International VLBI Service for
Geodesy and Astrometry

VGOS: The New VLBI Network

Proceedings of the 8th IVS General Meeting

Edited by
Dirk Behrend, Karen D. Baver, and Kyla L. Armstrong
NVI, Inc., Greenbelt, Maryland, USA

August 2014

Science Press, Beijing, China

Preface

This volume is the proceedings of the eighth General Meeting (GM2014) of the International VLBI Service for Geodesy and Astrometry (IVS), held in Shanghai, China, March 2–7, 2014.

Fig. 1 Logo of the eighth IVS General Meeting.

The keynote of the eighth General Meeting was the establishment of the VGOS (VLBI Global Observing System) network under the theme "VGOS: The New VLBI Network". The VGOS network continues to grow with many VGOS projects at various stages of accomplishment. By the end of 2014 as many as eight antennas are expected to have achieved broadband capability. The steadily growing VGOS network will gradually enter into full operations and provide daily products.

The eighth General Meeting was held at the Jianguo Hotel in Shanghai, China and was hosted by the Shanghai Astronomical Observatory (SHAO) of the Chinese Academy of Sciences. The goal of the meeting was to provide an interesting and informative program for a wide cross-section of IVS members, including station operators, program managers, and analysts.

This volume contains the following:

- **The papers presented at the meeting.** There are six major sections of this volume, each corresponding to a meeting session. Poster and oral papers are mixed. The six sessions cover the following topics:

  1. Evolution of the VGOS Network
  2. Technology Development for VGOS
  3. Stations, Correlators, and Operations Centers
  4. Progress in Data Structure, Software Development, and Analysis Strategies
  5. VLBI Results and Their Geodetic/Astrometric Interpretation
  6. New Horizons for VLBI

  This volume includes 106 papers. The program booklet with abstracts is available online at

  http://ivs2014.csp.escience.cn/dct/attach/Y2xiOmNsYjpwZGY6NjY2MzU=

  while the PDF versions of all oral presentations and many poster presentations are compiled at

  http://ivs2014.csp.escience.cn/dct/page/70045

  All papers of this volume were edited by the editors for usage of the English language, form, and minor content-related issues. Poster papers about IVS component status are not included in this volume; they have been published in the IVS 2013 Annual Report, available on the Web.
- **A list of registered participants.**
- **An author index.**

IVS 2014 General Meeting Proceedings

Fig. 2 Participants of the eighth IVS General Meeting at the VLBI Data Processing Center in Sheshan.

The contents of this volume also appear on the IVS Web site at

`http://ivscc.gsfc.nasa.gov /publications/gm2014`

142 registered participants attended the meeting, making this General Meeting one of the largest in IVS history. Over the span of four days, the participants made 134 presentations; 82 of these were talks, and 52 were poster presentations. The oral presentations consisted of seven invited talks and 75 contributed talks.

The April 2014 issue of the IVS Newsletter has a feature article about the meeting. The Newsletter is available at

`http://ivscc.gsfc.nasa.gov /newsletter/issue38.pdf`

Photographs taken at the icebreaker, during the conference sessions, during the visit to Sheshan Observatory, and at the conference dinner can be found online at

`http://ivscc.gsfc.nasa.gov /meetings/gm2014/`

We can only congratulate the meeting organizers on their excellent work. The event in Shanghai was very productive and trend-setting as well as very enjoyable and memorable at the same time. In short, GM2014 was exceptionally successful.

Fig. 3 The Director of SHAO, Prof. Xiaoyu Hong, welcoming the meeting participants.

Fig. 4 Meeting participants during an oral session.

Fig. 5 Huangpu River cruise boat, venue of the meeting banquet.

Fig. 6 Traditional Chinese music during the banquet.

Fig. 7 Bian Lian performance at the banquet.

Fig. 8 The new Tianma 65-m antenna at Sheshan.

Fig. 9 More oral presentations are given.

Fig. 10 IVS Chair, Prof. Axel Nothnagel, closing the meeting.

The editors would like to thank the contributing authors to this volume for the timely submission of their papers. Only this made it possible that these proceedings could be produced with such a short turnaround time. Thanks also to the publishing house of Science Press for printing this volume.

Dirk Behrend, Karen Baver, and *Kyla Armstrong*
GM2014 Proceedings editors
Greenbelt, MD · August 2014

Table of Contents

Session 3. Stations, Correlators, and Operations Centers 143

Session 1

Evolution of the VGOS Network

The Impact of NASA's SGP and USNO on VGOS

Chopo Ma[1], Stephen Merkowitz[1], Brian Luzum[2]

Abstract NASA's SGP (Space Geodesy Project) has completed a prototype core station at the Goddard Geophysical and Astronomical Observatory (GGAO) near Goddard Space Flight Center. It includes state-of-the-art VLBI, SLR, and GNSS systems as well as DORIS and a vector tie system between instruments. Broadband data have been acquired using GGAO and Westford. NASA intends to use the instruments it has developed to improve and expand the global space geodetic network. USNO has relied on VLBI for daily measurements of UT1 and is upgrading the Kokee Park station to VGOS specifications. We describe the NASA and USNO plans for implementing the next generation network.

Keywords VGOS, VLBI, DORIS, GNSS, SLR, vector ties

1 Supporting Future Requirements: NASA's Space Geodesy Project (SGP)

For years, it has been recognized that areas of science that use geodetic products, such as the International Terrestrial Reference Frame (ITRF), have a need for these products to have increased quality. For example, sea level studies will require an accuracy of 1 mm and a stability at 0.1 mm/year. This is a factor of 10–20 beyond the capability of the geodetic techniques that were standard at the beginning of the 21st century. It is estimated that ∼30 modern, integrated stations would be necessary to meet the new requirements.

In publications such as "Earth Science and Applications from Space" and "Precise Geodetic Infrastructure: National Requirements for a Shared Resource", the National Research Council has made several recommendations for accomplishing the required increases in accuracy and stability. Key recommendations are:

- upgrading U. S. stations with modern SLR and VLBI equipment,
- working with international partners to deploy additional stations,
- establishing and maintaining a high precision real-time GNSS/GPS national network,
- making a long-term commitment to maintaining the ITRF, and
- continuing to support the activities of the GGOS.

NASA's response is to contribute to building a new global network of integrated geodetic stations through the Global Geodetic Observing System (GGOS) and the international services. NASA proposes to provide six to ten of these stations.

A new NASA initiative SGP started at the end of 2011 in response to the Earth Science Decadal and the National Research Council study "Precise Geodetic Infrastructure". This initiative is part of the President's Climate Initiative. GSFC has led a partnership between it and JPL. The Smithsonian Astrophysical Observatory and the University of Maryland have also participated. The initiative has two goals. The initial goal is to establish and operate a prototype next generation space geodetic station with integrated next generation SLR, VLBI, GNSS, and DORIS systems, along

1. NASA GSFC
2. USNO

with a system that provides for accurate vector ties between them (see, for example, Figure 1e). The subsequent goal is to plan and implement the construction, deployment, and operation of a NASA network of similar next generation stations that will become the core of a larger global network of modern space geodetic stations. (Ideally, this should be done in time to support the coming Decadal Survey missions.)

Fig. 1 Components of an integrated station: a) a VLBI antenna, b) Next-generation SLR station, c) GNSS station, d) a DORIS beacon, and e) vector tie equipment to connect them.

2 Contributions of a Geodetic Measurement System

Each of the four techniques of an integrated station will provide different contributions to the ITRF, as well as to other things such as determination of Earth orientation parameters. VLBI and SLR stations have a low density global distribution, while GNSS has a high-density distribution, and DORIS has a well-spaced geographic distribution. The four components interact to fully define the ITRF, with each technique providing different contributions. VLBI determines the scale of the ITRF and its orientation with respect to the ICRF. SLR determines the origin of the ITRF (the Earth's CM), the ITRF scale, and the positions (orbits) of spacecraft within the ITRF. GNSS provides precise monitoring of the Earth's polar motion and rotation rate, the positions (orbits) of space craft in the ITRF, and the position of instruments on land and sea (e.g., tide gauges and buoys and geodetic instruments). DORIS provides the positions (orbits) of spacecraft within the ITRF, and it enhances the global distribution of ITRF station positions and velocities.

The vector tie system measures the co-location of the four techniques' instruments and connects the techniques. The full definition of the ITRF provided by the four components plus the improvement of the ITRF performance provided by the vector tie system combine to well-define the origin, the scale and the orientation of the ITRF.

3 Implementation of a Prototype Integrated Station at GGAO

NASA has implemented an integrated prototype station at its GGAO facility located in Greenbelt, Maryland. Substantial progress has been made towards implementing all five components of an integrated station (VLBI, SLR, GNSS, DORIS, and the equipment to tie them together).

Figure 2 shows the first component of the GGAO integrated station—its 12-meter VGOS VLBI antenna. The rest of Figure 2 shows the key front end components and back end rack.

Figure 3a shows the second component of the GGAO integrated station—its Next Generation SLR station with key personnel that have contributed to its development. The station has successfully completed a two-year development effort in which it demonstrated four key performance requirements. These were tracking the LAGEOS satellites with $\sim$mm-level precision, robust day time and night time satellite ranging from the LEO to GNSS altitudes (up to 22,000 km), maintaining system stability of under 1 mm (RMS) for over an hour, and operating semi-automatically. As one test, NGSLR and MOBLAS-7 simultaneously tracked the LAGEOS satellites, and NGSLR achieved excellent agreement with MOBLAS-7 with millimeter-level precision. Figure 3b shows NGSLR in the process of the simultaneous tracking.

Two new GNSS stations, GODN and GODS ("Goddard North and South"), form the third compo-

Fig. 2 Components of the VGOS VLBI system at GGAO: (top left) 12-m antenna, (top right) the cryogenic front end components, (middle left) a view of the quad ridge feed horn, (bottom left) low noise amplifier, and (bottom right) the fully assembled rack of the back end components.

Fig. 3 a) NGSLR station and key personnel in its development and support. b) NGSLR (left) and MOBLAS7 (right) perform simultaneous ranging on a LAGEOS satellite.

nent of the GGAO integrated station. They have been collecting data since 2012-01-17. Figure 4a shows the old GODE station, and Figure 4b shows the GODS station on a deep drilled braced monument. The stations are multi-constellation (i.e., they are compatible with GPS, GLONASS, and Galileo). The accuracy of GODN and GODS was tested by comparing the GODN—GODS baseline length calculated from GPS measurements taken by GODN and GODS to the baseline length measured by a local tie survey.

The fourth GGAO station component, a DORIS beacon shown in the foreground of Figure 5a, has been located at GGAO since June 2000. The GGAO

Fig. 4 GNSS stations: a) GODE and b) deep drilled braced monument GODS.

beacon is part of a global network of ∼57 stations, shown in Figure 5b. The beacons emit at 2 GHz and 400 MHz. The observable is dual-frequency one-way Doppler. DORIS receivers are located on altimeter satellites (e.g., TOPEX/Poseidon, Jason-1 and Jason-2, ENVISAT, Cryosat-2, and SARAL) and on remote sensing satellites (e.g., SPOT-2, SPOT-3, SPOT-4, and SPOT-5). DORIS receivers will be installed on future satellites, including Jason-3, SENTINEL-3, Jason-CS, and SWOT.

Fig. 5 a) The GGAO DORIS beacon (foreground). b) The global DORIS network.

The final component of the integrated station is its Vector Tie System (VTS). The VTS is a combination of a precise local-tie survey and a periodic monitoring system for measuring site stability. The system has demonstrated sub-millimeter accuracy at GGAO. The ability of the monitoring system to operate semi-autonomously has been demonsrated. It was able to find and identify a target prism, verify the prism correction, and process distance measurements to correct for atmospheric conditions. Figure 6a shows the robotic total station. Figure 6b schematically represents the local ties between the geodetic techniques at GGAO.

Fig. 6 a) The GGAO robotic total station. b) Diagram of the local reference frame tie to all geodetic stations at GGAO.

4 SGP Site Selection Strategy

The Global Geodetic Observing System (GGOS) has issued a call for participation in the Global Geodetic Core Network. This network is intended to be a foundation for measuring the Earth System, and it is intended to be a contribution to the Global Earth Observation System of Systems (GEOSS). To complement this call, the SGP has developed a strategy for developing a network of integrated stations. Based on simulations of a 32 site network, the SGP has developed a conceptual global site distribution as a starting point for identifying coverage by regions. The identification of actual sites to fill in this grid has three levels of focus. Consideration will be given to existing and projected sites of international groups, if the sites meet the required technological standards. Existing NASA and NASA partnership sites will also be examined as potential participants. An effort will be made to seek candidate sites with a reasonable chance of success in under-populated regions. The process for examining each candidate site will be to:

- examine the value that the site's geodetic position will add to the network,
- examine site conditions such as ground stability and typical cloud cover,
- examine human-imposed conditions such as RF/optical interference and air traffic,
- examine political and programmatic conditions, such as land ownership and control, the potential for an agreement and partnership arrangements, and
- examine site accessibility, logistics, infrastructure, security, power, and communications.

After examination, each site will be qualified as a good or a bad candidate. Three areas—French Polynesia, South America, and Africa—are under consideration by SGP using these criteria to fill existing gaps in the global distribution.

The island of Tahiti in French Polynesia has been evaluated. Some infrastructure for an integrated station already exists there at Punaaula. An SLR station, NASA's MOBLAS-8, has operated there since 1997, and the existing site has a co-located GNSS station and DORIS beacon. There is an existing agreement with CNES and the University of French Polynesia (UFP), and discussions are underway for a partnership. But the current site is not tenable, so a new site must be identified. Vairao has been identified as a potential location. Figure 7a shows the locations of Punaaula (larger section of the island) and Vairao (smaller section). Figure 7b and 7c show the actual locations at Punaaula and Vairao, respectively.

Fig. 7 a) Two station locations on Tahiti. Local conditions on Tahiti at b) Punaaula and c) Vairao.

Several South American sites are possible, as shown in Figure 8a. Discussions are underway with Colombia's Instituto Geográfico Agustín Codazzi (IGAC), and possible sites have been identified, including Barrancas and Marandua. Discussions are also underway with Brazil's National Institute for Space Research (INPE) concerning sites in Brazil, such as one near Brasilia. Several meetings have been held, and NASA is working with them on organization and presentation material. BKG's Transportable Integrated Geodetic Observatory (TIGO) (Figure 9b) is in the process of concluding operations at Concepcíon Chile and moving to a new site at La Plata, Argentina. There are existing SLR stations at Arequipa and San Juan but no SGP plans for augmentation at this time.

Two sites in Africa (Figure 8b) at Malindi, Kenya and Toro, Nigeria are under discussion. NASA and the Italian Space Agency (ASI) have begun discussions about forming a partnership to operate a site at Malindi (Figure 10a). NASA has no current agreement with ASI, but it has a long history of cooperation, and an agreement process is underway. Malindi is an established site with a large reservation funded by Italy,

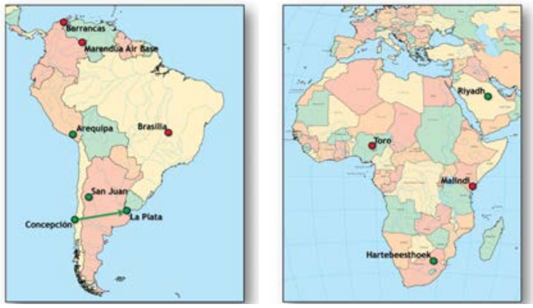

Fig. 8 Candidate integrated sites in a) South America and b) Africa.

Fig. 9 SLR stations in Argentina: a) San Juan and b) TIGO (moving to La Plata).

with a large staff and an existing ESA GNSS receiver. Discussions are also underway between NASA and Nigeria's National Space Research and Development Agency (NSRDA) about a partnership site at Toro (Figure 10b). This is also an established site which has a GPS station and a significant number of staff performing space geodesy. The Toro site was offered under the GGOS Call for Proposal.

Fig. 10 Candidate African sites at a) Malindi, Kenya and b) Toro, Nigeria.

5 Upgrade to an Existing Site (KPGO, Hawaii)

USNO (U. S. Naval Observatory) has relied on VLBI for daily measurements of UT1, so it is funding a new VGOS system at the Kokee Park Geophysical Observatory (KPGO) at Kokee Park, Hawaii, USA. KPGO is a well-established VLBI site with a long history of data. But a drawback for SLR is that it typically has very cloudy skies. A second Hawaiian site, Haleakala, is located ~380 km from KPGO. This site typically has clear skies and has a long history of SLR operations, but it will be very difficult to build a VGOS station nearby. The strategy is to use multitple GPS baselines to determine the co-location vector. Figure 11 shows the locations and local conditions at KPGO and Haleakala.

Fig. 11 Positions of KPGO and Haleakala, Hawaii with inset pictures of a) KPGO and b) Haleakala.

NASA and USNO are forming a partnership to build the new KPGO VGOS station. The SGP has completed an environmental categorical exclusion for two potential locations. USNO has awarded a contract to InterTronic Solutions to build a 12-m class antenna. The PDR was held on January 28 and 29. USNO has asked NASA to provide project oversight, site preparation, and signal chain development. Pad design will be done by a GSFC contractor. Pad construction will be done by NAVFAC or by a GSFC contractor. Signal chain fabrication, installation, integration, and testing will be done by MIT/Haystack Observatory. The new station will become an operational VGOS station as part of the new NASA Space Geodesy Network in 2016.

Acknowledgment. The invaluable assistance of NVI, Inc. personnel in preparing this paper is gratefully acknowledged.

UN Resolution About the Importance of Geodesy

A Global Geodetic Reference Frame for Sustainable Development (GGRF)

Line Langkaas, Anne Jørgensen

Abstract In order to reach the goal of GGOS there is a need for 20 to 30 core stations evenly distributed around the world. It is a challenge to manage a renewal of the existing infrastructure, and it is a huge effort to manage the establishment of new sites in "lacing areas," especially those who coincide with areas in developing countries. In Norway, we have been working hard for five years to obtain funds for our core station project in Ny-Ålesund. Our experience from this work is that the importance of geodesy, as critical infrastructure for society, is not well known by decision-makers, politicians, or people in the general public. Geodesy is in principle dependent on contributions from nations all around the globe. We have to move geodetic Earth observation from a "best-effort principle" to a multilateral collaboration under a UN mandate. The UN-GGIM (United Nations Committee of Experts on Global Geospatial Information Management, http://ggim.un.org) Working Group on a Global Geodetic Reference Frame for Sustainable Development has been established and is working on this issue. We outline the importance and status of this activity, and what is necessary to be successful. The goal is to get a resolution adopted by the UN General Assembly in May/June 2014.

Keywords UN, resolution, GGRF, Global Geodetic Reference Frame

Norwegian Mapping Authorithy

1 Introduction

Through the process to raise funds for our new core station in Ny-Ålesund, Norway we experienced that 'what geodesy is and why there is a need for a global reference frame' is not at all well known by politicians or the general populace. We really had to work hard to make the decision-makers understand the importance of geodesy and a sustainable global geodetic reference frame for our society today and in the future. We think this is the situation in other countries as well. It is our belief that, if there had been a common understanding and a commitment in the world that stated the importance of this, for example a UN resolution, the efforts regarding our project in Ny-Ålesund would have been less.

2 Manage to Take Decisions in Due Time

To make a sustainable global reference frame for the future, core sites, evenly distributed around the world, are necessary. This is not the situation today. Especially there is a huge lack of stations in the southern hemisphere. Today it is not possible to measure small changes, such as sea level variations, precisely enough in order to know what is going on. The global geodetic reference frame is not good enough. We have to be able to measure what is going on and establish time series; then we can make more reliable predictions for the future, allowing politicians and decision-makers to take action in due time. A huge amount of people live in equatorial areas, just above sea level. Our geodesists reckon that the sea level rise will be highest in these areas. When do these people have to be moved? A global geodetic reference frame allows us to relate measurements taken anywhere on the Earth to similar measurements taken at a different time or location. It provides the opportunity to monitor changes and is the basis for natural hazard and disaster management. It is essential for geospatial information and navigation used in many Earth sciences and societal applications as well as in a whole series of industries. The global geodetic reference frame is in growing demand, being important for environmental studies and the global economy.

3 Move from a Technical to a Diplomatic Community under a UN Umbrella

How geodesy contributes to strengthen the study of our planet and why a sustainable global geodetic reference frame is so important for our society has to get on the decision-makers agenda all over the world. The effort done by the geodetic communities, based on best effort principles, has been great, taking us to where we are today. But to manage to establish a sustainable global geodetic reference frame with a one-millimeter precision, something more has to be done. Professor Paul Cheung stated at the UN: “The game must be moved from the technical community to the diplomatic community.” To do this through the system of UN gives us an opportunity to get results on this. Make the decision-makers understand and adopt that a sustainable global geodetic reference frame for the future is necessary.

4 Actions Taken

On the basis of initiatives from the UN-GGIM Asian Pacific Group, GGOS, and several countries, a UN group of experts that handles geospatial questions took actions: United Nations Committee of Experts on Global Geospatial Information Management (UN-GGIM). This group was established by the UN Economic and Social Council (ECOSOC) in 2012. The UN-GGIM second high-level forum in Doha in February 2013 made a declaration in which they commit themselves to work together as an international community, under the coordination of the UN, to work with stakeholders to improve a sustained operational global geodetic reference frame and infrastructure as well as to support the increasing demand for positioning and monitoring applications with associated societal and economic benefits. The UN-GGIM decided in Cambridge in July 2013 to formulate and facilitate a draft resolution for a global geodetic reference frame (GGRF). They stated: “UN-GGIM recognizes the growing demand for more precise positioning services, the economic importance or a global geodetic reference frame and the need to improve the global cooperation within geodesy.” The resolution will be tabled at the 2013–14 Session of the UN General Assembly. In January 2014, a working group was established consisting of 20 countries and the International Association of Geodesy (IAG). Australia and Norway are co-chairing with Norway having the communication management. The work in this group is done the UN way: ‘keep the process open and inclusive.’

5 Main Goals

The two main goals are:

1. The UN General Assembly (UN-GA) adopts a resolution for a global geodetic reference frame for a sustainable development.
2. Develop a roadmap for enhancement of a global geodetic reference frame and multilateral cooperation on geodesy under a UN umbrella.

6 Time Frame

The time line of activities is staked out as follows:

- **February/March 2014:** Prepare draft concept note and draft resolution text, prepare communication material.
- **March/June 2014:** Transfer of understanding from us to the UN-missions, countries are encouraged to arrange meetings of their foreign affairs people with UN-delegates and UN-missions. Meetings and informal consultations will be held in New York for all the UN-missions in May/June, geodetic experts will give the information.
- **June 2014:** Hopefully the UN General Assembly adopts the GGRF resolution.

- **August 2014:** Present a draft roadmap at the UN-GGIM fourth meeting.
- **October 2014:** Present status of the roadmap work at UN-GGIM high-level meeting.

7 Communication Challenge

Geodesy and what-a-global-geodetic-reference-frame-is are not well understood by decision-makers, in particular at the political level. Politicians and UN delegates are not even familiar with the word 'geodesy.' The time you have for giving explanations is usually short. Typically there is no time to explain UT1, nutation, and so on. They want to know what is in it for them and for society. That is what we have to answer, using good examples that make them understand their benefits and why they should put priority on this. Ambassadors that can help to transfer this understanding to the politicians and decision-makers are more than welcome.

8 Collaboration

Global geodesy is dependent on contributions from nations all around the globe. We aim to change from the current system, where contributions to the development of a global geodetic reference frame are undertaken on a best effort basis, to one, where they are made through a multilateral collaboration under a UN umbrella.

The Most Remote Point Method for the Site Selection of the Future VGOS Network

Hayo Hase[1], Felipe Pedreros[2]

Abstract The VLBI Global Observing System (VGOS) will be part of the Global Geodetic Observing System (GGOS) and will consist of globally well distributed geodetic observatories. The most remote point (MRP) method is used to identify gaps in the network geometry. In each iteration step the identified most remote points are assumed to become new observatory sites improving the homogeneity of the global network. New locations for VGOS observatories have been found in La Plata, Tahiti, O'Higgins, Galapagos, Colombo, and Syowa.‡

Keywords VGOS, MRP method, Voronoi, network densification

1 Introduction

The International Association of Geodesy (IAG) has launched the GGOS aiming for the unification of traditionally separated geometric and geophysical reference systems and for the realization of a 3D-position error of 1 mm on the global scale and a reference point velocity error of no more than 0.1 mm/yr. To reach these goals, the operation of 30–40 globally well-distributed geodetic observatories is needed (Beutler and Rummel, 2012).

The International VLBI Service for Geodesy and Astrometry (IVS) will meet the GGOS requirements with its VGOS initiative (Hase et al., 2012) requiring a new type of very fast radio telescopes with broadband capabilities as described in Petrachenko et al. (2012). In this study only this upcoming VGOS network is considered as it will outperform the currently used IVS network infrastructure. We assume that all VGOS stations deliver identical data quality.

We introduce the most remote point (MRP) method, a tool to find the best new geometrical locations with respect to existing reference observing stations. It will provide the optimal network configuration for further simulations.

2 Evaluation and Improvement of Global Geodetic Networks

2.1 The Most Remote Point (MRP) Method

Given a point distribution on a limited surface area and a requirement to add points in order to make the distribution more homogeneous, Hase (2000) suggested an iterative approach where new points are always added at the most remote location with respect to the others.

Figure 1 shows the properties of the Delaunay triangulation and its counterpart, the Voronoi diagram. The most remote point coincides with the Voronoi vertex, even if a three dimensional spherical surface replaces the two dimensional plane surface (Hase, 1999).

For an ideal homogeneous point distribution, the area of each Voronoi facet will be equivalent to the mean spherical surface area of n reference points. This goal can be reached either by filling up the largest gaps

1. Bundesamt für Kartographie und Geodäsie
2. Universidad de Concepción

‡ This contribution is an excerpt of a work published in Journal of Geodesy (DOI: 10.1007/s00190-014-0731-y) covering the site selection for the GGOS.

in the network by adding new points or by removing points which have the shortest distance to each other.

For the purpose of modeling the point distribution of a global geodetic network, a spherical Earth model is sufficient. We apply the MRP method in a non-rigorous way. This means that the most remote point suggests a vicinity in which the definite location has to be chosen according to other selection criteria. A rigorous application of the MRP method is not practical. For instance, if the most remote point is calculated to be in the ocean, a nearby island or continental point has to be chosen instead.

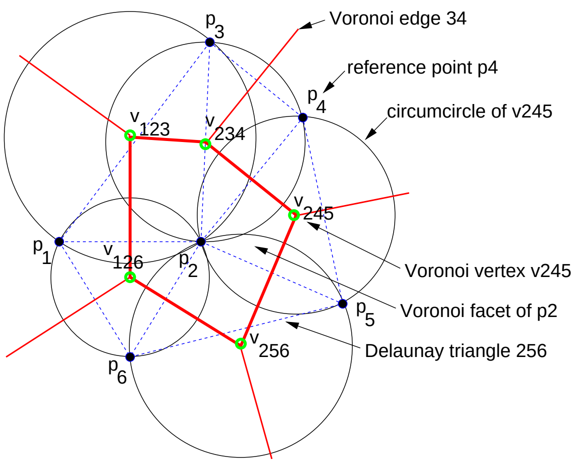

Fig. 1 Part of a network with reference points P_1, P_2, P_3, P_4, P_5, and P_6 as a given distribution showing the Voronoi facet of P_2. Within this facet no other reference point P_i is closer than P_2 itself. Therefore the Voronoi facet is the representative area of P_2. In this illustration the most remote point v_{123} is indicated by the largest circumcircle. If it will become a new reference point, i.e., P_7, the areas of the adjacent Voronoi facets of P_1, P_2, and P_3 will be decreased by a part which will surround P_7 (only the facet of P_2 is shown completely).

In this manner, the MRP method can be applied by the following sequence:

1. Compute the most remote point of the point distribution of a global network.
2. Define the new site to be added to the network close to the most remote point of the computation.
3. Continue iterating by computing and adding new most remote points to the network until a certain condition (i.e., total number of stations) is satisfied.

2.2 Network Quality Parameter

One criterion to measure the homogeneity of a point distribution can be derived from the Voronoi facet, which was introduced in Section 2.1. Thus, the standard deviation σ_i of a distribution of n Voronoi facet areas A_j in each iteration i will be a suitable parameter to measure the homogeneity of a global network. We introduce a quality parameter Q_i of the point distribution as:

$$Q_i := \frac{1}{\sigma_i} \tag{1}$$

The quality parameter increases in each iteration step as the homogeneity improves.

2.3 Improvement Parameter

The MRP method is iterative. The improvement in each iteration step can be quantified either a) by the achieved reduction of the largest radius of the circumcircle of the Delaunay triangles or b) by the achieved increase of the quality parameter (Equation 1). They can be expressed as percentages.

Based on the radius r of the circumcircle, the relative improvement parameter I^r_{rel} and, based on the radius r_0 of the initial network configuration, the absolute improvement parameter I^r_{abs} are expressed as:

$$I^r_{rel} := 1 - \frac{r_{i+1}}{r_i} \quad , \quad I^r_{abs} := 1 - \frac{r_i}{r_0} \tag{2}$$

In this study, the radius r of the circumcircle of the MRP corresponds to an arc of the great circle (and not to the baseline). The improvement of well placed new stations shortens the distance between neighboring stations.

The relative improvement parameter I^Q_{rel} is based on the area A of the Voronoi facets. In analogy to the previous formulae, an absolute improvement parameter I^Q_{abs} of the i-th iteration refers to the quality of the homogeneity of the initial configuration and can be expressed as:

$$I^Q_{rel} := \frac{Q_{i+1}}{Q_i} - 1 \quad , \quad I^Q_{abs} := \frac{Q_i}{Q_0} - 1 \tag{3}$$

The improvement parameter (Equation 3) is based on the spherical surface area of the Voronoi facet and indicates how efficiently a site selection contributes to a more homogeneous point distribution.

3 Applying the MRP Method to the VGOS Network

New VGOS radio telescope projects are in execution at the following sites: Wettzell, DE; Yebes, ES; Flores Island, PT; Santa Maria Island, PT; Tenerife Island, ES; Ny-Ålesund, NO; Onsala, SE; Metsahovi, FI; Kaliningrad, RU; Kazan, RU; Zelenchukskaya, RU; Badary, RU; Ussuriysk, RU; Ishioka, JP; Sheshan, CN; Changchun, CN; Nanshan, CN; Hartebeesthoek, ZA; Yarragadee, AU; Hobart, AU; Katherine, AU; Warkworth, NZ; Kokee Park, US; Greenbelt, US; and Haystack, US. This incomplete future network will form the VGOS which is an appropriate example to demonstrate the MRP method for network densification.

Following Subsection 2.1 we use this VGOS network for the initial computation of the Voronoi grid and hence the most remote points (iteration 0).

Figure 2 shows the network configuration and the results in an equal-area Hammer-Aitoff projection. The three most remote points are found in South America and the South-East Pacific area. The first choice to improve this network is to add a new VGOS site to the VGOS network in South America.

Recent contributions to the IVS from South America come from the German Transportable Integrated Geodetic Observatory (TIGO) and from Fortaleza in Brazil. In general it is easier to update an existing VLBI site rather than to set up a new one. Due to lacking financial support, TIGO will be moved from Concepción in Chile to La Plata in Argentina; both sites are closer to the computed remote point than Fortaleza. Therefore, a modernization project in La Plata to make the site VGOS compatible is meaningful. For this analysis, La Plata (LP) was chosen for the first iteration step (iteration 1). Figure 3 shows the consequence: a very significant improvement of 29.3% in the distance between the MRP and stations and of 11.2% of reduced inhomogeneity in the Voronoi facets.

Based on Figure 3, we chose Tahiti (Th) as the new site in the second iteration (Figure 4). This follows the

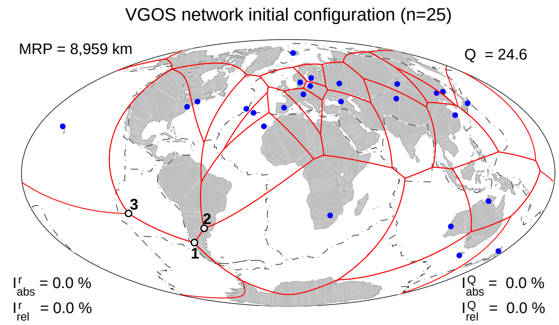

Fig. 2 The initial network configuration of the future VGOS network. New VGOS radio telescopes are marked with filled circles. The map shows the plate tectonic border lines (dotted lines) and the Voronoi edges (solid red lines) in an equal area projection. The Voronoi facets demonstrate the representative area of each individual station due to the given network configuration. The open black circles labeled with 1, 2, and 3 indicate the three most remote points with respect to the given network configuration or station distribution. The largest gaps in the network exist in the South America and South-East Pacific areas. The MRP is 8,959 km away from its nearest VGOS reference stations.

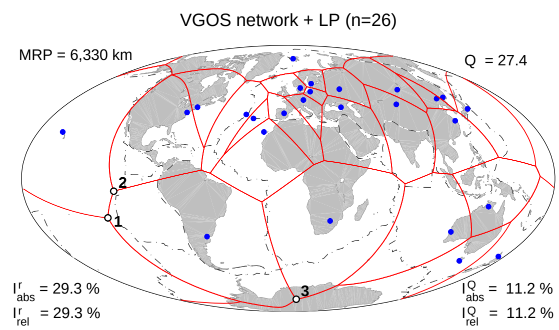

Fig. 3 The first iteration adds the site La Plata (LP) in Argentina to the initial network configuration of the future VGOS network. This improves the quality of the network by 11.2%. The largest gap in the network is shifted now to the South-East Pacific area.

idea of co-locating different geodetic space techniques at one site as we find already an SLR station on that island. A new VGOS radio telescope will improve the VLBI network further by 12.0% with respect to the previous iteration and create a very important fundamental reference point in the South Pacific.

The Antarctic region is very difficult for continuous VLBI operations. Only the German Antarctic Receiving Station O'Higgins and the Japanese base in Syowa are IVS network stations. The foundation of a radio telescope is restricted to areas with bedrock to obtain a long-term stable reference point. Access to the station is easier in the coastal regions. Both places are suitable

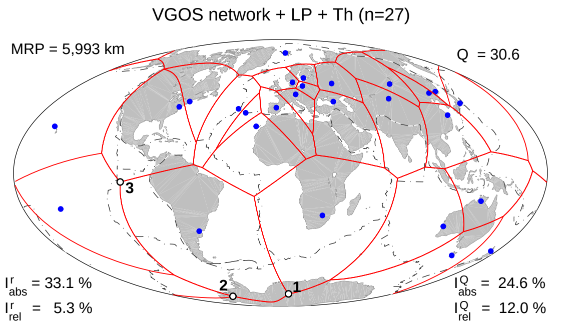

Fig. 4 The second iteration adds the site Tahiti (Th) in French Polynesia to the previous network configuration of the future VGOS network. This improves the network by 12.0% relative to the previous step and 24.6% relative to the initial configuration. The largest gap in the network is shifted to the Antarctic continent.

candidates for VGOS instrumentation. We selected in this step as the third added station to the VGOS network O'Higgins (Oh) site (Figure 5, iteration 3).

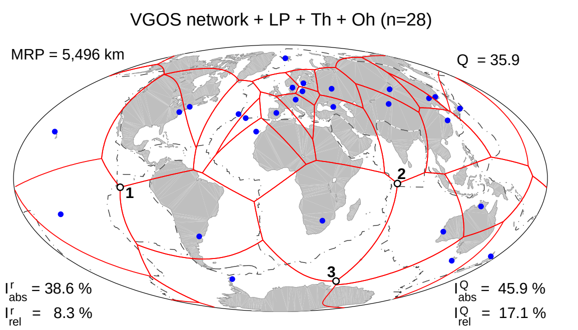

Fig. 5 The third iteration adds the site O'Higgins (Oh) in Antarctica to the previous network configuration of the future VGOS network. This improves the network by 17.1% relative to the previous step and 45.9% relative to the initial configuration. The largest gap in the network is shifted back to the East Pacific.

Due to the lack of continental surface the East Pacific does not offer many possibilities to set up a new observatory. In this fourth iteration, the Galapagos Islands (GI) have been chosen (Figure 6, iteration 4).

The Indian Ocean is populated with small and remote islands where it would be difficult to operate a VGOS station for logistical reasons. Therefore the town of Colombo (Co), Sri Lanka was chosen to become the fifth new site in the VGOS network (Figure 7, iteration 5).

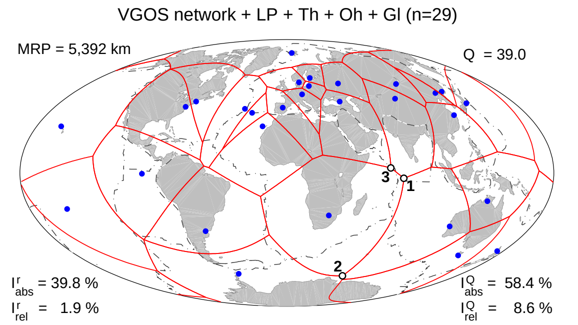

Fig. 6 The fourth iteration adds the site Galapagos Islands (GI) to the previous network configuration of the future VGOS network. This improves the network by 8.6% relative to the previous step and 58.4% relative to the initial configuration. The largest gap in the network is now shifted back to the Indian Ocean.

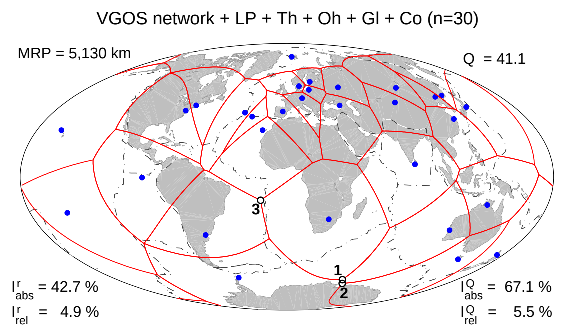

Fig. 7 The fifth iteration adds the site Colombo (Co) in Sri Lanka to the previous network configuration of the future VGOS network. This improves the network by 5.5% relative to the previous step and 67.1% relative to the initial configuration. The largest gap in the network is now shifted again to Antarctica.

Antarctica is a large and extended region. The sixth iteration adds Syowa base (Sy) as a new VGOS network station (Figure 8, iteration 6).

After six iterations, the improvements in the VGOS network have closed the largest gaps—all in the Southern hemisphere. The distance to the most remote point has almost halved (46.8%) and the network quality improved by nearly 86%. As one can easily see in the comparison of Figure 2 with Figure 8, the new Voronoi facets in the Southern hemisphere look much more equal in size compared to the Northern hemisphere. This confirms that the most remote point method is suitable for global network planning. It also underlines the argument that a network can be created in a much more efficient way with a global perspective.

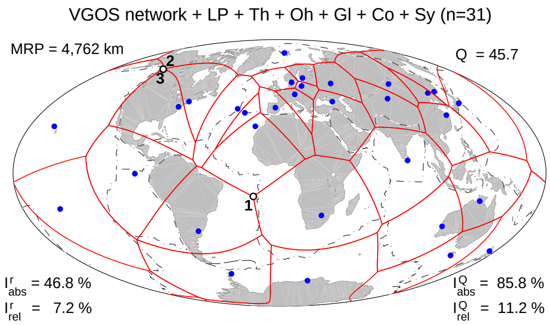

Fig. 8 The sixth iteration adds the site Syowa (Sy) in Antarctica to the previous network configuration of the future VGOS-network. This improves the network by 11.2% relative to the previous step and 85.8% relative to the initial configuration. With this iteration step the largest gaps in the network fall now into the Southern Atlantic and first time to the upper northern latitudes near Alaska.

Table 1 summarizes the convergence of radius of the MRP, of the improvement parameters (Equations 2 and 3) and of the quality parameter (Equation 1), indicating a much more homogeneous site distribution after adding six new sites with the MRP method.

Table 1 VGOS network: Improvement and quality parameters with six iterations. With only six additional VGOS stations the radius of the MRP shrinks from 8,959 km to 4,762 km, and a much more homogeneous global site distribution can be reached.

iter.	r_i of MRP	n	I^r_{rel} %	I^r_{abs} %	I^Q_{rel} %	I^Q_{abs} %	Q
0	8,959 km	25	0.0	0.0	0.0	0.0	24.6
1	6,330 km	26	29.3	29.3	11.2	11.2	27.4
2	5,993 km	27	5.3	33.1	12.0	24.6	30.6
3	5,496 km	28	8.3	38.6	17.1	45.9	35.9
4	5,392 km	29	1.9	39.8	8.6	58.4	39.0
5	5,130 km	30	4.9	42.7	5.5	67.1	41.1
6	4,762 km	31	7.2	46.8	11.2	85.8	45.7

The achievements by applying the MRP method to the densification of the global network can be illustrated by Figure 9, showing the circumcircles of the Voronoi-points in a concentric way comparing the initial and the sixth iteration. The circles are color-coded and distinguish Voronoi points of the Northern hemisphere from those of the Southern hemisphere.

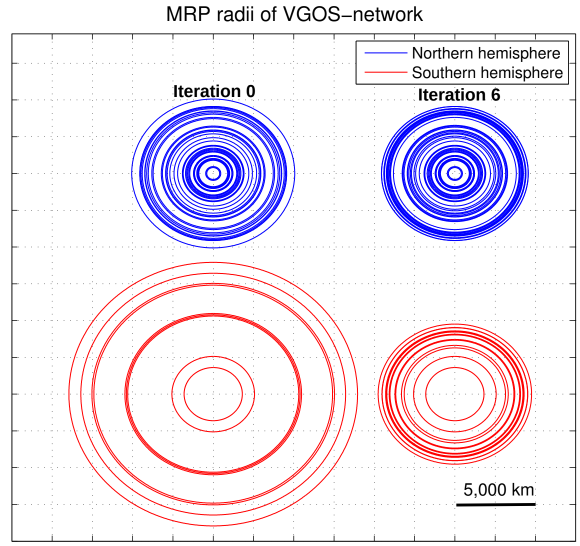

Fig. 9 Radii of the MRP of the initial VGOS network configuration (iteration 0) vs. those of the last iteration 6. This figure shows the MRP radii in the Northern hemisphere in blue above those in the Southern hemisphere in red. Initially the largest gaps were found in the Southern hemisphere indicated by large circumcircles. After the introduction of six new points with the MRP method, the situation has improved. The concentration of circles shows homogeneity as it can also be seen by comparing Figure 2 with Figure 8.

References

G. Beutler, R. Rummel. Scientific Rationale and Development of the Global Geodetic Observing System. Proceedings of the 2009 IAG Symposium, *Springer*, IAG Symp 136:987–993, 2012

H. Hase. Theorie und Praxis Globaler Bezugssysteme (in German). *Mitteilungen des BKG*, Band 13, 1999

H. Hase. New Method for the Selection of Additional Sites for the Homogenisation of an Inhomogeneous Cospherical Point Distribution. *Springer*, pp. 180–183, 2000 doi: 10.1007/978-3-642-59745-9_35

H. Hase, D. Behrend, C. Ma, B. Petrachenko, H. Schuh, A. Whitney. The Emerging VGOS Network of the IVS. NASA/CP-2012-217504, pp. 8–12, 2012

W.T. Petrachenko, A.E. Niell, B.E. Corey, D. Behrend, H. Schuh, J. Wresnik. VLBI2010: Next Generation VLBI System for Geodesy and Astrometry. *Springer*, IAG Symp 136:999–1006, ISBN 978-3-642-20337-4, 2012

VGOS Observing Plan

Bill Petrachenko[1], Dirk Behrend[2], John Gipson[2], Hayo Hase[3], Chopo Ma[4], Dan MacMillan[2], Arthur Niell[5], Axel Nothnagel[6], Xiuzhong Zhang[7]

Abstract Over the past several years, the VGOS broadband system has been under development; it is currently undergoing advanced testing. At the same time, commitments were made for a number of antenna projects with as many as 30 stations expected for VGOS observing by 2019. In order to focus activities into the future, a proposal was made by the VPEG for an observing plan with the long term goal of guiding the transition from S/X operations to VGOS operations. The plan anticipates that by the end of 2014 as many as eight antennas will be capable of broadband observing. These antennas will participate in a series of test campaigns during 2015 followed by a VGOS pilot project throughout 2016. Full operations with as many as 16 stations are expected to begin in 2017. The observing plan places a priority on early improvement in the quality of daily products. As a result, the pilot project involves a single weekly 24-hour session with reduced duty cycle sessions on each of the remaining days of the week. Correlator and data transmission requirements for the plan are currently being assessed.

Keywords VGOS, VLBI Global Observing System, Observing Plan, VPEG

1. Natural Resources Canada
2. NVI, Inc.
3. BKG Concepción
4. NASA GSFC
5. MIT Haystack Observatory
6. Institute of Geodesy and Geoinformation, Bonn University
7. Shanghai Astronomical Observatory

1 Introduction

In 2003, the IVS Directing Board recognized the need for a complete revision of geodetic VLBI infrastructure including antennas, systems, and processes [1, 2]. Bold goals for the new vision included 1-mm position accuracy, 24/7 operations, and the release of initial products within 24 hours of taking data. At the core of the new concept is a network of fast slewing antennas, a new broadband observing system, enhanced automation, and increased use of electronic networks to transmit data. When conceived, the new vision was called VLBI2010. Today the realization of the new network is being referred to as the VLBI Global Observing System (VGOS).

Over the past decade, technical development for the new system was coordinated by the VGOS Technical Committee (VTC, formerly the VLBI2010 Committee), and strategic leadership was provided by the VGOS Project Executive Group (VPEG, formerly the VLBI2010 Project Executive Group). About a year ago, it became apparent to the VPEG that system development and network expansion were sufficiently advanced that a roadmap was required to guide the transition from current style observations with the legacy S/X system to the operational realization of the new vision. To satisfy this need, the VPEG began to develop the VGOS Operations Plan.

The first priority of the plan is to deliver consistent daily products of high and uniform quality, especially Earth orientation parameters (EOP), as soon after observing as possible. A previous attempt to build up a 24/7 geodetic VLBI capability involved the addition of 24-hour sessions until all seven days of the week were filled. Each session would have used a different network as operational capacity increased. Unfortunately, the process ended with the scheduling of only two 24-hour sessions per week, R1 and R4, with the remaining days bridged by UT1 Intensive sessions typically involving a single baseline observing for only one hour per day. Scientifically, this mode of operation is suffering from inconsistent data quality through the week. Furthermore, staggered UT start times of the VLBI sessions has led to irregular reference epochs for the EOP results which hamper combination efforts with those of the other space geodetic techniques.

To avoid these problems, the VGOS operations plan takes a different philosophy for its ramp-up to full 24/7 operations. Since it is recognized that operational capacity for continuous observing will not be available at the outset, the initial years of the plan involve daily sessions using the complete available network but with a reduced duty cycle. In other words, instead of observing continuously 24 hours per day, sessions will consist of four equally spaced one-hour bursts at 3, 9, 15, and 21 UT. These four bursts will then be analyzed together to produce all EOP with as many as four UT1 values per day. Furthermore, the four bursts can be centered on the reference epoch of 12 UT, which is consistent with the reference epochs of the other space geodetic techniques. As operational capacity increases, stations can be scheduled to observe a larger number of one-hour bursts per day until each day is filled.

The first draft of the observing plan was completed in the summer of 2013. The plan was then circulated to the IVS Observing Program Committee (OPC) for comment, resulting in a significantly improved concept and a rewritten draft. It was realized that a full operations plan should also include estimates of correlator, data transmission, and analysis requirements and not just a schedule for the increase of observations. In the end it was decided, however, that the community needed to be informed as soon as possible of the planned roll out of observations and that the other requirements documents could be completed and released later. The title of the document was then changed from the VGOS Operations Plan to the VGOS Observing Plan [3]. It was accepted by the IVS Directing Board in February 2014.

2 Summary of the VGOS Observing Plan

The VGOS Observing Plan covers the five-year interval from 2015 through 2019, culminating in full 24/7 VGOS operations in 2020. It deals almost entirely with broadband observations, although it is recognized that an important part of the transition will also involve mixed-mode observing in which VGOS broadband antennas participate in S/X sessions. These are required to establish a strong tie between the new VGOS antennas and the legacy S/X network.

During the remainder of 2014, IVS technology development focuses on ensuring that VGOS systems and processes are ready for the first test campaigns to be carried out in 2015. The VGOS observing plan begins with a series of three test campaigns in 2015 with as many as eight sites expected to participate. Each of the three campaigns introduces a different aspect of the new VGOS mode of operation so that by 2016 the IVS will be ready to begin a VGOS Pilot Project. All campaigns will be roughly six weeks in duration to exercise the full "schedule-to-final-products" operational chain in a sustained format:

- The first campaign focuses on automation of processes unique to broadband operations and consists of a single 24-hour session. This has the benefit of allowing six days per week to prepare for the next session. Data will be recorded and shipped after each session (Figure 1).

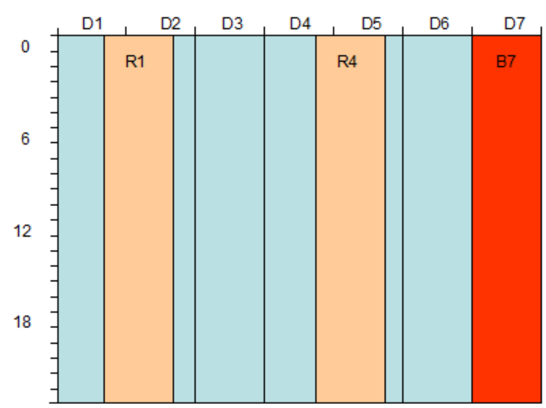

Fig. 1 Trial campaign 1: Sustained weekly 24-hour sessions, January–February 2015. The VGOS Day 7 broadband session (B7) is represented in red (dark gray).

- The second campaign focuses on producing a full set of EOP products on a daily basis. It involves observing four hours per day in equispaced one-hour bursts. As with the first campaign, data will be recorded and shipped once per week (Figure 2).
- The final campaign focuses on producing initial EOP products within 24 hours. Observationally it will be identical to the second campaign but the data will be e-transferred instead of being shipped (Figure 2).

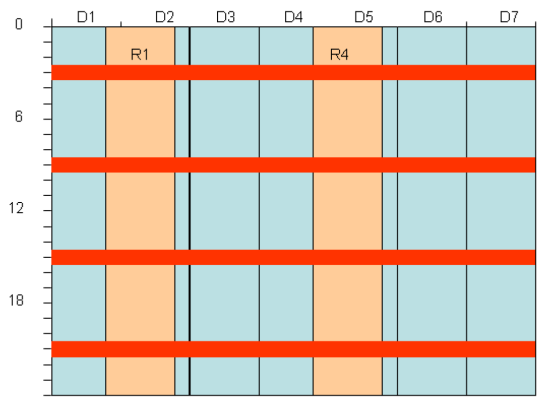

Fig. 2 Trial campaigns 2 and 3: Sustained daily VGOS EOP sessions, May–June 2015 and September–October 2015. The daily hour-long VGOS bursts are represented in red (dark gray).

The VGOS Pilot Project will be carried out throughout 2016. The project will imitate operations but without a full commitment to product delivery. As with the second and third trial campaigns of 2015, there will be four one-hour EOP sessions each day of the week along with a single 24-hour session per week (Figure 3). It is expected that perhaps one or two additional stations will come on-line during 2016.

By the end of the pilot project, VGOS will be ready to commit to product delivery. Daily EOP sessions and weekly 24-hour sessions will continue as in the pilot project, but the number of one-hour bursts in the daily sessions will increase as operational capacity increases. By the end of 2017, as many as 16 VGOS broadband stations are expected to be on-line, and by the end of 2019 the number of stations could be as large as 30. By 2020 it is expected that all or most stations will be observing nearly continuously, with sufficient time scheduled for maintenance.

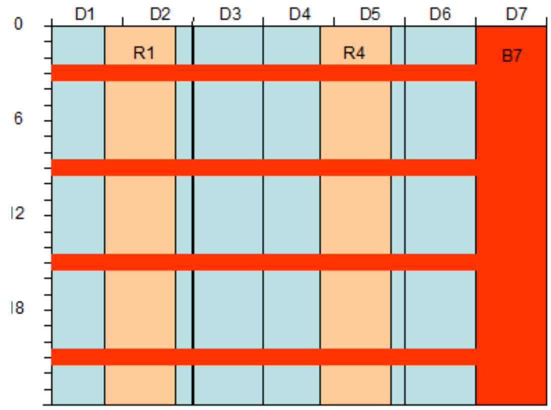

Fig. 3 VGOS Pilot Project: One 24-hour VGOS session and six daily VGOS EOP sessions per week during 2016. VGOS observing is represented in red (dark gray).

3 Simulated Performance

An attempt was made to predict performance for three scenarios from the VGOS Observing Plan (Table 1). The scenarios are: eight stations observing in four equally spaced one-hour bursts (2015–4h); 16 stations observing in eight equally spaced one-hour bursts (2017–8h), and 30 stations observing continuously for 24 hours (2019–24h). Performance was compared to that of the R1, R4, and CONT11 networks. To ensure a level basis for comparison, all performance estimates, including those for the R1, R4, and CONT11 networks, were derived using Monte Carlo simulations.

Table 1 Simulated performance for a number of observing scenarios.

	Observations [#/hr/stn]	UT1 [μs]	X-pole [μas]	Y-pole [μas]	Scale [ppb]
R1	10.8	3.0	71	58	0.47
R4	14.6	3.7	65	105	0.45
CONT11	15.8	2.0	34	27	0.35
2015–4h	87.5	2.0	83	96	0.41
2017–8h	52.3	1.4	38	43	0.26
2019–24h	58.2	0.4	9	9	0.08

The observing schedules for the R1, R4, and CONT11 simulations were taken from real sessions, while those for the VGOS predictions were generated using SKED assuming real antenna sensitivities and slew rates. In Table 1, it can be seen that, as expected, the number of observations/hour/station is significantly greater for the VGOS schedules than for the R1, R4, and CONT11 schedules. However, the VGOS schedules still fall significantly short of the VGOS target density of 120 observations/hour/station. For the 2015–4h schedule, this can be attributed to the inclusion of two slower legacy antennas in the network. However, the even greater shortfall for 2017–8h and 2019–24h is harder to understand. As a result, work continues towards improving scheduling algorithms for VGOS. Needless to say, performance for the VGOS simulations is expected to improve when observation densities are increased towards the 120-observations/hour/station target.

Generally speaking, the performance of the VGOS 2015–4h scenario is near that of the R1 and R4 scenarios, and VGOS 2017–8h is near that of CONT11, with UT1 and scale tending to be better in the VGOS simulations and X-pole and Y-pole being worse. Even considering the sub-optimal schedules used for the 2019–24h simulations, the predicted EOP and scale performance for this scenario is better than anything experienced to date.

4 Next Steps

- All relevant VGOS broadband processes, systems, and stations need to be completed in advance of the test campaigns scheduled for 2015.
- Requirements documents for correlation, data transmission, and analysis need to be completed to ensure that appropriate resources are available for all steps of the VGOS Observing Plan.
- Network expansion needs to remain a priority. Specifically, more Southern Hemisphere stations are required to support ICRF definition, and, in general, a more uniform global distribution of stations is required to support ITRF definition.

5 Conclusions

The VGOS Observing Plan provides a reasonable guideline for the IVS and for all observatories that are gearing up for the next generation of geodetic and astrometric VLBI observations. For the new radio telescopes yet to be installed, the operational requirements within VGOS are clear from the very beginning. In this respect, the operations of the VGOS network can evolve in a product-oriented fashion with very good results from the beginning. With more radio telescopes to participate in later years, the quality, stability, and redundancy of the VLBI results will define a new state of the art in space-geodetic EOP and reference frame results.

References

1. A. Niell, A. Whitney, B. Petrachenko, W. Schlüter, N. Vandenberg, H. Hase, Y. Koyama, C. Ma, H. Schuh, G. Tuccari, 2006, “VLBI2010: Current and Future Requirements for Geodetic VLBI Systems”. In Behrend & Baver (eds.), International VLBI Service for Geodesy and Astrometry 2005 Annual Report, NASA/TP-2006-214136, pages 13-40.
2. B. Petrachenko, A. Niell, D. Behrend, B. Corey, J. Böhm, P. Charlot, A. Collioud, J. Gipson, R. Haas, T. Hobiger, Y. Koyama, D. MacMillan, Z. Malkin, T. Nilsson, A. Pany, G. Tuccari, A. Whitney, J. Wresnik, 2009, “Design Aspects of the VLBI2010 System. Progress Report of the IVS VLBI2010 Committee”, NASA/TM-2009-214180, 58 pp.
3. B. Petrachenko, D. Behrend, H. Hase, C. Ma, A. Niell, A. Nothnagel, X. Zhang, “Proposal for VGOS Observing Plan”, In K. D. Baver, D. Behrend, and K. Armstrong, editors, International VLBI Service for Geodesy and Astrometry 2013 Annual Report, NASA/TP-2014-217522, pp. 70-79, 2014. in preparation.

An Atlantic Network of Geodynamical and Space Stations

The RAEGE Project

Jesús Gómez–González[1], José Antonio López–Fernández[1,2], Francisco Colomer[1], Luis R. Santos[3]

Abstract The National Geographic Institute (IGN) of Spain and the government of the autonomous region of Açores (Portugal) are jointly deploying an "Atlantic Network of Geodynamical and Space Stations" (project RAEGE). The first two radio telescopes of RAEGE were finished in Yebes (Spain) and Santa María (Açores islands, Portugal). The network will be completed with two additional stations on Tenerife (Canary Islands) and Flores (Açores). The RAEGE radio telescopes are of VGOS kind: azimuth/elevation turning head telescopes, reaching azimuth and elevation slew speeds of 12°/s and 6°/s, respectively. The optical design is based on a 13.2-m ring focus reflector. In its basic configuration, the observation frequency is in the range of 2–40 GHz. It can be enhanced up to 100 GHz by using additional options. First light at the Yebes radio telescope was achieved on February 9, 2014 on the tri-band receiver (S/X and Ka bands) developed at the laboratories at the Yebes Observatory. The RAEGE Santa María site will be in full swing in early 2015. The infrastructure project of RAEGE in Santa María includes the construction of the main control building, access roads, and a power distribution building scheduled for summer 2014. The Santa María site will include a completely isolated gravimetry pavilion, buried in a small hill, on top of which a permanent GNSS station will be installed. The Tenerife and Flores stations are scheduled for 2016. They also include new radio telescopes, permanent GNSS receivers, and gravimeter stations.

1. Instituto Geográfico Nacional (IGN)
2. IGN Yebes Observatory
3. DSCIG Açores

Keywords VGOS, radio telescope, networks, instrumentation

1 Introduction

The deployment of an Atlantic Network of Geodynamical and Space Stations (RAEGE, for "Red Atlántica de Estaciones Geodinámicas y Espaciales") consists of the construction of four Fundamental Geodetic Stations, in Yebes (Guadalajara, Spain), Tenerife (Canary Islands, Spain), and Santa María and Flores (Açores Islands, Portugal). Each RAEGE station is to be equipped with a VGOS-kind radio telescope, a permanent GNSS receiver, a gravimeter, and (at least at Yebes) an SLR instrument. The construction of the RAEGE station in Yebes is very advanced, since the VGOS 13.2-m radio telescope is already in place and first-light was obtained; therefore it is expected that it will start operations for IVS in the summer of 2014. The RAEGE station in Santa María (Açores) is progressing well; the radio telescope is erected, and the control and auxiliary buildings are being finalized. Once the receiver is installed, commissioning will start in order to become operational early in 2015.

Fig. 1 Location of the RAEGE stations.

2 The RAEGE Radio Telescope

The RAEGE radio telescopes follow the specifications for VGOS: azimuth/elevation turning head telescopes, with maximum azimuth and elevation slew speeds of 12°/s and 6°/s, respectively. The optical design is based on a 13.2-m ring focus reflector.

These radio telescopes were built under the supervision of MT Mechatronics. The concrete pedestal, which hosts an inner independent concrete pillar, is built by a local construction company. The mechanical elements are built by the Spanish company Asturfeito (following their design for the ALMA telescopes in Chile), and the reflector panels are provided by the Italian company COSPAL.

Fig. 2 The RAEGE VGOS radio telescope "Jorge Juan" at Yebes, Spain. At the back, the IGN 40-m radio telescope which is currently a network station in IVS.

3 RAEGE Receivers

The RAEGE radio telescopes in Yebes and Santa María are being equipped with cryogenic high-performance receivers of the S, X, and Ka bands (see Figure 5 and the paper by López-Fernández et al., in this volume).

IGN engineers at the Yebes Observatory are developing a VGOS broadband receiver. Low-noise amplifiers have been successfully developed at the Yebes laboratories for the 4–8 and 4–12 GHz bands, and research on broadband feeds is progressing (see the paper by López–Fernández et al., in this volume).

Fig. 3 The RAEGE VGOS radio telescope in Santa María, Açores Islands.

Table 1 RAEGE instrumentation parameters.

Parameter	Value	
RT Diameter	13.2 m	
Optics	Ring focus	
Surface RMS	180 μm	
Designer	MT Mechatronics GmbH	
Az/El slew speed	12°/sec / 6°/sec	
Receivers	triband (S, X, Ka)	
	dual pol (RCP+LCP)	
Band	Frequency (GHz)	Trec (K)
S band	2.2–2.7	21
X band	7.5–9.0	23
Ka band	28–33	25
DBBC type	European DBBC (IRA/INAF)	
Recorder	Mark 5B+/Mark 5C	
Yebes connectivity	10 Gbit/s fiber	

4 Other Instrumentation and Works Towards the Observatory Local-tie

4.1 GNSS

IGN has developed and maintained since 1998 a network of 41 permanent GNSS stations in Spain (ERGNSS), 20 of them included in EUREF. Two of these stations are part of the International GNSS Service (IGS): Yebes Observatory (YEBE) and La Palma (in Canary Islands, LPAL). IGN has also been a local Analysis Center for EUREF (known as IGE) since 2001 and processes the data of 50 stations in

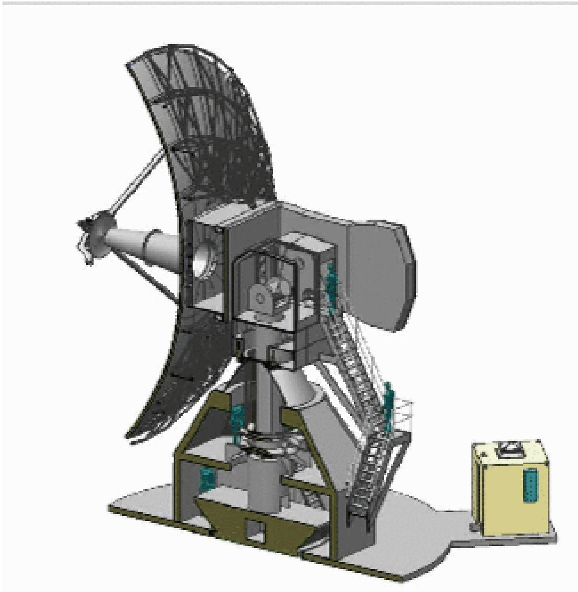

Fig. 4 Design of the RAEGE VGOS radio telescopes by MT Mechatronics (Germany).

Fig. 5 Tri-band (S/X/Ka) receiver for RAEGE radio telescopes, designed and built at the IGN Yebes Observatory.

Spain, Portugal, Morocco, France, Italy, and Great Britain.

4.2 Gravimeter

IGN Yebes Observatory hosts a state-of-the-art gravimetry pavillion, allowing very controlled thermal behavior (double chamber with air conditioning system in the external one) and structural behavior (isolated concrete pillars). Specially designed to host gravimeters given the high sensitivity of these instruments, it is offered for regional AG comparisons (RICAGs) for up to six instruments. The laboratory hosts a GWR Superconducting Gravimeter (permanently installed), and also available (but not always installed because they participate in different measurement projects) are an FG5 absolute gravimeter, an A10 absolute gravimeter, an L&R (LaCoste and Romberg) relative gravimeter, gPhone, Scintrex, etc. An artistic view of the gravimeter pavillion can be seen in the 2011 IGN annual report to IVS.

4.3 Satellite Laser Ranging

We have started studies aimed towards the construction of an SLR facility at the Yebes Observatory. Due to the current trends in the new SLR stations and the GGOS project, the future Laser Ranging Station at Yebes (CYLAR, Cdt Yebes LAser Ranging) should fulfill the main characteristics of the Next Generation Systems: low energy laser (taking into account the possibility of participating in one-way ranging and transponder experiments), high repetition rate (1000 to 2000 Hz), few picoseconds (ps) pulse width, pico event timer, single photon detection (CSPAD or APD detector) and high automation. The station should have the capacity to observe all satellites, from 400 to 24,000 km (navigation satellites: GPS, GLONASS, Compass, and Galileo). Other characteristics would be a lightweight biaxial Cassegrain-Coudé telescope for laser pulse transmission and reception ($\sim$ 50 cm and 10 cm respectively), Nd:YAG laser (532 nm), night and day operation, and air traffic protection, compatible with other activities at the observatory (VGOS and 40-m radio telescope). See Vaquero-Jiménez and López-Fernández (2011) for details.

4.4 Measurement of the Invariant Reference Point of the RAEGE Radio Telescope at the Yebes Observatory

The position of the invariant reference point (IRP) is very important in the determination of the local tie, which connects all the geodetic techniques in an observatory. It is defined as the intersection between the azimuth axis and the elevation axis of a radio telescope if this intersection exists. Otherwise it is defined as the projection of the elevation axis on the azimuth axis. Usually this point is inaccessible or it is not materialized. There are several methodologies for calculating it. The most classic method, which we have used, is based on the adjustment from measurements points on the radio telescope frame under circles in 3D constrictions. In this model, the radio telescope is rotated around one of its axes keeping the other one fixed; thereby the track of each target describes a circle. This process is repeated for different orientations of the radio telescope and for both axes. The details and measurement results are described in Appendix A.

5 Conclusions

The RAEGE network is being deployed, with important developments in infrastructures and instrumentation. The first VGOS antenna, in Yebes (Spain), will be operational for the IVS already in 2014 with a tri-band (S/X/Ka) receiver. Other developments towards a complete broadband system are underway and are described in other papers by the IGN team in this volume.

Appendix A: Measurements of the IRP at the RAEGE Radio Telescope at Yebes

The measurements at the 13-meter RAEGE radio telescope at the Yebes Observatory were performed inside the cabin with a Leica TS30 robotic total station, with an angular and distance accuracy of 0.5 and 0.6 mm respectively, located on the central pillar of the radio telescope pedestal. To do this, a tripod with optical plummet tribrach was established over the marked centered screw of the pillar. A measurement was taken of the position of a corner cube reflector "RRR Hexagon" with a manufacturing precision of 0.0001 mm, which was attached magnetically to the inner sides of both antenna counterweights. Measurements of the reflector (CCR) were taken every 30 seconds for the right counterweight by moving the antenna around the elevation and azimuth axis. The movement of the antenna taken in azimuth and elevation was performed in increments of 20^o. The sequence of actions were carried out by fixing one azimuth out of 18 possible azimuths and moving the telescope to five elevation positions (7^o, 27^o, 47^o, 67^o, 87^o). Then the azimuth angle was increased by 20^o and the procedure was done again but decreasing the elevation angle from 87^o to 7^o. The previous steps were repeated but placing the CCR at the left counterweight. A total of 180 (18*5*2) points were measured every 30 seconds, resulting in an automated observation of 90 minute duration. For each counterweight, it was possible to adjust five azimuth circles and 18 elevation arcs. For both counterweights, a total of ten azimuth circles and 36 elevation arcs were adjusted. From this, the 18 elevations axes were calculated.

The TS30 station was controlled by a laptop connected via Bluetooth, running software made by the observatory staff that handled the tasks of orientating, targeting, measuring, recording, and synchronization with the control center of the antenna.

The determination of the IRP for both the azimuth and the elevation axes was performed by adjusting the observation data with a Mixed Model Least Squares with constraints.

In the case of the azimuth axis, observations to the targets on the rotation of the radio telescope around the azimuth axis for different elevations were taken. Observations have been adjusted to circles in space, that is, the intersection of a sphere and a plane. Also, the center of the sphere must satisfy the plane equation. In this adjustment, the parameters for each sphere (center and radius) and for each plane were determined. A total of five circles for each counterweight (ten in total) were adjusted. Each circle was adjusted from 18 observed points. 52 parameters were adjusted from 360 observation equations.

In the case of the elevation axes, observations to the targets on the rotation of the radio telescope around the elevation axes for different azimuths were taken. Observations had to be adjusted to circular arcs in space. For each azimuth, measurements for both counterweights were done. Centers from both circular arcs generated the elevation axes. A total of 18 circular arcs for each counterweight (36 circular arcs in total) and 18 elevation axes were adjusted.

The obtained accuracy is below one millimeter, so we are in the required range to be able to relate the different available geodetic techniques in the observatory in the future by the local tie vector.

Table 2 Results from the measurements of the Yebes RAEGE radio telescope Invariant Reference Point.

	Value			Standard deviation		
IRP coordinates (m)	99.99774	199.99226	301.314795	0.00005	0.00005	0.000014
Eccentricity	0.000127			0.000074		
Azimuth axis inclination from the vertical ($''$)	-8.326001			0.320035		
Non-orthogonality angle between azimuth and elevation axes ($''$)	5.589358			0.901273		

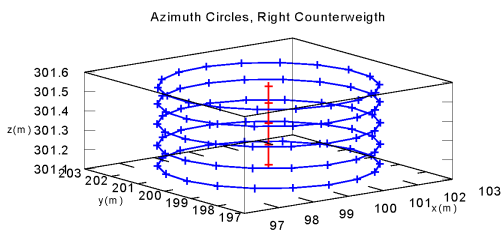

Fig. 6 Azimuth adjustments for the Yebes 13-m radio telescope IRP.

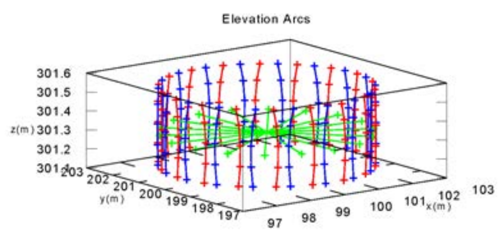

Fig. 7 Elevation adjustments for the Yebes 13-m radio telescope IRP.

Fig. 8 Robotic Total Station Leica TS-30 set up above the RAEGE radio telescope central pillar.

References

1. A. Santamaría-Gómez, S. García-Espada, "Simulating the estimation of the 40m radio telescope Invariant Reference Point at the Yebes observatory", IGN Yebes technical report CDT 2011-9
2. B. Vaquero-Jiménez, J. A. López-Fernández, "CYLAR Specifications (CDT Yebes Laser Ranging)", IGN Yebes technical report CDT 2011-11
3. J. M. Serna, P. Vaquero, S. Sainz-Maza, M. Calvo, B. Córdoba, J. López, C. López, J. A. López–Fernández, "FG5 Absolute Gravimeter", IGN Yebes technical report CDT 2012-1
4. J. M. Serna, B. Córdoba, J. López, M. Calvo, C. López, J. A. López–Fernández, P. Vaquero, S. Sainz-Maza, "Observatory Superconducting Gravimeter", IGN Yebes technical report CDT 2012-2
5. J. Dawson, P. Sardi, G. M. Johnston, L. Vittuari, "Indirect approach to invariant point determination for SLR and VLBI systems: an assessment", J. Geody. 81, 433-441, 2007
6. K. Fancher, D. Smith, S. Breidenbach, J. Olsen, N. Paudel, "Recent IERS Site Survey of Multiple Co-located Geodetic Techniques by NGS", in FIG Congress 2010, Facing the challenges- Building the Capacity, 2010.
7. P. Starti, P. Sillard, L. Vittuari, "Surveying co-located space-geodetic instrument for ITRF computation", Journal of Geodesy, 78, 210-222, 2004

Russian VLBI System of New Generation

Alexander Ipatov, Dmitri Ivanov, Gennadii Ilin, Sergey Smolentsev, Mikhail Varganov, Iskander Gayazov, Vyacheslav Mardyshkin, Leonid Fedotov, Mikhail Kajdanovsky, Alexander Vytnov, Alexander Salnikov, Andrey Mikhailov

Abstract The VGOS Program is being implemented in Russia to create the new generation of VLBI systems. The new generation radio interferometer provides implementation of perspective requirements for determining and predicting the Earth orientation parameters. The work was started in 2012, and the two-element radio interferometer will be created by the end of 2015 at the Badary and Zelenchukskaya co-location stations. The program includes the creation of two fast moving 13.2-m radio telescopes equipped with the receiving systems which will receive radio signals at three bands (S, X, and Ka) and two circular polarizations simultaneously. The digital broadband acquisition system provides a conversion to the 1 GHz band. The VDIF-formatted digitized data will be transferred to the St. Petersburg Correlation Processing Center by the communication channels. The current state of the program is presented.

Keywords VLBI, EOP, VGOS

1 Introduction

At the present time, high-precision determination of the Earth Orientation Parameters (EOP) and the well-timed determination of Universal Time (UT1) for GLONASS are provided by means of the QUASAR VLBI Network. At the same time, the QUASAR network works in cooperation with IVS and provides relevant data on the Earth rotation parameters and terrestrial and celestial reference frames.

Institute of Applied Astronomy, Russian Academy of Sciences

Characteristics of perspective GLONASS make higher demands on the full range of fundamental parameters, including determination and forecasting of EOP:

– *EOP determinations:* not worse than 3 mm for the pole coordinates, 10 μs for UT1 and 100 μas for precession and nutation;

– *Operational UT1 determinations:* 3–4 times a day with an error of 20 μs.

The achievement of the accuracy and rapidity are the most important for determination of Universal Time. The implementation of such Intensive sessions will be possible after principal modernization of the QUASAR network stations on the basis of small-diameter antennas. The antenna systems of the new VLBI network must work every day and on a 24-hour basis.

The simulation showed that the optimal diameter of the new antenna system should be about 13 m. This will cause the loss of flux sensitivity of the new antenna system by a factor of 7 compared to the QUASAR VLBI network antenna. This is compensated by an increase of bandwidth (not less than six times) and the number of observations of radio sources (not less than eight times). The first requirement is achieved by using wideband receivers with a registration frequency bandwidth of 1 GHz, and the second by a significant increase in the speed of antenna motion from one radio source to another (at least 5-6 deg/s in elevation and 12 deg/s in azimuth). The desired accuracy of UT1 determination can be achieved with the Badary-Zelenchukskaya baseline of the QUASAR network if the duration of observation scans will be up to 20 seconds. The number of observations obtained per day at such duration and speeds of antenna motion allows estimation of EOP with the desired accuracy.

The “Quasar-M” project, focused on constructing the two-element radio interferometer, is currently realized at the IAA.

2 VLBI2010 (VGOS) Antenna System

The IAA analyzed in detail all possible variants of the new generation antenna system (AS) for the purpose of fulfilling VLBI2010 (VGOS) requirements. Also taken into account were the possibility of placing the receiving equipment, the shipping cost, and the volume of work required to install the equipment. As a result, the 13.2-m AS produced by Vertex Antennentechnik GmbH was chosen (Figure 1). Vertex Antennentechnik GmbH also provided modernization of the AS to satisfy climatic and seismic conditions in the placements.

– Frequency range: 2–40 GHz;
– Main reflector diameter: 13.2 m;
– Overall surface accuracy: 0.2 mm (RMS);
– Mount: Elevation over Azimuth;
– Ring focus antenna;
– Subreflector mount: hexapod;
– Efficiency: 0.8;
– Max AZ velocity: 12 deg/s;
– Max EL velocity: 6 deg/s;
– Overall pointing accuracy: 16 arcsec.

Fig. 1 New 13.2-m VERTEX antenna in Badary (Feb. 2014).

3 Tri-band Receiving System

The tri-band receiving system provides signal amplification in S, X, and Ka frequency bands in both circular polarizations [1]. The main receiver system parameters are presented in Table 1. In order to improve the signal-to-noise ratio, the tri-band feed and the frontend LNAs are mounted in a single unit and cooled by closed cycle refrigerator to the temperature of liquid hydrogen (20 K) (Figures 2 and 3). The LNA outputs are connected to the inputs of the converter units. Each converter unit provides additional signal amplification, conversion of the signal frequency to the intermediate frequency (IF) band of 1–2 GHz, formation of the output signal bandwidth, and signal filtering. The commutator unit provides two modes of operation and forms four frequency channels in different frequency bands: 1S+3X or 1X+3Ka. Synchronization of the frequency converters is provided by the frequency-time synchronization system of the radio telescope. The radio telescope receiver units are placed in the focal cabin.

Table 1 Tri-band receiving system parameters.

Band	Freq. band GHz	Polarization	Estimated T_{sys},K	Radiation angle, deg	Number of channels	Working mode
S	2.2–2.6	RCP	23.2		2	1S+3X
X	7.0–9.5	+/−	29.7	130	6	or
Ka	28–34	LCP	44.5		6	1X+3Ka

4 Broadband Data Acquisition System

The BRoadband data Acquisition System (BRAS) is the digital backend of the radio telescope [2]. The system consists of eight identical Digital Converter Channels (Figure 4). Each channel has an input frequency range of 1 to 1.5 GHz and 512 MHz bandwidth. The

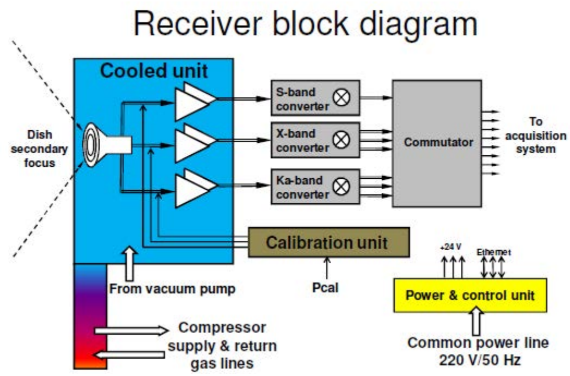

Fig. 2 Tri-band receiver block diagram.

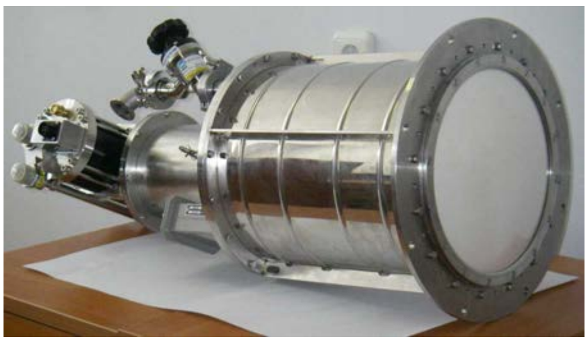

Fig. 3 Cooled unit.

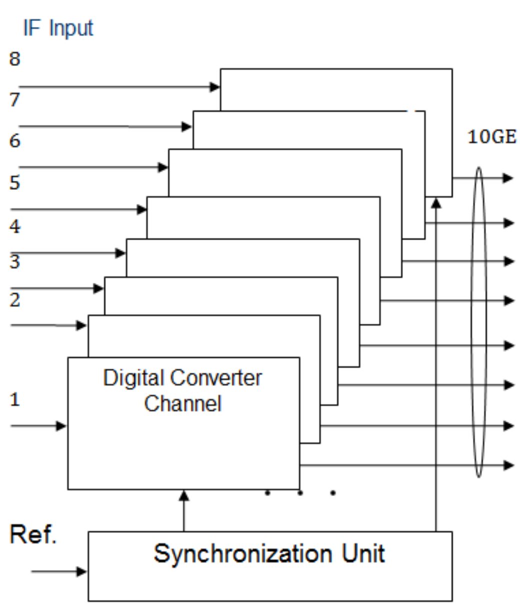

Fig. 4 The structure of BRAS.

input of each channel is connected to one of the IF outputs of the receiving system. Each channel has an ADC and an FPGA. The signal power measurement, 2-bit sampling, and data stream formatting are performed in the digital form. The Synchronization Unit is intended for formation and distribution of clock signals between all channels. Phases of these signals are synchronized with a 100 MHz signal from an H-maser and 1 PPS from the time scale of a radio telescope. Through the 10 GE interface data streams arrive at fiber lines. The total rate of the data stream at the system output is 16 Gbps. The system has built-in controls and diagnostics, including measurements of signal levels, current consumption, temperature on boards and chip, selection of the phase calibration signal, control of phase and amplitude characteristics, control of the locked-in state, and control of the statistics of the signal distribution on sampling levels. The system is controlled by computer. BRAS is implemented in a conventional 19" rack and located in the focal cabin of the antenna. Currently two samples of the system are ready to be installed on the antennas.

5 Time and Frequency Synchronization System

The time and frequency synchronization system (TFSS) provides transmission of high stable reference time and frequency signals to the focal cabin of the antenna where the tri-band receiving system and BRAS are located. For this purpose, special devices were designed, which allow reduction of the transmission loss of reference signals (Figures 5 and 6). For transmitting reference signals to the radio telescope, a new method is used. The reference signals are transferred through a fiber optic line that has better spectral characteristics than coaxial cable. For compensation of phase fluctuations due to the telescope motion, a phase stabilization scheme is used. The time synchronization unit provides time delay measurement and compensation in transmission lines. The p-cal signal generator with a frequency range up to 35 GHz was developed for wideband receiver phase calibration. All units of TFSS are placed into thermostabilized boxes.

Fig. 5 Unit for the formation reference frequency signal at an antenna.

Fig. 6 Time synchronization unit.

6 Center of Control and Scheduling

All systems developed for the new generation network are equipped by internal controllers with Ethernet interfaces. Monitoring and control are provided locally at the station and via Internet from the Center of control and scheduling at IAA RAS. We plan not to use pure remote control of operations. Session schedules should be loaded remotely from the Center and then run locally at the stations. This will improve reliability on unstable communication channels. However, remote control and monitoring capabilities will be improved relative to the existing system. The software development for remote control is in progress and is taking into account the security of the remote access.

7 Buffering and Data Transmission System

IAA RAS develops buffering and data transmission systems which realize VLBI2010 (VGOS) requirements [3]:

– recording of eight data streams (with scalability up to 16 data streams) in the VDIF format with 2 Gbps data speed from each channel;

– realizing data transfer to the Data Processing Center at 10 Gbps simultaneously with recording and buffering data;

– storing observational data up to 20 TB in size in the generic file structure with a set of disk pools.

The Data Recording System (DRS) is based on Commercial Off-The-Shelf (COTS) hardware [4, 5]. The DRS consists of a rack server Dell PowerEdge R720 with two Intel CPU Xeon E5-2643 3.30 GHz or Xeon E5-2650 2.0 GHz, 96 Gb RAM, and two disk enclosures Dell PowerVault MD1220 (up to 24 2.5″ hot-pluggable small-form-factor drives) (Figure 7). With this configuration, the disk subsystem of the server setup consists of three SAS backplanes, up to 64 2.5″ drives maximum. Each SAS-backplane is attached to an LSI SAS2008 based SAS HBA by two 24 Gbps SAS 2.0 channels. Up to four dual-port 10 Gigabit Ethernet Intel network cards (Intel X520) are used. The connection of DRS with digital backend was carried out in two ways: a direct connection from each BRAS channel to the 10 GbE network interface server and an Ethernet switched connection through the Cisco Catalyst c4900M switch, as seen in Figure 8. The DRS provides temporary storage for VDIF data of a single hour-long VLBI session that comes from BRAS (8 channels x 2 Gbps) placed at QUASAR network observatories and simultaneous data transmission from two observatories over fiber lines (the transmission rate is up to 8 Gbps). It also provides data storage for all three or four hour-long VLBI sessions at IAA RAS in St. Petersburg. This DRS is compatible with international registration systems. Data transmission is performed via Internet using broadband communication channels. The 10 Gbps Internet channel will let us carry out hour-long VLBI sessions three or four times a day.

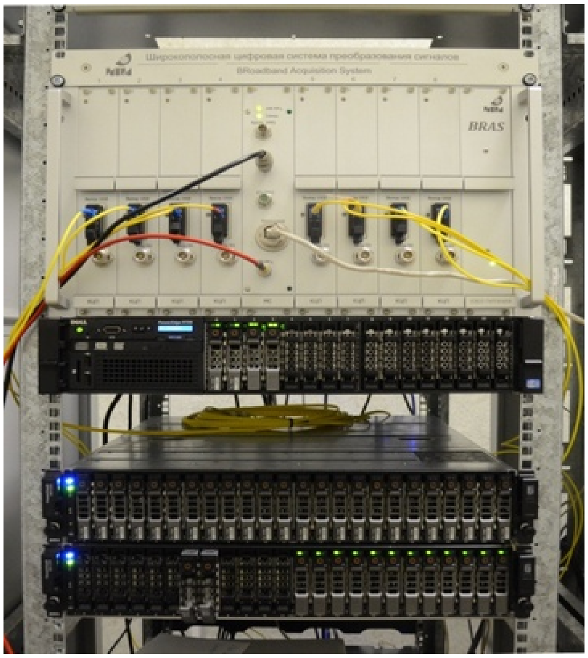

Fig. 7 Data Recording System: Server Dell PE R720 with storage Dell PV MD1220 (bottom) and digital backend BRAS (top).

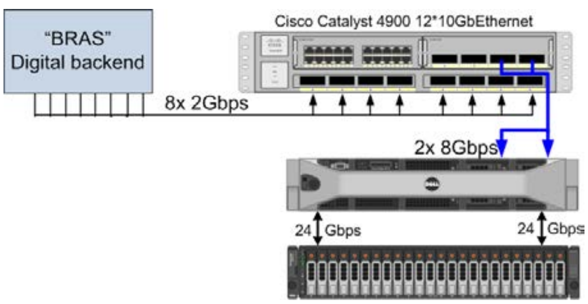

Fig. 8 Ethernet switched connection through the Cisco Catalyst c4900M switch.

8 Water Vapor Radiometer

Water vapor radiometers were constructed to have near real time information about tropospheric zenith wet delay (ZWD) in QUASAR network observatories for use in VLBI data processing and UT1 calculation. Two models of WVRs were tested at the Svetloe observatory [6]. One of them is fully steerable to have the ability to follow VLBI radio telescope RT-32 ,and another one is measuring ZWD. Comparing ZWD obtained with WVR and ZWD determined from GNSS observations demonstrates the coincidence with the accuracy of (3-5) mm (RMS) on an interval of several months, excluding periods of rainfall. WVRs are equipped with rain intensity sensors.

WVRs will be installed at the Badary and Zelenchukskaya observatories at the end of 2014.

For more accurate ZWD measurements, all QUASAR network sites will be equipped with atmosphere temperature profiles MTP-5 [6].

9 Summary

The two-element interferometer at the co-location stations Badary and Zelenchukskaya will be created in the framework of the "Quasar-M" project. This interferometer will determine UT1 3–4 times per day with an accuracy of 20 microseconds.

Milestones of the "Quasar-M" project are:

2013 – production of main equipment prototypes (feed, front-end, DAS);
2013 – building of the radio telescope foundation;
2014 – assembly of antenna parts at the observatories;
2015 – first VLBI observations.

The use of the created two-element radio interferometer in joint observation sessions with international global network stations will perform pole position determinations with an accuracy of 3 mm, nutation and precession angles with an accuracy of 100 μas, and determination of Universal Time with an error of 10 microseconds.

References

1. Alexander Ipatov, Irina Ipatova, Vyacheslav Mardyshkin, Alexander Evstigneev, Evgeniy Khvostov, Alexey Lavrov, Vitaliy Chernov. Tri-band System for the Russian Interferometer, 2014, this volume.
2. Evgeny Nosov, Anton Berdnikov, Sergey Grenkov, Dmitriy Marshalov, Alexey Melnikov, Leonid Fedotov. Current Development State of Russian VLBI Broadband Acquisition System. 2014, this volume.
3. I. Bezrukov, A. Salnikov, A. Vylegzhanin, Russian Data Recording System of New Generation, 2014, this volume.
4. Mark 6 VLBI data system: Web document http://www.haystack.mit.edu/tech/vlbi/mark6/index.html
5. FlexBuff The netmap project: Web document http://info.iet.unipi.it/ luigi/netmap/
6. G. Ilin, V. Bykov, V. Stempkovsky, A. Shishikin, WVRs for the "Quasar" Network, 2014, this volume.

An Introduction to the Seshan VGOS Station Project

Guangli Wang

Abstract SHAO has set up a team to push forward the building of the Seshan VGOS station. The task of the team is to present the station construction scheme based on the VGOS 'standard' and to investigate the capabilities of domestic companies and companies abroad for developing the different parts of the new station system. This report will introduce the progress of the team's work.

Keywords Seshan, VGOS, project

1 Project Status

In 2012, a project team, Seshan VGOS Station Project, was established to push forward the construction of the Seshan VGOS Station. In 2013, the team had received the operation fund from SHAO to support the pre-stage investigation under the name of "Study on the Key Technology of the Sheshan VLBI2010 Station Construction". The team consisted of members from two divisions: Division of Center for Astro-geodynamics Research including Chengli Huang (head), Jinling Li, Zhihan Qian, and Guangli Wang; and Division of Science and technology for Radio Astronomy including Weimin Zheng (head), Fengchun Shu, Xiuzhong Zhang, and Qingyuan Fan.

This team is to present "Shanghai Sheshan VLBI2010 Antenna Technical Specifications Requirements", to investigate the capabilities of the home industry according to the discussion of technical specifications, the comparison and the evaluation of the antenna design proposals, the antenna location, and the creation of a construction plan.

The team has completed the following work: (1) The selection of the Seshan VGOS station. The station will be located in the courtyard of the existing 25-m radio telescope. Considering that the Seshan 25-m antenna has a long history of participating in international geodetic VLBI sessions since 1988, this site is important in the Global Geodetic VLBI Network. The 25-m antenna is about thirty years old and, at some point in time, will break down. It is necessary to build a new VGOS antenna near to the old one and as its successor. In addition, an IGS station is located in this courtyard as well. (2) The RFI investigation. According to the measurement in 2010 at the Tianma 65-m telescope, which is not far from Seshan25, RFI occurs in S-band. It is difficult to use continuous broadband at S-band for VLBI observations. The Superconducting Filter is planned for use in the reduction of the RFI effects. (3) In the second half of 2013, consulting domestic manufacturers, determining the antenna design, and forming a construction plan.

Now the main technical specifications of the antenna and other parts consist of the following:

- Diameter: 13 m
- RF frequency range: 2–14 GHz, upgradable to Ka band
- Polarization: H&V Linear polarizations
- Optics: Ring focus
- Aperture efficiency: >50%
- Surface accuracy: <0.3mm
- Pointing accuracy: $<18''$
- Antenna mount: az-el turntable mount
- Slew rate: Az 12°/s, $3°/s^2$; El 6°/s, $3°/s^2$
- Slew range: Az $-270°\ldots+270°$; El $0°\ldots90°$

Shanghai Astronomical Observatory, CAS

- Reference point stability: ±0.3 mm
- Signal path length stability: ±0.3 mm
- Primary operating conditions:
  - Wind speed:11m/s
  - Temperature: -10°C…+50°C
  - Humidity: 0…100%
  - Rainfall: 50 mm/hr
- Antenna reliability:
  - Continuous operation:
    3,000 long slews per day
    for more than 30 days
  - Antenna mechanical structure's lifetime:
    >20 yr
  - Motors and gear boxes MTBF: >2 yr
  - Maintenance and repair: <10 days/yr
- System temperature: <40K excluding ATM noise
- Receiver temperature:
  <20K cryogenic front end output
- Digital UDC, 8 channels
  - Input 8 ch (four bands, two polarizations each)
  - Output 8 ch
    (70–512 MHz, 512–1024 MHz,
    70–1024 MHz)
- DAS and recording system
  - Input: 8 IF
  - sampling rate/IF:
    4 Gbps (BW 1 GHz, 2-bit sampling)
  - Total recording rate: 32 Gbps
- Time/Frequency: shared
- Meteorological system: shared

Now SHAO has determined to build the VGOS station by self-raised funds at Sheshan, near Shanghai. We are preparing for choosing an antenna manufacturing contractor. The Sheshan VGOS station will participate in IVS VGOS observations in the second half of 2015.

Construction of a VGOS Station in Japan

Yoshihiro Fukuzaki, Tadashi Tanabe, Jiro Kuroda, Shinobu Kurihara, Ryoji Kawabata, Takahiro Wakasugi

Abstract The Geospatial Information Authority of Japan (GSI) began a new project for constructing a VGOS station in Japan. The construction of the antenna (radio telescope) has been completed, and the necessary equipment (Front-end, Back-end, H-maser, and so on) has also been delivered. The name of the new station is Ishioka, which is located 17 km away from the Tsukuba 32-m antenna. We briefly report the current status of the construction of the new antenna.

Keywords VGOS, broadband receiving

1 Introduction

The Geospatial Information Authority of Japan (GSI) has carried out VLBI observations since 1981. In the first period from 1981 to 1994, we developed transportable VLBI systems with a 5-m antenna and a 2.4-m antenna and carried out domestic sessions using them. As a result, eight sites in Japan were observed, and precise positions were determined. In addition, Japan–Korea VLBI sessions were carried out by using a transportable 3.8-m antenna in 1995. In these sessions, the Kashima 26-m antenna, which was removed in 2002, was used as the main station. In the second period from 1994 to 1998, GSI established four permanent stations: the Tsukuba 32-m, Sintotsukawa 3.8-m, Chichijima 10-m, and Aira 10-m antennas. Up to the present, regular VLBI sessions using the four stations were carried out. The Tsukuba 32-m antenna is a main station for not only domestic but also international VLBI sessions now.

In 2011, GSI started a project for constructing a new antenna following the VLBI2010 concept, which is recommended by the International VLBI Service for Geodesy and Astrometry (IVS) as the next-generation VLBI system. This paper gives the outline of the project and the current status of the construction of the new antenna.

Geospatial Information Authority of Japan

2 Observing Facilities

In the new project, observing facilities are now being constructed. The conceptual design of the facilities consisting of six components is depicted in Figure 1. The Operation Building will be constructed by the Construction Department of Ministry of Land, Infrastructure, Transport, and Tourism a few years later than the original plan.

3 Components

3.1 Antenna

The antenna (radio telescope) is the main part of the observing system. Since a single antenna is employed, very high slew rates are specified in order to be compliant with the VLBI2010 concept. The specifications of the antenna are listed in Table 1. The photo of the new antenna is shown in Figure 2.

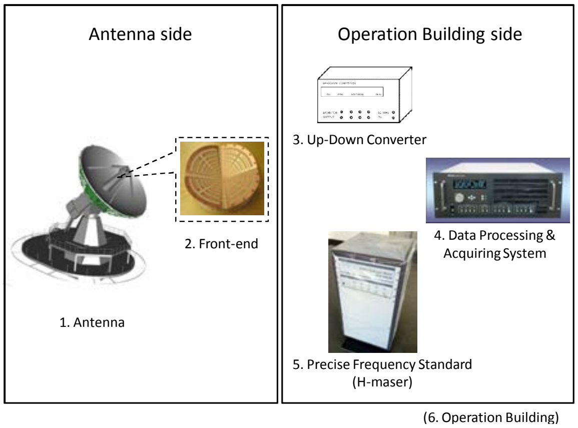

Fig. 1 Conceptual design of the new observing facilities.

Table 1 Specifications of the new antenna.

Parameter	**Value**
Diameter	13.2 m
RF frequency range	2–14 GHz
Surface accuracy	$\leq$ 0.08 mm (RMS) (at EL 45°)
Aperture efficiency	$\geq$ 50%
Antenna noise temperature	$\leq$ 10K (excluding atmospheric contributions)
System G/T	$\geq$ 45.882 dB (at 14 GHz) [T is the system noise temperature (Tsys), and Tsys excluding antenna noise temperature should be assumed as 30K.]
AZ maximum slew rate	$\geq$ 12°/sec
EL maximum slew rate	$\geq$ 6°/sec
AZ maximum acceleration rate	$\geq$ 3°/sec^2
EL maximum acceleration rate	$\geq$ 3°/sec^2
Cable for signal transfer	Optical fiber cable from antenna to building
Special feature	Reference point should be measured directly from the ground for co-location.

3.2 Front-end

According to the VLBI2010 concept, a broadband feed is necessary to achieve high aperture efficiency over 2–14 GHz. At present the Eleven feed, which was developed at Chalmers University of Technology in Sweden, and the Quadruple-Ridged Flared Horn (QRFH), which was developed at California Institute of Technology (Caltech), were practical as a broadband feed, so both feed systems were purchased. For the design of the antenna optics, employing the Eleven feed was assumed.

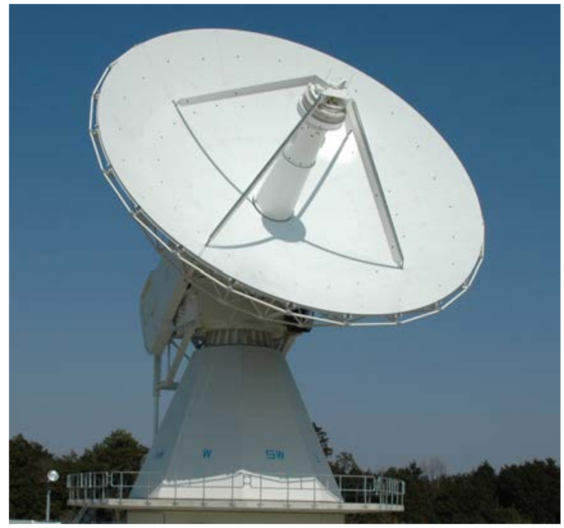

Fig. 2 Photo of the new antenna.

In both cases, the feeds and the Low Noise Amplifiers (LNAs) are integrated into each cryogenic system, whose physical temperature is less than 20 K. The measured receiver noise temperatures for a QRFH system are less than approximately 30 K (see Figure 3). The specifications of the front-end are shown in Table 2.

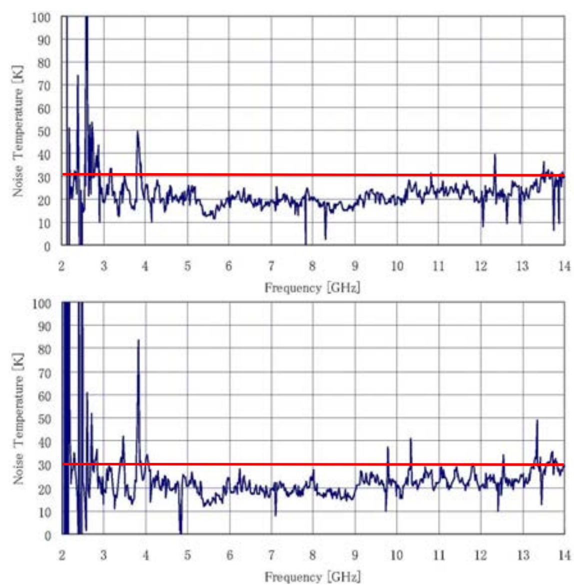

Fig. 3 Receiver noise temperature for QRFH system (upper: horizontal polarization, lower: vertical polarization).

Table 2 Specifications of the front-end.

Parameter	Value
RF frequency range	2–14 GHz
Polarization	Dual linear polarization
Feed	Eleven feed or QRFH
Dewar	Feed, LNAs, and other devices should be included and cooled by cryogenic system.
Physical temperature	$\leq$ 20 K (1st stage)
System noise temperature	$\leq$ 30 K (excluding antenna noise temperature)
Total gain	$\geq$ 45 dB
Output frequency range	2–14 GHz
Number of outputs	2 (for dual linear polarization)
Phase and delay calibration	New-type P-cal unit New cable calibration system developed by NICT
Injection of P-cal/noise-source	In the front of the feed or LNAs

3.3 Up-Down Converter

In order to convert the observed analog signal to digital data, the frequencies should be downconverted. For this purpose, a new Up-Down Converter is under development. The output signal frequencies are 1–2 GHz. The Lower Side Band (LSB) and the Upper Side Band (USB) need to be selectable in the Up-Down Converter, because the second Nyquist zone will be used in the sampler (see Section 3.4). The specifications of the Up-Down Converter are given in Table 3.

Table 3 Specifications of the Up-Down Converter.

Parameter	Value
Input frequency range	2–14 GHz
Output frequency range	1–2 GHz
Type of output signal	LSB or USB (selectable)
Number of units	4
Number of channels per one unit	2 (for dual linear polarization)
1st local oscillator	Programmable with 0.4-MHz step
2nd local oscillator	2 fixed LOs for LSB and USB
Total noise figure	$\leq$ 25 dB
Phase stability	$\leq 4^\circ$ with $\pm 2^\circ$C temperature change

3.4 Data Processing and Acquisition System

The data processing and acquisition system includes samplers, a Digital Back-end (DBE) function, and huge data storage. The sampling rate is 2048 Msample/sec, and the quantization is 1/2/4/8 bits (selectable). The second Nyquist zone will be used. The DBE function is equipped for the compatibility with the legacy observation system. Huge data storage of more than 400 TByte is installed. The specifications of the data processing and acquisition system are given in Table 4.

Table 4 Specifications of the data processing and acquisition system.

Parameter	Value
Sampling rate	2048 Msample/sec
Quantization	1/2/4/8 bits (selectable)
Digital Back-end	IVS recommended type
Data Storage	$\geq$ 400 TB

3.5 Precise Frequency Standard

Two hydrogen masers are installed as a frequency standard. In addition, a GPS time receiver and a clock comparison system are also installed. The specifications of the precise frequency standard are given in Table 5.

Table 5 Specifications of the precise frequency standard.

Parameter	Value
Number of hydrogen masers	2
Frequency stability	1 sec: $\leq 2.0 \times 10^{-13}$ 10 sec: $\leq 3.0 \times 10^{-14}$ 100 sec: $\leq 7.0 \times 10^{-15}$ 1000 sec: $\leq 3.2 \times 10^{-15}$
Output signal	5 MHz, 10 MHz, 100 MHz, and 1.4 GHz 1PPS
Other equipment	GPS time receiver Clock comparison system

3.6 Additional Facilities

Optical fiber cables are installed at the new site in order to establish a high-speed data link for data transmission. The initial transmission rate is 10 Gbps; then it can be increased to 32 Gbps and more in the future.

Two Global Navigation Satellite System (GNSS) continuous observation systems are installed at the new site to be registered as an IGS (International GNSS Service) station.

4 Site Information

The site name is Ishioka, which is near Tsukuba (about 40 minutes by car). The location is shown in Figure 4.

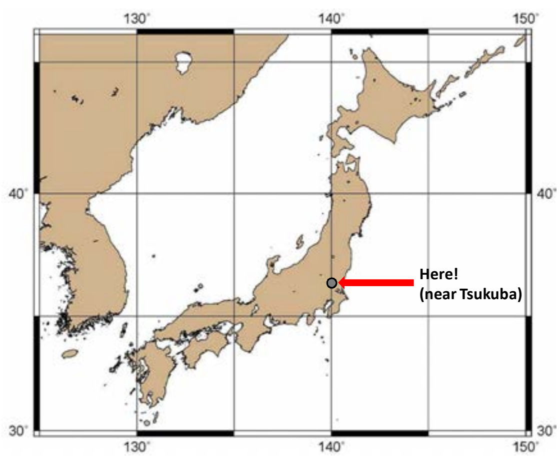

Fig. 4 Location of the site of the new observing facilities.

According to the results of a soil investigation of the site, there is bedrock very close to the surface (at less than 3 meter depth).

5 Summary

A new project for constructing a new antenna in Japan has started. The contract for the new antenna is complete, and the other components (front-end, back-end, and so on) were delivered. By integrating the whole set of components, the new station will be fully compliant with the VLBI2010 concept. In 2014, set-up and test observations will be carried out to make regular observing possible. After completion of the station, it will play an important role as a main station in the Asian region.

Atmospheric Modeling in the Data Analysis of Twin Telescope Observations

Tobias Nilsson[1], Benedikt Soja[1], Maria Karbon[1], Robert Heinkelmann[1], Li Liu[1,2], Cuixian Lu[1], Julian A. Mora-Diaz[1], Virginia Raposo-Pulido[1,3], Minghui Xu[1,2], Harald Schuh[1]

Abstract We investigate the possibility of combining the atmospheric parameters of the two antennas of a twin telescope in the VLBI data analysis. For this we perform simulations for a hypothetical future VGOS network, containing one twin telescope. The distance between the twin telescope antennas is varied between 0 m and 50 km to find out the distances over which it is possible to assume that the atmosphere above the antennas is identical. We find that the combination of the atmospheric parameters improves the station position repeatability when the distance between the antennas is less than 2–3 km. Thus, for the planned twin telescopes we expect that a common treatment of the atmosphere will increase the station position precision.

Keywords VLBI, Intensives, atmosphere, twin telescopes, VGOS

1 Introduction

In the upcoming year the VGOS (VLBI Global Observing System) network will start to operate [3]. It is expected that this system will result in about one order of magnitude improvement in accuracy compared to the current VLBI system. This will be achieved through using the more precise phase delays, as well as increasing the number of observations significantly by having faster antennas and observing a larger bandwidth. One idea is also to use so-called twin telescopes, i.e., equipping one station with two (or more) identical telescopes. This will further increase the number of observations—two telescopes should be able to make about twice as many scans as a single one—hence the accuracy will get even better. Furthermore, only with twin telescopes will continuous observations (24 h per day, seven days per week) be possible; when one telescope undergoes maintenance, the other one can still observe. For the VGOS network there are several twin telescopes planned, for example in Wettzell [5], Onsala [2], and Ny-Ålesund [4].

The idea is that the two antennas of a twin telescope can be treated as one in the data analysis. This requires that the local tie between the antennas be precisely known, that the antennas be connected to the same clock, and that the atmosphere above them can be assumed to be identical. All these assumptions may be challenging to achieve. For example, in order to consider the clock to be identical, it is not enough to just connect the two antennas to the same clock. The cable delays etc. need to be accurately calibrated as well. In this work, we have investigated the third assumption, i.e., whether the atmosphere above the antennas can be considered identical. Thus, in the following we have assumed that the local tie and the identical clock can be achieved without errors.

We investigated the atmospheric variations between the antennas of a twin telescope through simulations. To do this we applied an extended version of the simulation method presented by Nilsson and Haas (2010) [6], which is able to properly take into account the distance between the antennas. We then made simulations for a possible future VGOS network, including one twin telescope at Wettzell. The distance between

1. Helmholz Centre Potsdam, GFZ German Research Centre for Geosciences, Potsdam, Germany
2. Shanghai Astronomical Observatory, Chinese Academy of Sciences, Shanghai, China
3. Instituto Geográfico Nacional, Centro Nacional de Información Geográfica, Spain

the antennas was varied in order to determine how far away from each other it is possible to place the antennas and still assume a common atmosphere.

2 Simulations

To simulate the atmospheric delays we applied the method presented by Nilsson and Haas (2010) [6]. This method uses the theory of atmospheric turbulence to model the atmospheric fluctuations. The spatial variations in the refractive index n between the positions $\mathbf{r}_1$ and $\mathbf{r}_2$ can be described by the structure function [9]:

$$\left\langle [n(\mathbf{r}_1) - n(\mathbf{r}_2)]^2 \right\rangle = C_n^2 \frac{|\mathbf{r}_1 - \mathbf{r}_2|^{2/3}}{1 + \left[\frac{|\mathbf{r}_1 - \mathbf{r}_2|}{L}\right]^{2/3}} \quad (1)$$

Here C_n^2 is the refractive index structure constant, and L is the saturation scale length. The temporal variations can be modeled by assuming that these are caused by the air moving with the wind (the frozen flow hypothesis). Using Equation 1, it is possible to calculate a variance-covariance matrix for the variations in atmospheric delay, which can then be used to generate simulated atmospheric delays. In [6], the variations in time and as a function of the direction were considered. In this work we extend this to also contain the spatial variations between two antennas of a twin telescope.

For the simulations, we needed the structure constant C_n^2, the saturation scale length L, and the wind speed. We assumed that C_n^2 is constant up to a height of 2 km and zero above, and we obtained station specific values from GNSS data [6]. For all stations we used $L = 3000$ km and a wind speed of 8 m/s [9].

In this work we made simulations for a hypothetical future VGOS network consisting of 23 stations (see Figure 1), all equipped with very fast (12°/s slew speed) VGOS antennas. At Wettzell we assumed a twin telescope, and at the other stations, we assumed just single antennas. We generated an observing schedule for this network with the Vie_Sched software [8]. Then, for each scan of this schedule, we created simulated VLBI observations [7]. These were generated from the simulated atmospheric delays as well as simulated clock errors (assuming the clocks to have an Allan standard deviation of 10^{-14} @ 50 min) and white observation noise (standard deviation of 10 ps).

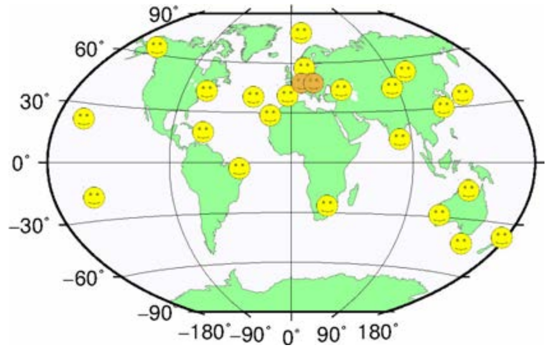

Fig. 1 The VGOS network used for the simulations in this work. At Wettzell (orange/dark gray) there is a twin telescope. All other stations (yellow/light gray) are assumed to have only one antenna.

The simulated observations were then analyzed with the Vienna VLBI Software, VieVS [1]. In the data analysis we estimated the clocks as piece-wise linear functions with 1-hour intervals, the tropospheric zenith wet delays with 10-minute intervals, tropospheric gradients with 30-minute intervals, daily station coordinates, and daily offsets of each of the five Earth orientation parameters. For the station-specific parameters of the twin telescope in Wettzell we tested four different options: (1) treating the two antennas completely independently, (2) combining the atmospheric parameters (zenith wet delays and gradients) of the antennas, (3) combining the atmospheric parameters and the clocks, and (4) combining atmospheric parameters, clocks, and station coordinates.

For the twin telescope in Wettzell, we varied the distance between the antennas between 0 m and 50 km. Of course, in reality a distance of 0 m is not possible, but it is in the simulations and corresponds to the case where the atmosphere above the two antennas is identical. For each distance we ran 100 independent simulations in order to have a sample size big enough for, for instance, the calculation of the station position repeatabilities.

3 Results

Figure 2 shows the station position repeatability of the Wettzell twin telescope as a function of the distance between the antennas for the four different analysis options. As can be seen, when no parameters are com-

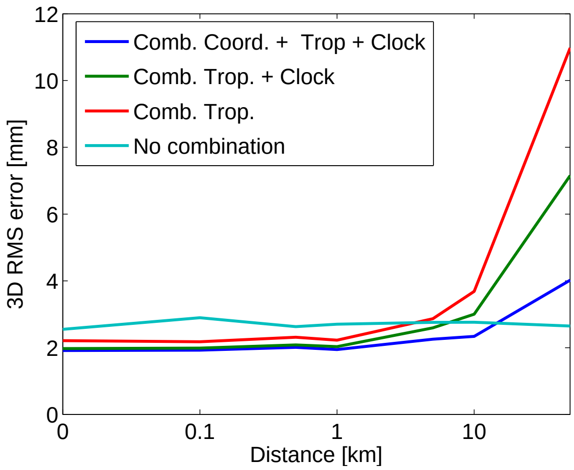

Fig. 2 3D station position repeatability of the Wettzell twin telescope as a function of the distance between the antennas. Shown are the results when treating the antennas independently in the data analysis (cyan), when combining the atmospheric delays (red), when combining atmosphere and clocks (green), and when combining atmosphere, clocks, and station coordinates (blue).

bined, there is no significant dependence on the distance. This is expected because we do not make any use of the fact that the two antennas are close to each other. When we combine the atmospheric parameters, the repeatability improves when the distance between the antennas is smaller than a few kilometers, and further improvements are obtained when also combining the clock and station coordinates.

For distances between the antennas above 5 km, the results get worse when combining the atmospheric delays. Obviously, for these large distances the assumption of an identical atmosphere above both antennas is no longer valid, which leads to errors in the estimated coordinates (and other parameters). When combining also the clocks and the coordinates the degradation of the repeatability for distances over 5 km is not that large. The reason is that unmodeled atmospheric delays mainly tend to be absorbed by a combination of station coordinates and clocks in the least squares adjustment. Thus, by limiting also these parameters, the possibility that the atmospheric variations cause errors in the station coordinates is reduced. It should however be noted that we assumed that the station coordinates and the clocks could be combined without errors, which will not be the case in reality.

4 Conclusions

The results show that combining the atmosphere for a twin telescope can reduce the errors of the estimated coordinates if the distance between the antennas is less than 2–3 km. Of course, the presented results are only valid for simulating a twin telescope in Wettzell. For another station the local conditions may be different (e.g., a more turbulent atmosphere), but we do not expect this would change the general conclusions of this work significantly. Thus, the combination of the atmospheric parameters should not be a problem for any of the planned twin telescopes but instead usually improves the station position; the actual distance between the antennas of the Wettzell twin telescope is about 75 m, and for the other planned twin telescopes, the distance will also be around 100 m.

Bigger problems will probably be obtaining an accurate enough local tie between the two antennas and connecting them to the same clock. How well this can and needs to be done is beyond the scope of this work. But the results show that even if the coordinates and clocks cannot be combined in the data analysis, the combination of the atmospheric parameters still leads to a significant increase in the station position repeatability (about 15–20%).

References

1. J. Böhm, S. Böhm, T. Nilsson, A. Pany, L. Plank, H. Spicakova, K. Teke, and H. Schuh. The new Vienna VLBI software. In S. Kenyon, M. C. Pacino, and U. Marti, editors, *IAG Scientific Assembly 2009*, number 136 in International Association of Geodesy Symposia, pages 1007–1011, Buenos Aires, Argentina, 2012. Springer. doi:10.1007/978-3-642-20338-1_126.
2. R. Haas. The Onsala twin telescope project. In N. Zubko and M. Poutanen, editors, *Proceedings 21th Meeting of the European VLBI Group for Geodesy and Astrometry*, pages 61–65, Espoo, Finland, 2013. Available from: http://evga.fgi.fi/sites/default/files/u3/Proceedings_EVGA2013.pdf.
3. H. Hase, D. Behrend, C. Ma, B. Petrachenko, H. Schuh, and A. Whitney. The Emerging VGOS Network of the IVS. In D. Behrend and K. D. Baver, editors, *IVS 2012 General Meeting Proceedings "Launching the Next-Generation IVS Network"*, NASA/CP-2012-217504, pages 8–12, 2012. Available from: http://ivscc.gsfc.nasa.gov/publications/gm2012/hase.pdf.

4. L. Langkaas, T. Dahlen, and P. E. Opseth. New fundamental station in Ny-Ålesund. In D. Behrend and K. D. Baver, editors, *IVS 2010 General Meeting Proceedings*, NASA/CP-2010-215864, pages 111–112, 2010. Available from: http://ivscc.gsfc.nasa.gov/publications/gm2010/langkaas.pdf.
5. A. Neidhardt, G. Kronschnabl, T. Klügel, H. Hase, K. Pausch, and W. Göldi. VLBI2010 - current status of the TWIN radio telescope project at Wettzell, Germany. In W. Alef, S. Bernhart, and A. Nothnagel, editors, *Proceedings 20th European VLBI for Geodesy and Astrometry (EVGA) Working Meeting*, pages 67–70, Bonn, Germany, 2011. Available from: http://www.mpifr-bonn.mpg.de/div/meetings/20thEVGA/pdf-files/EVGA-proccedings.pdf.
6. T. Nilsson and R. Haas. Impact of atmospheric turbulence on geodetic very long baseline interferometry. *J. Geophys. Res.*, 115:B03407, 2010. doi:10.1029/2009JB006579.
7. A. Pany, J. Böhm, D. MacMillan, H. Schuh, T. Nilsson, and J. Wresnik. Monte Carlo simulations of the impact of troposphere, clock and measurement errors on the repeatability of VLBI positions. *J. Geodesy*, 85:39–50, 2011. doi:10.1007/s00190-010-0415-1.
8. J. Sun, J. Böhm, T. Nilsson, H. Krásná, S. Böhm, and H. Schuh. New VLBI2010 scheduling strategies and implications on the terrestrial reference frames. *J. Geodesy*, 88(5):449–461, 2014. doi:10.1007/s00190-014-0697-9.
9. R. N. Treuhaft and G. E. Lanyi. The effect of the dynamic wet troposphere on radio interferometric measurements. *Radio Sci.*, 22(2):251–265, 1987. doi:10.1029/RS022i002p00251.

Session 2

Technology Development for VGOS

March 2-7, 2014

8th IVS

GENERAL MEETING

Shanghai, China

Dynamic Observing in the VGOS Era

James Lovell[1], Jamie McCallum[1], Stas Shabala[1], Lucia Plank[1], Johannes Böhm[2], David Mayer[2], Jing Sun[3]

Abstract What will VLBI observations be like in the VGOS Era? VGOS aims for continuous operations which will require a high level of automation and good connections between telescopes, correlators, schedulers, and operation centers. Here we describe a possible VGOS observing scenario, show some initial results from simulations, discuss some of the technology and software developments that are still required, and present some suggestions on how a fully dynamic observing system might be developed over the next few years as we transition from legacy systems to VGOS and from low to high network bandwidths.

Keywords VLBI, automation, scheduling

1 Introduction

One of the aims of VGOS is continuous VLBI observations. This is a significant departure from present IVS sessions which are typically 24 hours in length for EOP and astrometric observations at the rate of about 170 sessions per year and one hour for UT1 measurements every day of the year. Present sessions are scheduled in advance for an entire year and fixed in antenna, media, correlator, scheduling, and analysis resources.

One of the goals of VGOS is for initial data products to be made available within 24 hours of observation. It is hoped then that communication network capacities will have increased to allow stations to transfer data to the correlators in real time, doing away with the need for media and thus significantly reducing operating costs. Real time correlation also permits immediate feedback to the stations on their performance, allowing them to address many issues (hardware, software, pointing, RFI, etc.) quickly. This feedback also has the potential to allow for dynamic scheduling where, for example, sources can be rejected after their first observation if they prove unsuitable due to weaker than expected flux density. Observing bands can be shifted to avoid RFI. If an antenna is dropped due to poor performance or wind stow, the schedule can be re-optimized on the fly. Furthermore, data from the correlator could be analyzed in real time so that a scan could be observed for just the right amount of time to reach a target SNR.

Another measure to decrease operational costs that has been previously discussed is one in which there would be several VGOS Operation Centers (OCs) distributed globally. Staff at an OC would initiate an observation during their business hours and then hand over to another OC to the west at the end of their day. Sharing and transfer of antenna control is already possible, and has been successfully tested and used with the eRemoteCtrl software (Neidhardt et al., 2010).

Under VGOS, a block schedule might not need to be created for an entire year. Instead, network stations could make their antennas available whenever possible, and the OC could add them to the current session depending on need. The OC has, in effect, a pool of antennas to draw from at any given time and can select an array appropriate to the desired observing program. Antennas can be added and removed from a session dynamically.

Like the antennas, a correlator could also be treated as an allocatable resource. For example, a schedule

1. University of Tasmania
2. Vienna University of Technology
3. Shanghai Astronomical Observatory

Fig. 1 Formal errors in antenna positions (in cm) for three AUSTRAL sessions that demonstrate a successful observation (AUST11), one where an antenna drops out but no new schedule is created (AUST13) and when an antenna drops out but a new schedule is made (AUST12).

aimed at determining a full EOP solution will frequently divide the available antennas into two or more subarrays. Data from these subarrays could be distributed to different correlators to share the network load.

The first advantage of this type of dynamic observing scenario is that only the required on-source time to reach a target SNR is used, thus achieving the maximum possible number of useful scans per day. Only suitable sources are kept in the observing list and unsuitable ones rejected. Also, and more importantly, antenna-related problems are identified quickly, and schedules can be re-optimized. Real-time correlation also potentially allows for real time analysis, reducing the latency for UT1 and full EOP measurements.

2 Simulating Dynamic Observing

We have commenced work on simulations of various observing scenarios using existing data and VieVS [4] simulations to identify which of the Dynamic Observing strategies are likely to be most advantageous and how they can be implemented. Here we describe some initial results from studies of two scenarios.

Scenario 1: Loss of an antenna. We first consider a situation where an antenna is scheduled for a 24-h session but for some reason fails to participate and consider the consequences when the array is and is not re-scheduled to compensate. In this case we look at some existing observations from the AUSTRAL program (Lovell et al., 2014 these proceedings) where this was, in effect, simulated. The AUST11 session acts as our ’control’ where all five antennas (Hart 15 m, Yarragadee, Katherine, Hobart 12 m, and Warkworth) observed, and there were no significant problems. AUST13 represents a situation where one antenna (in this case Warkworth) did not observe and a new schedule was not created. Lastly, AUST12 is representative of a case where an antenna dropped out but a new schedule was made to compensate (in the actual case, Warkworth was not available for AUST12 and was not scheduled).

Figure 1 compares the observed formal errors in antenna position for these three sessions and shows a degradation of up to 40% when an antenna is dropped but the remainder are not re-scheduled (i.e. compare AUST11 to AUST13). Further, the data show that when an array is re-scheduled to compensate for a dropped antenna (AUST11 compared to AUST12) that the formal errors are maintained or even reduced to lower levels. In this case the significant improvement in errors for Hart is probably due to more scheduled scans involving this antenna as a result of not having restrictions caused by limited common source visibility with Warkworth.

Scenario 2: Antenna with low sensitivity. In this scenario we use VieVS to simulate a typical Rapid (R1) session where the Hobart 12 m antenna (Hb) was scheduled assuming an SEFD of 3,500 Jy when in fact it was 10,000 Jy. We look at the consequences of not rescheduling (the current observing paradigm) versus creating a new schedule using the new, poorer SEFD, something that could be picked up at a pre-experiment check in a Dynamic Observing mode. The results of this simulation are summarized in Figure 2 and show a clear advantage in rescheduling as the number and fraction of useful observations involving Hb returns to almost the same level as an unaffected session.

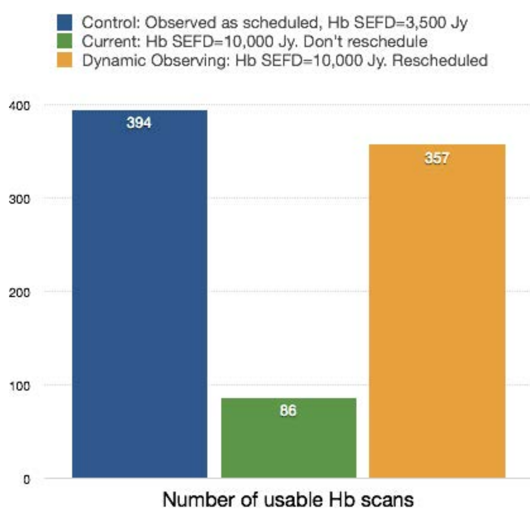

Fig. 2 Results of a VieVS simulation of an R1 session where the Hobart 12-m antenna had a significantly worse SEFD than expected.

3 The Dynamic Observing Cycle

A dynamic VGOS observing session would be divided into two main components: setup and observing. It should be possible for more than one observing session to be carried out simultaneously. It is envisaged that an operator would manage the setup stage, then initiate the main observing program. However, the main observing program would be managed by purpose-built software and be largely automatic.

Setup. The setup procedure would start with the operator in the OC allocating resources to an observing session. The operator might be starting an EOP session in which case they would choose an array of available antennas that have already been through system checks by local staff (pointing, SEFD, coherence checks, etc.) and made available to the pool. The next step would be to select the correlator or correlators that can be used to process the data. Local staff at the correlation centres would prepare their hardware and software, then make information on available resources (e.g., number of nodes) available to the OC so the correlator can be added to the correlator pool. The operator would choose other requirements, such as the desired scan SNR level, maximum number of sub arrays, data rates, default source catalog, etc.

The next step in the setup procedure is to make an observation of a bright source to obtain an initial fringe solution. The clock delays and rates obtained in this way are used in the main part of the observations. This fringe check also acts as a final array check. Absence of fringes to any antenna are indicative of a problem at the station that requires resolution before the antenna can join the array. The measured amplitude of the source on the various baselines can be used to estimate the SEFD of each antenna and verify that it meets with expectations. If fringes were weaker than expected or not found to a particular antenna, the operator would need to choose whether to leave the antenna out of the array until it is fixed, or to revise the antenna SEFD in the appropriate catalog before proceeding.

Observation. Once the setup procedure has been completed, the telescopes and correlators are ready, and the observations can begin. The operator would hand over operation of the array to the Observation Management Software (OMS).

At the heart of the OMS is the Scheduler. Much like existing scheduling software (SKED or the VieVS scheduling module), the Scheduler would choose the next source to observe given a number of constraints such as recently observed sky positions, minimum distance to move, SNR and integration time limits, the length of the experiment, etc. The Scheduler would draw on a catalog of suitable sources, a list of available antennas and correlators, all updated during the observations. Other constraints could also be accepted such as the observing schedule for a co-located SLR at a site in order to avoid pointing an antenna toward an aircraft avoidance radar transmitter. The Scheduler would allocate a source and correlator to each subarray, and the OMS would receive the information and instruct the antennas to move. Once the OMS has been notified by the antennas that they are on-source, an instruction would be sent to begin collecting data and the correlator would be instructed to commence processing. Data collection and correlation would continue until the desired SNR is reached or until a pre-specified maximum integration time had been exceeded. The key here is to make the observation as short as possible but to reach a level of sensitivity that will result in a useful baseline solution. Therefore, real-time feedback from the correlator during the observation is essential.

If the maximum specified integration time is exceeded then this indicates either an unsuitable source or a problematic antenna. The OMS would make a choice to exclude an antenna, revise its SEFD, or exclude a source as a result. Once the source observation is complete, the OMS would interrogate the Scheduler for a new source, correlator, and subarray and continue observing.

4 Technology and Software

The following paragraphs describe the current status of the key components required to make dynamic observing a reality.

Antenna control. In recent years, a significant amount of work has gone into remote control and monitoring of antennas with the eRemoteCtrl project (Neidhardt et al., 2010). This software is now used routinely for many IVS stations. For example, all three of the AuScope VLBI Array telescopes are controlled remotely using eRemoteCtrl as part of routine operations (Lovell et al., 2013). At the moment, all instructions to the antennas, samplers, and recorders are sent either manually by an operator or via a pre-prepared schedule file. However, an interface to eRemoteCtrl or to its associated server software on the host PC Field System computer could quite simply be built to allow instructions to be sent from the OMS.

Correlator control. Software correlators are now used in production geodetic VLBI and can be modified relatively easily to meet new requirements. Some of them already support e-VLBI observations but additions or modifications to the software and the interface will be required to support the observing mode described here. In the case of the DiFX software correlator (Deller et al., 2011), a client/server communications layer is required to allow interaction with the OMS.

Also, DiFX currently expects an input VEX format schedule file and a v2d file with information such as station clock offsets and rates and predicted EOPs. This information would need to be provided and processed dynamically. DiFX would also require an e-VLBI mode where a scan on a particular source could be stopped prematurely, triggered by feedback on SNR for example. This in turn requires software to monitor in real time the correlator output. Much of this already exists in DiFX through the difx_monitor software but additions would be required to trigger early integration stops and communicate back to the OMS.

Scheduling. Existing scheduling software such as SKED is already capable of automation. For example, given input parameters such as antennas, start and stop times, SNR targets, sky coverage requirements, source structure information, etc., the software can prepare an optimized schedule file for an observing session.

In some ways, programs such as SKED are already well-suited to the task. In an automated scheduling run, the next source is chosen based on what has previously been scheduled given the pre-specified requirements and constraints. This is precisely what is required for dynamic observing except one source is chosen at a time based on the success (or failure) of previous observations, rather than filling an entire 24 hours. The new challenges for scheduling software in a dynamic observing scenario are dealing with the changing input source list, antenna parameters, available antennas, and allocating subarrays to correlators (which may require changes to the VEX format).

As with the correlator, a client/server layer is also required for the scheduling software to allow communication with the OMS.

The OMS. The Observation Management Software (OMS) would coordinate the observations by accepting some initial parameters and constraints (e.g. experiment name and type, start and stop times, antenna, and correlator resources) and then conducting the observations through communications with the antennas, correlators and scheduling software. The design, building and testing of the OMS is likely to be a significant job given the need to manage several different types of experiment (simultaneously in some cases) with a high level of reliability and robustness.

High capacity networks. The high data recording rates required for VGOS will in turn require high capacity networks from the stations to the correlators to allow real-time data transfer and processing. This is discussed in more detail in the next section and is probably one of the more challenging requirements of VGOS as it spans national and international borders.

Development of Software and Operations Procedures. Probably the best approach in developing these new capabilities is to test the software and procedures at an IVS network station with two or more antennas, a software correlator, and a fast local network. This would eliminate the additional complications of managing long-distance network connections and allow developers to concentrate on building and debugging software.

5 The Transition to Dynamic Observations

There will inevitably be a period of transition from legacy systems to a fully capable VGOS network. During this time, some stations will have S/X systems and data recording rates of $\sim$1 Gbps or less, and others will have broadband VGOS systems and data rates of up to 32 Gbps. Some stations will have high capacity network connections capable of supporting the VGOS data rates in real time, while others will have VGOS recording capability but insufficient network capacity. Further, the correlation facilities must have a factor of N times the network bandwidth capability (where N is the number of stations to correlate) in order to achieve real-time processing. Unless all stations can transfer all data to the correlator in real time, data will need to be kept either at the station or the correlator until they can all be brought together for processing. Even though these network bottlenecks prevent a full VGOS implementation in the medium term, the possibility still exists to implement the most important aspects of dynamic observing with only modest network capacities.

Existing software on Mark 5 recorders such as jive5ab already permit simultaneous data streaming and local recording, so it is possible to send data for real-time processing for a subset of stations. Further, if a station or correlator has a limited connection, it may be possible to send a subset of a full data-stream (e.g. a single polarization, 1-bit data instead of 2-bit, and/or a single or sub-band) to the correlator for real-time analysis which would be sufficient for SNR measurement, dynamic scheduling, and initial data products within 24 hours, with the complete data set transferred later. If multiple correlators are available but the network bottlenecks are into the correlators rather than out of the stations, the data streams could be split by IF and sent to different correlators simultaneously. It should be noted that software development and/or testing is still required for simultaneous recording and data transfer on new recording systems such as Mark 6 and FlexBuff.

Pre-experiment checks such as fringe-finding can of course be carried out in non-real-time mode without a serious impact on observations. For example, a 10 s integration on a bright source at 32 Gbps recording rate would take a little over five minutes to transfer to a correlator with a 1 Gbps connection to the station. Even centrally coordinated pre-experiment checks, which would serve to check for telescope readiness and performance and allow the scheduling software to update antenna SEFDs and thus on-source time calculations, would be a significant step forward.

As total AGN flux density variability on timescales of months to years occurs in the sub-milliarcsec-scale jet [3], regular input from single-dish or short-baseline interferometer monitoring programs could also be used to keep flux density databases up to date. A flux density monitoring program could be coordinated between IVS stations to achieve this. Imaging of sources every few weeks from IVS data may be sufficient to determine the suitability of sources and therefore reduce the need for real-time SNR determination to optimize scan times. However, a more detailed study to assess the relative merits of these approaches is probably required.

References

1. Deller, A. T., et al. 2011. PASP, 123 , 275–287.
2. Neidhardt, A., et al. 2010. Proceedings of the 10th European VLBI Network Symposium and EVN Users Meeting: VLBI and the new generation of radio arrays. September 20–24, 2010. Manchester, UK
3. Shabala et al. 2014, J Geodesy 88, pp. 575–586
4. Sun, J., Böhm, J., Nilsson, T., Krásná, H., Böhm, S., and Schuh, H. 2014, J Geodesy, 88, pp. 449–461

Developments for the Automation and Remote Control of the Radio Telescopes of the Geodetic Observatory Wettzell

Alexander Neidhardt[1], Matthias Schönberger[2], Christian Plötz[2], Gerhard Kronschnabl[2]

Abstract VGOS is a challenge for all fields of a new radio telescope. For the future software and hardware control mechanisms, it also requires new developments and solutions. More experiments, more data, high-speed data transfers through the Internet, and a real-time monitoring of current system status information must be handled. Additionally, an optimization of the observation shifts is required to reduce work load and costs. Within the framework of the development of the new 13.2-m Twin radio Telescopes Wettzell (TTW) and in combination with upgrades of the 20-m Radio Telescope Wettzell (RTW), some new technical realizations are under development and testing. Besides the activities for the realization of remote control, mainly supported during the project "Novel EXploration Pushing Robust e-VLBI Services (NEXPReS)" of the European VLBI Network (EVN), autonomous, automated, and unattended observations are also planned. A basic infrastructure should enable these, e.g., independent monitoring and security systems or additional, local high-speed transfer networks to ship data directly from a telescope to the main control room.

Keywords Remote control, automation, e-RemoteCtrl

1. Forschungseinrichtung Satellitengeodäsie, Technische Universität München, Geodetic Observatory Wettzell
2. Federal Agency for Cartography and Geodesy, Geodetic Observatory Wettzell

1 Introduction

The visions for a VLBI Geodetic Observing System (VGOS) call for more than one antenna at one location, which will be operated continuously to derive the IVS products with a higher accuracy [Niell2005]. For a geodetic observatory, such as Wettzell, this is only possible with the same number of personnel staff and while keeping the high reliability and quality if the telescopes can be operated from one control room and if the automation is increased tremendously.

2 Remote Access and Control

The VGOS requires two or more antennas at a site, which share data recording and transmission resources, to increase the observing density [Niell2005]. For a geodetic observatory, such as Wettzell, this means that more than one antenna must be controlled by the operational staff at the same time. In the case of Wettzell, these are the 20-meter Radio Telescope Wettzell (RTW) and the two new 13.2-meter antennas of the Twin Radio Telescope Wettzell (TTW). As it is quite inefficient to have more than one responsible operator for the controlling of the different telescopes, and as it is also impractical to operate each antenna from another control room, the controlling facilities must be shared between the telescopes as well. One operator in one centralized control room must be able to control and monitor all telescopes at the location of the observatory.

Fulfilling this goal means that the operator is not directly in front of the telescope anymore while controlling it. Therefore it is necessary to enable a suitable

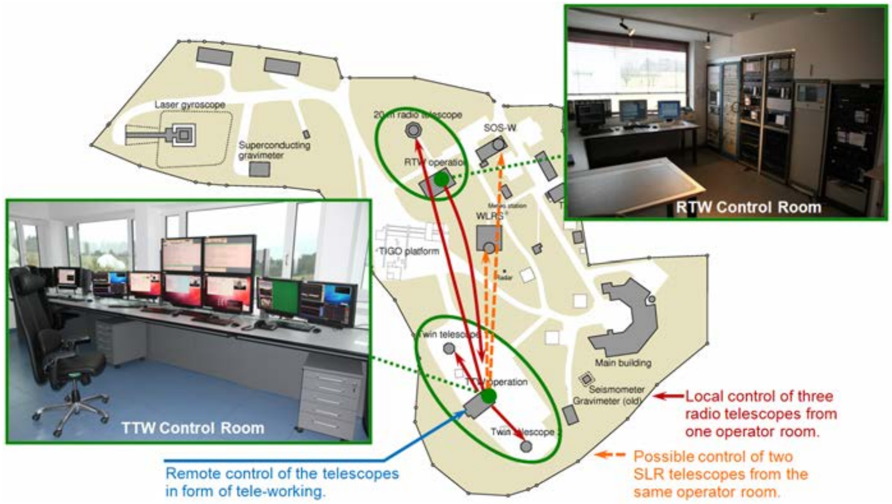

Fig. 1 The idea behind remote control at the observatory Wettzell is the control of three radio telescopes (and maybe in the future of two laser telescopes) from one operator room with an additional access from external.

remote control at the location of the observatory, which will forward the commands from the operator to the antennas and return the feedback again in a reliable way. Remote control then enables the following:

- Running all shifts of the three telescopes with the existing personnel staff will only be made possible by concentrating man power and reducing individual tasks.
- Some cases require remote supervision of student operators.
- Operator times can be shared between the different systems at the observatory.
- VLBI2010 calls for 24/7 operations, perhaps from a few centers across the globe [Lovell2013].
- Remote control can be more efficient and cost effective than local operation: one operator can be used for multiple telescopes [Lovell2013].

To allow such an operating center at Wettzell, a new operations building was constructed during the installation of the new TTW (see Figure 1). In this new building, there is enough space for a control room with at least three operator places and the corresponding facilities for information technology in a special server room. From there, all three telescopes should be controlled. Another possibility for the further future is to run the two laser ranging systems from this room, as well. Dedicated access points additionally allow connections from outside of the observatory for distant remote operators, who are at their homes or at other observatories. This should help to support operators from home during an error situation or to supervise student operators.

The used software is developed by the staff of Wettzell. It consists of two parts: an extension to the NASA Field System (FS), which forwards the monitoring and control of the FS to a remote operator, and a station specific code, supporting the FS in a dedicated way. For the first category of software, realizing remote access, the software extension “e-RemoteCtrl” is used. It is general enough to also be used at other observatories. It is set up on a generated communication middleware on the basis of Remote Procedure Calls. A server realizes the contact to the FS. Several clients can request monitoring data or can send orders in parallel. The middleware implements additional safety mechanisms, such as a process watchdog or semaphore-protected shared variables.

The whole communication is tunneled over a Secure Shell (SSH) connection and is therefore encrypted and quite safe. Additionally, each user must be authenticated and has a dedicated user role with clearly defined and monitored access rights [Neidhardt2013]. After login, each remote user is kept in his own home directory using a special setup of “rbash” as a command shell. The local systems controlling the telescopes are also situated in separate, physical networks. These “network enclaves” are at least protected by a package filter firewall from the rest of the observatory and the external Internet world.

"e-RemoteCtrl" also directly supports "IVS Live", a fully dynamic Web page for the monitoring of IVS sessions. With the injected real-time monitoring data from "e-RemoteCtrl", "IVS Live" can likewise be used to coordinate or check the global network and its current observations [Collioud2013]. Such features must be extended tremendously for the future VGOS network, to simplify the organization and to allow a general overview for coordinators, schedulers, and observatory people.

The secondly mentioned part, the station specific code, is the connection between the general FS programs and the local hardware and software. This software set consists of the antenna control (with the program "antcn"), the station module checking (with the program "cheks"), the interpreter of station-specific commands in the Standard Notation for Astronomical Procedures (SNAP) (with the program "stqkr"), a station error reporting tool (with the program "sterp"), and specific control programs. All of these programs must be developed by the observatory people to support the specific, local conditions [NASA1997]. Having regard to the planned automation, all of these modules follow a dedicated structure, which allows additional monitoring and access possibilities, separate from the FS (see Figure 2 and the following section about automation).

That additional software and equipment is necessary before the FS can be understood, taking a look onto the following points (compare [Lovell2013]):

- Nothing can be touched, moved, or turned directly (e.g., the changing of hard drive modules for the recording of VLBI data).
- Cables cannot be plugged off and on directly.
- Keyboards on location are not immediately accessible.
- Telescopes and their surroundings are not visible without additional equipment.
- Sky conditions are unratable.
- Racks and hardware equipment is not visible (e.g., lights on devices).
- Computer monitors, desktops, and module stores are not directly visible.

This requires amongst others (compare [Lovell2013]):

- Web cams to allow live video streams from the antennas to detect dangerous situations,
- network-based Video, Keyboard and Mouse (KVM) switches to forward monitor screens especially during the booting of the computers,
- network-based power switches to hardly reset hardware equipment,
- remote boot and reboot possibilities (e.g., the new antenna control at Wettzell allows a reset/reboot directly with a SNAP command in the Field System), and
- "cold stand-by" or better "hot stand-by" hardware[1].

At the observatory Wettzell, all of these equipments and possibilities are realized step-by-step and are already productive after the revision of the 20-m RTW. Successively, this equipment is additionally integrated into the system monitoring and control infrastructure, which is an extra, parallel system to detect critical or error states and warning situations [Ettl2010]. It makes its own decisions in substantially shorter time intervals, according to the given situation and parallel to the field system. Because of this, it also supports a higher degree of automation.

3 Automation

Having an additional look into the requirements for the VGOS, it becomes obvious that "continuous measurements for time series of station positions and Earth orientation parameters" [Niell2005] are planned. In principle, this calls for reliable 24/7 operations. This contrasts with the operational costs and required man power at the observatories. Taking the current situation of the VLBI group at Wettzell, currently operating the 20-m RTW, which is one of the most used geodetic radio telescopes, doubles the observation load to 24/7. This increase would require about 20 to 30 percent more man power (according to an internal investigation) if all current duties should be kept as usual. Unfortunately this is unrealistic. Enabling 24/7 while keeping the current state is only possible with an increase of automation.

Fulfilling this goal, this means that the operator is not always available at the telescope anymore. The system is started or starts automatically and processes the

[1] These are spare parts, which can be switched on or replaced quite fast ("cold stand-by") or which run parallel and take over control automatically if a hardware failure appears.

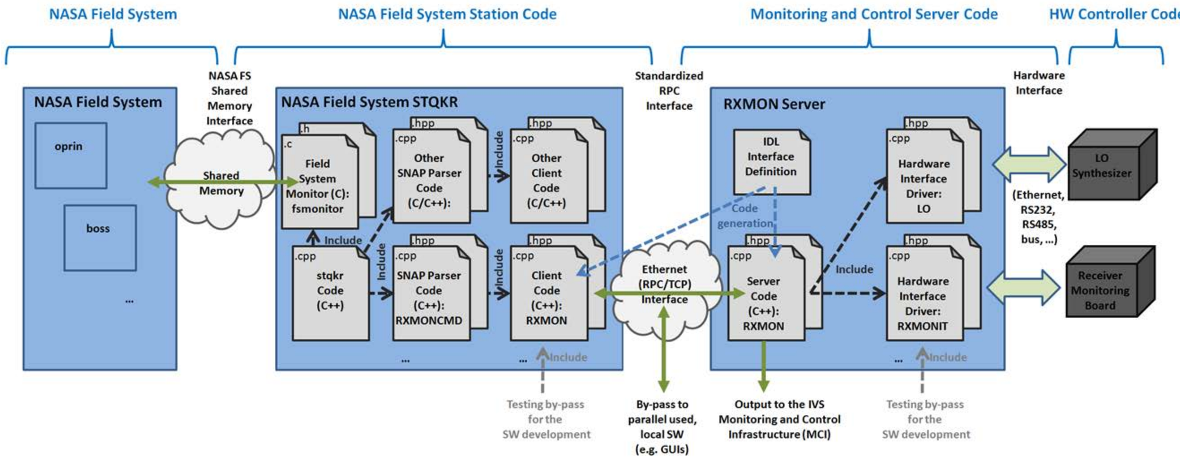

Fig. 2 The structure of local, station-specific programs, supporting a higher degree of automation and an additional system monitoring.

schedules autonomously while checking quality and safety parameters. Then automation enables the following possibilities:

- Surviving connection blackouts if the operator runs operations remotely.
- Simplification of operation workflows.
- Reduction of shifts at weekends and in the night.
- Reduction of monotonous work steps and therefore of error-prone tasks for the operator.
- Improvement of the observation quality because of a clearly defined runtime behavior.

To enable a higher autonomy of the systems at the observatory Wettzell, each hardware device is represented by a special monitoring and control server (see Figure 2), which builds a short feedback loop for the device. The server acts like an intelligent driver, checks the system state regularly, and makes decisions, keeping a stable and reliable state for the device. The local parameters and states are also forwarded to the nodes of the monitoring and control infrastructure, where all data are collected in an archive for real-time and historic data requests. These access points are used for further decisions at the following, higher control layers of monitoring and control nodes. Because the server and all other components of the central nodes are realized with the described RPC middleware, a simple, standardized access from everywhere is possible. This allows by-passes to directly control hardware, to realize Graphical User Interfaces (GUI) for dedicated devices, or to request data by faster checking loops than possible in the regular FS routine. Nevertheless, all data are also regularly available for the FS, realizing the mentioned station specific programs [NASA1997].

Nevertheless, the hierarchical system monitoring and control infrastructure offers a parallel and reliable possibility to check system states and quality parameters. It builds a safe instance to stop operations with interlock mechanisms if there are critical situations. This enables a higher degree of automation, which reduces shifts at unfavorable times, such as on weekends or during the night. It is the only possibility for allowing 24/7 VGOS observations.

3.1 Conclusion

Wettzell is on its way to realizing a site of the future VGOS. The challenges for doing this require new techniques and realizations to run the different telescopes and to operate the new 24/7 sessions. At the observatory Wettzell, this should be enabled by an increase of automated systems, which can be controlled remotely. First implementations and experiences are promising. The established solutions and the developed software are also interesting for other sites and are freely available. Over the past years, several sites made their own experiments with the software (see Figure 3). The Australian geodetic VLBI telescopes of AuScope can especially be seen as one very sophisticated and well advanced test site for such ideas.

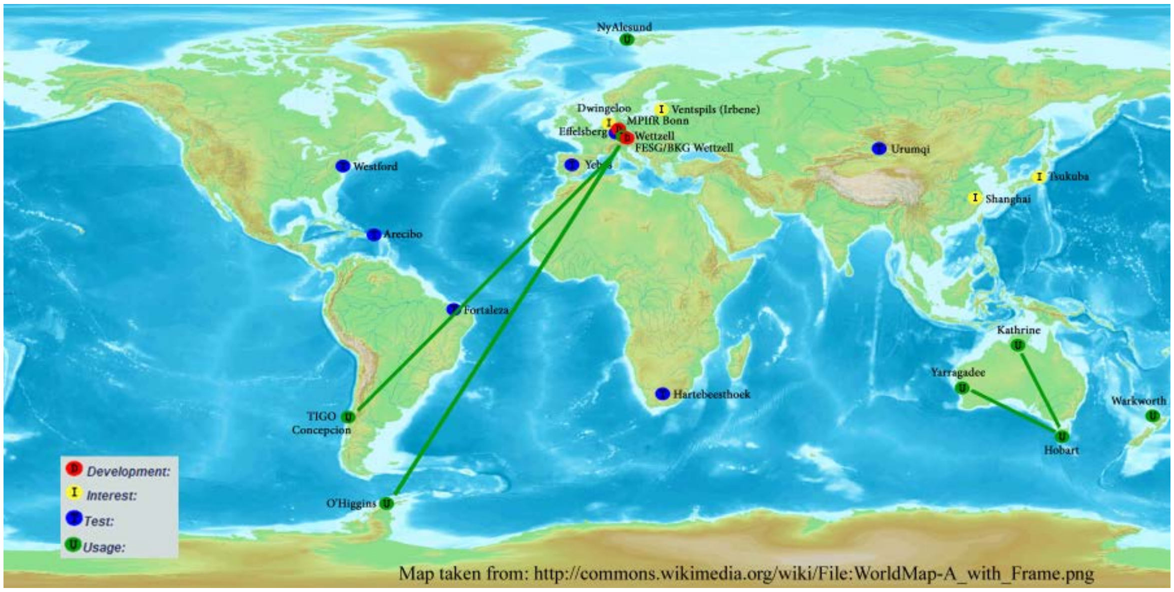

Fig. 3 The distribution of the software "e-RemoteCtrl" (beside several sites, where it was tested, a view observatories run the software regularly).

The three telescopes in Yarragadee, Katherine, and Hobart are controlled from the remote control room at the University of Tasmania, Hobart. Besides its own implementations, "e-RemoteCtrl" is an important pillar for the implementation. It demonstrates impressively that the new techniques are practical and work. Interested sites can register and download the software from: http://www.econtrol-software.de.

Acknowledgements

Special thanks should be acknowledged to all users of the software "e-RemoteCtrl", especially the people from the AuScope network in Australia, HartRAO in South Africa, and the guys from Ny-Ålesund on the island of Spitsbergen for their important and helpful feedback.

References

[Collioud2013] Collioud, A.; Neidhardt, A.: *When "IVS Live" meets "e-RemoteCtrl" real-time data ....* In: Zubko, N.; Poutanen, M. (eds.) Proceedings of the 21st meeting of the European VLBI Group for Geodesy and Astrometry, pp 17-20, *Finnish Geodetic Institute*, 2013.

[Ettl2010] Ettl, M.; Neidhardt, A.; Mühlbauer, M.; Plötz, C.; Beaudoin, C.: *The Wettzell system monitoring concept and first realizations.* In: Behrend, D.; Baver, K. D. (eds.), IVS 2010 General Meeting Proceedings, NASA/CP-2010-215864, pp 444-448, *NASA, Goddard Space Flight Center*, 2010.

[Lovell2013] Lovell, Jim; Neidhardt, A.: *Field System Remote Operations. Operation of the AuScope VLBI Array. Course script of the Seventh IVS Technical Operations Workshop*, Haystack, 2013.

[NASA1997] NASA, Goddard Space Flight Center: *Mark IV Field System. Volume 2. NASA, Goddard Space Flight Center*, 1993/1997.

[Neidhardt2013] Neidhardt, A.; Ettl, M.; Mühlbauer, M.; Kronschnabl, G.; Alef, W.; Himwich, E.; Beaudoin, C.; Plötz, C.; Lovell, J.: *Safe and secure remote control for the Twin Radio Telescope Wettzell.* In: Zubko, N.; Poutanen, M. (eds.) Proceedings of the 21st meeting of the European VLBI Group for Geodesy and Astrometry, pp 25-28, *Finnish Geodetic Institute*, 2013.

[Niell2005] Niell, Arthur; Whitney, Alan; Petrachenko, Bill; Schlüter, Wolfgang; Vandenberg, Nancy; Hase, Hayo; Koyama, Yasuhiro; Ma, Chopo; Schuh, Harald; Tuccari, Gino: *VLBI2010: Current and Future Requirements for Geodetic VLBI Systems. Report of Working Group 3 to the IVS Directing Board. NASA, Goddard Space Flight Center*, 2005.

A Cost and Complexity Survey on Emerging Technologies for the VGOS

Christopher J. Beaudoin, Peter Bolis, Brian E. Corey, Mark Derome, Christopher J. Eckert, Arthur E. Niell, Chester A. Ruszczyk, Russell McWhirter, Alan R. Whitney

Abstract Reduction of cost and complexity of VGOS technologies related to the signal chain plays an important role in the proliferation of the new VGOS stations. Focusing on hardware sub-systems ranging from the radio telescope frontend to the VLBI correlator, a survey of current and promising new VGOS-applied technologies is presented along with associated costs and implementation complexity. In the interest of brevity, we present technologies that are currently considered to be the most impactful to the VGOS.

Keywords VGOS, system, technology, survey, costs

1 Introduction

The cost of the geodetic VLBI technique is undoubtedly a limiting factor in realizing a dense network of VGOS stations. For example, the MIT Haystack Observatory is currently engaged in the development of a signal chain for the new KPGO 12-m antenna currently scheduled for installation in late 2015. The cost and installation of the signal chain for this 12-m antenna, designed and manufactured by Intertronics Solutions Inc., is nearly equivalent to the installed cost of the antenna.

The complexity of a system also plays an important role in the overall cost of a system. In the general case, reduction in the complexity of a system naturally results in a savings in overall system cost; not only in upfront costs but in operations and maintenance costs as well. For this reason, investigations of technologies that reduce the overall complexity of the VGOS signal chain can also significantly drive down the total cost of procuring and operating a VGOS system.

Fortunately for such investigations, technology advancement is a mainstay of our global society and these advancements are to the benefit of the VGOS in the interests of both cost and complexity reduction. In some cases, these technologies are the fruits of academic efforts [1, 2, 3, 4]. In commercial advancements, the economies of scale typically drive down the cost, size, and complexity of key sub-system components [5]. With emphasis on this theme, a survey of these technologies is presented in Section 2 and decomposed into 1) VGOS analog technologies, 2) VGOS mixed-signal technologies, and 3) VGOS digital technologies.

2 Emerging VGOS Technologies

Emergence of technologies with application in the VGOS is a very broad subject area spanning across physical hardware, firmware, and computer software, which can find implementations in the analog and/or digital domains. The full scope of this material cannot be covered within the limitations of this publication. Instead, we confine our survey to the presentation of hardware technologies with which Haystack Observatory is familiar and that are considered to be most critical to the VGOS signal chain. Analog, mixed-signal, and digital hardware technologies are presented in the following subsections.

MIT Haystack Observatory

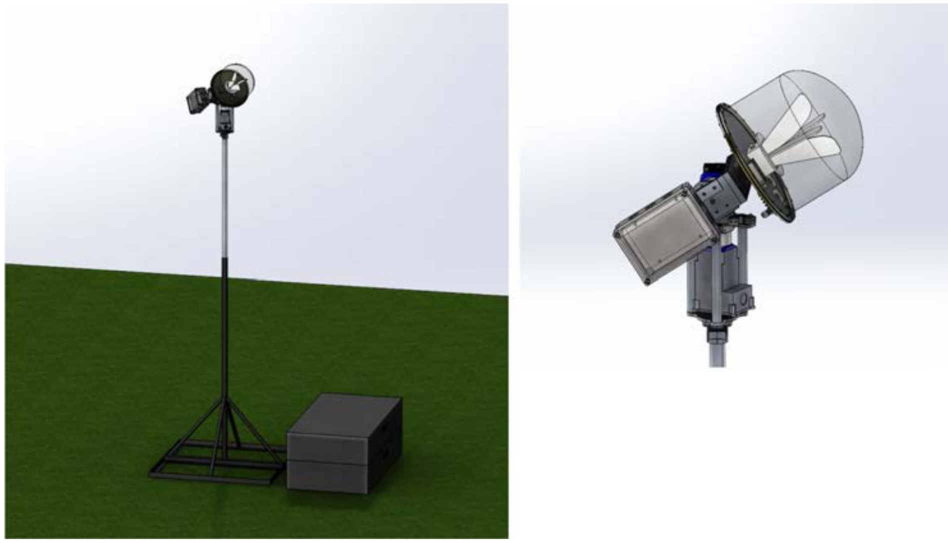

Fig. 1 3D model of the proof-of-concept (PoC) RFI monitoring system developed at MIT Haystack Observatory. The spectrum analyzer and data acquisition hardware reside in the black weatherproof enclosure. Replacement of the PoC quad-ridge survey antenna with a reflector-type antenna will improve the sensitivity and directivity of the surveying instrument.

2.1 VGOS Analog Technologies

2.1.1 RFI Surveying System

Arguably, Radio Frequency Interference (RFI) poses the most significant risk factor to the success of the VGOS. For this reason, it is necessary to conduct wideband RFI surveys as part of a VGOS site selection validation procedure to ensure that such a system can operate below a specified maximum threshold of degradation [6]. It is also desirable to carry out such surveys as part of VGOS standard operating procedures to quantify new sources of RFI and enable schedulers to develop frequency observing plans around these interferers. Portability is a desirable feature of such a surveying system to facilitate ease of deployment at prospective VGOS sites or to simply relocate the surveying antenna at an existing site.

The instrumentation needed to construct such a RFI surveying system consists of four main blocks: (1) 1–18 GHz directional surveying antenna (approximate cost 10,000–15,000 USD), (2) surveying antenna positioner (1,500 USD for the Haystack design), (3) Portable Spectrum Analyzer (20,000 USD), and (4) Data Acquisition and Logging software (Open Source). Figure 1 shows a 3D model rendering of a prototype surveying system developed by MIT Haystack Observatory to characterize RFI at the KPGO in preparation for the VGOS system installation.

2.1.2 Radio Telescope Feeds

The broad instantaneous/continuum frequency coverage specified for VGOS observations requires a radio telescope feed that possesses high aperture efficiency over nearly a decade of bandwidth. Such a feed must also facilitate integration with cryogenically-cooled low noise amplifiers to realize the system temperature specifications that have been set forth for VGOS. These two requirements impose a very challenging design problem to antenna engineers and for this reason selection of such feeds is limited. Figure 2 outlines three feeds that are reported to achieve the performance requirements and capabilities of such a design. To date, only the Eleven and Quadridged Flared Horn (QRFH) antennas have hardware realization and only the QRFH has been implemented at a VGOS station. When used as feeds for the Intertronics 12-m antenna, both antennas will provide 2–14 GHz aperture efficiency performance in excess of 50% [11].

As a two-port single-ended/unbalanced design, we consider the QRFH antenna to be the least complicated feed design. This is significant in that it facilitates

	Eleven	QRFH	Yebes-Feed
Frequency range (GHz)	1.2-14	2.2-14	2.2-14
Polarization	Dual-Linear	Dual-Linear	Dual-Circular
Port Configuration	Differential	Single-Ended	
LNAs per Polarization	4	1	1
LNAs per Feed	8	2	4
Calibration Signal Injection	Radiated or post-LNA	Radiated, pre-LNA, or post-LNA	-
Aperture Efficiency	> 50%		65% - 13.2m Telescope
Size	Diameter 210mm height 65 mm	diameter 160mm height 150mm	height 169 mm
Cost (USD)	Contact Omnisys	15K	TBD

Fig. 2 Performance and attribute comparison of the Eleven, QRFH, and Yebes radio telescope feeds.

immediate implementation as a radio telescope feed, since single-ended VGOS LNAs are readily available [1] while comparable differential LNAs are not. For this reason, the implementation cost of the QRFH is likely to be the least expensive of the designs considered in Figure 2.

2.1.3 VGOS Calibration Subsystem

The VGOS calibration subsystem plays a crucial role in mitigating instrumental biases in the signal chain, particularly those correlated with antenna pointing. If left uncalibrated, these instrumental fluctuations can degrade the accuracy of the observations and lead to systematic position errors in the geodetic solutions. MIT Haystack Observatory has designed and fabricated a 2–14 GHz calibration generator (Figure 3) that provides both amplitude and phase calibration signals, each of which possesses independent level control. Currently, this design will only support phase calibration pulses at a 5-MHz repetition rate.

This calibration signal generator also interfaces with a reference cable delay measurement system. Such a system has been developed at Haystack Observatory in response to a discovery that broadband observations were suffering from antenna-pointing-correlated reference cable delays at Westford and GGAO stations. A block diagram of this measurement system, that has demonstrated sub-picosecond scale accuracy, is shown in Figure 4. The overall cost of the VGOS calibration signal generator is approximately 30,000 USD; the cost of the cable measurement system is currently being evaluated. Designs for both components will be made available through the MIT technology licensing office.

2.2 VGOS Mixed Signal Technologies

2.2.1 Modular Monitor/Control Instrumentation

The VGOS signal chain is comprised of a variety of subsystems ranging from the receiver frontend on the telescope to the backend residing in the station operations center. Associated with these subsystems are a variety of monitor and control points that must be accessible through station infrastructure—the station's so-called monitor and control infrastructure (MCI). Examples of these monitor/control points include control of the receiver calibration noise diode, measurements

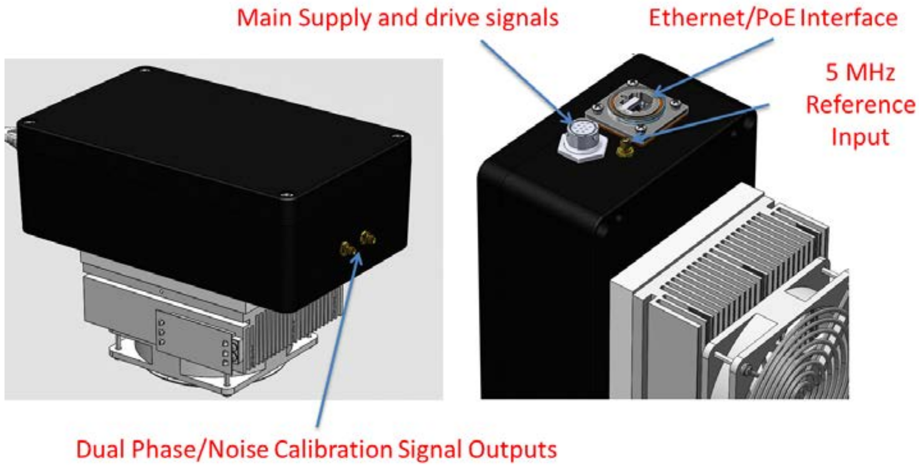

Fig. 3 3D model of the VGOS calibration signal generator developed by MIT Haystack Observatory.

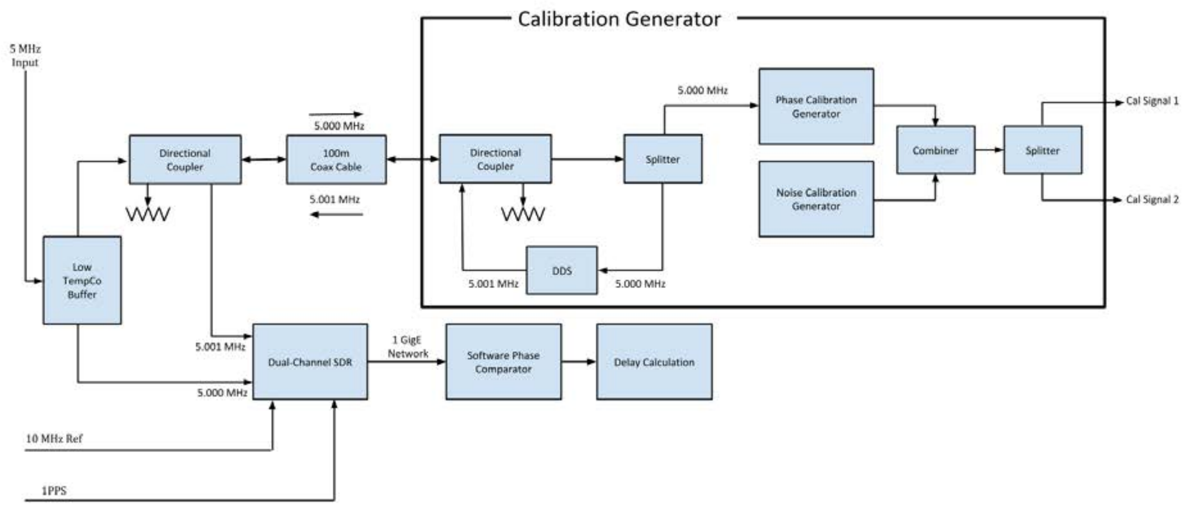

Fig. 4 Block diagram of the reference cable delay measurement system as integrated with the VGOS calibration signal generator. The instrumentation incorporated to realize this system has demonstrated sub-picosecond scale accuracy.

of ambient temperature/pressure/humidity, and control of signal level attenuators. If not carefully planned out, MCI can become a complex implementation in its own right when considering signal integrity, power supply distribution, and volume/space requirements. To minimize the need for station developers to address such considerations, MIT Haystack Observatory has developed the VLBI Data AcQuistion (VDAQ) module which is an open source hardware development expected to cost 2,000–3,000 USD and the design information will be made available through the MIT technology licensing office.

As a modular instrument, the VDAQ makes dual use of Ethernet infrastructure. The Ethernet backbone provides both a communications and electrical power interface to the module. This feature of the VDAQ and its small form factor ($13 \times 10 \times 2.5$ cm, see Figure 5) allow it to be deployed to space-limited locations where MCI is needed. This modular concept also serves to minimize issues related to signal integrity since sensors and signal monitors can be placed in close proximity to the module, which can also serve as a distributed power supply. The following provides a breakdown of the interfaces that the VDAQ module will support:

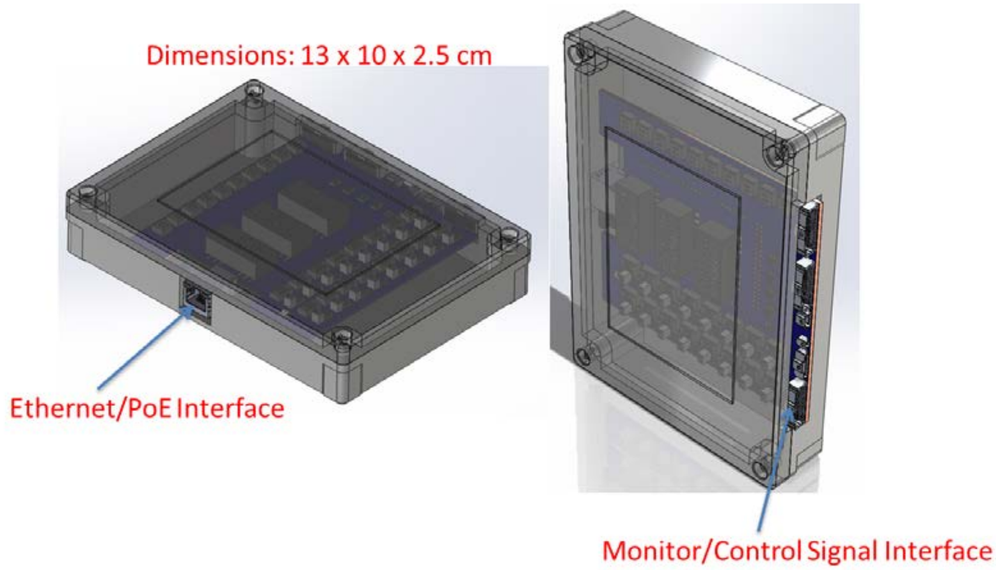

Fig. 5 Notional 3D model of the VLBI Data Acquisition (VDAQ) module.

- Digital Communications
  - RS232
  - I^2C
  - SPI
  - Ethernet
- Isolated DC Power Sources
- 16 Analog Monitors
  - Single-ended or Differential
  - Isolated or Non-Isolated
  - Configurable signal conditioning
- 40 Digital Monitors or Controls
  - Ten Isolated Monitors
  - Ten Isolated Controls
  - 20 Non-isolated Monitors and/or Controls

2.2.2 High Speed Samplers

In some sense, an analog-to-digital converter serves as the frontend to the VGOS signal chain backend. In order to support the 1-GHz IF band VGOS specification with quantizers possessing sufficient bit depth to accommodate RFI, high speed samplers, by current standards, are necessary to meet this specification [7]. Note that in this context, speed refers to data rate and not sampling rate; the latter is a component of the former. The Collaboration for Astronomy Signal Processing and Electronics Research (CASPER) has realized two such samplers of note to this end.

The first sampler, model ADC1-3000-8 [8], will clock at sample rates up to 3 GSps with an eight-bit quantizer and supports digitization of a single IF. The ADC1-3000-8 sampler demultiplexes the eight output data streams from the 3-GSps digitizer into 32 data streams at 375 MHz on both edges of the 375-MHz clock waveform (i.e., double data rate – DDR). This demultiplex operation provides relief on the clocking speed at which the FPGA data processor must operate, which is significantly limited relative to that of the digitizer. This sampler can be purchased from DIGICOM Electronics, Inc. at a cost of 2,500 USD.

The second sampler, model ADC1-5000-8 [9], will clock at an aggregate sample rate up to 5 GSps through the use of two digitizing cores. This sampler can be purchased in two configurations: (1) nondemux and (2) demux. The demux mode allows the full bit depth of the samples to be captured at a slower rate relative to the nondemux configuration which provides relief on the speed at which the FPGA data processor must be clocked. In both configurations, the sampler can be setup for interleaved operation (5 GSps digitization of a single IF) or dual IF operation (2.5 GSps digitization of two IFs). In either operating mode, the aggregate data rate remains the same. However, as a VGOS high speed sampler, the dual IF operating mode is far more attractive, since this mode will support digitization of two VGOS IF bands, whereas the ADC1-3000-8 will only support digitization of a single IF band. This sampler can also be purchased from DIGICOM Electronics Inc. for 1150 USD. This represents a savings of more than a factor of four in terms of Dollars per IF band relative to the ADC-3000-8.

2.3 Digital Technologies

2.3.1 FPGA Processing

The CASPER has also developed the next (2nd) generation of its Reconfigurable Open Architecture Computing Hardware (ROACH2) board [3] that is shown in Figure 6. This hardware integrates an FPGA processor and an integrated PPC onto one consolidated processing unit. The FPGA performs the processing-intensive digital operations, while the PPC serves as a communications and configuration interface into the FPGA. The ROACH2 FPGA is a Xilinx Virtex6 XC6VSX475T which is reported to support clock rates up to 625 MHz. At double data rate speed, this FPGA can support data transmission on a single physical transmission line (i.e., signal lane) up to 1.25 Gbps. Given that the ROACH2 possesses dual 40 lane signal lanes into the FPGA through its ZDOK interfaces, the ROACH2 can theoretically support a total aggregate data rate of $2 \times 40 \times 1.25 = 100$ Gbps. This represents a 10% improvement in speed relative to the Virtex5 XC5VSX95T FPGA which is integrated into the ROACH1 [3]. The significant gain in the Virtex6 over the Virtex5 are the gains in computing resources (e.g., 2,014 DSP slices V6 vs. 640 DSP slices V5) that facilitate more parallelized operations (e.g., 64 vs. 16 channel polyphase filter bank). The ROACH2 hardware can be purchased from DIGICOM Electronics, Inc. and the cost as of the submission date of this document is 12,000 USD.

For VGOS, the role of input data rate to the digital backend processor is twofold. Firstly, increased data rate facilitates consolidation of digital processing hardware. The more samplers that can be accommodated by a single digital processing hardware unit, the less complex the overall station hardware becomes. Secondly, for a given frequency IF sampling rate (VGOS standard IF bandwidth requires a rate of 2 GSps), increased data rate translates into allowance of digitizers possessing more dynamic range (i.e., more digitization states). This, in turn, provides more immunity to RFI and improves the saturation margin of the overall signal chain.

Fig. 6 Photo image of the Casper ROACH2 computing hardware circuit board.

2.3.2 Digital Recording

The Mark 6 16-Gbps data recorder [4] was developed at MIT Haystack Observatory through a commercial partnership with Conduant Corporation. The Mark 6 recorder was developed as an open-source software development and makes use of generic, high-performance commercial-off-the-shelf hardware. This recorder is available in 8 or 16 Gbps models. The latter requires a diskpack expansion chassis to circumvent the limitations on hard disk write speeds. With solid-state disk drives (SSDs), the recorder is expected to achieve rates up to 64 Gbps.

The cost of the 16-Gbps model of the Mark 6 is 14,000 USD while that of the 8-Gbps model is 11,000 USD. The diskpack carrier is identical for both models, costs 500 USD, and can be populated with up to eight recommended COTS SATA hard disks. As of the date of this publication (2014 Apr 30), a suitable 2 TB Seagate Barracuda hard disk can be purchased for 85 USD so that a 16-TB Mark 6 diskpack can be constructed for 1,180 USD including the cost of the diskpack carrier. The Mark 6 8/16 Gbps models require a total of two and four diskpacks, respectively, to sustain the maximum data rate. Therefore, the total minimum cost to operate the 8 and 16 Gbps models with 16-TB diskpacks is 13,400 USD and 18,700 USD, respectively.

Two Mark 6 recorders will satisfy the VGOS requirement on data recording rates (32 Gbps [10]) and SSDs promise to condense the requisite hardware to a single recorder. This feature of the Mark 6 significantly reduces the complexity of the VGOS signal chain. As a matter of example, a single Mark 6 recorder can sustain data storage at a rate equivalent to the aggregate data rate of four Mark 5C recorders, eight Mark 5B+ recorders, or 16 Mark 5B recorders. The reduction in complexity represents a significant savings in upfront procurement costs for the VGOS signal chain. Furthermore, the Mark 6 is capable of supporting diskpacks with much denser data storage than was possible by its predecessors. This fact also represents a significant cost savings in operations and maintenance, since more data can be stored onto fewer diskpacks, which translates to fewer diskpack procurements and reduced shipping costs.

3 Summary

Start-up procurement costs for a VGOS station are significant, as are the costs to operate and maintain these stations. For these reasons, administrators should be cognizant of the costs associated with emerging VGOS technologies and system developers with the associated complexities for operations and maintainability. To limit the scope of this survey, we presented only those technologies that are currently considered to be most impactful to the VGOS. The following outlines procurement costs for the technologies described in Section 2:

- RFI Monitoring System: ∼40,000 USD
- QRFH: 15,000 USD
- Calibration Signal Generator: ∼30,000 USD
- VDAQ: ∼2,000–3,000 USD
- High Speed Samplers
  - ADC1-3000-8: 2,500 USD
  - ADC1-5000-8: 1,150 USD
- ROACH2: 12,000 USD
- Mark 6
  - 16-Gbps Model: 14,000 USD
  - 8-Gbps Model: 11,000 USD
  - Empty Diskpack: 500 USD

References

1. "LNF-LNC1_12A 1-12 GHz Cryogenic Low Noise Amplifier." Low Noise Factory. Web. 2014 Apr 29. *http://www.lownoisefactory.com/files/6113/4599/9240/LNF-LNC1_12A.pdf*
2. A. Akgiray, S. Weinreb, Q.A. Imbriale, and C. Beaudoin, "Circular Quadruple-Ridged Flared Horn Achieving Near-Constant Beamwidth Over Multioctave Bandwidth: Design and Measurements," IEEE Trans.Ant. Propag., vol. 61, no. 3, pp. 1099–1108, March 2013.
3. "ROACH-2 Revision 2." Collaboration for Astronomy Signal Processing and Electronics Research. Web. 2014 Apr 29. https://casper.berkeley.edu/wiki/ROACH-2_Revision_2
4. Whitney, A.R., Beaudoin, C.J., Cappallo, R.J., Corey, B.E., Crew, G.B., Doeleman, S.S., Lapsley, D.E., Hinton, A.A., McWhirter, S.R., Niell, A.E. Rogers, A.E.E., Ruszczyk, C.A., Smythe, D.L., SooHoo, J., Titus, M., (2013) Demonstration of a 16 Gbps per Station Broadband-RF VLBI System. PASP, 125, pp. 196–203.
5. "Virtex-6 Family Overview." Xilinx. Web. 2014 Apr 29. http://www.xilinx.com/support/documentation/data_sheets/ds150.pdf
6. C. Beaudoin, B. Corey, B. Petrachenko: Radio frequency compatibility of VLBI, SLR, and DORIS at GGOS stations. American Geophysical Union, Fall Meeting 2010, abstract #G11B-0638. http://ivscc.gsfc.nasa.gov/technology/vlbi2010-docs/AGUPoster2010.pdf
7. B. Petrachenko. The Impact of Radio Frequency Interference (RFI) on VLBI2010, IVS 2010 General Meeting Proceedings, pp. 434–438.
8. "ADC1-3000-8." Collaboration for Astronomy Signal Processing and Electronics Research. Web. 2014 Apr 29. https://casper.berkeley.edu/wiki/ADC1x3000-8
9. "ADC1-5000-8." Collaboration for Astronomy Signal Processing and Electronics Research. Web. 2014 Apr 29. https://casper.berkeley.edu/wiki/ADC1x5000-8
10. B. Petrachenko et. al. "Design Aspects of the VLBI2010 System." Progress Report of the IVS VLBI2010 Committee, NASA/TM-2009-214180, Hanover, MD: NASA Center for AeroSpace Information, p. 10 and 27–28 June 2009.
11. C. Beaudoin. "A Cost and Complexity Survey on Emerging Technologies for the VGOS." IVS 2014 General Meeting Presentations. Web. 2014 Apr 29. *http://ivs2014.csp.escience.cn/dct/attach/Y2xiOmNsYjpwZGY6Njc3ODc=*

Broadband Feeds for VGOS

Miroslav Pantaleev[1], Leif Helldner[1], Bhushan Billade[1], Marianna Ivashina[2], Oleg Iupikov[2], Carlo Bencivenni[2], Jian Yang[2], Per-Simon Kildal[2], Terese Ekebrand[3], Jan Jönsson[3], Yogesh Karandikar[3], Anders Emrich[3]

Abstract The upcoming VGOS network aims at using dual polarization observations and a much wider bandwidth than traditional geodetic VLBI. This requires a new type of broadband feeds. Several such broadband feeds have been developed during the last years, among them the Eleven-feed and the Quadruple-Ridged Flared Horn (QRFH). In this paper we give an overview of broadband feeds for VGOS and compare their performance.

Keywords Very Long Baseline Interferometry, radio telescope, Eleven feed, QRFH, wideband feed, cryogenic technology

1 Introduction

The future development of geodetic VLBI (Very Long Baseline Interferometry) requires the design of observing systems based on small, fast-moving, single-beam, dual-reflector antennas covering the frequency range 2.2–14 GHz [1]. Similar are the requirements for the mid-frequency dish array of the SKA (Square Kilometer Array) [2] which currently entered design phase. Both projects pushed for the development of a variety of UWB (Ultra Wide Band) feeds. Among them are worth noting the ATA Feed [3], QSC (Quasy Self Complementary) Feed [4], and Inverted Conical Sinuous antenna [5] (see Figure 1). UWB feeds for different applications and different frequency ranges are

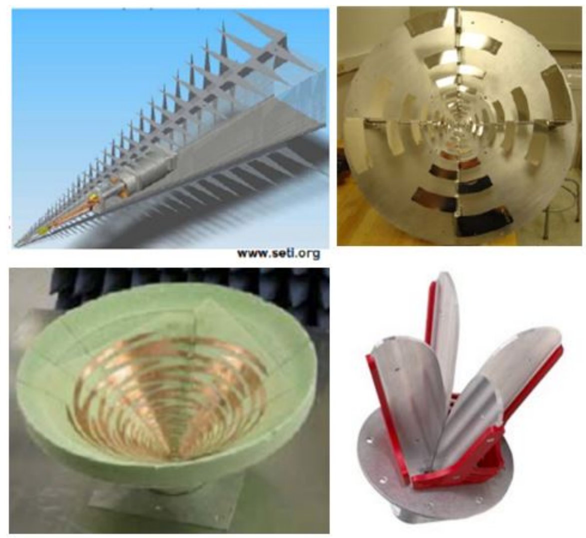

Fig. 1 Various UWB feeds: (top left) ATA feed, (top right) QSC feed, (bottom left) Inverted Conical Sinuous antenna, and (bottom right) ETS Lindgren feed.

also available as commercial products. For example, vivaldy type antennas from ETS Lindgren [6] were used for the VLBI2010 proof-of-concept tests at MIT Haystack Observatory [7]. Since the requirements imposed on the radiation performance and reflection coefficient for the UWB feeds for the VLBI2010 applications are quite complex and strict, not all of the research groups working on feed development were able to continue their work with the integration of the feed into a cryogenic system for use on a radio telescope. It is also that each UWB feed has certain disadvantages. For example, the ATA feed's beam width and phase center location vary with frequency, which leads to a low aperture efficiency. The quasi self-complementary antenna is also a log-periodic dual-dipole-like antenna,

1. Onsala Space Observatory
2. Antenna Group, Department of Signals and Systems, Chalmers University
3. Omnisys Instruments

but it has a polarization that squints with frequency and no hardware has yet been realized above 4 GHz.

The two feeds which have good radiation properties and were integrated into cryogenic systems for installation on a telescope are the QRFH (Quad-Ridged Feed Horn) [12] and Eleven Feed [13], and they are discussed and compared further in this paper with the main goal of providing a high level description of the two VGOS feed design alternatives using published results based on simulations, tests, and scientific observations performed by various research groups and institutions. References are cited for the detailed descriptions of various designs and tests. In this way, the interested reader may obtain more detailed information.

2 VGOS Antennas and Feed Requirements

Sensitivity calculations show that the goal of 2400 Jansky is achievable with 12-m antennas equipped with a receiver with a noise temperature of about 35–40K. For the VGOS frequency range the feed is compact enough for cryogenic integration. This approach reduces the contribution of feed resistive loss to the receiver noise and also simplifies the feed–LNA interface, since for a system with the feed at ambient temperature a vacuum feedthrough is required to interface to the LNAs in cryostat. This feedthrough introduces extra losses compared to an entirely cryogenically integrated feed. An additional disadvantage of a feed at ambient temperature is that the system is more complex mechanically. Consequently, size and cryogenic cooling concerns (such as outgassing and thermally induced mechanical stress) play important roles in the design of decade-bandwidth feeds for VGOS radio telescopes. Due to the wide opening angle of the UWB feeds the usual choice for the reflector optics design is the dual-reflector, axisymmetric design with ring-focus sub-reflector [14]. There are several antenna manufacturers (Intertronics Solutions, MT Mechatronics GmbH, and Vertex Antennentechnik GmbH) offering such designs with 12-m or 13-m main reflector diameter. The main advantage of the ring-focus design is that the aperture efficiency is kept at a reasonably good level and the blockage of the feed cone and supporting struts is minimized. In addition, the construction of the feed tower is mechanically very rigid and also allows easy access to the receiver and electronics as compared to primary a focus dish. The f/D for reflector systems from different manufacturers spans the range 0.35–0.5; thus, these systems are well suited for UWB feeds.

3 Eleven Antenna

The Eleven antenna is a decade-bandwidth, log-periodic, dual-dipole array. It was originally proposed in 2005 by P. S. Kildal [8]. It was designed as a feed for reflector antennas and has been demonstrated for radio telescope applications because of features such as a nearly constant beamwidth width, directivity of about 11 dBi, a fixed phase center location (over the entire decade bandwidth), and low profile and simple geometry. Several hardware implementations, operating in frequency bands ranging from 400 MHz to 2 GHz and 2–14 GHz, were realized. The first successful attempt to make a high frequency model working up to 10 GHz was developed in 2007, but it suffered from some mechanical and cryogenic problems. These problems were solved with the design developed in 2009 and described in [13]. The hardware realization of the current VGOS version of the Eleven feed is shown in Figure 2.

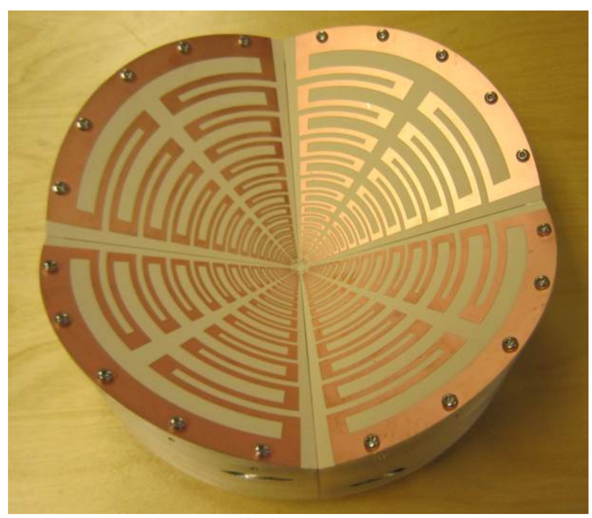

Fig. 2 Hardware realization of the current VGOS version of the Eleven feed.

The Eleven feed can receive dual linearly polarized waves, or, alternatively, it can be configured to receive circular polarization by means of quadrature combination of the two orthogonal linearly polarized ports, either by hardware or by software after detection. The antenna, for each linear polarization, consists of two oppositely-located log-periodic dipole arrays, i.e., two dipole petals. The opposite dipole pairs are separated by half a wavelength and located above a ground plane. Each pair constitutes a so-called petal and the pair of two opposite petals is forming one linear polarization. The dual-polarized Eleven antenna has four equal petals, as shown in Figure 2. The radiation field function of the Eleven feed is determined by the geometry of the four petals, which also has a strong impact on the input reflection coefficient. The goal of the electric design of the present Eleven antenna is to minimize the reflection coefficient at the input port of the petals, and at the same time to retain a good radiation performance, between 2.2 and 14 GHz.

An analytic or quasi-analytic analysis of the radiation field function of the Eleven antenna is only available for the basic geometry, i.e., for one pair of folded dipoles over an infinite ground plane, which provides the optimum ranges of the dimensions of each radiating dipole pair for the best radiation pattern shapes. An analytical impedance model for the multiple cascaded folded dipoles is not yet available. Therefore, the optimum dipole petal geometries for low input reflection coefficients must be determined by numerical analysis, using a general electromagnetic solver. Unfortunately, this is very time consuming, as the size of the whole log-periodic dipole petal geometry is very large in terms of wavelengths at the highest frequency. Numerical optimization becomes almost impossible, unless the log-periodic variation is accounted for in some way to reduce computation time. Therefore, a special computational approach, referred to as the partial array method for log-periodic geometries, was developed. The partial array method can be used to predict the reflection coefficient of a complete large log-periodic array from the S parameters of a sub-component of the log-periodic pattern. With this technique, the computation time is considerably reduced, and thereby allows for extensive optimizations. The partial array method and genetic algorithm is used to optimize the dimensions of the dipole petals, which provides the lowest reflection coefficient for a linearly polarized Eleven antenna. This means that only two opposing dipole petals are analyzed at a time, with both being correctly excited (equal amplitude and phase), and the dimensions that give the best radiation field functions are chosen. The radiation performance of the feed is judged by the values of the feed efficiency, i.e., the aperture efficiency of the blockage-free prime focus reflector with a certain subtended angle, as seen from the focal point. A goal of the simulation is also to keep the resulting reflection coefficient of the optimized linearly-polarized Eleven antenna, as simulated by CST Microwave Studio [9], low (preferably below -10 dB) over 2–14 GHz, when referred to an input balanced port impedance of 200 ohm on both dipole petals. The 200-ohm balanced input port impedance appears to be intrinsic to the Eleven antenna.

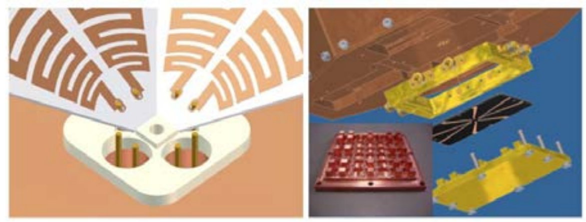

Fig. 3 View of the central region of the Eleven feed (left) and back side of the ground plane of the Eleven Feed with the 8-port and SMA connectors (right).

In the center of the geometry each dipole petal is connected to a balanced twin-lead transmission line, with a characteristic impedance of 200 ohms (Figure 3). The so-called center puck supports the petals and provides alignment for the twin lead lines. The two twin-lead transmission lines are connected to an impedance transformer realized in microstrip and located on the back side of the ground plane. The transformer output is a 50-ohm standard SMA connector. The four ports of the oppositely-located petals must be combined with the same amplitudes and phases in order to receive one linear polarization. This is usually achieved by connecting the two ports of each array to quadrature hybrid and then feeding the output of the hybrids connected to opposite placed dipole arrays via power combiner. Similarly, the two opposing pairs of orthogonal petals must be combined to receive the orthogonal linear polarization. The feeding network for a single polarization configuration is shown in Figure 4.

The reflection coefficient of the Eleven feed is overall less than -10 dB over the 2.2–14 GHz range. The simulated reflection coefficient of the Eleven feed is shown in Figure 5. The measured performance is quite close to the simulation. The same applies for the mea-

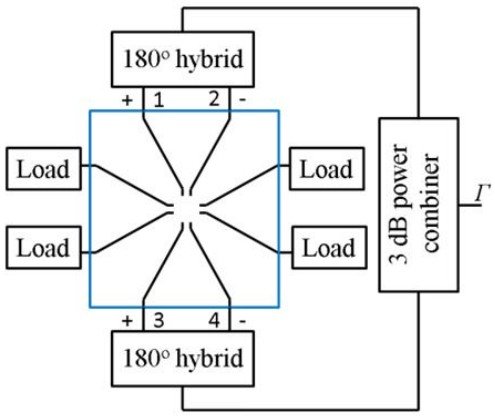

Fig. 4 Feeding configuration for the Eleven feed.

sured refection coefficient of the Eleven feed at cryogenic temperature. The use of SMA connectors and tin solder that are well suited for cryogenic applications minimizes the possibility of getting cracks in the solder after multiple thermal recycling.

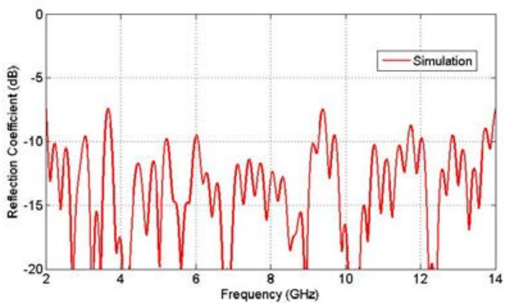

Fig. 5 Simulated reflection coefficient of the Eleven feed.

As seen in Figure 6, the beam width of the Eleven feed is nearly constant over the VGOS frequency range. The phase efficiency is high due to the nearly constant location of the phase center over the frequency range. The cross polarization level for the 2.2–14 GHz is relatively low. The radiation efficiency (ohmic loss) of the Eleven feed is between -0.1 dB and -0.4 dB over 2–8 GHz, and between -0.4 and -0.5 dB up to 14 GHz. The impact of the ohmic losses on the overall system noise is minimized since the petals are at a physical temperature of about 30 K. Y-factor tests done at Onsala Space Observatory showed that the receiver noise is about 20 K over the 4–10 GHz range slightly rising to about 30 K at the lowest and highest edges of the band.

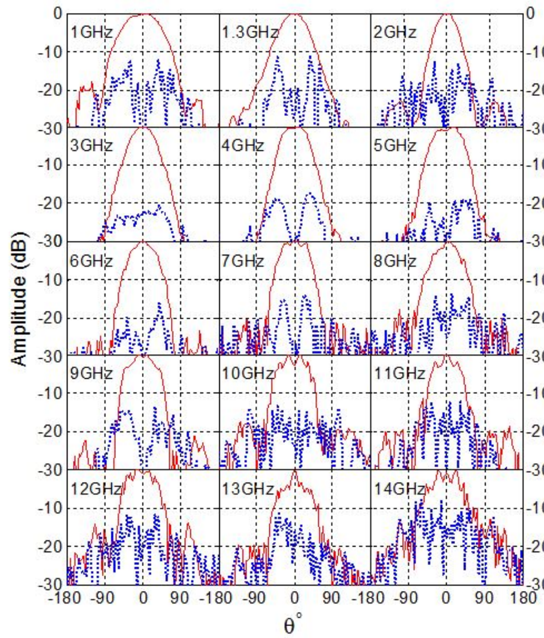

Fig. 6 Measured co-pol (red curve) and cross-pol (blue curve) patterns of the Eleven feed.

The cryogenic integration of the Eleven feed for commercial applications suitable for VGOS is done by Omnisys Instruments [10]. Figure 7 shows a CAD model of the cryostat developed at Omnisys. The Eleven feed is integrated at 20K physical temperature together with LNAs from Low Noise Factory [11] installed on a temperature-stabilized bracket to improve the gain and phase stability of the system. The system also incudes directional couplers for phase- and noise calibration signals injection.

4 QRFH

This section builds upon the recent publications of Akgiray [12, 16] and also on recent work done at Chalmers University during 2013 and reported in [18]. The most distinct feature of the Quad-Ridge Flare Horn (QRFH) with respect to the Eleven feed is its capability to form a nearly constant beam width pattern and to be optimized for a relatively large range of reflector subtended angles. This feed requires one single-ended

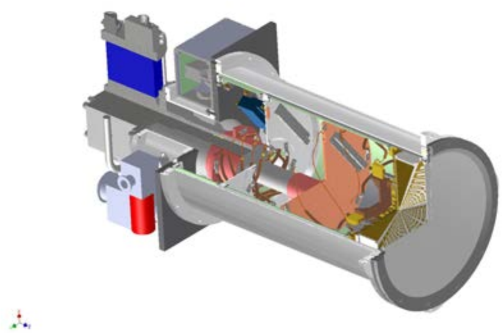

Fig. 7 Commercial realization of the cryogenic front-end for VGOS. [Courtesy of Omnisys Instruments.]

Low Nose Amplifier (LNA) per polarization; and its input impedance can be optimized for a reference (interface) impedance value between 50–100 ohms.

The QRFH is a circular horn with four perpendicular inset ridges. Three main sections are identifiable: (i) the tapered transition from the circular waveguide to the radiating aperture of the horn), (ii) the feeding section, and (iii) the back short section (see Figure 8). The taped profile realizes the transition from the circular waveguide to the radiating aperture, while supporting the dominant modes. Both the horn and profiles of the ridges are tapered. Each pair of the oppositely oriented ridged is associated with a separate polarization. The feeding of each pair is realized via a coaxial cable connected to a port on the external wall of the horn. Below the feeding section, a back short cavity is realized. This section is realized to support the transition from the coaxial line to the ridge propagation section, while radiating only in the direction of the horn aperture.

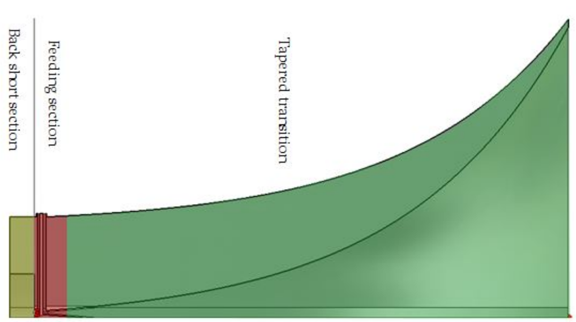

Fig. 8 Cross section of the QRFH.

Among all the parameters describing the quad-ridge horn geometry, parameters defining the ridge and sidewall profiles play a critical role in determining the performance of the horn. A number of different profiles were considered in [12], but the most promising type was found to be the exponential profile.

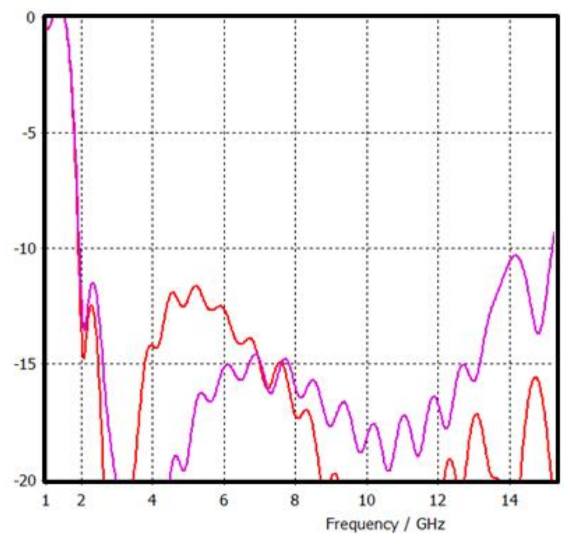

Fig. 9 Reflection coefficients of the QRFH – Chalmers design.

Reflection coefficients for different designs of the QRFH were presented in [16] and similar results were achieved in the design reported in [18]. The reflection coefficient for the QRFH design done at Chalmers is shown in Figure 9. Beam patterns from the same study are shown in Figure 10; as can be seen, the beam width is constant over the frequency range.

The QRFH designed at Caltech was successfully implemented and is currently used at MIT Haystack Observatory [17]. Figure 11 shows a 3D CAD drawing of the QRFH integrated in a 20 K physical temperature cryostat together with UWB LNAs from Caltech University. The system also incudes directional couplers for phase- and noise calibration signals injection.

5 Comparison

A document providing a comparison of the different VGOS feed alternatives was published in February 2013 [19]. In the document both the Eleven feed and

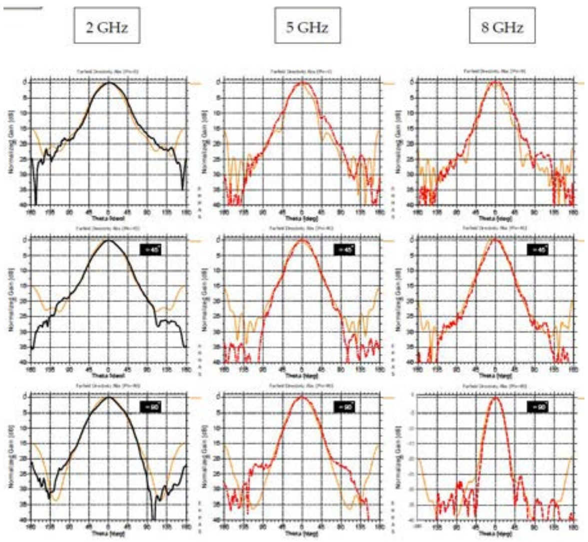

Fig. 10 Beam patterns of the QRFH – Chalmers design.

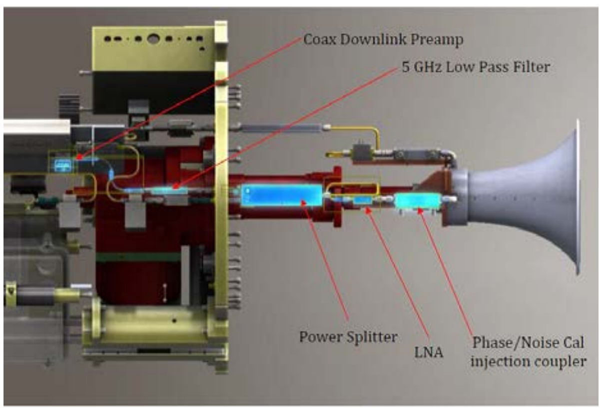

Fig. 11 QRFH integrated into a cryogenic front-end. [Courtesy of Chris Beaudoin, MIT Haystack Observatory.]

the QRFH feed as well as triple-band feeds were described. Here we concentrate on the UWB feeds and for completeness present the comparison table from [19]. The aperture efficiency calculations were performed in axisymetric, dual-reflector system with ring focus type sub-reflector. The data for the antenna geometry was provided by InterTronic Solutions Inc (Figure 12).

The beam pattern data set for the QRFH was provided by Ahmed Akgiray from Caltech University. The sampling in theta and phi was 1 and 15 degrees, respectively, with 100-MHz steps over the 2–12 GHz frequency range. The beam pattern data set for the Eleven feed was provided by Jian Yang from Chalmers University. The sampling in theta and phi was 1 and 5 degrees, respectively, with 150 MHz steps over the 1–14 GHz frequency range. Both data sets were for simulated feed patterns. The beam patterns were imported into GRASP with a MATLAB script and the position of the feed in the reflector system was optimized for the phase efficiency at the sub-reflector. Then GRASP was used to calculate the far-field pattern of the feed reflector system. The last step was to feed the far-field patterns into MATLAB and calculate the phase efficiency and cross-pol of the feed–reflector system.

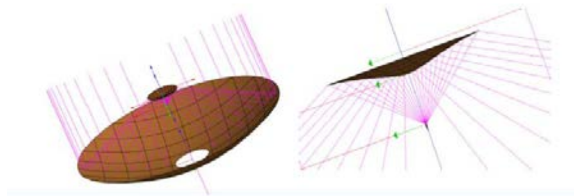

Fig. 12 Intertronics axisymetric, dual-reflector system with ring-focus sub-reflector.

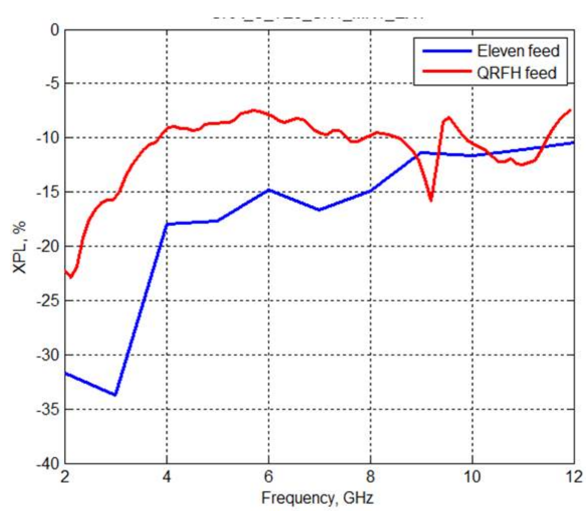

Fig. 13 Cross-pol for the Eleven feed and the QRFH feed.

The cross-pol for the QRFH and Eleven feeds are compared in Figure 13. As seen the cross-pol of the QRFH is worse than the Eleven feed. The dual reflection in the Cassegrain system minimizes this effect for both feeds but as Figure 14 shows the cross-pol level for the Eleven feed is well below -25 dB, while for the QRFH it is around -15 dB over the VGOS frequency range.

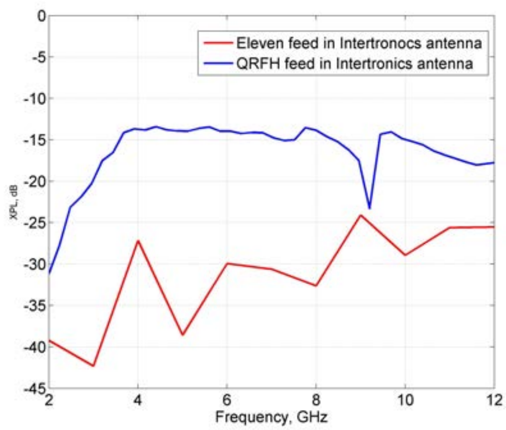

Fig. 14 Cross-pol for Eleven feed and QRFH in Intertronics axi-symetric dual reflector system with ring-focus sub-reflector.

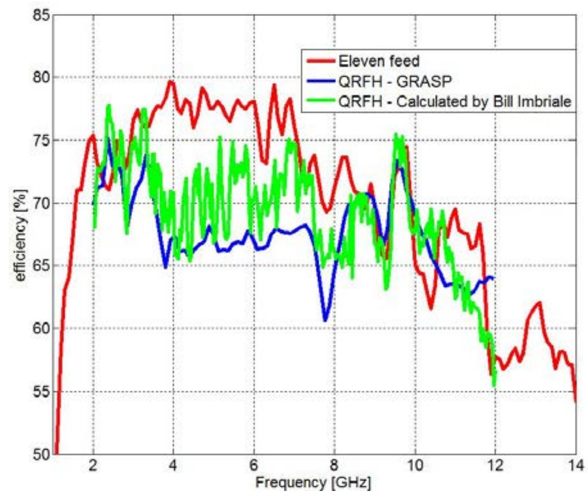

Fig. 15 Aperture efficiency for Eleven feed and QRFH in Intertronics axi-symetric dual reflector system with ring-focus sub-reflector.

The aperture efficiencies for the Eleven and QRFH feeds in the Intertronics axisymetric, dual-reflector system with ring-focus sub-reflector are shown in Figure 15. The GRASP analysis for both the Eleven feed and the QRFH feed used in the Intertronics reflector system was performed at Chalmers University using the method described above. The GRASP results are compared to aperture efficiency calculated by Bill Imbriale with Physical Optics Software available at Caltech University. The aperture efficiency of the Eleven feed is better over the 3–7 GHz band compared to the QRFH performance. The performance of both feed over the 2–3 GHz and 9–12 GHz bands is quite comparable. Data for the particular QRFH model was not available for the 12–14 GHz but according to [15] the aperture efficiency of the QRFH for this highest part of the band is similar to the Eleven feed. It should be noted that after providing the efficiency comparison plot for [19] an error in the convergency set-up for QRFH was discovered. Here in the problem in Figure 15 the results for QRFH are with the correct convergency setting.

Table 1 compares some of the main features and also the performance of the QRFH and Eleven feeds [19]. A disadvantage of the Eleven feed from a system integration point-of-view is that it requires a greater number of LNAs. On the other hand, the Eleven feed has better sensitivity and cross-pol for f/D in the 0.35–0.5 range. The QRFH has the advantage that it can be designed to match a wider range of f/D values, but currently (to our knowledge) there is no data about the efficiency of the QRFH in such systems over the VGOS frequency range.

6 Conclusions

As described above, both the Eleven feed and the QRFH feed are suitable for VGOS. The main advantage of the Eleven feed is the higher efficiency over some part of the band and better cross-pol, while the QRFH has the advantage that it is adaptable for a wider range of f/D values and requires less LNAs. Both systems are available for purchase as integrated in complete cryogenic system together with the LNAs. Depending on the particular antenna reflector system more detailed studies need to be done on the ground pick-up via the side lobes in order to get an accurate prediction of the Aeff/Tsys figure of merit.

Acknowledgements

The work on the Eleven feed has been supported by the Swedish VR Research Infrastructures Planning Grant "Swedish contributions to the SKA radio telescope in its pre-construction phase" Contract No C0546801. The work on the mechanical design, system integra-

Table 1 Feed comparison from [19].

	Eleven Feed	QRFH Feed
VLBI2010 compatibility	yes	yes
Frequency range (GHz)	1.2–14	2.2–14
Polarization configuration	dual-linear	dual-linear
Port configuration	differential	single-ended
LNAs per polarization	4	1
LNAs per feed	8	2
LNA balance requirements	1.6 dB amp 14° phase	none
Calibration signal injection	radiated or post-LNA	radiated, pre-LNA, or post-LNA
Aperture efficiency (f/D $\sim$ 0.375)	see Figure 15	see Figure 15
Ground noise contribution (f/D $\sim$ 0.4)	preliminary: 10–20K (needs research)	<20K (2.2–5 GHz) <10K (2.2–5 GHz)
f/D Range	0.35–0.5	adaptable for 0.3–2.5
Feed 10-dB half-beamwidth	65°	adaptable for 15°–70°
Size (half-beam-width $\sim$ 65°)	diameter 210 mm height 65 mm	diameter 160 mm height 150 mm
Cost	US$33,000 (to be confirmed)	US$15,000

tion, and tests for the Eleven feed (2008–2010) was supported by Onsala Space Observatory.

References

1. P. Petrachenko, et. al., "Design Aspects of the VLBI2010 System" Progress Report of the IVS VLBI2010 Committee, ftp://202.127.29.33/pub/VLBI2010/V2C/PR-V2C_090417.pdf.
2. P. Hall, The SKA: An Engineering Perspective, Springer, 2005.
3. G. Engargiola, "Non-planar log-periodic antenna feed for integration with a cryogenic microwave amplifier", Antennas and Propagation Society International Symposium, 2002. IEEE (Volume:4).
4. G. Cortes-Medellin, "Non-Planar Quasi-Self-Complementary Ultra-Wideband Feed Antenna", IEEE Transaction on Antennas and Propagation, Vol.59, No6, June 2011.
5. Gawande, R., Bradley, R. "Towards an Ultra Wideband Low Noise Active Sinuous Feed for Next Generation Radio Telescopes", IEEE Transaction on Antennas and Propagation, Vol.59, No6, June 2011.
6. "Open boundary quad-ridged horn", [online Available: http://www.ets-lindgren.com/pdf/3164-05.pdf
7. A. Niell et al., "First Broadband Results with a VLBI2010 System", IVS 2012 General Meeting Proceedings,p.13-17http://ivscc.gsfc.nasa.gov/publications/gm2012/Niell.pdf
8. R. Olsson, P.-S. Kildal, S. Weinreb, "The Eleven antenna: a compact low-profile decade bandwidth dual polarized feed for reflector antennas", IEEE Trans. Antennas Propogat., vol. 54, no. 2, pt. 1, pp. 368-375, Feb. 2006.
9. CST Microwave Studion, https://www.cst.com/Products/CSTMWS
10. Omnisys Instruments, http://omnisys.se/
11. Low Noise Factory, http://www.lownoisefactory.com/
12. A. Akgiray, S. Weinreb, W. Imbriale, and C. Beaudoin, "Circular quadruple-ridged flared horn achieving near-constant beamwidth over multioctave bandwidth: Design and measurements," IEEE Trans. Antennas Propag., vol. 61, no. 3, pp. 1099 — 1108, March 2013.
13. J. Yang, M. Pantaleev, Per-Simon Kildal, B. Klein, N. Wadefalk, M. Ivashinna "Cryogenic 2 — 13 GHz Eleven Feed for Reflector Antennas in Future Wideband Radio Telescopes," IEEE Treansactions on Antennas and Propagation, vol. 59, no. 6, pp. 1918-1934, 2011.
14. C. Granet, "A simple procedure for the design of classical displaced-axis dual-reflector antennas using a set of geometric parameters", Antennas and Propagation Magazine, IEEE (Volume:41 , Issue: 6).
15. A. Akgiray, M. Pantaleev, C. Beaudoin, Private communicaitons, 2013
16. A. Akgiray, "New Technologies Driving Decade-Bandwidth Radio Astronomy: Quad-Ridged Flared Horn & Compound-Semiconductor LNAs", http://thesis.library.caltech.edu/7644/1/Akgiray_PhDThesis_FinalVersion.pdf
17. C. Beaudoin, B. Corey, A. Niell, A. Whitney, "Haystack Observatory Technology Development Center", IVS 2011 Annual Report, ftp://ivscc.gsfc.nasa.gov/pub/annual-report/2011/pdf/tdhstk.pdf.
18. C.Bencivenni, M. Ivashina, "Quadruple-Ridge Flared Horn Feed design reoport", Onsala Observatory Internal Technical Report, June 2013.
19. B. Petrachenko, "VLBI2010 Feed Comparisson", In: International VLBI Service for Geodesy and Astrometry 2012 Annual Report, edited by K. Baver and D. Behrend, NASA/TP-2013-217511, 48–51, 2013.

A Dual-Circular Polarization Broadband Feed for Ring Focus Configuration

José Antonio López–Fernández[1,2], Enrique García[3], Alejandro Rivera–Lavado[3], Sergio Llorente–Romano[3], Francisco Javier Herráiz–Martínez[3], Javier Montero–de–Paz[3], Mario Méndez–Aller[3], Luis Santos[4], José Manuel Serna–Puente[2], José Antonio López–Pérez[2], Félix Tercero[2]

Abstract A new feed topology is presented that potentially can open new solutions for covering the new VGOS configuration and its associated frequency bands. In this approach a single band from 2 to 14 GHz is considered. A log-spiral antenna is printed on a conic surface. The whole structure is adjusted in order to obtain a pure circular polarization at broadside direction. An array of four elements is proposed for obtaining a dual-circular polarization feed. Simulations show an efficiency higher than 70% on a ring focus radio telescope illuminated with this feed.

Keywords VGOS, radio telescope, ring focus, broadband feed

1 The RAEGE Ring Focus Radio Telescope

The RAEGE radio telescope optical system is shown in Figure 1. It is composed of one main parabolic mirror and an elliptical subreflector. The entire system has rotational symmetry. The diameter of the main (Dm) and secondary (ds) mirrors are 13.2 m and 1.55 m, respectively. The distance between the highest focal point of the elliptical mirror and the vertex of the parabola (fp) is 3.7 m. The feed is placed into a cryostat below the subreflector.

1. Instituto Geográfico Nacional (IGN)
2. IGN Yebes Observatory
3. Carlos III University (UC3)
4. DSCIG Açores

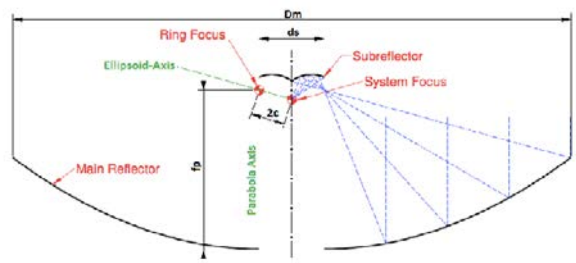

Fig. 1 The optical system of the RAEGE ring focus telescopes.

The optimum performance of this system is obtained with an ideal Gaussian feed placed in the focus of the subreflector, using a taper of −16 dB. GRASP tool has been used for analyzing the complete system. Figure 2 shows the maximum efficiency which goes from 72% to 81%. The sidelobe level is −13 dB and the antenna temperature goes from 30 to 2 Kelvin (Figure 3).

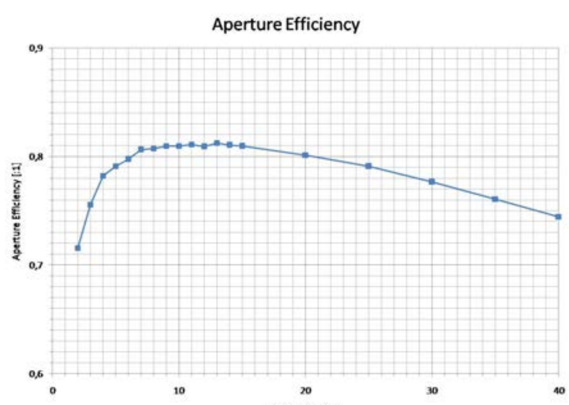

Fig. 2 Aperture efficiency of the RAEGE radio telescopes with an ideal feed and a taper of −16 dB.

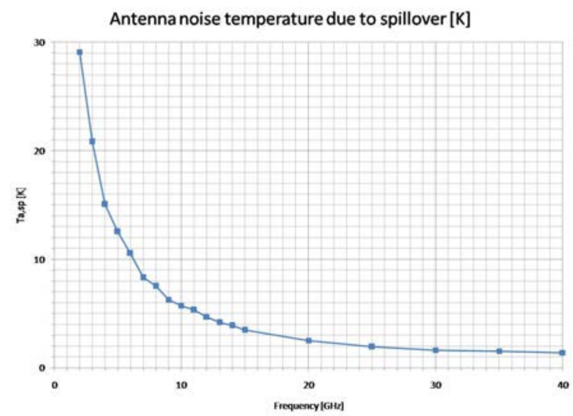

Fig. 3 RAEGE radio telescope antenna noise temperature.

2 The DYQSA Feed

The geometry proposed for the feed is based on a conical, log-spiral antenna (Dyson 1962, 1965). This is the origin of the name for the solution we have selected, devoted to the impressive work on this kind of antennas by Professor Dyson.

The antenna configuration is shown in Table 1. The full feed, based on the conical log-spiral antenna (see Figure 4), uses four units (see Figure 5).

Table 1 Parameters of the DYQSA feed.

Parameter	Value
ρ_o	2 mm
R_{max}	30 mm
α	85^o
θ_o	10^o
δ	$\pi/2$

Two antennas are devoted to one polarization (RHCP), while the other two antennas are devoted to the opposite one (LHCP). The angle between the axis of the cones and the z-axis is 16^o. The radiation pattern of the antenna was analyzed using the CST, Microwave Studio, and HFSS Ansoft softwares, obtaining the same results for both systems.

The phase center changes by 6 cm over the whole band. However, the variation is only 2 cm between 4 and 14 GHz. This will cause a reduction in efficiency for a fixed position of the antenna. However, this efficiency can be optimized to be always above 60% for different fixed positions of the feed from the focus, as is shown in Figure 9.

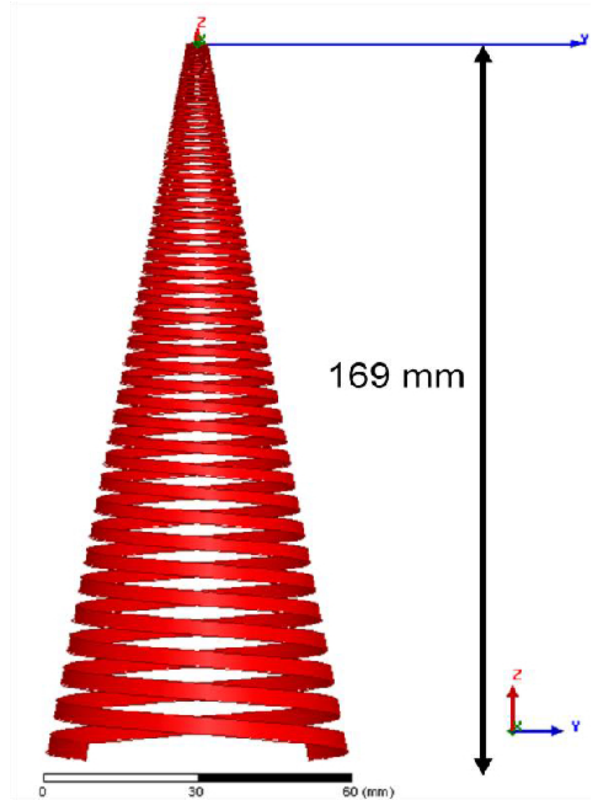

Fig. 4 Single element of the DYQSA feed.

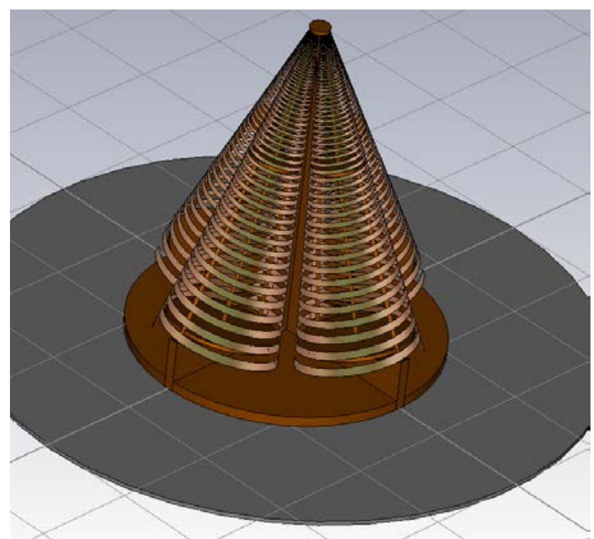

Fig. 5 The DYQSA full feed is made of four conical log-spirals. The result is a simultaneous dual-circular polarization feed.

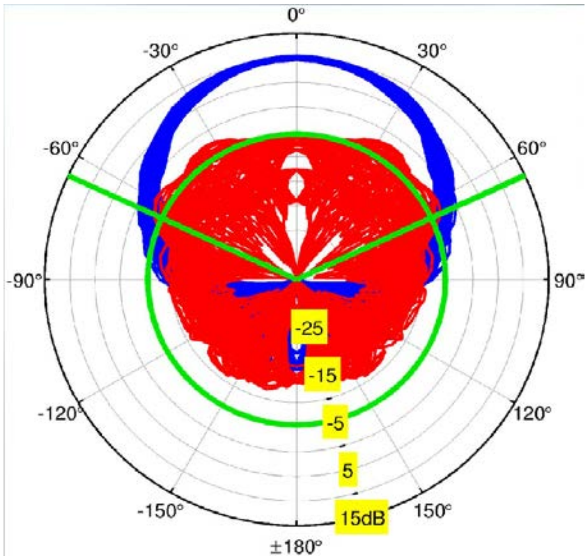

Fig. 6 Radiation patterns of the feed system from 2 GHz up to 14 GHz (step of 2 GHz) at the planes ϕ, with steps of 15^o from $\phi = 0^o$ up to $\phi = 180^o$. the blue line is copolar polarization and the red line is cross-polar polarization. Circular polarization is assumed. Green lines indicate the subtended angle from the focus of the subreflector. A pretty high symmetry in the radiation patterns at all frequencies is obtained with a maximum CP-XP level in broadside > 15 dB with a gain of 10 dB. The input impedance is also shown maintaining a quite constant behavior in the frequency band.

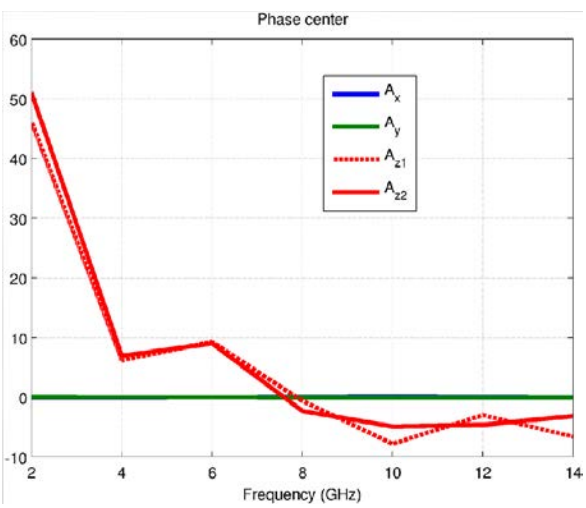

Fig. 7 Change of the phase center of the DYQSA feed.

3 First Measurements

A titanium first prototype of the feed single element has already been built (to assure no deformation of the feed). The measurements were done at the Yebes anechoic chamber and they show very good agreement with theory. Simulations with GRASP show that placing this feed at the focus of the system can reach efficiencies higher than 70% in the whole band.

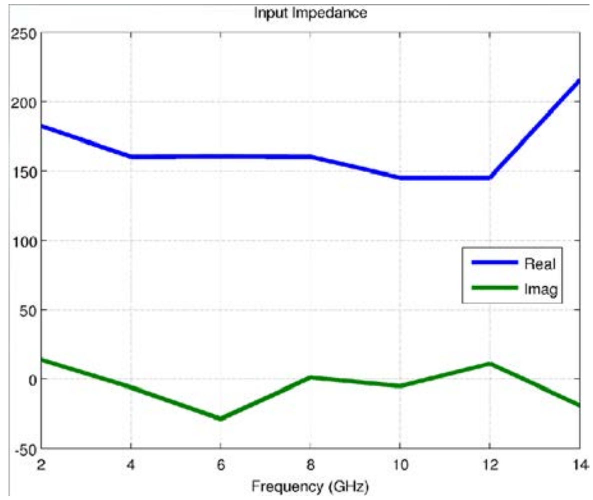

Fig. 8 Input impedance of the DYQSA feed.

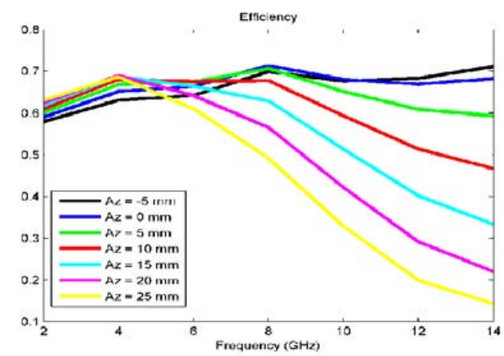

Fig. 9 Efficiency of the system obtained from GRASP allowing a geometrical displacement of the antenna along the z-axis.

4 Conclusions

A totally novel antenna topology for covering the requirements of the VGOS system has been presented. The DYQSA antenna is a new solution for broadband ring focus feeds. It offers simultaneous dual-circular polarization over the whole band of 2–14 GHz. The simulated efficiency of the ring focus using this feed is approximately 70%. The DYQSA feed is similar in

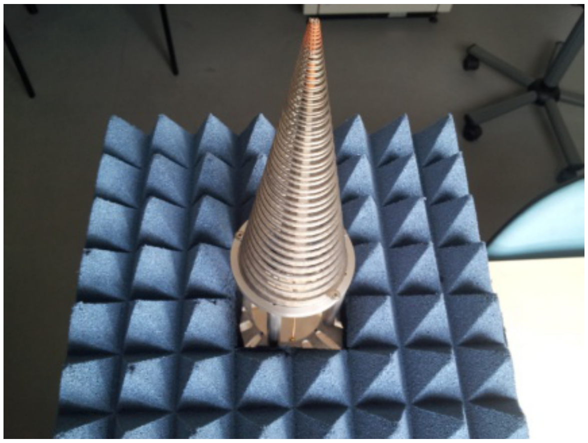

Fig. 10 First prototype of a single DYQSA element.

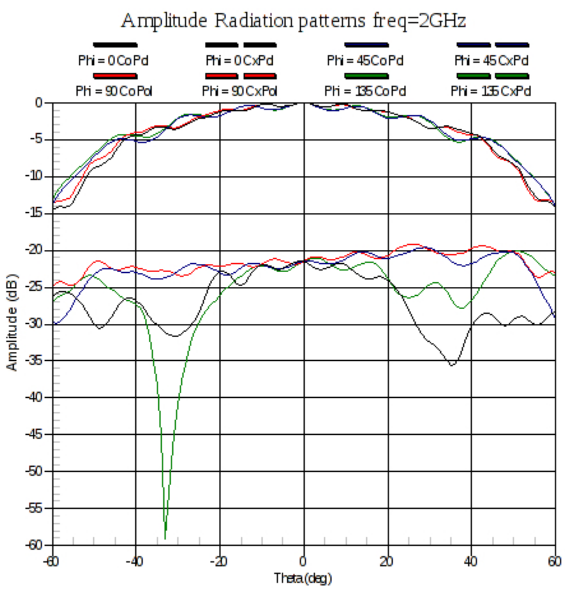

Fig. 11 Polar and cross-polar radiation patterns of a single element feed system at 2 GHz ($\phi = 0^o$, 45^o, 90^o, and 135^o).

volume to the QFRH feed. An already built prototype shows good agreement with theory. A final prototype will be finished in 2015.

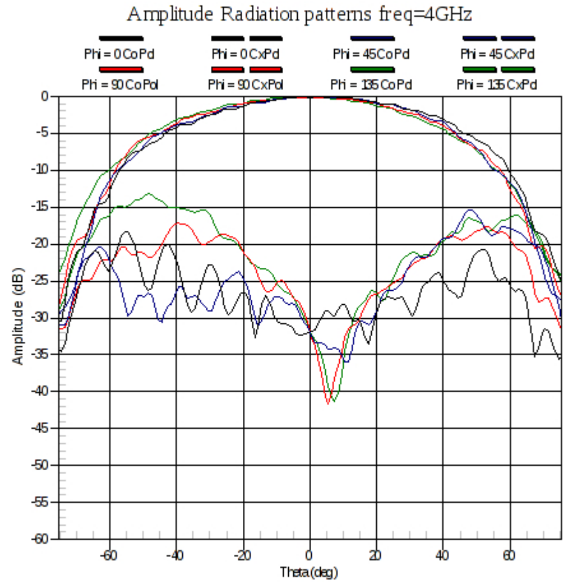

Fig. 12 Polar and cross-polar radiation patterns of a single element feed system at 4 GHz ($\phi = 0^o$, 45^o, 90^o, and 135^o).

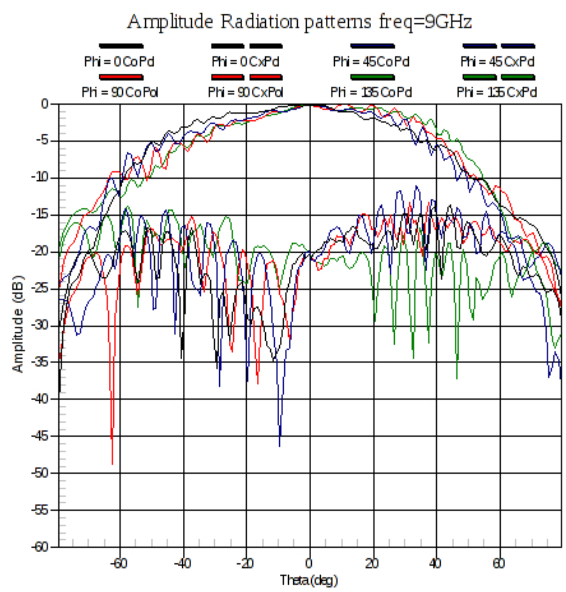

Fig. 13 Polar and cross-polar radiation patterns of a single element feed system at 9 GHz ($\phi = 0^o$, 45^o, 90^o, and 135^o).

Acknowledgements

This work was supported by the project FIS2012-38160 of the Spanish Ministry of Economy and Competitiveness.

References

1. Ticra GRASP.
2. J. D. Dyson, "The characteristics and design of the conical log-spiral antenna", IEEE Trans. On Antennas and Propagation, vol. AP-13. pp. 488–499. July 1965.

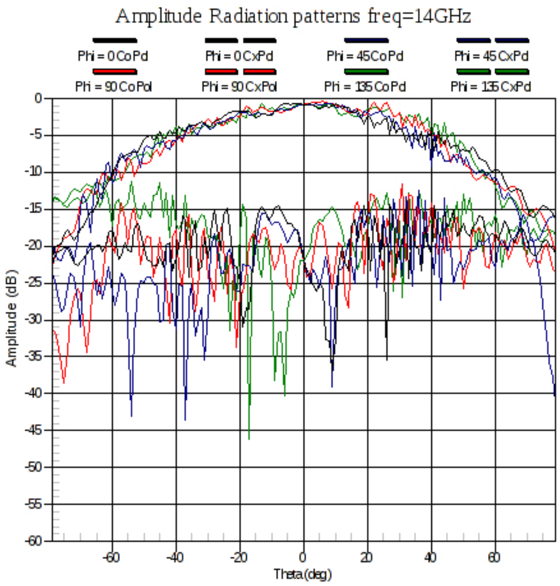

Fig. 14 Polar and cross-polar radiation patterns of a single element feed system at 14 GHz ($\phi = 0^o$, 45^o, 90^o, and 135^o).

3. J. D. Dyson, "The coupling and mutual impedance between conical log-spiral antennas in simple arrays", IRE International Convention Record, Vol. 10, pp. 165–182, Mar. 1962.
4. CST Microwave Studio, 2012.
5. Ansys HFSS 14.
6. J. A. López–Fernández, F. Tercero, S. López, J. M. Serna-Puente. "A Dyson Conical Quad-Spiral Array (DYQSA)", IGN CDTAC-14002 Technical Report, 2014.

Design of a Circularly-Polarized VGOS Frontend for Simplified Mixed-Mode VLBI Observations

Christopher J. Beaudoin

Abstract In the interest of minimizing the complexity and the associated development costs necessary to conduct mixed-mode legacy/VGOS observations, a linear-to-circular polarization conversion network for linearly-polarized VGOS-compatible feeds was designed. Because this network is an integral component of the receiver frontend and the conversion is performed in hardware, this solution provides relief to requirements for data rates and correlation processing for mixed-mode observations. Furthermore, this solution circumvents software developments that would be necessary to support linearly-polarized observations by the IVS. In this paper, a network designed to convert linearly-polarized signals to a circular-basis is outlined. Numerical simulation of the conversion network's cross-polarization isolation indicates that it meets the VGOS signal chain 20 dB cross-polarization isolation requirement.

Keywords VGOS, mixed-mode, linear, circular, polarization

1 Introduction

Broadband radio telescope feeds with hardware realizations that meet the VGOS requirements [1, 2] are linearly-polarized (LP). However, as concluded in MMA Memo 208 [3], the arguments against the LP feed outweigh the arguments against circularly-polarized (CP) feeds. In fact, the argument that circular feeds are inherently narrow bandwidth [3] is void in consideration of the conversion network design described in Section 3. Furthermore, the need to measure an absolute polarization angle is not a requirement for VGOS observations. Hence, based on the MMA Memo 208 [3], one could argue that there are no drawbacks or limitations associated with CP feeds for the VGOS application.

In contrast to VGOS compatible feeds, legacy IVS stations are outfitted with S- and X-band feeds that observe the CP basis. This polarization dissimilarity does not inhibit mixed-mode (i.e., legacy vs. VGOS) observations, but the difference would complicate such observations in two important ways.

MIT Haystack Observatory

1.1 Observing Implications

Observation complexity arises because the signal-to-noise ratio of a single correlation is coupled to the difference in parallactic angle between the two linearly-polarized VGOS stations. The signal-to-noise ratio can be decoupled from the difference in parallactic angle, but this necessitates recording and correlating twice the amount of data in the mixed mode scenario than is necessary if both receivers detected circular polarization. As such, dissimilar polarization sensing in mixed-mode observations has significant implications for those stations that are data transfer bandwidth limited and software correlators that are computing limited.

1.2 Operational Implications

Dissimilar polarization sensing also complicates the VLBI experimental setup relative to existing procedures. Assurance of accurate data flow through the IVS processing chain will require significant development, testing, and integration of software to support mixed-mode and new VGOS observing scenarios. The development of such software will extend across a major portion of the IVS processing chain from station scheduling to post-correlation data processing. Because the development of such software will necessarily span across multiple subsystems, the time and cost to develop and verify the performance of these efforts in the overall processing chain is quite significant.

2 Assessment of Conversion Network Performance

The performance of the LP-to-CP conversion network is assessed by exciting the proposed network with orthogonal phasor voltages V_x and V_y that are linear representations of right and left hand circularly-polarized wavefronts [4], RCP and LCP, respectively:

$$\begin{aligned} \left\{V_x = 1, V_y = e^{-i\frac{\pi}{2}}\right\} &\equiv RCP \\ \left\{V_x = 1, V_y = e^{i\frac{\pi}{2}}\right\} &\equiv LCP \end{aligned} \tag{1}$$

The phasors V_x and V_y are combined with appropriate 90° phase shifts to form phasors equivalent to those that would be detected at the RCP and LCP ports of a dual circular feed. An ideal 90° hybrid [5] implements the necessary combination to achieve this result which is described succinctly by the following:

$$\begin{bmatrix} V_{RCP} \\ V_{LCP} \end{bmatrix} = \begin{bmatrix} 1 & e^{i\frac{\pi}{2}} \\ 1 & e^{-i\frac{\pi}{2}} \end{bmatrix} \begin{bmatrix} V_x \\ V_y \end{bmatrix} \tag{2}$$

When the network is excited with the V_x and V_y RCP phasors given in Equation 1, the cross-polarization isolation (CP_{iso}) performance of the network is given by the following:

$$CP_{iso} = 20\log_{10}\left(\frac{V_{RCP}}{V_{LCP}}\right) \tag{3}$$

The matrix elements in Equation 2 are defined by the ideal hybrid and describe an equivalent amplitude and 90° phase relationship between the V_x/V_y phasors. In practice, it is not possible to maintain a perfect amplitude and phase match between V_x and V_y with physical components, particularly over more than a decade of bandwidth. Deviation from these match conditions results in cross-polarization contamination and degrades the performance of the network. In the following section, the expected level of contamination is outlined given the performance of a physically realizable hybrid and the LNAs necessary to support low noise operation of the receiver frontend.

3 Conversion Network Design

Figure 1 outlines a block diagram of the conversion design including the 90° hybrid, low noise amplifiers (LNAs), an amplitude matching attenuator, and a phase matching delay line.

The LNAs are both Caltech model CRYO1-11; serial numbers 127 and 128 were purchased by Haystack Observatory. The 90° hybrid is Krytar model 1830, and the delay line is Pasternack model PE8200, while the attenuator is a generic model (e.g., MiniCircuits). The attenuator and delay line are incorporated to improve the amplitude and phase matching between the V_x and V_y phasors in order to maximize the cross-polarization performance [6]. To assess the performance of the LP-to-CP conversion network, the 2–14 GHz electrical network parameters (i.e., S-parameters) of each component were measured individually. The cascade shown in Figure 1 was analyzed through numerical simulation by importing each set of network parameters into a MATLAB RF simulation to assess the performance of the conversion network design. For each frequency, the simulation computes the four elements of the matrix presented in Equation 2 given the imperfections in the individual components. The cross-polarization performance at each frequency is computed by applying Equation 3, and the resulting performance is shown in Figure 2. In order to achieve the performance shown in Figure 2, it was necessary to attenuate and delay the V_y phasor by 3 dB and 5.5 ps, respectively.

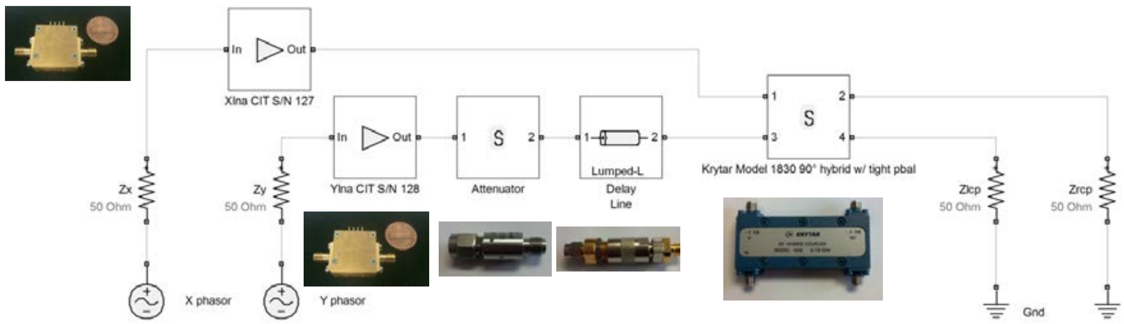

Fig. 1 Schematic diagram of the LP-to-CP conversion network. Also shown are the LNAs, attenuator, phase trimmer, and 90° hybrid that were measured to analyze the performance of the network.

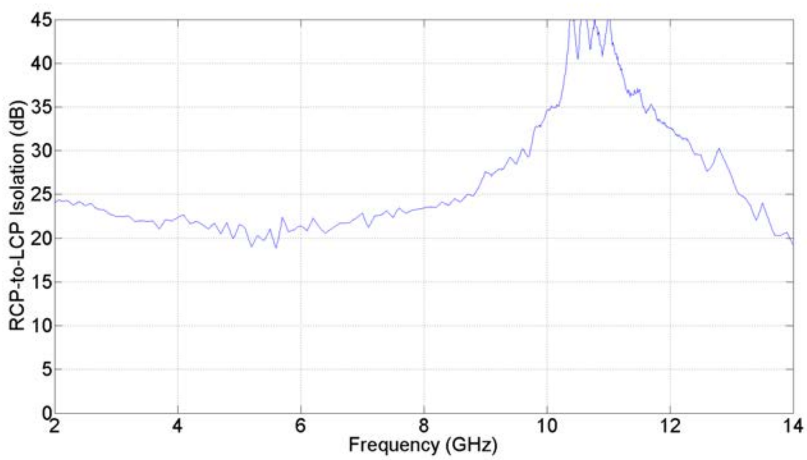

Fig. 2 Cross-polarization isolation performance of the conversion network shown in Figure 1. This performance was obtained from numerical simulation of the conversion network incorporating the measured electrical parameters of the components also shown in Figure 1.

4 Conclusions/Future Work

The drawbacks of a linearly-polarized VGOS radio telescope feed outweigh those of a circularly-polarized feed. Regarding IVS observations and operations in LP, the drawbacks are increases in data rate for mixed mode observations and operational software support for LP operations. Support of LP observations will require significant software development that spans IVS sub-systems from scheduling to post-correlation processing as outlined in Section 1. As described in Section 1, according to [3], one can argue that there are no drawbacks associated with CP feeds; however, this presupposes that such a radio telescope feed is in existence. While the design of a conversion network necessary to emulate a CP feed that will meet VGOS cross-polarization requirements [7] exists (see Section 3), this feed has yet to be fabricated and tested in an anechoic chamber. Fabrication costs are of order 5K USD with a one time verification testing cost of approximately 10K USD. The fabrication and testing of such a feed could be completed in approximately six months with dedicated efforts, which is considerably less time than to overhaul the various software packages from scheduling to post-processing so that they may support LP observations in the IVS network.

It should also be noted that other techniques were proposed for converting LP signals to CP in backend processing and/or post-correlation processing. These techniques suffer from the need to observe a fiducial source to calibrate the time-dependent amplitude and phase differences between the two LP channels. These differences are introduced by instrumental effects, and their removal through calibration is necessary to ensure adequate cross-polarization isolation between the RCP and LCP channels. One may argue that phase and noise calibration corrections can compensate for such instrumental errors; however, implementation of these corrective measures plays a crucial role in the utility of this information to perform polarimetric corrections. Specifically, it is crucial that phase and amplitude calibration signals be injected at the same physical point in the receiver chain (i.e. before the LNA). If not, systematic errors may be introduced through the correction procedure.

Such a calibration procedure is not necessary for standard operations with the design outlined in Section 3; the cross-polarization performance is verified through independent measurements in the anechoic chamber. Because this design incorporates a bare minimum of active components (i.e. only LNAs), this performance is not expected to drift over time. This assumption can be asserted if the conversion network is contained within the frontend vacuum chamber, though not necessarily cooled by the refrigerator. However, the LNA amplitude and phase must also remain stable over time to avoid degradation in the cross-polarization isolation performance of the conversion network. While there is no reason to expect the LNA's gain and phase to drift over time while cooled in the cryogenic chamber, this must be verified as part of the testing process. Furthermore, LNAs can fail for a variety of reasons. Because the conversion network is balanced based upon the characteristics of the LNAs, replacement of an LNA will require the network's amplitude and phase trim settings to be modified in order to maintain matching and good cross-polarization isolation performance.

Acknowledgements

I would like to acknowledge Lynn Matthews, Vincent Fish, and Brian Corey for sharing their knowledge on the subject of linear-to-circular polarization conversion as it relates to VGOS and the greater field of radio astronomical VLBI. I would also like to acknowledge Javier Gonzalez Garcia for his measurement support that facilitated the cross-polarization analysis that was presented in this document.

References

1. J. Yang, M. Pantaleev, P.-S. Kildal, Y. Karadikar, L. Helldner, B. Klein, N. Wadefalk, and C. Beaudoin, "Cryogenic 2-13 GHz eleven feed for reflector antennas in future wideband radio telescopes," IEEE Trans. Ant. Propag., vol. 58, no. 6, pp.1918,1934, June 2011. doi: 10.1109/TAP.2011.2122229
2. A. Akgiray, S. Weinreb, Q. A. Imbriale, and C. Beaudoin, "Circular Quadruple-Ridged Flared Horn Achieving Near-Constant Beamwidth Over Multioctave Bandwidth: Design and Measurements," IEEE Trans.Ant. Propag., vol. 61, no. 3, pp. 1099-1108, March 2013.
3. Cotton, D., Polarization Calibration of the MMA: Circular versus Linear Feeds, Main AMA Memo Series Memo 208.
4. Stutzman, W. L., Thiele, G. A., Antenna Theory and Design 2nd Ed. New York: John Wiley and Sons, Inc., 1998. Print.
5. Pozar, D.M., Microwave Engineering 3rd Ed. New York: John Wiley and Sons, Inc., 2005. Print.
6. Beaudoin, C., "Design of a Circularly Polarized VGOS Frontend for Simplified Mixed-Mode VLBI Observations." *http://ivs2014.csp.escience.cn/dct/attach/Y2xiOmNsYjpw ZGY6Njc3OTI=* Posted:April 1, 2014. Accessed: April 23, 2014.
7. Corey, B., "VLBI2010 Antenna and Site Recommendations." *http://www.fs.wettzell.de/veranstaltungen/vlbi/tecspec 2012/Session5/01_antenna_recommendations.pdf* Posted: March 29, 2012. Accessed: April 23, 2014.

Development of a Wideband VLBI System (GALA-V)

Mamoru Sekido, Kazuhiro Takefuji, Hideki Ujihara, Masanori Tsutsumi, Yuka Miyauchi, Shingo Hasegawa, Thomas Hobiger, Ryuichi Ichikawa, Yasuhiro Koyama

Abstract The VLBI group of the National Institute of Information and Communications Technology (NICT) has been developing a wideband VLBI observation system, which is semi-compliant with the VGOS system. Two small-diameter, transportable antennas and a 34-m antenna are prepared for wideband observations at the 3–14 GHz frequency range. This project, named "GALA-V", is intended to be used for precise frequency comparisons between widely separated atomic frequency standards. Several new challenges are being addressed in this project: (1) development of a wideband feed with narrow beam width for a large-diameter Cassegrain antenna, (2) development of a direct RF sampling data acquisition system, which samples the RF analog signal at 16 GHz. A prototype of the new wideband feed has been installed on the 34-m antenna at the end of 2013. The current status of this GALA-V project development is described in this report.

Keywords Broadband feed, direct sampling

1 Introduction

The unit of time, one second, which is currently defined by counting the microwave frequency emitted by a Cs atom, might be replaced by a new definition in which the second is realized by counting the optical frequency emission from some atoms (e.g., [1]). Such a development for a new atomic frequency standard is in progress in the field of quantum mechanics and metrology. NICT, as the Japanese Time Standard Authority, is in charge of keeping time and frequency, and it is developing new optical time standards too. Two-way satellite time and frequency transfer (TWSTFT) and GNSS observations have been used for frequency comparisons by domestic and international institutes [2]. Other space technologies, such as VLBI and SLR, are being investigated for T&F transfer applications [3, 4]. We are developing a VLBI system composed of a transportable, small-diameter antenna pair and a large-diameter antenna for distant frequency comparison. Two small-diameter antennas are to be placed at each site of atomic frequency standards, and their frequencies are compared via VLBI observations using those signals as the frequency reference at each station. We named this VLBI system (Project) "GALA-V". One of the small-diameter antennas and the 34-m diameter antenna as the component of the system are displayed in Figure 1. To compensate for the reduced sensitivity of the small-diameter antenna, two measures are taken to improve the system: (1) combi-

Fig. 1 A 1.5-m diameter antenna located at NICT headquarters in Koganei (left) and the 34-m diameter antenna at Kashima Space Technology Center (right).

National Institute of Information and Communications Technology, Kashima Space Technology Center

nation use with large-diameter antenna, and (2) use of wideband data acquisition and wide frequency range. The first measure is based on the fact that the sensitivity of the VLBI observation is proportional to the product of the diameters of an antenna pair. The second measure improves the SNR and the delay measurement precision in the same way as for the VGOS system [5]. The observation specifications of the GALA-V are designed to be compatible with those of VGOS, so that joint observations will be possible. Details of the technology developments in the GALA-V project are described in the following sections.

2 Observation Specification of the GALA-V Project

Four 1-GHz bandwidth radio frequencies were determined as the basic VLBI observation mode for the GALA-V project: 3500–4524 MHz, 5100–6124 MHz, 9900–10924 MHz, and 13100–14124 MHz. Its data acquisition mode is 2048 Msps/1 bit/4 ch. We decided on these fixed observation frequencies at the start of the design and development of the GALA-V system, while the VGOS specifications require a flexible choice for the observation frequency bands. However, as explained in a later section, the real data acquisition system of the GALA-V system has some flexibility w.r.t. the frequency selection allowing joint observations with VGOS stations. The radio frequencies were selected taking into consideration results from a radio frequency interference (RFI) survey and choosing a fine delay resolution function formed by synthesizing the observed signals. The radio frequency spectra obtained in the RFI survey are shown in Figure 2. The broadband radio frequency survey for 3.5–18 GHz was performed at the Kashima, Koganei, and Tsukuba sites in 2012 using a broadband receiver system.

Taking into account these RFI survey results, the observation frequency array of 1-GHz bandwidth was allocated to have zero-redundancy spacing to form the fine delay resolution function. Our choice for the four frequency bands is separated by the ratio of 1:3:2 with multiples of 1.6 GHz. Figure 3 shows the delay resolution function expected to be formed with this frequency array. This is based on the assumption that the correlation amplitudes are uniform for all bands, although this has to be confirmed with real data.

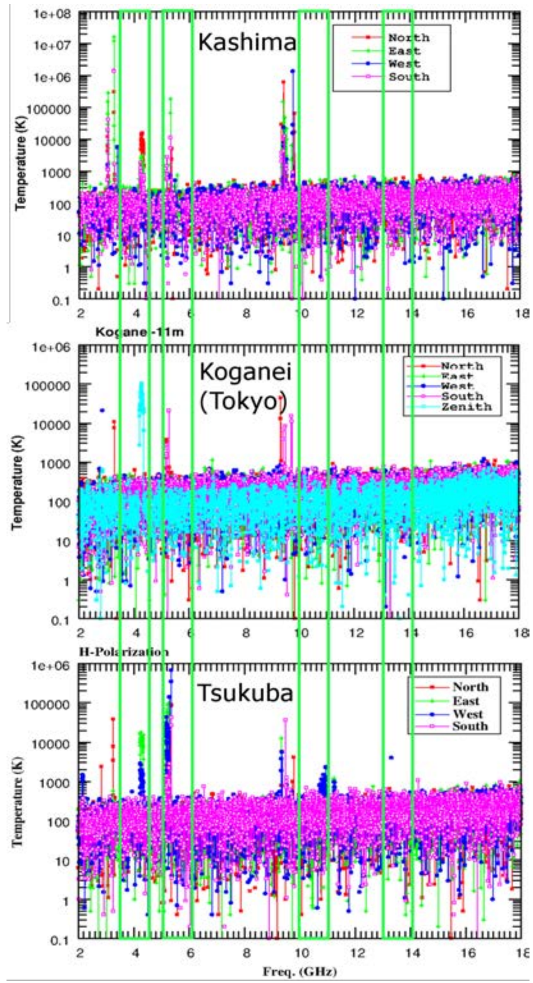

Fig. 2 Radio frequency spectra (MAX-HOLD) obtained in an RFI survey performed at the Kashima, Tsukuba, and Koganei sites in Japan. The received power is indicated by the antenna temperature in Kelvin. The broadband receiver system consisted of a double-ridged horn (SCHWARZBECK BBHA 9120 D), and room temperature LNAs (B&Z BZP118UD1 NF = 2 dB) were used in combination with HPF (Fc=3.5GHz Insertion Loss~ -0.3 dB) to avoid saturation due to strong RFI below 3 GHz. The amplified signal was fed into a spectrum analyzer (Rohde & Schwarz FSV30) and recorded. The measurements were made at four horizontal directions (NSEW) with a recording maximum value (RBW=1 MHz, VBW=1 MHz) during 30 seconds via the MAX-HOLD function of the spectrum analyzer. The four long rectangular boxes indicate the observation bands of the GALA-V system.

3 Small-Diameter Broadband Radio Telescopes

Small-diameter antenna system (1.6-m and 1.5-m diameters), each equipped with a Lindgren quad-ridge

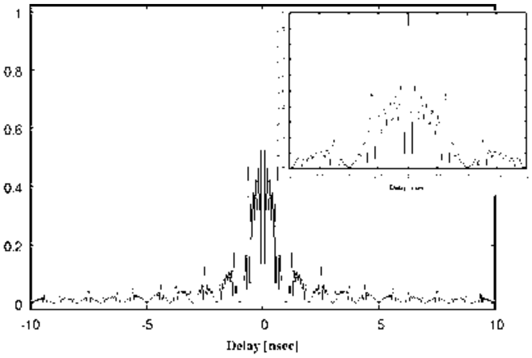

Fig. 3 Delay resolution function expected from the frequency array (3.5 GHz, 5.1 GHz, 9.9 GHz, and 13.1 GHz) with 1024-MHz bandwidth. The inset plot to the upper right shows a magnification of the center portion.

horn antenna (QRHA), are placed at Tsukuba (National Metrology Institute of Japan) and Koganei (NICT). The observation frequency of these antennas, which were originally developed for the MARBLE project [6], was modified from S/X -band to 3.5–15 GHz by exchanging the front-end microwave components. A broadband (1–18 GHz) optical signal transmission system with low noise figure characteristics (Sumitomo Osaka Cement, E18000) has been installed in place of the original frequency down-converter for both antennas. The phase calibration (PCAL) unit, whose pulse generation circuit was originally designed by Allan Rogers [7], was installed in the RF box of the antenna. The PCAL unit is used to generate 100-MHz intervals of frequency comb tones in the GALA-V system instead of the conventional 1-MHz interval. The reason for the 100-MHz interval is the improvement of the frequency characteristics of the PCAL signal, especially to get sufficient signal power at higher frequencies. Additionally, fewer injections of artificial signals are preferable to avoid an increase of the antenna system temperature. We believe that the 100-MHz interval tones will be enough for the phase calibration of 1024-MHz bandwidth and that a modern software correlator can handle any choice of PCAL frequency. The PCAL signal is an essential component for the calibration of the phase delay difference in the broadband bandwidth synthesis. The evaluation of the PCAL stability and phase behavior over the entire broadband is not sufficient yet and needs to be continued.

4 The Broadband 'Iguana' Feed for the 34-m Radio Telescope

One of the key issues of the GALA-V project is development of a receiver feed for a large-diameter antenna with long focal length. All of the broadband feeds currently known in the application to VGOS system have a wide beam size [8, 9]. This is one of the reasons why the ring-focus design was adopted for most of the new VGOS stations. We have started the development of a broadband feed of Cassegrain type for the Kashima 34-m parabolic antenna in 2012. The requested properties for the feed were (1) good efficiency at four frequency bands, which are described in the former section, and (2) constant and narrow beam width (HPBW $\sim 34^\circ$) for the target frequency bands. To satisfy these severe requirements, Dr. Ujihara investigated and proposed a new feed design. The new feed, called 'Iguana', is composed of two feeds: one for the higher frequency band and the other for the lower frequency band. At the end of 2013, a prototype of the higher frequency feed (Iguana-H) was mounted on the 34-m antenna with room temperature LNAs (Figure 4). The receiver system of the Kashima 34-m antenna is composed of four trolleys that are equipped with an S/X-band, L-band, C-band, and K/Q-band receiver, respectively. To change to a different receiver, the respective trolley is selected and moved up to the focal point of the antenna. The new Iguana-H receiver was installed in place of the C-band receiver system; thus, the S/X and other receivers were not changed at all and can be used as before. The lower panel of Figure 4 shows the SEFD and efficiency of the prototype feed. The Iguana-H feed demonstrated broad sensitivity over the frequency range 6–14 GHz. The development of the new broadband feed has been supported by a joint research development fund of the National Astronomical Observatory of Japan (NAOJ). The first light observation with the Iguana-H feed was made for the Methanol maser emission lines, which are known at 6.4 GHz and 12.3 GHz. The simultaneous observations of these two emission lines were performed for the W3OH maser source object on 17 January 2014 (Figure 5). Further improvement of the feed performance is under investigation for the final design, which is targeting good performance over the frequency range of 2–18 GHz. The broadband RF signal output from the front end is transferred to the observation room with a broadband optical signal transmission

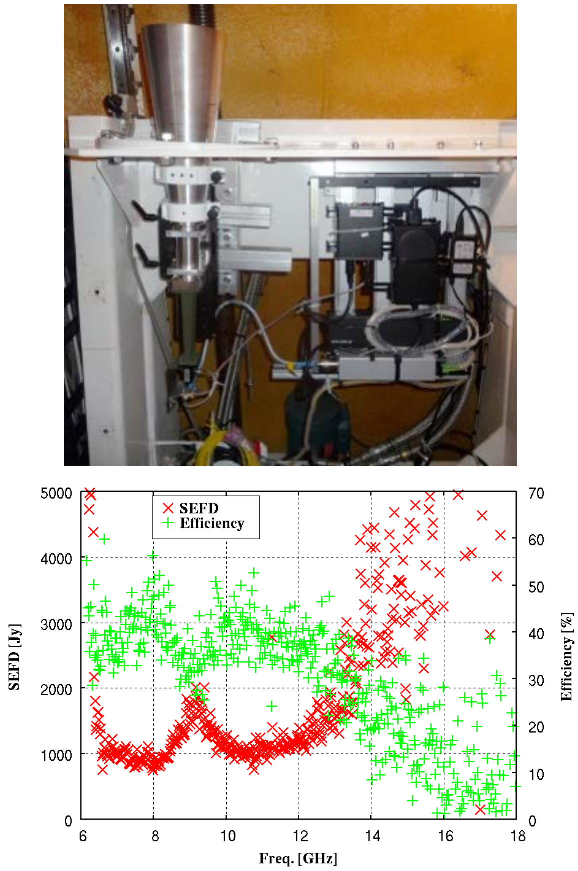

Fig. 4 A prototype of the higher frequency part of the broadband 'Iguana' feed was mounted on 34-m antenna (upper panel). System equivalent flux density (SEFD) and aperture efficiency measured with 'Cygnus-A' are indicated in the lower panel with '×' and '+', respectively.

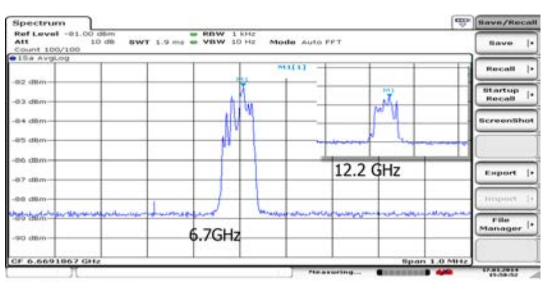

Fig. 5 The first light observation with the 'Iguana-H' feed was made on 17 January 2014 for the Methanol maser emission lines from W3OH at 6.4 GHz and 12.3 GHz, simultaneously.

system (E18000). The PCAL system of 100-MHz interval comb tones is to be injected after the LNAs via coaxial coupler, as is done with the small antennas.

5 RF Direct Sampler: K6/GALAS

One of the realizations of the data acquisition mode 2048 Msps/1 bit/4 ch uses a frequency converter, two sets of ADS3000+ samplers, and K5/PC-VSI (VSI-H) data recording systems. As another way for the data acquisition, employing a challenging new technology, we tried the direct sampling of the RF signal. The direct sampler K6/GALAS samples the analog RF signal at 16 GHz with 3-bit quantization; then frequency conversion and filtering is applied via digital signal processing. The data acquisition mode of 2048 Msps/1bit/4ch mode can be realized by one K6/GALAS sampler as indicated in the block diagram of Figure 6. The data stream over a 10G-Ethernet fiber link (10Gbase-SR) interface using the VDIF/VTP protocol and UDP/IP. The data recording system is composed of an off-the-shelf PC with 10Gbit Ethernet card and a Raid disk system. In addition to the simplicity and the reduction of the total cost, further benefits of the direct sampling approach are the homogeneous signal path length and the expected phase stability between the data at different frequency bands. Because the 'direct sampling' method captures the analog RF signal at once, the multiple frequency bands are separated by digital filtering. Thus, we can expect a uniform delay or an even delay adjustment between the data of each band. That might become advantageous for the broadband bandwidth synthesis. Further comparisons of the performance between the 'frequency conversion' and the 'direct sampling' methods have to be made using real data.

6 Remaining Tasks

An evaluation of the phase behavior of the 100-MHz interval PCAL signal and the frequency characteristics of the direct sampler remain to be done.

Correlation processing of the GALA-V project is performed with the GICO3 [10] software correlator developed at NICT. However, the post-correlation processing software is not ready yet. Synthesizing linear polarization correlation data and broadband bandwidth synthesis is a new feature of the bandwidth synthesis software. Data analysis is going to be done with CALC/SOLVE or C5++ [11]. The data processing path

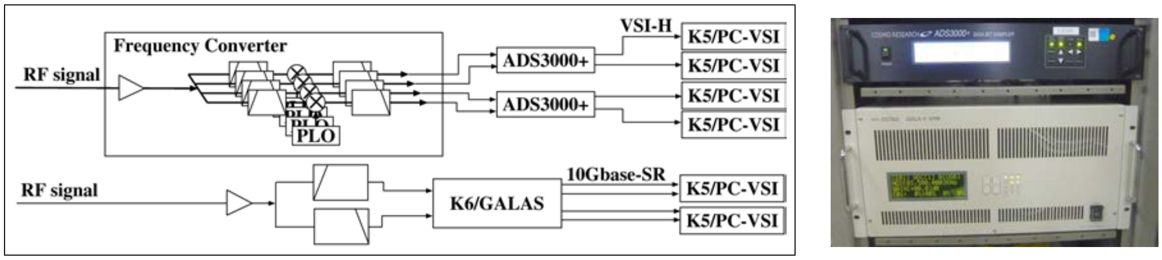

Fig. 6 Two ways of realizing the 2048 Msps/1 bit/4 ch data acquisition mode are illustrated in the left panel. The sampling frequency of the K6/GALAS is 16,192 MHz; higher and lower frequency signals than 8,096 MHz are separately input to avoid aliasing of the signal. The right panel displays a picture of the ADS3000+ sampler (top) and K6/GALAS (bottom).

from correlation processing to data analysis has to be established.

Acknowledgements

The broadband ‘Iguana’ feed development is supported by a Joint Development Research fund of NAOJ in 2013 and 2014. We thank Prof. K. Fujisawa of Yamaguchi University, Dr. M. Honma and Dr. N. Matsumoto of NAOJ, and Dr. H. Nakanishi of Kagoshima University for encouraging the development.

References

1. Riehle, F., Optical Atomic Clocks Could Redefine Unit of Time, Physics, vol. 5, Issue, id.126, 2012.
2. Jiang, Z, W. Lewandowski, Inter-comparison of the UTC time transfer links, Proc. of European Frequency and Time Forum (EFTF) 2012, pp.123-132, 2012.
3. Rieck, C., et al., VLBI and GPS-based Time-transfer Using CONT08 Data, Proceedings of IVS 2010 General Meeting “VLBI2010: From Vision to Reality”, Edited by Dirk Behrend and Karen D. Baver NASA/CP-2010-215864, pp.365—369, 2010.
4. Rieck, C., et al., VLBI Frequency Transfer using CONT11, Proceedings of European Frequency and Time Forum (EFTF) 2012, pp. 163-165. 2012.
5. Petrachenko, B., et al., Design Aspects of the VLBI2010 System – Progress Report of the IVS VLBI2010 Committee, NASA/TM-2009-214180, 2009.
6. Ichikawa, R., et al., MARBLE (Multiple Antenna Radio-interferometry for Baseline Length Evaluation): Development of a Compact VLBI System for Calibrating GNSS and Electronic Distance Measurement Devices, Proceedings of the IVS 2012 General Meeting “Launching the Next-Generation IVS Network”, Edited by Dirk Behrend and Karen D. Baver, NASA/CP-2012-217504, pp. 161-165, 2012.
7. Rogers, A. E. E., Test of new “digital” phase calibrator, BBDev. Memo #23, MIT Haystack Observatory, 25 Feb. 2010. `http://www.haystack.mit.edu/geo/vlbi_td/BBDev/023.pdf`
8. Yang, J, et al., Development of the Cryogenic 2-14 GHz Eleven Feed System for VLBI2010, 6th European Conference on Antennas and Propagation, DOI: 10.1109/EuCAP.2012.6206604, pp.621-625, 2011.
9. Akgiray, A., et al., Circular Quadruple-Ridged Flared Horn Achieving Near-Constant Beamwidth Over Multioctave Bandwidth: Design and Measurements, IEEE Trans. Antennas Propag., Vol. 61, No. 3, pp. 1099- 1108, 2013.
10. Kimura, M., and J. Nakajima, ‘The implementation of the PC based Giga bit VLBI system’, IVS CRL-TDC News No.21, pp.31-33, 2002.
11. Hobiger, T., et al.,c5++ - multi-technique analysis software for next generation geodetic instruments, Proceedings of the IVS 2010 General Meeting “VLBI2010: From Vision to Reality”. Held 7-13 February, 2010 in Hobart, Tasmania, Australia. Edited by D. Behrend and K.D. Baver. NASA/CP 2010-215864., p.212-216, 2010.

Current Development State of the Russian VLBI Broadband Acquisition System

Evgeny Nosov, Anton Berdnikov, Sergey Grenkov, Dmitriy Marshalov, Alexey Melnikov, Leonid Fedotov

Abstract The Institute of Applied Astronomy is currently creating a new radio interferometer consisting of two 13-meter antennas. A Broadband Acquisition System (BRAS) was developed and manufactured to equip the antennas with modern digital backends. BRAS contains eight 512-MHz channels. Each channel has a separate 10G Ethernet fiber link for transmitting the output data. The data consist of 2-bit or 8-bit samples packed into VDIF frames. We are currenlty performing tests of two created systems and are developing a new version of BRAS with 1024 MHz channels.

Keywords BRAS, MDBE, DAS, FPGA, Quasar network

1 Introduction

IAA RAS is creating a new radio interferometer consisting of 13-meter antennas. The collecting area of the antennas is relatively small in comparison to most of the existing VLBI antennas. To compensate for the resulting sensitivity loss, it is necessary to significantly increase the bandwidth of the recorded signal. This cannot be done with the existing data acquisition system R1002M DAS, which is currently used at the observatories of the “Quasar” network. To equip the antennas with a modern digital backend, the Broadband Acquisition System (BRAS) was developed and manufactured at IAA RAS [1].

Institute of Applied Astronomy, Russian Academy of Sciences

2 Broadband Acquisition System

BRAS consists of eight identical channels of 512-MHz bandwidth each (Figure 1). The channels receive the signals in the intermediate frequency (IF) range from 1024 MHz to 1536 MHz. Eight-bit analog-to-digital converters (ADC), used in BRAS to digitize the input signals, are clocked at 1024 MHz and have large enough input bandwidth to work in the third Nyquist zone. The 8-bit samples are processed by FPGA. The main purpose of FPGA is to pack the input samples into frames in the required format (VDIF) and with the corresponding timestamps, and to send the derived frames to the recording system through a 10 G Ethernet fiber-optic link. The output samples can be 8-bit or 2-bit. In the case of 2-bit data, FPGA measures the RMS level of the input signal and uses it as a threshold to requantize the signal to two bits. To provide time information, BRAS uses an internal clock synchronized to

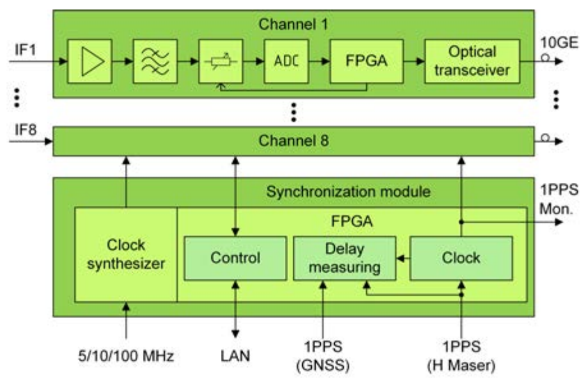

Fig. 1 Simplified structure of BRAS.

an external 1PPS signal from an H-maser. Each VDIF frame has the timestamp information in its header.

Fig. 2 Photo of the Broadband Acquisition System BRAS.

BRAS has a flexible output data formatter allowing different output modes. It provides a selectable VDIF payload size in a wide range of possible values from 1000 to 8192 bytes allowing the use of Jumbo frames. By default, BRAS encapsulates the VDIF frames into pure Ethernet frames without any overhead; but it is also possible to add IP and UDP headers. In addition, one can change the transmission medium from fiber to copper by replacing the transceiver. Besides the above-mentioned properties, FPGA performs several analysis features. It measures the input signal power with 0.25 second integration time. This data is used internally in the automatic gain control loop and is available in the control software. FPGA also collects 2-bit data statistics, which is useful for a quick analysis of the signal distribution and to detect strong signal distortions and interferences. Other useful features are the extraction of the phase calibration signal (PCAL) and the capture of the 1-microsecond input signal once per second. It gives rich possibilities for time and frequency domain analysis with software to evaluate the signal quality and system performance. Besides that, BRAS monitors the time difference between the internal 1PPS signal and any of the two 1PPS inputs. A BRAS prototype was successfully tested with real observations [2, 3]. Currently the system is ready for installation on the antennas (Figure 2). Key features of BRAS are summarized in Table 1.

Table 1 Key features of BRAS.

Number of channels	8
IF inputs	1024–1536 MHz
Channel bandwidth	512 MHz
ADC	8 bits, Fs=1024 MHz
Output samples width	2/8 bits
Total data rate	16/64 Gbps
Data frames format	VDIF
VDIF payload size	1000, 1024, 1280, 1600, 2000, ... , 8000, 8192 bytes
Output interface	10G Ethernet, X2 transceiver, fiber/copper
Output headers modes	Pure Ethernet frame, Ethernet + IP, Ethernet + IP + UDP
Control interface	10/100 Ethernet
Sync signals	5/10/100 MHz 1 PPS x2
Automatic gain control	For each channel, 31 dB
Analysis features	Signal power 2-bit data statistics PCAL extraction Both 8 and 2-bit signal capture (1024 samples) Spectrum analysis of captured signal and extracted PCAL (implemented in software) 1PPS int-ext delay monitoring
Telemetry	Power circuits current, temperature of PCBs and ADCs
Power consumption	75 W
Size	19″ case, 483x314x242 mm (WxHxD)

3 Multipurpose Digital Backend (MDBE)

The development of BRAS gave us the necessary experience to design a more complex and advanced backend— Multipurpose Digital Backend (MDBE). MDBE is intended to upgrade the backends of the “Quasar” network antennas and to allow it to operate both in conventional downconverter mode for compatibility with the existing data acquisition system and in broadband channel mode. MDBE has two four-channel ADCs with 1024-MHz sampling frequency giving overall eight channels with 512-MHz bandwidth (Figure 3). By using the ADC interleaving mode, MDBE can combine adjacent channels and operate in a four-channel mode with 1024 MHz bandwidth per channel. A powerful FPGA with embedded dual-core ARM processor used in the MDBE can perform quite complex digital signal processing. Along with the remote firmware reload supported by MDBE, it allows

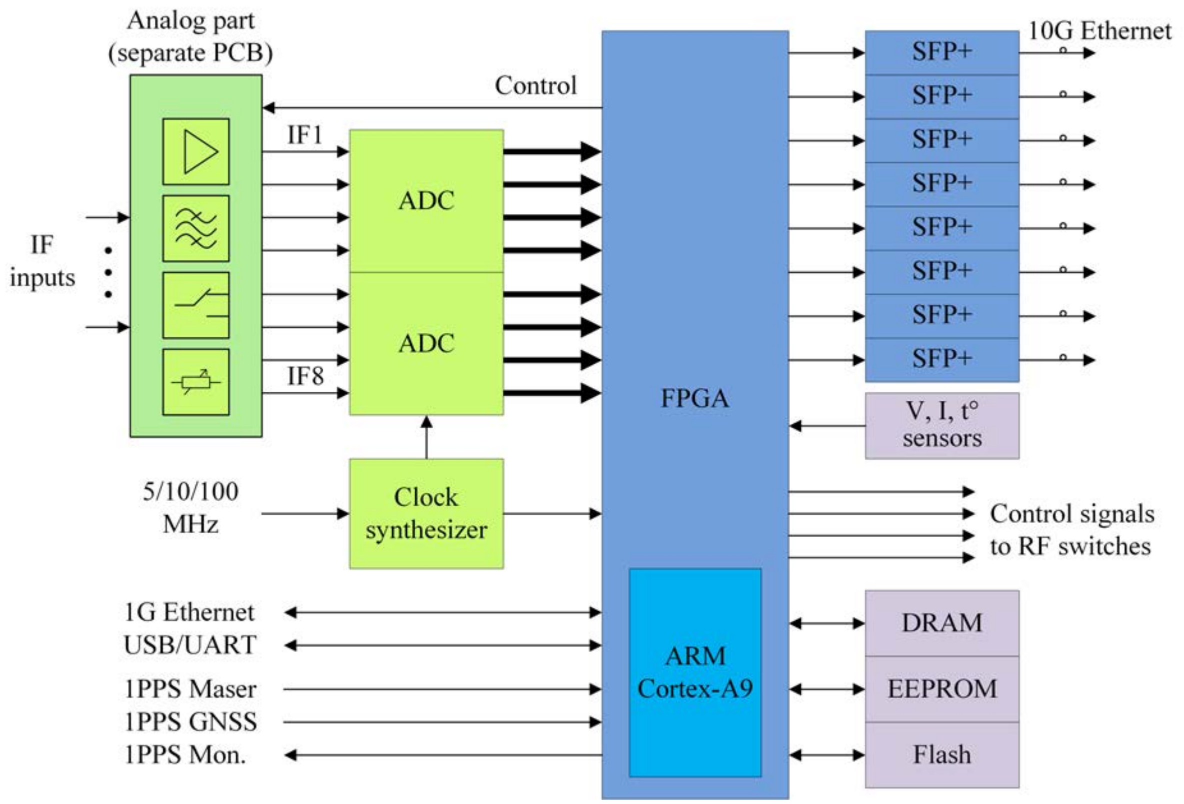

Fig. 3 Multipurpose Digital Backend structure.

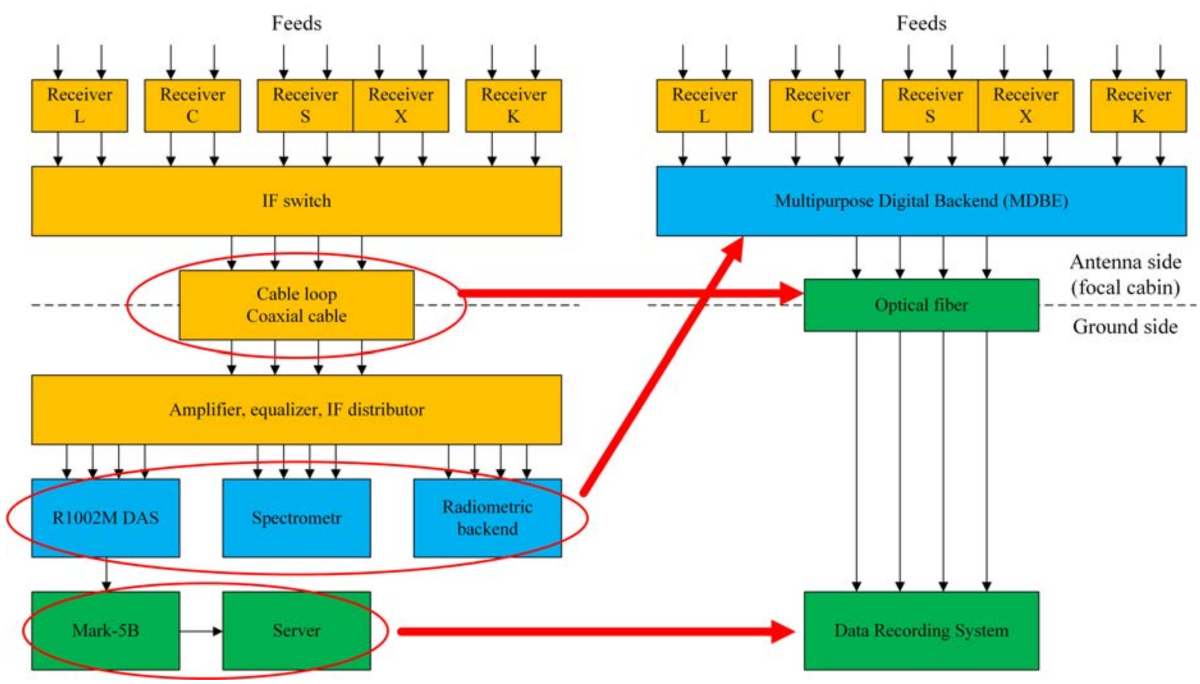

Fig. 4 Planned upgrade of the signal chain for RT-32 antennas.

to utilize the device for many radio astronomical tasks besides conventional VLBI applications. For example, spectrometer and radiometric backend modes are planned to be implemented. That means that the MDBE can combine all required backends into one device, greatly simplifying the signal chain structure (Figure 4). The MDBE will be located in the focal cabin of the antenna, which allows to eliminate long coaxial cables and auxiliary equipment used for signal transmission from the antenna to the control room and to replace it with fiber optic. Digital signals transmitted through fibers are insensitive to EMI, frequency response distortions, group delay variations, and so on. Using it can improve the quality of the VLBI data. The data recording system based on COTS components will be used to buffer the data [4]. It is also possible to copy data from the data recording system to Mark 5B for the case that the e-VLBI mode is not available. The MDBE is designed to be functionally compatible with the existing VLBI equipment, providing interoperability in international observations.

4 Conclusions

The Broadband Acquisition System for VLBI observations with 512-MHz bandwidth per channel was created. The prototype of BRAS was tested with real observations and first fringes were obtained. Currently the system is ready for installation on the new 13-meter antennas. In order to upgrade the existing equipment, to unify the instrumentation on all antennas of IAA RAS, and to provide a full set of modern radio astronomical backends, the development of the new Multipurpose Digital Backend was recently begun. The MDBE supports 1024-MHz bandwidth, remotely firmware reloading, and provides powerful computing resources.

References

1. Koltsov N. E., Marshalov D. A., Nosov E. V., Fedotov L. V. A data acquisition system of the S/X-wave range of the radio interferometer for the universal time on-line monitoring. *Instruments and Experimental Techniques*, 2013, Vol. 56, No. 3, pp. 339–346.
2. Grenkov S. A., Koltsov N. E., Marshalov D. A., Melnikov A. E., Nosov E. V., Fedotov L. V. Results of Testing a Radio Interferometer with Digital Signal Processing in a 400 MHz Band. *Instruments and Experimental Techniques*, 2014, Vol. 57, No. 1, pp. 45–49.
3. Melnikov, A., et al. First Fringes with BRAS on VLBI Network “Quasar”. This volume.
4. Ilya Bezrukov, Alexander Salnikov, Andrey Vylegzhanin. Russian data recording system of new generation. This volume.

DBBC3: An EVN and VGOS All-inclusive VLBI System

Gino Tuccari[1,2], Walter Alef[2], Salvatore Buttaccio[1], Simon Casey[3], Armin Felke[2], Michael Lindqvist[3], Michael Wunderlich[2]

Abstract The DBBC3 project is rapidly evolving in all its main components. The hardware of the astronomical L version is complete in the main parts, and the VGOS H version is progressing as planned. The DBBR receiver is under test and is expected to be placed in the antenna in the next few months. A first implementation of the L version includes the ability to support the VGOS requirements. A detailed status of the different structural parts is described, ranging from the front-end to the 32 Gbps disk and network capability, expandable up to 64 Gbps.

Keywords Backend, DBBC

1 Introduction

The development of the DBBC started in 2004, after in previous few years ad-hoc laboratory experiments and experiments with real sky signals had demonstrated that it would be possible to emulate with fully digital equipment the entire functionality of the Mark IV VLBI analog terminal. In the digital process, the signal available as IF from the receiver is immediately converted to a digital representation. This complete digital process could not be fully implemented at a reasonable cost, and moreover at that time it was a technical challenge due to the wideband and the high frequencies involved. During the first decade of 2000, with progressive improvements, the DBBC project evolved to cope with an input bandwidth of up to 4×1 GHz. The first DBBC version (DBBC1; 2004–2008) was a backwards compatible replacement of the existing VLBI terminal, while with the DBBC2 (2007 to date), additional observing modes, which did not exist in the analog backend, became available. The enhanced version of the DBBC2 for VGOS, the DBBC2010 (2009 to date), is compatible with the proposed VGOS observing, provided that an appropriate down-conversion of the broadband is realized in the analog domain. With new wideband receivers, the demand for backends which can handle bandwidths of several GHz has arisen. So both the new VGOS network and the EVN have been increasing their maximum data rate demand from a maximum of 1 Gbps with the Mark IV analog backend to something ranging between 32 and 64 Gbps. In particular for the EVN and the preparation for receivers and IF systems which will deliver up to 4 GHz (and later more) bandwidth to the backends, it was felt necessary to develop a system which can process an instantaneous bandwidth of 4 GHz per polarization as a minimum. The resulting output data rate for a dual polarization receiver should be at least 32 Gbps, with the option of 64 Gbps for a 4 IF system. Such a backend is the intermediate goal of the DBBC3 project. The specifications of VGOS define a set of features of the receiving/backend system to achieve the goal of greatly improved geodetic measurement precision. The telescopes will operate in a single broadband ranging from 2 to 14 GHz observing in dual linear polarization. Inside this frequency range a subset of four 1024 MHz wide pieces will be selected, in both polarizations. It is worth noting that then the actual selected input data rate will be equivalent in both EVN and VGOS. The wideband of the new VGOS network will realize bandwidth synthesis (phase slopes fitted over a wide frequency range) for a much wider portion of the spec-

1. INAF-Istituto di Radioastronomia
2. Max Planck Institute für Radioastronomie
3. Onsala Space Observatory

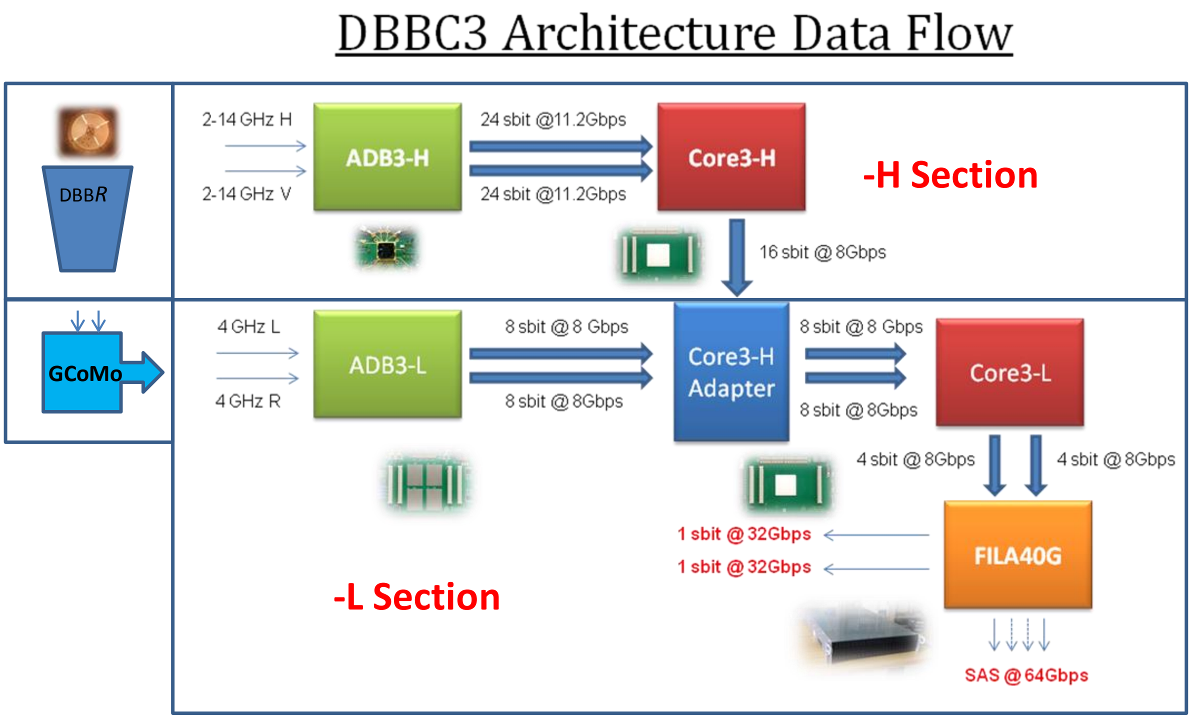

Fig. 1 General structure of the DBBC3.

trum than is possible with the present system. Such a wide input band could also be of great interest for astronomy because of the significant increase in sensitivity. Being able to process an entire 14 GHz-wide piece of band could be a quantum leap in digital radioastronomy data acquisition. This goal is very ambitious, and its implementation in a radio astronomy backend would be a novelty. To digitally sample and process the whole 14 GHz wideband or a number of sub-bands thereof is the final goal for the DBBC3 project.

2 DBBC3 Structure

The DBBC3 system needs to meet some compulsory requirements: backwards compatibility with the existing backends of the previous generations and the ability to realize the new functionality in the very wide band. It should also be able to accomplish all the required functionalities, for the planned EVN goals (minimum 2×4 GHz bandwidth) and VGOS (2×14 GHz bandwidth). Moreover, as many stations are active in both networks, a single system is mandatory, and flexibility is a requirement due to the different radio telescopes and their dissimilar receivers and IF systems in terms of their numbers and types of IFs. To be compatible with the existing systems, the new hardware needs to be mechanically and electrically level-compatible. This aspect is useful because existing DBBC terminals in the field could be upgraded to meet the new performance requirements by replacing the necessary parts. Components of the DBBC3 can be inserted into existing DBBC2 and DBBC2010 backends to augment their performance with additional functionalities.

The much higher performance of the new backends requires new hardware parts, to be supported by new firmware able to perform new functionality, that are a challenge for data volume and rate. A clear development path has been laid out to minimize the risk in the project. In a first step, a DBBC3-L will be developed which can be seen as a fully qualified 4 GHz DBBC and, at the same time, will allow us to study how best to achieve the final goal of a 14 GHz DDBC3-H. The first step is able to support both modes, EVN and VGOS, even if in this last case the input band is divided into four continuous progressive portions 4 GHz wide, up to 16 GHz.

The main features of the DBBC3-L system are:

- Maximum number of wide input IFs: four per polarization
- Instantaneous bandwidth in each IF: 4 GHz
- Sampling representation: 10 bit
- Processing capability N×5 TMACS (multiplication-accumulations per second), with N being the number of processing nodes
- Output data rate: maximum 64 Gbps
- Compatibility with the existing DBBC

The main features of the DBBC3-H system are:

- Maximum number of wide input IFs: four per polarization
- Instantaneous bandwidth in each IF: 14 GHz
- Sampling representation: 8 bit
- Processing capability N×5 TMACS
- Output data rate: maximum 896 Gbps
- Compatibility with the existing DBBC

This paper mainly describes the DBBC3-L version which is being specifically developed for the EVN network and is supported by RadioNet3. As already mentioned, this version will also be used in the first VGOS implementation. Figure 1 shows the overall structure of the DBBC3 including the data flow of both -L and -H.

The structure of the system is straightforward. Four IFs 4 GHz wide are sampled with 10-bit representation. This data is then transferred to one or more dedicated processing nodes, each with its own single element identity and functionality. The processors then extract from the digital data streams portions of the band (with digitally tunable mixers or fixed filters) and produce as VLBI-compatible output VDIF packets. The last element of the chain is the FILA40G subunit, whose function is to condense the data onto single optical fibers at 40 Gbps data rate and to handle the data at the network packet level. A dedicated version, the FILA40G-ST, will in addition have storage capabilities.

3 DBBR – Digital Broadband Receiver

The first unit mainly devoted to VGOS is the broadband receiver. The feed is coming from a deeply modified original project for telecommunication and renamed as “quad ridge in resonant chamber”. This is because having to cool it down at cryogenic temperatures, the performance is strongly influenced by the vacuum chamber and related shields. So it appeared convenient to have included as an active part the Dewar mechanics and to use it as an advantage more than to endure it as a side effect. The main characteristics of the DBBR are:

- Dual linear polarization
- 1 LNA per polarization
- Full range 1–16 GHz
- Radiation pattern versus frequency optimized for 3–14 GHz: 40–20 degrees @ -3dB
- Antenna factor versus frequency optimized for 3–14 GHz: 33–40 dB/m
- Optimized for cryogenic use (Dewar is active part)
- Entirely in copper
- Integration of custom cryogenic filters into the antenna body

The receiver is extremely compact and well-suited for 12-m class antennas. Its first use will be with the Noto antenna, where it will be adapted using a tertiary mirror.

4 GCoMo – Giga Conditioning Module

In a standard DBBC3 system, there could be from one to four units, available in more flavors with the capability of supporting a selection of four different frequency ranges: A (0–4 GHz), B (4–8 GHz), C (8–12 GHz), and D (12–16 GHz). For each range, the down-converted and the purely conditioned version will be available. This could help to simplify the receivers’ connections to the system. In the first VGOS implementation, this unit will allow access to the entire input range to be used with the ADB3-L samplers. Features of this unit are:

- Input: in real mode, four pre-filtered 4 GHz Nyquist bands; in complex mode, two pre-filtered 8 GHz bands
- Total power detectors independent in all the Nyquist zones
- Modular construction: any zone can be included
- Power level control in agc and manual mode
- Compatibility with the existing DBBC

5 ADB3-L Sampler

The massive 4 GHz sampling is performed by state of the art sampler chips. An extensive analysis is under way to determine the phase performance of those devices, as the interferometric use calls for high absolute phase stability and low temporal jitter. An alternative general method to increase the bandwidth is to make use of complex samples. Two channels in quadrature are sampled at a clock frequency equal to the full instantaneous bandwidth. A single ADB3-L has onboard four complete samplers, with the possibility of arranging them for a variety of functionalities, single and multiple, real or complex. Indeed, for example in real mode, the four samplers can be fed with a single input signal for the full 4 GHz functionality, so that they can be fed with two signals of 2 GHz instantaneous bandwidth each, or finally with four signals of 1 GHz bandwidth each. Sampled data are transferred to the processing units at a data rate of 80 Gbps for each ADB3-L board. The main features are:

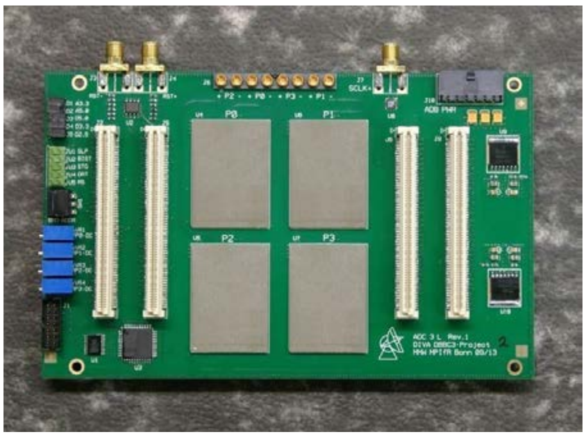

Fig. 2 ADB3-L board.

- Number of IFs: one to four
- Equivalent Sample Rate for full IF: 8 GSps
- Instantaneous bandwidth: 4 GHz
- Sampling representation: 10 bit
- Real/Complex Sampling
- Compatibility with existing DBBC

Figure 2 shows an ADB3-L board.

6 CORE3-L Processing Node

Data coming from the ADB3-L sampler board are routed to the processing node CORE3 using the lanes of the high speed input bus. This board is able to process data in different ways: DSC (Direct Sampling Conversion), DDC (Digital Down Converter), and PFB (Polyphase Filter Bank) functionalities. Additional capabilities will be spectroscopic and polarimetry observations. From the pool of channels, a subset is selected according to the desired output data rate defined by the observer or allowed by the recording or network media. The data is output through the high speed output bus. Additional input and output connections are available to maintain the compatibility with the DBBC2 stack. The large DSP resources available in the FPGA chosen for the CORE3-L allow digital filters in the class of 100 dB in/out band rejection. This feature is required for the expected presence of large RFI signals in the very wide input band. This very strong discrimination together with the tuning ability should be appropriate to obtain useful down-converted and clean pieces of the observed band. As an alternative input, the board will be able to receive data packets from a block of ADB3-H/CORE3-H units to be routed to the rest of the system for additional data processing. The functionality of the FILA10G used in the DBBC2 will be integrated in this unit for multiple 10G data I/O. In particular, this method is the output connection for the FILA40G unit. Figure 3 shows a

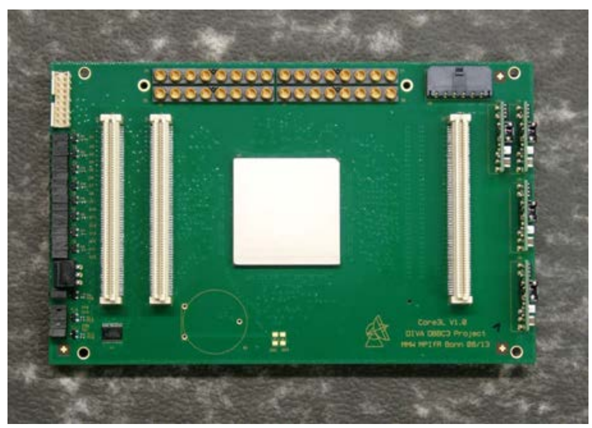

Fig. 3 CORE3-L board.

photo of the Core3-L board. The following list gives the main performance features:

- Number of I/O: maximum of 40 serial links, 12.5 Gbps
- Number of Output: maximum of 32 serial links, 11.2 Gbps
- Input Sampling Representation: 8–10 bit
- Processing capability: maximum of three TMACS
- Processing capability: WB-DDC, WB-PFB, WB-DSC
- Output: VDIF 10GE packets
- Compatibility with existing DBBC

7 FILA40G Network and Buffering Node

Data from the converted bands are finally transferred to the network controller FILA40G as multiple 10GE connections. The number of connections is then accumulated into a 40GE data stream to be transferred to the final destination points. Such final points could be recorders, nodes of VLBI correlators, or a buffer cloud. In addition to the 40G network capability, the FILA40G unit will be able to manipulate the data packets in order to perform functionalities such as corner-turning, pulsar-gating, packet filtering and routing, burst mode accumulation, and other functionalities that could be required at the packet level as soon as the VLBI methods evolve. In addition a dedicated version will be provided which can include storage elements for data buffering and recording. The general features are:

- 8 x 10GE Inputs
- 2 x 40GE Output
- Optional disk storage
- Expected recording rate of 32 Gbps
- Compatibilty with Mark 6 disk packs/chassis being investigated
- Stream aggregation
- Format conversion/VDIF threading
- Packet filtering
- Pulsar gating
- Timekeeping via NTP and/or GPS module
- Propagation of UTC to other connected devices via DBBC Local Network (DLN)

The available 10G skills are:

- Mark 5B up to 4 Gbps (native is 2 Gbps)
- VDIF Single Thread up to 8 Gbps
- VDIF Multiple Threads up to 8 Gbps
- RAW (no headers) up to 8 Gbps
- Threads can be fed by a selection of data channels eventually corner-turned
- The 10G Ethernet ports are independent in the destination address in VDIF-ST and Mark 5B
- The 10G Ethernet ports in multi-thread mode support an independent block of destination addresses coupled with the thread content selection
- Decimation and bit-mask are selectable at this level

Figure 4 shows a view of the FILA40G.

Fig. 4 FILA40G.

References

1. G. Tuccari, *Development of a Digital Base Band Converter (DBBC): Basic Elements and Preliminary Results*, in: New Technologies in VLBI, Astronomical Society of the Pacific Conference Series, ISSN 1050-3390, Vol. 306, 177–252, 2004.
2. G. Tuccari, *DBBC - a Wide Band Digital Base Band Converter*, in: International VLBI Service for Geodesy and Astrometry 2004 General Meeting Proceedings, NASA/CP-2004-212255, pp. 234–237, 2004.
3. A.E. Niell, A. Whitney, B. Petrachenko, W. Schlüter, N. Vandenberg, H. Hase, Y. Koyama, C. Ma, H. Schuh, and G. Tuccari, *VLBI2010: Current and Future Requirements for Geodetic VLBI Systems*, in: IVS 2005 Annual Report, NASA/TP-2006-214136, pp. 13–40, 2006.

Correlating and Fringe-fitting Broadband VGOS Data

Roger Cappallo

Abstract The great promise of increased precision and accuracy in the broadband VGOS system is accompanied by great challenges in processing the data it generates. The large spanned bandwidth necessitates ionospheric correction within the fringe-fitting process. Frequency sequences must be chosen not only on the basis of group delay precision and ambiguities, but also the ability to connect phase between bands, decouple delays from the ionosphere, and possibly to go to a phase-delay observable. The desire to use the system in conjunction with legacy S/X geodetic systems raises the issue of cross-correlating linearly- and circularly-polarized observations, mismatched bands, and unequal sample rates. This paper elaborates on these issues and describes how they are handled within the HOPS post-processing software.

Keywords VLBI, broadband, calibration

1 Introduction

As systems become more capable, there is generally a concomittant rise in complexity; the VGOS broadband geodetic VLBI system is no exception. Fortunately, there has been a parallel, even more dramatic increase in the capability of computing systems, so the tools are at hand to cope with the ensuing complexities. Here we document some of the new and modified algorithms used in the *fourfit* fringe-fitting program.

MIT Haystack Observatory

2 New Complexities Introduced by VGOS

Ultimately, the group delay observable is estimated by observing the change in interfereometric phase over a range of frequencies; the delay error is inversely proportional to the spanned bandwidth. By utilizing the full spectrum from about 3 GHz to 13 GHz, the VGOS system leverages a very wide spanned bandwidth compared to the legacy S/X band systems. At the same time, the *sampled* bandwidth has been significantly increased, to 2 GHz or more. Since the station sensitivity is directly proportional to the sampled bandwidth, this increase allows smaller, cheaper, and more agile antennas to be employed.

There is, however, a price to be paid for the increased frequency coverage and bandwidth, principally because:

- Single coherent fits across 8–10 GHz require treatment of ionosphere and source-structure effects at fringe-fitting time.
- VGOS uses dual linear polarization, since circularly polarized feeds that work well over a 2 octave frequency range are difficult to realize.
- The typical data volume has increased to 43 TB/day/antenna, assuming 8 Gb/s data rate and 50% observing duty cycle.
- Array homogeneity is reduced due to the mixture of VGOS and legacy S/X stations:
  - bandwidths/sample-rates are no longer equal,
  - there is a mixture of circular and linear polarizations,
  - frequency sequences mismatch,
  - sidebands mismatch.

In addition to these added complexities that are necessitated by the move to a wideband system, there are other challenges that have arisen as a by-product of general system improvement. The Mark 6 recording system (Cappallo et al. 2013) improves upon Mark 5 for performance and ease of use, but it constitutes another data format needing to be supported. Also, the move to complex sampling in the RDBE 3.0 offers efficiencies in both hardware and software, but it requires new code to deformat and correlate the data.

2.1 Phase Calibration and Connection

Phase calibration signals are injected at the receiver as a series of pulses at intervals of 200 ns, which can also be considered as a series of tones at 5 MHz spacings. These tones follow the same signal path as the radio-astronomical data down from the front end, and experience the same delay through the system prior to digitization (leg B in Figure 1). Since the upward path (leg A) can also experience time-varying delays due to phenomena such as cable stretching, leg A's delay will be measured independently by a cable delay calibration subsystem, and that delay contribution will be removed from the A + B − C combination. Leg C, which is typically a short cable run within the control room, combined with a small amount of timing electronics in the digitizer, is very stable over time, and appears simply as a clock offset.

The phases of all tones in each channel are extracted, and they are used to find out the instrumental delay in each channel. The 5 MHz tone spacing results in an ambiguity of the delay determination of 200 ns; i.e., the true delay is 0 or more increments of 200 ns in addition to the delay determination. This is handled within *fourfit* by allowing the user to specify *a priori* in which 200 ns range the delay is expected to lie. In modern digital backends, channels fed by the same IF and sharing the same cabling and anti-aliasing filter have very similar instrumental delays. Thus one can solve for a single delay per IF and apply it to all channels.

In current practice there are three parameters that are adusted during the fringe-fitting process:

1. **singleband delay** – the delay of each single channel

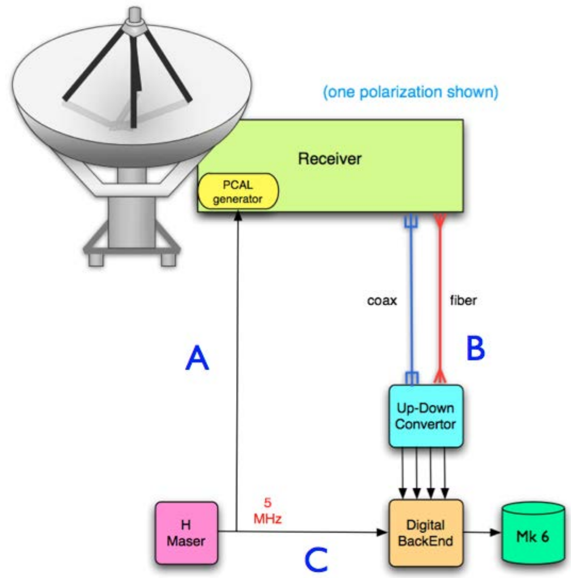

Fig. 1 Phase calibration paths: the delay measured by the phase cal tones is that of paths A + B − C. Path B is in common between the tones and the astronomical data, whereas the delay along path A must be measured by a cable delay calibration system.

2. **multiband delay** – the group delay found by estimating the linear phase change across multiple frequency channels
3. **delay rate –** the rate of change of delay

The historical reason for having two delays comes from instrumental causes: the single channels can have significant cabling and anti-aliasing filter differerences. With the move to digital backends, multiple channels share the same wideband anti-aliasing filter. Also, multiple phase cal tones are extracted from each channel, allowing the measurement and correction of each station's instrumental delays. In this manner we hope to use only a single delay in the fringe-fitting process.

2.2 Ionosphere Removal

In the S/X geodetic system independent group delay estimates are made for X-band and S-band, and a linear combination of these delays, $\tau_g = 1.081\tau_x - 0.081\tau_s$, is used to give a group delay measurement that is nearly free of ionospheric effects. One drawback of this system is that both the S and X band obervations have

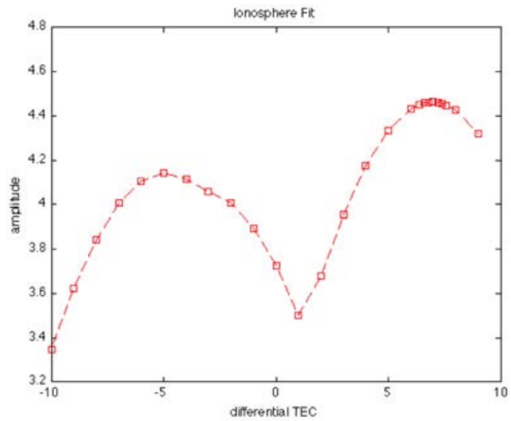

Fig. 2 Ionospheric fit – correlation amplitude as a function of differential TEC in TEC units. A complete fringe fit at multiple points for trial values of the ionospheric differential TEC is performed, and the code finds the interpolated maximum. The algorithm used is that a range of coarse values is specified, the maximum within the range is found, then a second pass fine search is done around the maximum. Although the efficiency of this algorithm could possibly be improved, it has proven a very robust mechanism for finding the maximum value. This example of the fitting process uses 19 coarse points spread over a dTEC from -10 to 10 TEC units.

to have a high enough signal-to-noise ratio so that a good detection can be made in each band. In constrast, the VGOS system is designed to work with very short scans, in which the individual bands may not provide a reliable detection, and in which all four bands need to be combined coherently in a fit. Since this fit also spans a wide frequency range, it is necessary to fit and remove the differential ionosphere from the group delay estimate.

The phase contribution in radians due to the ionosphere, $\Delta\phi$, is

$$\Delta\phi = -8.448x10^9 dTEC/f, \tag{1}$$

where f is the observing frequency in Hz, and $dTEC \equiv TEC_b - TEC_a$ is the differential TEC for baseline ab in TEC units (1 TEC unit = 10^{16} elec/m^2). Since phase is only measured modulo 2π, there is a non-linear dependence of phase upon the dTEC parameter in the model, which restricts the manner in which a fit might be performed (see Figure 2 for a brief description of the coarse-to-fine search algorithm used in *fourfit*).

2.3 Linear Polarization

In order to achieve reasonably good feed characterstics across the full frequency range, the VGOS design uses linearly polarized feeds. This adds significant complexity to the signal processing tasks, as all four polarization products must be produced and then combined in an optimal fashion to estimate group delay. A pseudo-Stokes-I (Intensity) observable can be formed, which is accurate to first order in the polarization leakage D-terms (Corey 2011). The pseudo-Stokes-I observable is formed as

$$I = (\overline{X_a \star X_b} + \overline{Y_a \star Y_b})cos(\delta p) + (\overline{X_a \star Y_b} - \overline{Y_a \star X_b})sin(\delta p), \tag{2}$$

where δp is the differential parallactic angle between sites a and b, and $\overline{X_a \star Y_b}$ is (for example) the time-averaged correlation product of site a's X polarization with site b's Y polarization.

2.4 Choice of Observable

Traditionally, geodetic VLBI has relied upon the group delay observable, as determined by the slope of phase vs. frequency across the span of several hundred MHz in a single band. The group delay can also be used with VGOS, with a much broader effective band; by connecting phase across multiple bands, we in effect form one large band – perhaps as much as an order of magnitude larger than was previously achievable. The error in the resulting group delay estimate, $\sigma(\tau_g)$, is given by

$$\sigma(\tau_g) = 1/(2\pi s\rho), \tag{3}$$

with signal-to-noise ratio s and rms spanned-bandwidth ρ.

If the system is sufficiently stable, then the residual phase left over after the best-fit delay model has been subtracted is slowly-varying. Its determination is equivalent to finding the y-intercept of a linear fit of phase vs. frequency. This means that the frequency span over which the phase is being determined is from 0 to the mean observing frequency, and thus

$$\sigma(\tau_p) = 1/(2\pi s\overline{f}) \tag{4}$$

with mean frequency $\overline{f}$. The error has then decreased by the ratio

$$\sigma(\tau_p)/\sigma(\tau_g) = \overline{f}/\rho, \quad (5)$$

which is ≈ 4 for the currently planned observing frequencies. If the phase delay observable is to be successful, then both the instrumental drifts in phase and the unmodeled phases due to source structure, which can vary as a function of both time and frequency, need to be sufficiently small.

2.5 System Complexity

The design choices described above lead to increased complexity in the execution of an experiment using the VGOS system. The placement of the frequency channels, for example, should be carefully considered, especially since there are somewhat contradictory criteria, whose effects need to be balanced:

- the channels should be spread apart to increase group delay precision;
- the channels should be spread fairly evenly to make phase connection between bands more robust;
- it is desirable to place the channels to decrease the correlation between the f group delay and the ionosphere's signature of 1/f;
- if there is a mixture of legacy stations, then the channels should be located where there is as much overlap with the legacy channels as possible.

In the VGOS system there are two polarizations, each with four bands of eight channels. Polarization-dependent phase corrections need to be determined for each antenna system, since the phases are dependent on some uncalibrated portions of the front end. The flood of data, with scans at intervals as low as 30 s or so and close to a petabyte of raw data per experiment, will stress the data-processing pipelines at the correlation centers. Efficient bookkeeping and quality control will be essential.

3 Transitioning from Legacy Systems

It is desirable to keep some compatibility between the broadband VGOS system and the legacy S/X band systems. This will establish continuity of the terrestial reference frame, and, through the ties of VLBI observations, there will also be better continuity of the celestial reference frame. For these reasons, it is expected that parallel observations will be made for some years after the introduction of the VGOS system. Thus the technical difficulties entailed in joint observations need to have satisfactory solutions.

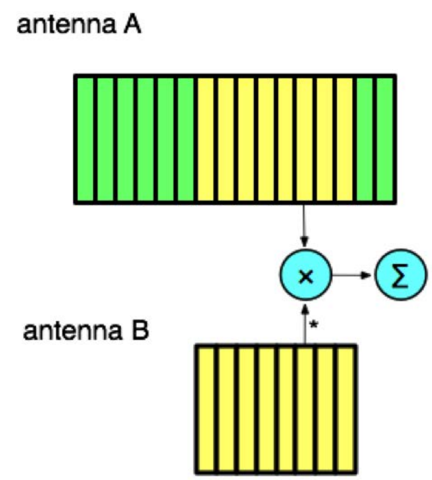

Fig. 3 Correlation of non-matching bandwidths by ensuring channel alignment within the F-stage of an FX correlation.

3.1 Mismatching Bandwidths, Sample Rates, and Channel Alignment

In general, recent practice with the legacy geodetic observing mode has been to use a bandwidth of 8 MHz, and thus a Nyquist sampling frequency of 16 MHz. On the other hand, the VGOS current standard is channels of 32 MHz bandwidth, sampled at 64 MHz. Furthermore, the local oscillator (LO) for the legacy setup is such that channels start at xxxx.99 MHz to try to preserve phase cal purity, while the broadband channels typically start at yyyy.40 MHz.

Cross correlations between the systems, in so-called "mixed mode" are accomplished (see Figure 3) by picking a narrow channel width, δf, in the F stage of an FX correlation, which satisfies the following two conditions:

- δf divides evenly into both station's channel bandwidths,
- the edges of the resulting narrow channels line up.

For the frequency setup mentioned above, $\delta f = 10\,\mathrm{kHz}$ satisfies these conditions. Then, in the cross-multiply, or X, stage of the correlation the corresponding narrow channels are paired off, multiplied, and summed.

In the *DiFX* program, which is a software correlator (Deller et al., 2011), this is accomplished using "zoom" mode. Zoom mode was originally intended for selectable high spectral resolution in portions of the processed band, but it also works as a way of implementing the necessary machinations for mixed mode. It handles the chore of sideband conversion of one of the signals, if the mismatching bands fail to match in sideband (i.e., upper x lower). New code was written to synthesize an output VEX file that correctly describes the narrower intersecting bands that result from zoom mode, in order to allow correct post-processing of the data.

3.2 Mixed Polarization

The legacy S/X band observing mode has been to use right circular polarization (RCP), whereas the new VGOS systems are dual linear polarization (XY). When there are multiple polarization products, the noise products contain statistically independent information, and we can maximize the sensitivity of the delay observation by coherently combining all available polarization products. In the most general case of dual circular polarization correlated against dual linear polarization, we have four products (XL, XR, YL, YR), and the appropriate linear combination for the complex visibility would be

$$V = (a_{xl}\overline{X\star L} + a_{yl}\overline{Y\star L})e^{i\delta p} + (a_{xr}\overline{X\star R} + a_{yr}\overline{Y\star R})e^{i\Sigma p}, \quad (6)$$

where δp and Σp are respectively the differenced and summed parallactic angles, and the a_{pq} are unit-magnitude complex phasors representing (minus) the calibration phase between polarization states p and q. The unit phasors are used to counter-rotate the complex fringes so that they will line up coherently. It is the expectation (and hope) that the phases will be very slowly varying, so that the calibration phasors need to be solved for only infrequently during an experiment, and they can subsequently be used over a long span of time. Note that this formulation for using the mixed polarization products differs from the earlier pseudo-Stokes-I in Equation 2, for there has been no effort here to correctly normalize the amplitudes. This simplification should only slightly affect the group delay estimate, but it would complicate the use of mixed-mode visibilities for imaging.

4 Future Work

Though many modifications have been made to the correlation and post-processing software to allow the efficient use of the VGOS broadband data, there are still desirable capabilities that have yet to be implemented:

- develop a $\phi(f)$ phase mode for source structure which would be calculated for each observation and applied in the fringe-fitting process, in order to permit phase connection across the bands for less point-like sources,
- correct for the known constant phase signature of the digital filters within each band,
- remove the current operational need for multiple passes (one per observing band) through the correlator,
- automate the generation of phase cal masks, which are used to exclude any phase cal tones that are corrupted by RFI,
- automate the generation of delay and phase calibrations for the VGOS multi-polarization-product data, and
- increase the size and efficienty of the computing clusters to handle the expected increase in observing and data rates.

Much of this work can be summarized simply, by noting that we need to achieve much better automation in the data pipeline for the anticipated needs of VGOS.

Acknowledgements

Many people have contributed to the HOPS post-processing software package through the years, with some of the most significant contributions coming from Alan Rogers, Colin Lonsdale, Alan Whitney, and Cris Niell. Much of the VGOS-related development work and ideas have come from Arthur Niell, Bill Petrachenko, and Brian Corey.

References

1. Brian Corey, private communication, 2011.
2. Adam Deller, Walter Brisken, Chris Phillips, John Morgan, Walter Alef, Roger Cappallo, Enno Middelberg, John Romney, Helge Rottman, Steven Tingay, and Randall Wayth. DiFX-2: A More Flexible, Efficient, Robust, and Powerful Software Correlator. PASP, **123**, pp. 275–287.
3. Roger Cappallo, Chester Ruszczyk, and Alan Whitney. Mark 6: Design and Status. Proceedings of the 21st Meeting of the European VLBI Group for Geodesy and Astronomy, pp. 9–12.

VGOS Operations and Geodetic Results

Arthur E. Niell[1], Christopher J. Beaudoin[1], Sergei Bolotin[2], Roger J. Cappallo[1], Brian E. Corey[1], John Gipson[2], David Gordon[2], Russell McWhirter[1], Chester A. Ruszczyk[1], Jason SooHoo[1]

Abstract Over the past two years the first VGOS geodetic results were obtained using the GGAO12M and Westford broadband systems that have been developed under NASA sponsorship and funding. These observations demonstrated full broadband operation, from data acquisition through correlation, delay extraction, and baseline estimation. The May 2013 24-hour session proceeded almost without human intervention in anticipation of the goal of unattended operation. A recent test observation successfully demonstrated the use of what is expected to be the operational version of the RDBE digital back end and the Mark 6 system on which the outputs of four RDBEs, each processing one RF band, were recorded on a single module at eight gigabits per second. The complex-sample VDIF data from GGAO12M and Westford were cross-correlated on the Haystack DiFX software correlator, and the instrumental delay was calculated from all of the phase calibration tones in each channel. A minimum redundancy frequency sequence (1, 2, 4, 6, 9, 13, 14, 15) was utilized to minimize the first sidelobes of the multiband delay resolution function.

Keywords Geodesy, VGOS

1 Introduction

The next generation geodetic VLBI instrument is being developed with a goal of 1 mm position uncertainty in twenty-four hours. The broadband signal chain, which is essential for obtaining the required delay accuracy from a network of relatively small antennas, has been implemented on the 12-meter antenna at Goddard Space Flight Center, Maryland, USA, and on the 18-meter Westford antenna at Haystack Observatory, Massachusetts, USA, in several phases over the past two years. Observing sessions to evaluate the status of the VGOS systems were conducted in October 2012 and in May 2013. Some results from these sessions are presented here.

Over the same period, improvements to the signal chains at both antennas continued. Desirable features were added to some of the components, and the entire recording system was replaced. These changes, which included installation of the Monitor and Control Instrumentation at Westford and implementation of complex samples in the RDBE, were evaluated in a successful fringe test in April 2014. The primary missing component is the cable delay measurement system, which is ready for proof-of-concept testing.

1. MIT Haystack Observatory
2. NVI, Inc.

2 Geodetic Results

2.1 October 2012

In October 2012, two six-hour sessions were carried out on successive days. The instrumentation configuration, observing procedures, correlation and observable extraction, and analysis are described in [1]. During early testing of the broadband system at GGAO it became apparent that the aircraft avoidance radar associated with the nearby (co-located) Satellite Laser Ranging systems is powerful enough to damage the VLBI front ends if the radar is pointed in the direction of the VLBI antenna. Thus, when the antenna is operating, either it must avoid pointing within a cone of approximately 40 degrees of the radar, or the SLR systems must not be operating. One scenario was exercised in each of the two sessions. The effect on the scheduled observations is seen in Figure 1 in which the azimuth and elevation for every scan is viewed as a projection on a horizontal plane. The loss of sky coverage reduces the positional accuracy along the direction of the missing data, but more importantly, reduces common visibility with other antennas in the network in that direction.

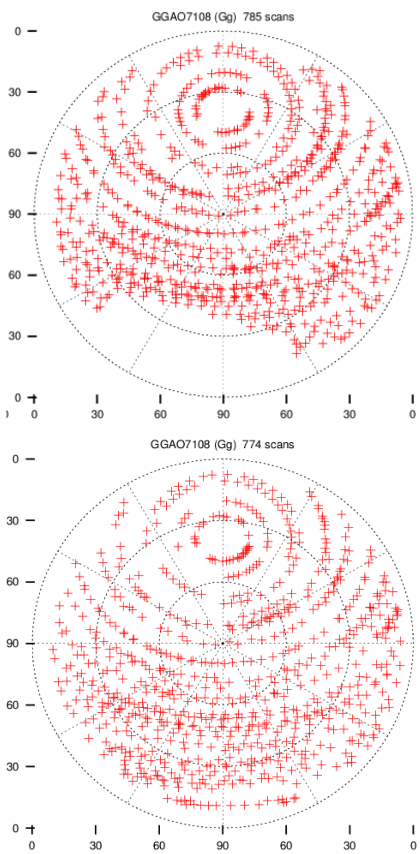

Fig. 1 Azimuth-elevation plots of the directions of all observations for 2012 October 4 (top) for which the direction to the SLR system was masked out, and October 5 (bottom) for which no mask was imposed (plots courtesy of GGAO).

The broadband signal chain provides the signal from two polarizations, vertical and horizontal, at the antenna. The two polarizations will be combined coherently in post-correlation for most sessions (and could be for these), but for these initial geodetic observations, they were processed separately in order to provide a measure of precision, because the two should agree to much less than the uncertainty for each. This is because the uncertainties are based on the scatter of the post-fit delay residuals, and these are probably dominated by errors in the atmosphere modeling and by other effects that are common-mode to the two polarizations. The components of the position of GGAO relative to Westford, and the baseline lengths, each relative to the mean of the values, are shown in Figure 2.

A new feature of the broadband technique is the need to estimate the 1/frequency term of the phase variation with frequency simultaneously with the other observables (single-band delay, group delay, delay rate, and phase). This is ascribed to the difference in total electron content (dTEC) along the lines of sight through the ionosphere to the radio source at each site. As a check on the consistency of the estimates of dTEC from the 2012 October 5 data, the values were compared with the same quantity derived from GPS TEC measurements. The results are shown in Figure 3.

2.2 May 2013

One goal of the 2013 May 22 session was the demonstration of unattended operation. This was the first full twenty-four hour VGOS session, and it required only the re-start of one RDBE when it timed out during the session. The antennas were controlled by the Field System, while the RDBEs and Mark 5Cs were run by a script generated from the same *sked* output file that provided the input to the Field System.

Another goal was to evaluate the fringe amplitude calibration of the interferometer. The frequencies of the four bands were chosen to span 3.3 GHz to 8.8 GHz so that the highest band (8.3 GHz – 8.8 GHz) overlaps the X-band from geodetic sessions [3]. The schedule took advantage of the high speed of both antennas to achieve an observing rate of approximately 45 scans/hour, limited by a minimum scan length chosen to be 30 seconds and by an excess latency in the startup motion of the Westford antenna, which has since been fixed. For this session, the SLR mask was on. Outside of this range, the minimum elevation was 5°.

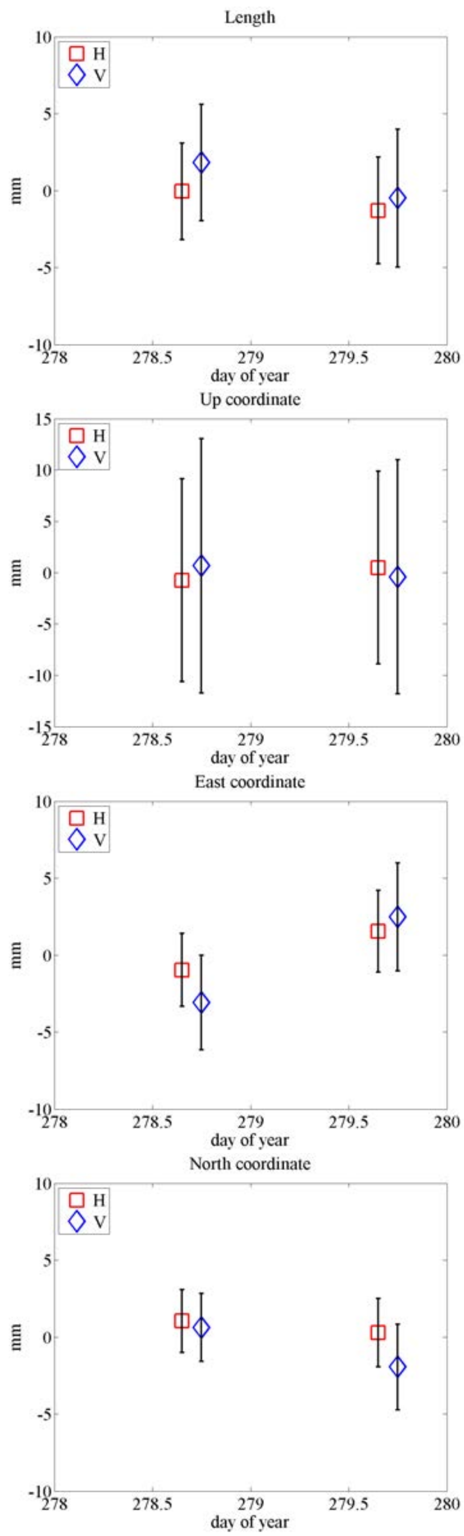

Fig. 2 Residual to the mean of the components of the position of GGAO relative to Westford.

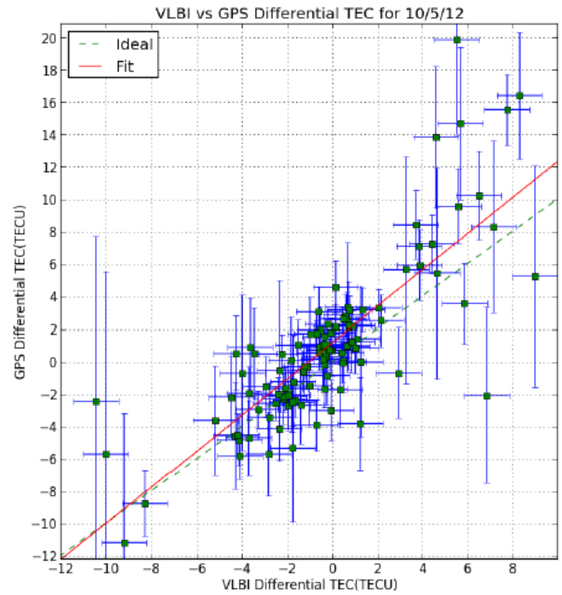

Fig. 3 Comparison of difference of TEC along line of sight from each antenna as estimated from the VLBI data of 2012 Oct 5 and from GPS TEC values.

Following correlation of the four bands in separate passes, the correlator outputs were merged into one file. The delay and dTEC were estimated for all 1,140 scans, and the position of GGAO was estimated relative to Westford using nuSolve with the clock and atmosphere parameters modeled as stochastic processes.

As a measure of the precision of the VGOS system, the position was estimated for separate, approximately six-hour segments for comparison with the full session. The results are shown in Figure 4.

2.3 Testing the Operational Configuration (April 2014)

Since the 2013 observations, several improvements have been made to various components of the system to bring both sites close to the operational configuration. At Westford the hardware for the Monitor and Control Instrumentation was installed. For both sites the RDBEs were upgraded by significant changes to the FPGA code and server software. At Westford two of the RDBEs were upgraded with a new synthesizer board and simpler attenuator components. Perhaps the

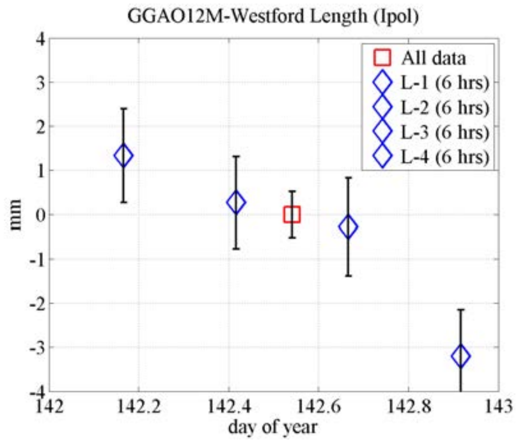

Fig. 4 Baseline length between Westford and GGAO12M on 2013 May 22. Red square: solution for all 24 hours of data; blue diamonds: independent six hour segments analyzed with the same parameterization as the full 24-hour solution.

most significant change was to make use of the Mark 6 recorder, which replaced four Mark 5C recorders.

The signal chain as currently implemented is illustrated in Figure 5. Previously, the output from each RDBE was recorded on a separate Mark 5C [2].

The RDBE upgrade provides many new features. The data samples are now complex representations and are output in VDIF (VLBI Data Interchange Format). This brings the RDBE into compliance with the VLBI standards, as well as reducing resource requirements in the FPGA fabric. Equally important, two capabilities were added: a) measurement of differences in the 1 pps epochs among the maser pulse, the external GPS time, and the internally re-generated 1 pps pulse; and b) extraction of the phase cal phases and amplitudes. The former allows continuous monitoring of the RDBE clock throughout a session, and the latter allows more thorough station checking both outside of an observing session and during the observations.

A short VLBI observation was made on 2014 April 17 to verify the operation of the new configurations. The new instrumentation performed as expected for the features that could be tested, and the correlator modifications required to process the data were validated as well. However, the two new capabilities were not able to be demonstrated, nor was the control and utilization of the noise diode switching for improved system temperature calibration.

The final development needed to complete the VGOS system is the cable delay measurement system.

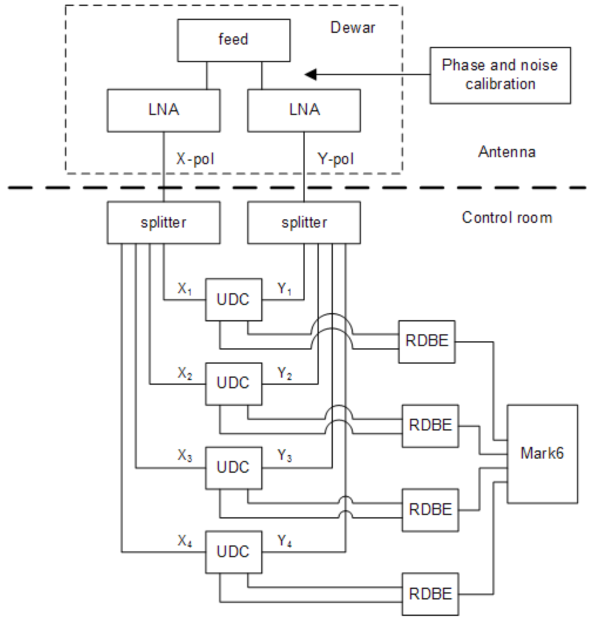

Fig. 5 Diagram of the Broadband Delay System. The dashed box indicates the components that are mounted on the antenna and cooled to approximately 20K. Phase and noise calibration signals are injected between the feed and each LNA. X-pol and Y-pol represent the two linear polarization signals produced by the QRFH feed.

A proof-of-concept unit has been thoroughly tested on the bench, and components are being constructed for installation of prototype units on both antennas. Testing of these units and the other features will be initiated on the GGAO antenna.

3 Summary

Operations on a regular basis using scripts as described above can begin as soon as the new features are verified and the delay calibrator is completed and checked out. However, full IVS usage also requires incorporation of the VGOS capabilities into the session preparation software (e.g., *sked*) and modification of the Field System to control the RDBE and Mark 6.

Finally, it is extremely important to develop a coordinated observing scheme with the SLR systems in order to avoid losing the geometric strength and common visibility that arises from loss of observations in the direction of the SLR.

Acknowledgements

Development of the VGOS system has been funded by the Earth Surface and Interior Focus Area of NASA through the efforts of John Labrecque, Chopo Ma, and Herb Frey.

The system could not have been put together without the work of Sandy Weinreb, Hamdi Mani, and Ahmed Akgiray of Caltech, whose designs of the Dewar, LNAs, and feed have been incorporated.

References

1. Niell, A. et al., Haystack Analysis Center, in International VLBI Service for Geodesy and Astrometry 2012 Annual Report, edited by K. D. Baver, D. Behrend, and K. Armstrong, NASA/TP-2013-217511, 265–268, 2013.
2. Niell, A. et al., First Broadband Results with a VLBI2010 System, in International VLBI Service for Geodesy and Astrometry 2012 General Meeting Proceedings, NASA/CP-2012-217504, D. Behrend and K. D. Baver (eds.), 13–17, 2012.
3. Niell, A. et al., Haystack Observatory Analysis Center, submitted to International VLBI Service for Geodesy and Astrometry 2013 Annual Report, edited by K. D. Baver, D. Behrend, and K. Armstrong.

WVRs for the “Quasar” Network

G. Ilin, V. Bykov, V. Stempkovsky, A. Shishikin

Abstract A prototype for dual frequency water vapor radiometers (WVRs) was developed at IAA and tested at the “Svetloe” observatory for more than a year. It was constructed according to the IAA plan to have near real time information about the zenith tropospheric wet delay (ZWD) in “Quasar” network observatories for use in VLBI data processing. Another two WVRs of the same type will be constructed in 2014 for the “Badary” and “Zelenchukskaya” observatories. The WVR prototype demonstrated very stable metrological characteristics in time intervals of several months. The values of ZWD assessed by WVR were compared with the same values determined from GNSS observations. The difference between the GNSS and WVR ZWDs is practically equal to zero with an accuracy of up to 3–5 mm (r.m.s), except for periods of intensive rain. This result was achieved due to precise measurements of the atmosphere brightness temperature.

Keywords Water vapor radiometers, wet delay

1 Introduction

IAA is realizing a special program to equip the “Quasar” VLBI Network observatories with WVRs. WVRs are designed for rapid evaluation of troposphere parameters. ZWD measured by WVR will be used in data processing of VLBI observations. We hope that WVRs will be very useful additional instruments for “Quasar” co-location sites [1], applied for determination and monitoring of ZWD and integrated water vapor (IWV) practically in real time mode.

Institute of Applied Astronomy of RAS

2 WVR Design

For effective application of the ZWD in VLBI data processing, it is necessary to measure it with maximum accuracy, up to 3 mm (r.m.s.). To solve this problem, WVRs should measure atmosphere brightness temperatures most accurately.

To realize this in regular automatic observations, WVR equipment must satisfy the following requirements:

- very stable microwave reference sources;
- maximum temperature stability of all RF units;
- temperature control (and logging) of all critical points;
- total gain variation control of the RF units;
- operation mode: “total power” + fast switching ($\sim$1 kHz) of input signals;
- guaranteed linearity of square law detector;
- reliable electronic unit;
- remote access and control facilities.

We tried to realize these requirements in the modern WVR design.

Two WVR models have been tested at the “Svetloe” observatory. WVR1 was installed in 2011, and WVR2 was installed in June 2013. The WVRs are operating in different modes. WVR1 is fully steerable to have the capability of following radio telescope RT-32. WVR2 is fixed and looks only at the zenith direction. The WVR3 model is designed for installation at the “Badary” and “Zelenchukskaya” observatories.

Fig. 1 (a) WVRs' location at the "Svetloe" observatory. (b) General view of the WVR3 box in a laboratory test board.

It will be fully steerable and capable of moving synchronously with the new RT-13 radio telescope.

WVR1 and WVR2 are located at the "Svetloe" observatory on the roof of the laboratory building at a distance of about 100 m from RT-32. A general view of the WVRs' location is shown in Figure 1a.

The construction of all WVR models is based on the ideas proposed in [2]. In the literature, this radiometer design is better known as absolutely stable radiometer [3].

WVR has two unified-in-design microwave radiometric blocks placed into the thermo-stabilized ($+30 \pm 0.1°$C) container. Each radiometric block has two internal waveguide-matched loads stabilized at a temperature of $+35 \pm 0.01°$C and $+60 \pm 0.01°$C. These loads are used as very stable reference signal sources [4]. All microwave units of radiometric blocks are placed on a thermostatic platform ($+30 \pm 0.01°$C). Radiometric blocks are equipped with horn-lens antennas. A general view of the WVR3 design is presented in Figure 1b. Specifications of the WVR are listed in Table 1.

Reference signals of WVR1 were calibrated with the tipping calibration method (tipcal) [5]. Tipcal was done exclusively in perfect weather conditions for determination of reference signal and atmosphere brightness temperature with a maximum accuracy.

As a calibration signal (T_{kA}) for the WVR, we use the combination of receiver noise signal ($T_{rec.A}$) and reference signal of "cold" waveguide matched load (T_{cA}) stabilized at a temperature of $+35 \pm 0.01°$C:

$$T_{kA} = T_{cA} + T_{rec.A}(t_{amb})$$

Table 1 Specifications of the WVR3.

Specifications:	Value
Frequency bandwidth 3 dB, GHz	
Channel A	20.7 ± 0.25
Channel B	31.4 ± 0.25
Receiver noise temperature, at the input, K,	
Channel A	150
Channel B	280
Gain, up to *Sq*. law detector, dB	
Channel A	65
Channel B	65
Brightness temper. sensitivity, K,	
$t = 1s$ (dry weather)	
Channel A	0.012
Channel B	0.025
Relative gain instability, 24 h, %, less than	0.03
HPBW(−3dB) / BW(−35dB)	$6°/22°$
Angular resolution Az, El, arc min.	5

The presence of small losses of the lens material leads to dependence of the receiver noise temperature on the value of ambient temperature (t_{amb}). This dependence was found and measured due to high accuracy of tipcal, made during the period of a year when t_{amb} changed from $-20°$C to $+20°$C. Temperature dependence of calibration signals was used in the data processing.

In the WVR3 model, we will apply more effective thermal isolation of the microwave units of the radiometric blocks to reduce the temperature dependence of the calibration signals or the temperature dependence of the receiver noise temperature.

The parameters of the WVR1 calibration signals are presented in Table 2.

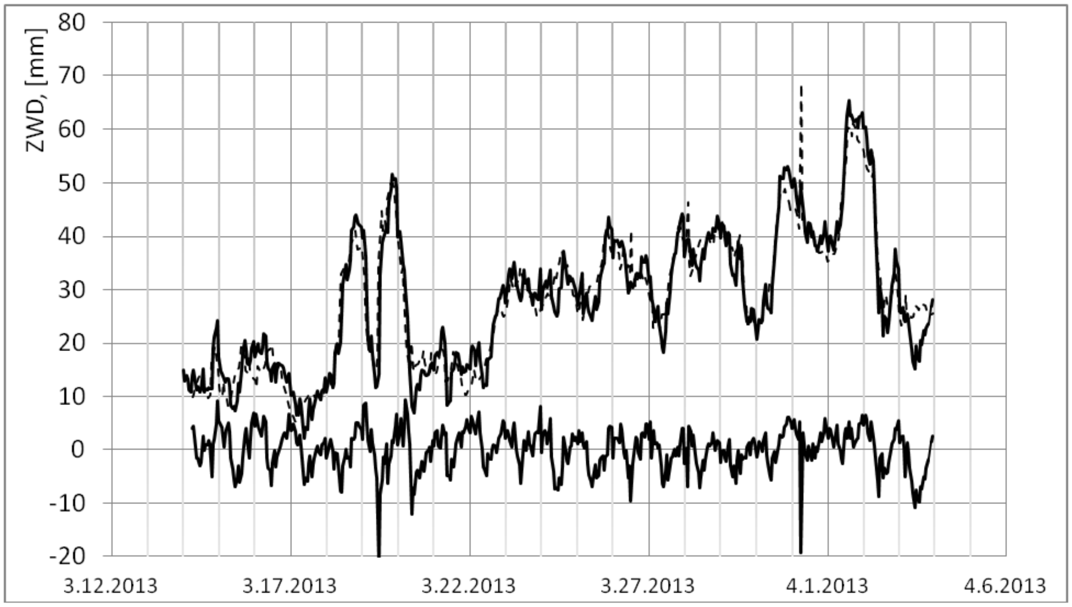

Fig. 2 ZWD, in mm, estimated by WVR1 (dashed line), retrieved from GNSS (solid line), and their difference (lower line).

Table 2 Parameters of WVR1 calibration signals.

Stability of the reference signal (“cold” loads), K, 1.5 year interval	
Channel A	313.02 ± 0.02
Channel B	313.38 ± 0.02
Effective noise temperature of the calibration signals, K, $t_{amb} = 0°$C	
Channel A	443.8
Channel B	571.0
Stability of the calibration signals (temperature dependence is excluded, K, (r.m.s.)	
Channel A	0.3
Channel B	0.4

3 Results

The retrieval of ZWD from the brightness temperatures measured by WVR proceeds as follows. First, an IWV value (g/cm^2) is determined, and ZWD (cm) can be calculated as [6]:

$$ZWD = (0.106 + 1722/T_{eff}) \cdot IWV,$$

where T_{eff} is the atmosphere mean temperature (K), calculated from radiosonde data, and can be modeled as a linear dependence on surface temperature. Now, at the “Svetloe” observatory T_{eff} can be measured by temperature profiler MTP-5 [7].

To estimate the accuracy of the retrieval algorithm, we compared ZWDs estimated by WVR1 with those from GNSS observations for the same time period. These values for a “dry” period from March–April 2013 are presented in Figure 2. Their difference is better than 3 mm (r.m.s.), when excluding two peaks associated with precipitation.

For a longer interval—from several months to one year—the standard deviation of the ZWD difference increases to 5 mm (incorrect WVR1 data for periods of rainfall are excluded).

4 Conclusions and Future Plans

WVR1 and WVR2 have shown stable metrological parameters and reliable, maintenance-free operation for intervals of more than six months.

The WVR3 model accumulates all the positive technological experience and will be more stable in operation under unfavorable weather conditions.

WVR3 models will be installed at the “Zelenchukskaya” and “Badary” observatories at the end of 2014. We also plan to install MTP-5 at “Zelenchukskaya” during May 2014. The data obtained by MTR-5 will be used in WVR data processing.

References

1. Finkelstein A., Ipatov A. et al. Co-location of Space Geodetic Instruments at the “Quasar” VLBI Network Observatories. *IVS 2012 General Meeting Proceedings*, NASA/CP-2012-217504, pp. 157–160.
2. Shmaonow T. A. Method of absolute effective radio emission temperature measurements characterized low equivalent temperature. Instruments and Experimental Techniques 1957, Vol. 2., No. 1, pp. 83–86 (in Russian).
3. Hach J. P. A very Sensitive Airborne Microwave Radiometer Using Two Reference Temperatures. IEEE Trans. On MTT, 1968, 16, 629–636.
4. Bykov V. Yu., Ilin G. N. K-band adjustable noise generators. Instruments and Experimental Technique. November 2012, Vol. 55., Issue 6, pp. 669–672.
5. Han Y., Westwater E. R. Analysis and improvement of tipping calibration for ground-based microwave radiometers. IEEE Trans. Geosci. Remote Sens., Vol. 38, No. 3, pp. 1260–1276, Apr. 2000.
6. Gaikovich K. P., Markina N. N., Naumov A. P. et al. Investigation of remote sensing possibilities of the low atmosphere in the microwave range and some aspects of statistical data use. Int. Journal of Remote Sensing, **1983**, Vol. 4, No. 2, pp. 419–431.
7. Kadygrov E. N., Miller E. A., Troitsky A. V. Study of Atmospheric Boundary Layer Thermodynamics During Total Solar Eclipses. IEEE Transactions and Remote Sensing, 2013, Vol. 51, Issue 9, pp. 4672–4677.

Research on Deep Space TT&C VLBI Digital Baseband Converting Methods Based on Parallel Down-conversion

Hong Ma, Xin Lian, Xueshu Shi, Zhu Chen, Shaojie Wei

Abstract Very Long Baseline Interferometry (VLBI) is a radio observation method that currently has the highest precision. To solve the problem of the requirement for the hardware to have an overly high processing speed, a wideband VLBI digital baseband converter based on parallel down-conversion is designed, combining parallel processing with polyphase filtering, which can greatly reduce the requirement for processing speed and relieve the pressure on the hardware and has helped to solve the bottleneck problem of digital signal processing. The simulation results show that this wideband VLBI digital baseband converter successfully realizes functions of down-converting, filtering, and decimation to a digital IF signal, and at the same time, the data rate is greatly reduced. So it could realize wideband receiving and processing and has helped for real-time signal processing.

Keywords VLBI, digital baseband converter, wideband, parallel down-conversion

1 Introduction

Very Long Baseline Interferometry (VLBI) is a somewhat new radio interferometry technique which was developed in the late 1960s [1], and it is an astronomical observation method that can obtain the highest resolution and measuring accuracy. Currently deep space exploration has become a hotspot which is researched by many different countries. With super high angle resolution, the VLBI technique has an important application value in the field of deep space exploration.

The VLBI digital baseband converter is an important part of the VLBI system, undertaking tasks of data acquisition, frequency band selection, and baseband conversion. It conducts digital down-conversion to the input IF signal and changes it into a baseband signal, then filters and decimates to improve signal quality and reduce the data rate, in preparation for the subsequent digital signal processing.

Currently there are two methods for implementing a VLBI digital baseband converter—uniform channelization filtering and direct down-conversion based on quadrature mixing [2]. [3] and [4] use the uniform channelization filtering method. It has high computational efficiency, but the band selection is not flexible enough, and it needs to consider the spectrum inversion phenomenon. [5] uses the direct down-conversion method containing quadrature mixing and multi-level low-pass filtering and decimation. This method has the capability of full spectrum processing, and the center frequency and band selection are flexible. However, considering the requirement of the wideband receiving and the rapid development of AD devices, the signal sampling rate continues to increase, and the data rate is correspondingly increased, which increases the hardware processing speed requirements. When the sampling rate is too high, the hardware processing speed cannot meet the requirements and would not work normally, leading to a digital signal processing bottleneck problem. How to solve this problem and realize wideband receiving and processing have important significance [6].

Addressing the shortcomings of the direct down-conversion method, this paper proposes a new kind of wideband VLBI digital baseband conversion method

The Academy of Equipment

based on parallel down-conversion. It can greatly reduce the requirement for processing speed and relieve the pressure on the hardware and has helped to solve the bottleneck problem of digital signal processing in the VLBI system.

2 Key Technology of VLBI Digital Baseband Conversion

The VLBI digital baseband converter is the first component after the AD device in the VLBI system. Its input is the digital IF signal which is gotten from the receiver via high-speed sampling. The receiver usually requires that different bandwidth signals can be processed, so the VLBI digital baseband converter is required to have flexible bandwidth and center frequency. VLBI digital baseband conversion mainly consists of key technologies such as digital down-conversion, digital filtering, and decimation.

2.1 Digital Down-conversion

The implementation structure of digital down-conversion is shown in Figure 1 [7].

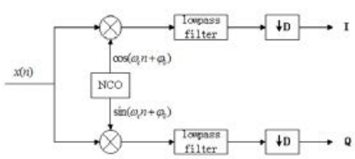

Fig. 1 Digital down-conversion implementation structure.

The numerically controlled oscillator (NCO) generates a quadrature digital local oscillator (LO) signal, whose frequency and initial phase can be set by the frequency control word and the phase control word. The digital IF signal gotten from AD sampling and the digital LO signal generated by the NCO are mixed, producing sum and difference frequency components. Then the high frequency components of the signal are filtered out by the low-pass filter and are decimated D times and decelerated. Finally, the zero center frequency output signal is obtained.

The NCO is one of the main factors that determine the performance of digital down-conversion. Its function is to generate a stable digital LO signal.

2.2 Polyphase Structure of FIR Filter

The polyphase structure of the FIR filter can geminately reduce the processing speed of hardware and relieve the pressure on the hardware.

Suppose the Z-transform of the impulse response of the FIR digital filter is

$$H(z) = \sum_{n=0}^{N-1} h(n) \cdot z^{-n} \tag{1}$$

After a series of derivations, Equation (1) can be turned into the following form:

$$H(z) = \sum_{k=0}^{D-1} z^{-k} \cdot H_k(z^D) \tag{2}$$

where $H_k(z) = \sum_{m=0}^{M-1} h(mD+k) \cdot z^{-m} = \sum_{m=0}^{M-1} h_k(m) \cdot z^{-m}$; $n = mD+k, (m = 0,1,2,\ldots,D-1; N = M \cdot D)$.

This is the polyphase structure of FIR filter $H(z)$. In the multi-rate signal processing, this structure is usually equivalently transformed into the form of filtering after decimation.

In the polyphase filter structure, branch filters are located behind the decimators, so filtering is conducted after deceleration, thus greatly reducing the processing speed requirements and improving the real-time processing capabilities.

2.3 Efficient Digital Filter

The half-band filter is a FIR filter whose frequency response $H(e^{j\omega})$ meets the following relation:

$$\omega_C = \pi - \omega_A \tag{3}$$

$$\delta_s = \delta_p = \delta \tag{4}$$

The stopband width of the half-band filter $(\pi - \omega_A)$ and the passband width (ω_C) are equal, and the passband and stopband ripple are also equal. The coefficients are all zeros at even points, except for the zero point. So it has high computational efficiency and needs only half the amount of computation, which is suitable for real-time processing, and it has a particularly important role in the multi-rate signal processing.

When the decimation rate D is a power of 2, M half-band filters can be used to accomplish decimation of the high multiples, whose decimation rate $D = 2^M$.

The cascaded integrator-comb (CIC) filter is a filter whose impulse response meets the following relation:

$$h(n) = \begin{cases} 1 \, , \, 0 \le n \le D-1 \\ 0 \, , \, \text{others} \end{cases} \tag{5}$$

where D is the order of the CIC filter and also the decimation factor. The coefficients of the CIC filter are all 1, so this kind of filter needs only addition and not multiplication. So it has small resource consumption and high calculation efficiency, and so it can complete decimation of any integral number of multiples.

3 Program Design Based on Parallel Down-conversion

3.1 Digital Down-conversion Based on Parallel Down-conversion

Briefly, digital down-conversion is multiplication of the input signal and the output LO signal of the NCO, and then to low-pass filter and decimate, so the final mixer output is obtained. Its mathematical expression can be written as:

$$y(n) = x(n) \times e^{j2\pi f_L n T_s} = x(n) \times e^{j2\pi \frac{f_L}{f_s} n} \tag{6}$$

where, f_L is the output LO frequency of the NCO and f_s is the sampling frequency and also the clock frequency. Suppose $n = iD + p$, $0 \le p \le D-1$, where is the number of branches. So

$$\begin{aligned} y(iD+p) &= x(iD+p) \times e^{j2\pi \frac{f_L}{f_s}(iD+p)} \\ &= x(iD+p) \times e^{j[2\pi \frac{f_L}{\frac{f_s}{D}} i + 2\pi \frac{f_L}{f_s} p]} \end{aligned} \tag{7}$$

Suppose $y_p(i) = y(iD+p), x_p(i) = x(iD+p)$, then the output of the p-th branch $0 \le p \le D-1$ is:

$$y_p(i) = x_p(i) \times e^{j[2\pi \frac{f_L}{\frac{f_s}{D}} i + 2\pi \frac{f_L}{f_s} p]} \tag{8}$$

It can be seen that the mixer output $y(n)$ can be divided into a timing combination of D output branches. Each branch is the mixture of the branch structure of the input sequence and the LO signal of the corresponding NCO. The output LO signal of each NCO is respectively:

$$S_p = e^{j[2\pi \frac{f_L}{\frac{f_s}{D}} i + 2\pi \frac{f_L}{f_s} p]} , 0 \le p \le D-1 \tag{9}$$

So the clock frequency of each branch is f_s/D, and the initial phase differences of the output LO signal of the NCO between adjacent branches are all $2\pi \cdot \frac{f_L}{f_s}$. As is seen, using this equivalent branch structure is equivalent to reducing the clock frequency of NCO from f_s to f_s/D, greatly reducing the processing speed of the hardware, thereby reducing the difficulty of the hardware implementation of the NCO.

From the above parallel structure, we can think of the polyphase structure of the FIR filter, so we can combine the parallel mixer outputs with the polyphase filter, so that the data rate of each branch can remain at a relatively low level, greatly reducing the processing speed of the hardware.

3.2 Design of the Whole Project

Based on the above derivation analysis, this paper intends to adopt an eight-branch parallel down-conversion structure to implement a wideband VLBI digital baseband converter; its implementation structure is shown in Figure 2.

The digital IF signal is obtained by high-speed AD sampling of the input analog IF signal, and it is divided into eight branches of parallel data streams through series-parallel conversion; the data rate of each branch is reduced to 1/8 of the original. The eight branches of the data stream are respectively mixed with the corresponding NCO output, and then a polyphase FIR filter structure is used to perform low-pass filtering on the eight branches of mixed output, so that the baseband signal is obtained. Then a two-time decimation polyphase filter structure is used again, to further improve signal quality and lower the data rate.

As to the NCO of each branch, f_{LO} is the LO frequency of the NCO output which is expected. When designing, it can be controlled by the frequency control word according to requirements, to get the equivalent

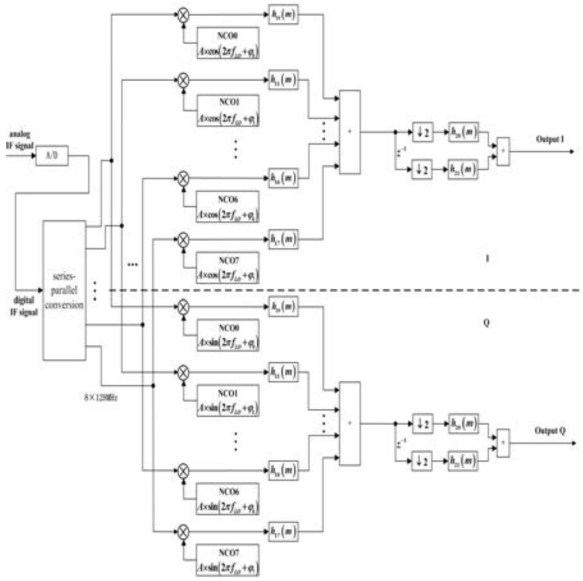

Fig. 2 Implementation structure of the wideband VLBI digital baseband converter.

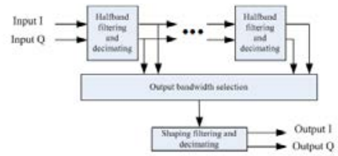

Fig. 3 Diagram of wideband mode processing.

LO frequency f_L that is wanted. In the above parallel down-conversion structure, the LO frequency of each branch NCO should be set to $f_{LO} = \mathrm{mod}(f_L, f_s/D)$, where f_s is the sampling frequency, D is the number of branches, and N is the digit of phase accumulator. And the initial phase difference of adjacent branch NCO output is $\Delta\varphi = 2\pi \cdot \frac{f_L}{f_s}$, so the initial phase of each branch NCO output is set to $\varphi_p = 2\pi \cdot \frac{f_L}{f_s} p$, where p is the serial number of the branch $(p = 0, 1, \cdots D-1)$.

According to the different bandwidths of the output signal, the working mode is divided into wideband mode and narrowband mode. The output bandwidth of wideband mode can be 16 MHz, 8 MHz, 4 MHz, 2 MHz, 1 MHz, or 0.5 MHz. Multi-stage half-band filtering and decimation are conducted on the above obtained I and Q signal, and the stage of the half-band filter is selected according to the output bandwidth requirement. At last, shaping filtering and decimation are conducted on the above output signal, and the final output is obtained. The implementation diagram is shown in Figure 3.

The output bandwidth of narrowband mode can be 200 kHz, 100 kHz, 50 kHz, 25 kHz, 16 kHz, 8 kHz, 4 kHz, 2 kHz, or 1 kHz. In this mode, multi-stage CIC filtering and decimation are conducted on the obtained I and Q signal, and the decimation time of the CIC filter is selected according to the output bandwidth requirement. At last, compensating filtering, shaping filtering, and decimation are conducted on the above output signal, and the final output is obtained. The implementation diagram is shown in Figure 4.

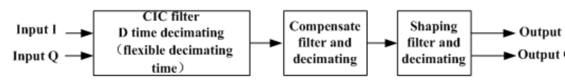

Fig. 4 Diagram of narrowband mode processing.

4 Simulation Verification

According to the above design scheme, simulations of the entire program are conducted using MATLAB software. At the same time, the scheme is implemented by writing VHDL codes, and the corresponding simulations are conducted too. Here suppose the input IF signal is a linear FM signal, whose frequency range is $f_{in} = 287$–290 MHz, sampling rate is $f_s = 1$ GHz, desired output LO frequency of NCO is $f_L = 288$ MHz, and number of branches is $D = 8$. In the simulation, the wideband output mode is used, and the stage of the half-band filter is set to 2.

Firstly, a linear FM signal as input is generated by MATLAB, whose frequency range is $f_{in} = 287$–290 MHz, and its frequency spectrum is shown in Figure 5.

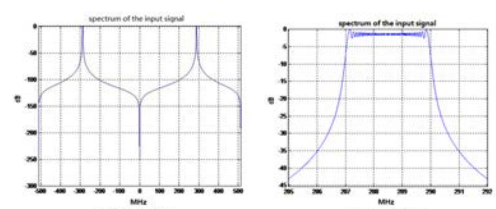

Fig. 5 Frequency spectrum of input signal.

Then the simulations of the entire scheme are conducted using MATLAB, the input signal is processed by the VLBI digital baseband converter, and the frequency spectrum of the output signal is shown in Figure 6.

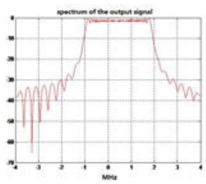

Fig. 6 Frequency spectrum of output signal in MATLAB simulation.

Meanwhile, the VHDL codes are programmed step by step to implement the wideband received VLBI digital baseband converter. Simulations are conducted using ModelSim software. The input signal is the same as with the above simulation, and the simulation time is 100 μs, so the corresponding output is obtained.

Then the above output data is read with MATLAB, and its frequency spectrum is obtained as shown in Figure 7. Figures 6 and 7 show that the input signal is processed by the VLBI digital baseband converter and the obtained output signal is a linear FM signal whose frequency range is $f = -1$–2 MHz. It shows that the frequency spectrum of the linear FM signal whose frequency range $f_{in} = 287$–290 MHz is moved to $f = -1$–2 MHz. And it is known, according to the theory of direct down-conversion, that the frequency range should be $f = (287 - 288)$ MHz – $(290 - 288)$ MHz $= -1$–2 MHz. So the simulation results of the scheme meet with the theoretical value, the output is correct, and the desired goal is achieved.

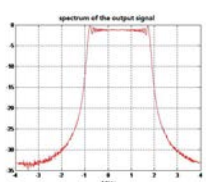

Fig. 7 Frequency spectrum of output signal in ModelSim simulation.

The scheme in this paper greatly reduces the requirement for processing speed and relieves the pressure on the hardware. Thus the hardware can support a higher sampling rate and wider band signal receiving and processing.

5 Conclusion

After the above scheme design and simulation verification, the proposed implementation method of wideband VLBI digital baseband converter based on parallel down-conversion can realize the functions of down-conversion, low-pass filtering, and decimation of the digital IF signal, and the output is correct. It has features for more than wideband receiving, the frequency can be set flexibly, and the output bandwidth can be optional. But also, the requirements for the processing speed of the hardware are greatly reduced, and this can solve the bottleneck problem of DSP. And it has helped to achieve wider bandwidth receiving and processing and also helped to achieve real-time signal processing. It has a high reference value and can promote the development of the VLBI system and fields such as software, radio, and data acquisition.

References

1. Qian Zhihan, Wu Linda. Very Long Baseline Interferometry. Beijing: Surveying and mapping press, 1998: 1–14.
2. Liang Sheng, Yang Wenge. Design of a VLBI Digital Baseband Converter Based on Polyphase Structure. Development & Innovation of Machinery & Electrical Products, 2011, 24(1): 149–151.
3. IVS Memorandum 2006-003v01, IVS-WG3 Report on the Backend System.
4. Chen Lan, Luo Jintao, Xiang Ying, et al. Polyphase based VLBI digital baseband converter with adjustable IF center frequency and bandwidth. Computer engineering and application, 2010, 46(2): 55–59.
5. Gino Tuccari, Walter Alef, Alessandra Bertarini, et al. DBBC Development Status. Proceedings of the 5th IVS General Meeting. St. Petersburg, Russia: IVS, 2008: 376–380.
6. Xiang Ying, Zhu Renjie, Gino Tuccari, et al. Wideband digital SSB down converter. Acta electronica sinica, 2006, 34(11): 1978–1980.

Mail adress: Optical & Electrical Equipment
The Academy of Equipment
Yanxi Town Huairou Dist.
Beijing 101416 CHINA

Control System and Tests for the 13.2-m RAEGE Antenna at Yebes

P. de Vicente, R. Bolaño, L. Barbas

Abstract The RAEGE network is being deployed. The antenna at the Yebes Observatory is the first one in the network, and its construction finished in October 2013. During the construction phase, the remote control system for the antenna and the receivers was developed, and during the commisioning time the software was tested by MT-Mechatronics. As a result, both the control system from MT-Mechatronics and the remote control system by the IGN-CDT were debugged. We have tested the basic functionality of the antenna operated as a single dish telescope. First light at S, X, and Ka band was achieved on February 10$^{\text{th}}$. Afterwards a pointing model for the whole sky was determined, together with an optimum focus position as a function of elevation. Commisioning is not finished yet, and the antenna will be totally delivered to the IGN-CDT in the next weeks. VLBI equipment will be installed within three months, and VLBI observations are foreseen by the end of 2014. In this paper, we provide an overview of the control system and of the main results achieved.

Keywords Antennas, control software

1 Introduction

RAEGE stands for "Red Atlántica de Estaciones Geodinámicas y Espaciales" and refers to a network including four 13.2-m radio telescopes located in Yebes (Guadalajara, Spain), Santa María (Azores islands, Portugal), Flores (Azores islands, Portugal), and Tenerife (Canary islands, Spain). The telescopes will be equipped with receivers at 2, 8, and 30 GHz at a first stage and later will include a wideband receiver. These telescopes were designed by MT-Mechatronics and built by Asturfeito in northern Spain.

The Yebes antenna is the first antenna of the series, and its construction was finished by October 2013. During the construction time, the remote control system for the antenna and the receivers was developed, and during the commisioning time by MT-Mechatronics, the software was tested. As a result, both the control system from MT-Mechatronics and the remote control system by the Instituto Geográfico Nacional – Centro de Desarrollos Tecnológicos (IGN-CDT), at Yebes were debugged.

2 An Overview of the Control System

The Antenna Control Unit, hereafter ACU, is composed of two computers: one which is devoted for the control of the main axes and located in a container on the ground and close by the antenna and a second one which controls the secondary reflector mounted on a hexapod and is located inside the azimuth cabin. Both computers run a real time extension under Windows XP called TwinCAT (by Beckhoff). The antenna can be controlled manually, through a local control panel, and remotely.

The remote control and monitoring of the antenna is achieved using two TCP sockets: one for commands and a second one for monitoring. The specifications for the commands and the monitoring are summarized in a document called the Interface Control Document which was agreed upon by MT-Mechatronics and the

Instituto Geográfico Nacional - Centro de Desarrollos Tecnológicos (Yebes)

IGN-CDT at Yebes. All commands are identified by a unique ID and provide an acknowledgement after being received. Although most of them are asynchronous, the acknowledgement provides information about the preprocessing of the command.

Commands allow tracking, superposition patterns on top of the tracking, and movements of the secondary reflector as a function of time and elevation. It is also possible to set the UTC and GST time and DUT1, move the antenna to any azimuth and elevation in the sky, stop it, and load a pointing model. The secondary reflector is operated using a hexapod device and can be positioned in space using six degrees of freedom. Tracking is achieved by sending tables with three columns: time, azimuth, and elevation or time, right ascension, and declination. If the latter mode is used, it is necessary to provide the GST and DUT1. Patterns are possible by loading a superposition table with three columns: time, azimuth offset, and elevation offsets. These patterns may be used to build pointing scans or position switch scans (on–off).

The ACU delivers the status of the antenna every 200 ms through a TCP socket on port 9001. The status is a structure composed of many variables which can be used to obtain a full view of the telescope, including any information regarding the last command sent and even diagnostics in case of malfunction. The timing of the ACU is obtained using an IRIG-B signal from a GPS receiver. The real time extension from Beckhoff guarantees that the time is kept locked to the UTC time provided by the GPS.

The remote control of the antenna, developed by the IGN-CDT personnel, uses ACS, ALMA Common Software, as the communication infrastructure. ACS is an open software framework used in the ALMA intereferometer and implemented by several telescopes in the world. ACS provides an implementation of the component/container paradigm via Common Object Request Broker Architecture (CORBA) and also provides general purpose utility libraries, hiding the complexity of CORBA to the developer.

A radio telescope is a distributed system in which individual components need to send and receive information to and from other components and keep synchronized with them. The ACS provides a powerful communication layer and a distributed component model with components implemented as CORBA objects. Each component exposes its public methods and variables to other components, which may be run in the same host or in different hosts. All communication is done in the Local Area Network. The deployment of components is highly flexible. Physical devices, such as receivers or auxiliary equipment, map into components, which have public and private methods. Public methods allow these devices to be controlled from third-party clients or by other components.

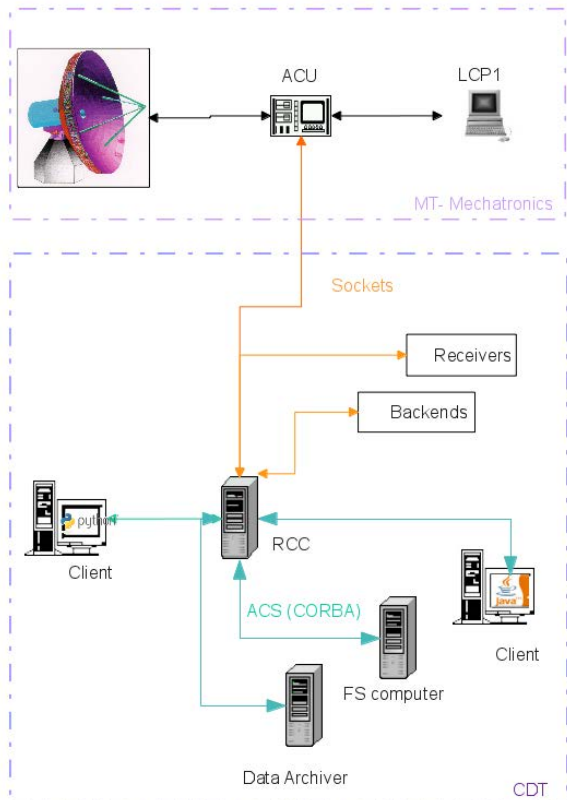

Fig. 1 Overview of the architecture.

Components are implemented using any of the following three programming languages: C++, Java, or Python. Usually C++ is reserved for components which require high speed. This is the case for the lowest level component which communicates with the ACU. IDL is reserved for declaring interfaces. Clients are usually written in Python or Java and can communicate with any component independently of the language in which it is written. All the control software runs on Debian Linux. The 13.2-m radio telescope uses two computers running Linux. Devices are available using embedded or standalone ethernet to serial converters. Receivers use I2C and a PIC with firmware developed at the IGN-CDT which is addressable via Ethernet.

Our control system provides several monitoring tools, individual graphical applications, and a command line shell which allow full control of the telescope for single dish observations.

For VLBI observations, the communication between the Field System and the control system is done at the Field System computer through shared memory. A C++ component runs in the Field System computer and reads FS local and global variables from the shared memory area and, according to the content of those variables (of which some work as semaphores), commands the antenna and receivers. Information from the antenna is also written onto shared memory by this component so that it is available for the Field System in real time. This method is fast and easy to implement, but it requires that the Field System and the control system, including the ACS, use the same version of the operating system, Debian 6.0.9 ("Squeeze") at the time of this report. In order to decouple the requirements for the FS and the ACS, so that they work in independent computers, we plan to investigate alternatives such as XML-RPC or e-RemoteCtrl (Ettl et al., 2012).

A simple snapshot of the architecture is displayed in Figure 1.

3 Basic Tests

During the comissioning of the telescope and the development of the control software, we performed basic tests to verify the correct behavior of the antenna. These tests included measuring the maximum speed in azimuth and elevation for different position separations, pointing scans at several elevations and tracking of a radio source. The maximum measured azimuth and elevation speed is 12 degrees/second and 6 degrees/second respectively. Acceleration is 6 degrees/second^2. Figure 2 shows the measurement when moving the antenna from azimuth 225 degrees to 45 degrees.

Tracking measurements have also shown that under low wind (less than 4 m/s), tracking errors are below 4 arcseconds peak to peak during a time interval 30 seconds long (see Figure 3).

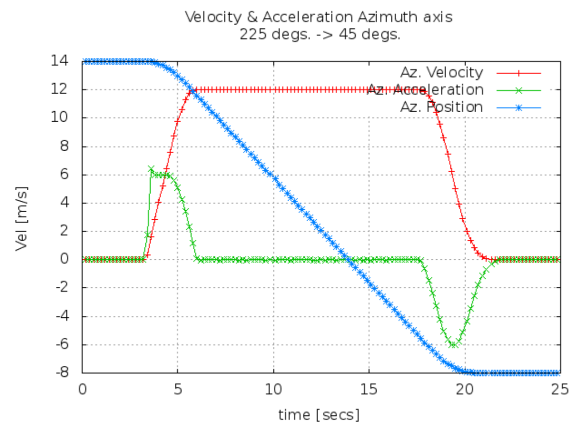

Fig. 2 Azimuth change, velocity, and acceleration versus slew time.

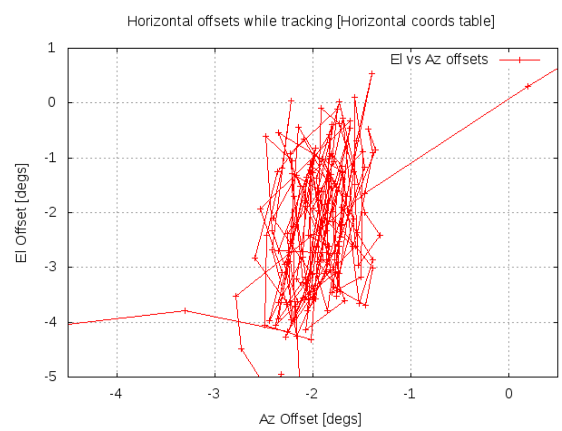

Fig. 3 Elevation versus azimuth while tracking a source for 30 seconds. Wind speed is 3 m/s.

Pointing scans at two different elevations show that the system performs as expected. The length of the horizontal arms depends on the elevation and results in equal arm length when using the source as the center of the reference system. Figure 4 shows the position of the antenna during a pointing scan composed of one azimuth drift and one elevation drift at 52 degrees elevation. It is important to distinguish between azimuth offsets in the encoder reference system and azimuth offsets in the sky, also known as "azimuth collimation" at some telescopes.

Once these basic tests were accomplished, more complex observations were performed. In particular, first light was achieved on February 2014 towards the sun at X band with a warm receiver. Figure 5 shows a

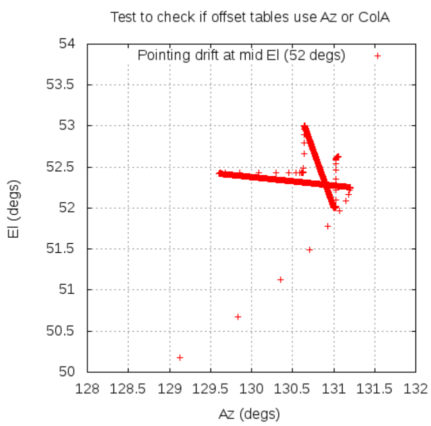

Fig. 4 Pointing scan composed of an azimuth and elevation drift. The azimuth arm is larger than the elevation one, but both have the same length in the sky, when taking the source as the center of the reference system.

pointing drift towards the Sun at S-, X-, and Ka-band under those conditions.

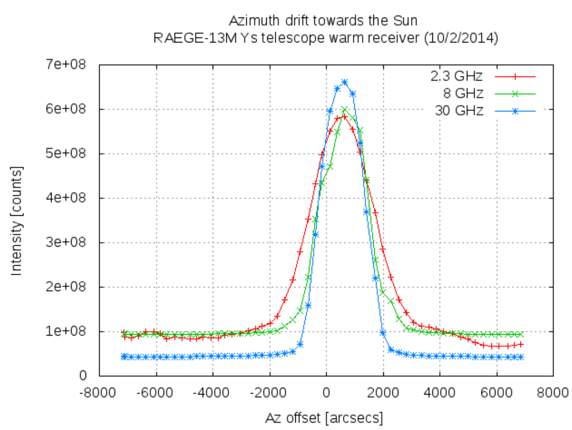

Fig. 5 First azimuth drifts towards the Sun at S-, X-, and Ka-band. The receiver was uncooled.

Later observations have been performed towards Cas A and Tau A with a cooled receiver to estimate the G/T, gain, and SEFD of the telescope. We have also determined a pointing model of the whole sky and optimized the focus position of the antenna in the X, Y, and Z axes.

We estimate an aperture efficiency of 50% and an SEFD of 1300 Jy at X-band. G/T is 43.2 dB/K at X-band. The determination of the gain and SEFD at S band has some uncertainties due to the presence of strong RFI in the band. Ka-band calibration is still preliminary, and some hardware changes are required.

4 Conclusions

The 13.2-m RAEGE antenna will be fully delivered from MT-Mechatronics in summer 2014. During the commissioning time, we debugged part of the MT-Mechatronics software and IGN-CDT remote control system, and as a result, the antenna is fully operational. Small hardware modifications are still pending. The antenna is equipped with a three band receiver, and single dish observations have already been performed. As a result, we already have a pointing model for the sky and an optimum position for the secondary reflector. During VLBI observations, the secondary will be locked to a fixed position. Gain observations are on the way and will be ready in the next month.

The VLBI backend, a DBBC plus a Mark 5B+, will be installed within three months, and VLBI observations are foreseen by the end of 2014.

Acknowledgements

The first light of the 13.2-m radio telescope is the result of the work of the engineers and technicians of IGN-CDT at Yebes, who have performed an excellent job. Without their work, this success would not have been possible.

References

1. Ettl M., Neidhardt A., Schönberger M., Alef W., Himwich E., Beaudoin C., Plötz C., Lovell J. and Hase H. "e-RemoteCtrl: Concepts for VLBI Station Control as Part of NEXPReS" In D. Behrend and K.D. Baver, IVS 2012 General Meeting Proceedings. NASA/CP-2012-217504, pages 128–132, 2012.

A Tri-band Cryogenic Receiver for VGOS Radio Telescopes

José Antonio López–Pérez[1,2], José Antonio López–Fernández[1,2], Félix Tercero[1,2], Beatriz Vaquero[1,2], José Manuel Serna[1,2]

Abstract The Yebes Observatory has developed a world class tri-band (S/X/Ka) cryogenic receiver for VGOS radio telescopes. The main advantages of this receiver are the simultaneous S/X/Ka operation with dual-circular polarization, the backward compatibility with the legacy VLBI stations, X/Ka VLBI measurements, the reduced feed size for cooling down to 15 Kelvin, and the easy cal signal injection in front of the LNAs. It also allows the characterization of radio telescope pointing, tracking, and gain at high frequencies (32 GHz).

Keywords VGOS, radio telescope, cryogenic receiver, instrumentation

1 The Tri-band Feed

The tri-band feed is actually made of three feeds in a coaxial arrangement, as can be seen in Figure 1. The largest feed is the S-band feed, inside which the X-band feed is located. Finally, a conventional conical feed for Ka-band is at the very center of the system. All feeds are working with the TE11 mode.

The S- and X-band feeds are fed by four symmetric ports 90 degrees apart. These ports are of SMA connector type for S-band and WR-112 waveguide flange for X-band. The Ka-band feed output is a circular waveguide that interfaces to a septum polarizer-coupler developed in house to achieve dual-circular polarization. In the S- and X-band, the dual-circular polarization is achieved by suitably combining the four port signals by means of microwave 180º and 90º hybrid circuits. The dimensions of the feed are 25 cm high and 20 cm in diameter, and it weighs 3 kg. The physical optic simulation of the feed, together with radio telescope reflectors, provides an aperture efficiency higher than 70% in all bands. Figure 2 shows the measured beam pattern for each band.

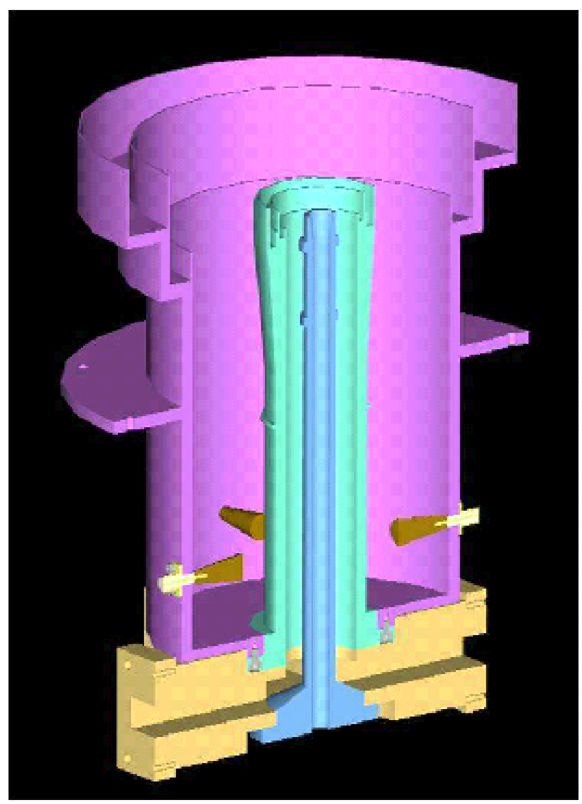

Fig. 1 Inside view of the tri-band feed (simulation).

1. Instituto Geográfico Nacional (IGN)
2. IGN Yebes Observatory

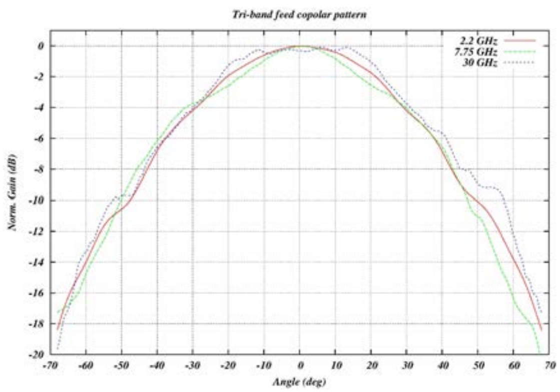

Fig. 2 Tri-band feed pattern.

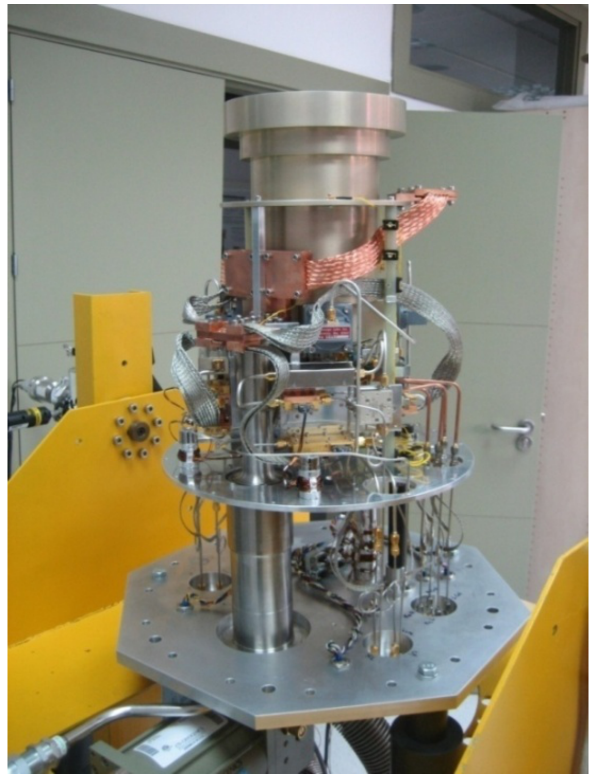

Fig. 3 Interior view of the tri-band receiver cryostat.

2 The Cryostat

The cryostat is built over a two-stage Sumitomo closed-cycle refrigerator inside a cylindrical Dewar made of steel with suitable multi-layer insulation. The top and bottom cover plates are made of aluminum. In the top cover, an infrared filter and a mylar sheet act as a vacuum window and let the radiation go to the tri-band feed. In the bottom cover, there are all RF connectors for the S/X/Ka output signals, vacuum flanges, pressure monitor, DC cabling, and housekeeping connectors. Figure 3 shows the interior of the cryostat with the feed and components.

The entire receiver has been assembled on a PVC structure that hold the different components: tri-band feed, the 180^{o} and 90^{o} hybrids, couplers for noise injection, microwave isolators, and S/X LNAs. The Ka septum-type polarizer/coupler and LNAs are attached directly to the feed. Copper braids are used for the thermal connection between the cold stage and the components. The cold and intermediate stages cool down to 7 Kelvin and 37 Kelvin, respectively. The vacuum pressure reaches 10^{-6} hPa and the cooling time is 12 hours, approximately.

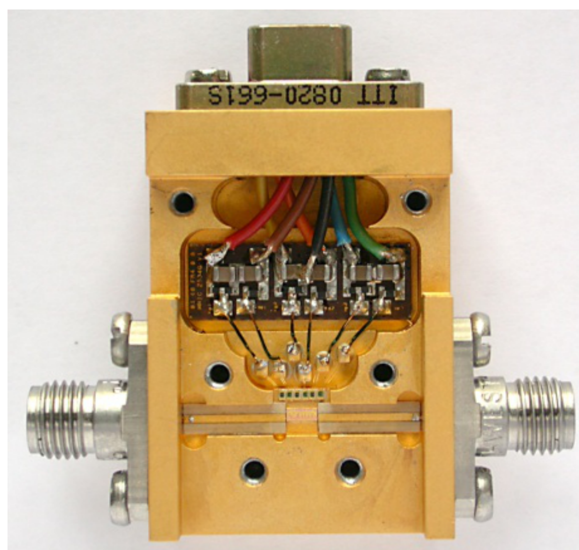

Fig. 4 Low noise amplifier (LNA) for Ka-band.

3 Low Noise Amplifiers

The cryogenic low noise amplifiers and 90^{o} hybrid circuits are in-house designs performed by Yebes Observatory laboratory. Figure 4 shows the Ka-band LNAs. The average LNA noise temperatures are < 6 Kelvin in S-band and X-band and < 21 Kelvin in Ka-band.

4 Measurements

The receiver noise temperature was measured for each frequency band with the Y-factor method. Microwave

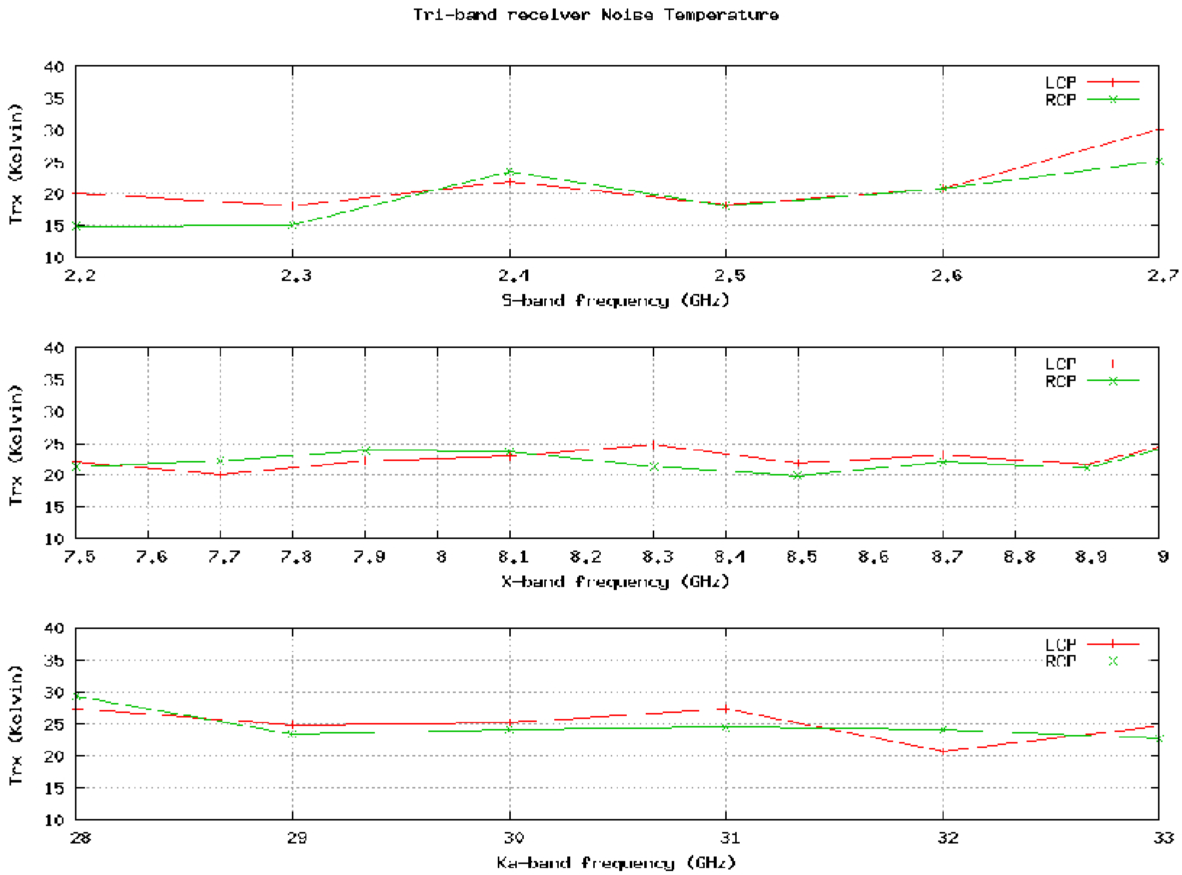

Fig. 5 Tri-band receiver noise temperature.

absorbers, dipped into liquid nitrogen and at room temperature, were used as calibration loads for the measurement. The results are plotted in Figure 5. The average receiver noise temperatures are 21 Kelvin in S-band, 23 Kelvin in X-band, and 25 Kelvin in Ka-band.

5 Conclusions

A cryogenically cooled tri-band receiver for VGOS radio telescopes has been successfully designed and developed at Yebes Observatory (IGN CDT). The main advantages of this receiver have been mentioned in the introduction section. Each of the three RAEGE project radio telescopes (`http://www.raege.net/`) will be equipped with one tri-band receiver as described here. In addition, a tri-band receiver has been constructed at Yebes Observatory for the Geospatial Information Authority of Japan (GSI).

Acknowledgements

This work was supported by the project FIS2012-38160 of the Spanish Ministry of Economy and Competivity.

Tri-band System for the Russian Interferometer

Alexander Ipatov, Irina Ipatova, Vyacheslav Mardyshkin, Alexander Evstigneev, Evgeniy Khvostov, Alexey Lavrov, Vitaliy Chernov

Abstract This report describes the tri-band receiving system for the 13.2-m antenna. Block diagrams and construction details are given. The measuring method for the noise temperature is described, and calculations and measurement results are compared. For the receiver feed, the results of the power pattern calculations and the measurements are presented.

Keywords VGOS, tri-band, receiver, cryogenic

1 Introduction

Two stations of the interferometer are under construction at the Zelenchukskaya and Badary observatories. The telescopes will use multiband feed and low noise amplifiers placed into a single unit (cryostat) of the receiver and cooled there to the hydrogen temperature level. This report describes the designed cryostat of the focal container for the radio telescope with a radio-transparent covering and a dielectric thermal screen to support the cooling process. The construction of the feed gives the possibility for cooling and operating with dual circular polarization simultaneously.

2 Tri-band Receiving System

This system operates in the following bands: S (2.2–2.6 GHz), X (7.0–9.5 GHz), and Ka (28–34 GHz). All receiver units are placed in the focal container (Figure 1), which is disposed in the secondary focus of the antenna.

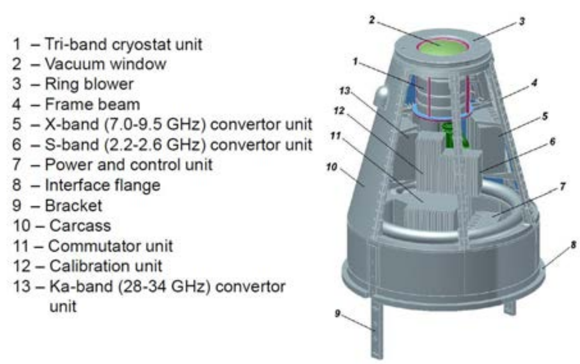

Fig. 1 Tri-band receiving system focal container.

The container is specially designed for an antenna with a 13.2-m dish, and it is housed in a rigid airtight framework. The construction of the focal container provides air circulation inside and its input has a window compatible with a cooled unit input. The external radio-transparent covering of this window is blown with warm air through a special hose to protect it from atmospheric precipitation.

The tri-band feed and input amplifiers with microwave isolators installed in the cryostat of the focal container are cooled there by the closed-cycle cryogenic system to the temperature of liquid hydrogen.

The aperture part of the feed is constructed with the use of circular waveguides of the S, X, and Ka bands placed coaxially (Figure 2). The Ka-band has a circular waveguide with a dielectric cone and waveguide septum polarizer. In the X-band, the signal reaches the horn, passes through the differential-phase section, and divides over the orthomode transducer. In S-band,

Institute of Applied Astronomy RAS

quarter-wavelength inductive pins and hybrid couplers are applied.

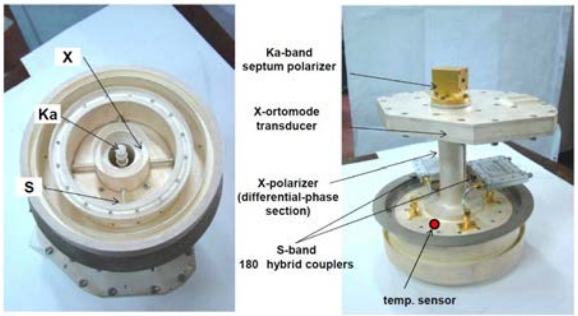

Fig. 2 The cooled unit feed.

During the development of the feed, it was modeled with software. Figures 3–5 show the calculated and measured power patterns. The measurements and calculations were made in co-polarization and cross-polarization. For the X-band, the influence of the differential-phase section was analyzed. The actual characteristics are enough close to the calculated ones. One of the main feed parameters is the beam width, and on the level of -15 dB, it is about 130 degrees.

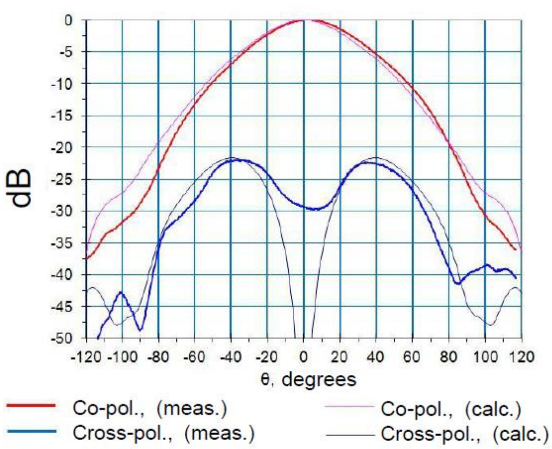

Fig. 3 Power patterns (S-band).

All the equipment of the cooled unit (Figure 6) for both polarizations of all three bands is tightly placed in the space between the feed and coldhead flange. The S and X band signal lines are coaxial, and the Ka-band is fully a waveguide. The equipment is closed with the metal heat shield. The infared filter is placed between

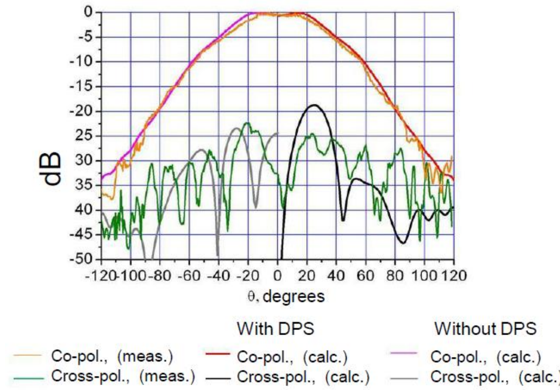

Fig. 4 Power patterns (X-band).

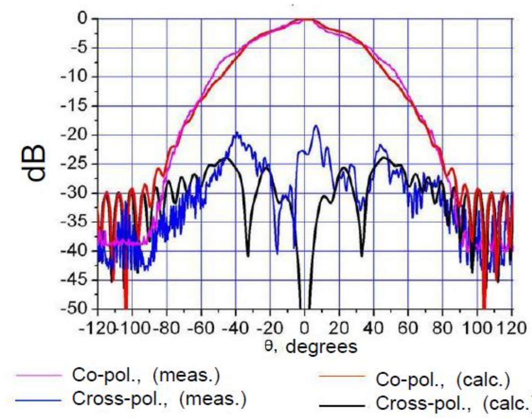

Fig. 5 Power patterns (Ka-band).

the feed and the vacuum window. It is 0.1 mm teflon film.

The vacuum window (Figure 7) is closed with a radiotransparent cover, which consists of two parts. The external sealing surface is made of Mylar film that is 0.05 mm thick. The film is supported by an inner layer of solid foam polyester that is 17 mm thick.

Focused with the antenna, electromagnetic waves get to the feed inside the cooled unit through the radiotransparent cover. They are separated to three bands and two circular polarizations, mixed with the noise and phase calibration signals and amplified with cooled low-noise transistor amplifiers (LNA). Almost all the equipment located inside the cryostat is cooled to the temperature of near 20 K, significally reducing the noise temperature of the "radio telescope-radiometer" system.

All amplified signals go to the intermediate frequency converter units. These units provide subchannel

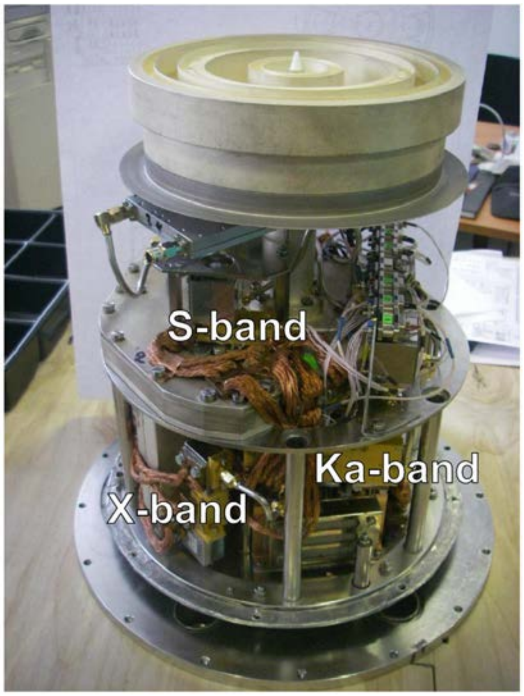

Fig. 6 The cooled unit assembly.

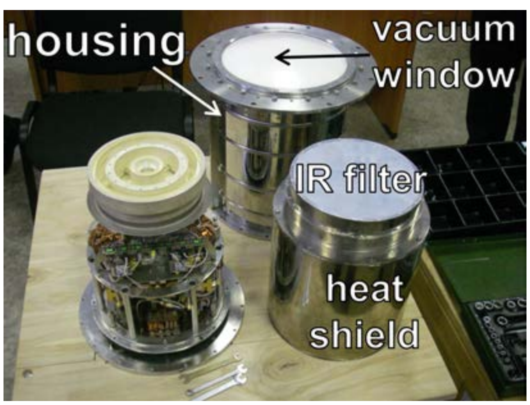

Fig. 7 Cooled unit heat shield, carcass, and vacuum window.

splittering and frequency converting to the band of the digital acquisition system. The subchannels to record are selected by the commutator unit.

The calibration unit contains an adjustable noise source for each band. External picosecond pulses for the phase calibration are used, and the calibration unit has a special input for them.

The receiving system is powered with a unified supply voltage and controlled via the Ethernet interface. A large amount of telemetric information such as temperatures, supply voltages, and consumption of current, is gathered.

3 Low Noise Amplifiers

The cryogenic low noise amplifiers (Figure 8) for S- and X-band are connected modules. They have a gain of more than 30 dB, and their noise temperature is not higher than 5 K. The Ka-band waveguide amplifiers are prototypes; they have excess gain and noise. Their parameters will be improved in the future.

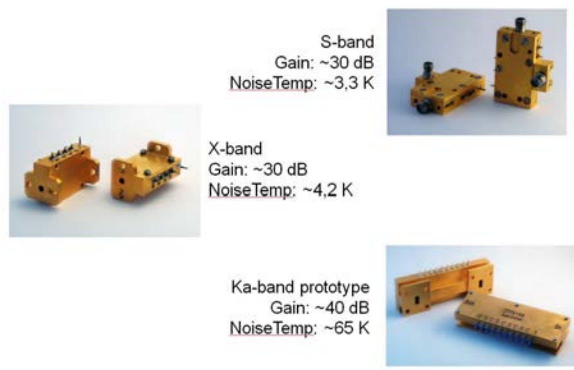

Fig. 8 Low noise amplifiers.

4 Cooled Unit Tests and Measurement Results

The cooling process (Figure 9) with the use of the Sumitomo closed cycle refrigerator takes seven hours. The measured feed physical temperature is about 26 K, and the temperature of the amplifiers is about 20 K.

For measuring the noise temperature of the cooled unit, a special broadband matched load was applied (Figure 10). It is a low temperature wide-aperture load, which is enclosed in a dewar with liquid nitrogen. The load is mounted on a mobile base, allowing it to be matched with the device under test during the movement. For matching the sizes of the vacuum window and the load aperture, the blends are located between the load and the cryostat. This equipment provides the <<cold>> load. The absorbent material plate with the room temperature is applied as a “hot” load.

Table 1 Cooled unit prototype measured and calculated parameters (S-band).

Parameter	Cover	IR-filter	Feed	Bridges	Dir. Coupler	From cal. input	Isolator	LNA	Isolator
Gain/Loss, dB	−0.02	−0.01	−0.35	−0.45	−0.1	−27	−0.2	30	−0.2
Phys. temperature, K	300	70	20	20	20	300	20	20	20
Noise temperature, K	1.4	0.2	1.5	2.0	0.5	0.6	0.9	3.3	0.9
Noise contribution, K	1.4	0.16	1.55	2.15	0.55	0.6	1.11	4.23	0.001
Total unit noise, K	11.8								
Measured noise, K	15 (RFI)								

Table 2 Cooled unit prototype measured and calculated parameters (X-band).

Parameter	Cover	IR-filter	Feed	Bridges	Dir. Coupler	From cal. input	Isolator	LNA	Isolator
Gain/Loss, dB	−0.03	−0.01	−0.15	−0.1	−0.1	−27	−0.2	30	−0.2
Phys. temperature, K	300	70	20	20	20	300	20	20	20
Noise temperature, K	2.1	0.2	0.7	0.5	0.5	0.6	0.9	3.3	0.9
Noise contribution, K	2.1	0.16	0.69	0.48	0.49	0.6	0.98	3.67	0.001
Total unit noise, K	9.1								
Measured noise, K	10								

Table 3 Cooled unit prototype measured and calculated parameters (Ka-band).

Parameter	Cover	IR-filter	Feed	Bridges	Dir. Coupler	From cal. input	Isolator	LNA	Isolator
Gain/Loss, dB	−0.04	−0.01	−0.2	−0.1	−0.1	−27	−0.2	40	−0.2
Phys. temperature, K	300	70	20	20	20	300	20	20	20
Noise temperature, K	2.8	0.2	0.9	0.5	0.5	0.6	0.9	64	0.9
Noise contribution, K	2.7	0.16	0.91	0.48	0.49	0.6	1.0	74.3	0.0001
Total unit noise, K	80.7								
Measured noise, K	80								

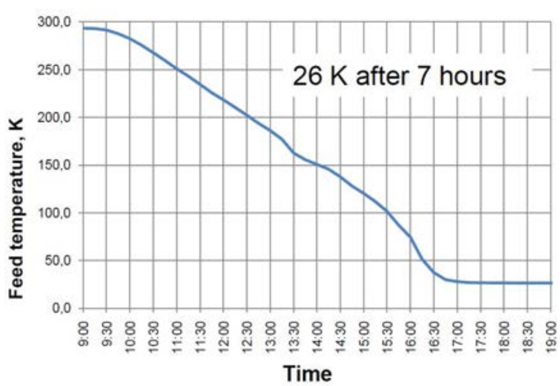

Fig. 9 The cooling process.

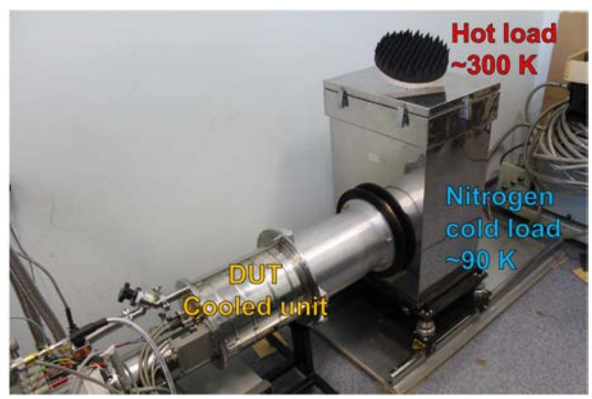

Fig. 10 Noise temperature measurements.

5 Conclusions

The results of the noise temperature measurements and calculations in different ranges are presented in Tables 1–3. The difference between the left and right circular polarization channels is insignificant. The main noise contribution comes from LNA. Other significant contributors are the radio-transparent cover, the feed, the bridges and polarizers, the direct coupler, and the ferrite isolators. The measurements of noise temperature in the S-band were obstructed by the strong RFI, but the result is not higher than 15 K. The measured and calculated temperature in X-band is about 10 K. The Ka-band is prototyped, and its noise temperature is about 80 K and will be improved.

The New Phase-calibration System of the Geodetic Observatory Wettzell

J. Kodet[1], K.U. Schreiber[1], Ch. Plötz[2], G. Kronschnabl[2], I. Prochazka[3]

Abstract In order to reduce systematic errors in VLBI operations, the one-way delays of the system are captured by injecting a narrow pulse train into the detection chain through an input coupler located near the front-end of the receiver chain. Such a pulse train generates calibration tones in the observation bandwidth, which are equally spaced by the repetition rate of the pulse train. In geodetic VLBI, tones with 1 MHz spacing are used. The tones propagate through the entire detection chain and are recorded along with the observed signal. They are extracted in post processing and are used for keeping track of the VLBI receiver delays. We are presenting the design and construction of the phase calibration unit, which will be used in the new 13.2-m Twin Radio Telescopes Wettzell (TTW) at the Geodetic Observatory Wettzell. It is also planned to be installed in the 20-m Radio Telescope Wettzell (RTW) as well. The design was inspired by A. E. E. Rogers' and B. Corey's phase calibration system. The new phase calibration operates either from 5, 10, or 100 MHz input frequencies and allows programming of the repetition rate of the output pulses. Together with the phase calibration tone generator, a low jitter programmable pulse generator was included. The pulse generator can be used for the additional timing of system delay aspects and therefore supports new approaches for the determination of systematic errors within the VLBI receiver chain.

1. Forschungseinrichtung Satellitengeodäsie, Technische Universität München, Germany
2. Bundesamt für Kartographie und Geodäsie, Geodätisches Observatorium Wettzell, Germany
3. Czech Technical University in Prague, Prague 1, Czech Republic

Keywords VLBI, pcal, cable delay, FPGA

1 Introduction

The VLBI technique is very dependent on phase stability measurements with respect to the reference frequency which is, in many cases, a hydrogen maser. To fulfill extreme phase stability measurements of the astronomical radio sources in the receiving chain (local oscillators, filter, cables, etc.), a test signal is injected near the VLBI input receiver. The use of such a signal allows monitoring of phase variations of the open loop detection system over the observation time by comparing received signals to a stable calibration tone locally generated in the detection bandwidth. For such a system, one of the most important things is to monitor the cable delay carrying the reference frequency for generating calibrations tones at the beginning of the receiver chain.

The currently implemented pcal system at the 20-m Wettzell Radio Telescope uses the cable delay measurement system, which is based on the mixing of a reference signal from an H Maser with the divided signal from the same source. Such a signal is then sent up to the phase calibration unit, where the signal is reflected back. After the reflection, the signal carries the phase modulation which is proportional to the cable length. In the VLBI room, there is a high resolution phase comparator comparing phase of the reflected signal with the H Maser reference. Thanks to the time expansion in phase comparator (2.5 ps of cable length is equal to 1 us phase difference), the phase can be measured using a common counter with high resolution [1]. The

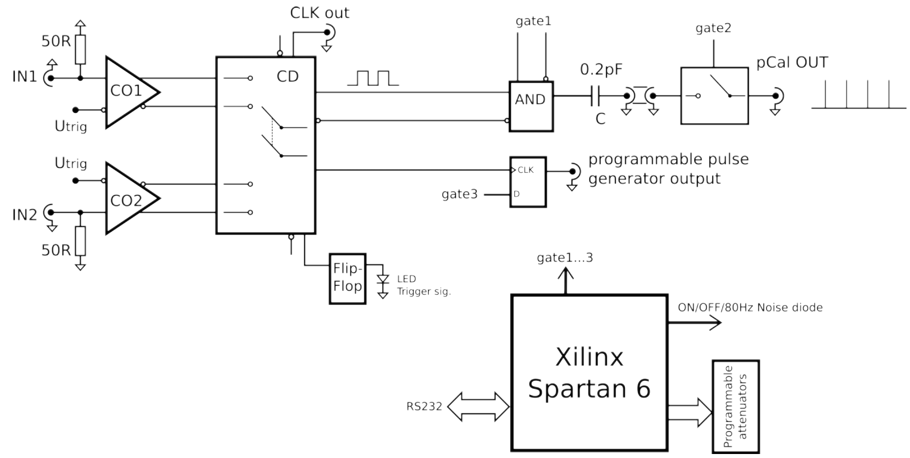

Fig. 1 Block diagram of the pcal unit.

approach described in this paper is based on TWTT using two Event Timing (ET) devices [2].

2 New Phase-calibration System Design

At the Geodetic Observatory Wettzell we have developed the new pcal system. The narrow pulses are formed by small capacitance at the output of the fast logic AND gate from the Hittite Microwave. The negative pulses are filtered out using the microwave switch HMC-C019. The entire end-stage of the circuitry was inspired by A. E. E. Roger's and B. Corey's phase calibration system [3]. In our pcal system, we have chosen another approach in the gating output stage to divide input frequency. We are buffering input frequency with common clock buffer circuitry and distributing this frequency in to the FPGA. In the FPGA we are generating synchronous gate signals with input reference. Those gate signals are used for dividing the input frequency by any integer N and for cutting out the negative pulses in the output pulse train. Figure 1 shows the block diagram, and Figure 2 is a photograph of the pcal system. The advantage of using the frequency divider implemented in the FPGA is that the user can connect any frequency in the range of 1 MHz up to 100 MHz to the input of the pcal system.

We have measured the output pulse shape using a 50 GHz Tetkronix sampling oscilloscope, shown in Figure 3. The pulse amplitude is 80 mV, and the rise and fall times of the pulse are better than 20 ps.

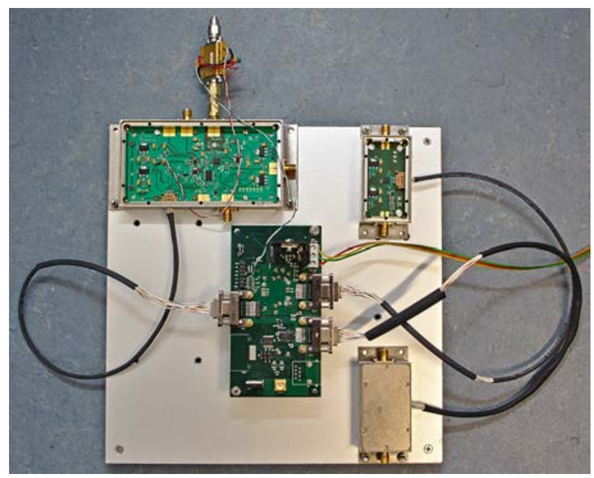

Fig. 2 Photograph of the pcal unit.

Thanks to modern low temperature dependent components, the delay temperature dependency is $+0.3$ ps/K for input frequency 100 MHz, and for 5 and 10 MHz, the temperature coefficient was measured to be -1 ps/K and -0.2 ps/K. The temperature dependancy for the input frequency of 100 MHz is shown in Figure 4. In addition to a standard generation of the pcal tones, the programmable low jitter pulse generator was implemented. This output can provide timing information suitable for triggering another devices like event timers. The programmable pulse generator was used for measuring cable delay temperature dependency and choosing suitable temperature stable cables for the new Twin Telescopes Wettzell.

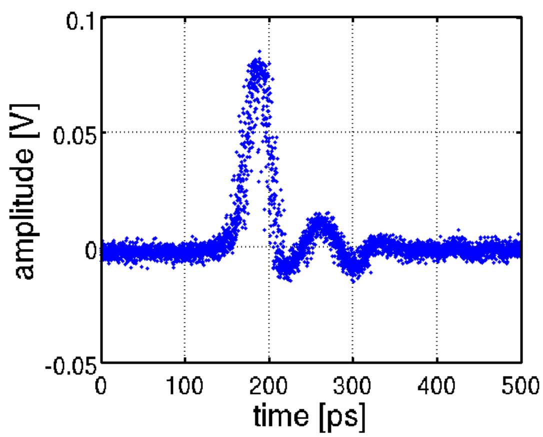

Fig. 3 Pulse shape of the output of the pcal, measured with a sampling oscilloscope.

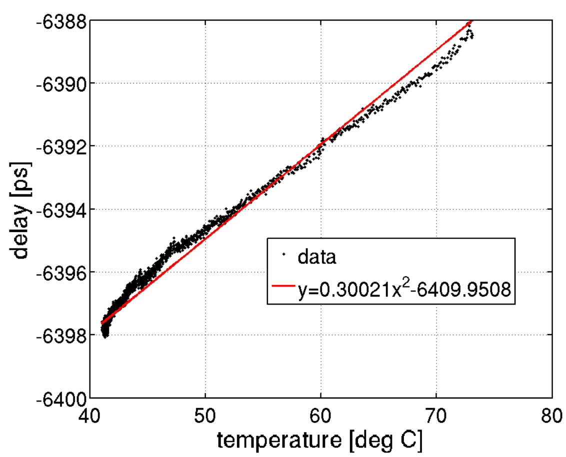

Fig. 4 The pcal unit timing delay temperature dependency.

The output power was measured using the Rohde and Schwartz spectrum analyzer. The output power varies within 2 dB in bands from 2 GHz up to 12 GHz slightly below −80 dBm, which is shown in Figure 5.

The new pcal system allows the measurement of the electrical cable delay of the reference frequency. The method is shown in Figure 6. The function of cable delay measurement is being developed. The reference frequency is power split in the VLBI control room. One part of reference frequency is sent to the VLBI antenna, where pcal tones and the pulse train suitable for triggering the event timer are generated. The second part of the reference frequency is used for triggering the event timer in VLBI control room. The two event timing devices are interconnected with another

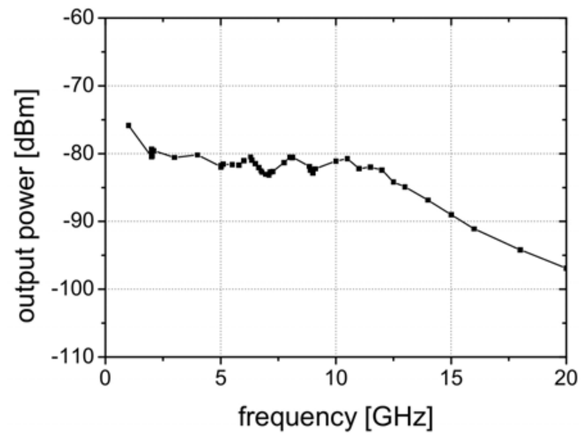

Fig. 5 The pcal output power level with tone spacing of 5 MHz.

cable. The built-in programmable pulse generators inside the event timers are activated alternately, and the generated pulse is sent through the interconnecting cable to the second event timing device, where the Time of Arrival (ToA) is measured. At the same time, this pulse ToA is measured by the event timer, which generated the pulse. This technique implements a two way measurement principle and is used to set the zero difference between both event timers [4]. After that measurement the event timers are switched to a second input, where pulse trains from a reference frequency are connected. The difference of the ToAs measured at the second input is directly proportional to the cable delay. The biggest advantage of such a method lies in the fact that the cable delay is measured at the output of pcal unit.

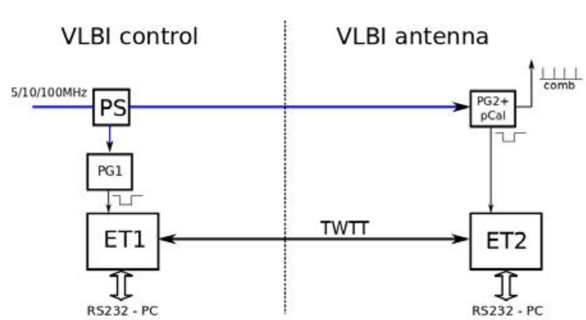

Fig. 6 Concept of the VLBI cable delay measurement.

Figure 7 shows an example of the cable delay measurement technique implementing two event timers with the two way technique. The cable delay was compared with an old measurement technique. The figure shows the dependency of the independent cable delays on azimuth and elevation (red—cable delay measured using the two way technique with event timers, green—cable delay of the new pcal system, and blue—currently implemented pcal cable delay technique). There is a large difference between the old and the new systems of a maximum of 10 ps. Unfortunately, due to limited experimental time, it was not possible to analyze where the difference is coming from.

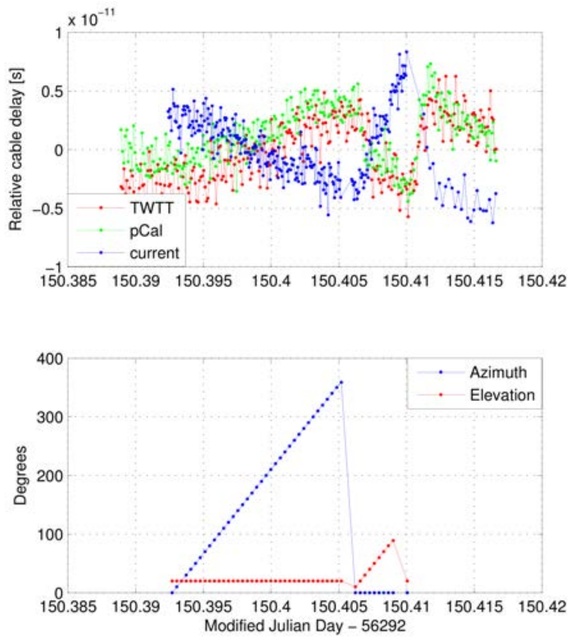

Fig. 7 Different VLBI cable delays' azimuth and elevation dependency.

3 Conclusions

We have designed and constructed the new pcal system generating any integer N pcal tone spacing from the reference frequency. The tones' output power is ~ 80 dBm in band spacing from 2 up to 12 GHz. The device has a very low temperature coefficient $+0.3$ ps/K for an input frequency of 100 MHz. In addition, the pcal has a built-in programmable pulse generator, which can generate pulses suitable for triggering external devices such as event timers or time interval counters. This output can be used for cable delay measurement or another timing application.

Acknowledgements

This work was carried out by support of the Technische Universität München, the Bundesamt für Kartographie und Geodäsie, and the Czech Technical University in Prague. We acknowledge funding through the Forschergruppe DFG FOR1503.

References

1. A. E. E. Rogers, *Phase and group delay calibration of a very long baseline interferometer by East Coast VLBI Group*, Radio Interferometry Techniques for Geodesy, NASA, July 1980, http://archive.org/details/nasa_techdoc_19800020297
2. P. Panek, *Time-Interval Measurement Based on SAW Filter Excitation* Instrumentation and Measurement, IEEE Transactions on, Vol. 57, pp. 2582–2588, 2008
3. B. Corey, *Phase calibration in prototype VLBI2010 systems* The 1st International VLBI Technology Workshop, http://www.haystack.mit.edu / workshop / ivtw / presentations / 2012.10.22_12-Corey.pdf
4. P. Panek, J. Kodet, I. Prochzka, *Accuracy of two-way time transfer via a single coaxial cable*, Metrologia, Vol. 50, pp. 60–65, 2013

Mark 6 16-Gbps Next-Generation VLBI Data System

Alan R. Whitney, Roger J. Cappallo, Chester A. Ruszczyk, Jason SooHoo, Geoffrey B. Crew

Abstract The Mark 6 VLBI data system has been developed as a next-generation disk-based VLBI data system capable of supporting the goals of VLBI2010 and other very-high-data-rate VLBI applications, with a maximum sustained recording rate of 16 Gbps. Based on COTS data hardware and open-source software, the Mark 6 is designed to transition easily from the widely used Mark 5 system. Its features include a 'scatter/gather' gather algorithm to ensure that data recording is not slowed by one or more slow or bad disks. The first field demonstration of a 16 Gbps/station VLBI experiment using Mark 6 in 2012 is reported. Existing Mark 5 systems are upgradeable to Mark 6, and existing Mark 5 SATA modules are upgradeable for compatibility with Mark 6.

Keywords Mark 6, data recorder, broadband recorder

1 Introduction

In this paper we report on the status of the 16-Gbps Mark 6 VLBI data system and its readiness to support VGOS operations that are expected to start in the near future. In particular, we describe a single-baseline dual-polarization VLBI experiment with a 4-GHz aggregate-bandwidth in which data were recorded on the Mark 6 system at 16 Gbps at each station.

MIT Haystack Observatory

2 Mark 6 Recorder

In contrast to the Mark 5 VLBI data system, which is based on proprietary hardware components, the 16-Gbps Mark 6 system utilizes only commercial-off-the-shelf (COTS) technology. The high data rate is achieved by adopting modern high-performance motherboards and components writing simultaneously to 32 conventional magnetic disks.

The open-source software operates under a Debian Linux distribution with application software written primarily in C/C++ for the 'data-plane' software and in Python for the 'control-plane' software.

The Mark 6 (Figure 1) can accept data into four 10GigE data ports, each operating independently at up to ~7 Gbps per port, with a maximum aggregate rate of ~16 Gbps. The system supports SATA-interface 8-disk modules that are inserted into the Mark 6 chassis and connected to the disk controllers via COTS external SATA cables. Each external SATA cable supports four disks, so that each module requires the connection of two such cables. Depending on the recording rate, different numbers of simultaneously-operating disk modules are required. A single 8-disk module will support 4 Gbps of continuous recording[1]; two modules (16 disks) are required for 8 Gbps, and four modules (32 disks) are required for 16 Gbps.

A 'scatter/gather' algorithm for writing data to disks has been implemented in Mark 6 to ensure that the aggregate real-time recording rate is sustained even when 'slow' disks are present; standard RAID

[1] Recent testing of Mark 6 using disks introduced in 2013/2014 has shown that eight such high-performance disks can support sustained 8 Gbps recording.

technology is not able to guarantee sustained recording rate in the face of even a single ‘slow’ disk.

Fig. 1 Photograph of prototype Mark 6 system.

VLBI has always pushed the technology of digital recording to the highest possible data rates primarily due to the fact that, for the majority of VLBI observations, the achievable signal-to-noise ratio of a given system increases as the square root of the recording bandwidth. Figure 2a shows the evolution of VLBI recording capability from the origins of VLBI in the late 1960s through the present. Over this period the record data-rate capability has increased by more than four orders of magnitude from less than 1 Mbps in 1967 (12″ open-reel magnetic tape) to 16 Gbps today (magnetic disks). At the same time, as shown in Figure 2b, the cost per Gbps of capability has dropped by almost five orders of magnitude and moved from highly proprietary tape-based systems to semi-proprietary disk-based systems (Mark 5 series), and now to the current 16-Gbps Mark 6 system which utilizes fully COTS data hardware with specially developed open-source software.

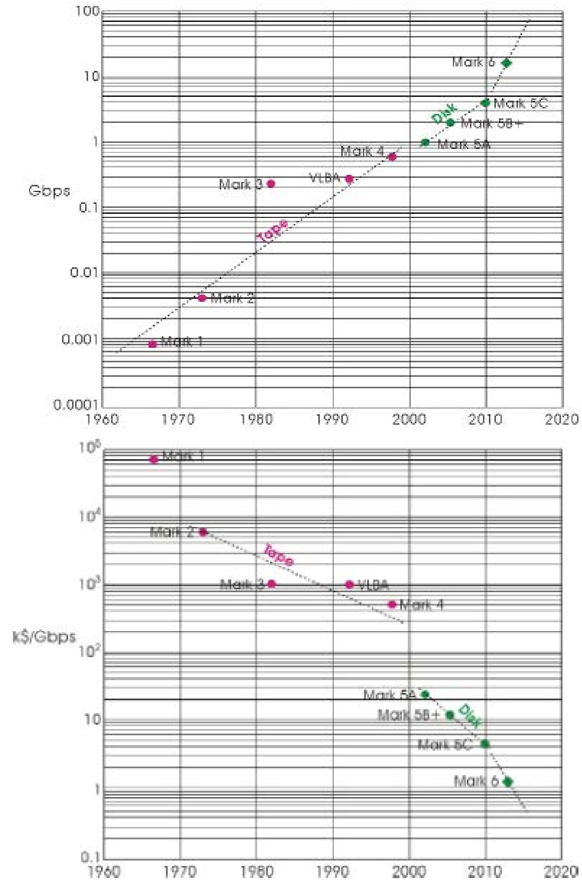

Fig. 2 a) Evolution of VLBI recording-rate capability from 1967 to 2012, progressing more than four orders-of-magnitude from original 1967 magnetic tape to modern magnetic disks, b) parallel evolution of cost of recording in k$ per Gbps, which has dropped by almost five orders-of-magnitude during the same period.

3 A 16-Gbps Experiment using Mark 6

VLBI observations were made in May 2012 using the 12-m diameter antenna recently installed at the Goddard Geophysical and Astronomical Observatory (GGAO), Goddard Space Flight Center, Maryland, and the 18-m diameter Westford antenna at Haystack Observatory, Massachusetts.

3.1 Receiver and Data System Block Design

The signal chain for each of these antennas (Figure 3) consists of a) a broadband dual-linear polarization feed; b) a broadband Low Noise Amplifier (LNA) for each polarization; c) four-way splitters for each polarization; d) four frequency converters for translation of

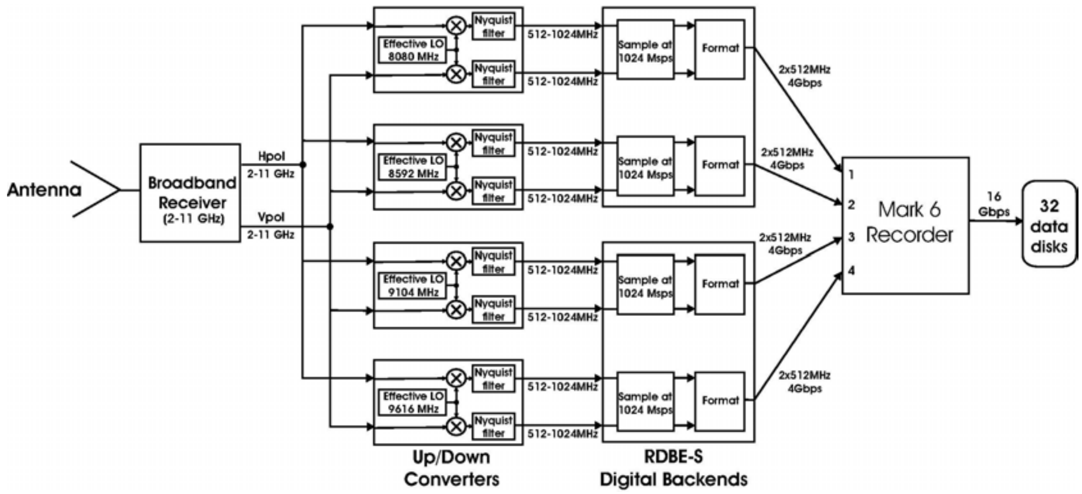

Fig. 3 Diagram of 2-GHz bandwidth dual-polarization system (4-GHz aggregate bandwidth) which records to the Mark 6 data recorder at 16 Gbps.

the signals from radiofrequency (RF) to intermediate frequency bands; e) two digital backend units [2], and f) a Mark 6 16-Gbps data recorder.

Each DBE accepts the two polarizations from two bands, quantizes all four 512-MHz bands to two-bit samples, time-tags and formats the data into VLBI Data Interchange Format (VDIF) format [3], and outputs the formatted data to two separate 10-Gigabit Ethernet datastreams at 4 Gbps each, one for each band. The four Ethernet 4-Gbps streams (two from each DBE) are fed to the Mark 6 recorder through two dual-port 10-Gigabit Ethernet network interface cards.

3.2 Correlation and Fringe Fitting

The data were cross-correlated on a 'DiFX' software-based correlation system [1], processing horizontal-to-horizontal and vertical-to-vertical polarizations between the two stations. Four passes through the correlator, one for each IF band, were required to process the complete dataset.

3.3 Results

Figures 4 and 5 show the results of a 16 Gbps/station observation of 3C84 of 10 seconds duration. Although there was no ability to do careful calibration of the system, the correlation amplitude and signal-to-noise-ratio of the scan (Figure 4) are within the expected range. The time-segmented band-by-band amplitude and residual-phase data (Figure 5) also appear nominal.

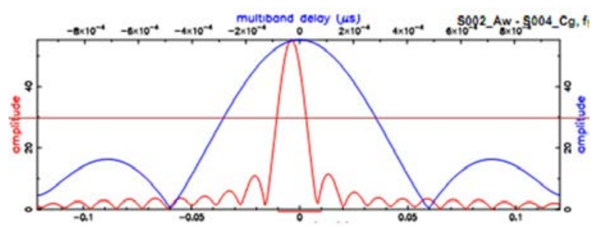

Fig. 4 Correlation amplitude vs. residual multi-band delay (larger, blue, three lobed curve, scale at top) from 10 second observation of 3C84 at 16 Gbps/station on 19 June 2012; smaller, red, multi-lobed curve shows correlation amplitude as a function of residual delay rate (nanoseconds/sec, scale at bottom). Correlation amplitude is $\sim 5.5 \times 10^{-3}$ (units in plot are 10^{-4}) with a signal-to-noise ratio of ~940; HH and VV cross-correlations for all four 512-MHz bands were combined coherently for this.

Although the results of the May 2012 observations were somewhat compromised by the failure of one of the up-down converter (UDC) units, 16 Gbps were recorded for a full 60 seconds on the Mark 6 system at each station, though only 12 Gbps of the recorded 16 Gbps could be processed to obtain fringes on the weak (~0.2 Jy) source 0550 + 356 (Figures 6 and 7);

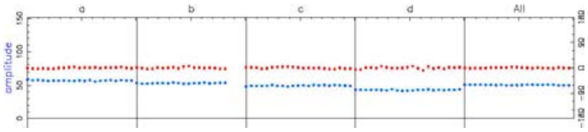

Fig. 5 Plot of correlation amplitude (blue/lower dotted line) and residual phase (red/upper dotted line) vs. time for each of the four 512-MHz-bandwidth bands (‘a’ through ‘d’) and vector sum (‘All’) over the 10-second duration of the observation.

as in the 3C84 observation above, only HH and VV correlations were done. Manual band-to-band adjustment phases for this source were obtained from observations of the nearby brighter source $0552+398$ (7 Jy at 5 GHz).

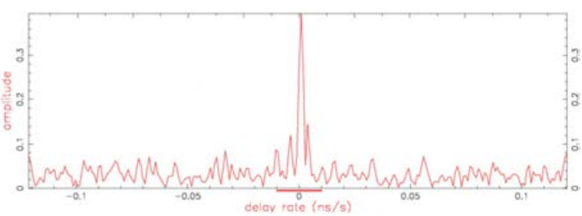

Fig. 6 Results from 60-second observation of $0550+356$ on 18 May 2012 showing correlation amplitude as function of residual delay rate in nanoseconds/sec (scale at bottom). Correlation amplitude at peak is $\sim 4.0\times10^{-5}$ with a signal-to-noise ratio of $\sim$14; HH and VV cross-correlation for the three good bands were combined coherently for this result.

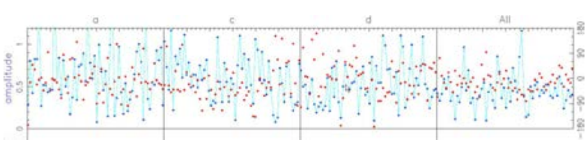

Fig. 7 Plot of correlation amplitude (blue) and residual phase (red) vs. time for each for each of the three 512-MHz-bandwidth bands (‘a’, ‘c’, ‘d’) and vector sum (‘All’) over the 60-second duration of the observation.

4 Summary

The Mark 6 VLBI data system is now a mature system with approximately 30 units currently in use around the world as of this writing; the open-source nature of the Mark 6 software invites anyone to augment and/or modify its capabilities. For full documentation of the Mark 6 system, please see http://www.haystack.mit.edu/tech/vlbi/mark6/index.html

The Mark 6 system is available from Conduant Corporation of Longmont, CO. The cost for a full 16 Gbps (without disk modules) is $\sim$ \$US14,000.

Acknowledgements

The Mark 6 VLBI data system is a joint collaborative development effort between MIT Haystack Observatory, NASA/GSFC High-End Network Computing Group, and Conduant Corporation.

References

1. Deller, A. T., Brisken, W.F. , Phillips, C.J., Morgan, J., Alef, W., Cappallo, R., Middelberg, E., Romney, J., Rottmann, H., Tingay, S.J., and Wayth, R.: DiFX-2: A More Flexible, Efficient, Robust, and Powerful Software Correlator, Publications of the Astronomical Society of the Pacific, 123, No. 901, pp. 275–287, 2011.
2. Niell, A. et al.: RDBE Development and Progress, in International VLBI Service for Geodesy and Astrometry 2010 General Meeting Proceedings, NASA/CP-2010-215864, D. Behrend and K. D. Baver (eds.), 396–399, 2010.
3. Whitney, A., Kettenis, M., Phillips, C., and Sekido, M.: VLBI Data Interchange Format — an Overview, in International VLBI Service for Geodesy and Astrometry Annual Report 2009, NASA/TP-2010-215860, pp. 15–35. (Also available at http://vlbi.org/vdif/).

Russian Data Recording System of New Generation

Ilya Bezrukov[1], Alexandre Salnikov[1], Andrey Vylegzhanin[2]

Abstract The IAA RAS is developing a data recording system for observations with radio telescopes of small diameter (13 m), which are also intended to realize the goals of the VLBI2010 international program. The main system goals are:

- recording of eight data streams (with scalability up to 16) in the VDIF format with a data speed of 2 Gbps from each channel;
- realizing data transfers to the Data Processing Centers at 10 Gbps transfer speed simultaneously with recording and buffering data;
- storing session data up to 20 TB in size in a generic file structure with a set of disk pools.

Keywords BRAS, DRS, VLBI

1 Features of the Data Recording System

In accordance with the experience of our colleagues [1, 2], we decided to create a Data Recording System (DRS) based on Commercial Off-The-Shelf (COTS) hardware.

Our development stand is a rack server (Figure 1) Dell PowerEdge R720 with two Intel CPUs: Xeon E5-2643 3.30 GHz or Xeon E5-2650 2.0 GHz, 96 Gb RAM, and two disk enclosures Dell PowerVault MD1220 (up to 24 2.5″ hot-pluggable small-form-factor drives). With this configuration, the disk subsystem of the server setup consists of three SAS backplanes, up to 64 2.5″ drives maximum. Each SAS-backplane is attached to LSI SAS2008 based SAS HBA by two 24 Gbps SAS 2.0 channels. Up to four dual-port 10 Gig Ethernet Intel network cards are used (Intel X520). The connection of the DRS with the digital backend was carried out in two ways: a direct connection of each channel BRAS to a server 10 GbE network interface (Figure 2a) and a connection through the Cisco Catalyst C4900M switch (Figure 2b). It also revealed first experimental data on registration of test signals and transmission of the data through a fiber

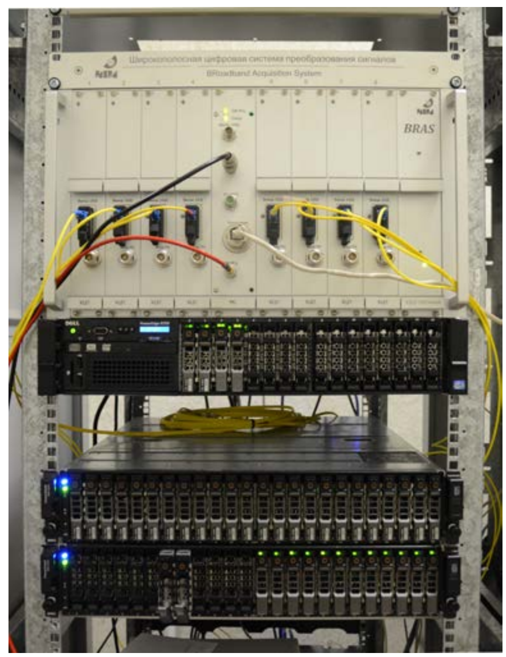

Fig. 1 The development stand. Up: digital backend BRAS [4]. Down: Server Dell PE R720 with storage Dell PV MD1220.

1. Institute of Applied Astronomy, Russian Academy of Sciences
2. Ioffe Physical Technical Institute, Russian Academy of Sciences

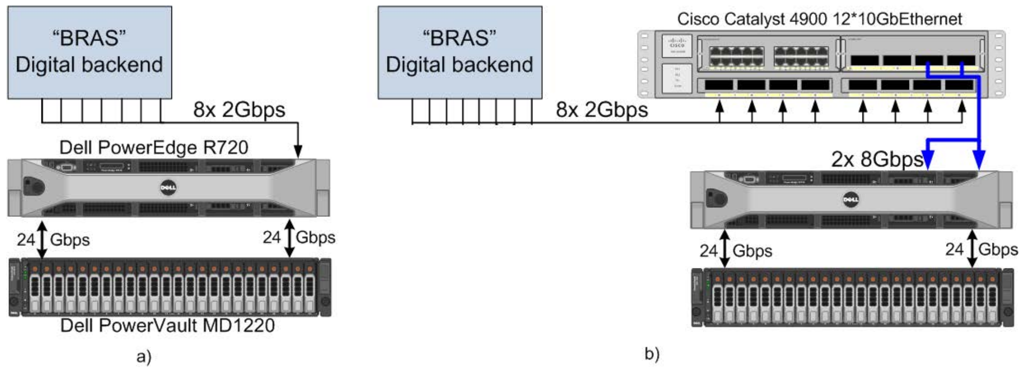

Fig. 2 Experiment diagram. a) direct connection and b) connection through 10 GbE switch.

optic channel with a maximum bandwidth of 10 Gbps between the IAA sites in St. Petersburg, Russia.

2 Packet Capturing and Recoding Algorithm

A block diagram of the data buffering software (application) is shown in Figure 3. The application has a multi-threaded architecture. Packet capture and management of the network interface is performed via a netmap [3] framework controlled by receiver thread. The receiver performs packet pre-processing and data transferring from the netmap circular buffer to an interim buffer. The data recording from the interim buffer on disk volumes is performed by a writer thread. The netmap is a framework for high speed packet I/O which has been a native part of a FreeBSD kernel since late 2011. This software interface, developed and maintained by Luigi Rizzo (member of FreeBSD team), can effectively process I/O packets at the maximum speed of the network interface, bypassing the standard kernel network stack interface. Unlike other frameworks for high packet processing, the netmap operates in user space memory, which excludes the possibility of a kernel crash. To achieve high speeds of packet processing, the application uses some of netmap's performance-boosting techniques, such as memory-mapping the network card's packet buffers and I/O batching. Network interface interrupt handlers and stream instances of thread <<receiver>> were also bound on the same CPU core, and features of Sandy Bridge processor architecture, memory management, and PCI express slot geographical addressing were taken into consideration.

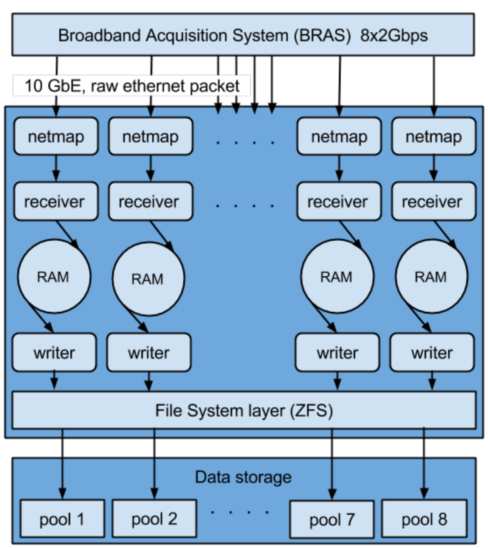

Fig. 3 Block diagram of the data buffering software.

3 Assessment of the Performance of the Disk Subsystem Data Buffering

The DRS is running under the FreeBSD 10.0-RELEASE operating system (in February 2014) with the ZFS (Zettabyte Filesystem). The ZFS is a stable FS actively developed by the world community that combines the functions of file system, logical volume manager, and software RAID. For a range of different disk configurations, we performed testing by simulating recorded data in Intensive session mode. To emulate this, a 10 GB random data set (white noise) was created in RAM and recorded 60 times by eight threads with 20 second intervals to eight ZFS pools. Data recording to the ZFS disk pools was performed with the standard Unix utility “dd”. Scoring of the writing speed to the ZFS pools was performed with utility “zpool iostat”. We tested SAS 10k rpm, low cost MLC SSD, NL SAS 7.2k rpm, and 3.5″ SATA 7.2k rpm drives.

Table 1 Disk performance.

Type of disk	Stripe pool, MBps			RAID-Z E5-2643		RAID-Z E5-2650	
	2 disk	3 disk	4 disk	3 disk	5 disk	3 disk	5 disk
SAS	**188**	**262**	**316**	140	**209**	117	143
NL-SAS	133	**200**	**241**	93	**185**	87	130
SSD	**274**	**338**	**403**	**189**	**236**	141	157
SATA	160	**189**	**192**	111	167	117	131

Table 1 shows the results of the disk types for stripe and RAID-Z (ZFS advanced RAID5 analog) pools. Results for the RAID-Z pools are given for two types of Intel Xeon processors: E5-2650 2 GHz and E5-2643 3.3 GHz. The red (thicker) numbers in Table 1 show transfer rates that fit requirements for DRS (180 MB/sec for 40 sec data streaming / 20 sec pause).

4 Experimental Research System Data Buffering from BRAS

During our research, we carried out data stream registration (recording) with 2 Gbps speed from each of the eight channels of BRAS. Figures 2a and 2b show the options of connecting BRAS to the DRS. We simulated the following mode of operation: a one hour session, eight data streams, each with 40 seconds of data recording and 20 seconds of pause. These total $60 \times 8 = 480$ files, 480×10 GB $= 4800$ GB total data. The recording was performed on the following configurations of ZFS disk pools:

- eight stripe pools, three SAS disks each;
- eight stripe pools, four NL-SAS disks each;
- eight RAID-Z pools, five SAS disks each;
- two stripe pools, 12 SAS disks each.

Additional testing was performed for simultaneous data transmission (with a transfer rate of 6 Gbps) to another server (Figure 4) and data recording of eight streams from BRAS (16 Gbps). For future DRS use, we performed successful preliminary testing for recording of a 32 Gbps data stream (4×8 Gbps BRAS channels) to four ZFS stripe pools, 12 SAS disks each (total 48 disks) with insignificant packet loss.

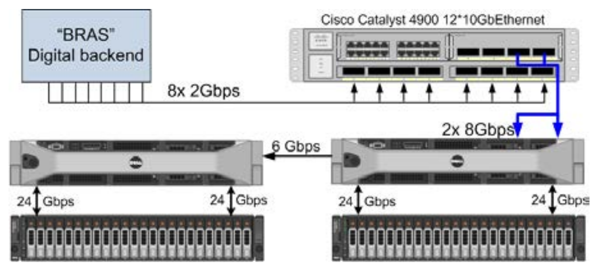

Fig. 4 Simultaneous data transmitting and data recording.

5 Future Plans

In the near future (2015), we plan to install our DRS on the RT-13 radio telescopes at the Badary (Siberia) and Zelenchukskaya (The Caucasus) observatories.

6 Main Results

The average data write speed for 60 scans (one scan/file size is 10 GB) to differently configured ZFS pools with the same disk type is about 2.5 GB/s, which is enough for recording 16 Gbps of a BRAS data stream.

With the multiple simulated Intensive session mode, we have demonstrated the ability to record eight data streams from a digital backend BRAS (total 2 Gbps $\times$ 8 $=$ 16 Gbps) without packet loss in two configurations:

- Direct connection of each BRAS channel to a DRS server;
- 10 Gbit Ethernet switched connection with $4\times$ BRAS channels (2 Gbps) to one 10 Gbit Ethernet port of the DRS server.

The average measured transfer rate for the Tsunami-UDP protocol is:

- Between IAI RAS sites in city area, 2.7 Gbps (with MTU 1500) with simultaneous BRAS data stream recording;
- In 10GBit LAN segment, 7 Gbps (with MTU 9000).

References

1. Roger Cappallo, Chester Ruszczyk, Alan Whitney. Mark6: Design and Status. `http://www.haystack.mit.edu/tech/vlbi/mark6/mark6_memo/05-Mark6_Design_and_Status.pdf`.
2. Tomi Salminen, Ari Mujunen. Nexpres WP8 — FlexBuff. `http://www.jive.nl/nexpres/doku.php?id=nexpres:nexpres_wp8`.
3. Luigi Rizzo. The netmap project. `http://info.iet.unipi.it/~luigi/netmap/`.
4. Evgeny Nosov, Dmitriy Marshalov. Current Development State of Russian VLBI Broadband Acquisition System. In this volume.

First Fringes with BRAS on VLBI Network “Quasar”

Alexey Melnikov, Anton Berdnikov, Sergey Grenkov, Dmitriy Marshalov, Andrey Mikhailov, Evgeny Nosov, Leonid Fedotov

Abstract Two 13-m antennas will be built at the Badary and Zelenchukskaya observatories of the VLBI network “Quasar”. These antennas will be equipped with new VGOS hardware being developed by the Institute of Applied Astronomy (IAA). While waiting for the small antennas, the first test sessions with VGOS technology were made with the 32-m antennas. A special VLBI session with the Broadband Acquisition System (BRAS) prototype was performed in late 2012 using the single baseline Svetloe–Zelenchukskaya. The main goals of this experiment were to test BRAS in a real environment and to compare it with the existing DAS R1002M.

Keywords BRAS, VLBI, fringe test

1 Introduction

A special VLBI session was performed in late 2012 to test BRAS, which was developed at the IAA [1, 2]. The test session was carried out using the Svetloe–Zelenchukskaya baseline, and the VLBI data was registered and recorded using the DAS R1002M with a Mark 5B recorder and using the BRAS prototype with a Mark 5C recorder. All scans were then transferred and correlated at the IAA Correlator [3]. Analysis and comparison of results were made using software packages PIMA, HOPS, and AIPS.

Institute of Applied Astronomy, Russian Academy of Sciences

2 Station Equipment and Setup

The Svetloe and Zelenchukskaya sites have 32-m antennas and are equipped with X/S receivers. Each station is equipped with DAS R1002M and Mark 5B+ for standard geodesy. The BRAS prototype and Mark 5C recording system were connected to the receiver output in parallel to the standard equipment.

For the standard system, a wideband geodetic X/S frequency setup was chosen. This setup includes 16 channels with center frequencies from 8212.99 to 8932.99 MHz and 16 MHz filters. Spanned bandwidths are 752 MHz in X band and 156 MHz in S band.

The BRAS prototype was able to record a single 512 MHz frequency channel, and it was adjusted to cover bandwidth from 8592.00 to 9104.00 MHz. The real BRAS bandwidth was reduced to 400 MHz by filters to fit the end of the receiver band.

In both cases, 2-bit sampling was used. The total sampling rate for the standard system was 1024 Mbps and, for the new system, was 2048 Mbps. Pcal was on.

3 Detection Limits and Source Choice

Using the following formula for the signal to noise ratio Q:

$$Q = 0.88 \cdot S\sqrt{\frac{2n\Delta f\tau}{SEFD_1 SEFD_2}},$$

a minimum detectable flux S_{min} can be estimated. SKED catalogs provide SEFD values for Svetloe and Zelenchukskaya equal to 400 Jy. Assuming lower s/n ratio for detection $Q_X = 10$, scan duration $\tau = 60$ s, and $n = 8$ X-band channels with $\Delta f = 16$ MHz, lower detectable flux density should be 37 mJy in case of a wideband geodetic setup. For the new system, a single 400 MHz bandwidth channel $S_{min} = 21$ mJy was used.

Table 1 Sources for Ru-TEST074 session.

IVS name	Number of observations	X band total flux, Jy	X band unresolved flux, Jy
4C39.25	239566	10.295	3.878
1803+784	201043	2.119	1.307
0059+581	289083	1.736	1.366
2320+506	2498	1.109	0.479
3C371	85725	1.021	0.415
0716+714	28223	0.755	0.646
1300+580	88230	0.474	0.400
0901+697	126	0.135	0.147
0611+665	117	0.099	0.024

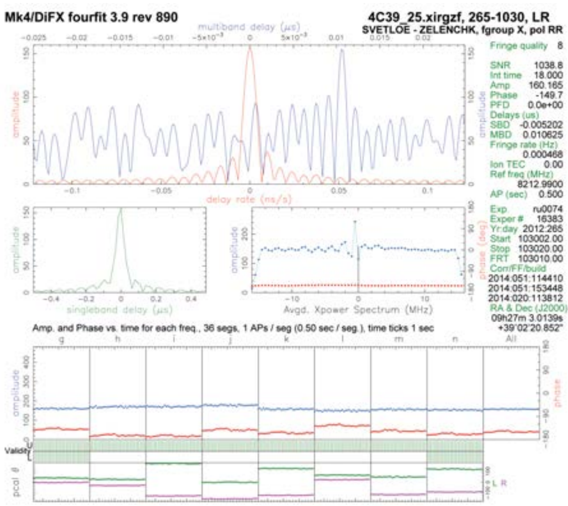

Fig. 1 HOPS fringe plots for scan at UT 10:30, source 4C39.25, standard geodetic X band.

Sources for the experiment were chosen according to the minimum flux density $S_{min} = 21$ mJy from the RFC 2012c catalog [5, 6, 7, 8, 9, 10] and the SKED source catalog. The list of sources and the parameters from RFC 2012c are presented in Table 1.

Source 0611+665 has never been observed with the "Quasar" VLBI network. Source 0901+697 was observed several times in the Ru-A observing program by 20-minute scans. Other sources are regularly observed. All sources have calibrator code "C".

4 Experiment Description

Test session Ru-TEST074 was carried out on September 21, 2012 and consists of three stages:

- the first — starting at UT 10:30, trial 20 s scan of bright source 4C39.25 during receiver cooling,
- the second — starting at UT 13:30, trial 20 s scan of 4C39.25, and
- the third stage — main experiment, starting at UT 17:00, consequent 60 s scans of remaining sources separated by five minute gaps to transfer data and maintain the Mark 5C recorder.

Data from Mark 5C was transferred manually after scan recording. The first scan was repeated at UT 10:40.

First scans were immediately transferred to the IAA Correlator via the Internet, and the fringe test was performed using the DiFX software correlator [4] to check that standard equipment works well and to find fringes with new DAS. Third stage scans were recorded at local storage and were transferred the next day.

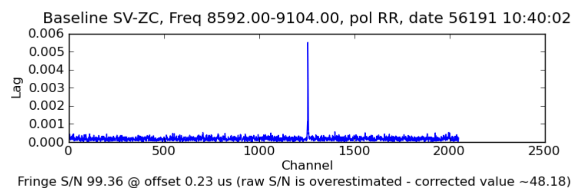

Fig. 2 First fringe with BRAS, DiFX plot of one second of data, 2 μs delay window, scan at UT 10:40, source 4C39.25.

5 Data Processing, Results and Analysis

The first three scans at UT 10:30, 10:40, and 13:30 of bright source 4C39.25 from Ru-TEST074 were correlated almost online right after recording and transferring to the IAA Correlator. Figure 1 shows fringes in X-band from HOPS for scan 10:30 recorded using standard geodetic equipment. The s/n ratio for scan 10:30 achieves 1038 units and for scan 13:30 — 1595. For broadband scans, several trial DiFX runs were performed with different delay windows and accumulation periods. Finally, a first fringe was found (Figure 2).

Table 2 Calculated signal to noise ratios for broadband and standard systems.

Software	Scan, Source/ Setup	17:00 1300+580	17:05 3C371	17:10 0901+697	17:15 1803+784	17:20 0716+714	17:25 0611+665	17:30 0059+581	17:35 2320+506
PIMA	1x16 MHz	48.22	64.03	13.86	151.95	107.31	7.87	370.5	23.01
AIPS	1x16 MHz	32.4	45.8	10.4	115.9	72.7	3.8	139.9	15.4
PIMA	8x16 MHz	143.81	199.14	42.46	452.31	309.34	27.36	1089.85	60.81
HOPS	10x16MHz	183.5	253.5	54.4	572.5	399.5	34.3	1391.4	79.0
PIMA	1x512 MHz	221.15	307.18	66.08	705.53	504.05	42.43	1737.14	111.01
HOPS	1x512 MHz	288.2	404.0	79.9	931.9	661.9	55.1	2299.3	147.2
AIPS	1x512 MHz	156.7	204.0	57.0	342.1	278.7	43.1	381.0	80.8

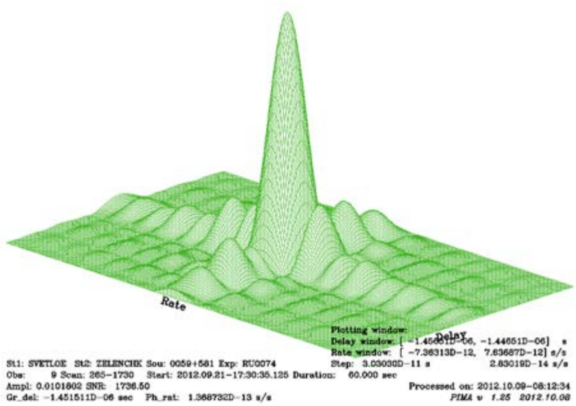

Fig. 3 PIMA 3D fringe plot of 0059+581 source at UT 17:30 using BRAS and Mark 5C.

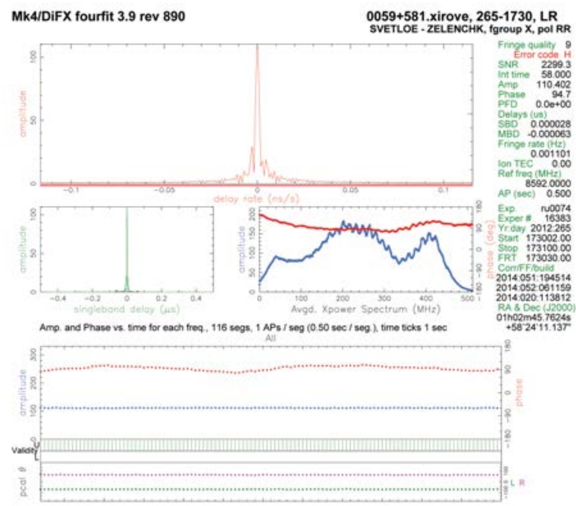

Fig. 4 HOPS fringe plot of source 0059+581, scan at UT 17:30 using BRAS and Mark 5C.

All data were correlated, and fits-idi and Mark IV format files were produced for standard and broadband systems. To estimate improvement from using the broadband system, s/n ratios were calculated. The ratio of broadband system s/n and standard system s/n with eight X-band frequency channels is proportional to the square root of the total bandwidth relation and should be equal to 1.76, because the broadband system has 400 MHz real bandwidth.

AIPS was used at first for data fringe fitting with task FRING, then s/n values were collected from output. Calculated values were a little bit confusing.

The next tool, HOPS, had some restrictions from the box. The maximum number of lags allowed is 2,048. Thus, the delay window for the 512 MHz band is only 2 μs, which is not enough for a fringe search with unknown clock offsets. Mark IV format files need to be produced specially for HOPS.

A much better tool for analysis is PIMA, which has a flexible setup for fringe search procedures and has no problems with only one frequency channel (IF) in a data set. It loads a fits file produced by DiFX. Also it produces beautiful 3D pictures of fringes (Figure 3). Equivalent HOPS fringe plots for the same scan are shown in Figure 4.

Calculated s/n values from the different software tools for both systems are gathered in Table 2. In the second column, the used frequency setup is given, which indicates the number of IFs and the bandwidth of each channel in MHz used in the s/n calculation. The IF bandwidth is 16 MHz for a standard system and 512 MHz for a broadband system.

The least square fit (LSF) average ratio between s/n values from PIMA for 8x16 MHz and 1x512 MHz is 1.6, a little bit less than the expected 1.76. This value was calculated for 400 MHz of bandwidth, but actually 512 MHz was recorded, so we can introduce the correction coefficient, which equals $\sqrt{\frac{512}{400}} = 1.13$. The corrected value is $1.6 \cdot 1.13 = 1.81$. Scan 17:35 got a G-code in HOPS and could be affected by local RFI at Zelenchukskaya. If this point would be removed, then the corrected value would be equal to 1.77, which agrees very well with the expected value. Calculated in the same way, corrected for the 10 IFs and 400 MHz bandwidth, the LSF average of s/n ratios for HOPS is equal to 2.01, which did not agree with expected value.

6 Conclusions

First fringes with BRAS were obtained. Source 0611+665 with only 24 mJy correlated flux density was detected.

The new broadband system BRAS is supposed to replace the previous digital DAS and provide an advantage by 1.77 over standard geodetic mode even with a single frequency channel.

Acknowledgements

Special thanks to Leonid Petrov for developing PIMA, the explanation, and the tutorial, and to Alessandra Bertarini for help on HOPS.

References

1. Fedotov, L. V., Kol'tsov, N. E., Marshalov, D. A., Nosov, E. V. A data acquisition system of the S/X-wave range of the radio interferometer for the universal time on-line monitoring. Instruments and Experimental Techniques, SP MAIK Nauka/Interperiodica, Dordrecht, 2013, 56, 3, 339–346.
2. Nosov, E., et al. Current Development State of Russian VLBI Broadband Acquisition System, in this volume.
3. Surkis, I., Ken, V., Melnikov, A., Mishin, V., Sokolova, N., Shantyr, V., Zimovsky, V. IAA Correlator Center. International VLBI Service for Geodesy and Astrometry 2012 Annual Report. NASA/TP-2013-217511, K. Baver, D. Behrend, and K. Armstrong (eds.), 201–203, 2013.
4. Deller, A. T., Tingay, S. J., Bailes, M., West, C. DiFX: A Software Correlator for Very Long Baseline Interferometry Using Multiprocessor Computing Environments. PASP, 2007, 119, 318.
5. Beasley, A. J., Gordon, D., Peck, A. B., Petrov, L., MacMillan, D. S., Fomalont, E. B., Ma, C. The VLBA Calibrator Survey — VCS1. Astrophys. J. Sup., 2002, 141, 13.
6. Petrov, L., Phillips, C., Bertarini, A., Murphy, T., Sadler, E. M. The LBA Calibrator Survey of southern compact extragalactic radio sources — LCS1. Mon. Not. of Roy. Astron. Soc., 2011, 414(3), 2528-2539.
7. Petrov, L., Kovalev, Y. Y., Fomalont, E. B., Gordon, D. The VLBA Galactic Plane Survey — VGaPS. Astron J, 2011, 142, 35.
8. Petrov, L., Taylor, G. Precise absolute astrometry from the VLBA imaging and polarimetry survey at 5 GHz. Astron. J., 2011, 142, 89.
9. Petrov, L. The EVN Galactic Plane Survey — EgaPS. MNRAS, 2012, 416, 1097–1105.
10. http://astrogeo.org/vlbi/solutions/rfc_2012c

Research on VLBI Digital Baseband Converting Methods Combining the Efficient Uniform Channelization with the Orthogonal Mixing

Shaojie Wei, Xin Lian, Xiaomin Hou, Hong Ma, Kun Jiang, Yiwen Jiao

Abstract To meet the special requirement of full spectrum processing in deep space TT&C, a new efficient VLBI baseband converting method, which can realize the processing of certain bandwidth without distortion and dead zone, is proposed. The method combines the efficient uniform channelization with the orthogonal mixing. By ingenious channelization and altering the coefficient of the low-pass prototype filter, the processing of the input signal analyzing bandwidth without distortion and dead zone in certain bandwidth is realized. Then with the flexibility of the orthogonal mixing, wide-band and narrow-band single-sideband output schemes are designed. Furthermore, the center frequency of the output signal can be changed arbitrarily and the bandwidth can be selected by different filter cascades.

Keywords VLBI, DBBC

1 Introduction

VLBI is a new interferometric measurement technique developed in the late 1960s with ultra-high precision of angle measurement [1]. At first, it was used in radio astronomy, geodesy, and geophysics. VLBI observations can provide complementary information on the three-dimensional with velocity and distance, it promotes the VLBI technology application and development of measurement and control in deep space. Currently, the U.S. National Aeronautics and Space Administration, the European Space Agency, and the Japanese Space Agency have developed measurement systems based on ΔVLBI (differential VLBI), and take it as the main tool to support spacecraft navigation in deep space [2]. DBBC (Digital baseband converter), which is an important part in VLBI receiving systems to complete data acquisition, channel selection, and baseband conversion, and some other functions, are the basis for the subsequent signal processing. Currently, the American Deep Space Network is using WVSR (Wideband VLBI Science Receiver) and VSR (VLBI Science Receiver) to complete broadband VLBI observations and ΔDOR [3], with the function of full spectrum recording. It requires DBBC that the center frequency of the output signal can be changed arbitrarily and the bandwidth can be selected according to the requirements. Orthogonal mixing and efficient uniform channelization are the main two methods in DBBC. A new VLBI baseband conversion method is proposed for special requirements of full spectrum processing in deep space TT&C. The method combines the efficient uniform channelization with the orthogonal mixing, which can realize the processing of certain bandwidth without dead zone and distortion.

Equipment Academy

2 Efficient Uniform Channelization without Dead Zone and Distortion in Certain Bandwidth

2.1 The Derivation of the Efficient Uniform Channelization Model

Figure 1 shows the multi-channel parallel processing model of the orthogonal mixing baseband conversion.

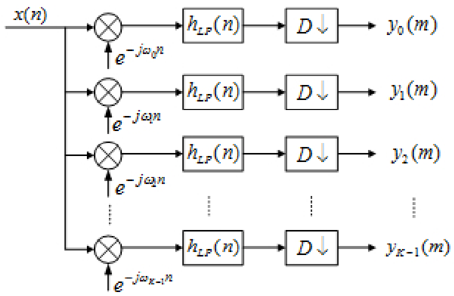

Fig. 1 Multi-channel parallel processing model of orthogonal mixing baseband conversion.

Achieving the multi-channel baseband conversion with this structure has the advantage of a flexible band selection. However, when the number of channels K is large, each channel requires an orthogonal mixer working at high speed. The hardware implementation pressure and resource consumption are large. Extraction is after the low-pass filter, so that a large number of data after conversion and low-pass filtering is not being used.

In order to reduce the front-end signal processing speed and to improve the overall operational efficiency, we can make the input signal uniform channelized filter over the entire frequency band, which can be analyzed when the following two conditions are met:

1. The bandwidth of each output channel is the same.
2. The difference between adjacent channel center frequency is (K is the number of channels). The output of the channel K is expressed as:

$$
\begin{aligned}
y_k(m) &= x(n)e^{-j\omega_k n} * h_{LP}(n)\,|_{n=m\mathrm{D}} \\
&= \sum_{i=0}^{\mathrm{N}-1} x(n-i)e^{-j\omega_k (n-i)} h_{LP}(i)\,|_{n=m\mathrm{D}} \\
&= \sum_{i=0}^{\mathrm{N}-1} x(m\mathrm{D}-i)e^{-j\omega_k (m\mathrm{D}-i)} h_{LP}(i)
\end{aligned}
\quad (1)
$$

Equation (1) is a convolution, N is the number of filter coefficients.

According to the number of channels K, let us make the low-pass prototype filter polyphase decomposed. Suppose (L is an integer), then:

$$
y_k(m) = \sum_{p=0}^{K-1} \sum_{i=0}^{L-1} x(mD-iK-p)e^{-j\omega_k (mD-iK-p)} \cdot h_{LP}(iK+p) \quad (2)
$$

Suppose $x_p(m) = x(m\mathrm{D}-p)$, $h_p(m) = h_{LP}(m\mathrm{K}+p)$, and $F = K/D$ then:

$$
\begin{aligned}
y_k(m) &= \sum_{p=0}^{\mathrm{K}-1} [\sum_{i=0}^{\mathrm{L}-1} x_p(m-i\mathrm{F})e^{-j\omega_k (m-i\mathrm{F})\mathrm{D}} h_p(i)]e^{j\omega_k p} \\
&= \sum_{p=0}^{\mathrm{K}-1} [\sum_{l=0}^{(\mathrm{L}-1)\mathrm{F}} x_p(m-l)e^{-j\omega_k (m-l)\mathrm{D}} h_p(\frac{l}{\mathrm{F}})]e^{j\omega_k p}
\end{aligned}
\quad (3)
$$

Let $h'_p(l) = h_p(\frac{l}{\mathrm{F}})$, that $h'_p(l)$ is F times the intervening sequence of $h_p(l)$, then:

$$
y_k(m) = \sum_{p=0}^{\mathrm{K}-1} \left\{ [x_p(m)e^{-j\omega_k m\mathrm{D}}] * h'_p(m) \right\} e^{j\omega_k p} \quad (4)
$$

In practical applications, depending on the channel division, we can get all kinds of high-channel structure by taking ω_k into Equation (4).

2.2 Real Signal Uniform Channelization Without Dead Zone

The different channel division decided a different channelized efficient structure. The literature [4] shows that the low-pass prototype filter cannot be ideal (rectangular factor of 1). So, there will be a dead zone in the conventional method of channel division. In order to achieve real signal processing without dead zone, using the symmetry of its positive and negative spectrum, the center frequency of each channel is divided into the following:

$$
\omega_k = -\frac{2\pi}{\mathrm{D}}k + \frac{\pi}{2\mathrm{D}} \qquad k = 0,1,2,\ldots,\mathrm{D}-1 \quad (5)
$$

In Equation (5), the multiple of the decimation D is equal the number of channels K. In order to ensure the spectrum of each channel signal after extraction does not overlap, we design the low-pass prototype filter as the magnitude response in Figure 2.

Usually, in order to realize easily, set the passband equal to transition (shape factor of 2). Based on the above channel division mode and low-pass prototype filter design, we can get the real signal uniform channelization without dead zone in Figure 3.

Since the input signal is a real signal, the signal spectrum in Figure 3 frequency axis in the positive

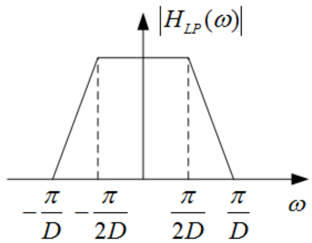

Fig. 2 Magnitude response of low-pass prototype filter.

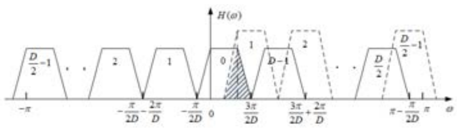

Fig. 3 Real signal uniform channelization without dead zone.

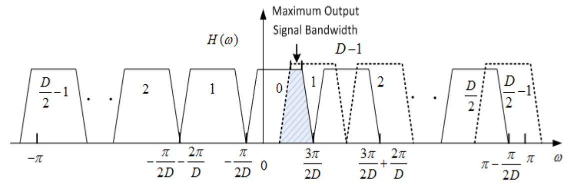

Fig. 4 Improved uniform channelization without dead zone.

"$0 \sim \pi$" and negative "$-\pi \sim 0$" are the mirror each other. Positive frequency spectrum in dotted line is the mirror spectrum of the axis of the negative frequency axis. The output signal from channel 1 to channel "$D/2-1$" is the mirror spectrum of the real input signal. By clever channelization, using the mirroring features of real signal spectrum, the receiving of the whole channel without dead zone is realized.

2.3 Uniform Channelization without Dead Zone and Distortion in Certain Bandwidth

In Figure 3 by clever channelization, the receiving of the whole channel without dead zone is realized. However, it cannot realize receiving without distortion in certain bandwidth. When the signal is located in the triangle shaded area as shown in Figure 3, because of the transition zone adjacent to the channel, it will cause the attenuation of the amplitude of the received signal, thereby causing signal distortion.

To solve this problem, we improve the amplitude-frequency characteristics of the low-pass prototype filter. We expand the low-pass prototype filter pass bandwidth, make the two equivalent adjacent channel passband overlapping ranges greater than or equal to the VLBI maximum output signal bandwidth, improved uniform channelization without dead zone is shown in Figure 4.

Take the center frequency of each channel in formula (5) into formula (4),we can get the output of channel K:

$$
\begin{aligned}
y_k(m) &= \sum_{p=0}^{\mathrm{D}-1} \left\{ [x_p(m)e^{-j\frac{\pi}{2}m}] * h_p(m) \right\} e^{j\frac{\pi}{2\mathrm{D}}p} e^{-j\frac{2\pi}{\mathrm{D}}kp} \\
&= \mathrm{DFT}[\left\{ [x_p(m)e^{-j\frac{\pi m}{2}}] * h_p(m) \right\} e^{j\frac{\pi p}{2\mathrm{D}}}] \qquad (6)
\end{aligned}
$$

Among (6), $x_p(m) = x(m\mathrm{D}-p), h_p(m) = h_{LP}(m\mathrm{D}+p), p = 0,1,...,\mathrm{D}-1, x_p(m)$ is the multiphase delay component of the input signal. $h_p(m)$ is polyphase branch low-pass prototype filter. The signal processing block diagram is shown in Figure 5.

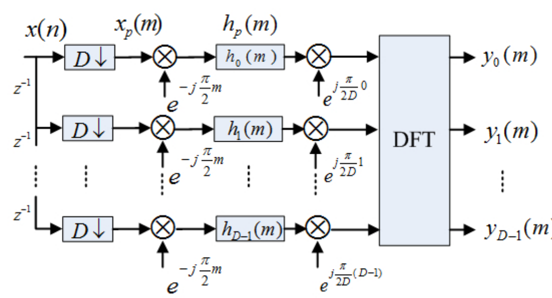

Fig. 5 Processing diagram of the improved uniform channelization without dead zone.

3 Wide-band and Narrow-band Single-sideband Output Schemes

The output signal after uniform channelization filter is lowering sampled baseband signal. The signal rate has been greatly reduced. So we can use the flexibility of orthogonal mixing. We can select the desired output signal from each uniform channel by changing the output frequency of the orthogonal local oscillator.

By loading different processing modes to achieve the bandwidth requirements of optional application.

Referring to the American Deep Space Network output bandwidth requirements for different observing modes [3], we design wide-band and narrow-band single-sideband output schemes.

3.1 The Design of Wide-band Single-sideband Output

In wide-band scheme, the bandwidth of the output real signal can be 16, 8, 4, 2, 1, or 0.5 MHz. Since the output bandwidth is a power of 2, the sampling rate of the input signal is usually a power of 2, we use half-band filter cascade to realize the wide-band output. The diagram of wide-band mode is shown in Figure 6.

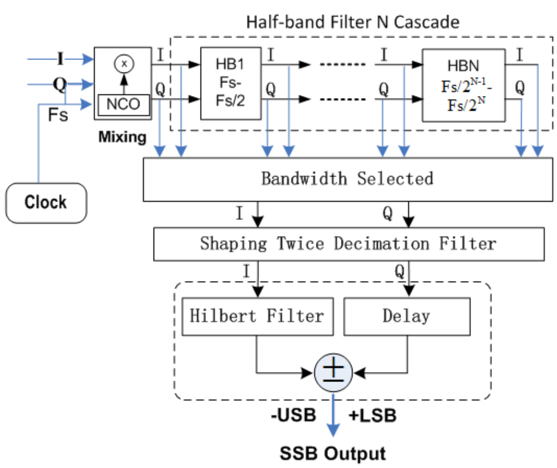

Fig. 6 Single channel diagram of wide-band mode.

3.2 The Design of Narrow-band Single-sideband Output

In narrow-band scheme, the bandwidth of the output real signal can be 200, 100, 50, 25, 16, 8, 4, 2, or 1 kHz. The literature [6] shows that, although the half-band filter passband ripple is small, if the high-power narrow-band signal decimation filtering, higher resource consumption but the filter order increase with the increase of filter progression. If the high-power narrow-band signal decimation filtering, the resource consumption is large. CIC, as an efficient filter, its stop-band attenuation and passband rolloff are only decided by the bandwidth scaling factor $b = \frac{B}{f_s/D}$, where B is the bandwidth and f_s/D is the sampling rate after decimation. The smaller b is, the greater is the CIC filter stopband attenuation of the aliasing signal bandwidth and the better the band flatness. So CIC filter is more suitable for narrow-band signal to filter and extract. The single channel diagram of narrow-band mode is shown in Figure 7.

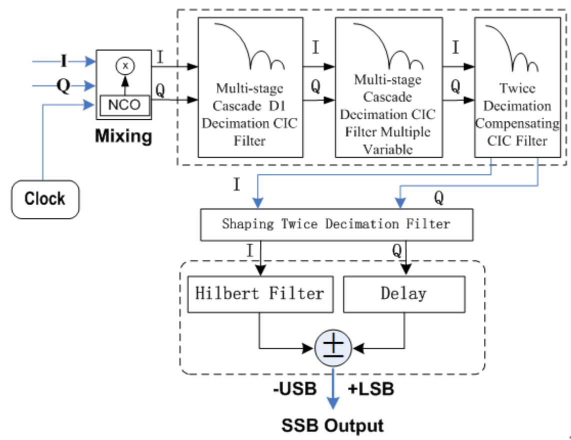

Fig. 7 Single channel diagram of narrow-band mode.

Because of the narrow-band output the signal bandwidth is narrow. So first reduce the signal rate by the high-powered CIC decimation filter, and then by changing the CIC decimation filter multiples to achieve the output signals with different bandwidths. As the CIC filter passband rolloff is large. Therefore, compensating for CIC compensation filter passband characteristic by the second stage of the CIC filter is needed, through the single sideband of the Hilbert transform to realize the SSB output.

4 VLBI Full Spectrum Digital Baseband Conversion Methods

Through the analysis above, the VLBI full spectrum digital baseband conversion method which the center frequency of output signal can be changed arbitrarily and the bandwidth can be selected is shown in Figure 8.

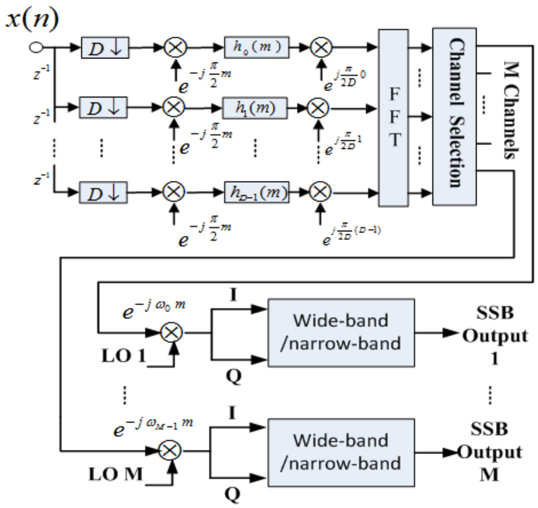

Fig. 8 Scheme of VLBI full spectrum digital baseband conversion.

First, the real input signal is done primary baseband conversion through efficient uniform channelized filtering, get down sampled complex baseband signal. Send the required signal into back-end orthogonal mixer unit by channel selection unit. In orthogonal mixer unit, we can realize the parallel multi-channel baseband signals output through multiple orthogonal mixer. In each orthogonal mixer unit, the frequency range of the desired output signal decides the oscillation frequency, the filter working methods, the output of the USB or LSB and so on. since the signal rate is low at this time, the realization difficulty and resource consumption of the multiple orthogonal mixer is small.

Compared with the orthogonal mixing method, this method has the advantage of low front-end signal processing pressure, high efficiency, and low consumption of resources. Compared with the efficient uniform channelization method, this method has the advantage that the center frequency of the output signal can be changed arbitrarily and the bandwidth can be selected.

5 Conclusions

A new VLBI baseband conversion method is proposed for special requirements of full spectrum processing in deep space TT&C. The method combines the efficient uniform channelization with the orthogonal mixing, which can realize the processing of certain bandwidth without dead zone and distortion. By clever channelization and change of low-pass prototype filter shape factor, the processing of input signal analyzing bandwidth without dead zone and distortion in certain bandwidth is realized. Using the flexibility of orthogonal mixing, wide-band and narrow-band single-sideband output schemes are designed. The center frequency of the output signal can be changed arbitrarily and the bandwidth can be selected by different filter cascades.

This VLBI baseband converting method has been used in CDBE (Chinese Digital Backend) developed by Equipment Academy. CDBE has played an important role in Chang'E-3 mission.

References

1. Qian Zhihan, Wu Linda. Very Long Baseline Interferometry. Beijing: SinoMaps Press. 1998:1–14
2. Hao Wan-hong, Dong Guang-liang, Li Hai-tao. An Introduction to Application of Radio Interferometry in Deep Space Navigation. Journal of Spacecraft TT&C Technology, 2009, 28(4)
3. DSMS Engineering Program Office. DSMS Telecommunications Link Design Handbook : 209, Rev. A Open-Loop Radio Science. California: JPL, 2010:5–17.
4. Yang Xiaoniu, Xu Caiyi, Xu Jianliang. Software Radio Technology and Application. Beijing: Beijing Institute of Technology, 2010:115–123.
5. Ouyang Changyue. The Basis of Information Transmission.Beijing, Beijing University of Aeronautics and Astronautics Press, 1996:75–86.
6. Yang Xiaoniu, Xu Caiyi, Xu Jianliang. Software Radio Technology and Application. Beijing: Electronic Industry Press, 2006:41–48.

Session 3

Stations, Correlators, and Operations Centers

March 2-7, 2014

8th IVS

GENERAL MEETING

Shanghai, China

Status of the Wettzell Radio Telescope Triple and the O'Higgins VLBI System at Antarctica

Gerhard Kronschnabl[1], Torben Schüler[1], Alexander Neidhardt[2], Christian Plötz[1], Thomas Klügel[1], Jan Kodet[2]

Abstract This contribution portrays the latest developments regarding the Wettzell and O'Higgins radio telescope systems devoted to geodetic VLBI. The technically revised 20-m RTW is currently the backbone of all VLBI operations at Wettzell. It will be superseded by the smaller 13.2-m VGOS-compliant TWIN radio telescopes. The first of this pair, TTW1, is currently prepared for operations and features a tri-band feed horn. A broadband feed horn is foreseen for integration into the second telescope, TTW2. It is planned to support further geodetic VLBI activities and special missions with the 20-m RTW in the future. In addition, the VLBI telescope at O'Higgins, Antarctica, is currently being revised for improved remote operation, which is a key to enhancing operational performance at this remote location.

Keywords TWIN, RTW, GARS O'Higgins

1 Overview

The Geodetic Observatory Wettzell is on its way to operate three radio telescopes completely devoted to geodetic services in the near future (see Figure 1): the 20-m Radio Telescope Wettzell (RTW) with its long time series of observations and the new 13.2-m TWIN radio Telescope Wettzell pair (TTW1 and TTW2), which fulfills the VGOS specifications [1].

1. Federal Agency for Cartography and Geodesy, Geodetic Observatory Wettzell, Germany
2. Forschungseinrichtung Satellitengeodäsie, Technische Universität München, Geodetic Observatory Wettzell, Germany

TTW1 was officially inaugurated in May 2013 after completion of the mechanical construction. At that time, it was equipped with a preliminary S-/X-band receiver for the demonstration of first-light capabilities. This telescope will be operated using a tri-band feed horn for S-, X-, and Ka-band in dual-polarization mode during a certain transition phase. In contrast, the second telescope, TTW2, is planned to feature a wideband feed horn ("Elevenfeed").

The existing 20-m RTW was revised in order to continue operations. It will be able to close the gap between the classic IVS sessions and the future VGOS network. In addition, some important technical improvements such as L-band tracking capabilities for special experiments were implemented. A demonstration was successfully carried out in January 2013 and in January 2014.

Finally, a 9-m antenna at O'Higgins, Antarctica is operated for geodetic VLBI by BKG for geodesy in partnership with the German DLR (remote sensing). It is currently enhanced with respect to dewar and receiver components. Efforts are carried out to enable an extension of the remote operation capabilities for a more effective use of this site in the future. First promising remote control tests were already performed in the year 2009 [4].

2 TWIN Telescope Status

2.1 Technical Characteristics

The TWIN telescopes were developed according to VGOS (VLBI2010) specifications (see [1]) and feature a ring focal design with a ratio of f/D = 0.29. This

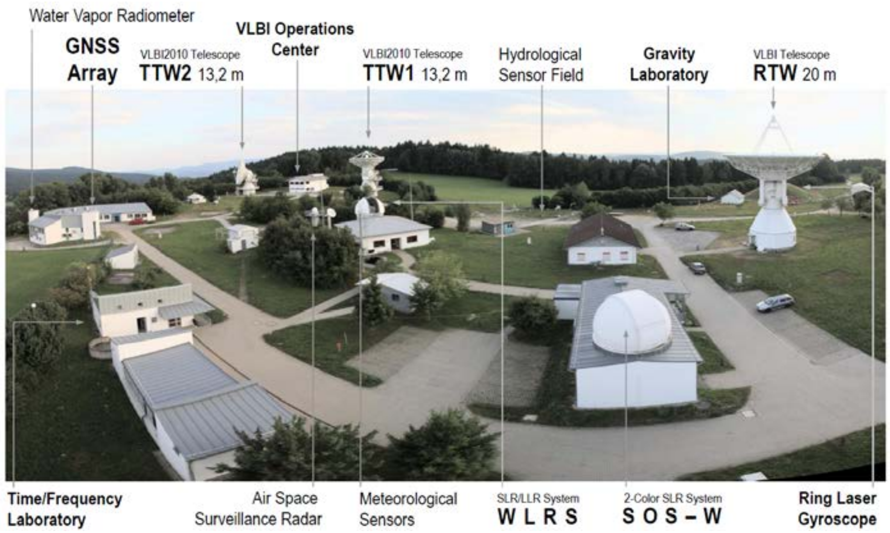

Fig. 1 Geodetic Observatory Wettzell, a fundamental station of geodesy featuring three VLBI radio telescopes.

choice is linked to the broadband design of the telescope. The surface finish of the main reflector is specified to be better than 0.3 mm RMS, where real control measurements reveal a finish even significantly below this threshold. An ALMA mounting was adopted for reasons of performance and quality. The slew rates are up to 12 degrees per second in azimuth and 6 degrees per second in elevation with a drive range from -90.0 to $+450.0$ degrees horizontally and 0 to 115 degrees vertically.

The overall antenna design of the TWIN telescopes is "balanced" in the sense that the antenna cannot pitch downwards in a powerless situation. Encoders with a discretization of 27 bits are in use yielding a resolution of 1 arc-second. The sub-reflector is adjustable by a hexapod, which is necessary and related to the stringent requirements for the surface finish that necessitates a mechanism for path length compensation especially for higher frequencies up to the Ka-band.

2.2 Milestones – History and Progress

The TWIN project officially started in 2009. The first antenna dish was mounted one year later in 2010, and finalization work was carried out until March 2012. The tri-band S-/X-/Ka-band feed horn was installed in the TTW1 in December of the same year, and the first test was carried out in March 2013, followed by the official inaugural act in April 2013. First light functionality was achieved in July with positive correlation results during several IVS Intensive sessions. The current plan foresees continuous test observations starting at the end of June 2014. Regarding the second TWIN telescope, TTW2, the critical design review for the broadband feed horn ("Elevenfeed", see Figure 2) is expected around mid-2014 with a possible integration until the end of that year.

2.3 Tri-band Feedhorn Efficiency Test, Receiver Design and Phase-calibration

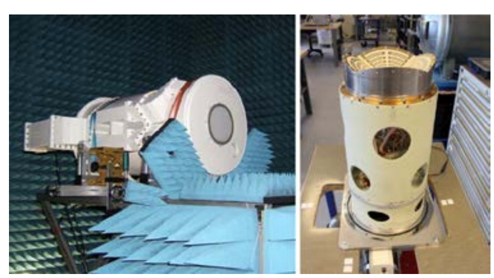

Fig. 2 S-/X-/Ka-band feedhorn by Mirad, Switzerland (left), Elevenfeed with cryogenic system by Omnisys, Sweden (right).

Fig. 3 A first assembly of the microwave wave part of the S-/X-/Ka-band receiver, as it will be used in the future (IF part and synthesizer are not shown in this picture).

S- and X-band efficiency measurements for the tri-band feed horn manufactured by Mirad, Switzerland, agree with the expected values at a very satisfactory level (see Figure 2). S-band efficiency is between more than 0.65 and partially slightly higher than 0.70 throughout the frequency band between 2.2 and 2.7 GHz. X-band efficiency is usually around 0.8 in the frequency band between 7.0 and 8.5 GHz and drops down to slightly better than 0.7 for 8.75 until 9.50 GHz. Measured SEFD (System-Equivalent Flux Density) is between 1400 and 1600 Jy for S-band and 700 to 840 Jy in X-band. The Ka-band calibration is still pending and will be performed with a suitable calibration source.

Note that the broadband feed horn for TTW2 ranging from 2 to 14 GHz has not been integrated yet. The critical design review is expected around mid-2014 so that its implementation into the system will likely not be performed before the end of 2014.

The receiver design and development is accomplished by the local Wettzell team of specialists. A preliminary receiver was set up for the time of the inauguration ceremony serving also to achieve first light functionality. It is now superseded by the final tri-band receiver as shown in Figure 3.

Similarly, a phase-calibration unit (see Figure 4) was developed, which can be used both for S-/X-band in TTW1 as well as for the broadband feed foreseen in TTW2. The output power level shows a linear to constant shape up to around 12 GHz and appears to be very suitable for phase calibration [6].

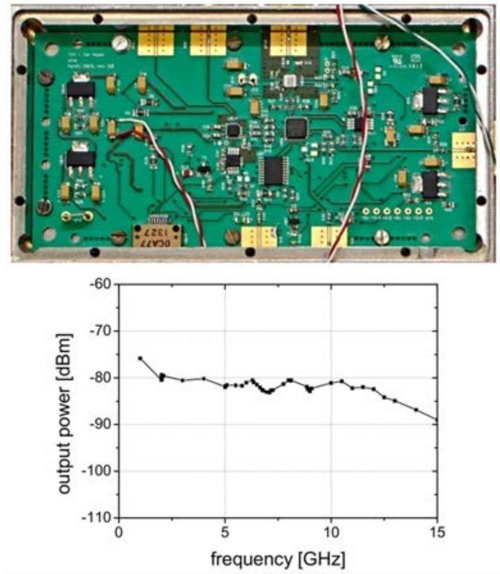

Fig. 4 Phase-calibration unit (top) and output power level versus frequency.

3 RTW - Technical Upgrades

The 20-m aperture RTW VLBI telescope has served the geodetic community reliably for 30 years now. Maintenance and repair efforts have been moderate so far. In order to preserve RTW for a sufficiently long period of time, a number of technical and mechanical enhancements were carried out in 2013. In particular, the obsolete servo motors and gears were replaced by a new digitally controlled servo system. The main and subreflector received a new coating. Moreover, the antenna control unit (ACU) was updated. It is now compatible with the TWIN ACU and supports “Green mode” and is capable of continuous satellite tracking, using Two-Line Elements (TLE). This is important for GNSS VLBI tracking experiments, for instance. Finally, the new ACU is Ethernet-controlled for a better integration into the in-house automation concepts.

3.1 Participation in Special Experiments

A number of special experiments were conducted with RTW between 2013 and 2014. In particular, it is worth mentioning that the receiving system is now able to track GNSS satellite signals in L-band, although this capability is currently limited to the L1 frequency, which is the lowest possible frequency transmitted over the existing S-band feed and waveguides. Successful correlation results from experiments between Onsala and Wettzell were demonstrated [5].

Moreover, RTW was also employed in support of EVN (European VLBI Network) with respect to observations of the Venus Express orbiter and PRIDE (Planetary Radio Interferometry and Doppler Experiment), testing a possible contribution to the upcoming ESA deep space missions. The first goal of these observations was to develop and test the scheduling, data capture, transfer, processing, and analysis pipeline. The high dynamic range of the detections allowed the extraction of the phase of the spacecraft signal carrier line. Apart from other important results, the measured phase fluctuations of the carrier line at different time scales can be used to determine the influence of the solar wind plasma density fluctuations on the accuracy of the astrometric VLBI observations [2].

3.2 Future of the RTW Telescope

Although the two TWIN telescopes will take over much of the routine observing load of RTW as soon as VGOS-related operations are started, it is planned to keep RTW as an active part of the IVS, based on the recommendations expressed for the future VGOS observing network (see [1], page 22). This concept "foresees the contribution of larger antennas [...] mostly for the densification and maintenance of CRF." The minimum VGOS network should "have at least 8 larger ($\geq$20 m) antennas (4 per hemisphere)." Currently it is guaranteed, that RTW operations are continued for the next five years. A corresponding concept for future operations is planned to be presented to the funds-giving agency within that period.

4 Geodetic VLBI at O'Higgins Station (Antarctica)

The GARS (German Antarctic Receiving Station) O'Higgins radio telescope (see Figure 5) is jointly operated by the German DLR (80%, mainly as a remote sensing—receiving station for the TerraSAR-X mission) and BKG (20%, geodetic VLBI). The site has been under the administration of the Chilean army with a corresponding station since 1948. The German receiving station has existed since 1993. Up to now, the VLBI campaigns have been conducted once or twice a year. In the future, the remote operations and remote control capabilities are planned to be significantly enhanced in order to increase the efficiency of the VLBI observations.

Fig. 5 The 9-m radio telescope at O'Higgins.

The O'Higgins site features a compact and stable antenna. The aerodynamic form of the VLBI telescope is resistant to wind speeds up to 300 km/h. It has a tilted elevation axis and can realize high slew rates of up to 11 degrees per second in azimuth and 6 degrees per second in elevation, which are almost VGOS-compliant. The diameter of the main reflector is 9 m. The VLBI receiver operates at frequencies in S-band (2.1–2.3 GHz) as well in X-band (8.1–8.9 GHz).

4.1 Contributions to IVS and Special Sessions

Due to the lack of VLBI sites in the southern hemisphere, as well as close to the South Pole, the O'Higgins site is of significant importance for geodesy (see Figure 6). Typically, the O'Higgins VLBI telescope contributes to the following IVS sessions:

- T2 (Terrestrial Reference Frame) experiments with radio telescopes distributed globally; participation of O'Higgins as one of the very few radio telescopes in the southern hemisphere improves VLBI solutions.

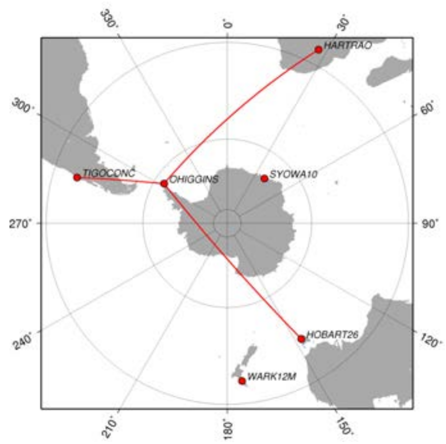

Fig. 6 Antarctica – VLBI stations around the South Pole.

- OHIG (Southern Terrestrial Reference Frame) experiments optimized to cover the Southern Terrestrial Reference Frame (TRF) with intent to supply precise measurements of the region around the south pole.

Moreover, a number of special experiments were supported by the O'Higgins VLBI telescope, in particular:

- IYA09 (International Year of Astronomy 2009)
- VIEPR01 (TU Vienna)
- TANAMI

The improved imaging capabilities of radio sources due to the increased resolution by integration of the O'Higgins telescope are revealed in [3].

4.2 Technical Upgrades and Remote Operation

A number of technical improvements of the VLBI system have been carried out so far. A new cryogenic dewar was manufactured by the team of the Centro Astronómico de Yebes, Spain, featuring new high performance LNAs and an extended stability of the cryo-temperature. Moreover, a newer hydrogen maser (EFOS-50) was brought to the site. Finally, the remote control of the VLBI system is getting extended using the e-RemoteCtrl software [4]. The Mark IV BBC is replaced by a digital baseband converter (DBBC/ADS3000). The ultimate goal of these measures is to reach an extended VLBI observation period in the future with help of better remote operation capabilities.

5 Conclusions

The Geodetic Observatory Wettzell will support the VGOS goals and is on the way to realize the design for GGOS core sites. The observatory will strongly continue the support of geodetic VLBI with the Wettzell Radio Telescope Triple and the O'Higgins VLBI System in Antarctica in the future.

References

1. Petrachenko, B.; Niell, A.; Behrend, D.; Corey, B.; Boehm, J.; Charlot, P.; Collioud, A.; Gipson, J.; Haas, R.; Hobiger, T.; Koyama, Y.; MacMillan, D.; Malkin, Z.; Nilsson, T.; Pany, A.; Tuccari, G.; Whitney, A.; Wresnik, J.: Design Aspects of the VLBI2010 System. Progress Report of the IVS VLBI2010 Committee. *NASA/TM-2009-214180*, June 2009.
2. Molera Calvés, G.; Pogrebenko, S. V.; Cimò, G.; Duev, D. A.; Bocanegra-Bahamón, T. M.; Wagner, J. F.; Kallunki, J.; de Vicente, P.; Kronschnabl, G.; Haas, R.; Quick, J.; Maccaferri, G.; Colucci, G.; Wang, W. H.; Yang, W. J.; Hao, L. F.: Observations and analysis of phase scintillation of spacecraft signal on the interplanetary plasma. *Astronomy & Astrophysics*, AA22925, 2014.
3. Müller, C.; Kadler, M.; Ojha, R.; Wilms, J.; Böck, M.; Edwards, P. G.; Fromm, C. M.; Hase, H.; Horiuchi, S.; Katz, U.; Lovell, J. E. J.; Plötz, C.; Pursimo, T.; Richers, S.; Ros, E.; Rothschild, R. E.; Taylor, G. B.; Tingay, S. J.; Zensus, J. A.: Dual-frequency VLBI study of Centaurus A on subparsec scales. The highest-resolution view of an extragalactic jet. *Astronomy & Astrophysics*, Volume 530, Article L11, June 2011.
4. Neidhardt, A.; Ettl, M.; Plötz, Ch.; Mühlbauer, M.; Dassing, R.; Hase, H.; Sobarzo, S.; Herrera, C.; Alef, W.; Rottmann, H.; Himwich, E.: e-control: new concepts for remote control of VLBI-telescopes and first experiences at Wettzell. Proceedings of Science, PoS(EXPReS09)038, 2009.
5. Kodet, J.; Plötz, Chr.; Schreiber, U.: Co-location of space geodetics techniques in Space and on the ground. *Geophysical Research Abstracts, EGU General Assembly*, Vol. 15, ISSN (Online) 1607–7962, 2013.
6. Kodet, J.; Schreiber, U.; Plötz, C.; Kronschnabl, G.: The new Phase-Calibration system of the Geodetic Observatory Wettzell. In: Behrend, D.; Baver, K.D. (eds.): VGOS: The New VLBI Network. *IVS 2014 General Meeting Proceedings, National Aeronautics and Space Administration*, 2014.

Status Report on the Tsukuba VLBI Station
– Damage to the Substructure of the Antenna and Its Repair –

Takahiro Wakasugi, Ryoji Kawabata

Abstract The Geospatial Information Authority of Japan (GSI) has carried out a lot of VLBI experiments with the Tsukuba VLBI Station since 1998. On the other hand, repeating loads of the antenna has weakened the substructure gradually, and we had to suspend all sessions from May 2013 due to the damage. Investigations revealed the distortion of the rail track and the gaps under the sole plate, which caused the antenna to subside 6 mm at maximum. We repaired the damage and confirmed that the subsidence of the antenna was improved significantly. Finally, we resumed observations from November 2013.

Keywords Repair, wheel and track structure, damage

1 Introduction

The Tsukuba VLBI Station, which is one of the leading VLBI stations in Eastern Asia, was installed at the site of Geospatial Information Authority of Japan (GSI) in 1998. Recently we carried out more or less 200 sessions per year (Figure 1). On the other hand, a lot of loads were applied to the substructure of the antenna. Some phenomena concerning the damage to the substructure occurred from a few years ago. For example, outflow of the farinaceous grout occurred around the substructure, and vertical movement of the rail track was found when the wheel passed through. The pointing offset in April 2013 revealed that the offset was so large that it would affect observations. In response to this, we decided to suspend all observations from early May 2013. We investigated the substructure in order to know the damage in detail. In this article, we report the analysis result of the investigation and the repair work.

Geospatial Information Authority of Japan

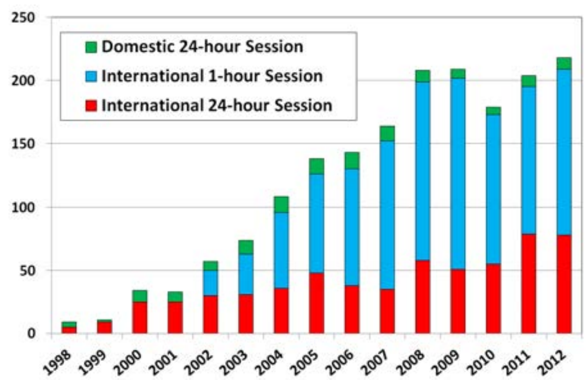

Fig. 1 The number of sessions carried out by using the Tsukuba VLBI Station.

2 Investigations

2.1 Pointing Offset

Figure 2 shows the result of the pointing offset in April. Large offsets occurred at specific azimuths in both the azimuth and the elevation plots. The maximum elevation offset was 170 arcseconds at the azimuth angle of 115 degrees, which was large enough to disturb observations because the beam half-value width of the Tsukuba antenna for X-band was about 250 arcseconds.

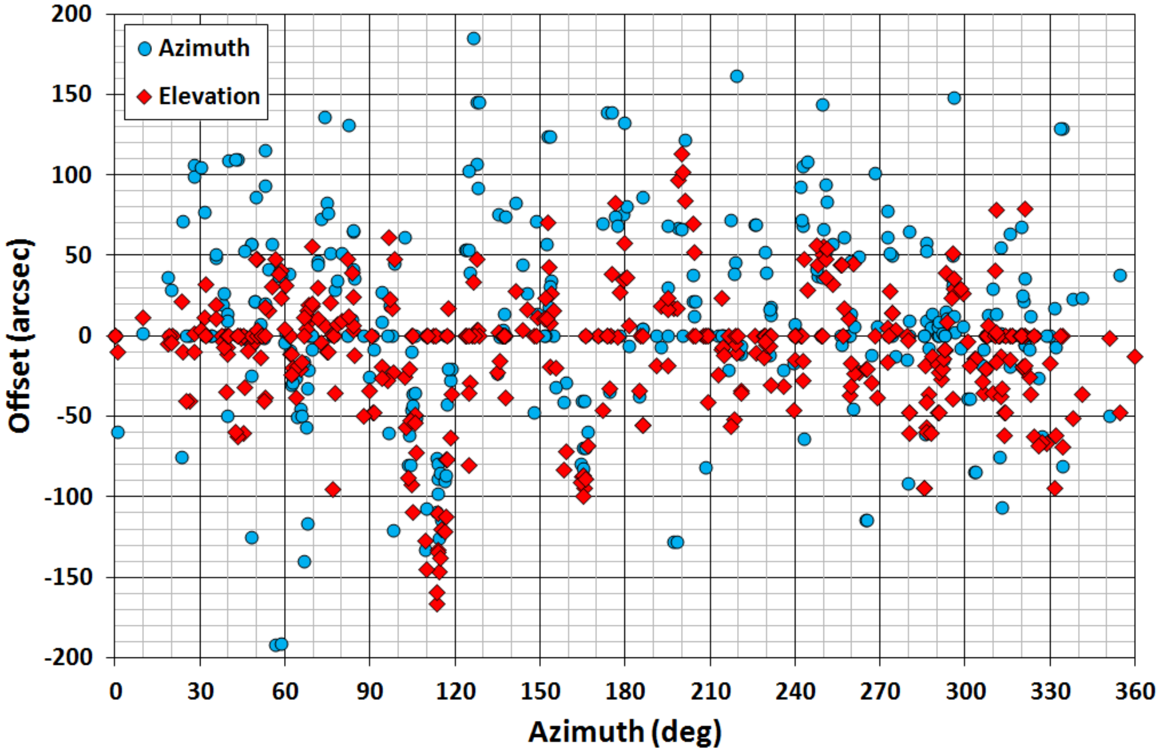

Fig. 2 The pointing offset of azimuth and elevation in April 2013 plotted as a function of the azimuth direction.

2.2 Investigations

Figure 3 is the schematic cross section of the substructure of the antenna. The rail track is mounted on the sole plate, and the sole plate is locked to the basement concrete by some anchor bolts. The space between the rail track and the sole plate is filled with cementitious grout. Additionally, the rail track and the sole plate are divided into several pieces, and those boundaries are arranged alternately.

In order to know the damage in detail, we conducted two kinds of investigations. One was leveling on the rail tracks under a no load condition. The other was the measurement of the vertical movements of the sole plates to the grout when the wheel passed through. Adding these results, we can understand the subsidence amount of the antenna from the reference level.

Figure 4 shows the results of the leveling and the vertical movement. It turned out from the leveling that almost all the rail tracks were distorted in a convex shape while only one rail track at the azimuth angle of 250 degrees was deformed concavely. The range of

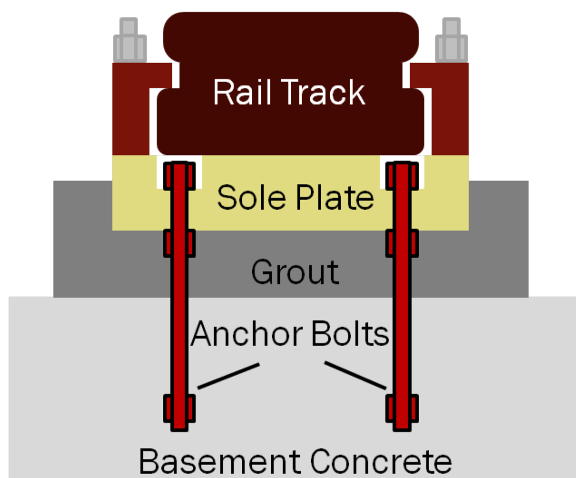

Fig. 3 A schematic cross section of the substructure of the antenna.

the level reached to 4 mm. The second investigation revealed the vertical movements of almost all the sole plates at their boundaries. The maximum amount of the vertical movement was up to 3.5 mm. The estimated

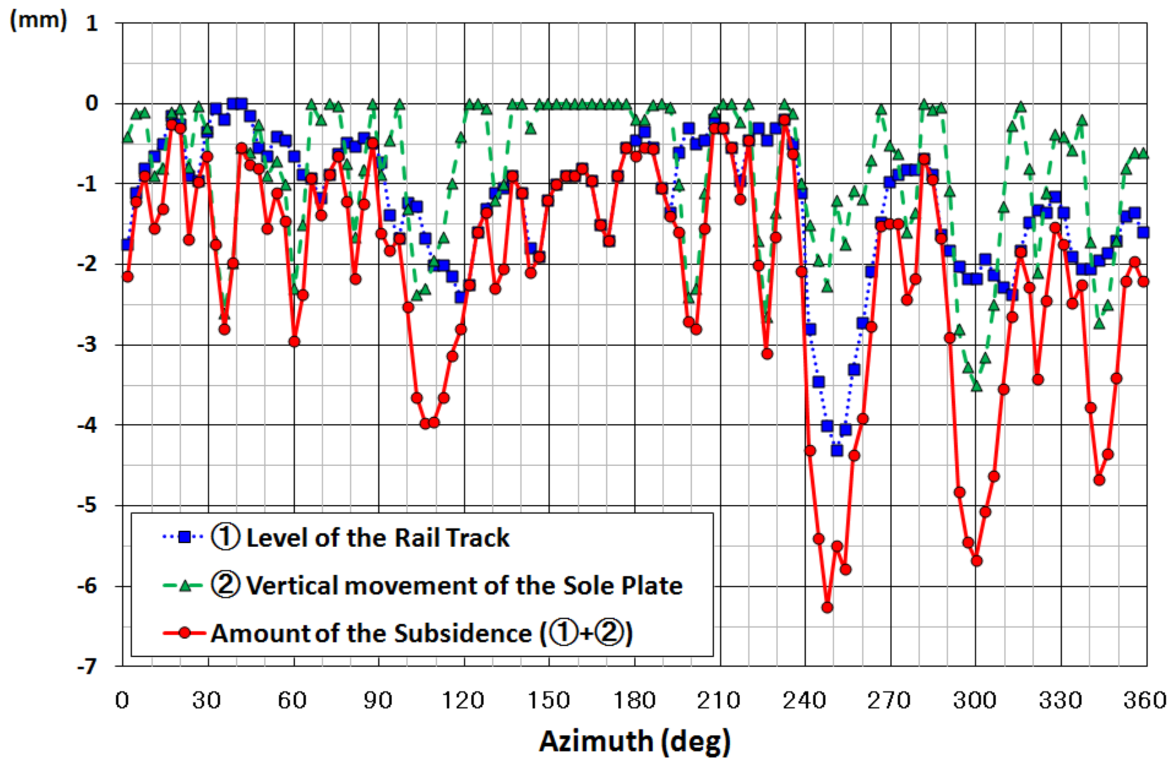

Fig. 4 The results of the leveling, the vertical movements, and the estimated subsidence amounts of the antenna. The blue squares, the green triangles, and the red circles show the level of the rail tracks, the vertical movements of the sole plates, and the estimated subsidence of the antenna respectively.

subsidence amount of the antenna was also plotted in Figure 4. The maximum subsidence came to 6 mm.

2.3 The Relationships Between the Elevation Offsets and the Subsidences

Assuming that the superstructure of the antenna is a rigid body, the antenna will miss the target when the wheels are located on subsidence spots (Figure 5). For example, we consider the case that one of the wheels is located on the maximum subsidence spot. In this case, both of the front wheels subside about 5 mm while both of the rear wheels scarcely subside (Figure 6). Five millimeters of the subsidence of the front wheels causes 52 arcseconds of the offset. The actually measured elevation pointing offset in such an arrangement of the wheels was 51 arcseconds (see Figure 2). That is, the subsidence of the antenna is able to cause the measured offset.

We reviewed the relationships between the measured elevation offsets and the estimates of the offsets caused by the subsidences. In almost all the cases, the positive/negative sign coincided with each other between both the measured and the estimated offsets. However, the estimated offset was insufficient to produce the whole amount of the measured offset in many cases. Considering these relationships, the fundamental cause of the measured offset was the subsidence of the antenna.

3 Repair

In order to prevent the antenna from subsiding and to reduce the offset, we conducted two kinds of repairs. One repair was the lifting up of the concavely deformed rail track. The other repair was the filling up of the gaps under the sole plates with new firm grout. It was con-

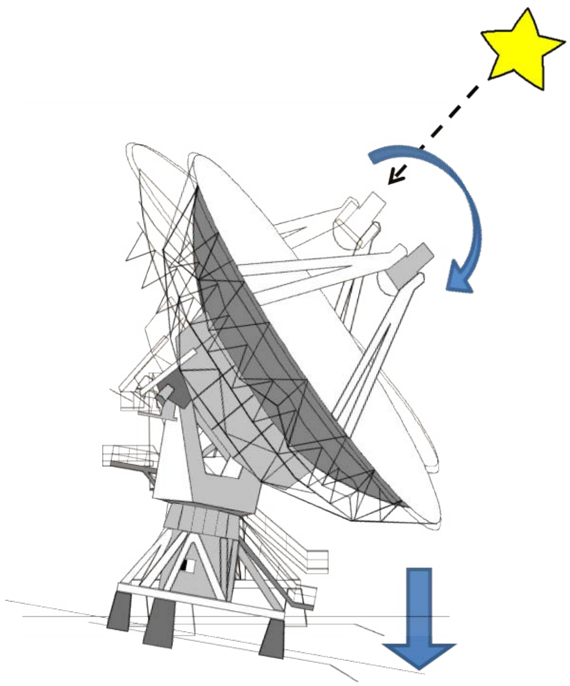

Fig. 5 Missing the target if some wheels subside.

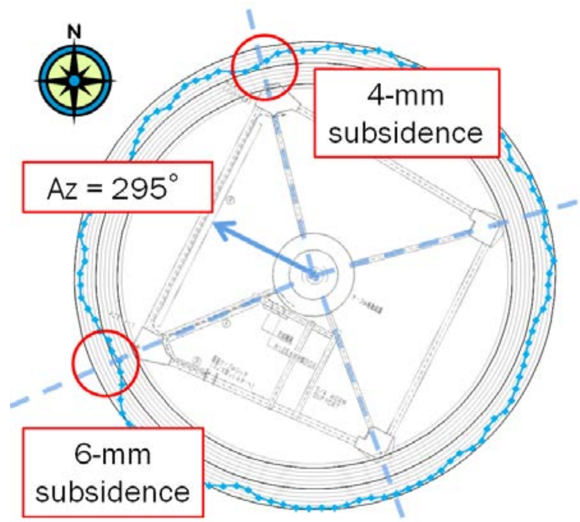

Fig. 6 The configuration of the antenna when one of the wheels is located on the maximum subsidence spot.

ducted under high pressure in order to fill every corner of the gaps.

After the repair, we measured the level and the vertical movements again. As a result, the concavely deformed rail track was raised by 1.5 mm, and almost all the vertical movements of the sole plates no longer existed. Eventually, the range of the subsidence was reduced to 2.5 mm (Figure 7).

We checked the pointing accuracy of the antenna after those measurements. Although some of the offsets remained, most of the offsets were improved. The maximum offset was reduced to 100 arcseconds, which did not have harmful influence on observations (Figure 8). At last, we resumed observations from the end of November.

4 Conclusions

All observations at the Tsukuba VLBI station were interrupted by the damage to the substructure of the antenna. Investigations revealed the deformations of the rail tracks and the vertical movements of the sole plates. By checking the relationship between the measured elevation offsets and the estimates of the offsets caused by the subsidence of the antenna, it turned out that the subsidence was the fundamental cause of the measured offset. Most of the subsidences were cleared, and the pointing offset was improved substantially by the repair. Finally, the Tsukuba VLBI station returned to sessions from November 2013.

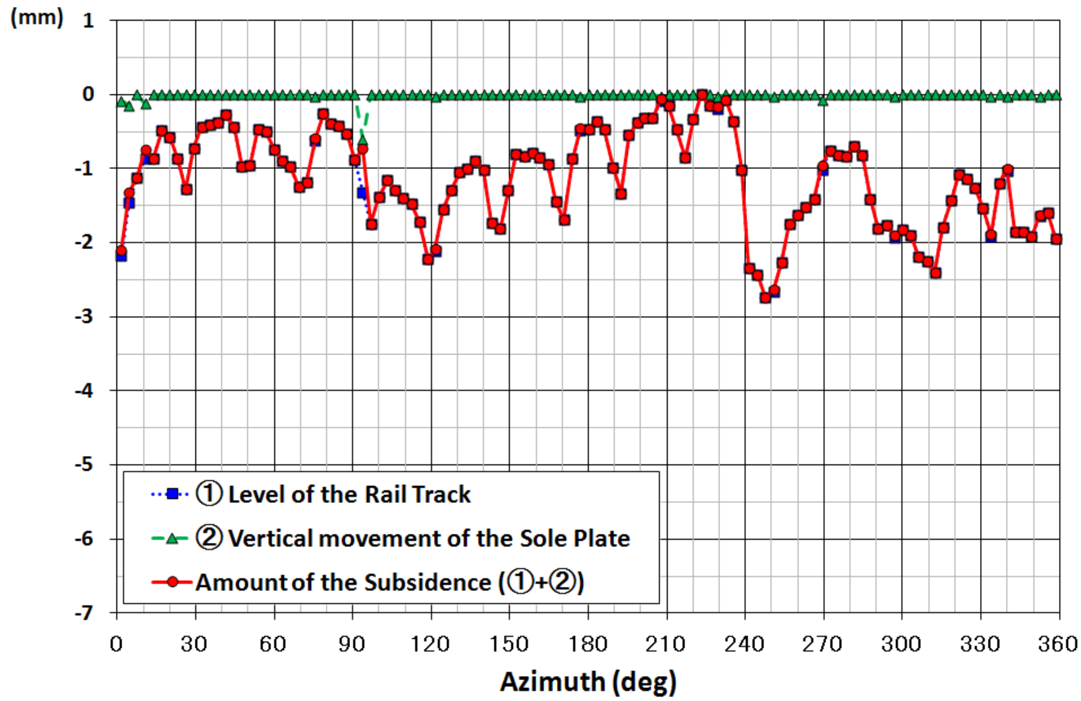

Fig. 7 The results of the investigations after the repair. The blue squares, the green triangles, and the red circles show the level of the rail tracks, and the vertical movements of the sole plates and the estimated subsidence, respectively.

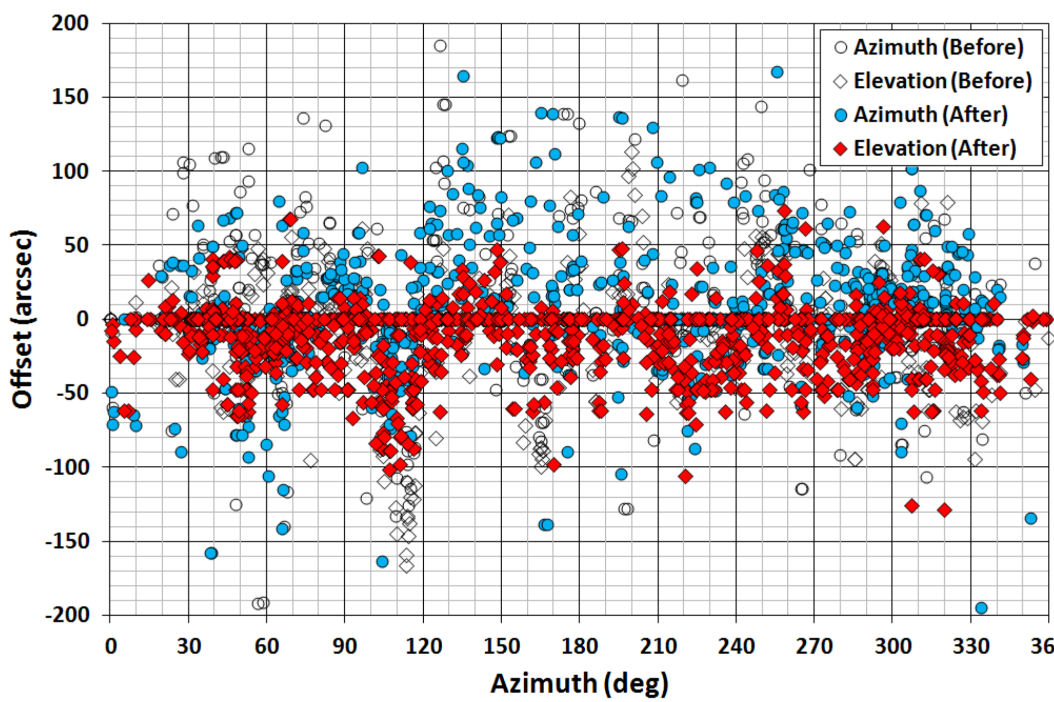

Fig. 8 The azimuth and elevation pointing offsets after the repair plotted as a function of the azimuth direction. The offsets before the repair are also plotted by open circles and rhombuses.

New Geodetic Observatory in Ny-Ålesund

Leif Morten Tangen

Abstract This paper gives a short presentation of what has been done and what will be done to build our new geodetic observatory. We built a part of the road last year, and it will be finished this summer. We have chosen a telescope supplier and are planning how the station area will be. The station will be a core station with DORIS, VLBI, SLR, GNSS, an absolute gravity meter, and a superconducting gravity meter.

Keywords Core station, twin telescope, fiber cable

1 Introduction

Our existing telescope was built in 1993–1994. Our first observation was in October 1994. The lifetime for the telescope is 20 years, and we have the 20-year celebration this year. So, we need a new telescope to continue with VLBI observations. Ny-Ålesund is on the top of the world at 79 degrees north. We are the northernmost observatory in the world. Our position is unique, and we decided to build a core station after the VGOS recommendation with a twin telescope.

2 Budget

Basis cost: 253M NOK (ca. 32M Euro)
Expected cost: 293M NOK (ca. 36.5M Euro) (P50)
Maximum cost: 329M NOK (ca. 41M Euro) (P85)

Norwegian Mapping Authority

The basis cost is what the project manager can use. If something goes wrong, the project owner has a limit in the expected cost. The department has the maximum cost. All this money is allocated in the national budget, and we will not need to send a new application for more money if we stay inside these limits.

3 Time Schedule

The project will be finished in 2018, and then a three-year parallel run with the old telescope will start. When the parallel run is finished, the old telescope will be removed in 2021. April 2016 is a very important time. The new telescopes will arrive, and all construction work for fundaments and other buildings must be finished by then. All VLBI equipment will also be at the station in spring 2016.

4 Environment

The Norwegian government has decided that Svalbard will be the best protected wilderness in the world. Because of this, we must be very careful with everything we do. We shall monitor bird life before, during, and after the construction work. In total, the Governor has given 24 items that we shall follow.

Fig. 1 New bridge.

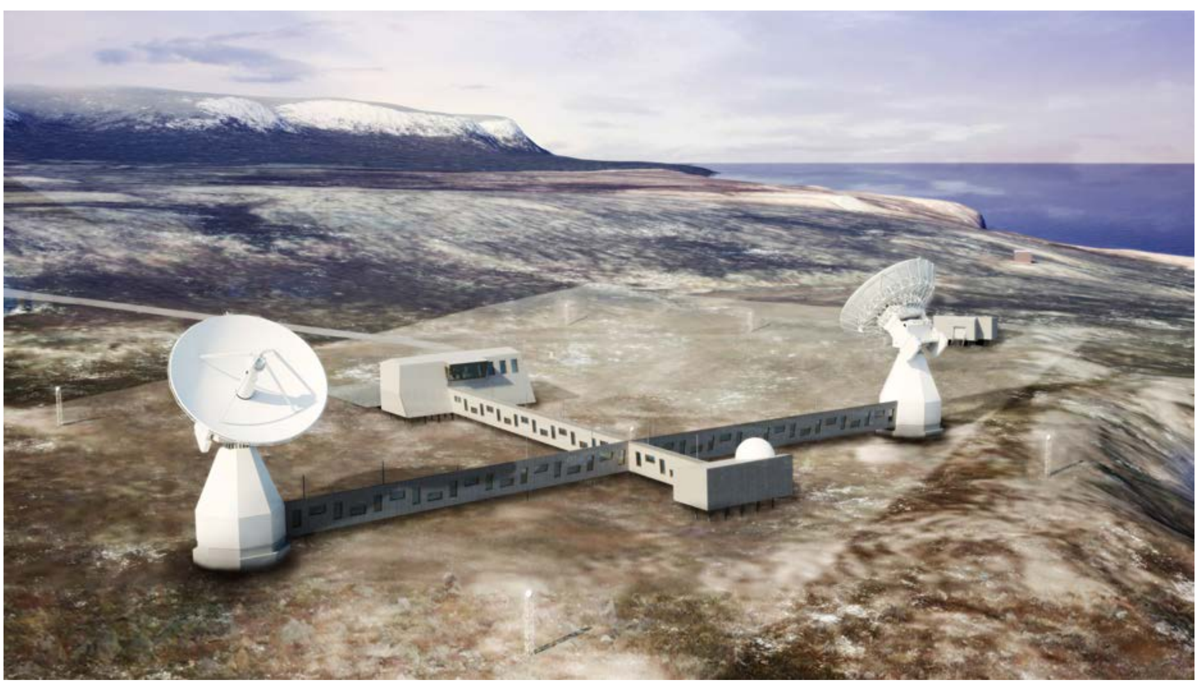

Fig. 2 New site.

5 Work

In summer 2013, half of the road was built, approx. 800 m. It consists of one bridge and a culvert. Power cable and communication lines have also been laid beside the road. In summer 2014, the rest will be done, and construction work at the new site can start in October. To find the best position for all geodetic fundaments, test drilling has been done. It is 4 m down to the bedrock, where the twin telescope fundaments will stay.

6 Telescope Supplier

On February 4, the Norwegian Mapping Authority signed a contract with MT Mechatronics. Our telescopes are of the same type as RAEGE.

7 Fiber Optical Cable

Preparing for fiber cable from the sea to the station was done in 2013. The cable will be laid in summer 2014. Then we will be prepared for e-VLBI.

Gravitational Deformation Effects: The Yebes 40-m Telescope Case

Axel Nothnagel[1], Anne Springer[1], Erik Heinz[1], Thomas Artz[1], Pablo de Vicente[2]

Abstract The determination of gravitationally induced deformation effects of the parabolic mirror of a radio telescope on the VLBI group delays is closely related to the concept of illumination functions. In our study, these serve as a weighting function of the individual rays in the coherent integration of phase and amplitude at the focal plane of the feed horn. An introduction to illumination functions precedes the manuscript for a better understanding of the implications.
A ray tracing program has been developed and is further extended at the Institute of Geodesy and Geoinformation of the University of Bonn, Germany. This is used to calculate an effective path length from the individual lengths of the rays for the undeformed and the deformed case considering gravitational deformation effects at different elevation angles. After having looked at the Effelsberg 100-m radio telescope in a previous study, we now investigate possible applications of the deformation model for the Yebes 40-m telescope near Madrid, Spain. A preliminary correction model is developed which can be applied for alignment of the station height results of sessions with and without deliberate sub-reflector shift which were employed for gain optimization.

Keywords Radio telescopes, gravitational deformation, illumination function, YEBES40M

1. Institut für Geodäsie und Geoinformation der Universität Bonn, Germany
2. Yebes Observatory, Instituto Geográfico Nacional, Spain

1 Introduction

In recent years, the effect of gravitational deformation has gathered some attention in a few publications, e.g., [4, 5, 6]. Abbondanza and Sarti (2010) [2] investigated illumination functions as weighting function of the individual rays in the coherent integration of phase and amplitude at the focal plane of the feed horn. This weighting function is an important part of a ray tracing program which has been developed for the 100-m Effelsberg radio telescope [1]. This program is now extended for the 40-m radio telescope of the Yebes Observatory (Instituto Geográfico Nacional, IGN), near Madrid, Spain.

The reason for this endeavor is twofold: first, as for any other radio telescope with a homologous design, the VLBI delay observations gathered with the Yebes 40-m telescope need to be corrected for the deformation effects due to movements of the main reflector. When we talk about movements in this article, we mean the movements which take place when the telescope is tilted with different elevation angles. Second, on November 11, 2011, the operations of the telescope was changed from an automatic, deliberate elevation-dependent readjustment of the sub-reflector for maximizing the gain to a fixed sub-reflector position throughout all geodetic and astrometric VLBI sessions. Necessarily, this leads to a discontinuity in the site position, especially in the vertical component.

The aim of this investigation is to produce a correction model for gravitational deformations, which can be applied to the observations with deliberate shift of the sub-reflector or with the fixed sub-reflector to align the two incompatible time series of the telescope positions. The basis of this model development are the ray tracing program, the illumination function, and the function of the sub-reflector shift. Prior to November 11, 2011, the model function of the latter was

$$\Delta R_d(\varepsilon)[mm] = -1.0 - 24.0 \cdot \sin(\varepsilon). \qquad (1)$$

Today, ΔR_d equals zero, as the sub-reflector is fixed.

2 Illumination Function

The illumination function of a radio telescope is the Fourier transform of the antenna beam pattern of a radio telescope. Assuming that the latter is radially symmetric, the illumination function can, to first order, just be expressed as a two-dimensional function depending on the radial distance of the impact point on the reflector from the vertex or optical axis.

The antenna beam pattern is constructively mostly dependent on the feed horn characteristics. For completeness, it should be mentioned that the telescope itself with, for example, the quadrupod, i.e., the struts holding the sub-reflector, affects the beam pattern as well. The feed horn is in general designed so that the efficiency drops as sharp as possible at the edge of the reflector. For this reason, the drop in level of sensitivity is also called edge taper. The edge taper is the best compromise because feed horns cannot be built with a Dirac function at the edge. Other, equally important reasons for the edge taper are the optimal suppression of sidelobes and the avoidance of signal pick-up from beyond the aperture of the telescope.

Figure 1 shows the basic construction elements of a prime focus antenna with the normalized sensitivity (in logarithmic scale) superimposed at the location of the feed horn, while Figure 2 does the same for a secondary focus telescope. In general, only the part between the optical axis and the edge (taper) is of interest and the situation can be depicted in a two-dimensional plot of the normalized sensitivity w.r.t. the opening angle or linear distance from the optical axis in the form of an illumination function (Figure 3).

The selection of the function itself mainly depends on the available measurements of the beam pattern, i.e., the gain w.r.t. the opening angle. Mostly only one value, the edge taper, is known and the selection of the best function is rather subjective. Abbondanza et al. [2] favor exponential or binomial functions, while Artz et al. [1] have shown that cosine-squared functions may be preferable. The most reliable answer to that question can, of course, only be given if the beam pattern has been measured in detail.

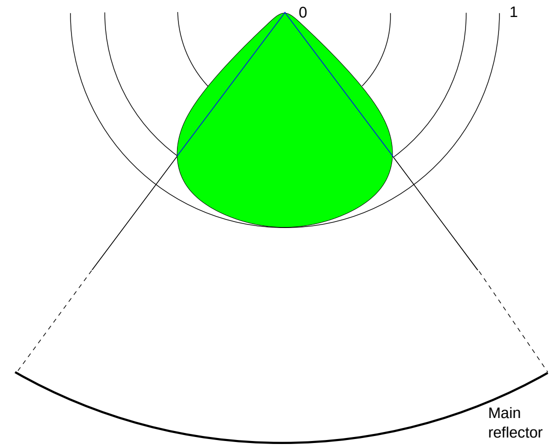

Fig. 1 Prime focus antenna with generic beam pattern. The green/shaded area represents the normalized gain which is "1" towards the vertex of the paraboloid (along the optical axis) and dropping to "0" outside of the reflector area.

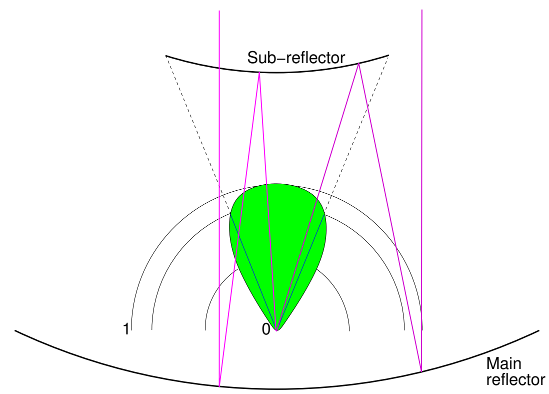

Fig. 2 Secondary focus antenna with generic beam pattern and rays near and away from the optical axis.

3 The Yebes Case

The Yebes 40-m radio telescope of IGN is a secondary focus system with a hyperbolic sub-reflector with a long focal length of the sub-reflector and multiple mirrors in front of the stationary feed horn (Nasmyth system). In an undeformed situation, e.g., at 90° eleva-

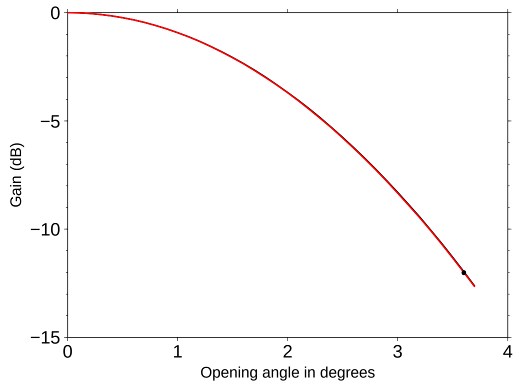

Fig. 3 Gain function of the Yebes 40-m telescope w.r.t. the opening angle of the sub-reflector (γ) for an exponential and a $\cos^2\gamma$ function which cannot be distinguished at this scale.

tion, the telescope geometry is adjusted so that all rays have the same length and are combined in the focal point of the feed horn. To compensate for gravitational deformation effects at other elevation angles, the telescope is built following the homologous deformation concept, i.e., gravitational deformation always leads to a parabolic shape, although with varying focal length, which is the only form parameter of a paraboloid. To compensate for the shift in focal length, an empirical model for movements of the sub-reflector depending on the elevation was determined for optimal gain of the telescope at any elevation angle (Equation 1).

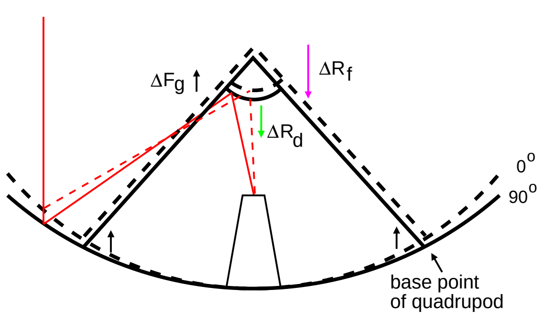

Fig. 4 Form and deformation at 90° and 0° elevation angle with displacement vectors ΔF_g being the focal length change due to gravitation, ΔR_f being the unintended shift of the sub-reflector as a consequence of focal length change through the shift of the base points of the quadrupod and ΔR_d being the deliberate shift coming from empirical gain optimization.

Since no survey of any kind has been carried out at the telescope, only this model for the adjustment of the position of the sub-reflector is known at this point. However, this model does not only comprise the homologous deformation of the paraboloid and the resulting change in focal length. It also includes the unintended gravitational shift of the sub-reflector, which is caused by displacements of the base points of the quadrupod and of the sub-reflector itself through bending of the struts of the quadrupod. So, the deliberate movements of the sub-reflector according to Equation 1 (ΔR_d) compensate for an aggregate of effects which have different impacts on the path lengths of the incoming electro-magnetic rays:

$$\Delta R_d(\varepsilon)[mm] = -(\Delta F_g(\varepsilon) - \Delta R_f(\varepsilon) - \Delta R_g(\varepsilon)), \quad (2)$$

with ΔF_g being the focal length change due to gravitation, ΔR_f being the unintended shift of the sub-reflector as a consequence of focal length change through the shift of the base points of the quadrupod, and ΔR_b being the unintended shift of the sub-reflector due to the remaining gravitational forces.

To deconvolve the three effects, we have to do some reverse engineering. The only solid information which we have right now is how the base points of the quadrupod move as a consequence of the change in focal length. In an iterative process, this shift is computed with the dimensions of the paraboloid and Equation 1, because the same shift applies to the sub-reflector (short black arrows in Figure 4). If we assume that the struts were constructed very rigidly, the remaining gravitational forces on the sub-reflector can be guessed as being negligible.

Computing $\Delta F_g(\varepsilon)$ and $\Delta R_f(\varepsilon)$ from Equation 1 and the dimensions of the telescope, inserting these in the ray tracing program, and applying the illumination function

$$I = -3043.638 + 3043.638 \cdot \cos^2\gamma, \quad (3)$$

with γ being the opening angle w.r.t. the optical axis, permits to compute delay corrections for discrete elevation angles at 10° intervals. A fit to these discrete values yields the continuous correction function

$$\Delta\tau(\varepsilon)[s] = -\frac{1}{c}(51.63 \cdot \sin(\varepsilon) - 0.007 \cdot \cos(\varepsilon) \quad (4)$$
$$-51.63 \cdot \sin^2(\varepsilon) - 50.27 \cdot \cos^2(\varepsilon)).$$

This function has its minimum at 90° elevation (0 mm) and a maximum at 0° elevation with

−50.3 mm. It is surprising that a cosine-squared component has such a serious impact on the fit. An explanation is not possible at this time. We can only speculate that it has to do with the fact that the effect amplifies through the aperture of the telescope which goes by the square.

4 Impact on the VLBI Solutions

Finally, the model according to Equation 5 was applied in a standard VLBI solution to all sessions after November 11, 2011, with the Yebes 40 m coordinates being treated as arc parameters. Then, differences to the results of a reference solution without these corrections were computed and depicted in Figure 5. At first

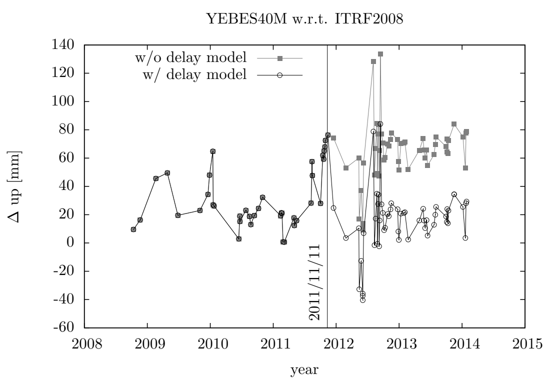

Fig. 5 Relative local height components of the Yebes 40-m telescope with and without delay corrections for deliberate sub-reflector movements.

glance, the obvious jump of approximately 50 mm in the vertical position in the original series after November 11, 2011, definitely disappeared applying the corrections. Most of the corrected data points pretty well match the height level of the 2008 and 2010 results. However, just prior to November 11, 2011, there seem to be a few sessions which might belong to the group of sessions with fixed sub-reflector as well. Likewise, there are sessions in early and late 2009 or in the middle of 2012 which show extra-ordinary height results and need to be checked. This requires some more tedious investigations.

5 Conclusions

The change in operational procedures at the Yebes 40-m telescope on November 11, 2011, with respect to deliberate movements of the sub-reflector have led to a severe discontinuity in the time series of the height results. The correction model developed in this study seems to compensate correctly for the effect which is caused by gravitational deformation of the paraboloid and the counter-acting deliberate shift of the sub-reflector, but the remaining outliers still need to be investigated for a final confirmation.

In view of the computation of any new International Terrestrial Reference Frame, like ITRF2014, further considerations are necessary. For the final coordinates, the VLBI data needs to be re-analyzed with applying the $\Delta R_f(\varepsilon)$, $\Delta F_g(\varepsilon)$, and $\Delta R_d(\varepsilon)$ corrections to the observations prior to November 11, 2011, while for the sessions thereafter, only $\Delta R_f(\varepsilon)$ and $\Delta F_g(\varepsilon)$ have to be applied.

Of course, in this study we neglected the presumably small contribution of the remaining shifts of the sub-reflector due to a possible bending of the quadrupod support struts. This needs to be verified by local surveys like the ones performed at Medicina [5] or Effelsberg [3].

References

1. Artz T, Springer A and Nothnagel A (2014). “A complete VLBI delay model for deforming radio telescopes: The Effelsberg case.” *J Geod*, submitted
2. Abbondanza C and Sarti P (2010). “Effects of illumination functions on the computation of gravity-dependent signal path variation models in primary focus and Cassegrainian VLBI telescopes.” *J Geod*, 84 (8), 515–525, DOI: 10.1007/s00190-010-0389-z
3. Holst C, Zeimetz P, Nothnagel A, Schauerte W, Kuhlmann H (2012) Estimation of Focal Length Variations of a 100 m Radio Telescope’s Main Reflector by Laser Scanner Measurements. *J Surv Eng*, 138 (3), 126–135, DOI: 10.1061/(ASCE)SU.1943-5428.0000082
4. Nothnagel A, Eichborn M, Holst C (2013): Improved focal length results of the Effelsberg 100 m radio telescope. In: Proceedings of the 21st Meeting of the European VLBI Group for Geodesy and Astrometry, N. Zubko and M. Poutanen (eds.), Reports of the Finnish Geodetic Institute, 2013:1, Kirkkonummi, ISBN: 978-951-711-296-3, Finland, 55–59

5. Sarti P, Abbondanza C, Vittuari L (2009b) Gravity-dependent signal path variation in a large VLBI telescope modelled with a combination of surveying methods. *J Geod*, 83 (11), 1115–1126, DOI: 10.1007/s00190-009-0331-4
6. Sarti P, Abbondanza C, Petrov L, Negusini M (2011) Height bias and scale effect induced by antenna gravitational deformations in geodetic VLBI data analysis. *J Geod* 85(1):1–8.

Determination of the Telescope Invariant Point and the Local Tie Vector at Onsala using GPS Measurements

Tong Ning, Rüdiger Haas, Gunnar Elgered

Abstract At Onsala Space Observatory, two gimbal-mounted GPS antennas were installed on each side of the 20-m VLBI radio telescope. The coordinates of the GPS antennas estimated for different VLBI telescope angle readings, at different epochs, were used to calculate the invariant point (IVP) of the telescope. The GPS data, with 1-s sampling rate, were recorded for five semi-kinematic observing campaigns. Two different methods, Precise Point Positioning (PPP) and single difference analysis, were used to estimate the GPS coordinates. The results show that the local tie vector between the Onsala IVS and the IGS reference points can be determined with an accuracy of a few millimeters. The single difference data processing gives a better accuracy ($\sim$1 mm) in determining the axis offset of the telescope.

Keywords GPS, invariant point, local tie vector, axis offset

1 Introduction

In order to measure the local tie vector between a GPS and a VLBI reference point, we need to determine the invariant point (IVP) of the VLBI telescope. The IVP is the intersection of the primary axis with the shortest vector between the primary, rotated by azimuth, and secondary axis, rotated by elevation [1]. For the VLBI telescope at the Onsala Space Observatory (OSO), the primary and secondary axes do not intersect, and the IVP is thus the projection of the secondary axis onto the primary axis. Therefore, the IVP can only be measured by indirect surveying methods [2]. In the years of 2002 and 2008, two classical geodetic measurement campaigns were performed at OSO where the local tie vector was determined with very high accuracy on the sub-mm level for both campaigns. The difference of the estimated local tie between the two campaigns is 0.7 mm [3]. However, the whole working time consumed for the classical measurements was also significant.

Department of Earth and Space Sciences, Chalmers University of Technology, Onsala Space Observatory

Based on a model first presented by [4, 5] proposed a modified model in which the telescope axes can be presented in the same three-dimensional Cartesian system as the observed coordinates. This is well suited to measurements obtained by GPS antennas that are attached to the telescope structure. Following this approach, in the summer of 2013 two gimbal-mounted GPS antennas were installed on each side of the 20-m VLBI radio telescope at OSO. GPS data were acquired, with a sampling rate of 1 s, for five semi-kinematic observing campaigns. The data were analyzed using two different processing methods, Precise Point Positioning (PPP) and single difference analysis. Both the local tie vector between the IGS and the IVS reference points and the axis offset of the telescope were determined.

2 Methodology

We used a model developed for the Metsähovi telescope in order to calculate the IVP of the VLBI telescope from the time series of estimated GPS coordinates [5].

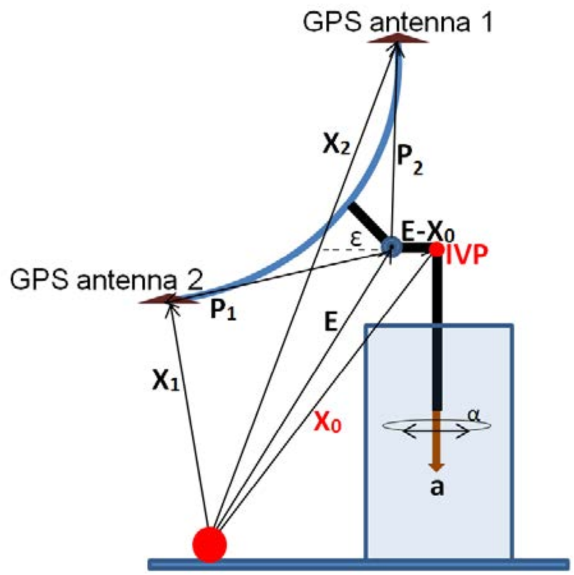

Fig. 1 The schematic diagram of the model parameters in a local reference frame. Note that the actual positions of the GPS antennas are on the sides of the telescope (see Figure 2).

$$X_n = X_0 + R_{\alpha,a}(E - X_0) + R_{\alpha,a} R_{\varepsilon,e} P_n \quad (1)$$

where the coordinate vector of the GPS antenna X_n (n=1, 2) in an arbitrary reference frame is determined by the sum of three vectors (see Figure 1): the coordinate vector of the IVP of the telescope X_0, the horizontal axis offset vector $E - X_0$ rotated by the angle α about the azimuth axis a, and the vector from the eccentric point E to the antenna point P_n (n=1, 2) rotated about the elevation axis e by the angle ε and about the azimuth axis by the angle α.

The input data to Equation 1 are the estimated coordinates of the two GPS antennas, together with the azimuth and the elevation angles of the VLBI telescope for each time epoch.

Since the axes are unit vectors, we have two condition equations for the azimuth axis and the elevation axis.

$$a_x \cdot a_x + a_y \cdot a_y + a_z \cdot a_z = 1 \quad (2)$$

$$e_x \cdot e_x + e_y \cdot e_y + e_z \cdot e_z = 1 \quad (3)$$

Meanwhile the offset vector $E - X_0$ is perpendicular to both the azimuth and elevation axes, so we have two more condition equations:

$$(E - X_0)_x \cdot a_x + (E - X_0)_y \cdot a_y + (E - X_0)_z \cdot a_z = 0 \quad (4)$$

$$(E - X_0)_x \cdot e_x + (E - X_0)_y \cdot e_y + (E - X_0)_z \cdot e_z = 0 \quad (5)$$

All unknown parameters in Equation 1 were estimated as corrections to their approximate values starting from a priori values by solving a least squares mixed model including all condition equations and the main function. The solution is reached by iterations until convergence is found, i.e., the correction of the IVP coordinates to the previous estimates are less than 0.1 mm.

3 GPS Observations and Data Processing

We first mounted two Leica AS10 multi-GNSS antennas on both sides of the telescope dish using two rotating holders. Both holders have counterweights in order to make the two antennas point to the zenith regardless of the position of the VLBI telescope (see Figure 2). Then we conducted five observing sessions in which the movement of the VLBI telescope was scheduled for different azimuth and elevation angles. The duration of each session was 24 hours. For the first two sessions (July 9 and 10, 2013), the telescope was positioned at elevation angles 10°, 15°, 20°, 25°, 30°, 35°, 40°, 45°, 55°, 65°, 75°, and 85°. For each elevation angle, the telescope was positioned at four different azimuth angles with an interval of 90°. In total, we had 48 telescope positions. After every 30 minutes, the telescope moved to a new position. For the later three sessions (September 21–23, 2013), the telescope moved through the same elevation angles as for the first two sessions, but with four more azimuth angles for each elevation angle with an interval of 45°, which gave us a total of 96 telescope positions.

The sampling rate of GPS measurements was 1 Hz. We first processed the GPS data using GIPSY/OASIS II v.6.2 where the Precise Point Positioning (PPP) strategy was implemented for a kinematic solution. The GPS orbit and clock products were provided from a reprocessing of existing archives. In a kinematic solution, it is difficult to estimate tropospheric delay with a high accuracy. Considering the short distance (∼78 m) between the IGS station (ONSA) and the VLBI telescope, the Zenith Wet Delay (ZWD) and its horizontal gradients estimated from ONSA should be approximately the same as the ones estimated from the two GPS antennas on the telescope. Therefore, we first estimated ZWD and gradients from the data obtained at

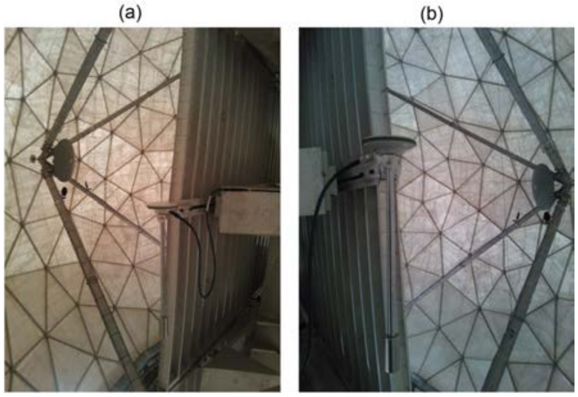

Fig. 2 The installation of the GPS antennas on (a) the left side and (b) the right side of the 20-m radio telescope.

ONSA using a static solution. Thereafter, the ONSA-estimated ZWD and gradients were input to the data processing for the two GPS antennas, while the hydrostatic delay was modeled with a scale height parameter given by the nominal position without adjustments.

Besides PPP, we also processed differenced GPS data considering that the two GPS antennas on the telescope and the IGS station ONSA have a common ionospheric delay and the common delay of the neutral atmosphere. We took advantage of this feature in our data processing by forming two baselines (GPS1–ONSA and GPS2–ONSA) in order to avoid the estimation of those common parameters. As a start, we used single differenced observations from only the L1 frequency in order to achieve a low level of noise where the baseline coordinates were solved after the ambiguities were fixed as floats.

For both processing methods, PPP and single difference analysis, the absolute calibration of the Phase Center Variations (PCV) of the GPS antennas is necessary. However, it is complicated to implement in our case, because the orientation of the GPS antenna on the radio telescope varies while the telescope is rotating. The true azimuth angle of the satellite seen from the GPS antenna changes with the VLBI telescope azimuth. If we would apply the standard absolute PCV calibration directly, it would cause systematic errors in the estimated GPS coordinates and the resulting IVP. In order to solve this problem, we calculated the orientation of the two GPS antennas based on the position of the telescope for each epoch. Then the true azimuth angle seen in the direction of the GPS satellite was calculated, and the corresponding PCV correction reading from the standard IGS table was applied in the RINEX files. Eventually, the corrected RINEX files were used in the GPS data processing.

Finally, the estimated GPS coordinates and the telescope angle reading (azimuth and elevation) for each epoch were input to the linearized least squares mixed model with condition equations (see Equations 1 to 5). After the first two iterations, residuals larger than 50 cm were removed, and after another two iterations, the threshold value was set to 25 cm. Then, after two more iterations, the data points with residuals larger than three times the standard deviation were removed. Thereafter, we let the model run for another two iterations in order to reach convergence. On average, about 50% of the input data points were removed as outliers.

4 Results

Figure 3 depicts the estimated baseline between the two GPS antennas mounted on the VLBI telescope for two different sessions in which the telescope moved to 48 positions (July 9) and to 96 positions (September 23), respectively. The mean value and standard deviation given by PPP are 20.7778 m and 2.7460 m, and 20.7590 m and 2.8292 m for the two sessions, respectively. The corresponding values for the single difference data processing are 20.7465 m and 0.0384 m, and 20.7450 m and 0.0496 m. It is clear that the baseline estimated by single difference analysis has a much smaller variability. Figure 3 also gives the number of satellites, with an elevation cutoff of 15°, included in the data processing for each epoch. It indicates that the variations for both methods are correlated to the number of observed satellites.

The estimated local tie vector between the IGS and the IVS reference points together with the estimated axis offset of the VLBI telescope are shown in Figure 4. For comparison, we also calculated the local tie vector in ITRF2008 coordinates referring to the epoch of July 1, 2013, while for the axis offset we used values given by two local surveys as references [3]. The results for the estimated east and north components of the local tie vector show no significant differences between the two processing methods in terms of the mean value and the standard deviation over five sessions. For the vertical component, the single difference data processing gives

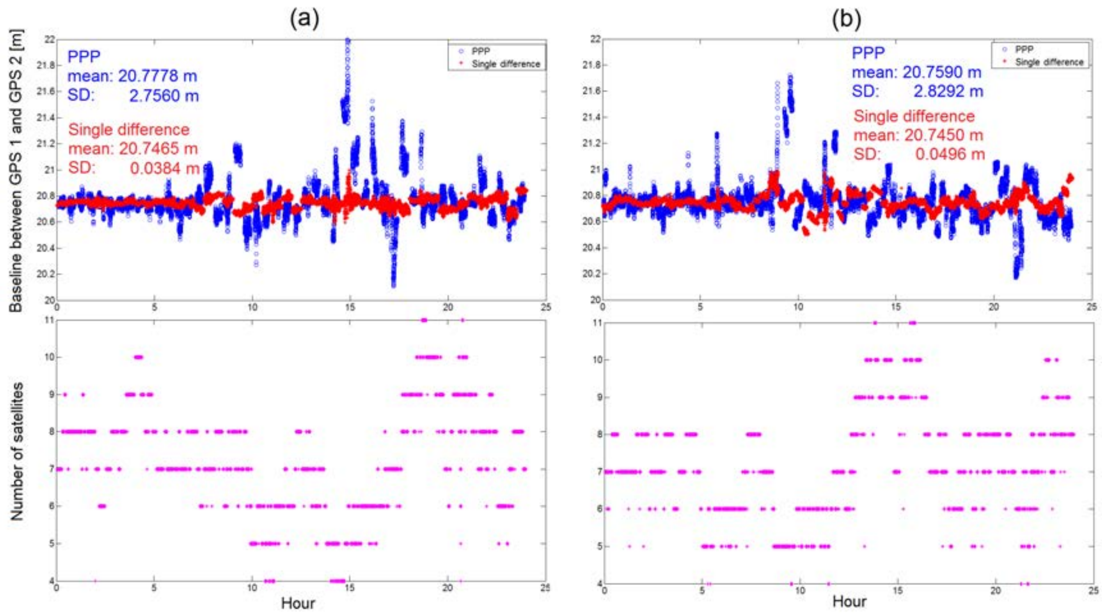

Fig. 3 The baseline between the two GPS antennas on the sides of the telescope, estimated from both PPP (blue circles) and single difference analysis (red stars), for two sessions in which (a) the telescope moved for 48 positions and (b) the telescope moved for 96 positions.

a smaller standard deviation (0.0027 m) than the one derived by PPP (0.0079 m). The differences between our estimated and the ITRF local tie vector are within 0.007 m. The comparison of the axis offset (see Figure 4d) shows a much better result for the single difference data processing, which gives a mean axis offset of −0.005 m with a standard deviation of 0.0021 m over five sessions. A difference of about 0.001 m is seen with respect to the two local surveys (−0.0060 m for 2002 and −0.0062 m for 2008). The result from the PPP data processing shows a significant difference, the mean axis offset of −0.0224 m with a standard deviation of 0.0077 m, from the reference values.

5 Conclusions and Future Work

We carried out five semi-kinematic observing sessions in which the coordinates estimated for two GPS antennas mounted on the rim of the main reflector of the Onsala 20-m radio telescope for different telescope angle readings, at different epochs, were used to calculate the local tie vector between the Onsala IGS and the IVS reference points. Two different methods, PPP and single difference analysis, were used for the GPS data processing. The result shows no significant differences in the estimated local tie vector using the two different processing methods, while the mean difference between the estimated local tie vector and the ITRF calculated local tie vector is within 0.007 m. We also estimated the axis offset of the VLBI telescope, where the single difference data processing gives a better result with a difference of 0.001 m from the reference axis offset given by two local surveys, while the difference seen from the PPP result is at the centimeter level.

As shown in Figure 3, larger variations in the estimated baseline, seen for both processing methods, are correlated with the number of satellites. For future work, in order to increase the number of observables, measurements from other GNSS, e.g., GLONASS, will be included.

Due to the blockage by the telescope, a significant number of cycle slips occurred in the GPS phase measurements, and this introduces more ambiguity parameters. Therefore, a higher sampling rate of GPS measurements, e.g., 10 Hz or 20 Hz, would be good in order to have more data available for the ambiguity estimation.

The final goal of the work is to use only GPS measurements obtained during standard geodetic VLBI sessions, in which no extra telescope time will be re-

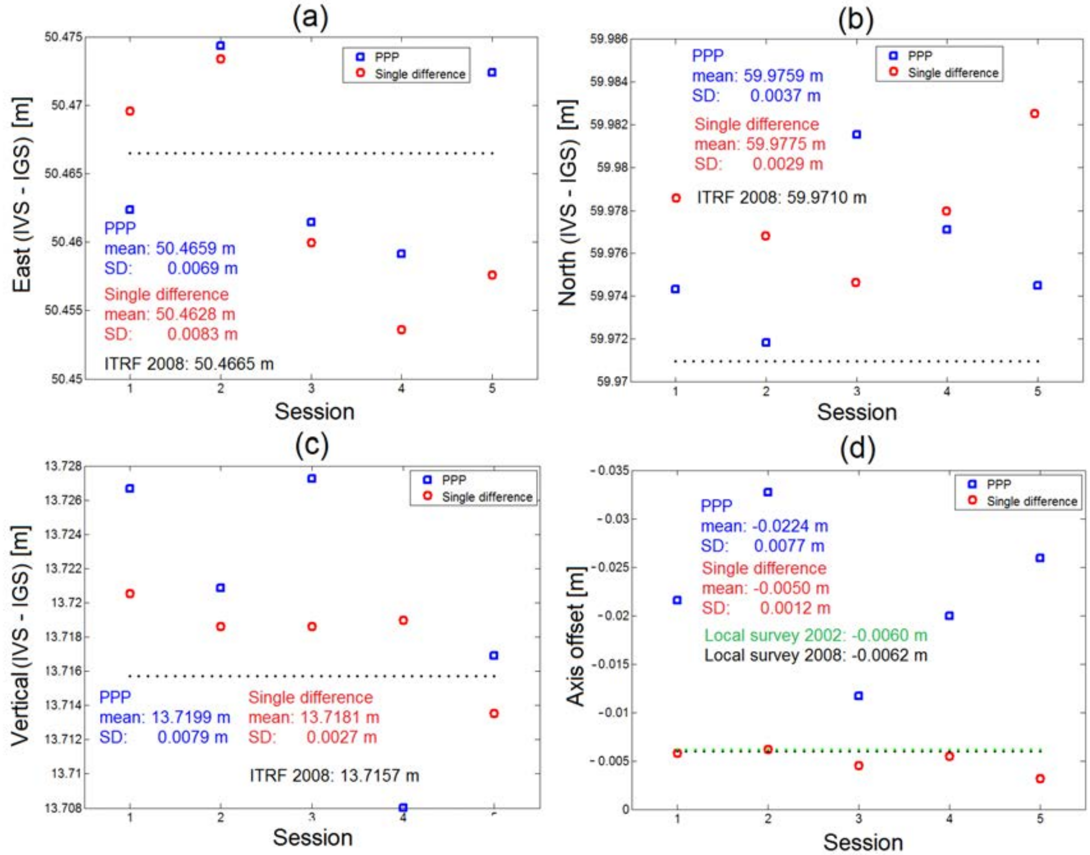

Fig. 4 The estimated local tie vector between the IGS and IVS reference points shown for (a) East, (b) North, (c) Vertical components, and (d) the axis offset of the telescope, given by both PPP (blue squares) and single difference data analysis (red circles). The calculated ITRF local tie vectors are given by black dotted lines, while the axis offsets obtained from two local surveys are given by black and green dotted lines.

quired. In that case, the GPS antenna will only be static for very short observational time spans, in which the ambiguities, when estimated as floats, become poorly separable from the baseline coordinates. This will result in a poor accuracy of the estimated GPS coordinates. In order to solve this problem, a double difference data processing with ambiguity fixing to integer values will be used.

References

1. J. Dawson, P. Sarti, G.M. Johnston, and L. Vittuari. Indirect approach to invariant point determination for SLR and VLBI systems: an assessment, *J. Geod.*, 81(6–8), doi:10.1007/s00190-006-0125-x, 433–441, 2007.
2. C. Eschelbach and R. Haas. The 2002 Local Tie Survey at the Onsala Space Observatory, In: Proc. IERS Workshop on site co-location, edited by B. Richter, W. Schwegmann, and W.R. Dick, IERS Technical Note, 33, Verlag des Bundesamts für Kartographie und Geodäsie, 55–63, 2005.
3. M. Lösler. New mathematical model for reference point determination of an azimuth-elevation type radio telescope. *J. Surv. Eng.*, 135(4): 131–135, 2009.
4. M. Lösler and R. Haas. The 2008 Local-tie Survey at the Onsala Space Observatory, In Charlot P., A. Collioud, and G. Bourda, (Ed.) Proceedings of the 19th European VLBI for Geodesy and Astrometry Working Meeting, March 24–25, 2009, Bordeaux, France, p. 97–101, 2009.
5. U. Kallio and M. Poutanen. Simulation of Local Tie Accuracy on VLBI Antennas, In IVS 2010 General Meeting Proceedings, (Eds. Dirk Behrend and Karen Baver), NASA/CP-2010-215864, p. 360–364, 2010.
6. G. Blewitt. Carrier phase ambiguity resolution for the Global Positioning System applied to geodetic baselines up to 2000 km, *J. Geophys. Res.*, 9j, (B8), 10,187–10,203, 1989.

Local Survey at the Shanghai Tianma 65-m Antenna

Jinling Li[1], Fuwen Xiong[2]

Abstract A local survey was implemented at the newly constructed Shanghai Tianma 65-m radio telescope in June and July of 2013. The survey implementation and data analysis are described in this report. The outcome provides an important reference for the subsequent activities of antenna maintenance and scientific applications. It is also important archive data for monitoring possible subsidence and lateral displacement of the antenna foundation as well as deformation of the antenna tracking-rail and structure.

Keywords VLBI, radio telescope, reference point, axis offset, local survey

1 Introduction

In October of 2012, the Shanghai Tianma 65-m radio antenna was equipped with S/X-band reception facilities and initially applied to deep space tracking of Chang'E-2, a lunar satellite of China, during its extended exploration mission to fly by the asteroid 4179 Toutatis. The L, C, K, and Ka-band reception devices were equipped and tested successively. The antenna also tracked the Chang'E-3 lunar satellite at the end of 2013. Based on the need for the establishment of a precise antenna orientation model, antenna orientation guidance, the extraction of VLBI observations, scientific applications, and analysis studies of the observations, a local survey to this telescope was conducted in June and July of 2013. This report describes the LCN (Local Control Network) layout, survey implementation, data analysis, and final results.

1. Shanghai Astronomical Observatory
2. Shanghai Institute of Geological Survey

2 Local Control Network, Observation Instrument, and Survey Implementation

Figure 1 shows a satellite map of the yard of the 65-m antenna. Figure 2 shows the horizontal projection of the LCN. A1 to A4 are the control pillars with forced-centering devices on top. G5 indicates a permanent GPS antenna, which is used for the delay correction of the transmission medium in the lunar exploration project of China. 65m indicates the horizontal projection of the vertical axis of the 65-m antenna, and the circle around it represents the antenna dish.

Fig. 1 Satellite map of the Shanghai Tianma 65-m antenna yard.

Pillar A1 is on the northwest corner of the control building and near to the western fencing wall. Pillar A2 is at the northwest corner of the fencing wall and is very near to the 65-m antenna. If targets connected

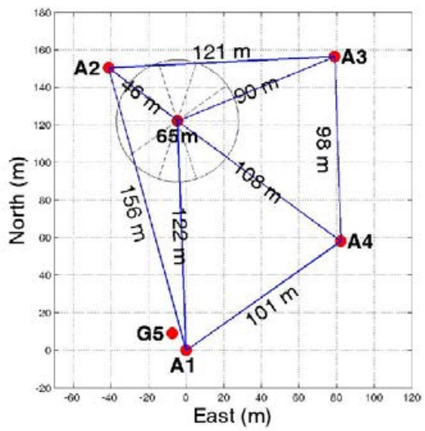

Fig. 2 Horizontal projection of the Local Control Network.

to the antenna are observed from this point, the elevation angle will be very high, and the visible dynamic range will be very limited. So A2 is inconvenient for instrument operation. But it can be a reference direction when observing targets on the antenna from other control pillars. Pillar A3 is on the right side of the entrance of the yard (near to the northeast corner of the yard). A4 is located near the turning corner of the southern fencing wall. Due to blocking by the antenna base pillars, A2 and A4 are not directly visible to each other, but every other pair of pillars is mutually visible.

The main optical instruments in the survey were the Leica Total Station TM30 and TS30, with an observation uncertainty in direction of 0.5 as (arc second) and in range of 0.6 mm + 1 ppm. The GPS receivers were dual-band geodetic type ASHTECH UZ-12 and Trimble 5700. Other auxiliary devices were cooperation targets, data transfer cable, batteries, calipers, and so on.

On 23 June 2013, an optical survey of the LCN was conducted. GPS observations of the LCN were carried out from 23 June to 7 July 2013. On 7 July, surveys to the vertical axis were also done at azimuths 30, 60, 90, and 120°. On 8 July, surveys to the vertical axis were continued at azimuths 150, 180, 240, 270, 300, 330, and 0°. On 9 July, surveys to the horizontal axis were done at an azimuth of 150° and elevations of 7, 10, 20, 30, 40, 50, 60, 70, 80, and 88°. On 13 July, surveys were also done to the horizontal axis at azimuths 120 and 188°. For the 120° azimuth, the elevations were sequentially 15, 30, 40, 50, 60, 70, 80, and 88°. For the 188° azimuth the elevations were 8, 18, 28, 38, 48, 58, 68, 78, and 88°.

3 Data Reduction

Data reduction includes the reduction of LCN observations and the reduction of spatial intersection survey observations of targets. The reduction of LCN observations is firstly to determine the relative local coordinates of pillars from optical observations, secondly to determine the geocentric 3D coordinates of pillars from GPS measurements of the LCN, and thirdly to determine the coordinate transformation relationship from the local to the geocentric 3D coordinates. In the data reduction of the spatial intersection survey of targets, there are multiple steps, including those to determine the local coordinates of targets at various antenna orientations, the local coordinates of the centers of the circular loci of targets, the location and orientation of the vertical and horizontal axes in the LCN, the plane holding the horizontal axis, the coordinates of the intersection point of this plane with the vertical axis, and the length of axis offset. Finally the local coordinates of the reference point are transformed into geocentric 3D coordinates.

3.1 The LCN Observations

Optical measurement of the LCN involved setting up the optical instrument on the pillars on A1 and A4 in turn and performing a spatial survey to all the other pillars in the LCN. The observations are the horizontal and vertical directions and the radial distance. In the data reduction, pillar A1 is taken as the origin of the local coordinate frame, the horizontal direction from A1 to A2 as the x-axis, the zenith direction of A1 as the z-axis, and xyz as constituting a right-handed frame. Table 1 shows the local coordinates of pillars resulting from weighted least squares adjustment of the optical observations, in which σ_x etc. denote the formal errors of coordinate components and "/" indicates parameters that were not adjusted. The weighted mean post-fit residuals of the horizontal and vertical directions and the radial distance are respectively -0.7 as, -1.9 as, and -0.01 mm.

Although G5 in Figure 2 is a permanent GPS station, due to some equipment failure, only some of the observations were available during the GPS survey of the LCN, and the precise coordinates of this point are still unavailable. Therefore in the GPS data anal-

Table 1 Adjustment results of the LCN optical observations.

Pillar	x/m	y/m	z/m	σ_x/mm	σ_y/mm	σ_z/mm
A1	0.0000	0.0000	0.0000	/	/	/
A2	155.9572	0.0000	−0.0066	0.02	/	0.07
A3	129.8441	−117.6418	0.0044	0.02	0.02	0.07
A4	34.2157	−94.7139	0.0004	0.03	0.02	0.07

ysis, SHAO, an IGS permanent station in the yard of the Shanghai Sheshan 25-m antenna which is about 6 km from the 65-m antenna, is taken as the reference station. The GPS data analysis software GAMIT was adopted, and through spatial adjustment of the baseline length solution, the geocentric 3D coordinates of the LCN pillars in the frame of ITRF2008 were obtained as shown in Table 2, in which σ_X etc. denote the formal errors of coordinate components. The middle epoch of the GPS survey of the LCN was UTC 0h 29 June 2013, when (−2831733.7669, 4675665.8529, 3275369.3294) m was adopted as the geocentric 3D coordinates of SHAO in ITRF2008.

Table 2 Adjustment results of the LCN GPS survey data.

Pillar	X/m σ_X/mm	Y/m σ_Y/mm	Z/m σ_Z/mm
A1	−2826729.534	4679262.767	3274544.855
	0.4	0.4	0.4
A2	−2826653.989	4679217.667	3274673.627
	0.4	0.4	0.4
A3	−2826755.409	4679152.789	3274678.772
	0.4	0.4	0.4
A4	−2826784.426	4679194.559	3274594.605
	0.4	0.4	0.4

By comparison of the LCN local and geocentric 3D coordinates as shown in Table 1 and 2, it is clear that there are large translations (on the magnitude of the Earth radius) and relative rotations between them. During the data analysis of the local survey of Shanghai Sheshan 25-m antenna in July 2008, theoretical analysis and numerical tests showed that, for the different dimensions and different magnitudes of the seven parameters in the transformation of two sets of 3D Cartesian coordinates, to adjust the parameters by multiplying different factors and so to let the resulting formal errors be basically close to each other, the condition of the normal equation could be effectively improved when the parameters are small in magnitude, and the solution stability of the parameters could be improved when the parameters are large in magnitude. In the case of large rotations, via simple and effective iterative solution mode, programming could be facilitated, and the solution would be characterized by fast convergence and by a wide dynamic range of initial parameters. Finally, in the case of large translations, applying a coordinate transformation to partly deduct the translation beforehand would benefit the stable and precise solution of the parameters. Here, all of the above strategies are directly adopted to get the transformation relationship from the LCN local coordinates *xyz* to the geocentric 3D coordinates XYZ. Specifically, the data in Table 2 are transformed from geocentric 3D coordinates into topocentric coordinates at pillar A1, and the coordinate origin is translated from the geocenter to pillar A1, i.e., to deduct the geocentric distance U_0 of pillar A1 from the transformed dataset. The transformation relationship from *xyz* to XYZ is expressed as:

$$\mathbf{X} = \mathbf{R}_{TOP}\left[\mathbf{T} + (1+D)\mathbf{R}_x(R_1)\mathbf{R}_y(R_2)\mathbf{R}_z(R_3)\mathbf{x} + \mathbf{U_0}\right] \tag{1}$$

where $\mathbf{X} = [X,Y,Z]^T$, $\mathbf{x} = [x,y,z]^T$, $\mathbf{U_0} = [0,0,U_0]^T$, and $\mathbf{T} = [T_1,T_2,T_3]^T$ are the 3D translation parameters. Superscript T indicates the transpose matrix. D is the scale factor. $\mathbf{R}_x(R_1)$ is the rotational matrix around the first coordinate axis by a counterclockwise rotation R_1, and $\mathbf{R}_y(R_2)$ and $\mathbf{R}_z(R_3)$ are analogous. $\mathbf{R}_{TOP}$ is the transformation matrix from the topocentric coordinate frame (TF) at pillar A1 to the geocentric 3D coordinates, which is related to the specific definition of the TF orientation.

The upper ends of the four pillars in the LCN are almost co-planar, which leads to exceptional solutions to the parameters in *Equation (1)* as mathematically right but physically wrong. By application of a simple identification criterion to solutions, the transformation parameters from the LCN local frame to geocentric 3D coordinates are finally determined as follows:

$$\begin{gathered}\mathbf{T} = [-0.53, 2.48, 0.77]^T \pm [0.30, 0.30, 0.36]^T \text{ mm},\\ D = (0.5 \pm 2.4)\times 10^{-6},\\ \begin{bmatrix} R_1 \\ R_2 \\ R_3 \end{bmatrix} = \begin{bmatrix} 0.0000100 \\ -0.0029992 \\ -0.2682713 \end{bmatrix} \pm \begin{bmatrix} 0.0000038 \\ 0.0000031 \\ 0.0000024 \end{bmatrix} \text{rad},\\ U_0 = 6372483.33920 \text{ m},\\ \mathbf{R}_{TOP} = \\ \begin{bmatrix} 0.2657010819 & 0.8559418582 & -0.4435836680 \\ -0.4398316729 & 0.5170720796 & 0.7342918793 \\ 0.8578758853 & 0.0000000000 & 0.5138569504 \end{bmatrix}.\end{gathered} \tag{2}$$

Table 3 shows that the post-fit residual is less than 3 mm in magnitude for all coordinate components, which is in accordance with the expectations of the survey.

Table 3 Post-fit residuals from local to geocentric 3D coordinates.

Pillar	X/m	Y/m	Z/m
	σ_X/mm	σ_Y/mm	σ_Z/mm
A1	0.0005	−0.0025	−0.0008
A2	0.0016	0.0009	0.0005
A3	−0.0003	0.0002	−0.0010
A4	−0.0019	0.0014	0.0012

3.2 Target Intersection Survey

Taking the local coordinates of A1 through A4 as known in order to determine the directions and radial distance of a target connected onto the 65-m antenna, an intersection survey is used to determine the local coordinates of the target. Taking the survey of the vertical axis as an example, the elevation of the antenna is kept unchanged while the azimuth is changed by steps, and an intersection survey of the target is performed at every azimuth. Multiple position determinations of a target describe a circle in space, centered at a point on the vertical axis. With an intersection survey of multiple targets, the position and orientation of the vertical axis can be determined relative to the LCN. The survey of the horizontal axis can be done similarly. The plane holding the horizontal axis could be determined in the LCN by surveying the horizontal axis at more than one azimuth, and by combination with the survey of the vertical axis, the local coordinates of the reference point can be determined.

Intersection surveys of four targets at 11 antenna azimuths were performed on 7 and 8 July 2013 (denoted as v_130707). Surveys of the horizontal axis at azimuths 120, 150, and 188° were performed on 9 and 13 July, denoted respectively as h_130713_120, h_130709_150, and h_130713_188. The local coordinates of the targets were obtained through weighted least squares adjustment of the observations, and the weighted mean of the post-fit residuals are given in Table 4. It is shown that the residuals for the horizontal and vertical direction (H.r. and V.r.) are less than 0.5 as in magnitude. The corresponding positioning uncertainty for targets within 0.2 km (the LCN's geometric scale) would be less than 0.5 mm. The radial distance residual (R.r.) is less than 0.1 mm in magnitude.

Table 4 Weighted mean of the post-fit residuals in the data reduction of the intersection survey of targets.

Session	H.r./as	V.r./as	R.r./mm	Orient.	Azimuth
V_130707	0.40	0.18	−0.05	11	
h_130713_120	0.28	−0.15	0.00	8	120°
h_130709_150	−0.30	−0.02	−0.04	10	150°
h_130713_188	−0.19	0.27	−0.05	9	188°

The usual method of spatial circle fitting is to project the spatial sample points onto the coordinate plane. Data simulations and tests show that the sample points should be as dense as possible and should uniformly cover the spatial circle. Otherwise, a very low noise level would lead to divergence of parameter solutions. In the local survey of the radio antenna, especially in the survey of the horizontal axis, due to the limitations in the structure design and physical dimensions of the working site, the sample points could only cover at most one fourth of a spatial circle. Therefore, the usual method of projecting onto the coordinate plane would not be applicable. In order to get the coordinates of the locus center of a target in the antenna survey, the method that firstly gets the normal direction of the plane holding the spatial circular arc and secondly gets the coordinates of the locus center is adopted in order to suppress the detrimental effects of observation noise and uneven spatial coverage of sample points, and to improve the stability and precision of parameter solutions. Specifically, for some given 3D vectors $\mathbf{r}_1$, $\mathbf{r}_2$, and $\mathbf{r}_3$, suppose all begin at the coordinate origin and end at a spatial circle. Then the unit vectors of the vector products $(\mathbf{r}_2-\mathbf{r}_1)\times(\mathbf{r}_3-\mathbf{r}_1)$ and $(\mathbf{r}_3-\mathbf{r}_2)\times(\mathbf{r}_1-\mathbf{r}_3)$ should be in the direction of the normal vector of the plane holding the circle. In real data analysis due to the observation errors the weighted mean is taken as the normal direction of the plane. Take all the locus points of each target in the survey as vector ends, and then the plane normal direction is deduced. Via coordinate transformation, two-dimensional (2D) circle fitting and the corresponding inverse coordinate transformation, the local coordinates of locus centers (x_c, y_c, z_c) and formal errors $\sigma_{(x_c,y_c,z_c)}$ as well as the plane normal direction vector $\mathbf{n}(n_x, n_y, n_z)$ are deduced.

The post-fit residuals of the spatial circle fit are important indicators of the completeness and quality of the antenna survey. Results show that the distance of the target position to the plane holding the spatial circle and the distance to the fitted circle in the plane are less than 1 mm in magnitude, indicating that the implementation of the survey and the data analysis are reliable.

In order to determine the position and orientation of the spatial line (the vertical or horizontal axis), it is again the intuitive way to project the points onto the coordinate plane and then to perform a 2D line fit. But data simulation and tests show that the parameter solution is not stable and is low in precision in the case of the local survey. Therefore the coordinate transformation method is applied again. That is, taking the average of the normal direction as the temporary z-axis, after the coordinate transformation the resulting ideal coordinates x, y of points should be zero. Taking into account the observation noise, the weighted average is adopted. After the inverse coordinate transformation the coordinates of the ends of the measured segment on the vertical and horizontal axes are deduced. It is then easy to get the coordinates of the foot of the common perpendicular on the vertical axis and the axis offset.

Take the reference point as the intersection of the vertical axis and the plane holding the horizontal axis. The solution procedure of parameters is designed as the following steps.

a Three times, measure vector segments in a survey of the horizontal axis. The vector product of every pair of vectors will be in the direction of the normal of the plane holding the horizontal axis. After normalization, the normal direction is taken as the weighted mean of the three vector products.
b Take the normal direction as the temporary z-axis. After a coordinate transformation, the weighted mean of the resulting z-coordinate component of the end points of the measured segments on the horizontal axis is taken as the z-coordinate of the reference point, denoted as z_w.
c In the temporary coordinate frame, on the vertical axis, the x- and y-components corresponding to z_w are the planar coordinates of the reference point, denoted as x_w and y_w.
d By applying the inverse coordinate transformation to (x_w, y_w, z_w), then the local coordinates of the reference point are determined.

The solutions of the local coordinates of the reference point are as follows:

$$\begin{bmatrix} x \\ y \\ z \end{bmatrix} = \begin{bmatrix} 118.8666 \\ -27.8894 \\ 35.2401 \end{bmatrix} \mathrm{m} \pm \begin{bmatrix} 0.03 \\ 0.03 \\ 0.00 \end{bmatrix} \mathrm{mm} \tag{3}$$

By using Equations (1) and (2) the geocentric 3D coordinates of the reference point in ITRF2008 are:

$$\begin{bmatrix} X \\ Y \\ Z \end{bmatrix} = \begin{bmatrix} -2826708.6045 \\ 4679237.0542 \\ 3274667.5314 \end{bmatrix} \mathrm{m} \pm \begin{bmatrix} 0.42 \\ 0.45 \\ 0.43 \end{bmatrix} \mathrm{mm} \tag{4}$$

The reference epoch is the middle epoch of the GPS observations in this survey, UTC 0h 29 June 2013.

The weighted average of the axis offset determined by the length of the common perpendicular of the vertical and horizontal axes at azimuths 120, 150, and 188°, $\bar{f}$, is as follows:

$$\bar{f} = 2.95\ \mathrm{mm} \pm 3.26\ \mathrm{mm} \tag{5}$$

It is shown that at the precision level of 3 mm, the axis offset is not significant, indicating that the framework rigidity of the antenna reaches a very high level.

4 Discussion

This survey lasted only about 20 days, and so the determination precision is limited. However, the precision is absolutely adequate for the establishment of an antenna orientation model and the guidance of antenna orientation, and the survey can act as a historical data archive to study factors affecting the stability of the antenna reference point.

Acknowledgements

This work is supported by NSFC (No. 11178024, 10973030, U1331205), Chinese lunar exploration project CE-1, National 863 project of China (2012AA121603), STC of Shanghai Municipality (06DZ22101).

Co-location of Space Geodetic Techniques at the “Quasar” VLBI Network Observatories

A. Ipatov, I. Gayazov, S. Smolentsev, D. Ivanov, G. Ilin, N. Shuygina, Yu. Bondarenko

Abstract The current status of the co-location of space geodetic techniques at the observatories of the “Quasar” VLBI network is considered. The main technical characteristics, co-located high-precision observational instruments, and their systems as well as some results of sessions are presented.

Keywords VLBI, SLR, GNSS, DORIS, co-location

1 Co-location stations of the “Quasar” VLBI Network

The “Quasar” VLBI network is a unique astronomical instrument in Russia created in the Institute of Applied Astronomy. The network consists of three radio astronomical observatories—Svetloe near St. Petersburg, Badary in Eastern Siberia, and Zelenchukskaya in the North Caucasus attached to the Correlation processing center in St. Petersburg (Figure 1). All observatories have been linked by optical fiber lines with 1 Gb/s average data transfer rate, providing operational determinations of Universal time in e-VLBI mode.

2 VLBI Systems

The main instrument in each of three observatories is a 32-m radio telescope (RT-32), which provides a completely automatic process of observing the radio sources and satellites. The main technical characteristics of the antennas are presented in Table 1. Sessions can be carried out both in radiometric mode, when the telescope is working alone, and in radio interferometric mode, when several telescopes operate synchronously in the same network. The data obtained by the “Quasar” VLBI network are equivalent to the space-time resolution of a radio telescope having a mirror diameter of about 5,000 km. One of the fundamental problems solved by using the “Quasar” VLBI network is a high-precision monitoring of the Earth’s rotational irregularity. The data obtained by “Quasar” are used for implementation of a number of space projects, including support of the operation of global navigation satellite systems GLONASS.

Table 1 RT-32 specifications.

Configuration	Cassegrain (with asymmetrical subreflector)
Mount	AZEL
Main reflector diameter	32 m
Subreflector diameter	4 m
Focal length	11.4 m
Azimuth range	$\pm 270°$ (from south)
Elevation range	from $-5°$ to $95°$
Max. velocity AZ	0.83 °/s
Max. velocity EL	0.5 °/s
Pointing accuracy	$< 10''$
Frequency range	1.4–22 GHz

The radio telescopes meet all the international standards and work as part of the global radio interferometric networks. The observatories have actively participated in both international (IVS, EVN) and domestic (Ru) observation programs since 2006. Activities of the observatories in VLBI programs in 2013 are presented in Table 2.

Institute of Applied Astronomy of RAS

Fig. 1 Co-location stations of the "Quasar" VLBI Network.

Table 2 VLBI observations in 2013.

Programs		**Svetloe**		**Zelenchukskaya**		**Badary**	
		days	sessions	days	sessions	days	sessions
IVS	24h	29	29	31	31	31	31
	1h	1.5	36	–	–	–	–
EVN		16.5	75	16.2	78	15	73
Ru	24h	48	48	48	48	48	48
	1h	0.9	23	14.7	353	14.3	344

3 The Combined GNSS Receivers and the DORIS Antenna

The combined GNSS (GPS/GLONASS/Galileo) receivers have performed continuous observations in the framework of IGS global and European permanent networks since 1996, sending the observational data in daily and hourly regimes. In 1991, the DORIS equipment was installed at Badary observatory. The same year, the station (BADA) was included in the International DORIS Service (IDS). Receiving and pre-processing of radio signals is performed on satellites of the DORIS system.

4 SLR Systems

The new satellite laser ranging systems "Sazhen-TM" by "Precision Systems and Instruments" company were installed at all observatories of the "Quasar" Network in 2011. SLR is designed to obtain high-precision range and angular coordinates of geodetic and navigation satellites (Lageos 1, Lageos 2, GLONASS, etc.). The optical mounts of SLR systems were installed on concrete pillars inside of specially built towers covered with the "Astro Haven" dome. The towers are 2–4 m in height and are located at distances 2–35 m from the laboratory buildings of the observatories. These locations provide a full view in all azimuths at elevations more than 20°. Electronic blocks of the SLR systems, including the equipment for laser pumping, control and management, are installed in laboratory buildings of the observatories. The main technical characteristics of the “Sazhen-TM” system are presented in Table 3.

Table 3 “Sazhen-TM” specifications.

Ranging distance (night)	400–23000 km
Ranging distance (day)	400–6000 km
Aperture	25 cm
Wavelength	532 nm
Beam divergence	5″
Laser pulse frequency	300 Hz
Laser pulse width	150 ps
Pulse energy	2.5 mJ
Mass	120 kg
Normal points precision	1 cm
Angular precision	1–2″

All stations of the “Quasar” Network joined ILRS in 2012. Activities of SLR stations in 2013 are presented in Table 4.

5 Observatories Equipment

All of the observatories are equipped with the identical time standards and meteorological stations which are used when carrying out all types of observations. The automatic digital weather transmitter “Vaisala” is used to obtain meteorological data in real time. A water vapor radiometer being designed at the Institute of Applied Astronomy is currently working at the Svetloe observatory. It is planned to equip all stations with the analogous radiometers. The water vapor radiometer is designed to measure the effective radiation temperature of the atmosphere.

6 Co-located Instruments of the Observatories

These days, each observatory of the “Quasar” network is supplied with at least three co-located instruments of different techniques: VLBI, GPS/GLONASS, SLR and DORIS (Table 5). The Svetloe and Zelenchukskaya observatories are the co-location stations with three types of high precision space geodetic instruments, while the Badary observatory is one of those few stations with four types of instruments.

The status of the observatories as the stations of different global and continental space geodetic networks is presented in Table 6.

7 Reference Points of Instruments

The local geodetic network of the observatory is designed for monitoring the displacement of radio telescope reference points and GPS antennas caused by constructions deformation and local ground motions. Local tie parameters between reference points of the VLBI antenna (intersection of axis taking into account axis offset), SLR system (intersection of axis taking into account height of the system mount), GNSS, and DORIS antenna markers were determined with about 2 mm accuracy. Consistency of VLBI- and GNSS-derived coordinates with local geodetic measurements is about 5 mm. As a result, all three observatories were approved to be included in the list of GGOS Legacy Co-location Sites, which means that they were acknowledged as operational, well calibrated systems with episodic intersystem vector determinations. Values of eccentricity vectors from GNSS markers to VLBI antenna reference points are presented in Table 7.

8 Radio Interferometer of New Generation

Under the state program of VLBI network “Quasar” modernization, construction of two 13-m radio telescopes (RT-13) are planned up to 2015 of the new generation (at the Zelenchukskaya and Badary observatories) for operational and high-precision polar coordinates and Universal Time data support of the GLONASS system, and for communication with the international VLBI network and other international agencies. Construction of the new 13.2-m radio telescopes have already begun at the Badary and Zelenchukskaya observatories. The main specifications of the RT-13 antenna system are presented in Table 8. These new antennas will meet all requirements of the VGOS program.

Table 4 SLR observations in 2013.

Observatory	GLONASS, etc		Lageos 1 and 2		Total	
	sat. passes	NP	sat. passes	NP	sat. passes	NP
Badary	1100	10285	178	1145	1278	11430
Zelenchukskaya	581	3468	163	1254	744	4722
Svetloe	234	2215	119	825	353	3040

Table 5 Observatories' co-located instruments.

Technique	Svetloe	Zelenchukskaya	Badary
VLBI	Radio telescope with 32-m antenna (circular polarization L, C, S\X, K cryogenic receivers, Mark 5B+ recorder, DAS P1002M)		
GNSS	Javad GNSS Delta-G3T (Javad RingAnt-DM)		
	Topcon GNSS NET-G3 (Choke Ring CR-G3)		
SLR	"Sazhen-TM" (25-cm aperture, 300 ps pulse, 300 Hz)		
DORIS	–	–	DORIS Beacon model 3.0 (Starec 52291)
Other equipment	Time synchronization system (Active Hydrogen Maser VCH-1003M)		
	Vaisala WXT 510 automatic digital weather transmitter		
	Water vapor radiometer		

Table 6 Global and regional network stations.

Technique	Network	Svetloe	Zelenchukskaya	Badary
VLBI	IVS	Sv(2003)	Zc(2005)	Bd(2006)
	EVN	7380(2003)	7381(2005)	7382(2006)
GNSS	IGS	SVTL(2004)	ZECK(1997)	BADG(2001)
	EPN			
SLR	ILRS	1888(2012)	1889(2012)	1890(2012)
DORIS	IDS	–	–	BADB(1992)

Table 7 Eccentricity vectors VLBI-GNSS.

Difference	Sv-SVTL	Zc-ZECK	Bd-BADG
ΔN	-57.5932 ± 0.002 m	-64.7489 ± 0.003 m	61.8824 ± 0.002 m
ΔE	58.4824 ± 0.002 m	7.9544 ± 0.003 m	-73.4973 ± 0.002 m
ΔH	9.3495 ± 0.003 m	8.7813 ± 0.003 m	10.2001 ± 0.002 m

Table 8 RT-13 specifications.

Manufacturer	Vertex Antennentechnik GmbH
Mount	alt-azimuth
Main reflector diameter	13.2 m
Azimuth speed	12 °/s
Elevation speed	6 °/s
Tracking accuracy	16 arcsec
Frequency range	2–40 GHz
Surface accuracy	0.2 mm

9 Conclusion

Implementation of the new technologies and the improved procedures allows the “Quasar” VLBI Network observatories to achieve the status of the “New Technology Sites”, which implies that we strive for millimeter level accuracy in our data products.

Going Digital – The Transition from Mark IV to DBBC at Onsala

Niko Kareinen[1], Rüdiger Haas[1], Laura La Porta[2], Alessandra Bertarini[2,3]

Abstract The Onsala Space Observatory is currently equipped with both a VLBI Mark IV rack and a digital BBC (DBBC). The Mark IV rack at Onsala has been used operationally for both astronomical and geodetic VLBI for more than 40 years. In 2011, Onsala purchased a DBBC and we started to test it and to gain experience with the new device, both for astronomical and geodetic VLBI. The DBBC was upgraded several times and the Field System (FS) interface was implemented. We did parallel recordings, with both the old Mark IV/Mark 5A system and the new DBBC/Mark 5B+ system, during numerous geodetic VLBI sessions. Several R1, T2, and Euro sessions were correlated during the last two years by the Bonn correlator with Onsala being included both as an analog station (two-letter code On) and as a digital station (two-letter code Od). We present results from these parallel sessions, both results from the original correlation and results from the analysis of the corresponding databases.

Keywords VLBI, backends, DBBC, geodesy

1 Introduction

The Onsala Space Observatory has a long history in VLBI going back all the way to 1968, participating both in the field of geodetic and astronomical VLBI within IVS, EVN, and GMVA. At the moment, VLBI observations are carried out with two telescopes: a 25-meter telescope operating from 18 cm (L-band) to 5 cm (C-band) and a radome-enclosed 20-meter telescope in the frequency range from 13 cm (S-band) to 3 mm (115 GHz). In the foreseeable future these two telescopes will be joined by the VLBI Global Observing System (VGOS) twin telescopes. In 2011 the Mark IV rack was complemented with a DBBC VLBI backend. With the observing mode requirements for VGOS and the limitations of the old analog systems compared to digital backends, the transition to DBBCs is unavoidable. By adopting DBBCs at Onsala we had the opportunity to get hands-on experience with the evolving system and ensure that we can obtain satisfactory results with the system. Furthermore, maintaining the old Mark IV equipment provides challenges on its own.

The DBBC acquired in 2011 was a DBBC2 [1] and since then it has been upgraded several times. Zero-baseline tests have been conducted for both IVS and EVN, and with EVN the DBBC is operational since mid-2013. The aim is to have the DBBC in operation in the IVS sessions as well. Currently the equipment used consists of a Mark 5A connected to the Mark IV rack and a Mark 5B+ connected to the DBBC. Furthermore, we have a Mark 5C, which is used as an e-transfer machine, and a PC-EVN for real-time e-VLBI, which is to be replaced by FlexBuff as the future e-VLBI machine.

Recording in parallel with both Mark IV and DBBC setup during several geodetic VLBI sessions, correlated at Bonn, we obtained databases in which Onsala was included both as analog and digital station. We compared the results from these databases to find whether there were any differences, random or systematic, in both the raw delays and the derived geodetic parameters, i.e., station positions, earth orientation parameters, and zenith wet delays.

1. Chalmers University of Technology, Department of Earth and Space Sciences, Onsala Space Observatory
2. Institut für Geodäsie und Geoinformation der Rheinischen Friedrich-Wilhelms Universität Bonn
3. Max-Planck-Institut für Radioastronomie

2 Parallel Observations with Mark IV and DBBC

Numerous parallel observations with the Mark IV and DBBC were recorded during the period between 2012–2014. The session types included R1, R&D, EUR, and T2 sessions. The sessions are listed in Table 1.

Table 1 Sessions recorded in parallel at Onsala with Mark IV and DBBC.

Session type	Session name
IVS-R1	R1553, R1563, R1566, R1567, R1569, R1570, R1572, R1573, R1585, R1592, R1598, R1601, R1602, R1604, R1612, R1615, R1616
IVS-R&D	RD1201, RD1301, RD1303, RD1306
EUROPE	EUR118, EUR120, EUR123, EUR125
IVS-T2	T2090, T2093, T2094

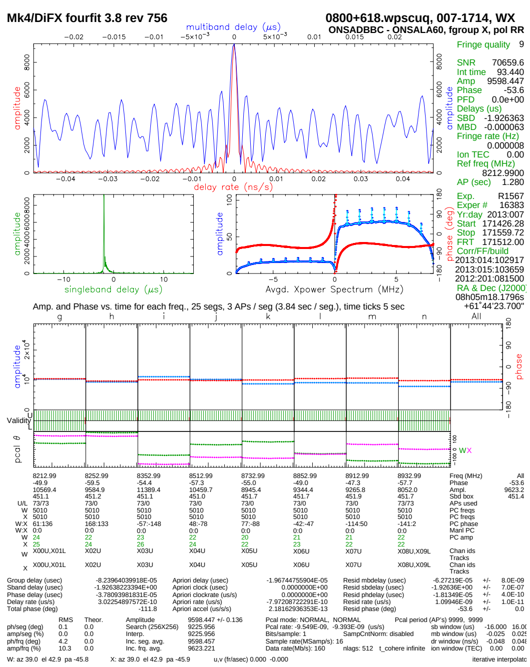

Fig. 1 Fringe plot for X-band for the R1567 zero-baseline test.

Zero-baseline tests were conducted for these sessions using the DiFX installation at Onsala. Fringe plots for X- and S-band for one such zero-baseline test (R1567) are shown in Figures 1 and 2. Furthermore, as mentioned earlier, in several cases both the Mark IV/Mark 5A and DBBC/Mark 5B+ data from the sessions were sent to Bonn for correlation. The Bonn correlator did fringe-testing and as a result produced databases in which the analog and digital data were added as separate Onsala stations, ONSALA60 (On) and ONSADBBC (Od). From here on the analog and digital stations will be referred to as On and Od, respectively.

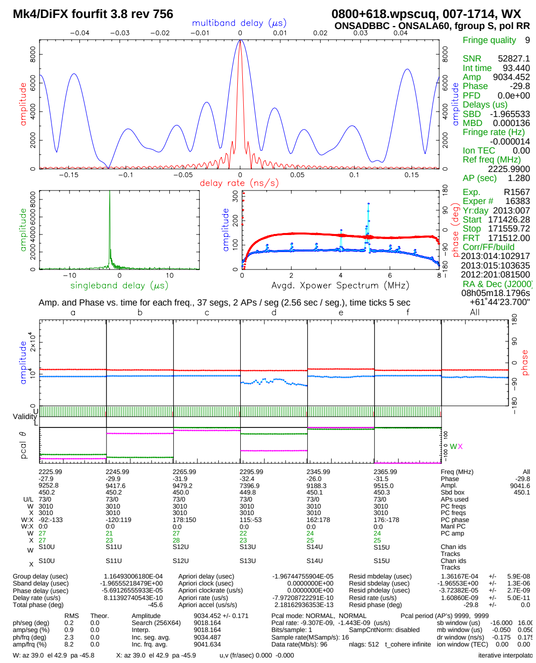

Fig. 2 Fringe plot for S-band for the R1567 zero-baseline test.

3 Correlation and Analysis

The sessions that were recorded in parallel and correlated at Bonn were used as a basis in the comparison analysis. The analyzed sessions are listed in Table 2. In total, six sessions were used in the analysis, which covered a time period of approximately 13 months.

All sessions were analyzed using the Calc/Solve VLBI analysis software [2]. Both On and Od were included as separate stations in these databases. The databases were processed in two ways to yield results for the session: either On or Od was turned off. The

Table 2 Analyzed sessions with Onsala as analog and digital station.

Observing date	Session name
2012 October 01	IVS-R1553
2012 December 10	IVS-R1563
2013 January 02	IVS-R1566
2013 January 07	IVS-R1567
2013 July 01	IVS-R1592
2013 Novermber 18	IVS-R1612

databases were calibrated using cable and weather data extracted from the individual station log files. There were no gross errors apparent in either of the log files in any of the sessions. A small, noise-like difference could be seen in the cable calibration data, but it is negligible because the differences between the cable calibration data were within 1.5–3 μs RMS, which is less than 0.1% of the total values. We first resolved ambiguities, clock breaks, and possible other issues with the sessions. Then we estimated station positions, earth orientation parameters, and zenith wet delays by switching either On or Od on/off. Station positions were estimated for digital and analog Onsala, and—due to post-seismic motion—for TIGO and Tsukuba. The clocks and the troposphere were modeled as piecewise linear functions with 60-minute intervals. Then the set of parameters associated with On and Od were compared to determine whether there were any significant differences in the results. In addition, we translated the database version 2 into NGS format to compare the raw delays for On and Od.

To assess whether the differences were noticeable, we computed a weighted RMS difference for station positions, UT1–TAI and rate, polar motion, and atmospheric parameters. The On–Od difference values are listed in Table 3.

Table 3 WRMS differences between the estimated parameters.

On–Od	WRMS differences
Up	8.2 mm
East	1.3 mm
North	3.5 mm
UT1–TAI	0.98 μs
$-\Delta$LOD	1.14 μs
Xpol	11.0 μas
Ypol	11.6 μas
dX	8.9 μas
dY	10.3 μas
ZWD	3.2 mm

In general, there is a relatively good agreement between On and Od in the estimated parameters. There is, however, a noticeable fluctuation in the station position when comparing the two solutions. The largest variation was found in the vertical coordinate; it was about 1 cm. The east and north coordinates show better agreement, with East being the best. As can be seen from Figure 3, this difference is mostly due to fluctuation, which is scattered around the zero-line. This indicates that it is likely that there is no systematic bias between the station positions from On and Od. Almost all the differences fall within the error limits with respect to zero.

The estimates for UT1–TAI and rate, as well as polar motion and nutation, all lie within their limits of uncertainty from zero. The difference in ZWD was within 20 mm with approximately 91% of the values within one standard deviation from zero. The distribution of differences in the hourly ZWD estimate is illustrated in Figure 4. Session R1553 has the largest deviation from zero, and has also the greatest offset in the station position, with a distinct deviation in the North-component. This indicates that there might be unresolved problems within that session.

Table 4 Biases and standard deviations of the observed delays between ONSADBBC–ONSALA60.

Od–On	Bias [ns]	Std. dev. [ps]
IVS-R1553	−657300.04	32.0
IVS-R1563	−657350.06	26.8
IVS-R1566	−657350.09	14.4
IVS-R1567	−657300.08	11.6
IVS-R1592	−657300.08	19.4
IVS-R1612	−657350.03	16.4

Table 5 Biases and standard deviations of the differences between observed delays on the baselines (ONSADBBC–WETTZELL)–(ONSALA60–WETTZELL).

(Od–Wz)–(On–Wz)	Bias [ns]	Std. dev. [ps]
IVS-R1553	−1900.03	33.9
IVS-R1563	−1950.08	65.1
IVS-R1566	−1950.08	20.8
IVS-R1567	−1950.08	14.8
IVS-R1592	−1950.07	21.2
IVS-R1612	−1900.02	17.3

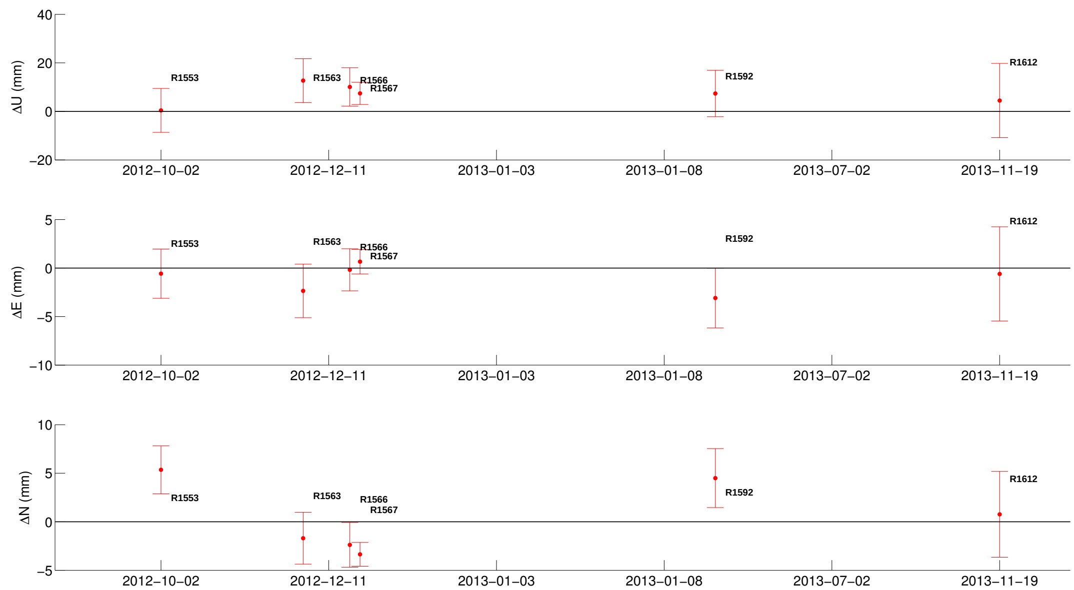

Fig. 3 Differences between On–Od in the East, North, and Up components.

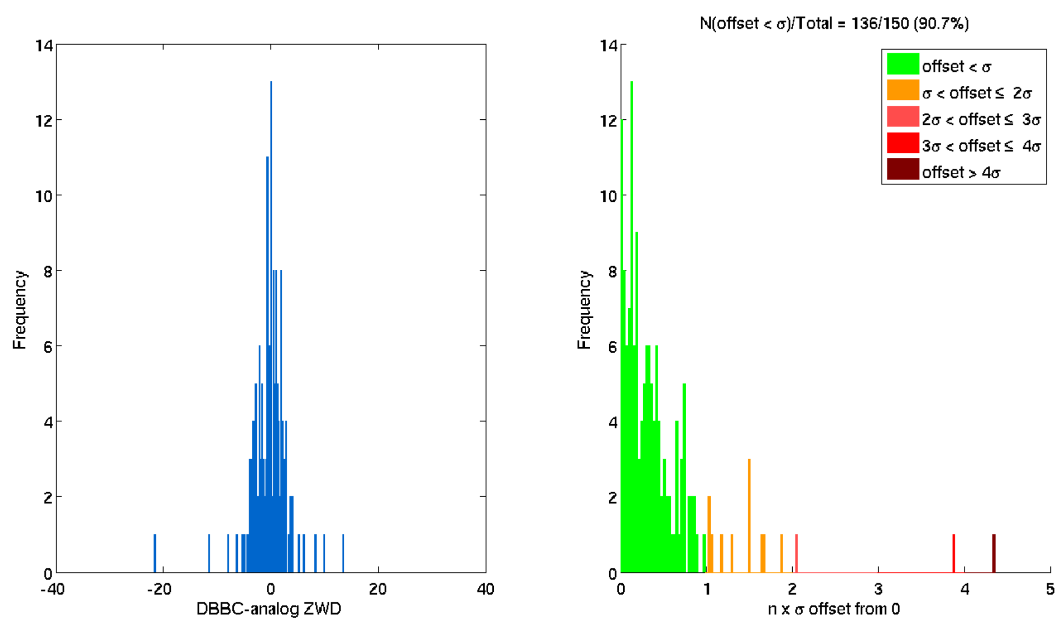

Fig. 4 (left) Distribution of differences in the ZWD estimate between Od and On. (right) Distribution of the level of significance of the Od–On differences.

When the observed delays are compared between On and Od as well as among On, Od, and a third station, the unbiased values lie approximately under 50 ps with even scattering. The delays on the ONSADBBC-ONSALA60 baseline obtained from the converted NGS cards for each database are illustrated in Figure 5. There was a constant bias of approximately -657 μs present in each database with standard deviations from 12–30 ps. In addition to the constant term, three of the databases had a 50-ns ambiguity with respect to the other four. The constant biases are absorbed into the clock parameters in the analysis. The biases and standard deviations are listed in Table 4. A similar inspection was done with On,

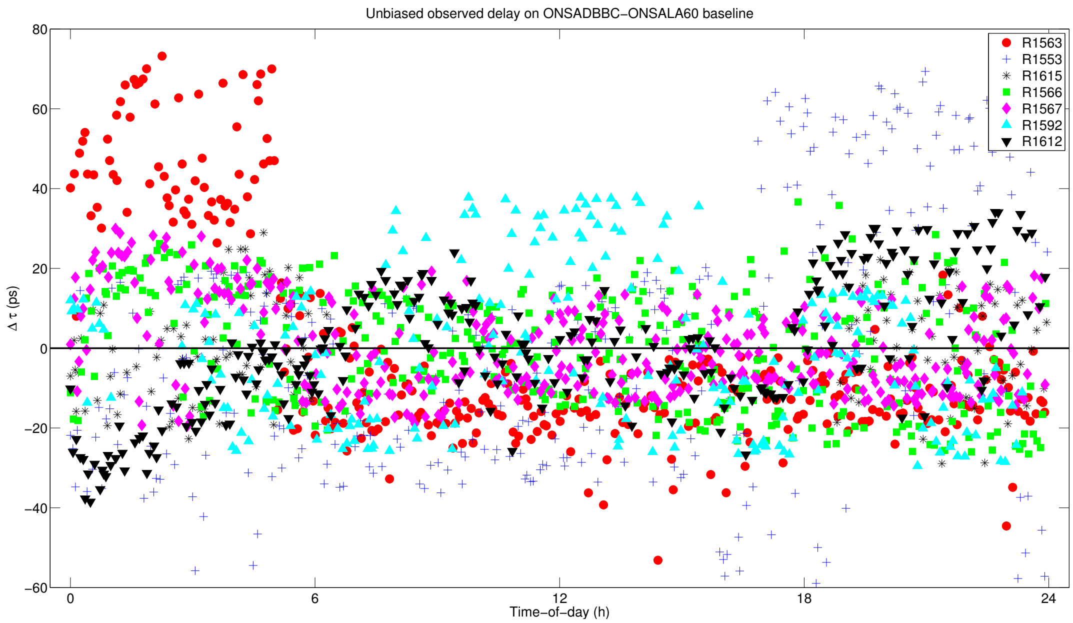

Fig. 5 Unbiased observed delays on the zero-baseline ONSADBBC–ONSALA60.

Od, and WETTZELL. The approximate bias between the differences is within −1900 ns to −1950 ns with standard deviations ranging from 15 ps to 65 ps. The biases and standard deviations for the differences between (Od–Wz)–(On-Wz) are listed in Table 5.

for the raw observed delay between Od and On differ in the range of ±20 ps. The non-systematic nature of the differences suggests that the source for errors is likely in the analysis and parametrization rather than in the instrumentation.

4 Conclusions

The differences between Od and On are relatively small. Due to the small number of sessions in which both On and Od are correlated, the sample size is relatively limited. No systematic errors could be discerned from the estimates obtained in this analysis. The DBBC at Onsala has performed reliably in numerous IVS sessions and no significant differences between the analog and digital backend have been found in the zero-baseline tests. Based on these sessions the values

References

1. Tuccari, G., Alef, W., Bertarini, A., Buttaccio, S., Comoretto, G., Graham, D., Neidhardt, A., Platania, P. R., Russo, A., Roy, A., Wunderlich, M., Zeitlhöfler, R., and Ying, X., 2010. DBBC2 Backend: Status and Development Plan. *International VLBI Service for Geodesy and Astrometry 2010 General Meeting Proceedings*, 392–395.
2. Ma, C., Sauber, J. M., Bell, L. J., Clark, T. A., Gordon, D., Himwich, W. E., Ryan, J. W., 1990. Measurement of horizontal motions in Alaska using very long baseline interferometry. *J. Geophys. Res.* 95 (2), 21991–22011.

Design of a VGOS Software Correlator Based on GPUs

Voytsekh Ken, Vladimir Mishin, Dmitry Pavlov, Nadezda Sokolova, Igor Surkis

Abstract The design of a new FX software correlator intended for the new small antenna VLBI network was started at IAA RAS in 2012. The main principles, topology, hardware, and software solutions for the design of a six-station, near-real-time correlator with the ability to process 16 Gbps data are presented. Benchmark test results are given. First fringes with wideband observations were obtained.

Keywords Correlator, GPU, VLBI, VGOS

1 Introduction

The design goal is to realize a near-real-time, six-station correlator to process a data stream of up to 16 Gb/s from each observatory. VLBI data are recorded on four frequency bands at a bandwidth of up to 1024 MHz for each circular polarization or up to 512 MHz for two linear polarizations using 2-bit sampling. The input data format is VDIF. The correlator computes cross-spectra at a resolution of 4,096 spectral channels and extracts 32-phase calibration tones in each frequency band for each station in near-real time. A two-station prototype was designed in 2013 [1].

2 Why GPU?

The most significant distinctive feature of our correlator from existing VLBI software correlators is the usage of graphical processing units (GPUs) for the main computations such as bit repacking, Fourier transformation, doppler tracking, spectra multiplication, and phase calibration signal extraction. The choice of the GPUs was dictated by the fact that a GPU contains hundreds of ALUs, which are able to simultaneously operate the same instructions. Besides the global memory with large latency, a GPU also contains shared, texture, and constant memories, which are of cache-type. This allows different threads to access the same data almost simultaneously. Thus, usage of GPUs should sufficiently decrease the amount of the central processing units. A corrrelator design using traditional processors requires approximately 3,000 cores or 375 eight-core CPUs.

Another key feature is that data transformation from bit-type to float-type is perfomed during the GPU's kernel execution in the GPU's DRAM. It allows a decrease in traffic between all modules of the cluster of up to 32 times.

3 High-perfomance Computing Cluster

The correlator's hardware is based on hybrid-blade-server technology. The hardware of the current single-baseline correlator prototype contains five blade servers, which are installed into one chassis (Figure 1). Each blade server contains two Intel Xeon E5 CPUs and two Nvidia Tesla M2090 GPUs based on Fermi technology. The cluster also includes power supply and power distribution units, two cache servers (which are similar to blade servers but having 256 GB RAM and 2x10 GbE optic input), one head (master) server, data storage with a capacity of 20 TB, an infiniband

Institute of Applied Astronomy, Russian Academy of Sciences

data commutator, and a fiber optic commutator. The cluster components are mounted in one cabinet.

Fig. 1 HPC cluster with five blade servers for a two-station correlator prototype at IAA RAS.

In 2014 the cluster will be upgraded to 40-blade servers, eight cache servers, and 75 TB data storage. Also, the existing ten GPUs will be changed to Tesla K20 (Kepler technology). These components require four cabinets.

4 Correlator Topology

The correlator's topology consists of head, station, and correlation software modules. The head module controls all interblock processes and collects the results. Each station module processes a data stream from one station and provides phase calibration signal extraction, data synchronization, delay tracking, and bit repacking. Each correlation module provides cross- and autocorrelation spectra computing for all the stations. Figure 2 illustrates the principle of the station module (SM). SM decodes a VDIF input stream and transfers to delay tracking block.

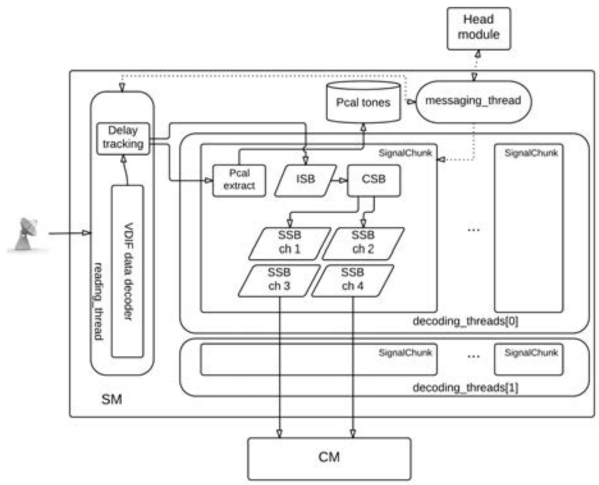

Fig. 2 Station module algorithm.

During tracking, the signal from the station is being transformed to the reference of the Earth center time scale. During the transformation, samples are inserted/removed (Figure 3) into/from the input stream buffer (ISB). The VDIF decoder is continuously being asked for portions of samples to fill the ISB between the inserted/removed samples, or for the whole ISB at once for the case that there are no inserted/removed samples in the ISB. In parallel, the genuine signal (without added or removed samples) is being copied into a separate ISB, which we call "ISB-Genuine".

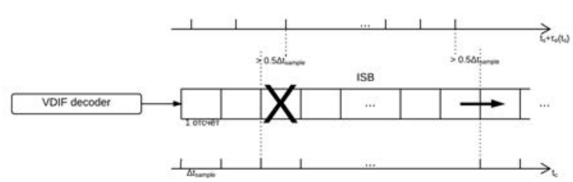

Fig. 3 Delay tracking scheme.

The ISB is separated into channels in the channel separation block (CSB). The CSB essentially repacks bits using the GPU. As a result, the station signal buffers (SSB) are formed and are ready to be transferred to the correlation modules (CM).

ISB-Genuine is used for the pcal extraction operations, which are also perfomed with the GPU. Pcal extraction is implemented using the method proposed by Pogrebenko [2]. If the pcal offset is equal to zero, then the phase tones have an equidistant frequency spacing. The shifted data is divided into frames with a size of doubled pcal tones, and then all the frames are summed. We used a reduction algorithm [3] to accelerate the computation. As a result, white noise from the cosmic data is averaged to zero, and only the phase tone information remains. Then the FFT is run to get the pcal data.

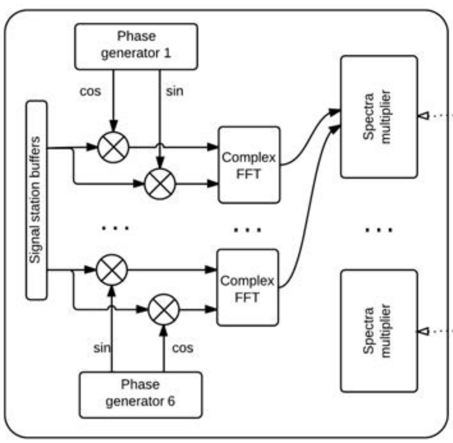

Fig. 4 Correlation module algorithm.

The cross-spectra computation algorithm is shown in Figure 4. First the fringe rotation is produced on the input stream. This operation is perfomed in conjunction with a bit transformation into the float type. Then the FFT operation is completed; and, finally, the obtained data are transferred to the spectra multipliers, where they are multiplied together and averaged within the chosen time period.

When using computation with GPUs, we are able to use several approaches in order to improve the performance by optimization of the operations with memory. Constant memory was used when the precomputed values of the trigonometrical functions for fringe rotation were saved. Different threads had multiple access to these values, so we took sufficient advantage of the memory caching. To sum up the spectra, shared memory was used to decrease the number of requests to global memory.

5 Benchmark Tests

Time and perfomance estimation tests were perfomed in order to check the SM and CM algorithms. The tests were made using Tesla M2090 and Tesla K20x. The pass criterion is to provide the delay tracking and pcal extraction operations in real time for the SM. The input signal is a wideband VDIF data stream written in 2-bit, eight-channel 512-MHz mode.

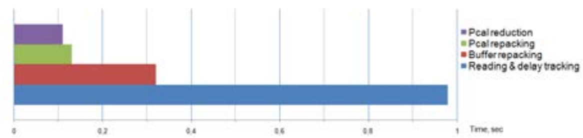

Fig. 5 Station module time benchmark test for one second of a 16 Gbps signal (Tesla M2090).

Fig. 6 Correlation module time benchmark test (Tesla M2090).

Figure 5 and Table 1 show the time intervals to perform the required operations for SM. The reading and delay tracking operation as well as other operations are provided by parallel threads so the total time does not exceed the period of one second for one second of data.

Table 1 Required time for station module operations, in seconds.

Operation	Tesla M2090	Tesla K20x
Reading and delay tracking	0.98	0.98
Buffer repacking	0.32	<0.32
Pcal repacking	0.13	0.21
Pcal reduction	0.11	0.19

Benchmark tests were also done for the CM in order to estimate the amount of blade servers needed to

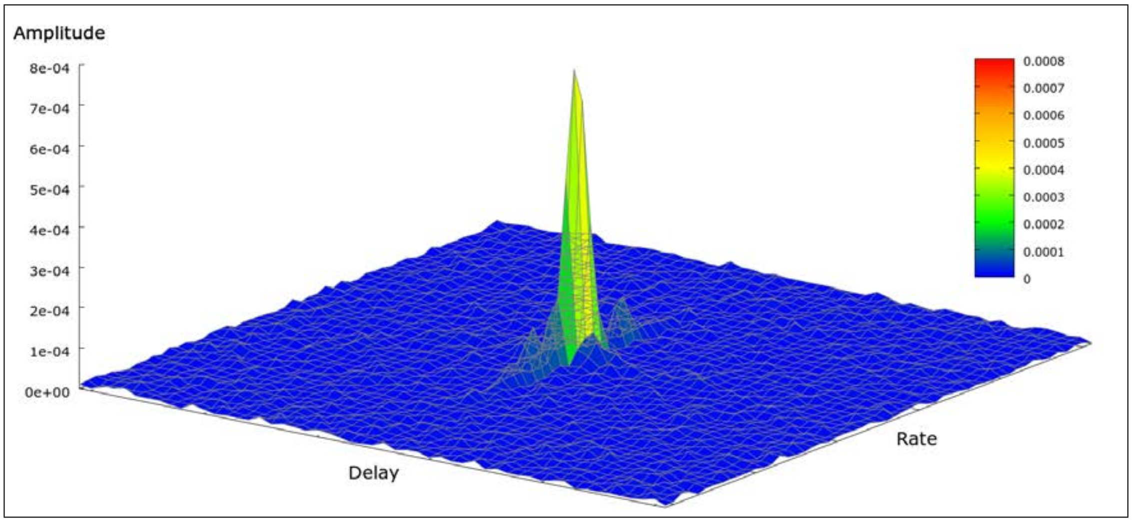

Fig. 7 3D fringe plot for the source 1300+580.

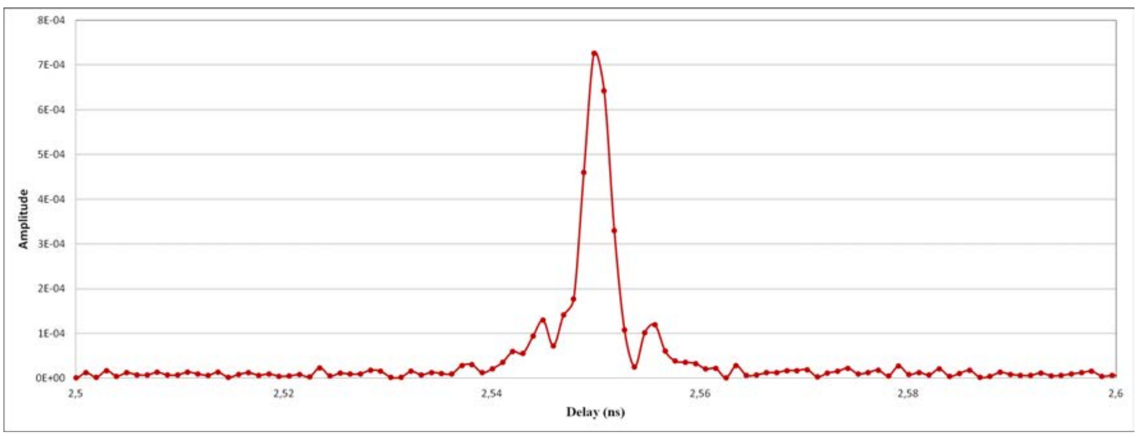

Fig. 8 Fringe plot for the source 1300+580, delay vs. amplitude.

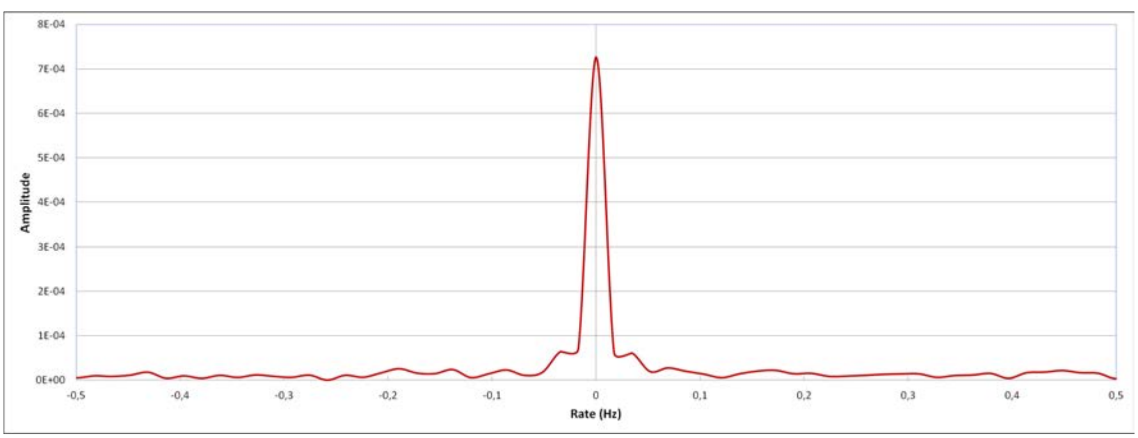

Fig. 9 Fringe plot for the source 1300+580, delay rate vs. amplitude.

process a 16-Gbps data stream in near-real time. Figure 6 illustrates the interval distribution during spectra computation. The bits unpacking and fringe rotation operations are the most intensive, because high-latency DRAM is used. The comparison results between M2090 and K20x are compiled into Table 2. According to the results, the implementation of the algorithms requires eight Fermi M2090 blades or seven Kepler K20x blades for near-real-time processing of one wideband (512 MHz, 2 Gbps) data stream.

Table 2 Required time for correlation module operations, in microseconds.

Operation	Tesla M2090	Tesla K20x
Bits unpacking & fringe rotation	31	23
FFT	8.4	6.5
Spectra multiplication	7.4	6.6

6 First Fringes

A test session, Ru-TEST074, was carried out on September 21, 2012. A scan of the source 1300+580 was chosen to find fringes. The 56-s scan was recorded with the BRoadband Acquisition System (BRAS) prototype on the single baseline Svetloe–Zelenchukskaya. Figures 7–9 illustrate the fringe fitting results. More information about this experiment is presented in [4].

7 Conclusions

The two-station, near-real-time FX-correlator prototype was designed. An HPC cluster was developed and installed at IAA RAS. A six-station correlator is under development. This work will be completed in 2015. All well-parallelized algorithms are perfomed using GPUs. The algorithms require 76 GPUs. Fringes were found for the source 1300+580 with a fringe rate of 1.4 MHz.

References

1. Surkis, I., Ken, V., Kurdubova, Ya., Melnikov, A., Mishin, V., Pavlov, D., Sokolova, N., Shantyr, V., Zimovsky, V. IAA Correlator Center. International VLBI Service for Geodesy and Astrometry 2013 Annual Report. Submitted.
2. Wagner, J., Pogrebenko, S. Fast multi-tone phase calibration signal extraction. http://www.metsahovi.fi/∼jwagner/pcal_extraction_practicals.pdf
3. Harris, M. Optimizing parallel reduction in CUDA. http://developer.download.nvidia.com/assets/cuda/files/reduction.pdf
4. Melnikov, A., et al. First fringes with BRAS on VLBI network “Quasar”. This volume.

Software Correlator in the Chang'E-3 Mission

Weimin Zheng[1,2], Juan Zhang[1,2], Yun Yu[1], Wenbin Wang[1], Tong Li[1]

Abstract During the real-time phase of the Chang'E-3 lunar exploration mission, the VLBI group delay accuracy was better than 1 ns, and the delay turnaround time was less than 45 seconds. The software correlator was the primary correlator of the VLBI center and worked for nearly one month with high stability and real-time ability. Compared with the versions in the previous lunar missions, this correlator can process data in parallel mode on multiprocessors using MPI and OpenMP. This paper introduces the software correlator structure and its current situation.

Keywords Software correlator, Lunar exploration, e-VLBI, fast fringe search, phase calibration tone extraction

1 Introduction

The CVN real-time software correlator (CRSC) is used in the Chang'E-3 (CE-3) mission. The CVN (Chinese VLBI Network) consists of five stations (Shanghai Tianma 65-m, Shanghai Sheshan 25-m, Yunnan 40-m, Urumqi 25-m, and Beijing 50-m) and one data processing center at the Shanghai Astronomical Observatory. The Shanghai Sheshan station is the backup of the Tianma station. CRSC is the key component of the data processing center. According to the CE-3 mission requirements, the design objectives of CRSC focus on stability and real-time performance. During the mission, the software correlator's continuous working period was up to approximately 11 hours per day, and the data latency for CRSC should be less than 25 seconds. Development of CRSC was begun in 2007. The early version of CRSC took part in the CE-1 and CE-2 missions as primary equipment and did a good job in 2007 and 2010. In 2012, the basic parallel version correlator executed the CE-2 extended mission of flying over the second Solar-terrestrial Lagrange point. Last year, the real-time parallel version software correlator completed the CE-3 task successfully based on e-VLBI technology. CRSC is written in high-level languages such as C, Python, Matlab, and so on. It implements a parallel algorithm using MPI (Message Passing Interface) and OpenMP (Open Multi-Processing). CRSC runs on commodity computer hardware. It has high scalability and flexibility. It also has a good degree of parallelism. The code of CRSC is accelerated using the Intel Performance Primitive Library (IPP) vector arithmetic libraries. After several years of development, CRSC has many capabilities such as Fast Fringe Search, Phase Calibration (PCAL) tone extraction and FITS-IDI format transformation, and real-time visibility monitoring.

2 Main Functions

As an FX-style correlator, the data latency of CRSC was less than 25 seconds during the CE-3 mission. If it was not in the fringe search mode, the latency could be less than 10 seconds. Besides, it has the function of PCAL extraction.

The hardware platform is a commercial blade cluster. It has five I/O nodes (one quad-core CPU of E7-

1. Shanghai Astronomical Observatory, Chinese Academy of Sciences
2. Key Laboratory of Radio Astronomy, Chinese Academy of Sciences

Table 1 CRSC specifications.

Processing Mode	Real-time & post-processing
Station number	1–20
Real-time fast fringe search	4 stations
IF number	1, 2, 4, 8, 16
Frequency channel	24–4096/IF
Integration period	0.1–60 seconds
Input data format	Mark 5
Output data format	CVN, FITS-IDI
Maximum data speed	1.4 Gbps/station

4820, 128 GB memory, 300 GB + 12 TB storage), 16 computation nodes (six CPUs/node, dual-core CPU of E5-2640, 32 GB memory, 300 GB storage), and two management nodes (one dual-core CPU of E5-2620 24 GB memory, 900 GB + 214 GB storage). The management network is 10G Ethernet, and the computation network is InfiniBand.

Fig. 1 The computational platform of the CRSC in CE-3.

The station data were transported to the data receiving server in the Data Center through the fiber link in the real-time mission. The different correlator items exchange data through NFS (Network File System).

2.1 Real-time Fast Fringe Search

In general, during orbital maneuver phases, the accurate orbit cannot be provided in advance, so the correlator cannot work properly in such conditions. The fast fringe search module first extracts the main car-

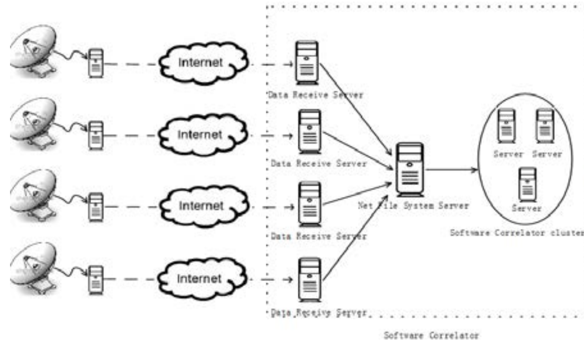

Fig. 2 Data flow diagram of the Chang'E 3 Mission.

rier frequencies from the signals of different stations, produces the delay rate, and then compensates for the delay and delay rate. After several iterations, the accurate delay and delay rate are found. They are used to modify the predicted model. Following the reconstructed delay model, the software correlator can produce the correct results (Figure 3). MPI, OpenMP, and IPP are adopted to increase the computing speed. This on-site fringe search and delay model reconstruction procedure takes place every five seconds in the CE-3 mission to guarantee real-time correlation.

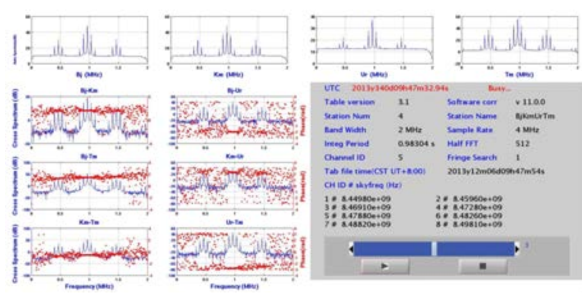

Fig. 3 The cross-correlation phase spectrum (red points) and amplitude spectrum (blue points) of every baseline using the fast fringe search function from Quick Viewer GUI.

2.2 Phase Calibration Tone Extraction

PCAL tones are injected at the front end of a VLBI antenna in order to provide a convenient means to estimate instrumental delays [2]. CVN antennas rely on the software correlator to extract the PCAL tones. CRSC can extract all tones in CE-3 (eight channels, 2 MHz bandwidth).

2.3 Real-time Visibility Monitoring

The new Quick Viewer (QV) module was added to monitor CRSC output results in real time with a Graphical User Interface (Figure 3). The information of channel frequency, station names, sample rate, integration period, FFT point, fast fringe search mode, and cross-correlation amplitude/phase spectrum can be displayed on the GUI. It is very convenient to monitor the important status of the software correlator and even the CVN in the CE-3 mission.

2.4 FITS and CVN Output Format

The preceding software correlator only supported CVN output format specifically designed for satellite navigation. Considering the astronomical and geodetic data processing usage, the new CRSC version supports the standard FITS-IDI format output and can be processed by AIPS directly.

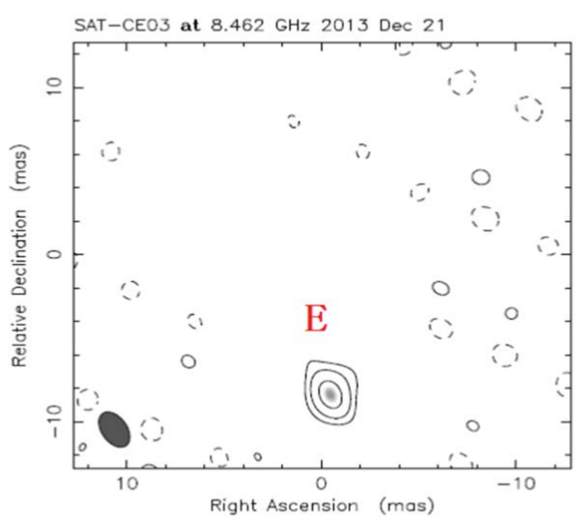

Fig. 4 CE-3 Rover image obtained from CRSC FITS output using Difmap.

3 Conclusions

The CRSC has already been utilized in the CE-3 mission successfully. A number of significant improvements have been made. However, the real-time ability and the robustness also need to be improved, and astronomical application functions will be added. Besides the lunar exploration missions, more astronomy and geodesy data will be processed by CRSC in the future.

Acknowledgements

This paper is sponsored by the Natural Science Foundation of China General Program (11173052, 11373061), the state CNGI demonstration project, the State High-tech 863 R&D project (2012AA121603), the Key Laboratory of Radio Astronomy of Chinese Academy of Sciences, the Science & Technology Commission project of Shanghai Municipality (06DZ22101), the Program of Shanghai Subject Chief Scientist (14XD1404300), and the Chinese lunar exploration project. The authors appreciate the support from the CVN data center.

References

1. Weimin Zheng et al.: The Software Correlator of the Chinese VLBI Network, IVS 2010 General Meeting Proceedings, pp. 157–161.
2. A.T.Deller, W.F.Brisken et al.: DiFX2: A more flexible, efficient, robust and powerful software correlator, Publications of the Astronomical Society of the Pacific, Vol. 123, No. 901 (March 2011), pp. 257–385.

Southern Hemisphere Geodesy and Astrometry with AUSTRAL

Jim Lovell[1], Stas Shabala[1], Jamie McCallum[1], John Dickey[1], Lucia Plank[1], Cormac Reynolds[2], Sergei Gulyaev[3], Tim Natusch[3], Stuart Weston[3], Jonathan Quick[4], Johannes Böhm[5], Jing Sun[6], Oleg Titov[7], Patrick Lovell[8], Sarah Lovell[8]

Abstract The AuScope VLBI array is currently participating in geodetic and astrometric programs at the level of 150 days per year. Sixty of these days are dedicated to southern hemisphere focused AUSTRAL sessions. Here we describe the aims of the AUSTRAL program and new simulation and observing techniques under trial. We report on the progress to date, with a particular focus on our first 15-day southern hemisphere 'CONT' campaign carried out in November/December 2013.

Keywords VLBI, reference frame, astrometry

1 Introduction

The AuScope geodetic VLBI array [1] consists of three new 12-m radio telescopes and a correlation facility in Australia. The telescopes, all operated by the University of Tasmania, are at Hobart (Tasmania), Katherine (Northern Territory), and Yarragadee (Western Australia). They are co-located with other space geodetic techniques including GNSS, gravity, and, in the case of Yarragadee, SLR and DORIS facilities. The correlator is located at Curtin University in Western Australia.

Between July 2013 and July 2015 the array is participating in IVS programs at the level of 150 days per year. Sixty of these days are dedicated to AUSTRAL sessions with scheduling in VieVS [3], observations with the three AuScope antennas plus the Hobart 26 m, Warkworth 12 m, and Hartebeesthoek 15 m and 26 m (Figures 1 and 2), and correlation at Curtin University.

Fig. 1 Hobart 12 m schematic. (credit: P. Lovell)

The AUSTRAL observing program is divided into three streams focussed on high priority geodetic and astrometric aims in the southern hemisphere:

1. Astrometric observations to monitor and enhance the southern hemisphere reference frame in preparation for ICRF3;
2. Regular observations to improve the density of the geodetic time series for the southern antennas and to measure and monitor the motion and deformation of the Australian plate;
3. Four 15-day CONT-like campaigns over two years to demonstrate the full capabilities of the array,

1. University of Tasmania, Australia
2. Curtin University, Australia
3. Auckland University of Technology, New Zealand
4. Hartebeesthoek Radio Astronomy Observatory, South Africa
5. Vienna University of Technology, Austria
6. Shanghai Astronomical Observatory, China
7. Geoscience Australia, Australia
8. Mount Stuart Primary School, Australia

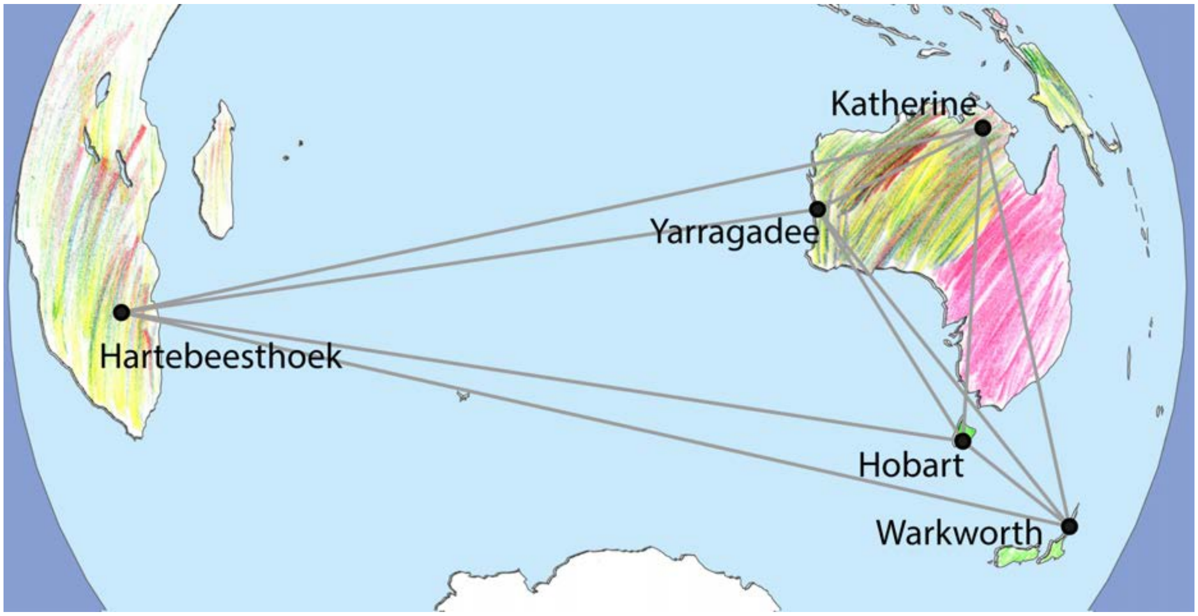

Fig. 2 The AUSTRAL Array, consisting of the three 12-m Australian AuScope antennas, the Hartebeesthoek 15 m, and the Warkworth 12 m. (credit: S. Lovell)

characterize the level of systematic errors caused by the troposphere and source structure, and develop and test error mitigation strategies.

2 Understanding the Systematics

Baseline length repeatability is a fundamental measure of the precision of the VLBI technique. In Figure 3 we show residuals for a typical long baseline between Hobart 12 m (Hb) and Kokee Park, Hawaii (Kk) ($\sim 8,300$ km). The two sets of points represent different observing campaigns, with filled points representing the CONT11 campaign.

The weighted RMS (WRMS) for the Hb-Kk baseline length during the CONT11 campaign is 0.010 m. This suggests that centimeter level accuracy in position measurements is achievable even with present techniques. By comparison, the WRMS of the baseline residuals for all other available observations is 0.021 m (Figure 4).

Our results highlight an important point. While formal uncertainties in station positions and baseline lengths can be reduced by increasing the number of observations, this is not particularly useful when attempting to assess the quality of individual position

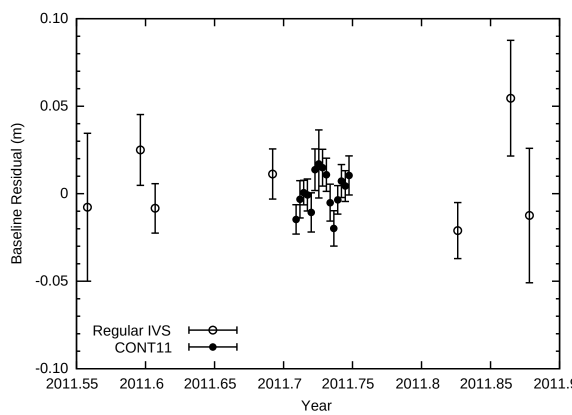

Fig. 3 Time series for residuals for the Hobart-12-m–Kokee (Hb–Kk) baseline. Filled circles represent data from the CONT11 campaign. Open circles are standard IVS sessions. Figure reproduced from [1].

measurements. It is clear that the main factor at present limiting the accuracy of VLBI observations lies in systematic biases inherent to the analysis. For example, ignorance of quasar structure and variability (which can exhibit different temporal behavior at S and X bands; e.g., Shabala et al., these proceedings, and [2]) will map into source and station positions. Furthermore, the magnitude and sign of these effects

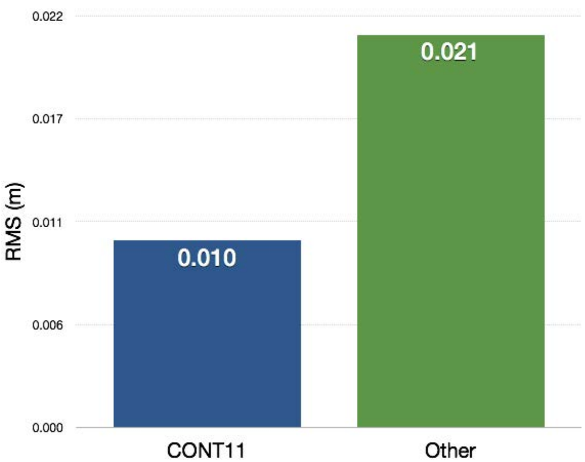

Fig. 4 A comparison of weighted RMS baseline residuals on the Hobart 12 m to Kokee baseline for CONT11 and all other observations. This demonstrates a clear improvement when systematic biases (such as array geometry) are removed.

will in fact depend in a complicated fashion on network geometry and the observing schedule.

One of the main aims of the 15-day continuous AUSTRAL campaigns is to further understand these systematic effects and develop strategies to mitigate against them.

As well as the 15-day campaigns, for four 24-h experiments during 2014, the 26-m antennas at Hartebeesthoek and Hobart will join the AUSTRAL array. With the same atmosphere and clocks at each site, and with baselines to each pair observing the same source structure, we hope to further understand the systematic uncertainties due to troposphere and source structure.

3 The 15-day AUSTRAL Observing Strategy

In the two-year period between July 2013 and July 2015, we plan to observe four 15-day CONT-like campaigns with the AUSTRAL array. The first of these campaigns has already taken place (November/December 2013) with the second one planned for November 2014. For each of the systematic effects we have identified, we are implementing the following strategies:

1. Array geometry can play an important factor in the solutions as the CONT11 results demonstrate. We will use the same array for all of the 15-day AUST campaigns.
2. Source structure. For the November/December 2013 campaign, we selected two source samples based on their Structure Index (SI):

   - The "good" sample containing sources with median SI < 2.5, observed on eight out of the 15 days.
   - The "bad" sample containing sources with median SI > 2.5, observed on seven out of 15 days.

   There are two schedules, one for the good sources and one for the bad. The schedules are repeated in sidereal time so that baseline orientation to source structure is fixed, removing random effects due to structure but preserving systematic effects.
3. Troposphere. For every sidereal day, we alternated between the "good" and "bad" source schedules so that, as much as possible, the weather conditions between consecutive days are comparable.

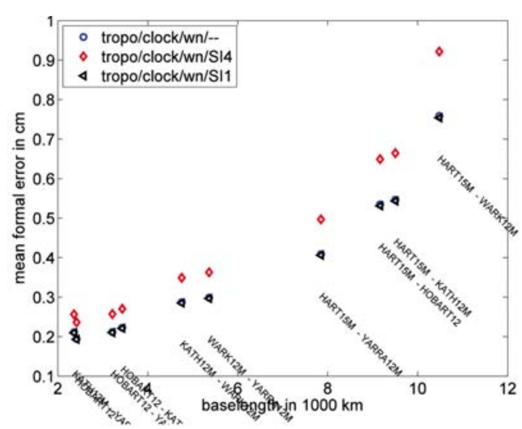

Fig. 5 Formal uncertainties for baseline lengths from simulations of the November 2013 AUSTRAL 15-day campaign. There is a clear indication that the uncertainties will be lower for sources with small Structure index (black triangles) than high Structure Index (red diamonds).

4 Simulations

Simulations of the AUSTRAL 15-day campaigns were conducted in VieVS, making use of the new source

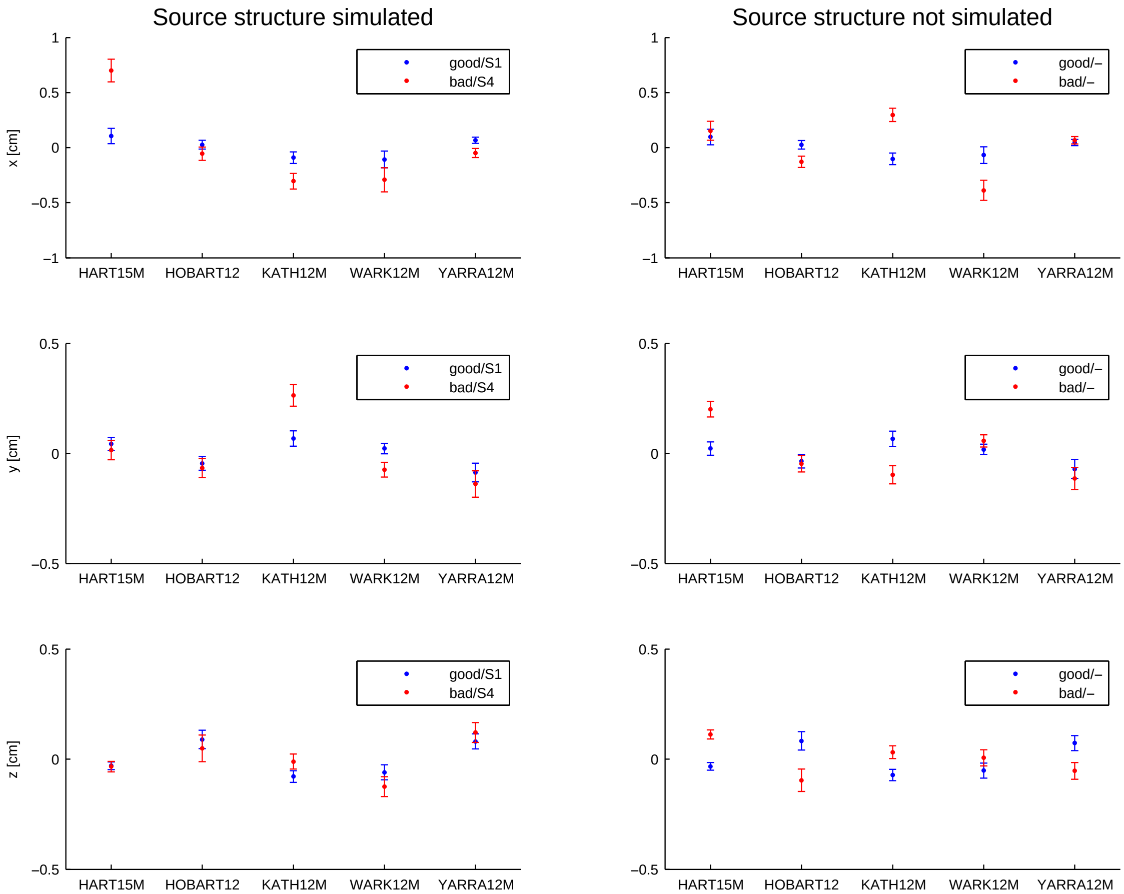

Fig. 6 Station cartesian coordinate residuals from simulations of the November 2013 AUSTRAL 15-day campaign for the "good" (blue) and "bad" (red) source selections. Panels on the left show results when source structure is simulated, and panels on the right are from simulations when structure is not simulated (i.e., point sources are assumed).

structure simulator [3]. The actual schedule files used in the November/December 2013 AUST 15-day campaign were used with 30 realizations each. Moderate values of Cn and H were used to characterize the troposphere, but this was still the dominant error over clock and white noise. The "good" and "bad" sources were simulated with Structure Index values of 1 and 4, respectively. While this is a reasonably crude approximation to real sources (which exhibit a distribution of structure indices), such simulations allow us to make an estimate of the source structure effect.

The simulations clearly show an improvement in the formal uncertainties for the low SI (good) sources over the high SI (bad) sources. In Figure 5 we show the simulated formal uncertainties as a function of baseline length, and in Figure 6 the station cartesian coordinates with formal errors derived from the VieVS global solution.

Lastly, in Figure 7 we show source coordinates as a function of declination. Once again the difference between low and high SI sources is clearly apparent.

5 Conclusions

We will use our analysis of the first 15-day campaign to validate the simulations and provide feedback to further develop our scheduling and observing strategies for the AUSTRAL program. Data from AUSTRAL sessions are released to the VLBI community in the same way as other IVS-coordinated programs.

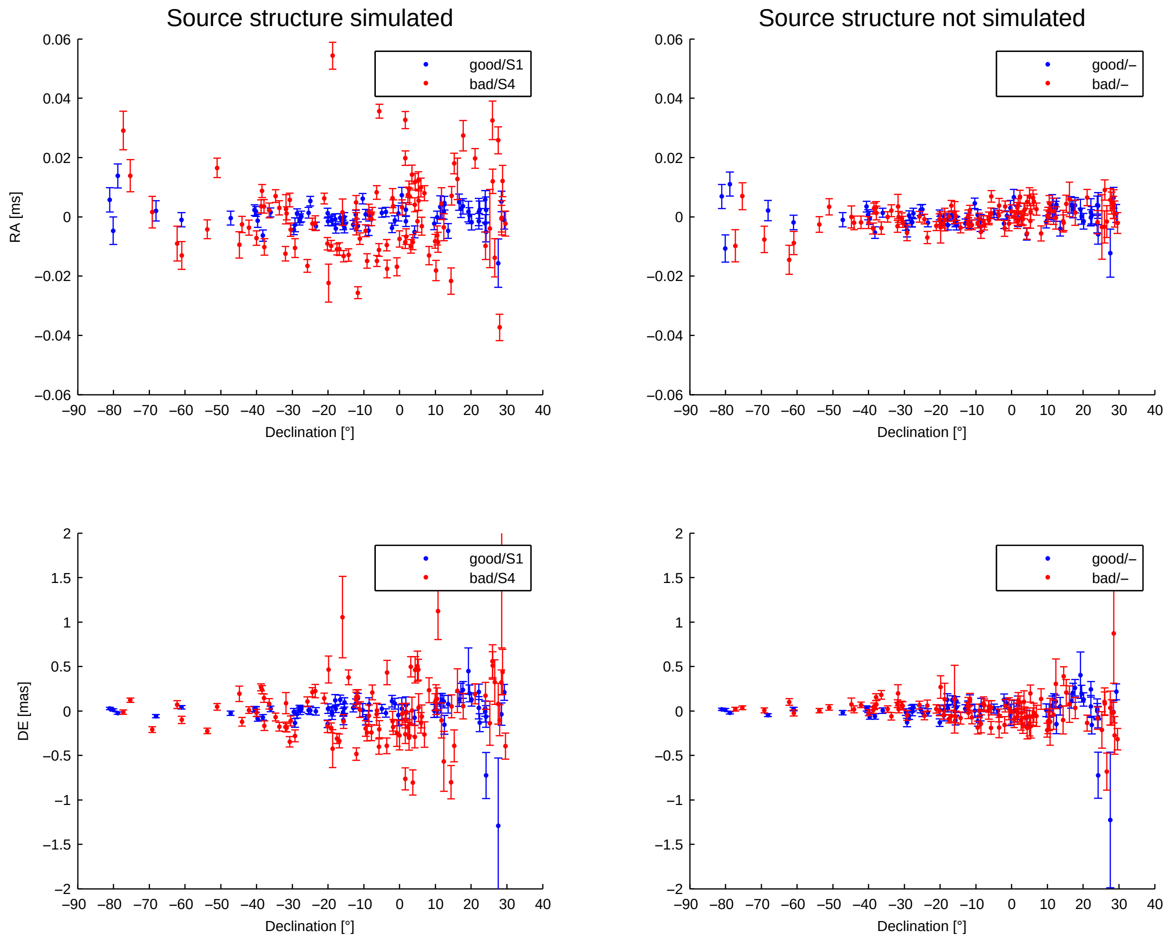

Fig. 7 Source position estimates from simulations of the November 2013 AUSTRAL 15-day campaign for the "good" (blue) and "bad" source selections. Panels on the left show results when source structure is simulated, and panels on the right are from simulations when structure is not simulated (i.e., point sources are assumed).

References

1. Lovell, J. E. J. et al. (2013). The AuScope geodetic VLBI array. J. Geodesy, 87, pp. 527–538
2. Shabala et al. (2014), J. Geodesy, 88, pp. 575-586
3. Sun, J., Böhm, J., Nilsson, T., Krásná, H., Böhm, S., and Schuh, H. (2014), J. Geodesy, 88, pp. 449–461

CONT14: Preparation and Prospects

Dirk Behrend, Cynthia Thomas, Ed Himwich, Dan MacMillan

Abstract In May 2014, a network of seventeen stations at sixteen sites will observe the next continuous VLBI campaign named CONT14. From May 6 through May 20, ten northern hemisphere and seven southern hemisphere stations will record S/X VLBI data for fifteen continuous UT days at a rate of 512 Mbps. This campaign is the continuation of similar campaigns loosely organized every three years. We discuss the preparation work such as allocation of station, media, and correlator resources and the observational procedure that will ensure that the best possible S/X VLBI data set be recorded. With a network size of seventeen stations, CONT14 is a precursor of continuous VGOS-type observing but with the S/X system. In the next several years, continuous VGOS observing on the broadband system will become a reality. With this in mind, we provide an outlook on future prospects of CONT campaigns.

Keywords CONT14, media, stations

1 Introduction

The Continuous VLBI Campaign 2014 (CONT14) will be a continuation of the series of very successful continuous VLBI campaigns that were observed at irregular intervals since 1994. The most recent CONT campaigns were observed in roughly three-year intervals (see Table 1).

The planning and organization of CONT14 commenced more than a year before the actual observing date. First, the general time frame was decided by the IVS Coordinating Center and the Observing Program Committee (OPC) to be spring 2014 (to sample a different time of the year). Then, the actual observing dates were fixed in correspondence with the EVN and other VLBI groups to May 6–20, 2014.

NVI, Inc.

Table 1 History of CONT campaigns.

Campaign	Network size	Observing month
CONT94	two 7-station networks	January 1994
CONT95	6-station network	August 1995
CONT96	5-station network	September/October 1996
CONT02	8-station network	October 2002
CONT05	11-station network	September 2005
CONT08	11-station network	August 2008
CONT11	14-station network	September 2011
CONT14	17-station network	May 2014

2 Resource Allocation: Media, Correlator, and Stations

The next step of the preparation was resource allocation. In an iterative process, the station, correlator, and media resources were evaluated and then eventually fixed. For the media it was determined that in order to keep the same observing rate as in the CONT11 campaign, additional media purchases were necessary.

We estimated that 142 modules were needed to support CONT14. Most of those are supported through new purchases and loans (110 modules). Several stations/agencies agreed on purchasing media to support the CONT14 campaign (see Table 2).

In order to allow the Hobart 26-m antenna (Ho) to participate, UTas will provide their own modules to

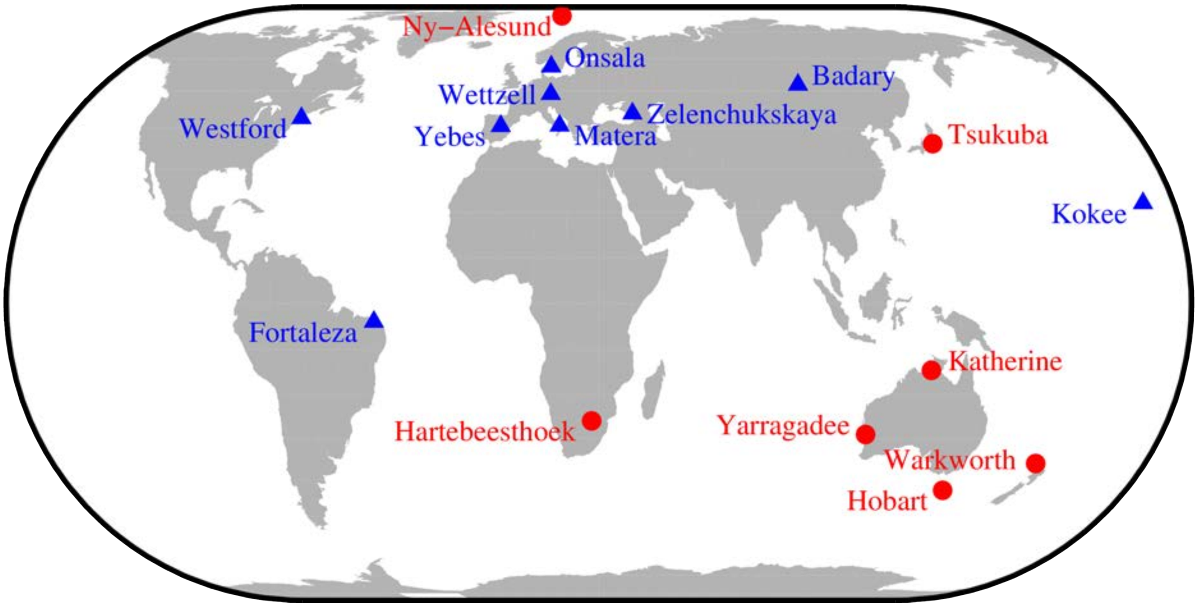

Fig. 1 The observing network of seventeen stations at sixteen sites for the CONT14 campaign. The sites in red (circles) will e-transfer their data to the correlator, whereas the blue sites (triangles) will physically ship their recording modules.

Table 2 Media purchases in support of the CONT14 campaign.

Agency	Module size	Quantity	Comment
AuScope	16 TB	24	Hb, Ke, Yg (on loan)
HartRAO	16 TB	12	
IAA	8 TB	10	Bd, Zc (on loan)
Matera	8 TB	10	
NASA	8 TB	20	Ft, Wf
Ny-Ålesund	8 TB	10	
Onsala	8 TB	10	
Wettzell	4 TB & 8 TB	6 & 4	6*4-TB, 4*8-TB
Yebes	16 TB	4	

support their participation. The remaining 32 modules come from the geodetic media pool.

Correlation will be done at a single correlator. This will simplify the logistics and ensure consistency of results; furthermore, it will provide the correlator with experience in handling a VGOS-type load. The Bonn Correlator at MPIfR agreed to take on the task of being the correlation facility for the entire campaign. Bonn will use their implementation of the DiFX software correlator.

There will be sixteen VLBI sites participating in the campaign (see Figure 1). At Hobart, both the 26-m and the 12-m telescopes will observe, resulting in seventeen VLBI observing stations in total for CONT14. The observing network can be characterized by the following items:

- ten northern hemisphere and seven southern hemisphere stations;
- reasonable global coverage with network size reaching VGOS requirements; a more optimal coverage would require more stations in Africa, North America, and South America, as well as Southeast Asia and Oceania;
- no broadband station will participate in CONT14: the processing of mixed-mode observing is not operational yet.

Because of the latter item, the 12-m antenna at GGAO dropped out of the original station list, and Westford will observe using their legacy S/X system.

Four R&D sessions (RD1309, RD1310, RD1401, and RD1402) were dedicated to check out the observing mode at the participating stations and to ensure that the stations are in good operating condition before CONT14.

3 Observational Procedure

An hour before the start of CONT14, a station sanity check in the form of a rapid fringe test will be performed. All stations will observe one or two 20-second scans and immediately e-transfer their data to the Bonn Correlator. Finding fringes for all stations will verify that all stations are in good working condition and set up correctly. Otherwise corrective action can be taken.

The schedules of CONT14 have the following characteristics:

- Fifteen consecutive session days are observed with three minutes between days for schedule changes (continuous VLBI).
- The observing days run from 0 UT to 24 UT (UT-day observing) in order to yield the most accurate combination and comparison of results from other space geodetic techniques.
- The observational data rate is 512 Mbps, which is identical to the setup of the CONT11 campaign.
- The Int1, Int2, and Ru-U Intensive sessions will take place as scheduled and have precedence over CONT14. There is no Int3 Intensive session scheduled during CONT14. The Intensives were considered in the CONT14 schedules.

The total number of scans scheduled for the campaign is 24,336, resulting in 302,115 campaign observations. These numbers, however, include the tag-along periods during the maintenance checks (see below). The actual observation count will thus be slightly smaller.

In order to avoid observational gaps in the overall network, station check times were fixed in staggered fashion at convenient and well-coordinated times for the stations (see Figure 2). These station check times are used from the second to the fourteenth day of CONT14; no maintenance checks are scheduled for the first and last days of CONT14.

For the case that a station completes its checks before the end of the check time slot, each station is tagged along for its check period. The two-hour slots for the Intensive stations (Bd, Kk, Ts, Wz, and Zc) are aligned with their respective Intensive (Int1, Int2, or Ru-U) observation periods. These stations first observe their Intensive sessions (90 min) and then perform their checks (30 min).

For recording purposes, the individual days of CONT14 are grouped into sets of session days (recording groups) in order to share modules between days. One, two, three, or four session days will be recorded onto one module. The recording groups will typically end with an equivalent of an R1 or R4 session (rapid-turnaraound session, R-session, cf. Table 3). This alignment allows the data of the R-sessions to be transported (shipped or e-transferred) immediately after the session so that the 15-day time delay goal for the R-sessions can be met.

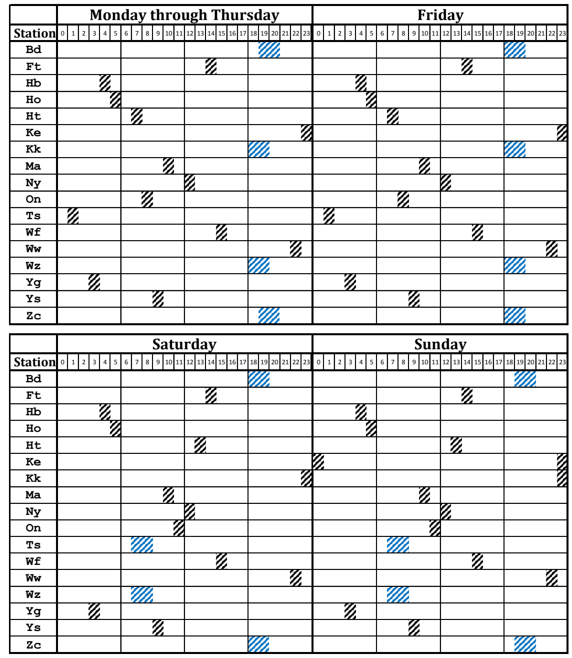

Fig. 2 Graphical display of the slots for station checks for the regular stations (1-hour slots, black) and the Intensive stations (2-hour slots, blue). The 2-hour slots actually commence 15 min past the hour.

Table 3 R1 and R4 equivalents of the CONT14 session days.

CONT14 day	Actual date	Day of year	Equivalent
C1401	May 06, 2014	126	R1
C1403	May 08, 2014	128	R4
C1407	May 12, 2014	132	R1
C1410	May 15, 2014	135	R4
C1414	May 19, 2014	139	R1

The R-sessions will be correlated and analyzed immediately and the results posted to the Data Center. Once the entire campaign has been analyzed, the results will be updated with a final version.

With up to four sessions recorded onto one module, a single module may contain more than 1,023 scans. As 1,023 scans per module was the upper limit for the Mark 5 directory listing, an upgrade to the Mark 5 software was prepared and rolled out under the leadership of Chet Ruszczyk from Haystack Observatory. The updated version of the Mark 5 software now supports a large directory structure with up to 65,536 entries.

The data transport to the correlator is done either by the physical shipment of modules or by the electronic transfer of data (e-transfer). As indicated in Figure 1, seven sites (eight stations) e-transfer all of their data to the correlator, whereas nine stations ship their modules. Fortaleza, which was included in the count of nine, is a special case: the station ships the modules to the Washington Correlator, and from there it is e-transferred to the Bonn Correlator. Hence, about half of the data of the CONT14 campaign are electronically transferred. This is a significant step towards realizing VGOS-type operations.

4 Simulation Results

Accompanying the steps of resource allocation and schedule writing, simulations have been run using the *Solve* software in order to determine the optimal network and scheduling parameters. The optimization was based on simulated formal errors for the EOP, number of observations, number of scans per hour, sky coverage, and robustness. In a final step, the eventually chosen schedules were analyzed w.r.t. their EOP performance and compared to the performance of previous CONT campaigns.

The simulation results for the individual fifteen days of CONT14 only vary marginally; hence, their differences are not reported here. The picture changes when comparing the simulation results of the first day for the last five CONT campaigns (including CONT14). For this purpose the formal EOP uncertainties were computed using two different *Solve* solutions.

The first solution is a standard TRF-type solution with station velocities estimated, i.e., similar to operational analysis except that the simulation databases were added to the analysis of all sessions observed from 1980 through 2013 (see Table 4). It is interesting to note that the CONT session formal errors for the ERP (X, Y, and dUT1) increased since CONT05. The reason for this is that the uncertainties of the station positions increase as the campaign epochs occur further away from the midpoint of the data span of the solution. This increase is due to the error in the estimated positions caused by the error in the estimated site velocities. It is simply a consequence of making a linear fit of a span of data.

Table 4 Simulated EOP formal errors with station velocities estimated in the *Solve* run.

Campaign	X [μas]	Y [μas]	dUT1 [μs]	ψ [μas]	ε [μas]
CONT02	43.1	33.6	1.7	83.2	36.8
CONT05	29.7	29.4	1.3	60.0	22.2
CONT08	30.1	30.6	1.3	41.4	16.5
CONT11	32.9	34.1	1.4	32.6	13.2
CONT14	36.2	38.2	1.5	31.1	11.7

In the second *Solve* solution, no velocities were estimated (see Table 5). In this solution we note a clear and steady improvement in ERP formal errors since CONT02. The effect of the increase in network size and global coverage and, to a lesser extent, of the increased data rate becomes apparent, while it was diluted by the effect of the velocity error in the first solution. The improvement of results from CONT11 to CONT14 is small because they have networks of similar sizes (14 versus 17 stations) and a very similar geographic distribution.

Table 5 Simulated EOP formal errors with station velocities fixed in the *Solve* run.

Campaign	X [μas]	Y [μas]	dUT1 [μs]	ψ [μas]	ε [μas]
CONT02	40.0	29.7	1.6	83.2	36.8
CONT05	21.2	20.8	1.0	60.0	22.2
CONT08	16.2	16.1	0.8	41.4	16.5
CONT11	12.9	13.2	0.7	32.6	13.2
CONT14	11.2	12.1	0.7	31.1	11.7

While the simulated formal errors for the ERP are too optimistic in the second solution, the relative quality of the CONT campaigns is represented correctly. More representative error estimates could be obtained using Monte-Carlo simulations with realistic troposphere, clock, and observation noise models.

5 Conclusions and Outlook

The preparation work for the CONT14 campaign was completed, and the stage is set for another successful continuous VLBI campaign. CONT14 is the largest such campaign in terms of network size and number of observations/scans. It also ranks first in the amount of data being transferred electronically (about half of the data).

Because of its network size, CONT14 is a precursor of continuous VGOS-type observing but with the S/X system. Assuming three-year gaps between future CONT campaigns, we can anticipate that by 2017, an extended VGOS pilot project with the broadband system will be in place, and by 2020, continuous 24/7 VGOS observing will be fully operational.

In 2020, the main purpose for a CONT campaign—namely continuous VLBI observing—will already be fulfilled by the standard VGOS observing. With this in mind, the following scenarios could be envisioned for future CONT campaigns:

- observe a CONT campaign with the legacy S/X system in parallel to the VGOS system;
- observe a mixed CONT campaign of legacy S/X stations and broadband VGOS stations.

It is conceivable that both types of CONT campaigns will be organized. A mixed CONT campaign could be observed in 2017 (CONT17) and a final legacy CONT in 2020 (CONT20). Further discussions are needed before a final decision can be made.

More information about CONT14 can be found at: `http://ivscc.gsfc.nasa.gov/program/cont14/`.

Evolution of the Geodetic Media Pool

Cynthia C. Thomas, Dirk Behrend, Ed Himwich

Abstract Over the years, VLBI has upgraded its recording capabilities by transitioning from thick to thin tapes, then thin tapes to disks, and currently the plan is to transition from Mark 5 disk recording with proprietary hardware and software to Mark 6 disk recording with open source software, commercial off-the-shelf hardware, and higher bandwidth for VGOS stations. The purpose of this paper is to show how this process will affect the geodetic media pool. Currently there are about 34 legacy stations participating in the IVS Observing Program that use the Mark 5 recording system. According to the VGOS Observing Plan [1], eight VGOS stations, including three converted legacy stations, will be operational by the end of 2014. We show the impact of the VGOS Trial Operations in 2015 and the VGOS Pilot Project in 2016 on the geodetic media pool. This includes the projected number of modules needed to maintain the Mark 5 pool for legacy stations and the projected number of Mark 6 modules needed to support the Trial Operations and the Pilot Project. We will also provide an estimate for the number of Mark 6 modules that need to be purchased by each station to support regular VGOS observing as well as an annual purchase of Mark 6 modules needed to mitigate media pool attrition.

Keywords Media, legacy stations, Mark 6, VGOS

NVI, Inc.

1 Introduction

Over the years, VLBI has transitioned from thick to thin tapes and then to disks. The geodetic media pool is currently comprised of Mark 5 modules from various stations and institutions. Each module contains eight disks, all of one type, either PATA (Parallel ATA) or SATA (Serial ATA). Most of the older and smaller

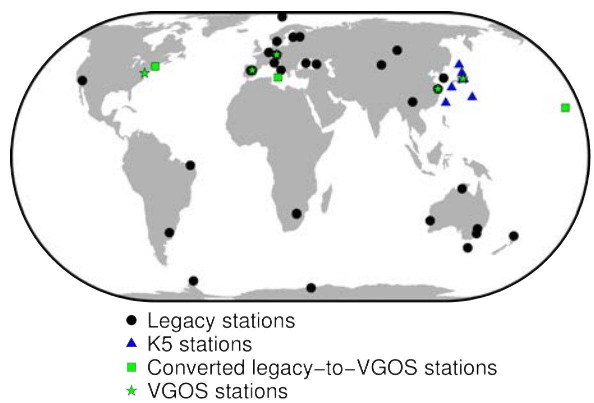

Fig. 1 A world map displaying a graphic view of the various types of geodetic stations that will support VGOS observing starting during 2015, according to [1]. The networks will increase from a proposed eight in 2015 to 16 in 2016 to 30 by 2018. Legacy stations use Mark 5 SATA and PATA modules only. Many of the legacy stations e-transfer their data to the correlators, which cuts down on shipping costs. K5 stations do not require modules at their site because the data is recorded on their servers. The K5 stations' data is e-transferred to the correlator from their servers. There are three stations that are converted legacy-to-VGOS stations: Kokee, Westford, and Noto. Westford currently switches from S/X to VGOS by changing receivers manually. Soon Westford will switch between the two receivers electronically. There are five VGOS stations that are tentatively scheduled to be operational by 2015: Ishioka, Sheshan, GGAO, Yebes, and Wettzell. GGAO has recorded broadband data.

modules are PATA, and all of the newer larger modules are SATA. The SATA modules can be converted from Mark 5 to Mark 6 by replacing the chassis for a nominal price. Although our plan is to use new Mark 6 modules for the VGOS observing, eventually we may have to convert some Mark 5 SATA modules to Mark 6 due to budgetary reasons. The Mark 6 geodetic pool may consist of the converted Mark 5 modules and newly acquired Mark 6 modules. The size of the modules in the geodetic media pool currently ranges from 0.96 TB (A-size) to 16 TB (L-size), and the modules are used for recording Mark 5 data only. Our plan is to transition from legacy Mark 5 recording to VGOS Mark 6 recording. According to the VGOS Observing Plan [1], eight VGOS stations, including three converted legacy stations, will be operational by the end of 2014 (see Figure 1). The focus of this paper is to determine what effect this change will have on the current media pool, future purchases, and maintenance of two geodetic media pools (Mark 5 and Mark 6).

2 Mark 5 Media Pool

We anticipate that the Mark 5 media pool will be static except for replenishment. Figure 2 shows how many modules of a particular size (A-size - 0.96 TB, B size - 1.4 TB, etc.) are needed to support the legacy stations for 2015 and beyond based on the 2014 media requirements. Also displayed are the available modules in a particular size and how many of those modules are PATA or SATA modules. There are not enough D-size (2 TB) and G-size (4 TB) modules. The correlators can ship the larger modules to the stations to compensate for the lack of smaller modules.

As in Figure 2, Figure 3 shows information about the number and the size of modules when adding a future CONT campaign. There are not enough modules of certain sizes. Some of the larger modules will be used to supplement the smaller modules. In addition, the 56 modules listed in Table 1 will be requested as a loan or purchase to support the next potential CONT campaign. Table 1 displays the number of modules needed per station to support regular legacy observing based on the 2014 observing level. The replenishment rate is based on a 5% failure rate, which is an estimate.

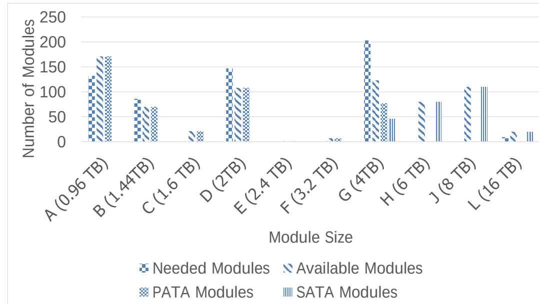

Fig. 2 Number of modules needed to support regular geodetic legacy observing.

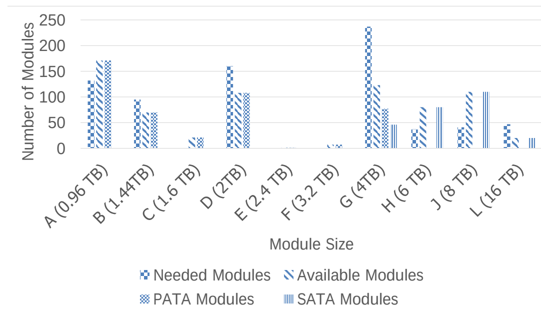

Fig. 3 Number of modules needed to support regular geodetic legacy observing plus a CONT campaign.

3 VGOS Observing Plan

As stated in the VGOS Observing Plan [1], there will be three trial VGOS campaigns starting in 2015. Each campaign will span a six-week period. It is estimated that one or two 32 TB modules per station, per day will be needed to support the three campaigns. The data will be processed and the modules released before the start of the next campaign. The first test campaign will need at most 12 32 TB modules per station to support the six 24-hour B7 sessions, a total of 96 modules. The B7 sessions will start on Sunday at 00:00 UT and end on Monday at 00:00 UT. The first trial campaign will be scheduled during a six-week period between January and April 2015. The tentative participating stations are Kokee, Ishioka, Seshan, GGAO12, Westford, Yebes, Wettzell, and Noto. The S/X observing will not conflict with the first VGOS Observing Plan trial.

The second test campaign will consist of four one-hour sessions every six hours for six consecutive weeks. The six new VGOS stations will not participate in the S/X sessions. The new VGOS stations will

Table 1 Modules needed to maintain legacy geodetic observing. First, this table represents the total annual usage based on the current level of observing. Second, media has to be replenished based on failure rate and TB used.

Station	Bd	Ft	Ht	Hh	Ho	Hb	Ke	Kk	Km	Ma	Mc	Mh	Nt	Ny	Oh	On	Kv	Sh	Sm	Sv	Ag	Ur	Ww	Wf	Wz	Yg	Ys	Zc	Total
Regular Observing Usage	11	21	21	16	8	28	28	28	5	24	19	6	10	28	5	17	23	11	7	11	24	11	20	20	28	28	20	28	506
Annual Failure Rate - 5% (Replenish)	1	2	2	1	1	2	2	2	1	2	1	1	1	2	1	1	2	1	1	1	2	1	1	1	2	2	1	2	40
Additional CONT Need (2017)	8	0	0	0	8	8	8	0	0	0	0	0	0	0	0	0	0	0	0	0	8	0	8	0	0	0	0	8	56

record the one-hour sessions every six hours without any interruption. Noto does not participate in the regular weekly R1/R4 sessions. Noto can be scheduled to avoid switching between S/X and broadband observing, but Noto has decided that they do not want to participate in the last two test campaigns. Kokee and Westford both participate in at least one of the weekly R-series. Westford will be able to switch electronically between S/X and broadband, so the second test campaign should not be a problem for them. It is unknown at this time how the transition between S/X and VGOS will operate at Kokee. According to the VGOS Observing Plan [1], the broadband media will be shipped out once a week. This is a potential complication that needs to be worked out, because the R-series are shipped as soon as the sessions are completed. The second trial campaign will be scheduled during a six-week period between May and August 2015. No additional modules will be needed because it is anticipated that the first trial campaign will be processed before the start of the second test campaign.

The third test campaign will be scheduled like the second test campaign but the data will be e-transferred to the correlators during the five-hour gaps. The third trial campaign will be scheduled during a six-week period between September and December 2015.

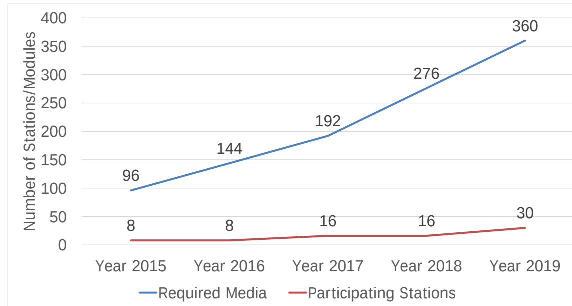

Fig. 4 The number of modules needed to support VGOS Operations from 2015 through 2019 is being displayed. 32 TB modules will be required. The initial 96 modules will have to be purchased in 2014 to support the 2015 Trial periods.

4 VGOS Geodetic Media Pool

The first proposed eight VGOS stations are GGAO12, Ishioka, Kokee, Noto, Sheshan, Westford, Wettzell, and Yebes. There are now no 32 TB Mark 5 or Mark 6 modules in the geodetic pool. As shown in Table 2, the first eight stations will need to purchase 12 Mark 6 modules per station to have sufficient media. The modules will need to be purchased during 2014 to be available for recording during January through April 2015. The additional eight stations scheduled to participate in 2016 are Santa Maria, Tenerife, Flores, Onsala, Metsahovi, Changchun, Kunming, and HartRAO. In preparation for 2016 VGOS observing, these stations should purchase half of the needed modules in 2015 and the remainder in the first quarter of 2016. The two smaller purchases should be easier on each station's budget. The additional 14 stations scheduled to participate in 2018 are Ny-Ålesund, Badary, Zelenchukskaya, Ussurisk, Kaliningrad, Kokee, Hobart, Katherine, Yarragadee, Warkworth, and four new NASA stations. Each of the 14 participating stations should purchase 12 modules for the Mark 6 geodetic media pool. Each of the 14 stations should purchase six modules in 2017 and the remaining six in the first quarter of 2018 to put less strain on their budgets. In order to keep the media pool up to date with respect to attrition, each of the 30 stations should replenish the media pool with one module annually starting the following year after their initial purchase.

5 Special Considerations

In addition to the information already presented in this paper, there are some special considerations that should

Table 2 Start-up and maintenance of the VGOS media pool.

Information	8-Station Network	Additional 8 Stations	Additional 14 Stations
Total Purchase in 2014	96		
Total Purchase in 2015		48	
Total Purchase in 2016		48	
Total Purchase in 2017			84
Total Purchase in 2018			84
Failure – 5%	5	5	8
Replenish per station & year	1	1	1

be addressed when making final decisions about the legacy Mark 5 and VGOS Mark 6 media pools.

First, the PATA Mark 5 modules cannot be converted to Mark 6. As more Mark 5 legacy stations convert to Mark 6, the older PATA modules will be used less.

Second, the SATA Mark 5 Modules can be converted to Mark 6 by replacing the chassis for approximately 495 USD per module. The decision will have to be made, based on how many Mark 5 legacy stations will convert to Mark 6, and whether it is preferable to keep all of the current Mark 5 modules as Mark 5 or convert them to Mark 6. The failure rate of the older PATA modules will have to be factored into the decision as well.

Third, Kokee, Noto, and Westford will not contribute to the legacy geodetic pool once they become VGOS-only stations and do not switch between S/X and VGOS observing.

Fourth, the TRACK program needs to be updated or replaced and maintained to support the Mark 5 and Mark 6 geodetic pool. The TRACK program was developed by NRAO to keep up-to-date information on media (initially tapes and later modules) in the media pool. Fortunately, we just learned that NRAO is in the midst of a major TRACK overhaul. NRAO asked for input regarding the overhaul, and input will be provided.

Fifth, the 5% failure rate is an estimate, because currently there is no program or tool that can be used to keep track of the statistics. This is an additional feature that will be suggested to NRAO for the new version of TRACK.

6 Conclusions

The geodetic media pool will transition from Mark 5 to Mark 6 over the next several years, until VGOS is fully established. This paper shows the necessary media purchases to establish and maintain the geodetic media pool. An update or replacement of the TRACK program, which is in progress through NRAO, is needed to manage the media pools properly.

References

1. Bill Petrachenko, Dirk Behrend, John Gipson, Hayo Hase, Chopo Ma, Dan MacMillan, Arthur Niell, Axel Nothnagel, Xiuzhong Zhang, “VGOS Observing Plan”, in International VLBI Service for Geodesy and Astrometry 2014 General Meeting Proceedings, D. Behrend, K. D. Baver, and K. L. Armstrong, editors, 2014, this volume.

Twin Telescope and Tide Gauge Plans for the Onsala Space Observatory

Rüdiger Haas, Gunnar Elgered, Johan Löfgren

Abstract We report on the present status of the installation of two new instruments at the Onsala Space Observatory: a twin telescope dedicated to geodetic and astrometric Very Long Baseline Interferometry (VLBI) and a tide-gauge station equipped with several different sensors to complement the experimental set-up of the Global Navigation Satellite Systems (GNSS) tide gauge. The twin telescope project is now at the stage where procurement will start. The tide-gauge station is just starting to be constructed, while the sensors have been bought and will now be calibrated and characterized in the laboratory.

Keywords Onsala Twin Telescope, tide gauge

1 Introduction

The Onsala Space Observatory has been involved in geodetic and astrometric VLBI observations since 1968 [1]. Currently about 40–50 sessions per year are observed in IVS programs. Onsala participated in all CONT campaigns. In April 2012 we received a decision for funding of a twin telescope at Onsala, to be part of the VLBI Global Observing System (VGOS) network. The project has been delayed by approximately one year due to difficulties to get the necessary building permits [2]. In late February 2014, finally all necessary permits were issued and the project is continued. The procurement of the equipment will start in 2014, and we plan that the Onsala Twin Telescope (OTT) will become operational in 2016.

With plans for a significant improvement in accuracy within the VGOS project, the need for complementary instrumentation and observations will increase. Particularly at the Onsala site, being located at the coast, loading effects on the Earth's crust are important. The modeling of the sea level in the Kattegatt strait is complicated and the available tide gauge data today are from Gothenburg and Ringhals at a distance of 33 km and 18 km, respectively. This together with the fact that the Onsala site will be very well determined in the International Terrestrial Reference Frame (ITRF) motivates the installation of an official tide gauge station of the Swedish national network. This network is operated by the Swedish Meteorological and Hydrological Institute (SMHI) and an agreement for a joint responsibility in constructing and operating a tide-gauge station has been signed.

Chalmers University of Technology (Sweden)

2 The Onsala Twin Telescope Project

The telescope sites identified have received the necessary permissions from the authorities and the procurement phase of the project has started. As is indicated in Figure 1, the twin telescopes will be located at a 500-m distance from the 20-m radome enclosed telescope, which presently is used for all geodetic VLBI observations, approximately in the south direction. The distance between the two telescopes will be approximately 75 m. We foresee a period of several years during which the 20-m telescope will be used in parallel with the twin telescopes.

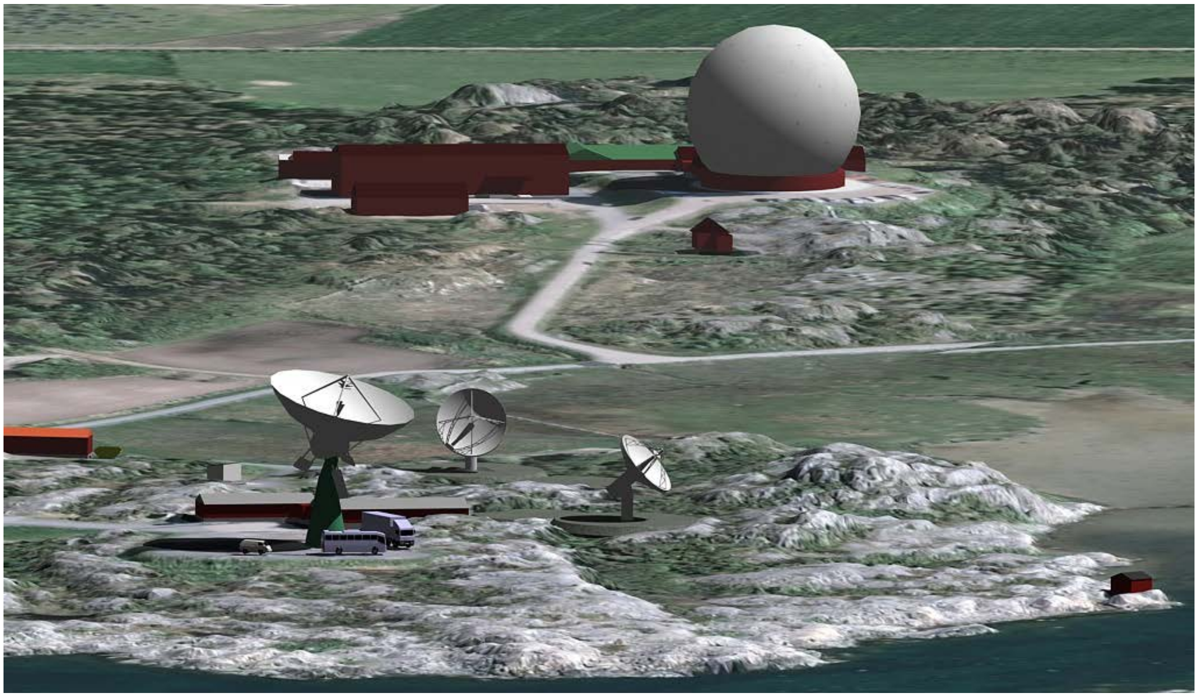

Fig. 1 An artist's impression of the twin telescopes at the Onsala site, roughly looking towards the north-east. The almost zenith looking telescope in the left foreground of the picture is the 25-m telescope from 1964, which is used primarily for astronomical VLBI. The new twin telescopes (OTT1, right, and OTT2, left) will be located in a distance of about 75 m and 125 m, respectively, from the 25-m telescope. The white radome in the upper part of the picture encloses the 20-m radio telescope from 1976 that is currently used for all geodetic VLBI observations. The distance to the twin telescopes will be about 475 m and 540 m, respectively.

The expected horizon masks of the new telescopes are presented in Figure 2. The common horizon of both telescopes together will be obstruction-free above 7.5° and only blocked to 7.5% at elevation 5°.

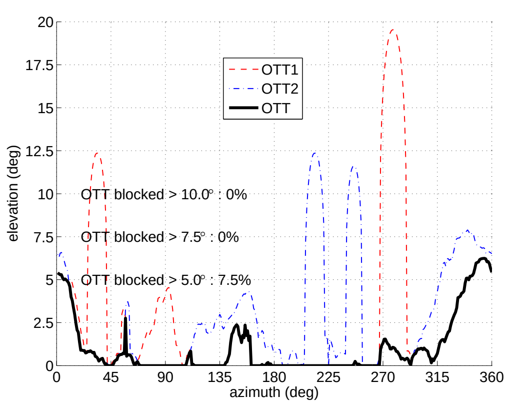

Fig. 2 Expected horizon masks for the individual twin telescopes, OTT1 (dashed line, red) and OTT2 (dashed-dotted line, blue), and combined for both OTT antennas together (solid line, black), as seen from the lower edge of the prime reflectors. The OTT telescopes will see each other (at about 30° and 240° azimuth), and they will see the 25 m telescope at about 210° and 290° azimuth. However, the common horizon is completely free above 7.5° and only blocked by 7.5% at elevation 5°.

We plan to establish a local control network around the twin telescopes. It will include several GNSS-monuments and several ground markers for classical geodetic survey. We aim at installing a fully automated local survey system for the twin telescopes with redundant automized and motorized total stations. A corresponding system has been developed and tested in the past few years [3]. This system will be used in a pilot project during the CONT14 campaign to determine reference point and local-tie information during the whole campaign. The experience gained from this pilot project will be very useful for the system to be implemented for the twin telescopes.

3 The Onsala Tide Gauge Project

Since 2010 we operate a so-called GNSS tide gauge utilizing reflected GNSS signals [4]. The GNSS tide

Fig. 3 A panorama of the GNSS tide gauge at the coastline, looking towards south.

gauge consists of geodetic GNSS equipment in the form of one zenith-looking and one nadir-looking antenna, connected to one receiver each. The installation records both the direct satellite signals and the satellite signals that are reflected off the sea surface. Through analysis of the phase delay of the signals or the signal-to-noise ratio given by the receiver, the sea level can be determined. The GNSS tide gauge is complimented by three pressure-sensor-based tide gauges at the same location, shown in Figure 3.

In the autumn of 2013 a pneumatic tide gauge sensor (called the bubbler sensor) was installed at the small hut, in the lower right corner in Figure 1. The sensor driver unit is shown in Figure 4.

This new location will host the official tide gauge station of the Swedish national network mentioned in the introduction. When finished, a radar sensor and a pneumatic sensor (CS471, Campbell Scientific) will be mounted in a special concrete culvert with heating, in order to ensure operating conditions also when the sea is covered by ice. An artist's impression is shown in Figure 5.

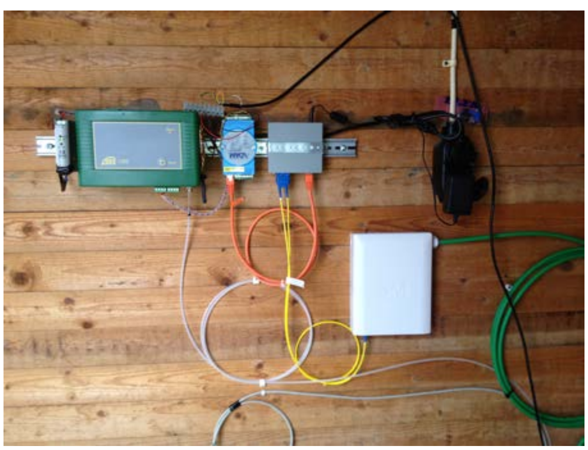

Fig. 4 The bubbler sensor installed in the hut. Compressed air flows from the green unit (to the left) through a plastic tube to a bubble chamber below the sea level. The pressure in the measuring tube is proportional to the height of the water column above the bubble chamber.

The bubbler sensor determines the sea level from differential pressure measurements. One value is the pressure of compressed air necessary in order to release bubbles from a tube at a fixed position, well below the sea level, and the other pressure value is that of the air at the sea level. Examples of one month of sea level observations are shown in Figure 6.

The data presented in the upper graph of Figure 6 are from the bubbler sensor, one pressure sensor, and the GNSS tide gauge. Differences with respect to the bubbler data are presented in the lower graph. As can be seen in the upper graph, the tides on the Swedish west coast are small and the large variations are caused by air pressure, wind, and ocean currents. The storm "Sven" on December 5–6 with wind speeds of up to 34 m/s caused the strong signal in sea level.

The most accurate (i.e., giving the smallest uncertainty) of the current sensors is, as expected, the bubbler: ± 3 mm according to the specifications [5]. The two other techniques both result in an agreement with the bubbler on the order of 48 mm (standard deviation after bias removed).

An improved accuracy is expected from the radar sensor (CS476, [6]) to be installed in the autumn of 2014. Until then extensive characterization of the radar and the second pneumatic (bubbler) sensor will be carried out. Calibration measurements with respect to repeatability, linearity and drifts are performed. The experiment setup is shown in Figure 7 and preliminary results of the sensor repeatability are presented in Figure 8.

Fig. 5 An artist's impression of the planned official tide gauge station of the Swedish national network. The red hut exists and will be used to accommodate instrumentation for the tide-gauge station. A first preliminary installation is shown in Figure 4.

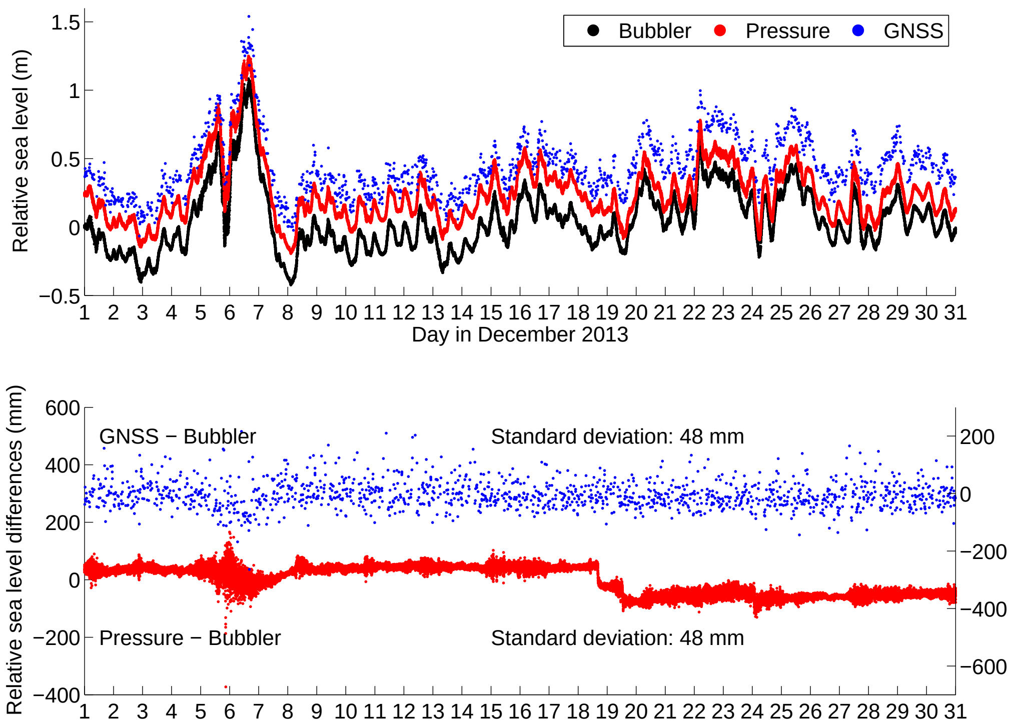

Fig. 6 One month of sea level observations from the Onsala site. Data from the bubbler sensor, one pressure sensor, and the GNSS tide gauge are shown in the upper graph. Differences with respect to the bubbler data are presented in the lower graph. As can be seen in the upper graph, the tides on the Swedish west coast are small and the large variations are caused by air pressure, wind, and ocean currents.

Fig. 7 The plastic tube with the bubble chamber lowered into the water (to the left) and the radar sensor (to the right) being tested in one of the showers at the observatory.

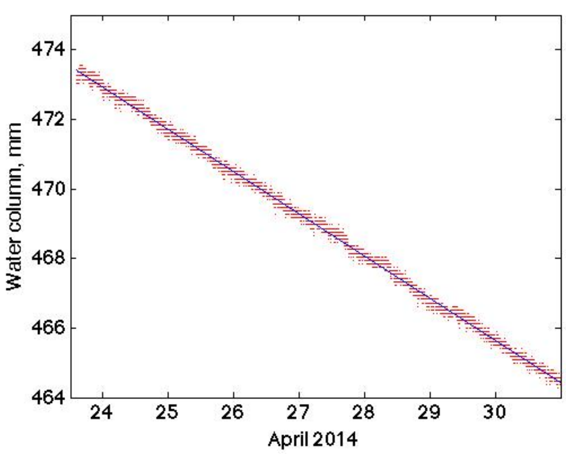

Fig. 8 Measurements of the water column with the bubbler sensor (see Figure 7) give an evaporation rate of 1.2 mm/day and a root-mean-square scatter about this model of 0.1 mm.

4 Outlook

We foresee an intensive period of construction work at the observatory. The plans are that the new tide-gauge station will be inaugurated in the autumn of 2014, whereas the installation of the twin telescopes will continue until 2016.

Acknowledgements

The authors gratefully acknowledge the support received from the staff at the national facility for radio astronomy, the Onsala Space Observatory.

References

1. Elgered, G., and R. Haas (2000). VLBI in the Service for Geodesy 1968–2000: An Onsala Perspective, *Proc. of the 5th European VLBI Network Symp.*, Eds. J.E. Conway, A.G. Polatidis, R.S. Booth and Y. Pihlström, Onsala Space Observatory, Chalmers University of Technology, Gothenburg, Sweden, pp. 209–216.
2. Haas, R. (2013). The Onsala Twin Telescope Project, Reports of the Finnish Geodetic Institute, *Proceedings of the 21st Meeting of the European VLBI Group for Geodesy and Astronomy*, Ed. by N. Zubko and M. Poutanen. 2013:1 (1), 61–65, 2013.
3. Lösler M., Haas R., Eschelbach C. (2013). Automated and continual determination of radio telescope reference points with sub-mm accuracy: results from a campaign at the Onsala Space Observatory. *J. Geod.*, 87(8), 791–804, 2013.
4. Löfgren J. and Haas R. (2014). Sea level measurements using multi-frequency GPS and GLONASS observations *EURASIP J. Adv. in Signal Processing*, 50, doi: 10.1186/1687-6180-2014-50.
5. Campbell Scientific (2010). *CS470 and CS471 OTT CBS Compact Bubbler Sensors*, Logan, Utah, www.campbellsci.com.
6. Campbell Scientific (2011). *CS475, CS476, CS477 Radar Ranging Sensors*, Logan, Utah, www.campbellsci.com.

Development of an Electromagnetic Interference Monitor from 1 GHz to 18 GHz

G. Gancio, J. J. Larrarte, E. Diaz, F. Aquino, S. Spagnolo

Abstract After conducting an interference monitoring campaign using equipment from Wettzell [1], the IAR decided to develop a new transportable RFI measuring system covering the range from 1 GHz to 18 GHz. For this, new components like a new antenna with a proper calibration certificate and a spectrum analyzer were acquired in order to improve the frequency range of the observations and the sensitivity of the system.

Keywords RFI monitoring, VLBI sites, TIGO, IAR, transportable

1 Motivation

When evaluating a location for a radio telescope, either to make astronomical observations or for geodetic VLBI observations (such as at TIGO), from the point of view of electromagnetic interference (RFI) it is to be expected that the selected site is as quiet or free from interference as possible. To assess these characteristics at a particular site, a system for monitoring electromagnetic interference is needed that is compatible with the radio telescope to be used, and for studying and monitoring the same frequency bands as to be used by the observing system. This equipment should have high sensitivity and allow the detection of signals from very low power, which would greatly affect the observations made by the telescope.

The duration of the monitoring for RFI signals at a selected site is also important, as there are likely sporadic signals that may or may not repeat over a day or on different consecutive days. The measurement duration is conditional upon the time available for site selection. It is desirable to have as many measurements as possible, in order to obtain a database of the site for the evaluation of the progress with time, or in subsequent measurements since the operation of the radio telescope. This is of importance when making the effort (along with the appropriate agencies) to maintain the spectrum allocated for scientific use [2] free from interferences which may occur during operation of the telescope.

Instituto Argentino de Radioastronomía – CONICET

2 System Overview

The monitoring system of interference is divided into three stages. In this article we will focus on the stage of radio frequency and data processing:

- RF stage: includes the measuring antenna, RF amplifiers, low noise, system calibration using noise diode, and spectrum analyzer.
- Status of control and monitoring: includes the hardware to monitor the status of the RF amplifiers and control system calibration and monitoring of the input voltages.
- Stage of acquisition: the acquisition and control software for measurement is linked to the stage of monitoring and control, as well as the spectrum analyzer in order to make the RFI measurements.

The software was developed in the programming language “C” on a Linux platform, allowing portability to other platforms if necessary. For RFI measurements, the software uses data from a configuration file editable by the user with the different observation parameters

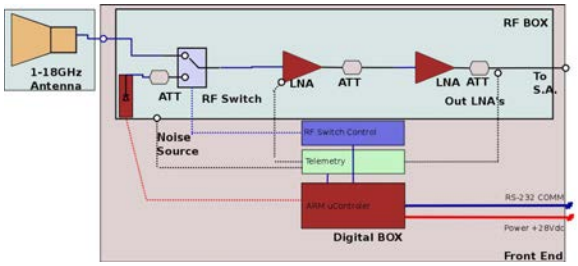

Fig. 1 RF Stage, block diagram.

such as start and end frequency, number of repetitions, resolution bandwidth or RBW, and pointing directions. The RF stage, or frontend, with its associated control is mounted on a custom antenna rotor, which allows observations on the horizontal plane orienting the antenna in different directions. The number of measuring points will be defined by the minimum bandwidth of the antenna, to the highest frequency. The polarization is changed mechanically, by rotating the axis of the antenna 90°. This system is in development at the time of writing this article. From the RF box, or frontend, an RF cable is routed to the spectrum analyzer. This cable should be short in order to minimize the signal attenuation; depending on the cable to be used the maximum length will be calculated.

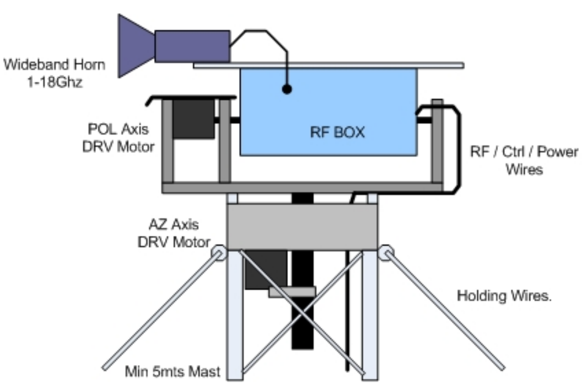

Fig. 2 Schematic view of the antenna rotor.

3 RF Stage Description

The RF stage is designed based on the following components, which were acquired for the present development.

Fig. 3 Picture of the antenna rotor under development.

- RF Antenna: EST-Lindgren model 3117 with radome, operational frequencies 1 GHz to 18 GHz, HPW 85°@ 2 GHz — 40°@ 18 GHz (E-Plane), Gain 3–10 dBi.
- RF Switch: HP8761B, insertion loss: 0.8dB @ 18 GHz.
- Low noise amplifiers: Miteq model AFS42 NF 2.5 dB, operational frequencies 1 GHz to 18 GHz, Gain 39 dB.
- Noise Source: NoiseWave NW346D, ENR:23 dB.
- Spectrum Analyzer: Agilent N9344C, DANL −144 dBm.
- RF Down link cable: Heliax, Insertion Loss 12 dB/10 mtrs.

To evaluate the system properties the different parameters of each component are analyzed according to the Figure 1 block diagram, resulting in the total system gain and system temperature and thus knowledge about the sensitivity of the system.

- **System gain:**
  The system gain is given by the sum of the gain of each component. For this the minimum gain values of each component are evaluated.

$$G_{sys} = G_{rfSwitch} + G_{amp} + G_{att} + G_{amp} + G_{rfCable}$$

$$G_{sys} = (-0.8 + 39 - 6 + 39 - 12)\ \mathrm{dB} = 58.2\ \mathrm{dB}$$

- **Receiver temperature:**
  The system temperature is given by the following equation, with the temperature or noise figure from the first amplifier being the most critical. In the equation, the temperature from the spectrum analyzer (DANL) should be included as the last parameter to evaluate; but as this is very low, the aggre-

gate value of temperature is negligible, and thus is not included to simplify the equations.

$$T_{rx} = T_1 + \frac{T_2}{G_1} + \frac{T_2}{G_1} + \ldots + \frac{T_2}{G_1}$$

where:
T_{rx}: Receiver temperature
T_n: Each stage temperature
G_n: Each stage gain (linear)
For Passive or active componentes must be used

$$T_{passive} = (L-1) \cdot T_a$$

$T_{passive}$: Passive component temperature
L: Loss factor
T_a: Physical component temperature

$$T_{active} = (F-1) \cdot T_a$$

T_{active}: Passive component temperature
f: Noise Figure $F = 10^{(F[dB]/10)}$
T_a: Physic component temperature

$$T_a = 290^{\circ} K$$

Evaluating the different component parameters gives:

$$T_{rx} = 330.28^{\circ} K$$

- **Receiver sensitivity:**
The receiver sensitivity is the parameter related to the minimum signal to be detected, thus allowing comparisons with other receiver systems.
Taking into account parameters from the antenna and observed resolution band width, the sensitivity is calculated in the form of flux density units as follows:

$$S_o = \frac{k \cdot T_{sys}}{\rho \cdot A_e \cdot \sqrt{B \cdot t}} \ [\mathrm{Wm^{-2}Hz^{-1}}]$$

where:
T_{sys}: Receiver temperature plus antenna temperature
A_e: Antenna effective area
"k" Boltzmann's constant
"B" Resolution bandwidth
"t" Integration time
"ρ": 1/2 due to the linear polarization of the "H" or "V" antenna
Using the relationships between the parameters of the antenna A_e, G_i, and K_a and maintaining an impedance of Z=50 ohms, the sensitivity can be expressed as:

$$S_o = \frac{0.133}{\rho} \cdot \frac{k \cdot T_{sys} \cdot K_a^2}{\sqrt{B \cdot t}} [Wm^{-2}Hz^{-1}]$$

where:

$$K_a = 3.24 \cdot 10^{-8} f(Hz) \sqrt{\frac{1}{G_i}}$$

$f(Hz)$: Observed frequency
G_i: Isotropic antenna gain [dBi]
Thus leaving the sensitivity according to the observed frequency.
Using the following parameters as an example we get a sensitivity of:
F_o =1413.5Mhz
B = 10KHz
T_{Int} = 0.1mSeg
G_i=5dB
T_{ant} = 12K
ρ=1/2

$$K_a = 3.24 \cdot 10^{-8} f(1413.5 \cdot 10^6) \sqrt{\frac{1}{5}} = 20.29$$

$$S_o = \frac{0.133}{\rho} \cdot \frac{k \cdot (330.28+12) \cdot 20.29^2}{\sqrt{10 \cdot 10^3 \cdot 0.1 \cdot 10^{-3}}} = 5.17 \cdot 10^{-19} \ \mathrm{Wm^{-2}Hz^{-1}}$$

$$S_{o[dB]} = -182.86 \ \mathrm{dBWm^{-2}Hz^{-1}}$$

In order to obtain a better time resolution, multiple iterations of the same set of observations are made. This provides a larger number of samples allowing for a better evaluation of the presence of possible interfering signals.

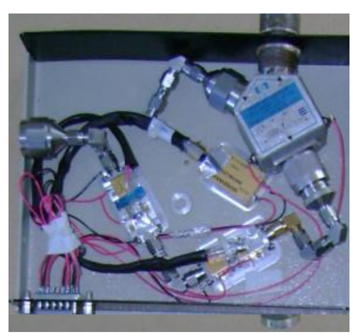

Fig. 4 Components of the RF stage.

- **System calibration:**
The system calibration is performed using a noise diode with an "excess noise ratio" (ENR) of 23 dB; in addition, an attenuator is used in order to maintain a similar value for the expected system noise. At the end of each measurement cycle, two measurements are realized with the same settings as used before: the first with the noise diode off and the second with the noise diode on.
With this measuring cycle, similar to a three-state Dicke type receiver, one can obtain a measure of the gain of the system and the temperature of the receiver, allowing the data to be calibrated and understand the functioning of the system.
The temperature of the receiver is evaluated as follows:

$$ENR = 10^{\frac{ENR_{dB}}{10}}$$

$$T_o = T_{amb}$$

$$T_hot = T_o \cdot (ENR + 1)$$

$$Y = \frac{P_{on}[W]}{P_{off}[W]}$$

$$T_{rcv} = T_o \cdot (\frac{ENR}{Y-1} - 1)$$

$$G_{ercv} = \frac{P_{on}[W]}{k \cdot B[Hz] \cdot (T_{hot} + T_{rcv})} .$$

Figures 5 and 6 show the actual measurements and a system evaluation. It can be seen that the segment of 10 GHz to 14 GHz has a higher gain ripple level and the behavior translates into an increase in the system temperature. This is probably due to an adaptation mismatch of the amplifiers operating in that frequency.
It can also be seen that the temperature of the receiver is above 400 K when the calculation showed a system temperature of 330 K. This is due to a mismatch in the real components parameters or additional attenuation in the input transmission line, as well as the RF switch. In order to enhance the system parameters and reduce the input attenuation, higher quality RF cables and connectors should be used at the input stages.

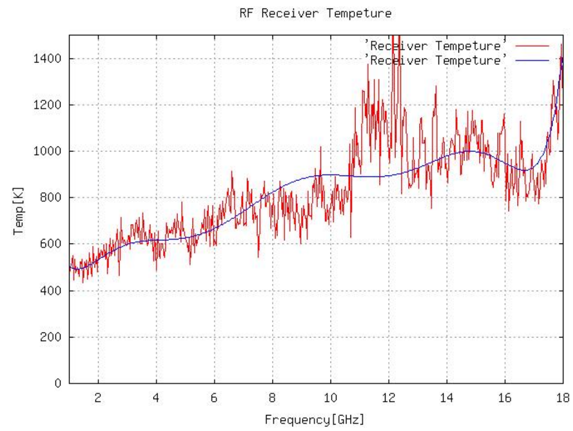

Fig. 6 System temperature.

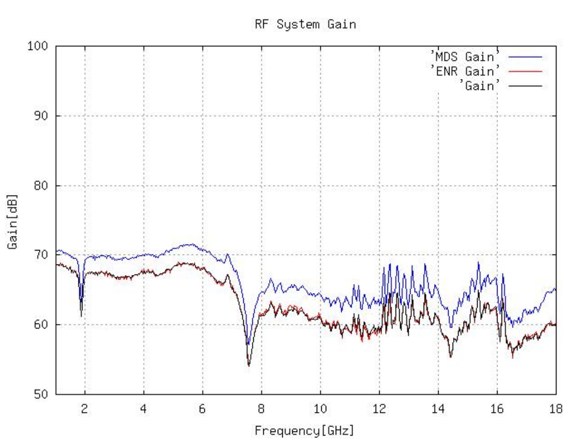

Fig. 5 System gain.

4 Post-Processing of the Measurements

The raw data from the spectrum analyzer as well as from the control and monitoring modules are published online on a Web page for a visual check of system functionality. Go to http://www.iar-conicet.gov.ar/ggancio/rfi/rfi_stat.html for online RFI data.

After generating the measurement files, according to the previously set modes, the off-line processing is realized. In principle two analyses were performed: The first analysis takes all measurements made without distinguishing pointing direction or antenna polarization in order to obtain a global profile of the observed spectrum. With this set of measurements the maximum and minimum percentiles of 10 and 90 were obtained. These indicate the detected interference over a percentage depending on the number of samples, thus giving an idea of spectrum occupancy versus time observed. The second analysis evaluates each observed polarization and each measured direction separately, thus giving an idea of the RFI direction from which it came or some mode interference. This analysis is carried out the moment an RFI is identified in order to characterize and analyze its features in more detail. If the case allows it, with an RFI located in a frequency band allocated for passive use only, one may give notice to the national regulatory agency to intercede in the case. In both cases raw data is processed in the same manner; the difference lies in the number of files to process. Taking all the files in the first case and by filtering in polarization and direction in the second one. The

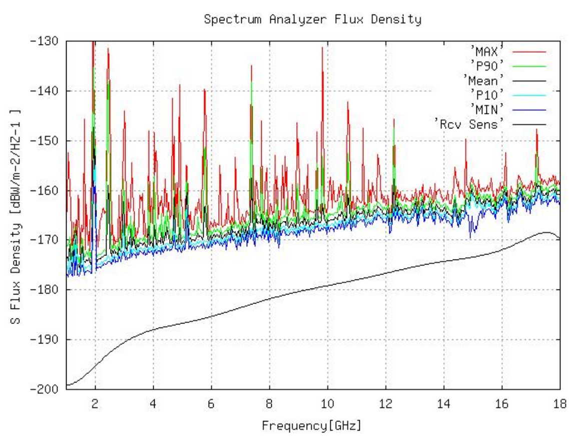

Fig. 7 Resulting spectrum.

raw data, in units of dBm given by the spectrum analyzer, are transformed into flux density units, related to the antenna input. With this the system parameters such as gain variations or antenna parameters are removed from the resulting plots. This unit also permits to evaluate according to the recommendations of the ITU [3] if the interference levels are detrimental or not for a radio astronomy station. The simplified equation for transforming units is as follows [4]:

$$S_{dB} = P_{SA[dBm]} - 10log_{10}B - G_{rcv[dB]} + K_A - 35.77$$

$$S_{dB} = [\mathrm{dBWm^{-2}Hz^{-1}}]$$

Figure 7 shows a sample image, which was obtained from 56 measured scans using a resolution of 30 kHz RBW in the range from 1 GHz to 18 GHz in the geographical location of the IAR (La Plata, Argentina). Figure 8 depicts a direction analysis for RFI incidence angles using data from [1].

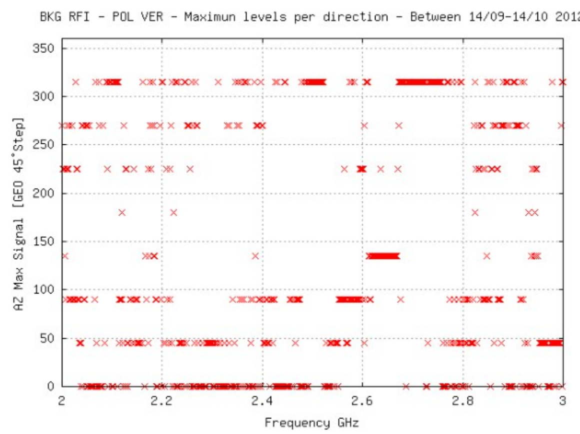

Fig. 8 Amount of RFI detected vs. direction.

5 Conclusions

A development of a new instrument for measuring electromagnetic interference "RFI" in order to perform a site characterization in order to evaluate potential sources of interference was presented. The development was designed to be portable, allowing their installation virtually anywhere. Once installed for evaluation in the IAR, it will generate a database for local RFI, operating continuously, allowing to assess their performance and to make improvements to the system.

References

1. "Radio Frequency Interference Observations at IAR La Plata" EVGA 2013 Proceedings, p. 49, 2013.
2. http://www.cnc.gov.ar/infotecnica/espectro/cabfra.asp (CNC Comision Nacional de Comunicaciones).
3. http://www.itu.int/rec/R-REC-RA.769 (ITU RA Recomendation 769).
4. SSSM System Design Considerations (R.P. Millenaar — Astron).

A New Generation of Platforms for CDAS

Renjie Zhu[1,2], Xiuzhong Zhang[1], Yajun Wu[1,2], Shaoguang Guo[1], Ying Xiang[1]

Abstract A new platform was finished by the end of 2013. It contained two Xilinx K7 FPGAs for data processing, in addition to the capability of supporting two channels that each sample 512 MHz bandwidth or a single channel that samples 1024 MHz bandwidth. Compared with the previous platform, which consists of four Xilinx V4 FPGAs, the new one not only updates the key chips for DSP but also adds two 10-Gigabit Ethernet SFP+ ports for data transmission. The new platform also improves the performance and lowers the cost.

Keywords Backend, platform, CDAS

1 Introduction

With the development of VLSI technology, the capacity and performance of the FPGAs are growing exponentially. Therefore, we can achieve more and more complex algorithms in one chip.

With the previous platform used in CDAS, each module could sample 512 MHz bandwidth and convert it with four BBCs using a DDC algorithm with four Xilinx Virtex4 LX series FPGAs. As the CDAS has the capability of four input IF channels and 16 output BBCs, more than four modules are needed.

In contrast, with the new platform, one module has the capability of using dual channels to sample 512 MHz bandwidth apiece or using one channel for 1024 MHz bandwidth sampling. Compared with the previous platform, it not only updates the key chips from Xilinx Virtex4 series FPGAs to Kintex7 series FPGAs for DSP but also adds two 10-Gigabit Ethernet SFP+ ports for data transmission. The new platform also improves the performance and lowers the cost. It can deal with two input IF channels and produce output with at least eight BBCs using one chip. Furthermore, the output data can be recorded by commercial disk array server with the 10-Gigabit Ethernet. The new platform will be used in CDAS2.

After that, another platform, which will be implemented with a 5-Gsps ADC, will be put on the agenda in the near future.

2 The New Platform

As shown in Figure 1, the new platform consists of one ADC for sampling, two FPGAs for data processing, and two SFP+ ports for data transfer. PPC and other peripherals make the system run in standalone mode.

Platform characteristics:

- Dual channel ADC with 8-bit resolution
- 1 Gsps sampling rate per channel
- 2 Gsps in Interlaced Mode
- One Xilinx Virtex4 FX for control
- Two Xilinx Kintex7 for data processing
- Two SPF+ for 10-Gigabit Ethernet
- One RTC for system time

The FPGA1 is the master chip with two 10-Gigabit Ethernet ports attached. The FPGA2 is a servant chip, and there is no high speed port for data output. If the

1. Shanghai Astronomical Observatory, Chinese Academy of Sciences
2. Key Laboratory of Radio Astronomy, Chinese Academy of Sciences

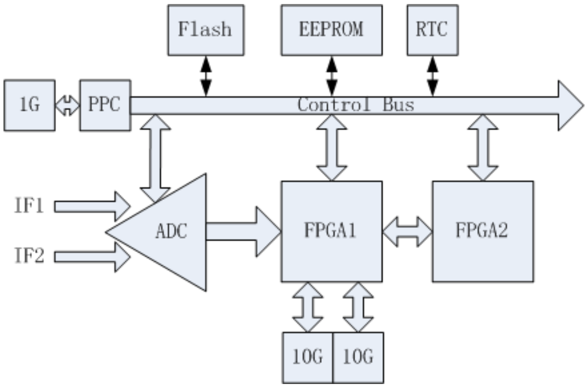

Fig. 1 The construction of the new platform.

Fig. 2 The module of the new platform.

master chip can meet the requirements for data processing, the other chip can be omitted. The control system is set up by PowerPC405, which is embedded in Xilinx Virtex4 FX series FPGAs. With peripherals such as flash, EEPROM, RTC, and Gigabit Ethernet attached, it can work in standalone mode.

The FPGAs used by the new platform can be selected from the Xilinx Kintex7 series, whose package is FFG901. Table 1 shows the differences between Xilinx Virtex4 LX160, which was used in the previous platform, and Xilinx Kintex7 480T, which can be used in the new platform for the same amount of resources. Compared to the Virtex4 LX160, Kintex7 480T has more than ten times as many DSP slices and six times as many RAMs, which are more useful for the complex algorithms.

Table 1 Virtex4 LX160 and Kintex7 480T Resources.

Parameters		XC4VLX160 [1] -10FF1148C	XC7K480T [2] -1FF901C
Logic Cells		152,064	477,760
CLB	Distrubuted RAM (Kb)	1,056	6,788
	DSP Slices	96	1,920
Block RAM	18 Kb	288	1,910
	36 Kb	—	955
	Max	5,184	34,380
DCMs/CMTs		12	8
PCIe		–	1
GTXs		–	28
XADC		–	1
Total I/O banks		17	8
MAX User I/O		960	380

3 PFB Version of CDAS2

With the new platform, a PFB version of CDAS2 is undergoing testing now. As Figure 3 shows, it consists of one module with only the master Kintex7 FPGA on it.

CDAS2 now works in two modes:

- 512 MHz Dual IF Mode:
  For each IF, it has
  - 512 MHz bandwidth input
  - 16 output channels
  - 32 MHz bandwidth for each output channel
- 1024 MHz Single IF Mode: 16 channels x 64 MHz baseband output
  - 1024 MHz bandwidth input
  - 16 output channels
  - 64 MHz bandwidth for each output channel

Fig. 3 PFB version of CDAS2.

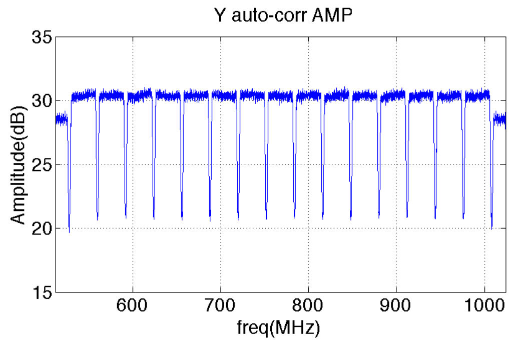

Fig. 4 The bandpass of PFB.

Due to the PFB algorithms, the first channel in each mode is different from the others. Figure 4 shows the characteristics of the 512 MHz (512–1024 MHz) bandwidth.

4 Future Plan

In the near future, a 5-Gsps ADC platform will be applied. This platform consists of two modules—an ADC module (Figure 5) and a DSP module (Figure 6). These two modules are connected by the backplane.

- ADC module
  - Quad channel ADC with 10-bit resolution
  - 1.25 Gsps sampling rate in four-channel mode
  - 2.5 Gsps sampling rate in two-channel mode
  - 5 Gsps sampling rate in one-channel mode
- DSP module
  - ARM7 for control
  - Xilinx Kintex7 480T for data processing
  - 6 SPF+ for TenGiga Ethernet
  - 8 GB DDR3
  - 1 Gsps DAC output

After connecting these two modules, it can be a new backend.

For this backend in the future:

- Wider bandwidth can be processed in one chip
- Original sampling data can be transmitted over the network
- Intermediate results can be temporarily stored in DDR3
- DAC (analog) output will be possible.

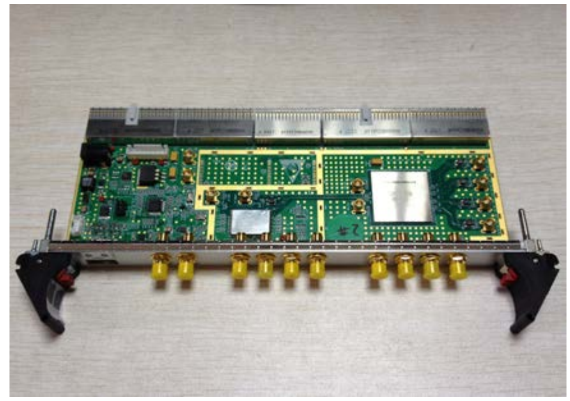

Fig. 5 5-Gsps ADC module.

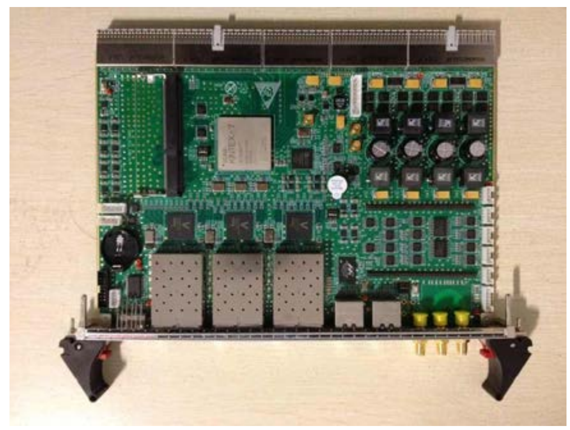

Fig. 6 5-Gsps DSP module.

Table 2 Comparison among the three platforms.

Platform	CDAS	CDAS2	Future
Number of input IFs	1	2	4
Sample mode [CH@Msps]	1 @ 1024	2 @ 1024 1 @ 2048	4 @ 1024 2 @ 2048 1 @ 4096
FPGA series	4 × Virtex4 LX160	2 × Kintex7 480T	1 × Kintex7 480T
Interface	VSI	2 × 10-GigE	6 × 10-GigE
Memory	No	No	8 GB DDR3
DAC	No	No	Yes
Planned schedule	complete	2014	2015

5 Summary

Comparing the three platforms described above, Table 2 shows the differences among the three platforms.

We plan to test the CDAS2 in our VLBI stations this year and prepare the 5-Gsps platform for the future.

References

1. Virtex4 Famaliy Overview, DS112(V3.1), 1, August 30, 2010
2. 7 Series FPGAs Overview, DS180(V1.13), 3, November 30, 2012

VLBI Data Playback in FPGA

Jiangying Gan, Zhijun Xu, Xiuzhong Zhang, Shaoguang Guo, Renjie Zhu, Ying Xiang

Abstract The correlator as the VLBI core data preprocessor is a complex, high-speed, and real-time signal processing system. We have successfully used it to process VLBI observations of the Chang'E mission. For the VLBI hardware correlator (HCORR), the original VLBI data of the stations must be read and preprocessed before correlation. We focus on VLBI data playback at the correlator for Chang'E-3 data of 2013. The VLBI playback system uses a 1-Gb Ethernet network to transmit station data and design some preprocessing method such as data correction and data decoding specific to VLBI data. The Chang'E-3 results show that the system is able to playback VLBI data in real-time, while ensuring data validity and meeting the requirements of the VLBI observations. We conclude with an outlook on future research plans for the VLBI data playback system.

Keywords VLBI, correlator, playback, pre-processing

1 Introduction

Very Long Baseline Interferometry (VLBI) is an important radio astronomy technique (Zheng) that is widely used for high-precision measurements of deep-space probes. We have successfully used VLBI to perform observations for the Chang'E mission. In China, the VLBI infrastructure is comprised of the VLBI stations, data pre-processing, correlator, post-correlator, SKD, orbit, location, and so on. The correlator is the core device of the VLBI data preprocessing unit able to calculate important parameters such as the delay, delay rate, correlation amplitude, and interferometric phase. The correlator can be divided into hardware correlator and software correlator. High-speed, large-scale correlators are mostly hardware correlators, so the hardware correlator is very important. The hardware correlator and its data playback system use a special hardware platform such as a Field Programmable Gate Array (FPGA). The rapid development and optimized mutual integration of the FPGA with high-speed networks made miniaturization possible for a low-power, high-speed, and real-time VLBI data playback system.

Shanghai Astronomical Observatory, Chinese Academy of Sciences

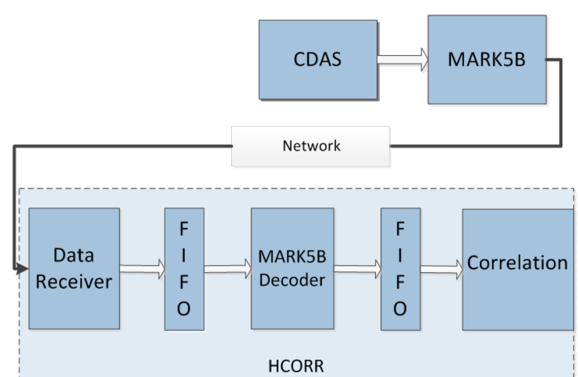

Fig. 1 Diagram of the VLBI data system.

Figure 1 shows the VLBI data system. The system uses the Chinese Data Acquisition System (CDAS) to collect original VLBI data and the Mark 5B system to record and playback the observed data. The HCORR shall receives the VLBI data from the Mark 5B system via Internet and calculates the delay, delay rate, correlation amplitude, and interferometric phase with proper control parameters given from the correlator control computer, and then transmits the correlation results to the post-correlator. HCORR uses FPGA as the hardware platform and mainly includes the data playback system and correlation module. The VLBI data playback of the correlator includes the network control data playback module, the data receiver, and the cache module. In December 2013, the VLBI system was used in the Chang'E-3 mission. We used the HCORR real-time mode and post-correlation and the results proved that the requirements of the Chang'E-3 mission can be met.

2 System Description

For the Chang'E-3 mission, the specifications for the correlator are the following (Zhang, 2012):

- Number of stations: four
- Bandwidth per station: 64 MHz
- Input resolution (max): 1–32 bits
- Correlation points: 1024 or 2048
- Data input format: Mark 5B

The hardware correlator design can reach 128-MHz bandwidth per station in real-time data processing. Figure 2 shows the conceptual configuration of the hardware correlator system. There can be four observation stations, e.g., Beijing (BJ), Kunming (KM), Urumchi (UR), Shanghai (SH), or any other station that can participate in the VLBI observations. The stations' data is transmitted through the network and is recorded to the data cache and distributed components (DDU). One DDU corresponds to one station. Finally, the DDUs distribute the data to the correlator across the 1-Gb Ethernet network. The dotted line encircles the hardware correlator modules. The hardware correlator VLBI data playback interface module (VSIDOM) receives the VLBI data from the DDU system, pre-processes the data w.r.t. the data format, and then dumps the pre-processed data into the correlation system. The correlation system is the core algorithm of data server, which is used to calculate the correlation of stations. The correlation system includes the Fourier transformation and cross-multiplication module (FFT and MAC) as well as the Long Time Accumulation module (LTA). The Computer Control (CCC) is the correlator and operation computer, which is used to send proper control parameters and to save the correlation data as a structured file system for the post-correlator.

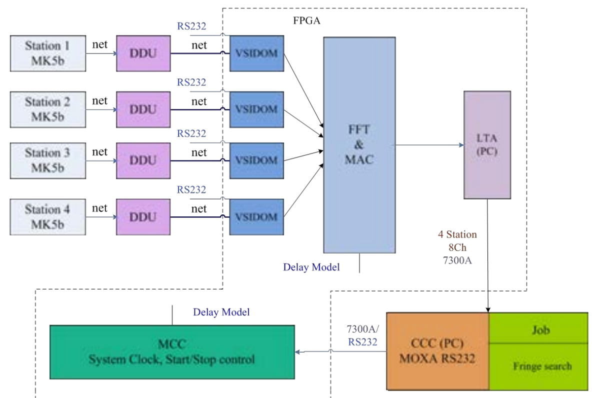

Fig. 2 Diagram of the HCORR system (Xu, 2006).

The VLBI data playback system is an indispensable part of the hardware correlator system. It reads station data and pro-processes raw VLBI observation data needed for the correlation system. The overall scheme for the VLBI data playback of HCORR is shown in Figure 3 for one station (VSIDOM).

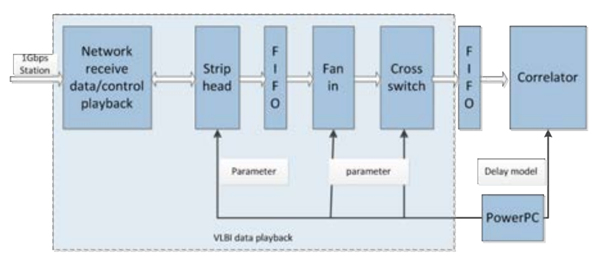

Fig. 3 The VLBI data playback of the HCORR.

2.1 Network Module

The network module has a 1-Gb Ethernet input port to connect to the data cache and distributed components (DDU) for data playback. It allows the user to read data via the 1-Gb Ethernet interface and to write data to registers for the next module. It will feedback full mark to control the DDU data playback continue. Data are transmitted from the stations in Mark-5B-formatted UDP packets. The cache space of the hardware correlator in real-time mode is limited because of the use of FPGA. When all stations' data is synchronized all the time, just process continuously. When checked, if some stations data reach synchronization time but other stations do not, then wait for the feedback client to stop sending data, otherwise it will cause data overflow. When all stations are synchronized, tell the client to send data continuously, then recorded data can be processed validly. In this network interface data are transmitting from the stations in Mark5B-formatted UDP packets, and improving response mode, to ensure that the data transmission is more reliable. The network interface module of the VLBI data playback system (VSIDOM) and the data playback module in DDU form a complete set of network transmission system, using the client/server mode, data playback module in DDU send part for the client network, network interface module of VSIDOM for the server. When the DDU through Ethernet received data from the observatory stations, began to prepare to send data to the VLBI data playback system. There are several steps:

1. Connection to the Ethernet, the client sends an ARP request frame to ask the server MAC address, after the server receives an ARP request frame and send ARP reply frame, if client receives an ARP reply from the server then start data transfer.
2. The client sends a packet and waits for feedback data. At the same time, the timeout timer is started. If received server response frame, continues to send the next frame, timeout timer resets at the same time, if the timeout timer more than set threshold, argues that the UDP packet loss, client resends just the frame data.
3. The server receives packets from the determined client. When the FPGA pre-process data rate is less than the capacity of client send data, not send reply to the client server network. If the recorded data can be processed continuously as per real time data, then send the reply packet to client.

2.2 Parameters

The VLBI data pre-processing parameters are provided by the CCC. The FPGA communicate with the CCC through the Peripheral Component Interface (PCI) bus which will drive by the PCI drive module. The PCI rate can reach 264 MB/s, which can meet the real-time data playback mode. The VLBI data pre-processing parameters adhere to a specific format and include:

- Strip head parameters: correlation start time and end time, frame number.
- Fan in parameters: the number of valid bit streams.
- Cross switch parameters: each bit need in position.
- And other parameters such as system reset, system start, FFT start and so on.

2.3 Pre-process Module

The main specification of the pre-processing interface module was described in Figure 3. The infrastructure of course provides the FPGA top-file, connecting three modules includes the strip head module, the fan in module, and the cross switch module. The pre-processing module has the capability to frame header parsing, CRC checking, get the raw and valid data, arrange data in the required format, send the frame header information and error number to the correlator control and operation computer which is used to check playback time synchronization. As normally, there are four stations playback and process at the same time, but at some special status, fewer than four station, then need do some special processing. There are several situations:

- Before the start of the HCORR system. To shield the station which cannot playback VLBI data, and pad with zeros as the station data.
- In running. If stop data playback, there will timeout overflow and give up the scan data all station. If cannot restore at a long time, then need to stop the HCORR system, turn off the station, restart HCORR system.

The function of the strip head module is strip frame head and get the data. Mark 5B format data has frame header and data field. A frame size is 10016 bytes includes 16 bytes frame head and 10000 bytes data. From the frame header we can get synchronous word such as ABADDEED, can get frame number within seconds, BCD time stamps and CRC code. The mainly functions of strip head module are:

- Determine synchronous word. In normally, ever frame set synchronous word to constant ABAD-

DEED, only find the constant means the frame is start.

- BCD time stamps. The time stamp in the header also is used to determine the data playback start or stop. As the hardware correlation actions must be required to synchronize timing between the stations. When the start time is reached, the correlator requests the DDU to send data and process recorded data. By comparing the time stamp in the header with stop time from CCC, if the same then the data processing stop.
- CRC. Calculate synchronous word, custom information, seconds time frame number, BCD code calculation to a check code, comparing with the CRC of frame header, if the same, can be concluded that the frame header information is correct, so as to start recording data.
- Finally combined the time stamps (48 bit) from frame header and error number (16 bit) which count the error frame into two 32-bit data, send to the CCC system.

Fan in module according to the number of effective bit-stream which given from the CCC, recovering data word from Mark 5B recording equipment each time sampling to get valid data bits, such as effective for 1 bit, need 32 times to recover a 32-bit data and one bit for each time, from low to high, each bit combine with 31-bit zeros to 32-bit data, will rearrange data in chronological order, and transfer to the cross selection module. Cross switch module shall cross the restoration bit-stream with cross parameters given from the CCC to the new order data, and finally record data to the buffer.

3 Conclusions

The data is Chang'E-3 (Chinese Lunar Exploration Program) observations of lunar flight information on December 13, 2013. There are four observation stations: Beijing (BJ), Kunming (KM), Urumchi (UR), and Tianma (TM). The HCORR can support the recording and playing back speed is 256 Mbps. Figure 4 shows the time delay analysis of HCORR for the collected satellite data. Each point represents a processing unit (scan), is a satellite data point, each scan is 5-s data. Figure 4 is the difference between the two scan begin processing time. From the figure you can see that the time delay is 4 s to 6 s, normal for 5 s. When more than 5 s is because the process data rate is less than the capacity of playback real-time data, and less than 5 s because is the processing of the correlator faster than real-time. The result was checked to make sure the VLBI data playback system can meet the needs of the real-time playback. Figure 5 is the result of real-time correlator, while the left six graphs present the correlation delay and the right six graphs show the correlation delay rate. There are four stations (BJ, KM, UR, and TM). BK means BJ and KM, BU means BJ and UR, BT means BJ and TM, KU means KM and UR, KT means KM and TM, UT means UR and TM. Using the real-time mode of

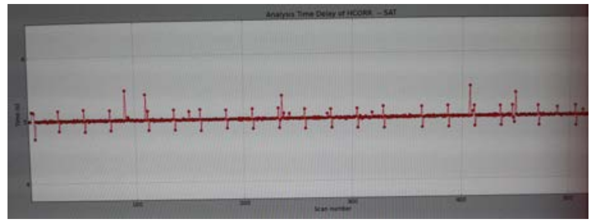

Fig. 4 Time delay analysis of HCORR.

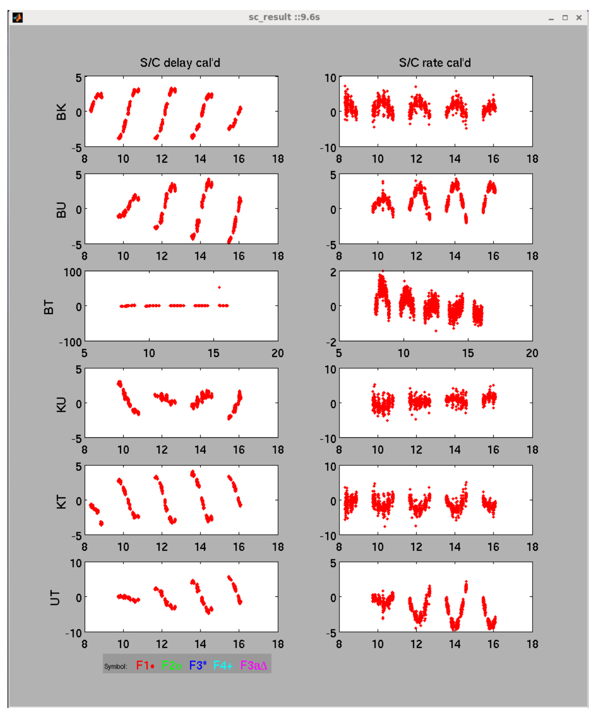

Fig. 5 Delay and delay rate.

HCORR and post-correlator, we can handle the result of the correlation processing at the same time.

4 Future Plans

The SHAO participated in the Uniboard development with JIVE as a member of international consortium. So, in the near future our group will port the whole system to Uniboard for speed improvement and supporting more modes. The next generation hardware correlator design goal are (Hargreaves, 2011):

- Number of stations: four
- Sample rate per station: 2 Gbps
- Input resolution (max): 1–32 bits
- Correlation points: 1024 or 2048
- Data Input Format: Mark 5B
- VLBI data input interface: 10-Gb Ethernet
- CCC control interface: 1-Gb Ethernet

References

1. Weimin Zheng, Yan Yang. VLBI software Correlator Progress and Its Applications in Deep Space Exploration. *World Sci-tech R and D*, 27(5), pp. 7-15, 2005
2. Zhjun Xu. Real Time Correlator in FPGA. *IVS 2006 General Meeting Proc.*, pp. 89-92, 2006
3. X.Z.Zhang. CVN Correlator and Its Future. *New Technologies in VLBI Astronomical Society of the Pacific Conference Series*, pp. 287300, 2012
4. Jonathan Hargreaves, Harro Verkouter. EVN Correlator Design, Version 2.0 *http://www.radionet-eu.org/fp7wiki/lib/exe/fetch.php?media=jra:uniboard:evn correlator design mar2011.pdf*

Recent Geodetic Activities of the Shanghai VLBI Correlator

Wu Jiang, Fengchun Shu, Fengxian Tong, Weimin Zheng

Abstract Recent geodetic activities concerning the Shanghai VLBI Correlator are reported in this paper. A more accurate delay model was implemented in the domestic correlator job generating software, which has been used for the VLBI sessions for tracking satellites and the Chinese domestic geodetic VLBI program. The comparison results of model delays with Calc9.0 will be shown. We also managed to develop an offline software function to convert the correlator output into FITS-IDI format. Furthermore, we obtained some experience in processing a few geodetic sessions with an ad hoc DiFX correlator and the HOPS software, the final results were very promising. A new hardware cluster dedicated to DiFX was constructed. It will expand to a platform of more than 300 cores, 300TB RAID, and eight Mark 5 units by 2014.

Keywords Geodesy, VLBI, correlator, DiFX

1 Introduction

Shanghai Astronomical Observatory (SHAO) organizes the Chinese VLBI network (CVN) and operates the correlator center. The correlators including hardware correlator and software correlator were developed at the beginning of this century. They have already played an important role in the missions of Chinese lunar explorations. Recently, SHAO also adopted the well known DiFX correlator in the correlator center, named SHAO-DiFX. It is aimed to correlate the astrophysical and geodetic VLBI observations.

Shanghai Astronomical Observatory, Chinese Academy of Sciences

2 Activities of Shanghai Correlator

2.1 Events of Domestic Software Correlator

The domestic software correlator (SCORR) is dedicated to the data processing of the Chinese domestic VLBI observing programs, inclusive of the Chinese deep space exploration project for tracking spacecrafts and the CMONOC project for monitoring the Chinese regional crustal movements. Recently, a more accurate delay model was implemented in the correlator job

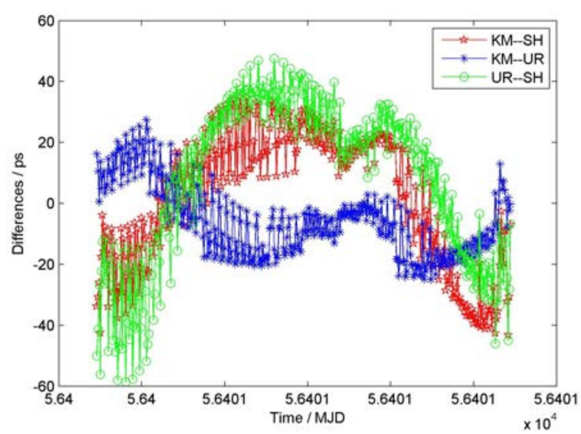

Fig. 1 Comparison results of model delays between SCORR and DiFX-Calc9.0.

generating software, which was used for VLBI sessions of tracking satellites and the Chinese domestic geodetic VLBI observing program. Comparison tests of model delay calculations were carried out between the software in SCORR and DiFX-Calc9.0. Figure 1 shows the comparison results of the model delays in a hypothetical 24-h geodetic experiment. A special schedule file was generated with SKED for the experiment. 360 scans and 67 sources were scheduled. Each scan spanned two minutes and always included the same three Chinese stations. The model delays on the three baselines were calculated separately with the software of the two correlators. The level of the delay differences is in several tens of pico-seconds.

2.2 SHAO-DiFX Correlator

As the DiFX correlator is of high performance and has comprehensive output formats for astrophysics and geodesy, it has been adopted and operated in worldwide correlator centers. Since September 2012, DiFX 2.1 was installed in an ad hoc 36 Intel X5650 (2.67 GHz) core cluster at SHAO. After testing and operating for about one year, a new DiFX platform was constructed in January 2014 (see Figure 2). Features of the DiFX platform are listed in Table 1. The maximum speed of the cluster is about 1 Gbps for each station in a four station correlation pass.

Fig. 2 Diagram of the DiFX platform and Mark 5 units.

Table 1 Deployment of the first stage SHAO-DiFX system.

Device	Parameters
DiFX version	DiFX 2.2, DiFX 2.3 and trunk
Head node	2x6 cores, Intel E5-2620 CPU, (2.0 GHz) 64 GB Memory
Computing nodes	3 nodes, each has 2x8 cores, Intel E5-2609 CPU (2.4 GHz), 64 GB Memory
I/O nodes	3 RAID6 60TB
Network connection	10G Ethernet,1G Internet
Mark 5 units	6, Mark 5A/B/B+
Output formats	FITS and Mark IV
Post processing	HOPS3.8, HOPS3.9, AIPS

3 Some Results

In 2013, four domestic geodetic VLBI experiments were carried out using 16 frequency channels allocated at the S/X bands. Three experiments were recorded at a data rate of 256 Mbps with 8 MHz bandwidth and one at 1024 Mbps with 32 MHz of bandwidth in each channel. The data correlation was performed by both the SCORR and the SHAO-DiFX. The output of the DiFX correlator in Mark IV format was further processed with the HOPS software. Figure 3 shows the fringes of the newly built Tianma 65-m telescope (T6) to the Seshan 25-m antenna in one of the experiments. The observing was carried out in a way similar to that of IVS sessions. The fringes in both the S and the X bands were detected. The output of DiFX in Mark IV format was processed with HOPS to generate the geodetic database, and the position of the T6 station was estimated with Calc/Solve.

The 1024 Mbps data rate experiment was carried out to detect and estimate the positions of 85 selected faint sources with a higher sensitivity attributed to a wider bandwidth. Through the experiment, 18 out of 85 selected sources were newly determined. One of the fringes at X-band from the Seshan—Urumqi baseline in the experiment is presented in Figure 4.

Meanwhile, two milli-second pulsar (MSP) VLBI astrometric experiments with CVN were successfully

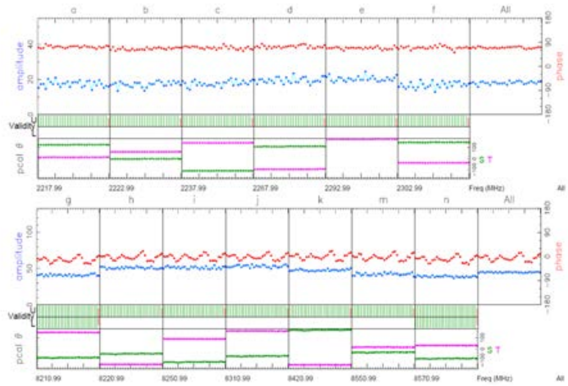

Fig. 3 Fringes of Tianma (T6) 65-m telescope to Seshan 25 m in S/X band.

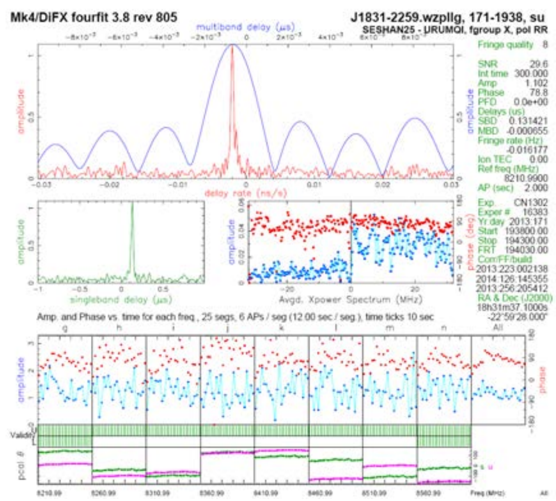

Fig. 4 Fringes of the CVN 1 Gbps observational data.

correlated with the DiFX correlator in 2013. The target pulsar was MSP J1939+2134. The experiments were carried out in S-band with 256 MHz bandwidth in total. The parallaxes of J1939+2134 were reduced through the phase referencing mapping method. The image of the target pulsar is plotted in Figure 5.

Off-line FITS format conversion software was developed and used at the SCORR correlator. Some comparison tests were made between the FITS format outputs of SCORR and DiFX. Figure 6 presents the results for the same geodetic observational data. The outputs of correlating all ten X-band frequency channels in a scan were converted to the FITS format. In Figure 6, the top shows the means and the deviations of the phase differences in each channel. The bottom shows the differences of phases and amplitude in a frequency channel.

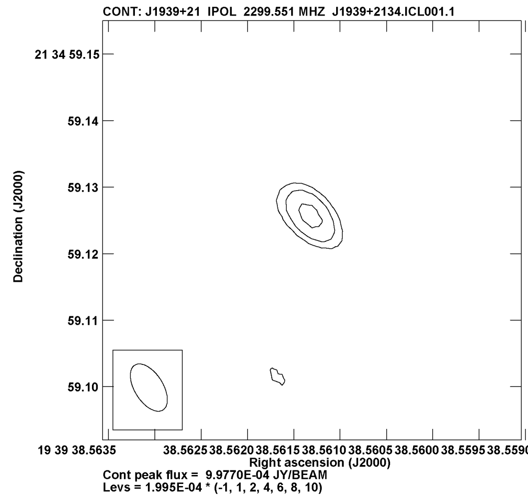

Fig. 5 Image of MSP J1939+2134 with CVN (beam size=7.95*4.28 mas).

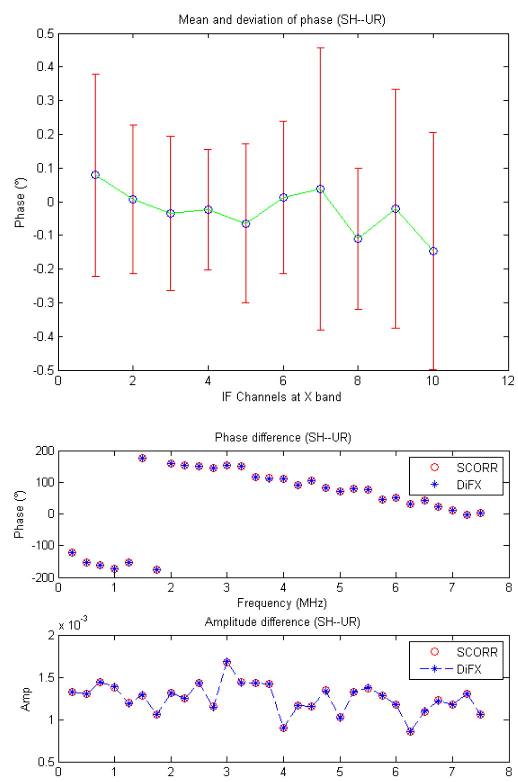

Fig. 6 Comparison results of the FITS format outputs of two correlators.

It implies that the phase differences of the two FITS format outputs are within 0.5 degrees.

4 Conclusions and Future Plans

The precision of delay measurement and reliabilty of SCORR correlator will be improved further for future deep space missions. At the same time, it will provide some support for astronomical and geodetic observations. SHAO-DiFX will be dedicated to correlating astrophysical and geodetic VLBI sessions. More computing nodes and redundant arrays of inexpensive disks (RAID) sources, including 300 cores, 300 TB RAID, and Infiniband network, are planned to be added to the cluster system in 2014. It will provide services for domestic and international VLBI observations. For example, it can process some IVS sessions if possible.

Acknowledgements

The work was supported by the National Natural Science Foundation of China (U1331205).

References

1. Deller A T, Brisken W F, Phillips C J, et al. DiFX-2: a more flexible, efficient, robust, and powerful software correlator. Publications of the Astronomical Society of the Pacific, 2011, 123(901): 275-287.
2. Brisken W F. A Guide to the DiFX Software Correlator, version 2.2. http://cira.ivec.org/dokuwiki/lib/exe/fetch.php/difx/difxuserguide.pdf. Jun, 2013.
3. HOPS. http:// www.haystack.mit.edu/ tech/vlbi/hops.html.
4. Shu F, Zheng W, Zhang X et al. Shanghai correlation system upgrade for geodetic application, in Proceedings of the 19th European VLBI for Geodesy and Astrometry Working Meeting, edited by G. Bourda, P. Charlot, and A. Collioud, pp.87-91, 2009.
5. Jiang W, Shen Z, Shu F, et al. The progress of adapting DiFX correlator for Chinese VLBI network.(In preparation)
6. Calc/Solve. http://gemini.gsfc.nasa.gov/solve/.

Hardware Correlator Development at SHAO

Zhijun Xu[1], Jiangying Gan[1], Shaoguang Guo[1], Xiuzhong Zhang[1], Renjie Zhu[1,2], Yajun Wu[1,2], Ying Xiang[1]

Abstract The CE-1 and CE-2 hardware correlators have been used for the Chinese Chang'E-1 and Chang'E-2 missions. Recently, the CE-3 hardware correlator has been successfully used for the Chang'E-3 mission. This paper presents the development of the hardware correlator at SHAO and some results of the Chang'E-3 mission.

Keywords Hardware correlator, FPGA, Chang'E

1 Introduction

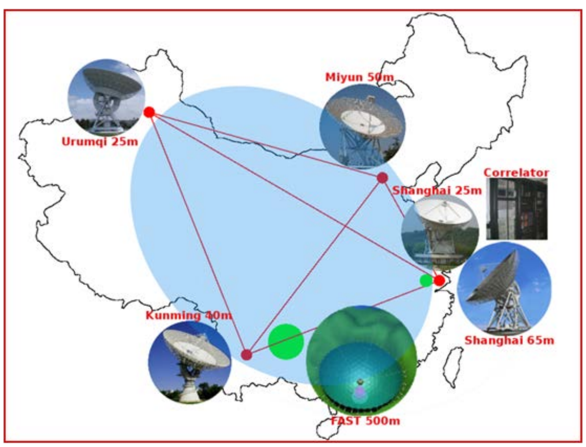

Fig. 1 Chinese VLBI Network.

1. Shanghai Astronomical Observatory, Chinese Academy of Sciences
2. Key Laboratory of Radio Astronomy, Chinese Academy of Sciences

The Chinese VLBI Network (CVN) has stations located in Shanghai, Beijing, Kunming, and Urumqi as well as a VLBI Center in Shanghai that processes four-station data in real time. For the Chang'E-1 project a Mark IV hardware correlator [1] and for the Chang'E-2 project a Mark 5B hardware correlator [2], both shown in Figure 2, were used to process four-station data in real time.

Fig. 2 Chang'E-1 and Chang'E-2 hardware correlators.

2 Chang'E-3 Hardware Correlator

In the recent Chang'E-3 mission, the Chang'E-3 hardware correlator has been used and has performed well. The hardware correlator includes five FPGA boards. All of the FPGA boards have the same hardware: one Xilinx Virtex-4 FX60 and four LX160 FPGAs.

The FX60 FPGA includes a 1-Gigabit Ethernet port and embedded two PowerPC405 processors to send and receive processing data and control information to and from the outside network.

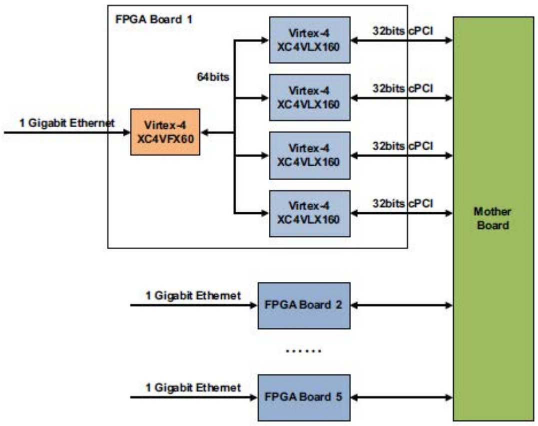

Fig. 3 Diagram of the Chang'E-3 hardware correlator.

The FX60 also connects to four LX160 FPGAs via a 64-bit bus to send and receive processing data and control information to and from each LX160 FPGA. Each LX160 FPGA has a 32-bit cPCI bus connected to the mother board, which connects all five FPGA boards. The FPGA board and the correlator picture are shown in Figure 4.

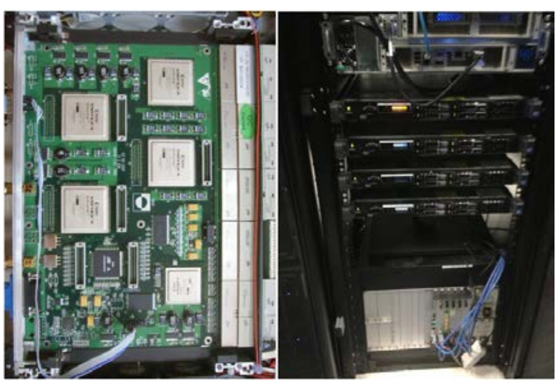

Fig. 4 Chang'E-3 hardware correlator.

3 Results from the Chang'E-3 Mission

Figure 5 shows a comparison between the results of Delta-DOR observations correlated via a hardware correlator and a software correlator. The red points show the results from the hardware correlator, and the black points show the results from the software correlator. Please see the on-line pdf version of this paper to compare the red and the black points in detail. The hardware correlator skips the observation data of third radio source, so there is some difference between the hardware and software correlator outputs in the next two satellite scans and back to the same in the following.

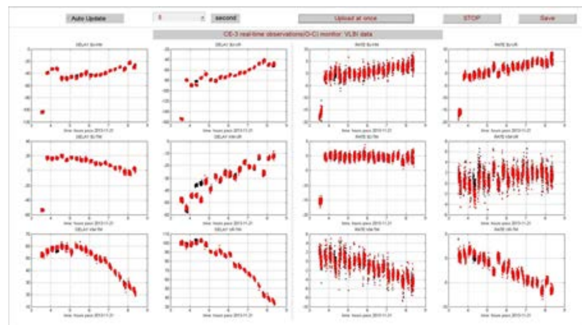

Fig. 5 Comparison between the hardware and software correlators.

Figure 6 shows the final delays from the results sent to Beijing Center from the s3c13a session. The first two scans used the software correlator results, and the following used the hardware correlator results. Between scans two and three there is a small drop, which shows that the hardware correlator delay is about three seconds less than the software correlator delay.

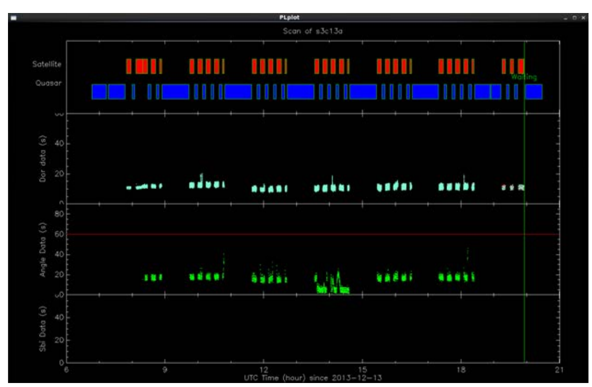

Fig. 6 Hardware and software correlator delays.

4 UniBoard-based Hardware Correlator

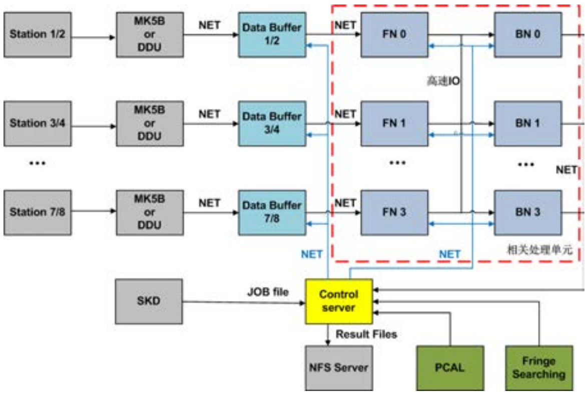

Fig. 7 UniBoard-based hardware correlator.

Currently, we are designing a UniBoard version of the hardware correlator as the next generation correlator. Its features are:

- Outside data are transmitted to a Data Buffer server using the TCP/IP Protocol.
- The Data Buffer server sends data to the Uniboard Front Node via a 10GbE port using the UDP Protocol.
- Data is processed in four Front Nodes and sent to the Back Node via high speed I/O on the Uniboard.
- The results on the Back Node are sent to a PC via a 1GbE port using the TCP/IP Protocol.
- The data is sent to the Front Node via a 10GbE interface.

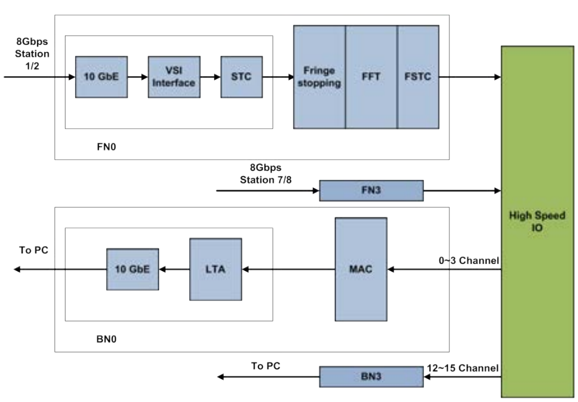

Fig. 8 Diagram of the UniBoard-based hardware correlator.

- The VSI Interface gets the data from the 10GbE interface, then synchronizes and reformats the data.
- The Sample Time Correction (STC) block takes the integer part of the delay model.
- The data is sent for Fringe Stopping using Phase Model coefficients.
- After Fringe Stopping, the data is sent to an FFT, which can be set to between 1,024 and 65,536 FFT points. The output data will be in the natural order.
- Fraction Sample Time Correction (FSTC) uses the fractional part of the delay model.
- Output data is sent to the Back Node FPGA via high speed I/O.
- In the Back Node, data is sent to a Multiply-Accumulate (MAC) unit.
- After the MAC, the data is sent to the Long Term Accumulator (LTA).
- The results are sent to a PC via a 1GbE port using the TCP/IP Protocol.

5 Future Plans

Our future plans include:

- Expansion to an eight-station 32-channel system;
- Update to a single precision floating point FFT and MAC;
- Update to a 10GbE Ethernet;
- Update to a VDIF interface;
- Update to a JIVE UniBoard.

References

1. Xu, Z. J., et al. Real Time Correlator in FPGA. IVS 2006 General Meeting Proceedings, NASA/CP-2006-214140, pp. 89–92.
2. Zhang, X. Z., et al. VLBI Technology Development at SHAO. IVS 2010 General Meeting Proceedings, NASA/CP-2010-215864, pp. 383–387.

Control System and Visualization of the VLBI Hardware Correlator at SHAO

Shaoguang Guo, Zhijun Xu, Jiangying Gan, Xiuzhong Zhang, Renjie Zhu, Yajun Wu, Ying Xiang

Abstract The VLBI system is comprised of VLBI stations, data preprocessing, correlator, post-correlator, SKD, orbit, location, and so on. The corrlator processor is the core equipment of the VLBI data preprocessing device; we can calculate important parameters such as the delay, delay rate, correlation amplitude, and interferometric phase from the correlator. Now our group has realized a complete software control system and an FPGA core for the hardware correlator on a CPCI board through the playback interface. We have also achieved the visualization of the processing data for convenience and the C/S architecture for controlling the PBI interface. In the future, our group will port the whole system to the Uniboard board—for speed improvement and supporting more modes. Recently, the real-time mode and post-correlation were tested during the CE-3 mission. The result was also checked to make sure our hardware correlator is fine. This paper describes the whole control system and its realization.

Keywords VLBI, hardware correlator, FPGA, fringe search, Uniboard

1 Introduction

The technique of Very Long Baseline Interferometry (VLBI) has been employed to achieve extremely high angular resolution in the study of radio sources. VLBI has been used in the Chinese Lunar Exploration Program with the participation of the CVN (Chinese VLBI Network) stations. As shown in Figure 1, the Shanghai Astronomical Observatory's VLBI Center includes four VLBI stations (including Shanghai station, Beijing station, Kumming station, and Urumqi station; later to be joined by Seshan station), data preprocessing, correlator, post-correlator, SKD, orbit, location, and so on.

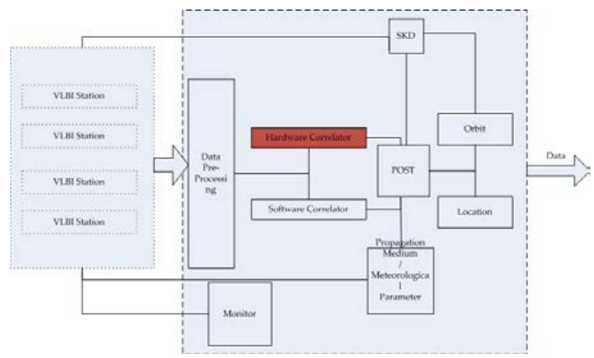

Fig. 1 Diagram of the Chinese VLBI Center.

The hardware correlator is the core equipment of the VLBI data preprocessing device with a complicated high speed processing system. It produces the signal's correlation function and complex visibility function (mutual spectral-density function), from which important parameters can be derived such as the delay, delay rate, correlation amplitude, and interferometric phase. There are two types of correlators; we chose the FX hardware correlator. It completes the data format transition, time synchronization, time-delay compensation, FFT calculation, plural cross-multiplication accumulation, long-term accumulation, and eventually produces the correlation output for post-processing [1].

The Shanghai VLBI Correlator is hosted and operated by the Shanghai Astronomical Observatory, Chi-

Shanghai Astronomical Observatory

nese Academy of Sciences. It is dedicated to the data processing of the Chinese domestic VLBI observing programs, inclusive of the CMONOC project for monitoring the Chinese regional crustal movement and the Chinese deep space exploration project for tracking spacecraft [2].

2 Correlator Procedure

The VLBI correlator is the "glue" that brings the data from separate antennas together and processes it to form the basic observables used in astronomy and geodesy [3]. The correlation procedure goes through the following steps: transfer of observation data from the antenna to the correlator unit through the 10 GbE Internet interface, decoding of the real data to original data by unpacking the frame header information, integer sample time compensation (ISTC), integer sample bit delay compensation, fringe rotation, FFT and fractional sample time compensation (FSTC), transport of the processed data to back-end chips via the high speed serial bus for cross-multiplication in the baseline unit after synchronization, and derivation of the visibility function. The final data are sent to the NFS server in a special data format. The whole system is running under the arrangement of a JOB file. The JOB file contains the following: observed object, observed time, observed frequency, observed bandwidth, observed channels, model, and so on. The hardware correlator also operates by using the JOB file [4].

3 Hardware Correlator System Architecture

Suppose there are two signals f(t) and g(t) as shown in Figure 2. The corresponding FFT transforms are F(w) and G(w).

As we all know, correlators can be grouped into FX and XF types by the sequence of the FFT and multiplication operations. The name "FX" was originated by Chikada (Chikada et al., 1987), who also built the first such correlator, to indicate this reversal of the order of operations compared to the conventional lag correlator. The VLBA correlator group, while considering one

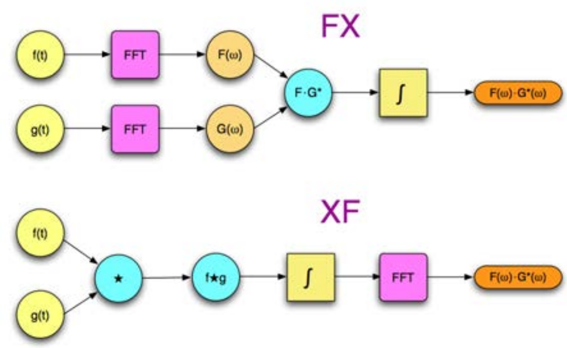

Fig. 2 Equivalence of the FX and XF correlator architectures.

design of each type, adopted the term "XF" which is sometimes used for the latter architecture. Both the FX and the XF correlators include:

- model: delay compensation, fringe rotation
- data sources
- fringe detection & observable parameter estimation
- technical details: discrete samples, integration, correlator beam

There are many advantages of FX; e.g., the cost for the spectral channels grows only with the

$$\log_2(N) \qquad \text{vs.} \qquad N$$

(linear) for XF and there is little loss due to delay quantization.

We chose the FX correlator after taking many factors into consideration. The hardware correlator system includes:

- CCC: center control computer, which controls the whole flow;
- Five FPGA boards: include the core algorithm of the correlator process;
- PBI: the playback interface will playback the raw data to FPGA.

The CCC commuticates with the FPGA through the Peripheral Component Interface (PCI) bus, which is driven by the PCI drive module. As the PCI rate can reach 264 MB/s, which already reaches the command of the current hardware correlator system.

As shown in Figure 3, the PCI bus connects the CCC and the POWERPC (PPC) on the FX60. They access the 64-MB memory at the same time. The PCI interface carries out the definitions and introductions of the memory.

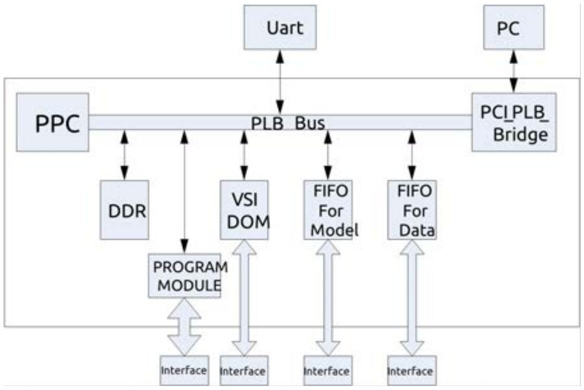

Fig. 3 Hardware correlator system architecture.

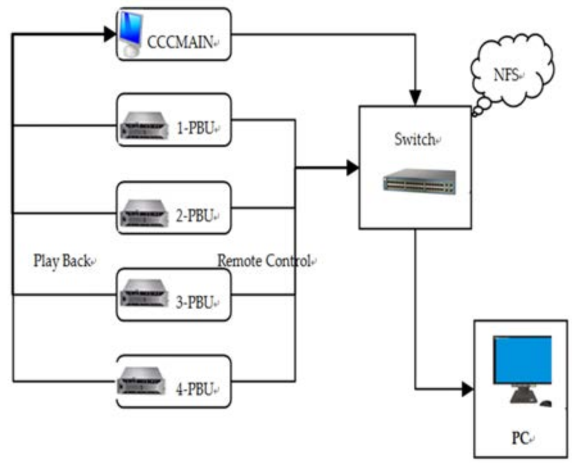

Fig. 4 Layout of the hardware correlator.

The CCC sends control commands and parameters to the FX60 to control the relevant FPGA chips, and the status is fed back to the CCC. The concrete functions of the CCC are:

- Load LX160: download the bin file into the FPGA through the PCI bus,
- Initialize FPGA: initialize the FPGA to original status,
- Set parameters: include 50 bytes to control the FPGA,
- Set modules: generate the modules for the correlator,
- Read parameters: feed back the status of FPGA to CCC,
- Record the correlator data: save the correlator data to NFS.

4 Realization of the Hardware Correlator

Figure 4 shows how the CCC connects the PC node and the playback unit (PBU) via the local area network. Thus the CCC can control the PBU by the client/server (C/S) mode, which starts the PBI program automatically. Five FPGA cards connect directly via the network to the PBU.

The playback data is mounted on the NFS, so that the same data can be shared with the software correlator.

A correlator must cross-multiply the signals from different antennas that correspond to the same arriving wave front. But the antennas are at different distances from the source, so the wave front arrives at different times (the delay). Also they are moving at different speeds along the direction to the source, causing different Doppler shifts (the fringe rate). An estimate of these time and rate offsets is removed in the correlator hardware.

5 The Result of Visualization

Figures 5 and 6 are the result of the visualization of the real-time correlator. The magenta (dark gray) lines represent the correlation amplitude and the cyan (light gray) points represent the interferometric phase. The data is the real data from the CE-2 (Chinese Lunar Exploration Program). There are four stations in total. Based on the shared memory technology, we can handle the correlation process and watch the result at the same time. In this way, we can immediately find if there was any error. Also, after using the fringe search technology, the result shows that it has some influence on the delay.

6 Conclusions

It is important to understand that the model we used is never quite accurate; however, it is accurate enough so that the differences between the model and reality are small and are within the search range of the correlator processing. These differences are called the

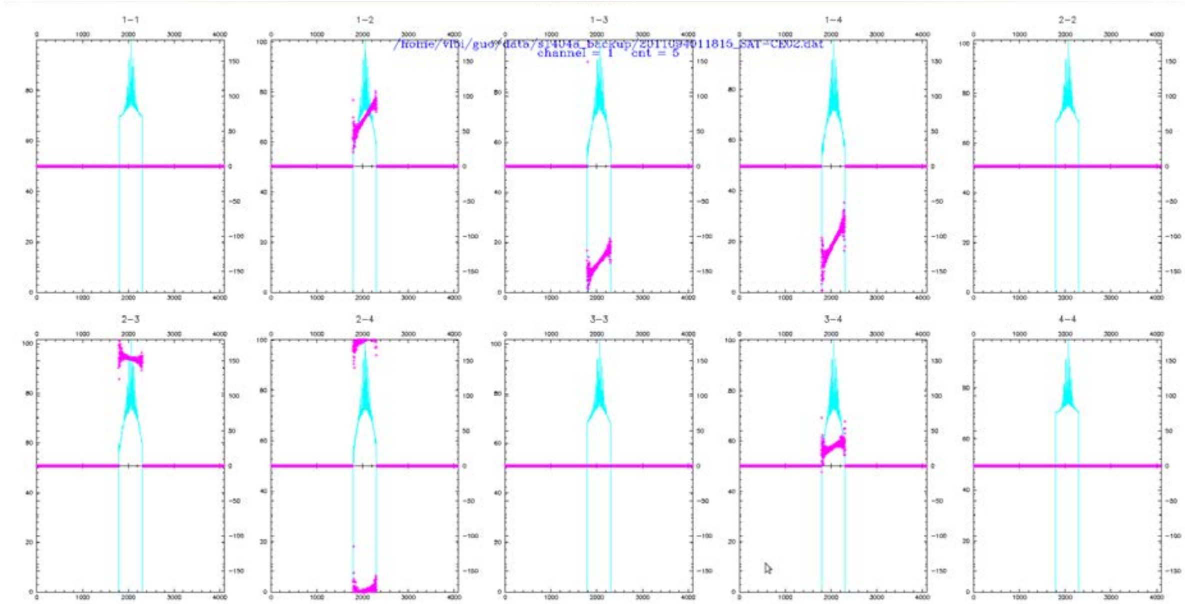

Fig. 5 Result without fringe search. There are four stations involved in the observations, so the figure includes four autocorrelation products and six cross-correlation products. The magenta (dark gray) lines represent the correlation amplitude and the cyan (light gray) points represent the interferometric phase.

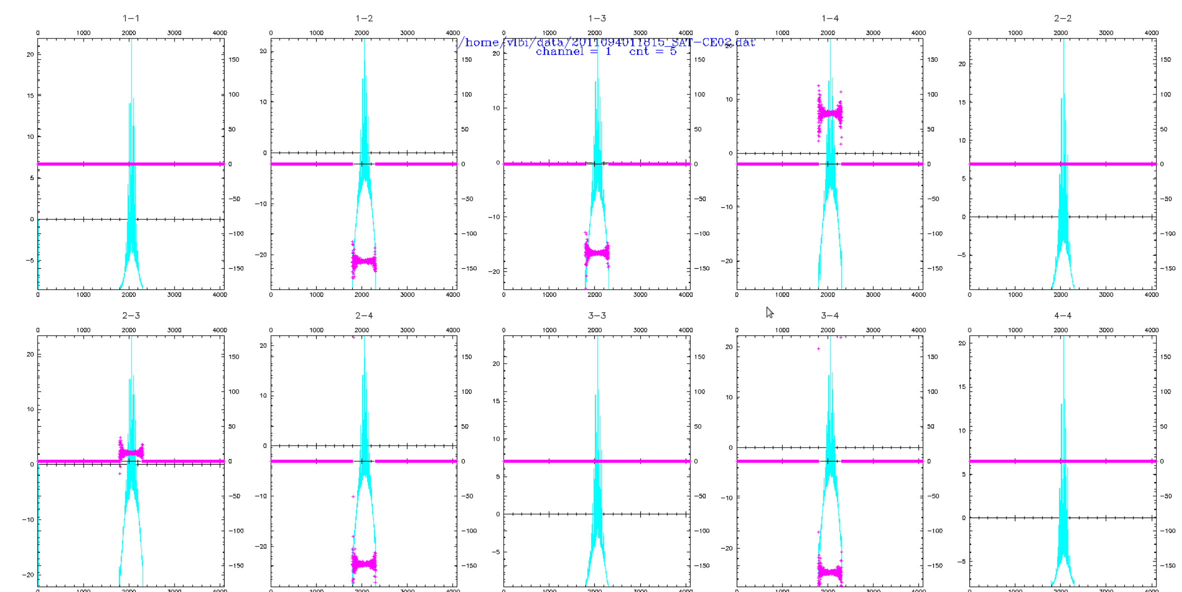

Fig. 6 Result with fringe search. We can see the fringes become flat after the fringe search function, indicating that the residual delay is very low compared to the figure above.

residual differences, or just residuals. In the discussion of single-band and multi-band delay determinations, we are dealing with residuals to the computer model and trying to determine the best estimate delay, delay rate, and phase of these residuals. Once determined, the residuals are added to the original model parameters to arrive at the total observables (e.g., delay, rate, phase) that are used in post-correlation analysis [3].

The usual fringe search technique for VLBI is correlator-based. We can get the conclusion that the result is better when we use the fringe search function.

Of course, this method can solve for motion that is not very intense, but for violent motion we need to further reduce the integration time. This may cause a sharp increase in the amount of data, requiring the algorithm to be optimized further. For future development, we are considering the use of the GPU for the compute-intensive part.

After handling the same data with and without fringe search (Figures 5 and 6), we can see the change of delay and delay rate between the two figures. The result without fringe search has an offset delay of about 200 ns. When using the fringe search module, the delay can be reduced to about 10 ns, which can be ignored for the final result. Here we just modify the delay by the model mentioned before [5]. The tiny change in the trend of the delay rate will be added in the future.

Acknowledgements

We would like to thank the Shanghai Astronomical Observatory (SHAO) for their financial support, Radio Astronomy Science and Technology Laboratory (RASTL) for their technical support, and Zhang Xiuzhong, Xu Zhijun and Gan Jiangying for their thoughts and suggestions on the design of various parts of the whole system. We also thank the hard work and dedication of our team members Zhu Renjie, Xiang Ying, and Wu Yajun for their constructive critiques. This work was in part supported by the Chinese Lunar Exploration Program fund.

References

1. Zhu Renjie, Zhang Xiuzhong, Xiang Ying, Xu Zhijun. An Introduction to the VLBI Correlator Used in the Chinese Lunar Exploration Program. *PROGRESS IN ASTRONOMY*, Vol.26, No.1, pp. 62–72, March 2008.
2. Shu Fengchun, Zheng Weimin, Chen Zhong. IVS 2012 Annual Report *ftp://ivscc.gsfc.nasa.gov/pub/annual-report/2012/pdf/coshao.pdf*
3. Alan R. Whitney. How Do VLBI Correlators Work?, in International VLBI Service for Geodesy and Astrometry 2000 General Meeting Proceedings, edited by Nancy R. Vandenberg and Karen D. Baver, NASA/CP-2000-209893, 2000.
4. Zhang Xiuzhong, Zheng Weimin, Ren Fangbin, Zhu Congxin, Shu Fengchun, Xiang Ying. The High-speed FX Correlator of Chinese VLBI Network? A Super Spectrum Analyzer Based on Programmable ASIC Circuits and Systems, 2000. IEEE APCCAS 2000. The 2000 IEEE Asia-Pacific Conference, pp. 854–858.
5. Shu F. C., Zhang X. Z. The accuracy analysis of model using in correlator process software system, Progress in Astronomy, No. 22, pp. 100–106, 2001.

The XF-Type Correlator for Delta-DOR in Deep Space Navigation

Maoli Ma[1,2], Weimin Zheng[1], Yidan Huang[1], Guangli Wang[1]

Abstract The Delta-DOR technique provides high-precision angular position data for the Chinese Chang'E-3 satellite. The standard DOR tones are comprised of several single-frequency signals that are spaced several MHz or several tens of MHz apart. The correlator in China is of FX type. It is suitable for quasars with a flat spectrum, while the spectral resolution limits the accuracy of the phase from the satellite. Or the DOR tones must have harmonics that share energy, but it is useless for SNB and measurement precision. We report on the XF correlator, which is a tailor-made correlator for single-frequency signals.

Keywords Delta-DOR, Delta-VLBI, correlator

1 Introduction

Delta-DOR (Delta Differential One-Way Ranging) is a Very Long Baseline Interferometry (VLBI) technique that can be used in conjunction with Doppler and ranging to improve spacecraft navigation by more efficiently determining spacecraft angular position in the plane of sky. The standard DOR tones are comprised of several single frequency signals (Figure 1). A narrow tone spacing is required for integer cycle phase ambiguity resolution, while a wider tone spacing is required for high measurement accuracy [1]. It is quite different from quasars with a flat spectrum. The Chinese correlator is of FX type. It is suitable for quasars, while in order to distinguish single frequency signals, a high FFT resolution is required, especially for weak signals, and the FFT resolution limits the accuracy of the phase from the satellite.

The DOR tones in China are not a single-frequency signal as the standard ones. They have harmonics with certain bandwidths. These harmonics will share the total limited energy with the DOR tones, while they do not improve the precision of the tone phase. If all total energy is given to the DOR tones, the higher SNB will improve the precision of the tone phase.

NASA and ESA have already developed special correlators for DOR tones [1, 2]. We report on an XF-type correlator, which is tailored for single frequency signals. The definition of Delta-DOR we got is different from the one (we call Delta-VLBI) in China. We discuss the transformation of Delta-VLBI and Delta-DOR.The reliability of Delta-DOR is further validated.

1. Shanghai Astronomical Observatory CAS
2. University of Chinese Academy of Sciences

2 Delta-VLBI and Delta-DOR

Although Delta-DOR is a VLBI technique, the geometric delay definition of Delta-DOR at NASA and ESA is different from the traditional Delta-VLBI. Delta-VLBI measures the geometric time delay when the same wave front of a signal reaches two geographically separated stations (Figure 1).

$$\tau_{VLBI} = \frac{r_1 - r_2'}{c} = t_1 - t_0. \tag{1}$$

For Delta-DOR, two VLBI stations receive radio signals at the same time and the difference of the transmission times is measured (Figure 2).

$$\tau_{DOR} = \frac{r_1 - r_2}{c} = t_2 - t. \tag{2}$$

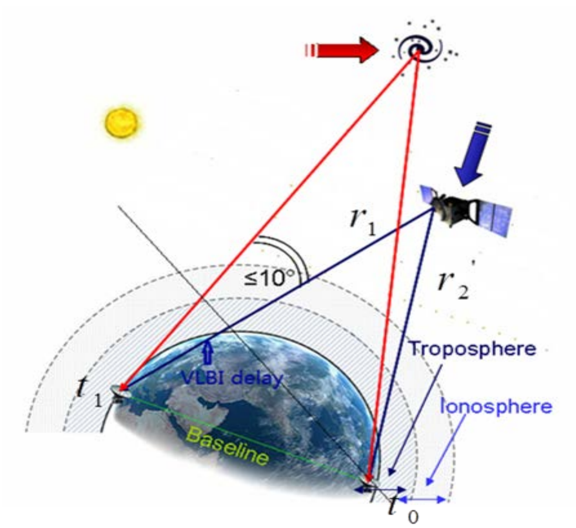

Fig. 1 Geometric principle of Delta-VLBI.

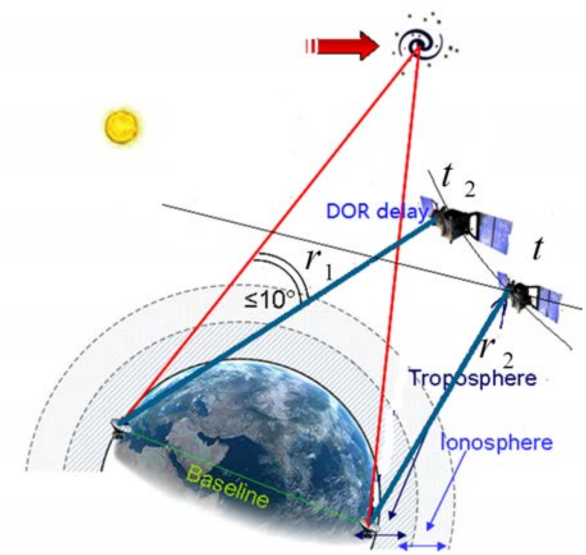

Fig. 2 Geometric principle of Delta-DOR.

There is a relationship (3) between them:

$$c \cdot \tau_{VLBI} = c \cdot \tau_{DOR} + \frac{\partial r_2}{\partial t} \tau. \quad (3)$$

3 XF Correlator in s1404a

s1404a is an experiment about China CE2 satellite. The sample rate is 16 Mbps/s, bandwidth 8 MHz, and quantization 1 bit. We processed data from the Shanghai 25-m (Sh), Kunming 40-m (Km), and Urumchi 25-m (Ur) antennas. Figure 3 shows the DOR tones distribution. DOR1 and DOR4 are wider tones for high accuracy; DOR3 is one of the narrow tones used in conjunction with the main carrier to resolve ambiguity. Figure 4 depicts the spectrums of the main carrier for Sh–Km–Ur. The signal at Ur is nearly 7 dB weaker than for Sh and Km. The other eight signals with frequency exactly .9 MHz and 1 MHz interval are phase calibration signals (pcals). The power of the main carrier is larger than the pcal, while the DOR tones are much weaker than the pcals.

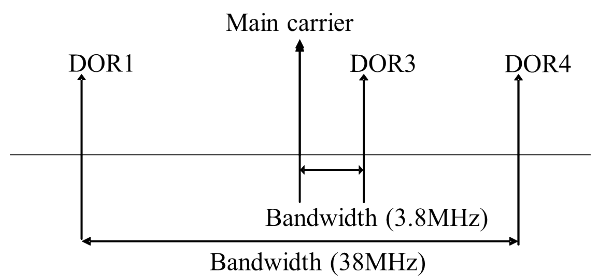

Fig. 3 DOR signal distribution in s1403a.

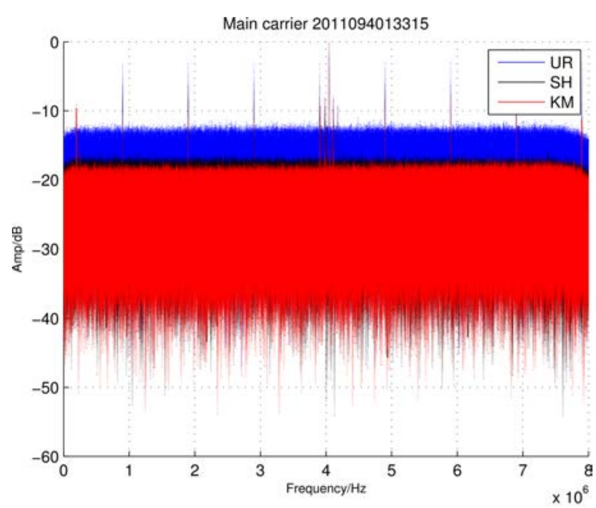

Fig. 4 Spectrums of main carrier. Blue is Ur, black is Sh, and red is Km.

A dynamical model will be used for the phase rotation on the raw data. At NASA and ESA, DOR is a one-way range. There is no uplink, and the satellite directly transmits the signal to the receiving station. In

China, on the other hand, the satellite first locks signal to the uplink station and then re-transmits to the VLBI station. In s1404a, the uplink station was Kashi. The dynamical model must include the uplink light time in addition to the downlink time. After rotation, a signal with low frequency is received. In order to decrease jamming signals and computation, the signal is filtered and downsampled to 100 Hz. Then we do the correlation in the time domain. The signal after correlation is also around 0. A low sample number is enough for FFT. The residual frequency and phase will be estimated in the frequency domain. The quasar's phase and delay is used to correct for system errors, the atmosphere, and the ionosphere. The quasar data, atmosphere, and ionosphere are from the VLBI Center of the Shanghai Astronomical Observatory (SHAO). Figure 5 shows a flow chart of the XF correlator.

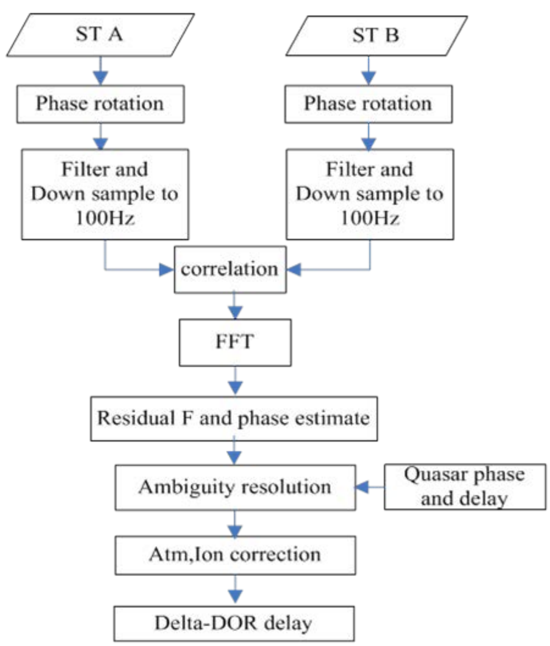

Fig. 5 Flow chart of the XF correlator.

4 Results

In order to confirm our Delta-DOR results, we compared them to Delta-VLBI from the VLBI Center. There is a significant difference because of the different definitions of Delta-DOR and Delta-VLBI (see the upper panel in Fig. 6). They are consistently below 0.3 ns and within the error limit (Table 1) after we corrected the difference with Equation (3). Table 1 lists the residuals of Delta-VLBI and Delta-DOR from the XF correlator. For Sh–Km, they are about 0.34 ns for both Delta-VLBI and Delta-DOR. For Sh–Ur and Km–Ur, the errors are much larger because of the lower SNB for Ur.

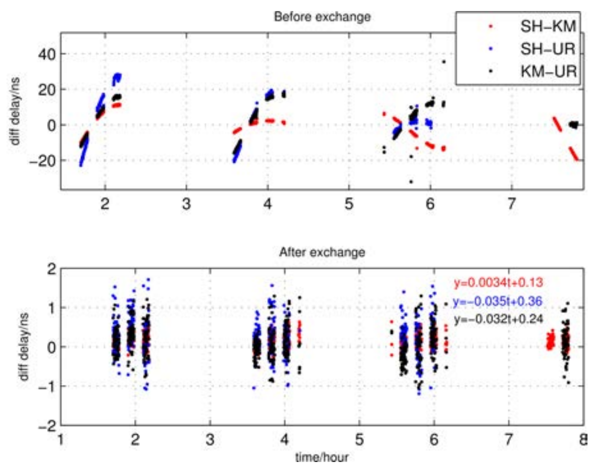

Fig. 6 Difference between Delta-DOR and Delta-VLBI.

Table 1 Residuals of Delta-VLBI and Delta-DOR.

	Sh–Km	Sh–Ur	Km–Ur
Delta-VLBI	0.34	0.9	0.76
Delta-DOR	0.34	0.91	0.8

We also compared the close delay of the above three baselines about Delta-DOR and Delta-VLBI (Figure 7). They are at about the same level.

5 Future Plans

In this paper, the DOR is three-way, and a dynamical model including uplink is considered. We intend to process one-way DOR in the future, where the frequency shift of ultra-stable crystal oscillator must be considered. We will also analyze each error, such as instrumental errors, clock jitters, and transmission medium errors in Delta-DOR.

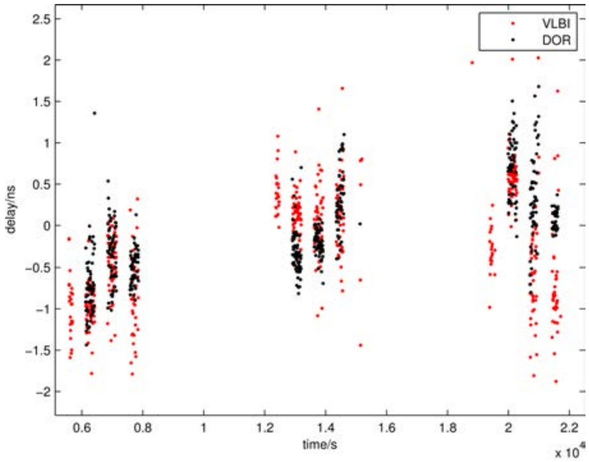

Fig. 7 Close delay about Delta-DOR and Delta-VLBI.

Acknowledgements

The work was supported by the Opening Project of Shanghai Key Laboratory of the Space Navigation and Position Techniques (No. Y224351002) and NSFC (No. Y247041001, Y347471001).

I'm very grateful to Professor Luciano Iess for providing a nearly two-months learning opportunity at Radio Science Laboratory, Sapienza University of Rome. Thanks to Francesco Barbaglio and Alessandro Ardito for the disscussions on Delta-DOR.

References

1. J. S. Border and J. A. Koukos, Technical Characteristics and Accuracy Capabilities of Delta Differential One-Way Ranging (ΔDOR) as a Spacecraft Navigation Tool, CCSDS Meeting of RF and Modulation Standards Working Group, Munich, Germany, 09/20/1993.
2. L. Iess, R. Abello, A. Ardito et al., The European ΔDOR correlator, 57th International Astronautical Congress, Valencia, 2–6 October 2006 (IAC-06-B3.1.05).
3. Yong Huang, Orbit Determination of the First Chinese Lunar Exploration Spacecraft CE-1.

Session 4

Progress in Data Structure, Software Development, and Analysis Strategies

March 2-7, 2014

8th IVS

GENERAL MEETING

Shanghai, China

IVS Combination Center at BKG: ITRF2013 Preparations and Source Position Combination

Sabine Bachmann, Linda Messerschmitt, Daniela Thaller

Abstract The IVS Combination Center at BKG is responsible for the IVS contribution to the ITRF2013. In preparation for the submission of the combined VLBI data, a detailed analysis of the individual input data of the IVS analysis centers have to be performed. Data format, station positions and EOP have to be investigated, e.g., for format correctness, systematic behavior, and outliers. For the first time, the IVS is advised to provide also combined source positions in the SINEX files. The source positions are estimated consistently with EOPs and the terrestrial reference frame (TRF). We present the generation of combined source position time series and a combined celestial reference frame as well as the combination approach, the current status of the analysis, and the combined results obtained so far for TRF, CRF, and EOPs.

Keywords VLBI, intra-technique combination, terrestrial reference frame, IVS

1 Introduction

Every few years the IERS ITRS Product Center initiates the generation of an inter-technique combined international terrestrial reference frame (ITRF), containing data from each of the four space-geodetic techniques, i.e., Satellite Laser Ranging (SLR), Global Navigation Satellite Systems (GNSS), Very Long Baseline Interferometry (VLBI), and Doppler Orbitography and Radiopositioning Integrated by Satellite (DORIS). The last ITRF (called ITRF2008) contains data until the end of 2008 and has been published in 2009 [3]. The upcoming ITRF will contain data up to 2013 and is called ITRF2013, which means five years of additional data are available compared to the ITRF2008. The contribution of the International VLBI Service for Geodesy and Astrometry (IVS) consists of a combined solution of individual submissions of Analysis Centers (AC). Individual solutions are based on datum free normal equations, which are transformed to equal epochs and equal a priori values for all parameters. Stacking the individual normal equations leads to a combined solution, which is then submitted to the IERS ITRS Product Center as official IVS contribution to the ITRF2013. Details on the combination process can be found in [1].

The call for participation has been sent out by the IERS ITRS Product Center in March 2013, proposing February 10, 2014 as submission deadline for all services. This deadline has been postponed by the IVS due to analysis software developments and preparation issues. Several ACs have already announced their participation, including some new institutions with their own developed analysis software, which implies a more heterogeneous combined solution. Overall, about ten contributions are expected for the IVS combination, which means a total amount of ∼60,000 SINEX files. The preparation for the ITRF2013 started already at the end of 2013 with several discussions on submission instructions, axis offsets, EOP parameterization, and source position handling. First test files have been made available in the IVS Data Center on February 10, 2014 (go to ftp://ivs.bkg.bund.de/pub/vlbi/ITRF2013/daily_sinex/). Other submissions have been submitted since that time or are expected to follow.

Federal Agency for Cartography and Geodesy

Table 1 Institutions and software packages contributing to the ITRF2013 effort.

Abbreviation	Institution	Software	Contribution to operational products
AUS	Geoscience Australia, Australia	Occam	no
BKG	Federal Agency for Cartography and Geodesy, Germany	Calc/Solve	yes
DGFI	German Geodetic Research Institute, Germany	Occam	yes
GFZ	German Research Center for Geosciences	VieVS	no
GSFC	Goddard Space Flight Center, USA	Calc/Solve	yes
IAA	Institute of Applied Astrometry, Russia	Quasar	yes
NMA	Norwegian Mapping Authority, Norway	Geosat	no
OPAR	Observatory of Paris, France	Calc/Solve	yes
SHAO	Shanghai Observatory, China	Calc/Solve	no
USNO	US Naval Observatory, USA	Calc/Solve	yes
VIE	Vienna University of Technology, Austria	VieVS	no

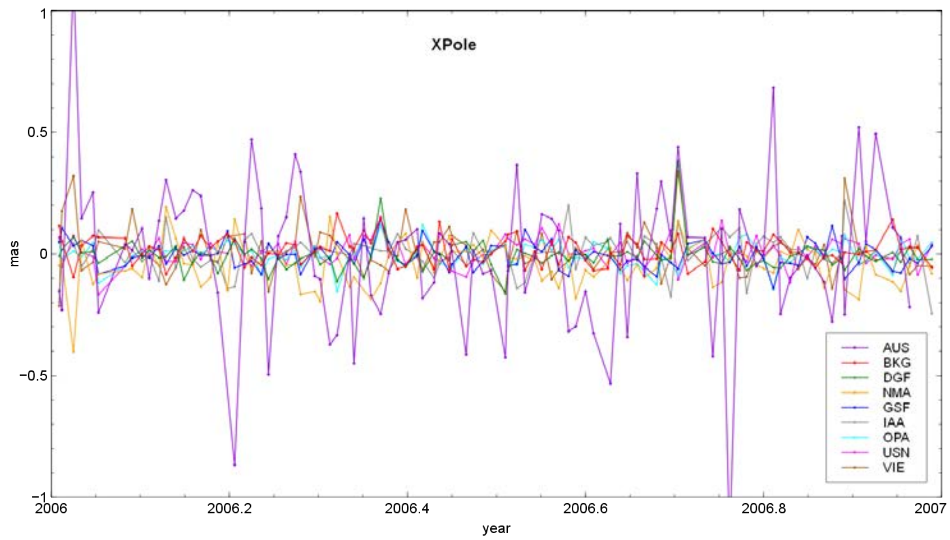

Fig. 1 X-Pole for the year 2006 estimated by different ACs w.r.t. the IVS combination.

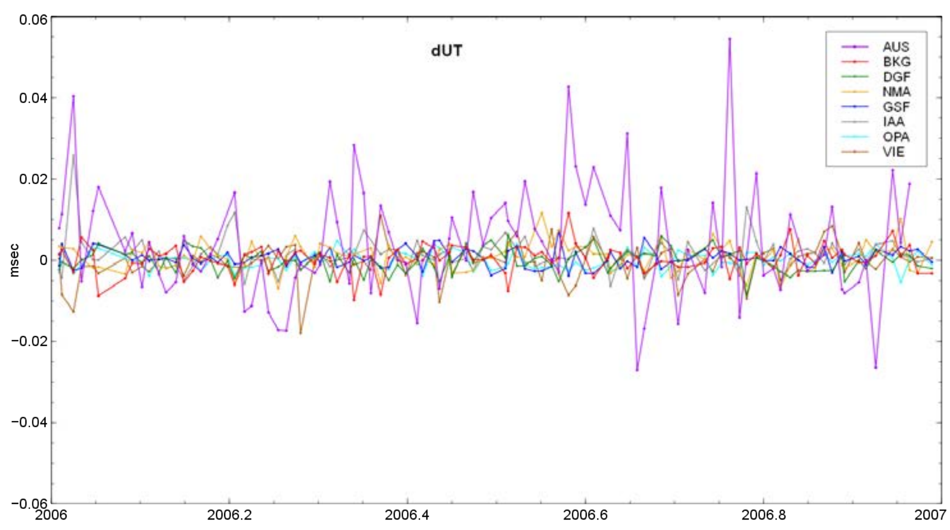

Fig. 2 dUT for the year 2006 estimated by different ACs w.r.t. the IVS combination.

2 Data

The data comprises 24-hour VLBI sessions until the end of 2013. The analyzed sessions are submitted in SINEX file format[1] to the IVS data center. In general, the ACs are free to decide which sessions are analyzed back to the beginning of VLBI observations in the early 1980s. The overall combination process is close to the operational quarterly combination. Parameters are station coordinates and Earth orientation parameters (EOPs). Source positions are left out, but further investigations are foreseen for the post-ITRF2013 era. A robust outlier test for station coordinates and EOPs is applied based on Least-Median-of-Squares method and a group-wise software package variance-component estimation (VCE) is applied as described in [2]. As of March 2013 the following software packages are expected to contribute to the IVS combination: Calc/Solve, QUASAR, OCCAM (LSM[2], LSC[3]), GEOSAT, and VieVS.

Also some further institutions announced their participation, i.e., AUS (Australia), NMA (Norway), and VIE (Austria) with whom iterative development of format issues, parameterization, and modeling (among other things) have been discussed within the last weeks. Table 1 gives an overview of the expected contributions and software packages.

3 Analysis

Some test combination series have been generated in order to set up the combination software and the databases for the storage of the estimates which will be used for quality analysis of the submitted data later on. The general IVS submission is behind ITRF schedule; not all ACs have submitted data yet. Comparisons are thus performed using test series provided in advance and/or sessions provided in the IVS Data Center which are used for operational rapid and quarterly combination, but which are not generated for ITRF2013 combination explicitly.

Figure 1 shows the X-Pole for sessions in 2006 by different ACs w.r.t. the combined solution. The plot does not show a systematic behavior for any of the ACs, and the solutions are nicely scattered around zero. One of the ACs (i.e., AUS) still shows a larger amplitude, where the AC is already working on an improvement. In Figure 2 dUT1 is shown for the same time span and the same data source. Similar to Figure 1 no systematics can be seen. At the time of writing (March 2014) only a common data set for one year has been provided by the ACs and not every AC which announced their participation provided test data for comparisons. For conclusive studies of EOP and station coordinates concerning systematic behavior, offsets, or drifts in the time series more data have to be considered which will be submitted by the ACs within the upcoming weeks.

In Table 2 the weighted root mean square (wrms) over the one-year time span w.r.t. the combined solution is shown. This value is computed by summing up the weighted residuals after the combination and represents a quality indicator for the individual contribution within and w.r.t. the combined solution.

Table 2 WRMS of the residuals for EOPs for 2006.

	X_P [μas]	Y_P [μas]	dUT [μs]	X_P Rate [μas/day]	Y_P Rate [μas/day]	LOD [μs/day]	dX [μas]	dY [μas]
AUS	183	207	9	386	376	84	N/A	N/A
BKG	46	49	3	171	140	7	47	48
DGFI	30	40	2	136	135	6	N/A	N/A
GSFC	44	36	2	124	112	5	29	31
IAA	58	59	3	190	206	12	50	41
NMA	64	68	3	219	214	26	50	44
OPAR	42	39	2	120	104	4	26	32
USNO	49	68	7	183	157	8	44	55
VIE	58	51	3	195	172	9	63	58

Generally, the table shows a good agreement between the ACs and good results for the test data for one year. Comparisons between the contributed solutions over the whole time span of ~30 years of data and all contributions will follow as soon as the submission for ITRF contributions is completed.

The individual weighting of the contributions is done by a variance component estimation (VCE). As in the operational rapid and quarterly combinations (http://ccivs.bkg.bund.de/) a number of ACs are using the same software package (highlighted in red (gray) in Table 2) a group-wise VCE was introduced which forms groups of software packages. Contrary to a VCE

[1] http://www.iers.org/

[2] LSM = Least Squares Method

[3] LSC = Least Squares Collocation Method

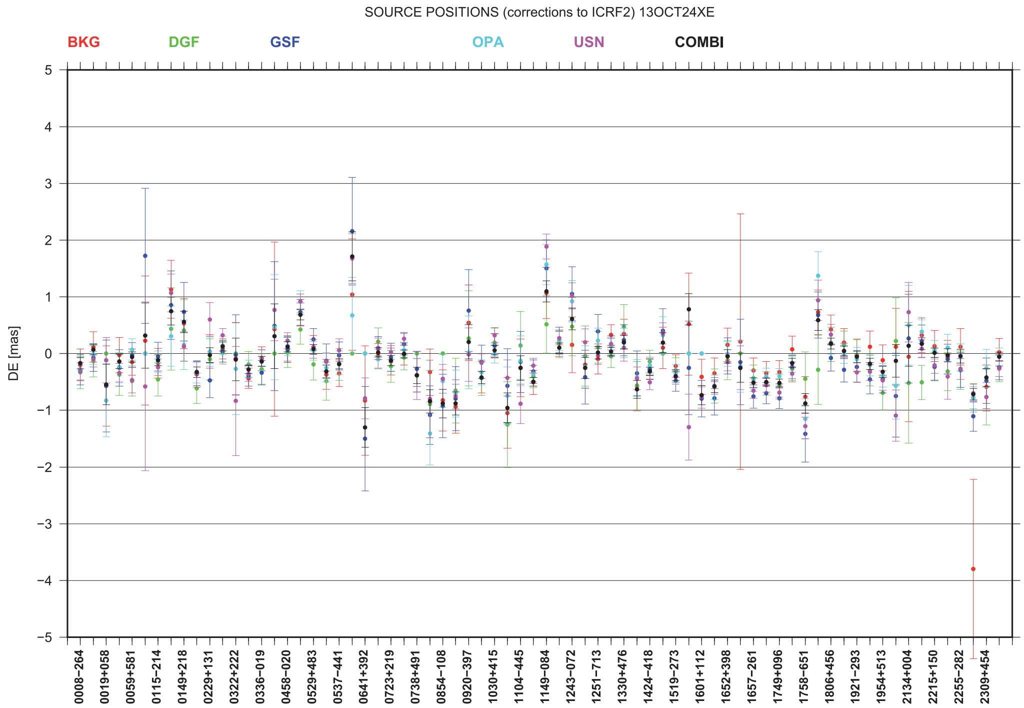

Fig. 3 Estimated source positions (declination) for session 13OCT24XE (R4608).

where each AC is represented by one group, this approach compensates for a disproportional impact of one software package. Meanwhile, eleven ACs (six ACs are currently contributing to the operational rapid and quarterly combination) announced their participation for the IVS contribution with different software packages. Using all the contributions (once they are all submitted) the above mentioned effect can be investigated using a larger number of contributions and a broader variety of software packages. This investigation and other comparisons will be performed when all institutions have submitted their contributions for the ITRF2013 to the IVS Data Center.

3.1 Combination of Source Positions

Source positions are provided by most of the IVS Analysis Centers. Initially, the combination and submission of source positions was foreseen for the ITRF2013. After some discussions within the IVS it was decided not to include them in the IVS submission for ITRF2013, but to perform further investigations after the calculations for the ITRF2013 have been finished. Nevertheless, combination routines for source positions have been set up and tested for a limited amount of data. First single sessions have already been combined and a global solution for the celestial reference frame (CRF) was generated. The results are promising. As an example, Figure 3 shows the results of source positions for session 13OCT24XE (R4608) for individual ACs and the combined solution w.r.t. the ICRF2 positions (cf. http://hpiers.obspm.fr/icrs-pc/). The differences are in a range of ± 0.5 to 1 mas, with some possible outliers for single sources only.

Figure 4 shows the result of a global source solution (CRF) generated with the CONT11[4] campaign data. The combined solution is the result of stacking all combined normal equations for the individual sessions. The comparison of the combined CRF and the source positions given in the ICRF2 shows differences in the order of ± 0.2 mas in right ascension (RA) and declination (DE).

Further investigations of source position combination are foreseen after the IVS submission for the ITRF2013 was completed.

[4] http://ivs.nict.go.jp/mirror/program/cont11/

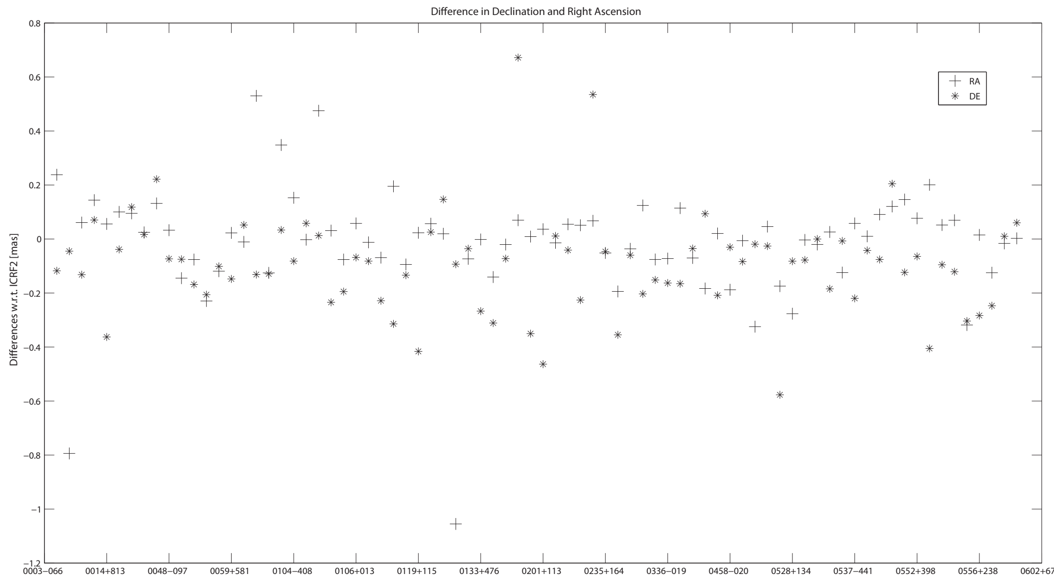

Fig. 4 Source positions w.r.t. ICRF2 estimated from the CONT11 data as a combination of 5 Analysis Center contributions.

4 Summary and Conclusions

For the ITRF2013 preparations test data are available, but not even half of the expected submissions have been submitted to the IVS data center. The data that have been tested for the new institutions look promising. Contributions from manifold software packages and many contributors are expected, which helps to expand the heterogeneity of the combined solution. First contributions have been submitted to the IVS data center. A first combined IVS solution including all contributions that were promised is expected to be ready in May 2014 (status quo April 2014).

Concerning the source position combination, an inclusion of source positions into the ITRF combination has originally been envisaged for ITRF2013, but further investigations on source position analysis and combination were postponed by the IVS to the post-ITRF2013 era. Nevertheless, the combination software was already expanded so that the inclusion of source positions has been integrated in the combination routines. First results are looking promising both for the single session combination and for the global CRF solution.

References

1. Böckmann, S., Artz, T., Nothnagel, A., Tesmer, V.: International VLBI Service for Geodesy and Astrometry: Earth orientation parameter combination methodology and quality of the combined products, J. of Geophysical Research, Vol. 115, doi:10.1029/2009JB006465, 2010.
2. Bachmann, S. and Lösler, M.: IVS combination center at BKG - Robust outlier detection and weighting strategies. In Behrend, D. and Baver, K.D., editors, *IVS 2012 General Meeting Proceedings*of *NASA/CP-2012-217504*, pages 266–270, Madrid, 2012.
3. Altamimi, Z., Collilieux, X., Métivier, L.: ITRF2008: an improved solution of the international terrestrial reference frame, J. of Geodesy, Vol. 84, pages 457–476, doi:10.1007/s00190-011-0444-4, 2011.

IVS Working Group IV and the New Open Format Database

John Gipson

Abstract IVS Working Group IV was established to "design a data structure that meets current and anticipated requirements for individual VLBI sessions including a cataloging, archiving, and distribution system. Further, it will prepare the transition capability through conversion of the current data structure as well as cataloging and archiving softwares to the new system." Working Group IV successfully met these goals and was disbanded in March 2013. I describe the new VLBI data format, the use of the format by various software packages, and plans to transition to the new format.

Keywords Data structures, VLBI

1 Introduction and Brief History

At the 15 September 2007 IVS Directing Board meeting I proposed establishing a "Working Group on VLBI Data Structures". This proposal was unanimously accepted, and the Board established IVS Working Group 4 on VLBI Data Strucures (IVS-WG4). The first meeting of IVS-WG4 was at the IVS General Meeting in St. Petersburg in 2008 [1]. In 2009 I circulated a draft proposal within IVS-WG4, and this was presented to the wider VLBI community at the 2010 General Meeting in Hobart [2]. At that meeting I also solicited input on naming the data structure. At the IVS GM in Madrid [3] I presented a progress report and announced that the new structure would be called 'openDB'. The name acknowledges the long history of Mark III databases, and emphasizes the open nature of the new structure. The final report of IVS-WG4 was presented to the IVS Directing Board in March 2013. With its acceptance WG4 was disbanded. Since it turned out that the name 'openDB' is already taken, the format was renamed to vgosDB. A slightly modified version of the final report reflecting the name change was published in the 2013 IVS Annual Report [4].

It often happens that something that makes sense in theory does not work well in practice. To ensure that this did not happen, Calc/Solve and VieVS were modified to use 'draft' versions of the proposed structure. In 2010 I wrote a utility to convert a subset (the data contained in NGS format) of the data in a Mark III-database (MK3-DB) to the new format. This subset was chosen because many software packages use NGS format as input. VieVS was successfully modified to use this format. Solve was also modified to take some input from the new format, taking the rest of its input from Solve 'superfiles'. The original utility was expanded to convert more of the data in MK3-DB to vgosDB format, and by 2012 the vgosDB format could be used as a replacement for Solve 'superfiles'. Timing tests (see Figure 1) showed that the new format is faster for large sessions. Concurrently, nuSolve was modified to be able to read and write the new format. In the remainder of 2012 and the beginning of 2013 programs were written to handle other stages in the processing chain. By June 2013 it was possible to process a VLBI session in the vgosDB format, starting at correlator output and ending with a 'version 4' vgosDB where the ambiguities were resolved and the data edited. The first public release of Calc/Solve which used vgosDB was made in February 2014.

1. NVI, Inc.

Alpha-testing of the new format using Calc/Solve, nuSolve, and VieVS was very important. Although there were no fundamental changes in the overall scheme, there were many incremental changes that improved the final product. For example: we changed variable names to make them more consistent; we modified which variables were stored in which files to reflect our experience in processing the data (with the original specification, the standard processing would have required updating some files—something we wanted to avoid if possible); we made some files more self-contained, and we also reduced redundancy for variables which are sometimes constant for a session (e.g., ambiguity spacing) by introducing the ‘Repeat’ attribute.

The remainder of this note describes vgosDB and concludes with a transition plan. In a note of this size it is impossible to do more than present an overview of the vgosDB format. A fuller description of an earlier version of vgosDB can be found in [5]. This documentation is in the process of being updated to reflect the final version and should be available via anonymous ftp at the same location later in 2014.

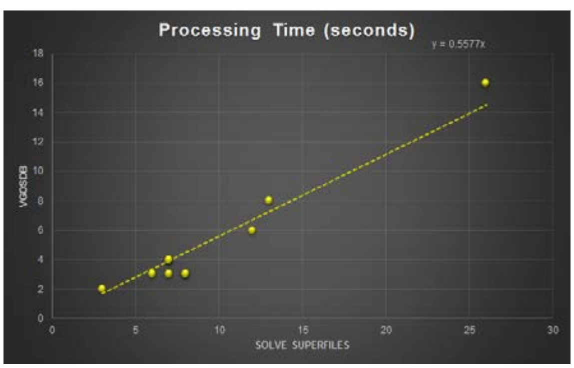

Fig. 1 Large sessions run much faster in the vgosDB format.

2 Design Goals

Table 1 summarizes some of the important design goals of IVS-WG4 and how they were achieved. We divide the goals into two classes: format is related to how the data is stored and structure to how the data is organized. This is an important distinction, because these are independent. For example, T. Hobiger [6] wrote routines which store the information contained in a MK3-DB in netCDF files while preserving the original organization of the data. This format would have met most of the goals in the top of the table, but not those in the bottom.

Table 1 Design Goals.

Goal	Format	Structure	How
Low Level Goals			
Reduce Redundancy		X	Scope
Ease of Access	X		NetCDF
Speed of Access	X		NetCDF
Open format	X		NetCDF
Many Languages, Platforms	X		NetCDF
High Level Goals			
Flexibility		X	Wrappers Separation
Exchange subsets of data	X	X	Separation
Separate observables, models, theoreticals		X	Separation
Data at different levels of abstraction		X	Completeness, Separation

Scope is how broadly applicable the data is. The Mark III databases (MK3-DB) recognize two scopes: 1) session-dependent data is valid for the entire session (e.g., station positions and names) and is stored in type 1 lcodes, and 2) observation-dependent data is valid for a given observation and is stored in type 2 and type 3 lcodes. Everything that is not session-dependent is automatically observation-dependent. This results in great redundancy, since some items, such as station meteorological data are really station/scan-dependent (that is, are constant for a given station in a scan), and not observation-dependent. For an N-station scan, this information is currently stored N–1 times in the MK3-DB and NGS format. vgosDB enlarges the concept of scope to include the following additional categories: 3) scan-dependent, where the data depends only on the scan (e.g., EOP) and 4) station/scan-dependent (Met data, cable-cal), where the data depends only on the station and a scan. Separating data by scope reduces redundancy at the cost of extra book-keeping.

NetCDF is a commonly used binary format used to store scientific data. Figure 2 is a schematic depiction of a netCDF file. NetCDF was designed for fast data access. It is open-source, and there are interfaces for most common computer languages (e.g., C, C++, FORTRAN, Matlab, Java) and most common operating sys-

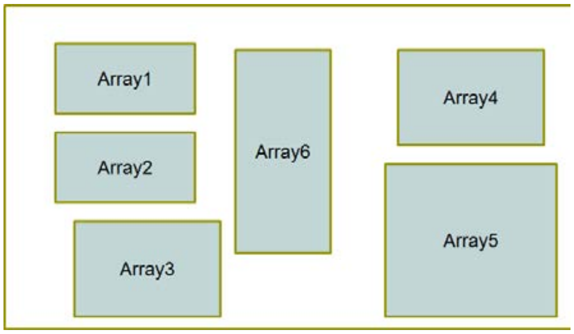

Fig. 2 A netCDF file can be viewed as a container for arrays.

tems (Linux, Windows, Mac OS). There are other data-storage formats with similar characteristics, and there are utilities for converting from one format to another. We chose netCDF because several members of IVS-WG4 had prior experience with it. All data in vgosDB is stored in either netCDF or ASCII files. This ensures that it can be read by anyone.

Separation is the concept that data should be split up depending on its origin and use. This is in contrast to MK3-DB and NGS format where in principle all of the data required to analyze a session is stored in a single file. In contrast, in the vgosDB format, observables (which should never be modified) are kept separate from theoreticals, partials, and the results of derived quantities such as ionosphere corrections.

An advantage of Separation is that it allows you to do a partial update of the data, for example, using alternative met-data, without updating all of the files. This is in contrast to the MK3-DB format where changing a single variable requires an entirely new database.

Completeness is the concept that we should include sufficient data so that the the complete processing chain can be redone from scratch. The proposed format does allow for this to happen, but this would require archiving the raw correlator output. In the current implementation we do not go quite this far, but we do include all data present in Version 1 MK3-DB. This allows other software packages besides Calc/Solve to do data editing and ambiguity resolution. Because many session log-files from 1990 onwards are available at the IVS Data Centers, other packages can also add cable-calibration and meteorological data.

Wrappers are special ASCII files that organize the data. These are necessary because, in contrast to MK3-DB or NGS format where all of the data is one file,

```
Begin History
Begin Program Calc/Solve Processing
Version   Mixed
CreatedBy John M. Gipson
Default_dir History
RunTimeTag 2014/04/21 17:21:51
History    10JAN04XU_kMK3DB_V005.hist
End Program Calc/Solve Processing
...
End History
!
Begin Session
Session I10004
AltSessionId 10JAN04XU
Head.nc
Default_Dir Apriori
Eccentricity.nc
Antenna.nc
Station.nc
Source.nc
Default_Dir CrossReference
StationCrossRef.nc
SourceCrossRef.nc
End Session
!
Begin Station KOKEE
Default_Dir KOKEE
TimeUTC.nc
Met.nc
AzEl_V005.nc
End Station KOKEE
!  ... Wettzell omitted
Begin Observation
!
Default_Dir Observables
TimeUTC.nc
DataFlag_bS.nc
DataFlag_bX.nc
AmbigSize_bS.nc
AmbigSize_bX.nc
Baseline.nc
GroupDelay_bS.nc
Source.nc
GroupDelay_bX.nc
Default_Dir ObsEdit
NumGroupAmbig_bX.nc
NumGroupAmbig_bS.nc
GroupDelayFull_bX.nc
GroupDelayFull_bS.nc

Default_Dir CrossReference
ObsCrossRef.nc
Default_Dir ObsDerived
EffFreq_bS.nc
EffFreq_bX.nc
End Observation
```

Fig. 3 Wrapper grammar is simple and human-readable.

vgosDB splits the data into many files. The wrapper contains pointers to all of the different pieces.

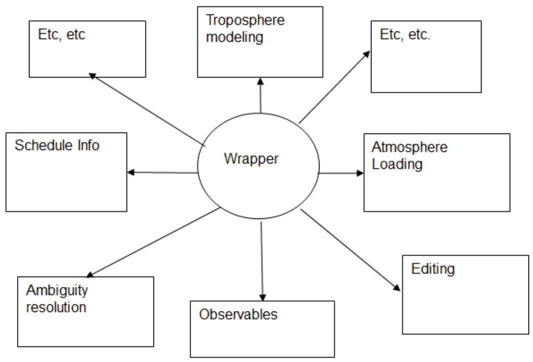

Fig. 4 A wrapper organizes vgosDB data.

3 Organization

In this section, we give an overview of how the vgosDB data is organized.

3.1 Directories

vgosDB sessions are organized by year and then by session. The name of the session directory is the same as the associated MK3-DB name. For example, the directory $vgosDB/2010/10JAN04XA$ and its sub-directories contains all of the data for 10JAN04XA. There is one sub-directory for each station (e.g., *KOKEE*) which contains all of the station/scan-dependent data. The *Session* and *Scan* sub-directories contain session-dependent and scan-dependent data, respectively. There are several observation-dependent directories containing different types of data: *Observables* contains observables; *ObsEdit* contains the data editing flags; *ObsCal* and *ObsPart* contain calibration and partial information; and so on. The *History* sub-directory contains ASCII files summarizing the history of the experiment. In addition there is a provision for software specific directories, e.g., *Solve* or *VieVS*, which contain information of interest only to a particular analysis package.

3.2 vgosDB Variable

A vgosDB variable is an array of data together with associated meta-data. Roughly speaking, a variable corresponds to an MK3-DB lcode. The meta-data is stored using netCDF attributes, some examples of which are shown in Table 2. Each variable name is almost unique: it is permissible to use the same name if the variables differ in Station, Band or Kind. (Kind is described more fully below.) For example, the temperature data at all stations is called TempC. The X and S band group delay are both called GroupDelay but reside in different files.

Table 2 Some vgosDB variable attributes.

Name	Comment
Definition	Required
Units	Required if appropriate
Origin	Optional
Repeat	Indicates repeating value
Lcode	Optional
CreateTime	Optional

3.3 Time Dependence

There are two kinds of time dependence for vgosDB variables. If the time dependence is explicit, then the time information must be contained in the same file as the variable. If it is implicit, then the time dependence is contained in external files called *TimeUTC.nc*. This file contains two arrays: 1) YMDHM is an integer array that contains the Year, Month, Day, Hour and Minute part of the time-tag and 2) Second is a double precision array that contains the seconds part of the time-tag. Each station directory contains a *TimeUTC.nc*. The files *Scan/TimeUTC.nc* and *Obs/TimeUTC.nc* contain the time tags for the scan-dependent and the observation-dependent data, respectively.

3.4 Files

Related vgosDB variables are stored together in NetCDF files. These files have header information which provides information about when the files were made, their contents, and some information used for consistency checks. An example is given in Table 3.

Table 3 Sample vgosDB header information.

Name	Example
Stub	Cal-Cable
CreateTime	2013/06/27 17:56:41
CreatedBy	John Gipson NVI, Inc.
Program	db2vgosDB 2014Feb04
Subroutine	write_station_file 2012Dec11
DataOrigin	Data extracted from i1004kk.log
TimeTag	StationScan
TimeTagFile	TimeUTC.nc
Session	I1004
Station	KOKEE

Data is grouped together depending on scope, origin, how the data is used, and how the data is processed. One guiding principle in deciding where to put the data was that in routine data processing, although it may be necessary to make a new NetCDF file, you should avoid having to update an existing one. Most of the vgosDB files contain only a few vgosDB variables. For example, the meteorology data for each station usually comes from an on-site sensor. This data is stored in the file Met.nc in the appropriate station directory. Met.nc files contain pressure, temperature, and humidity of a site. The GroupDelay_bX.nc file contains the measured group delay and sigma. (A notable exception to the rule that 'each file contains only a few variables' is the CorrInfo*.nc file which contains the output of the fringing process and has $\sim$ 100 variables, most of which are seldom or rarely used.)

Table 4 vgosDB file-naming conventions.

Stub_kAAAA_vBBBB_iCCCC_bDD.nc Fields are separated by _ Field type indicated by k, v, i, b Field length is arbitary		
Part	Field	Comment
Stub	First	Specifies type of data
_k	Kind	e.g., NMF, VMF, ...
_v	Version	Arbitrary version control
_i	Institution	Individual/Institution
_b	Band	e.g., X, S, Ku..
Examples: Met_kNMF.nc Cal-Cable.nc Part-NutationEQX_kIAU2000 GroupDelay_bX.nc		

Table 4 summarizes the filenaming convention. The first part of the file-name is the *stub* and completely specifies the type of data in the file. Files with the same stub are 'plug compatible', i.e., you can replace one file with another and the analysis software will continue to work correctly. The *kind* field differentiates between different functionally equivalent models, e.g., mapping functions such as VMF1 and GMF.

4 Transition Plans and Next Steps

The first Calc/Solve release, using vgosDB, was made in February 2014. This release can use vgosDB to replace superfiles. Also, nuSolve, which was released at the same time, can read and write the vgosDB format. VieVS is able to use vgosDB instead of NGS cards. The Goddard VLBI group has developed programs to create vgosDB files from correlator output and to use these files in all other stages in the processing chain.

Currently the Calc/Solve Analysis Centers (ACs) are responsible for producing the 'Version 4' databases which serve as the basis for all VLBI analysis. (Other software packages use NGS cards which are derived from the MK3-DB.) In 2014 the Calc/Solve ACs will transition to producing vgosDB files and submitting them to the IVS Data Center. Until this transition is complete the Goddard VLBI group will make available all IVS sessions in vgosDB format. By the end of 2014 the Calc/Solve ACs will stop producing MK3-DB, and we will fully transition to the new format.

References

1. J. Gipson, IVS Working Group 4 on VLBI Data Structures, in IVS 2008 General Meeting Proceedings, pp. 143–152.
2. J. Gipson, IVS Working Group 4: VLBI Data Structures, in IVS 2010 General Meeting Proceedings, NASA/CP-2010-215864, pp. 187–191.
3. J. Gipson, IVS Working Group 4: VLBI Data Structures, in IVS 2012 General Meeting Proceedings, NASA/CP-2012-217504, pp. 212–221.
4. J. Gipson et al., Final Report of IVS Working Group 4 on Data Structures, in IVS 2013 Annual Report, in press.
5. J. Gipson, OpenDB Manual, ftp:://gemini.gsfc.nasa.gov/pub/misc/jmg/VLBI_Structure_2013Jun11.pdf
6. T. Hobiger, Y. Koyama, T. Condo, MK3TOOLS and NetCDF-Storing VLBI data in a machine independent oriented data format, Proceedings 2007 EVGA Meeting.

The VLBI Data Analysis Software νSolve: Development Progress and Plans for the Future

S. Bolotin, K. Baver, J. Gipson, D. Gordon, D. MacMillan

Abstract The program νSolve is a part of the CALC/SOLVE VLBI data analysis system. It is a replacement for interactive SOLVE, the part of CALC/SOLVE that is used for preliminary data analysis of new VLBI sessions. νSolve is completely new software. It is written in C++ and has a modern graphical user interface. In this article we present the capabilities of the software, its current status, and our plans for future development.

Keywords VLBI, data analysis, software

1 Introduction

The currently used software CALC/SOLVE for data analysis of geodetic VLBI observations has been developed since the end the 1970s. It is written mostly in FORTRAN and its design reflects hardware restrictions that existed at the time of its active development phase. The software evolved into a large system that is widely used in many areas of space geodesy. At the same time the system grows stiffer and harder to modify. Continuous commissioning of new VLBI stations, an enormous increase in the observation data rate, and realization of the VLBI Global Observing System (VGOS) technology led to new requirements for data analysis software as well as for the software development process.

Having long experience with the development of the CALC/SOLVE VLBI data analysis software, the VLBI group at the NASA Goddard Space Flight Center initiated creation of the new generation software.

NVI, Inc.

The first step in developing new data analysis software was made in 2007, when the IVS Working Group on VLBI Data Structures (IVS WG4) was created [6]. Efforts undertaken by the group were eventually realized in the creation of the new VLBI data format, vgosDB. In mid-2009 a design of system architecture of νSolve was elaborated and presented at the IVS 2010 General Meeting in Hobart ([2]). A prototype of the software was demonstrated in 2011 at the 20th EVGA Meeting in Bonn [3]. The first version of νSolve was presented at the IVS 2012 General Meeting in Madrid [4]. A public release of the software was made on February 20, 2014.

Currently νSolve is used for routine data analysis of the IVS-R4 and IVS-INT sessions at the NASA GSFC VLBI Analysis Center. It was also used in data analysis of the first VGOS observations.

2 New VLBI Data Analysis Software

νSolve is a replacement for interactive SOLVE. It is designed to analyze a single VLBI session by performing necessary calibrations and data editing and storing results in an appropriate format. Later νSolve will evolve into a powerful session editor that allows us to fix all known anomalies of the VLBI observations, for example subambiguities.

We should note that νSolve does not make global solutions. A separate executable (a driver) will be developed later to perform data analysis of multiple sessions of VLBI observations.

The architecture of νSolve was discussed in detail in [2] and [4]. Here we just outline the main features of the architecture.

The software is written in the *C++* programming language. It is being developed with the Linux/GNU operating system, but its use is not limited only to Linux. We tried to use a minimal set of external libraries for its functionality. In addition to the standard system libraries, *libc* and *libm*, the *Qt* library is used for the graphical user interface, data containers, and auxiliary tools. To realize input and output operations in the new vgosDB format we use the *netCDF* library [8].

The software consists of two parts:

1. The Space Geodesy Library, a library where data structures and algorithms are implemented (about 90% of the total source code);
2. An executable `nuSolve` – a driver that calls the library functions and organizes work with an end-user (about 10% of total source code).

Such organization of the software allows us to reuse the source code in other applications. In the first public releases, while we have only one executable, `nuSolve`, the distribution and the whole software package is called "nuSolve". Later, the library and drivers will be distributed in separate packages.

The modular structure of the software makes it flexible and stable. By a *module* we mean a logical block of the source code that is loosely tied with other parts of the software. A detailed description of modules is given in [2].

3 Features of the Software

The general features of the software are the following. It is able to read and write data in the Mark III DBH format as well as in the new vgosDB format. There are no limitations on the numbers of stations and sources that participate in one session or the number of observations. The software can work either through the CALC/SOLVE catalog subsystem or in a standalone mode. The process of data analysis can be automated to some extent. Special efforts were made to reproduce CALC/SOLVE results. If a user selects the option "Interactive SOLVE compatible mode", νSolve makes a solution that is very close to the solution obtained with interactive SOLVE (the post fit residuals differ by not more than 0.2 ps) using the same set of models, external a priori data, and so on.

3.1 Functionality

The capabilities of νSolve are evolving in accordance with the adopted model of the software production process (see [2]). All necessary key functional points are implemented in the software. νSolve is able to: 1) read/write files in Mark III DBH and vgosDB formats, 2) display on plots various information that were stored in the files, 3) perform least squares parameter estimation, 4) process a single VLBI session and save obtained results, 5) detect and process clock breaks, 6) resolve group delay ambiguities, 7) evaluate ionospheric corrections, 8) calibrate weights of observations to make a normalized χ^2 equal to unity, 9) eliminate outliers, restore previously eliminated observations, 10) use different geophysical models in data analysis, and 11) apply alternative a priori information from external files.

These key functional points have allowed us to use the software in routine data analysis of all IVS-INT and IVS-R4 VLBI sessions since July 2012.

3.2 Plotting Subsystem

A simple plotting subsystem has been developed for νSolve. By design, the subsystem is a separate generic module that is independent of VLBI data structures, estimated parameters, or other parameters. Instead, it provides a mechanism to communicate with other parts of the software. This feature makes it possible to use the plotting subsystem in various aspects of VLBI data processing and other applications.

The use of the plotting subsystem allows a user to display various values that are either stored in files, evaluated "on the fly", or estimated from VLBI data analysis. Also, it permits a user to edit observations by eliminating outliers and manually adjusting the number of group delay ambiguities.

In Figures 1–3, several examples of using the plotting subsystem are shown.

3.3 Estimator

The module Estimator of νSolve performs a least squares estimation of the following parameter types:

- *local parameter*: an unbiased parameter that is determined for a whole session;
- *arc parameter*: an unbiased parameter estimated for an interval specified by the user (e.g., 1 hour);
- *piecewise linear function*: coefficients of a continuous linear function estimated from data, where the interval between nodes is specified by the user;
- *stochastic parameter*: an alternative to a piecewise linear function, a time varying parameter is modeled as a stochasic process.

The realization of the least squares estimation is made with a square-root information filter (SRIF) [1]. Using SRIF and its derivations makes it possible to implement a model where the arc and piecewise linear functions can have different lengths of segment intervals or have overlapping segments.

The software can estimate the following parameters:

- coefficients of the polynomial model for station clocks,
- tropospheric zenith delays and horizontal gradients,
- station positions,
- antenna axis offsets,
- source coordinates,
- polar motion offsets and rates,
- Earth rotation, $d(UT1-UTC)$ and its rate,
- angles of nutation,
- baseline clock offsets, and
- baseline vectors.

The user can assign any of the parameter types to each of these parameters. The user can select a list of stations to estimate their positions or sources to estimate their coordinates. If all available stations or sources are selected, the user can specify what station or source *a priori* coordinates will be used in the equations of No-Net-Rotation and/or No-Net-Translation constraint.

4 Data Processing Operations

The following essential operations that are necessary to perform to make a VLBI session usable in a batch solution are: clock break detection and correction, ambiguity resolution, evaluation of ionospheric correction, adjusting of weights of observations, and outlier processing. We now discuss these operations.

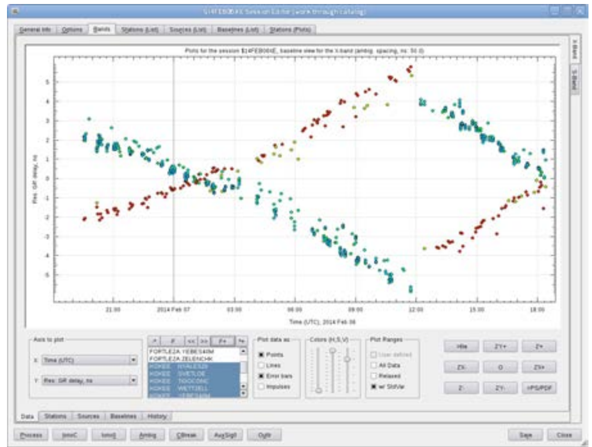

Fig. 1 A clock break at station KOKEE during session \$14FEB06XE. The group delay residuals are shown only for selected baselines.

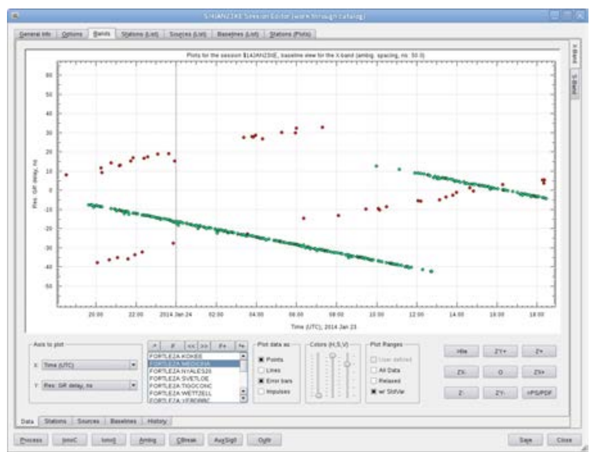

Fig. 2 Group delay residuals with unresolved ambiguities for the FORTLEZA–MEDICINA and MEDICINA–WETTZELL baselines of the \$14JAN23XE session.

A clock break is a discontinuity in the recorded time marks of the observations due to hardware problems at the station. There are also other effects (e.g., manually applied phase calibration which consists of several segments) that manifest themselves as clock breaks as shown in Figure 1. The standard SOLVE software estimates parameters of a clock break as additional parameters of the solution. In contrast, *v*Solve estimates clock break parameters in a separate solution and then applies them in further data analysis. Such an approach allows processing of rare cases of multiple clock breaks during a short interval of time.

Clock breaks can be detected and corrected in automatic, semi-automatic, and manual mode.

Ambiguity resolution of group delays (see Figure 2) is done using the same ideas as implemented in interactive SOLVE. The algorithms implemented in νSolve are less restrictive. The software can process VLBI sessions that have different ambiguity spacing of group delays on different baselines or even on one baseline. In addition, νSolve allows the user to adjust the number of ambiguities manually.

The ionosphere corrections for group delays, phase delay rates, and phase delays are evaluated using dual band VLBI observations. Since the group delays are determined up to an arbitrary number of ambiguity spacings, the evaluated ionospheric correction is not unique. It is a good practice to process clock breaks and resolve group ambiguities before evaluating the ionospheric corrections.

We perform corrections of observation weights to make the normalized χ^2 equal to unity. Complementary standard deviations can be computed in two modes: in a session-wide mode (one weight correction is evaluated for the whole set of observations) and a baseline-dependent mode. Weight corrections change the solution and the distribution of post fit residuals, making the process of weight correction an iterative process. The complementary standard deviations can be imported from an external file. Reweighting is performed in conjunction with the next operation, outlier elimination.

An outlier is an observation with an absolute value of a normalized residual greater than a user-specified threshold. There can be various scales used for normalization of residuals. In the interactive SOLVE compatibility mode νSolve uses a dispersion to normalize the residuals [7]. The dispersion, d is expressed as

$$d = \sqrt{\frac{\sum_{i=1}^{N}(p_i \varepsilon_i)^2}{N-1}},$$

where p_i is a weight of ith observation and ε_i is its residual. The sum is done, depending on options, either over all processed observations or only for a particular baseline. In this case, the normalized residual will be

$$\rho_i = \frac{p_i \varepsilon_i}{d}.$$

As one can see, the normalized residuals are unitless. Distributions of the residuals and the normalized residuals are different. In Figure 3 both types of values are shown for one baseline.

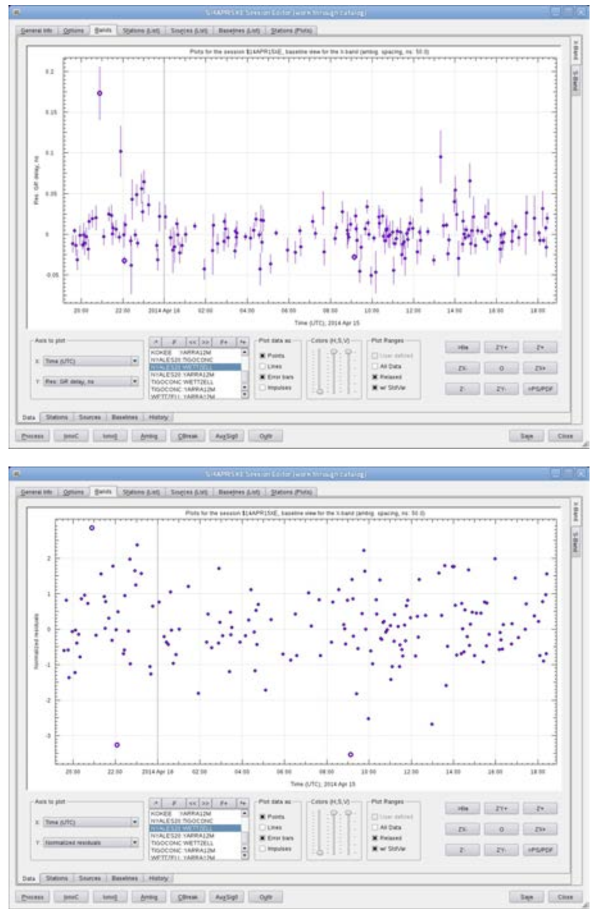

Fig. 3 Group delay residuals (upper screenshot) and the corresponding normalized residuals (lower screenshot) of the baseline NYALES20–WETTZELL obtained for the session $14APR15XE.

Typically, the threshold for normalized residuals is 3 or 5. In some circumstances this corresponds to 3σ or 5σ thresholds of the residuals. The normalized residuals can be evaluated either for the whole set of processed observations or on a baseline basis. The process of outlier exclusion is an iterative process. After excluding an outlier from a solution, a new solution and normalized residuals are calculated. Also, the user can include previously excluded observations if the absolute values of their normalized residuals become less than the specified threshold. This action is called restoration and is performed iteratively. Both actions, outlier elimination and restoration, are performed in conjunction with the reweighting operation.

5 Conclusions

The first public release of the software νSolve was made in February 2014 along with a new CALC/SOLVE release. At the time of writing it can be accessed at the URL:

ftp://gemini.gsfc.nasa.gov/pub/misc/slb/

After the release, we have received user comments and suggestions and the software now is in a permanent process of updates. This is why it was released in a directory separate from the CALC/SOLVE directory. As for next major public releases, these will be distributed in the general CALC/SOLVE source tree.

In addition to the source code, a user guide on νSolve has been created. Currently it is available as a separate PDF file in the same FTP directory.

In the next releases we will focus on the following issues: 1) optimization of data processing time; 2) improvement of the plotting system; 3) extension of the functionality; and 4) introduction of the elements of automatic data processing.

References

1. G. J., Biermann, *Factorization Methods for Discrete Sequential Estimation. V128, Mathematics in Science and Engineering Series*, Academic Press, 1977.
2. S. Bolotin, J. M. Gipson and D. MacMillan. *Development of a New VLBI Data Analysis Software*. In D. Behrend, and K.D. Baver, editors, *IVS 2010 General Meeting Proceedings*, NASA CP 2010-215864, NASA GSFC, Maryland, pages 197–201, 2010.
3. S. Bolotin, J. M. Gipson, D. Gordon and D. MacMillan, *Current Status of Development of New VLBI Data Analysis Software* In W. Alef, S. Bernhart and A. Nothnagel, editors, *Proc. of the 20th Meeting of the EVGA*, Bonn, Germany, pages 86–88, 2011.
4. S. Bolotin, K. Baver, J. Gipson, D. Gordon and D. MacMillan *The First Release of νSolve.* In D. Behrend, and K.D. Baver, editors, *IVS 2012 General Meeting Proceedings*, NASA CP 2012-217504, NASA GSFC, Maryland, pages 222–226, 2012.
5. S. Bolotin, K. Baver, J. Gipson, D. Gordon and D. MacMillan *Current Status of νSolve.* In N. Zubko, and M. Poutanen, editors, *Proc. of 21st Meeting of the European VLBI Group for Geodesy and Astronomy*, p.77–80, ISSN: 0355-1962, Kirkkonummi 2013.
6. J. M. Gipson *The Report of IVS-WG4.* In D. Behrend, and K.D. Baver, editors, *IVS 2012 General Meeting Proceedings*, NASA CP 2012-217504, NASA GSFC, Maryland, pages 212–221, 2012.
7. L. Petrov *Memo about outliers elimination* CALC/SOLVE documentation, available at http://lacerta.gsfc.nasa.gov/mk5/help/elim_02_hlp.ps.gz
8. R. K. Rew and G. P. Davis *NetCDF: An Interface for Scientific Data Access* IEEE Computer Graphics and Applications, Vol. 10, No. 4, pp.76–82, 1990.

Vienna VLBI Software: Current Release and Plans for the Future

Johannes Böhm[1], Hana Krásná[1], Sigrid Böhm[1], Vasyl Choliy[2], Andreas Hellerschmied[1], Armin Hofmeister[1], Maria Karbon[4], David Mayer[1], Jamie McCallum[3], Matthias Madzak[1], Tobias Nilsson[4], Lucia Plank[3], Stanislav Shabala[3], Benedikt Soja[4], Jing Sun[5], Kamil Teke[6]

Abstract The Vienna VLBI Software (VieVS) is a geodetic VLBI data analysis software written in Matlab. It has been developed and maintained at the Department of Geodesy and Geoinformation of the Vienna University of Technology since 2008. Recent improvements and extensions include a source structure simulator, additional estimable parameters in the global solution such as harmonic station position variations, and tools to observe satellites with VLBI radio telescopes and to analyze these observations. A highlight each year is the VieVS User Workshop which is held in September at TU Vienna. The VieVS Web site can be accessed at http://vievs.geo.tuwien.ac.at/.

Keywords VLBI analysis software

1 Introduction

The Vienna VLBI Software (VieVS) is VLBI data analysis software written in Matlab (Böhm et al., 2012 [1]). VieVS has been developed and maintained by the research group *Höhere Geodäsie* (Higher Geodesy) at the Department of Geodesy and Geoinformation of the Vienna University of Technology (TU Vienna) since 2008. Important contributions from other groups have been made by the Shanghai Astronomical Observatory (scheduling), Hacettepe University (least squares adjustment), and the University of Tasmania (source structure simulation and other features).

1. Vienna University of Technology
2. Main Astronomical Observatory
3. University of Tasmania
4. GeoForschungszentrum
5. Shanghai Astronomical Observatory
6. Hacettepe University

The current version, VieVS 2.1, was released in August 2013. The next version, VieVS 2.2, will be freely available to registered users in the middle of 2014. These registrations allow us to provide information to the users in the case of new releases or bugs in the software.

VieVS has been written in Matlab, which is commercial software and rather expensive. Nonetheless, we decided to use Matlab, because the source code is compact and easy to understand and to modify, and because Matlab provides many built-in functions to write concise code. Furthermore, Matlab provides tools to set up a Graphical User Interface (GUI). Since our students at TU Vienna are familiar with Matlab, it is rather easy for them to write bachelor or diploma theses with VieVS by developing small add-ons to the software. The disadvantages are that Matlab is costly and slower compared to other programming languages; however, a global solution with all geodetic VLBI sessions can be run in one or two days on a standard PC, which is fast enough for most of our purposes.

2 Structure of VieVS

VieVS consists of several modules which are connected in one common GUI (see Figure 1). Typically, the modules VIE_INIT, VIE_MOD, and VIE_LSM are run to analyze a single VLBI session. Additionally, VIE_SCHED can be used to schedule a VLBI session with the classical station-based approach and with the newly developed source-based approach (Sun et al., 2014 [8]). If required, these schedules can then be supplemented with simulated observations based on thermal noise as well as correlated clock and troposphere noise (Pany et al., 2011 [4]). The simulation of source structure effects (Shabala et al., 2014 [9]) will be available with the simulator in the new release.

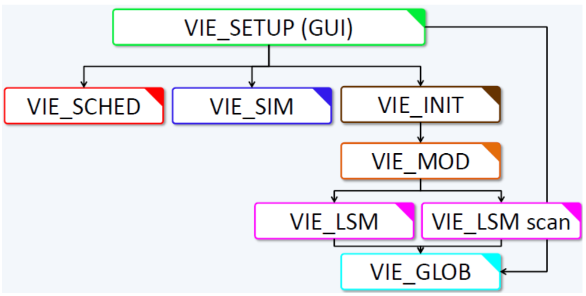

Fig. 1 Structure of VieVS: All modules are connected and can be accessed by a common GUI. Additionally, the modules can also be run in batch mode.

The module VIE_GLOB can be used to stack normal equations from single sessions to run a global VLBI solution (Krásná et al., 2014 [3]) to, e.g., determine global terrestrial and celestial reference frames. Alternatively to starting the jobs with the GUI, it is also possible to run VieVS in batch mode, i.e., without graphical user interface. This is particularly well suited to run longer jobs on a server remotely or to perform automatic processing.

VieVS is capable of following the Conventions of the International Earth Rotation and Reference Systems Service (IERS; Petit and Luzum, 2010 [5]). More specifically, VieVS applies the concept of piecewise linear offsets to nearly all parameters (Böhm et al., 2012 [1]). In terms of Earth orientation parameters, this is in agreement with the goals of the Global Geodetic Observing System (GGOS), but it is not in full agreement with other solutions by Analysis Centers of the International VLBI Service for Geodesy and Astrometry (IVS). However, ways have been found to include solutions with VieVS in the VLBI combination for the International Terrestrial Reference Frame 2013 (ITRF2013) (Thomas Artz, Andreas Iddink, and Sabine Bachmann, personal communication).

3 AUST Campaigns

The scheduling module VIE_SCHED in VieVS has been successfully applied for scheduling VLBI sessions with the telescopes in Australia (Hobart, Katherine, and Yarragadee), in South Africa (Hartebeesthoek), and New Zealand (Warkworth) (see Figure 2). The overall plan for those sessions is accessible at: http://auscope.phys.utas.edu.au/opswiki/doku.php.

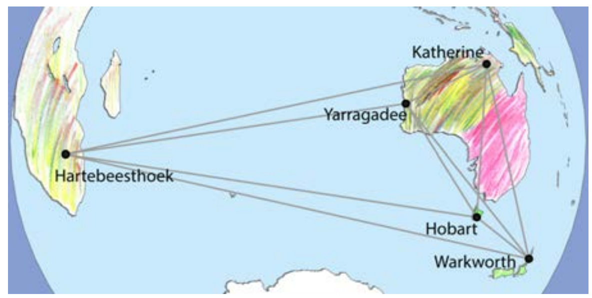

Fig. 2 Stations participating in the 15-day continuous AUST campaign (provided by Sarah and Jim Lovell).

In particular, the AUSTRAL sessions since July 2013 have been scheduled in geodetic and astrometric mode, and a continuous AUST campaign was designed for 15 days from 28 November to 15 December 2013. This continuous campaign will demonstrate the capabilities of the telescopes in the South, and it will serve to investigate source structure effects on geodetic parameters. In particular, alternate observations of 8 and 7 days with *good* structure index (SI < 2.5) and *bad* sources (SI > 2.5), respectively, have been carried out to demonstrate the impact of source structure on geodetic results. The schedules are repeated every sidereal day in order not to mitigate systematic effects by observing sources at different angles on different days.

In Figures 3 and 4, we illustrate the simulated effects (mean values and mean formal uncertainties) on the estimates of right ascension of the sources and of x-components of station coordinates. It should be clearly stated that we have used 30 sessions with structure indices 1 and 4, respectively, instead of 8 and 7 sessions with structure indices <2.5 and >2.5, respectively, and we find a clear mitigation of mean values and mean formal uncertainties if *good* sources are observed. As soon as the real observations become available, we will analyze them. However, we are aware that with the real observations, the effects will not be as obvious.

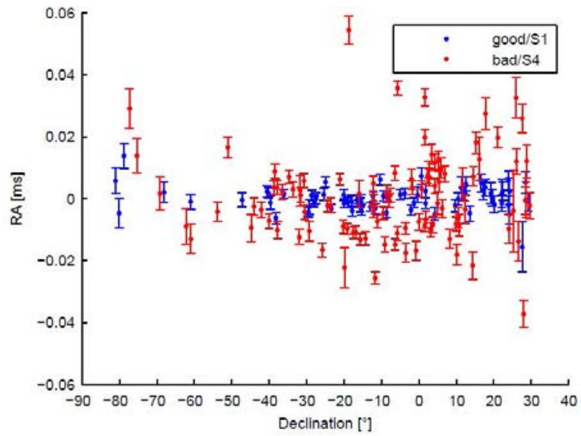

Fig. 3 Mean values of the estimates of right ascension and mean formal uncertainties (error bars) from 30 simulated sessions. In the case of good sources, the structure indices are assumed to be 1. The bad sources were simulated with a structure index of 4.

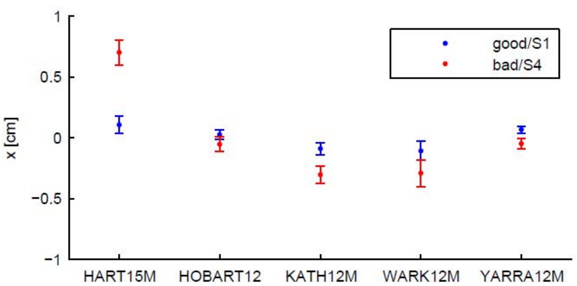

Fig. 4 Mean values of the estimates of X-components in station coordinates and mean formal uncertainties (error bars) from 30 simulated sessions. In the case of good sources, the structure indices are assumed to be 1. The bad sources were simulated with a structure index of 4.

4 New Features and Ongoing Developments

New features to become available with the new release VieVS 2.2 comprise the source structure simulator (Shabala et al., 2014 [9]), updates to the scheduling module VIE_SCHED such as the tag-along mode, and the ability to estimate axis offsets and harmonic station position variations in the global solution.

Ongoing activities are related to the observation of satellites with VLBI radio telescopes. Hellerschmied et al. (2014 [2]) developed a Satellite Scheduling Module in VieVS, providing the possibility to plan satellite observations flexibly for arbitrary station networks and satellite constellations. With the schedule files issued in VEX format, it is possible to carry out actual satellite observations. These schedules have been successfully applied to observe GLONASS satellites on the baseline Wettzell–Onsala in January 2014. Plank et al. (2014a [6], 2014b [7]) have analyzed simulated observations to satellites with an internal version of VieVS and found that the frame ties between the dynamical frame realized by satellites and the celestial reference frame benefits greatly from a combined estimation of tropospheric parameters from both quasar and satellite observations.

5 Future Plans

A major restructuring of VieVS will be required by a rigorous change to the new VGOS databases which are provided as netCDF files. On the other hand, the new format will ease the exchangeability of data between different software packages.

Furthermore, we are considering replacing the Matlab-based GUI by graphical user interfaces built with Qt. By doing so, we could remove the dependency on the commercial software Matlab, because VieVS in batch mode could also be run with Octave, a free Matlab alternative. First steps towards that goal have already been taken.

Other main VieVS activities in the future will be related to observing satellites with VLBI radio telescopes, tropospheric delay modeling with ray-traced delays, scheduling legacy antennas together with new VGOS telescopes, geophysical and astronomical parameter estimation (e.g., galactic rotation), contributions to ICRF3, and filter solutions for the analysis of observations.

6 VieVS User Workshops

There has already been a series of four VieVS User Workshops at TU Vienna. The 5th User Workshop will be held from 17 to 19 September 2014, and everybody is welcome to attend. More information about the VieVS User Workshops can be found at http://vievs.geo.tuwien.ac.at/.

Acknowledgements

We would like to acknowledge the Austrian Science Fund (FWF) for supporting our work in projects Integrated VLBI (P23143-N21) and Radiate VLBI (P25320-N29).

References

1. J. Böhm, S. Böhm, T. Nilsson, A. Pany, L. Plank, H. Spicakova, K. Teke, and H. Schuh, The New Vienna VLBI Software, in: International Association of Geodesy Symposia, Vol. 136, edited by S. Kenyon, M.C. Pacino, and U. Marti, ISBN 978-3-642-20337-4, pp. 1007–1012, 2012.
2. A. Hellerschmied, L. Plank, A. Neidhardt, R. Haas, J. Böhm, C. Plötz, and J. Kodet, Observing satellites with VLBI radio telescopes – practical realization at Wettzell, Proceedings of the IVS General Meeting 2014, edited by D. Behrend, K.D. Baver, and K. Armstrong, Science Press, 2014.
3. H. Krásná, J. Böhm, L. Plank, T. Nilsson, and H. Schuh, Atmospheric Effects on VLBI-Derived Terrestrial and Celestial Reference Frames, in: International Association of Geodesy Symposia, Vol. 139, edited by C. Rizos and P. Willis, pp. 203–208, 2014.
4. A. Pany, J. Böhm, D. MacMillan, H. Schuh, T. Nilsson, and J. Wresnik, Monte Carlo simulations of the impact of troposphere, clock and measurement errors on the repeatability of VLBI positions, Journal of Geodesy, 85(1), pp. 39–50, doi: 10.1007/s00190-010-0415-1, 2011.
5. G. Petit and B. Luzum (eds.), IERS Conventions (2010), IERS Technical Note 36, Frankfurt am Main: Verlag des Bundesamts für Kartographie und Geodäsie, ISBN 3-89888-989-6, 2010.
6. L. Plank, J. Böhm, and H. Schuh, Precise station positions from VLBI observations to satellites: a simulation study, Journal of Geodesy, doi: 10.1007/s00190-014-0712-1, 2014a.
7. L. Plank, J. Böhm, and H. Schuh, VLBI satellite tracking of the GNSS constellation - observing strategies, in: International Association of Geodesy Symposia, submitted, 2014b.
8. J. Sun, J. Böhm, T. Nilsson, H. Krásná, S. Böhm, and H. Schuh, New VLBI2010 scheduling strategies and implications on the terrestrial reference frames, Journal of Geodesy, 88, pp. 449–461, 2014.
9. S.S. Shabala, J.N. McCallum, L. Plank, and J. Böhm, Simulating the effects of quasar structure on parameters from geodetic VLBI, Journal of Geodesy, submitted, 2014.

Real-time Data Streams from “e-RemoteCtrl” to Central VLBI Network Status Monitoring Services Like IVS Live

Alexander Neidhardt[1], Arnaud Collioud[2]

Abstract A central VLBI network status monitoring can be realized by using online status information about current VLBI sessions, real-time, and status data directly from each radio telescope. Such monitoring helps to organize sessions or to get immediate feedback from the active telescopes. Therefore the remote control software for VLBI radio telescopes “e-RemoteCtrl” (http://www.econtrol-software.de), which enables remote access as extension to the NASA Field System, realizes real-time data streams to dedicated data centers. The software has direct access to the status information about the current observation (e.g., schedule, scan, source) and the telescope (e.g., current state, temperature, pressure) in real-time. This information are directly sent to “IVS Live”. “IVS Live” (http://ivslive.obs.u-bordeaux1.fr/) is a Web tool that can be used to follow the observing sessions, organized by the International VLBI Service for Geodesy and Astrometry (IVS), navigate through past or upcoming sessions, or search and display specific information about sessions, sources (like VLBI images), and stations, by using an Internet browser.

Keywords IVS Live, e-RemoteCtrl, real-time status

1 Introduction

In the future, and especially for the expected VLBI Global Observing System (VGOS), a fast and informative feedback about the status of the observing network of globally distributed radio telescopes is essential to derive health states, error situation, or session setup mistakes. Real-time data streams with relevant information from the telescopes such as current activity, observed source, meteorology, or disk states, help to realize such a quick feedback to schedulers, coordinators, and the telescope staff. Therefore a new attempt realizes for the first time a sophisticated way for such status information, which can easily be requested with Internet browsers over the World Wide Web. This solution combines the functionality of the remote control software “e-RemoteCtrl” with the presentation abilities of the IVS Web tool “IVS Live”. “e-RemoteCtrl” is used to standardize the sending of status information to a centralized presentation server, while “IVS Live” integrates this real-time information into its functionalities to follow observing sessions live. This new status workflow under the name “e-QuickStatus” is also flexible enough to integrate legacy systems, which do not have or do not want to upgrade to “e-RemoteCtrl”.

1. Forschungseinrichtung Satellitengeodäsie, Technische Universität München, Geodetic Observatory Wettzell, Germany
2. Laboratoire d’Astrophysique de Bordeaux, Université de Bordeaux – CNRS, France

2 Participation

A participation in the real-time status of the IVS network is possible for all telescopes. The only requirement is that they regularly send status files of a dedicated format (see Figure 1) to the Web server of the Technische Universität München (Technical University Munich, TUM), Germany. In the best case, the status file is updated for each of the following events:

- Field system startup
- Field system terminated
- Starting schedule

- Schedule finished
- Pointing/slewing
- Recording
- Recording stopped
- e-RemoteCtrl startup
- Halt
- Continue

The status file should also be updated after each occurrence of an error from the extended error message facility of the NASA Field System (FS) log. The errors consist of an error code, an error number, and an error message from the control files “fserr.ctl” and “sterr.ctl” in the control directory of the FS [2]. At least the error codes and error numbers should be added to the status text in the sent status file. “e-RemoteCtrl” additionally evaluates and prioritizes the errors with different warning levels to separate critical errors from less critical. These warning levels are also printed in the status field.

```
<eQuickStatusInfo>
    Service = IVS
    Stationname = WETTZELL
    StationIVSCode = Wz
    Schedule = rd1403wz
    Status = [eRC] Recording
    DateTime = 2014.113.20:55:32
    TimeNext = 20:55:33
    Source = 2353+816
    Scan = rd1403_wz_113-2055
    Mark5VSN = USN-0121
    Mark5Volume = 3984.5
    Mark5Used = 3.3
    RightAscension = 23h56m22.79s
    Declination = 81d52m52.30s
    Azimuth = 359.8751
    Elevation =  41.1038
    CableDelay = 0.006513
    SystemTemperatureIFA = 36
    SystemTemperatureIFB = 75
    SystemTemperatureIFC = 27
    SystemTemperatureIFD = 0
    MeteorologyTemperature = 13.5
    MeteorologyHumidity =  54.3
    MeteorologyPressure =  947.9
</eQuickStatusInfo>
```

Fig. 1 An example status file showing the required structure.

2.1 Legacy Systems

While the status update is already part of the “e-RemoteCtrl” software, legacy systems without this remote control functionality have to setup their own realization of the status injection if they want to participate. The injection can be done, using scripts or other programs, which send the status files to the Web server at the TUM with Secure Copy (SCP) or Secure File Transfer Protocol (SFTP). A potential participant should follow the following steps:

1. Request a Secure Shell (SSH) key for the access to the Web server “econtrol.iapg.bv.tum.de” from the TUM (by sending an email to *neidhardt@fs.wettzell.de*).
2. Create a status file in the defined form (see below) for each specific event and status change while running an observation schedule.
3. Send the status files with SCP or SFTP to the Web server “econtrol.iapg.bv.tum.de” into the directory “statusincoming”, by using the user account “equickstatus” and the SSH key file, e.g., with:
   /usr/bin/scp -I ./iapg_key ./WETTZELL.info
   equickstatus@econtrol.iapg.bv.tum.de:
   ./statusincoming/[1].
4. Check your status data at:
   http://econtrol.iapg.bv.tum.de
   and at:
   http://ivslive.obs.u-bordeaux1.fr/
   (under the tab “Real time”).

2.2 VGOS Systems with “e-RemoteCtrl”

For stations, using the “e-RemoteCtrl” software (e.g., possible VGOS sites), it is much easier to send out the status information automatically, as all required parts are already integrated into “e-RemoteCtrl”. It can be switched on with a section in the configuration file for the server “ercd”. A possible configuration section is shown in Figure 2.

A potential participant should do the following steps:

1. Request an account for the download of the “e-RemoteCtrl” software (by sending an email to *neidhardt@fs.wettzell.de*) and install the software according to the manual.
2. Request an SSH key for the access to the Web server “econtrol.iapg.bv.tum.de” from the TUM (by sending an email to *neidhardt@fs.wettzell.de*).

[1] “*iapg_key*” must be replaced by the name of the requested SSH key file.

```
<eQuickStatus>
  SendStatus     = yes                    # Send status (yes) or not (no)
  SSHCopyClient  = /usr/bin/scp           # Used secure copy client
  SSHServer      = econtrol.iapg.bv.tum.de # Server, to which the status
                                          # should be sent to
  SSHUsername    = equickstatus           # User on the e-QuickStatus server
  # ATTENTION: The user rights of the following key file must fit to the user,
  # who starts the ercd (e-RemoteCtrl server), e.g. "-rw------- oper rtx",
  # if oper should start the remote control server.
  SSHKeyfilePath = ${HOME}/.ssh/iapg_key   # Key file, used for login
  LocalInfoPath  = /tmp/                  # Temporary path, from where is
                                          # copied from
  RemoteInfoPath = ./statusincoming/.     # Remote location, to which should
                                          # be copied to
</eQuickStatus>
```

Fig. 2 An example configuration of the automatic status sending service of the “e-RemoteCtrl” server (“*iapg_key*” must be replaced by the name of the requested SSH key file).

3. Configure the <eQuickStatus> section of the configuration file for the “e-RemoteCtrl” server, e.g., as shown in Figure 2 and configure the rest of the server according to the “e-RemoteCtrl” manual.
4. Start the server “ercd” with the changed configuration file.
5. Check your status data at:
   http://econtrol.iapg.bv.tum.de
   and at:
   http://ivslive.obs.u-bordeaux1.fr/
   (under the tab “Real time”).

2.3 Technical Background to Provide Real-time Data Automatically with “e-RemoteCtrl”

“e-RemoteCtrl” is a software extension to the NASA FS to operate and control radio telescopes remotely. Its server has access to the shared memory of the NASA FS and also reads the log file information, which is parsed to find defined patterns. Usually the data are prepared to be requested by the “e-RemoteCtrl” clients that are used to enable a safe and secure remote control possibility on the basis of SSH-encrypted remote procedure calls [3].

Additionally, the available status data can be broadcast as a status file stream (“e-QuickStatus”). Every file contains the status information after each schedule or radio telescope status change or if errors occur. After a status change, a new file is created and copied with SCP to the data collecting Web server, which is located at the TUM, Germany. To enable the secure copy, a key for SSH is required, which is used to authenticate the participating station at the TUM server. The key can be requested by any station from the distributor of the “e-RemoteCtrl” software, as described before. Also legacy systems can send in their status information in a similar way.

The TUM server scans the directory for incoming files every second. Each scan updates the local e-QuickStatus Web page. From there, “IVS Live”, located at the University of Bordeaux / CNRS, France, fetches the data regularly to present them interactively.

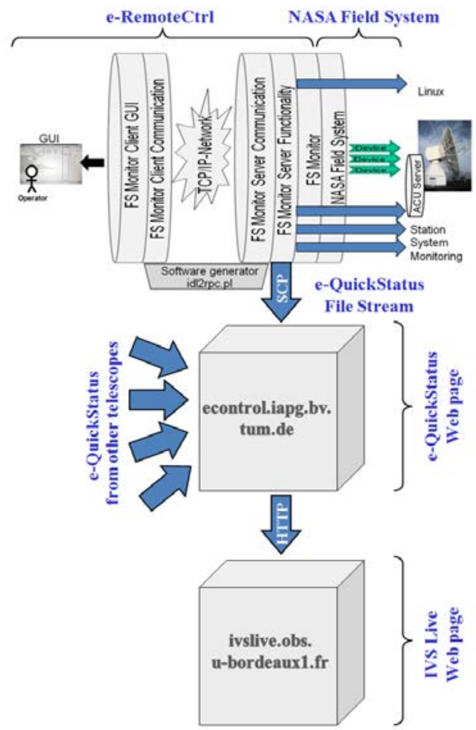

Fig. 3 Providing real-time data from radio telescopes to “IVS Live”: “e-RemoteCtrl” provides a status file stream to the e-QuickStatus server, where a Web page is updated every second. From there “IVS Live” fetches the data sets and presents the information centrally in a compact way.

2.4 “IVS Live” and Real-time Data

The main reason for the existence of “IVS Live” is the monitoring of IVS sessions. It is a fully dynamic Web site, developed with Javascript and PHP, with a MySQL database as back-end, which contains almost 6,000 sessions (starting from 2 January 2003), more

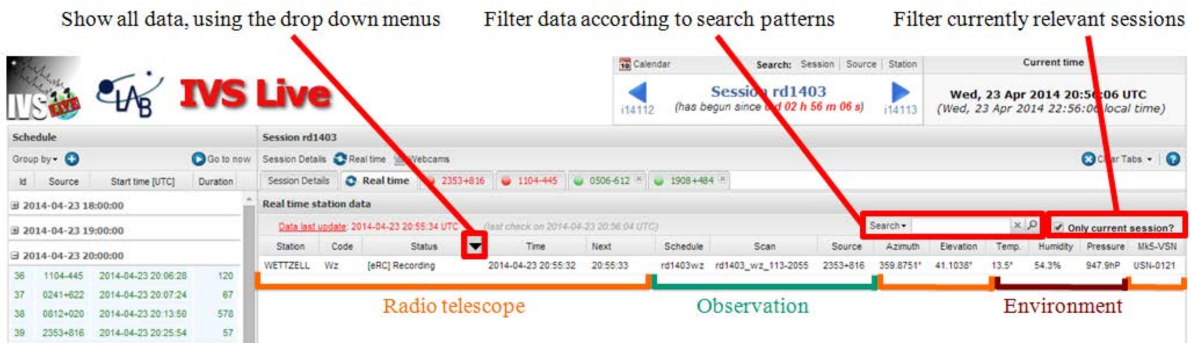

Fig. 4 Example of a presentation of real-time data in "IVS Live", captured during the IVS session rd1403 (2014-04-23) at 20:56:06 UTC from the 20m Radio Telescope Wettzell (RTW), Germany.

than 1,750 sources, and 68 stations at present. "IVS Live" is organized as a single user interface divided into several sub-panels (schedule of the session, main panel with an overview of the session, etc.). By default, the ongoing IVS session (if any) or the upcoming session is displayed. While the session is running, the main interface is automatically updated by a synchronization procedure with the displayed master clock. It offers a calendar tool to search for IVS sessions and allows to navigate through all IVS master schedules since 1979. Additional facts, e.g., station and source positions, source images, map locations, Web cam link, and several more, give detailed information about the IVS network and its work [1].

All information displayed in "IVS Live" (with exception of the Web cam streams/images) come from the IVS session schedules, which are frozen before the sessions start. In contrast, the "e-RemoteCtrl" software gives access to real-time information about the current observation (schedule name, scan name, source name, source coordinates), the telescope (station name and code, current state and errors, pointing azimuth and elevation, recording Mark 5 VSN number, volume and filling level), and the environment (temperature, pressure, humidity, cable delay measurement), stored on a global monitoring server. All this information is available in the "IVS Live" main interface as a separate tab with the name "Real time" (see Figure 4). This tab contains a table, which displays information related to all radio telescopes, participating in the status updates in a legacy mode or automatically with "e-RemoteCtrl".

An example of a table with real-time values in "IVS Live" is displayed in Figure 4. The user can select the different columns, which should be shown or hidden, using a drop-down menu. The data table also can be filtered by any specific value or string, which have to be entered into the search field located above the table. In addition, the right-hand side check-box allows to only display the real-time data of the session, which is currently operated and presented on the "IVS Live" page.

3 Conclusion

Thanks to the "IVS Live" Web page, which can be used to monitor the IVS observing sessions, in combination with the "e-RemoteCtrl" software, which streams real-time status information, a wealth of information is accessible to the IVS coordinators, schedulers and users. Stations are encouraged and are very much welcome to participate with their real-time status streams to increase the real-time information about the VLBI network and its observations. Having these data centrally available, provides a convenient global network view of the VLBI network and of any IVS session.

References

1. A. Collioud: IVS Live: All IVS on your desktop. In: Alef, W.; Bernhart, S.; Nothnagel, A. (eds.): *Proceedings of the 20th Meeting of the European VLBI Group for Geodesy and Astronomy (EVGA)*, Schriftenreihe des Instituts für Geodäsie und Geoinformation, Heft 22, pp 14–18, Universität Bonn, ISSN 1864-1113, 2011.
2. NASA, Goddard Space Flight Center: Mark IV Field System. Volume 1. *NASA, Goddard Space Flight Center*, 1993/1997.

3. Neidhardt, A.; Ettl, M.; Mühlbauer, M.; Kronschnabl, G.; Alef, W.; Himwich, E.; Beaudoin, C.; Plötz, C.; Lovell, J.: Safe and secure remote control for the Twin Radio Telescope Wettzell; In: Zubko, N.; Poutanen, M. (eds.) Proceedings of the 21st meeting of the European VLBI Group for Geodesy and Astrometry, pp 25-28, *Finnish Geodetic Institute*, 2013.

Balancing Sky Coverage and Source Strength in the Improvement of the IVS-INT01 Sessions

Karen Baver, John Gipson

Abstract The USNO NEOS Operation Center uses two alternating strategies to schedule IVS-INT01 sessions—the original "STN", which uses a relatively small set of strong geodetic sources, and the USS, which uses all sources from the 10AUG23 geodetic source catalog that are mutually visible at the main IVS-INT01 stations. The USS' larger number of sources is meant to maximize sky coverage but also results in a set of sources that is weaker, on average. Improved sky coverage should lower the UT1 formal error, but weaker sources should raise it. We have seen that where the STN already provides good sky coverage, adding weaker sources through the USS can degrade performance, indicating that the USS may be adding too many sources. Here we give a preliminary report on trying intermediate numbers of sources in an effort to find a better balance of average source strength and sky coverage and improve performance against metrics such as the UT1 formal error. We identify a promising source set.

Keywords Intensive, scheduling, UT1

1 Development of Alternative Source Sets and Schedules

USNO schedules the INT01 sessions, using the Sked program [1]. USNO uses two infrequently updated source sets based on contrasting strategies of source strength and sky coverage to schedule the sessions. The original set ("STN") is a relatively small set of (currently 32) strong geodetic sources. (The STN also has 19 sources that are not mutually visible at Kokee and Wettzell, the two stations that mainly observe in the INT01 sessions.) The USS set is all sources (currently 91) from the 10AUG23 geodetic catalog that are mutually visible at Kokee and Wettzell sometime during the year. The USS' larger number of sources is meant to maximize sky coverage but also results in a set of sources that is, on average, weaker. Improved sky coverage should lower the UT1 formal error, but weaker sources should raise it, resulting in a trade-off. We have seen that where the STN already provides good sky coverage, adding weaker sources through the USS can degrade performance, indicating that the USS may be adding too many sources. Here we try intermediate numbers of sources in an effort to find a better balance of average source strength and sky coverage. We create two series of source sets with varying numbers of sources using two selection strategies through Sked's *BestSource* command. Then we create schedules from the source sets and test them against three metrics.

The *BestSource* command selects a list of "good" sources from an initial catalog for a given network and observing span, based on source strength, mutual visibility, and sky coverage. The command takes three arguments. Argument 1 (N) is the desired number of sources. Argument 2 (*Mode*) takes values of 1, 2, and 3 and determines how the sources are initially ranked. Argument 3 (*NumCov*) determines how many sources to consider at a time when considering sky coverage. The algorithm works as follows. The first step gives all sources in the starting catalog an overall score which depends on the *Mode*. It does so by scheduling a series of hypothetical scans for each source at 10-minute intervals over the du-

NVI, Inc.

ration of the schedule. For each scan, the source is given a sub-score, and the total score is the sum over all scans. For *Mode=1,2,3* the sub-score is, respectively, 1) the number of observations in the scan; 2) 1/(scan_duration)—a measure of the source's strength, and 3) (number_of_observations)/(scan_duration). Sked then builds an output source list iteratively, starting with the highest ranked source. Sked considers the improvement in sky coverage that would result by adding, individually, each of the remaining sources to the output list. From among the top *NumCov* sources, it picks the source that has the highest *Mode* ranking. This process repeats until Sked has selected *N* sources or there are no more sources left in the input list. (The latter happens if the number of observable sources is $<$ N.) In this study we always used *Mode=2*—that is, sources were ranked by 1/(scan_duration), i.e., source strength—and *NumCov=3*, which meant that coverage played an important but not overwhelming role.

We used *BestSource* to make two series of six source sets apiece with varying numbers of sources, to be used to schedule 26 test Intensives apiece. The basis for both series was the current (13SEP23) geodetic source catalog, a set of sources used for generating geodetic schedules. In series 1, for each source set, our strategy was to choose one group of sources that would be visible at any time at Kokee and Wettzell, so that the source set could be used for all schedules regardless of their observing times. The number of sources in the six source sets ranged from 40 to 90 in increments of 10. We call these source sets BA_x, where x is the number of sources in the set and *BA* stands for "Best-All" because the same source set is used for all schedules. (We call the source set with the most sources BA_{90} although the *BestSource* command found only 89 sources.) In series 2, for each of the six source sets, we chose 26 independent groups of sources, one per proposed, individual schedule, from the sources that could be observed during the corresponding schedule. The number of sources in each group in a source set was the same. This number ranged from nine to 24 in increments of three. We call the source sets composed of these groups BI_x for "Best-Individual".

The purpose of varying the number of sources in each series was to compare the strategies of maximizing source strength (as in the STN), maximizing sky coverage (as in the USS), and using a balance of these two characteristics (new cases). We chose 40 sources as the *BA* series' lower limit because the STN catalog has had ~40 to 50 sources in recent years. (We did not realize that not all of the STN's sources are usable. In retrospect, the *BA* lower limit should have been lower.) We chose 90 sources as the upper limit because the USS currently has ~90 sources. We chose nine sources as the lower *BI* limit because operational STN schedules tend to have nine or fewer sources, and USS schedules tend to have 10 or more sources. We chose 24 as the upper limit because operational experience suggested that this is probably the maximum number of sources that can be currently scheduled in USS schedules.

Our main interest is the varying number of sources in the *BA* and *BI*, but we also compare the two series.

We included the operational STN and USS source sets from the start of 2014 in order to use them to evaluate the test source sets as potential alternative operational source sets. But for consistency with the test sets, we used the current (14FEB06) flux models. We call the resulting sets STN_{rf} and USS_{rf}, where "rf" means reselected fluxes.

We used Sked to generate schedules for 26 days of the year spaced two weeks apart, starting at 18:30 UT. Because the schedules started at the same time, they differed in the part of the sky that was visible. The visible sky at session start time can be identified by GST. In comparing scheduling strategies, it is important to compare them at the same GST and also to evaluate them at many GSTs, because, depending on the GST, one strategy may be superior. For all 26 GSTs, we created schedules using the six *BI* sets, the six *BA* sets, STN_{rf}, and USS_{rf}. To improve statistical significance, we created multiple schedules per combination of GST and source set by 1) creating a schedule template and determining the initially available sources and 2) creating one schedule per initial source by selecting each source in turn, then running Sked's autosked mode to complete the schedule. If a schedule's final observation began fewer than 55 minutes into the schedule, we discarded the schedule as too short.

Due to space limitations, this paper only considers each source set's data averaged over all 26 GSTs. Also, please note that we have not yet calculated the statistical significance of any result.

2 Comparison of Source Sets

In comparing source sets, it is useful to consider all 26 BI_x source groups for a given x together. We call this set BIU_x where U means "union". Figure 1 plots the STN_{rf} and USS_{rf} sets by right ascension and declination, along with the sets at each end of the two series—BIU_9 and BA_{40} and BIU_{24} and BA_{90}. Venn diagrams show the number of sources shared by adjacent sets.

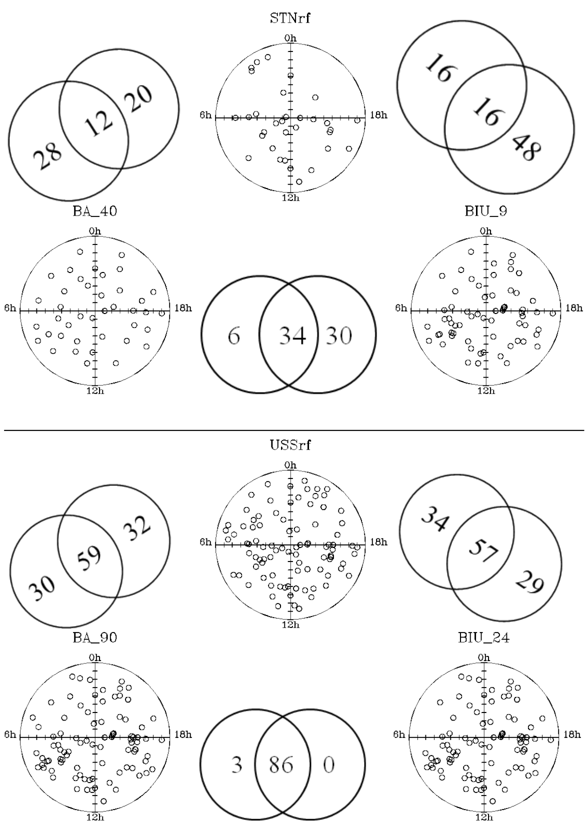

Fig. 1 Source distributions in the three source sets at the lower limits (top two rows) and upper limits (bottom two rows) of the *BIU*, *BA*, and STN_{rf}/USS_{rf} series. The Venn diagrams show the number of sources in the adjacent source sets.

The *BIU* and *BA* series have good sky coverage throughout. Their most notable difference is that the first *BA* source set, BA_{40}, is fairly uniform, but the first *BIU* source set, BIU_9, has redundant sources—sources that are close together and provide little improvement in sky coverage. But BA_{40} has 24 fewer sources than BIU_9, and this might play a role in its lack of redundancy. The *BA* series shows redundancy by its final source set, BA_{90}. The final *BIU* source set, BIU_{24} has similar redundancy, and in fact, BIU_{24} is a subset of BA_{90} with three fewer sources, indicating that the *BI* and *BA* strategies converge as sources are added. The differences between the STN_{rf} source set and the BIU_9 and BA_{40} source sets are striking. STN_{rf} has large gaps in its sky coverage, even though it has only eight fewer sources than BA_{40}. This is not surprising, because the STN sources were picked largely for strength. USS_{rf} has a similar number of sources to BIU_{24} and BA_{90}, but it shares only ∼2/3 of its sources with those sets, because it came from a different source catalog. But it has a similar degree of sky coverage to the other two sets, as well as some redundancy.

Table 1 compares the 14 source sets and the schedules made from them. Averages are taken over all 26 GSTs in a source set.

The total source count applies to the *BA* and *BIU* sets. The mid-session count is the number of sources available for scheduling at mid-session in a representative schedule from each GST. Of the two counts, the mid-session count has the more direct effect on scheduling, and it strictly increases in each series as sources are added to the source sets. In general, more sources are available in the *BA* series than in the *BI* (11.4–23.5 vs. 7.8–19.6), an important advantage for scheduling. The BI_{12}/BA_{70} and the BI_{21}/BA_{80} pairs have comparable total numbers of sources, permitting reasonably direct comparisons. These pairs also indicate that the *BA* series provides more sources for scheduling. Every set but BI_9 provides more sources at mid-session than STN_{rf}, and five sets (BI_{21}, BI_{24}, BA_{70}, BA_{80}, and BA_{90}) provide more sources than USS_{rf}.

The schedules are compared by the average number of scheduled sources, sky coverage (measured by sky gap, as discussed below), and source strength (measured by scan length). In each series, more sources were scheduled as more sources were added to the source sets. More sources were scheduled for the *BA* than the *BI* series (13.1–17.1 vs. 8.9–16.3). For source sets with fewer than 15 sources at mid-session, more sources were scheduled than were available at mid-session, indicating that the schedules took advantage of sources that rose or set during the schedule. For source sets with more than 15 sources at mid-session, fewer sources were scheduled than were available at mid-session, indicating that the larger source sets provided more sources than were needed for scheduling. Every set but BI_9 scheduled more sources than the STN_{rf}. Seven sets (BI_{21}, BI_{24}, BA_{50}, BA_{60}, BA_{70}, BA_{80}, and BA_{90}) scheduled more sources than the USS_{rf}.

Sky gap is the average distance of a point in the sky to the nearest observation. It is an inverse measure of

Table 1 Characteristics of the source sets (top section) and the schedules generated from them (bottom section).

averages are over all GSTs in a set	STN_{rf}	BI_9	BI_{12}	BI_{15}	BI_{18}	BI_{21}	BI_{24}	BA_{40}	BA_{50}	BA_{60}	BA_{70}	BA_{80}	BA_{90}	USS_{rf}
#sources: total	32	64	69	72	75	79	86	40	50	60	70	80	89	91
mid-session (avg)	8.1	7.8	10.3	12.8	15.2	17.6	19.6	11.4	14.6	16.4	18.5	21	23.5	17
Avg number of scheduled sources	9.6	8.9	11.6	13.7	15.0	16.1	16.3	13.1	15.4	16.3	16.7	17.0	17.1	15.3
Avg sky gap	12.6	11	9.9	9.5	9.4	9.2	9.1	9.5	9.1	9.0	8.9	8.9	9.0	9.5
Avg scan length (seconds)	126.5	130.3	135.1	137.5	139.9	140.9	141.5	132.8	137.7	142.7	144.0	143.1	143.2	145.7

sky coverage. Adding sources reduces the sky gap in the *BI* schedules, but the *BA* schedules have little difference in sky gap after BA_{40}. The *BA* schedules provide lower sky gap values (better sky coverage) than the *BI* schedules. It takes the 72-source BI_{15} set to produce schedules with as low a sky gap (9.5) as those produced from the 40-source BA_{40} set. In addition, the BA_{70} and BA_{80} schedules have lower sky gap values than the corresponding BI_{12} and BI_{21} schedules. The STN_{rf} schedules have the largest average sky gap of any set (12.6), which is not surprising given its sparse source distribution. The USS_{rf} value, 9.5, is smaller than the STN_{rf} value but larger than most of the sky gap values, including the analogous BI_{24} and BA_{90} sets.

Source strength is inversely proportional to average scan length; it takes longer to observe weaker sources. In the *BI* schedules, adding new sources always increases the scan length, implying that weaker sources are being scheduled. In the *BA* schedules, adding new sources increases the scan length through BA_{70}, then decreases it. The *BI* scan lengths are less than the *BA* lengths (130.3–141.5 vs. 132.8–143.2 seconds), indicating that the *BI* selects stronger sources. The BI_{12}/BA_{70} and BI_{21}/BA_{80} pairs support this. As expected, the average scan length is shortest for the STN_{rf} schedules. It is longest for the USS_{rf} schedules.

The schedule characteristics generally show the expected trade-offs. Adding sources within a series generally increases sky coverage but weakens source strength. But changes in the characteristics generally slow down or reverse towards the end of each series. So adding sources eventually becomes useless or counterproductive. The *BI* schedules have greater source strength but worse sky coverage than the *BA* schedules. The STN_{rf} is similar to the *BI* series but has even greater source strength and even worse sky coverage. The USS_{rf} is the exception to the trade-offs. It has the weakest source strength but does not compensate with the greatest sky coverage. Instead it is inferior in all three schedule characteristics to BI_{21} through BI_{24} and BA_{50} through BA_{90}.

3 Simulation Results

We evaluated the 26 schedule sets made from each of the 14 source sets using the following three metrics.

Unscaled UT1 Formal Error. We used the simulation capability of Solve to determine the unscaled formal error of the UT1 estimate from each Intensive schedule. The unscaled formal errors depend only on the observations used and the errors in the observations. By assumption, there are no modeling errors, so the formal errors give lower limits on the real errors. All things being equal, lower formal errors are better.

Atmospheric Turbulence. A session is robust if its UT1 estimate does not change much with random noise such as atmospheric turbulence. We used the metric 1 Solve configuration but added random noise that simulated atmospheric turbulence to each schedule's simulated observations. We did this 300 times per schedule and then calculated each schedule's RMS of the UT1 estimates about the mean. We then averaged the RMS values for each source set. A lower average RMS indicates that the schedules generated from a source set are less vulnerable to atmospheric turbulence.

Source Loss. A session is robust if its UT1 estimate does not change much when it fails to observe one of its scheduled sources. We ran a set of Solve solutions for each schedule in which we suppressed the schedule's sources, one at a time. We then calculated the RMS of each schedule's UT1 estimates about the mean, and we averaged the RMS values for all schedules from a given source set. A lower average RMS indicates that the schedules generated from a source set are less vulnerable to source loss.

Table 2 summarizes the performance of the source sets' schedules against the metrics.

Unscaled UT1 Formal Error. In each series, the UT1 formal error generally increases as the number of sources increases. Source redundancy is probably a factor; as new (and weaker) sources are added to the source sets, some are close to previous sources, and if

Table 2 Performance under the metrics: unscaled UT1 formal error and vulnerability to atmospheric turbulence and source loss (UT1 estimate RMSs), averaged over all GSTs in each source set. The units are μs. The best values in each series are in bold type.

		STN_{rf}	BI_9	BI_{12}	BI_{15}	BI_{18}	BI_{21}	BI_{24}	BA_{40}	BA_{50}	BA_{60}	BA_{70}	BA_{80}	BA_{90}	USS_{rf}
Unscaled UT1	Average	7.9	7.3	**7.2**	7.3	7.6	7.7	7.8	**6.6**	6.9	7.3	7.4	7.5	7.6	8.2
Formal Error	St. dev.	1.4	1.5	**1.4**	1.4	1.3	1.0	1.0	**1.0**	1.1	1.1	1.0	1.0	1.2	1.4
Atmospheric	Average	15.5	**14.1**	14.5	14.8	15.6	15.9	16.2	**14.3**	15.3	16.1	16.4	16.8	16.9	17.1
Turbulence	St. dev.	4.6	**2.8**	2.9	2.7	2.5	2.2	2.4	**2.3**	2.3	2.0	2.0	2.2	2.1	3.2
Source	Average	21.1	18.3	14.6	12.6	12.5	**11.5**	11.9	12.6	11.8	11.5	11.6	**11.4**	11.5	13.0
Loss	St. dev.	8.2	3.9	3.0	2.8	3.0	**2.8**	2.7	2.8	2.3	2.4	2.4	**2.2**	2.2	2.6

scheduled, they can add little sky coverage improvement to offset the loss of source strength. The *BA* series yields a better (lower) range of UT1 formal errors than the *BI* series (6.6–7.6 vs. 7.2–7.8 μs). The improved performance is due to BA_{40} and BA_{50}; the range of formal errors for the other *BA* sets is comparable to the *BI*. Again, the lower source redundancy of BA_{40} and BA_{50} may be a factor. Overall, BA_{40} is the best choice for this metric, giving the lowest UT1 formal error (6.6 μs). The STN_{rf} and the USS_{rf} have the highest values (7.9 and 8.2 μs, respectively) and are the worst choices for this metric.

Atmospheric Turbulence. In each series, vulnerability to atmospheric turbulence increases as the number of sources increases. The *BI* is less vulnerable to atmospheric turbulence than the *BA* is, with lower RMS values (14.1–16.2 vs. 14.3–16.9 μs). BI_{12} and BI_{21} also provide lower RMS values than BA_{70} and BA_{80}. Overall, BI_9 is the best choice for this metric, with an RMS of 14.1 μs, followed closely by BA_{40} (14.3 μs). Five choices are better than the STN_{rf}, and every choice is better than the USS_{rf}.

Source Loss. Previously, we assumed that increasing the number of scheduled sources strictly decreases vulnerability to source loss. However, although the number of scheduled sources strictly increases in each series, the *BI* RMS increases after BI_{21}, and the *BA* RMS fluctuates within 0.2 μs starting with BA_{60}. This suggests that adding sources might only be helpful up to a point, perhaps ∼16 sources. The *BA* series is less vulnerable to source loss than the *BI* is, with lower RMS values (12.6 to 11.4 vs. 18.3 to 11.5 μs). This is supported by the superiority of BA_{70} over BI_{12} (11.6 vs. 14.6 μs), although BA_{80} and BI_{21} are comparable. BI_{21} and BA_{80} provide the lowest RMS averages. But BI_{15} through BI_{24} and all *BA* schedules are better than the USS_{rf}, making them reasonable choices. The worst choice is the STN_{rf}.

Overall, no number of sources and neither selection strategy is superior for all three metrics, so tradeoffs must be considered. But the STN_{rf} and the USS_{rf} were each the worst or second worst choice for two metrics, so the STN and USS should be replaced. The BA_{40} source set provided the best UT1 formal error, the second lowest vulnerability to atmospheric turbulence, and vulnerability to source loss that is better than the STN_{rf}'s and USS_{rf}'s. This source set should be evaluated for short-term replacement of the STN and USS, and the selection of 40 sources under the *BA* strategy from any starting source catalog should be evaluated as a general method of INT01 source selection.

4 Conclusions

We selected varying numbers of the best overall sources (*BA*) and the best sources for individual schedules (*BI*) from the current geodetic source catalog. Within both strategies, adding sources yielded schedules with better sky coverage and more, but weaker, sources. The additions worsened the schedules' UT1 formal errors and vulnerability to atmospheric turbulence, but reduced their vulnerability to source loss, up to a point. *BA* gave schedules with better sky coverage and more, but weaker, sources than *BI*. The *BA* schedules had better UT1 formal errors and less vulnerability to source loss, but more vulnerability to atmospheric turbulence. The BA_{40} source set performed the best overall. This set and the strategy that produced it should be investigated for operational use.

References

1. http://lupus.gsfc.nasa.gov/files_user_manuals/sked/sked.pdf J. Gipson, Sked User Manual, 2012.

VLBI Analyses using Covariance Information from Turbulence Models

Sebastian Halsig, Thomas Artz, Judith Leek, Axel Nothnagel

Abstract Refractivity variations in the troposphere represent a dominant contribution to the error budget of the observations of Very Long Baseline Interferometry (VLBI). In fact, they limit the accuracy of the VLBI target parameters. These refractivity variations also lead to elevation-dependent uncertainties and affect the correlations between observations. However, such stochastic properties are generally not considered in VLBI data analysis leading to deficiencies in modeling the stochastic properties of the observations. Thus, formal errors are generally too optimistic.
In this study, the stochastic model is modified. The standard stochastic information from the VLBI correlation process is now augmented by the variance-covariance information derived from atmospheric turbulence models based on the Kolmogorov turbulence theory. Thus, we obtain a fully populated variance-covariance matrix of observations, which is incorporated in the VLBI analysis. In order to validate our results, this approach will be applied to the continuous VLBI campaign 2011 (CONT11).

Keywords VLBI, stochastic properties, refractivity variations, Kolmogorov turbulence theory, turbulence model

1 Introduction

The observations of space-geodetic techniques, such as Very Long Baseline Interferometry (VLBI) or Global Navigation Satellite Systems (GNSS), are affected by refractivity variations in the neutral atmosphere. Today, only long-periodic variations are considered routinely. Micro-scale meteorological phenomena are not taken into account, limiting the attainable accuracy of the VLBI target parameters.

In general, the total tropospheric delay can be modeled by a hydrostatic (index h) and a wet (index w) component [3]. Each of these terms consists of a zenith delay (ΔL_h^z and ΔL_w^z) and a corresponding mapping function ($mf_h(\varepsilon)$ and $mf_w(\varepsilon)$) for the transformation from zenith to an arbitrary elevation angle ε,

$$\Delta L(\varepsilon) = mf_h(\varepsilon)\Delta L_h^z + mf_w(\varepsilon)\Delta L_w^z. \quad (1)$$

The hydrostatic delay on the one hand mainly depends on the air pressure and is generally taken into account by using surface pressure measurements and applying an adequate model [3]. Due to the high temporal and spatial variability of water vapor in the atmosphere, the variations of the wet component on the other hand are unpredictable. Thus, the zenith wet delay is estimated as an additional correction parameter within the VLBI estimation process.

Dynamic processes in the atmosphere, particularly refractivity fluctuations, also lead to elevation-dependent uncertainties and induce physical correlations between observations. However, the stochastic model in the VLBI analysis only includes uncertainties from the VLBI correlation process [14]. Other error sources, such as remaining correlator related errors, uncertainties in the phase calibration, source position and structure errors, deficits in modeling the station coordinates or model errors (e.g., atmosphere, clocks), are not modeled in the VLBI standard approach. Thus, the variance-covariance matrix (VCM) in the VLBI analysis is only sparsely populated and formal errors

Institute of Geodesy and Geoinformation, University of Bonn

for the derived parameters, such as station coordinates, and Earth orientation parameters, are too optimistic. An indication for the fact that other noise sources should be taken into account and that there are deficiencies in the current stochastic modeling is given by the χ^2 statistics, i.e., $\chi^2 = \frac{\sigma_0^2}{\hat{\sigma}^2}$, where σ_0^2 and $\hat{\sigma}^2$ denote the a priori and a posteriori variance, respectively. Regarding χ^2 values from individual session solutions, they are in general much larger than they should be [4]. The standard approach in Calc/Solve is to re-weight the observations by iteratively adding additional noise until $\chi^2 \approx 1$.

Earlier studies have been carried out to investigate the stochastic properties of VLBI observations. For instance, Tesmer and Kutterer [11] refined the traditional stochastic model by means of expending the variances of the observations by source-, station-, and elevation-dependent components. Gipson et al. [4] included station-dependent noise in the VLBI analysis which leads to an increase of the observational noise. Romero-Wolf et al. [8] presented a simplified application of the turbulence-based stochastic model for tropospheric delays developed by Treuhaft and Lanyi [12] to a set of VLBA catalog runs. Nilsson and Haas [6] used simulations of atmospheric delays to validate the impact of atmospheric turbulences on VLBI observations during the continuous VLBI campaigns CONT05 and CONT08.

This contribution extends the existing approaches by an external way to model physical correlations due to refractivity variations in the neutral atmosphere. For this purpose, the more general atmospheric turbulence model of Schön and Brunner [9] is used to obtain a fully populated variance-covariance matrix of the observations which is incorporated in the VLBI analysis in a second step. This leads to a more adequate modeling of the stochastic properties in the VLBI analysis.

2 Modeling Atmospheric Turbulence

Atmospheric turbulence can be best described stochastically following the widely accepted turbulence theory of Kolmogorov. In turbulence theory, the stochastic properties are usually described by the so-called structure function that contains information of scatter and statistical covariance. An integration of the structure function of refractivity along the line-of-sight (LOS) leads to a VCM of the tropospheric delays (for more detail see, e.g., [6, 12]).

As an alternative approach, Schön and Brunner developed a turbulence model [9] for GPS carrier phase data, based on a 3D spectrum representation. Since restrictive conditions, such as inhomogeneity and anisotropy, can be taken into account, this approach leads to a more general description of the VCM in comparison to the structure function expression [9].

Since the initial formulation of the spectral representation by Kolmogorov has a singularity for $\kappa = 0$, the 3D spectrum Φ_n for refractivity fluctuations is expressed by the van Karman spectrum [13],

$$\Phi_n(\kappa) = \frac{0.033 C_n^2}{\left(\kappa^2 + \kappa_0^2\right)^{\frac{11}{6}}} \sim \kappa^{\frac{-11}{3}}, \qquad 0 < \kappa < \kappa_s. \quad (2)$$

Here, C_n^2 denotes the structure constant of refractivity which, roughly speaking, expresses the strength of turbulence. κ represents the wave numbers with κ_0 and κ_s being the wave numbers corresponding to the outer and inner scale length, respectively [13].

Integrating the refractivity variations along the line-of-sight, the spectrum of refractivity, which can be best described by the Fourier wave number decomposition, can be related to the covariances of the tropospheric delay [9],

$$\left\langle \tau_A^i(t_A), \tau_B^j(t_B) \right\rangle = \int_0^\infty \int_0^\infty \int_{-\infty}^\infty \int_{-\infty}^\infty \int_{-\infty}^\infty \Phi_n\left(\hat{\kappa}, \frac{\mathbf{r}_A^i + \mathbf{r}_B^j}{2}\right) e^{i\hat{\kappa}^T \mathbf{d}} \mathbf{d}^3 \hat{\kappa} ds_1 ds_2. \quad (3)$$

Here, $\mathbf{r}_A^i$, $\mathbf{r}_B^j$ are the LOS vectors between station A and source i, and station B and source j, respectively. Please note that for a more specific VLBI configuration two stations (A and B) and only one source ($i = j$) are used. The 3D vector of wave numbers is denoted by $\hat{\kappa}$,

$$\mathbf{d} = \mathbf{r}_B^j(ds_2) + \varphi_A^B - \mathbf{v}\Delta t - \mathbf{r}_A^i(ds_1), \quad (4)$$

represents the vector separating the integration points and φ_A^B denotes the baseline.

Besides the spatial correlations, temporal correlations are taken into account using Taylor's frozen flow model [13]. It is assumed that the turbulent medium is frozen during the observation time and travels in wind direction with a constant velocity $v > 0$. The temporal separation Δt is multiplied with the constant wind vector $\mathbf{v}$. Thus, the temporal separation is transformed to a spatial separation and can be added to Equation 4.

After a few modifications (for more details, see [9]) and transforming the integration over the slant direction to an integration over the zenith direction ($dz_i = \sin\varepsilon_i ds_i$) yields the following expression for the covariances of the tropospheric delays,

$$\left\langle \tau_A^i(t_A), \tau_B^j(t_B) \right\rangle = \frac{12}{5}\frac{0.033}{\Gamma\left(\frac{5}{6}\right)}\frac{\sqrt{\pi^3}\kappa_0^{-\frac{2}{3}}2^{-\frac{1}{3}}}{\sin\varepsilon_A^1 \sin\varepsilon_B^2}C_n^2 \cdot \int_0^H\int_0^H (\kappa_0 d)^{\frac{1}{3}} K_{-\frac{1}{3}}(\kappa_0 d)\, dz_1 dz_2, \tag{5}$$

where d represents the separation distance between the actual integration points [9], Γ denotes the gamma function [1] and K is the modified Bessel function of second kind [1]. Similarly, we receive a representation for the variances. Here, all expressions can be analytically integrated, yielding

$$\left\langle \tau^2 \right\rangle = \frac{12}{5}\frac{0.033}{\Gamma\left(\frac{5}{6}\right)}\frac{\sqrt{\pi^3}\kappa_0^{-\frac{2}{3}}2^{-\frac{1}{3}}}{(\sin\varepsilon)^2}C_n^2 H^2 \cdot \left\{ \frac{\pi 2^{\frac{1}{3}}}{\sqrt{3}\Gamma\left(\frac{2}{3}\right)} F_3^2\left(\left[\frac{1}{2},1\right],\left[\frac{2}{3},\frac{3}{2},1\right],\frac{z^2}{4}\right) - \frac{27}{80}2^{\frac{2}{3}}\Gamma\left(\frac{2}{3}\right) z^{\frac{2}{3}} F_2^1\left(\left[\frac{5}{6}\right],\left[\frac{11}{6},\frac{7}{3}\right],\frac{z^2}{4}\right)\right\}. \tag{6}$$

Here, F denotes the hypergeometric function [1] and it holds that $z = \frac{p\kappa_0 H}{\sin\varepsilon}$, where H is the effective tropospheric height and p describes the impact of anisotropy on the variance [9].

3 Analysis Setup

The atmospheric turbulence model is applied to the CONT11 campaign provided by the International VLBI Service for Geodesy and Astrometry (IVS, [10]). The databases are initially processed using the VLBI analysis software Calc/Solve [5], which was modified to export the normal equation system. A stand-alone C++ back-end to Calc/Solve is used to incorporate the additional variance-covariance matrix into the least-squares adjustment. The new ensemble variance-covariance matrix is the square sum of the weight matrix of the correlation process and the additional matrix from turbulence modeling. Then, the program is used to build and solve the normal equation system. The modeling and analysis setup described in [2] is used for all solutions.

4 Results

Different solution setups have been analyzed which differ primarily in the parametrization of the structure constant C_n^2, the effective tropospheric height H, and the wind vector $\mathbf{v}$ (cf. Table 1). In particular, the structure constant is either assumed to be equal for each station (setups 3 and 4) or estimated from radar measurements, radiosonde data or GNSS data (setups 5, 6, and 7). In the latter case, the station-dependent C_n^2 values are taken from [6] or [7]. Different methods for estimating C_n^2 are presented by Nilsson and Haas [6].

Table 1 Solution setups w.r.t. the Calc/Solve re-weighting option and the parametrization of the structure constant (equal for all stations or station-dependent estimates), the tropospheric effective height (equal for all stations or station-dependent estimates), and the wind vector. The mean χ^2 value [-] and WRMS post-fit residuals for the delay observables, converted to [mm], are given for the CONT11 interval.

	re-wt.	C_n^2	H	$\mathbf{v}$	χ^2	WRMS
1	+	-	-	-	0.83	25.07
2	-	-	-	-	3.68	26.32
3	-	C_n^2 = 1.0	1 km	8 $\frac{m}{s}$	3.25	17.22
4	-	C_n^2 = 1.0	2 km	8 $\frac{m}{s}$	2.99	16.50
5	-	est.,[7]	2 km	8 $\frac{m}{s}$	2.32	14.55
6	-	est., [6]	est., [6]	8 $\frac{m}{s}$	2.27	14.39
7	-	est.,[7]	2.5 km	8 $\frac{m}{s}$	2.17	14.01

To validate the different solutions, the χ^2 value (Figure 1) and the weighted root mean squared (WRMS) post-fit residuals of the delay observables are given in Figure 1 and Figure 2, respectively, for each day of the CONT11 campaign. The mean values over the CONT11 time period are shown in Table 1.

The χ^2 value is a criterion whether the global test for an adjustment is fulfilled or not, which would be the case if $\chi^2 \approx 1$. As expected, this is true for the standard Calc/Solve solution (black diamonds), because

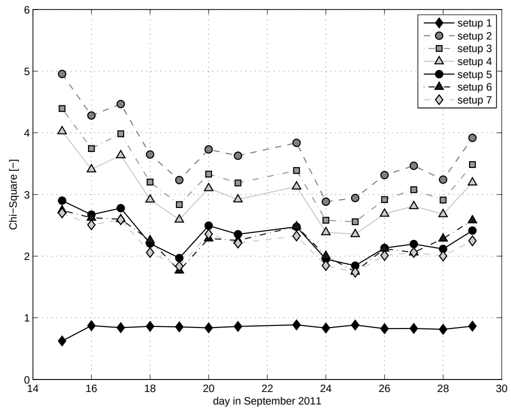

Fig. 1 Validation of the different solution parametrizations for the CONT11 campaign: χ^2 values [-].

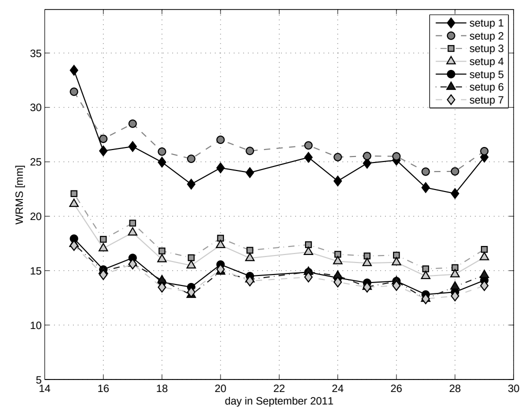

Fig. 2 Validation of the different solution parametrizations for the CONT11 campaign: weighted root mean squared (WRMS) post-fit residuals of the delay observables, converted to [mm].

additional noise is iteratively added to the observations as described above. Turning off the re-weighting option, typical values are $\chi^2 \approx 3-4$ [4], which is equal to our solution (setup 2, dark gray points). Compared to this reference value, the solutions with constant atmospheric parameters (setup 3, dark gray squares or setup 4, light gray triangles) lead only to a little decrease in the χ^2 value. Using estimated structure constants (setup 5, black circles; setup 6, black triangles, setup 7, light gray diamonds) leads to a reduction of the χ^2 value. However, the χ^2 values are still little too high for all cases.

For the same solution setup, Figure 2 shows the weighted root mean squared (WRMS) scatter per solution based on the post-fit residuals. It is obvious that for some solutions, particularly those using the more realistic C_n^2 values (setup 5, black circles; setup 6, black triangles; setup 7, light gray diamonds), the WRMS post-fit residuals decrease sharply compared to the reference solution defined above. There are only small differences in the three solution types using estimated C_n^2 values.

Besides the given statistics, the baseline length repeatabilities are calculated for a Calc/Solve solution re-weighting the observations (setup 1, black diamonds) and a least-squares adjustment with additional turbulence modeling (setup 3, dark gray squares). The results are shown in Figure 3(a). Both solutions are quite similar and the root mean squared (RMS) error for the baseline length repeatabilities decreases sharply compared to a solution without re-weighting (setup 2, dark gray points). Further, a quadratic polynomial is estimated for all baseline lengths. It should be noted here that for the different solution setups (2–7) only minor variations in the baseline length repeatabilities are observed (not shown here).

The RMS differences between the Calc/Solve solution re-weighting the observations and the solution concerning atmospheric conditions are presented in Figure 3(b). Whereas black bars indicate an improvement, light gray bars denote a degradation. In this comparison, about 25% of the baselines are improved by at least 1 mm, whereas 12% get worse by at least 1 mm and 63% remain unchained.

5 Conclusion and Future Work

The turbulence model developed by Schön and Brunner [9] is used to obtain information about the stochastic properties of tropospheric refractivity variations. The resulting VCM is added to the weights from the VLBI correlation process and the ensemble VCM is incorporated into the VLBI analysis. This approach has been applied to the CONT11 campaign for different solution types w.r.t. the structure constant, the tropospheric height, and the wind vector parametrization.

It was shown that the WRMS post-fit residuals decrease sharply when using estimated C_n^2 values, e.g., from GNSS estimation. The baseline length repeatabilities improve slightly, but only minor variations between the different solution setups are observed. Al-

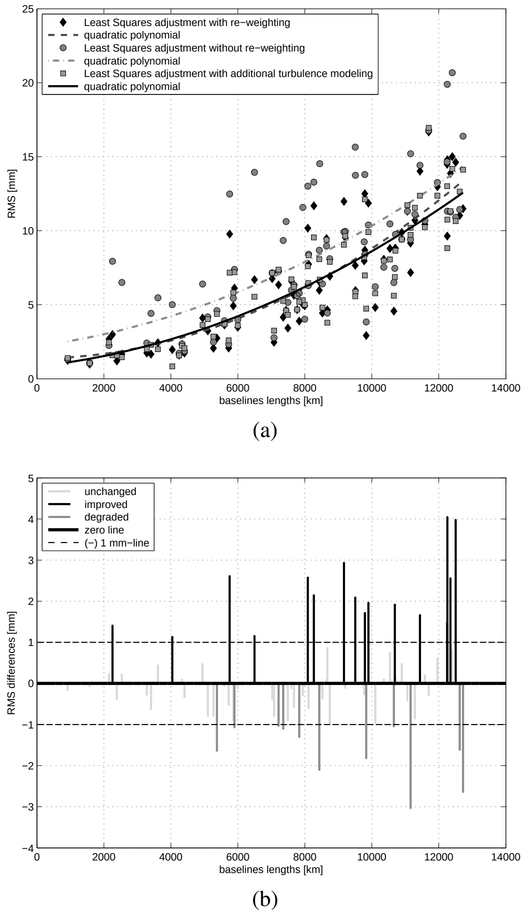

Fig. 3 Baseline length repeatabilities (a) for a least-squares adjustment with (setup 1, black diamonds) and without (setup 2, dark gray points) re-weighting the observations as well as for a least-squares adjustment with turbulence modeling (setup 3, dark gray squares). RMS differences (b) between setup 1 and 3. Black bars show an improvement, dark gray bars denote a degradation and light gray bars indicate unchanged baseline lengths.

though the χ^2 values decrease for the new approach, they are still a little too high indicating that the observational noise is still underestimated or that there are some other terms that are not adequately modeled.

In a next step, special consideration should be given to the parametrization of the wind velocity and direction that is assumed to be constant in this study. Further, and even more important, other error sources—e.g., source position and structure errors, remaining correlator related errors, uncertainties in phase calibration, or further model errors—have to be investigated and modeled adequately as well.

Acknowledgements

The authors thank the German Research Foundation (Deutsche Forschungsgemeinschaft, DFG) for its financial support (contract NO 318/10-1).

References

1. M. Abramowitz and I. A. Segun. Handbook of mathematical functions. *Dover Publications*, New York, 1972
2. T. Artz, S. Böckmann, A. Nothnagel, P. Steigenberger. Subdiurnal variations in the Earth's rotation from continuous Very Long Baseline Interferometry campaigns. *J Geophys Res*, 115, B05404, doi: 10.1029/2009JB006834, 2010
3. J. L. Davis, T. A. Herring, I. I. Shapiro, A. E. E. Rogers, G. Elgered. Geodesy by radio interferometry: Effects of atmospheric modeling errors on estimates of baseline length. *Radio Sci*, 20(6), pp. 1593–1607, 1985
4. J. Gipson, D. MacMillan, L. Petrov. Improved Estimation in VLBI through Better Modeling and Analysis. *IVS 2008 General Meeting Proc.*, pp. 157–162, 2008
5. C. Ma, J. M. Sauber, T. A. Clark, J. W. Ryan, L. J. Bell, D. Gordon, W. E. Himwich. Measurement of horizontal motions in Alaska using very long baseline interferometry. *J Geophys Res*, 95(B13), doi: 10.1029/JB095iB13p21991, 1990
6. T. Nilsson and R. Haas. Impact of atmospheric turbulence on geodetic very long baseline interferometry. *J Geophys Res*, 115, B03407, doi: 10.1029/2009JB006579, 2010
7. T. Nilsson, R. Heinkelmann, M. Karbon, V. Raposo-Pulido, B. Soja, H. Schuh. Earth orientation parameters estimated from VLBI during the CONT11 campaign. *J Geodesy*, 88, doi: 10.1007/s00190-014-0700-5, pp. 491–502, 2014
8. A. Romero-Wolf, C. S. Jacobs, J.T. Ratcliff. Effects of Tropospheric Spatio-temporal Correlated Noise on the Analysis of Space Geodetic Data. *IVS 2012 General Meeting Proc.*, pp. 231–235, 2012
9. S. Schön and F. K. Brunner. Atmospheric turbulence theory applied to GPS carrier-phase data. *J Geodesy*, 82, doi: 10.1007/s00190-007-0156-y, pp. 47–57, 2008
10. H. Schuh and D. Behrend. VLBI: A fascinating technique for geodesy and astrometry. *Journal of Geodynamics*, 61, doi: 10.1016/j.jog.2012.07.007, pp. 68–80, 2012
11. V. Tesmer and H. Kutterer. An advanced Stochastic Model for VLBI Observations and its Applications to VLBI Data Analysis. *IVS 2004 General Meeting Proc.*, pp. 296–300, 2004
12. R. N. Treuhaft and G. E. Lanyi. The effect of the dynamic wet troposphere on radio interferometric measurements. *Radio Sci*, 22(2), pp. 251–265, 1987
13. A. D. Wheelon. Electromagnetic Scintillation - I. Geometrical Optics. *Cambridge University Press*, Cambridge, 2004
14. A. Whitney. How Do VLBI Correlators Work? *IVS 2000 General Meeting Proc.*, pp. 187–205, 2000

Using External Tropospheric Delay in VLBI Data Processing

Sergei Kurdubov, Gennady Ilin

Abstract The zenith wet tropospheric delay is one of the parameters that need to be estimated in routine VLBI data processing. Stations of the Russian national VLBI network "Quasar-KVO" will be equipped with water vapor radiometers in the next year, and we performed several experiments in order to estimate how the external tropospheric data can improve the accuracy of VLBI astrometry results. We process hourly UTC–UT1 estimation sessions using VLBI and GPS estimated tropospheric delays. In the first case, one can see potential improvement from external tropospheric data in the UTC–UT1 formal errors. The second case shows that, when we use truly external data from GPS, the results can be improved.

Keywords VLBI, troposphere, WVR

1 Introduction

The tropospheric delay can be divided into "dry" and "wet" components. The "dry" component can be calculated using the Saastamoinen formula from the atmospheric pressure. In routine VLBI data processing, we estimated only Wet Zenith Delay (WZD) and gradients. It can be assumed that using a priori tropospheric data (from GNSS or WVR) can improve EOP and coordinate results. We expect maximum effect for the hourly UT1–UTC sessions.

Institute of Applied Astronomy, Russian Academy of Sciences

2 Simulation

We performed simulations in order to estimate the maximum possible improvement from external tropospheric delays. Hourly one-baseline sessions from the Ru-U program (31 sessions from 14.09.2012 to 14.10.2012, Zelenchukskaya–Badary) were processed with the QUASAR software:

1. No a priori WZD, estimated parameters: UT1–UTC; linear clock + stochastic; WZD + stochastic.
2. A priori WZD from solution 1, estimated parameters: UT1–UTC; linear clock + stochastic; WZD + stochastic.
3. A priori WZD from solution 1, estimated parameters: UT1–UTC; linear clock + stochastic; No WZD.

We obtained for the first solution a UT1–UTC mean formal error of 41 μs, for the second solution 29 μs, and for the third solution 19 μs. Thus, the maximum improvement can be up to two times if the external tropospheric delay is set to a VLBI estimate.

3 GPS Tropospheric Delay in VLBI Processing

We processed VLBI data with tropospheric delays taken from GNSS data. We took sessions of the Ru-U program from 2012.11.01 to 2013.01.27, 60 hourly one-baseline Zelenchukskaya–Badary sessions. The tropospheric delay data came from the JPL GPS products database. Only total zenith delays (TZD) are available from GPS. The WZD was obtained using the Saastamoinen formula. Five solutions were obtained:

1. Standard solution, no stochastic, no a priori troposphere: Est: (+clock,+dUT1,+WZD), Apr: -TZD, -WZD
2. Standard solution, +stochastic, no a priori troposphere: Est: (+clock,+dUT1,+WZD+random), Apr: -TZD, -WZD
3. Estimation only clock and UT1-UTC; a priori WZD and TZD from GPS: Est: (+clock,+dUT1), Apr: +TZD, +WZD (GPS)
4. Estimation only clock and UT1-UTC; a priori WZD from GPS: Est: (+clock,+dUT1), Apr: -TZD, +WZD (GPS)
5. Estimation only clock and UT1-UTC; a priori WZD from GPS; station positions from QUASAR global solution (2011): Est: (+clock,+dUT1), Apr: -TZD, +WZD (GPS)

Table 1 Differences of the Ru-U UT1 estimations to the IERS series, μs.

Solution ID	RMS	WRMS	Mean formal error, μs	TRF
1	49	41	38	ITRF2008/Q2011
2	48	42	42	ITRF2008
3	44	41	34	ITRF2008
4	48	46	39	ITRF2008
5	41	36	33	Q2011

4 Conclusion

Real external tropospheric data can improve Intensive UT1–UTC results up to 20%. Station coordinates are crucial, because the WZD parameter in one-baseline sessions takes on station coordinate errors. We obtain the best improvement from the GPS troposphere when using more correct station coordinates. Our plans are to obtain new results after WVRs are installed at all QUASAR network stations.

Troposphere Delay Raytracing Applied in VLBI Analysis

David Eriksson[1], Daniel MacMillan[2], John Gipson[2]

Abstract Tropospheric delay modeling error is one of the largest sources of error in VLBI analysis. For standard operational solutions, we use the VMF1 elevation-dependent mapping functions derived from European Centre for Medium Range Forecasting (ECMWF) data. These mapping functions assume that tropospheric delay at a site is azimuthally symmetric. As this assumption does not reflect reality, we have instead determined the raytrace delay along the signal path through the three-dimensional troposphere refractivity field for each VLBI quasar observation. We calculated the troposphere refractivity fields from the pressure, temperature, specific humidity, and geopotential height fields of the NASA GSFC GEOS-5 numerical weather model. We discuss results using raytrace delay in the analysis of the CONT11 R&D sessions. When applied in VLBI analysis, baseline length repeatabilities were better for 70% of baselines with raytraced delays than with VMF1 mapping functions. Vertical repeatabilities were better for 2/3 of all stations. The reference frame scale bias error was 0.02 ppb for raytracing versus 0.08 ppb and 0.06 ppb for VMF1 and NMF, respectively.

Keywords Troposphere, raytracing

1 Introduction

Tropospheric delay modeling is still a significant source of random and systematic error in the analysis of VLBI data. In current tropospheric delay modeling, the elevation dependence of tropospheric delays is described by hydrostatic and wet mapping functions. It is assumed that the atmosphere has no horizontal refractivity variation. Both the NMF mapping functions [4], which used the radiosonde tropospheric profile data, and the VMF1 mapping functions [1], which used the ECMWF weather model data, were derived by computing raytrace delays through uniform atmospheric layers of constant refractivity. In the work described here, we have computed the total (hydrostatic & wet) delays and the wet mapping functions from a numerical weather model for each VLBI observation by raytracing through the three-dimensional refractivity field at the observation epoch.

1. Chalmers University of Technology
2. NVI, Inc.

2 Data and Raytracing Algorithm

Troposphere data is taken from the NASA GSFC GEOS 5.9.1 data assimilation model, which has a temporal resolution of three hours, a horizontal resolution of $0.5^\circ \times 0.625^\circ$, and troposphere profiles with 72 vertical levels. From the model pressure, temperature, relative humidity and geopotential heights, we have calculated the corresponding three-dimensional refractivity fields. For each VLBI observation, the refractivity along the signal raypath was then calculated by spatial interpolation of the refractivity field interpolated to the VLBI epoch. A piecewise linear approach similar to one proposed by Hobiger [3] was used to determine the path of the ray and then to compute the hydrostatic and wet delay components along the path. To minimize computation time, the propagation of the ray is constrained to a plane of constant azimuth.

3 Analysis

In a first test, we investigated how much of the observed wet zenith delay is modelled by the raytraced wet zenith delay. The observed VLBI residual zenith delay was estimated in a solution where the a priori tropospheric delay was the NMF hydrostatic delay so that the residual delay is predominantly the wet zenith delay. Figure 1 shows how closely the raytraced wet zenith delay agrees with this estimate of the observed delay for Westford (Massachusetts) over the CONT11 time period. The average correlation for CONT11 sites between the observed estimate of wet zenith delay and the raytraced wet zenith delay was 0.93. The raytraced wet zenith delay accounts for about 90% of the RMS of the estimated wet zenith delay estimates.

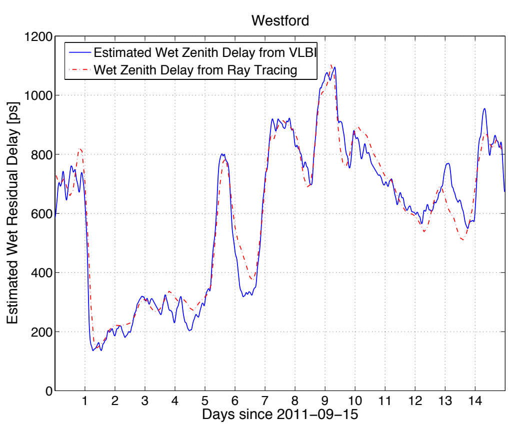

Fig. 1 Comparison of the raytraced wet zenith delay at Westford and the wet residual delay estimated from observed VLBI data.

We then ran a VLBI solution for the CONT11 series of sessions applying as the a priori delay the total raytraced delay for each observation. It is still necessary to estimate the usual troposphere parameters; residual wet zenith and gradient delays were estimated as piecewise linear functions with 20-minute and six-hour intervals, respectively. The wet mapping function was computed from calculated wet raytraced delays for each observation. For comparison, two additional solutions were performed that used: 1) NMF mapping functions and 2) the VMF1 total delay as the a priori troposphere delay and the residual wet delay estimated using the VMF1 wet mapping function. We also evaluated three different data weighting strategies: 1) baseline reweighting, 2) elevation-dependent weighting, and 3) correlated noise. Baseline reweighting adds a constant noise contribution in quadrature to the observation uncertainties such that the χ^2 per degree of freedom is unity. Elevation-dependent weighting instead adds noise of the form $\alpha/\sin(elev)$ to the observation uncertainties. Correlated noise [2] includes an elevation-dependent off-diagonal correlation between simultaneous observations on baselines that share a common station. Table 1 summarizes the results of these test solutions in terms of the average baseline length WRMS repeatability. The best weighting strategy for all three troposphere options was correlated noise, and the best troposphere modeling choice was to use raytraced delays and mapping functions.

Table 1 CONT11 baseline length WRMS.

	NMF	VMF1 Total	Raytrace
Weighting	Average	Average	Average
Baseline	6.89	6.75	6.41
Elevation-dep	6.50	6.31	6.04
Correlated noise	6.35	5.96	5.73

Figure 2 shows the improvement in baseline length repeatability using raytraced delays versus using VMF1. For each site, the baseline length improvement is shown for all baselines to the site. The measure of improvement is the reduction (in quadrature) of the WRMS (weighted root mean square) repeatability. Because the baselines are ordered by length, it can be seen that the improvement generally increases with length. Most baselines improve except for Kokee (Hawaii). Length repeatabilities are improved for 72% of the baselines. Kokee is located on the Hawaiian island of Kauai at an elevation about 800 m higher than the ocean surface. The GMAO grid cells that contribute to the raytrace delay calculation may not reflect the true local troposphere behavior at Kokee. Improvement of site position repeatabilities (raytrace versus VMF1) are shown in Figure 3, where site vertical coordinate repeatabilities are improved for 11 of 13 sites.

Whenever mapping function improvements have been made in the past, reference frame scale errors

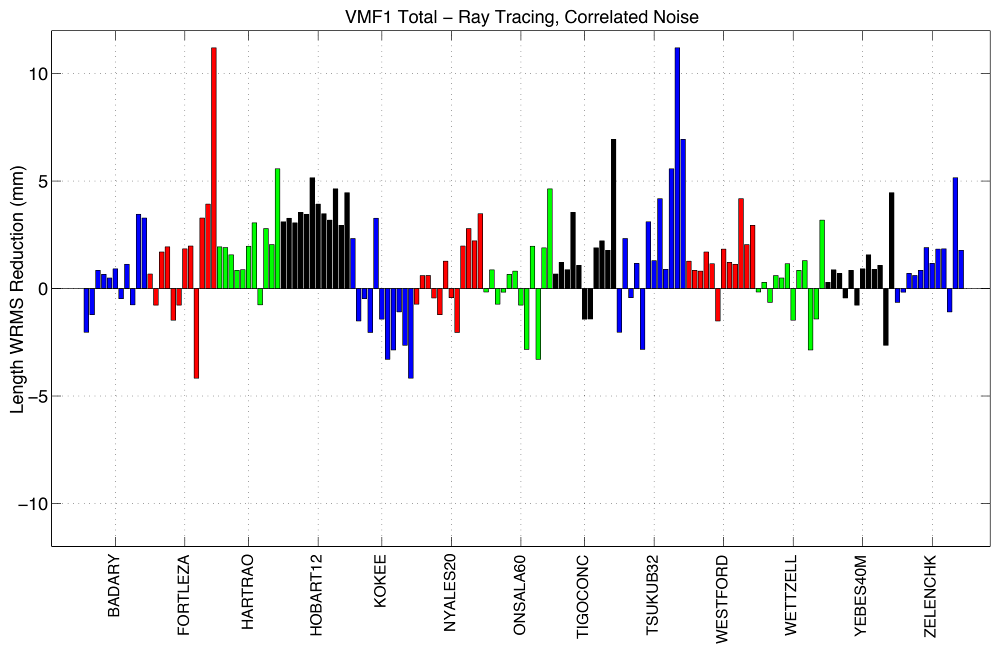

Fig. 2 Improvement in baseline length for different baselines of the CONT11 sessions. Baselines for each site are ordered by length.

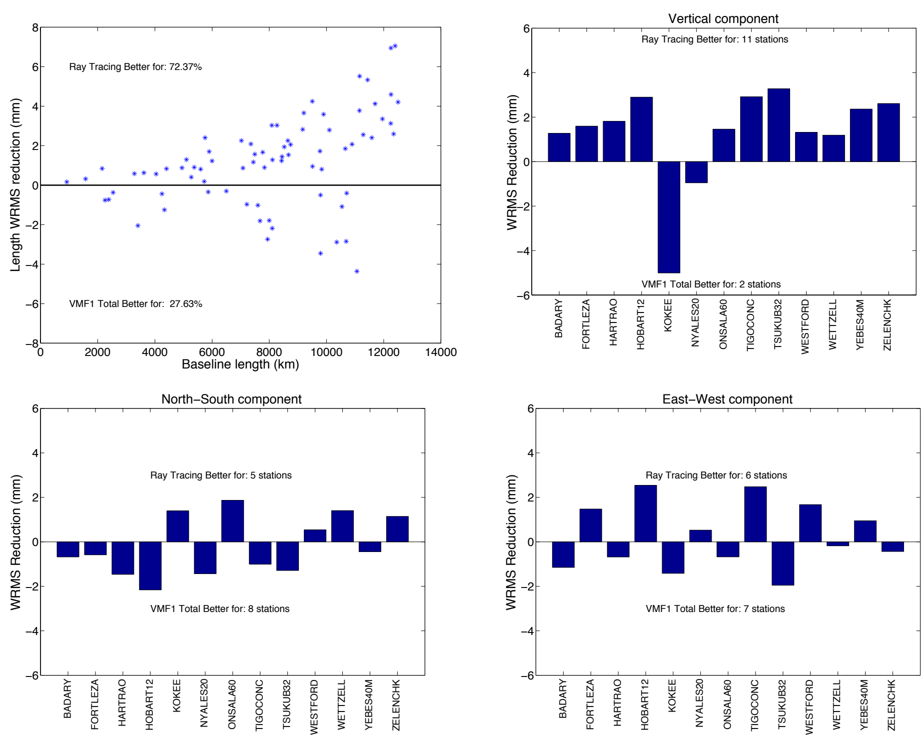

Fig. 3 Improvement in baseline length and in station position (up, east, north) estimates for the CONT11 experiment sessions.

have been reduced. We have estimated the scale bias error by performing an elevation cutoff test using two solutions, one with a minimum elevation cutoff of 5° and the other with a cutoff of 12°. The idea of the cutoff test is that troposphere modeling error increases as elevation decreases and that a measure of this error is given by how much position estimates at the higher cutoff change when low elevation data is included in a solution. For each baseline, the mean baseline length difference between the baseline length series estimated from each of the cutoff solutions was computed. The scale bias is the slope of the best-fitting line in Figure 4 through the differences as a function of baseline length.

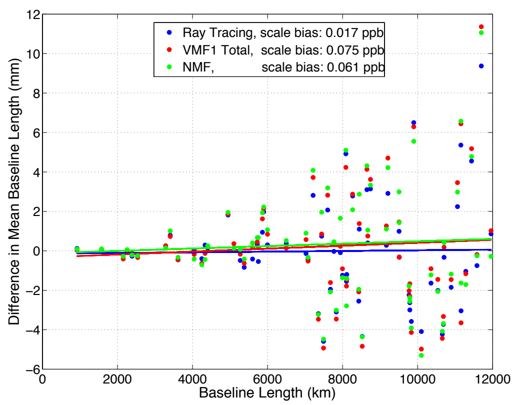

Fig. 4 Scale bias from mean baseline length differences between solutions with minimum elevation cutoff at 5° and 12°.

For the raytrace delay solution, the scale bias was 0.017 ppb. For solutions where VMF1 or NMF were used, the scale biases were 0.061 ppb and 0.075 ppb, respectively.

4 Conclusions

Raytracing has the potential to significantly improve VLBI analysis. Applying raytraced delays in the analysis of the CONT11 experiment sessions improves the baseline length repeatabilities for 72% of baselines and vertical repeatabilities for 11 out of 13 sites compared with using the VMF1 model. We are currently producing raytracing results for the entire GEOS-5 time period (2000 to the present) as part of a raytracing service to provide tropospheric delay corrections for all VLBI sessions at http://lacerta.gsfc.nasa.gov/tropodelays/. The current latency is 24 hours, which allows the raytracing service to provide delays to the VLBI community for application of tropospheric corrections within one day after a session is observed.

Acknowledgements

The numerical weather model GEOS 5.9.1 was provided by the NASA Global Modeling and Assimilation Office (GMAO) at Goddard Space Flight Center.

References

1. J. Boehm, B. Werl, and H. Schuh. Troposphere Mapping Functions for GPS and Very Long Baseline Interferometry From European Centre for Medium-Range Forecasts Operational Analysis Data. *Journal of Geophysical Research*, 111, B02406, doi:10.1029/2005JB003629, 2006.
2. J. Gipson. Incorporating Correlated Station Dependent Noise Improves VLBI Estimates. *Proc. 18th European VLBI for Geodesy and Astrometry Working Meeting*, edited by J. Boehm, A. Pany, and H. Schuh, pp. 129–134, Tech. Univ. Wien, Vienna, 2007.
3. T. Hobiger, R. Ichikawa, Y. Koyama, and T. Kondo. Fast and Accurate Ray-tracing Algorithms for Real-time Space Geodetic Applications Using Numerical Weather Models. *Journal of Geophysical Research*, 113, D20302, doi:10.1029/2008JD010503, 2008.
4. A. E. Niell. Global Mapping Functions for the Atmosphere Delay at Radio Wavelengths. *Journal of Geophysical Research*, 101(B2), 3227–3246, 1996.

Ray-traced Delays in the Atmosphere for Geodetic VLBI

Armin Hofmeister, Johannes Böhm

Abstract The application of ray-traced slant path delays has the potential to enhance geodetic Very Long Baseline Interferometry (VLBI) analysis through improving the correction of the tropospheric effects on the observations. The utilization of directly estimated ray-traced slant path delays calculated from true meteorological data has the potential to overcome the shortcomings of the commonly used method of indirectly determined slant path delays via zenith delays mapped to the actual observation angle. Within our project RADIATE VLBI (Ray-traced Delays in the Atmosphere for geodetic VLBI) we are developing a new ray-tracing program for application in geodetic VLBI analysis. We introduce our project and present an overview of the current development status of our ray-tracer. In order to verify our results, we compare our ray-traced delays to results of a ray-tracer comparison campaign by Nafisi et al. (2012b), [4]. The RADIATE piecewise-linear solution for the slant total delay calculated from mapping factors at 5° elevation agrees with most of the other ray-tracers, with mean differences below 1 cm and standard deviations below 0.6 cm at the station Tsukuba and mean differences below 2.5 cm and standard deviations below 1 cm at the station Wettzell.

Keywords Ray-tracing, troposphere, VLBI

Department of Geodesy and Geoinformation, Vienna University of Technology, Austria

1 Derivation of Slant Path Delays

The influence of the troposphere is one of the major error sources in space geodetic applications such as Very Long Baseline Interferometry (VLBI) or Global Navigation Satellite Systems (GNSS) (Böhm (2012), [1]). Besides the common way of determining zenith delays and mapping them to the elevation angles, it is possible to use ray-tracing algorithms to directly determine the slant delays for each observation.

The great advantage of this approach is the possibility of using the true meteorological data along the exact ray path of each individual observation to determine the slant total delays, whereas in the standard approach only surface-based data serve as input to calculate zenith hydrostatic delays and the zenith wet delays are only estimated within the VLBI analysis using the wet mapping factors as partial derivatives (Böhm (2012), [1]). Therefore the currently common method to determine the slant delays shows some disadvantages because of its indirect approach through the use of zenith delays and mapping functions.

In the following the ray-tracing technique for application in geodetic VLBI will be discussed.

2 Ray-tracing Technique

In order to determine the slant path delays for geodetic VLBI observations, it is necessary to reconstruct the original signal path for each observation as accurately as possible. For this task different approaches of ray-tracing can be used, some more sophisticated than others, but more detailed methods often lead to increased computation times.

For the signal path determination, information about the state of the atmosphere in the form of pressure, temperature, and humidity is needed. These data are delivered through numerical weather models with certain resolutions in the horizontal and vertical directions. From the information gained by a numerical weather model, the refractivities at the different height levels can be calculated, and with them the signal path can be determined.

After deriving the true signal path of the observation, the slant path delay is calculated again using the refractivities.

3 Project RADIATE VLBI

One main goal of project RADIATE VLBI (Ray-traced Delays in the Atmosphere for geodetic VLBI), funded by the Austrian Science Fund (FWF), is to determine ray-traced delays for all VLBI observations since 1979 (about 5 Mio.) (Böhm (2012), [1]).

Through the development of the new ray-tracer called RADIATE within the project, we want to enhance the processing of VLBI sessions in order to improve the resulting geodetic parameters such as station coordinates and the scale of the terrestrial reference frame or Earth orientation parameters (EOP) (Böhm (2012), [1]).

3.1 Ray-tracer RADIATE

For our RADIATE ray-tracer we use meteorological data from the European Centre for Medium-range Weather Forecasts (ECMWF) in the form of a global numerical weather model (ECMWF pressure level data) with a horizontal resolution of 0.125° x 0.125°, a vertical span of 25 pressure levels, and a time resolution of six hours with epochs at 0h, 6h, 12h, and 18h. Interpolation of the meteorological parameters in the vertical direction is carried out prior to the ray-tracing to establish also a high vertical resolution besides the originally already high horizontal resolution. The temperature is linearly interpolated, and the total pressure and the water vapor pressure are logarithmically interpolated as described by Nafisi et al. (2012a), [3].

Above the ECMWF-supported pressure levels, a model of a standard atmosphere is used to extend the data up to 84 km.

RADIATE is currently capable of three different 2D ray-tracing approaches, forcing the ray to stay within a vertical plane of constant azimuth:

1. Piecewise-linear method:
   A fast, but less sophisticated approach. This method will be further referred to as RADIATE pwl.

2. Refined piecewise-linear method:
   A kind of improved version of the piecewise-linear approach designed for ray-tracing with lower vertical resolution. The refractivities along the signal path are determined in a refined way. This method will be further referred to as RADIATE ref. pwl.

3. Thayer method:
   A more sophisticated approach since curved ray-traces are introduced for enhanced reconstruction of the true signal path. This method will be further referred to as RADIATE Thayer.

For detailed information on the ray-tracing methods 2 and 3 please refer to the paper of Hobiger et al. (2008), [2].

In order to estimate the slant delays at the actual VLBI observation time, linear interpolation between the delays calculated at the two sequent epochs of meteorological data directly surrounding the observation is done.

3.2 Future Goals for RADIATE VLBI

It is planned to additionally set up a 3D ray-tracing approach, where the ray paths are not limited to a certain azimuthally fixed vertical plane.

Furthermore, ray-tracing for (near) real-time applications of geodetic VLBI such as the IVS Intensive sessions is planned to be realized within the project (Böhm (2012), [1]).

The program code will be converted from MATLAB® to FORTRAN or C.

4 Comparison of Different Ray-tracers

In order to verify the RADIATE ray-tracer and its results from the different ray-tracing approaches, we have carried out a comparison of the determined zenith and slant delays to results of a past comparison campaign, described in Nafisi et al. (2012b), [4], where ray-tracers of five institutions took part. Table 1 gives a brief overview of the ray-tracing packages from the institutions that were part of the past comparison campaign.

4.1 Data for the Comparison

For comparing the RADIATE results, ray-tracing has been done using the same data sets (numerical weather models and geoid undulations) as for most of the participants in the past comparison campaign. This means that ray-tracing has been carried out for the stations Tsukuba (Tsukub32) at 12 August 2008, 0 UTC and Wettzell at 1 January 2008, 0 UTC using regional ECMWF numerical weather models with a horizontal extent of 20° x 20° and a resolution of 0.1° x 0.1° containing 25 pressure levels. Slant delays have been determined for a fixed elevation of 5° at full azimuthal coverage using a step width of 2°. Since the artificial observations are set exactly to the epochs of the numerical weather models, no time interpolation of the calculated delays has been necessary in order to match the observation times (Nafisi et al. (2012b), [4]).

There is one important difference in the input data used by the ray-tracers GFZ and Horizon concerning the utilized numerical weather model. Those two ray-tracers used the ECMWF-native model level data containing 91 model levels, whereas all other ray-tracers used the ECMWF-pressure level data containing 25 pressure levels (Nafisi et al. (2012b), [4]).

Please refer to Nafisi et al. (2012b), [4] for more details on the data sets and calculation settings used in the past comparison campaign.

4.2 Results

Looking only at the different RADIATE results for the zenith total delays (ZTD), shown as a difference plot to the RADIATE pwl results for the stations Tsukuba and Wettzell in Figure 1, it can be seen that all three different ray-tracing approaches yield the same results. This is because the three different ray path determination approaches do not influence the zenith delays, and therefore differences should only occur in the slant delays.

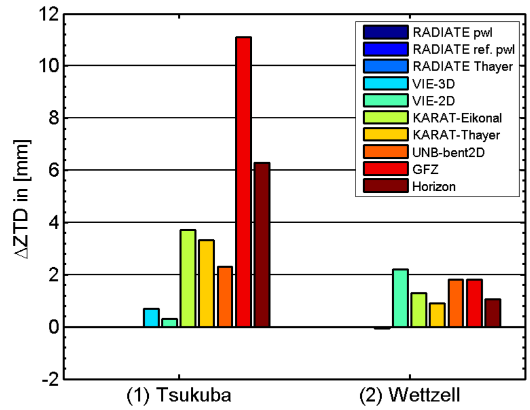

Fig. 1 Differences in zenith total delay (ZTD) [ZTD from a specific ray tracer minus ZTD from RADIATE pwl]. The reference ZTD taken from RADIATE pwl has the following absolute values: (1) Tsukuba: 2.5716 m, (2) Wettzell: 2.2057 m. Please refer to the Web version of the Proceedings to see the original color-coded version of this figure.

Compared to the other ray-tracers, the agreement of the zenith total delay is quite good for the station Wettzell (see right part of Figure 1) with differences up to a maximum of about 2 mm. Looking at the results for the station Tsukuba (see left part of Figure 1), increased differences can be seen. As stated earlier, GFZ and Horizon used a different numerical weather model for their calculations, which obviously results in significant differences in the determined zenith total delay. This is mainly because of the wet part of the zenith delay, as the different numerical weather model apparently shows the largest difference in this part. Also the other ray-tracers have slightly increased differences to the RADIATE zenith delays of up to 4 mm, but most of them are still on a quite low level, yielding a fine agreement.

For some ray-tracers also the zenith hydrostatic delays determined from the equation by Saastamoinen (1972), [5] are presented in Nafisi et al. (2012b), [4]. Compared to the RADIATE results (see Figure 2), we

Table 1 Ray-tracing packages of the five institutions that participated in the past comparison campaign described by Nafisi et al. (2012b), [4].

Ray-tracing package	Method	Institution	Developers
GFZ	2D	GFZ (German Research Centre for Geosciences)	Florian Zus and Jens Wickert
Horizon	Eikonal (2D)	GRGS (Groupe de Recherche de Géodésie Spatiale)	Pascal Gegout
KARAT	Thayer (2D) and Eikonal (3D)	NICT (National Institute of Information and Communications Technology)	Thomas Hobiger and Ryuichi Ichikawa
UNB-bent	2D and 3D	UNB (University of New Brunswick)	Landon Urquhart, Marcelo Santos, Felipe Nievinski
VIE	2D and 3D	Vienna University of Technology	Vahab Nafisi, Johannes Böhm, Dudy D. Wijaya

can again see a good agreement of the RADIATE solutions with the other ray-tracers. Once more the difference to the GFZ ray-tracer is significantly larger, probably again due to the different numerical weather model from which the total pressure at the surface has been retrieved, which is needed for calculating the zenith hydrostatic delay when using the equation by Saastamoinen (1972), [5]. The differences of the RADIATE results to the other ray-tracers are mainly around 0.1 mm at both stations Tsukuba and Wettzell, if the GFZ solution is neglected.

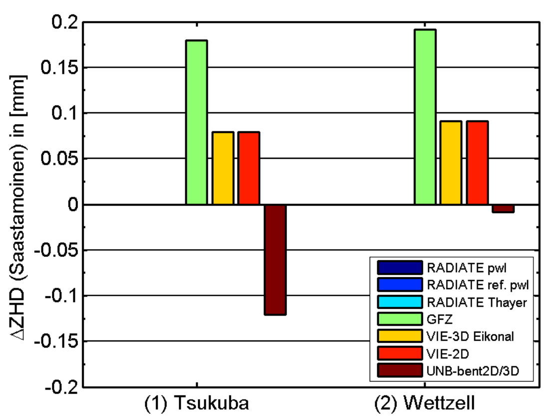

Fig. 2 Differences in zenith hydrostatic delay determined from the equation by Saastamoinen (1972), [5] [ZHD (Saastamoinen) from a specific ray tracer minus ZHD (Saastamoinen) from RADIATE pwl]. The reference ZHD (Saastamoinen) taken from RADIATE pwl has the following absolute values: (1) Tsukuba: 2.2948 m, (2) Wettzell: 2.1662 m. Please refer to the Web version of the Proceedings to see the original color-coded version of this figure.

If we look at the slant total delays (STD) for the station Tsukuba in Figure 3, it is again obvious that the RADIATE results agree quite well with the other ray-tracers except for GFZ and Horizon due to the previously described reason. Especially when just the trends of the slant total delays are taken into account, the RADIATE results match with the other ray-tracers, if the results of GFZ and Horizon are not considered. The RADIATE pwl approach agrees with the other ray-tracers with mean differences below 4 cm and standard deviations of the differences below 0.6 cm.

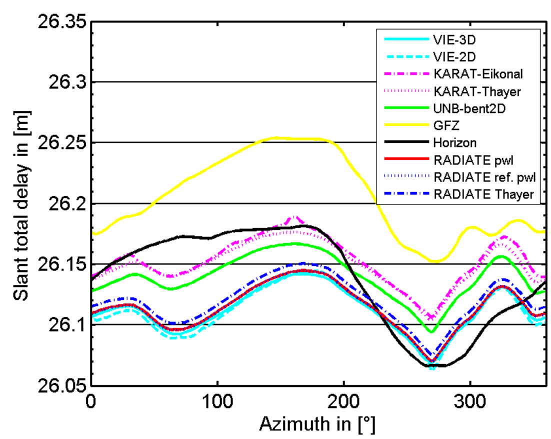

Fig. 3 Slant total delays calculated by different ray-tracers for Tsukuba (Tsukub32) at 5° elevation for 12 August 2008, 0 UTC. Please refer to the Web version of the Proceedings to see the original color-coded version of this figure.

Also for the station Wettzell, the RADIATE ray-tracing approaches deliver slant total delays fitting very well, as RADIATE pwl has mean differences below 2.5 cm and standard deviations of the differences below 1 cm, if the GFZ and Horizon solutions are not considered.

Due to the usage of a high vertical resolution after the interpolation of the original ECMWF numerical weather model, the results of RADIATE pwl and RADIATE ref. pwl are almost the same, as the refined approach only has an advantage if reduced vertical resolution is used.

In the case of the slant total delays (STD) calculated from the total mapping factors (TMF) of the different ray-tracers using the zenith total delay (ZTD) from RADIATE pwl (see Equation 1), the agreement between the RADIATE results and the other ray-tracers is even better for station Tsukuba (see Figure 4), with mean differences of below 1 cm and standard deviations of the differences below 0.6 cm, not considering the results of GFZ and Horizon.

$$STD = TMF * ZTD \tag{1}$$

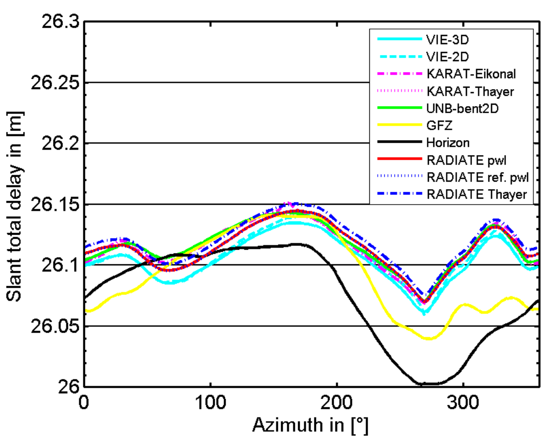

Fig. 4 Slant total delays (STD) calculated from the total mapping factors (TMF) of different ray-tracers for Tsukuba (Tsukub32) at 5° elevation for 12 August 2008, 0 UTC. The STD is calculated with the TMF of the different ray-tracers and the zenith total delay (ZTD) of RADIATE pwl (2.5716 m). Please refer to the Web version of the Proceedings to see the original color-coded version of this figure.

The general agreement of the slant total delays calculated from the total mapping factors for the station Wettzell stays the same compared to the directly computed slant total delays, yielding for the RADIATE pwl approach mean differences below 2.5 cm and standard deviations of the differences below 1 cm, again not taking the results of GFZ and Horizon into account.

5 Conclusions

The comparison showed a good overall agreement of the RADIATE results with the other ray-tracers. Especially with respect to the slant total delays calculated from the total mapping factors for both stations Tsukuba and Wettzell, our results have a fine conformity with all other ray-tracers where direct comparison is possible through the use of the same numerical weather model.

Further investigation into the zenith total delay differences, particularly for the station Tsukuba, may reveal some starting points for quality enhancement of the RADIATE ray-tracer.

Acknowledgements

Johannes Böhm and Armin Hofmeister are very grateful to the Austrian Science Fund (FWF) for financial support of the project “Ray-traced Delays in der Atmosphäre für geodätische VLBI” (RADIATE VLBI) (P25320).

References

1. Böhm J. (2012). *RADIATE VLBI*. Project proposal for the FWF, Vienna University of Technology.
2. Hobiger T., Ichikawa R., Koyama Y., and Kondo T. (2008). *Fast and accurate ray-tracing algorithms for real-time space geodetic applications using numerical weather models*. In Journal of Geophysical Research, Vol. 113, D20302, doi:10.1029/2008JD010503.
3. Nafisi V., Madzak M., Böhm J., Ardalan A.A., Schuh H. (2012a). *Ray-traced tropospheric delays in VLBI analysis*. In Radio Science, Vol. 47, RS2020, doi:10.1029/2011RS004918.
4. Nafisi V., Urquhart L., Santos M.C., Nievinski F.G., Böhm J., Wijaya D.D., Schuh H., Ardalan A.A., Hobiger T., Ichikawa R., Zus F., Wickert J., and Gegout, P. (2012b). *Comparison of Ray-Tracing Packages for Troposphere Delays*. In IEEE Transactions on Geoscience and Remote Sensing, Vol. 50, No. 2, February 2012, pp. 469–481, doi: 10.1109/TGRS.2011.2160952.
5. Saastamoinen J. (1972). *Atmospheric Correction for the Troposphere and Stratosphere in Radio Ranging of Satellites*. In S.W. Henriksen, A. Mancini and B.H. Chovitz (eds): The Use of Artificial Satellites for Geodesy, Vol. 15, Geophysical Monograph Series, pp. 247–251, American Geophysical Union, Washington, D.C., ISBN 0-87590-015-1.

Tropospheric Modeling for the Intensive Sessions

Tobias Nilsson[1], Benedikt Soja[1], Maria Karbon[1], Robert Heinkelmann[1], Li Liu[1,2], Cuixian Lu[1], Julian A. Mora-Diaz[1], Virginia Raposo-Pulido[1,3], Minghui Xu[1,2], Harald Schuh[1]

Abstract We investigate different possibilities for improving the modeling of the tropospheric delays in the data analysis of the Intensive VLBI sessions. These possibilities include using external information from GNSS or ECMWF, as well as extending the parametrization in the data analysis by also estimating tropospheric gradients or constraining the tropospheric variations using a turbulence model. In general, the results show that estimating gradients in the data analysis improves the results. The best strategy, however, depends on the type of Intensive session and the quality of the a priori tropospheric data.

Keywords VLBI, Intensives, troposphere, UT1

1 Introduction

The Intensive VLBI sessions are VLBI sessions performed approximately every day in order to monitor UT1–UTC. In most cases just two stations on a long East-West baseline are used, and the sessions are only one-hour long. Because of this, the number of observations is rather low (20–30), and the geometrical distribution of the observed radio sources on the skies above the stations is relatively poor. This limits the number of parameters that can be estimated in the data analysis of these sessions. Normally, just clock offsets, clock drifts, one constant zenith wet delay (ZWD) per station, and one UT1–UTC offset are estimated. In particular for the troposphere this parametrization may not be sufficient, e.g., the tropospheric gradients are not estimated but fixed to a priori values. Hence, if large tropospheric gradients are present, these will lead to errors in the analysis results, e.g., in the UT1–UTC estimates.

The tropospheric modeling of Intensive sessions was investigated by Nilsson et al. (2011) [6]. They created Intensive-like sessions by extracting single-baseline observations from the CONT08 data set. They found that, if good a priori information about the troposphere is available, the accuracy of the UT1–UTC estimates improves. Furthermore, they also found an improvement if tropospheric gradients were estimated in the data analysis. This improvement was confirmed for the actual Intensive sessions by Böhm et al. (2010) [2].

In this work we investigate different possibilities for the modeling of the troposphere in the data analysis of the Intensives. We test using a priori information of the troposphere estimated from GNSS (Global Navigation Satellite Systems) or ECMWF (European Centre for Medium-range Weather Forecasts) analysis data. Furthermore we also consider the possibility of extending the tropospheric modeling in the data analysis, e.g. by estimating also tropospheric gradients or by modeling the tropospheric delays using a turbulence model.

1. Helmholz Centre Potsdam, GFZ German Research Centre for Geosciences, Potsdam, Germany
2. Shanghai Astronomical Observatory, Chinese Academy of Sciences, Shanghai, China
3. Instituto Geográfico Nacional, Centro Nacional de Información Geográfica, Spain

2 The Intensive Sessions

In this work we analyzed the data from the 2012–2013 Intensive sessions. We considered three different types

Table 1 The different types of Intensives used in this work. The table gives the baselines, the observation time, the baseline length, and the length of the baseline projected onto the equatorial plane

	Stations	Observation time	Baseline length [km]	Equatorial proj. [km]
INT1	Wettzell, Kokee Park (Svetloe, occasionally)	Monday–Friday	10357	10072
INT2/INT3	Wettzell, Tsukuba (Ny-Ålesund, INT3) (Sheshan, occasionally)	Weekends Monday (INT3)	8445	8378
Ru-U	Zelenchukskaya, Badary (Svetloe, occasionally)	Every day	4405	4364

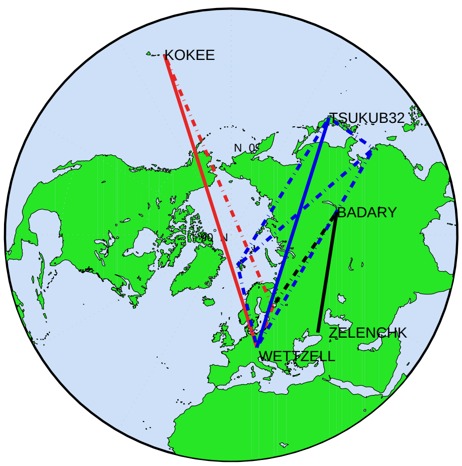

Fig. 1 The baselines observed in the Intensive sessions used in this work. Shown are the INT1 (red), the INT2/3 (blue), and the Ru-U (black) baselines. Solid lines are baselines included in most sessions, and dashed lines denote baselines only occasionally used.

of Intensive sessions, which are presented in Table 1. The baselines of these sessions are plotted in Figure 1.

3 Data Analysis

The data were analyzed with the Vienna VLBI Software (VieVS, [1]). In the data analysis we estimated clock offsets, linear clock drifts, and UT1–UTC. For the troposphere we tested several different parametrizations, as listed below. Unless otherwise noted, one ZWD per station was estimated.

Standard Tropospheric gradients fixed to zero.

DAO grad. Tropospheric gradients fixed to constant station-wise values derived from data of the Goddard Data Assimilation Office (DAO) [5].

ECMWF grad. Tropospheric gradients fixed to values derived from ECMWF operational analysis data [3].

GNSS grad. Tropospheric gradients fixed to the GNSS estimates (the IGS (International GNSS Service) tropospheric product [4])

GNSS trop. Both ZWD and tropospheric gradients taken from the IGS tropospheric product. No ZWD estimated in the data analysis.

Est grad. Tropospheric gradients were estimated in the data analysis. These were constrained to the DAO values using a σ of 1 mm.

Turbulence One tropospheric delay per station was estimated for every scan. These were constrained with a variance-covariance matrix estimated using turbulence theory (Treuhaft and Lanyi, 1987 [9]).

For the *turbulence* solution, the variance-covariance matrix was calculated assuming that the fluctuations in the refractive index, n, between $\mathbf{r}_1$ and $\mathbf{r}_2$ can be expressed by the structure function:

$$\left\langle [n(\mathbf{r}_1) - n(\mathbf{r}_2)]^2 \right\rangle = C_n^2 \frac{|\mathbf{r}_1 - \mathbf{r}_2|^{2/3}}{1 + \left[\frac{|\mathbf{r}_1 - \mathbf{r}_2|}{L} \right]^{2/3}} \quad (1)$$

where C_n^2 is the refractive index structure constant and L is the saturation scale length. Station specific C_n^2 values were estimated from GNSS data (Nilsson et al., 2010, [7]). For the temporal variations we assumed the frozen flow hypothesis, i.e., that the fluctuations are moving with the wind. Since no precise wind information was available for the stations, we calculated variance-covariance matrices for 18 different

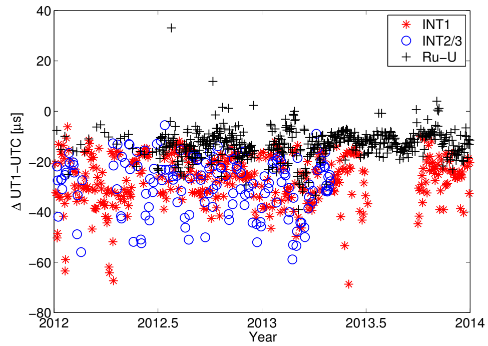

Fig. 2 The UT1–UTC error that would be caused by an unmodeled 1 mm East gradient at all stations in the 2012–2013 Intensive sessions.

wind vectors (velocity varied between 5 m/s and 15 m/s in steps of 5 m/s, direction between 0° and 300° in steps of 60°), and then calculated the average variance-covariance matrix.

As a reference solution we analyzed all IVS-R1, IVS-R4, IVS-T2, and RDV sessions from 2012–2013. In the analysis we estimated all five EOP (for polar motion and UT1–UTC one offset and one rate per EOP, and for nutation one offset for each component).

4 Results

We first investigated which UT1–UTC errors could be caused by unmodeled tropospheric gradients. This was done by changing the a priori East gradients of all stations by 1 mm in the standard solution, and then we checked what impact this had on the UT1–UTC estimates. The results can be seen in Figure 2. On average, the gradients cause a UT1–UTC error of -26.9 μs for the INT1 sessions and -27.7 μs for the INT2/3 sessions. This agrees with the results of Nilsson et al. (2011) [6], who found that the UT1-UTC error is -24 μs to -20 μs for a mean unmodeled East gradient of 1 mm. However, for the Ru-U sessions, the sensitivity to unmodeled gradients is lower; on average, the UT1–UTC error is 12.9 μs. The reason is probably because of different scheduling options being used for the Ru-U sessions compared to the INT1 and INT2/3 sessions. In particular, the Ru-U sessions generally make observations at higher elevation angles. For most of the Ru-U sessions the lowest elevation angle is 18° or larger, while for the INT1 and INT2/3 sessions it is between 5° and 10°. Since the effect of gradients is larger for low elevation angles, it is not surprising that the impact of gradients on the Ru-U results is lower.

Table 2 WM and WRMS differences between UT1–UTC values estimated from the Intensives and those from the reference solution.

Solution	INT1 WM [μs]	INT1 WRMS [μs]	Ru-U WM [μs]	Ru-U WRMS [μs]
Standard	3.0	20.7	21.9	45.0
DAO grad.	2.0	20.7	20.8	45.0
ECMWF grad.	2.4	20.7	21.5	45.2
GNSS grad.	−0.8	20.2	23.7	45.7
GNSS trop.	−0.4	21.2	25.4	44.5
Est. grad.	2.6	20.2	21.2	45.3
Turbulence	2.5	20.2	30.5	52.7

In Table 2 the weighted Mean (WM) and Weighted Root-Mean-Square (WRMS) differences between the different Intensive solutions and the reference solution are shown. These were calulated using all Intensives observed within one of the sessions of the reference solution. Since none of the sessions of the reference solution took place on weekends (nor Monday mornings), only the results for the INT1 and Ru-U sessions are shown. Mostly there are only minor differences between the different solutions. For the INT1 sessions the lowest WRMS values are obtained when fixing the gradients to the GNSS estimates, or when using an extended modeling in the data analysis (estimating gradients or using a turbulence model). For the Ru-U sessions, however, the turbulence model clearly gives the worst results. One reason could be that the Ru-U sessions normally do not include observations at low elevation angles. Thus, it is not possible to extend the parametrization for the troposphere. For the Ru-U sessions, there are relatively high WM values (around 20 μs).This is likely caused by inconsistencies in the station coordinates.

Using the UT1 values estimated from Intensives occurring on consecutive days we calculated daily length of day (LOD) values. We then compared these to LOD estimated by GNSS. The WM and WRMS differences can be seen in Table 3. The best results (lowest WRMS values) are here obtained when using gradients from GNSS (INT1), when estimating gradients in the data analysis (INT2/3), and when simply using the DAO gradients (Ru-U). However, here also the differences between the solutions are small. The exceptions are

Table 3 WM and WRMS differences between LOD values estimated from the Intensives and those from GNSS.

	INT1		INT2/3		Ru-U	
Solution	WM [μs]	WRMS [μs]	WM [μs]	WRMS [μs]	WM [μs]	WRMS [μs]
Standard	3.4	23.7	−0.7	20.7	1.6	53.1
DAO grad.	3.4	23.9	−0.8	20.5	1.6	53.0
ECMWF grad.	3.9	23.2	−0.5	20.0	1.7	54.1
GNSS grad.	3.1	22.2	−1.2	21.2	1.5	53.5
GNSS trop.	3.3	23.5	3.0	25.9	2.3	53.3
Est. grad.	3.5	23.3	−1.9	18.5	2.0	52.8
Turbulence	3.7	23.2	−2.3	18.6	2.4	62.3

for the turbulence model with the Ru-U sessions (see above), and when fixing all tropospheric parameters to the GNSS estimates for the INT2/3 sessions (probably because of biases in the GNSS ZWD estimates).

5 Conclusions

As we have seen, tropospheric gradients can—if not properly modeled in the data analysis—cause significant errors in the estimated UT1–UTC values. One way of reducing the impact of the gradients is to increase the elevation cut-off angle, like what is done for the Ru-U sessions. However, this makes the geometrical configuration worse, which will generally increase the uncertainty of the estimated parameters and the correlation between them. As seen in Tables 2 and 3, the WRMS values from the Ru-U sessions are higher than for the INT1 and the INT2/3 sessions, although this is also partly due to much shorter baselines being observed in the Ru-U sessions.

External tropospheric gradients from ECMWF or GNSS improve the results in some cases, but not always. Probably the accuracy of the external gradients varies from station to station; thus, whether or not the results are improved by external gradients depends on which stations are included in the Intensive sessions. Good quality of the external information is particularly important if also the ZWD are fixed to a priori values. In principle, because this reduces the number of unknown parameters, it should improve the precision. However, if there are systematic errors in the external ZWD values, the errors in the UT1–UTC estimates will increase. This is clearly the case for the INT2/3 sessions when fixing the tropospheric parameters taken from the IGS (Table 3).

Improving the tropospheric modeling by estimating more tropospheric parameters can improve the results. However, it is then important that the geometrical distribution of the observations be good enough to allow a separation of the different estimated parameters in the data analysis. This seems to be a problem when applying the turbulence model for the Ru-U sessions, while for INT1 and INT2/3 this strategy works well. For all session types the estimation of gradients in the data analysis gives satisfactory results. Thus, it is recommended that this strategy should be used when analyzing the Intensive sessions.

Acknowledgements

We would like to thank The International VLBI Service for Geodesy and Astrometry (IVS) [8] for providing the VLBI data used in this work.

References

1. J. Böhm, S. Böhm, T. Nilsson, A. Pany, L. Plank, H. Spicakova, K. Teke, and H. Schuh. The new Vienna VLBI software. In S. Kenyon, M. C. Pacino, and U. Marti, editors, *IAG Scientific Assembly 2009*, number 136 in International Association of Geodesy Symposia, pages 1007–1011, Buenos Aires, Argentina, 2012. Springer. doi:10.1007/978-3-642-20338-1_126.
2. J. Böhm, T. Nilsson, and H. Schuh. Prospects for UT1 measurements from Intensive sessions. In D. Behrend and K. D. Baver, editors, *Proc. 6th IVS General Meeting*, pages 251–255, Hobart, Tasmania, Australia, 2010. Available from: http://ivscc.gsfc.nasa.gov/publications/gm2010/boehm.pdf.
3. J. Böhm and H. Schuh. Tropospheric gradients from the ECMWF in VLBI analysis. *J. Geodesy*, 81(6-8):409–421, 2007. doi:10.1007/s00190-006-0126-9.

4. S. H. Byun and Y. E. Bar-Sever. A new type of troposphere zenith path delay product of the international GNSS service. *Geodesy*, 83(3-4):1–7, 2009. doi:10.1007/s00190-008-0288-8.
5. D. S. MacMillan and C. Ma. Atmospheric gradients and the VLBI terrestrial and celestial reference frames. *Geophys. Res. Lett.*, 24(4):453–456, 1997. doi:10.1029/97GL00143.
6. T. Nilsson, J. Böhm, and H. Schuh. Universal time from VLBI single-baseline observations during CONT08. *J. Geodesy*, 85(7):415–423, 2011. doi:10.1007/s00190-010-0436-9.
7. T. Nilsson and R. Haas. Impact of atmospheric turbulence on geodetic very long baseline interferometry. *J. Geophys. Res.*, 115:B03407, 2010. doi:10.1029/2009JB006579.
8. H. Schuh and D. Behrend. VLBI: A fascinating technique for geodesy and astrometry. *J. Geodyn.*, 61:68–80, 2012. doi:10.1016/j.jog.2012.07.007.
9. R. N. Treuhaft and G. E. Lanyi. The effect of the dynamic wet troposphere on radio interferometric measurements. *Radio Sci.*, 22(2):251–265, 1987. doi:10.1029/RS022i002p00251.

A New Empirical Ocean Tide Model for Improved High-Frequency Earth Rotation Variations

Matthias Madzak[1], Sigrid Böhm[1], Johannes Böhm[1], Wolfgang Bosch[2], Jan Hagedoorn[3], Harald Schuh[3,4]

Abstract We seek to improve the current model for high-frequency Earth rotation variations induced by ocean tides. For empirical models, we derive oceanic currents, which are required for the ocean tidal angular momentum. We use the hydrodynamic FES2012 to derive a preliminary test model and analyze the CONT11 campaign to compare it to the IERS recommended model. We find an improvement for yp at the semi-diurnal frequencies. The xp component agrees to a level of about 10 μas, those from UT1–UTC to a level of about three μas.

Keywords Earth rotation, ocean tides, VLBI analysis, project SPOT

1 Introduction

Accurate a priori models are essential for Very Long Baseline Interferometry (VLBI) analysis to derive precise geodetic parameters. In particular orbit prediction for Global Navigation Satellite Systems (GNSS) requires a model for the effect of ocean tides on Earth rotation in the diurnal and sub-diurnal band. The recommended prediction model of this effect is described in the IERS Conventions 2010, Chapter 8 [1].

However, there are significant differences between the model prediction values and the estimated parameters for polar motion and UT1–UTC. Figure 1 shows those differences for UT1–UTC in the frequency domain. The large peaks coincide with the frequencies of the major ocean tides, for example O1 and S1 in the diurnal band and M2 and K2 in the semi-diurnal band.

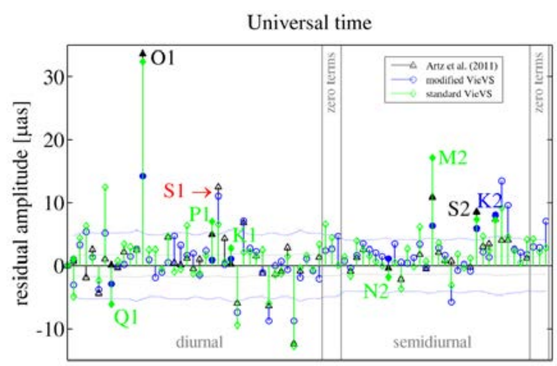

Fig. 1 Spectrum: Residuals of model values and estimated UT1–UTC from VLBI analysis.

The Project SPOT, supported by the Austrian Science Fund (FWF), deals with this issue and seeks to close the gap between model predictions and observations. We develop a new model for high frequency Earth rotation parameter (ERP) variations induced by ocean tides. This could be one step further to meet the GGOS requirements regarding the accuracy of geodetic results (Plag and Pearlman, 2009 [2]).

2 Ocean Tide Models

When using ocean tide models for the calculation of ocean tidal angular momentum (OTAM), there are basically two types of models available. Empirical models, derived solely from satellite altimetry data, include

1. Vienna University of Technology, Austria
2. German Geodetic Research Institute (DGFI), Germany
3. Berlin University of Technology, Germany
4. GeoForschungszentrum Potsdam, Germany

only tidal heights of the ocean surface. Hydrodynamic models, on the other hand, also contain oceanic currents, which are required for the motion term of the angular momentum.

Ocean tide models usually include eight major tides: Q1, O1, P1, and K1 in the diurnal band and N2, M2, S2, and K2 in the semi-diurnal band. Due to the long time span of satellite altimetry observations, it is nowadays possible to estimate further tides in the tidal analysis. The new FES2012 for example includes a total of 27 semi-diurnal and diurnal constituents.

Spatial resolutions of current ocean tide models are 0.125° or even smaller.

3 Worksteps

The workflow to derive a new high-frequency ERP model is shown in Figure 2.

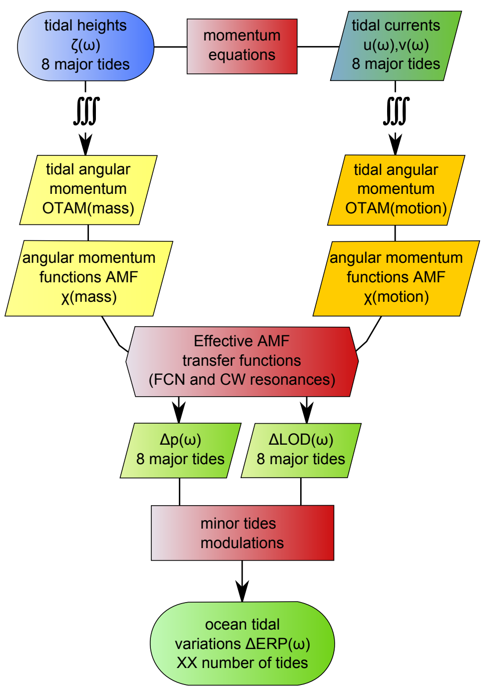

Fig. 2 Workflow of Project SPOT.

The first major task is to derive oceanic currents from tidal heights when an empirical model is used. More details about hydrodynamic equations can be found in Section 4. After numerical integration, we derive ocean tidal angular momentum, both for mass and motion terms.

Time-varying and frequency-dependent OTAM can be converted to ERP using effective angular momentum functions (e.g., Gross, 1993 [3]), which account for Free-Core-nutation and Chandler-wobble resonances.

If minor tides are not included in the ocean tide model, they have to be accounted for during the ERP model derivation using nodal corrections and admittance functions. Lunar tides are affected by the lunar node cycle (18.6 years), which requires amplitude and phase corrections of those tidal constituents [4]. Minor tides can be interpolated using admittance functions: according to Munk and Cartwright (1966) [5], the ratio of the tide generating potential and the tidal height is assumed to be a slowly varying function of frequency. Hence, minor tides can be interpolated from major tides if the tide generating potential is known, e.g., from the Hartmann and Wenzel (1995) tidal potential catalog.

4 Hydrodynamics

The shallow water equations (linearized, simplified, and depth-averaged Navier-Stokes equations) describe the hydrodynamic flow of the ocean. The momentum and continuity equations read (Ray, 2001 [6])

$$\frac{\partial \mathbf{u}}{\partial t} + \mathbf{f} \times \mathbf{u} = -g\nabla(\zeta - \zeta_E - \zeta_s) - \frac{\mathbf{F}}{\rho D}$$

$$\frac{\partial \zeta}{\partial t} = -\nabla \cdot D\mathbf{u},$$

where u is the horizontal velocity vector, f is the Coriolis parameter, g is gravity acceleration, ζ is tidal height, ζ_E is the equilibrium tide, ζ_S is a term accounting for self-attraction and Earth loading, F is bottom friction force, ρ is density, and D is ocean depth.

The parameters, namely horizontal, barotropic tidal oceanic volume transports (velocity multiplied by depth) can be estimated in a least-squares algorithm. Due to the large number of equations, an iterative least-squares solver is advantageous.

Tests of this algorithm were performed using the model HAMTIDE11a, a hydrodynamic model containing (1) tidal heights from which to calculate ocean ve-

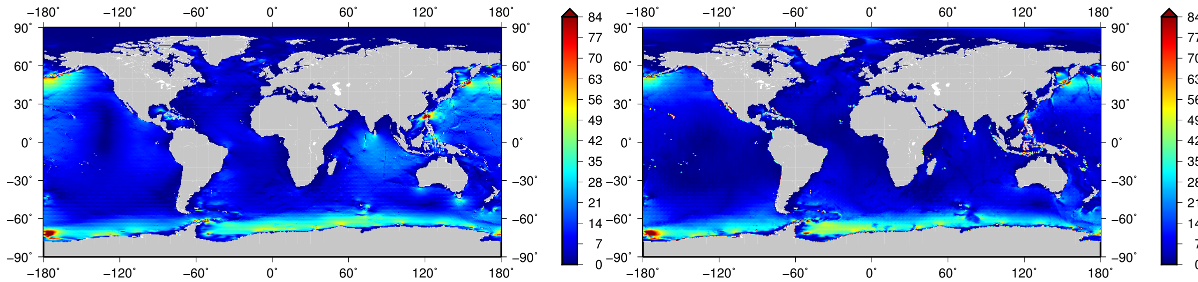

Fig. 3 Volume transport amplitudes (m^2/s) in East direction. Left: Model HAMTIDE11a, right: Estimated from HAMTIDE11a heights using shallow water equations.

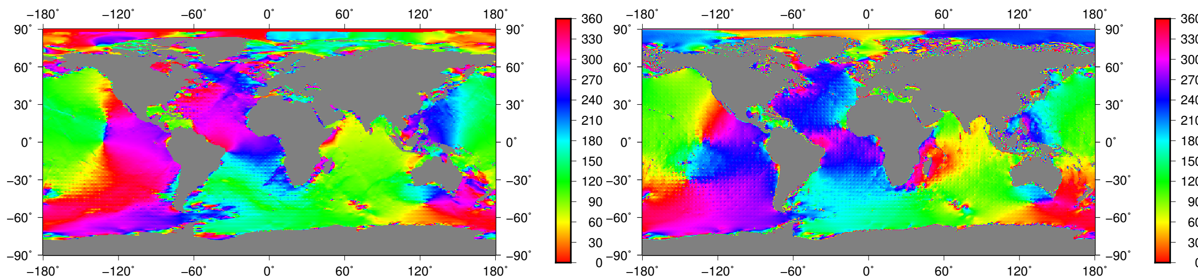

Fig. 4 Volume transport phases (°) in East direction. Left: Model HAMTIDE11a, right: Estimated from HAMTIDE11a heights using shallow water equations.

locities and (2) tidal velocities to perform a validation of the estimated results.

Figure 3 shows model values and estimated volume transport amplitudes for the East component.

A similar global pattern can be recognized; differences occur mostly in coastal regions, where no-flow boundaries are used. As expected, the phase (Figure 4) shows larger differences. Likewise the semi-diurnal tides seem to be less accurately estimated.

One possible explanation for problems at different frequencies is the simple friction term in the shallow water equations: $F = r^* \rho u$, where r^* is a friction coefficient. Although there is no physical reason for a frequency-dependent friction coefficient, the simple form of F could absorb other physical mechanisms. Hence, different r^* values for different frequencies might lead to better results.

One possibility of finding the "best" r^* values for each tide is to calculate these coefficients from hydrodynamic model values of tidal heights and currents.

Figure 5 shows the estimated friction parameter values for eight major tides for the models FES2012 and HAMTIDE11a. The diurnal tides seem to have significantly smaller r^* values than the semi-diurnal tides. However, more research needs to be done in this regard; the results shown in Figures 3 and 4 comprise constant r^* coefficients for all tides.

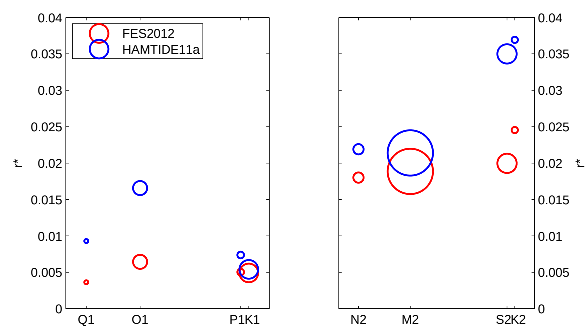

Fig. 5 Estimated friction parameter r^* from hydrodynamic models. The circles are scaled by the tide generating potential of the particular tide.

5 Angular Momentum

Time-varying ocean tidal angular momentum functions are derived for three models. They are summarized in Table 1. The OTAM values of four major constituents are given in Table 2. The mass terms (height component) agree very well between the two hydrodynamic models (Model A and Model B). The motion terms (current component) are still in good agreement between Model A and Model B. However, Model C shows large differences, especially in phase. It should be noted that diurnal tides show smaller discrepancies than semi-diurnal tides.

Our currents estimated from the shallow water equations are not yet accurate enough to derive an improved ERP model.

Table 1 Overview of models used for the derivation of ocean tidal angular momentum.

Model	Mass term	Motion term
A	FES2012	FES2012
B	HAMTIDE11a	HAMTIDE11a
C	HAMTIDE11a	Estimated*

* *Estimated from HAMTIDE11a heights*

6 Test Model

Using a hydrodynamic model—and thus not having to calculate oceanic currents—we derive a preliminary test model. We use the FES2012 ocean tide model including a total of 27 tides: six diurnal tides, 13 semi-diurnal tides, and eight tides with even higher frequencies (from one-third to one-eighth of a day). As a numerical integration method, we use Simpson cubature. To convert OTAM to Earth rotation variations, we use the equations and values from Gross (1993) [3].

7 Validation

To validate the test model versus the IERS Conventions 2010 model, we analyze VLBI data from the CONT11 campaign—a 15-day continuous VLBI experiment in September 2011.

In a prior step, we estimate nutation offsets for the time period of CONT11. This is needed, because in the normal parameterization we cannot estimate high-frequency ERP and nutation offsets at the same time. Those nutation offsets dX and dY are used as a priori nutation model for all further processing.

All CONT11 sessions were analyzed using (1) the test model and (2) the IERS Conventions 2010 model for a priori high-frequency ERP values. For the post-fit residuals of all three ERP, namely xp, yp and UT1–UTC, a discrete Fourier transform is calculated. The amplitude spectra were subtracted ("IERS minus test model"), and those spectrum differences allow a validation of the test model: small residuals show a better agreement between observations and the model, and they also yield smaller Fourier coefficients. Because of the order of subtraction ("IERS minus test model"), positive values in the Fourier coefficient differences show a better agreement between the test model and the observations than the IERS model and the observations. Figures 6, 7, and 8 show the Fourier spectrum differences.

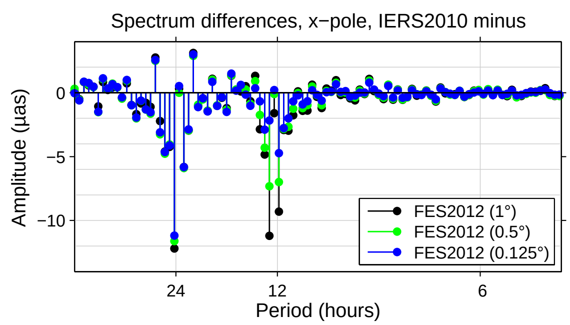

Fig. 6 Fourier spectrum differences between the IERS Conventions 2010 and the test model of the x-pole residuals.

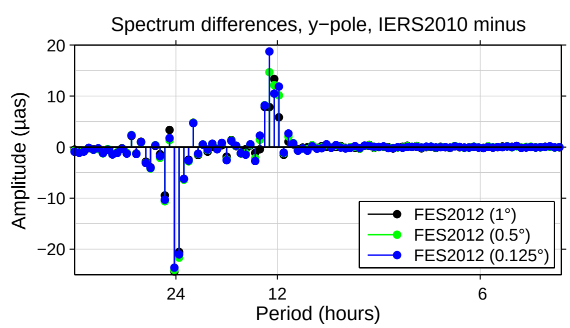

Fig. 7 Fourier spectrum differences between the IERS Conventions 2010 and the test model of the y-pole residuals.

The only improvement compared to the IERS Conventions 2010 model can be seen for yp at the semi-diurnal frequencies (12-hour period). The semi-diurnal band for xp and UT1–UTC is of similar accuracy as the IERS model, or slightly worse. Less accurate re-

Table 2 Ocean tidal angular momentum for three models and four major tides. Amplitudes in 10^{25} kg m^2/s, phases in degrees.

Tide		Model A				Model B				Model C			
		Heights		Currents		Heights		Currents		Heights		Currents	
	x	0.5	−52°	0.6	−71°	0.4	−54°	0.6	−76°	0.4	−54°	0.3	−175°
K1	y	1.4	−136°	0.8	−168°	1.3	−137°	0.8	−172°	1.3	−137°	0.7	178°
	z	0.2	1°	0.8	128°	0.2	34°	0.7	131°	0.2	34°	0.3	110°
		0.5	−30°	0.3	−60°	0.5	−31°	0.3	−60°	0.5	−31°	0.2	133°
O1		1.2	−138°	0.4	−154°	1.1	−139°	0.4	−155°	1.1	−139°	0.2	177°
		0.2	171°	0.7	115°	0.2	154°	0.5	119°	0.2	154°	0.3	127°
		0.1	39°	0.6	−61°	0.1	40°	0.6	−64°	0.1	40°	0.2	89°
S2		0.3	9°	1.0	−162°	0.3	8°	1.0	−159°	0.3	8°	0.0	−31°
		0.2	132°	0.8	−13°	0.2	132°	0.8	−19°	0.2	132°	0.2	9°
		0.5	10°	1.0	−100°	0.5	10°	1.2	−101°	0.5	10°	0.6	37°
M2		0.3	−56°	1.8	166°	0.3	−58°	1.8	165°	0.3	−58°	0.2	−150°
		0.6	86°	1.5	−45°	0.5	89°	1.7	−41°	0.5	89°	0.6	−13°

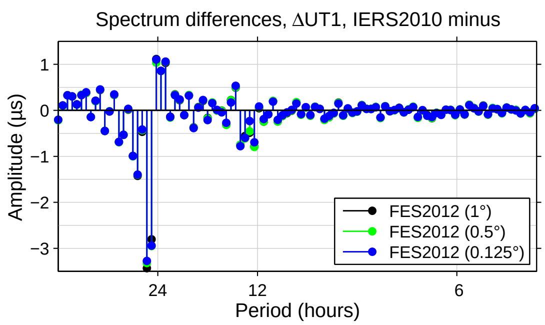

Fig. 8 Fourier spectrum differences between the IERS Conventions 2010 and the test model of the UT1–UTC residuals.

sults can be seen in the 24-hour periods. All three ERP show a better agreement between the IERS Conventions model and the observations than the test model and the observations.

The three figures (6, 7, and 8) show results for the test model in three different spatial resolutions: 1°, 0.5°, and 0.125°. An improvement for higher resolutions can be seen. For example, the values of the 12-hourly xp differences increase from about -10 μas at 1° to about -5 μas at 0.125°.

8 Conclusions

When we use an empirical ocean tide model to derive a new model for high-frequency ERP variations, we need to apply hydrodynamic equations to calculate oceanic currents. Our estimated oceanic currents are not yet accurate enough to be used in an ERP model.

If a hydrodynamic model such as FES2012 is used, results are reasonable and comparable to the IERS Conventions 2010 model. Even though there are slight punctual improvements using the test model, it is not yet possible to revise the IERS recommended model.

However, there are several possibilities, such as higher spatial resolutions of ocean tide models or the use of (more) minor tides, which may lead to improved high-frequency ERP predictions.

Acknowledgements

The authors would like to thank the Austrian Science Fund for supporting this work within Project SPOT (P24813).

References

1. G. Petit and B. Luzum (eds.). IERS Conventions (2010). (IERS Technical Note; 36) Frankfurt am Main: Verlag des Bundesamts für Kartographie und Geodäsie, 179 pp., ISBN 3-89888-989-6, 2010.
2. H.-P. Plag and M. Pearlman (eds.). Global Geodetic Observing System. 376 pp., ISBN 978-3-642-02687-4, 2009.
3. R. Gross. The effect of ocean tides on the Earth's rotation as predicted by the results of an ocean tide model. In *Geophysical research letter*, Vol. 20, No. 4, pages 293–296, 1993.
4. IHO. Harmonic constituents with Nodal Corrections. Harmonic constants, Product Specification, Edition1, 2006.
5. W. H. Munk and D. E. Cartwright. Tidal Spectroscopy and Prediction. In *Phil. Trans. R. Soc.*, Vol. 259, No. 1105, pages 533–581, 1966.
6. R. D. Ray. Inversion of oceanic tidal currents from measured elevations. In *Journal of Marine Systems*, Vol. 28, pages 1–18. 2001.

ERP Estimation using a Kalman Filter in VLBI

M. Karbon, B. Soja, T. Nilsson, R. Heinkelmann, L. Liu, C. Lu, J.A. Mora-Diaz, V. Raposo-Pulido, M. Xu, H. Schuh

Abstract Geodetic Very Long Baseline Interferometry (VLBI) is one of the primary space geodetic techniques, providing the full set of Earth Orientation Parameters (EOP), and it is unique for observing long term Universal Time (UT1). For applications such as satellite-based navigation and positioning, accurate and continuous ERP obtained in near real-time are essential. They also allow the precise tracking of interplanetary spacecraft. One of the goals of VGOS (VLBI Global Observing System) is to provide such near real-time ERP. With the launch of this next generation VLBI system, the International VLBI Service for Geodesy and Astrometry (IVS) increased its efforts not only to reach 1 mm accuracy on a global scale but also to reduce the time span between the collection of VLBI observations and the availability of the final results substantially. Project VLBI-ART contributes to these objectives by implementing an elaborate Kalman filter, which represents a perfect tool for analyzing VLBI data in quasi real-time. The goal is to implement it in the GFZ version of the Vienna VLBI Software (VieVS) as a completely automated tool, i.e., with no need for human interaction. Here we present the methodology and first results of Kalman filtered EOP from VLBI data.

Keywords VGOS, Kalman filter, EOP

Deutsches GeoForschungsZentrum Potsdam, 1.1 GPS/Galileo Earth Observation

1 Introduction

At the moment the VLBI products have a latency of about two weeks. However, as the need for near real-time estimates of the parameters is increasing, e.g., for satellite based navigation and positioning or for enabling precise tracking of interplanetary spacecraft [Ichikawa et al., 2004], the efforts to shorten the time span between observation and final results have been increased considerably. To reach these goals, the VLBI Global Observing System (VGOS; Petrachenko et al. [2009]) was proposed, where a dense network of very fast moving antennas (slewing speed $>6°$/s) is foreseen, providing a high number of observations per time unit. The aim is to reach an accuracy of 1 mm (position) and 1 mm/year (velocity) from a global solution of 24-hour sessions, and near real-time operation with the help of electronic data transfer to the correlators. In order to retrieve the analysis results in near real-time, a solution algorithm applying completely automated processes is also required. One way to achieve these goals is by implementing an adaptive Kalman filter in place of the classical least-squares method (LSM) in VLBI analysis software packages. Herring et al. [1990] had proposed such an approach already in the 1990s, where the clock and atmosphere parameters are modeled as stochastic processes, which can authentically represent the geodetic parameters as well as the dynamics of the system processes. Various software packages include such a Kalman filter approach, e.g., Occam [Titov et al., 2004]. However, the existing software packages implemented the Kalman filter in the form of a post-processing tool, as at that time continuous VLBI observations were utopistic and VLBI was not designed for true real-time applications. Within project VLBI-ART, a Kalman filter will be realized that is in particular designed for analyzing VLBI data in (near) real-time. This method has the advantage that simultaneously both the deterministic estimation of parameters, which usually change slowly throughout time, e.g., station positions, and the tracking of highly variable parameters showing a stochastic behavior, like clocks or atmospheric parameters, are possible. The filter is able to perform the VLBI parameter estimation without any manual interaction, making it a completely autonomous tool. In this paper we describe the filter and discuss its application for ERP determination.

2 Mathematical Principle of a Kalman Filter in VLBI

Traditional VLBI analysis software uses the least-squares method (LSM) or least-squares collocation for the estimation of the desired parameters, in which most of the parameters showing a stochastic behavior, such as clock and atmospheric disturbance, are approximated by piecewise linear functions. The length and order of these polynomials have to be chosen manually by the analyst according to session type and duration and may vary from analyst to analyst, and thus they are subjective. For this method, the observations have to be artificially bundled as they cannot handle a continuous data flow. All this hinders the efficiency of the data processing and makes a continuous data analysis almost impossible.

The Kalman filter was especially developed for real-time applications and is widely applied in various fields of research and development including the analysis of space geodetic data (cf. Herring et al. [1990]; Morabito et al. [1988]; Nilsson et al. [2011]). The advantage of such a filter over ordinary least-squares is that the estimation is carried out sequentially, epoch by epoch, by combining the observations at each time step with the estimation of the previous ones, making it ideal for real-time applications [Kalman, 1960]. Further, stochastic models replace the polynomial parameter models and thus more appropriately describe the physics behind the processes.

The Kalman filter should follow the sequence of observations, using the state at the epoch $(t-1)$ to predict the state at the next epoch t. Finally the predicted value is combined with the new information to get an optimal estimation for t. If $\mathbf{x}_t$ is the state vector containing all unknown parameters to be estimated at epoch t, it can be related to the estimates at a previous epoch $\mathbf{x}_{t-1}$ through

$$\mathbf{x}_t = \mathbf{F}_t \mathbf{x}_{t-1} + \mathbf{w}_t \ , \tag{1}$$

where $\mathbf{F}_t \mathbf{x}_{t-1}$ is the prediction of $\mathbf{x}_t$ based on $\mathbf{x}_{t-1}$ and $\mathbf{w}_t$ is the error in the prediction. $\mathbf{F}$ is called the state transition matrix. The covariance matrix of the total error $\mathbf{P}_t^-$ can be calculated by

$$\mathbf{P}_t^- = \mathbf{F}_t \mathbf{P}_{t-1} \mathbf{F}_t^T + \mathbf{Q}_t \ , \tag{2}$$

with $\mathbf{P}_{t-1}$ denoting the variance-covariance matrix of $\mathbf{x}_{t-1}$ and $\mathbf{Q}_t$ the variance-covariance matrix of the prediction error $\mathbf{w}_t$. The observations $\mathbf{z}_t$ at epoch t are introduced through

$$\mathbf{z}_t = \mathbf{H}_t \mathbf{x}_t + \mathbf{v}_t \ . \tag{3}$$

$\mathbf{H}_t$ is the observation matrix and $\mathbf{v}_t$ is the observation noise. To get the optimal estimation for $\mathbf{x}_t$ and its covariance matrix $\mathbf{P}_t$ the prediction $\mathbf{x}_t^-$ and the observation $\mathbf{z}_t$ can be combined using

$$\mathbf{x}_t = \mathbf{x}_t^- + \mathbf{K}_t (\mathbf{z}_t - \mathbf{H} x_t^-) \ , \mathbf{P}_t = (\mathbf{I} - \mathbf{K}_t \mathbf{H}_t) \mathbf{P}_t^- \ , \tag{4}$$

with the Kalman gain $\mathbf{K}_t$

$$\mathbf{K}_t = \mathbf{P}_t^- \mathbf{H}_t^T (\mathbf{H}_t \mathbf{P}_t^- \mathbf{H}_t^T + \mathbf{R}_t)^{-1} \ , \tag{5}$$

where $\mathbf{R}_t$ is the variance-covariance matrix of the observation noise $\mathbf{v}_t$.

In our filter the state transition matrix $\mathbf{F}$ is realized as a unit matrix with the dimensions $[n \times n]$ with n being the number of unknowns. Since all the deterministic models are already applied within VieVS [Böhm et al., 2012], only the stochastic processes are left to be modeled. Exceptions are the clock parameters, where the relationship between offset and rate is described through a parameter of the primary diagonal. The noise parameters for the process noise covariance matrix $\mathbf{Q}$ are taken from literature (e.g., [Herring et al., 1990]). For the clock, these noise parameters were determined empirically. The observation matrix $\mathbf{H}$ consists of the partial derivatives of the delay w.r.t. the unknowns. For most cases these are identical to the ones used in the LSM approach.

3 First Results

Here first results of session 08JUN19XE_N004 are shown. We chose this session as it represents an average state-of-the-art IVS VLBI session and falls into the time span where ERPs from GPS [Steigenberger et al., 2006] are available to us. It involved seven antennas and contains 1,576 observations within 596 scans over 24 hours. The filter was set up to estimate x- and y-pole, dUT1, station coordinates, and zenith wet delays for all stations, as well as clock and clock rate for all stations except the reference clock. Here, only the results for polar motion and dUT1 are shown (Figure 1).

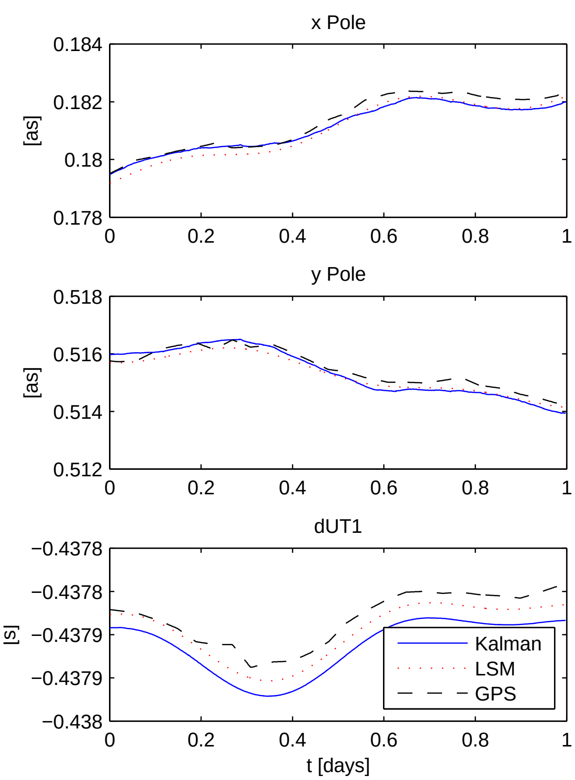

Fig. 1 The upper plot shows x-pole, the middle shows y-pole, and the lower shows dUT1. The solid graph depicts the results for the Kalman filter, the dotted line shows the results for the LSM solution, and the dashed line shows the GPS parameters.

Although the noise parameters were chosen independently of the LSM solution, i.e., no tuning towards the LSM solution was performed, the results show a very good agreement. The adjustments to the IERS 08 C04 [Bizouard et al., 2009] a priori of dUT1 differ at the microsecond level. See Table 1 for RMS values of the various approaches. For an external validation, an ERP time series derived from GPS was used. Because not all the models involved in the determination are known, only the final ERP series can be compared. In spite of biases, the agreement is good, although the differences in general are larger in comparison to the LSM solution. For y-pole the Kalman solution agrees slightly better with the GPS results. Further investigations are needed and other sessions have to be chosen to verify these results, as also the GPS time series show some small unexpected peaks (see Figure 1).

Table 1 RMS of the three solutions, i.e., Kalman (KAL) and LSM in comparison to the GPS time series.

	RMS KAL adjustments only	RMS (KAL–LSM) adjustments only
x-pole [μas]	0.2152	0.1834
y-pole [μas]	0.1347	0.1796
dUT1 [ms]	0.0135	0.0176
	RMS (LSM–GPS) a priori included	**RMS (KAL–GPS) a priori included**
x-pole [mas]	0.2778	0.3235
y-pole [mas]	0.2187	0.1488
dUT1 [ms]	0.0154	0.0325

4 Current Status and Outlook

A first version of the Kalman filter was implemented and is now in the debugging phase. We showed preliminary results for the ERP and compared them to the classical LSM, and we found a very good agreement. The comparison of Kalman filter with GPS also shows a good agreement between the results. All results are still under investigation and validation, as well as the GPS time series itself, as it shows some unexpected peaks. Further, the clock models will be improved, so that clock breaks are automatically detected. This is the first step towards full automation. Later the filter will be extended to other parameters such as source coordinates or station velocities. The improvement of the system dynamics and the fine tuning of the process noise as well as the refinement of the deterministic and stochastic models are ongoing as well. We plan to have the filter fully operational for the analysis of the CONT14 campaign.

References

C. Bizouard, and D. Gambis. The combined solution C04 for Earth Orientation Parameters consistent with International Terrestrial Reference Frame 2008. *Geodetic reference frames*, Springer Berlin Heidelberg, 265–270, 2009.

J. Böhm, S. Böhm, T. Nilsson, A. Pany, L. Plank, H. Spicakova, K. Teke, and H. Schuh. The new Vienna VLBI software. In: S. Kenyon, M. C. Pacino, and U. Marti (eds.), *IAG Scientific Assembly 2009*, 1007–1011, 2012.

T. A. Herring, J. L. Davis, and I. I. Shapiro. Geodesy by radio interferometry: The application of Kalman filtering to the analysis of Very Long Baseline Interferometry data. *J. Geophys. Res.* , 95(B8): 12, 561–581, 1990.

R. Ichikawa, M. Sekido, H. Ohsaki, Y. Koyama, T. Kondo, T. Ohnishi, M. Yoshikawa, W. Cannon, A. Novikov, M. Bérubé and NOZOMI DVLBI Group, An Evaluation of VLBI Observations for the Deep Space Tracking of the Interplanetary Spacecrafts. In: N. R. Vandenberg and K. D. Baver (eds.), *International VLBI Service for Geodesy and Astrometry 2004 General Meeting Proceedings*, NASA/CP-2004-212255, 253–257, 2004.

R. E. Kalman. A new approach to linear filtering and prediction problems. *J. Basic Eng.*, 82D: 35–45, 1960.

D. D. Morabito, T. M. Eubanks, and J. A. Steppe Kalman filtering of earth orientation changes. In: A. Babecock and G. A. Wilkins (eds.), *The Earths rotation and reference frames for geodesy and geodynamics*, 257–267, Dordrecht, Holland, 1988.

T. Nilsson and L. Gradinarsky. Water vapor tomography using GPS phase observations: Simulaton results. *IEEE Trans. Geosci. Remote Sensing*, 44(10): 2927–2941, 2006. doi:10.1109/TGRS.2006.877755.

B. Petrachenko, A. Niell, D. Behrend, B. Corey, J. Böhm, P. Charlot, A. Collioud, J. Gipson, R. Haas, T. Hobiger, Y. Koyama, D. MacMillan, Z. Malkin, T. Nilsson, A. Pany, G. Tuccari, A. Whitney, and J. Wresnik. Design Aspects of the VLBI2010 System. In: D. Behrend and K. Baver (eds.), *International VLBI Service for Geodesy and Astrometry 2008 Annual Report*, NASA/TP-2009-214183, 13–67, 2009.

P. Steigenberger, M. Rothacher, R. Dietrich, M. Fritsche, A. Rülke, and S. Vey. Reprocessing of a global GPS network. *J. Geophys. Res.*, 111, B05402, 2006, doi:10.1029/2005JB003747.

O. Titov, V. Tesmer, and J. Böhm. OCCAM v. 6.0 Software for VLBI Data Analysis. In: N. R. Vandenberg and K. D. Baver (eds.), *International VLBI Service for Geodesy and Astrometry 2004 General Meeting Proceedings*, 267-271, NASA/CP-2004-212255, 2004.

Analysis of Error Sources of Very Long Baseline Interferometry in Deep Space Exploration

Jia Wang[1,2], Gongyou Wu[1,2], Dong Zhang[1,2], Ke Xu[1,2], Xiaojuan Ou[1,2]

Abstract The Very Long Baseline Inteferometry (VLBI) technique is currently one of the hottest research topics in the domain of deep space exploration. Aiming at exploring whether error items are sufficient and finding out their impact on the VLBI delay and delay rate, the paper analyzes the error sources of VLBI in deep space exploration and teases out the major error items in different observation modes. The conclusion is very important to advancing the precision of VLBI data processing and provides technique support for the construction of the VLBI system.

Keywords Deep space exploration, Very Long Baseline Interferometry, error sources, geometric delay

1 Introduction

Deep space exploration is a new domain in space technique after satellite and manned space applications. The first step is lunar exploration, and then, we will explore Mars and farther space. Deep space exploration, especially lunar exploration, has a higher demand on the precision and real-time performance of the orbit measurement, which guarantees that the lunar Lander landed at its destination accurately and that its return equipment is returned to earth in its scheduled orbit. To master the high precision measurement of the deep space explorer orbit will support and promote the advancement of high tech and quicken up the development of deep space exploration science in our country.

Very Long Baseline Interferometry (VLBI) is one of a finite list of methods which can be depended upon in deep space exploration. VLBI has been widely used in the fields of astrophysical radio astronomy and mother earth survey since its inception in 1965 [1]. Furthermore, VLBI has been widely used in tracking and navigation of satellites, lunar explorers, and even interplanetary explorers from the 1970s because of its high precision ability of measuring angles. It is the prerequisite for precise orbit determination in deep space explorer to investigate error sources and analyze their impact on the orbit determination precision correctly, because the main factor of credibility and effect is all sorts of errors of measuring equipment in the course of measurement [2, 8]. The paper aims at error sources of VLBI and analyzes its correct model.

2 VLBI Observation Modes in Deep Space Exploration

In Differential One-way Ranging (DOR) and Differential One-way Doppler (DOD) in aerospace engineering, the measurement elements of the deep space VLBI system are differential one-way ranges and their rates. For eliminating time synchronization and station site, ionosphere and troposphere errors, the project of time-sharing work, ranking observations of deep space spacecraft and quasars, and subtracting corresponding common errors has been adopted, which is called Delta Differential One-way Ranging (Delta-DOR) and Delta Differential One-way Doppler (Delta-DOD). Furthermore, it is called Same-Beam Interferometry (SBI), which is designed for measuring

1. China State Key Laboratory of Astronautic Dynamics
2. China Xi'an Satellite Control Center

the relative positions of two spacecraft in the same beam.

2.1 Differential One-way Ranging and Differential One-way Doppler

In DOR/DOD observation, the steps include two stations pointing to the same target, a data collection system for collecting data, and recording it onto disks after formatting. After observation, the steps include giving data to the data processing center, decoding, and correlating processing to get a measurement outcome, which is the delay difference and its rate for a spacecraft signal arriving at two stations.

2.2 Delta Differential One-way Ranging, Delta Differential One-way Doppler

In Delta-DOR and Delta-DOD observations, the steps include a) two stations pointing to a quasar near a spacecraft, collecting signals and recording data, making DOR/DOD to get delay difference and delay difference rate values for a quasar signal arriving at two stations, then b) two stations pointing to a spacecraft, collecting signals and recording data, making DOR/DOD to get delay difference and delay difference rate of the spacecraft signal arriving at two stations, and c) subtracting quasar's outcome to get final result.

2.3 Same-Beam Interferometry

In SBI observation, the steps include antennas simultaneously tracking two spacecraft which are in the same beam, making DOR and DOD measurements, and subtracting to get difference results, which contain the relative angle position and its rate.

3 Non-geometric Delay

The delay and delay rate are the primary observation elements in VLBI. But the geometric delay precision is influenced by several factors, such as observation station, target, reference frame, and so on. Moreover, additive delays which are affected by transmission have been included in factual observation. In other words, the error sources that influence the geometric delay can be divided into three kinds approximately. The first is systematic errors which can be treated as constant, such as clock bias. The second relates to measurement target orientation which can be described as a model, such as tropospheric delay, ionospheric delay, and antenna axis offset. The third belongs to random distribution which can be expressed as a random function, such as observation noise. The influence of the above error sources on the geometric delay is a non-geometric delay, which is the sum of systematic errors and random errors in observations, including clock bias, tropospheric delay, ionospheric delay, antenna axis offset and noise. It is described as Equation (1).

$$\tau_{err} = \tau_{tropo12} + \tau_{iono12} + \tau_{axis12} + Cl + R(n) \qquad (1)$$

$\tau_{tropo12}$ is tropospheric delay of station No.1 to No.2, τ_{iono12} is ionospheric delay of station No.1 to No.2, τ_{axis12} is antenna axis offset of station No.1 to No.2, Cl is clock bias of station No.1 to No.2, described as constant, R(n) is noise of station No.1 to No.2, described as random function.

4 Analysis of Error Sources

4.1 Tropospheric Delay

Neutral atmosphere refraction delay is the primary error in deep space exploration, especially in the low elevation observation because of the complexity of the atmosphere model space-time transformation and the non-integral character of the atmosphere refraction integral function [3]. The impact on the signal delay of the neutral atmosphere includes a dry and a wet part [4].

4.1.1 Tropospheric Delay Correction Model

As a commonly used software system in VLBI data processing, CALC makes use of Marini continued fraction at a given latitude to interpolate the Marini continued fraction to the observing station's latitude, then gets the Niell dry and wet mapping function.

$$m_{d,w} = \frac{1 + a/(1 + b/(1 + c))}{\sin E/a + (\sin E + b/(\sin E + c))} \qquad (2)$$

Firstly, the height of the station above the geoid, the latitude of the station, the pressure and rate of change of pressure are used to calculate the zenith delay for the "hydrostatic" component of the atmosphere using Saastamoinen formula and constants.

$$F = 1 - 0.00266 \cdot \cos(2l_{sta}) - 0.0028 \cdot \frac{h_{sta}}{1000.0} \qquad (3)$$

$$Z_d = 0.0022768 \cdot \frac{P}{F} \qquad (4)$$

Secondly, the relative humidity, temperature, and time derivative of relative humidity and temperature are used to calculate the zenith delay due to the "wet" (non-hydrostatic) component of the atmosphere using Saastamoinen [1] formula.

$$Z_w = 0.002277 \cdot (\frac{1255.0}{T} + 0.05) \cdot RH \cdot P_{sta} \qquad (5)$$

Finally, the contributions to the delay and rate due to tropospheric refraction at each observation site are computed.

$$\tau_{tropo} = m_d \cdot Z_d + m_w \cdot Z_w \qquad (6)$$

We make use of two deep space stations' weather data for parameter pick-up, zenith delay computing, and polynomial fitting. Figure 1 shows two deep stations' tropospheric zenith delay and fit. Figure 2 shows the ESA Cebreros station's tropospheric zenith delay and its fit. It is easy to conclude that three stations' dry and wet zenith delays have the same trends in Figure 1 and Figure 2. Compared to Figure 2, there is less measurement data in Figure 1. So in later work, we should make use of deep space stations' long period measurement data (Figure 3) to fit a high order polynomial in order to correct measurement errors in orbit determination software.

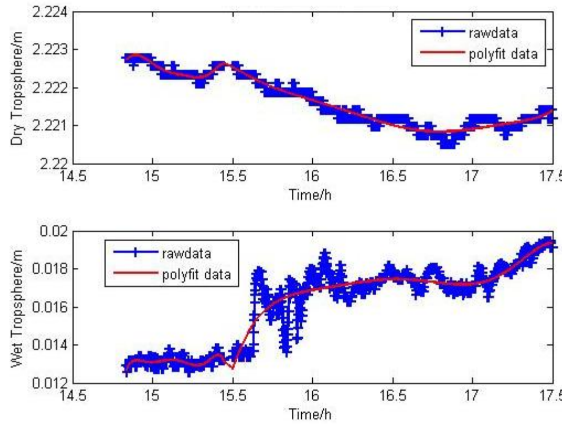

Fig. 1 Measurement data and polynomial fit results of short-term troposphere zenith.

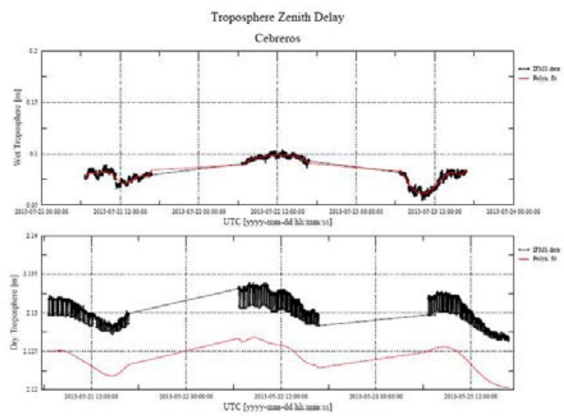

Fig. 2 Measure datum and polynomial outcome of troposphere zenith delay for the station of Cebreros.

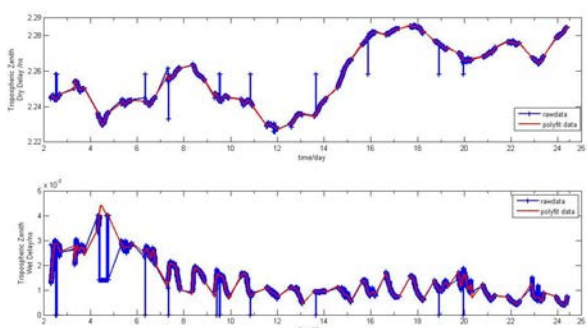

Fig. 3 Measure datum and polynomial outcome of long-term troposphere zenith delay.

4.1.2 Microwave Vapor Radiometer Measurement Model

The models mentioned above for the dry part are good, but the wet part is not easy to model. This is because the dry ingredients' mapping function model error is small, and it is easy to set up the south-north gradient model, while the atmospheric wet part is not easy to model, and in time, space distribution is extremely unstable and is not about the horizontal isotropic. In order to correct the wet component, the ground meteorological measurement alone is not enough. It is also necessary to estimate the influence of water vapor in data analysis. In order to obtain high accuracy results, microwave water vapor measurements must be used. The microwave water vapor radiometer principle is measuring in any direction the sky brightness temperature and establishing the relationship between the sky brightness temperature and the propagation path of growth, to realize the measurement of water vapor content.

4.2 Ionospheric Delay

Ionospheric delay is another error source in deep space VLBI observations. It can be measured in real time and corrected if a dual-frequency technique is adopted. But if dual-frequency observing is not guaranteed, an ionosphere correction model should be adopted.

4.2.1 Dual Frequency Ionospheric Delay Correction Model

According to ionosphere refractive index and transmission theory of carrier wave spreading, we can get a formula for carrier wave delay in the ionosphere, which is shown as Equation (7).

$$\tau_{iono} = 40.28 \cdot \frac{N_e}{f^2 \cdot c} \tag{7}$$

We can eliminate the influence of the ionosphere on delays if a spacecraft sends a dual-frequency signal. Ionosphere delay corrections in S frequency and X frequency are shown as Equations (8) to (10).

$$\tau_S = \tau + \tau_{S_{iono}} = \tau + 40.28 \cdot \frac{N_e}{f_S^2 \cdot c} \tag{8}$$

$$\tau_X = \tau + \tau_{X_{iono}} = \tau + 40.28 \cdot \frac{N_e}{f_X^2 \cdot c} \tag{9}$$

$$\tau = \frac{f_X^2 \cdot \tau_X - f_S^2 \cdot \tau_S}{f_X^2 - f_S^2} \tag{10}$$

4.2.2 Ionosphere Correction Model

Without dual-frequency observing, the Bent model, VTEC model, IRI model, Klobuchar model, and GIM/CODE model are in common use [5]. Because the influence of the ionosphere at night is smaller than in the day time, it is suggested that VLBI observing be carried out at night. Figure 4 shows the ionospheric delay graph of the deep space station in CE03.

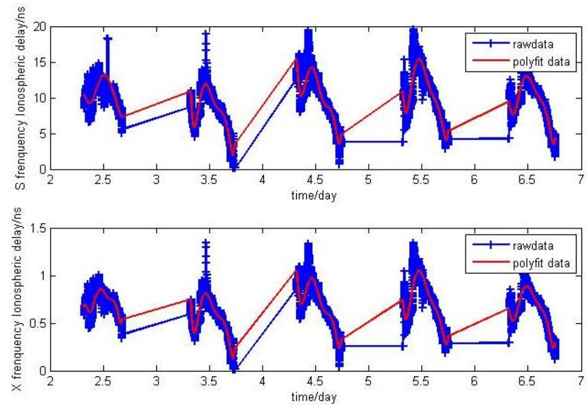

Fig. 4 Measure datum and polynomial outcome of S/X frequency ionospheric delay.

4.3 Clock Bias

The observation precision of VLBI relies on the precision of time and frequency which is used in the observation and recording. For the synchronization error of two stations' clocks and the change in clock stability, the clock bias must be corrected [6]. A linear model describing a station's clock bias is often adopted, which means that the clock has a constant offset at the start time of observation and a constant rate of change during the whole observing session.

4.4 Antenna Axis Offset

Antenna structure refers to the additional geometry delay caused by two disjoint antenna axes. This influence can be explained by the antenna pointing in the direction of tropospheric refraction of slight disturbance.

Modeling can be used to modify the antenna phase center deviation and error analysis [7] for the basis of orbit determination.

5 Conclusion

The paper comes up with theoretical formulas for the non-geometric delay, which impact on geometry delay by analyzing error components in the different observation modes. Moreover, it analyzes central error sources and establishes tropospheric delay, ionospheric delay, and antenna axis offset error models and gives its conditions of use and extension. All of the above provide a base for error analysis for later precision analysis of VLBI in deep space exploration and have an important value in advancing data processing precision and separating error items. In addition, as the important error sources, clock bias, and atmospheric effect modeling have significant meaning in improving the precision of parameter computation. Although the paper gives some correct steps and means, what was just described is the delay's main part but not the whole. Furthermore, we must pay more attention to the residual error in later research.

References

1. Saastamoinen, J: *The use of Artificial Satellite for Geodesy*, Geophys. Monograph Service, vol. 15, ed. by S.W.Henriksen et al, AGU, Wash, D.C., pp. 247–251,1972
2. Wang Guangli: *Research on the Application of VLBI to Reference Frame and Constituting and Modern Crustal Motion Surveying*, Shanghai: Shanghai Astronomical Observatory, 1999
3. Wang Jing: *A Sort of Realization Blue Print of Spacecraft Differential VLBI Surveying*, Shanghai: Shanghai Astronomical Observatory, 2007
4. Wei Erhu, Li Guan, Liu Jingnan, et al: *Analysis and Research of Tropospheric Delay Based on VLBI Data*, Bulletin of Surveying and Mapping, 2010,56(2):1–4
5. Zhang Hanwei, Zheng Yong, Ma Gaofeng, et al: *Research Progress on the Neutral Atmospheric Refraction Delays for VLBI Correction Model of the Mapping Function*, Science of Surveying and Mapping, 2005, 28(4):22–26
6. Guo Li, Li Jinling: *On the Ionospheric Delay Correction in the Processing of Satellite VLBI Observations*, Journal of Institute of Surveying and Mapping, 2003, 22(2):91–93,96
7. Zhang Bo, Li Jinling, Wang Guangli: *On the Modeling of the Residual Effects of the Clock Behavior and the Atmosphere Effects in the Analysis of VLBI Data*, Annals of Shanghai Observatory Academic Sinica, 2002(23):40–45
8. Kong Qiaoli, Han Litao: *Error Sources of Satellite-borne GPS and Accuracy Analysis of Precise Orbit Determination*, Hydrographic Surveying and Charting, 2010, 30(3):13–15, 19
9. He You, Zhang Caisheng, Ding Jiahui, et al: *The impact of time synchronization error on passive coherent pulsed radar system*, Scientia Sinica Informationis, 2011, 41(6):749–760

A DOR Signal Correlation Processing Method

Ke Xu, Gongyou Wu, Xiaojuan Ou, Dong Zhang, Jia Wang

Abstract We research a correlation processing method suitable for the DOR signals. First, we preprocess the raw data to achieve the Doppler dynamic information of the received signal. Then we generate a signal, which has a similar frequency on board locally, and utilize the signal to do correlation processing with the raw data. The local generated signal phase model is adjusted continuously by using the Doppler dynamic information from preprocessing; it eliminates the frequency dynamic changes caused by the relative motion of the spacecraft and the earth. Finally, we processes the different channel DOR signal differential phase with Bandwidth Synthesis and calculate the final DOR delay. This method was utilized in CE3 interferometry test data correlation processing; the residual delay is relatively stable and verifies the correctness of this method.

Keywords DOR Signal, local correlation, Doppler dynamic

1 Introduction

The conventional interferometry data processing algorithm for each observation station makes integer bit delay compensation, fringe stop, Fourier transform, fraction bit delay compensation, multiply accumulation, and so on [1, 2, 3]. This method is quite practical for broadband continuous spectrum signal. The spacecraft DOR signals are point-frequency signals, which have a few MHz interval with each other. Processing the DOR signals with the conventional FX correlation method requires a very high spectral resolution to achieve a sufficient SNR and accuracy, and most of the output data are noise data, so the accuracy is relatively low [4].

2 DOR Signal Processing Algorithm

2.1 Local Correlation Algorithm

References [4] and [5] provide a complete description of the DOR signal local correlation algorithm.

Assume that the one-way light time signal from the spacecraft to Station 1 is p_1 and to Station 2 is p_2. Then the relation of the transmission times t_1 and t_2 with the reception time t is:

$$t_1 = t - p_1 \tag{1}$$

$$t_2 = t - p_2 \tag{2}$$

Assume the spacecraft DOR signal expression at transmission time to be:

$$s_i(t) = e^{j(2\pi f_i t + \Phi_{oi})}$$

,

where f_i is the DOR signal frequency, Φ_{oi} is the original phase of the DOR signals, so that the received signals to the two stations are expressed respectively:

$$s_{rec1}(t) = e^{j(2\pi f_i (t-p_1)+\Phi_{o1})} \tag{3}$$

$$s_{rec2}(t) = e^{j(2\pi f_i (t-p_2)+\Phi_{o2})} \tag{4}$$

The spacecraft transmits a radio-frequency signal, but the stations receive a baseband signal after down-

China State Key Laboratory of Astronautic Dynamics

conversion, and add the equipment phase delay and the clock delay. The two stations record actual signals that may be expressed as:

$$s_{rec1-f_i}(t) = e^{j(2\pi(f_i - f_{0i})t - 2\pi f_i p_1 + \Phi_{o1} + \Phi_{1i})} \quad (5)$$

$$s_{rec2-f_i}(t) = e^{j(2\pi(f_i - f_{0i})(t-\Delta\tau_c) - 2\pi f_i p_2 + \Phi_{o2} + \Phi_{2i})} \quad (6)$$

f_{0i} is the sky-frequency. $\Delta\tau_c$ is the clock error of two stations. Φ_{1i} and Φ_{2i} are the signal phase delays through the two stations.

The noiseless local model signals of the two stations are expressed as:

$$s_{mod1-f_i}(t) = e^{j(2\pi(f_i^m - f_{0i})t - 2\pi f_i^m p_1^m)} \quad (7)$$

$$s_{mod2-f_i}(t) = e^{j(2\pi(f_i^m - f_{0i})(t-\Delta\tau_c) - 2\pi f_i^m p_2^m)} \quad (8)$$

f_i^m is the estimated transmitting frequency of the spacecraft signal. p_1^m and p_2^m are the delay models of the received signal.

The DOR signal real frequency of Station 1 can be obtained from test data. Then the transmitting frequency of the spacecraft signal can be estimated.

The playback data of the station can be cross-correlated with the local noiseless model signal giving the two point-frequency signal correlation phase of Station 1 expressed as:

$$\varphi_{cor1}^i = 2\pi(f_i - f_i^m)t - 2\pi f_i(p_1 - p_1^m) + \varphi_{o1} + \varphi_{1i}$$

Without considering the impact of the initial phase noise introduced by phase noise and instrument, so:

$$\varphi_{cor1}^i = 2\pi(f_i - f_i^m)t - 2\pi f_i(p_1 - p_1^m)$$

Similarly, the correlation phase of the two point-frequency of the two stations can be expressed as:

$$\varphi_{cor2}^i = 2\pi(f_i - f_i^m)t - 2\pi f_i(p_2 - p_2^m)$$

The difference phase of the two stations corresponds to the transmitting frequencies f_1 and f_2 and can be expressed as:

$$\varphi_{dif}^{f_1} = 2\pi f_1(p_2 - p_1) + 2\pi f_1(p_1^m - p_2^m) \quad (9)$$

$$\varphi_{dif}^{f_2} = 2\pi f_2(p_2 - p_1) + 2\pi f_2(p_1^m - p_2^m) \quad (10)$$

Differencing Equations 9 and 10 gives the DOR delay:

$$p_2 - p_1 = \frac{\varphi_{dif}^{f_1} - \varphi_{dif}^{f_2}}{2\pi(f_1 - f_2)} - (p_1^m - p_2^m)$$

2.2 Frequency and Phase Correction Based on Polynomial Fitting

During the data processing, the residual frequency has much Doppler influence because of the error between the delay model and the real propagation delay and the error between the estimated transmitting frequency and the real transmitting frequency. To obtain the final DOR delay we have to correct the frequency and phase of the dynamic variation.

The correlation residual frequency of the actual signal and the local signal is $f_{res}(t)$ and the residual phase is $\phi_{res}(t)$. Then $f_{res}(t)$ can be expressed through an N-order polynomial fitting :

$$f_{res}(t) = \sum_{i=0}^{N} a_i \cdot t^i$$

Then the residual phase is:

$$\phi_{res}(t) = 2\pi \cdot \int f_{res}(t)dt = 2\pi \cdot \sum_{i=0}^{N} (\frac{a_i \cdot t^{i+1}}{i+1} + \phi_0)$$

,

where ϕ_0 is a constant. There are two steps to correct the local model signal based on the polynomial fitting of the residual phase:

(1) Obtain the single station residual phase correction term by fitting a polynomial to the residual frequency, and correct the phase of the local signal to let the residual frequency in several Hz after the correlation of the raw signal and the corrected local model signal.

(2) Based on Step 1, cross-correlate the results of the two raw data and local signal, extract the phase of the tone, fit a polynomial to the phase variation, and correct it in the phase model of Station 2 to make the residual frequency equal for the two stations.

3 Measured Data Processing and Analysis

We processed the Station A and B data of the CE3 mission. The measured data is in six channels, quantized in 8-bit with a bandwidth of 200 kHz. The duration is 300 s. The third channel is the main carrier signal; the first, second, fifth, and sixth channels are the DOR signal. The fourth channel is the ranging tone. The frequency spectrogram is shown in Figure 1 and Figure 2.

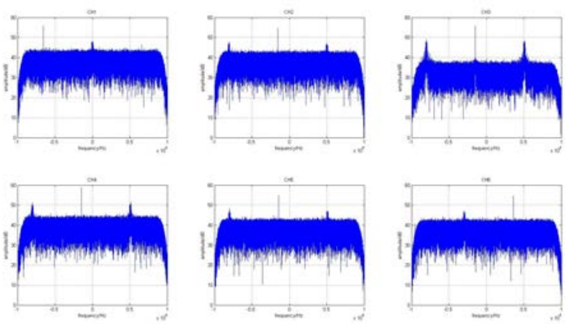

Fig. 1 Frequency spectrogram for Station A.

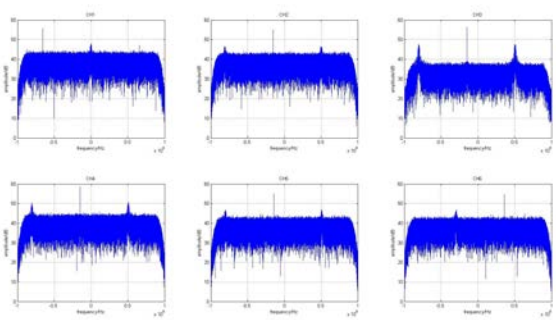

Fig. 2 Frequency spectrogram for Station B.

Cross-correlating the recorded raw data and the local model signal resulted in the DOR signal residual frequency variation shown in Figure 3. Then we fit a polynomial to the residual frequency and corrected the residual phase to the local model signal. The corrected residual frequency of each channel is shown in Figure 4.

The residual frequency variation decreases in 300 s, the maximum variation is about 1.5 Hz. The tiny fluctuation is caused by the instability of the oscillator on board. The variations of Station A and B are similar; this is consistent with the expected result. The difference residual phase of corresponding channel is shown in Figure 5. The difference residual phase variation tendency of each channel is steady and similar, the difference residual phase of 20-s accumulation is shown in Figure 6.

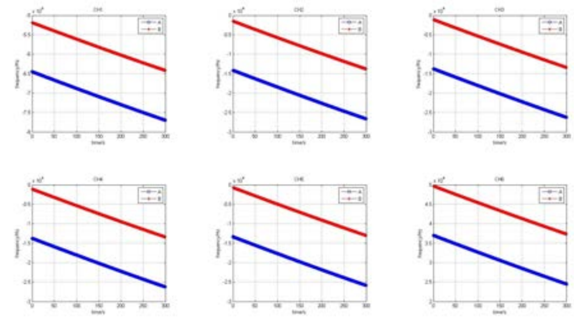

Fig. 3 Residual frequency dynamic variation of Station A and B.

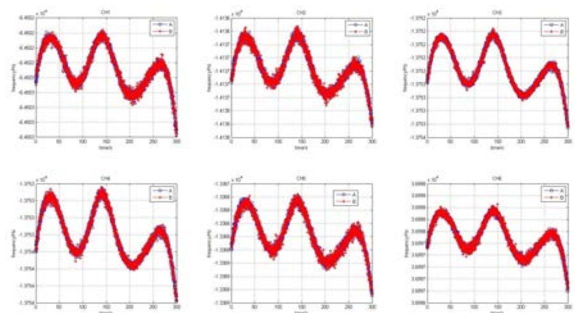

Fig. 4 Residual frequency dynamic variation of Station A and B after polynomial fitting correction.

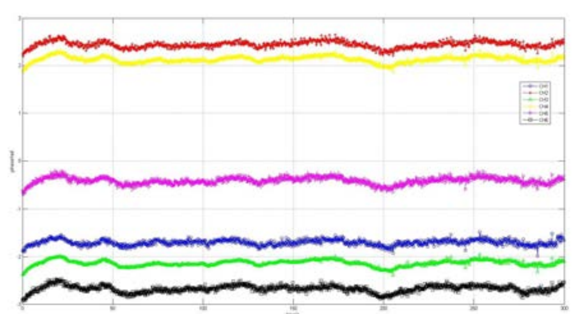

Fig. 5 Difference residual phase.

The variation tendency of difference residual phase decreases via accumulation. The average residual delay is 1090.625 ns, the mean square error is 0.127 ns. The big residual delay (about $1\mu s$) is due to the inaccuracy of the initial delay model. However, the stability of the residual delay verifies the correctness of the algorithm.

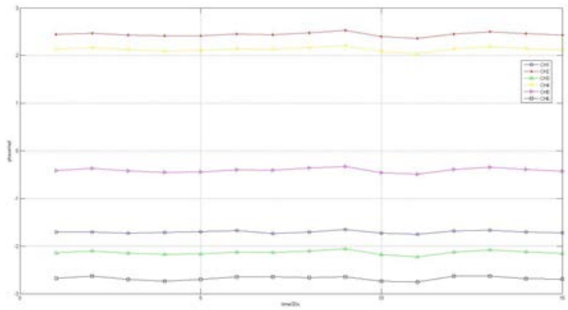

Fig. 6 Difference residual phase via accumulation.

4 Conclusions

The polynomial fitting method is utilized to correct the local signal model and eliminate the residual frequency dynamic variation and the frequency error of corresponding channels. We can compare the results with the spacecraft precise orbit subsequent for further comparative analysis.

References

1. Zensus J A, Diamond P J, Napier P J, et al. Very Long Baseline Interferometry and the VLBA,New Mexico: Publications of the Astronomical Society of the Pacific, 1995: 17-37.
2. Deller A T, Tingay S J, Bailes M, et al. DiFX: A Software Correlator for Very Long Baseline Interferometry Using Multiprocessor Computing Environments. Publications of the Astronomical Society of the Pacific, 2007: 318-336.
3. Li Yuanfei. Study on VLBI Data Software Correlation Pocessing Method. Shanghai Astronomical Observatory Chinese Academy of Sciences, 2004: 10-14.
4. Shu Fengchun, Ping Jingsong, Zheng Weimin, et al. Local Correlation Model of DOR Tones for Tracking Deep Space Probes, The 7th China Deep Space Exploration Conference, 2010: 79-83.
5. Chen Lue, Tang Geshi, Han Songtao, et al. Modeling and Simulation of Local Correlation Processing of Spacecraft DOR Signals. Journal of Spacecraft TT&C Technology, 2012, 31(4): 15-19.

Algorithm and Simulation Analysis of VLBI Data Correlation Processing

Dong Zhang[1,2], Gongyou Wu[1], Jia Wang[2]

Abstract As a radio astronomical technique with very high angular resolution, Very Long Baseline Interferometry (VLBI) has been widely used in the high precision deep space probe tracking activities. VLBI correlation processing consists of integer and fractional sample delay correction, fringe stopping algorithms, and so on. Simulation results have proven that the algorithm is correct and valid. Moreover, the mission data used in the correlative calculation yield clear interference fringes residual delay and residual delay rate through the bandwidth synthesis. We compared the fringes obtained using different integration times; it has high significance for the further development of VLBI research.

Keywords Correlation processing, VLBI, delay correction, fringe stop

1 Introduction

Very Long Baseline Interferometry (VLBI) is a radio interferometry technique developed since the 1960s. The principle of VLBI is receiving a signal from a distant source at two radio telescopes where the signals are recorded on storage media. After a subsequent correlation processing parameters are estimated that reflect the position and state of motion of the source space. It is currently the highest angular resolution astronomical observation technique, reaching sub-mas resolution and better. With the development of China's aerospace industry, spacecraft extend from near-Earth orbit to the moon and deeper space, resulting in higher requirements for aerospace measurements and control ability. VLBI is one of a limited number of deep space exploration methods we can rely on; therefore, it can provide high-precision measurement information for deep space navigation [1, 2, 3].

The VLBI system consists of two or more observation antennas and a data processing center. The VLBI data correlation processor is the core equipment of the data processing center and is a complex high-speed signal processing system. Its main function is to detect interference fringes and to calculate the correlation value or the corresponding cross power spectrum for each frequency channel. While in the early days VLBI data processing mainly used hardware correlators, in recent years the software correlation technology, based on modern high performance PCs or server platforms, has been highly valued in Europe and the United States. Software correlation has become a research hotspot in VLBI [4, 5, 6]. This paper summarizes the FX algorithm of the VLBI software correlator. Using this algorithm we obtain clear interference fringes residual delay and residual delay rate through bandwidth synthesis. This is very important for the future development of VLBI research.

2 The Basic Principle of VLBI

2.1 VLBI Measurement Principle

The basic principle of VLBI observations is shown in Figure 1. When two radio telescopes on Earth at different locations align a radio source simultaneously,

1. China State Key Laboratory of Astronautic Dynamics
2. China Xi'an Satellite Control Center

they receive the radio radiation of pulsar together. The observed radio source is a very distant extragalactic object; therefore, radio waves can be considered as a plane wave when they arrive at the Earth [7]. Due to the different distances of the two antennas to the radio source, there is a distance difference L. The time of the radio signal to reach the two antennas will be different, resulting in a time delay τ_g and delay rate $\dot{\tau}_g$.

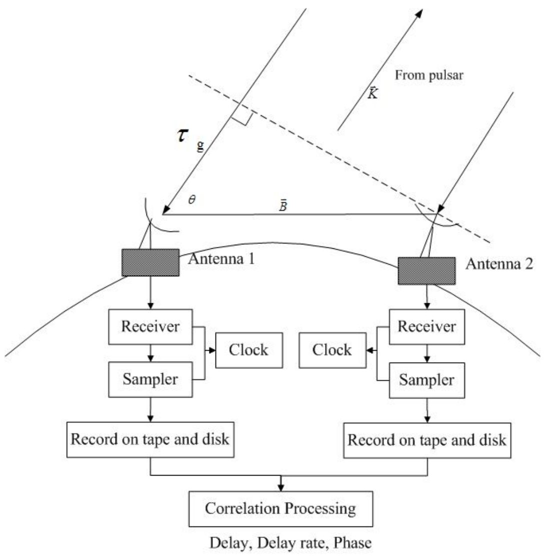

Fig. 1 The basic principle of VLBI observations.

The geometric relationship of the VLBI observation is

$$L = c \cdot \tau_g, \tag{1}$$

where c is the velocity of light. If D is the baseline between the two antennas and θ is the angle between the observed pulsar direction and the baseline, then

$$\tau_g = \frac{1}{c}(D \cdot \cos(\theta)). \tag{2}$$

Due to the motion of the Earth, the baseline vector position changes, so τ_g is a function of time t and the time derivative, called time delay rate $\dot{\tau}_g$, is

$$\dot{\tau}_g = \frac{1}{c}\frac{\partial}{\partial t}(D \cdot \cos(\theta)). \tag{3}$$

The observed data of each station are transmitted to the data processing center through a certain way, and the delay and delay rate of signal reaching each station can be calculated by correlation processor, so as to determine the angle of the source relative to the station. The VLBI observation principle for spacecraft is similar: correlation processing of the spacecraft signal received at two stations provides the angle between the spacecraft and the two measuring stations. This can be used to determine the orbit information of the spacecraft.

2.2 The Basic Principle of the Correlation Processing

The correlation processing is the core of the VLBI data processing, and it is divided into XF type and FX type. The XF correlator calculates the cross-correlation function and Fourier transform first, and then gets the power spectrum. But FX does the Fourier transform of the signal first and then the cross-correlation power spectrum is calculated. The performance of FX is better, but the development is difficult. It has many advantages such as less operation scale and hardware overhead, modularity, and extensibility.

At present, the processing mode of the FX is further advanced. The principles of its data correlation processing is that using the initial value provided by the delay and delay rate model and doing a series of correlation operations such as integer bit correction, fringe stop, FFT, fractional bit correction, and cross multiplication to get the cross-correlation power spectrum of the radio source and spacecraft. Then the correlation fringe is obtained through phase unwrapping; the slope of the correlation phase fringe relative to frequency is the residual delay that we seek. Accurate delay results corrected by residual are used to determine the spacecraft orbit.

2.3 The VLBI Correlation Algorithm

The mathematical model of correlation processing has been introduced in several papers [3, 4, 5], e.g., integer sample time compensation, fringe stopping, FFT, fractional sample time compensation, cross multiplication, and cross spectrum accumulation. We do not describe it here further.

Finally, the actual delay and delay rate can be received by residual delay and residual delay rate plus the model value of the delay and delay rate. All the stations must do the delay compensation and fringe stopping when the geocenter is the reference, and then the cross-spectral estimation can be used to get the residual delay and residual delay rate.

3 Calculation and Analysis

3.1 Simulation Analysis

The correlation processing algorithms are verified through simulation and calculation. Reference station is 1, the length of the baseline between two stations is 30,000 m, frequency sampling of signal is 1 MHz, the sampling time interval is 1 μs, the initial delay equal to 5*10-5 s, and the ideal fringe rate is -629.804 Hz.The Gaussian white noise signal S1 is generated by Matlab as signal of the station 1, and we do correlation calculation using the signal S1 and S2 which is constructed by the delay.

Under the condition that the fringe rate is constant, we calculate the time delay for the initial values to 46 μs, 47 μs, 50 μs, 51 μs, 52 μs, and 54 μs. Assuming the delay to be constant, we calculate the time delay rate for the initial values of -633.804 Hz, -630.804 Hz, -629.804 Hz, -628.804 Hz, -626.804 Hz, and -625.804 Hz. The results of the residual delay and residual fringe rate are shown in Table 1 and Figure 2.

Table 1 Statistics for the residual delays and residual fringe rates.

Initial delay/μs	Residual delay/s	Precision/s
46	$+4.000076 \cdot 10^{-6}$	$7.66 \cdot 10^{-11}$
47	$+3.000089 \cdot 10^{-6}$	$5.61 \cdot 10^{-11}$
50	$-7.606533 \cdot 10^{-25}$	$5.24 \cdot 10^{-11}$
51	$-1.000062 \cdot 10^{-6}$	$5.48 \cdot 10^{-11}$
52	$-1.999952 \cdot 10^{-6}$	$6.01 \cdot 10^{-11}$
54	$-3.999984 \cdot 10^{-6}$	$7.19 \cdot 10^{-11}$

Initial fringe rate/Hz	Residual fringe rate/Hz	Precision/Hz
-633.804	$+3.998936$	0.000360
-630.804	$+0.999742$	0.000259
-629.804	$+5.8473 \cdot 10^{-17}$	0.000256
-628.804	-0.999742	0.000259
-626.804	-2.999213	0.000273
-625.804	-3.998935	0.000360

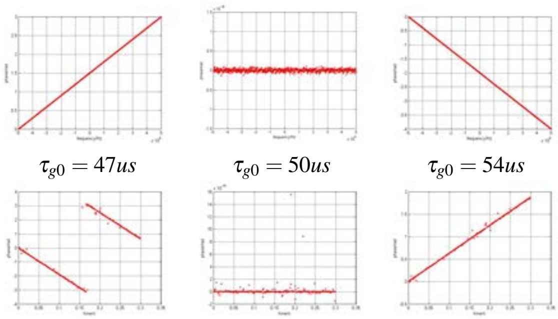

$\tau_{g0} = 47us$ $\tau_{g0} = 50us$ $\tau_{g0} = 54us$

$f_{r0} = -630.804hz$ $f_{r0} = -629.804hz$ $f_{r0} = -626.804hz$

Fig. 2 Schematic diagram of the simulated signal interference fringe.

3.2 Mission Data Analysis

We complete the correlation processing of a single baseline by using the CE-3 database with the data processing method described above. Since the measurement data of the mission is DOR tone signal, a clear interference fringe could be obtained in the main carrier channel when doing the correlation calculation. The residual delay and residual delay rate could be calculated by the phase of the tone signal of the other channel based on the bandwidth synthesis technique. The spectrum analysis of the original data is shown in Figure 3. We can clearly see the tone signal in the four channels.

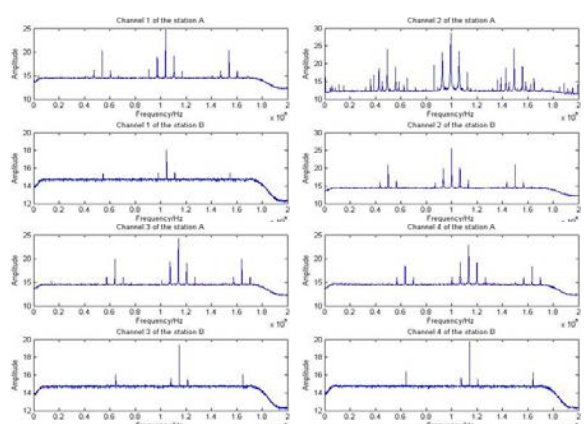

Fig. 3 The spectrum of the raw data in the four channels.

We finish the correlation processing with the mission data by setting the integration time to 5 s and 60 s, respectively. The results of the interference fringes are shown in Figure 4. The residual delay and residual delay rate are shown in Figure 5; the long time integral is better when the model value is accurate.

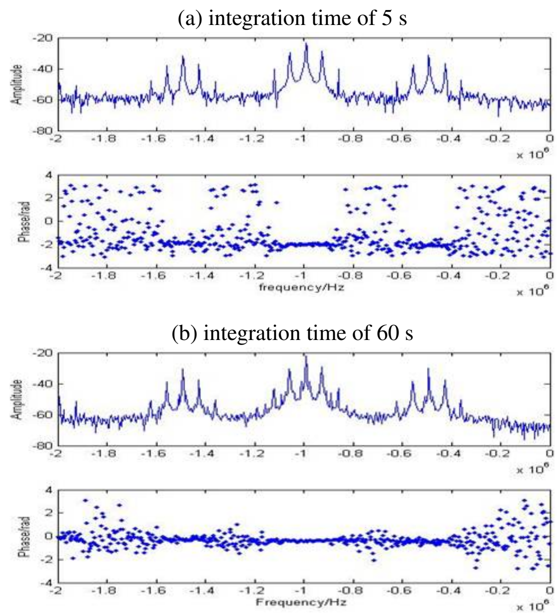

Fig. 4 The interference fringes with different integration times.

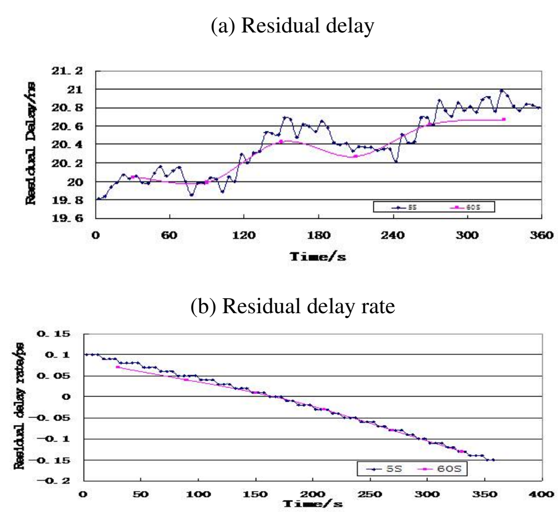

Fig. 5 The resulting residual delay and residual delay rate.

4 Conclusions

Based on the introduction of VLBI software related processing method, the paper has given the model and calculation formula of the integer sample time compensation, fringe stopping, FFT, fractional sample time compensation, cross multiplication, and cross-spectrum accumulation. The clear interference fringe, accurate value of delay and fringe rate can be determined by simulation and mission data. We can see from the simulation results that the residual delay precision is up to 10^{-11} s and the residual fringe rate precision is up to 10^{-4} Hz. This proves the validity of the correlation algorithm. Finally, using mission data in the correlative calculation, we obtained clear interference fringes residual delay and residual delay rate through the bandwidth synthesis and compared the fringes of different integration time. It has high significance for further VLBI research.

References

1. A. Richard Thompson, et al. Interferometry and Synthesis in Radio Astronomy, John Wiley, Sons, Inc, 1986: 29–33
2. James Ulvestad, Miller Goss, Radio Astronomy's Resolution Machine: The Very Long Baseline Array C: How radio astronomers can hit the 'zoom' button and scrutinize unusual objects with unprecedented clarity, Sky and Telescope, 1999, 98(4): 36–46.
3. ZHENG Wei min, SHU Feng chun, ZHANG Dong, Application of Soft ware Correlator to Deep Space VLBI Tracking, Journal of Astronautics, 2008, 29(1): 18–23.
4. QIAN Zhi han, Li JinLing. Very Long Baseline Interferometry and Its Applications in Deep Space Exploration. Beijing: China science and technology Press, 2012.
5. ZHU Xin ying, LI Chun lai, ZHANG Hong bo, A Survey of VLBI Technique for Deep Space Exploration and Trend in China Current Situation and Development, Journal of Astronautic,2010,31(8): 1893–1899.
6. HONG Xiao yu. VLBI techniques and application in the Chang'e lunar orbiter.Chinese Journal of Nature, 2007,29(5): 297–299.
7. ZhENG Yong, Geodetic VLBI, PLA Publishing House, 1999.

Session 5

VLBI Results and Their Geodetic/Astrometric Interpretation

First Geodetic Results from the Australasian VLBI Network

Oleg Titov[1], Jim Lovell[1,2], Hiroshi Takeguchi[3], Jonathan Quick[4], Stanislav Shabala[2], Jamie McCallum[2], Jing Sun[5], John Dawson[1], Aletha de Witt[4], Cormac Reynolds[6], Hayley Bignall[6], Tim Natusch[3], Stuart Weston[3], Sergei Gulyaev[3]

Abstract The Australasian geodetic Very Long Baseline Interferometry (VLBI) array consisting of three new 12-meter radio telescopes in Australia (Hobart, Katherine, and Yarragadee), a 12-meter radio telescope in New Zealand (Warkworth), and a correlation facility in Perth started operations in 2011. The daily positions of the AuScope array are estimated with a precision of a few mm, whereas their daily estimates vary within a range of 20–30 mm on the annual scale. Analysis of geodetic VLBI sessions also reveals small linear trends in the time series of baseline lengths between the Australian and New Zealand stations. A seasonal signal with amplitude of about 10 mm was detected for the baseline Hobart–Katherine. This signal is consistent with seasonal variations of baselines between co-located GNSS stations. We argue this signal should be incorporated in the fitting model to improve the estimates of positions and linear velocities.

Keywords VLBI, AuScope, tectonic velocities

1 Introduction

In the framework of the AuScope project [1] and in a partnership with Geoscience Australia, UTas operates three 12-m radio telescopes located in Hobart (HOBART12), Yarragadee (YARRA12M), and Katherine (KATH12M). Located on the Australian tectonic plate, both AuScope and WARK12M [2] radio telescopes are ideally placed for measurements of intra-plate deformation. Additionally the six baselines of the AuScope+WARK12M array are long enough to contribute to Earth Orientation Parameter (EOP) observations, particularly when coupled together with a Japan–New Zealand baseline.

In this paper, we present a summary of the baseline length variations between AuScope antennas and WARK12M from IVS results for a three-year period, from the beginning of 2011 to the end of 2013. We analyze baseline length variations for the co-located GNSS stations [3, 4, 5].

2 Analysis of VLBI and GNSS Baselines for the Australasian Geodetic Network

AuScope and WARK12M VLBI stations are co-located with GNSS stations HOB2, KAT1, YAR2, and WARK [6, 7]. In this section we compare GNSS vs. VLBI baseline lengths and their linear rates for this Australasian array.

The first AuScope VLBI station, HOBART12, has participated in global IVS sessions regularly since 2010. KATH12M and YARRA12M have regularly taken part in IVS observations since 2011. Regular WARK12M–AuScope observations started in July 2012. In 2012, HOBART12 and KATH12M achieved over 90% sessions analyzed. Unfortunately, this percentage is lower for WARK12M because of a serious problem with the Symmetricom Hydrogen Maser experienced in 2012. Once rectified WARK12M was

1. Geoscience Australia
2. University of Tasmania
3. Auckland University of Technology
4. Hartebeesthoek Radio Astronomical Observatory
5. Shanghai Astronomical Observatory
6. Curtin University

able to resume participation in IVS sessions from January 2013.

Baseline lengths and their rates of change were estimated by using the IVS analysis centers results. Only accurate position measurement data (1-σ < 10 mm) were used. These results are summarized in Table 1 for all types of sessions (e.g., R1, R4, AUST).

We analyzed the VLBI databases applying a uniform strategy across all session types. It is important to do this because the different types of IVS sessions are optimized for different purposes. For example, R1 and R4 sessions are optimized for providing twice weekly EOP results. The purpose of AUST sessions is to determine the station coordinates and their evolution in the AuScope+WARK12M network. We analyzed 134 databases of four types (R1, R4, AUSTRAL, and CRDS) using the Calc/Solve software. In the analysis of R1 and R4 sessions, we excluded TIGOCONC and the Japanese stations (TSUKUM32, KASHIM34, and KASHIM11) in order to avoid the effects of earthquake after-slip. In the analysis of AUST and CRDS sessions, we used only AuScope and WARK12M station data.

Figure 1 shows the VLBI baseline length variations vs. time for six baselines. The linear trends of baselines estimated for different types of sessions are provided in Table 1. For all CRDS sessions, the baseline length standard deviations (sigmas) were all greater than 10 mm. The poor accuracy of the baseline measurements in CRDS sessions can be explained by a specific character of the distribution of scheduled sources—they were all clustered in the celestial south pole direction.

Table 1 Weighted linear rates for six baselines in mm/year.

Baseline	VLBI (OCCAM)	VLBI (CALC/SOLVE)	GNSS
Hb – Ke	7.1 ± 1.8	5.3 ± 0.9	0.3 ± 0.2
Hb – Yg	-0.5 ± 1.6	3.0 ± 1.1	0.8 ± 0.1
Ke – Yg	6.1 ± 1.6	5.6 ± 1.0	-0.8 ± 0.1
Hb – Ww	-0.2 ± 0.5	4.5 ± 2.4	-1.6 ± 0.2
Yg – Ww	20 ± 12	9.9 ± 4.9	-0.6 ± 0.3
Ke – Ww	18 ± 17	11.9 ± 3.7	0.1 ± 0.3

GNSS data from the co-located IGS and PositioNZ stations were analyzed using the GAMIT/GLOBK software. We combined the results with the SOPAC global network file. Figure 2 shows the baseline length residuals and the corresponding rates of change of the six baselines. The rates of change indicated in Table 1 were estimated by formally fitting linear functions to all sets of GNSS baseline data. All GNSS rates of change proved to be very small (about 1 mm/yr or less), which seems realistic as all four stations are located on the Australian Plate. There is a clear annual/seasonal periodic pattern in GNSS baseline data. We argue that this is also evident in the most heavily sampled VLBI baseline data, e.g., for HOBART12–KATH12M baseline. The amplitude of these periodic changes is about 10 mm.

Geodetic VLBI data were also analyzed using the OCCAM software. Estimates obtained by fitting the data with a linear function are presented in Table 1. These numbers indicate, for example, that VLBI antenna KATH12M moves with respect to the two other Australian stations at a rate of 5–7 mm/year. With the Australian continent assumed to be located on a single, quite solid tectonic block, such high rates of linear motion between radio telescopes was not predicted. The New Zealand site belongs to the same tectonic plate. However, the margin between the Australian and Pacific plates is located nearby, therefore the WARK12M site sits on a deformation zone near the tectonic plate margin. As a result, the Trans-Tasman baselines might be expected to show a more substantial linear trend. However, the GNSS results do not support this conclusion. Unfortunately the number of VLBI observations is currently insufficient for robust estimation of these linear trends.

The uncertainties in the linear trend estimates (Table 1) are exaggerated by strong seasonal signals present in both the VLBI and GNSS times series [5]. The seasonal trends, clearly seen in the plotted baseline time series, are likely to be caused by hydrological signals with annual and semiannual periods. However, these signals are not purely harmonical, so temporal changes in periods and amplitudes are expected. Figure 2 shows all six baseline length variations measured with GNSS. The seasonal signals are very indicative with peak amplitudes of 3–6 mm for annual signals and 1–3 mm for semi-annual signals (Table 2).

Figure 3 shows variations of the KATH12M vertical component measured with VLBI and GNSS data, respectively. The GNSS time series shows a steady rate of 6 mm/year with obvious signs of seasonal variation superimposed, whereas the VLBI time series displays a higher annual rate of 14 mm/year and quasi-regular variations. We believe that the quasi-regular variations

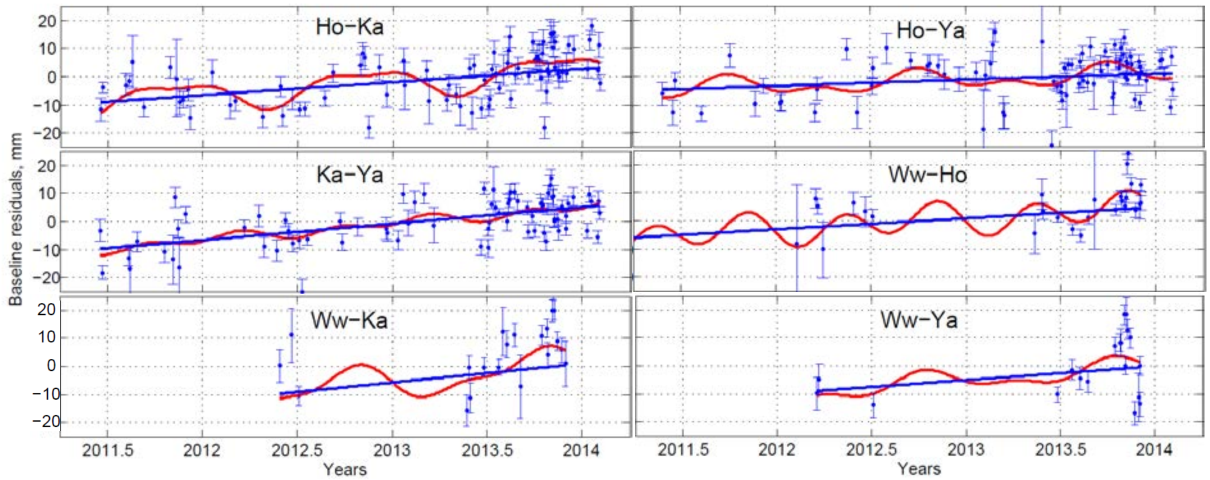

Fig. 1 VLBI derived baselines.

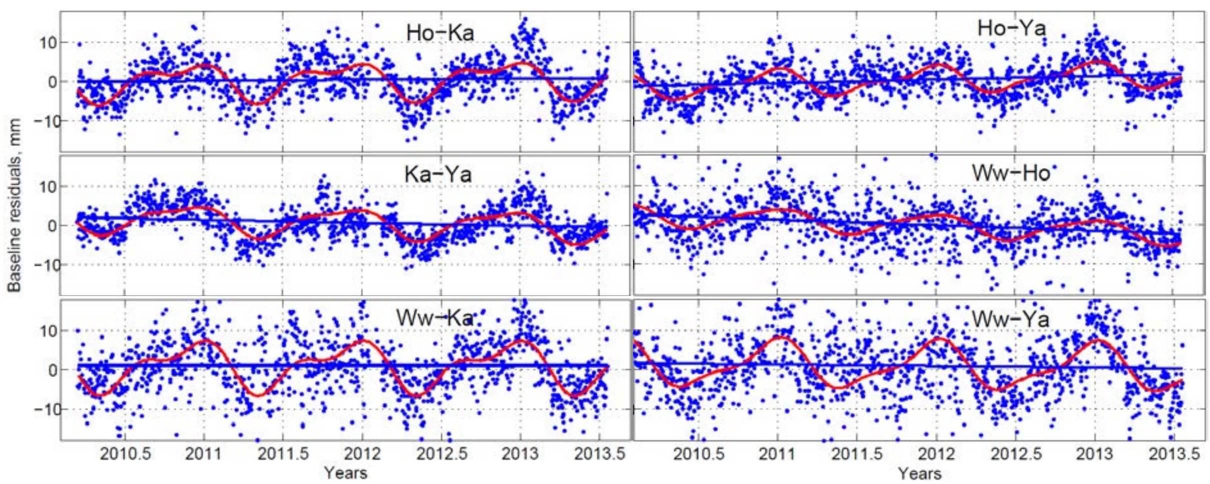

Fig. 2 GNSS derived baseline data.

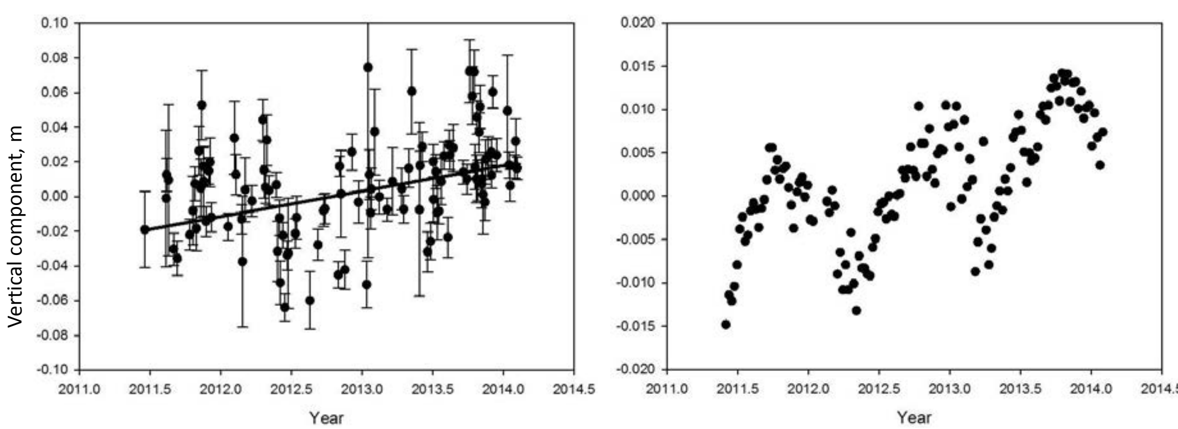

Fig. 3 Vertical components for the Katherine station derived from VLBI (left) and GNSS (right).

Table 2 Peak amplitude of annual and semi-annual signals from GNSS data, units mm.

Baseline	Annual	Semi-annual
Hb – Ke	4.0	2.2
Hb – Yg	2.9	1.4
Ke – Yg	3.5	1.2
Hb – Ww	2.8	0.6
Yg – Ww	5.5	1.9
Ke – Ww	5.5	2.8

of the vertical component may be responsible for the higher rate of the vertical component measured with VLBI. The nature of the uplifting of this area over the three-year period is likely to be caused by hydrological effects. Analysis of a longer times series (since 2010) from the co-located GNSS at KATH12M indicates that the 6 mm/year vertical component rate is a part of long term variations. We suggest therefore that the VLBI-measured rate may have the same explanation. A longer observational time span for VLBI data is necessary to verify this suggestion.

3 Conclusions

The Australasian VLBI network of four 12-meter radio telescopes has been operational since 2011. We have analyzed almost three years of observations and compared the baseline length changes with the corresponding GNSS results. Two Australian baselines including the KATH12M station show a statistically significant linear trend in the VLBI data, but this is not supported by the corresponding GNSS data. At the same time both types of observations reveal quite significant seasonal variations, which may affect the linear rate estimates. The third Australian baseline HOBART12–YARR12M does not show a statistically significant linear trend in accordance with expectations.

The Trans-Tasman baseline changes are difficult to estimate with VLBI due to insufficient observational data. The baseline HOBART12–WARK12M shows no significant tectonic motion, whereas the two longer VLBI baselines KATH12M–WARK12M and YARR12M–WARK12M display somewhat controversial linear rates, arguably due to the sparseness of the time series collected to date. More data must be collected to improve the linear rate estimates.

Acknowledgements

This paper is published with the permission of the CEO, Geoscience Australia.

References

1. Lovell, J. E. J., McCallum, J. N., Reid, P. B., McCulloch, P. M., Baynes, B. E., Dickey, J. M., ... Bignall, H. E. (2013), The AuScope geodetic VLBI array. Journal of Geodesy, 1–12. doi:10.1007/s00190-013-0626-3
2. Takiguchi, H., S. Gulyaev, T. Natusch, S. Weston, and L. Woodburn (2011), Towards Synergy of VLBI and GNSS Geodetic Techniques in Geologically Dynamic New Zealand, Advances in Geosciences, Vol. 31, 33–42.
3. H.-P. Plag, M. Pearlman (eds.) (2009), Global Geodetic Observing System, DOI 10.1007/978-3-642-02687-4_1.
4. GGOS Vision, Mission and Goals. (2011). Officially adopted by the Global Geodetic Observing System Steering Committee at its 21st Meeting on July 2, 2011 at the IUGG XXV General Assembly, Melbourne, Australia. http://www.ggos.org/
5. Beavan, R. J. (2005), Noise properties of continuous GPS data from concrete pillar geodetic monuments in New Zealand, and comparison with data from US deep drilled braced monuments. Journal of geophysical research. Solid earth, 110(B8): B08410, doi:10.1029/2005JB003642.
6. The IGS Tracking Network http://www.igs.org/ network/ complete.html
7. GNS Science, http://www.gns.cri.nz/Home/Our-Science/ Earth-Science/Plate-Tectonics/Deformation-of-NZ.

Comparison of Russian Ru-U and IVS Intensive Series

Sergei Kurdubov, Alexey Melnikov

Abstract This article presents results of a comparison of the Russian national UT1–UTC estimation observing program Ru-U and the international IVS Intensive program. It is shown that the Ru-U sessions performed with good accuracy and that the Ru-U results can be included in the international VLBI data processing scheme. A comparison of different distributions shows that the problem of the lack of correlation between single delay formal errors and UT1 estimates are present both in the Ru-U and the IVS Intensive series.

Keywords VLBI, Intensive, Ru-U, UT1–UTC, "Quasar"

1 Introduction

The Russian national VLBI network "Quasar" started to operate in 2006. In 2009, it was adopted that the "Quasar" network would provide the fundamental time-positioning service of the GLONASS [1, 2]. The Quasar network performs regular 24-h VLBI sessions in standard IVS VLBI S/X wideband for EOP estimations every week and hourly sessions for UT1–UTC estimation every day. Hourly sessions are observed on the baseline Zelenchukskaya–Badary. The observations are delivered to the IAA Correlation Center (hardware correlator ARC) by e-VLBI data transfer [3]. UT1–UTC sessions have been observed daily since 01.07.2012. The time delay between the session start and the UT1–UTC results is between two and six hours. Observations are available for analysis in NGS card format at the IAA Web site.

Institute of Applied Astronomy, Russian Academy of Sciences

What is the Ru-U observation program?

- Russian national UT1–UTC estimation
- One-baseline S/X VLBI sessions
- Zelenchukskaya–Badary or Svetloe–Badary baseline
- e-VLBI data transfer
- IAA hardware correlator
- Daily sessions since 01.07.2012
- Two to six hours between observation start and dUT1 results
- Duration: one hour
- Available for analysis in NGS card format at the IAA website:
  ftp://quasar.ipa.nw.ru/pub/EOS/IAA/ngs/
  http://www.ipa.nw.ru/vlbi/

We use the "QUASAR" software [4] for VLBI data processing and obtaining the UT1–UTC results. All calculations meet the IERS Conventions [5].

2 Mean Formal Uncertainty of Single Delay

The mean formal errors of single delay from the Ru-U sessions are presented in Figure 1. As one can see, the accuracy of the observations differs up to 4–5 times from one session to another. (It is not a secondary processing result. It is the mean correlator formal error.) The differences can be explained by the fact that some sessions were observed with cold receivers and others with warm receivers. The minimum points in Figure 1 correspond to the moments of 24-h EOP-oriented Ru-E sessions performed with cold receivers.

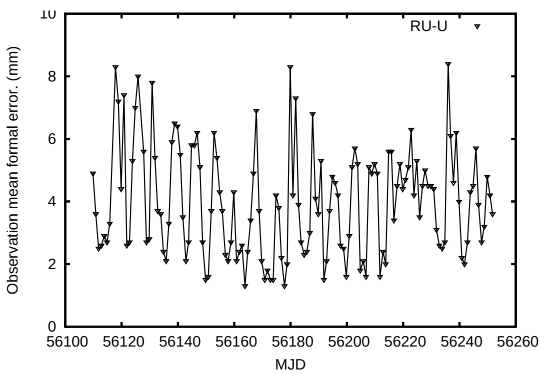

Fig. 1 Mean formal uncertainty of single delay in Ru-U sessions.

It should be noted that the RMS after the solution has no correlation with the formal errors of single delay as seen in Figure 2. The problem looks similar both for the Ru-U and the IVS Intensive sessions. The RMS after the solution is a crucial parameter and directly affects the accuracy of the UT1–UTC estimation (Figure 4).

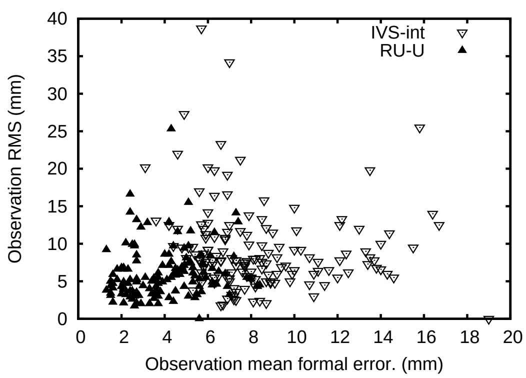

Fig. 2 Mean formal errors of single delay vs. RMS after solution for Ru-U and IVS Intensive sessions.

3 Ru-U UT1–UTC Statistics and Scheduling

Observations were carried out with cold receivers weekly using the single schedule pattern with scans of 60-second length. In July 2012, observations became daily, but use of the same scheduling pattern continued. Sessions from Thursday to Saturday always had cooled receivers, and sessions from Sunday to Wednesday had warm or cool receivers, depending on the time schedule for a particular station. The next major change in observing strategy occured in April 2013. It was separate scheduling depending on the state of the stations' receivers: the warm (hot) and the cool (cold) state were scheduled with different patterns. The last important change in observing strategy was scans with arbitrary durations from 22 to 127 seconds. The comparison of the UT1 series from IAA observations and IERS finals is presented in Table 1. All values are in μs. The table has RMS in the 3rd column, calculated bias in the 4th column, and weighted RMS without bias in the 5th column. The table shows that the last scheduling change significantly improves our results.

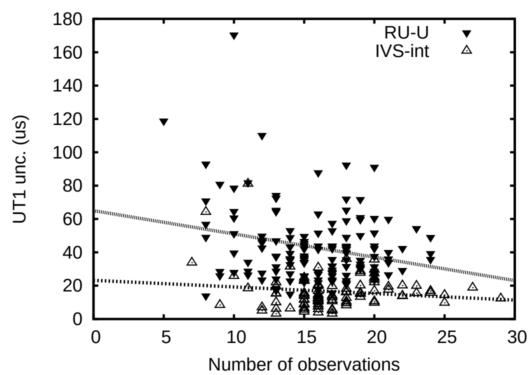

Fig. 3 Number of observations vs. UT1–UTC uncertainty.

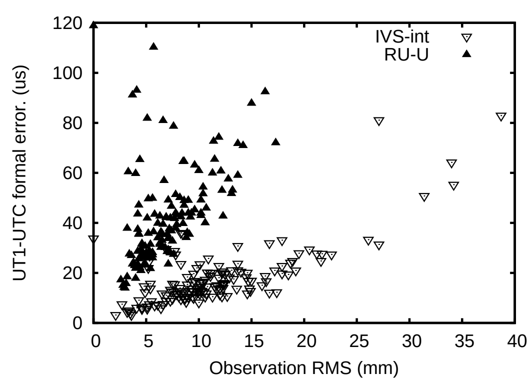

Fig. 4 RMS after solution vs. UT1–UTC formal errors for the IVS Intensive and Ru-U sessions.

The following important changes in schedule pattern were made since the Ru-U sessions became daily (schedules are in the SKED software format):

1. 2012/07/01 — Ru-U sessions became daily. $OP section: estimated parameters DUT, AOFF, ARAT, COFF, and CRT1 for SvZcBd; optimized for ZcBd baseline only, used reference station Bd;
2. 2012/09/01 — Slew time additive constants C1 and C2 (in $STATIONS: A-line) were changed for Sv, Zc, and Bd from 60 to 40 seconds;
3. 2012/12/01 — Source NRAO190 was removed from the $SOURCES section. 158 sources remained in the pattern;
4. 2013/01/21 — Source 0723-008 was removed from the $SOURCES section (based on Ru-U190, 192, 201, 203, 418, and 419). 157 sources remained in the pattern;
5. 2013/02/10 — Separate session patterns for HOT and COLD receivers state at stations. In the HOT pattern, $MAJOR MIN_BETWEEN was changed from 25 to 20 and BEST% from 85 to 100;
6. 2013/04/24 — In the HOT Ru-U pattern, the $SOURCES list was replaced with a new list of 38 selected sources;
7. 2013/04/25 — ARAT was removed from the optimization and estimation parameters in the $OP section;
8. 2013/06/14 — Sources 4C67.05 and 1038+52B were removed from the COLD session pattern. The first was too weak in S-band, and the second was too weak in X-band (based on Ru-U558, 559, and 560). Probably, RFI at Zc in the North direction affected the 4C67.05 scans;
9. 2013/12/01 — The scan durations became arbitrary. The HOT and COLD Ru-U patterns' basic parameters were changed: CORSYNCH was changed from 3 to 0, MINSCAN from 60 to 30, SNR X from 20 to 40, and SNR S from 15 to 40. Both SNR MARGINS were set to 0. Several weights changed in $MINOR. In $MAJOR, MIN_BETWEEN was changed from 25 to 40 and BEST% from 85 to 100. This was a trial period to look for optimal parameters;
10. 2013/12/15 — In the HOT Ru-U pattern, the $SOURCES list was replaced with a new list of 151 COLD sources, except for the following sources: CTA26, 0400+258, 0657+172, and 0945+408. Basic parameters were changed: CORSYNCH from 0 to 3, MINSCAN from 30 to 22, MAXSCAN from 300 to 200, SNR X from 40 to 38, and SNR S from 40 to 37. In $STATIONS, SEFD X changed from 400 to 1200 and SEFD S from 600 to 1200;
11. 2013/12/24 — Changes were made to the COLD Ru-U pattern's basic parameters: CORSYNCH changed from 0 to 7, MINSCAN from 30 to 22, MAXSCAN from 300 to 127, SNR X from 40 to 38, and SNR S from 40 to 37. This restricted the maximum scan duration to 120 seconds at the correlator. Source 2021+614 was removed from the HOT Ru-U pattern due to low S flux. Changes were made to the HOT Ru-U pattern's basic parameters: CORSYNCH changed from 3 to 7, MAXSCAN from 200 to 127, and SNR S from 37 to 38;
12. 2013/12/29 — Changes were made to the HOT Ru-U pattern's basic parameters: ELEVATION changed from 18.0 to 10.0, and in $MAJOR, MIN_BETWEEN changed from 40 to 30.

Table 1 Comparison of the Ru-U UT1 estimates with the IERS series.

Period covered	Scheduling strategy changes	Ru-U–IERS, μs		
		RMS	BIAS	WRMS
2012/07/20 –2013/04/23	Ru-U became daily	61	18±3	50
2013/04/24 –2013/11/30	Different cold and hot sessions	62	8±4	54
2013/12/01 –now	Arbitrary scan length	44	25±4	35

4 IVS Intensive UT1–UTC Statistics

IVS Intensive sessions can be divided into two parts: the XK sessions with baseline Wettzell–Tsukuba and XU sessions with baseline Wettzell–Kokee. We processed sessions for year 2013 (78 XK and 266 XU sessions) and calculated statistics for the complete set and for XU and XK separately. The obtained RMS and unbiased WRMS vs. the IERS finals series for the XK and XU series are presented in Table 2. It can be assumed that the XK series shows worse results due to the unstable Tsukuba position. The two series have different biases, and the XK series has better unbiased WRMS values than the total Intensive series. The relation between the Ru-U and the IVS Intensive estimations are in good agreement with the baseline length relation. Our results for the IVS Intensive sessions are also consistent with the results of other VLBI data analysis centers.

Table 2 Differences of IVS Intensive vs. IERS finals (from 01.01.2013 to 01.01.2014).

	XU+XK	XU	XK
RMS, μs	43	27	46
WRMS, μs	29	15	26

5 Conclusion

The main result of this article is that the IAA Ru-U UT1–UTC estimations have comparable accuracy to the IVS Intensive results and can be used by IERS and IVS as contributions to the IERS UT1–UTC series. Raw observation data and the results of UT1–UTC estimations can be obtained at the IAA ftp sites:

ftp://quasar.ipa.nw.ru/pub/EOS/IAA/ngs/

ftp://quasar.ipa.nw.ru/pub/EOS/IAA/veopi-ru.dat

Moreover it should be noted that:

- Ru-U sessions have better single delay formal errors (see Figure 2).
- Ru-U sessions show a faster decrease in error with an increase in the number of observations (see Figure 3).
- There is a lack of correlation between the delay formal error and the RMS both for the Ru-U and IVS Intensive series (see Figure 2).
- The scheduling significantly affects the accuracy of UT1–UTC estimation. A complex investigation of the scheduling algorithms is needed.

References

1. Finkelstein, A. M.; Skurikhina, E. A.; Surkis, I. F.; Ipatov, A. V.; Rakhimov, I. A.; Smolentsev, S. G. Using the Quasar VLBI network for the fundamental time-positioning service of the GLONASS space system. Astronomy Letters, Volume 34, Issue 1, pp. 59–68, 2008 doi: 10.1134/S1063773708010076.
2. Finkelstein, A. M.; Ipatov, A. V.; Skurikhina, E. A.; Surkis, I. F.; Smolentsev, S. G.; Fedotov, L. V. Geodynamic observations on the Quasar VLBI network in 2009-2011. Astronomy Letters, Volume 38, Issue 6, pp. 394–398, 2012 doi:10.1134/S1063773712060023.
3. Finkelstein, A. M.; Kaidanovskii, M. N.; Salnikov, A. I.; Mikhailov, A. G.; Bezrukov, I. A.; Skurikhina, E. A.; Surkis, I. F. Prompt determination of universal time corrections in e-VLBI mode. Astronomy Letters, Volume 37, Issue 6, pp. 431–439, 2011 doi: 10.1134/S1063773711060028.
4. Kurdubov, S. L.; Gubanov, V. S. Main results of the global adjustment of VLBI observations. Astronomy Letters, Volume 37, Issue 4, pp. 267–275, 2011 doi: 10.1134/S1063773711010063.
5. D. D. McCarthy and G. Petit. IERS Conventions (2003). IERS Technical Note, No. 32, Frankfurt am Main, Germany: Verlag des Bundesamts für Kartographie und Geodäsie, ISBN 3-89888-884-3, 2004, 127 pp., 2004.

Some New Results of the VLBI Data Analysis in the IAA RAS

Vadim S. Gubanov, Sergei L. Kurdubov

Abstract At the Institute of Applied Astronomy, the multi-purpose software package QUASAR created by I. Surkis, V. Gubanov, and S. Kurdubov has been used for processing VLBI observations since 2000. In this paper, some scientific results derived recently by means of QUASAR are presented.

Keywords VLBI, reference frames, Earth rotation

1 Introduction

QUASAR is used mainly for the analysis of 24-h series of VLBI observations in IVS geodetic programs for more precise definition of the CRF and TRF reference frames and for geodynamic investigations. Current variations of unstable Earth rotation and local parameters are determined by independent solutions of each series. Stable parameters are determined from global solutions.

A number of interesting new results have been obtained recently with the help of the software package QUASAR analyzing the 30-year series of VLBI observations in connection with IERS Convention (2010) [1]:

1. It is stated with high reliability that the linear trend of the Retrograde Free Core Nutation (RFCN) phase changed four times during this time, which can be explained by the fact that the period of these oscillations is changeable [3, 4].

2. A complete global adjustment of all available observations has been achieved in order to obtain new versions of terrestrial and celestial coordinate systems as well as Earth orientation parameter series [5].

3. New estimates have been made with an accuracy of 10^{-4} for the integral (not frequency dependent) complex values of Love/Shida tidal numbers and for diurnal and semi-diurnal bands. A new effect has been discovered for 49 VLBI stations—the tidal asymmetry of horizontal displacement in the direction of their tectonic motions [6].

Institute of Applied Astronomy of RAS

2 Results

2.1 VLBI Global Solutions

Arc parameters: Earth orientation (Xp, Yp, UT1–UTC, Xc, and Yc), station clock quadratic + stochastic model, station troposphere linear + stochastic model.

Global parameters: source coordinates $\Delta\alpha$ and $\Delta\delta$ and station coordinates and velocities.

NNR for 212 ICRF1 defining sources, NNT/NNR for 15 stations (BR-VLBA, FD-VLBA, FORTLEZA, HN-VLBA, KP-VLBA, LA-VLBA, MATERA, NL-VLBA, ALGOPARK, WESTFORD, WETTZELL, HARTRAO, KOKEE, NYALES20, and ONSALA60). Soft constraint for sources with fewer than 15 observations, no velocity estimation for stations with less than a year of observations. The sum of the clock parameters in each session equals zero. EOP is fixed for low geometry sessions. Velocities for stations at the same site (such as NRAO) are made equal.

Results are presented as tables iaa2012a, iaa2011a, iaa2009b, iaa2008b, and iaa2007b at: http://ivscc.gsfc.nasa.gov/products-data/products.html, ftp://ivs.bkg.

bund.de/pub/vlbi/ivsproducts/trf/iaa2013a.trf.gz, ftp://ivs.bkg.bund.de/pub/vlbi/ivsproducts/trf/iaa2013a.crf.

2.2 Direct Estimations of ICRF2 Systematic Errors

The distribution of systematic errors in the coordinates of 1,217 extragalactic radio sources of the latest version of the International Celestial Reference Frame (ICRF2) has been mapped by processing VLBI observations by geodetic programs spanning the period 1980–2012 [7].

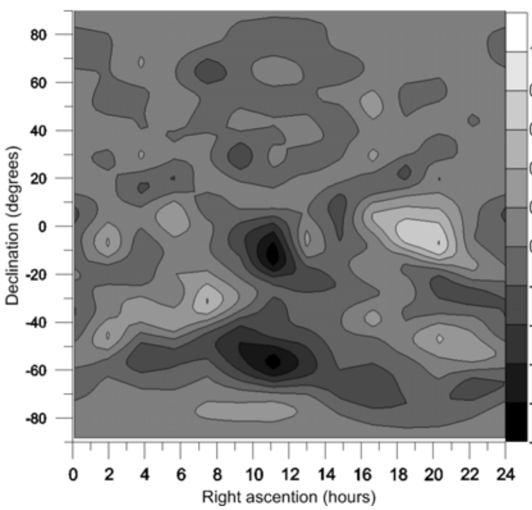

Fig. 1 Map of ICRF2-1217 $\Delta\alpha$ systematic errors.

These errors are shown to reach ± 1.0 mas (milliarcsecond). This accuracy cannot be considered satisfactory, especially in order to determine Earth orientation parameters (EOP). For this task, we must collect a specific list of sources with more accurate coordinates (ICRF-EOP). For example, the list of 752 sources observed more than 100 times may be adopted as system ICRF-752, the systematic errors of which do not exceed ± 0.2 mas (see Figures 3 and 4).

2.3 Instability of CRF and TRF Objects

The individual stability of many of the extragalactic radio sources and VLBI stations included in the latest versions of ICRF2 and ITRF2005 has been investigated [7]. For example, Figures 5–7 and 8–10 show the displacements in time for the source 0923+392 and the station Pie Town, respectively. The position and proper motion of 0923+392 are $\Delta\alpha = (0.019 \pm 0.002) + (0.131 \pm 0.003)T$, $\Delta\delta = (0.014 \pm 0.002) - (0.041 \pm 0.003)T$, where T is in centuries from the epoch 1997.1. Anomalous shifts reaching ± 20 μas for sources and ± 3 mm for stations have been detected.

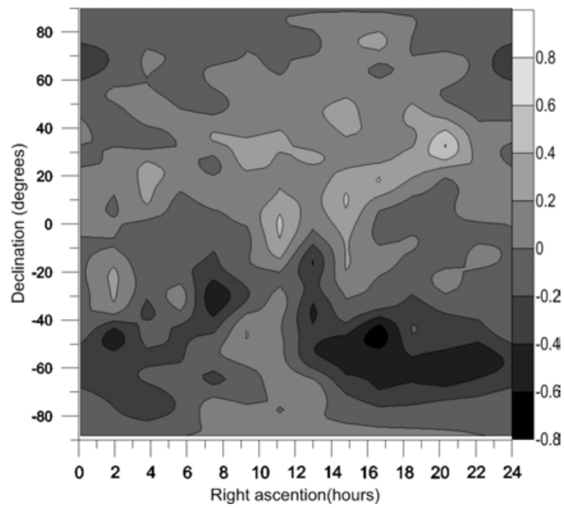

Fig. 2 Map of ICRF2-1217 $\Delta\delta$ systematic errors.

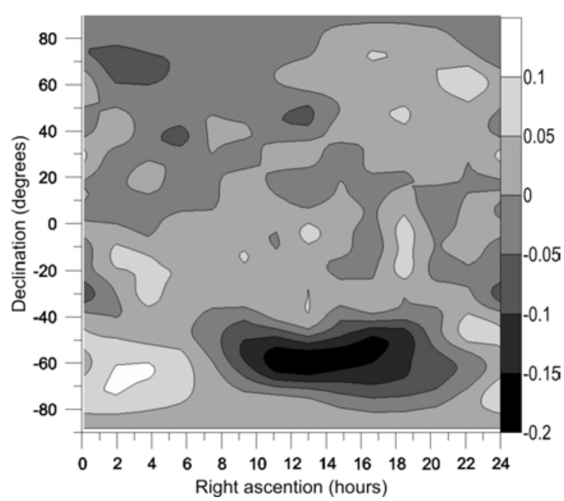

Fig. 3 Map of ICRF2-752 $\Delta\alpha$ systematic errors.

The displacements of the Pie Town station in the directions North and South shown in Figures 8–9 are generally consistent with those obtained in [2].

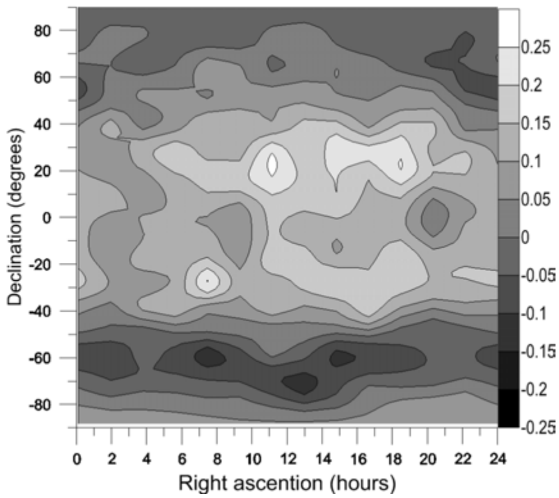

Fig. 4 Map of ICRF2-752 $\Delta\delta$ systematic errors.

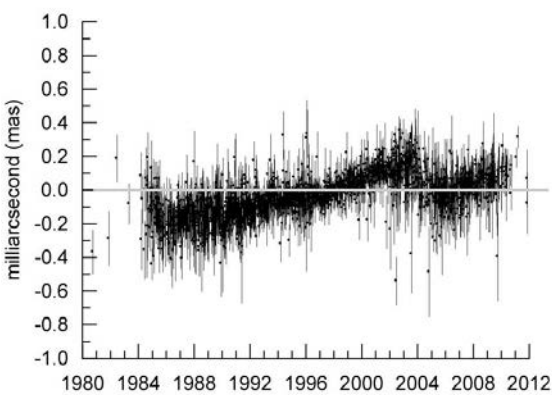

Fig. 5 Displacements of source 0923+392 in α direction.

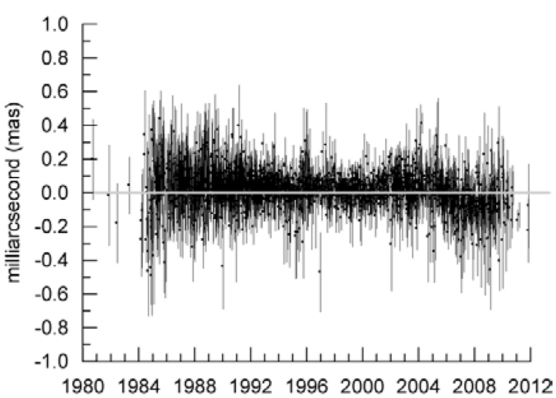

Fig. 6 Displacements of source 0923+392 in δ direction.

2.4 RFCN Parameters

On the basis of available determinations of the Celestial Intermediate Pole (CIP) coordinates (X, Y)

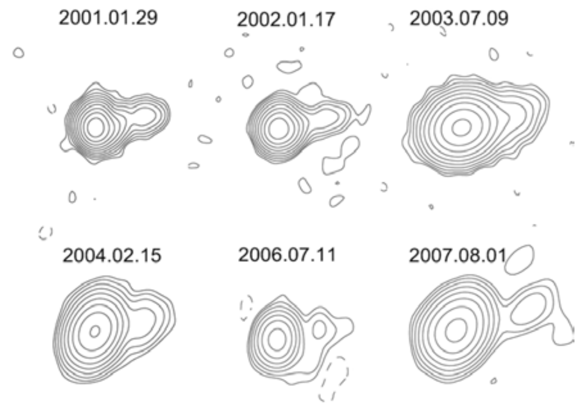

Fig. 7 Images of source 0923+392 by A. Fey (USNO).

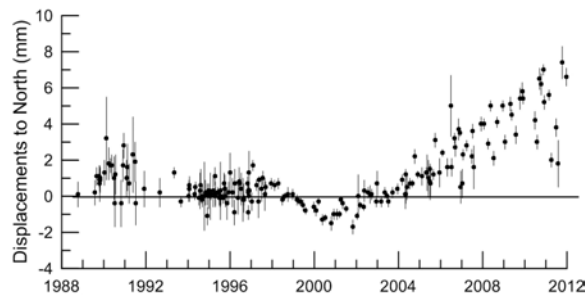

Fig. 8 Displacement of Pie Town VLBI station.

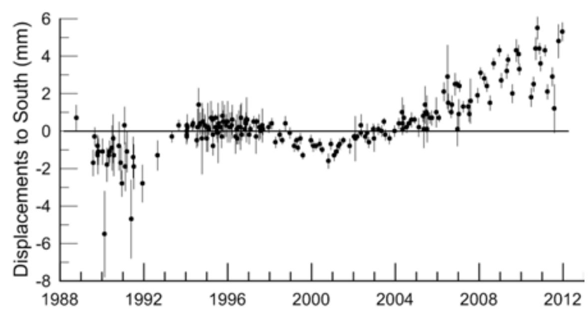

Fig. 9 Displacement of Pie Town VLBI station.

from VLBI observations over the last 25 years, a new combined series, gvscomb, has been created [3, 4]. The amplitude-and-phase analysis of this series by Moving Least-Squares filter (MLSF) has allowed the estimation of the Retrograde Free Core Nutation (RFCN) parameters as functions of time to be obtained. It has been shown that during this time interval the period RFCN was not constant $P = -430.21$ solar days as it is adopted in MHB precession-nutation theory but changed a few times. Until 1992.1, it was equal to

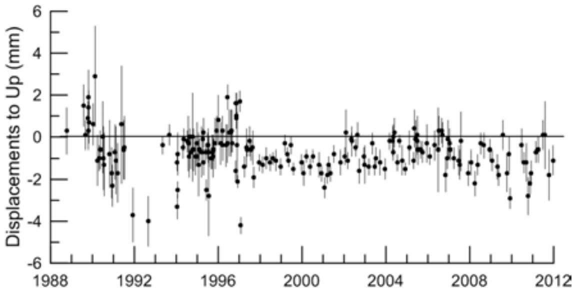

Fig. 10 Displacement of Pie Town VLBI station.

-418.1 ± 0.2 days, and then up to 1999.0 it was equal to -431.6 ± 0.2 days. In 1999 there was almost full damping of CIP oscillation and its reconstruction. Since 2000 the amplitude of this oscillation has begun to increase, and its period has appeared equal to -450.7 ± 0.1 days.

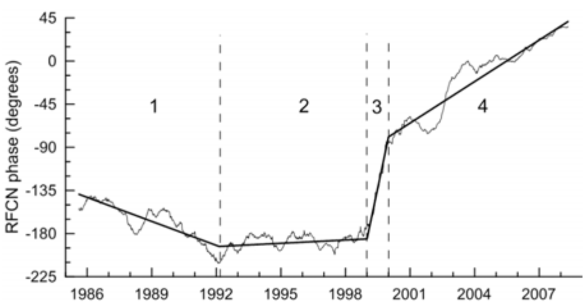

Fig. 11 RFCN phase variation.

Uncertainties of 3,216 points on the thin line in this figure are in the range of two to six degrees.

The discovered instability of the RFCN frequency indicates the presence of quasi-regular disturbances for which a geophysical explanation has not yet been found. They may be connected with unstable electromagnetic and coupling forces on the border of the Earth's liquid core and lower mantle or existence of the scale convection of the matter in this envelope.

2.5 Frequency Independent Love/Shida Numbers and Tide Lag

The partial derivatives of the total tidal displacement $\Delta\vec{s}$ with respect to the nominal Love/Shida numbers are [6]

$$\frac{\partial(\Delta\vec{s})}{\partial h^{(0)}} = H\frac{3p^2-1}{2}\widehat{r}, \quad \frac{\partial(\Delta\vec{s})}{\partial l^{(0)}} = 3Hp(\widehat{R}-p\widehat{r}),$$

where $\widehat{R}$ is the geocentric unit vector to the Moon or Sun, $\widehat{r}$ is the geocentric unit vector to the VLBI station, $p = (\widehat{R}\cdot\widehat{r})$ is the scalar product, H is the amplitude total tidal displacement in meters, and $h^{(0)}, l^{(0)}$ are the nominal Love and Shida numbers independent of latitude.

The partial derivative of the total tidal displacement with respect to tidal phase lag is the following:

$$\frac{\partial(\Delta\vec{s})}{\partial\theta} = 3H\{[(h_2-2l_2)p\widehat{r}+l_2\widehat{R}](\boldsymbol{L}\widehat{R}\cdot\widehat{r})+l_2p\boldsymbol{L}\widehat{R}\},$$

where $\boldsymbol{L}$ is a 3×3-matrix with rows: $(0,-1,0), (1,0,0), (0,0,0)$.

Values from a global solution for nominal tidal numbers and phase lag are [6]

$$\Delta h^{(0)} = +0.00348 \pm 0.00027,$$
$$\Delta l^{(0)} = -0.00039 \pm 0.00006,$$
$$\Delta\theta = -0.^\circ 110 \pm 0.^\circ 014.$$

2.6 Asymmetry of Horizontal Tidal Displacement

Intuitively, one would expect that some point on the Earth's surface, moving under the action of horizontal tectonic forces has an additional degree of freedom, and its displacement in this direction under tidal action will be somewhat larger than in all other directions. Assuming tidal forces act on a point equally in all directions, the movement of the point of these forces will not occur in a circle, but in an ellipse, whose major axis is elongated along the tectonic movement of the point. The compression of the ellipse is called the asymmetry parameter. The hypothesis is confirmed, if the parameter is positive. If it is negative or zero, then the hypothesis is rejected. Figure 12 shows that the expressed proposal is confirmed in 49 cases out of 72 (68 percent), which is not too bad [6].

2.7 Frequency Dependent Tidal Numbers

Based on an analysis of the VLBI observations performed in 1985–2010 within the framework of IVS

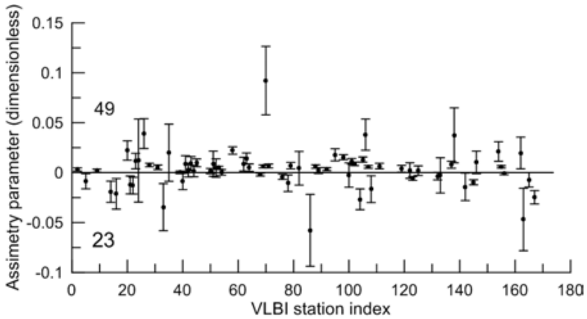

Fig. 12 Asymmetry parameters for 72 VLBI stations.

geodetic programs on global networks, we have obtained the parameters of lunisolar tides as the nominal complex Love/Shida numbers without considering diurnal resonance effects [6]. The new estimates of such "integral" values of these numbers (in 10^{-4}) are for:

total tides:

$h^{(0)} = (6113 \pm 3) - (33 \pm 2)i,$
$l^{(0)} = (843 \pm 1) - (5 \pm 2)i,$

diurnal tides:

$h^{(0)} = (6106 \pm 3) - (10 \pm 6)i,$
$l^{(0)} = (843 \pm 1) - (8 \pm 1)i,$

semi-diurnal tides:

$h^{(0)} = (6106 \pm 3) - (24 \pm 3)i,$
$l^{(0)} = (843 \pm 1) + (3 \pm 1)i$.

Acknowledgements

The authors are grateful to Dr. Alan Fey (Astrometry Department of USNO, USA) for permission for the publication of the images of source 0923+392.

References

1. G. Petit, B.Luzum (eds). IERS Conventions (2010). *IERS Technical Note*, No. 36, 1–179, 2010.
2. M. Seitz et al., The 2008 DGFI realization of the ITRF: DTRF2008. *J Geod*, 86: 1097–1123, DOI 10.1007/s00190-012-0567-2, 2012.
3. V. Gubanov. Dynamics of the Earth's core from VLBI observations. *Astronomy Letters*, 35(4), 270–277, 2009.
4. V. Gubanov. New estimates of retrograde free core nutation parameters. *Astronomy Letters*, 36(6), 444–451, 2010.
5. S. Kurdubov, V. Gubanov. Main results of the global adjustment of VLBI observations. *Astronomy Letters*, 37(4), 267–275, 2011.
6. V. Gubanov, S. Kurdubov. Tidal deformations of the Earth from VLBI observations. *Astronomy Letters*, 38(6), 399–410, 2012.
7. V. Gubanov, S. Kurdubov. On the errors and stability of reference frames. *Astronomy Letters*, 39(12), 866–875, 2013.

The GFZ VLBI Solution: Characteristics and First Results

Robert Heinkelmann[1], Tobias J. Nilsson[1], Maria Karbon[1], Li Liu[1,2], Cuixian Lu[1], Julian A. Mora-Diaz[1], Elisabeth Parselia[1,3], Virginia Raposo-Pulido[1,4], Benedikt Soja[1], Minghui Xu[1,2], Harald Schuh[1,3]

Abstract At GFZ, we have created a contribution for ITRF2013 following the analysis configuration specified by the IVS Analysis Coordinator. The models mostly comply with the IERS Conventions (2010). For the sake of consistency, the ICRF2 defining sources were fixed on their catalog positions. The positions of other sources, including the special handling sources, were estimated together with the coordinates of the terrestrial network stations and the Earth orientation parameters. The standard auxiliary parameters—clock, tropospheric zenith delays and gradients—were estimated as well, applying a 1-h resolution for clock and zenith delays and a 6-h resolution for gradients. The resolution of auxiliary parameters was changed, if the density of observations demanded it. The solution contains 5,813 24-h VLBI sessions between 1979 until the end of 2013. The analyses were done with the VieVS VLBI software.

Keywords ITRF2013, GFZ Analysis Center

1. Helmholtz Center Potsdam, GFZ German Research Center for Geosciences
2. Shanghai Astronomical Observatory, Chinese Academy of Sciences
3. Technical University Berlin, Institute of Geodesy and Geoinformatics
4. Instituto Geográfico Nacional, Centro Nacional de Información Geográfica

1 Introduction and General Characteristics

At the IVS Associate Analysis Center (AC) at GFZ Potsdam, a VLBI solution has been obtained using the VLBI analysis software VieVS (Boehm et al., 2012). With this effort the AC GFZ aims to contribute to the upcoming realization of the International Terrestrial Reference System (ITRS), the International Terrestrial Reference Frame ITRF2013. Currently, the GFZ VLBI solution starts at the post-processing level with the NGS file (`http://lacerta.gsfc.nasa.gov/mk5/help/dbngs_format.txt`), which is created from the database format vers. 4 or higher. At this stage, the ambiguities from broadband synthesis have been fixed and the ionospheric delays have been determined. We have downloaded the complete historical archive available from IVS Data Centers, more specifically from the BKG Data Center (`ftp://ivs.bkg.bund.de/pub/vlbi/ivsdata/ngs/`). By the end of February 2014 when the GFZ VLBI solution was completed, the archive contained 5,984 non-Intensive sessions. The GFZ solution includes 5,813 of those sessions (97%). The neglected sessions mainly suffer from larger numbers of bad observations due to a variety of reasons, e.g., radio frequency interference, or from bad station or baseline performances due to sub-ambiguities.

In general, the number of observations per session has been increasing since 1979 (Figure 1). In the middle of the 1990s a smaller group of sessions significantly exceeds the mainstream: the sessions featuring the VLBA (`http://www.vlba.nrao.edu/`). Those sessions generally have many more observations than the average and also include the session with the most observations: 99DEC20XA (30,510 observations), a session observed by the ten VLBA antennas plus a global network of ten IVS antennas.

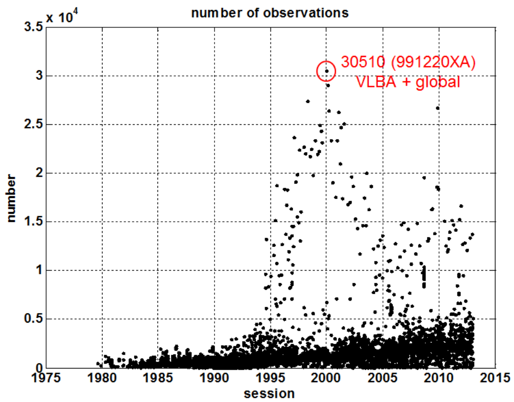

Fig. 1 GFZ VLBI solution: the number of observations per session has been increasing since the beginning in 1979.

The generally increasing number of stations per session (Figure 2) does not exceed 20, with one exception: the International Year of Astronomy (IYA) session, 09NOV18XA (`http://ivscc.gsfc.nasa.gov/program/iya09/`). With 32 stations, this individual session features the largest number.

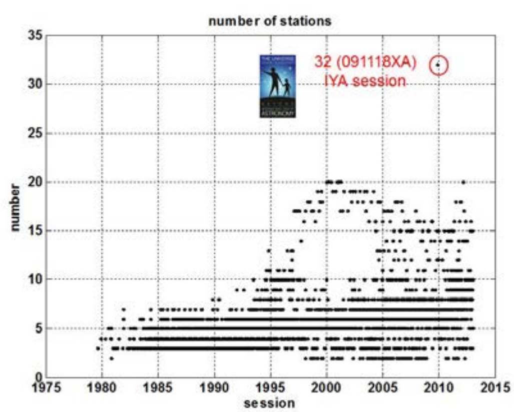

Fig. 2 GFZ VLBI solution: the number of stations per session does not exceed 20 with only one exception: the IYA session.

Figure 3 shows the number of sources observed per session. In the first years from 1979 until about 1989, one can see that there were not more than about 20 radio sources observed in a single 24-h VLBI session. Then, in 1990, the number of sources started to increase until about 2002 when the average number of sources per session settled roughly around 50. Some groups of sessions contain significantly larger numbers of sources. The session type with the largest number of sources is the VLBA Calibrator Survey (VCS). Among them we find the session with the most radio sources observed, 05JUL09XV, a VCS-5b session (Kovalev et al., 2007) with 268 sources.

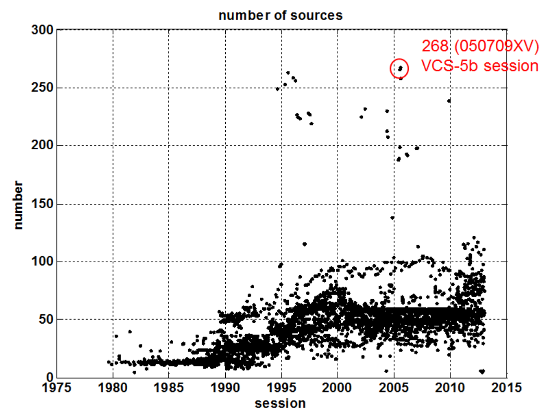

Fig. 3 GFZ VLBI solution: the number of sources per session.

The duration of the sessions has not varied a lot from 1979 until the end of 2013. With a few exceptions, it has stayed around 24-h. With 62-h, the longest session is also the earliest of our archive: 79AUG03XX. While the duration mostly stays the same, the starting time of the sessions varies significantly, in particular in the early years. Since about 1995, well-defined starting times of individual session types have been introduced mainly varying between 12:00 and 18:30 UTC (Figure 4). With its starting time at 0 h UTC since 2008, the CONT (`http://ivscc.gsfc.nasa.gov/program/cont08/`) type of session is an important exception. CONT05 has also been re-correlated to provide sessions between integer UTC days. Because the observation period fits to the ones of the other space geodetic techniques and due to the superior quality, the CONT type of session is specifically suitable for comparisons with other space geodetic techniques.

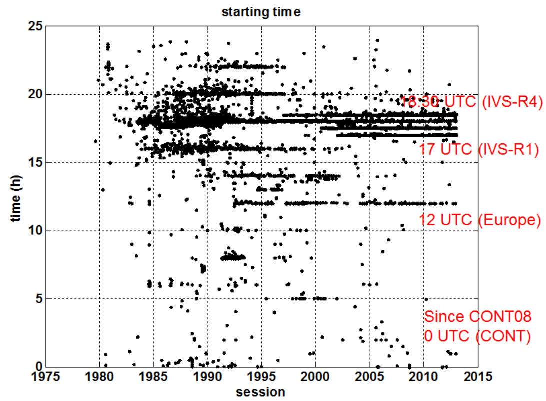

Fig. 4 GFZ VLBI solution: the starting time of the sessions.

2 Analysis Options and Parameterization

The analysis options applied for the GFZ VLBI solution follow the specifications given by the IVS Analysis Coordinator for contributions to ITRF2013 (`http://lupus.gsfc.nasa.gov/IVS-AC_ITRF2013.htm`). Most of the applied models are valid for several space geodetic techniques and are thus specified by the IERS Conventions (Petit & Luzum, 2010). Those will not be discussed explicitly here. This section focuses on the analysis options which are not specified by the IERS Conventions or are treated in a different way. The Conventions recommend a model of S1-S2 tidal atmosphere pressure loading. For the sake of consistency, atmosphere pressure loading is not applied because the IGS contribution to ITRF2013 does not consider it. Apart from the Conventions, which recommend the use of APG a priori gradients (Boehm et al., 2013), an updated version of the DAO a priori gradient model (MacMillan & Ma, 1998) was specified for the ITRF2013 contribution. The axis offset correction is based on axis offset lengths given in the updated list (`http://lupus.gsfc.nasa.gov/files_IVS-AC/gsfc_itrf2013.axo`) provided by GSFC. For the antenna thermal expansion model (Nothnagel, 2008) some of the dimensions of the antennas (`http://vlbi.geod.uni-bonn.de/Analysis/Thermal/antenna-info.txt`) have been added; others have been revised.

The most prominent difference between a standard solution and this ITRF2013 contribution is the handling of the radio sources. The positions of the ICRF2 (Fey et al., 2009) defining sources were fixed on ICRF2 catalog values, while the positions of ICRF2 special handling and other sources were estimated (and reduced from the reported normal equations). Coordinates of all terrestrial stations are estimated as session-wise offsets. For the EOP, the 24-h sessions of the ITRF2013 contribution fall into two categories:

- > 3 station networks, for which standard EOP parameterization including adjustments to the celestial pole coordinates X and Y, terrestrial pole coordinates x-pole and y-pole, UT1–UTC, and their first time derivatives has been applied, or
- the 2–3 station networks, for which a limited parameterization has been applied for EOP: x-pole, y-pole, and UT1–UTC.

These and other technical solution characteristics are summarized in a document (`http://lupus.gsfc.nasa.gov/files_IVS-AC/ITRF2013_checklist_v2014Feb07.pdf`) issued by the IVS Analysis Coordinator.

With the version of VieVS modified at GFZ it was possible to follow the specified solution requirements. However, the EOP parameterization in VieVS is a linear spline with equally spaced supporting points at integer UTC days, labeled by some authors as piecewise linear function, while the IVS requirements for ITRF2013 specify the offset and rate parameterization referring to an epoch close to the middle of the VLBI session. In addition to these two parameterizations, the ITRF2013 input for EOP of the other space geodetic techniques (GNSS, SLR, and DORIS) refers to 12 h UTC. For ITRF2013, the IVS Combination Center at BKG will transform both VLBI EOP parameterizations to the offset and rate representation at 12 h UTC. Consequently, for the first time the IVS input to ITRF2013 will be at the same epoch as the other space geodetic techniques. Since the EOP determined by several VLBI groups refer to an epoch close to the middle of the session, the large differences of the starting times (Figure 4) may cause an inconsistency of the EOP if the parameter definition epoch is not exactly considered. In the future, AC GFZ intends to contribute to ICRF, ITRF, and EOP time series solutions within the framework of IVS, IERS, and IAU.

3 GFZ VLBI Solution: First Results

In this section we present a selection of results obtained with the GFZ VLBI solution.

The GFZ VLBI solution includes in principle all IVS stations, currently 157, which have ever participated in an astrometric or geodetic IVS session. Since some of the VLBI sessions are observed by networks of rather low numbers of antennas, the terrestrial constraints are most reliable if the maximal number of stations is included. Thus, all available ITRF2008 VLBI stations were used for the session-wise NNR and NNT constraints. In the cases where an episodic motion (earthquake, seismic event, antenna repair) had significantly affected a station, the station was excluded from the constraint after the event but kept before. Figure 5 shows such an event, the Tōhoku earthquake, which affected the coordinate time series of adjacent sites, for example the time series of the 32-m antenna in Tsukuba, Japan. A big advantage of ITRF2013 compared to ITRF2008 will be that it will contain many more stations located in the southern hemisphere. Figure 6 exemplarily shows the time series of coordinate adjustments of the new VGOS antenna KATH12M in Katherine, Australia, where the time series are now long enough to reliably estimate velocities.

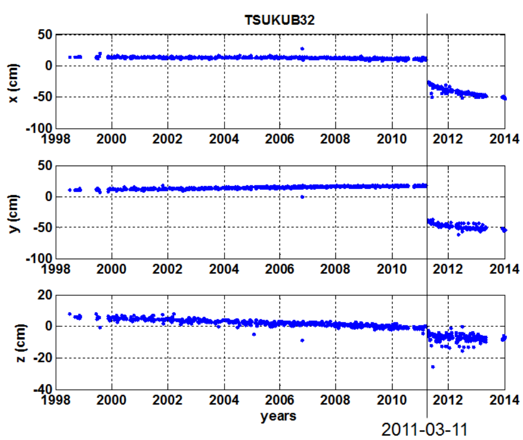

Fig. 5 GFZ VLBI solution: coordinates of TSUKUB32 relative to the respective mean value.

All of the observed radio sources were in principle included in the GFZ VLBI solution. Occasionally, for the sake of a positive redundancy, it was necessary to exclude single radio sources with insufficient

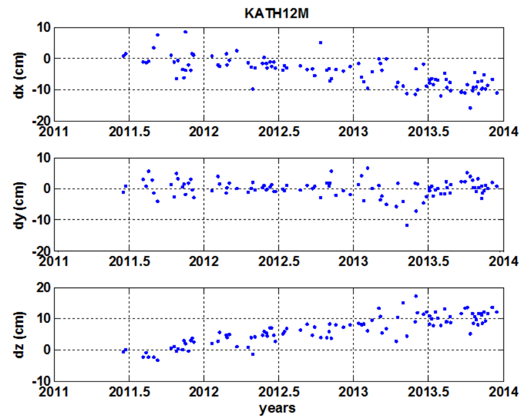

Fig. 6 GFZ VLBI solution: adjustments to the coordinates of KATH12M.

number of observations from the session-wise analysis. Since the GFZ VLBI solution includes more recent sessions than the solution served for the creation of ICRF2, it is evident that the number of sources of the GFZ solution (3,559) is slightly larger than the number of ICRF2 sources (3,414). For some of the radio sources, we observed significant non-linear variations (see Mora-Diaz et al., this volume). One example is shown in Figure 7. Because the ICRF2 defining source positions were fixed to their ICRF2 catalog values (see Section 2), no local celestial NNR constraint had to be used.

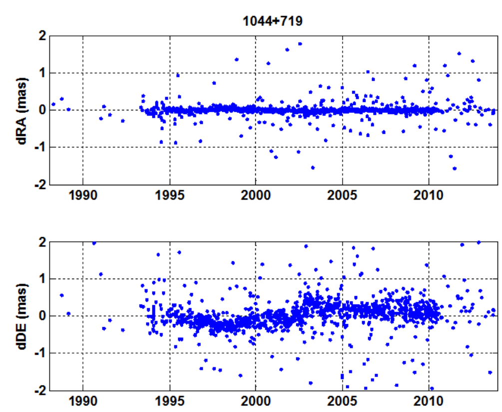

Fig. 7 GFZ VLBI solution: adjustments to the coordinates of 1044+719.

The EOP have been determined by our solution as well. We found that a large effect on the EOP is due to the relatively strong variation of the terrestrial station network. To illustrate this effect, Figure 8 shows the adjustments to the celestial pole coordinate X, color-coded for the ten most recent and black for the other session types. Depending on the type of session, large differences of the RMS can be found for all EOP. As an example, Table 1 gives the numerical results for the celestial pole X coordinate.

Table 1 RMS of the celestial pole X coordinate depending on the type of session.

Type of session	RMS [μas]
IVS-R1	394
IVS-R4	232
IVS-T2	314
APSG	486
VLBA & global + VLBA	183
CRF	1420
R&D	422
EUR	1051
JADE	2147
CONT	144
Other	1378

The RMS varies between 144 μas for the various CONT sessions and 2,147 μas for the JADE type of session. In general, it can be found that spatially limited networks, e.g., national (JADE) and regional (EUR) networks, cause large RMS values, while networks with a global extension (IVS-R1, IVS-R4, and CONT) result in smaller RMS values for the EOP. Session types in which the EOP are not among the original scientific purposes, e.g., CRF sessions, also do not provide good RMS values. The CONT RMS is about half as large as the respective values of the standard IVS types of session (IVS-R1, IVS-R4), which is due to the larger number of observations obtained by a denser network. This shows that with the future VGOS networks and schedules, one can expect further improvement for the EOP RMS. Note that from the celestial pole coordinates, which were derived w.r.t. the conventional IAU2000/2006 models, the free core nutation model has not been considered. Thus, the RMS derived and discussed here can only be compared and interpreted relative to each other, and they do not reflect the current accuracy capability of VLBI for the determination of EOP.

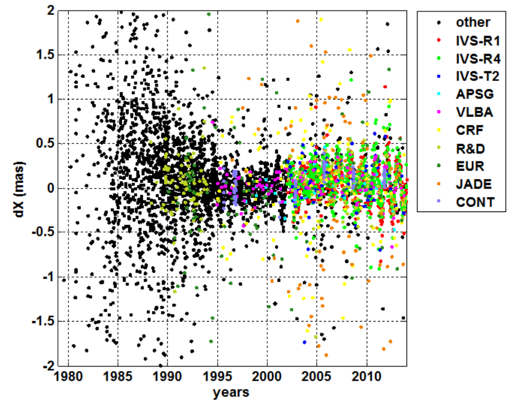

Fig. 8 GFZ VLBI solution: adjustments to the celestial pole X coordinate.

References

1. Boehm J., S. Boehm, T. Nilsson, A. Pany, L. Plank, H. Spicakova, K. Teke, & H. Schuh. The new Vienna VLBI software. In S. Kenyon, M. C. Pacino, and U. Marti (eds.) International Association of Geodesy Symposia, 136, doi:10.1007/978-3-642-20338-1_126, 1007–1011, 2012
2. Boehm J., L. Urquhart, P. Steigenberger, R. Heinkelmann, V. Nafisi, & H. Schuh. A priori gradients in the analysis of space geodetic observations. In Z. Altamimi, and X. Collilieux (eds.) International Association of Geodesy Symposia, 138, doi:10.1007/ 978-3-642-32998-2_17, 105–109, 2013
3. Fey A.L., D. Gordon, & C.S. Jacobs. The Second Realization of the International Celestial Reference Frame by Very Long Baseline Interferometry. IERS Technical Note. 35, Verlag des Bundesamts für Kartographie und Geodäsie, Frankfurt am Main, 2009
4. Kovalev Y.Y., L. Petrov, E.B. Fomalont, & D. Gordon. The fifth VLBA calibrator survey: VCS5. *The Astronomical Journal*, 133, doi:10.1086/511157, 1236–1242, 2007
5. MacMillan D.S., & C. Ma. Using meteorological data assimilation models in computing tropospheric delays at microwave frequencies. *Phys. Chem. Earth*, 23, 97–102, 1998
6. Mora-Diaz J.A., V. Raposo-Pulido, R. Heinkelmann, M. Xu, T.J. Nilsson, M. Karbon, L. Liu, B. Soja, C. Lu., & H. Schuh. Modeling special handling source positions in the GFZ VLBI solution. in Proc. of the 8th IVS General Meeting, this volume
7. Nothnagel A.. Conventions on thermal expansion modelling of radio telescopes for geodetic and astrometric VLBI. *Journal of Geodesy*, 83, doi:10.1007/s00190-008-0284-z, 787–792, 2008
8. Petit G., & B. Luzum. IERS Conventions (2010). IERS Technical Note. 36, Verlag des Bundesamts für Kartographie und Geodäsie, Frankfurt am Main, 2010

A Strategic Independent Geodetic VLBI Network for Europe

Denise Dale[1,2], Ludwig Combrinck[1,2], Alet de Witt[2]

Abstract Irregularities of the rotation of the Earth in space are described by the Earth Orientation Parameters (EOPs). An independent EOP network, applying the Very Long Baseline Interferometry (VLBI) technique and using the Vienna VLBI Software (VieVS), are strategically essential for Europe to minimize its reliance on foreign global support in terms of required infrastructure for the realization of such a network. The generation of independent EOPs is already achievable by countries such as the USA, the People's Republic of China, and the Russian Federation due to their large extent of land mass that allows for long baselines in both the North-South and East-West directions and thus allows for accurate determination of all EOPs. These three countries need not rely on foreign partnerships to generate EOPs, as they all have independent geodetic VLBI networks capable of determining EOPs for precise positioning, navigation, and satellite launch/orbital purposes. They also have or are developing independent Global Navigation Satellite Systems (GNSS) constellations; so does the European Union (EU). Accurate EOPs are essential for long-term orbital maintenance of GNSS constellations, leaving the EU GALILEO GNSS vulnerable and reliant on the three superpowers. Generation of accurate EOPs by Europe is not possible due to its much smaller land mass and thus smaller achievable baselines. Even though there are many radio telescopes spread across Europe, these are separated by relatively short distances. The proposed stations that will be used to investigate this independent EOP network for Europe are the WETTZELL radio telescope in Germany, two German owned radio telescopes, TIGOCONC in Concepción, Chile, and OHIGGINS in Antarctica, as well as the HartRAO radio telescope in South Africa.

1. University of Pretoria (UP), Department of Geography, Geoinformatics and Meteorology
2. Hartebeesthoek Radio Astronomy Observatory (HartRAO)

Keywords Independent European EOP network, VLBI, Earth Orientation Parameters, VieVS, GALILEO

1 Introduction

The Very Long Baseline Interferometry (VLBI) technique and equipment are currently in a period of upgrade and modernization (Schuh and Böhm, 2013). The use of VLBI has seen rapid extension for the past three decades and has gained widespread recognition (Clark, 2003). The ground-breaking precision and resolution made possible by VLBI has provided substantive contributions not only to astronomy but also to the areas of geodesy, astrometry, and spacecraft tracking. The VLBI technique is unique in that it provides milliarcsecond (mas) or even sub-milliarcsecond resolution of astronomical radio sources and allows us to measure the positions of radio sources with sub-milliarcsecond accuracy (Walker, 1999), (Thompson et al., 2007). Accurate positions of extragalactic radio sources, made possible by VLBI measurements, currently define and maintain the International Celestial Reference Frame (ICRF). Geodetic VLBI observations of extra-galactic reference sources (quasars) are used to measure the positions of participating antennas separated across continents to mm precision. The technique is also the most accurate method in both astrometry and geodesy (Sovers et al., 1998). In addition, several geodynamic, atmospheric, and astronomical parameters can be derived from the long history of VLBI measurements, which commenced in the late 1970s. Only geodetic VLBI provides the link (the Earth Orientation Parameters, or EOPs) between the ICRF and the ITRF. The EOPs provide the Earth's orientation in inertial space at a given epoch and need to be measured continuously. Furthermore, VLBI is the only technique that provides the full set of EOPs, which are indispensable for positioning and navigation on Earth and in space.

Precise tracking of satellites for Earth monitoring, gravity field and other studies (Satellite Laser Ranging (SLR)), laser ranging for studying lunar motion (Lunar Laser Ranging (LLR)), long-baseline radio interferometric observations for deciphering extra-galactic radio sources (VLBI) and the precise manoeuvring of interplanetary flights all require a precise measurement of the motions of the Earth's rotation axis. At the same time, these different geodetic observational techniques such as SLR, LLR, GNSS, and Doppler Orbitography and Radio Positioning Integrated by Satellite (DORIS) contribute to the generation of EOPs. However, only geodetic VLBI permits the changes in rotation to be measured with an unprecedented precision and resolution (Lambeck, 1988). The other geodetic systems are Earth-centered, whereas VLBI relies on the fixed positions of selected extra-galactic radio sources, which create an absolute and fixed reference frame. These measurements are crucial for the determination of Earth orientation with respect to inertial space and to the ITRF, which is a precondition for long-term monitoring, and they are crucial for the determination of other geodetic parameters, for Earth studies, including the maintenance of the ITRF and the ICRF.

The importance of determining EOPs is critically linked to the maintenance of the accuracy of GNSS orbits upon which much of the world depends for navigation in space and locating positions on Earth. Furthermore it is also essential for satellite orbit determination and spacecraft navigation, as well as deciding to insert or delete leap seconds in the UTC, which is the primary time standard by which the world regulates clocks. The EOPs are also used to obtain positions and velocities of radio antennas that define a VLBI-based ITRF, and lastly to accurately determine the geometric delay of observations in astronomy and astrometry. Providing the basis for precise positioning and navigation, geodesy is also crucial for supporting or enabling many activities and processes in a modern society.

2 Surveys and Experiments

Geodesy provides the foundation for most Earth observations as well as crucial observations of changes in the Earth's geometry, gravity field, and rotation, which are all related to mass transport in the Earth system and system dynamics. Thus, it is driven to meet many requirements of observations of global changes and observations supporting studies of the Earth system. The International VLBI Service for Geodesy and Astrometry (IVS) is an international collaboration of organizations which operate and support geodetic and astrometric VLBI work on reference systems and Earth science research in general and provides the basis for all operational activities. The geodetic VLBI data products currently available are the full set of EOPs, the TRF, the CRF, and tropospheric parameters. These are provided on a regular basis by the IVS and stem from a continuous program. The IVS currently has more than 30 network stations across the globe and is roughly supported by 40 institutions in 20 countries (Figure 1). Global participation in VLBI observations is required to obtain accurate EOPs.

To accurately determine EOPs with VLBI, very long North-South and East-West baselines between antennas are needed. North-South baselines are most sensitive to polar motion, and the East-West baselines are most sensitive to UT1 (Schuh, 2000). It is therefore crucial to include stations in high and low latitudes if pole coordinates are to be estimated with the highest accuracy. The proposed stations to be used for the independent EOP European network research are indicated in Figure 1. Covering the period from 2003 to 2014, 13 existing T2 sessions were utilized. All stations were used in the processing of the sessions. Consequently a subset of stations using only the proposed EU strategic network were then processed, to test the stability and the accuracy of the EOPs for the proposed network relative to the larger network.

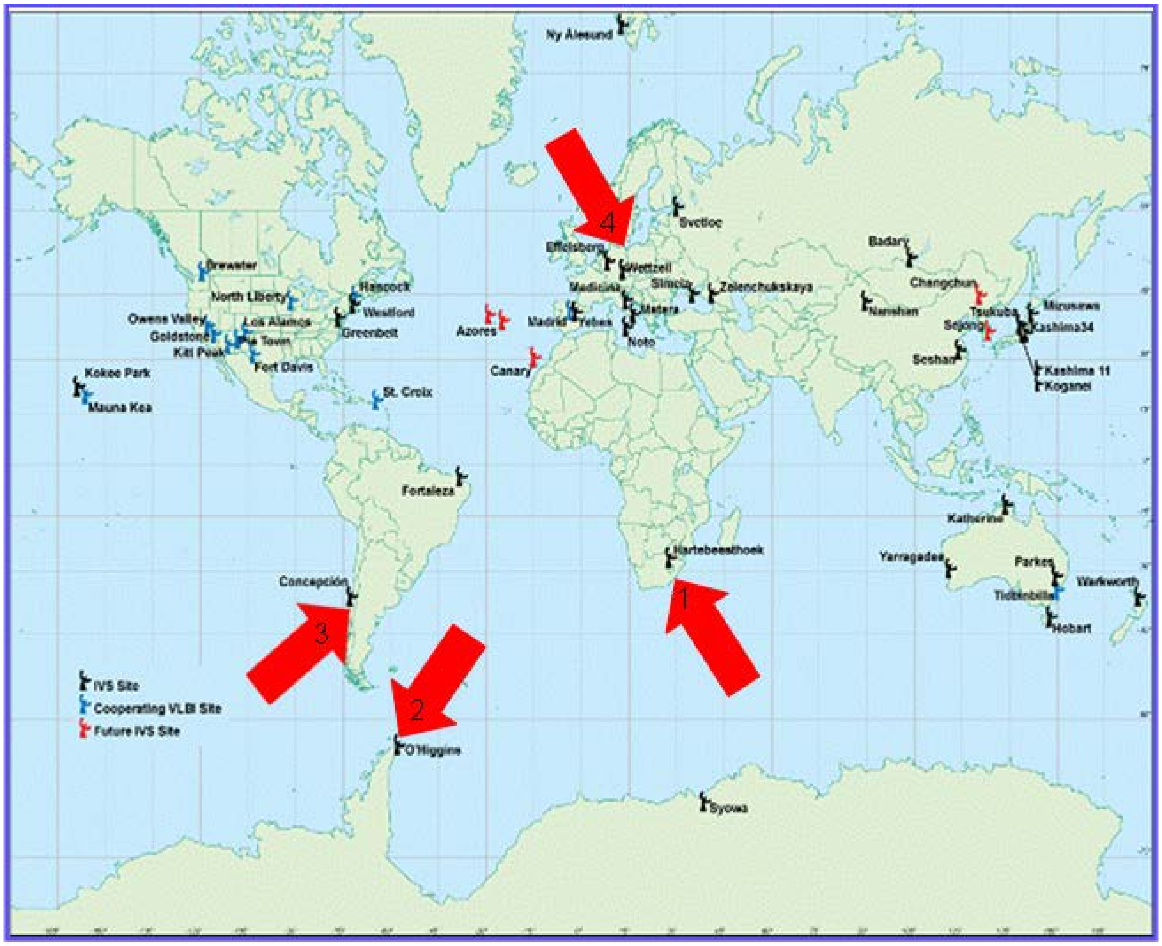

Fig. 1 World map illustrating the stations participating in the current international geodetic networks. Arrows show the proposed stations for investigating the independent EOP network for Europe: the HartRAO radio telescope in South Africa (1), OHIGGINS in Antarctica (2), TIGOCONC in Concepción, Chile (3), and WETTZELL in Germany (4).

3 Data Reduction

The VieVS software, developed by the Department of Geodesy and Geoinformation, of the Vienna University of Technology, is a MATLAB based program with an easy to use Graphical User Interface (GUI) (Böhm et al., 2012). This software is used for data analysis and evaluation of alternative strategies and network configurations. Network configurations will be changed to evaluate the impact of network density, data quality and quantity and baseline length. From the T2 sessions, the 2008 T2053 was chosen as the first session for preliminary EOP analysis. The T2053 session has 11 stations in total that participated in observations, including the proposed EU EOP network stations. The EOP results were obtained for the whole network and then for the proposed EU EOP network stations only. These results are listed in Table 1.

4 Preliminary Results

To evaluate the EOP results we obtained, a comparison was made with the EOP results obtained by the IERS; this provided a first order validation. Table 1 contains the EOPs for the whole session and for the four stations only, as well as the IERS EOP values. The IERS values should be taken as reference values for this comparison. Comparing the EOP values obtained from the four stations against the 11 stations reveals a small difference, although there are larger differences between the IERS and the four station or 11 station values. The largest difference is between the 11 station network and the IERS Ypol that showed a difference of 3.004 mas. The dut1 for all possible differences is less than 0.85 milliseconds. A special session to test this network might show an improvement of these values as scheduling will optimize source acquisition.

Table 1 The EOP results for the four-station strategic network and the complete network, as well as the IERS EOP values obtained for that session. The second row contains the estimated dut1 with errors, the third and fourth rows provide the Xpol and Ypol values with errors, and the fifth and sixth rows the dx and dy with errors.

EOPs	Strategic network	Complete network	IERS
dut1 (ms)	-306.00 ± 0.04	-306.057 ± 0.004	-305.207 ± 0.001
Xpol (mas)	-122.16 ± 0.62	-121.26 ± 0.1	-120.82 ± 0.06
Ypol (mas)	343.69 ± 0.28	344.15 ± 0.16	341.14 ± 0.06
dx (mas)	0.1 ± 0.15	0.14 ± 0.04	0.15 ± 0.04
dy (mas)	-0.09 ± 0.15	0.02 ± 0.03	0.06 ± 0.03

5 Conclusions

We demonstrated that fairly accurate EOP values can be obtained with a small network with appropriately long baselines. The fact that the TIGOCONC radio telescope is being moved to La Plata (Argentina) (i.e. changing the East - West baseline length) might change the values. The existing (small and not VGOS-compatible) TIGOCONC should be replaced by a modern fast-slewing VGOS antenna similar to the new antennas at Wettzell, instead of relying on the old antenna. This will greatly facilitate the generation of accurate and reliable EOPs using the proposed EU EOP network.

Acknowledgements

The authors acknowledge the International VLBI Service for Geodesy and Astrometry (IVS) and all its components for providing VLBI data. We are grateful to the National Research Foundation (NRF), South Africa, for supporting this project.

References

1. Böhm J., Böhm, S., Nilsson, T., Pany, A., Plank, L., Spicakova, H., Teke, K. and Schuh, H. (2012) The new Vienna VLBI Software VieVS. *IAG Symposium 2009*, 136. Ed. Kenyon S., M.C. Pacino and U. Marti, 1007–1012.
2. Clark B. G. (2003) In Radio Astronomy at the Fringe. *Astronomical Society of the Pacific Conference Series, ed. J. A. Zensus, M. H. Cohen & E. Ros*, Vol. 300, 1-58381.
3. Hale, B. (2007) Astronomy Methods. *Cambridge University Press*, p. 66. ISBN 978 0 521 53551 9.
4. International VLBI Service for Geodesy and Astrometry Network Stations `http://ivscc.gsfc.nasa.gov/stations/ns-map.html`
5. Lambeck K. (1988) Geophysical Geodesy: The Slow Deformation of the Earth. *Oxford University Press*.
6. Schuh H. (2000) Geodetic Analysis Overview, *In: IVS 2000 General Meeting Proceedings, Nancy R. Vandenberg and Karen D. Baver, editors*, p. 219-229.
7. Schuh, H and Böhm, J. (2013) Very Long Baseline Interferometry for Geodesy and Astrometry, in Guochang Xu (ed.): Sciences of Geodesy II, Innovations and Future Developments, Springer Verlag, ISBN 978-3-642-27999-7, doi: 10.1007/978- 3-642-28000-9, pp. 339-376.
8. Sovers O. J., Fanselow J. L. and Jacobs C. S. (1998) Astrometry and geodesy with radio interferometry: experiments, models, results. *Reviews of Modern Physics*,70, 1393.
9. Thompson A. R., Moran J. M. and Swenson, G. W. (2007) Interferometry and Synthesis in Radio Astronomy. *John Wiley & Sons*.
10. Walker R. C. (1999) Synthesis Imaging in Radio Astronomy II. *Astronomical Society of the Pacific Conference Series, ed. G. B. Taylor, C. L. Carilli & R. A. Perley*, Vol. 180, 433.

Axis Offset Estimation of VLBI Telescopes

Hana Krásná[1], Marisa Nickola[2], Johannes Böhm[1]

Abstract Axis offset models have to be applied for VLBI telescopes with pointing axes which do not intersect. In this work, we estimated the axis offsets for VLBI antennas in a global adjustment of suitable IVS 24-hour sessions (1984.0–2014.0) with the Vienna VLBI Software (VieVS). In particular, we focused on the two radio telescopes of the Hartebeesthoek Radio Astronomy Observatory (HartRAO) in South Africa. For the older 26-m telescope we compared the estimated axis offset values before (6699.2 ± 0.5 mm) and after (6707.3 ± 0.8 mm) the bearing repair in 2010. A comparison with axis offset estimates from other geodetic techniques, such as GNSS or conventional local survey, was made. The estimated axis offset for the newer 15-m telescope (1495.0 ± 3.4 mm) agrees with the estimated value from the GPS survey in 2007. Furthermore, we assessed the influence of differences in the axis offsets on the estimated geodetic parameters, such as station coordinates or Earth Orientation Parameters.

Keywords Axis offset, Earth Orientation Parameters, global reference frames, HartRAO

1 Introduction

The antenna axis offset (AO) is the distance between the pointing axes. Moving the antenna around its pointing axes causes a change in the position of the receiver with respect to the incoming wavefront. An additional delay τ_{AO} is created, which depends on the unit vector $\boldsymbol{s}$ in the radio source direction and on the unit vector in the direction of the fixed axis $\boldsymbol{l}$ (Sovers et al., 1998 [6]; Nothnagel, 2009 [5]):

$$\tau_{AO} = \frac{1}{c} AO \cdot \sqrt{1 - (\boldsymbol{s} \cdot \boldsymbol{l})^2} \tag{1}$$

The projection of the axis offset onto the time delay depends on the mount type of the telescope. There are three major mount types: Altitude-Azimuth mount, Equatorial (or Polar) mount, and XY mount (Figure 1).

2 Estimation of Axis Offset

Using the 24-hour IVS sessions from 1984 to 2014, we estimated the axis offsets of the VLBI telescopes within a global adjustment of the measured data in an updated version of VieVS (Böhm et al., 2012 [1]). We ran three identical global solutions where we—apart from the axis offsets—determined the terrestrial reference frame (station coordinates and linear velocities) and celestial reference frame (coordinates of the distant radio sources). Earth Orientation Parameters, clock parameters, and tropospheric parameters, such as zenith wet delays and tropospheric gradients, were estimated session-wise by a reduction from the normal equation systems. We also reduced the positions of the so-called special handling sources and of stations where the time span of included data did not allow for velocity determination. The only difference between these three solutions was the selection of the telescopes for which the axis offset was computed. In the first solution S1, the axis offset was estimated for all stations in the global adjustment.

1. Vienna University of Technology
2. Hartebeesthoek Radio Astronomy Observatory (HartRAO)

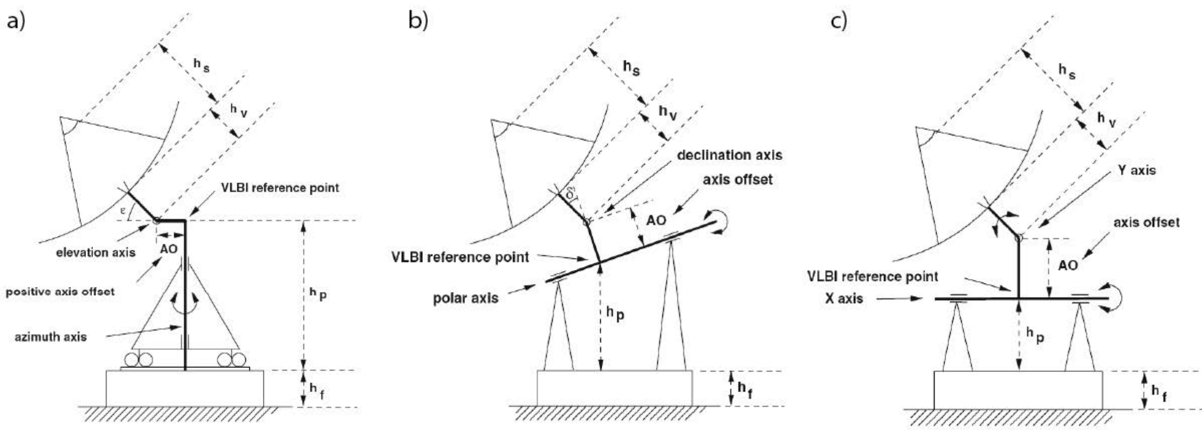

Fig. 1 (a) Altitude-Azimuth, (b) Equatorial (Polar) and (c) XY telescope mounts. Nothnagel (2009) [5].

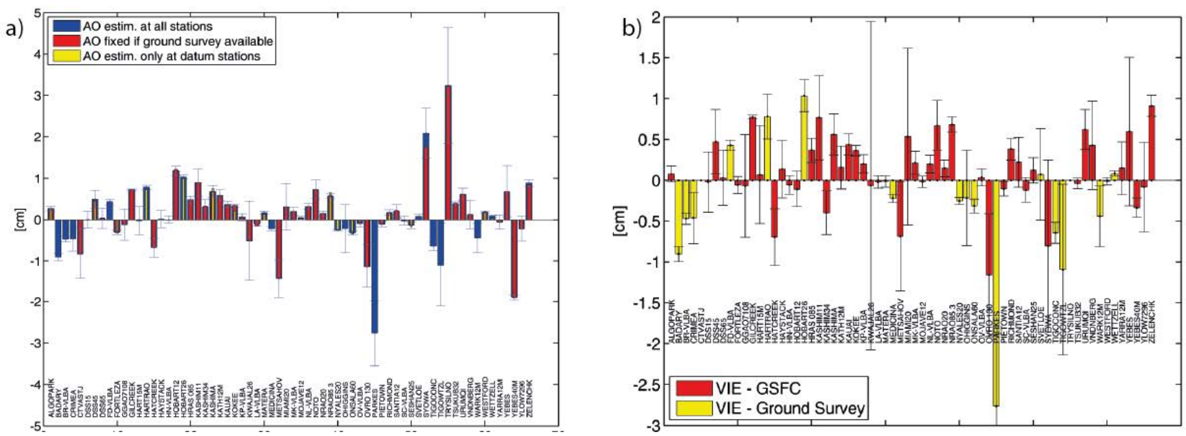

Fig. 2 a) Comparison of our three solutions: S1 (blue), S2 (red), and S3 (yellow) with respect to the a priori values of axis offsets given in `antenna-info.txt` (December 2013 version); b) Differences between our solution S2 and the solution `MacMillan2014` in red color, and between S1 and the axis offsets from ground surveys where available in yellow color.

In the second solution S2, we fixed the axis offsets to the values measured with conventional survey methods at stations where available, and in the third solution S3, the axis offset was determined only at stable stations with longer observational history used for the datum definition. The a priori values for the axis offset of the telescopes were taken from the file `antenna-info.txt` (December 2013 version) provided by the IVS analysis coordinator. In Figure 2a, the differences of the three solutions with respect to the values in `antenna-info.txt` are shown. At all stations the differences between the three individual solutions (S1, S2, and S3) agree in the range of their formal errors. Concentrating on the solution S2 (red bars)[1], where the locally estimated values were fixed to their a priori values, the largest difference w.r.t. the values given in `antenna-info.txt` is found for the telescope Trysilno, exceeding 3.2 cm (`antenna-info.txt` provides a zero value for Trysilno's axis offset). The second largest difference is found for Yebes40M, where the deviation from the reported value (value according to construction specifications) is -1.9 cm, and for the telescope Syowa we get a difference of 1.8 cm w.r.t. the value reported by L. Petrov in `antenna-info.txt`.

The file `antenna-info.txt` was updated in January 2014 with a new estimation of axis offsets by Daniel MacMillan from the GSFC VLBI Group.

[1] `http://vievs.geo.tuwien.ac.at/results`

We name this new solution `MacMillan2014` in our paper. The axis offset value for the Trysilno telescope was not updated. The comparison of the axis offsets for Yebes40M and Syowa shows that the difference of our estimates to the values computed by `MacMillan2014` decreases to -0.3 cm and -0.8 cm, respectively. The WRMS between our solution S2 and `MacMillan2014` computed over all common stations is 3.8 mm.

In Table 1 we summarize estimated values of axis offset from our solutions S1 (second column) and S3 (fourth column) for telescopes where a value from a ground survey is available (third column). As mentioned before, the estimates from S1 and S3 agree with each other within the formal errors. The WRMS error for the differences between S1 and the ground survey over the 16 antennas reaches 4.3 mm. It is close to the WRMS w.r.t. `MacMillan2014` and it can be understood as a real accuracy with which the axis offsets from the adjustment of VLBI data can be estimated.

Table 1 Axis offsets for stations where the value of axis offsets is known from local survey. Second column shows the estimated axis offset from solution S1, third column gives the value from ground survey (provided in `antenna-info.txt`), and the fourth column shows results from solution S3. Values are given in millimeters.

Telescopes	solution S1	ground survey	solution S3
Badary	-6.5 ± 0.9	$2.5 \pm$ —	
BR-VLBA	2129.9 ± 0.7	$2134.6 \pm$ —	
Crimea	-6.4 ± 2.9	-1.8 ± 0.2	
FD-VLBA	2134.1 ± 0.7	$2129.8 \pm$ —	
HartRAO	6703.1 ± 0.4	6695.3 ± 2.3	6702.6 ± 0.4
Hobart26	8201.6 ± 0.4	8191.3 ± 1.5	8201.3 ± 0.4
Medicina	1827.9 ± 0.5	$1830.1 \pm$ —	
NyAles20	521.7 ± 0.2	524.2 ± 0.2	521.6 ± 0.2
OHiggins	-2.2 ± 5.8	$0.0 \pm$ —	
Onsala60	-9.2 ± 0.4	-6.0 ± 0.4	-9.6 ± 0.4
Parkes	-27.0 ± 7.9	0.6 ± 1.0	
Svetloe	-6.8 ± 0.6	-7.5 ± 5.0	
TigoConc	-6.4 ± 1.0	0.0 ± 0.3	
TigoWtzl	-11.0 ± 10.2	0.0 ± 0.3	
Wark12M	-3.4 ± 3.5	1.0 ± 0.2	
Wettzell	0.7 ± 0.2	-0.1 ± 0.1	0.3 ± 0.2

3 HartRAO 26-m and 15-m Telescopes

The HartRAO 26 m is an equatorially mounted Cassegrain radio telescope built by Blaw Know in 1961. In October 2008 the bearing of the polar shaft of the HartRAO 26-m telescope failed. In August 2010 the telescope took part in its first post-repair geodetic VLBI observing session. Antenna axis offset values for the 26 m determined prior to the bearing failure, as given by Combrinck (1997) [2], are displayed in Table 2. Also shown are the values as determined in our current study for the period preceding the bearing failure (6699.2 ± 0.5 mm), the period following the bearing repair (6707.3 ± 0.8 mm) as well as the entire period from 1986 to 2014 (6703.1 ± 0.5 mm). The change in the axis offset after the repair does not seem to be realistic. The most probable explanation for this discrepancy is that a change in station position occurred due to the bearing failure and replacement, which then propagated into the axis offset estimation.

Table 2 HartRAO 26-m antenna axis offset determined by independent techniques.

Method	Determined by	Value
Standard value	JPL, 1961	6 706 mm
Conventional survey	M. Newling, 1993	6695 ± 3 mm
VLBI solution	C. Ma, 1995	6693.6 ± 2.5 mm
VLBI solution	M. Eubanks, 1995	6692.5 ± 1.5 mm
HartRAO GPS	L. Combrinck, 1995	6695.6 ± 2.3 mm
VLBI solution	C. Ma, 1996	6688.8 ± 1.8 mm
Local tie survey	Michel et al. (2005) [4]	6695 ± 2.5 mm
VieVS solutions:		
Before repair (1986–2008.8)	our estimate	6699.2 ± 0.5 mm
After repair (2010.6–2014.0)	our estimate	6707.3 ± 0.8 mm
1986–2014.0	our estimate	6703.1 ± 0.5 mm

Table 3 HartRAO 15-m antenna axis offset determined by independent techniques.

Method	Determined by	Value
GPS survey	A. Combrink, 2007	1495 mm
VLBI solution (from 1st IVS sessions)	GSFC, D. Gordon & S. Bolotin, 2012	1464 mm
VLBI solution	*MacMillan*2014	1494.1 ± 2.6 mm
VieVS solution	our estimate	1495.0 ± 3.4 mm

Hart15M is a 15-m altitude-azimuth radio telescope built as a Square Kilometre Array (SKA) prototype in 2007 and converted to an operational geodetic VLBI antenna during 2012. In October 2012, Hart15M started its observations within the IVS schedules. In Table 3, the antenna axis offset values for the 15 m as determined from a GPS survey by Attie Combrinck in January 2007 and a first VLBI solution by David Gordon and Sergei Bolotin from GSFC using data from October 2012 geodetic VLBI experiments R4554 and R4555, are taken from the HartRAO Web page [3]. Our estimate of the axis offset value 1495.0 $\pm$ 3.4 mm agrees within the formal error with the estimates from `MacMillan2014`.

4 Comparison of EOP and TRF

In Figures 3 and 4 the propagation of a mismodeled axis offset into the coordinates and velocities, respectively, of the estimated terrestrial reference frame (TRF) is shown. Plotted are the differences between our solution S2 and a solution where the axis offsets for the telescopes were fixed to the values in `antenna-info.txt`. The projection of axis

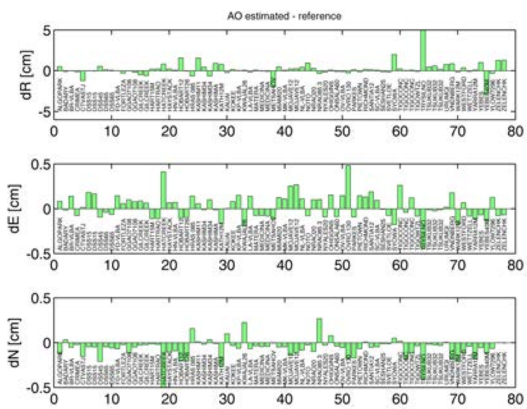

Fig. 3 Differences in the estimated TRF (coordinates): solution S2 minus solution where axis offsets were fixed to values provided in `antenna-info.txt` (December 2013 version).

offset onto the measured time delay changes with the cosine of the elevation angle; therefore, if not enough observations under various elevation angles at the particular stations are provided, it comes to the propagation of errors into the estimated coordinates and velocities of the stations. The largest difference can be seen in the height component of station Trysilno, i.e., 5.9 cm, followed by the difference at stations Yebes40M and Syowa, where the co-estimation of the axis offset changed the value of the estimated height by -2.9 cm and 2.0 cm, respectively. The differences in the horizontal plane are below 0.5 cm at all stations. The estimated velocities of the two solutions differ by up to 2 mm/yr in the height component and by up to 0.5 mm/yr in the east and north components.

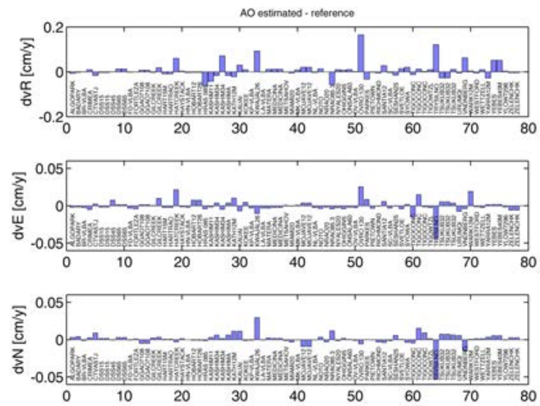

Fig. 4 Differences in the estimated TRF (velocities): solution S2 minus solution where axis offsets were fixed to values provided in `antenna-info.txt` (December 2013 version).

Differences in all five Earth Orientation Parameters estimated in solution S2 w.r.t. the solution with antenna axis offsets fixed to values given in `antenna-info.txt` are shown in Figure5. Affected are the three Earth Rotation Parameters (ERP)—x-pole, y-pole and dUT1—which are connected to the terrestrial reference frame. For sessions which included telescopes with a larger correction of the axis offset, the difference in the estimated ERP reaches up to 0.5 mas for the pole coordinates and 0.03 μs for dUT1.

5 Conclusions

An axis offset is projected onto the time delay with the cosine of the elevation angle; therefore a correlation with tropospheric delay, clock parameters, and station position can occur. We compared our estimates of the axis offsets with the latest values (January 2014) provided by D. MacMillan (GSFC VLBI Group). The largest differences reach up to 1 cm. The WRMS between both solutions for common stations is 3.8 mm. We focused on the HartRAO 26-m telescope, which had undergone a critical south polar bearing failure

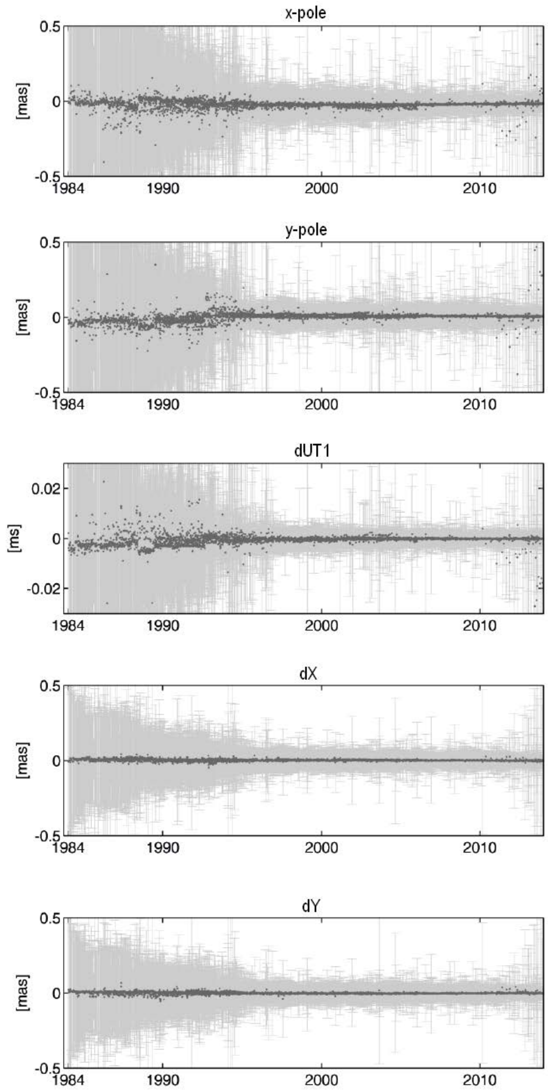

Fig. 5 Differences in the Earth Orientation Parameters estimated in solution S2 w.r.t. a solution with fixed antenna axis offsets to values given in `antenna-info.txt` (December 2013 version).

in 2008, and on the newly operational Hart15M. The estimated axis offset of the 26-m telescope before and after the bearing repair in 2010 differs by 8.1 ± 1.3 mm, while the estimated value for the 15 m agrees to within its formal error with the values obtained by `MacMillan2014` and by GPS (HartRAO Web page [3]). Our estimates will be compared with values from a local tie survey, which took place at HartRAO during March 2014, as soon as the survey results become available.

Acknowledgements

The authors acknowledge the International VLBI Service for Geodesy and Astrometry (IVS) and all its components for providing VLBI data. Johannes Böhm and Hana Krásná are grateful to the Austrian Science Fund (FWF) for supporting the project Integrated VLBI P23143-N21.

References

1. Böhm J., S. Böhm, T. Nilsson, A. Pany, L. Plank, H. Spicakova, K. Teke and H. Schuh. The new Vienna VLBI Software VieVS. *IAG Symposium 2009*, 136. Ed. Kenyon S., M.C. Pacino and U. Marti, 1007–1012, 2012.
2. Combrinck W. L. and C. L. Merry. Very long baseline interferometry antenna axis offset and intersection determination using GPS. *J Geophys Res*, 102(B11), 24,741–24,743, 1997.
3. Hartebeesthoek Radio Astronomy Observatory (HartRAO). HartRAO 15m radio telescope details. *http://www.hartrao.ac.za/ht15m_factsfile.html*
4. Michel V., G. Roesch and J. Long. Hartebeesthoek Colocation Survey. *IERS Technical Note*, 33, 100–109, 2005.
5. Nothnagel A. Conventions on thermal expansion modelling of radio telescopes for geodetic and astrometric VLBI. *J Geodesy*, 83(8), 787–792, 2009.
6. Sovers O. J., J. L. Fanselow and C. S. Jacobs. Astrometry and geodesy with radio interferometry: experiments, models, results. *Rev. Mod. Phys.* 70(4), 1393–1454, 1998.

The Usage of Recursive Parameter Estimation in Automated Reference Point Determination

Torsten Lossin[1], Michael Lösler[2], Alexander Neidhardt[3], Rüdiger Lehmann[1], Swetlana Mähler[4]

Abstract The Geodetic Observatory Wettzell (GOW) is one of the core stations within the International Earth Rotation and Reference Systems Service (IERS). The research facility is operated by the Federal Agency for Cartography and Geodesy (Bundesamt für Kartographie und Geodäsie, BKG) and the Research Institute for Satellite Geodesy (Forschungseinrichtung Satellitengeodäsie, FESG) of the Technische Universität München (Technical University Munich, TUM). The observatory hosts several geodetic space techniques, including permanent receivers for the Global Navigation Satellite Systems (GNSS), optical telescopes for Satellite Laser Ranging (SLR), and radio telescopes for Very Long Baseline Interferometry (VLBI). To combine these techniques the geodetic reference points of each technique and therefore the relative geometries (local ties) must be known with higher-level accuracy. To enhance the reliability, the Global Geodetic Observing System (GGOS) calls for continuous measurements and automated determination of the reference points. In 2013 the monitoring system HEIMDALL was installed at the GOW to derive the reference point of one of the TWIN radio telescopes in an automated way. Thirty single epochs were carried out from March to July 2013. The results of these epochs were combined by recursive parameter estimation. The advantage of this approach is the consideration of all former results and uncertainties. These combined results enable a reliable assessment to prove the stability of the reference point of the new radio telescope.

1. University of Applied Sciences Dresden, Germany
2. University of Applied Sciences Frankfurt am Main, Germany
3. Forschungseinrichtung Satellitengeodäsie, Technische Universität München, Geodetic Observatory Wettzell, Germany
4. Federal Agency for Cartography and Geodesy, Geodetic Observatory Wettzell, Germany

Keywords Recursive parameter estimation, Kalman filter, IVS, reference point, automated determination

1 Introduction

The GOW with its co-located geodetic space techniques is one of the core stations within the IERS [Schlüter et al., (2007)]. In order to derive a high-precision reference frame like the International Terrestrial Reference Frame (ITRF), the geometric relationships (local ties) between the single reference points of the co-located instruments of these space techniques have to be known with higher-level accuracy. In this context the GGOS calls for a sub-mm estimation of the local ties along with continuous measurements and an automated determination of the reference points to increase the reliability (cf. [Niell et al., (2006)], [Plag and Pearlman, (2009)]). To achieve these requirements, the monitoring system HEIMDALL was first installed in 2010 for stability testing of the monument of the Radio Telescope Wettzell (e.g., [Neidhardt et al., (2010)]). Based on these investigations, HEIMDALL was installed at GOW in 2013 in order to monitor and determine the geodetic reference point of the southern antenna of the TWIN Radio Telescope Wettzell (TTW2) in an automated and continuous way. In total, 30 single reference point determinations were carried out under different configurations. To enhance the reliability of the parameter estimation, the recursive Kalman filter technique was used to combine these single results.

2 Brief Description of Kalman Filter

Recursive least squares adjustment and Kalman filter techniques can be introduced, if observations are only available from time to time and if interim solutions are required. The main areas of applications are e.g., the navigation and control of vehicles or the monitoring of buildings (cf. [Heunecke et al., (2013)]). With the advent of automated IVS reference point determination, recursive filters were introduced for data handling and processing (e.g., [Lösler et al., (2013a), Lösler et al., (2014)]). Based on an existing solution $\mathbf{\hat{x}_{k-1}}$ an improvement $\delta\mathbf{\hat{x}_{k-1}}$ should be achieved by adding further observations $\mathbf{l_k}$. For this purpose, the vector of observations can be separated into two uncorrelated vectors $\mathbf{l_{k-1}}$ and $\mathbf{l_k}$ and two associated variance-covariance-matrices $\mathbf{C_{l_{k-1}}} = \sigma_0^2\mathbf{Q_{l_{k-1}}}$ and $\mathbf{C_{l_k}} = \sigma_0^2\mathbf{Q_{l_k}}$, where k denotes the different observation epochs and σ_0^2 is the a-priori variance factor. The solution is given by

$$\begin{aligned}\mathbf{\hat{x}_k} = (\mathbf{A_{k-1}^T Q_{l_{k-1}}^{-1} A_{k-1}} + \mathbf{A_k^T Q_{l_k}^{-1} A_k})^{-1} \\ (\mathbf{A_{k-1}^T Q_{l_{k-1}}^{-1} l_{k-1}} + \mathbf{A_k^T Q_{l_k}^{-1} l_k})\end{aligned} \tag{1}$$

or by

$$\begin{aligned}\mathbf{\hat{x}_k} = (\mathbf{Q_{\hat{x}_{k-1}}^{-1}} + \mathbf{A_k^T Q_{l_k}^{-1} A_k})^{-1} \\ (\mathbf{Q_{\hat{x}_{k-1}}^{-1} \hat{x}_{k-1}} + \mathbf{A_k^T Q_{l_k}^{-1} l_k})\end{aligned} \tag{2}$$

if

$$\begin{aligned}\mathbf{\hat{x}_{k-1}} &= (\mathbf{A_{k-1}^T Q_{l_{k-1}}^{-1} A_{k-1}})^{-1}(\mathbf{A_{k-1}^T Q_{l_{k-1}}^{-1} l_{k-1}}) \\ &= \mathbf{Q_{\hat{x}_{k-1}} n_{k-1}},\end{aligned} \tag{3}$$

and its associated cofactor-matrix $\mathbf{Q_{\hat{x}_{k-1}}}$ is derived by the observations $\mathbf{l_{k-1}}$, where $\mathbf{A}$ is a Jacobi matrix, which contains the partial derivatives with respect to the unknown parameters (cf. [Koch, (1999)]). The cofactor-matrix $\mathbf{Q_{\hat{x}_k}}$ of the estimated parameters $\mathbf{\hat{x}_k}$ can be derived by

$$\begin{aligned}\mathbf{Q_{\hat{x}_k}} &= (\mathbf{Q_{\hat{x}_{k-1}}^{-1}} + \mathbf{A_k^T Q_{l_k}^{-1} A_k})^{-1} \\ &= \mathbf{Q_{\hat{x}_{k-1}}} - \mathbf{K_{k-1,k} A_k Q_{\hat{x}_{k-1}}}\end{aligned} \tag{4}$$

where $\mathbf{K}$ is the Kalman gain matrix.

$$\mathbf{K_{k-1,k}} = \mathbf{Q_{\hat{x}_{k-1}}} + \mathbf{A_k^T}(\mathbf{Q_{l_k}} + \mathbf{A_k Q_{\hat{x}_{k-1}} A_k^T})^{-1} \tag{5}$$

Substituting $\mathbf{K}$ in Equation 2, the parameter vector follows recursively by adding the observations $\mathbf{l_k}$ to the prior results.

$$\begin{aligned}\mathbf{\hat{x}_k} &= \mathbf{\hat{x}_{k-1}} + \delta\mathbf{\hat{x}_{k-1,k}} \\ &= \mathbf{\hat{x}_{k-1}} + \mathbf{K_{k-1,k} d_{k-1,k}} \\ &= \mathbf{\hat{x}_{k-1}} + \mathbf{K_{k-1,k}}(\mathbf{l_k} - \mathbf{A_k \hat{x}_{k-1}})\end{aligned} \tag{6}$$

If the vector $\mathbf{\hat{x}_{k-1}}$ contains time-dependent state parameters in a dynamic system, the linear differential equations

$$\mathbf{\tilde{x}_k} = \mathbf{T_{k-1,k} \hat{x}_{k-1}} + \mathbf{Bw} \tag{7}$$

$$\mathbf{Q_{\tilde{x}_k}} = \mathbf{T_{k-1,k} Q_{\hat{x}_{k-1}} T_{k-1,k}^T} + \mathbf{BQ_w B^T} \tag{8}$$

can be introduced to transform the state vector and its cofactor-matrix between the times t_{k-1} and t_k. Here, the matrix $\mathbf{T_{k-1,k}}$ contains the state-transition model and $\mathbf{Bw}$ describes the process noise together with the variance-covariance-matrix $\mathbf{C_w} = \sigma_0^2\mathbf{Q_w}$ (e.g., [Heunecke et al., (2013)]). Again, Equations 4–6 can be used to merge the transformed parameters $\mathbf{\tilde{x}_k}$ and the newer observations $\mathbf{l_k}$ w.r.t. the time t_k. Tests of significance can be applied to find an optimal set of (additional) parameters (cf. [Lösler et al., (2014)]).

Recursive least squares and Kalman filter methods allow a continuing estimation of the state parameters, which include all available observations and uncertainties. As it can be seen in Equations 4 and 5, the recursion requires less memory.

3 Monitoring of TWIN Telescope

From March to July 2013, the monitoring system HEIMDALL was installed to observe the reference point of the VGOS radio telescope TTW2 ("southern tower"). Due to the inaccessibility of the geodetic reference point, indirect observation strategies have to be performed (e.g., [Dawson et al., (2007)]). For this reason 26 1.5″ Corner Cube Reflectors (CCR) were installed on the turnable part of the radio telescope. Figure 1 shows the mounted CCRs at the telescope cabin and the back-structure of the antenna. In order to determine the geodetic reference point, the positions of these CCRs must be observed in different telescope orientations. The resulting trajectories can be used to estimate the reference point and additional telescope parameters, such as the axis-offset (cf. [Dawson et al., (2007), Lösler, (2009)]).

Fig. 1 Reflections from the installed 1.5″ CCR at the cabin and the timbering of the TTW2.

Based on the azimuth and elevation angles from a calibration schedule for the antenna, HEIMDALL predicts the position of each mounted target and selects the observable ones with respect to the known coordinates of the observing total station. Depending on the azimuth and elevation angles of the radio telescope, the angle of incidence of each mounted target is changing. Glass body prisms cause systematic errors because of the refraction on the surface of the glass body (e.g., [Rüeger, (1990)]). These errors can be divided into lateral and radial effects. The order of magnitude depends on the dimension of the glass body and the angle of incidence and can exceed the 1-mm level. Thus, the observed polar elements of the total station (direction, zenith angle and slope distance) should be corrected (cf. [Lösler et al., (2013a)]). Moreover, air temperature, pressure and humidity were observed for an Electronic Distance Measurement (EDM) compensation. The temperature of the monument was also recorded to reduce the spatial influence of the radio telescope expansion (cf. [Nothnagel, (2009)]). In order to collect reliable data, a high-precision total station TS30 (Leica) was used, which was partially supported by a TCA2003 (Leica). Table 1 summarizes the manufacturer's specifications of both instruments.

Table 1 Manufacturer specifications of the total stations.

Type	TS30	TCA2003
Direction	0.15 mgon	0.15 mgon
Zenith angle	0.15 mgon	0.15 mgon
Distance	0.6 mm + 1 ppm	1.0 mm + 1 ppm

To analyze the impact of the configuration on the spatial position of the reference point and its uncertainty, different monitoring configurations were realized. In total, three campaigns including 30 single monitoring epochs were carried out from March to July 2013, which differ in the number of telescope orientations, the number of involved total stations and the number of stand points (cf. [Lossin, (2013)]. A selection of different network designs is shown in Figure 2.

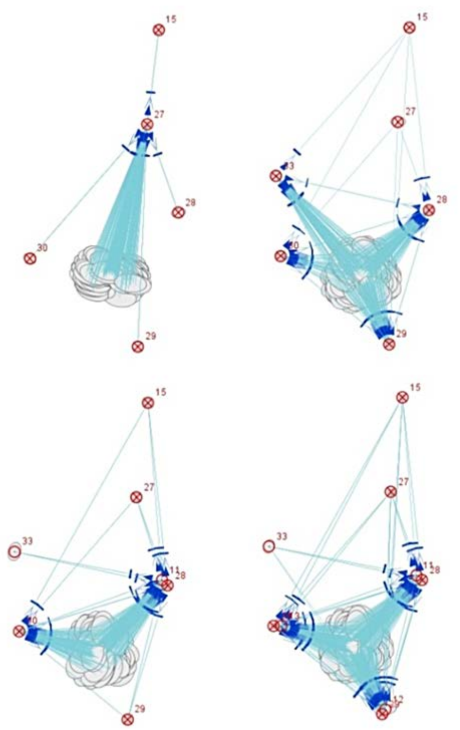

Fig. 2 Results of free adjustment with different monitoring configurations. Monitoring epochs carried out by one total station (top) and two total stations (bottom).

4 Analysis and Results

A free network adjustment was carried out to process the redundant observations in order to connect multiple survey points and to get the coordinates and the uncertainties of the observed points for each single measurement experiment. Six stable concrete pillars of the ground-fixed reference system at the GOW were used to define the geodetic datum of the local site network. The estimated coordinates of the observed CCRs at the telescope and the corresponding telescope orientation angles were used to determine the reference point and additional telescope parameters. A detailed description is given in [Lossin, (2013)].

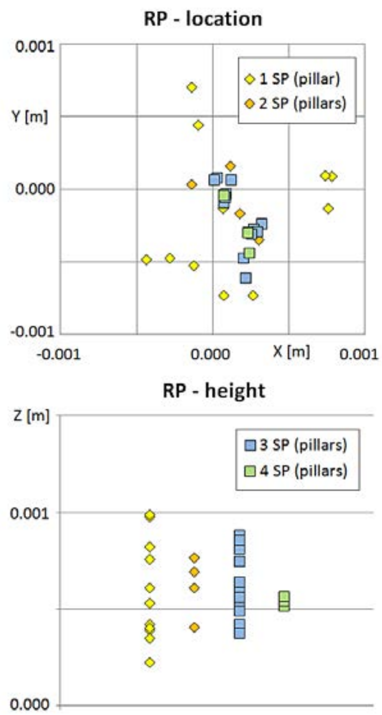

Fig. 3 Results of the reference point w.r.t. the number of stand points within a single monitoring epoch.

As shown in Figure 3, the quality of the results depends on the configuration of the monitoring epoch. If only one pillar is used as observation stand point, the 3D position of the reference point scatters within 2 mm. Including at least one additional stand point, the scattering is reduced to the 1-mm level. To increase the reliability of the results, the use of more than one pillar is recommended. According to the monitoring configuration, the uncertainties of the reference point reflect the number of used stand points within an epoch, cf. Table 2. A benefit of a second total station could not be detected and confirm prior investigations (e.g., [Lösler et al., (2013b)]).

Table 2 The changing average standard deviation of monitoring configuration according to the number of stand points.

Type	Pillar 1	Pillar 2	Pillar 3	Pillar 4
$\hat{\sigma}_{RP_x}$ [mm]	0.58	0.38	0.31	0.30
$\hat{\sigma}_{RP_y}$ [mm]	0.54	0.37	0.32	0.30
$\hat{\sigma}_{RP_z}$ [mm]	0.55	0.42	0.35	0.32

To overcome the configuration deficit and to receive a higher reliability, the determined coordinates and uncertainties of the reference point are combined by recursive parameter estimation. With respect to the elapsed time between each single epoch the coordinates and uncertainties of the reference point are concatenated.

The advantage of this method is the consideration of all former results and uncertainties with the intention to smooth and to straighten the temporal progression of the filtered results. Moreover, less favorable observation configurations can be combined by using the Kalman filter. The spatial uncertainties of the filtered reference point all remain below 1 mm during the observation period (cf. Figure 4).

5 Conclusions

The Global Geodetic Observing System suggests an automated monitoring of the reference points of the space geodetic techniques and calls for a position uncertainty within the 1-mm level. Both requirements are fulfilled at the GOW. The usage of the recursive parameter estimation is introduced to combine single epochal results. The uncertainties of the filtered reference points are 0.7 mm or even better, and confirm the stability of the examined TTW2.

Acknowledgements The authors would like to thank the colleagues of BKG Leipzig for the straightforward loan of their total station for the campaigns at the GOW.

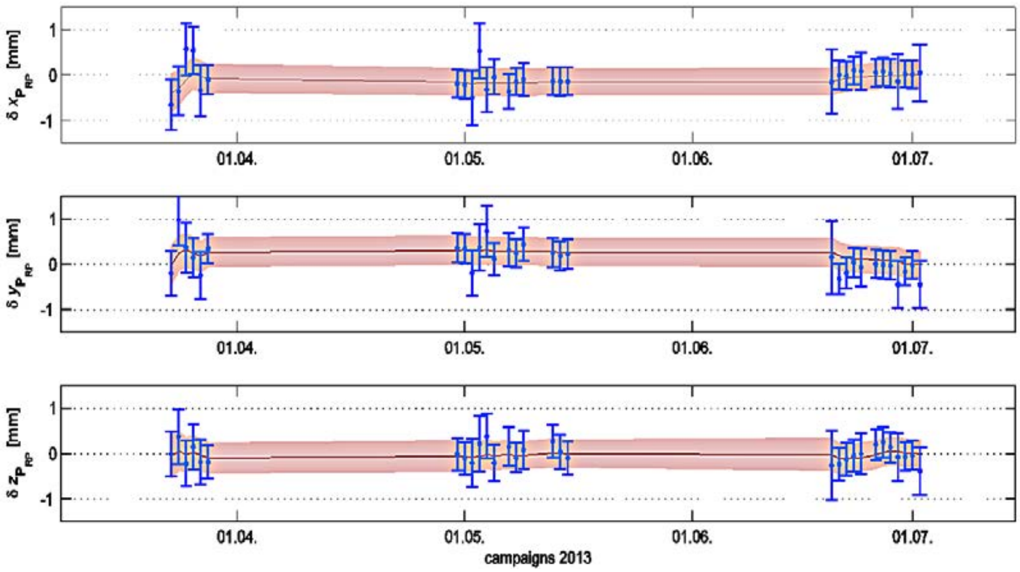

Fig. 4 Time series of the coordinates of the reference point with a 1σ error bar (blue) and the additionally calculated sequence from the recursive estimation with a 1σ error band (red).

References

[Dawson et al., (2007)] Dawson, J.; Sarti, P.; Johnston, G.M.; Vittuari, L.: Indirect approach to invariant point determination for SLR and VLBI systems: an assessment. *Journal of Geodesy*, 81(6-8), doi: 10.1007/s00190-006-0125-x, 433–441, 2007.

[Heunecke et al., (2013)] Heunecke, O.; Kuhlmann, H.; Welsch, W.; Eichhorn, A.; Neuner, H.: Handbuch Ingenieurgeodäsie: Auswertung geodätischer Überwachungsmessungen. *Wichmann*, 2nd edn, 2013.

[Koch, (1999)] Koch K.R.: Parameter Estimation and Hypothesis Testing in Linear Models. *Springer, Berlin*, 2nd edn, 1999.

[Lösler et al., (2014)] Lösler, M.; Lossin, T.; Lehmann, R.; Neidhardt, A.: Langzeitmonitoring zur Überwachung des geodätischen Referenzpunktes eines VLBI2010-Radioteleskops. In: Neuner, H. (eds.): 129. *DVW-Seminar: Zeitabhängige Messgrößen*, Wissner, 249–269, 2014.

[Lösler et al., (2013a)] Lösler, M.; Haas, R.; Eschelbach, C.: Automated and Continual Determination of Radio Telescope Reference Points with Sub-mm Accuracy - Results from a campaign at the Onsala Space Observatory. *Journal of Geodesy*, 87(8), doi: 10.1007/s00190-013-0647-y, 791–804, 2013.

[Lösler et al., (2013b)] Lösler, M.; Neidhardt, A.; Mähler, S.: Impact of Different Observation Strategies on Reference Point Determination - Evaluations from a Campaign at the Geodetic Observatory Wettzell. In: Zubko N., Poutanen, M. (eds.): *Proceedings of the 21th EVGA Working Meeting*, Finnish Geodetic Institute, 255–259, 2013.

[Lösler, (2009)] Lösler, M.: New Mathematical Model for Reference Point Determination of an Azimuth-Elevation Type Radio Telescope. *Journal of Surv Eng*, 135(4), doi: 10.1061/(ASCE)SU.1943-5428.0000010, 131–135, 2009.

[Lossin, (2013)] Lossin, T.: Untersuchungen zur Automatisierung von kontinuierlichen Bestimmungen des IVS-Referenzpunkts am Twin Radioteleskop Wettzell. *Master Thesis*, Dresden/Munich, unpublished, 2013.

[Neidhardt et al., (2010)] Neidhardt, A.; Lösler, M.; Eschelbach, C.; Schenk, A.: Permanent Monitoring of the Reference Point of the 20m Radio Telescope Wettzell. In: Behrend, D.; Baver, K. D. (eds.): *IVS 2010 General Meeting Proceedings*, Greenbelt MD, NASA/CP-2010-215864, 133–137, 2010.

[Niell et al., (2006)] Niell, A.; Whitney, A.; Petrachenko, B.; Schlüter, W.; Vandenberg, N.; Hase, H.; Koyama, Y.; Ma, C.; Schuh, H.; Tuccari, G.: VLBI2010: Current and Future Require-ments for Geodetic VLBI Systems. In: Behrend, D., Baver, K. D. (eds.): *IVS Annual Report 2005*, NASA/TP-2006-214136, 131–135, 2006.

[Nothnagel, (2009)] Nothnagel, A.: Conventions on thermal expansion modelling of radio telescopes for geodetic and astrometric VLBI. *Journal of Geodesy*, 83(8), doi: 10.1007/s00190-008-0284-z, 787–792, 2009.

[Plag and Pearlman, (2009)] Plag H. P.; Pearlman, M. (eds.): The Global Geodetic Observering System. Meeting the Requirements of a Global Society on a Changing Planet in 2020. *Springer, Berlin*, 2009.

[Rüeger, (1990)] Rüeger, J.M.: Electronic Distance Measurement - An Introduction. *Springer, Heidelberg/Berlin*, 3rd edn, 1990.

[Schlüter et al., (2007)] Schlüter, S.; Brandl, N.; Dassing, R.; Hase, H.; Klügel, T.; Kilger, R.; Lauber, P.; Neidhardt, A.; Plötz, C.; Riepl, S.; Schreiber, U.: Fundamentalstation Wettzell - ein geodätisches Observatorium. *zfv*, 3, 158–167, 2007.

Impact of Seasonal Surface Displacement on Earth Rotation and Global Reference Frames

Hana Krásná, Johannes Böhm

Abstract The calculation of actual station positions requires several corrections, which are recommended by the International Earth Rotation and Reference Systems Service (IERS) Conventions (e.g., solid Earth tides and ocean tidal loading) as well as other corrections, e.g. for hydrology or atmospheric loading. To investigate the pattern of omitted non-linear seasonal motion, we estimated empirical harmonic models for selected stations within a global solution of suitable Very Long Baseline Interferometry (VLBI) sessions as well as mean annual models by stacking yearly time series of station positions. To validate these models we compare them to displacement series obtained from the Gravity Recovery and Climate Experiment (GRACE) data and to hydrology corrections determined from global models. Furthermore, we assess the impact of the seasonal station motions on the celestial reference frame as well as on Earth Orientation Parameters (EOP) derived from VLBI analysis. Additionally, we demonstrate that a harmonic signal in the station east coordinate with an amplitude of 3 mm propagates into dUT1 (UT1–UTC) with an amplitude of 0.01 ms, by using a set of artificial VLBI observations.

Keywords seasonal surface displacement, Earth Orientation Parameters, global reference frames

Vienna University of Technology

1 Introduction

The position of a station is defined in a terrestrial reference frame as a sum of the position at a certain time epoch and a linear velocity trend. For a better approximation of the actual station position, several tidal and non-tidal corrections are recommended by the International Earth Rotation and Reference Systems Service (IERS) Conventions to be applied to the station coordinates. Krásná et al. (2014) [5] showed that the difference between the modeled time series of the station position and the estimated position series includes a long-periodic signal which is omitted in the recommended a priori models. We developed two empirical models to describe the signal. The first one is a harmonic model at annual and semi-annual periods, where the corresponding amplitudes for the selected stations were estimated within a global adjustment of VLBI data, and the second model is based on a mean annual signal obtained from a stacked time series in a local coordinate system of the stations. In this work we compare our models to the GRACE-derived surface displacement monthly time series provided by M. Weigelt and T. van Dam and to hydrology loading displacement computed from the monthly GLDAS NOAH model provided by the NASA GSFC VLBI group[1] (Eriksson and MacMillan, 2014 [3].) In Section 3 we examine the propagation of the omitted seasonal signal in the station coordinates to the Earth Orientation Parameters (EOP) and the Celestial Reference Frame (CRF).

[1] `http://lacerta.gsfc.nasa.gov/hydlo`

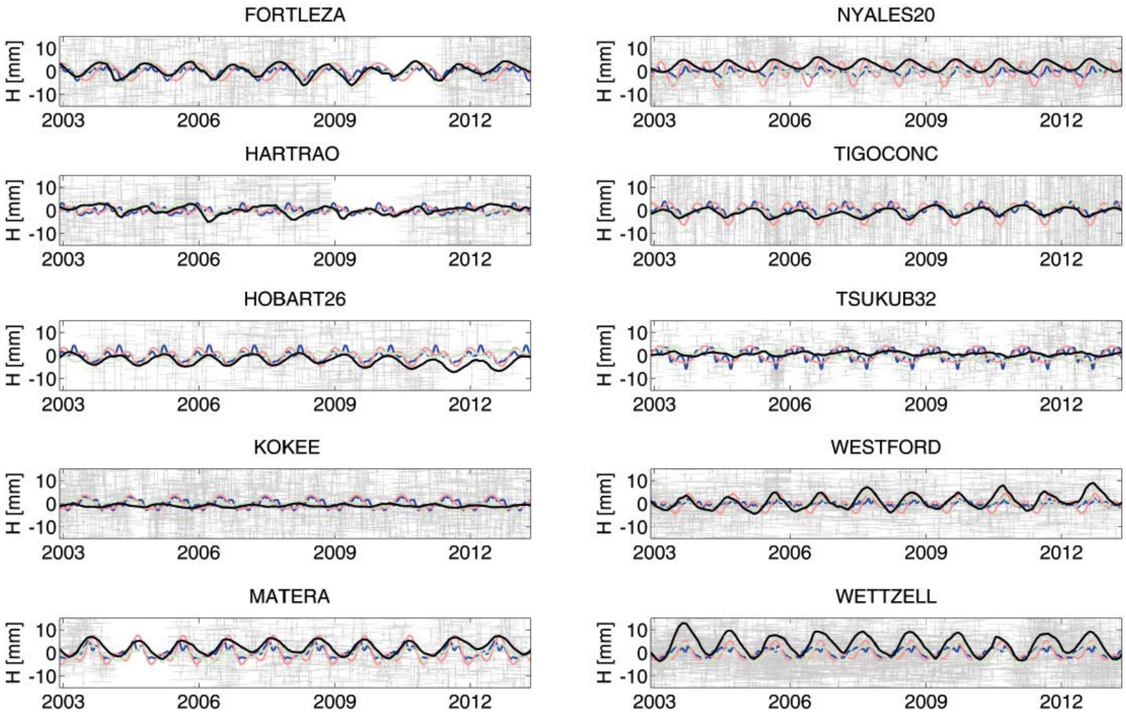

Fig. 1 Monthly GRACE time series (green color) together with the harmonic model at annual and semi-annual periods estimated from VLBI (light red color) and with the mean annual models from VLBI (blue color) at ten selected VLBI stations. In black color, the hydrology loading is plotted. The session-wise corrections of the height component from a VLBI solution without applying the seasonal models' a prioris to station positions are shown as grey error bars. For the colors, we refer to the electronic version of the paper.

2 Analysis

In our analysis, we included about 3,700 24-hour IVS sessions starting in the year 1984 until April 2013, which represent 5.6 million observations. The GRACE deformation series was provided as a monthly time series in the local coordinate system for the location of the VLBI telescopes. The analysis settings to derive the displacement from the GRACE measurements are summarized in Table 1. Figure 1 shows the surface displacement in height at ten stations which have the largest number of observations during the included time span of data. The visualization of the data starts in 2003 because this is the year when GRACE started to observe. The light red and blue curves show our empirical models: the harmonic model and the mean annual, respectively. The displacement of the VLBI telescopes derived from the GRACE data is plotted in green color. In black, we show the hydrology loading corrections. In Table 2, the correlation coefficients between the seasonal models and the displacement series from GRACE measurements (first and second columns) and from the hydrology loading model (third and fourth columns) are listed. At most of the stations, the correlation for the estimated models is higher with the hydrology loading model rather than with the displacement derived from the GRACE time series, i.e., at 70% of the stations for the harmonic model and at 80% of the stations for the mean annual model. The reason for this is that GRACE can only provide a model with a particular resolution so that the loading at specific sites cannot be retrieved.

3 Differences in Estimated EOP and CRF

To examine the propagation of the omitted signal in the station coordinates to the Earth Orientation Parameters, we artificially constructed the VLBI measurements and

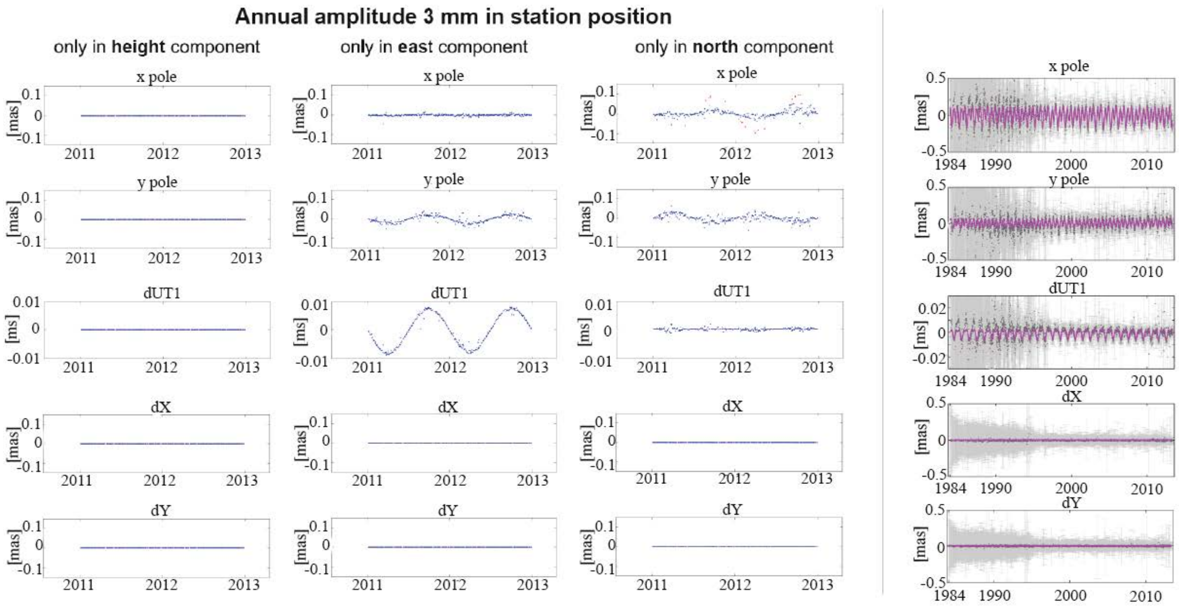

Fig. 2 Estimated EOP from artificial observations (first three columns) and from real observations (fourth column).

Table 1 Settings for GRACE deformation series. Courtesy of M. Weigelt and T. van Dam.

Source	University of Texas CSR
C20	replaced by SLR Rel05 from Cheng and Tapley (2004) [2]
Degree 1	replaced by time series of Swenson et al. (2008) [6]
Descripting	yes
Filtering	Gaussian with 350 km
GAC	not added
Frame	center of figure

Table 2 Correlation coefficients between the seasonal models and the displacement series obtained from GRACE measurements and from hydrology loading models.

VLBI telescope	Harmonic model x GRACE	Mean Annual model x GRACE	Harmonic model x Hydrological loading	Mean Annual model x Hydrological loading
Fortleza	0.65	0.61	0.41	0.71
HartRAO	0.20	0.08	0.23	0.10
Hobart26	0.11	0.02	0.66	0.71
Kokee	0.29	0.10	0.14	0.33
Matera	0.58	0.49	0.70	0.67
NyAles20	0.35	0.29	0.20	0.09
Tigoconc	0.31	0.22	0.73	0.64
Tsukub32	0.00	0.02	0.34	0.21
Westford	0.28	0.60	0.41	0.59
Wettzell	0.67	0.62	0.73	0.74

analyzed them in a standard analysis approach using the software VieVS (Böhm et al., 2012 [1]). We took the real schedules of the IVS sessions over two years from 2011.0 until 2013.0, and we filled up these schedules with the so-called zero-input time delay, i.e., with a time delay which is equal to the calculated delay from the models. In total we ran four data analyses, and in each of them, the five EOP were estimated. The first solution was the reference. In the three further analyses, a harmonic signal with an amplitude of 3 mm was added into one of the station local coordinate components (height, east, and north) at all VLBI telescopes. The difference in the estimated EOP between these three solutions with respect to the reference is plotted in the first three columns of Figure 2. It can be seen that the annual harmonic signal in the station height component does not propagate into the EOP (first column), but the neglected signal in the east coordinate (second column) propagates directly into dUT1 (causes differences up to 0.01 ms) and into the y-pole coordinate (difference up to 0.04 mas). Signals in the north station coordinate influence both the x- and y-pole coordinates. Especially in regional European networks (red dots in the upper plot in column three of Figure 2), the omitted harmonic displacement propagates directly into the x-pole coordinate, where the difference reaches up to 0.1 mas. The estimated celestial pole coordinates dX and dY are not affected. The last column of Figure 2 shows the difference in estimated EOP from the real VLBI observations between the solutions from data analysis with and without applying the harmonic displacement model. The range of the difference in the estimated EOP corresponds to the results from the simulations.

To investigate the effect of the seasonal displacement in the station coordinates on celestial reference frames, we ran the following three global solutions in which we estimated the terrestrial and celestial reference frames together with EOP. The first solution S1 was the reference, in the second solution S2 the harmonic model was applied a priori to the station coordinates, and in the third solution S3 the mean annual model was applied. We plot the differences in the estimated CRF with respect to the solution S1 for three sets of radio sources. The upper plot in Figure 3 contains only datum sources where larger differences between the estimated positions at sources in the southern hemisphere are present, which were observed only in a limited number of sessions. The middle plot of Figure 3 shows sources which were observed more than twenty times in at least two sessions. Note that the scale of this plot is two times larger than for the defining sources. The lower plot contains all radio sources. The scale of the obtained differences is five times larger when the sources with fewer than twenty observations are examined.

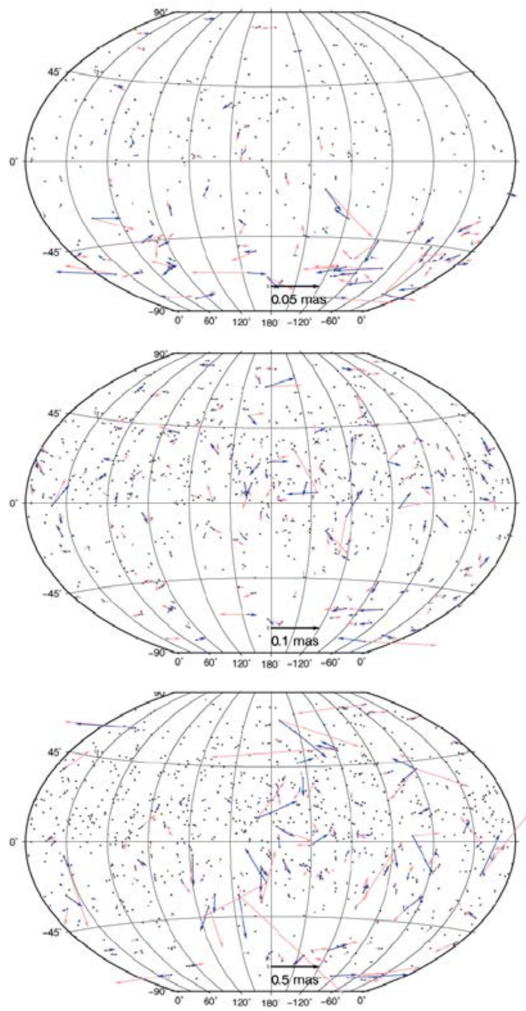

Fig. 3 Comparison of CRF from solution S2 (light red) and S3 (blue) with respect to S1 for datum sources (upper plot), sources with more than 20 observations (middle plot), and all sources (lower plot).

4 Conclusions

Two kinds of empirical models were created for unmodeled seasonal signals in station coordinates. For validation, we compared them to displacement series obtained from the GRACE data and to hydrology loading corrections. We showed that the unmodeled harmonic signal propagates from station coordinates into the Earth rotation parameters. Especially the signal in the station east coordinates with an amplitude of 3 mm propagates into dUT1 with an amplitude of 0.01 ms. The seasonal station movements do not yield any significant systematic effect on the CRF but can cause a significant change in the positions of radio sources from a small number of sessions unevenly distributed over the year.

Acknowledgements

We gratefully acknowledge Tonie van Dam and Matthias Weigelt (University of Luxembourg) for providing the surface displacements derived from GRACE gravity fields for VLBI stations. The authors acknowledge the International VLBI Service for Geodesy and Astrometry (IVS) and all its components for providing VLBI data. We are grateful to the Austrian Science Fund (FWF) for supporting the project Integrated VLBI P23143-N21.

References

1. Böhm J., S. Böhm, T. Nilsson, A. Pany, L. Plank, H. Spicakova, K. Teke, and H. Schuh. The new Vienna VLBI Software VieVS. *IAG Symposium 2009*, 136. Ed. Kenyon S., M.C. Pacino and U. Marti, 1007–1012, 2012.
2. Cheng M. K. and B. D. Tapley. Variations in the Earth's oblateness during the past 28 years. *J Geophys Res*, 109(B9), 9, 2004.
3. Eriksson D. and D. S. MacMillan. Continental hydrology loading observed by VLBI measurements. *J Geodesy*, published online, DOI 10.1007/s00190-014-0713-0, 16, 2014.
4. Petit G. and B. Luzum. IERS Conventions 2010. *IERS Technical Note* 36, 179, 2010.
5. Krásná H., Z. Malkin, and J. Böhm. Impact of seasonal station displacement models on radio source positions. *Proceedings of the Journées* 2013, In press, 2014.
6. Swenson S., D. Chambers, J. Wahr. Estimating geocenter variations from a combination of GRACE and ocean model output. *J Geophys Res*, 113(B8), 12, 2008.

IVS Rapid Tropospheric Parameter Re-combination and Comparison with GNSS Products

Cuixian Lu[1], Robert Heinkelmann[1], Julian A. Mora-Diaz[1], Christian Schwatke[2], Tobias Nilsson[1], Li Liu[1], Maria Karbon[1], Virginia Raposo-Pulido[1,3], Benedikt Soja[1], Harald Schuh[1]

Abstract Within the International Very Long Baseline Interferometry (VLBI) Service for Geodesy and Astrometry (IVS), the combination of the tropospheric zenith total delays (ZTD) and zenith wet delays (ZWD) is done for the rapid turnaround sessions IVS-R1 and IVS-R4 on a weekly basis. In this paper, the combination method is discussed. The re-combination of data sets from January 2002 to December 2013 submitted by eight IVS ACs is presented and the various submissions are compared with each other. A discussion on inhomogeneity is done and a possible future extension is treated as well. Furthermore, the combined IVS zenith delays are compared with products provided by the International Global Navigation Satellite System (GNSS) Service (IGS) for co-located stations.

Keywords VLBI, GNSS, tropospheric parameters, recombination

1 Introduction

The IVS rapid tropospheric product is a combination of ZTD and ZWD provided by various IVS Analysis Centers (ACs). Such a combination allows identification and exclusion of outliers of the individual solutions submitted by the ACs and assessment of the internal precision of tropospheric parameters derived from VLBI. The rapid combination is carried out weekly with a delay of about four weeks after the observation files were released on the IVS Data Centers [2]. Recently, the IVS tropospheric parameters rapid combination service has been migrated from DGFI [3] to GFZ. The release of the re-combined data sets from January 2002 to December 2013 has been completed (`kg6-dmz.gfz-potsdam.de/ivs/php/tropospheric_combination.php`).

There are three main user groups of the IVS tropospheric product. The first one is the IGS Troposphere Working Group (IGS TWG) [1], which aims at monitoring GNSS tropospheric parameters and comparing them with available co-located techniques. The Chair, Christine Hackman (USNO), has asked for an extension of the IVS tropospheric product to include gradients and more co-location sites [4]. The second user is EU COST Action ES1206 – GNSS4SWEC: Advanced Global Navigation Satellite Systems tropospheric products for monitoring severe weather events and climate. This action is designed to address new and improved capabilities of monitoring severe weather from concurrent developments in both the GNSS and meteorological communities. As reported in the work plan of its Working Group 3 (WG3) – GNSS for climate monitoring, one of the main tasks is to validate GNSS ZTD data by comparison with data from other techniques, e.g., VLBI [5]. The third user group is the European Permanent Network (EPN) of EUREF. One responsible EUREF AC (BKG), uses the IVS rapid troposphere product for routine comparison and achieves quite good results (`http://www.epncb.oma.be/_networkdata/siteinfo4onestation.php?station=WETT`).

In this paper, the re-combination of data from 2002 to 2013 is reported, and the results are presented. The

1. Helmholtz Centre Potsdam, GFZ German Research Centre for Geosciences, Potsdam, Germany
2. Deutsches Geodätisches Forschungsinstitut (DGFI), München, Germany
3. Instituto Geográfico Nacional, Centro Nacional de Información Geográfica, Spain

combination method, including the outlier elimination process and the weighting scheme, is also re-visited. Furthermore, a discussion on inhomogeneities is done, and the effects of earthquakes and inconsistencies in the meteorological data are treated as well. Finally, the combined IVS ZTD are compared with ZTD from the IGS at several co-locations.

2 Re-combination and Results

Currently, there are six contributing ACs, as listed in Table 1. Three other ACs (OSO, IGG, and GFSC) also participated in the past and are still welcome to re-join. Other IVS groups are invited for participation as well.

Table 1 Analysis Centers that are currently making contributions.

IVS Analysis Centers	Institutions
BKG	Bundesamt für Kartographie und Geodäsie, Leipzig, Germany
CGS	Centro di Geodesia Spaziale, Matera, Italy
DGFI	Deutsches Geodätisches Forschungsinstitut, Munich, Germany
IAA	Institute of Applied Astronomy, St. Petersburg, Russia
INA	Istituto di Radioastronomia, Istituto Nazionale di Astrofisica, Bologna, Italy
MAO	Main Astronomical Observatory, National Academy of Sciences of Ukraine, Kiev, Ukraine

The tropospheric parameters are combined on the parameter level, and the current inputs are ZTD/ZWD parameters and their formal errors. The combination strategy is a two-step approach as described in detail by Schuh and Böhm (2003) [6]. However, since the effect of inhomogeneous meteorological data is not taken into account in the combination, a further improved scheme will be considered in the future. For instance, the new ZWD can be derived by subtracting from the combined ZTD unique zenith hydrostatic delays (ZHD) that are obtained with homogeneous meteorological data instead of the directly reported ones used before.

In the re-combination, the submissions of various ACs are combined and compared with each other as well as with the combined solution. Figure 1 shows the weekly biases and standard deviations of ZTD of each AC and the combined solution at Westford, USA.

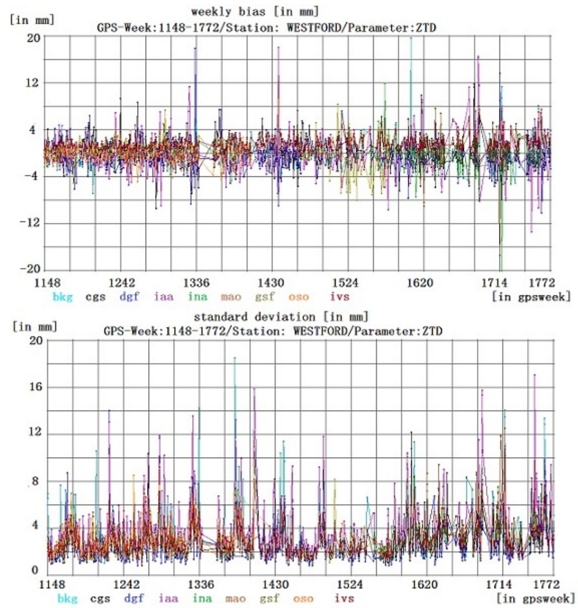

Fig. 1 Weekly bias (top) and standard deviation (bottom) of ZTD of each AC compared to the combined solution at Westford, USA.

It can be noticed that the ZTD submitted by various ACs agree well within a few millimeters, and the standard deviations are at the millimeter level. The combined series is much more smooth, stable, and robust. However, the solution from IAA shows a little larger standard deviation, which may be caused by the usage of Kalman filtering instead of the least squares adjustment adopted by the other ACs, or other differences in the software package. For this case, a factor could be applied to account for this kind of offset during the combination process.

For modeling the ZHD at the stations, the surface air pressure is needed. Thus, consistent meteorological data are of great importance to achieve the goal of homogeneous tropospheric parameters. Figure 2 gives the weekly biases of ZWD at Wettzell, Germany. A significant part of ZWD difference occurs for the DGFI solutions, where the mean value of the local pressure records are shifted to the European Centre for Medium-Range Weather Forecasts (ECMWF) mean value, while the other ACs do not apply this shift. This effect cannot be seen in the ZTD series. Therefore, more attention should be focused on the homoge-

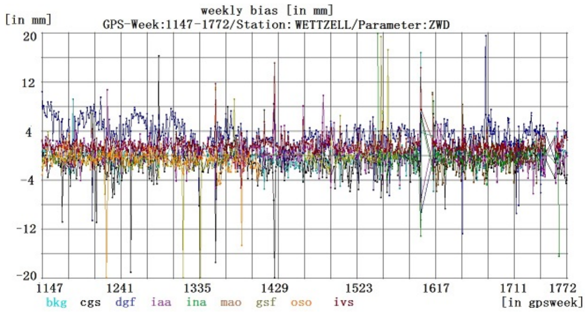

Fig. 2 Weekly bias of ZTD at Wettzell, Germany.

neous meteorological data to obtain a more consistent and stable tropospheric product.

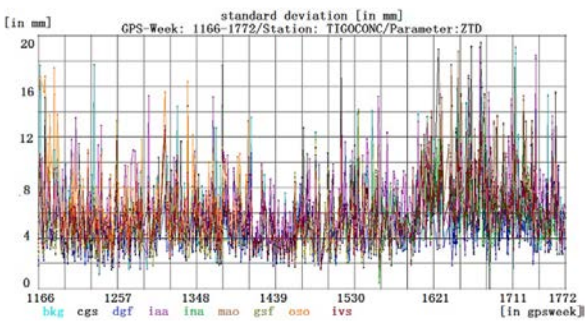

Fig. 3 Standard deviation of ZTD at Tigoconc, Chile.

An indirect effect of earthquakes on the tropospheric product can be seen in Figure 3: for TIGO/Concepción, an increase of the standard deviation from 3 mm to 6 mm happened in GPS week 1560, which is right after the 2010 Maule Earthquake in Chile. This effect results from worse a priori station coordinates. To prevent this type of distortion in the product, revised station coordinates would have to be derived and distributed among the ACs right after a major earthquake.

3 Comparison with IGS ZTD

The IVS combined ZTD are available at each UTC hour within an IVS observing session, while the IGS ZTD (`http://www.igs.org/components/dcnav/cddis_products_trop.html`) are given at UTC hours as well, but with a sampling interval of two hours. Therefore, only data at the common epochs at co-location sites are considered. Figure 4 shows the ZTD time series of both the IVS combined solution and the IGS solution at co-location site Westford, USA.

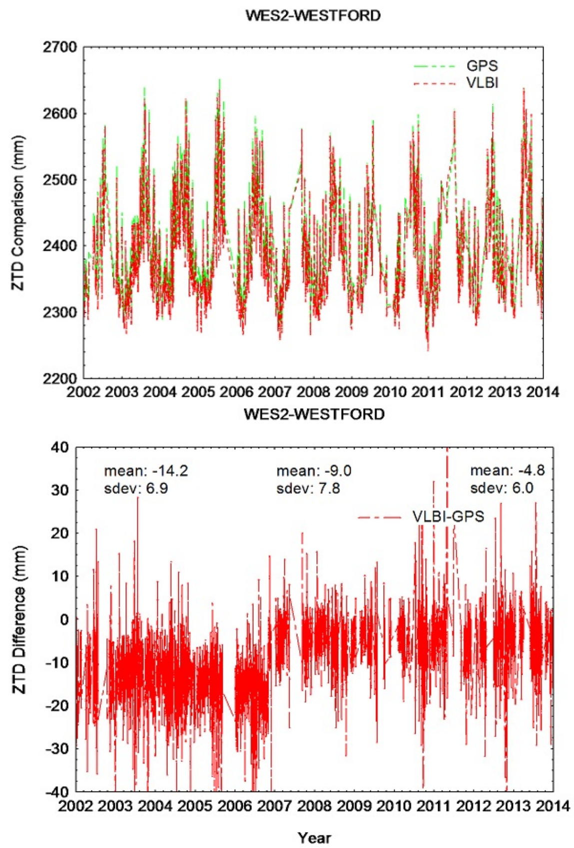

Fig. 4 ZTD time series of VLBI combined solution and IGS product (top) and the difference (bottom) at co-location site Westford, USA.

It can be seen from the top figure that the two time series show a good overall agreement. However, a significant shift of the running mean value in the ZTDs' difference (bottom figure) appeared at the end of 2006 when the mean bias decreased from -14.2 mm to -4.8 mm. The shift was caused by the change of phase center model, i.e., the adoption of absolute phase center offsets/variations (PCO/PCV) model since 5 November 2006 by the IGS. Generally, the absolute antenna model shows a significant effect on the station position, troposphere, and clock parameters [7], resulting in smaller ZTDs in this case. Similar effects of variable size occurred at all the other co-located sites.

Table 2 ZTD comparison of the VLBI combined solution and IGS product for several co-location sites.

site	IGS acronym	height diff. [m]	bias1 [mm]	bias2 [mm]	bias3 [mm]	std1. (IVS –IGS)[mm]	std2. (IVS –IGS)[mm]	std3. (IVS –IGS)[mm]
Algopark	algo	23.0	−15.0			6.3		
Kokee	kokb	10.2	−8.9	−1.6	−3.8	7.5	6.5	7.8
Nyales20	nya1	3.1	−3.8	−0.2	−1.4	4.2	3.9	4.6
Westford	wes2	1.8	−14.2	−4.8	−9.0	6.9	6.0	7.8
Wettzell	wtzr	3.1	−2.7	−0.9	−1.5	5.0	4.8	5.2
Tigoconc	conz	−9.8	−8.0	0.4	−2.1	9.0	8.4	10.4

Table 2 shows the statistics of the ZTD comparison between the IVS combined solution and IGS product at several co-locations with a breakpoint at the epoch when the IGS sites' antenna model changed (November, 2006). Bias1 and bias2 refer to the mean bias before and after the breakpoint, respectively; bias3 denotes the overall mean bias for the whole duration. The standard deviations are described in a similar way (std1, std2, and std3). In general, the IGS mean ZTDs are larger than the IVS rapid combination except for Tigoconc, which needs to be explained. The IGS ZTDs may present a systematic error regarding the PCO/PCV effect, but much better agreement can be achieved after the antenna model change of the IGS sites. The mean bias is usually smaller than 2 mm, except for Westford, where additional inhomogeneities may come from equipment changes such as an antenna receiver change or the usage of a radome of the GPS antenna. The standard deviations are about 5 mm. Such inhomogeneities do not occur in reprocessed products. However, the scope of rapid combination products is not to avoid these kind of inconsistencies but to detect and quantify them to enable them to be considered through the reprocessing. Furthermore, the height difference between GNSS and VLBI reference points will be considered in future studies.

4 Summary and Conclusions

The service of the IVS tropospheric parameter rapid combination has been recently migrated from DGFI to GFZ. At GFZ, we did a consistent re-combination of the complete IVS troposphere rapid combination product starting with the IVS-R1 and IVS-R4 sessions in January 2002. A quite good agreement and consistency can be seen between individual submissions by various ACs. The mean agreement of all AC biases at all sites are within ±1.5 mm, and standard deviations are around 3 mm. The combined solution is more robust and stable. A possible improvement of the combination strategy has been discussed. Also, both the effects of inhomoheneous meteorological data and earthquakes on the product were investigated. The results of comparison with IGS ZTDs show better agreement after the antenna model change of the IGS sites. To avoid the influence of inhomogeneous IGS zenith delays, reprocessed data are suggested for further analysis.

In future studies, we would like to extend the IVS rapid troposphere combination product to include not only IVS-R1 and IVS-R4 sessions but also the other current session types. Another goal is to decrease the time delay from four weeks to two weeks or one week between the release of the database and of the troposphere products. Besides, more information from individual ACs about their submissions are required, e.g., if the parameters are provided right at integer hours or at ±30 min. Better communication about missing or outlying results between the troposphere combination center (GFZ) and the contributing ACs are needed. Furthermore, the joint contribution of all the IVS ACs is proposed to supply the tropospheric gradients, due to the call for participation from IGS TWG for comparison with GNSS data. Ultimately, a new homogeneous IVS tropospheric long-term series at GFZ is in planning and preparation.

Acknowledgements

We would like to acknowledge all the contributing IVS Analysis Centers for their continuous efforts to provide the tropospheric parameters.

References

1. Gendt G.: Comparison of IGS tropospheric estimates, In: Proceedings of the IGS Analysis Center Workshop, edited by R.E. Neilan, P.A. van Scoy, J.F. Zumberge, Silver-Spring, USA, March 19–21, 1996, pp. 151–164
2. Heinkelmann R. and C. Schwatke: The Tropospheric Products of the International VLBI Service for Geodesy and Astrometry, IVS 2010 General Meeting Proceedings, NASA/CP-2010-215864, pp. 340–344, 2010
3. Heinkelman R.: IVSTrop: Status and recommendations of the IVS rapid troposphere combination, Proceedings of the 19th European VLBI for Geodesy and Astrometry Working Meeting, 24-25 March 2009, Bordeaux, pp. 180–182
4. Heinkelmann R.: IVS Rapid Troposphere Product – A Possible Extension Regarding the IGS TWG (C. Hackman), in: 21st Meeting of the European VLBI Group for Geodesy and Astrometry (EVGA) and 14th IVS Analysis Workshop, Espoo, Finland, 2013
5. Pacione R.: WG3: GNSS for climate monitoring WG3.2 Methodology [R], the 1st ES1206 — GNSS4SWEC Workshop, Munich, Germany, 26–28 February 2014
6. Schuh H. and J. Boehm: IVS Pilot Project - Tropospheric Parameters, Österreichische Zeitschrift für Vermessung und Geoinformation, Heft 1/2003, pp. 14–20, Wien, Österreich, 2003b
7. Schmid, R., P. Steigenberger, G. Gendt, M. Ge and M. Rothacher, Generation of a consistent absolute phase center correction model for GPS receiver and satellite antennas. Journal of Geodesy, doi 10.1007/s00190-007-0148-y, 2007

Plan and Schedule VLBI Observations of Close Approaches of Jupiter to Compact Extragalactic Radio Sources in 2016

Anastasia Girdiuk[1], Oleg Titov[2]

Abstract Very Long Baseline Interferometry is capable of measuring the gravitational delay caused by the sun's and the planets' gravitational fields. The post-Newtonian parameter γ [1] is now estimated with an accuracy of $\sigma_\gamma = 2 \cdot 10^{-4}$ using a global set of VLBI data since 1979 [2] and $\sigma_\gamma = 2 \cdot 10^{-5}$ by the Cassini spacecraft [3]. Unfortunately, VLBI observations very close to the solar limb are not possible due to strong turbulence in the solar corona. Instead of that, close approaches of the big planets to the reference quasars could be also used for testing of the general relativity theory with VLBI. Jupiter is the most appropriate among the big planets due to its large mass and relatively fast apparent motion across the celestial sphere. Here we discuss two approaches of Jupiter to reference radio sources in 2016 and propose to observe these events using the existing VLBI facilities.

Keywords VLBI, general relativity

1 Introduction

Einstein predicted the deflection of light passing by a massive body, in particular, at the solar limb about $1''.75$. This theoretical prediction was later confirmed using optical observations of stars during a total solar eclipse. In 1964, Shapiro [4] found that the light travelling in a static gravitational field undergoes additional time delay known as "Shapiro delay". The difference between two Shapiro's delays measured by two radio telescopes makes a gravitational delay [5],[6] which may be directly linked to Einstein's light deflection [7]. The gravitational delay measured with VLBI since 1979 is used to probe general relativity and estimate the post-Newtonian parameter γ. Due to the effect of the solar corona, VLBI observations closer than 4-5° from the sun are not possible. Therefore, a large set of data collected over many years is required to provide sufficient accuracy.

In contrast, close approaches of the big planets, especially Jupiter, could be observed at a very small angular distance equal to the planet's angular radius. As a result, the general relativity effects may become significant and could be observed with a set of large radio telescopes on a short time scale (1–2 days). Three appoaches of Jupiter to quasars have been observed with VLBI by now. In 1988 [8] and in 2002 [9], Jupiter passed by radio sources in observed approaches at the angular distance of more than $3'$. A large observational campaign in 2002 was arranged using the VLBA network and the 100-meter Effelsberg radio telescope. In 2008 Jupiter passed by radio source 1922-224 at the angular distance of $1.'4$. But, due to poor observing conditions and a small network (Parkes, Hobart26, Kokee, and Tsukub32), this event was observed only during four hours. (Certain of these details are included in another paper in these Proceedings).

There will be two close approaches of Jupiter to radio sources in 2016 at angular distances of less than an arcminute, including a unique event—an occultation on 9 April, 2016. Both radio sources are weak; therefore, only big antennas should be included in the provisional VLBI network. We have investigated observing conditions of these events for all suitable radio telescopes. Our results are presented in the next sections.

1. Institute of Applied Astronomy
2. Geoscience Australia

2 Theoretical Background

Recently, we have developed the formulae to link the VLBI gravitational delay and Einstein's deflection angle (details are provided in another paper of these Proceedings). It is essential that the gravitational delay may be formulated in terms of the angles between vectors (Figure 1).

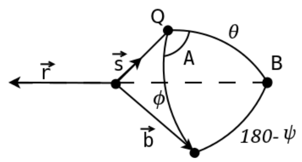

Fig. 1 Angle θ—the impact parameter, angle φ between vectors **b** and **s**, and angle ψ between vectors **b** and **r**.

The gravitational delay expressed in terms of the angles is given by

$$\tau_{GR} = \frac{2GM_J}{c^3}\frac{b\ \sin\varphi\sin\theta\cos A}{r(1-\cos\theta)} + \text{small terms} \quad (1)$$

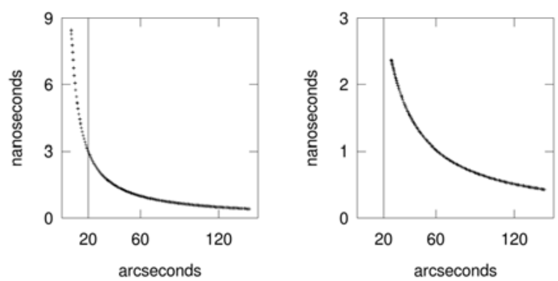

Fig. 2 Major term (Equation (1)) with respect to θ for Jupiter's approach to 1101+077 (left) and 1107+072 (right) of a baseline of length of up to 10,000 km. The vertical line separates two areas covered and uncovered by the Jupiter's disk.

The most important parameter is angle θ—the angular distance between Jupiter and the encountered quasar (Figure 2). The minimum observable distance between the radio source and Jupiter's center is equal to Jupiter's apparent radius (about 20″). For approximation of small angles, Equation 1 could be replaced by

$$\tau_{GR} = \frac{4GM_J}{c^3}\frac{b\ \sin\varphi\cos A}{R} + \text{small terms} \quad (2)$$

where R is the physical radius of Jupiter—about 70,000 km.

The small terms depending on the baseline length are negligible for larger impact parameters but should be implemented for very small angles between two objects.

Once the separation between Jupiter and the quasar approaches this limit, the gravitational delay and deflection angle grow rapidly.

3 Events of 2016

There will be two close approaches in 2016 between Jupiter and reference radio sources (1107+072 on 26 March, 2016 and 1101+077 on 9 April, 2016) (Table 1). The minimum angular distances are 26″ and 8″ for the first and second event, respectively. Jupiter's angular size is about 20″. Therefore, a unique event, occultation of the radio source 1101+077 by Jupiter, will be observed. The radio source will not be seen for about four hours during this occultation. Variations of θ with respect to UT are shown in Figure 3, while Figures 4 and 5 show the light deflection angle with respect to θ for the major and minor terms. For 1101+077, the effect of light deflection achieves its maximum value, approximately 16 mas on Jupiter's limb. The small terms grow faster ($\frac{b^2}{R^2}$), and the deflection angle measured at a very close angular separation will be dependent on the baseline length. It will reach about 3 mas for longer baselines (10^4 km). Therefore, the baseline-dependent effect could be measured by the existing geodetic VLBI facilities.

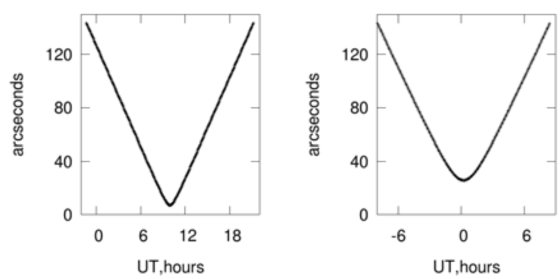

Fig. 3 Impact parameter (θ) with respect to UT for 1101+077 (left) and 1107+072 (right).

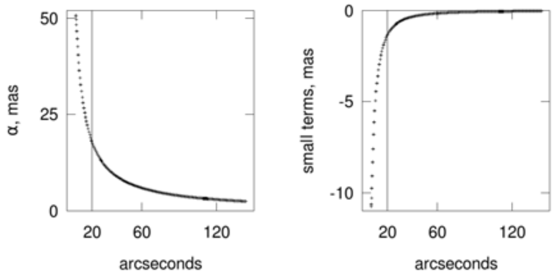

Fig. 4 Deflection angle calculated from Equation (1) (left) and from small terms (right) for 1101+077 and baseline length of 10,000 km. The vertical line separates two areas covered and uncovered by Jupiter's disk.

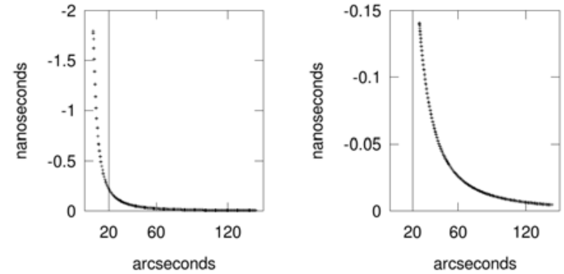

Fig. 6 Small terms (Equation (1)) with respect to θ for 1101+077 (left) and 1107+072 (right) and a baseline length of 10,000 km. The vertical line separates two areas covered and uncovered by Jupiter's disk.

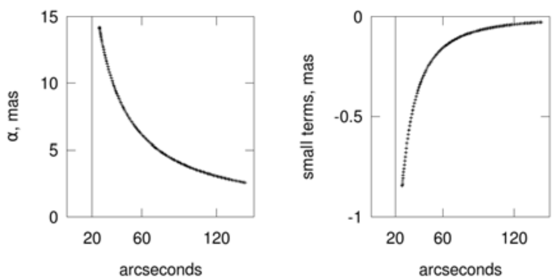

Fig. 5 Deflection angle calculated from Equation (1) (left) and from small terms (right) for 1107+072 and baseline length of 10,000 km. The vertical line separates two areas covered and uncovered by Jupiter's disk.

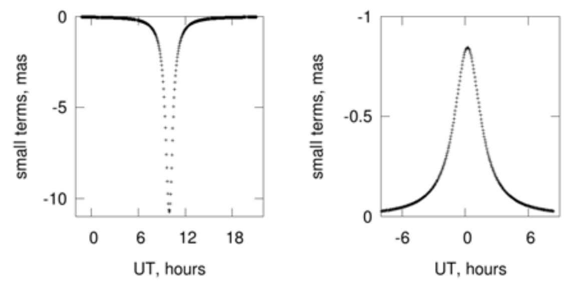

Fig. 7 Deflection angle converted from small terms (Equation (1)) with respect to UT for 1101+077 (left) and 1107+072 (right) and a baseline length of 10,000 km.

Table 1 Information about quasars.

quasar	date	θ''	Flux X(S), mJy	α, mas	other, ps
1107+072	26.03	26	~ 10 (20)	14.5	140
1101+077	09.04	20(8)	~ 38 (68)	16(46)	200(1600)

Basic information about these events in Table 1 also includes data flux densities of the radio sources in S- and X-bands. Unfortunately, both radio sources are weak; therefore, large radio telescopes are required for planning the experiments in order to keep the integration time at a reasonable level (less than five minutes).

Figure 6 shows additional contributions of the minor terms to the total delay with respect to the angle θ during the both events. The same additional contribution expressed in seconds of arc with respect to UT during both events is shown in Figure 7 (for a 10,000 km baseline).

It is important to note that the time delay for each baseline should be converted to the light deflection angle using the angle A between directions to the baseline vector and the vector to the barycentric position of the deflecting body (as shown in Figure 1). Angle A is individual in every baseline; therefore, multiplication by the factor $\cos A$ in Equation (2) is necessary to calculate the path of the observed source position correctly for each time epoch. Then the meaning of the deflection angle for every epoch will be common for all baselines regardless of their lengths (Figure 8).

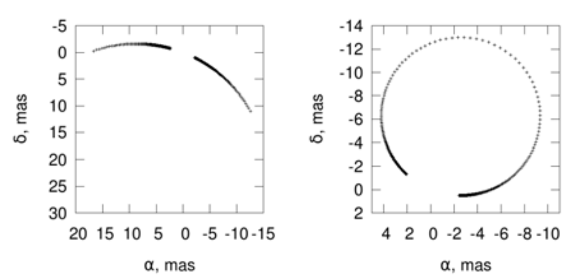

Fig. 8 Einstein's light deflection angle for 1101+077 (left) and 1107+072 (right).

4 Observational Goals

We are planning to arrange two dedicated geodetic VLBI sessions in 2016 to observe the unique astronomical events. The primary goal of this project is to test the previously proposed formulae, especially to indicate the tiny effect of minor terms at the closest angular distance between the radio source and the limb of Jupiter using a combination of baselines with different lengths, including lengths as much as 9,000 km and longer. It would be interesting to probe the predictions at the small impact parameter approach, first of all, whether the deflection angle is actually proportional to the baseline length due to effect of the minor terms in Equation (2).

Technically, we are aiming to obtain the deflection angle and the radio source positions at each observational epoch. For accurate estimation of the deflected position, one has to 1) collect as many single scans during the event as possible and 2) use as many VLBI antennas for each individual scan as possible. But, due to rather low fluxes of both radio sources, a compromise between the scan length and the number of observations must be the subject of careful consideration.

5 Technical Setup

The length scan for a single baseline is calculated as follows

$$\mathrm{scanlen} = \left(\frac{\mathrm{k} \times \mathrm{SNR}}{\mathrm{F}}\right)^2 \times \frac{\mathrm{SEFD}_1 \times \mathrm{SEFD}_2}{\mathrm{Rate}} \quad (3)$$

where k is the efficiency coefficient for S- or X-band, SNR is the adopted signal-to-noise ratio, F is the flux density of a radio source in S- or X-band, Rate represents the antenna recording rate parameters, and SEFD (System Equivalent Flux Density) represents the antenna technical parameters. Table 2 shows SEFD values for several radio telescopes suitable for observing weak radio sources.

Table 2 List of stations SEFD_X.

Svetloe	250	Zelenchuk	255
Badary	300	VLBA network	500
Parkes	200	Tsukub32	320
Kunming	600	Seshan25	700

We have calculated observing schedules of both events in different modes to provide as many observations as possible keeping the parameters below. All simulations were done with the VieVS software [10].

- SNR (S) = 20, SNR (X) = 15
- SEFD (1, 2) = 200/700
- number of channels = 14
- bandwidth = 4/16 MHz and bandwidth = 128/512 MHz
- rate ≈ 16/64 Mbps and rate ≈ 512 Mbps / 2 Gbps

Expected scan lengths at different bandwidths and other parameters kept fixed are presented in Table 3.

Table 3 Table of rates.

bandwidth	scan length 1107+072, 26.03.16 flux = 10 mJy in X band	scan length 1101+077, 09.04.16 flux = 38 mJy in X band
16 MHz		8/24 min
32 MHz		4/12 min
128 MHz	20 min	50 sec/2 min
512 MHz	4 min	40 sec/56 sec

6 Conclusions

Two close appoaches of Jupiter to weak reference radio sources will happen in 2016. These events are favorable to test some predictions of general relativity, in particular, fast changes of the light deflection angle and small baseline-dependent effects. Two 24-hour specially scheduled sessions should be organized within IVS to observe the rare astronomical events.

Acknowledgements

Anastasia Girdiuk is thankful for support by the IAG Travel Award in order to attend the IVS 2014 General Meeting.

References

1. C. Will “Theory and Experiment in Gravitational Physics”, Cambridge University Press, 1991

2. S. Lambert, A. Gontier, "On radio source selection to define a stable celestial frame", A&A , vol. 493, Issue 1, 2009, pp. 317-323, 2009.
3. B. Bertotti, L. Iess, P. Tortora, "A test of general relativity using radio links with the Cassini spacecraft", Nature, vol. 425, Issue 6956, pp. 374-376, 2003.
4. I. Shapiro "Fourth Test of General Relativity", Phys. Rev. Lett., vol. 13, Issue 26, pp. 789-791, 1964.
5. T. Eubanks (ed.) Proc. of the U. S. Naval Observatory Workshop on Relativistic Models for Use in Space Geodesy, United States Naval Observatory, Washington, D. C., 1991.
6. G. Petit, B. Luzum (eds.) IERS Conventions (2010), IERS Technical Note 36, Frankfurt am Main: Verlag des Bundesamts für Kartographie und Geodäsie, 2010.
7. A. Einstein "Die Grundlage der allgemeinen Relativitatstheorie", Annalen der Physik, vol. 354, Issue 7, pp. 769-822, 1916.
8. H. Schuh, M. Fellbaum, J. Campbell, M. Soffel, H. Ruder, M. Schneider, "On the deflection of radio signals in the gravitational field of Jupiter", Phys. Lett. A, vol. 129, Issue 5-6, pp. 299-300, 1988.
9. E. Fomalont, S. Kopeikin, "The measurement of the light deflection from Jupiter: experimental results", AJ , vol. 598, Issue 1, pp. 704-711, 2003.
10. Matthias Madzak, Sigrid Böhm, Hana Krásná, and Lucia Plank. Vienna VLBI Software Version 2.1 User Manual Web document http://vievs.geo.tuwien.ac.at/.../vievsDoc.pdf.

Simulations of Minimum Elongation from the Sun

Jing Sun[1,2], Harald Schuh[3], Geshi Tang[1]

Abstract Based on the typical IVS (International VLBI Service for Geodesy and Astrometry) networks, we evaluate how the minimum elongation angle from the Sun affects the estimation of the Earth orientation parameters (EOP). In particular, we investigate the better sky coverage and the uniform distribution of radio sources in the sky if sources closer to the Sun than 15 degrees are included in the schedule, i.e., if the minimum elongation angle is set to 4 degrees. In addition to thermal measurement noise and clock errors, tropospheric turbulences are simulated based on realistic station-dependent turbulence parameters derived from GPS time series of zenith wet delays. The improvement in the estimation of EOP is investigated by Monte Carlo simulations, which are realized by running a sequence of different solutions using the VieVS software (Vienna VLBI Software).

Keywords Elongation, schedule, Monte Carlo simulations, VieVS

1 Introduction

The quasar's elongation is the angle between the Sun and the quasar, as viewed from the Earth. As seen from Figure 1, the elongation is the angle α. In the history of IVS (International VLBI Service for Geodesy and Astrometry) geodetic VLBI observations, the minimum elongation was set to 15 degrees between 2002 and November 2013; before 2002 it was 5 degrees.

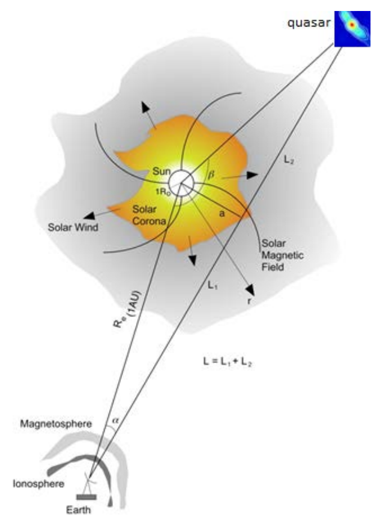

Fig. 1 The definition of quasar's elongation angle from the Sun.

If we schedule VLBI observations closer to the Sun, one of the disadvantages is the possible loss of observations because of stronger solar wind, plasma, and corona. Even worse, observations too close, e.g., on the limb of the Sun, could have an impact on antenna hardware. On the other hand, we can benefit a lot from the observations closer than 15 degrees to the Sun. Based on the data from RDV (R&D sessions with the VLBA stations) and VCS (VLBA Calibrator Survey) experiments, Lambert and Poncin-Lafitte [1] expected that the inclusion of sources closer to the Sun can improve the determination of the post-Newtonian parameter γ by 15% (even with a modest number of observations below 15 degrees per session; for instance, one to two

1. National Key Laboratory of Science and Technology on Aerospace Flight Dynamics, China
2. Shanghai Astronomical Observatory, China
3. GFZ German Research Centre for Geosciences, Germany

observations per session). Secondly, the observations closer to the Sun would be helpful to probe the solar corona as demonstrated by Soja et al. [2].

In this paper, we study the improvement of Earth orientation parameter (EOP) determination by observations closer to the Sun using Monte Carlo simulations, which are realized by running a sequence of different solutions of the VieVS software (Vienna VLBI Software) [3].

2 Scheduling Parameters

Two networks are employed here to evaluate the influence of the minimum elongation angle from the Sun. The first network is a typical nine-station network used for IVS-R1 sessions (see Figure 2). The second network is artificial and only used for this study; it includes eight stations (see Figure 3).

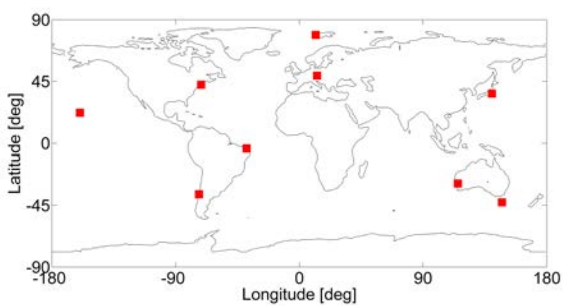

Fig. 2 A typical IVS-R1 nine-station network.

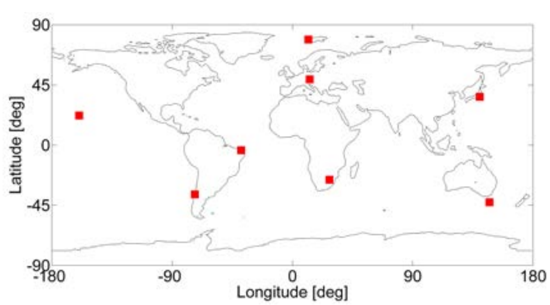

Fig. 3 An artificial eight-station network.

All the antennas are assumed to be identical in this study. The slew rate parameters are 3 deg/s and 2 deg/s in the azimuth and elevation axes, respectively. The slew acceleration in both axes is 3 deg/s^2. The same SEFD (System Equivalent Flux Density) of 2500 is used for all the antennas. The data rate is 512 Mbps. SNRs of 20 at X-band and 15 at S-band are used for all stations. A cutoff elevation angle of 5 degrees is used.

The pre-selected source list is established considering the strength, compactness, and distribution, which includes 61 suitable radio sources in total (see Figure 4). Three out of 61 sources have an elongation angle from the Sun less than 15 degrees, i.e., source 1958−179 (13.9 degrees), source 1921−293 (8.0 degrees), and source 1920−211 (4.5 degrees). As seen from Figure 4, the distribution of observed sources on the celestial sphere is improved if we consider more sources closer to the Sun.

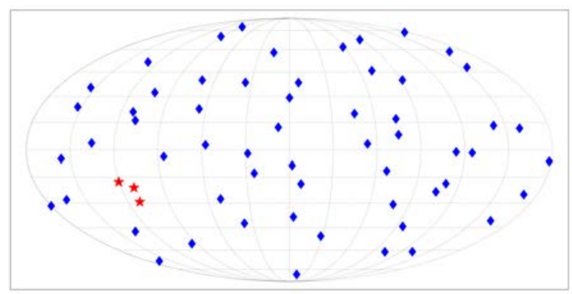

Fig. 4 Distribution of all 61 radio sources (blue diamonds) on the celestial sphere, including the three special radio sources (red stars) having an elongation angle from the Sun less than 15 degrees.

The source-based scheduling strategy of Vie_Sched (scheduling package of VieVS) with fill-in mode was employed, and one source was scheduled each time to generate all the schedules in this study [4]. The same source was not observed again within 30 minutes.

For either network, two schedules were generated with different thresholds of elongation angles. The first schedule (Schedule1) considered a minimum elongation angle of 15 degrees. The other one (Schedule2) included three special radio sources having elongation angles less than 15 degrees (the minimum elongation angle was set to 4 degrees). It is found from Schedule2 that all the stations except NYALES20 have observations on these three radio sources.

3 Simulation Parameters

In this paper Monte Carlo simulations are employed to study how the minimum elongation angle from the Sun affects the estimation of the EOP.

The Vie_Sched is directly connected to the other packages of VieVS and the simulation studies are realized by running a sequence of different packages of VieVS. Simulated VLBI observables are generated taking into account the three most important stochastic error sources in VLBI, i.e., wet troposphere delay, station clock, and measurement error [5]. In order to simulate the wet delays as realistically as possible, the turbulence theory with a dedicated strategy proposed by Nilsson and Haas [6] is applied. Those wet delays following turbulence theory take into account the covariance information between all observations at a station, and a particular series of equivalent zenith wet delays is triggered by random numbers. The turbulent troposphere is modeled using site-dependent structure constants C_n [7], effective wet heights H, and components of wind velocity (V_n and V_e). The zenith wet delay at the beginning of the time series (*zwd*0), the correlation interval (*dhseg*), and the height increment for the numerical integration (*dh*) are set to standard values. Stochastic errors of station clocks can be simulated as the sum of random walk and integrated random walk stochastic processes. Our simulations are performed with power spectral densities corresponding to Allan Standard Deviations (ASD) of 1×10^{-14} at 50 minutes, which is a typical frequency stability of current H-masers. The contribution of the measurement error to the simulated delay observables is small compared to the contributions of troposphere and clock. In our simulations a white noise (WN) of 8 ps 1-sigma Gaussian random variable is used to represent all system errors. The simulation parameters are summarized in Tables 1 and 2.

For Monte Carlo simulations, 50 sessions are simulated to detect the small difference of the EOP sigmas using the same 24-hour schedule but different realizations of noise delays, each time creating new values for zenith wet delays, clocks, and white noise. The analysis is performed for each of the simulated files, and the sample of output parameters is analyzed statistically.

Table 1 Simulation parameters.

H [m]	2000
V_n [m/s]	0.00
V_e [m/s]	8.00
zwd_0 [mm]	250
dhseg [h]	2
dh [m]	200
clock ASD	10^{-14}@50 min
WN [ps]	8

Table 2 Site-dependent C_n in $m^{-1/3}$.

Station	$C_n \cdot 10^{-7}$	Station	$C_n \cdot 10^{-7}$
FORTLEZA	2.46	TSUKUB32	3.45
HOBART12	1.60	WESTFORD	2.30
KOKEE	1.39	WETTZELL	1.50
NYALES20	0.65	YARRA12M	1.76
TIGOCONC	2.08	HARTRAO	1.34

4 Results

In the least squares parameter estimation part of VieVS, most of the estimated parameters are modeled by piecewise linear offset functions. The parameters to be estimated are troposphere parameters, clock parameters, and station positions, as well as daily EOP. The main goal of the estimation process in the simulations is to investigate the impact of observations closer to the Sun on the estimation of EOP.

Tables 3 and 4 show the detailed information on the observations to the three special radio sources for the typical IVS-R1 network and the artificial network.

Table 3 Detailed information on the observations to the three special radio sources for the typical IVS-R1 network.

Source	Elongation angle	Num of scans	Num of obs
1958-179	13.9°	5	13
1921-293	8.0°	10	10
1920-211	4.5°	9	43

Table 4 Detailed information on the observations to the three special radio sources for the artificial network.

Source	Elongation angle	Num of scans	Num of obs
1958-179	13.9°	4	11
1921-293	8.0°	11	13
1920-211	4.5°	10	30

Tables 5 and 6 show the EOP results estimated from the two schedules for the two networks. Schedule2 has great advantages for providing EOP estimation, as a consequence of its better source distribution.

Table 5 EOP determination from the two schedules for the typical IVS-R1 network.

EOP Parameter		Schedule1 (elong_min = 15°)	Schedule2 (elong_min = 4°)
Mean uncertainty [μas, μs]	xp	25.55	24.52
	yp	24.47	24.02
	dUT	1.76	1.72
	dX	21.71	21.25
	dY	20.93	20.83

Table 6 EOP determination from the two schedules for the artificial network.

EOP Parameter		Schedule1 (elong_min = 15°)	Schedule2 (elong_min = 4°)
Mean uncertainty [μas, μs]	xp	22.49	21.61
	yp	25.81	25.18
	dUT	1.63	1.59
	dX	21.50	21.28
	dY	21.57	21.26

To have a closer look at the small difference, Figure 5 plots the relative improvement of EOP determination. The average improvement of EOP determination is up to 4% just by adding three radio sources that are between 4 and 14 degrees from the Sun.

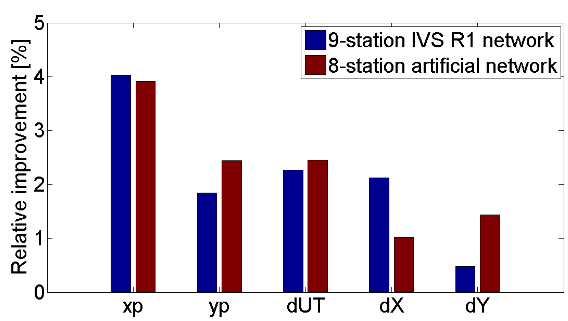

Fig. 5 Relative improvement of EOP determination.

5 Conclusions

According to the above results, a 4% improvement in the estimation of the x-pole is obtained from the second schedule. The average improvement of the pole coordinates is 3%, of the Earth rotation parameter dUT 2.4%, and of the nutation parameters 1.3%. Thus, just by adding a few radio sources with elongation less than 15 degrees to the observing schedule, an improvement of the main geodetic parameters between 0.5% and 4% is obtained. This can be explained by the better coverage of the complete sky if radio sources closer to the Sun are included in the schedule. In the future, it would also include the consideration of solar activity for the setting of minimum elongation angle.

References

1. S. Lambert and L. Poncin-Lafitte. Improved determination of γ by VLBI. *Astronomy & Astrophysics*, Volume 529, doi:10.1051/0004-6361/201016370, 2011.
2. B. Soja, R. Heinkelmann, and H. Schuh. Sun corona electron densities from VLBI and GIM data. *Proceedings of the IAG General Assembly 2013*, accepted, 2013.
3. J. Böhm, S. Böhm, T. Nilsson, A. Pany, L. Plank, H. Spicakova, K. Teke, and H. Schuh. The New Vienna VLBI Software VieVS. *Geodesy for Planet Earth, Proceedings of the 2009 IAG Symposium*, Springer Verlag, edited by St.C. Kenyon, M.C.Pacino, U.J. Marti, ISBN 978-3-642-20337-4, doi:10.1007/978-3-642-20338-1, 1007–1012, Buenos Aires, Argentina, 2012.
4. J. Sun, J. Böhm, T. Nilsson, H. Krásná, S. Böhm, and H. Schuh. New VLBI2010 scheduling strategies and implications on the terrestrial reference frames. *Journal of Geodesy*, 88(5), doi:10.1007/s00190-014-0697-9, 449–461, 2014.
5. A. Pany, J. Böhm, D. MacMillan, H. Schuh, T. Nilsson, and J. Wresnik. Monte Carlo simulations of the impact of troposphere, clock and measurement errors on the repeatability of VLBI positions. *Journal of Geodesy*, doi:10.1007/s00190-010-0415-1, 85, 39–50, 2011.
6. T. Nilsson and R. Haas. Impact of Atmospheric Turbulence on Geodetic Very Long Baseline Interferometry. *Journal of Geophysical Research*, doi:10.1029/2009JB006579, 115(B03407), 2010.
7. T. Nilsson, J. Davis, and E. Hill. Using ground based GPS to characterize atmospheric turbulence. *Geophysical Research Letters*, doi:10.1029/2009GL040090, 36, L16807, 2009.

Investigations of the Solar Corona by VLBI

Benedikt Soja, Robert Heinkelmann, Harald Schuh

Abstract The solar corona is an important target for solar research and the understanding and prediction of space weather. Several techniques have been applied in the past to determine properties of the corona, most notably, its electron density. Recently, for the first time, it was shown by the authors that Very Long Baseline Interferometry (VLBI) is capable of assessing the characteristics of the solar corona. For this paper, further investigations were performed. The electron density models were compared to those from spacecraft tracking, and correlations between solar activity, characterized by Sunspot numbers, and the electron density have been studied. In addition, the temporal variations of the density and turbulence of the corona were investigated. Here, a comparison between VLBI and coronagraph data shows that VLBI is sensitive to transient events such as coronal mass ejections.

Keywords Solar corona, ionosphere, VLBI, electron density, Coronal Mass Ejection

1 Introduction

The solar corona is a dispersive medium for electromagnetic waves. By conducting radio measurements to targets with small angular distances to the Sun, it is possible to determine the electron density of the coronal plasma. In the past 45 years, models of the electron density have been derived by various techniques [1], most notably spacecraft tracking during superior solar conjunctions [2].

Recently, geodetic VLBI data has been used to successfully determine electron density models of the corona [3, 4]. A slightly different approach, combining VLBI and GNSS data, has led to similar outcomes [5]. While VLBI is not as precise as spacecraft tracking in sensing the coronal electron content, it offers the possibility of probing the corona on a regular basis because it does not depend on superior solar conjunctions with spacecraft. Furthermore, VLBI is able to observe several radio sources at the same time, allowing the study of electron density variations in various regions around the Sun.

2 Data and Methodology

The electron density models from VLBI data are based on twelve R&D experiments performed by the International VLBI Service for Geodesy and Astrometry (IVS) [6] in 2011 and 2012. Each of the sessions utilized a global network of up to nine radio telescopes, lasted 24 hours, and included observations with solar elongation angles less than 15°, which had been the cut-off elongation angle between 2002 and 2013. The derived group delays in S- and X-band allowed the computation of the dispersive contribution to X-band $\tau_{disp,x}$ which is the observable used in a least-squares adjustment to estimate instrumental dispersive delays, parameters of the Earth's ionosphere, and, of most interest, of the solar corona. The coronal electron density is parameterized using a radial power-law

$$N_e(r) = N_0 \cdot r^{-\beta} \tag{1}$$

GFZ German Research Centre for Geosciences, Potsdam, Germany

with the electron density at the Sun's surface N_0, the fall-off parameter β, and the heliocentric distance r in units of solar radii $R_\odot$. More details about the dataset and methodology can be found in [4].

3 Results and Discussion

3.1 Comparison with Electron Density Models from Spacecraft Tracking

We have compared the average electron density model derived from the twelve VLBI experiments with previous models obtained from radio measurements to spacecraft during superior solar conjunctions. In Table 1, models derived between 1970 and 2008 are included (spacecraft Mariner 6/7, Viking 1/2, Voyager 2, Ulysses, Mars Express, and Rosetta [2]), as well as the model from VLBI data. The spacecraft tracking data are distributed over a period of almost 40 years and were obtained during very different solar conditions. The different fall-off parameters β range from about 2.1 to 2.5. The electron density at a distance of 14 $R_\odot$ varies by a factor of two (excluding the value for Voyager in 1988 – the electron density is about four to eight times larger compared to other models). The model from VLBI data agrees well with the spacecraft-based ones.

Table 1 Power-law parameters N_0 and β of the models derived from spacecraft tracking and VLBI data are given. Additionally, for each data set, the minimum elongation, smoothed Sunspot numbers during the data acquisition, and the electron density at a distance of 14 $R_\odot$ are included.

Mission / data set	Year	Min. elongation	N_0 $[10^{12}\ \mathrm{m}^{-3}]$	β	$N_e(14\ R_\odot)$ $[10^9\ \mathrm{m}^{-3}]$	SSN
MAN 6/7	1970	1.6°	0.60	2.06	2.61	105
VIK 1/2	1976	0.8°	0.99	2.32	2.17	13
VOY 2	1985	1.7°	1.92	2.36	3.79	18
VOY 2	1988	1.4°	6.04	2.25	15.93	100
ULS	1991	1.4°	2.85	2.47	4.21	145
MEX	2004	1.0°	1.68	2.46	2.55	40
ROS	2006	2.2°	0.84	2.14	2.96	15
MEX	2008	2.5°	0.49	2.07	2.08	3
VLBI	2012	3.9°	1.24	2.3	2.87	58

3.2 Dealing with the Parameter β

Using VLBI data, it has only been possible to determine one of the power-law parameters N_0 and β due to correlations between them. In this section, we investigate, to which extent different fixed values of β affect the estimated electron density models from VLBI.

Table 2 shows the estimated power-law parameter N_0 for several β values 2.0, 2.3, and 2.6. Additionally, the corresponding electron densities at distances 14 and 20 $R_\odot$ are displayed. It is evident that N_0 and β are correlated (correlation coefficient 0.97 for a sample of seven β values between 2.0 and 2.6). Larger values of β (i.e., a steeper decline) lead to higher theoretical electron densities at the surface of the Sun. At 3.9° elongation ($\approx$ 14 $R_\odot$) and farther away (i.e., the distances at which observations were performed), the difference in the electron density N_e is significantly lower compared to N_0. When assuming $\beta = 2.3$ for our VLBI model, the difference to the other estimates shown in Table 2 is about $4 \cdot 10^7\ \mathrm{m}^{-3}$ at 14 $R_\odot$, about 4% of the standard error (68% confidence interval). Within the range, where the VLBI model is valid, the largest absolute difference is found at 20 $R_\odot$: about $1.5 \cdot 10^8\ \mathrm{m}^{-3}$ with a gradient $\Delta N_e / \Delta \beta$ of about $-5 \cdot 10^8\ \mathrm{m}^{-3}$. Here, the difference amounts to roughly $\frac{1}{3}\sigma$, which is still insignificant.

Table 2 The table shows the average electron density models derived from all twelve R&D sessions fixing the value of β to 2.0, 2.3, and 2.6. Included are the electron densities at 1 (theoretical value N_0), 14, and 20 $R_\odot$ (3.8° and 5.4° elongation) together with their standard errors.

β	N_0 $[10^{12}\ \mathrm{m}^{-3}]$	$N_e(14\ R_\odot)$ $[10^9\ \mathrm{m}^{-3}]$	$N_e(20\ R_\odot)$ $[10^9\ \mathrm{m}^{-3}]$
2.0	0.57 ± 0.18	2.91 ± 0.92	1.42 ± 0.45
2.3	1.24 ± 0.42	2.87 ± 0.97	1.26 ± 0.43
2.6	2.70 ± 0.98	2.83 ± 1.03	1.12 ± 0.41

Figure 1 shows the VLBI model for three different values of β (see Table 2) compared to previous models developed from spacecraft tracking (Table 1). The differences between the three VLBI models are small at the elongations at which VLBI observations have been performed. At closer elongations, e.g. 2°, the differences are larger, but the electron densities are still within the range suggested by previous models. The deviation of the 1988 Voyager 2 model (uppermost line

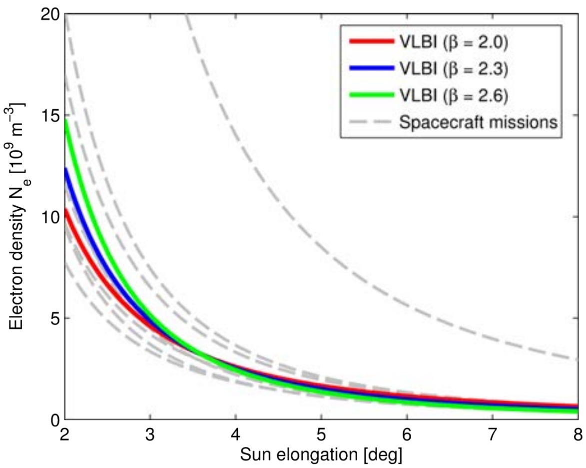

Fig. 1 The electron density models from VLBI data using three different values of β (see Table 2) are compared to models from spacecraft tracking. The electron densities of the coronal plasma are plotted as functions of solar elongation.

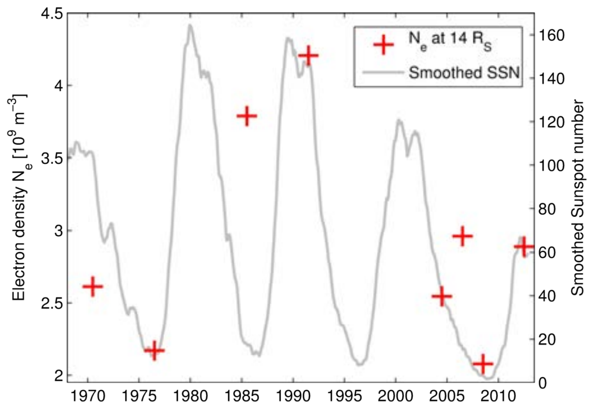

Fig. 2 The electron densities at a heliocentric distance of 14 $R_\odot$ from the models in Table 1 are plotted together with a time series of smoothed Sunspot numbers (SSN). The model from the 1988 Voyager 2 conjunction was excluded.

in Figure 1, separated from all other models) is much larger than those caused by different β values.

Bird et al. [2] have suggested that a correlation between β and solar activity exists. Since our data is from a period of medium solar activity, a medium value of $\beta = 2.3$ is appropriate.

3.3 Comparison to Sunspot Numbers

In Figure 2 we investigate whether correlations between the models from Table 1 and smoothed Sunspot numbers, which are indicators for overall solar activity, can be found. The electron densities in this figure are assessed at a distance of 14 $R_\odot$ (cf. Table 1). The reason for not using N_0 in this comparison is the strong correlation between N_0 and β as explained in Section 3.2.

Besides the model from 1988 (which was not considered in Figure 2), the ones from 1985 and 2006 (spacecraft Voyager 2 and Rosetta, respectively) also show, to a minor extent, anomalous electron densities when compared to smoothed SSN. The correlation between $N_e(14\,R_\odot)$ and SSN is 41% for all models, 55% when excluding the one from 1988, and 88% when further excluding the ones from 1985 and 2006.

For the outlying model from 1988 and also for the slightly anomalous models from 1985 and 2006, observations in regions of higher electron density are responsible [7, 8]. The average VLBI model is not affected to the same extent by such regional anomalies because the spatio-temporal sampling of the observations is more broadly distributed when compared to spacecraft tracking.

3.4 Coronal Mass Ejection Identifications through Coronagraph and VLBI Data

Coronal mass ejection (CME) events cause a regional and time-limited increase in electron density and turbulence. Increases in coronal total electron content (TEC) observed by spacecraft could be linked to such events in the past [7]. Thus, it is of interest studying the VLBI observations for similar TEC time variations. The problem is, a single VLBI observation is only sensitive to the difference in TEC along the lines-of-sight of the two telescopes, which strongly depends on the orientation and length of the baseline. If the electron density was strictly radially symmetric, this dependency could be removed by scaling with the inverse of the projected baseline $b_\perp \doteq p_2 - p_1$ with the impact parameters p_i of the two ray paths. However, the scatter due to turbulance and small-scale variations in electron density is unnaturally amplified for small $b_\perp$ which makes the detection of time variations in TEC impossible.

Instead, the increase in turbulence caused by the CMEs was investigated using the formal errors of the dispersive group delays. The formal errors (in terms of 1σ standard deviations) are determined during the correlation of the VLBI signals and are indirectly proportional to the geometric mean of antenna temperatures [9, 10]

$$\sigma_\tau \propto \frac{1}{\sqrt{T_{A_1} \cdot T_{A_2}}} \quad , \tag{2}$$

which are in turn proportional to the effective flux density of the observed source. Thus, if the flux density is reduced due to perturbations, e.g., in the corona, the formal errors σ_τ are expected to increase. The formal errors of the dispersive contribution in X-band can be derived from σ_τ in S- and X-band by

$$\sigma_{\tau_{disp,x}} = \sqrt{\sigma_{\tau_x}^2 + \sigma_{\tau_s}^2} \cdot \frac{f_s^2}{f_x^2 - f_s^2} \quad . \tag{3}$$

During the twelve R&D sessions, two CMEs took place in coronal regions through which radio sources were observed. Figure 3 shows time series of the formal errors $\sigma_{\tau_{disp,x}}$ for the observations of radio source 2008-159 (RD1201) and 1243-072 (RD1208) during CME events. The radio source 1958-179 was even closer to the path of the CME during RD1201, but was only observed during the first half of the session, i.e., before the CME happened. Also included in this figure are LASCO [11] coronagraph images depicting the evolution of the CMEs and the positions of the observed radio sources (more details about these images, as well as animations can be found in [4]). Since the observations in Figure 3 are from different baselines with telescopes of different sizes and receiver hardware, the standard deviations are scattered. Still, a trend is visible. At about the same time when the brighter plasmas arrive at the ray paths of the telescopes pointing to the respective radio sources (about 12 PM for RD1201 and 9 AM for RD1208), a strong increase in the formal errors appears.

In both cases the standard deviations increase even a bit earlier. Consequently, there seems to be an increase in turbulence before the bright plasma of the CME arrives at the line-of-sight as seen in the LASCO images. Another reason could be disturbances in the Earth's ionosphere, but time series of ionospheric TEC do not show any anomalies in this specific time period.

Also indicated in Figure 3 are the quality codes from the correlation. Diamonds represent observations of low quality which are not used in standard VLBI analysis (and also not in this study for estimating the coronal electron density). At roughly the same time when the CMEs pass the ray paths, most observations are flagged as low quality.

4 Conclusions

We have shown that the model from VLBI data fits well to ones from spacecraft tracking. A correlation close to 90% between selected electron density models of the past (including the one from VLBI) and Sunspot numbers exists. While we cannot give an independent estimate of the power-law parameter β, we have demonstrated that the arbitrary choice does not affect the resulting electron density models significantly. Finally, the effects of coronal mass ejections, identified through coronagraph images, have also been detected in the VLBI data.

Acknowledgements

The authors thank the IVS for observing, correlating, and providing the VLBI data used in this work. The LASCO data used here are produced by a consortium of the Naval Research Laboratory (USA), Max-Planck-Institut für Radioastronomie (Germany), Laboratoire d'Astronomie (France), and the University of Birmingham (UK).

References

1. P. B. Esposito, P. Edenhofer, and E. Lueneburg. Solar corona electron density distribution. *J. Geophys. Res.*, 85:3414–3418, 1980.
2. M. K. Bird, M. Pätzold, B. Häusler, S. W. Asmar, S. Tellmann, M. Hahn, A. I. Efimov, and I. V. Chashei. Coronal radio sounding experiments with the ESA spacecraft MEX, VEX, and Rosetta. In *511th WE-Heraeus-Seminar, Bad Honnef, Germany, Jan 31 - Feb 3 2012*. 2012.
3. B. Soja, J. Sun, R. Heinkelmann, H. Schuh, and J. Böhm. Sun Corona Electron Densities Derived from VLBI Sessions in 2011/2012. In *Proceedings of the 21st Meeting of the European VLBI Group for Geodesy and Astrometry*, N. Zubko and M. Poutanen, editors, pages 159–163, 2013.

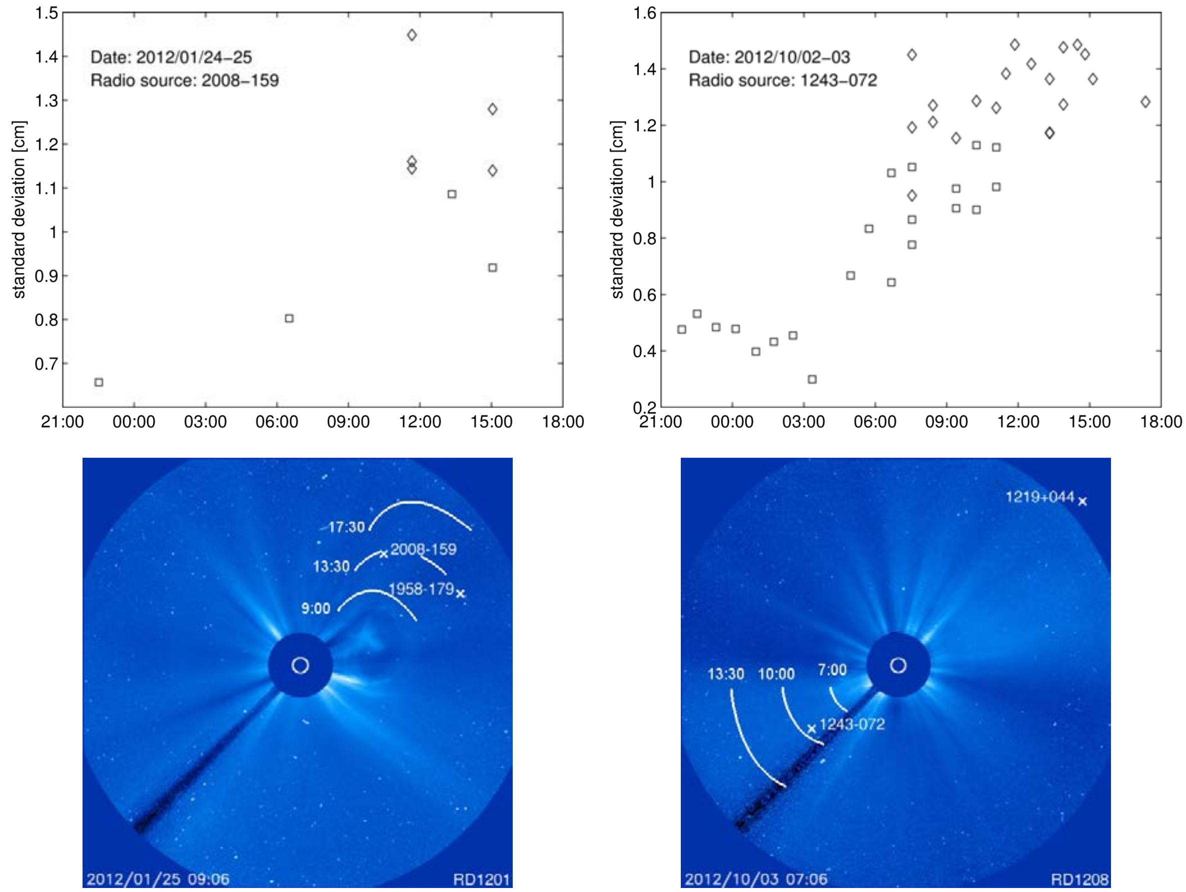

Fig. 3 The a priori standard deviations of the dispersive delay observations, as estimated in the correlation of the VLBI data, for sessions RD1201 on 2012/01/24–25 (top left) and RD1208 on 2012/10/02–03 (top right). Squares indicate decent quality observations, and diamonds stand for observations with bad correlation quality flags. The bottom figures show the positions of the radio sources (white crosses) in the vicinity of the Sun with respect to images of the LASCO C3 coronagraph. The temporal evolution of the CMEs is indicated by white curves.

4. B. Soja, R. Heinkelmann, and H. Schuh. Probing the Solar Corona with Very Long Baseline Interferometry. *Nature Communications*, submitted, 2014.
5. B. Soja, R. Heinkelmann, and H. Schuh. Solar corona electron densities from VLBI and GIM data. In P. Willis and C. Rizos, editors, *Proceedings of the IAG Scientific Assembly 2014*, accepted, 2014.
6. H. Schuh and D. Behrend. VLBI: A fascinating technique for geodesy and astrometry. *J. Geodyn.*, 61:68–80, 2012.
7. M. Pätzold, M. Hahn, S. Tellmann, B. Häusler, M. K. Bird, G. L. Tyler, S. W. Asmar, and B. T. Tsurutani. Coronal Density Structures and CMEs: Superior Solar Conjunctions of Mars Express, Venus Express, and Rosetta: 2004, 2006, and 2008. *Solar Physics*, 279(1):127–152, 2012.
8. M. K. Bird, H. Volland, M. Pätzold, P. Edenhofer, S. W. Asmar, and J. P. Brenkle. The coronal electron density distribution determined from dual-frequency ranging measurements during the 1991 solar conjunction of the ULYSSES spacecraft. *Astrophysical Journal*, 426(1):373–381, 1994.
9. H. Schuh and J. Böhm. Very Long Baseline Interferometry for Geodesy and Astrometry. In G. Xu, editor, *Sciences of Geodesy II: Innovations and Future Developments*. Springer Berlin Heidelberg, 2013.
10. A. Whitney. *Precision Geodesy and Astrometry Via Very-long-baseline Interferometry*. PhD thesis, Massachusetts Institute of Technology, 1974.
11. G. E. Brueckner, R. A. Howard, M. J. Koomen, C. M. Korendyke, D. J. Michels, and J. D. Moses. The Large Angle Spectroscopic Coronagraph (LASCO). *Solar Physics*, 162:357–402, 1995.

The Evaluation of the Earth's Dynamical Flattening Based on the IAU Precession-nutation and VLBI Observations

Nicole Capitaine[1], Jia-Cheng Liu[2]

Abstract The dynamical flattening H_d is a fundamental Earth's parameter and a crucial scale factor in constructing the precession-nutation models. Its value has generally been derived from astronomical observations of the luni-solar precession in longitude at epoch, or from geophysical determinations of the Earth's moment of inertia. It should be noted that the observed precession rates in longitude and obliquity result from several theoretical contributions, some of them, as well as the nutation amplitudes, being also dependent on H_d. This paper discusses the rigorous procedure to be used for deriving H_d from the best available astronomical observations. We use the IAU 2006/2000 precession-nutation and VLBI observations of the celestial pole offsets spanning about 32 years in order to calculate the observed position of the CIP (Celestial intermediate pole) in the GCRS (Geocentric celestial reference system). Then, the value of H_d is evaluated by a least squares method with a careful consideration of the various theoretical contributions to the precession rates and of the largest terms of nutation. We compare the results with an indirect fit of H_d to the estimated corrections to the linear term in precession and the 18.6-yr nutation. We discuss the limit of accuracy, given the characteristics of the available observations and the uncertainties in the models, as well as the parameters on which H_d is dependent.

Keywords Astrometry, precession-nutation, VLBI, reference systems

1. SYRTE, Observatoire de Paris, CNRS, UPMC, France
2. School of Astronomy and Space Science, Nanjing University, China

1 Introduction

Precession and nutation of the Earth originate from the tidal forces exerted by the Moon, the Sun, and the planets on the equatorial bulge of the Earth, for which the oblateness is described by the dynamical flattening H_d:

$$H_\mathrm{d} = \frac{C-(A+B)/2}{C} \tag{1}$$

where A, B, and C are the principal moments of inertia of the whole Earth. H_d is an essential parameter for the precession-nutation theory since the effect of luni-solar and planetary torques is proportional to this parameter; it is directly linked ($H_\mathrm{d} = e/(1+e)$) to the parameter e, which is one of the Basic Earth Parameters of the IAU 2000 precession-nutation (Mathews et al., 2002). Values of H_d deduced from precise astro-geodetic techniques, such as VLBI and LLR, have been used in developing recent precession nutation theories; some of them, along with the associated precession models, are listed in Table 1. The relative differences between these values are ranging from tenths to tens of parts per million (ppm).

Table 1 Values at J2000.0 used for computing the precession of the equator for various precession models.

Authors	$H_\mathrm{d} \times 10^3$	$f_{01}\|_{\mathrm{LS}}$ in ″/cy	Model
Lieske et al. (1977)	3.2739935	5494.3861	IAU 1976
Williams (1994)	3.2737634	5494.01083	W94
Mathews et al. (2002)	3.27379492		IAU 2000
Capitaine et al. (2003)	3.27379448	5494.062986	IAU 2006

Traditionally, the Earth's dynamical flattening has been derived from astronomical observations of the luni-solar precession in longitude at epoch, considering the first order-lunisolar precession rate at J2000.0, which is the most significant contribution (at the order of 5500″/cy), denoted $f_{01|_{\mathrm{LS}}}$ (cf. column 3 of Table 1). However, other minor contributions to the precession rates in both longitude and obliquity as well as nutation are affected by H_{d}. This should be properly considered for a rigorous computation of H_{d}.

2 Estimation of H_{d} from the Observed Motion of the Celestial Intermediate Pole

The purpose of our work is to use a rigorous procedure for deriving the Earth's dynamical flattening H_{d} from the best available astronomical observations.

The first method we have used is a direct fit of H_{d} to the time series of the observed CIP (Celestial intermediate pole) location, which can be expressed by the coordinates, X and Y, of the CIP in the GCRS (Geocentric celestial reference system).

We have first computed the observed quantities X_{obs} and Y_{obs} by using the theoretical expressions of the CIP coordinates X_{IAU} and Y_{IAU}, based on the IAU 2006/2000 precession-nutation (Mathews et al., 2002, Capitaine et al., 2003, 2005) and the time series of the "celestial pole offsets" observed by VLBI, denoted dX and dY, as follows:

$$\begin{aligned} X_{\mathrm{obs}} &= X_{\mathrm{IAU}} + \mathrm{d}X \\ Y_{\mathrm{obs}} &= Y_{\mathrm{IAU}} + \mathrm{d}Y. \end{aligned} \qquad (2)$$

The series for X_{obs} and Y_{obs} are shown in Figure 1.

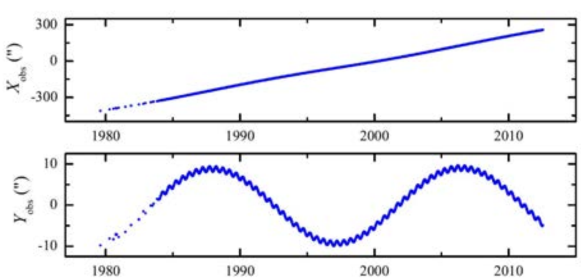

Fig. 1 Time series of the X and Y coordinates of the observed CIP in the GCRS over the period 1980–2012.

The quantities X_{IAU} and Y_{IAU} are calculated using the IAU SOFA software, while the quantities (dX, dY) used in this analysis are those of the IVS solution opa2012a (of Paris Observatory): the time span is about 32 years (1980–2012) and the free core nutation (FCN) is removed using the empirical model provided in the IERS Conventions (2010). The weighted mean root square for dX and dY are 0.137 and 0.173 mas, respectively.

We have then expressed the X_{obs} and Y_{obs} quantities as a function of H_{d}:

$$X_{\mathrm{obs}} = H_{\mathrm{d}}\left(\dot{X}_{\mathrm{th}}\,t + X_{\mathrm{nut}}\right) + \left(\dot{X}_{\mathrm{g}} + \dot{X}_{\mathrm{nl}}\right)t + \delta X \qquad (3)$$
$$Y_{\mathrm{obs}} = H_{\mathrm{d}}\left(\dot{Y}_{\mathrm{th}}\,t + Y_{\mathrm{nut}}\right) + \dot{Y}_{\mathrm{nl}}\,t + \delta Y, \qquad (4)$$

where the subscripts "th", "nut", "g", and "nl" represent the theoretical contributions to precession rates, contributions from nutation, geodesic precession, and non-linear effect, respectively. The time t is measured in Julian centuries since J2000.0.

The Earth's dynamical flattening H_{d} has been estimated from the above equations by using a weighted least squares fit among the time series of X_{obs} and Y_{obs}. The expressions for $\dot{X}_{\mathrm{g}} + \dot{X}_{\mathrm{nl}}$ and $\dot{Y}_{\mathrm{g}}$ are taken from Capitaine et al., (2003) and Capitaine et al., (2005), respectively. A rigorous expression of $\dot{X}_{\mathrm{th}}$ as a function of H_{d} can be obtained from Bourda and Capitaine, (2004). Different fits have been performed by using (i) equation (3) only, (ii) equation (4) only, and (iii) both equations (3) and (4) simultaneously. As the most significant effect of H_{d} is in the X component, especially for the contribution of the first order lunisolar term, the relative errors (for both theoretical and observational) in precession and nutation in the X component are much smaller than those in the Y component.

The value for H_{d} obtained in this way, from (i), is such that its relative difference with respect to the reference value H_{P03} of the IAU 2006 precession is about -14 ppm, which is much larger than expected.

The second method we have used in this work is an indirect estimation of H_{d} from the celestial pole offsets. We have used the time series, opa2012, of VLBI celestial pole offsets corrected for the FCN, but this time for determining H_{d} from the estimated corrections to the two most sensitive terms of the IAU precession-nutation to H_{d}, namely the t^1 term in precession and the 18.6-yr term of nutation. The celestial pole offsets dX and dY can then be written as follows (Capitaine et al., 2009):

$$\begin{aligned} \mathrm{d}X &= A_0 + A_1 t + A_{\mathrm{s}} \sin\Omega + A_{\mathrm{c}} \cos\Omega \\ \mathrm{d}Y &= B_0 + B_1 t + B_{\mathrm{s}} \sin\Omega + B_{\mathrm{c}} \cos\Omega, \end{aligned} \qquad (5)$$

where Ω is the mean longitude of the ascending node of the Moon.

The coefficients of the above equations have then been derived by a weighted least squares fit as shown in Table 2. Then, we have fitted to A_1 the correction $\mathrm{d}H_\mathrm{d}$ to the reference value H_{P03}. This gives a correction of 0.071 ppm in the Earth dynamical flattening, which is quite negligible.

Table 2 Weighted fits of a linear term plus a 18.6 yr periodic term to the opa2012 time series (1980–2012) of VLBI celestial pole offsets.

	coefficient	value (mas or mas/cy)	uncertainty
	A_0	0.02745	0.00221
X	A_1	0.14252	0.03139
	A_s	-0.01397	0.00267
	A_c	0.05762	0.00263
	B_0	-0.08655	0.00254
Y	B_1	0.09964	0.03614
	B_s	0.01886	0.00307
	B_c	-0.07189	0.00298

3 Discussion

Possible ways to derive an accurate value for H_d using the best available precession-nutation models and VLBI observations are investigated; for that purpose, various theoretical contributions are considered for the first time in studying this Earth's global parameter.

The differences between the results obtained by two different methods of least squares fit need to be further investigated with considering all error sources for each term in the CIP X and Y coordinates. A possible reason for the discrepancy is due to the out-of-phase components of the main nutation terms, because most of the effects in those terms are not proportional to H_d. This paper is a first step of the work, which will be continued by the authors. Publication of this work is under preparation and is planed to be submitted to A&A in the near future.

Acknowledgements

J.-C Liu's contribution to this work is funded by the National Natural Science Foundation of China (NSFC) under grant no. 11303018.

References

1. Bourda, G., Capitaine, N., Precession, nutation, and space geodetic determination of the Earth's variable gravity field, Astron. Astrophys. 428, 691–702 (2004)
2. Capitaine, N., Wallace, P. T., Chapront, J.: Expressions for IAU 2000 precession quantities. Astron. Astrophys. 412, 567–586 (2003)
3. Capitaine, N., Wallace, P. T., Chapront, J.: Improvement of the IAU 2000 precession model. Astron. Astrophys. 432, 355–367 (2005)
4. Capitaine, N., Mathews, P. M., Dehant, V., Wallace, P. T., Lambert, S. B.: On the IAU 2000/2006 precession-nutation and comparison with other models and VLBI observations. Celest Mech Dyn Astr 103:179–190 (2009). DOI 10.1007/s10569-008-9179-9
5. IERS Conventions (2010), IERS Technical Note 36, G. Petit and B. Luzum (eds), Frankfurt am Main: Verlag des desamts für Kartographie und Geodäsie, 2010
6. Lieske, J. H., Lederle, T., Fricke, W., Morando, B.: Expressions for Precession Quantities Based upon the IAU (1976) System of Astronomical Constants. Astron. Astrophys. 58, 1–16 (1977)
7. Mathews, P. M., Herring, T. A., Buffett B. A.: Modeling of nutation and precession: New nutation series for nonrigid Earth and insights into the Earth's interior. J. Geophys. Res. 107, B4, ETG 3-1-C3-26 (2002). doi:10.1029/2001JB000390
8. Williams, J. G.: Contributions to the Earth's obliquity rate, precession and nutation. Astron. J. 108(2), 711–724 (1994)

An Alternative Model of the Gravitational Delay

Anastasia Girdiuk[1], Oleg Titov[2], Laura Stanford[2]

Abstract A massive body causes a time delay in the gravitational field of a body. The conventional gravitational delay model was expanded into a Taylor series on $O(\frac{b}{r})$. The results of the expression show a dependence on the positions of the two antennas, the observed source (quasar), and the massive body (Sun or Jupiter). In this paper we compare the Taylor series expansion approach with the conventional gravitational delay. The total difference of these models stays below the accuracy limit.

Keywords VLBI, gravitational delay model, general relativity

1 Introduction

The conventional gravitational delay model for the reduction of geodetic VLBI [1] observations was developed in the 1980s and its use was recommended by the IAU General Assembly in 1991. We propose an alternative model by using the Taylor series expansion of the gravitational delay on the small parameter. A numerical comparison of these two models shows their consistency at the 1 picosecond (ps) level for the Sun's gravitational field (at an angular distance of about 4°). Although the new formula is more complex, because it comprises several terms, there are some advantages: 1) direct analytical link to the effect of the light deflection, 2) exclusion of the coordinate terms (total potential of the solar system bodies) in the gravitational and geometric delays, and 3) applicability to a wide selection of related effects.

1. Institute of Applied Astronomy
2. Geoscience Australia

2 The Conventional Formula

Besides the three classical tests, the fourth test of General Relativity—the delay of a signal propagating in the gravitational field—has been proposed by Shapiro [2] and is known as the Shapiro delay. The difference between the two Shapiro delays as measured with two radio telescopes gives a gravitational delay which must be considered at the standard reduction of the high-precision geodetic VLBI data. The IERS Conventions 2010 [3] contain the conventional formula for the gravitational delay, which is valid for most cases unless a distant quasar and a deflecting body are too close. This formula is presented as follows

$$\tau_{grav} = \frac{(\gamma+1)GM}{c^3} \ln \frac{|\mathbf{r_1}| + \mathbf{s} \cdot \mathbf{r_1}}{|\mathbf{r_2}| + \mathbf{s} \cdot \mathbf{r_2}}, \tag{1}$$

where γ is the PPN-parameter of General Relativity [4], G is the gravitational constant, M is the mass of gravitational body, c is the speed of light, $\mathbf{s}$ is the barycentric unit vector towards the radio source, and $\mathbf{r_i}$ is the vector between the center of mass of the gravitating body and the i-th telescope.

3 Two Examples of Geodetic VLBI Sessions

One close approach of Jupiter to the radio source 1922–224 on 18/19 November 2008 was observed during the OHIG60 session. Four stations (Hobart26, Kokee, Tsukub32, and Parkes) were tracking the radio source over twelve hours. The minimum approach distance was $1.4'$. A special "hand-made" schedule was prepared by Dirk Behrend (GSFC).

Several radio sources were observed in close angular proximity to the Sun during the R&D session RD1208 on 2/3 October 2012. The radio source 1243–072 was tracked at the range of angular distance from of 3.7° to 4.3°. Five stations (Kokee, Tsukub32, HartRAO, Wettzell, and Onsala60) participated in this session.

4 General Relativity Delay Model

An expression that links the gravitational delay and the formula for the light deflection angle [5] is yet to be developed. To obtain it we have expanded the gravitational delay using a Taylor series expansion on $O(\frac{b}{r})$. We keep the terms of order $(\frac{b}{r})^2$ that correspond to an accuracy of about 1 ps.

We expand Formula (1) as a series of $\frac{b}{r_2}$ where r_2 is the barycentric vector of the second station:

$$\begin{aligned}\tau_{grav} = &-\frac{(\gamma+1)GM}{c^3}\frac{b}{r_2}\cos\varphi && \{\text{coordinate term}\}\\ &+\frac{(\gamma+1)GM}{c^3}\frac{b}{r_2}\frac{\sin\varphi\sin\theta\cos A}{1-\cos\theta} && \{\text{term } t_1\}\\ &-\frac{(\gamma+1)GM}{2c^3}\left(\frac{b\sin\varphi\sin\theta\cos A}{r_2(1-\cos\theta)}\right)^2 && \{\text{term } t_2\} \qquad (2)\\ &+\frac{(\gamma+1)GM}{2c^3}\frac{b^2}{r_2^2}\frac{1-\cos^2\varphi\cos^2\theta}{1-\cos\theta} && \{\text{term } t_3\},\end{aligned}$$

where the vectors $\mathbf{b}$ and $\mathbf{r}$ and the angles φ, ψ, θ, and A are shown in Figure 1. In order to provide more accurate modeling of the gravitational delay, in the calculations one has to use the vector $\mathbf{r_2}$ for the second station instead of the barycentric vector $\mathbf{r}$ of Figure 1.

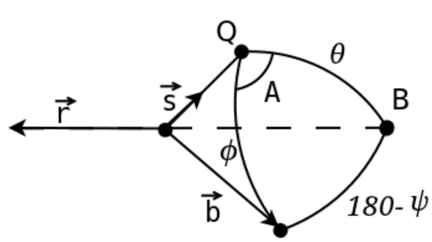

Fig. 1 Angle θ – the impact parameter, angle φ between vectors $\mathbf{b}$ and $\mathbf{s}$, and angle ψ between vectors $\mathbf{b}$ and $\mathbf{r}$.

Figure 1 shows the positions of the quasar Q, the deflecting body B (e.g., Jupiter or Sun), the baseline vector $\mathbf{b}$, the vector $\mathbf{r}$ from the body to the geocenter, and the barycentric unit vector $\mathbf{s}$ to the quasar Q.

Surprisingly, we found that the first term in Formula (2) is equal to the term including the PPN parameter γ of the geometric delay, but with opposite sign, and consists of distance r. We want to bring your attention to the fact that, although the distances are different, the terms are equal to within about 0.1 ps. Keeping in mind that ($\mathbf{b}\cdot\mathbf{s} = |\mathbf{b}|\cos\varphi$), the formula for the total group delay recommended by the IAU [3, 6] becomes:

$$\tau_{group} = \frac{\tau_{grav} - \frac{\mathbf{b}\cdot\mathbf{s}}{c}(1-\frac{(\gamma+1)GM}{c^2 r}+\ldots)}{1+\frac{1}{c}(\mathbf{s}\cdot(\ldots))} = \frac{\tau_{\mathrm{GR}}+\ldots}{1+\frac{1}{c}(\mathbf{s}\cdot(\ldots))}, \quad (3)$$

where τ_{GR} is the resultant contribution of General Relativity (GR) effects to the τ_{group}, including two relativistic terms which cancel each other out. Then, τ_{GR} may be written as follows for $\gamma = 1$

$$\tau_{\mathrm{GR}} = \frac{2GM}{c^3}\ln\frac{|\mathbf{r_1}|+\mathbf{s}\cdot\mathbf{r_1}}{|\mathbf{r_2}|+\mathbf{s}\cdot\mathbf{r_2}} + \frac{2GM(\mathbf{b}\cdot\mathbf{s})}{c^3 r_2} \quad (4)$$

or, from Formulas (2) and (4), as

$$\begin{aligned}\tau_{\mathrm{GR}} = &\frac{2GM}{c^3}\frac{b}{r_2}\frac{\sin\varphi\sin\theta\cos A}{1-\cos\theta} - \frac{GM}{c^3}\left(\frac{b\sin\varphi\sin\theta\cos A}{r_2(1-\cos\theta)}\right)^2 +\\ &+\frac{GM}{c^3}\frac{b^2}{r_2^2}\frac{1-\cos^2\varphi\cos^2\theta}{1-\cos\theta} \qquad (5)\end{aligned}$$

—the total effect of GR in the group delay.

4.1 The Approximation of Small Angles

Given that $\gamma = 1$ in GR and ignoring the minor terms of $O(\frac{b^2}{r^2})$ for the sake of simplicity, then

$$\tau_{\mathrm{GR}} = \frac{2GM}{c^3}\frac{b\sin\varphi\sin\theta\cos A}{r_2(1-\cos\theta)} \underset{\theta\to 0}{=} \frac{4GM}{c^3}\frac{b\sin\varphi\cos A}{R}, \quad (6)$$

where $R = \theta\cdot r_2$ is the linear impact parameter. It is now easy to note that Formula (6) corresponds to the formula of the light deflection developed by Einstein in 1916: $\alpha'' = \frac{4GM}{c^2 R}$.

The light deflection angle α'' and τ_{GR} are linked by

$$\tau_{\mathrm{GR}} = \alpha''\frac{b}{c}\sin\varphi\cos A. \quad (7)$$

For an arbitrary angle θ, α'' is

$$\alpha'' = \frac{2GM}{c^2 r_2} \frac{\sin\theta}{1-\cos\theta} \quad (8)$$

Formula (8) proves that the deflection angle as measured with geodetic VLBI is independent of the baseline length in a first approximation. Figure 2 shows the modeled curve of the light deflection angle variations for the approach of Jupiter to the radio source 1922–224. This arc is common for all four baselines (Hobart26–Parkes, Hobart26–Tsukub32, Tsukub32–Kokee, and Parkes–Tsukub32).

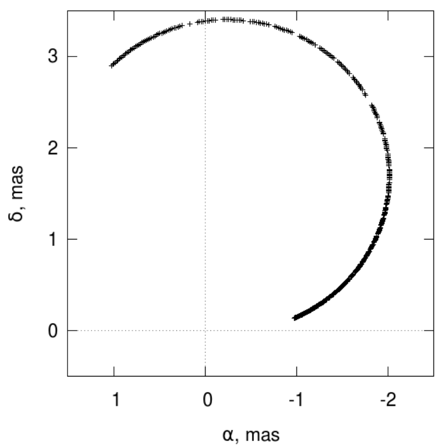

Fig. 2 The light deflection angle α''_A for the baselines Hobart26–Tsukub32, Parkes–Tsukub32, Hobart26–Parkes, and Tsukub32–Kokee for Jupiter to quasar 1922–224.

We can present the resultant contribution of GR in the approximation of small angles to the total group delay in terms of b/R as follows:

$$\tau_{\text{GR}} = \frac{4GM}{c^3}\left[\frac{b}{R}\sin\varphi\cos A - \frac{b^2}{2\,R^2}\sin^2\varphi\cos 2A\right] \quad (9)$$

4.2 Major Term t_1 and Effect of Minor Terms t_2 and t_3

The alternative Formula (5) for an arbitrary angle θ consists of three terms: the term t_1 from Formula (2) gives a major contribution to the GR effects, while the terms t_2 and t_3 from Formula (2) are much smaller than t_1 for the case of the Sun. However, for a very close approach of Jupiter to radio sources (less than 30″) all three terms become comparable.

The four curves of Figure 3 reflect the variations for four VLBI baselines of different length: Kokee–Tsukub32, HartRAO–Wettzell, Onsala60–Wettzell, and HartRAO–Onsala60. Figure 3 shows the dependence of the term t_1 on Universal Time (UT) and the angle θ for the approach of the Sun to the radio source 1243–072. This term varies steadily due to the relatively slow apparent motion of the Sun.

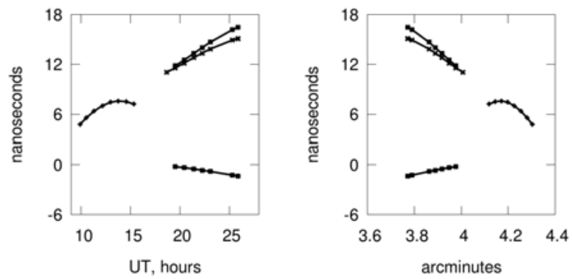

Fig. 3 Major term t_1 vs. UT (left) and vs. angle θ (right) for the case of 1243–072 for the baselines Kokee–Tsukub32, HartRAO–Wettzell, Onsala60–Wettzell, and HartRAO–Onsala60.

The approach of Jupiter to the radio source 1922–224 is more interesting due to the small minimum angular distance. The angle θ increases from 1.4′ to about 5′ rather quickly (in about 12 hours) followed by a fast change in the deflection angle (Figure 2). Figure 4 shows the variations of the term t_1 depending on UT and θ during this event. This term reaches its maximum near 12 UT and becomes negligible over a short period of time.

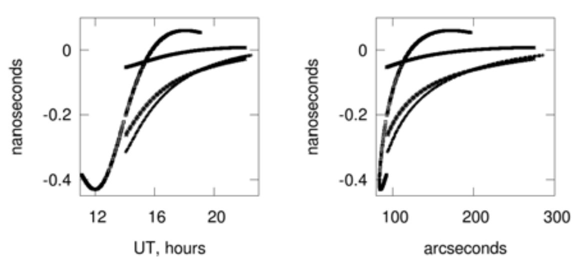

Fig. 4 (left) Major term t_1 from date; (right) t_1 from θ for Jupiter to the radio source 1922–224 for the baselines Hobart26–Tsukub32, Parkes–Tsukub32, Hobart26–Parkes, Tsukub32–Kokee.

Figure 5 shows variations of the sum of the two minor terms (t_2+t_3) depending on UT and θ for the case of 1922–224. Although the angle θ is larger than $1'$, we clearly see wide swings in amplitude in the small terms. In accordance with Formulas (5) and (9), these terms are proportional to $(\frac{b}{R})^2$ (Figure 6); therefore, this sum is becoming very large for longer baselines (Hobart26–Tsukub32) with respect to shorter ones

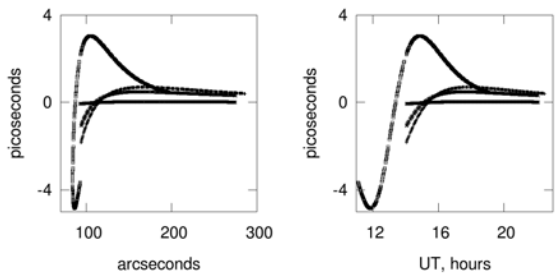

Fig. 5 Variations of the sum (t_2+t_3) for the approach of Jupiter to the radio source 1922–224 vs. θ (left) and vs. UT (right) for the baselines Hobart26–Tsukub32, Parkes–Tsukub32, Hobart26-Parkes, and Tsukub32–Kokee.

(Hobart26– Parkes) even at the same impact parameter θ. For a very close approach (less than $30''$) the sum (t_2+t_3) for long baselines will be of the same order of magnitude as the major term t_1.

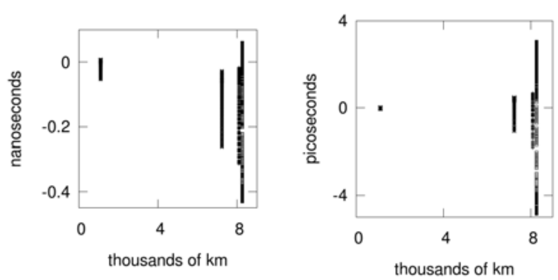

Fig. 6 Variations of the term t_1 (left) and the sum t_2+t_3 (right) for the approach of Jupiter to the radio source 1922–224 vs. baseline length for the baselines Hobart26–Tsukub32, Parkes–Tsukub32, Hobart26–Parkes, and Tsukub32–Kokee.

5 Comparison of the Two Models

The sum of the conventional gravitational delay model (1) and the GR coordinate term $\frac{2GM(\mathbf{b}\cdot\mathbf{s})}{c^3 r_2}$ from the geometric delay can be approximated by Formula (5). Figure 7 shows the variations of the coordinate term and the difference between models (4) and (5) with respect to UT for the approach of the Sun to the radio source 1243–072. This coordinate term does not exceed 1 ns even for a small angle θ.

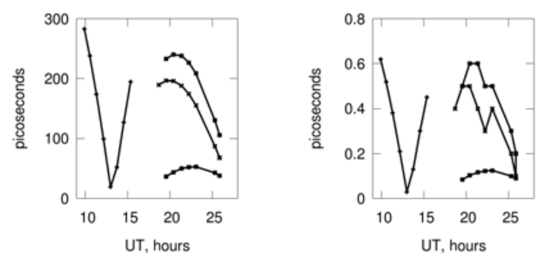

Fig. 7 Variations of the coordinate term (left) and comparison of the two models for the approach of the Sun to the radio source 1243–072 for baselines Kokee–Tsukub32, HartRAO–Wettzell, Onsala60–Wettzell, and HartRAO–Onsala60.

Figure 8 shows the same values as Figure 7 but for the case of 1922–224. The coordinate term here is also negligible. The discrepancies between models (4) and (5) do not exceed 0.1 ps and can be ignored.

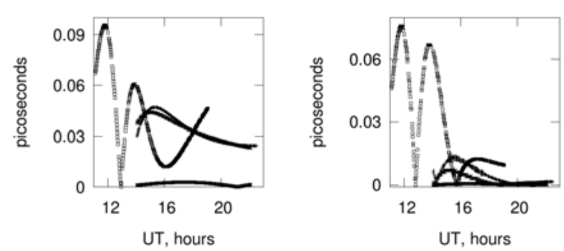

Fig. 8 Variations of the coordinate term (left) and comparison of the two models for the approach of the Jupiter to the radio source 1922–224 for baselines Hobart26–Tsukub32, Parkes–Tsukub32, Hobart26–Parkes, and Tsukub32–Kokee.

6 Conclusion

We proposed an alternative presentation of the effect of GR in the total VLBI group delay model. We showed a new formula, which combines the GR effects from the gravitational and geometric delays with a precision of as much as 1 ps along all ranges of the angular distance between a gravitational body (Sun, Jupiter) and an encountered radio source. In addition, this alternative formula could be easily linked to the light deflection angle at an arbitrary angular distance.

Acknowledgements

Anastasia Girdiuk is thankful for the support by the IAG Travel Award to attend the IVS 2014 General Meeting.

References

1. H. Schuh, D. Behrend (2012). "VLBI: A fascinating technique for geodesy and astrometry", Journal of Geodynamics, Vol. 61, pp. 68–80, October 2012. DOI 10.1016/j.jog.2012.07.007.
2. I. Shapiro (1964). "Fourth Test of General Relativity", Phys. Rev. Lett., vol. 13, Issue 26, pp. 789-791, 1964.
3. G. Petit, B. Luzum (eds.) (2010). IERS Conventions (2010), IERS Technical Note 36, Frankfurt am Main: Verlag des Bundesamts fur Kartographie und Geodasie.
4. C. Will (1991). "Theory and Experiment in Gravitational Physics", Cambridge University Press.
5. A. Einstein (1916). "Die Grundlage der allgemeinen Relativitatstheorie", Annalen der Physik, vol. 354, Issue 7, pp. 769-822, 1916.
6. T. Eubanks (ed.) (1991). Proc. of the U. S. Naval Observatory Workshop on Relativistic Models for Use in Space Geodesy, U. S. Naval Observatory, Washington, D. C.

Space Geodesy, VLBI, and the Fourth Pillar of Geodesy – Spacetime Curvature

Ludwig Combrinck

Abstract Typically geodesy is described as having "three pillars": the variations in Earth's shape, gravity field, and rotation. These pillars form the conceptual and observational basis for the celestial and terrestrial reference frames required for Earth and space observations. However, it is no longer adequate to base the conceptual and observational basis on only three pillars. Spacetime curvature as described by the General Theory of Relativity (GTR) is an integral component of all space geodesy techniques and influences all measurements, techniques, and data reduction. Spacetime curvature is therefore the fourth pillar. It is the measurement of the shape of spacetime and its variations. Due to accuracies of Very Long Baseline Interferometry (VLBI) and optical celestial reference frame measurements reaching the tens of micro-arcsecond level in the near future, it is essential to recognize the impact of spacetime seeing on the accuracy objectives of the Global Geodetic Observing System. Spacetime seeing (resulting from spacetime curvature) is analogous to astronomical seeing (resulting from atmospheric conditions), as all of spacetime is affected by microlensing/weak lensing to some extent as a result of mass (normal baryonic and darkmatter) distribution, placing a limit on the realization of the celestial reference frame.

Keywords ICRF, VLBI, General Theory of Relativity, microlensing, weak lensing, spacetime curvature seeing, space geodesy

Hartebeesthoek Radio Astronomy Observatory

1 Introduction

Currently the focus of the International Association of Geodesy (IAG) is Earth-centric to a large extent; the IAG's main perspective is towards Earth. This is reflected in the structure and tasks of its four commissions. These are briefly summarized as:

- Commission 1: Reference Frames
- Commission 2: Gravity Field
- Commission 3: Earth Rotation and Geodynamics
- Commission 4: Positioning and Applications

These commissions fulfill valuable roles in the continued maintenance and improvement of the terrestrial and celestial reference frames, gravity field modeling and measurement, determination of orbits and their modeling, Earth orientation, tectonic measurement and modeling, ocean level changes, planetary and lunar dynamics, precise positioning, and applications of space geodesy for ionospheric and atmospheric studies. This list is not comprehensive as the applications and implications of geodesy are diverse and encompass subfields of many disciplines. In addition to the four commissions, there are nine joint study groups.

1. JSG 0.1: Application of time series analysis in geodesy
2. JSG 0.2: Gravity field modeling in support of height system realization
3. JSG 0.3: Comparison of current methodologies in regional gravity field modeling
4. JSG 0.4: Coordinate systems in numerical weather models
5. JSG 0.5: Multi-sensor combination for the separation of integral geodetic signals

6. JSG 0.6: Applicability of current GRACE solution strategies to the next generation of inter-satellite range observations
7. JSG 0.7: Computational methods for high-resolution gravity field modeling and nonlinear diffusion filtering
8. JSG 0.8: Earth system interaction from space geodesy
9. JSG 0.9: Future developments of ITRF models and their geophysical interpretation

It is quite clear that these study groups cover a wide field; they are however Earth-centric. That is of course no surprise, as the commissions and joint study groups support the requirements of the three classical pillars of geodesy. These basically are:

1. changes in Earth's shape (geokinematics),
2. its gravity field, and
3. rotation and orientation of Earth.

Taken together, these three classical pillars provide an underlying conceptual framework as well as observational and technological systems for the realization of the reference frames required for Earth observation. In addition, these 'three pillars' are synergistically interlinked and relate to one another through the Earth system processes.

2 Roles of the Reference Frames

The most important component in all of geodesy and in particular space geodesy is the International Celestial Reference Frame (ICRF) as determined by Very Long Baseline Interferometry (VLBI). No doubt this statement will be frowned upon by some, but this is simply due to the fact that the ICRF provides the only absolute frame of reference, which needs to be of the highest possible accuracy. In addition, all Earth-bound reference frame requirements, which depend on the International Terrestrial Reference Frame (ITRF), access the ICRF through the Earth orientation parameters (EOPs). This necessitates ultra-high accuracy EOPs. These accuracy requirements spill over into specifications for the Global Geodetic Observing System (GGOS), where the long-term accuracy and maintenance of the reference frames at very high level are major requirements. The ICRF, ITRF, and EOPs are the mandate of the International Earth Rotation and Reference Systems Service (IERS). EOPs and the ITRF are determined as multi-technique solutions and rely on high quality contributions from the different space geodetic techniques. High accuracy objectives such as maintenance of the ITRF at an accuracy level of 1 mm and stability level of 0.1 mm per year are difficult objectives (a factor of ten or more improvement on the current ITRF2008), which can only be attained if the ICRF and its variations in time can be maintained and the ICRF can be densified at a sufficiently accurate level. In addition to extreme demands by users on Earth (e.g., requirements of ocean level variation due to climate change), more demands for high accuracy space geodetic products for application in the solar system, as well as for astrometric VLBI, tests of GTR, interplanetary (and beyond) navigation will soon become common. When one therefore considers the combination of space and terrestrial geodetic techniques, measuring the complexities of the Earth system, through the three classical pillars of geodesy, the reference frames are the most important common denominator, with the ICRF being the crème de la crème. If the ICRF cannot be measured and maintained to a very high level (eventually micro-arcsecond level), which includes the optical and radio reference frames, it will not be possible to meet the GGOS objectives for the ITRF. From the viewpoint of its instrumental capacity, GGOS has six major levels of instrumentation and reference objects. These are not all fully developed.

- **Earthbound:**
  - **Level 1:** Terrestrial geodetic infrastructure (e.g., VLBI, SLR, GNSS, DORIS, and InSAR).
- **Spacebound:**
  - **Level 2:** LEO satellite missions;
  - **Level 3:** GNSS and the Lageos-type SLR satellites;
  - **Level 4:** Planetary missions and geodetic infrastructure on the Moon and planets;
  - **Level 5:** Specialized geodetic space platforms (e.g., orbiting laser transponders, VLBI satellites, Moon-bound tethered reference satellites, optical reference frame satellites); and
  - **Level 6:** Extragalactic objects.

3 Geodesy is Not *Ge*odesy Anymore

The term *geodesy* has become a bit of a misnomer ("terme inapproprié") as geodesy is not Earth-centric anymore. The term *ge* (earth) must be read in a wider context today. As example, what does the 'geodesy of the Moon' mean? Geodesy is derived from the Greek $\gamma\varepsilon\omega\delta\alpha\iota\sigma\iota\alpha$ (geodaisia), of which the literal meaning is 'division of the Earth'. However, in modern times, components of geodesy, in particular 'space geodesy', are moving towards measurement and representation of the solar system, and its place in spacetime curvature, which brings us to the Greek *chronochora*, an abstract model of space and time, i.e., *chronochora-daisia*, or *spacetimedesy*. As example, measuring the deflection of a star's light or a quasar's radio emission as it bends in the spacetime curvature of a massive object such as the Sun or Jupiter is spacetimedesy, not space geodesy. The VLBI technique in particular measures in spacetime curvature, through vast distances, through the 'local universe' and beyond. Observing through the galactic bulge must be considered as a current spacetime curvature problem and has to be accounted for when ICRF sources are being observed. Space geodesy is a good tool to test GTR. In particular, VLBI is suitable for deflection tests (Müller et al., 2008; Heinkelmann and Schuh, 2009). If GGOS is developed to its full potential, space geodesy will remain a strong contender in reliable tests of relativity, possibly reaching adequate test accuracy to evaluate alternative (scalar-tensor) theories, which predict small deviations from GTR values at a level of $|\gamma| \approx 10^{-6} - 10^{-7}$ (Combrinck, 2012).

4 Through the Looking Glass of Spacetime Curvature

The effect of weak gravitational lensing on the stability of the ICRF was already considered to some extent (*cf.* Hosokawa et al., 1997; Zharov et al., 2000), concluding that weak gravitational lensing places a limit on the realization of the ICRF. The implications on GGOS objectives have not been quantified. A certain amount of effort will have to be dedicated to improving our understanding of how spacetime affects our observations and long term reference frame stability. Spacetime curvature, i.e., the 'gravity field' of space is already incorporated in space geodesy measurements and data analysis as a matter of routine to some level as it affects VLBI, SLR, and GNSS measurements. Locally, in the solar system, VLBI has to account for deflection of the radio signal emitted from the VLBI source due to spacetime curvature caused by the Sun and large planets such as Jupiter. In the case of GPS, one has to consider that due to spacetime curvature a clock runs faster in a weaker 'gravity field', but slower due to relativistic motion. In the case of GPS, spacetime curvature wins, so the onboard clocks are set slower before being placed in orbit. The SLR model includes acceleration described by the Schwarzschild metric, frame dragging (Lense-Thirring) and geodetic (de Sitter) precession, and correction for spacetime curvature (Shapiro delay). These models and relativistic corrections are discussed in detail in Combrinck (2013) and with considerable detail concerning VLBI in Schuh and Böhm (2013).

5 So Spacetime Is Not 'flat'

Known gravitational lenses in the VLBI databases are excluded from ICRF solutions as discussed in IERS Technical Note 35 (IERS, 2009). As spacetime curvature (microlensing/weak lensing) has become an observable (Figure 1), and will become so more and more as the geodesy community strives to meet GGOS requirements (GGOS requirements for the ICRF is 25 μas accuracy, with a stability of 3 μas per year) the fourth pillar of geodesy must be taken into account. As a summary of the four pillars of geodesy we then have measurements of:

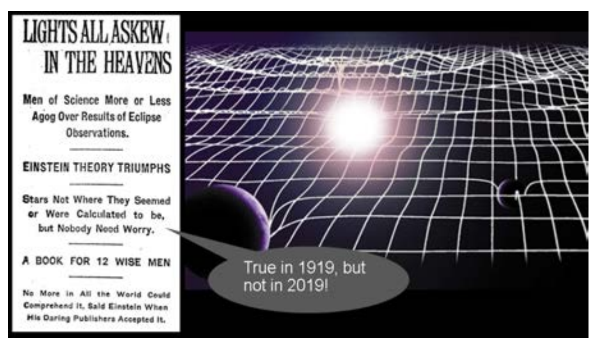

Fig. 1 Spacetime curvature has become an observable as we move into μas measuring accuracies.

- **First pillar:** changes in Earth's shape (geokinematics),
- **Second pillar:** its gravity field,
- **Third pillar:** rotation and orientation of Earth, and
- **Fourth pillar:** spacetime curvature:
  - Positions and orientation in spacetime,
  - reference frames in spacetime, and
  - how these affect the three classical pillars.

Spacetime curvature (i.e., the gravity field of space) thus becomes the fourth pillar of modern geodesy, or if you want to, 'spacetimedesy'. This fourth pillar affects all high accuracy space geodesy measurements.

6 Current Assumptions

For most general cases relevant to gravitational lensing, the assumption is made that the Friedmann-Lemaître-Robertson-Walker metric describes the geometry of the universe and that the matter which leads to the lensing are no more than local perturbations (Naryan and Bartelmann, 1995).

When considering microlensing (temporary increase of source amplitude as a result of magnification) some assumptions are usually made:

- The effect of spacetime curvature is dominated by a single localized collection of matter at some point between source and observer (thin lens approximation).
- Therefore lensing is assumed to occur at a single distance.
- In most astronomical cases this is justified as the 'lens thickness' and it is relatively small compared to the typical distances of order few Gpc between observer and lens or lens and background quasar/galaxy, respectively (and galaxy sizes ~50 kpc, galaxy cluster ~2 Mpc).

These assumptions are only valid if the Newtonian potential is small $|\Phi| \ll c^2$ and if the relative velocities of lens, source, and observer are small compared to the velocity of light so that $v \ll c$.

A complex two-dimensional magnification distribution in the plane of the source results from the microlenses which is made up of many caustics which correspond to locations of formally infinite magnification. Apparent brightness and positional changes can occur as a function of time due to relative motion of the observer, lens, and source (Wambsganss (1998). In terms of the ICRF, the effects due to amplitude variation and apparent positional changes should be evaluated. Microlensing effects will have to be considered individually for each reference quasar, with the possible development of a subset of 'super stable' ICRF sources, i.e., those with minimal microlensing position and amplitude distortion. There are several problems with the basic assumptions normally made for microlensing:

- Dark matter: baryon acoustic oscillations have left voids regularly of ~150 Mpc diameter, surrounded by the galaxies, but what is in between? Dark matter creates the gravitational framework for baryonic material, it thus creates a spacetime framework for the ICRF. Deflection of VLBI source signals is dependent on the total matter density and does not differentiate between dark or ordinary matter. What do we know about the halo's of dark matter around galaxies concerning the ICRF?
- Dark energy.
- The 'thin lens' may be stacked lenses (multiple lenses).
- Ultra-weak lensing effect for high-resolution, high-accuracy astrometry may be a cumulative effect creating 'spacetime curvature seeing' effects.
- Eventually, we will find that all VLBI source structure stability is affected by spacetime curvature dynamics at some level, impacting on our 'stable' ICRF.

As example, the galaxy cluster Abell 2218 is the widest separation lens system to be detected in the radio spectrum so far; maximum source separation is 41 arcsec. We have to consider that 'subtler' curvature effects than is seen in Abell 2218, e.g., weak lensing (which may have light bending effects that cannot be determined under the assumptions previously mentioned, but rather in a statistical way) could have an adverse impact on the ICRF, leaving us with the question: how much do we know about the effects of microlensing/weak lensing on the stability of the ICRF? Weak lensing is likely to be the main problem considering the ICRF, as basically all of spacetime is effected by the geometric distribution and variations in spacetime curvature, which is also dynamic in time, demanding continuous monitoring and maintenance of a spacetime curvature defined ICRF.

7 Recommendations

- The three pillars of geodesy should be extended to have a fourth pillar (spacetime curvature) as achieving the GGOS objectives of 1 mm accuracy in the ITRF (i.e., all the space geodetic techniques) and 0.1 mm ITRF stability is finally constrained by our understanding of the geometry of spacetime (and its variations in time).
- A working group, in close collaboration with the IERS/IVS Working Group should be formed to consider aspects of spacetime curvature (microlensing, weak lensing, local solar system deviations from asymptotically flat space) and its effects on the ICRF and how it will affect the three classical pillars of geodesy. To some extent this exists, but not formally, so this issue is perhaps not being addressed to the extent it should.

8 Conclusions

Support by GGOS for VLBI, SLR, and LLR will improve validations of GTR, but only to its fullest extent if all aspects of GGOS are addressed: networks, spacetime curvature, equipment, models, observing strategy, and processing strategies. Spacetime curvature dynamics could create "spacetime curvature seeing" effects. The possible effects of spacetime seeing should be considered in the light of extreme accuracy requirements for the ICRF and ITRF. In the near future, spacetime curvature as an observable cannot be excluded from any ICRF measurements and maintenance. It is suggested that a sub-set of super stable ICRF sources be identified which show minimum positional distortion and amplitude variation due to microlensing or weak lensing to ensure high level integrity of the ICRF.

Acknowledgements

Funding received from the National Research Foundation (NRF), South Africa, towards this project is appreciated. This work is based on research supported by NRF grant IFR2011041500034.

References

1. Combrinck, L. (2012) A Comparison of General Relativity Theory Evaluations using VLBI and SLR: Will GGOS Improve These Results? In: D. Behrend and K. Baver, editors, *International VLBI Service for Geodesy and Astrometry 2012 General Meeting Proceedings*, NASA/CP-2012-217504, pages 357—361.
2. Combrinck, L. (2013) General Relativity and Space Geodesy, in: Guochang Xu (ed.): Sciences of Geodesy II, Springer Verlag, ISBN 978-3-642-27999-7, doi: 10.1007/978- 3-642-28000-9, pp. 53-95.
3. Heinkelmann, R. and H. Schuh (2009) Very long baseline interferometry: accuracy limits and relativistic tests, in: Relativity in Fundamental Astronomy: Dynamics, Reference Frames, and Data Analysis, eds. S. A. Klioner, P. K. Seidelmann and M. H. Soffel, Proceedings IAU Symposium No. 261, Cambridge University Press, Proceedings IAU Symposium No. 261, S. A. Klioner, P. K. Seidelman and M. H. Soffel, eds., 2009
4. Hosokawa, M., Fukushiwa, T. and Ohnishi, K. (1997) Fluctuation of ICRF due to gravitational lensing, in: The New International Celestial Reference Frame, 23rd meeting of the IAU, Joint Discussion 7, 22 August 1997, Kyoto, Japan, meeting abstract, [Online Article]: cited 24 April 2014, http://adsabs.harvard.edu.
5. IERS (2009) IERS Technical Note 35, The second realization of the Interntaional Celestial Reference Frame by Very Long Baseline Interferometetry, in: Fey, A. L., Gordon, D. and Jacons, C. S. (eds.) Verlag des Bundesamts für Kartographie und Geodäsie, Frankfurt am Main, (http://www.iers.org/TN35).
6. Müller, J., M. Soffel, and S. A. Klioner, (2008) Geodesy and relativity, J. of Geodesy, 82, pp. 133-145.
7. Narayan, R., and Bartelmannn, M. (1995) Lectures on Gravitational Lensing, in: A. Dekel and J.P. Ostriker (eds.) Formation of Structure in the Universe, Proceedings of the 1995 Jerusalem Winter School.
8. Schuh, H. and Böhm, J. (2013) Very Long Baseline Interferometry for Geodesy and Astrometry, in: Guochang Xu (ed.): Sciences of Geodesy II, Innovations and Future Developments, Springer Verlag, ISBN 978-3-642-27999-7, doi: 10.1007/978- 3-642-28000-9, pp. 339-376.
9. Wambsganss, J., 'Gravitational Lensing in Astronomy', Living Rev. Relativity, 1, (1998), 12. [Online Article]: cited on 22 April 2014, http://relativity.livingreviews.org/Articles/lrr-1998-12/fulltext.html.
10. Zharov, V. E., Sazhin, M. V., and Kalinina, T. A. (2000) Weak Gravitational Lensing and Instability of the Celestial Reference Frame, in: R. Rummel et al. (eds.), Towards an Integrated Global Geodetic Observing system (IGGOS), Springer-Verlag Berlin, Heidelberg, pp. 126-127.

Revisiting the VLBA Calibrator Surveys for ICRF3

David Gordon

Abstract ICRF2 contains two classes of sources. Approximately 1/3 are sources observed in many sessions, and the other ∼2/3 are single epoch sources whose average formal errors are ∼5 times worse. About 300 of these single epoch sources have since been re-observed in RDV sessions, but around 1,900 remain. A second epoch VCS campaign is underway to re-observe these remaining single epoch sources. Results from the first of these sessions is shown to improve the position formal errors by factors of ∼5-10.

Keywords ICRF2, ICRF3, RDVs, VLBA, VCS, VCS-II

1 Introduction

ICRF2 [1] contained positions for 3,414 sources. However, two classes of sources were distinguished – those observed in many sessions (1,448 sources) and those observed in a single session (1,966 sources). If we look more closely though, we see that there are ∼2,200 sources that were observed in between one and three sessions over a short time period, which we will refer to as 'single epoch' sources. Most of these sources are from the original Very Long Baseline Array (VLBA) Calibrator Surveys (VCS) [2, 3, 4, 5, 6, 7]. These were a series of seven observing projects that used the National Radio Astronomy Observatory's (NRAO) VLBA to accurately measure the positions of as many compact radio sources as possible. The average formal position errors for the single epoch sources is approximately five times greater than that of the other ∼1,200 sources. Figure 1 shows the Right Ascension (RA) and Declination formal errors vs. the number of sessions for each source in ICRF2, using the original (unscaled) solution (gsf008a) that was used for ICRF2. The distinction between the two classes is quite clear.

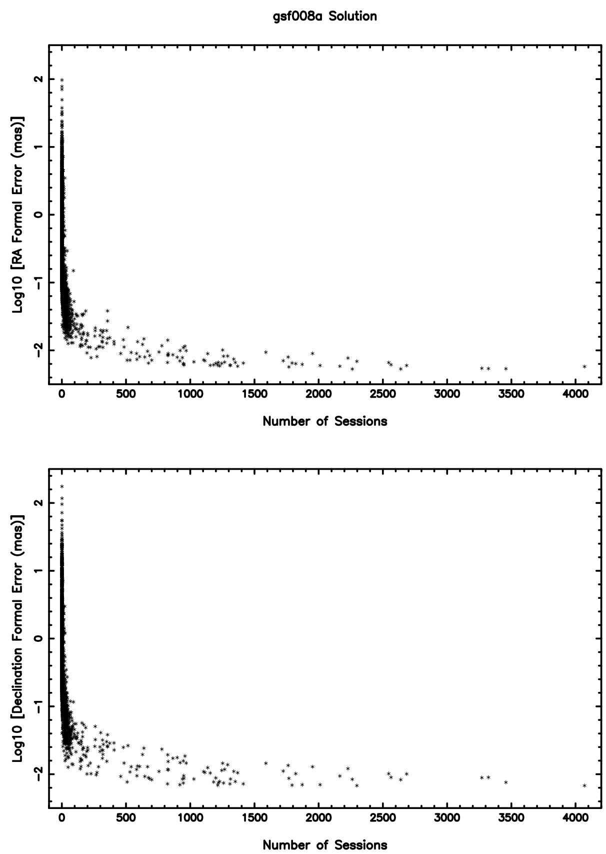

Fig. 1 Unscaled ICRF2 formal errors in Right Ascension and Declination vs. number of sessions each source was observed in.

NVI, Inc.

Table 1 shows some statistics for the ICRF2 sources by the number of sessions in which they were observed for sources at the low end of Figure 1. ICRF2 had so many weak sources observed in three or fewer sessions that it has not been practical or possible to significantly reduce their numbers through the regular IVS observing program. If we look at the distribution of formal errors among the 1,903 one-session sources, we see a wide range, from around ∼100 mas for sources with the fewest number of observations, to ∼0.1 mas for sources with the largest number of observations. This is plotted in Figure 2, which shows a fairly smooth decrease in formal errors with an increasing number of observations. Table 2 gives the statistics of ICRF2 for sources with ten or fewer observations. There were 36 sources with only three observations, 31 with only four observations, etc. These were smaller numbers that could be addressed by re-observing these sources in the regular RDV sessions.

Table 1 Distribution of sources in gsf008a (ICRF2) by number of sessions.

Sessions	Sources	Average RA-sigma (mas)	Average Dec-sigma (mas)
1	1903	1.35	2.29
2	477	1.28	2.22
3	120	0.87	1.41
4	49	0.57	0.81
5	48	0.98	1.08
6	44	0.79	0.74
7	34	0.49	0.64
8	31	0.56	0.54
9	18	0.44	0.48
10	19	0.79	0.57
15	21	0.27	0.33
20	20	0.20	0.20
25	12	0.14	0.19
30	8	0.06	0.07
35	7	0.04	0.05
40	10	0.04	0.06
45	4	0.04	0.05
50	3	0.05	0.06

Beginning in May 2009, while ICRF2 was still being finalized, we began to add a few of these poorly observed, one-session sources to each RDV session. We also re-observed some VCS sources that were originally detected in X-band only, as well as many sources whose positions were requested by members of the astronomical community for use in phase calibrating or

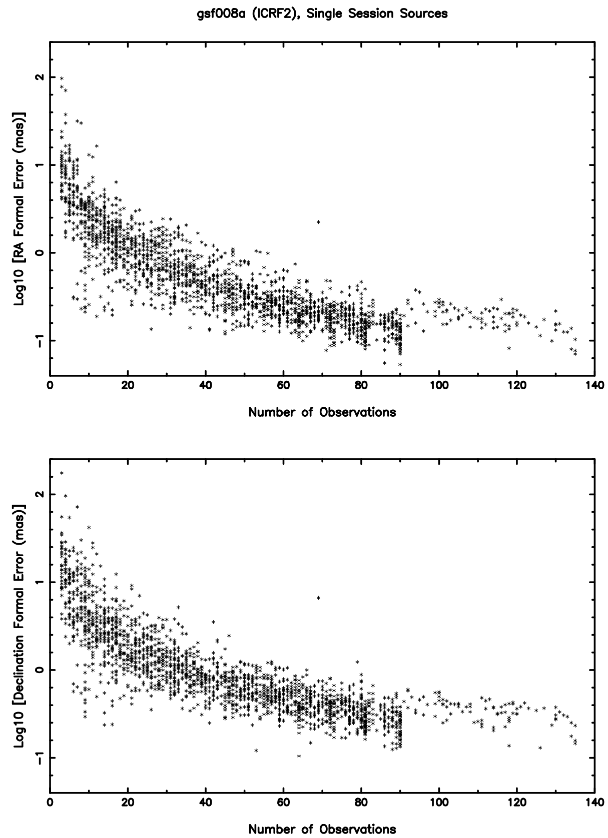

Fig. 2 Unscaled ICRF2 formal errors in Right Ascension and Declination vs. number of observations, for single-session sources.

Table 2 Distribution of sources in gsf008a (ICRF2) by number of observations for sources with ten or fewer observations.

# Obs	# Sources	Average RA-sigma (mas)	Average Dec-sigma (mas)
3	36	14.87	24.28
4	31	10.38	15.48
5	42	6.91	11.30
6	34	4.95	6.77
7	30	5.78	10.09
8	32	4.34	7.69
9	49	3.41	6.25
10	41	2.93	5.46

other purposes. In RDVs 75–102, (May 2009—Dec. 2013), some 341 ICRF2 few-observation and X-only sources have been successfully re-observed. 118 new requested sources have also been observed and detected. Table 3 gives the current numbers for sources observed ten times or less, to be compared with Table 2. Most of the sources with six or fewer observations in ICRF2 have been re-observed. Those remaining are sources that are too far south to be observed with the VLBA. These RDV re-observations are more sensitive than the original VCS sessions because we use longer integration times, 2-bit sampling (since October 2009), and fourfit fringing (since February 2011). We currently have 3,670 sources with three or more X/S observations (256 more than ICRF2). But there are still ∼1,900 single epoch sources remaining.

Table 3 Distribution of sources by number of observations after RDV75—RDV102, for comparison with Table 2.

# Obs	# Sources	Average RA-sigma (mas)	Average Dec-sigma (mas)
3	7	37.59	31.03
4	5	8.96	7.34
5	5	3.64	4.46
6	7	3.02	3.03
7	23	3.76	6.37
8	30	3.62	6.14
9	48	2.82	5.06
10	40	2.52	4.30

2 The VCS-II Proposal

To address the many single epoch sources that remain, a group was formed to request VLBA time to re-observe them in a second epoch VCS campaign. The VLBA can now observe at 2 Gbps with 2-bit sampling, which is a vast improvement over the original VCS sessions (64 and 128 Mbps, 1-bit sampling). It was estimated that ∼300 sources could be observed twice in a 24-hr session. A request was made for eight 24-hr sessions to observe ∼2,400 sources. This also included several hundred sources observed but not detected in the original VCS sessions. This proposal was approved.

The primary goals of the VCS-II campaign are: to improve or obtain the positions of ∼2,400 sources for ICRF3; improve the VLBA calibrator list; produce images of all the sources; and obtain many more apparent proper motions for secular aberration drift studies. The members of the VCS-II campaign are: D. Gordon/PI, A. Beasley (NRAO), C. Jacobs (JPL), A. Fey (USNO), R. Gaume (USNO), C. Ma (GSFC), O. Titov (Geosciences Australia), D. Boboltz (USNO/NSF), A. Peck (NRAO/ALMA), and P. Charlot (Bordeaux Observatory). The observations will use the RDBE/Mark 5C system with 16 32-Mhz channels, 12 in X-band and four in S-band. Each session will make two scans each of ∼300 single epoch sources. Slewing times will be minimized by observing a troposphere calibrator (∼20-30 seconds) and six nearby single epoch sources (∼60-120 seconds each). Scheduling will be done with the NRAO SCHED program.

3 VCS-II Observations and Analysis

Only one VCS-II session, BG219A, has been run so far, on January 4/5, 2014. Six of the VLBA antennas were used successfully for the full 24 hours, and a seventh (FD-VLBA) for ∼six hours. We did not get any BR-VLBA or HN-VLBA data, so the declination formal errors are somewhat larger than expected. However, all 300 target sources were detected, most with 20-30 observations.

Figures 3 and 4 compare the formal errors for these 300 sources, before and after this first VCS-II session. Before, the formal errors for these sources were in the range of .2–15 mas. Afterwards, the formal errors are all below 1.7 mas, and most are below 0.5 mas in RA and 1.0 mas in Declination.

4 Conclusions

Position uncertainties for many of the noisiest sources in ICRF2 have been greatly improved through re-observation in the RDV sessions since 2009, and many new sources were also added to the current catalog. The first session of the VCS-II campaign has shown that formal position errors of the single epoch sources can be improved by factors of ∼5—10. The VCS-II campaign could potentially eliminate the second class of ICRF2 sources with large formal errors. The VCS-II campaign is also expected to add several hundred additional sources to ICRF3.

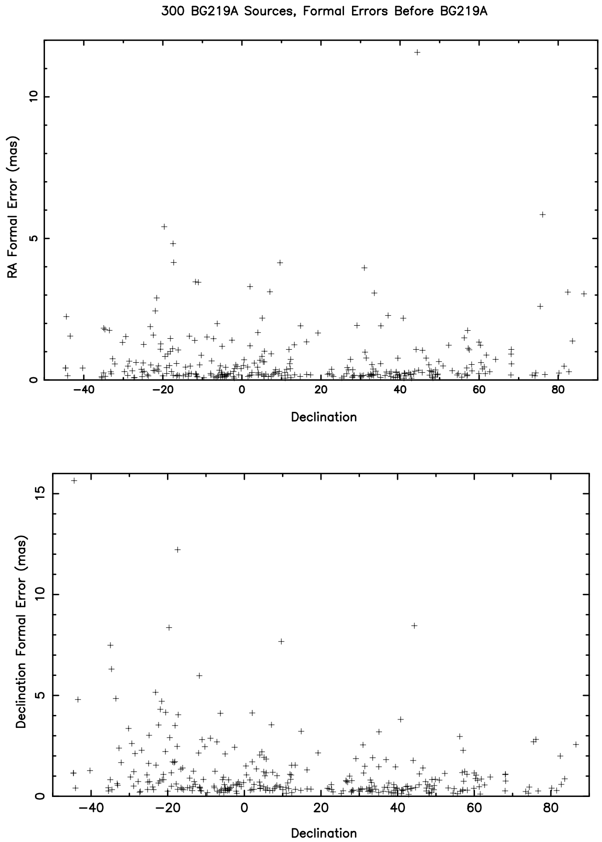

Fig. 3 Formal errors of the 300 sources in BG219A before re-observations,

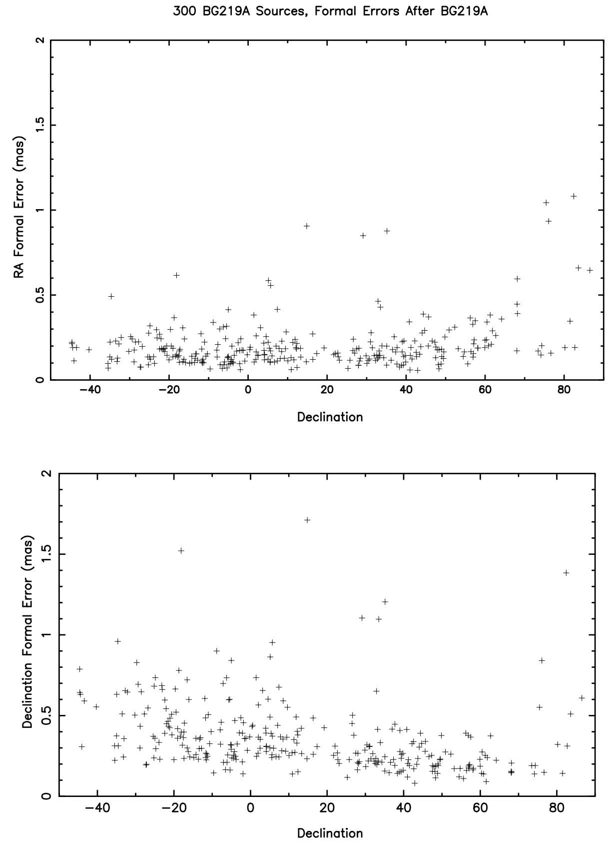

Fig. 4 Formal errors of the 300 sources in BG219A after re-observations. Note the change in scales.

Acknowledgements

The VLBA is operated by the National Radio Astronomy Observatory (NRAO) from the Pete V. Domenici Science Operations Center (SOC) in Socorro, New Mexico. The National Radio Astronomy Observatory is a facility of the National Science Foundation, operated under cooperative agreement by Associated Universities, Inc.

References

1. "The Second Realization of the International Celestial Reference Frame by Very Long Baseline Interferometry", IERS Technical Note No. 35, A.L. Fey, D. Gordon, C.S. Jacobs (editors), 2009. http://www.iers.org/TN35.
2. "The VLBA Calibrator Survey - VCS1", Beasley, A. J., D. Gordon, A. B. Peck, L. Petrov, D. S. McMillan, E. B. Fomalont, C. Ma, Asrophys. J., Supp., vol. 141, p. 13-21, 2002.
3. "The Second VLBA Calibrator Survey - VCS2", E. Fomalont, L. Petrov, D. S. McMillan, D. Gordon, C. Ma, Astronomical Journal, vol. 126 (N5), p. 2562-2566, 2003.
4. "The Third VLBA Calibrator Survey - VCS3", L. Petrov, Y. Y. Kovalev, E. Fomalont, D. Gordon, Astronomical Journal, vol. 129, p. 1163-1170, 2005.
5. "The Fourth VLBA Calibrator Survey - VCS4", L. Petrov, Y. Y. Kovalev, E. Fomalont, D. Gordon, Astronomical Journal, vol. 131, pp. 1872-1879, 2006.
6. "The Fifth VLBA Calibrator Survey - VCS5", Y. Y. Kovalev, L. Petrov, E. Fomalont, D. Gordon, Astronomical Journal, 2007, Vol. 133, p. 1236-1242.
7. "The Sixth VLBA Calibrator Survey - VCS6", L. Petrov, Y. Y. Kovalev, E. Fomalont, D. Gordon, Astronomical Journal, vol. 136, p. 580-585, 2008.

The NASA Goddard Group's Source Monitoring Database and Program

John Gipson[1], Karine Le Bail[1], Chopo Ma[2]

Abstract Beginning in 2003, the Goddard VLBI group developed a program to purposefully monitor when sources were observed and to increase the observations of "under-observed" sources. The heart of the program consists of a MySQL database that keeps track of, on a session-by-session basis: the number of observations that are scheduled for a source, the number of observations that are successfully correlated, and the number of observations that are used in a session. In addition, there is a table that contains the target number of successful sessions over the last twelve months. Initially this table just contained two categories. Sources in the geodetic catalog had a target of 12 sessions/year; the remaining ICRF-1 defining sources had a target of two sessions/year. All other sources did not have a specific target. As the program evolved, different kinds of sources with different observing targets were added. During the scheduling process, the scheduler has the option of automatically selecting N sources which have not met their target. We discuss the history and present some results of this successful program.

Keywords Scheduling, sources

1 Problem: Under-observed Sources

In June 2003 we noticed that some sources were being observed a lot, while other sources, including many of the ICRF1 defining sources, were observed scarcely at all. Because there are literally thousands of sources that have been observed in VLBI, we decided to restrict our attention to two subsets. 'Geodetic' sources are in the geodetic catalog and are used for most IVS geodetic schedules. An ideal geodetic source is strong and compact. The other category, which we called 'Astrometric', consisted of the 212 defining sources of ICRF1 plus an additional 90 sources suggested by Martine Feissel. About a third of these sources were also Geodetic. After internal discussions, we decided that a reasonable observing target was that all 'Geodetic' sources should be scheduled and succesfully observed in 12 sessions/year, and the 'Astrometric' sources in two sessions/year. The remaining sources have no set observing target. Figure 1 plots the observing frequency of the Astrometric sources beginning in 2003 and continuing through 2004. In the

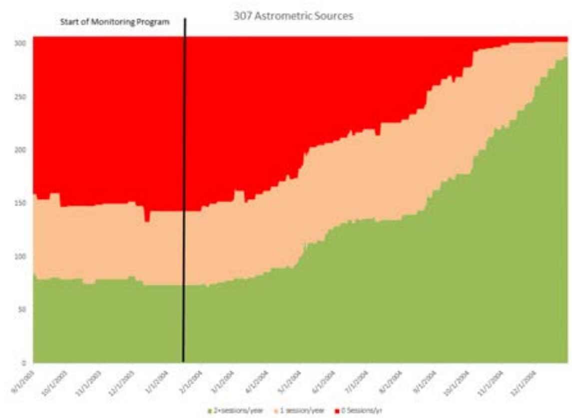

Fig. 1 Prior to the start of the Source Monitoring Program almost half of the Astrometric sources had not been observed during the prior year. Once the program starts the number of sources that do not meet their target (in red and orange (the top two layers)) decreases sharply.

1. NVI, Inc.
2. NASA Goddard Space Flight Center

remainder of this paper, we describe our approach to meeting these observing goals.

2 Source Monitoring Program

In principle, scheduling under-observed sources could be done by hand by the scheduler. The scheduler would need to do the following: 1.) find the under-observed sources; 2.) find out which ones are visible with the current network, and 3.) choose a set of these sources to observe. However, we wanted a solution that was more or less automatic and that required minimal human intervention. All of the above steps would still have to be done–but they would be done by the computer.

2.1 Overview of Database

Our approach to this was to design a database that kept track of when sources were observed. This database, called VDB, could be queried by humans or programs to extract the relevant information. We also decided to include additional information that would be useful outside of the needs for source monitoring. Table 1 summarizes the important tables in the database.

Table 1 Tables in the source monitoring database.

Name	Description
Master	Summary Information
SrcExp	Session specific source information
StatExp	Session specific station information
SrcObsDens	Source observing target
History	Database history

Master contains summary information about each VLBI session. This includes all of the information in the IVS Master files as well as additional information, for example, when the session is scheduled and when it is analyzed, and also individual session fits. This table is updated 1.) whenever the IVS Master files are updated; 2.) when the session is posted to CDDIS, and 3.) when the session is analyzed at GSFC to produce a Version 4 database.

SrcExp contains session-by-session information about each source. For each session, this table includes: the number of scheduled observations per source; the number of correlated observations per source, and the number of observations per source used in the solution. This table is updated: 1.) when a session is posted to CDDIS and 2.) when a session is analyzed at GSFC to produce a Version 4 database.

StatExp contains information about the stations. Its format and use is entirely analogous to SrcExp. This table is updated 1.) when a session is posted to CDDIS and 2.) when a session is analyzed at GSFC to produce a Version 4 database.

SrcObsDens contains source-specific information about the sources. This includes what kind of source it is (ICRF2, Defining, Special Handling, etc.) and the observing targets for each source. The only sources that are required to be in this table are sources that have some specific observing target. This table is only updated when we add new sources to the monitoring program or we change the observing targets of the source.

History contains a record of when the database is updated and is used primarily for debugging purposes.

2.2 Source Monitoring Dataflow

The Source Monitoring database is updated whenever 1.) the Master File is updated; 2.) a schedule is put on CDDIS, and 3.) a database is analyzed at GSFC. A schematic diagram of this is presented in Figure 2. The stages in this are described below.

Update_vdb_master keeps the Master Table current. This is run to create new entries in the Master Table when a new Master Schedule is created, for example, prior to the start of a new observing year. The program is also run whenever the Master Schedule is changed, which happens many times during the course of a year. When this is done, existing entries are updated to reflect the changes. This process happens automatically as part of posting the Master Schedule to the IVS Web pages.

Update_vdb_out is run whenever a new VLBI schedule appears on CDDIS. This program runs *sked* to extract information about the schedule. It checks to make sure that the schedule is in the Master Table, and if so, updates the Master Table indicating when the session was scheduled. In addition, it also updates SrcExp and StatExp indicating how many times each Source and Station in the schedule were scheduled.

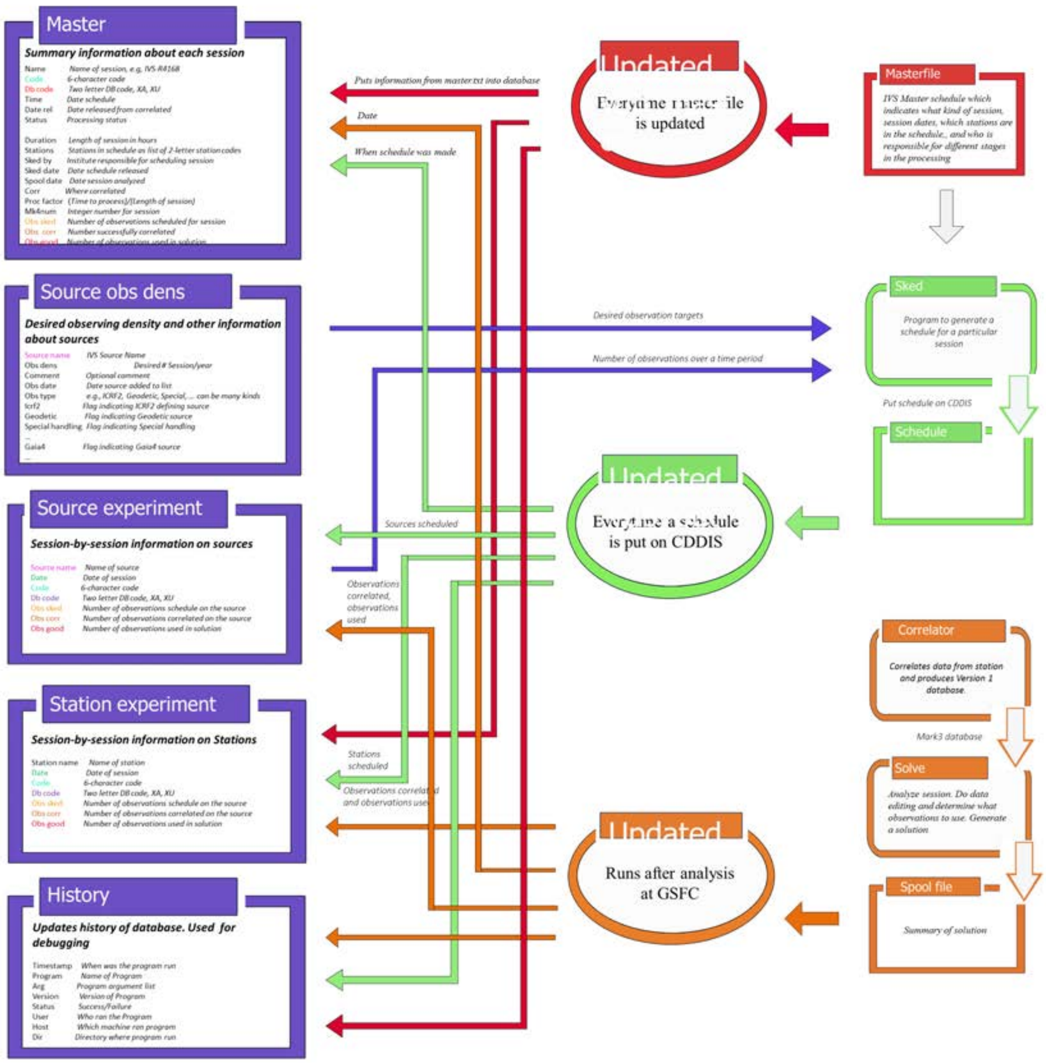

Fig. 2 Events that update the Source Monitoring Database.

This program is run automatically as part of posting the schedule the IVS data centers.

Update_vdb_in is run whenever GSFC analyzes an IVS session as part of its regular data analysis. The program reads the session spool-file (which contains the results of the analysis). It then updates the Master Table indicating when the analysis was done, as well as the session fit of the solution. It then updates SrcExp and StatExp with the number of observations that were correlated and used in the solution for each source and station. This program is run automatically as part of posting the Goddard solution to the IVS Web site.

The above describes how we keep the database updated to reflect the state of processing and the analysis of VLBI data. An equally important part of the source monitoring program is the ability to query the database. We built an interface between *sked* and the source monitoring database. If the user types "monitor *N*", *sked* will attempt to select *N* under-observed sources to include in the current schedule. These schedules are put in the $ASTROMETIC section with observing targets of 1% to 1.5%, and *sked* will devote up to $1.5 \times N\%$ of the observations in the schedule to these sources. We do not have space to completely describe the process, but here is a summary. Using SQL commands, *sked* queries the database to find out how many successful sessions the sources in the monitoring program have been observed during the last year. Here *successful* means that they were scheduled and at least three observations were used in the solution. It then compares this against the target for the sources and gives each score a rank by how much it has been under-observed. *Sked* will then select up to N sources from this list (starting at the top) that are observable with the current network. For a more complete description of *sked* and its commands, see [1].

3 History and Applications

The monitoring program started on February 1, 2004 and is now entering its tenth year. Initially only NASA was involved in this effort, and only R1s and RDV sessions participated in the program. In each of these sessions we scheduled up to ten monitoring sources and used up to 15% (although the actual number is typically less). We chose this number because we felt that this would not significantly degrade the measurement of EOP, which was the primary purpose of the R1s.

3.1 Starting the Monitoring Program

Figure 1 shows the observing history of the sources initially in the Astrometric source list before and after the Source Monitoring program. Initially only 25% of the sources in the list met their observing target of two sessions/year. We began to see results almost immediately, and by the end of the first year, 95% of the Astrometric sources met their target. The sources that did not meet their targets tend to be southern sources that are not visible by most stations in the IVS.

3.2 Enlarging the Geodetic Catalog

In 2008, GSFC decided to significantly enlarge the geodetic catalog. A series of four R&D experiments scheduled in April (RD0803), May (RD0804), September (RD0807), and October (RD0808) was devoted to observing these sources and establishing a baseline flux model. Once the sources were successfully observed, they were added to the catalog. Figure 3 shows the observing history of the new enlarged geodetic catalog.

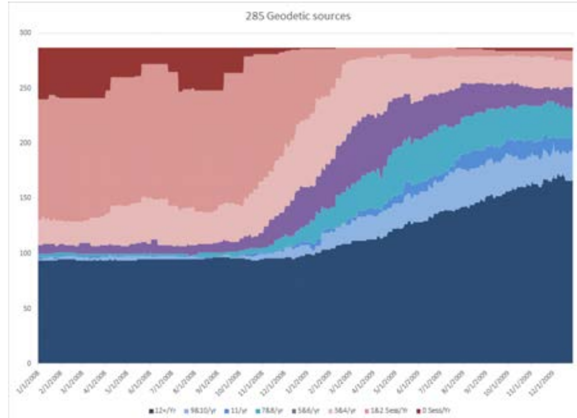

Fig. 3 Updating the geodetic catalog.

3.3 USNO Joins the Effort

In August 2010, USNO joined the Source Monitoring program, scheduling up to ten sources in each of the R4s. Because of security reasons, they could not directly access the database over the Internet. Instead we used the following work-around. Every evening the mysql database is tarred and gzipped and made available via anonymous ftp. USNO picks up the database the next morning and makes a local copy. This local copy is queried by sked when USNO generates schedules.

3.4 Gaia Transfer Sources

In mid-2013, we began introducing the Gaia transfer sources to the source monitoring program. This is a set of 195 sources submitted by the Laboratoire d'Astrophysique de Bordeaux (LAB) that will be used to tie the ICRF and the Gaia Reference Frame. These 195 sources are divided into four categories. The first two contain sources already in the IVS monitoring program, with a yearly observation target of 12. Categories 3 (16 sources) and 4 (24 sources) contain sources that are not in the monitoring program, and, for category 4, have a poor position accuracy. These sources are now scheduled in R&D and RDV sessions. We can see preliminary results in Figures 4 and 5.

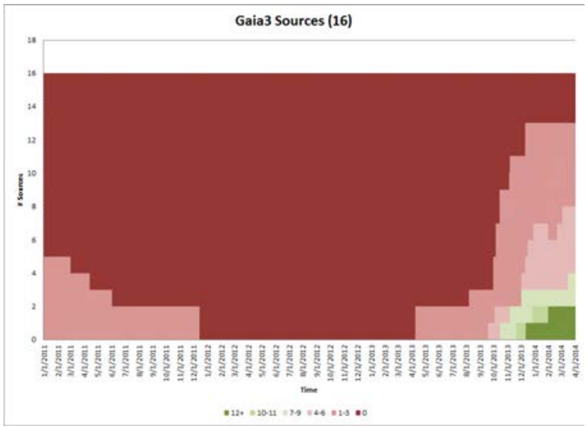

Fig. 4 Category 3 of the Gaia transfer sources.

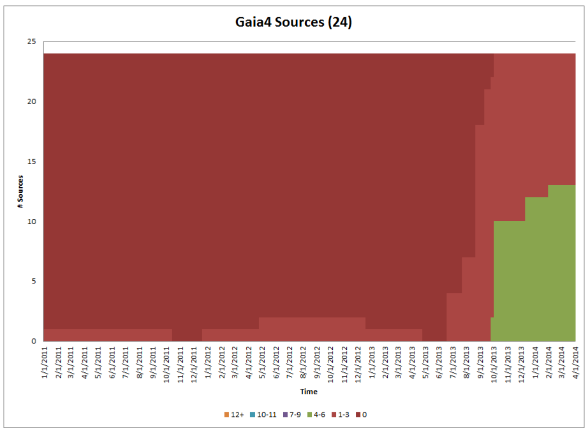

Fig. 5 Category 4 of the Gaia transfer sources.

4 Using SQL to Query the Database

The VDB database can be used for purposes other than to automate the observing of sources. The figures displayed previously were the results of querying the database about the frequency of observation of various source sets. Other queries are also possible. For example, in the query below (Figure 6) we inquire about all sources in the Intensives over a one-year period. More complex queries are possible, such as asking about: 1.) all sessions involving Kokee; 2.) all sessions involving Kokee and Ny-Ålesund which scheduled 3C84; 3.) observations of sources in different declination bands; and 4.) all observations of a source in the RDVs. Because of space limitations, we forgo further examples.

```
mysql> select src_name, count(*)
from srcexp where date
> "2007-8-31" and date <
"2008-9-1" and code like "i0%"
group by src_name;

+----------+----------+
| src_name | count(*) |
+----------+----------+
| 0014+813 |        2 |
| 0059+581 |      156 |
| 0119+115 |        9 |
| 0201+113 |        4 |
. . .
| 3C371    |      178 |
| 3C418    |       98 |
| 4C39.25  |       78 |
| DA426    |        2 |
| OJ287    |       24 |
+----------+----------+
31 rows in set  (0.07 sec)
```

Fig. 6 Sample SQL query and results.

5 Conclusion

The source monotiring mySQL database was originally designed as a tool to facilitate the automatic monitoring of sources. It has been very successful in this capacity. However, because it is a full relational database, you can use it to examine the data in different ways. In this note, we have presented some of the ways that we use database. A copy of the database is tarred and gzipped on a daily basis and made available via the Web at ftp://gemini/pub/vdb/gsfc_mysql_db.out.gz

References

1. J. Gipson, Sked User Manual, http://lupus.gsfc.nasa.gov/files_user_manuals/sked/sked.pdf

Evaluation of the Stability of ICRF2 in the Past Five Years Using the Allan Variance

Karine Le Bail, David Gordon, John Gipson

Abstract This preliminary study is a re-evaluation of the work done in 2010 on the stability of ICRF2, using the most up-to-date source positions catalog from GSFC and comparing to the solution computed in 2009. The example of source 3C418 shows how five more years of data can strengthen statistical studies. The Allan variance shows a threshold of 50 μas for the noise level (flicker noise) for both coordinates in 2010. With five more years of data, the threshold is passed, and for the declination, the white noise reaches a level of 10 μas. Using methods similar to those used in 2010, we also show that the ICRF2 defining sources realize a more stable frame, suggesting the solutions are getting more consistent, and the latest solution shows a better statistical stability.

Keywords ICRF2, stability, Allan variance

1 Introduction

In 2010, we presented a method of analyzing VLBI source time series and evaluating the statistical time stability of VLBI sources, generating a stability index function of time for each source (see Le Bail and Gordon, 2010 [2]). This method is inspired by the paper of Martine Feissel-Vernier "Selecting stable extragalactic compact radio sources from the permanent astrogeodetic VLBI program" [1].

Four years later, we use the same method to study current solutions and compare the evolution of the stability of ICRF2.

NVI, Inc.

In the first part of this study, we look at a particular source we studied in 2010: 3C418, and we determine by the Allan variance if the previous determination of noise is confirmed by the additional data. The second part of the study looks at the stability of Celestial Reference Frames by using the stability index to quantify each source stability. A look at the ICRF2 defining sources is also given.

2 Studied VLBI Solutions

In this study, we consider three different solution sets: 09GSF005, TS2012a, and TS2014a, all computed at GSFC/NASA with *Calc/Solve*. These time series solution sets were all generated in the same manner.

Five separate *Solve/Globl* solutions were run for each solution set. In the first solution, the positions of all 295 ICRF2 defining sources were estimated as global parameters (a single position for the entire data span) and constrained to their ICRF2 positions using a no-net-rotation constraint. All other source positions were treated as arc parameters; that is, a separate position was estimated for each source in each session. In the second solution, one-fourth (74) of the defining sources were removed from the global parameter list and the no-net-rotation constraint (every fourth source by right ascension). Positions for those 74 sources (along with all the others from the first solution) were estimated as arc parameters. In the third, fourth, and fifth solutions, the next successive 1/4 of the ICRF2 defining sources (74, 74, and 73 sources) were treated as arc parameter sources. The time series for the 295 defining sources were taken from the second, third, fourth, and fifth solutions. All other sources were taken from the first solution.

For these solutions, sessions with small and regional networks were excluded, because they do not yield highly accurate source positions. Also no VCS sessions were used, because most of the VCS sources were observed only once or twice.

The three solution sets differ by the period they cover: 1979 to 2009 for 09GSF005 (29 years and 7.5 months), 1979 to 2012 for TS2012a (32 years and 11 months), and 1979 to 2014 for TS2014a (34 years and 5.5 months). The number of sources in the catalog increases 41% from 1,204 for 09GSF005 to 1,696 for TS2014a (see Table 1).

Table 1 The three solution sets of this study.

	Period	Number of sources
09GSF005	1979-Aug-03 to 2009-Mar-16	1204
TS2012a	1979-Aug-03 to 2012-Jul-02	1517
TS2014a	1979-Aug-03 to 2014-Jan-16	1696

3 The Case of 3C418 with Five More Years of Observations

We use the Allan variance to study source 3C418. This is a statistical tool used to determine the type and level of noise of time series by computing the Allan variance over various sampling times τ. The slope of the Allan variance curve indicates the type of noise as illustrated in Figure 1: -1 indicates white noise, 0 flicker noise, and $+1$ random walk.

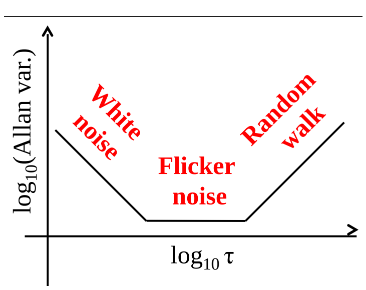

Fig. 1 Using the Allan variance to determine the type of noise.

3C418 is a good example of non-stationarity. From the 09GSF005 solution, the Allan variances computed from 1989–1993 show white noise at the level of 100 μas for both coordinates. The Allan variances computed from 1997 to 2009.5 show a combination of white noise and flicker noise, with a level for the flicker noise as low as 50 μas for both coordinates.

We extend this study to 2014 using the solution TS2014a (see Figure 2). The Allan variances computed from 1989–1993 show white noise at the level of 200 to 400 μas. This is the same four-year period as in the previous study. The results can be explained by the short period on which the Allan variances are computed, as well as the improvement of the technique after 1993. The Allan variance computed from 1997–2014 shows a combination of white noise and flicker noise. However, for the declination, the Allan variance curve is characteristic of white noise with a periodic signal with a period close to one year: the declination time series do not reach the same threshold of 50 μas reached by the right ascension. The five more years of observations strengthen the previous statistical study and brings more details on the noise in the time series.

4 Stability Study

To judge the stability of a subset of chosen sources, we compare two Celestial Reference Frames realized by this subset: one is the yearly mean realization $(CRF)_i$ while the other is the mean computed over the full period. To do so, we process $(A1,A2,A3)$, three rotation angles around the X, Y, and Z axes, respectively, and a fictitious declination bias dz. This is illustrated in Figure 3.

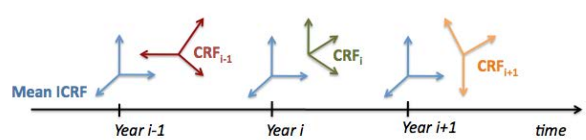

Fig. 3 Method used to compute the parameters $(A1(i),A2(i),A3(i),z(i))$ to access the stability of Celestial Reference Frame.

First, we apply this to study the 295 ICRF2 defining sources. The three solution sets are studied over the same period 1989.5–2009.5. Figure 4 shows the $(A1,A2,A3)$ obtained. We repeat this study for a longer period for TS2014a (1989.5–2013.5), and the results

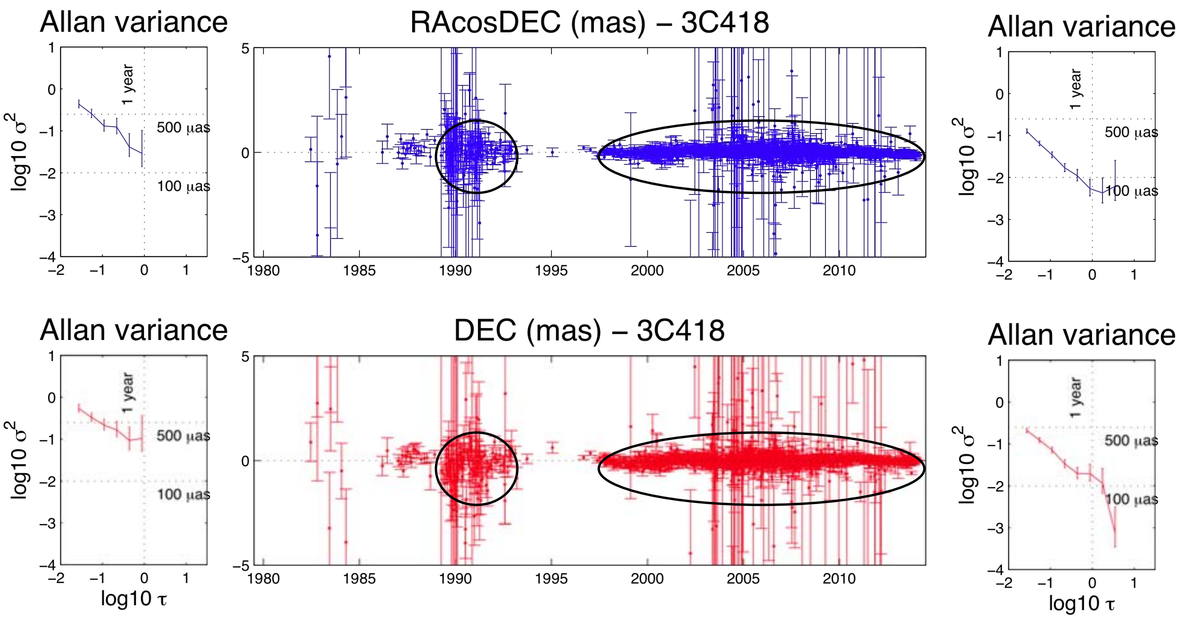

Fig. 2 Position time series of 3C418 (middle plots), Allan variances computed from 1989 to 1993 time series (left plots) and Allan variances computed from 1997 to 2014.1 times series (right plots).

are shown in Figure 5. The standard deviation and the mean are reported in Table 2.

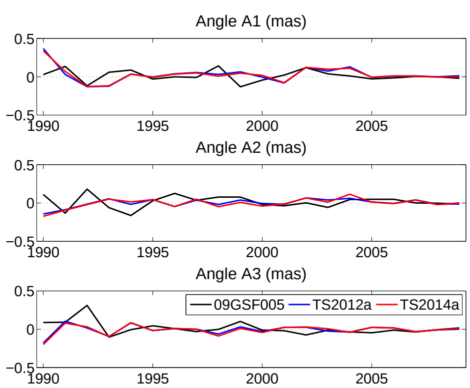

Fig. 4 Stability of the frame realized by the ICRF2 defining sources in each solution 09FSF005, TS2012a, and TS2014a studied, over the same period 1989.5–2009.5.

For the latest solution sets (TS2012a and TS2014a), the means and standard deviations are smaller than for solution set 09GSF005. The stability of A3 is improved by a factor of two. The curves in Figures 4 and 5 are significantly more stable, especially after 1995. The ICRF2 defining sources realize a more stable frame, suggesting the solutions are getting more consistent.

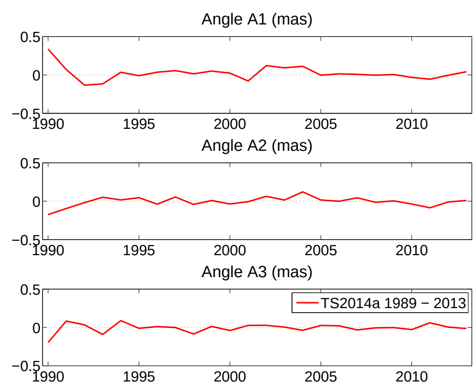

Fig. 5 Stability of the frame realized by the ICRF2 defining sources in the solution TS2014a over the period 1989.5–2014.1.

In the second part of this study, we look at the stability of each source and build sets of stable sources for each solution set. The method is described in Le Bail and Gordon, 2010 [2] and summarized hereafter. Using statistical metrics such as the Allan variance at a one-year sampling time and the normalized values of the drifts for both coordinates (right ascension and

Table 2 Standard deviations and means of (A1,A2,A3) in Figures 4 and 5.

Statistics		09GSF005 (1989.5 - 2009.5)	TS2012a (1989.5 - 2009.5)	TS2014a (1989.5 - 2009.5)	TS2014aL (1989.5 - 2013.5)
Std	A1	0.0756	0.0703	0.0692	0.0644
	A2	0.0839	0.0415	0.0494	0.0488
	A3	0.0901	0.0473	0.0482	0.0443
Mean	A1	0.0127	0.0131	0.0148	0.0103
	A2	0.0108	0.0089	0.0061	0.0026
	A3	0.0090	0.0016	-0.0006	0.0021

declination), we calculate a stability index for each analyzed source. The sources are then sorted from the most stable to the least stable. Reference Frames are built using sets of the i^{th} most stable sources. For each of these Reference Frames, we compute a set of $(A1(i), A2(i), A3(i), dz(i))$ for each year i, and then calculate the standard deviation and the mean for the quantity $A1 + A2 + A3 + dz$.

Figure 6 shows the standard deviation and the mean as a function of the number of sources used, for the solutions 09GSF005, TS2012a, and TS2014a studied over a common period 1989.5–2009.5.

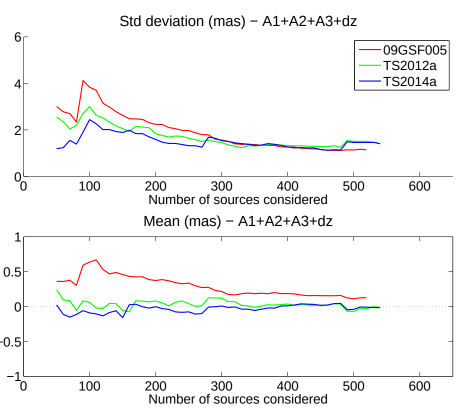

Fig. 6 Stability of subsets of stable sources selected in each solution set: 09GSF005, TS2012a, and TS2014a over the period 1989.5–2009.5.

The solution set TS2014a shows better stability than 09GSF005 and TS2012a. A set of 280 sources gives an optimal stability.

Let us note that the improvement in stability of TS2014a compared to TS2012a may be due in part to a reprocessing of *DiFX* correlated data from 2011.0 to 2012.5 to fix a *difx2mark4* error.

5 Discussion

We compare solution sets done with data through the beginning of 2009 (09GSF005), through the middle of 2012 (TS2012a), and through the beginning of 2014 (TS2014a). The latest solution set has five more years of data.

The current solution set is more consistent, and the frame realized by the defining sources seems more stable. Thanks to efforts such as the IVS monitoring program, IVS observing is becoming more consistent and uses more resources.

References

1. Martine Feissel-Vernier. Selecting stable extragalactic compact radio sources from the permanent astrogeodetic VLBI program. *A&A*, 403, doi:10.1051/0004-6361:20030348, 105–110, 2003.
2. Karine Le Bail and David Gordon. Time-dependent Selection of an Optimal Set of Sources to Define a Stable Celestial Reference Frame. In D. Behrend and K. Baver, editors, *International VLBI Service for Geodesy and Astrometry 2010 General Meeting Proceedings*, NASA/CP-2010-215864, pp. 280–284, 2010.

On the Selection of Core Sources

Sergei Kurdubov, Elena Skurikhina

Abstract In earlier work [3, 4], we had suggested a method of ranking source sets in order to select the list of sources that better define the orientation parameters of rigid rotation transformation from one system to another. The transformation parameters' formal errors were selected as a characteristic of the source set. For all catalogs, IVS WG2 selected a special order for the source lists and obtained an accuracy for the transformation parameters as a function of the number of sources. For all catalogs with a minimum between 300 and 400 sources, adding sources after the minimum leads to increasing formal errors of the orientation parameters. After that, we selected the common sources which were selected before the minimum, and we obtained the "optimal set". Source position time series were obtained and analyzed for the optimal set of sources. It was shown that some of the core sources have unstable positions and need to be excluded from the optimal set. Nevertheless, the time series show that the stable sources compose a mainly optimal source set.

Keywords VLBI, CRF, ICRF, core, defining sources

1 Introduction

We try to select the set of sources that minimizes formal errors of the orientation parameters of the rigid rotation transformation model.

Institute of Applied Astronomy Russian Academy of Sciences

2 List Characteristic Definition

We do not use ranking of sources. Instead, we construct ranking parameters that can characterize the list of sources. Then we can compare not individual sources, but instead a set of them. The main advantage of our method is that it takes into account both geometrical distribution of the sources in the set and source position accuracy.

Let's say we have two catalogs (*RA*, *DE*) and (*ra*, *de*); we can then represent the differences

$$dRA = RA - ra$$

$$dDE = DE - de$$

between them and form

$$dRA = A1\tan(DE)\cos(RA) + A2\tan(DE)\sin(RA) - A3$$

$$dDE = A1\sin(RA) + A2\cos(RA),$$

where A_1, A_2, and A_3 are the transformation parameters. If we select the set of common sources in the two catalogs then we can calculate parameters $\mathbf{A} = (A1, A2, A3)$ and formal errors σ_{A1}, σ_{A2}, and σ_{A3} by the Least Square method:

$$\mathbf{A} = \mathbf{N}^{-1}\mathbf{b}$$

$$\sigma_{A1} = \sigma_0\mathbf{N}^{-1}[0,0]$$

$$\sigma_{A2} = \sigma_0\mathbf{N}^{-1}[1,1]$$

$$\sigma_{A3} = \sigma_0\mathbf{N}^{-1}[2,2].$$

We form normal equation matrix $\mathbf{N} = \mathbf{C^T P C}$ where $\mathbf{C} = \partial(dRA, dDE)/\partial A$ with the $\mathbf{P} = \mathbf{E}$ unitary matrix. The diagonal elements of inverted normal matrix

$\mathbf{N}^{-1}[0,0]$, $\mathbf{N}^{-1}[1,1]$, $\mathbf{N}^{-1}[2,2]$ are not affected by the differences between the two catalogs and depend only on the set of sources. For the calculation of σ_0, we use the formal errors of the selected set of sources

$$\sigma_0 = \frac{\sum(\sigma_{RA})^2 + \sum(\sigma_{DE})^2}{N-3} \tag{1}$$

Thus we calculate σ_{A1}, σ_{A2}, and σ_{A3}, which are not affected by the differences between the two catalogs and depend only on the geometrical distribution of the sources in the set and formal errors of source coordinates.

We do not use σ_0 for the standard formula

$$\hat{\sigma_0} = \frac{\sum(r_{RA})^2 + \sum(r_{DE})^2}{N-3} \tag{2}$$

where r_{RA} and r_{DE} are the residuals after transformation, because all CRF catalogs are obtained from the same data, and using σ_{RA} and σ_{DE} gives more adequate results.

For source list ranking parameter q, we select the maximum of the orientation parameter formal errors:

$$q = MAX(\sigma_{A1}, \sigma_{A2}, \sigma_{A3}).$$

3 Optimized List Construction

If we want to define the orientation of the catalog in the best way, we need to select the set of sources that minimizes parameter q. The obtained set of sources can be considered as a set of "defining" sources.

We take into account only sources that are presented in the ICRF-ext.2 catalog [1] and have more than 10 session in the gsf008a catalog.

We use the next algorithm for the selection of the set of sources:

- Triple loop over all sources to select three sources that give a minimum value of q. At this step, we have the optimal set for $N_{sources} = 3$.
- Search over all remaining sources in order to minimize q for N+1 sources Remove the identified source from the list of remaining sources and add it to the final set.
- Repeat Step 2 for all remaining sources.

After that, we have a sequence of the lists that contains the optimal set of sources for a given $N_{sources}$ (see the red line on the Figure 2). We obtained for all catalogs MAX(σ_{A1}, σ_{A2}, σ_{A3}) as a function of the number of sources (Figure 1). All of the catalogs have a minimum between 300 and 400 sources. Adding sources after the minimum leads to increasing formal errors of orientation parameters.

The first three sources in the set after step 1 are $0851+202$, $0955+476$, and $2037+511$.

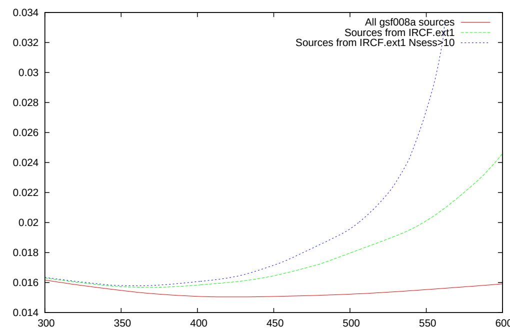

Fig. 1 Normalized MAX(σ_{A1}, σ_{A2}, σ_{A3}) vs. the number of sources for different catalogs.

4 Comparison of Our Optimized List and the OPA-ranked List

We have compared our optimized list with the OPA-ranked list. Also we calculated parameter q for the ICRF 212 defining list and for some lists of common sources. The results are presented in Figure 2.

The $\sqrt{q}$ plotted on the graph can be considered as the maximum formal error of the orientation parameters for the given set of sources. One can see that the ICRF 212 defining list gives worse results than the subset of the first sources from the OPA or IAA lists. Excluding from it seven sources not presented in the OPA list gives significant improvement. The first 380 sources from the OPA list recommended by Sebastien and Anne-Marie Gontier [2] show much better results than the 205 ICRF defining sources. But if we take common sources from the first 380 sources of the OPA list and the first 380 of the IAA list, we obtain almost two times better results by our criteria. The common set contains 288 sources.

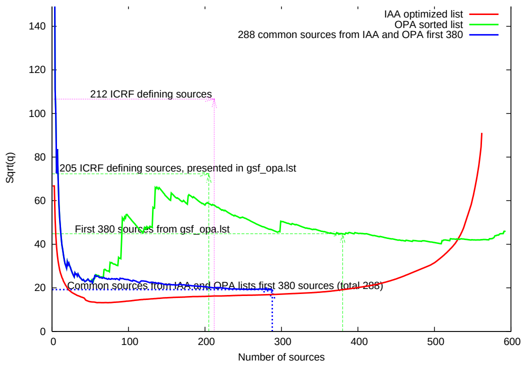

Fig. 2 MAX(σ_{A1}, σ_{A2}, σ_{A3}) vs. the number of sources for different subsets of the gsf2008a catalog.

5 Conclusion

It seems that transformation parameters for ICRF2 by the first 380 sources of the OPA-ranked list will not be estimated with the best accuracy. We suppose it would be better to use part of our optimized list or the common part of the N sources from our OPA list for the calculation of the transformation parameters. The function $q(N)$ for our optimized list rapidly increases only after N=400 sources. Thus if one takes the common part of any list of sources with our list for N$\leq$400, it will increase the accuracy of the transformation parameters.

The presented algorithm can be used for the selection of core sources for new catalogs. We plan to use selected sources for the actual computation of the transformation parameters between catalogs for ICRF3. The algorithm needs to be reviewed in the case of upcoming of multi wavelength reference frame.

References

1. The Second Realization of the International Celestial Reference Frame by Very Long Baseline Interferometry, Presented on behalf of the IERS / IVS Working Group, Alan Fey, David Gordon, and Christopher S. Jacobs (eds.). IERS Technical Note 35, Verlag des Bundesamts für Kartographie und Geodäsie, Frankfurt am Main, 2009. 204 p., ISBN 3-89888-918-6
2. S. Lambert, A.-M. Gontier, On Radio Source Selection to Define a Stable Celestial Frame, A&A, vol. 493, issue 1, pp. 317–323, Jan. 2009. http://www.aanda.org/articles/aa/abs/2009/01/aa10582-08/aa10582-08.html
3. Kurdubov S. L., Skurikhina E. A. Dependence of Catalogue Orientation Parameters Accuracy from Sources Set Selection. Proceeding of the 19th European VLBI for Geodesy and Astrometry Working Meeting. eds.: G. Bourda, P. Charlot, A. Collioud. Bordeaux, 2009. pp. 5–9.
4. Kurdubov S., Skurikhina E. Source selection for NNR constraints from source position time series “Measuring the future”, Proc. of the Fifth IVS General Meeting, A. Finkelstein, D. Behrend (eds.), St. Petersburg, “Nauka”, 2008, pp. 279–283.
5. D. D. McCarthy and G. Petit. IERS Conventions (2003). IERS Technical Note, No. 32, Frankfurt am Main, Germany: Verlag des Bundesamts für Kartographie und Geodäsie, ISBN 3-89888-884-3, 2004, 127 pp., 2004.

Modeling Special Handling Source Positions in the GFZ VLBI Solution

Julian A. Mora-Diaz[1], Virginia Raposo-Pulido[1,3], Robert Heinkelmann[1], Minghui Xu[1,2], Tobias J. Nilsson[1], Maria Karbon[1], Li Liu[1,2], Benedikt Soja[1], Cuixian Lu[1], Harald Schuh[1]

Abstract Based on the GFZ VLBI solution obtained using the Vienna VLBI Software (VieVS), we estimate time series of the ICRF2 special handling sources. We investigate their time-variable positions based on our VLBI solution, which compared to ICRF2 includes the more recent VLBI observations. In a next step, the parameterization of the special handling sources is appropriately extended by allowing a linear variation in time. We present our first results, and we propose further studies with the aim of improving our research.

Keywords VLBI, radio sources, AGNs, apparent proper motions, special handling sources

1 Introduction

Very Long Baseline Interferometry (VLBI) is the space geodetic and astrometric technique for determining the International Celestial Reference Frame (ICRF) (Ma et al., 1998). The current catalog (ICRF2) is made up of 3,414 radio sources which are classified into three categories: i) defining sources: the sources are included in the axes definition, being a part of the global NNR condition; ii) special handling sources: the sources are not estimated as a global parameter, and iii) other sources: the sources are estimated as a global parameter but not considered in the axes definition.

1. Helmholtz Centre Potsdam, GFZ German Research Centre for Geosciences
2. Shanghai Astronomical Observatory, Chinese Academy of Sciences
3. Instituto Geográfico Nacional, Centro Nacional de Información Geográfica

The special handling sources (hereafter, SHS) are a subset of 39 sources which exhibit non-constant positions in time due to source structure changes (MacMillan & Ma, 2007). These radio sources exhibit time-variable extended structure and hence are not good candidates for very precise geodesy and astrometry (Charlot, 1990). Furthermore, the SHS show strong instability either in right ascension or declination (Figure 1) up to the level of 1 mas (Titov, 2007). Variations can be observed over days, weeks, or longer time scales (Fey et al., 2009).

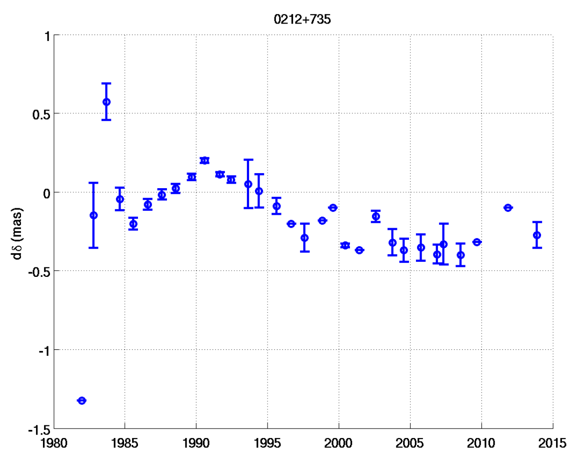

Fig. 1 Time series of declination of the special handling source 0212+735.

Based on the GFZ VLBI solution (Heinkelmann et al., 2014), we study the variability of the SHS positions to provide better a priori coordinates by applying extended parameter models to the celestial coordinates. As a first trial, we test linear apparent proper motions.

The ICRF2 is the actual realization of the International Celestial Reference System (ICRS), which contains precise coordinates of extragalactic radio sources observed by VLBI. In it, the SHS are not treated as global parameters in order to avoid distortions of the frame (Altamimi et al., 2013). When studying session-wise estimates of radio source coordinates, the SHS show significant non-constant systematics. These are not considered by the radio source coordinate model of the ICRF. The source positions are treated as constant, and all variations are believed to be measurement errors and are expressed by an error bar which is reported along with the position. This error bar can be made much smaller, if more sophisticated coordinate models are introduced.

This preliminary study is the first implementation of an extended radio source coordinate model. Later, having realized optimized models, we expect to be able to include special handling and other radio sources into the datum by likewise extension of the datum constraints. Then, we will obtain a more reliable celestial reference frame and correspondingly more reliable Earth orientation parameters.

2 Data Analysis

The GFZ VLBI solution contains 5,793 sessions solved by using the Vienna VLBI software VieVS. The analysis options follow the IERS 2010 Conventions and the ITRF2013 specifications. For the estimation of the SHS coordinates, the ICRF2 defining sources were fixed to their a priori coordinates in order to have consistency between celestial and terrestrial reference frames, while SHS and other sources were adjusted (Heinkelmann et al., 2014).

Based on the almost complete VLBI solution, we plot time series of declination and right ascension times cosine declination of the special handling radio sources, which were not included in the datum and were, therefore, independently adjusted (see Figure 2 and Figure 3). By visual inspection, we detected that estimates of a few sessions showed larger scatter than those of the majority of sessions. For the determination of the linear trend, we decided to ignore those outlying sessions in order to not distort the trend determination.

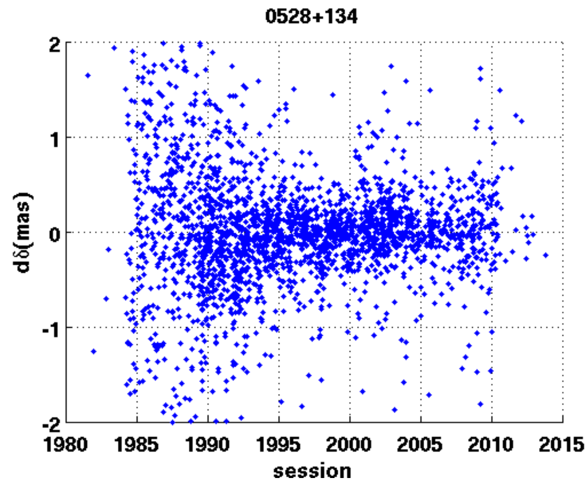

Fig. 2 Declination of 0528+134 from the GFZ VLBI solution. The same analysis was applied to all SHS.

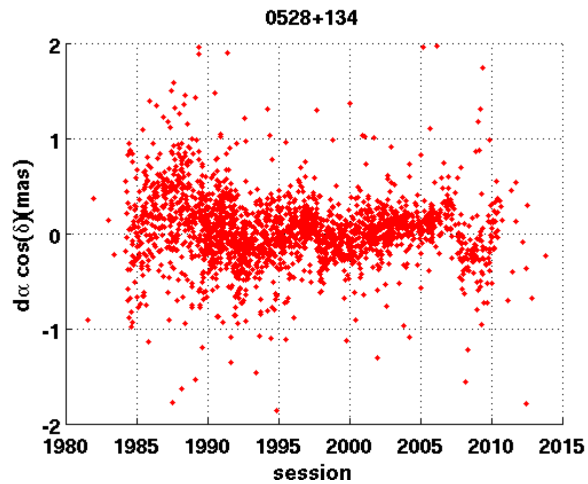

Fig. 3 Right ascension of 0528+134 from the GFZ VLBI solution. The same analysis was applied to all SHS.

3 Time Series of Source Positions

We determine yearly weighted means of source coordinates from the time series as follows:

$$\bar{X} = \frac{\sum_{i=1}^{n} w_i x_i}{\sum_i w_i} \tag{1}$$

where $w_i = 1/\sigma_i^2$ and σ_i is the formal error of the radio source coordinate estimate.

Time series of all of the 39 ICRF2 SHS were analyzed in that way. We estimate linear trends in the time series

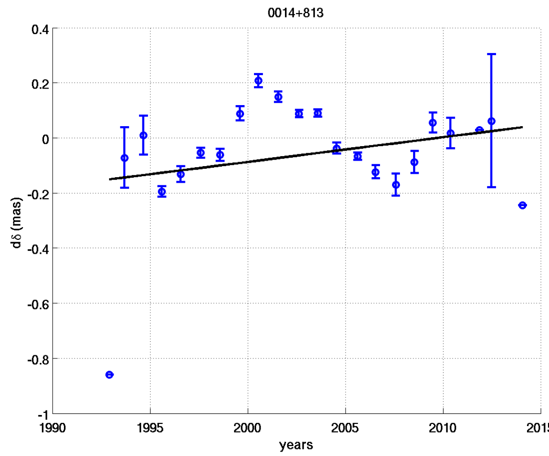

Fig. 4 Weighted mean with yearly resolution of declination for 0014+813. The error bars were determined as the yearly root-mean-square error.

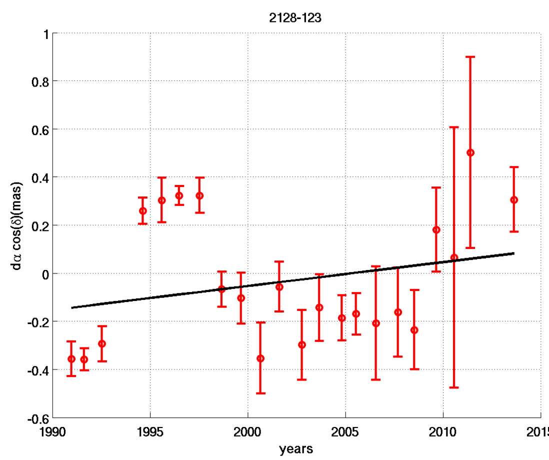

Fig. 5 Weighted mean with yearly resolution of right ascension for 2128-123. The error bars were determined in the same way as described in Figure 4.

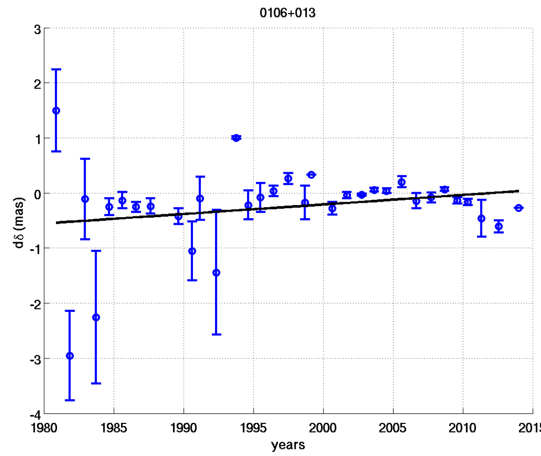

Fig. 6 Linear trend of declination of 0106+013.

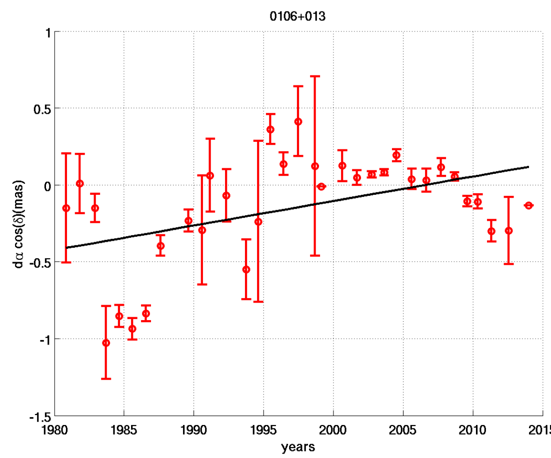

Fig. 7 Linear trend of right ascension of 0106+013.

of the source positions based on the annual weighted mean values for all SHS (see Figures 4 through 7). Most of the SHS exhibit significant non-constant positions (Figures 6 and 7). However, to our surprise, in some cases we found no evidence for significant positional variations in at least one component (Figure 4 and Figure 5). Using a linear interpolation, we compute apparent proper motion displacements (Table 1), which allows us to see what are the yearly rates of changes in source coordinates. To properly understand what the main causes are of such long-term variations in the coordinates of the SHS, more studies should be done, especially with respect to the underlying astrophysics. On the other hand, we bring up an example already given in the literature which is useful for the purpose of discussing and comparing our results. Radio source 4C39.25 has been showing interesting astrophysical behavior since the first time that it was observed in 1979. This source showed significant proper motion during 1986–1997 due to superluminal motion (Fey et al., 1997) that caused a fast change in right ascension (Titov, 2007). We notice this fact in our plots (Figure 8). According to our measurements, the right ascension of the source varies approximately 0.05 mas per year.

Table 1 Linear apparent proper motion displacements. There are very few data for the radio source 2134+004. Therefore we do not take it into account in the present study.

Source	$\alpha\cos\delta$ (mas year^{-1})	δ (mas year^{-1})
0014+813	-0.0283 ± 0.0401	0.0090 ± 0.0128
0106+013	0.0159 ± 0.0282	0.0173 ± 0.0307
0202+149	-0.0102 ± 0.0156	0.0218 ± 0.0334
0208-512	0.0008 ± 0.0001	0.0017 ± 0.0025
0212+735	0.1148 ± 0.1937	-0.0081 ± 0.0136
0235+164	-0.0029 ± 0.0050	-0.0257 ± 0.0445
NGC1052	-0.0709 ± 0.1223	-0.0853 ± 0.1468
3C84	-0.0014 ± 0.0037	0.1079 ± 0.2464
3C120	-0.0029 ± 0.0054	-0.0627 ± 0.1162
0438-436	-0.0426 ± 0.1831	0.0271 ± 0.1162
0451-282	0.0342 ± 0.0507	0.0892 ± 0.1317
0528+134	-0.0033 ± 0.0058	-0.0061 ± 0.0110
0607-157	0.0314 ± 0.0497	0.1034 ± 0.1638
0637-752	0.0061 ± 0.0093	0.0011 ± 0.0018
0711+356	-0.0259 ± 0.0616	-0.0560 ± 0.1299
0738+313	0.0012 ± 0.0027	0.0986 ± 0.2128
0919-260	-0.0460 ± 0.0680	-0.0104 ± 0.0154
4C39.25	0.0475 ± 0.0862	-0.0105 ± 0.0190
OK290	0.0211 ± 0.0377	0.0475 ± 0.0853
1021-006	0.2564 ± 0.7216	0.2033 ± 0.5723
1044+719	0.0137 ± 0.0188	0.0151 ± 0.0208
3C273B	0.0080 ± 0.0142	0.0147 ± 0.0269
3C279	0.0273 ± 0.0530	-0.0519 ± 0.0996
1308+326	-0.0134 ± 0.0234	-0.0160 ± 0.0277
OQ208	-0.0097 ± 0.0167	0.0044 ± 0.0077
1448+762	-0.2001 ± 0.2865	-0.0030 ± 0.0044
3C309.1	0.0420 ± 0.0695	-0.0699 ± 0.1156
1611+343	-0.0243 ± 0.0410	0.0087 ± 0.0146
1610-771	0.1636 ± 0.2521	-0.0369 ± 0.0566
3C345	0.0694 ± 0.1384	-0.0131 ± 0.0264
1739+522	0.0036 ± 0.0055	-0.0029 ± 0.0044
2121+053	-0.0026 ± 0.0043	-0.0153 ± 0.0248
2128-123	0.0220 ± 0.0341	0.0152 ± 0.0237
2145+067	-0.0102 ± 0.0176	0.0027 ± 0.0046
2201+315	0.0223 ± 0.0321	-0.0364 ± 0.0522
2234+282	-0.0174 ± 0.0282	-0.0126 ± 0.0204
2243-123	-0.0643 ± 0.1061	-0.0081 ± 0.0131
3C454.3	0.0275 ± 0.0524	-0.0029 ± 0.0054

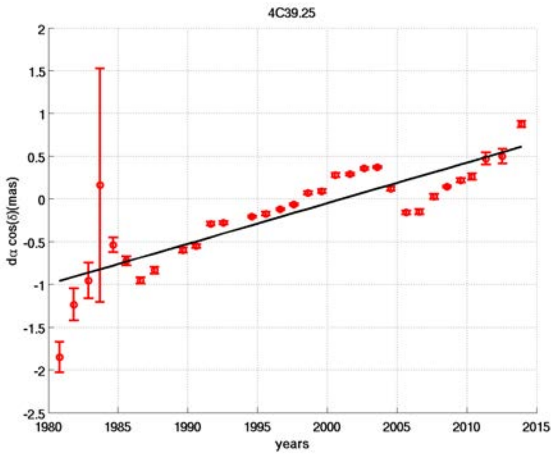

Fig. 8 Linear trend of right ascension of 4C39.25.

4 Conclusions

We successfully obtained time series of source coordinates based on the new GFZ VLBI solution. We first looked into the ICRF2 list of the SHS to check the variability of those sources by studying their linear trends. Long-term trends are seen in the time series of the source coordinates (Table 1). Checking our preliminary results, for some sources there are no significant changes in coordinates, bringing us to several questions: (1) What were the criteria in which the ICRF2 defined the selection of SHS? (2) If some sources exhibit no significant proper motion, why not consider them as "defining sources"? (3) Hence, what should be the exact definition of SHS?

The information about the variability in source positions of the SHS could be used as improved a priori source coordinates. Thus, more precise a priori coordinates could be used, which would allow us to improve the theoretical delays and in the end the VLBI estimates.

We need to study in more detail global solutions with different settings, i.e., parameterization, datum definitions, and so on. An implementation of a suitable time-variable coordinate model is needed in order to assess the impact on the global parameters such as EOP and station coordinates. Finally, we have to investigate different mathematical models for the extension of the radio source coordinate model, for example using Chebyschev polynomials, linear spline functions, and so on and including those in a time dependent NNR (No-Net-Rotation) condition.

References

1. Altamimi, Z. and Collilieux, X. (eds.). Reference Frames for Applications in Geosciences. *Effects of ICRF2 on the TRF, CRF, and EOP*. Gordon D., Ma C., MacMillan D., Bolotin S., Le Bail K., and Gipson, J. Chapter 26, pp. 175–179, 2013.
2. Charlot, P. Radio-source structure in astrometric and geodetic very long baseline interferometry. *Astronomical Journal*.

Vol. 99, No. 4, 1990.
3. Fey, A. L. The proper motion of 4C 39.25. *American Astronomical Society*. 191st AAS Meeting, #22.13; Bulletin of the American Astronomical Society, Vol. 29, p. 1249, 1997.
4. Fey A.L., Gordon D., Jacobs C.S. (eds.). The Second Realization of the International Celestial Reference Frame by Very Long Baseline Interferometry *IERS Technical Note No. 35*. Presented on behalf of the IERS / IVS Working Group. Frankfurt am Main: Verlag des Bundesamts für Kartographie und Geodäsie, 2009. 204 pp., available at http://www.iers.org/TN35
5. Feissel-Vernier, M. Stability of the VLBI-Derived Celestial Reference Frame *IVS 2004 General Meeting Proceedings*, NASA/CP-2004-212255, pp. 346–350, 2004.
6. Heinkelmann, R. The GFZ VLBI Solution — Characteristics and First Results. *IVS 2014 General Meeting Proceedings*, this volume.
7. MacMillan, S. D. and Ma C. Radio source instability in VLBI analysis *J. Geod.*, 81: pp. 443–453, 2007.
8. Titov, O. A. Apparent proper motions of radio sources from Geodetic VLBI data *Astronomy letters*, Vol. 33, No. 7, pp. 481–487, 2007.

Datum Effects on the Stability of the Celestial Reference Frame Determined by VLBI

Virginia Raposo-Pulido[1,2], Robert Heinkelmann[2], Julian A. Mora-Diaz[2], Minghui Xu[2], Tobias Nilsson[2], Maria Karbon[2], Li Liu[2], Cuixian Lu[2], Benedikt Soja[2], Harald Schuh[2]

Abstract In this work, we investigate the small differences in realizations of the Celestial Reference Frame (CRF) by applying different celestial datum definitions to our new GFZ VLBI solution. The approaches are based on the geometric distribution, the astrophysical quality, and the number of radio sources. The effects on the axes stability of the frame are assessed by several statistical measures. The results show how the differences among the rotation angles are more sensitive to the astrophysical quality than to the number of radio sources chosen to define the datum. The global rotations show values up to 21 μas when comparing datums with different numbers of radio sources and up to 45 μas when comparing datums with different astrophysical quality, where radio sources with declinations below $-50°$ are not found. Besides, the regions where more radio sources need to be observed (generally below $-50°$ in declination) are plotted in the conclusions.

Keywords celestial datum, Vienna VLBI Software (VieVS), Celestial Reference Frame (CRF)

1 Introduction

When estimating a CRF in VLBI analysis, usually a number of radio sources with a long history of observations and stable positions are used to determine the orientation of the estimated frame w.r.t. the previous frame. Thereafter an additional small set of rotations relates the frame to the initial orientation as given by the International Celestial Reference System (ICRS). For the second realization of the International Celestial Reference Frame (ICRF2), 295 radio sources called "defining sources" were chosen to define the orientation of the axes, following the criteria specified by the IERS Technical Note 35 (Fey et al., 2009). For the improvement of the axes definition, the ICRF2 defining sources were chosen not only depending on their astrometric and astrophysical qualities, but also depending on their geometrical distribution, particularly in the south. Consequently, some radio sources were possibly included in spite of being variable in both flux and structure. Positions of those radio sources could become significantly variable with time, which would degrade the accuracy of the datum.

1. IGN, National Geographic Institute, Madrid, Spain
2. Helmholtz Centre Potsdam, GFZ German Research Centre for Geosciences

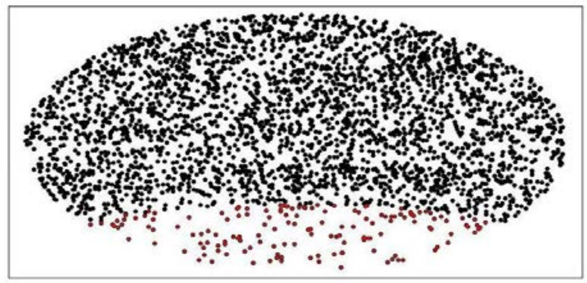

Fig. 1 Radio sources included in the GFZ global VLBI solutions. 151 radio sources have declinations below $-40°$.

2 Data and Methods

In order to assess the celestial datum effects, global VLBI solutions were calculated with the new GFZ VLBI solution (Heinkelmann et al., 2014). 3,341 sessions were analyzed with the GFZ version of the Vienna VLBI Software (VieVS, Böhm et al., 2012), applying the IERS Conventions (Petit and Luzum, 2010). In this work, we only use sessions that are from the period 1990–2013 and have more than three stations. The sessions were selected taking into account the small number of radio sources with good astrophysical quality before 1990 and the limitations of the VLBI networks at that time. The terrestrial datum was realized by applying no-net-translation (NNT) and no-net-rotation (NNR) conditions for all stations except those affected by earthquakes and the recently built ones, which are not included in the International Terrestrial Reference Frame 2008 (ITRF2008, Altamimi et al., 2011). With this criterion, the stations left out of the datum were: TSUKUB32, KOGANEI, KASHIM11, KASHIM34, TIGOCONC, SINTOTU3, VERAMZSW, YARRA12M, WARK12M, and KATH12M. Furthermore, 14 additional stations were found with not enough data to estimate reliable velocities, most of them being mobile occupation or radio astronomy telescopes. Therefore, they were reduced session-wise in the analysis. The global solutions considered only radio sources with more than two observations (see Figure 1), excluding the remaining sources to avoid singularity problems. The 39 special handling sources were reduced session-wise due to their time-dependent large structures.

The axes stability was assessed by estimating the angles of a 3D rotation (A_1, A_2, and A_3) and two shearing or deformation parameters (D_α and D_δ):

$$d\alpha = A_1 tan\delta_1 cos\alpha_1 + A_2 tan\delta_1 sin\alpha_1 - A_3 + D_\alpha \delta_1$$

$$d\delta = -A_1 sin\alpha_1 + A_2 cos\alpha_1 + D_\delta \delta_1$$

where (α_1, δ_1) are the a priori source coordinates taken from the ICRF2 and ($d\alpha$, $d\delta$) the differences of coordinates in the two frames.

3 Analysis Based on the Number of Radio Sources

The concept used in this analysis was to divide the celestial sphere into an equally spaced 20° by 20° grid, i.e., 18×9 fields. The effects due to the number of radio sources, the density, were assessed by keeping the geometrical distribution constant. For the datum definition, NNR conditions were applied for five levels of densification (see Figs. 2–6): A (156 radio sources), B

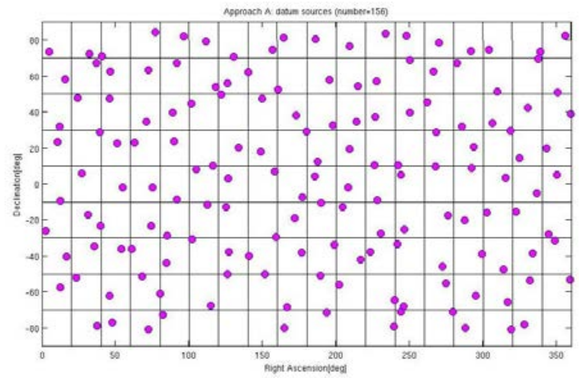

Fig. 2 Radio sources included in the datum for approach A (156 sources).

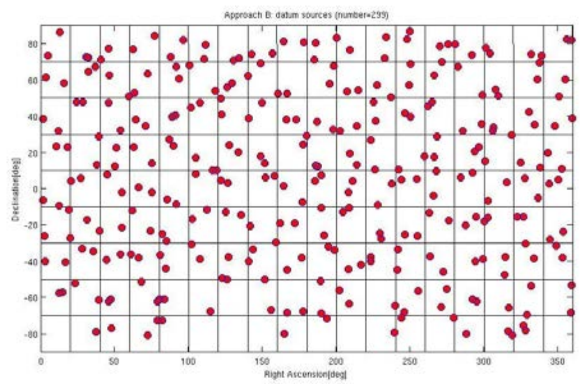

Fig. 3 Radio sources included in the datum for approach B (299 sources).

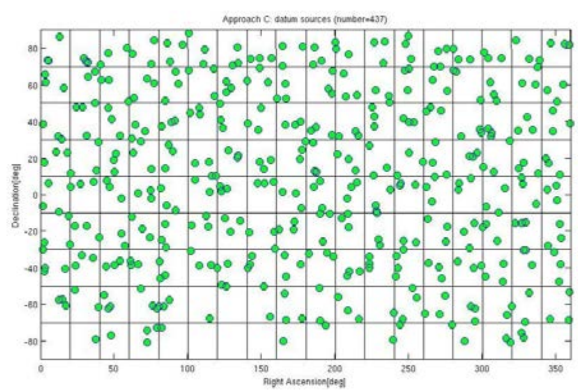

Fig. 4 Radio sources included in the datum for approach C (437 sources).

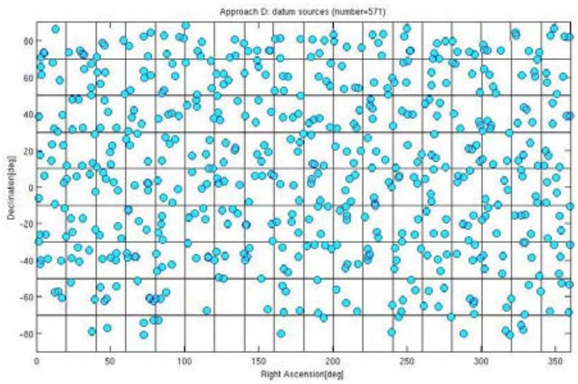

Fig. 5 Radio sources included in the datum for approach D (571 sources).

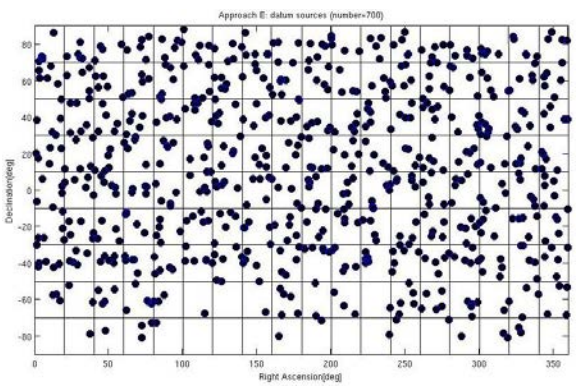

Fig. 6 Radio sources included in the datum for approach E (700 sources).

(299 radio sources), C (437 radio sources), D (571 radio sources), and E (700 radio sources).

Table 1 Transformation parameters w.r.t. ICRF2 using different approaches (A, B, C, D, and E).

	A_1 [μas]	A_2 [μas]	A_3 [μas]	D_α [μas/deg]	D_δ [μas/deg]
A	10.8 ± 6.0	17.5 ± 6.9	9.1 ± 7.7	0.3 ± 0.2	0.2 ± 0.1
B	13.0 ± 4.7	17.1 ± 5.3	2.6 ± 5.7	0.1 ± 0.2	0.1 ± 0.1
C	16.7 ± 5.1	15.9 ± 5.8	1.2 ± 6.1	0.1 ± 0.2	0.1 ± 0.1
D	17.8 ± 5.3	13.9 ± 5.9	2.2 ± 6.1	0.2 ± 0.2	0.2 ± 0.1
E	20.2 ± 5.1	14.5 ± 5.8	0.5 ± 5.9	0.2 ± 0.2	0.2 ± 0.1

The orientation parameters (see Table 1) show variations between the different approaches smaller than 10 μas, the current level of axes stability specified for ICRF2. However, A_1 and A_2 frame rotations are all positive between about 10 to 20 μas for all the investigated densifications. This is due to the comparison of different selected data (1979–2009 for ICRF2 vs. 1990–2013 in this work). The formal errors are between about 5 and 6 μas. The rotation around the z-axis A_3 shows differences among the approaches that are relatively larger, but of less significance. The values are smaller than 21 μas but indicate a systematic rotation w.r.t. ICRF2. The deformation parameters w.r.t. ICRF2 are negligible and almost insignificant.

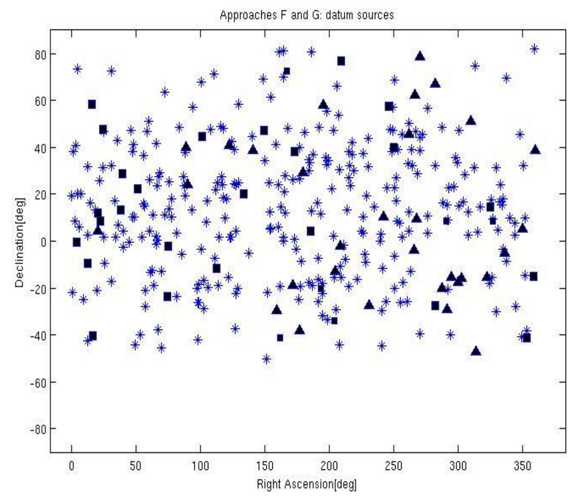

Fig. 7 Datum sources for approaches F and G: 296 radio sources in common (asterisk), 31 sources for approach G with an S-band SI larger than 2 (triangle), and 31 sources different from the approach G sources for approach F (square).

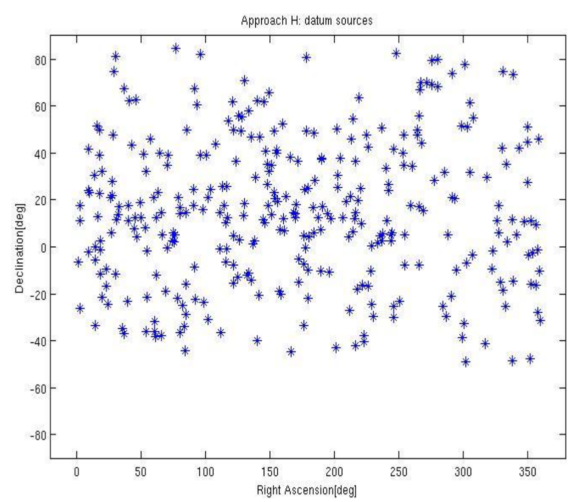

Fig. 8 Datum sources for approach H: 327 radio sources different from approaches F and G.

4 Analysis Based on the Astrophysical Quality

The concept used in this analysis was to choose sets of radio sources with different structure indices (SI, Fey et al., 1997). The effects due to astrophysical quality were assessed by keeping the number of radio sources constant. For the datum definition, three sets of datum sources were investigated: F, G, and H. Set F includes only those radio sources with X-band SI and S-band SI smaller than three, G considers only radio sources with an X-band SI smaller than three (see Figure 7), and H considers radio sources with an X-band SI greater than two (see Figure 8). Datum subsets F to H all contain 327 radio sources in total, which was the maximum number of radio sources with X-band and S-band SI smaller than three in the GFZ global solution. A total of 358 radio sources were found with X-band SI smaller than three (31 out of 358 with S-band SI larger than two) and 370 with X-band SI larger than two. For that reason, 296 radio sources in common between the approaches F and G were selected, and 31 alternate sources (around 10% of the total number) were selected. Approach H does not contain any radio source in common with F and G.

Table 2 Transformation parameters w.r.t. ICRF2 using different approaches F, G, and H.

	A_1 [μas]	A_2 [μas]	A_3 [μas]	D_α [μas/deg]	D_δ [μas/deg]
F	14.2 ± 6.0	44.5 ± 6.8	-24.7 ± 6.7	0.3 ± 0.2	0.0 ± 0.1
G	14.2 ± 6.3	39.5 ± 7.2	-19.3 ± 6.9	0.2 ± 0.2	0.0 ± 0.1
H	16.8 ± 7.1	-8.0 ± 7.7	-10.6 ± 7.6	0.0 ± 0.2	0.2 ± 0.1

The orientation parameters (see Table 2) reach significant values up to 45 μas. This results in significant frame rotations, which are partly due to the comparison of data based on different periods (1979-2009 vs. 1990-2013) and the deficient geometry considered by this approach. The three sets of datum sources do not contain radio sources below about $-50°$ in declination. Consequently, the transformation parameters should only be interpreted relatively w.r.t. each other. In that case, the orientation parameters (see Table 2) show variations between approaches F and G smaller than 6 μas and up to 53 μas when approach H is considered in the comparison. The formal errors are between about 6 and 7 μas, being the largest for approach H. The deformation parameters w.r.t. ICRF2 are negligible and almost insignificant.

5 Conclusions

The current number of defining sources is 295. The first analysis shows that this number can be increased with no significant detriment to the frame. The second analysis deals with approaches F, G, and H with approximately the same geometry but different radio sources depending on the SI. The relative rotation angles are larger for the second analysis than for the first analysis. The differences are more significant when the astrophysical quality is considered instead of the number of radio sources.

The X-band and S-band SI information was available for 728 and 701 out of 3,254 radio sources, respectively (www.obs.u-bordeaux1.fr/BVID/). The plots of the second analysis show the lack of radio sources with small SI or SI information for declinations below $-50°$. It means that more observations for imaging are necessary in the south to cover that declination range. Regions have been found for declinations below $-45°$ (see Figure 9) with no radio sources (for extreme right ascensions) or just one source. More observations in these regions should be done to have a uniform distribution over the sky.

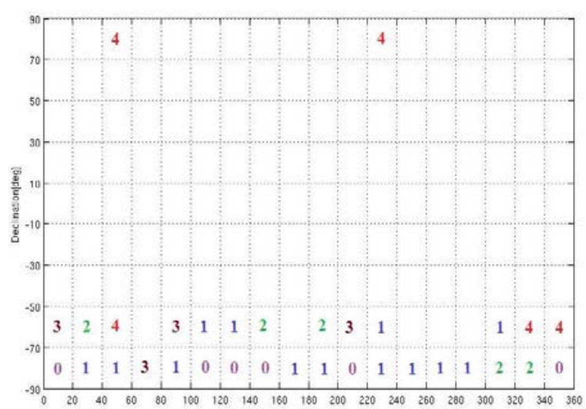

Fig. 9 Grids, where the radio sources are missing (0 radio sources) or no radio sources could be added for densification (1, 2, 3, or 4 radio sources) for the first analysis. The empty grids contain more than 4 radio sources

Acknowledgements

We acknowledge IGN for its support and IVS for providing the data analyzed in this study.

References

1. Z. Altamimi, X. Collilieux, and L. Métivier (2008). ITRF2008: an improved solution of the international terrestrial reference frame. *Journal of Geodesy, Volume 85, Issue 8, pp. 457–473*. doi: 10.1007/s00190-011-0444-4,
2. J. Böhm, S. Böhm, T. Nilsson, A. Pany, L. Plank, H. Spicakova, K. Teke, and H. Schuh (2012). The New Vienna VLBI Software VieVS. *S. Kenyon et al. (eds.), Geodesy for Planet Earth, International Association of Geodesy Symposia 136. Springer-Verlag Berlin Heidelberg, 2012*. doi: 10.1007/978-3-642-20338-1_126.
3. A. L. Fey and P. Charlot (1997). VLBA Observations of radio reference frame sources. III: Astrometric suitability of an additional 225 sources. *The Astrophysical Journal Supplement Series, 128, pp. 17–83*.
4. A. L. Fey, D. Gordon, and C. S. Jacobs (eds.) (2009). The Second Realization of the International Celestial Reference Frame by Very Long Baseline Interferometry. *Presented on behalf of the IERS / IVS Working Group (IERS Technical Note No. 35). Frankfurt am Main: Verlag des Bundesamts für Kartographie und Geodäsie, p.204*. ISBN 3-89888-918-6.
5. R. Heinkelmann, T. Nilsson, M. Karbon, L. Liu, C. Lu, J. Mora-Diaz, E. Parselia, V. Raposo-Pulido, B. Soja, M. Xu, and H. Schuh (2014). The GFZ VLBI Solution — Characteristics and First Results. *IVS General Meeting 2014 Proceedings*, this volume.
6. G. Petit and B. Luzum (2010). IERS Conventions (2010). *(IERS Technical Note No. 36) Frankfurt am Main: Verlag des Bundesamts für Kartographie und Geodäsie, p. 179*. ISBN 3-89888-989-6.

The Acceleration of the Origin of the ICRF

Minghui Xu[1,2], Robert Heinkelmann[2], Harald Schuh[2], Ming Zhao[1], Guangli Wang[1]

Abstract From VLBI observations we have determined the Solar acceleration, based on the assumption that the proper motions of the extragalactic sources observed by VLBI are of a random pattern over the sky, with much higher accuracy than that predicted from the Galactic model (Xu et al., 2012, 2013). Our result, however, differs from that obtained by Titov et al. (2011) and Titov & Lambert (2013) using a different estimating method due to the significant vertical acceleration obtained by us. In this paper, we validate our results and investigate the vertical component. The possibilities for it are presented and discussed. In contradiction to the essence of the inertial reference frame, therefore, the origin of the ICRS, and consequently the ICRF, has an acceleration with respect to the background of the extragalactic radio sources. Finally, the impact of the acceleration on the ICRF2 is discussed.

Keywords Solar system barycenter's acceleration, vertical component, VLBI, astrometry

1 Introduction

In 1728, the English astronomer James Bradley discovered the aberration effect, which describes the apparent variation in the direction of the object as a result of the motion of the observer with respect to the coordinate system (Xu et al., 2014). Due to the aberration effect, different observers would have obtained different positions for an object. As a result, we always choose the Solar System Barycenter (SSB) as a fictitious observer to reduce and compare the positions of celestial objects obtained by all earth-based observations.

However, the SSB accelerates in the universe even though the acceleration is quite small. This leads to apparent proper motions of the observed objects. It was first predicted by Eubanks et al. (1995) in the 1990s and detected from VLBI observations in recent years. On the basis of two different methods, values for the acceleration of the SSB in the Galactic plane were determined to coincide well with each other and also with those predicted from the Galaxy model. But there is a big difference in the component perpendicular to the Galactic plane due to the significant vertical acceleration detected by us (Xu et al., 2012). From that work, this component is 3.95 ± 0.47 $mm{\cdot}s^{-1}{\cdot}yr^{-1}$, and its magnitude is about 53 percent of that of the Galactocentric acceleration.

We will discuss this component and investigate the possibilities for it in this paper and also focus on the impact of this acceleration on the ICRF. In Section 2, the validation of this acceleration will be presented, and we will investigate the vertical component in Section 3. The impact of the acceleration will be discussed in Section 4, and finally conclusions will be made in Section 5.

2 Validation

The SSB's acceleration wss determined to be (7.47 ± 0.46, 0.17 ± 0.57, 3.95 ± 0.47) $mm{\cdot}s^{-1}{\cdot}yr^{-1}$ in the Galactic coordinate system by using VLBI 24-hour

1. Shanghai Astronomical Observatory, Chinese Academy of Sciences
2. Helmholtz Center Potsdam, GFZ German Research Center for Geosciences

observations and the Calc/Solve software (Xu et al., 2012). In order to check if the determination is sensitive to the a priori, we take this result as an a priori value of the acceleration and estimate its correction based on the same data analysis strategy. It turns out to be insignificant with respect to its formal error as (0.04 $\pm$ 0.46, 0.08 $\pm$ 0.57, 0.06 $\pm$ 0.47) $mm{\cdot}s^{-1}{\cdot}yr^{-1}$.

The effect of the acceleration on positions of radio sources has a dipole structure over the sky with the magnitude of 5.8 $\mu as/yr$. And, in turn, this apparent proper motion should be present in the time series of source positions. In order to make this effect visible, one of the ICRF2 defining sources, 2136+141, was selected to make a special experiment for two reasons. First of all, it lies on the great circle of the celestial sphere normal to the acceleration vector; thus it maximizes the effect of the acceleration, which has an apparent proper motion of 5.7 $\mu as/yr$ and 1.3 $\mu as/yr$ in the directions of right ascension ($\Delta\alpha \cdot cos\delta$) and of declination, respectively. Secondly, as a defining source, it has a long observational history. In this circumstance the position of 2136+141 is treated as a local parameter to get its time series. So this means that the No-Net-Rotation constraint is imposed on the remaining 294 ICRF2 defining sources. Two solutions were made based on this solution strategy. In one, the observations used to determine the acceleration included the observations of 2136+141, and in the other, the observations did not include those of 2136+141. When we speak of not including one observation, in practice, it means that for that observation the derivation of the group delay with respect to the acceleration is set to be zero instead of to the calculation from the model. Consequently, two time series were obtained, and the differences between them are shown in Figures 1 and 2. As we can see, this difference clearly reveals the apparent proper motion caused by the acceleration. It demonstrates that the code used for the estimation is correct, and the VLBI observation and the Calc/Solve software are exactly sensitive to the level of μas. This experiment shows us that if there is a systematic effect on the position of a radio source at the level of μas, it can be extracted from VLBI observations.

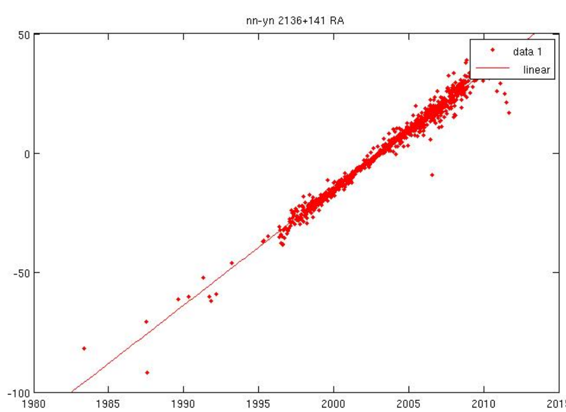

Fig. 1 The time series of right ascension of 2136+141. The linear trend is 5.7 μas per year.

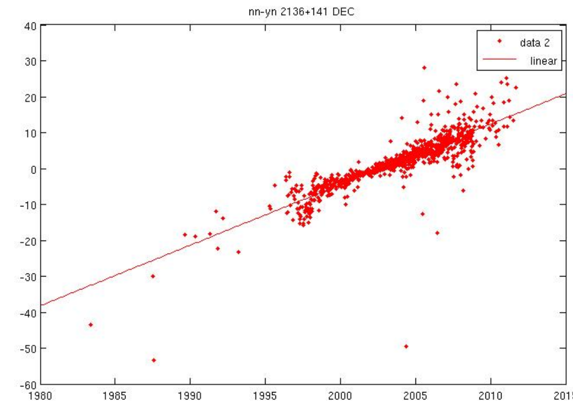

Fig. 2 The time series of declination of 2136+141. The linear trend is 1.3 μas per year.

3 Investigation of the Vertical Component

From the results we have obtained, the vertical acceleration is half of the domain component, the Galactocentric acceleration. As we know, the acceleration in the Galactic plane can exactely be validated by the current Galactic model. Contrary to that, there is not enough knowledge to directly identify the vertical acceleration, and there are not enough other observations to make a clear comparison.

Nevertheless, the oscillation of the Solar system over the Galactic plane is evident according to the researches in astronomy, even though the exact period and vertical distance of this oscillation has not been obtained yet. In the past 30 years, this oscillation has been pervasively used to explain phenomena with ultra-long periods on the Earth, such as the terrestrial mass extinction, cometary impacts, climate change, the inversion of the Earth magnetic field and so on (see, e.g., Rampino & Stothers 1984, Bahcall & Bahcall 1985, Shuter & Klatt 1986, Stothers 1998, Binney & Tremaine 2008, and Bailer-Jones 2009). The gravity potential can be established from the mass distribution model of the Galaxy, and as a result of other assumptions, such as the location and the vertical velocity of the Solar System, the period of this motion was expected to lie in the range of 52 $\sim$ 87 Myr. However, we should not expect that it can be used to validate the vertical component we obtained because of the large uncertainty of these studies.

The pulsar timing is another observation that may provide information about the motion of the SSB within the Galaxy, because the time of arrival (TOAs) of pulses is affected by the relative motion of the pulsar and the SSB. The effect in TOAs caused by the rotations of the SSB and pulsars round the Galactic center can be taken into account directly from the Galactic model. Therefore, if an ensemble of pulsars selected nevertheless manifests a common motion from the TOA observations, this collective motion can be assumed as, or at least used to constrain, the motion of the SSB apart from the rotation around the Galactic center. Harrison (1977) first suggested that the Sun has an undetected companion star as an explanation of the decrease in the period of a small group of pulsars. Later this was discussed in more detail by Cowling (1983) and Thornburg (1985). However, these studies could only constrain the SSB's remaining acceleration to $\sim$ 32 $mm{\cdot}s^{-1}{\cdot}yr^{-1}$, which is much higher than that of the vertical acceleration determined from VLBI data, 3.95 $mm{\cdot}s^{-1}{\cdot}yr^{-1}$ when expressed in the same unit. Recently, Zakamska & Tremaine (2005) used the timing data of millisecond pulsars, pulsars in binary, and pulsating white dwarfs to constrain the limit of the acceleration. The results showed that the SSB's remaining acceleration was on the upper limit of 4.73 $mm{\cdot}s^{-1}{\cdot}yr^{-1}$, comparable with the vertical component but without information for the direction. Thus, this method would be insufficient to check our result effectively.

As we have discussed before, it is very likely that this vertical component arises from the oscillation motion of the Sun over the Galactic plane. If this is the real case, this means that the dynamical plane near the Sun is tilted with respect to the current Galactic plane in an unusually large angle, and the mass model for the Galaxy may need to be investigated. Because the Sun is probably located in the north of the Galactic plane (see, e.g., Humphreys & Larsen 1995; Perryman 2009, Chap. 9), the vertical acceleration should point to the south pole of the Galaxy, which is the inverse direction of our result. Moreover, the Sun is considered to be near the plane, and the vertical component is supposed to be one order of magnitude smaller than the Galactocentric component (Kopeikin & Makarov 2006).

On top of that, there are two other possibilities. One is that the Galaxy accelerates toward its north pole in the universe. But currently no one knows. The second one is that the proper motions of the ICRF2 sources, especially of the 295 defining sources, have a systematic pattern. It is obvious that if they also have a dipole structure toward north pole, then the acceleration determined would include this effect. In this case, even though it cannot be interpreted as the SSB's acceleration, it should be taken into account as well for the celestial reference frame.

4 The Impact of the Acceleration

The SSB's acceleration changes the apparent positions of radio sources over time by approximately 5.8 $\mu as/yr$ based on our results, which breaks the rules of the establishment of the current ICRF. Table 1 shows the magnitude of this effect from different studies. The first two results were predicted from the Galaxy model, whereas the last two ones were determined from VLBI observations. If this effect is not taken into account, the position discrepancy for the 295 defining sources will exceed 100 μas for the approximately 30-year history of VLBI observations. The aberration

Table 1 The magnitude of the apparent proper motion caused by the SSB's acceleration. Unit: $\mu as \cdot yr^{-1}$

Reference	Magnitude
Kovalevsky 2003	4.0
Malkin 2011	5.0
Xu et al. 2012	5.8
Titov et al. 2011, 2013	6.4

effect, which has a dipole pattern, in essence would not lead to any global rotation, but the distribution for the 295 defining sources is obviously not uniform on the sky. This global rotation is identified to exist in the

ICRF2. The main term is the rotation around the z-axis of the ICRF2 with a magnitude of 25 μas per century (Xu et al., 2013).

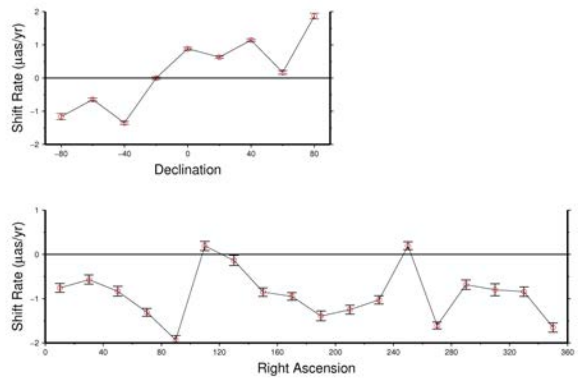

Fig. 3 The impact of the SSB's acceleration.

Figure 3 shows the impact of the SSB's acceleration on the equator plane and the zero right ascension. As we can see, the equator is moving toward the south pole with the speed of one μas per year on average.

5 Conclusions

Currently, it seems impossible to clearly explain and validate the vertical acceleration. The practical way is to keep monitoring it with more VLBI data in the future or to detect it from Gaia observations that are expected to be available in 2020. However, it was for the first time obtained directly from observations with high accuracy. As a real signal extracted from VLBI observations, it would be meaningful for the research of the Galaxy.

Although there are still some differences between the SSB's accelerations from various studies, it is apparent that it cannot be ignored. We propose a pilot program in the International VLBI Service for Astrometry and Geodesy community (IVS; Schuh & Behrend, 2012) to validate it and make it useful for VLBI data analysis.

Acknowledgements

Minghui Xu would like to thank the CAS-DAAD joint scholarship for supporting his exchange study at GFZ, Potsdam.

References

1. Bahcall, J. N., and S. Bahcall (1985), "The Sun's motion perpendicular to the galactic plane", Nature, 316, 706–708.
2. Bailer-Jones, C. A. L. (2009), "The evidence for and against astronomical impacts on climate change and mass extinctions: a review", International Journal of Astrobiology, 8(03), 213–219.
3. Binney, J., and S. Tremaine (2008), "Galactic dynamics", Princeton University Press, Princeton, N.J.
4. Cowling, S. A. (1983), "The Pulsar P/P Distribution and the Postulated Solar Companion", Mon Not R Astron Soc, 204(3), 1237–1244.
5. Eubanks, T., D. Matsakis, F. Josties, B. Archinal, K. Kingham, J. Martin, D. McCarthy, S. Klioner, and T. Herring (1995), "Secular Motions of Extragalactic Radio-Sources and the Stability of the Radio Reference Frame", International Astronomical Union (IAU) Symp. 166.
6. Harrison, E. R. (1977), "Has the sun a companion star", Nature, 270, 324–326
7. Humphreys, R. M., and J. A. Larsen (1995), "The Sun Distance above the Galactic Plane", Astronomical Journal, 110(5), 2183–2188.
8. Kopeikin, S. M., and V. V. Makarov (2006), "Astrometric effects of secular aberration", Astronomical Journal, 131(3), 1471–1478.
9. Kovalevsky, J. (2003), "Aberration in proper motions", Astronomy & Astrophysics, 404(2), 743–747.
10. Malkin, Z. M. (2011), "The influence of galactic aberration on precession parameters determined from VLBI observations", Astronomy Reports, 55(9), 810–815
11. Perryman, M. A. C. (2009), "Astronomical applications of astrometry: ten years of exploitation of the Hipparcos Satellite data", Cambridge University Press, Cambridge.
12. Rampino, M. R., and R. B. Stothers (1984), "Terrestrial mass extinctions, cometary impacts and the Sun's motion perpendicular to the galactic plane", Nature, 308(5961), 709–712.
13. Schuh, H., and D. Behrend (2012), "VLBI: A fascinating technique for geodesy and astrometry", Journal of Geodynamics, 61, 68–80.
14. Shuter, W., and C. Klatt (1986), "Phase modulation of the sun's Z oscillations", The Astrophysical Journal, 301, 471–477.
15. Stothers, R. B. (1998), "Galactic disc dark matter, terrestrial impact cratering and the law of large numbers", Mon Not R Astron Soc, 300(4), 1098–1104.
16. Thornburg, J. (1985), "An Upper Limit for the Solar Acceleration", Mon Not R Astron Soc, 213(1), P27–P28.

17. Titov, O., and S. Lambert (2013), "Improved VLBI measurement of the solar system acceleration", Astronomy & Astrophysics, 559, 95.
18. Titov, O., S. B. Lambert, and A. M. Gontier (2011), "VLBI measurement of the secular aberration drift", Astronomy & Astrophysics, 529, 91.
19. Xu, M. H., G. L. Wang, and M. Zhao (2012), "The solar acceleration obtained by VLBI observations", Astronomy & Astrophysics, 544, 135.
20. Xu, M. H., G. L. Wang, and M. Zhao (2013), "A new concept of the International Celestial Reference Frame: the epoch ICRF", Mon Not R Astron Soc, 430, 2633–2637.
21. Xu, M. H. and G. L. Wang (2014), "The Definition of Aberration", International VLBI Service for Geodesy and Astrometry 2014 General Meeting Proceedings, this volume.
22. Zakamska, N. L., and S. Tremaine (2005), "Constraints on the acceleration of the solar system from high-precision timing", Astronomical Journal, 130(4), 1939–1950.

Effects of AGN Jet Evolution on VLBI Astrometric Positions

Romuald Bouffet[1,2], Patrick Charlot[1,2], Sébastien Lambert[3]

Abstract Astrometric positions of extragalactic radio sources derived from VLBI data are used to build highly-accurate reference frames such as the International Celestial Reference Frame. Despite their distant locations, instabilities in the position of these sources are often seen on time scales of months to years, which is generally thought to be caused by source structure evolution. In this paper, we compare position instabilities and structural evolution for a sample of 68 sources observed over a ten-year period (1994–2003). Our results indicate that the two phenomena are linked at some level although the correlation is not perfect.

Keywords Reference frames, astrometry, active galactic nuclei, quasars, VLBI

1 Introduction

The current IAU fundamental celestial reference frame, namely the ICRF2 (second realization of the International Celestial Reference Frame), which has been in use since January 1, 2010, includes positions for a total of 3414 extragalactic radio sources distributed over the entire sky. Such positions were determined from VLBI data acquired at 8.4 and 2.3 GHz over 30 years (1979–2009). The ICRF2 has a floor of 40 microarcseconds (μas) in the individual source coordinate accuracies and an axis stability of 10 μas (IERS, 2009). Joint observational efforts of the VLBI community aiming at a denser and even more accurate celestial frame continue in order to further improve the quality of the frame.

One limitation in improving the accuracy of the individual VLBI source positions originates in actual astrometric instabilities which are found in these positions. Due to their location at cosmological distances, no proper motions are expected for these sources and their astrometric positions should thus be stable with time. While this is indeed the case on the long term, it is not true for shorter time scales (months to years) where instabilities at the level of several hundreds of microarcseconds are commonly detected (IERS, 2009). Such instabilities are usually attributed to varying source structure which is often spatially extended at the level of the VLBI resolution (Fey and Charlot,, 2000). Structural variations are generally due to ejection of material from the central VLBI core in a recurrent although unpredictable manner, causing shifts in the brightness centroid of the radio emission and hence potential VLBI astrometric instabilities.

In this paper we compare source position instabilities and structural variations based on astrometric and imaging VLBI data covering a period of ten years (1994–2003). The datasets are presented in Section 2 while Section 3 describes the analysis scheme. Section 4 reports our findings and discusses correlations between the two phenomena. In the last section, we draw prospects for further work in this area.

2 Observations

The data used to derive astrometric positions were acquired during numerous VLBI sessions conducted by the International VLBI Service for Geodesy and As-

1. Univ. Bordeaux, LAB, UMR 5804
2. CNRS, LAB, UMR 5804
3. Observatoire de Paris/SYRTE, CNRS/UMR 8630, Université Pierre et Marie Curie

trometry (IVS) over the past 30 years (Behrend,, 2013). A large number of observations is available for many sources which permits monitoring of their astrometric positions on time scales of days to weeks. Analysis was carried out in a similar way as that described in Gontier et al., (2006). For our study we averaged the individual session-based positions over monthly intervals in order to have a sampling similar to that of the imaging data.

Structural variations were taken from the analysis of VLBI jet kinematics reported in Piner et al., (2012). This analysis has made use of 2753 images at 8.4 GHz obtained from 50 Research & Development VLBI sessions organized by the IVS and the Very Long Baseline Array between 1994 and 2003. Six such sessions are carried out every year with a sampling of approximately two months. The network includes 15–20 stations, yielding high-quality VLBI images. Sixty-eight sources observed at 20 epochs or more (with a median of 43 epochs per source) are included in the present study.

3 Analysis

For our study, we used a simplified representation of the source structures in the form of a limited number of Gaussian components obtained through model-fitting (as available in Piner et al., (2012)). Such a representation was preferred, because it identifies the VLBI core of each source from epoch to epoch and aligns automatically the brightness distributions over time, assuming that the core position is stable. This alignment is crucial since the absolute map position is lost during the imaging process due to self-calibration.

Processing further the source structural information, we calculated the centroid of the brightness distribution (i.e., the centroid of the Gaussian components) at every epoch, allowing us to assess the relative motion of the brightness centroid with time. This calculation was carried out for 68 sources observed at 20 epochs or more for which model-fits are available in Piner et al., (2012). The result is a time series of centroid positions which may be compared with the monthly-averaged VLBI astrometric positions. This comparison assumes that the source motion as seen from the astrometric data is well matched with the motion of the centroid of the brightness distribution detected from VLBI imaging.

4 Results and Discussion

An example of the comparisons that we carried out using the scheme explained in the previous section is presented in Figure 1. The upper panels show the evolution in right ascension and declination of the astrometric position of the source 1308+326 from 1996–2003, while the lower panels show the motion of its brightness centroid over the same period of time. Uncertainties in the astrometric positions were derived as weighted averages (over monthly intervals) of the individual session-based uncertainties. Declination has higher uncertainties due to the predominantly East-West baselines of current VLBI networks. No error bars are given for the centroid positions, because model-fitting does not provide a direct means to estimate reliable uncertainties for the Gaussian components representing the structures.

Examination of the plots in Figure 1 indicates similar trends in the evolution of the astrometric and brightness centroid positions. This is also confirmed when calculating correlation coefficients between the two series, which are 0.30 in right ascension and 0.63 in declination. Applying the same calculation to all sources, an overall positive correlation is found (median value of 0.22 in right ascension and 0.19 in declination) as shown in Figure 2. This indicates that structural variations and astrometric instabilities are linked at some level.

Looking at Figure 2, one also notes that a fraction of the sources shows a negative correlation. At this stage, it is not understood however whether this negative trend is real or whether it results from the lack of significance of some of the correlation coefficients. For example, the correlation coefficients may be questionable when there is no notable evolution in both the astrometric and brightness centroid positions. Further studies are thus necessary to assess the significance of the correlation coefficients. Ultimately, every source may have to be examined separately to understand any discrepancy that may happen between the two series of positions.

Different trends in the astrometrically derived and structurally derived positions (possibly leading to negative correlation) may result from misidentification of the core component over the successive epochs (thereby affecting the alignment of images and the brightness centroid relative locations) or from effects

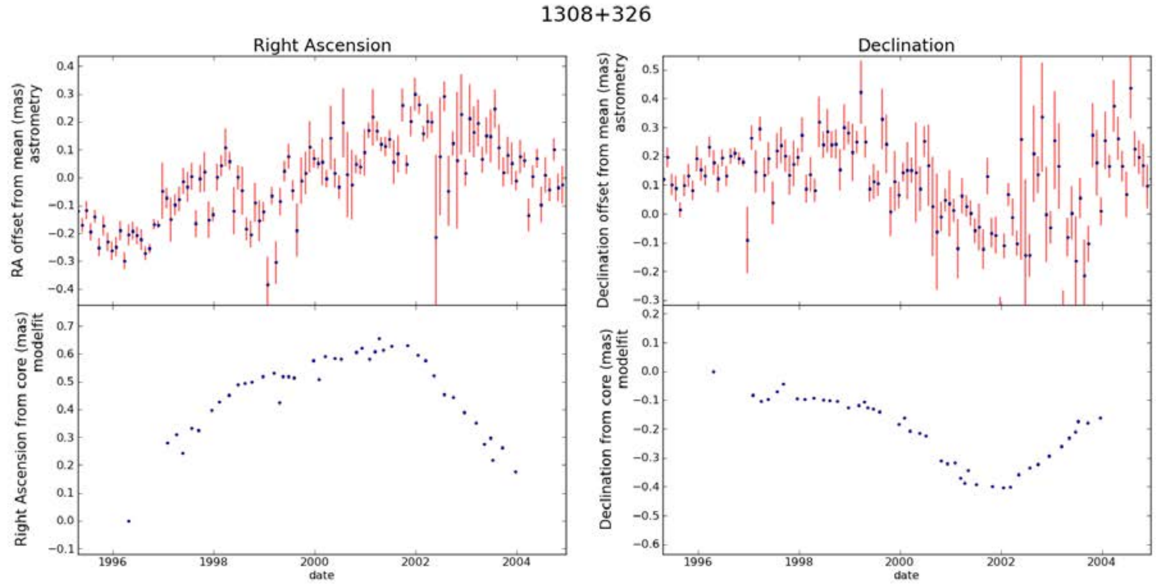

Fig. 1 Comparison of the astrometric position instabilities (upper panels) and brightness centroid motions (lower panels) for the source 1308+326 between 1996 and 2003. The left panels are for right ascension, while the right panels are for declination. The vertical scale is in milliarcseconds (mas).

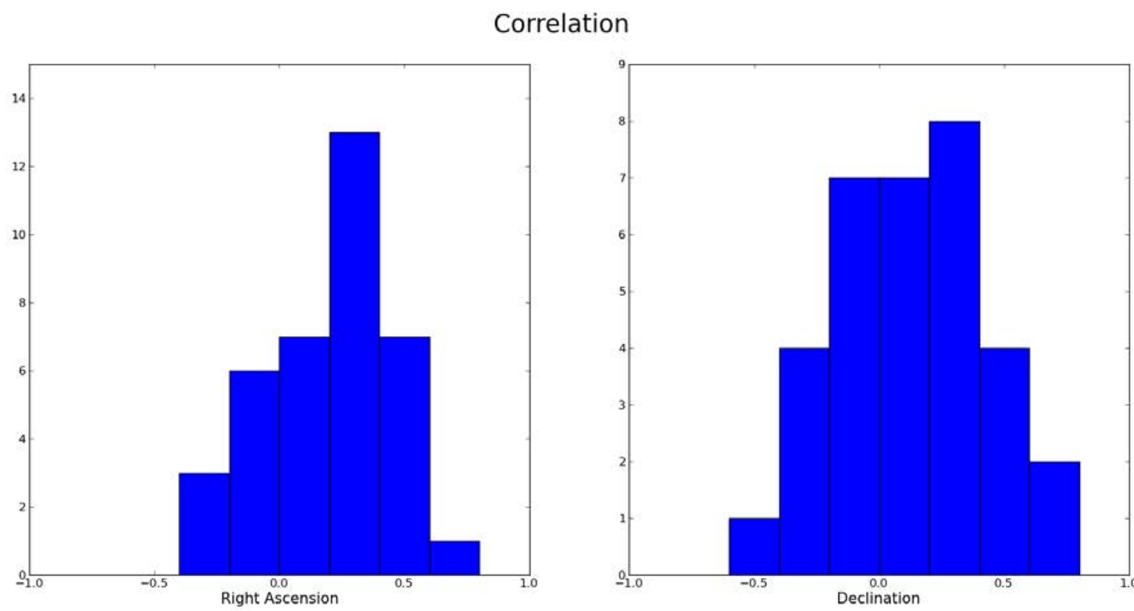

Fig. 2 Distribution of correlation coefficients between astrometric position instabilities and structural variations for all sources with significant astrometric instabilities (reduced $\chi^2 > 4$). Note that the source 0923+392, which shows atypical evolution, was removed from the sample for the purpose of this histogram.

coming from the S-band (2.3 GHz) data. For a full analysis, the S-band structures should indeed be considered as well, since the astrometric positions are derived from a combination of the data at the two frequencies, whereas only the X-band (8.4 GHz) structures have been considered in the above comparisons. The S-band data have a lower weight though and are thus a priori less likely to affect strongly the positions, hence the reason for neglecting them in the first stage.

5 Conclusions

A comparison between the evolution of astrometric positions and the variations of source structure (characterized as the motion of the centroid of the brightness distribution) was carried out for a sample of 68 sources observed over a period of ten years between 1994 and 2003. This comparison reveals similar trends in the astrometric and structural time series of positions for some sources showing significant motions like 1308+326. On the other hand, the correlation for sources with smaller motions is more difficult to assess. Overall, a positive correlation is found between the two time series, which favors an explanation of VLBI position instabilities in terms of structural variations.

In the future, we plan to refine this comparison by examining carefully each individual source in the sample. In some cases the comparison may not be reliable, because the position errors are too large and the motions are not significant, while in other cases different trends are seen, which needs to be understood. Possible explanations for such discrepancies include misidentification of the core components over the epochs and effects of the S-band data. In the longer term, enlarging the source sample and expanding the time span covered by the astrometric and imaging data up to recent years would be desirable.

Acknowledgements

The authors gratefully acknowledge support from the CNRS through the "Action Spécifique GRAM" for this project.

References

IERS and the IVS Working Group. The Second Realization of the International Celestial Reference Frame by Very Long Baseline Interferometry. *IERS Technical Note* **35**. Eds. A. L. Fey, D. Gordon and C. S. Jacobs. Verlag des Bundesamsts für Kartographie und Geodäsie, Frankfurt am main (2009).

A. L. Fey, P. Charlot. VLBA Observations of Radio Reference Frame Sources. III. Astrometric Suitability of an Additional 225 Sources. *ApJS* **128** (2000) 17-83.

D. Behrend. Data Handling within the International VLBI Service. *Data Science Journal* **12** (2013) WDS81-WDS84.

A.-M. Gontier, S. B. Lambert, & C. Barache. The IVS team at the Paris Observatory: how are we doing? Proceedings of *SF2A-2006: Semaine de l'Astrophysique Francaise*. Eds. D. Barret, F. Casoli, T. Contini, G. Lagache, A. Lecavelier and L. Pagani (2006) 23.

B. G. Piner, A. B. Pushkarev, Y. Y. Kovalev, et al. Relativistic Jets in the Radio Reference Frame Image Database. II. Blazar Jet Accelerations from the First 10 Years of Data (1994-2003). *ApJ* **758** (2012) 84.

Simulating the Effects of Quasar Structure on VLBI Observations

Stanislav Shabala[1], Jamie McCallum[1], Lucia Plank[1], Johannes Böhm[2]

Abstract The structure of quasars making up the celestial reference frame has long been recognized as a potential issue in the quest to achieve a millimeter-level VLBI terrestrial reference frame. We present Monte Carlo simulations of quasar structure in geodetic VLBI observations using the Vienna VLBI Software (VieVS) package. We outline our simulation strategy, including generation of mock quasar catalogs and calculation of structure group delays, and we present results. The effects of source structure on VLBI observables such as station coordinates and Earth orientation parameters are important at the level of a few millimeters and tens of microarcseconds, respectively, for existing networks. We suggest various strategies for minimizing and correcting for the source structure effect.

Keywords Source structure, celestial reference frame

1 Introduction

Quasars used to define the celestial reference frame are not perfect, stable point sources. Instead, they evolve on timescales as short as months, with bright jet components appearing and disappearing in addition to the stable point-like cores [1]. Source structure is usually quantified using the *structure index* (SI; [2]), a quantity related to the logarithm of the median time delay due to quasar structure observed with all terrestrial baselines. Quasars with median SI greater than 3 are considered unsuitable for geodesy [3] and can pose a challenge to the VGOS targets of 1 mm accuracy in position and 0.1 mm/year in velocity [4].

The effect of quasar structure on geodetic observables is not easy to quantify and depends on a number of factors including the relative brightness of the various quasar components and their projected separation as viewed from a baseline subtended by two antennas. In the present contribution, we simulate the effects of quasar structure on geodetic solutions.

2 Source Structure Simulator

The Vienna VLBI Software (VieVS; Böhm et al., these proceedings) contains a simulation capability. Until now, this simulation module has allowed the user to generate synthetic observations containing contributions from various stochastic sources of error including the wet troposphere, clock variance, and instrumental errors. We have extended this simulator to include the systematic effects of source structure. This capability will be included in the next public release of VieVS.

We model radio sources as two-component structures. The brighter component corresponds to the so-called core, while the secondary component (which may be as far as a few milli-arcseconds away) represents the jet. The amount of structure a source has depends on the relative brightness ratio and separation of the two components. For sources with no structure, only the core is seen.

The measured quantity in geodetic VLBI is the X-band ionosphere-corrected group delay, defined as the slope of phase against frequency across the 750 MHz bandwidth centered at 8.6 GHz. In sources that are not point-like, multiple components beat in and out

1. School of Physical Sciences, University of Tasmania
2. Department of Geodesy & Geoinformation, Vienna University of Technology

of phase in a complicated way that depends on observing frequency. As a result, the extra phase due to source structure is slightly different in the eight X-band channels (due to the different central frequency of each channel). This additional *structure phase* can be plotted against frequency (Figure 1), and the slope of this plot yields the group delay contribution due to source structure.

In the VieVS source structure simulator, this additional *structure group delay* is added to the simulated group delay for each observation (i.e., each baseline–scan pair).

3 Quantifying the Effects of Source Structure

3.1 Mock Catalogs

To investigate the effects of source structure on geodetic observables, we constructed six mock catalogs: (1) one catalog of perfect point sources (i.e., no structure); (2–5) four catalogs where every source has the same structure index of either 1, 2, 3, or 4; and (6) one catalog where structure indices are assigned to individual sources at random but with the constraint that the distribution of structure indices in this catalog matches the observed distribution for ICRF2 sources [3]. For all catalogs, we used the celestial positions of actual ICRF2 sources but assigned fictitious structures to each source.

For each source, we generated mock images (as shown, for example, in Figure 1) from structure indices as follows. The jet direction (i.e. the direction of the vector joining the two components) was assigned at random. The ratio of the relative brightness of the two components was also chosen at random from the range 0.04–0.44. Together with the structure index, this brightness ratio then determined the component separation; this was typically ≤ 5 mas, consistent with astronomical imaging of many ICRF2 sources.

This procedure was repeated for each source in each of the six catalogs described above.

3.2 Simulations

To quantify the effects of different levels of source structure on geodetic observables, we ran simulations using schedules from the CONT11 campaign. CONT11 has a number of advantages over the usual R1 and R4 experiments, including a larger number of observations and a fixed, large network that minimizes the effects of network geometry.

We ran 30 simulations for each day of CONT11 using our six mock catalogs. Two types of simulations were performed: (a) those including only source structure and (b) those including tropospheric turbulence and clock instabilities in addition to source structure. We added 1 picosecond of white noise to each simulation. For each day in each simulation, we calculated station positions and Earth Rotation Parameters. The quality of solutions was gauged using three metrics: (1) difference between median estimated parameter value and the original input value; (2) standard deviation in the estimated value, and (3) formal uncertainty.

The left panel of Figure 2 shows the effects of different levels of source structure on station coordinates in structure-only simulations. A clear decrease in both accuracy (green line) and precision (red and blue lines) is seen as the amount of source structure is increased. For full simulations (right panel of Figure 2) this signal is less obvious due to the dominant contribution from the troposphere, but still present. Overall, source structure contributes to position uncertainties at the millimeter level and must therefore be corrected or mitigated if the VGOS targets of 1 mm accuracy in position and 0.1 mm/year in velocity are to be achieved.

Figure 3 similarly shows that inclusion of source structure degrades the quality of solutions for Earth Rotation Parameters. Further details on these simulations and results can be found in [5].

4 Mitigation Strategies

There are two main strategies for mitigating the effects of source structure: selecting quasars to have little structure or applying appropriate corrections.

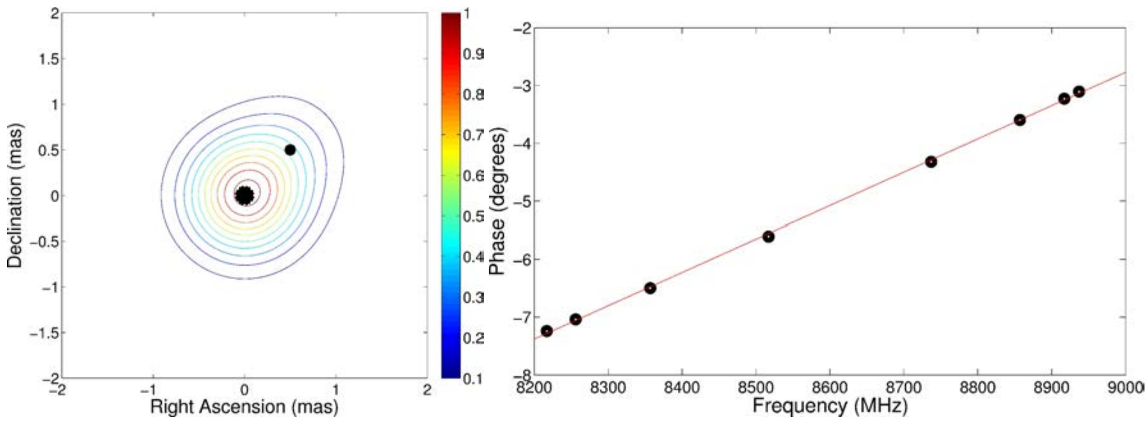

Fig. 1 *Left panel*: Simulated two-component source with structure index 2.7. The flux density ratio of the two components (filled circles) is 5:1. Each component is modeled as a δ-function, and the structure is convolved with a 1 mas beam. Colors represent scaled flux density. *Right panel*: Structure phase as a function of frequency for this source observed with a 9,280 km baseline parallel to the source jet axis. The structure contribution to the group delay is given by the slope of phase against frequency. Black points represent the eight X-band channels.

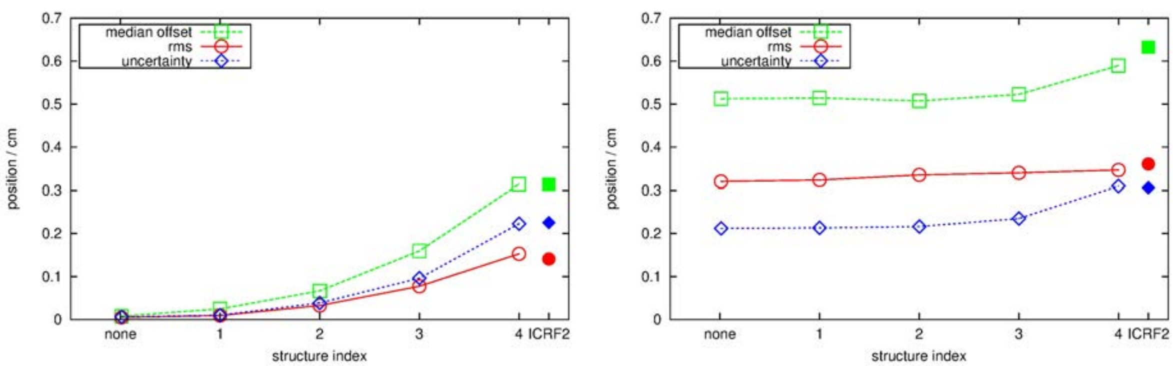

Fig. 2 Effects of source structure on station coordinate offsets (measured−true value, shown in green), debiased rms (red), and median formal uncertainty (blue) over 15 days of CONT11. Left panel: structure-only simulations; right panel: full simulations. Median values over all stations are shown. Filled symbols are for the ICRF2 distribution of structure indices.

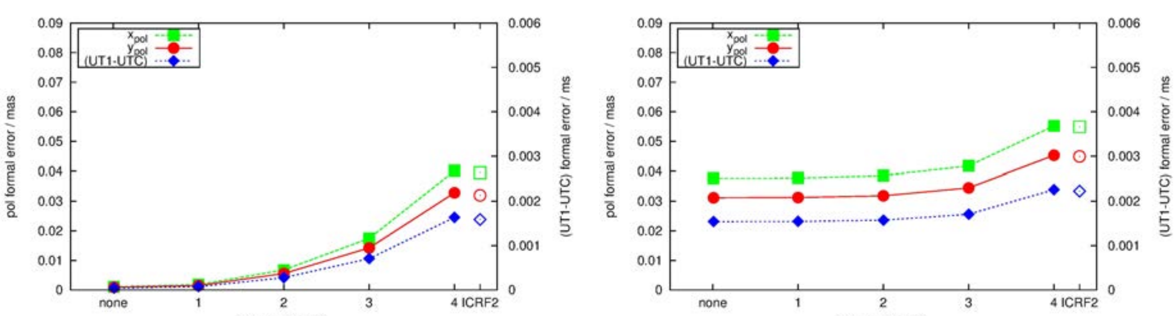

Fig. 3 Effects of source structure on the median formal uncertainty for $x_{\rm pol}$, $y_{\rm pol}$, and (UT1-UTC). Left panel: structure-only simulations; right panel: full simulations. Open symbols are for the ICRF2 distribution of structure indices.

4.1 Quasar Selection

In the first approach, ICRF2 sources are imaged at regular intervals [2, 6], and those sources with large structure indices (typically SI ≥ 3 [3]) are scheduled less often than sources that exhibit less structure. This is the standard strategy currently used in scheduling IVS observations. There are two potential difficulties with this approach.

First, the reduction in quasar structure by excluding many sources significantly limits the density (and homogeneity of distribution) of sources in the celestial reference frame. Most quasars brighter than $\sim$100 mJy at X-band have already been identified, and this situation will therefore not be improved with additional observations, unless a move to much higher frequencies (e.g., 32 GHz [7]) is made.

Secondly, quasars evolve significantly on timescales of months to years, and care must be taken when deciding which quasars are "stable" on any given day. Fortunately, a number of astrophysical metrics can be used to evaluate or even predict the amount of structure a source has. These include direct VLBI imaging [8, 2, 3], or variability properties of radio sources [9, 10]. It should therefore be possible to flag sources as being presently unsuitable for observation; this list would be updated continuously.

4.2 Structure Corrections

An alternative approach uses VLBI images of radio sources to correct for structure. Quasar variability is again a problem, as corrections applied using an outdated model for the quasar are likely to cause more harm than good. This, however, should not be a problem for future VGOS-style observations, in which source images will be a standard data product [11, 12]. An important issue is whether the expected astrometric accuracy and amplitude calibration will allow for structure corrections of sufficient quality to be applied to the data. We aim to investigate these issues in the near future with the source structure simulator described in this paper.

5 Scheduling with Respect to Source Orientation

A very different approach to the source structure problem is to use some a priori knowledge of quasar physics to schedule quasars. Although quasar structure varies appreciably on human timescales, it invariably consists of either a core or a core plus jet. The *direction* of the jet does not change appreciably (although some jets do precess). It has been suggested by R. Porcas [13] that jet direction information can be used in scheduling, since even for sources with significant jet components, structure effects are zero if the jet is oriented perpendicular to the observing baseline. Figure 4 shows the impact of jet–baseline orientation on simulated group delays due to source structure.

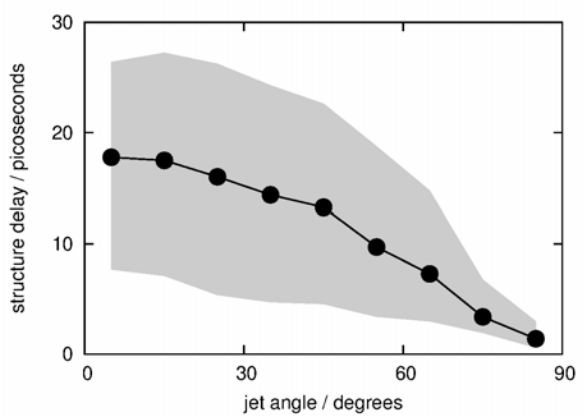

Fig. 4 Structure group delays per observation as a function of relative jet–baseline orientation, for an SI=3 simulated mock catalog. The points are medians, and the shaded region is the interquartile range. Even high structure index sources contribute very little to the structure group delay if the jet direction is almost orthogonal to the observing baseline.

Single-baseline scans are rare in geodetic VLBI. It is therefore likely that, for any scan of an extended source, at least one baseline will have an unfavourable orientation with respect to the jet direction. Given some crude knowledge of source structure, however, it should be possible to optimize the observing strategy for that particular source. For example, our simulations in Figure 4 suggest that for two equal-length orthogonal baselines, smaller total structure delays may be obtained by having one baseline be orthogonal and the other parallel to the quasar jet axis, rather than two baselines at 45°. A more sophisticated approach would also include baseline length information, since shorter baselines suffer less from source structure effects. In this way, a combination of source structure, jet orientation, and baseline information could inform the scheduling process.

6 Broadband Observations

Some additional complications relating to source structure arise in the case of broadband (2–14 GHz or similar) observations. Quasar structure is frequency-dependent in the sense that sources typically exhibit less structure at higher frequencies. Time-variable properties of quasars also depend on observing frequency. Finally, even quasars showing little structure exhibit *core shifts*, a synchrotron self-absorption effect that causes the location of the observed quasar core to change with frequency. Understanding the multi-frequency behavior of quasar structure (and its temporal evolution) is necessary for making any meaningful corrections to broadband VGOS data.

Acknowledgements

We thank Jim Lovell, Arthur Niell, Richard Porcas, and Bill Petrachenko for useful discussions. SS, JM, and LP are grateful to the Australian Research Council for Research Fellowships.

References

1. Lister, M. L., Cohen, M. H., Homan, D. C., Kadler, M., Kellermann, K. I., Kovalev, Y. Y., Ros, E., Savolainen, T., Zensus, A. 2009, MOJAVE: Monitoring of jets in Active Galactic Nuclei with VLBA experiments. VI. Kinematics analysis of a complete sample of blazar jets, Astronomical Journal, 137, 3718
2. Fey, A. L., Charlot, P. 1997, Astrophysical Journal Supplement Series, 111, 95
3. Ma, C., et al. 2009, in IERS Technical Note. No. 35, ed. A. L. Fey, D. Gordon, C. S. Jacobs
4. Petrachenko, B., Niell, A., Behrend, D., Corey, B., Böhm, J., Charlot, P., Collioud, A., Gipson, J., Haas, R., Hobiger, T., Koyama, Y., MacMillan, D., Malkin, Z., Nilsson, T., Pany, A., Tuccari, G., Whitney, A., Wresnik, J. 2009, Design Aspects of the VLBI2010 System - Progress Report of the IVS VLBI2010 Committee, NASA/TM-2009-214180
5. Shabala, S. S., McCallum, J. N., Plank, L., Böhm, J. 2014, J. Geodesy, submitted
6. Fey, A. L., USNO Radio Reference Frame Image Database, URL: http://rorf.usno.navy.mil/RRFID
7. Jacobs, C. S., et al. 2012, The potential for a Ka-band (32 GHz) worldwide VLBI network, Proc. Journées 2011 "Systèmes de référence spatio-temporels", ed. H. Schuh, S. Böhm, T. Nilsson and N. Capitaine, Vienna University of Technology, p. 78
8. Charlot, P. 1990, Astronomical Journal, 99, 1309
9. Schaap, R. G., Shabala, S. S., Ellingsen, S. P., Titov, O. A., Lovell, J. E. J. 2013, Scintillation is an indicator of astrometric stability, Monthly Notices of the Royal Astronomical Society, 434, 585
10. Shabala, S. S., et al., 2014, J. Geodesy, 88(6), p. 575–586, DOI: 10.1007/s00190-014-0706-z
11. Collioud, A., Charlot, P. 2010, VLBI2010 Imaging and Structure Corrections, IVS GM Proc., Hobart, ed. D. Behrend and K. D. Baver, NASA/CP-2010-215864, p. 45
12. Collioud, A., Charlot, P. 2012, VLBI2010 Imaging and Structure Correction Impact, IVS GM Proc., Madrid, ed. D. Behrend and K. D. Baver, NASA/CP-2012-217504, p. 47
13. Porcas, R. 2010, VLBI2010: the Astro-Geo connection, IVS GM Proc., Hobart, ed. D. Behrend and K. D. Baver, NASA/CP-2010-215864, p. 8

Multi-epoch Study of Source Morphology in the Southern Hemisphere

S. Basu[1,2], A. de Witt[1], J. F. H. Quick[1], A. Bertarini[3], L. Leeuw[2]

Abstract The International Celestial Reference Frame (ICRF) has been constructed using catalogs of radio quasars observed using the Very Long Baseline Interferometry (VLBI) technique. The VLBI technique defines the current ICRF and helps to improve its precision. The angular resolution available from VLBI measurements is on a scale of milliarcseconds to submilliarcseconds and provides the highest accuracy available at present. On this scale most extragalactic radio sources exhibit extended structures. In order to define the ICRF with the highest accuracy, observational efforts are required to find more compact sources and to monitor them. We report here our efforts to provide multi-epoch VLBI maps for southern sources observed through existing astrometric sessions. These images will be used to identify compact southern sources and to correct observations for source structure, thereby allowing improved relative astrometric accuracy.

Keywords Celestial Reference Frame, VLBI, imaging, astrometry, quasar

1 Introduction

Since the late 1970s, Very Long Baseline Interferometry (VLBI) observations have been used to determine the positions of radio sources with milliarcsecond precision. In recent years, the accuracy of the VLBI technique has improved substantially, and high precision VLBI measurements of positions of extra-galactic radio sources are now used to define and maintain celestial radio reference frames with sub-milliarcsecond precision. The current realization of the International Celestial Reference Frame (ICRF2, [9]), is based on dual frequency 2.3-GHz (S-band) and 8.4-GHz (X-band) VLBI observations of 3,414 extra-galactic radio reference sources, and it forms the basis for positional astronomy. Catalogs of positions of radio reference sources with the highest precision are needed for many applications, for example, the imaging of faint radio sources in phase-referencing mode, accurate differential astrometry, spacecraft tracking, space navigation, and space geodesy.

The primary sources used as reference sources in VLBI are radio-loud quasars. In radio-loud quasars, the radio emission originates with a relativistic jet launched from the vicinity of the black hole. The ones useful as reference sources are those where the scale of this jet is small compared to the resolution such that the radio emission is compact or core-dominated and appears almost point-like. Unfortunately, many of the radio-loud quasars that make up the ICRF exhibit spatially extended intrinsic structures, with VLBI imaging showing jets in addition to compact cores. The extended emission structures in these sources may also evolve significantly over time on scales of months to years, and in addition they also exhibit flux density variations on timescales of years to weeks.

Charlot *et al.* [2] showed that the effect of source structure on VLBI astrometric positions can be significant, where any departure from the point source approximation, commonly made in astrometric analysis, introduces errors in the observable quantities of group delay and delay rate. It is therefore important to map the structures of these sources on a regular basis. Reg-

1. Hartebeesthoek Radio Astronomy Observatory
2. University of South Africa
3. IGG/Max-Planck-Institut für Radioastronomie

ular imaging of Northern hemisphere ICRF sources is made through the ongoing astrometric and geodetic Research and Development VLBI (RDV) experiments using the Very Long Baseline Array (VLBA) (e.g. [3, 6]). The results of the imaging and analysis of these studies prove to show the importance of continual observing and analysis in order to monitor the sources for variability or structural changes so that their astrometric quality can be continuously evaluated.

Catalogs of compact radio sources, including the ICRF2, are weak in the south, especially at declinations south of $-45°$, the limit of the reach of northern baselines. There have been many efforts in recent years to increase the number of known Southern hemisphere reference sources, in particular the astrometric observations from the Long Baseline Array (LBA) Calibrator Survey (LCS), which has already produced a significant improvement at X-band [12]. Dedicated astrometric observations at S/X band to densify the ICRF in the south are currently underway, as proposed in Lovell *et al.* [8]. There have also been a few dedicated imaging observations of southern sources (e.g., [7, 10, 11]), and the first images from the LCS astrometric experiments have been produced [5].

However, dedicated imaging observations to map the structures of sources on a regular basis have proven to be very resource intensive, with the availability of antennas being one of the most limiting factors in the south. Based on these considerations, we have investigated the possibility of imaging source structure from existing geodetic or astrometric observations in the south. Imaging of source structure from the LCS experiments has proven to be successful, and we will continue to image more of the LCS experiments. The details of the LCS experiments are discussed in more detail in Section 2. We have also identified the Celestial Reference Frame Deep South (CRDS) astrometric VLBI observations (see Section 3) to be potentially suitable for mapping purposes, and in this paper we present our first imaging results. In addition to yielding source structure information for astrometric purposes, such images will also allow us to study the properties of such sources that will be valuable in the investigation of a wide range of astrophysical phenomena.

2 LBA Calibrator Survey (LCS)

The LCS[1] is an ongoing VLBI project to observe at 8.4 GHz a list of flat-spectrum radio sources below $-30°$ declination using the LBA. This array is stretched out along Australia's east coast in a north-south direction, which limits the uv-coverage (Figure 1 (a)).

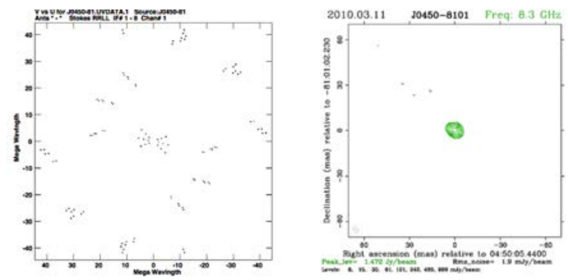

(a) (b)

Fig. 1 uv-coverage (a) and source structure (b) of the source J0450-8101. Image credit: de Witt *et al.* [5].

The LCS seeks to systematically increase the density of compact extra-galactic radio sources in the Southern hemisphere and to determine their positions with milliarcsecond accuracy. To date, the positions of 924 new objects have been determined from analysis of 14 LBA experiments, and a total of 170 sources from two of these experiments have been successfully imaged to determine the structure at 8.4 GHz. Figure 1 (b) shows an example of source structure which was imaged from LCS experiment v271e [5].

The main aim of the LCS project is to determine the suitability of potential new sources for phase referencing observations and as target for astrometry and geodesy observations. Most sources are observed at a single epoch only, and so variability and structural changes cannot be monitored. However, the LCS provides a very valuable pool of potential new sources that can be added to existing observing projects, such as the CRDS sessions, that will provide observations of such sources on a continual basis.

In our efforts to complete the imaging and determine the source morphology of all LCS sources, we selected as our first target the most recent experiment

[1] Information on the LCS is available on the Web at *http://astrogeo.org/lcs/*

from the LCS, V271m. Observations for LCS experiment V271m were made on 15–16 June 2013 at a central frequency of 8.344 GHz and a total bandwidth of 128 MHz, and they were recorded at RCP. The antennas that participated were ASKAP, ATCA, Ceduna, Tidbinbilla 34-m, Parkes, Mopra, Hobart 26-m, Hobart 12-m, HartRAO 26-m, and Warkworth. A total of 101 sources were observed in this experiment with 2–4 scans of 2–6 minutes duration per source. The data were correlated at the Curtin University of Technology using the DiFX correlator [4]. Data reduction for v271m is still in progress.

3 Celestial Reference Frame Deep South (CRDS)

The CRDS[2] astrometric observing sessions are part of a program to strengthen the ICRF in the south and are coordinated by the International VLBI Service for Geodesy and Astrometry (IVS). The aim of the CRDS sessions is to provide astrometric results from dual frequency (S/X band) observations for improving the current ICRF, but also to extend and densify the ICRF by observing new sources. The CRDS observing program started in 2011 with six sessions scheduled per year. Since 2013, observations have been scheduled using a regular network of six southern stations: the HartRAO 26-m telescope in South Africa; the Hobart 26-m and the Hobart, Katherine, and Yarragadee 12-m telescopes in Australia; and the Warkworth 12-m telescope in New Zealand.

A total of 97 sources have been observed through CRDS sessions with the majority of sources being south of -30° declination. On average, most sources are observed in at least two to three sessions per year with around two to seven scans of nine minutes duration per source. As opposed to more typical astrometric sessions where only two-station scans are required, the majority of scans in the CRDS sessions observed since 2013 include at least four to six stations per scan, making these observations more suitable for mapping purposes.

In order to test the suitability of CRDS sessions for imaging of source structure, we have chosen the most recent CRDS session at the time, which is CRDS63. Observations for CRDS63 were made on 14–15 June 2013 and 38 sources were observed. All six stations as mentioned above were scheduled for observing, but, unfortunately, in the end both the Hobart 12-m and Warkworth 12-m antennas did not participate. Data was recorded at RCP with six IFs at 2.3 GHz and eight IFs at 8.4 GHz with a bandwidth of 4 MHz per IF[3]. The data was correlated at the Washington Correlator (WACO) in Washington, DC.

4 Data Reduction and Preliminary Results

The data reduction for the CRDS 8.4-GHz data was done using AIPS. The correlated data was fringe-fitted with `fourfit` using the '-X' option which is used to produce data suitable for import into AIPS. The correlated data was then imported into AIPS using `MK4IN` [1].

Amplitude gains were derived from nominal system temperatures. Thereafter, data inspection, initial editing, and fringe fitting were done in the standard manner. We did an initial round of fringe-fitting to find approximate residual rates and delays. The main editing was carried out using this approximate calibration, and then, using the edited data, we proceeded to a second round of fringe-fitting to refine the calibration, with each source being fringe-fitted individually. The visibility data for source J1427-4206 were Fourier inverted and deconvolved using the CLEAN algorithm, and the amplitude gains were further refined by self-calibration using CLEAN models. For the final CLEAN image, we used complex weighting using the square root of the statistical visibility weights, which increases the robustness of the image.

So far we have only produced preliminary imaging results for source J1427-4206 at 8.4 GHz (see Figure 2). We have chosen source J1427-4206 for our initial attempt, as this source has the highest flux density from the sample of sources in CRDS63 and was observed during four scans that included all four antennas. J1427-4206 has also previously been observed with both the VLBA and LBA (see Figure 2) which

[2] Information about the CRDS sessions is available on the IVS Web site at *http://ivscc.gsfc.nasa.gov*

[3] Bandwidth was increased to 8 MHz from CRDS66 session in June 2013.

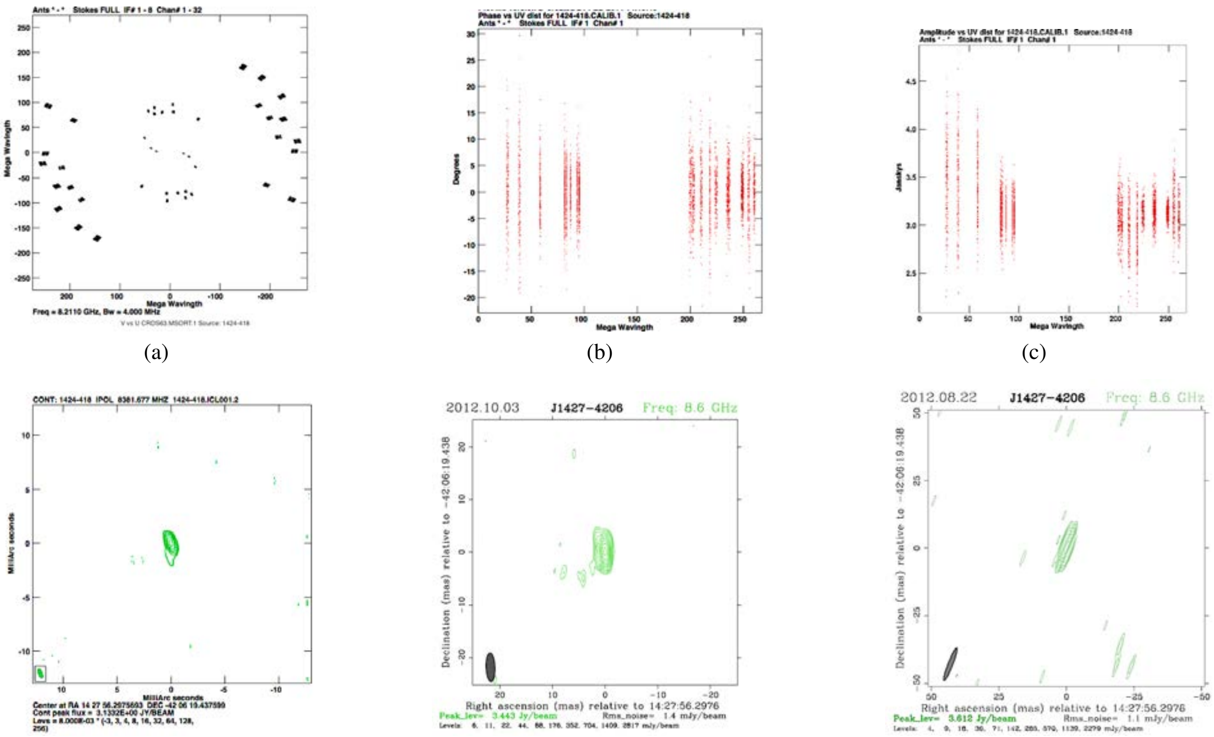

(a) (b) (c)

(d) (e) (f)

Fig. 2 (a) uv-coverage plot for source J1427-4206 from the CRDS63 experiment. (b) Phase vs. uv-distribution plot of the source J1427-4206. (c) Amplitude vs. uv-distribution plot of the same source. (d) Map of source J1427-4206 from the CRDS63 experiment. (e) and (f) Multi-epoch source structure images of J1427-4206 available from the RFC VLBI Global Solution Catalogue (available on the Web at http://astrogeo.org/vlbi/solutions/rfc_2014b/). North is UP and East is to the LEFT in all of the above maps.

provides us with an opportunity to compare our results with available images from existing experiments.

We show a representative contour plot of the CRDS63 image of J1427-4206 at 8.4 GHz in Figure 2. The total CLEAN flux density is 3.33 Jy, and the image background rms is 7.9 mJy beam^{-1}.

5 Summary and Outlook

We present preliminary imaging results for one source from the CRDS63 astrometric observing session. Our aim is to complete imaging of all CRDS sessions in order to evaluate the astrometric quality of these ICRF sources for future astrometric and geodetic use.

At present we are working on the calibration and imaging of the remaining sources in the CRDS63 session at 8.4 GHz. We also plan to analyze the 2.3-GHz data from the CRDS63 session. In the future we plan to set up a pipeline for automated imaging of CRDS sessions. These dual-frequency observations will give us an opportunity to test the frequency dependence of the source structure and to monitor the sources for variability or structural changes on a continuous basis.

Acknowledgements

We thank Alan Fey, Maria Davis, and David Hall from USNO for use of the data from the CRDS observing sessions. We wish to thank HartRAO, NRF-DST, and the University of South Africa for financial support. This research has made use of the IVS and LCS databases.

References

1. W. Alef and D. A. Graham. The New Bonn Mk IV - AIPS Data Export Path., *in proceedings of the 6th European VLBI Network Symposium*, 31, 2002.
2. P. Charlot. Radio-source structure in astrometric and geodetic very long baseline interferometry., *AJ*, 99, pp. 1309, 1990.
3. A. Collioud and P. Charlot. The Bordeaux VLBI Image Database., *in Proceedings of the 19th European VLBI for Geodesy and Astrometry Working Meeting*, pp. 19, 2009.
4. A. T. Deller et al. DIFX: A Software Correlator for Very Long Baseline Interferometry Using Multiprocessor Computing Environments., *PASP*, 119, 318, 2007.
5. A. De Witt and M. Bietenholz. Analysis of Potential VLBI Southern Hemisphere Radio Calibrators., *in Proceedings of the 11th European VLBI Network Symposium & Users Meeting*, 2012
6. A. L. Fey and P. Charlot. VLBA Observations of Radio Reference Frame Sources. III. Astrometric Suitability of an Additional 225 Sources., *ApJS*, 128, pp. 17, 2000.
7. F. Hungwe et al. Characterization of long baseline calibrators at 2.3 GHz., *MNRAS*, 418, pp. 2113, 2011.
8. J. E. J. Lovell et al. The AuScope geodetic VLBI array., *Journal of Geodesy*, 87, pp. 527, 2013.
9. C. Ma et al. The Second Realization of the International Celestial Reference Frame by Very Long Baseline Interferometry., *IERS Technical Note*, 35, pp. 1, 2009.
10. R. Ojha et al. VLBI Observations of Southern Hemisphere ICRF Sources. I., *AJ*, 127, pp. 3609, 2004.
11. R. Ojha et al. VLBI Observations of Southern Hemisphere ICRF Sources. II. Astrometric Suitability Based on Intrinsic Structure., *AJ*, 130, pp. 2529, 2005.
12. L. Petrov et al. The LBA Calibrator Survey of southern compact extragalactic radio sources - LCS1., *MNRAS*, 414, pp. 2528, 2011.

Session 6

New Horizons for VLBI

March 2-7, 2014

8th IVS
GENERAL MEETING
Shanghai, China

Completing the K-band Celestial Reference Frame in the Southern Hemisphere

A. de Witt[1], A. Bertarini[2], S. Horiuchi[3], C. S. Jacobs[4], T. Jung[5], J. E. J. Lovell[6], J. N. McCallum[6], J. F. H. Quick[1], B. W. Sohn[5], C. Phillips[7], R. Ojha[8]

Abstract K-band (22 GHz) radio observations have the potential to form the basis for the most accurate Celestial Reference Frame (CRF) ever constructed. Relative to the standard S/X (2.3/8.4 GHz) observing bands, K-band is expected to exhibit a reduction in extended source morphology and core-shift. This reduction in astrophysical systematics should allow for a more stable CRF at K-band and should also be advantageous in tying the VLBI radio frame to the Gaia optical frame. K-band CRF observations currently exist only from the all-northern Very Long Baseline Array (VLBA) and therefore must be complemented by observations from southern arrays in order to realize this potential. A collaboration was formed with the goal of completing sky coverage at K-band with specific emphasis on the Southern hemisphere where K-band CRF coverage is weak. Southern hemisphere observations to densify the CRF at K-band are under way and preliminary astrometric observations were carried out on 23 August 2013 between telescopes in Australia (Hobart 26 m), Korea (Tamna 21 m), and South Africa (HartRAO 26 m). More extensive astrometric observations were carried out on 21/22 December 2013 that also included the Tidbinbilla 70-m DSN antenna in Australia. A proposal for imaging source structure at K-band has been submitted to the Australian Telescope-Long Baseline Array (AT-LBA). We discuss some of our results as well as the implications for K-band CRF work.

1. Hartebeesthoek Radio Astronomy Observatory
2. IGG/Max-Planck-Institut für Radioastronomie
3. CSIRO/Canberra Deep Space Communications Complex
4. Jet Propulsion Laboratory, California Institute of Technology/NASA
5. Korea Astronomy & Space Science Institute
6. University of Tasmania
7. ATNF/CSIRO
8. Goddard Space Flight Center/NASA

Keywords Celestial Reference Frame, VLBI, astrometry, K-band, quasar

1 Introduction

In recent years, VLBI radio source angular position accuracy has improved to the sub-milliarcsecond level. High precision VLBI measurements of positions of extragalactic radio sources define and maintain the current International Celestial Reference Frame (ICRF-2, [10]), which forms the underlying basis for positional astronomy. The ICRF-2 is based on dual frequency S-band (2.3 GHz) and X-band (8.4 GHz) VLBI observations of 3,414 reference sources. Catalogs of positions of extragalactic radio reference sources with the highest precision are needed for many applications. Among these are imaging of faint radio sources in phase-referencing mode, accurate differential astrometry, spacecraft tracking, space navigation, and space geodesy. Extragalactic radio sources that are relatively bright at the frequency of observation, compact, or core-dominated on VLBI scales and that have no or little detectable motion are well-suited for high-accuracy reference frame work. Quasars, being at great distances, do not exhibit any measurable proper motion or parallax, making them ideal reference sources.

Unfortunately, at the standard S/X frequencies, many ICRF sources exhibit spatially extended intrinsic structures that may vary with time, frequency, and baseline projection. This departure from the point-source approximation commonly made in astrometric VLBI analysis can have a significant effect on the measured VLBI positions. Extended source structures, if not corrected for, will limit the ability to further improve the accuracy of individual VLBI source positions and thus the improved stability of future celestial reference frames (CRFs). However, mapping the structures on a regular (approximately monthly) basis for hundreds of sources has proven to be too resource intensive to be a sustained solution.

Our solution is to observe at higher radio frequencies such as K-band (22 GHz), where, on VLBI scales, sources tend to be more compact (e.g., [1] and [2]), and hence the structure effects on astrometric position estimation should be reduced. VLBI observations of quasars have also shown that the location of the peak brightness often varies with observing frequency due to opacity effects, a phenomenon known as "core-shift". In particular, VLBI images of quasars show that the observed position of the peak brightness moves closer to the central black hole as the frequency increases (e.g. [13]). Thus by observing at frequencies higher than the standard S/X bands, we can expect to see more compact structure and also reduce the effect of core shift [7]. This reduction in astrophysical systematics should allow for a more accurate and stable reference frame at these higher frequencies and be particularly advantageous in tying the VLBI reference frame to future optical reference frames such as Gaia.

2 Reference Frames at Higher Radio Frequencies

At present there are far fewer observations of extragalactic reference sources at high radio frequencies compared to the standard S/X observing bands. One of the major challenges of observing at higher radio frequencies is the decrease in system sensitivity. At higher radio frequencies, the sources themselves are in general weaker and many sources are resolved, antenna performance (e.g. antenna pointing) becomes degraded, system temperatures are higher and more susceptible to degradation from bad weather, and coherence times are shorter. Fortunately the rapidly decreasing costs of recording higher data rates allows us to compensate for sensitivity issues that result from observing at higher radio frequencies. In the last few years, considerable work has been done and significant progress made on defining reference frames at higher radio frequencies.

Astrometric VLBI observations at Ka-band (32 GHz), a combined project of NASA's Deep Space Network and ESA, have already developed a catalog of ~ 631 observable sources (134 south of $-45°$ declination) with highly accurate positions for improved deep-space navigation [6], showing that there are sufficient strong sources suitable for astrometric use at higher frequencies. However, all the data from the Ka-band effort is from single baseline passes only, and thus no source images could be made. Astrometric and imaging observations by Lanyi et al. [8] and Charlot et al. [2] provided a foundation for the development of a reference frame at K-band. The current K-band frame consists of only 279 sources with weak coverage in the southern hemisphere, showing a rapid drop in source density at declinations south of $-30°$.

Because many stations across the globe have K-band receivers, there is now an opportunity to create a worldwide K-band network with potential for high resolution imaging and astrometry. The advantage of observing at K-band is that radio observatories typically have K-band receivers, while Ka-band receivers are typically only available at tracking stations, which are very few in number. For very long baseline observations at K-band, calibrator reference sources are also needed, in particular for trigonometric parallax distances to H_2O (22 GHz) masers (e.g. [12]), as well as phase referenced observations to image the sub-milliarcsecond structure of the most compact regions of emission in AGN. High-resolution K-band observations would also be of much value to study wavelength dependent systematic errors due to the core-shift effect.

3 Why Observe in the Southern Hemisphere?

VLBI observations in the southern celestial hemisphere have always been more difficult both because there are fewer radio telescopes in the south than in the north, and because there are fewer known reference sources in the south. There have been many efforts in recent years to increase the number of known calibrator reference sources in the south, in particular the Australian Telescope - Long Baseline Array (AT-LBA) calibrator survey (LCS), which has already produced a significant improvement at X-band [11]. There have also been a few observations at S-band, for example, Hungwe et al. [5], and southern observations are planned at 1.6 GHz (L-band), to improve the number of calibrator sources for phase-referencing at low frequencies. In 2012, an International Astronomical Union (IAU) working group was formed with the goal of the realization of the next generation International Celestial Reference Frame (ICRF-3), with specific emphasis on improving the accuracy and coverage in the southern hemisphere. Dedicated astrometric observations to improve the southern celestial reference frame at S/X band are currently underway, as proposed in Lovell et al. [9]. However, at present there are virtually no VLBI observations of reference sources at K-band. All these low frequency programs thus invite complementary work at K-band.

4 Observational Plan and Network Geometry for Southern Hemisphere VLBI at K-band

We have undertaken a program to observe potential K-band reference sources in the Southern Hemisphere. These observations are motivated by the need to complete sky coverage at K-band and thus extend CRFs to higher radio frequencies. Astrometric observations to complete sky coverage at K-band, as well as VLBI imaging observations to characterize the nature of the sources at K-band, are underway. Preliminary astrometric observations were carried out on 23 August 2013 between telescopes in Australia (Hobart 26 m), Korea (Tamna 21 m), and South Africa (HartRAO 26 m). More extensive astrometric observations that also included the Tidbinbilla 70 m DSN antenna in Australia were carried out on 21 December 2013, and similar observations are planned for 4 May 2014. Details of the observational setup and preliminary results are presented in Section 5. The Korea to South Africa baselines will extend K-band CRF coverage down to about $-45°$ declination, and observations between Australia and South Africa will extend coverage to the south polar cap and thus gain full sky coverage for the K-band CRF. Observations between Tamna and HartRAO are limited to about $\pm 45°$ declination and less than four hours of mutual visibility.

Fig. 1 A map showing the proposed telescopes for the Southern hemisphere K-band observations.

For imaging of source structure, as opposed to astrometry, a larger network of telescopes is needed in order to provide a variety of baseline lengths and orientations. For this purpose we have also submitted a proposal to observe and image a set of potential K-band reference sources at declinations below $-30°$. We will use the full AT-LBA which adds the ATCA (6-m and 22-m), Ceduna (30-m), Mopra (22-m), and Parkes (64-m) telescopes in Australia to our observing network (see Figure 1). It should be noted, however, that although the AT-LBA provides a large network of antennas, we are still missing intermediate baseline lengths of a few thousand kilometers.

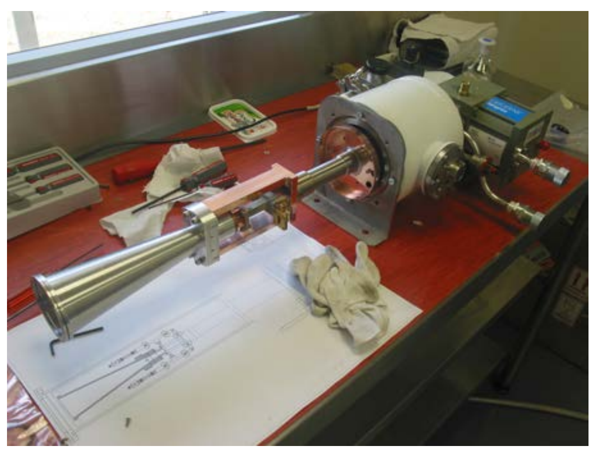

Fig. 2 New cryogenically cooled K-band receiver during development at HartRAO. The feed horn and waveguide components for the receiver were included inside the cryogenic vacuum package and cooled down with the low noise amplifiers. This resulted in a very low receiver noise temperature of 20–25 K.

We have identified the uncooled K-band receiver on the HartRAO 26-m antenna as one of the major error sources in our K-band CRF work and thus made it high priority to develop a cooled receiver. Although the current K-band receiver at HartRAO is VLBI-capable and regularly detects fringes from VLBI observations, it has a high noise temperature (250 K), limiting observations to the brightest sources only (> 500 mJy). A new cryogenically cooled K-band receiver is under development at HartRAO (see Figure 2) to replace the experimental ambient receiver currently on the antenna. The receiver is undergoing lab testing, and we hope to have it installed and ready for VLBI use by the time we run our next K-band observations in May 2014.

5 Observations and Preliminary Results

Our first test observations ran for four hours on 23 August 2013, and about 20 sources from the LCS catalog were observed ([4]) . Given that we found fringes to all stations, we proceeded with a similar 24-hour experiment starting 21 December 2013, in which we observed a total of 106 sources at K-band (see Figure 3).

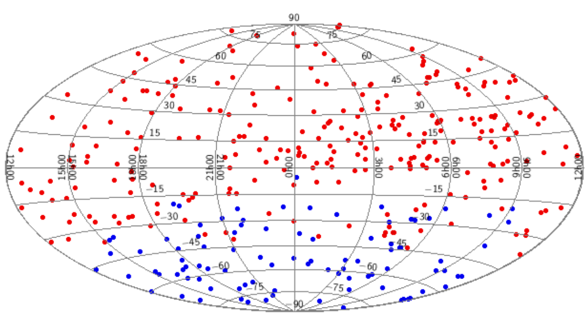

Fig. 3 The distribution of CRF sources at K-band. The 279 sources from Lanyi et al. [8] and Charlot et al. [2] are shown in red. The 106 sources observed at K-band during 21–22 December 2013 are shown in blue. There are 12 overlapping sources.

These observations included also the Tidbinbilla 70-m antenna using their recently installed VLBI digital backend called the Deep Space Station VLBI Processor (DVP) and their old Mark IV terminal for redundancy. The trial correlation proved that data from both the DVP and the KVN digital backend can be successfully correlated using DiFX ([3]). However, inadvertently, after a few scans, the setup of the DVP was changed. This change requires special DiFX modes that are not functional yet; therefore, the correlation is still pending.

Figure 4 shows, as an example, the detection of ICRF J1427-4206 from both observations. Table 1 shows some of the detections on the baseline between Tidbinbilla (Mark IV terminal) and Hobart. One should also keep in mind that the Mark IV rack was observing at half the speed (512 Mbps, instead of 1 Gbps), and only three 16 MHz wide channels were usable, i.e., the bandwidth was reduced from 256 MHz to 48 MHz.

Table 1 SNRs of some of the observed sources in the baseline Tidbinbilla (Mark IV terminal) to Hobart. The flux densities of these sources are not yet available, as no amplitude calibration has been applied yet.

Source	No. Obs	SNR
J0049-5738	1	24
J0058-5659	1	27
J0309-6058	1	12
J0403-3605	1	15
J0519-4546	1	20
J0522-6107	1	8
J0529-7245	1	56
J0550-5732	2	23
J0845-5458	1	22
J1038-5311	1	65
J1147-3812	1	17
J1206-6138	3	15
J1254-7138	2	10
J1515-5559	2	24
J1617-7717	3	22
J1703-6212	1	23
J1834-5856	1	8
J1932-4536	1	8
J1940-6907	1	10
J2056-4714	1	48
J2147-7536	1	40
J2239-5701	1	36

6 Summary and Outlook

As radio frequency increases, sources are expected to exhibit more compact source morphology and reduced core-shift. Astrometric VLBI observations of reference sources at K-band will therefore allow for a more accurate and stable reference frame to be constructed. For this reason, we began an observational program to

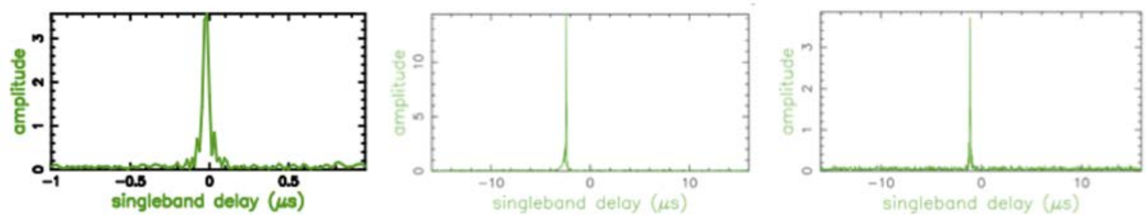

Fig. 4 HOPS fourfit plots, showing the single-band delay for ICRF J1427-4206 betweenHartRAO and Hobart (SNR $\sim$ 70, left) from the August 2013 observations, and the between Hobart and Tidbinbilla (SNR $\sim$ 338, middle) and HartRAO and Tidbinbilla (SNR $\sim$ 95, right) from the December 2013 observations.

densify the CRF at K-band. Our initial focus will be on the Southern hemisphere, where K-band coverage is weak. We have successfully detected fringes from our first test observations to demonstrate the feasibility of our experimental approach. We have also demonstrated that data taken with the KVN digital backend as well as the Tidbinbilla DVP backend system can be successfully correlated with DiFX. The new cryogenic K-band receiver for the HartRAO 26-m antenna, as well as improvements in the instrumental calibration at HartRAO, provides hope that significant progress in the Southern hemisphere is achievable within the next one to two years.

Our goals for K-band are the realization of a full sky CRF by 2018, in time for the Gaia optical reference frame. Our first goal is to obtain comparable density and accuracy in the south to that obtained from the astrometry that was done with the VLBA in the north. The second goal will be further densification of the K-band frame in the north using the VLBA as well as the European VLBI Network (EVN). We will also make use of EVN and HartRAO baselines to improve the accuracy of source positions in declination. Our ultimate goal is to reach accuracies better than 70 μas to match the Gaia predicted accuracy for V = 18 visual magnitude quasars.

References

1. M. F. Bietenholz, N. Bartel and M. P. Rupen. The Location of the Core in M81, *ApJ*, 615, pp. 173, 2004.
2. P. Charlot et al. The Celestial Reference Frame at 24 and 43 GHz. II. Imaging., *AJ*, 139, pp. 1713, 2010.
3. A. T. Deller et al. DiFX: A Software Correlator for Very Long Baseline Interferometry Using Multiprocessor Computing Environments, *PASP*, 119, pp. 318, 2007.
4. A. de Witt et al. Extending the K-band Celestial Frame Emphasizing Southern Hemisphere, *in Proceedings of the Journées "Systèmes de référence spatio-temporels"*, 2013.
5. F. Hungwe et al. Characterization of long baseline calibrators at 2.3 GHz, *MNRAS*, 418, pp. 2113, 2011.
6. C. S. Jacobs et al. The X/Ka-band (8.4/32‘GHz) Celestial Reference Frame: Results from combined NASA-ESA baselines including Malargüe, Argentina, presented at the IVS 2014 General Meeting, Shanghai, China, March 2014.
7. Y. Y. Kovalev et al. Opacity in compact extragalactic radio sources and its effect on astrophysical and astrometric studies, *A&A*, 483, pp. 759, 2008.
8. G. E. Lanyi et al. The Celestial Reference Frame at 24 and 43 GHz. I. Astrometry., *AJ*, 139, pp. 1695, 2010.
9. J. E. J. Lovell et al. The AuScope geodetic VLBI array, *Journal of Geodesy*, 87, pp. 527, 2013.
10. C. Ma et al. The Second Realization of the International Celestial Reference Frame by Very Long Baseline Interferometry, *IERS Technical Note*, 35, pp. 1, 2009.
11. L. Petrov et al. The LBA Calibrator Survey of southern compact extragalactic radio sources - LCS1, *MNRAS*, 414, pp. 2528, 2011.
12. M. J. Reid et al. Trigonometric Parallaxes of High Mass Star Forming Regions: the Structure and Kinematics of the Milky Way, *ApJ*, 783, pp. 130, 2014.
13. K. V. Sokolovsky et al. A VLBA survey of the core shift effect in AGN jets. I. Evidence of dominating synchrotron opacity, *A&A*, 532, pp. A38, 2011.

Combining Datum-free Normal Equation Systems and Solutions with Full Covariance Information for Upcoming CRF Realizations

Andreas Iddink, Thomas Artz, Axel Nothnagel

Abstract Combination approaches within the International VLBI Service for Geodesy and Astrometry (IVS) are solely performed on the level of datum-free normal equations (NEQs). The procedure is used to compute the two major products of the IVS, i.e., time series of Earth orientation parameters (EOPs) and station coordinates. One shortcoming of the datum-free NEQ-based combination is the limitation to contributions based on the classical least squares adjustment and to analysis software packages supporting the output of datum-free NEQs. Hence, in order to increase the potential number of contributions, it would be a big gain to be able to include contributions based on solutions of a constrained NEQ.

In this paper, we present a method to mix the combination on the level of datum-free NEQ and on the solution level with full covariance information. We show the implementation of this approach in our existing software environment BonnSolutionCombination (BoSC) and discuss the prerequisites and the limitations. Furthermore, we show the benefits for upcoming Celestial Reference Frame (CRF) realizations.

Keywords VLBI, ICRF, intra-technique combination, datum-free normal equations, full variance-covariance information

1 Introduction

At present, six analysis centers regularly contribute their independent solutions to the International VLBI Service for Geodesy and Astrometry (IVS) [3, 6] for the computation of intra-technique combined products. This includes rapid solutions of Earth orientation parameters (EOPs) and quarterly solutions [2] of VLBI Terrestrial Reference Frames (VTRFs) [4] containing station positions and velocities. In multiple studies it has already been highlighted that the use of an intra-technique combination improves the stability and robustness of the combined results compared to the individual results [5]. In order to avoid that contributions are distorted by any constraints before combining them, the intra-technique combination is performed at the level of datum-free normal equation systems (NEQs). Thus, the same datum reference frames and an identical datum can be initially applied during the combination process. By using datum-free NEQs, it is guaranteed that the full variance-covariance information of all parameters and all individual contributions is rigorously transferred. The delivery and exchange of the NEQs is performed with the Solution Independent Exchange Format (SINEX).

Despite the advantages of the combination on the level of datum-free NEQs, some shortcomings can be identified. In the first place, the combination is limited to contributions based on the classical least squares adjustment. However, the similar parameterization of auxiliary parameters by linear splines in all solutions may lead to systematic effects. These might be mitigated by using solutions based on filter techniques as well since these are based on a different, i.e., stochastic, representation of the auxiliary parameters.

Secondly, analysis software packages which does not support the export of datum-free NEQs are excluded and cannot contribute to the combination. Hence, in order to overcome these shortcomings and to improve the robustness and stability of the combined

Institute of Geodesy and Geoinformation, University of Bonn

products even more, it would be a substantial progress to be able to include contributions based on solutions of constrained NEQs. Furthermore, by including source positions in the rigorous VLBI intra-technique combination, an improvement will be exploited for the Celestial Reference Frame (CRF) combination as well.

2 Reconstruction of Datum-free NEQs

In order to be able to compute TRFs, CRFs, and corresponding EOPs, it is essential that all contributing analysis centers (ACs) and software packages support the output of the entire set of parameters, including EOPs, all station coordinates, and all source positions. The common intra-technique combination is based on VLBI input data provided in the SINEX format in form of datum-free NEQs. In order to be able to include solutions with full covariance information in this combination procedure, the datum-free NEQs need to be reconstructed using information about the applied constraints. Due to the fact that the SINEX format allows for the storage of NEQs as well as of solutions of constrained NEQs, all necessary information for the reconstruction can be stored in the SINEX files.

In this case the file must contain the solution vector $\hat{x}$, the full covariance information of the estimated parameters $C_{\hat{x}\hat{x}}$, the a posteriori variance factor $\hat{\sigma}^2$, and the weighted square sum of residuals $\hat{v}^T P \hat{v}$ [1]. Furthermore, the most critical and important fact is that the full a priori variance-covariance matrix C_{xx} needs to be booked in the SINEX file as well. In order to be able to entirely reconstruct the datum-free NEQ matrix N, this matrix has to contain all applied constraints that were used for the parameter estimation. Under these prerequisites N can be reconstructed using [8]

$$N = \hat{\sigma}^2 C_{\hat{x}\hat{x}}^{-1} - \hat{\sigma}^2 C_{xx}^{-1} \quad (1)$$

$$y = \hat{\sigma}^2 C_{\hat{x}\hat{x}}^{-1} \hat{x} \quad (2)$$

$$l^T P l = (\hat{v}^T P \hat{v}) + y^T \hat{x} \quad (3)$$

Constraints which were used to stabilize the solution and refer to already reduced parameters are particularly critical. These hidden constraints are basically not booked in the SINEX file and consequently cannot be subtracted from the NEQs. In this case, the datum-free NEQs are not fully reconstructable. Existing correlations between remaining and reduced parameters can lead to deformations and systematic effects due to the fact that hidden constraints and new applied constraints might influence each other [7]. To avoid such incidents and in order to get an insight into the constraint characteristics, the number and type of rank defects need to be determined in a preceding step [9].

3 Software Implementation

The reconstruction of datum-free NEQs has been implemented in our existing software environment called BonnSolutionCombination (BoSC) (Figure 1).

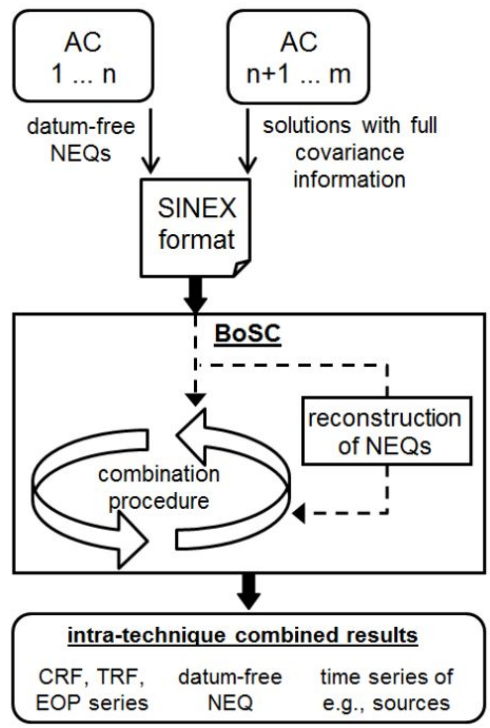

Fig. 1 Reconstruction of datum-free NEQs implemented in our software environment BonnSolutionCombination (BoSC).

Through this addition, the software obtains the capability to include contributions based on solutions with full variance-covariance information in the common combination strategy on the level of datum-free NEQs. Based on this, BoSC offers several capabilities and final products. It is possible to compute consistent VLBI intra-technique CRF and TRF with corresponding EOP series. Furthermore, a monolithic datum-free NEQ can be determined or time series of sources, stations, and EOPs can be illustrated. The full variance-covariance matrix of all parameters is carried forward from each AC and each observing session to the final products. All upcoming CRF investigations can profit from these capabilities, because the complemented software is not only suitable to generate a combined CRF but also to support any studies and investigations required previously.

4 Conclusion and Future Work

In this paper, an approach for combining datum-free NEQs and solutions with full variance-covariance information has been presented. Up to now the implemented reconstruction has been successfully tested with well-chosen and self-generated input data. In the next step we plan to use this new implemented feature for an inclusion of stand-alone catalogs with full variance-covariance information like K-band and Ka-band reference frames. Investigations concerning the properties and features of such a combined CRF have to be made in upcoming studies. This includes also the expectable difficulty with hidden constraints in real input data.

References

1. D. Angermann, H. Drewes, M. Krügel, B. Meisel, M. Gerstl, R. Kelm, H. Müller, W. Seemüller, V. Tesmer. ITRS Combination Centre at DGFI - A terrestrial reference frame realization 2003. *Deutsche Geodätische Kommission*, Reihe B, Nr. 313, Munich, 2004
2. S. Bachmann, M. Lösler. Activities and Products at IVS combination center at BKG. In: N. Zubko and M.Poutanen (Eds.): *Proceedings of the 21st Meeting of the European VLBI Group for Geodesy and Astrometry*, pp. 169–173, ISBN: 978-951-711-296-3, 2013
3. D. Behrend. Data Handling within the International VLBI Service. *Data Science Journal*, Vol. 12, pp. WDS81–WDS84, ISSN 1683-1470, 17 February 2013. DOI 10.2481/dsj.WDS-011
4. S. Böckmann, T. Artz, A. Nothnagel. VLBI terrestrial reference frame contributions to ITRF2008. *Journal of Geodesy*, 84, pp. 201–219, doi: 10.1007/s00190-009-0357-7, 2010.
5. S. Böckmann, T. Artz, A. Nothnagel, V. Tesmer. International VLBI Service for Geodesy and Astrometry: Earth orientation parameter combination methodology and quality of the combined products. *Journal of Geophysical Research*, Vol. 115, doi:10.1029/2009JB006465, 2010.
6. H. Schuh and D. Behrend. VLBI: A fascinating technique for geodesy and astrometry. *Journal of Geodynamics*, 61, doi: 10.1016/j.jog.2012.07.007, pp. 68–80, 2012
7. M. Seitz. Kombination geodätischer Raumbeobachtungsverfahren zur Realisierung eines terrestrischen Referenzsystems. *Reihe C 630 Deutsche Geodätische Kommision*, Munich, 2009
8. M. Seitz, D. Angermann, M. Bloßfeld, H. Drewes, M. Gerstl. The 2008 DGFI Realization of the ITRS: DTRF2008. *Journal of Geodesy*, Volume 86, Issue 12, pp. 1097–1123 , DOI:10.1007/s00190-012-0567-2, 2012
9. R. Kelm. Rank Defect Analysis and Variance Component Estimation for Inter-Technique Combination. In: B. Richter, W. Schwegmann and W. Dick (Eds.): *Proceedings of the IERS Workshop on Combination Research and Global Geophysical Fluids*, Bavarian Academy of Sciences, Munich, Germany, 18–21 November 2002. (IERS Technical Note 30) Frankfurt am Main: Verlag des Bundesamts für Kartographie und Geodäsie

Observing Satellites with VLBI Radio Telescopes
– Practical Realization at Wettzell –

Andreas Hellerschmied[1], Lucia Plank[2], Alexander Neidhardt[3], Rüdiger Haas[4], Johannes Böhm[1], Christian Plötz[5], Jan Kodet[3]

Abstract A concept of an operational path for VLBI satellite observations from scheduling to actual observations is introduced in this report. It is based on a recently developed satellite scheduling module for the Vienna VLBI Software (VieVS) in connection with dedicated satellite tracking functions of the NASA Field System (FS) and the station specific realizations. This concept has been exemplarily realized with the radio telescope Wettzell.

Keywords VieVS, satellite observations, scheduling

1 Introduction

Satellite observations with VLBI is a promising topic and has been vividly discussed in the community for the last few years. Although several experiments were carried out successfully [10], a clear strategy for realizing such observations operationally has not been shown by now.

The difficulties already start with the observation planning, because standard VLBI scheduling programs are not able to routinely schedule satellites as targets. Furthermore, the standard data formats used for VLBI schedule files do not provide the possibility of including information on satellite orbits in a suitable way. Although the most recent version of the NASA FS [13] provides dedicated functions for satellite tracking with VLBI antennas, it does not yet support the generation of local control files with DRUDG [11], including the necessary commands. For those reasons, previous satellite observations meant a large expenditure compared to classical geodetic VLBI observations of quasars. Experiments had to be done with hand-written schedules and numerous manual interactions were necessary at the stations.

In order to overcome those deficiencies, a joint initiative in cooperation with the Geodetic Observatory Wettzell was started to investigate options for an operational path to implement VLBI satellite observations.

2 Tracking Satellites with VLBI Radio Antennas

Standard VLBI antennas do not provide dedicated functions for the tracking of satellites. Therefore, in previous experiments, the antennas were steered by using a step-wise approach [8, 9, 10]. Sequences of celestial positions in terms of topocentric right ascension (RA) and declination (DEC) angles were commanded consecutively, separated by a defined time interval of, e.g., 15 seconds, to track the satellite on its orbit. The great advantage of this approach is that it is feasible with every VLBI antenna, if the slewing rate is fast enough and if it is able to process celestial coordinates. No additional dedicated satellite tracking software is requested.

The drawback is, however, that due to the step-wise repositioning, it is not possible to keep the satellite ex-

1. Vienna University of Technology
2. University of Tasmania
3. Forschungsgruppe Satellitengeodäsie, Technische Universität München, Geodetic Observatory Wettzell
4. Chalmers University of Technology, Onsala Space Observatory
5. Federal Agency for Cartography and Geodesy, Geodetic Observatory Wettzell

actly centered within the antenna beam all the time during an observation. According to Tornatore et al. [9], this may produce some glitches in the resulting data of the residuals with a period equal to the duration of the guidance interval. Hence it would be preferable to track satellites in a continuous fashion.

Some kind of orbit information is needed at the station during an observation to calculate the position of the currently observed satellite and accurate pointing data to control the antenna continuously. NORAD Two Line Elements (TLE, [5]) provide that ability. They are freely available over the Internet for a vast number of spacecrafts and facilitate a precise enough orbit determination by dedicated analytical models.

The way in which the orbit data, such as TLE, has to be prepared, processed, and formatted to satisfy the demands of satellite tracking at the location of the telescope depends on the requirements of the local Antenna Control Units (ACU) and is therefore strictly station specific. When the ACU of a dedicated VLBI antenna does not provide the ability to process the satellite orbit data directly, software is needed to prepare that information as required. SATTRACK [7], a module for the FS, provides the capability of doing these translations. Furthermore, FS versions 9.11.2 and higher are able to process TLE data [4]. Both programs provide new FS commands intended for satellite tracking. They convert TLE data to discrete satellite positions in terms of RA/DEC or azimuth/elevation.

3 Scheduling of VLBI Satellite Observations

The setup of a VLBI experiment for the entire station network is defined in a dedicated schedule file. A commonly used file format is VEX 1.5b [14].

Prior to a VLBI experiment, the program DRUDG [11] is used at all participating stations to extract locally necessary information from the VEX file and to generate a local control file in the Standard Notification for Astronomical Procedures (SNAP) format. Such SNAP files consist of sequences of FS commands (SNAP commands) in order to set up the local station configuration and to perform the observations as scheduled. Although the FS already has some features implemented for the realization of satellite tracking, neither the current releases of the VEX format nor the current version of DRUDG provide the feasibility of including satellites in the appropriate way (the same way as radio sources). Therefore local workarounds are necessary.

To have software available for the planning of VLBI satellite sessions, VieVS [2] was updated with a Satellite Scheduling Module. The program leads the user through an interactive scheduling process. Initially it calculates positions of all selected satellites, e.g. the GLONASS constellation, on the basis of TLE data and checks whether they have shared visibility from the particular station network for the chosen date and time. After checking of further conditions, such as observation restrictions due to limited antenna slew rates, etc., a list of observable satellites is presented, and the user is asked to assemble a sequence of desired sources. Automated source selection is not yet included. Finally a VEX file is generated, containing all required data to run the scheduled observations. Due to the inadequate satellite support of the current VEX format, the satellites are still defined as step-wise stationary sources (like quasars) in terms of topocentric RA and DEC. Topocentric indicates that RA/DEC satellite positions depend on the geographic location of the observing station and therefore have to be defined separately for each site in the schedule. Using these schedule files, it is possible to track satellites "step-wise" and, with the following station adaptations, also continuously.

4 Satellite Tracking at Wettzell

There are three VLBI radio telescopes at the Geodetic Observatory Wettzell: the 20-m Radio Telescope Wettzell (RTW) and the twin telescope consisting of two 13.2-m antennas. After a hardware update in 2013, each of them is equipped with an identical ACU from Vertex Antennentechnik GmbH and is able to operate in a *Two Line Track Mode* and capable of processing TLE data directly for satellite tracking purposes [12]. The ACU satellite tracking capability has the advantage that the antenna movement is precisely adjusted to the internally predicted satellite movement, without the detour of calculating discrete satellite positions in the FS.

The satellite tracking procedure is illustrated in Figure 1. DRUDGing a VEX file issued by VieVS generates a SNAP file (SNP_s), defining each satellite scan as a sequence of SNAP commands, (*source=<sourcename><RA><DEC><epoch>*), which point the antenna to specified celestial positions. To enable the continuous tracking, a perl script (*SNAP File Translator*) was implemented to translate these SNAP files: it simply replaces the source-command sequence for each scan by a single satellite SNAP command. Although the new satellite tracking functions of the FS were already activated for the twin telescope, they could not be used for satellite experiments with the RTW, because an older FS version (9.10.4) was installed. For that reason a new SNAP command (*antenna=tle,<tle_filename>*) was implemented in the station specific part of the FS. Both the "satellite" and the "antenna=tle" command read the TLE data either from the shared memory of the FS or from a separate TLE file and send them to the ACU. There the tracking points are calculated and the mode is switched to the Two Line Track, which starts the continuous orbit track.

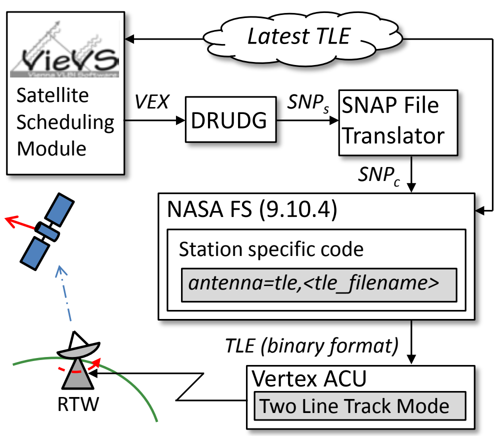

Fig. 1 Satellite Tracking Procedure for the Radio Telescope Wettzell (RTW). The latest TLE data sets are obtained from a Web-service before an experiment. A perl script (SNAP File Translator) is used to convert SNAP files intended for step-wise tracking (SNP_s) to enable continuous tracking (SNP_c).

5 Satellite Observation Experiments

Several VLBI observations of L1 signals of the GLONASS satellites were carried out in January 2014 to validate the proper functionality of the newly implemented satellite tracking features at Wettzell and the VieVS Satellite Scheduling Module in general.

5.1 Experiment Description

Two sessions were carried out on January 16, 2014 (G140116a and G140116b), and another two were carried out on January 21, 2014 (G140121a and G140121b) on the baseline Wettzell–Onsala. Each of them had a duration of one hour and scheduled several GLONASS satellites consecutively.

For all sessions, the scheduling and further on the creation of VEX files was performed with the new VieVS Satellite Scheduling Module. A detailed listing of the selected GLONASS satellites, the related observation intervals for each scan, and the emitted frequencies for all four sessions can be found in Tables 1 and 2.

Table 1 Observation setup from 16 January 2014.

Session Name	Glonass Number	Scan Period [UT]	L1 Carrier Frequ. [MHz]
G140116a	743	12:30 – 12:45	1605.3750
	723	12:50 – 13:05	1602.0000
	730	13:10 – 13:30	1602.5625
G140116b	743	14:00 – 14:15	1605.3750
	723	14:20 – 14:35	1602.0000
	730	14:40 – 15:00	1602.5625

At Wettzell, all sessions were carried out by the 20-m RTW. The RTW's front end receiver was basically designed for observations in the S- and X-band domain, as is common for geodetic VLBI. When trying to observe GLONASS L1-band signals (1592–1609 MHz) with the existing S-band receiver system, these signals were blocked due to a narrow S-band band pass filter (2210–2350 MHz). To enable the reception of L1 signals with the existing antenna hardware, the S-band front end system of the RTW was upgraded and split to create a new L1 receiver module [6]. This enables the acquisition of L1-band in addition to S/X-band without changing the receiver hardware. At the first experiment (G140116a), the antenna was guided, using a step-wise approach with a re-positioning interval of 15 seconds to test if the scheduling was principally functional. In the other three sessions, the satellites were tracked continuously by means of the new FS functions.

Table 2 Observation setup from 21 January 2014.

Session Name	Glonass Number	Scan Period [UT]	L1 Carrier Frequ. [MHz]
G140121a	743	13:30 - 13:35	1605.3750
	732	13:37 - 13:43	1603.6875
	743	13:44 – 13:49	1605.3750
	732	13:51 – 13:56	1603.6875
	743	13:59 – 14:04	1605.3750
	735	14:08 – 14:13	1603.1250
	735	14:14 – 14:19	1603.1250
	732	14:25 – 14:30	1603.6875
G140121b	735	15:00 – 15:04	1603.1250
	735	15:05 - 15:09	1603.1250
	735	15:10 – 15:14	1603.1250
	746	15:20 –15:24	1604.2500
	746	15:25 – 15:29	1604.2500
	746	15:30 – 15:34	1604.2500
	723	15:45 – 15:49	1602.0000
	723	15:50 – 15:54	1602.0000
	723	15:55 – 16:00	1602.0000

Onsala's 25-m radio telescope (ONSALA85) used its L-band front end receiver. This qualifies it to receive strong L1 signals, but acquisition of S/X-band signals is not possible without changing the receiver. Because Onsala's SATTRACK module was not installed when the experiments were carried out, all satellites were tracked step-wise there with a 15 second re-positioning interval, controlled by the VieVS schedules.

5.2 Observation Results

The DiFX software [3] was used to correlate the acquired data. The correlation was done with 0.25 seconds of integration time, and the results were fringe-fitted with the Astronomical Image Processing System software (AIPS, [1]). Continuous phases and strong amplitudes were found for all satellites, indicating that the described concepts for satellite observations worked correctly at both stations. The fringe plot (amplitude and phase) for GLONASS-732 is shown exemplarily in Figure 2.

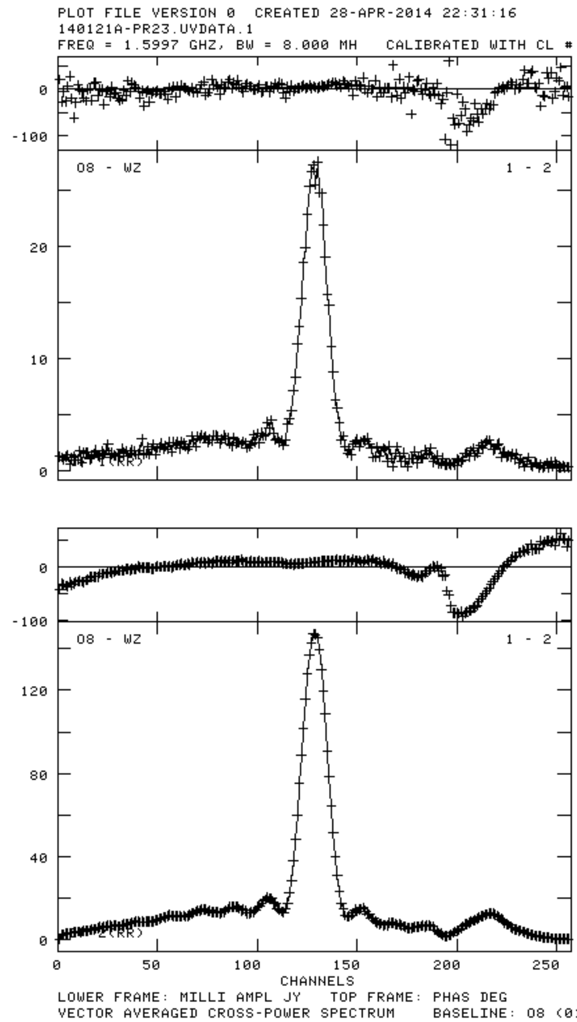

Fig. 2 Fringe plots for GLONASS-732. Data acquired during the G140121a session (2^{nd} scan).

6 Summary and Outlook

The VieVS Satellite Scheduling Module provides a flexible tool for scheduling real VLBI satellite observations, even for large station networks and arbitrary satellites. It generates VEX files able to perform satellite tracking directly in a step-wise fashion. For the future it would be important to extend the current VieVS module with further functionalities, such as the possibility of combining satellite observations with classical observations to quasars or providing automated source selection, based on a dedicated scheduling optimization approach.

Fully operational application and process automation of VLBI satellite observations, comparable to the traditional geodetic VLBI observation of quasars, is presently restricted due to limitations in the schedule file format (VEX) and generation of local control files (SNAP files) with DRUDG. Although the upcoming release of VEX 2.0 will provide possibilities to define satellites as radio sources in terms of TLE data appropriately (personal communication with E. Himwich), currently the best option seems to be to define satellite orbits by sequences of celestial coordinates in the schedule. This directly allows step-wise satellite tracking with all suitable VLBI antennas. Despite there being different ways to realize continuous tracking (SATTRACK, FS, ACU), it still depends on local implementations and antenna features. Because the current version of DRUDG does not support dedicated satellite commands, a way has to be found to include the satellite SNAP commands in the control files. At Wettzell, this was done by modifying the SNAP files with a perl script which can also be shared with other stations.

Based on several satellite tracking experiments on the baseline Wettzell–Onsala, two things could be validated so far: first, that the schedule files (VEX) prepared with VieVS were applied successfully to control the satellite observations and second, that satellite tracking with both approaches, step-wise and continuous, worked properly at the involved stations.

The developments in satellite tracking and scheduling allow VLBI satellite observations in an easy and nearly automated manner. This is an important step to promote further developments regarding satellite observations with VLBI, such as investigations related to link budget, signal attenuation, correlation of satellite signals, etc., and finally the co-location of different space geodetic techniques.

References

1. Astronomical Image Processing System, Web resource: http://www.aips.nrao.edu/index.shtml, 2014.
2. J. Böhm, S. Böhm, T. Nilsson, A. Pany, L. Plank, H. Spicakova, K. Teke, and H. Schuh. The new Vienna VLBI Software VieVS, Proc. of IAG Scientific Assembly 2009, International Association of Geodesy Symposia Vol. 136, edited by S. Kenyon, M.C. Pacino, and U. Marti, pp. 1007-1011, 2012, doi: 10.1007/978-3-642-20338-1_126.
3. A. T. Deller, M. Tingay, M. Bailes, and C. West. DiFX: A Software correlator for very Long Baseline Interferometry using Multiprocessor Computing Environments, The Astr. Soc. of the Pacific, 119, pp. 318-336, 2007.
4. E. Himwich and J. Gipson. GSFC Technology Development Center Report, IVS 2011 Annual Report, NASA/TP-2012-217505, pp. 280–282, 2012.
5. F. R. Hoots and R. L. Röhrich. Spacetrack Report No. 3 – Models for Propagation of NORAD Elemets Sets, Project Spacetrack Reports, Office of Astrodynamics, Aerospace Defense Center, Peterson, 1988.
6. J. Kodet, K. U. Schreiber, Ch. Plötz, A. Neidhardt, G. Kronschnabl, R. Haas, G. Molera Calvés, S. Pogrebenko, M. Rothacher, B. Maennel, L. Plank, and A. Hellerschmied. Co-locations of Space Geodetic Techniques on Ground and in Space. IVS 2014 General Meeting Proceedings, 2014, this volume.
7. M. Moya Espinosa and R. Haas. SATTRACK - A Satellite Tracking Module for the VLBI Field System, Proc. 18th European VLBI for Geodesy and Astrometry Working Meeting, edited by J. Böhm, A. Pany, and H. Schuh, Geowissenschaftliche Mitteilungen, Schriftreihe der Studienrichtung Vermesung und Geoinformation, Technische Universität Wien, 79, 53–58, 2007.
8. V. Tornatore, R. Haas, G. Maccaferri, S. Casey, S. V. Pogrebenko, G. Molera Calvés, and D. Duev. Tracking of Glonass satellites by VLBI radio telescopes, 5th ESA International Workshop on Tracking, Telemetry and Command Systems for Space Applications, 21–23 September 2010.
9. V. Tornatore, R. Haas, D. Duev, S. V. Pogrebenko, S. Casey, G. Molera Calvés, and A. Keimpema. Single Baseline GLONASS observations with VLBI: data processing and first results, 20th EVGA work meeting proceedings, MPIfR Bonn, 29–31 March 2011.
10. V. Tornatore, R. Haas, S. Casey, D. Duev, S. Pogrebenko, and G. Molera Calvés. Direct VLBI Observations of Global Navigation Satellite System Signals, Proc. of the IAG General Assembly 2011, International Association of Geodesy Symposia Volume 139, edited by C. Rizo & P. Willis pp. 247–252, 2014, doi: 10.1007/978-3-642-37222-3_32.
11. N. Vandenberg. DRUDG: Experiment Preparation Drudge Work - Program Reference Manual, VLBI Software Documentation, Scheduling Program, NASA/Goddard Space Flight Center – Space Geodesy Program, 15 March 1997.
12. Vertex Antennentechnik GmbH. Umrüstung 20m RTW. Betriebshandbuch Servo-Subsystem, Technische Beschreibung und Allgemeine Bedienungsanleitung, OM-1012043-30000-01, pp. 78–79, Vertex Antennentechnik GmbH, Duisburg, 2013.
13. VLBI Field System Documentation, NASA GSFC, http://lupus.gsfc.nasa.gov/software_fs_main.htm, 2007.
14. A. Whitney, C. Lonsdale, E. Himwich, and N. Vandenberg. VEX File Definition/Example, Rev. 1.5b1, 30, January 2002, http://www.vlbi.org/vex/docs/-vex%20definition%2015b1.pdf.

Co-locations of Space Geodetic Techniques on Ground and in Space

J. Kodet[1], K.U. Schreiber[1], Ch. Plötz[2], A. Neidhardt[1], G. Kronschnabl[2], R. Haas[3], G. Molera Calvés[4], S. Pogrebenko[4], M. Rothacher[5], B. Männel[5], L. Plank[6,7], A. Hellerschmied[6]

Abstract Systematic error sources are of great concern in space geodesy. Subtle in nature, they are currently limiting the performance of all the major techniques—GNSS, VLBI, and SLR. Co-locations of these techniques on fundamental stations provide the chance to identify such systematic errors. In order to provide a better tie between GNSS, SLR, and VLBI, we have designed and implemented a fully calibrated receiver unit that allows GNSS observations with the 20-m Radio Telescope Wettzell (RTW). The Wettzell 20-m antenna is equipped with S- and X-band receivers, which cannot be used for receiving the GNSS L1 signal without significant changes. We are reporting the design and construction of the new receiving chain and enabling observation of the GNSS L1 signal together with the required changes in the NASA Field System using the satellite tracking module. The receiver was installed in the 20-m RTW, and the first common observation with Onsala Space Observatory was performed. Finally, we give a rough estimation of the expected signal strength and also outline suitable observation scenarios.

Keywords GNSS, VLBI, co-locations. L1 receiver

1. Forschungseinrichtung Satellitengeodäsie, Technische Universität München
2. Bundesamt für Kartographie und Geodäsie, Geodätisches Observatorium Wettzell
3. Chalmers University of Technology, Department of Earth and Space Sciences, Onsala Space Observatory
4. Joint Institute for VLBI in Europe
5. Institute of Geodesy and Photogrammetry ETH
6. Vienna University of Technology, Institute of Geodesy and Geophysics,
7. University of Tasmania, Australia

1 Introduction

All the major measurement techniques of space geodesy are characterized by a very high measurement sensitivity, which resolves the measured quantities, such as the range to satellites or signal delays from quasar sources between radio telescopes to about one part in 10^9. While all the different observing stations have impressive precision, the accuracy still carries biases well in excess of estimated measurement precision.

Within each of the techniques, these errors are minimized by a non-linear data fitting process. Fundamental stations on the other side are important, because they provide a link from one measurement technique to the other. However, this is also the link where discrepancies between precision and accuracy become evident. There are several co-location strategies between GNSS, SLR, and VLBI. One possibility is to observe GNSS satellites with all relevant techniques at the same time. Unfortunately, until now there has been no real chance to observe GNSS satellites at the Geodetic Observatory in Wettzell, because the 20-m RTW is equipped only with an IVS-compatible S/X receiver. But the previous work at Onsala and Medicina [2, 3] was a driving motivation to make required upgrades of the Wettzell S/X receiver chain.

2 Wettzell 20-m S/X Receiver

The Wettzell 20-m Radio Telescope is equipped with a classical IVS-compatible S/X receiver. However, the GNSS signals are well below the lowest S-band frequency. In order to receive GNSS signals using this in-

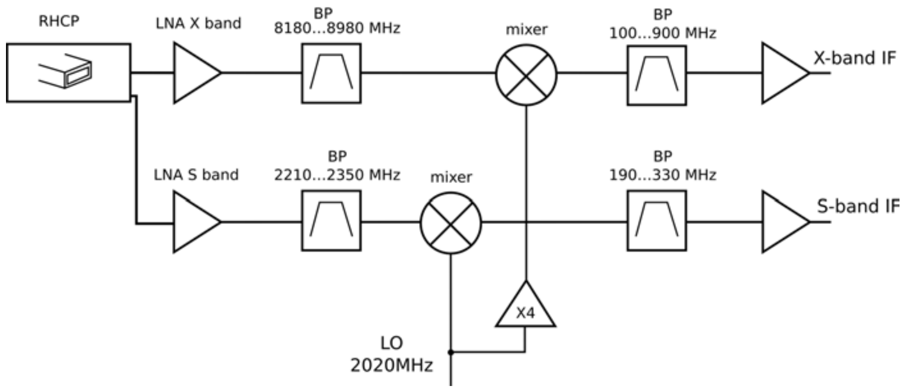

Fig. 1 Simplified block diagram of the Wettzell 20-m S/X receiver.

strument, it is necessary to revise the frequency passband and to adjust the signal levels. The GPS L1 signal is transmitted at a frequency of 1575.42 MHz, and GLONASS satellites transmit L1 signals in the band of 1592–1609 MHz, while each satellite transmits at a different frequency. According to the specification, the received RF signal level at the output of a 3 dBi linearly polarized antenna is not less than -160 dBW for GPS C/A code and -161 dBW for GLONASS in the L1 sub-band[1]. The maximum differential power level from different satellites is affected by the distance of the satellites. The shortest distance is at zenith and the longest distance to the satellite is at the horizon. Because the power level is inversely proportional to the distance square, the difference in power level can be written as

$$\Delta = 10log_{10}\left(\frac{R^2_{zenith}}{R^2_{horizon}}\right), \tag{1}$$

where R_{zenith} is the distance to the satellite at zenith and $R_{horizon}$ is the distance to the satellite at the horizon. Using the above equation, one obtains a maximum differential power level of ~ 2 dB for GPS and of ~ 3 dB for GLONASS [1].

Reviewing the Wettzell 20-m S/X Receiver, which is shown in Figure 1, one can divide the receiving chain into three main parts. At first the signal passes through the antenna dish with the feed horn and the wave-guides. Then the signal is fed into the low noise amplifier (LNA) in the cryo-box, followed by the bandpass filters and S or X receiver mixers. The wave-guide

[1] Expressed in Jansky: GPS ∼4900 Jy and Glonass ∼7800 Jy.

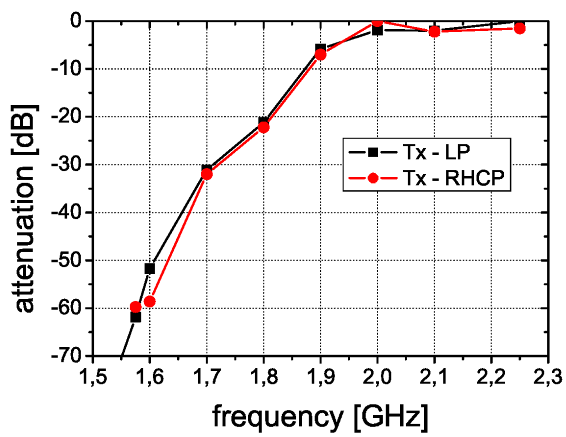

Fig. 2 Dependency of the attenuation on frequency in the S-band receiver chain.

of the X-band receiver has dimensions which do not allow the GNSS L1 signal to be received. The S-band wave-guide system uses the wave-guide type WR430 with a cut-off frequency of 1.375 GHz, so that L1 transmission is possible. For this reason we focused on the S-band receiver part[2] in order to detect the L1 GNSS signal.

In a first approach, we tested the antenna dish, feed horn, and microwave guides with artificially generated signals. Linear Polarization (LP) and Right Hand Circular Polarization antennas were used and were mounted in Wettzell TWIN radio telescope at a distance of 136 m. The dependency of the 20-m RTW

[2] It should be noted that the cut-off frequency of the 20-m RTW is 1.375 GHz, and hence L2 is outside of this pass-band.

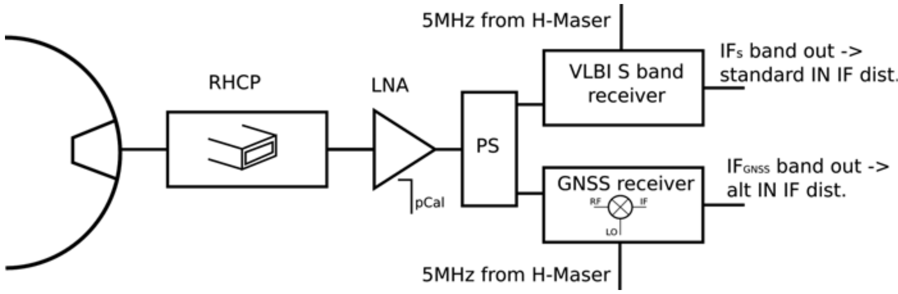

Fig. 3 The simplified diagram of the Wettzell 20-m S/X receiver upgrade.

gain on frequency is shown in Figure 2. One can see that the attenuation of the receiving chain up to the input of the LNA is 60 dB in the GNSS L1 band. On the other hand, the 20-m parabolic dish antenna has 47 dBi gain in this band. The GNSS signal power level at the input of the LNA in a bandwidth of 1 MHz[3] is

$$P_{LNAin} = P_{GNSS} + G_a - A = -144dBm\ , \qquad (2)$$

where P_{GNSS} is the GNSS signal power level on the ground, G_a is the antenna gain and A is the attenuation. That means that the GNSS signal power is approximately 30 dB below the noise floor. This fact precludes the detection of the GNSS signal with spectrum analyzers, as would be possible with a complete L-band feed chain.

The next part in the receiver chain is the S-band LNA, which has a gain of 35 dB in S-band. In the L1 band, the gain of the LNA is slightly lower and was measured to be 33 dB. Behind the LNA there is a bandpass filter with a passband of 2210–2350 MHz, which completely blocks the L1 GNSS signal.

3 Wettzell 20-m S/X Receiver Upgrade

The previous section showed that the bottleneck of the complete receiver chain is located in the electronic section of the heterodyne receiver. In order to overcome this problem we are bypassing the main receiver by adding a power splitter behind the initial S-band LNA. One part of the signal is used for the standard S-band receiver chain, and the second part of the signal path is used for the newly developed L1-band VLBI receiver, which will be referred to as the VLBI(GNSS) receiver in the text below. The block diagram of the updated 20-m RTW S-band receiver is shown in Figure 3. Splitting the signal behind the LNA will not influence the standard VLBI observation, because the system temperature is defined mainly by the noise temperature of the LNA. In order to avoid additional losses, it is necessary to adjust the power level by changing the attenuation of the IF band. Another advantage of connecting the VLBI(GNSS) receiver behind the LNA was that the phase calibration tones are now also present in the GNSS observations.

[3] Valid for GLONASS.

The photograph of the receiver is presented in Figure 4. The VLBI(GNSS) hardware is installed in a metal box and comprises a classical heterodyne receiver. The local oscillator can be locked to the 5 or 10 MHz reference frequency[4]. We are using a VBF-1575 image filter with a pass-band of 1530–1620 MHz, which defines the receiver bandwidth. Behind the passive mixer (MiniCircuits ZX05-C42), an IF band filter BFP-A410 is inserted. In order to compensate for cable losses of the cable guiding the IF band signal from the 20-m RTW antenna to the VLBI control room, the overall gain of the receiver was set to 71 dB.

4 The First Experimental Results

The VLBI(GNSS) receiver was tested in several experiments. The biggest obstacle is that the GNSS signal is well below the noise floor; therefore, a standard spectrum analyzer cannot be used to check whether the VLBI antenna is detecting the satellite or not.

[4] The SNM-H201 low phase noise programmable frequency synthesizer from Serenum, a.s. was used. The programmable synthesizer has a custom firmware version allowing it to generate frequencies up to 2.2 GHz.

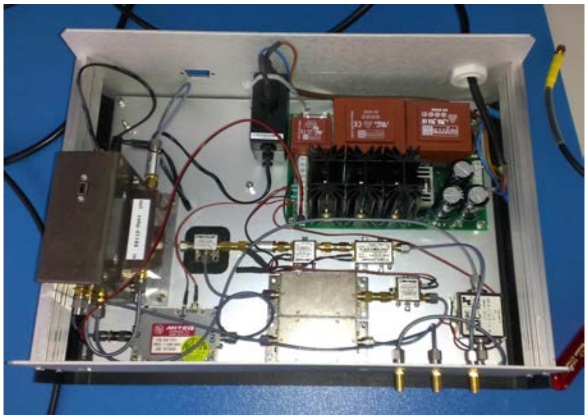

Fig. 4 Photograph of the VLBI(GNSS) receiver suitable for the split S-band receiver channel of the RTW.

For the first acquisition test, we have used a standard GNSS antenna in connection with VLBI(GNSS) receiver. The data was stored for the correlation process, using the MIT Mark 5A/B recording systems. In Matlab, we have developed correlation software which implements a parallel code phase search algorithm of the GPS and the GLONASS signals[5]. The sensitivity of the search algorithm is improved by coherent and non-coherent integration. Once this test was successfully completed, we installed the receiver in the 20-m RTW. Using the Vienna VLBI Software (VieVS) and an additional implementation allowing the scheduling of satellite targets, we were able to create schedules for the observation of satellites with different telescopes. With an additional program extension of the NASA Field System, it was possible to track the GNSS satellites successfully in a continuous way. For more details please refer to [4].

Based on the described sessions, we have demonstrated that we are able to adequately receive the GNSS L1 signal. Therefore, we have organized a series of common observations of GLONASS signals together with the Onsala Space Observatory. The first common observation, Wettzell—Onsala, was recorded in January 2013 (G130128), and the details of the experiment were reported in [5]. At this time the first observation schedules were provided and correlation was performed by the Joint Institute for VLBI in Europe (JIVE). The latest progress in VLBI satellite observing was made in January 2014. During several observation days, the (VieVS) satellite tracking capability and the entire system settings were optimized. The fact that we could look at the observed signal by using our Matlab search algorithm almost in real-time played one major role for the optimization process for the Wettzell station. Figure 5 shows an example of GNSS data analysis for a data set of GLONASS 735 made with the Matlab search algorithm. One can obtain the carrier-to-noise ratio and account for the system noise temperature. Considering the GNSS signal power level, we were able to confirm the calculated signal transmission of the receiving chain. The observed attenuation resulted in $-62dB$, which is in a good agreement with the earlier measurements using an artificial signal from a signal generator.

[5] The purpose of this proceedings paper is not to describe basic algorithms used for acquisition of the GNSS signals, in detail. For further information see [1].

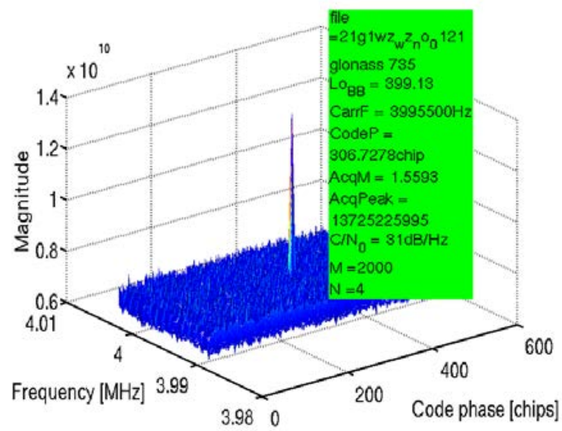

Fig. 5 The obtained GNSS signal data acquisition extracted by a Matlab script.

5 Conclusions

The Global Geodetic Observing System (GGOS) requires both a reduction in measurement errors and a considerable reduction of systematic errors within the measurement techniques of space geodesy. Co-locations of these techniques on fundamental core stations provide the chance to identify such systematic errors. One of the possible ways to tie GNSS, SLR, and VLBI is to perform common observations of the GNSS satellites using all these space techniques.

We have designed and implemented a receiver unit called the VLBI(GNSS) receiver, that allows GNSS observations with the 20-m RTW in Wettzell. With that hardware we are able to overcome the problem that the 20-m RTW was only equipped with a classic S/X receiver. The functionality of the updated receiver was demonstrated in several experiments at the Wettzell Observatory and in common observations with the Onsala Space Observatory.

Acknowledgements

This work has been supported by the Technische Universität München, the Bundesamt für Kartographie und Geodäsie. We acknowledge funding through the Forschergruppe DFG FOR1503.

References

1. James Bao-Yen Tsui, Fundamentals of Global Positioning System Receivers: A Software Approach, 2nd Edition *ISBN: 978-0-471-70647-2*, 352 pages, January 2005
2. Tornatore, V., R. Haas, D. Deev, S. Pegrebenko, S. Casey, G. Molera-Calves, A. Keimpema, *Single baseline GLONASS observations with VLBI: data processing and first results*, In: 20th Meeting of the European VLBI Group for Geodesy and Astronomy, 162—165, 2011.
3. Tornatore, V, R. Haas, S. Casey, D. Deev, S. Pegrebenko, G. Molera-Calvs, *Direct VLBI Observations of Global Navigation Satellite System Signals*, In: International Association of Geodesy Symposia, Proc. IAG General Assembly, Melbourne - 2011, 247-252, 2014.
4. A. Hellerschmied, L. Plank, A. Neidhardt, R. Haas, J. Böhm, C. Plötz, J. Kodet, *Observing satellites with VLBI radio telescopes — a practical realization at Wettzell*, this issue.
5. Haas, R., A. Neidhardt, J. Kodet, C. Plötz, U. Schreiber, G. Kronschnabel, S. Pogrebenko, D. Duev, S. Casey, L. Plank, *The Wettzell-Onsala G0128 Experiment*, this issue.

The Wettzell–Onsala G130128 Experiment
– VLBI Observations of a GLONASS Satellite –

Rüdiger Haas[1], Alexander Neidhardt[2], Jan Kodet[2], Christian Plötz[3], Ulrich Schreiber[2], Gerhard Kronschnabl[3], Sergei Pogrebenko[4], Dmitry Duev[4], Simon Casey[1], Ivan Marti-Vidal[1], Jun Yang[1], Lucia Plank[5]

Abstract We describe the Wettzell-Onsala G130128 experiment, where for the first time a GLONASS satellite was observed in VLBI mode with the new L-band system on the 20-m radio telescope in Wettzell. Fringes were successfully found using two independent software correlators and three independent a priori delay models. The RMS scatter of the derived phase delays is below 10 ps for solution intervals of 2 s and larger. The RMS scatter of the derived group delays is below 1.5 ns for solution intervals of 30 s and larger. The total delays, using the three different a priori delay models, agree on the level of 0.8–0.9 ns and 0.2–0.4 ns, for groups delays and integrated delay rates, respectively.

Keywords GNSS-VLBI, GLONASS, a priori delay models, SFXC, DiFX

1 Introduction

During recent years the topic of an improved connection of the VLBI and GNSS reference frames has been discussed. Currently, these techniques are linked together at ground-based co-location stations only. This kind of connection relies on local surveys at the sites to be able to link the reference points of the different instruments used for geodetic VLBI observations and GNSS observations, respectively. To improve the connection of the techniques, the idea of observing GNSS satellites with VLBI has been brought up, e.g. [1, 2]. Several such GNSS-VLBI experiments have been performed during recent years, where a stochastic delay measurement noise of 80 ps in 1 s and 4 ps in 15 min could be achieved [2]. Because GNSS signals are in the L-band, radio telescopes with L-band receivers are needed for such observations. However, geodetic radio telescopes are usually only equipped with S/X-band receivers. Thus these telescopes cannot be used for GNSS-VLBI experiments. To overcome this restriction, an L-band system that extracts the L-band signal from the S-band signal chain has been developed at Wettzell [3, 4]. To test this new instrumentation, a test experiment was conducted in early 2013.

2 The Observations

The G130128 experiment was conducted on January 28, 2013, on the Onsala–Wettzell baseline. At Onsala, the 25-m telescope with an L-band receiver was used, while at Wettzell, the 20-m telescope with the specially developed L-band receiver was utilized. The observations concentrated on one GLONASS satellite (Norad # 37139, GLONASS-736, PR09), that was observed for 45 minutes, in nine scans of four minutes length each and one minute breaks. Four IF channels of 8 MHz bandwidth were observed with the central frequency at 1586.87 MHz. The observing plan was prepared by JIVE (Joint Institute for VLBI in Europe) and included a stop-and-go tracking of the satellite with 15 second updates. Because the primary goal was to test the L-band receiver at Wettzell, no calibrator source was observed.

1. Chalmers University of Technology (Sweden)
2. Technische Universität München (Germany)
3. Federal Agency for Cartography and Geodesy (Germany)
4. Joint Institute for VLBI in Europe (The Netherlands)
5. University of Tasmania (Australia)

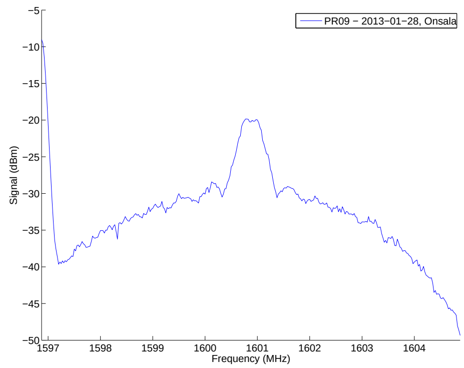

Fig. 1 Signal spectrum of PR09 (Norad # 37139, GLONASS-736) observed on 2013-01-28 at Onsala.

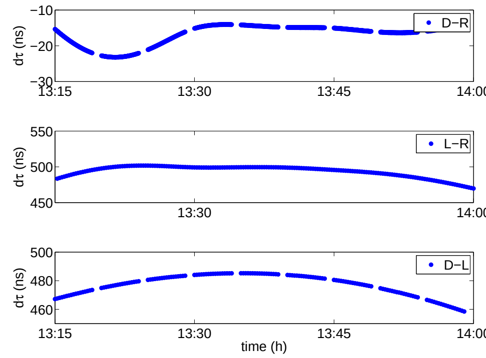

Fig. 2 Comparison of a priori delay values. Shown are the differences between the D- and R-model (top), L- and R-model (middle), and D- and L-model (bottom).

As the Onsala 25-m telescope is equipped with a dedicated L-band receiving system, the satellite signal strength had to be attenuated in the RF regime by 30 dB, in order to avoid saturation. A picture of the resulting signal spectrum is presented in Figure 1 and clearly shows the GLONASS signal.

On the other hand, the L-band signal at Wettzell is extracted via the S-band horn that is attenuating the L-Band frequencies by about 60 dB. Thus, here the signal had to be amplified by 30 dB before the receiver. The spectrum of the signal was not visible at the station.

3 A priori Delay Modeling and Data Correlation

A priori delay values were modeled with three different approaches. The first set of a priori delays was calculated by Dmitry Duev as described in [5]. These values included the geometrical, ionospheric, and tropospheric contributions, as well as the axis offset at the Onsala 25-m telescope. In the following discussion, these a priori delay values are referred to as D-model.

The second set of a priori delay values was calculated by Lucia Plank [6], following [7]. These values included only the geometrical contributions and will be referred to as L-model in the following discussion.

The last set of a priori delays were calculated by Rüdiger Haas following [8] and also only included the geometrical contributions. The satellite positions for these calculations were based on final ephemerides with 15 min temporal resolution provided by CODE (Center for Orbit Determination in Europe). These a priori values will be referred to as R-model.

Figure 2 depicts a comparison of the geometrical part of the three sets of a priori delays. The D- and R- model, both calculating geocentric delays, agree on the level of about 15 ns. Probably, part of the detected differences is due to different treatment of the a priori satellite orbit information and necessary interpolation between satellite positions that are only given at discrete epochs. The differences between the L-model and the other two models are larger and on the order of about 490 ns. This rather large difference is due to the L-delays being topocentric.

4 Preliminary Analysis

The correlation of the observed data was done with two different software correlators, the SFXC [9] at the Joint Institute for VLBI in Europe (JIVE) and the DiFX [10], installed at the Onsala Space Observatory. The SFXC correlation explicitly used the a priori delays of the D-model, while the DiFX correlation was done with all three sets of a priori delays.

As an example, the amplitudes and phases, as derived from the correlation with DiFX using the D-model, are presented in Figure 3. The DiFX correlation was done with 0.25 s integration time, and the figure depicts the average of the nine scans of four minutes length each. In all four IF channels, a rapid phase change is clearly visible, and clear and strong amplitudes are detected.

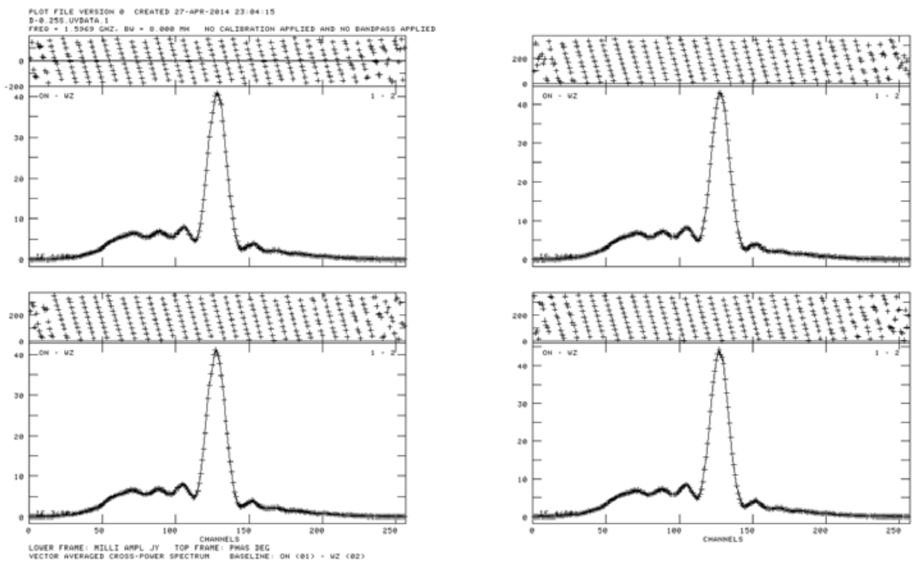

Fig. 3 Amplitudes and phases in the four IF channels after correlation with DiFX using the a priori delay values of the D-model.

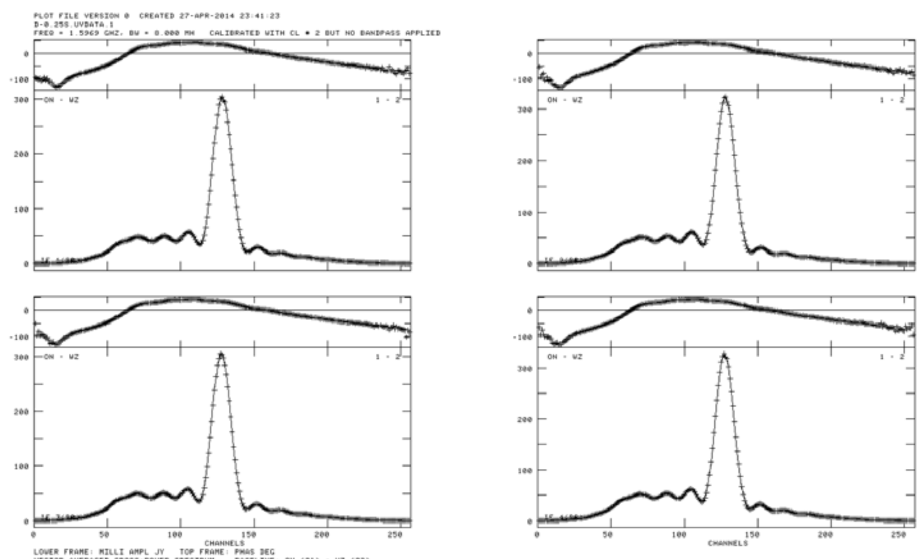

Fig. 4 Amplitudes and phases in the four IF channels after fringe-fitting with AIPS [11] with a 30 s solution interval.

Fringe-fitting with AIPS [11] was done for 0.25 s, 1 s, 2 s, and 30 s solution intervals. Figure 4 depicts the corresponding amplitudes and phases after fringe-fitting with a 0.25 s solution interval. The phases in the four IFs are now stable. The remaining non-flat phase residual and the amplitude bandpass shape are due to the instrument response and can be calibrated in future observations.

After fringe-fitting with AIPS, group delays, delay rates, and phases were compared for the three correlations. Figure 5 depicts the raw phases after fringe-fitting with a 30 s solution interval. For the correlation using the D-model, the raw phases (black triangles in Figure 5) could be unwrapped without problems, and phase delays could easily be determined. However, for the correlations with the L- and R-models, some problems occurred with phase unwrapping. This indicates

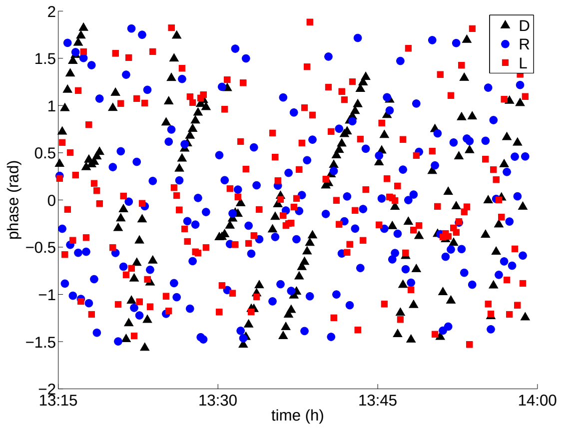

Fig. 5 Raw phases after fringe-fitting with AIPS with a 30 s solution interval. The phases need to be unwrapped before phase delays can be obtained. The unwrapping worked fine for values from the correlation with the D-model (black triangles), but failed for the other two (R-model, blue circles; L-model, red squares) where not all phase ambiguities could be resolved.

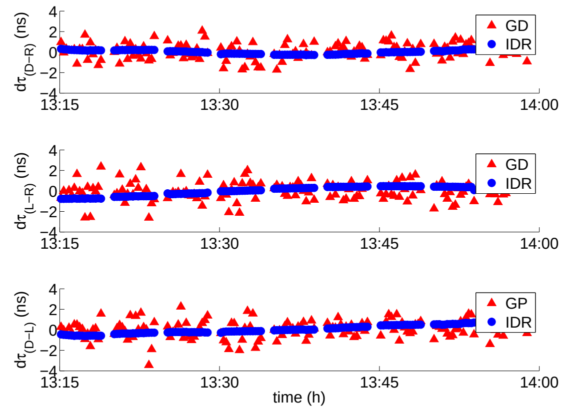

Fig. 7 Comparison of total delays, i.e., a priori delays plus residual delays from the the DiFX correlation and post-processing. Shown are the differences between processing with the D- and R-model (top), L- and R-model (middle), and D- and L-model (bottom). Results based on group delays (GD) are shown as red triangles, based on integrated delay rates (IDR) as blue circles.

that improvements are still necessary for these two a priori models.

For all three correlation sets, the delay rates could be integrated. As an example, Figure 6 depicts the group delays, integrated delay rates, and phase delays of the DiFX correlation using the D-model and subsequent fringe-fitting with AIPS with a 30 s solution interval. It is clearly visible that the group delays have a much larger scatter than both the integrated delay rates and the phase delays. Table 1 presents the RMS scatter for different solution intervals. Already for a solution interval of 2 s, phase delays and integrated delay rates reach an RMS scatter level of about 10 ps, while group delays do not reach an RMS scatter below 1.5 ns before a solution interval of 30 s.

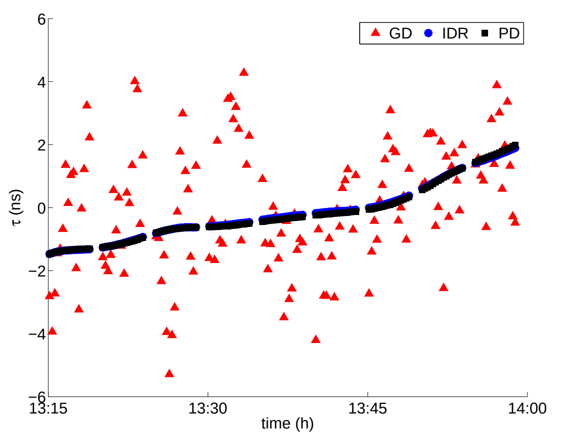

Fig. 6 Group delay (red triangles), integrated delay rate (blue circles), and phase delay (black squares) results from the DiFX correlation using a priori delay values of the D-model.

Table 1 RMS scatter after fringe-fitting with different solution intervals. The correlation itself was done using a priori delay values according to the D-model and the DiFX software correlator.

Solution interval	RMS scatter		
	group delays	integrated delay rates	phase delays
1 s	5.9 ns	17.6 ps	12.5 ps
2 s	3.9 ns	9.5 ps	8.7 ps
30 s	1.4 ns	9.1 ps	8.8 ps

The fringe-fitted delay residuals from AIPS were added to the corresponding a priori delay models to give total delays. The differences for the total delays for the three models are presented in Figure 7, and the corresponding RMS scatter of these differences are given in Table 2. The agreement is on a level of 0.8–0.9 ns for group delays and 0.2–0.4 ns for phase delays (approximated by integrated delay rates).

5 Conclusions and Outlook

The G130128 experiment verifies that the L-band system on the Wettzell 20-m radio telescope, which is

Table 2 RMS scatter of the total delay differences between the three different correlations using the three different a priori delay models, the D-, R- and L-model.

Difference	RMS group delays	RMS integrated delay rates
D–R	0.76 ns	0.22 ns
L–R	0.88 ns	0.22 ns
D–L	0.86 ns	0.42 ns

regularly used for geodetic VLBI, works fine. Fringes were successfully found on the Wettzell-Onsala baseline with two independent software correlators, SFXC and DiFX. For the DiFX correlations, three different and independent a priori delay models were used, and fringes were found with all three approaches. The correlation results were post-processed with AIPS. For the correlation using the D-model, group delays, integrated delay rates, and phase delays could be determined successfully. For correlations using the two other a priori models, group delays and integrated delay rates could be determined, but the phase delay determination suffered from unresolved phase ambiguities.

The RMS scatter of the phase delays was on the level of 10 ps for solution intervals of 2 s, while group delays reached an RMS scatter below 1.5 ns for solution intervals not shorter than 30 s.

Total delay values, i.e., a priori delay models plus fringe-fitted delay residuals from AIPS, agreed on a level of 0.8–0.9 ns for group delays and 0.2–0.4 ns for phase delays (approximated by integrated delay rates) between the three different correlations. This indicates that the L- and R-model for a priori delay values need to be improved, which was also evident from the unresolved ambiguities for the phase delay determination.

For the future, we are planning improvements of post-processing by, e.g., bandpass calibration and doppler tracking to remove time-dependent phase residual errors. We are also planning further experiments to observe GLONASS satellites with VLBI, involving more VLBI stations and observing several GLONASS satellites, which shall also be simultaneously observed with satellite laser ranging (SLR). Furthermore, we plan for a dedicated L/S/X session involving the 20-m radio telescope at Wettzell, which is able to receive all three frequency bands, and the two radio telescopes at Onsala, the 25-m telescope with L-band capability, and the 20-m telescope with S/X capability. This approach will allow us to observe geodetic radio sources with the S/X systems and GLONASS satellites with the L-band systems in the same experiment.

References

1. Tornatore V., Haas R., Duev D., Pogrebenko S., Casey S., Molera Calvés G., Keimpema A. Single baseline GLONASS observations with VLBI: data processing and first results. *Proc. 20th European VLBI for Geodesy and Astrometry Working Meeting*, 162–165, 2011.
2. Tornatore V., Haas R., Duev D., Pogrebenko S., Casey S., Molera Calvés G. Direct VLBI Observations of Global Navigation Satellite System Signals. *Proc. of the IAG General Assembly 2011*, International Association of Geodesy Symposia Volume 139, Eds.C. Rizo & P. Willis, 247–252, 2014. doi:10.1007/978-3-642-37222-3_32
3. Kodet J., Plötz Ch., Schreiber K. U., Neidhardt A., Pogrebenko S., Haas R., Molera Calvés G., Prochazka I. Co-location of space geodetics techniques in space and on the ground. *Proc. 21st European VLBI Group for Geodesy and Astronomy Working Meeting*, Eds. N. Zubko & M. Poutanen, 2013:1, 223–226, 2013.
4. Kodet J., Schreiber K. U., Plötz Ch., Neidhardt A., Kronschnabl G., Haas R., Molera Calvés G., Pogrebenko S., Rothacher M., Maennel B., Plank L., Hellerschmied A. Co-locations of Space Geodetic Techniques on Ground and in Space. *IVS 2014 General Meeting Proceedings*, 2014, this volume.
5. Duev D. A., Molera Calvés G., Pogrebenko S. V., Gurvits L. I., Cimó G., Bocanegra Bahamon T. Spacecraft VLBI and Doppler tracking: algorithms and implementation. *Astronomy & Astrophysics*, 541, A43, 2012. doi:10.1051/0004-6361/201218885
6. Plank L. VLBI satellite tracking for the realization of frame ties. *Veröffentlichungen des Departments für Geodäsie und Geoinformation*, Vienna University of Technology, Geowissenschaftliche Mitteilungen, Nr. 95, 2014.
7. Klioner S. A. General Relativistic Model of VLBI Observables. In: *Proc. AGU Chapman Conference on Geodetic VLBI: Monitoring Global Change*, 188–202, NOAA Technical Report 137, NGS 49, 1991.
8. Moyer T. D. Formulation for Observed and Computed Values of Deep Space Network Data Types for Navigation. *Deep Space Communications and Navigation Series, Monograph 2*, JPL Publication 00-7. Jet Propulsion Laboratory, California Institute of Technology, 2000.
9. Keimpema K. A., Duev D. A., Pogrebenko S. V., et al. Spacecraft tracking with the SFXC software correlator. In: *URSI-BeNeLux 2011*, ESTEC, The Netherlands, 2011.
10. Deller A. T., Tingay S. J., Bailes M., West C. DiFX: A Software Correlator for Very Long Baseline Interferometry Using Multiprocessor Computing Environments. *The Publications of the Astronomical Society of the Pacific*, Volume 119, Issue 853, 318–336, 2007.
11. http://www.aips.nrao.edu/index.shtml

New Progress in VLBI Tracking of GNSS Satellites at GFZ

L. Liu[1,2], R. Heinkelmann[1], V. Tornatore[3], R. Haas[4], A. Neidhardt[5], D. Duev[6], J. Kodet[7], J. Li[2], T. Nilsson[1], M. Xu[1,2], C. Plötz[5], U. Schreiber[7], S. Pogrebenko[6], G. Kronschnabl[5], J.A. Mora-Diaz[1], B. Soja[1], M. Karbon[1], C. Lu[1], V. Raposo-Pulido[1], H. Schuh[1]

Abstract The topic of VLBI tracking of GNSS satellites has lately emerged as a new way for linking the dynamic reference frame realized by GNSS satellites to the ICRF. Recently, a few related experiments and studies were carried out to test and further develop this technique. In this contribution, we present preliminary results of post-correlation with the observations from a recent VLBI tracking of a GLONASS satellite experiment performed by the radio telescopes in Wettzell and Onsala in January 2013 [1]. To determine and evaluate the ability of these observations, the appropriate way to fringe fit the correlation data from artificial signals is studied, and some graphs after calibrations from AIPS are analyzed.

Keywords GLONASS, VLBI satellite tracking, GNSS, clock model, fringe-fitting, narrow band, AIPS, calibration

1. Helmholtz Centre Potsdam, GFZ German Research Centre for Geosciences, Potsdam, Germany
2. Shanghai Astronomical Observatory, Chinese Academy of Sciences, Shanghai, China
3. Politecnico di Milano, DIIAR, Sezione Rilevamento, Milano, Italy
4. Chalmers University of Technology, Onsala Space Observatory, Onsala, Sweden
5. Federal Agency for Cartography and Geodesy, Geodetic Observatory Wettzell, Germany
6. Joint Institute for VLBI in Europe, The Netherlands
7. Technische Universität München, Geodetic Observatory Wettzell, Germany

1 Introduction

While the ITRF (International Terrestrial Reference Frame) is realized by the combination of the various space geodetic techniques, VLBI (Very Long Baseline Interferometry) is the only technique to determine the ICRF (International Celestial Reference Frame) through its observations of extragalactic radio sources. According to combinations of parameters derived by GNSS (Global Navigation Satellite Systems) and VLBI, e.g. troposphere delays [2], gradients, and UT1–UTC [3], evidence of discrepancies between the two systems becomes obvious. Terrestrial local ties can provide a way to interlink the otherwise independent technique-specific terrestrial reference frames, but only to some degree [4]. It is evident that errors in the determination of the terrestrial ties, e.g. due to the errors during the transformation from the locally surveyed coordinates into global Cartesian three dimensional coordinates, introduce significant errors in the combined analysis of space geodetic techniques. A new concept for linking the space geodetic techniques might be to introduce celestial ties, e.g. realized by several techniques co-located on board a satellite [5]. A small satellite carrying various space geodetic techniques is under investigation at GFZ. Such a satellite would provide a new observing platform with its own additional unknowns, such as the orbit or atmospheric drag parameters. A link of the VLBI and GNSS techniques might be achieved in a more direct way as well: by VLBI tracking of GNSS satellites with the extragalactic radio sources nearby as calibrators. This new kind of hybrid VLBI–GNSS observation could comprise a new direct inter-technique tie without the involvement of surveying methods and would improve the consistency of the two space geodetic techniques VLBI and GNSS, in particular of their celestial frames. Several tests of this type of observation were already successfully carried out. First results were obtained from the GLONASS satellites tracking data in cooperation with JIVE using the software SWSpec and SCTracker [6]. In our work, to test this kind of innovative observation, we also analyzed the observations from an experiment where the PR09 GLONASS satellite was tracked [1] in this work.

2 “VLBI Tracking GLONASS” Experiment Description

With the new L-band receiver equipped at the 20-m Wettzell telescope [7], the PR09 GLONASS satellite was successfully tracked from 13:15:00 UT to 13:59:59 UT on January 28th, 2013 for the first time together with the 25-m Onsala telescope (experiment G130128, Figure 1 and Figure 2) [1]. Data were recorded in L1 format with 8 MHz bandwidth and RHCP (Right Hand Circular Polarization) [7] and correlated with the JIVE Software Correlator SFCX in the Nertherlands, which is based on the original design developed for VLBI tracking of the Huygens Probe. It is able to support both the far-field and the near-field delay models and processing data in various “flavors” of the Mark 5 format [8].

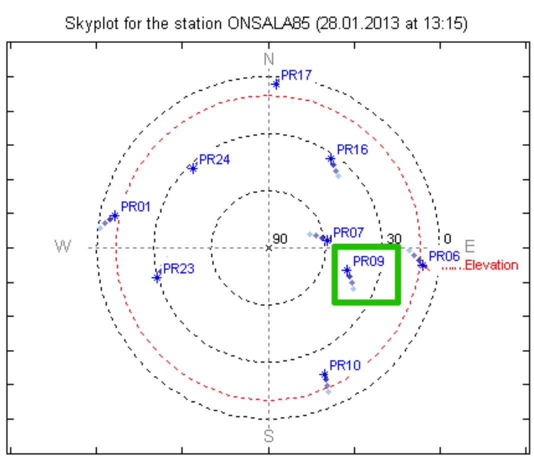

Fig. 1 Skyplot for station Onsala85.

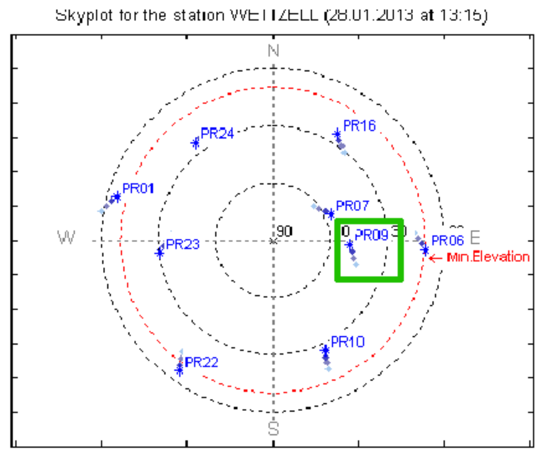

Fig. 2 Skyplot for station Wettzell.

3 Data Reduction for Artificial Signals

The artificial GLONASS signals are quite narrow, which differs from the broad continuous spectrum from natural extragalactic radio sources. The spectral resolution of the narrow band observations from GLONASS is 15.6 Hz, i.e., 512 channels per IF (Intermediate Frequency). The lower edge frequencies in the four IFs are displayed in Table 1 [9]. The whole bandwidth spreads from 1595 MHz to 1603 MHz. This situation limits the observation accuracy, and multi-band delays (the derivation of the phases over the wide-spreading bandwidth in different IFs with respect to the frequencies) could not be derived because the signals are all centered to almost the same frequency and differ only by 10 kHz. After correlation, the data were stored in files of the FITS-IDI (Flexible Image Transport System-Interferometry Data Interchange) [10] format with 0.5 s and 1 s integration time, respectively. To get the delay and rate for the geodetic parameter estimation, fringe-fitting should be done first.

Table 1 The lower edge IF frequencies (in MHz).

Pass	IF 1	IF 2	IF 3	IF 4
Frequency	1594.87	1594.88	1594.89	1594.90

3.1 Fringe-fitting

The aim of fringe-fitting is to get the delay and the rate, and the basic theory is as follows,

$$\Delta\phi_{t,v} = \phi_0 + (\frac{\partial\phi}{\partial v}\Delta v + \frac{\partial\phi}{\partial t}\Delta t) \quad (1)$$

$\frac{\partial\phi}{\partial v}$ denotes the delay, and $\frac{\partial\phi}{\partial t}$ is the rate [11]. The fringe-fitting was conducted by the Astronomical Imaging Processing System (AIPS), developed and maintained by NRAO. The algorithm determining the residual delay, rate, and phase in the AIPS software is realized by the task 'FRING'. Through FFT (Fast Fourier Transform) and least squares solution, single-band group delays and rate residuals were independently obtained from each of the four IFs. In the comparison between the results from 0.5 s and 1 s integration times, we set Wettzell as the reference station and chose the solution interval of 15 s (antenna stop and go in every 15 s [1]).

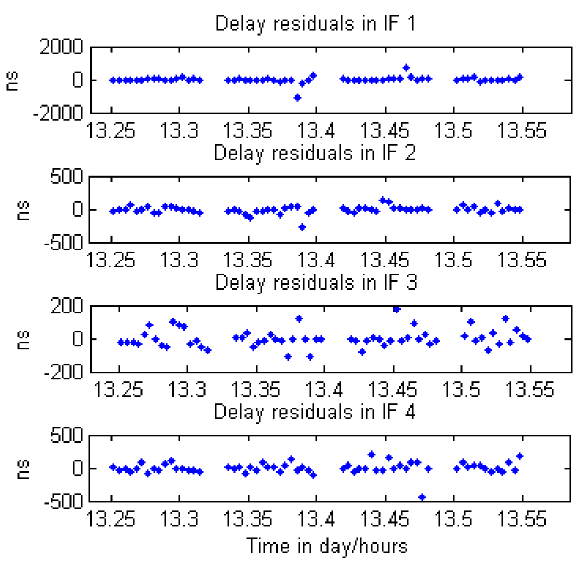

Fig. 3 Delay residuals correlation data with 1 s integration time.

From Figure 3, it is obvious that big outliers (IF 1) exist in delay residuals from the FITS-IDI data with 1 s integration time, while the 0.5 s FITS-IDI data improve the results by almost one order of magnitude (Figure 4). The delay residuals at a level of 10 ns in Figure 4 could come from the difference between the observations and the a priori delay model, the instrument,

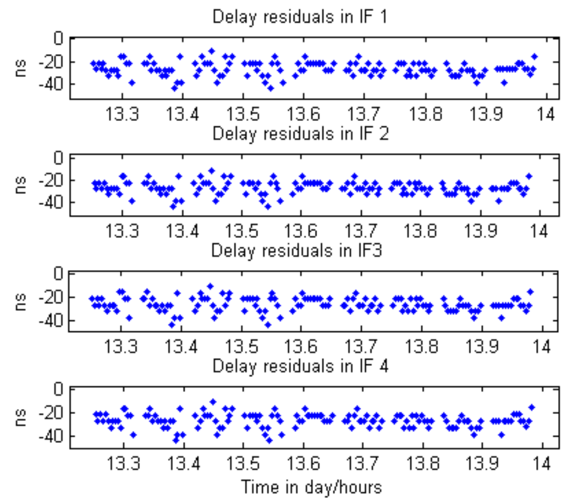

Fig. 4 Delay residuals correlation data with 0.5 s integration time.

the clock, etc. The delay residuals are below zero, indicating that there are some systematic errors which need further analysis. Results with a smaller integration interval, i.e., 0.25 s, were also tested and analyzed in [1]. In the fringe-fitting for the 0.5 s FITS-IDI data, the SNR cutoff is 10 dB.

$$\Delta\tau \sim \frac{1}{2\Delta v}\frac{1}{SNR} \quad (2)$$

Δv is the bandwidth (8 MHz). We can tell from Equation 2 that the delay accuracy should be less than 6 ns. Through the fringe-fitting, the results were fitted to the midpoint of the epoch. The RMS of the phase, delay and rate with different solution intervals in the first scan are presented in Figure 5. The solution interval of 15 s (30 integrations) shows the best stability and highest precision. The average RMS (Root Mean Square) of the phase, delay, and rate are 1.43 degrees, 0.98 ns, and 0.34 mHz, and the SNR is 40.28 dB if we set the solution interval to 15 s. In conclusion, a smaller solution interval in the fringe-fitting lowers the accuracy with the SNR decreasing, while the larger solution intervals such as 30 s may have less stability, which is possibly caused by the rapid movements of the satellite. In a real time satellite tracking experiment, a small solution interval, i.e., 3 s could be more suitable with the correspondingly relatively lower average precision of 2.3 ns for delay residuals.

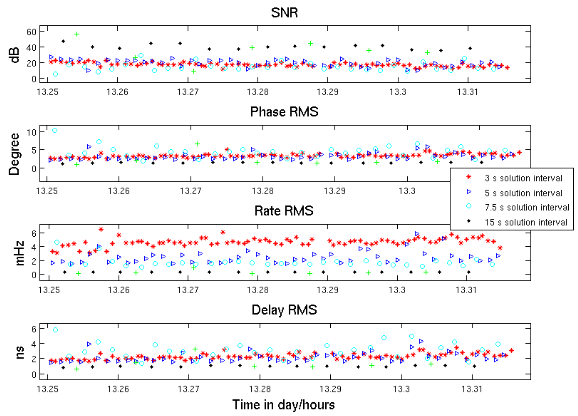

Fig. 5 SNR and RMS of phase, rate, and delay with different solution intervals.

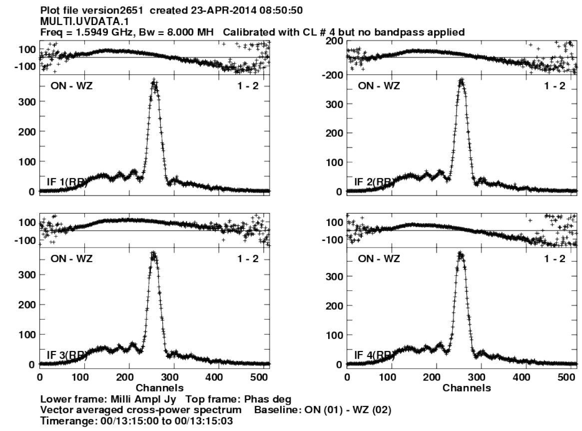

Fig. 7 Cross-power spectrum and phase against frequency with 3 s solution interval.

3.2 Calibrations and Graphic Analysis

There are several calibrations in AIPS, which are important for imaging, such as amplitude calibration, band pass calibration, self-calibration, etc. The task 'CLCAL' can apply the SN table from fringe-fitting to the CL table for the calibration [12]. With these calibrations, we can plot the results by the 'POSSM' task to present the cross-power spectrum and phase against frequency. The graphics in Figure 6 and Figure 7 show that the correlation process and fringe-fitting were successful.

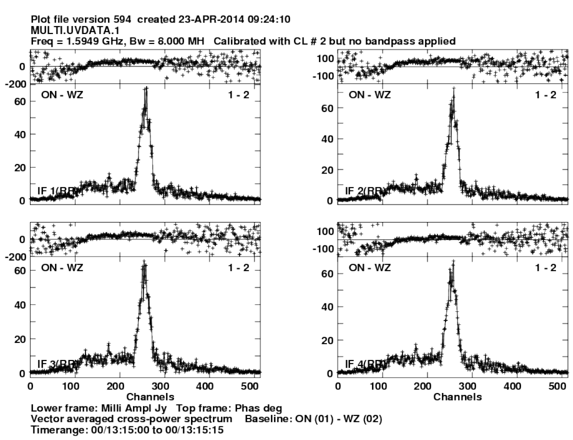

Fig. 6 Cross-power spectrum and phase against frequency with 15 s solution interval.

From Figure 6 and Figure 7, we can see that the smaller solution interval in fringe-fitting can cause a stronger amplitude and less noise in the results, while the delay (phase vs. frequency) is not as flat as that of a larger solution interval, which means that the delay residuals have some kind of deviations. To take into account the graphic results and the above mentioned RMS, a 15 s solution interval could be suitable for precise processing in VLBI satellite tracking.

4 Conclusions

Fringe-fitting with results of 0.5 s integration time is better than with 1 s integration time. The delay residuals improve by one order of magnitude. Precision of a level of 10 ns is obtained in the former case. The figures of cross-power spectrum and phase against frequency verify the reliability of the correlation and fringe-fitting in AIPS. A solution interval of 15 s is suitable in fringe-fitting in this experiment with FITS-IDI data of 0.5 s integration time; the corresponding RMS for phase, delay, and rate are 1.43 degrees, 0.98 ns, and 0.34 mHz. A small solution interval such as 3 s may be useful for real-time tracking. More data from future similar experiments with more stations are needed. Extending the observation duration and observing more satellites would also help to improve the results. Radio sources as calibrators with broader bandwidth added into GNSS tracking experiments may improve the GNSS observation accuracy.

References

1. Haas R., A. Neidhardt, J. Kodet, C. Plötz, U. Schreiber, G. Kronschnabl, S. Pogrebenko, D. Duev, S. Casey, I. Marti-Vidal, J. Yang, L. Plank, The Wettzell-Onsala G130128 experiment, *IVS 2014 General Meeting Proceedings*, this volume, 2014
2. Krügel, M., D. Thaller, V. Tesmer, M. Rothacher, D. Angermann, R. Schmid. Tropospheric parameters: combination studies based on homogeneous VLBI and GPS data. *Journal of Geodesy*, 81(6–8), doi: 10.1007/s00190-006-0127-8, 515–527. 2007
3. Thaller, D., M. Krügel, M. Rothacher, V. Tesmer, R. Schmid, D. Angermann. Combined Earth orientation parameters based on homogeneous and continuous VLBI and GPS data. *Journal of Geodesy*, 81(6-8), doi: 10.1007/s00190-006-0115-z, 529–541. 2007
4. Ray, J. and Z. Altamimi. Evaluation of co-location ties relating the VLBI and GPS reference frames. *Journal of Geodesy*, 79(4–5), doi: 10.1007/s00190-005-0456-z, 189–195. 2005
5. Tornatore, V., R. Haas, S. Casey, D. Duev, S. Pogrebenko, G. Molera Calvés. Direct VLBI Observations of Global Navigation Satellite System Signals, *Earth on the Edge: Science for a Sustainable Planet*, 139, doi: 10.1007/978-3-642-37222-3_32247-252, ISBN (online): 978-3-642-37221-3, 247-252,2014
6. Tornatore, V., R. Haas, et al. Single baseline GLONASS observations with VLBI: data processing and first results. *Proceedings of the 20th Meeting of the European VLBI Group for Geodesy and Astrometry*, 162–165, 2011
7. Kodet, J., K.U. Schreiber, Ch. Plötz, A. Neidhardt, G. Kronschnabl, R. Haas, G. Molera Calvés, S. Pogrebenko, M. Rothacher, B. Maennel, L. Plank, A. Hellerschmied. Co-locations of Space Geodetic Techniques on Ground and in Space. *IVS 2014 General Meeting Proceedings*, this volume, 2014
8. Duev, D. A., G. Molera Calvés, S. V. Pogrebenko, L. I. Gurvits, G. Cimó, and T. B. Bahamon. Spacecraft VLBI and Doppler tracking: algorithms and implementation. *Astronomy & Astrophysics*, 541, doi: 10.1051/0004-6361/201218885, 2012
9. Petrov, L., D. Gordon, J. Gipson, D. MacMillan, C. Ma, E. Fomalont, R. C. Walker, C. Carabajal. Precise geodesy with the Very Long Baseline Array. *Journal of Geodesy*, 83(9), doi: 10.1007/s00190-009-0304-7, 859–876, 2009
10. Greisen, E., The FITS Interferometry Data Interchange Convertion. AIPS Memo114r, 2011
11. Cotton, W. D., Fringe fitting. *Very Long Baseline Interferometry and the VLBA ASP Conference Series*, 82, 1995
12. Moran, J. M., Dhawan, V. An Introduction to Calibration Techniques for VLBI. *Very Long Baseline Interferometry and the VLBA ASP Conference Series*, 82, 161–188, 1995

GLONASS Satellites Simultaneously Observed by VLBI, GNSS and SLR

Benjamin Männel[1], Markus Rothacher[1], Jan Kodet[2], Ulrich Schreiber[2], Ralf Schmid[3]

Abstract In recent years, the tracking of GNSS satellites by radio telescopes has become possible for a number of VLBI stations. Due to hardware limitations these measurements will usually be limited to one frequency, and ionospheric delay corrections have to be taken into account. Beyond the possibility of using ionospheric models, we present a method to correct these ionospheric delays by using observations from co-located GNSS receivers. The VLBI observations of quasars and simultaneous GNSS observations with comparable azimuth and elevation from different sessions in 2013 were used for validation. Station coordinates are a major result from simultaneous tracking of satellites using different space techniques. By combining real GNSS and SLR observations with simulated SLR and VLBI data for a number of European stations, the accuracy of station positions is assessed.

Keywords VLBI, SLR, ionosphere, GNSS

1 Introduction

The co-location of geodetic space techniques allows the investigation of technique-specific error sources and errors related to the links between them, by providing an alternative possibility of combining these techniques using on-board satellite offsets (space ties). Using present co-locations between GNSS, SLR, DORIS, on-board low Earth orbiters, and GNSS satellites, very promising results were presented in recent years (e.g., [1, 2]). Unfortunately, VLBI could not be considered for co-location in space due to the impossibility of tracking near-Earth satellites by radio telescopes and bandwidth limitations of the receiver chain. Thanks to recent hardware developments at some stations, tracking of GLONASS satellites will become the first possibility of combining VLBI with other space techniques in space. The first GLONASS tracking sessions were already carried out for the baselines Medicina–Onsala and Wettzell–Onsala, see [3], [4], and [5]. As usual L_1 GNSS signals are tracked, this kind of observations will not be possible for all VLBI stations and, depending on hardware characteristics, may consist of only one frequency. Therefore, our first goal was to analyze possibilities for correcting the remaining ionospheric delays. In a second stage, prospective accuracies for station coordinates were estimated from real and simulated GNSS, SLR, and VLBI data.

2 Real Observations and Simulation Method

We used real VLBI and GNSS data collected at the European stations Matera, Onsala, and Wettzell in 2013 to investigate ionospheric corrections. For accuracy studies, GNSS and SLR data of GPS week 1774 (5–11 January 2014) were used, together with simulated SLR and VLBI observations of GLONASS satellites for the same time span. Table 1 gives an overview of all observations and synthetic data. The simulation of VLBI data included a turbulence model for wet troposphere delays and receiver clock behavior following [6]. White noise of 2 cm and 67 ps for SLR and VLBI were added to the computed distances. These simula-

1. Institute of Geodesy and Photogrammetry, ETH Zurich
2. Geodetic Observatory Wettzell
3. Deutsches Geodätisches Forschungsinstitut, Munich

tions were repeated 26 times to allow statistical interpretation (based on [7]). To obtain a realistic scenario, measurements of three GLONASS satellites within one hour per day by *n* stations were simulated using an observation interval of 60 s. The SLR simulation was only performed for one laser station at Wettzell, and VLBI was simulated both for a single baseline and for a small European network. For both simulation and processing, a modified version of the Bernese GNSS Software V5.2 was used.

3 Ionospheric Delay Correction

3.1 GNSS-based Ionospheric Models

A well-investigated method for correcting single-frequency VLBI observations for ionospheric delays is the usage of a GNSS-based ionospheric model (e.g., [8, 9]). To check the quality of different models, data from VLBI session R1615 were used (see Table 1). Figure 1 shows the impact of applying such models for three European baselines. The differences of the baseline lengths w.r.t. ITRF2008 positions caused by applying or ignoring the ionospheric corrections from NGS Card files are shown in black (1st bar) and red (2nd). The green (3rd) and blue bars (4th) represent the differences for a global ionosphere model provided by the Center for Orbit Determination in Europe (CODE) and for a regional model based on smoothed, undifferenced GPS code observations of eight well-distributed European IGS stations. The regional model could not fully compensate for the ionospheric delay, resulting in an elongation of the baselines. As a global model cannot represent local structures, the results are not satisfactory either. It has to be mentioned that ionospheric delays might also be compensated by other parameters such as wet tropospheric delays and receiver clock offsets. Here, depending on the solution type, differences of up to ±5 cm for tropospheric wet delays and changes in receiver clock offsets of up to ±0.1 ns could be detected. In general, GNSS-based ionospheric models are a possibility for correcting VLBI observations for ionospheric delays. However, if GNSS satellites are observed, it might be worth trying to derive ionospheric delay corrections from co-located GNSS observations.

Table 1 Data used for investigations: I_1 = ionosphere model; I_2 = ionosphere from GNSS observations; I_3 = accuracy investigation; Ma = Matera, On = Onsala60, Wz = Wettzell, Mc = Medicina, Ys = Yebes40m, [1]IGS station name [2]ILRS station name.

session	I_1	I_2	I_3	stations	date (year, doy)
R1615	x			Ma, On, Wz	2013, 343/344
R1566		x		Ma, On, Wz	2013, 002/003
R1567		x		Ma, On, Wz	2013, 007/008
R1569		x		On, Wz	2013, 022/023
R1570		x		Ma, On, Wz	2013, 028/029
R1578		x		Ma, On, Wz	2013, 084/085
R1580		x		On, Wz	2013, 098/099
EUR123		x		Ma, On, Wz	2013, 126/127
R1585		x		On, Wz	2013, 133/134
R1591		x		On, Wz	2013, 175/176
EUR124		x		On, Wz	2013, 185/186
R1606		x		Ma, Wz	2013, 280/281
R1615		x		Ma, On, Wz	2013, 343/344
R1616		x		Ma, On, Wz	2013, 350/351
GNSS (*real*)			x	GOPE[1],ONSA[1] POTS[1],WTZR[1]	2014, 005-011
SLR (*real/sim*)			x	WLRS[2]	2014, 005-011
VLBI_1 (*sim*)			x	On, Wz	2014, 005-011
VLBI_2 (*sim*)			x	Mc, On, Wz, Ys	2014, 005-011

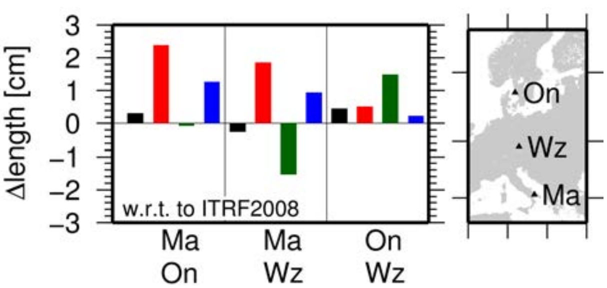

Fig. 1 Changes of the baseline length w.r.t. ITRF2008 for different options for correcting ionospheric delays: standard processing (*1st bar*), without ionospheric correction (*2nd*), CODE model (*3rd*), regional model (*4th*).

3.2 Ionospheric Delays from GNSS L_4 Residuals

When combining GNSS L_1 and L_2 phase observations using the geometry-free linear combination L_4,

$$L_4 = L_1 - L_2 = \lambda_1 N_1 - \lambda_2 N_2 + \left(1 - \frac{f_1^2}{f_2^2}\right) \delta ion_1 \quad (1)$$

only phase ambiguities and ionospheric delays remain in the observable. After fixing the ambiguities, the remaining residuals resulting from a least-squares adjustment contain the ionospheric delay. As it is necessary to form double differences between two stations and two satellites for ambiguity fixing, these residuals have to be split up into two satellite components $R^B_{S1,2}$ for each individual baseline B. Because there are only $n-1$ linearly independent double differences for n single baselines, an additional and independent constraint has to be introduced ([10]). This regularization step can be performed by fixing one satellite S or by introducing a zero-mean condition over a certain period of time. For the following investigations, an epoch-wise zero-mean condition was used. As the resulting residuals R^B_S only provide relative information, a bias parameter has to be added to get absolute values. An epoch-wise mean slant delay correction $\bar{I}_{model}$ based on a CODE ionosphere model is able to provide this absolute information. The ionospheric delay correction I^B_S can be written as

$$I^B_S = R^B_S + \bar{I}_{model}, \quad (2)$$

i. e., the estimated values will be model-mean values instead of zero-mean values. In principle, this method could be applied to all baseline lengths as visibility conditions are nearly identical for co-located VLBI and GNSS stations. Unfortunately, fixing ambiguities for GLONASS observations might be difficult for very long baselines using the Bernese GNSS Software ([11]). As a solution, the regularization step described above could be repeated to obtain undifferenced residuals. Then, ambiguity fixing could be done using shorter baselines w.r.t. additional GNSS stations.

3.3 Validation of Delays Based on GNSS L_4 Residuals

To evaluate this method, real VLBI and GNSS observations were screened to find corresponding observations, i. e. observations in the "same" direction at the "same" epoch. As we split the residuals only into single differences, this condition should be fulfilled at both VLBI stations, which hardly occurs. Therefore, thresholds for direction and observation time differences were defined. If deviations in elevation and azimuth are smaller than 2° and 5°, resp., and if the time difference is smaller than 15 min, the GNSS observation was accepted as a so-called associated observation. Besides, only baselines shorter than 1,000 km, namely Onsala–Wettzell and Matera–Wettzell, were analyzed. For a typical 24 h session, we found 15–25 quasar observations associated with 200–300 GNSS observations. In Figure 2, associated observations are shown for session R1615 at Wettzell. To validate the estimated GNSS-based ionospheric

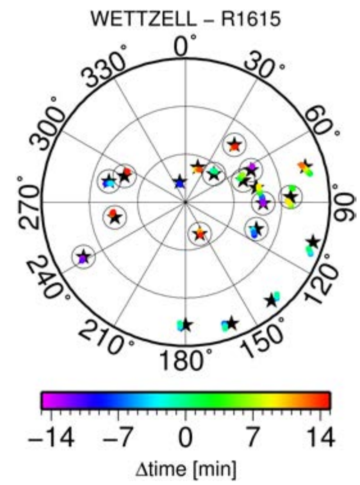

Fig. 2 Associated observations to quasars (asterisks) and GNSS satellites (*colored dots*) for session R1615 at Wettzell, including baselines w.r.t. Matera (*without circle*) and Onsala (*with circle*).

delay corrections ($L4R$) available for each associated observation, VLBI-derived ionospheric corrections contained in the X-band NGS Card observation files (NDC) were used. These corrections $\tau'_{X,ion}$ are computed as [12]

$$\tau'_{X,ion} = \frac{f_S^2}{f_X^2 - f_S^2}(\tau_X - \tau_S) + \tau_{1,inst} - \tau_{2,inst} \quad (3)$$

with $\tau_{1,inst}$ and $\tau_{2,inst}$ representing the receiver-specific offsets. Hence, the difference $L4R - NDC$ also contains an unknown receiver offset, which can be considered as constant over 24 h [12]. As a consequence, a baseline-specific mean difference can be assumed to represent the receiver offsets of the corresponding VLBI stations. Therefore, the baseline-specific standard deviation of

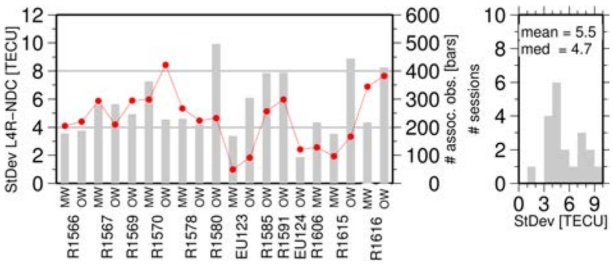

Fig. 3 Validation of ionospheric delay corrections based on GNSS L_4 residuals by means of ionospheric correction values from NGS Card files. *Left:* standard deviation of the mean difference *L4R-NDC* (*dots*) and number of associated observations (*bars*) for different sessions; *right:* histogram of the standard deviations. OW = Onsala–Wettzell, MW = Matera–Wettzell.

the mean difference $L4R-NDC$ is used as a validation criterion. In Figure 3, results from various sessions in 2013 are shown. The standard deviations of the mean differences are between 1 and 10 TECU[1]. Considering all 4,599 associated observations, mean and median values of 5.5 and 4.7 TECU can be found. Differences in the resulting standard deviations arise from remaining unresolved ambiguities in the L4R approach, the distribution of associated observations over each session, and also the ionospheric activity. The impact of the thresholds is below 1 TECU as regards time and elevation (see Figure 4). As the standard deviations increase with increasing azimuth thresholds, azimuth differences of associated observations should be kept small for future validation scenarios. At this point the balance between the number of remaining associated observations and small standard deviations is important. Further validation steps will be based on GNSS observations only, comparing solutions using our approach and results based on the ionosphere-free linear combination L_3, and tests with real VLBI tracking data of GLONASS satellites will be provided.

4 Simultaneous Observation Time Series

Real and simulated tracking data of GLONASS satellites by GNSS, SLR, and VLBI (see Section 2) are used to derive station coordinates. As input files, GNSS orbits and clocks as well as ERP final products from CODE were used. Coordinates, troposphere (GNSS and VLBI), and receiver clock offsets (VLBI) were set up in the data processing. For GNSS and VLBI, an NNR and NNT condition was applied, whereas single SLR station coordinates are estimated w.r.t. the GNSS orbits. Table 2 shows the number of observations, the formal errors and the repeatability of the station coordinates for real and simulated data. Comparing real and simulated SLR data reveals a higher number of simulated observations, as we do not take weather and clear sky conditions into account. Therefore, smaller formal errors are reasonable. Using the simulated VLBI data for the baseline Onsala–Wettzell, formal errors of 1.2 cm for the north and up components can be found. The significantly smaller value for the east component might be a result of the orientation of the baseline. This effect also shows up in the repeatability values, where the north component is around 1.5 cm and the other values are below 1 cm. If a small network is used, the results get worse. Only the formal errors for the up component are improved, perhaps due to the higher number of observations. The degradation of the other components might be associated with sky coverage and observation scheduling, as the simulated satellites were chosen randomly from different orbit planes.

5 Conclusions and Outlook

The presented method based on GNSS L_4 residuals for the estimation of ionospheric delay corrections will be applied and further validated by using real VLBI satellite tracking data. Referring to standard deviations of 5 TECU (80 cm for GNSS L_1) for the presented validation approach, the method will be more accurate for real tracking data as a consequence of using the same signal from the same source. Further investigations related to the influence of the ambiguity resolution quality on the ionospheric corrections should be done in terms of satellite tracking observations based on longer baselines. According to simulations, a station coordinate repeatability of 1–2 cm can be expected for a baseline such as Onsala–Wettzell when observing different GLONASS satellites under good sky coverage. Analyses of different scenarios (e.g., single-pass tracking and shorter observation intervals per satellite including careful scheduling) and assessment of their prospective benefits will be the subject of further research.

[1] 1 TECU corr. to 0.6 cm (X-band) and 80 cm (GNSS L_1)

Table 2 Results from real and simulated tracking data (GNSS also includes IGS stations GOPE and POTS; $VLBI_1$ = baseline Onsala–Wettzell; $VLBI_2$ = European network; number of observations per station for SLR and within the network for GNSS and VLBI).

		real			simulated						
		GNSS		SLR	SLR	$VLBI_1$		$VLBI_2$			
stations		ONSA	WTZR	WLRS	WLRS	On	Wz	Mc	On	Wz	Ys
observations		250,000 each		216	378	377		957			
formal error [cm]	N	0.012	0.012	0.39	0.19	1.26	1.16	2.10	1.68	1.48	1.50
	E	0.012	0.012	0.76	0.28	0.74	0.72	1.70	0.97	1.42	1.57
	U	0.003	0.004	0.70	0.14	1.22	1.33	0.76	0.36	1.15	0.33
repeatability [cm]	N	-	-	-	0.13	1.58	1.49	2.00	1.51	1.88	2.39
	E	-	-	-	0.20	0.65	0.65	2.22	1.58	2.71	2.29
	U	-	-	-	0.32	0.76	0.93	0.38	1.62	1.08	0.52

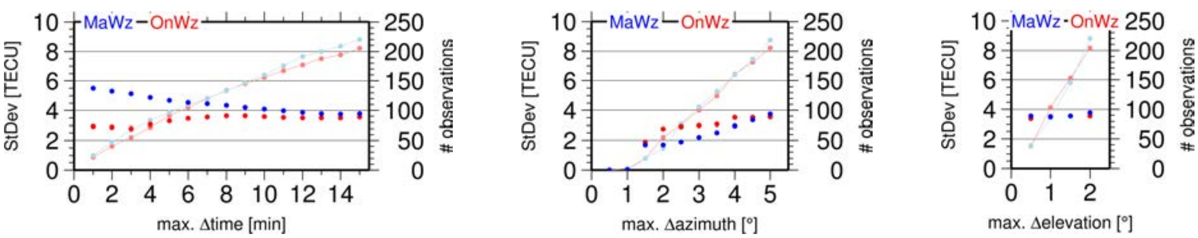

Fig. 4 Impact of different thresholds for differences in time, azimuth, and elevation on the standard deviation (session R1566).

Acknowledgements

The authors wish to thank the IVS, the IGS, and the ILRS for providing observation data and CODE for providing precise GNSS-related products. This work was done within the project "Co-location of Geodetic Space Techniques on Ground and in Space", part of the DFG Research Unit on reference systems (FOR1503).

References

1. Flohrer, C., M. Otten, T. Springer, J. Dow, Generating precise and homogeneous orbits for Jason-1 and Jason-2, Adv Space Res, 48(1), 152–172, 2011. doi:10.1016/j.asr.2011.02.017
2. Thaller, D., R. Dach, M. Seitz, G. Beutler, M. Mareyen, B. Richter, Combination of GNSS and SLR observations using satellite co-locations, J Geod, 85(5), 257–272, 2011. doi: 10.1007/s00190-010-0433-z
3. Tornatore, V., R. Haas, D. Duev, S. Pogrebenko, S. Casey, G. Molera Calvés, A. Keimpema, Single baseline GLONASS observations with VLBI: data processing and first results, In: Proc 20th Meeting of the European VLBI Group for Geodesy and Astrometry, 162–165, 2011.
4. Tornatore, V., R. Haas, S. Casey, D. Duev, S. Pogrebenko, G. Molera Calvés, Direct VLBI observations of Global Navigation Satellite System signals, In: IAG Symposia 139, 247–252, 2014. doi:10.1007/978-3-642-37222-3_32
5. Haas, R., A. Neidhardt, J. Kodet, C. Plötz, U. Schreiber, G. Kronschnabl, S. Pogrebenko, D. Duev, S. Casey, I. Marti-Vidal, J. Yang, L. Plank, The Wettzell-Onsala G130128 experiment, In: IVS 2014 General Meeting Proceedings, 2014, this volume.
6. Böhm, J., J. Wresnik, A. Pany, Simulation of wet zenith delays and clocks, IVS Memorandum 2006-013v03, 2007.
7. Plank, L., VLBI satellite tracking for the realization of frame ties, TU Vienna, Department of Geodesy and Geoinformation, 2013.
8. Sekido, M., T. Kondo, E. Kawai, Evaluation of GPS-based ionospheric TEC map by comparing with VLBI data, Radio Sci, 38(4), 1069, 2003. doi:10.1029/2000RS002620
9. Tierno Ros, C., J. Böhm, H. Schuh, Use of GNSS-derived TEC maps for VLBI observations, In: Proc 20th Meeting of the European VLBI Group for Geodesy and Astrometry, 114–117, 2011
10. Alber, C., R. Ware, C. Rocken, J. Braun, Obtaining single path phase delays from GPS double differences, Geophys Res L, 27(7), 2661–2664, 2000. doi:10.1029/2000GL011525
11. Dach, R., Bernese GNSS Software: New features in version 5.2, Astronomical Institute, Unversity of Bern, 2013.
12. Hobiger, T., VLBI as a tool to probe the ionosphere, TU Vienna, Institute of Geodesy and Geophysics, 2006.

Real-time and High-Accuracy VLBI in the CE-3 Mission

Weimin Zheng[1,2], Yong Huang[1], Zhong Chen[1,2], Guangli Wang[1,2], Qinghui Liu[1,2], Fengxian Tong[1], Peijia Li[1], Li Tong[1], Fengchun Shu[1,2]

Abstract On 14 December 2013, the Chang'E-3 (CE-3) lunar probe successfully landed on the Moon and then released the Yutu rover. To support this mission, the Chinese VLBI Network (CVN) made important upgrades: the new VLBI Center and the 65-m Tianma antenna were built in Sheshan on the periphery of Shanghai. To get high-precision delay results, the beacon onboard the CE-3 probe was designed to emit a set of special X-band Differential One-way Range (DOR) signals. The CVN used the real-time ΔDOR technique to track the lander and to eliminate systematic errors as much as possible. During the circum-lunar orbit, the VLBI delay residuals after orbit determination were $\sim$0.5 ns (using a 5-second integration time). The absolute position accuracy of the lander using the VLBI group delay is approximately 100 meters. The e-VLBI technique reduced the turnover time for the observations to $\sim$15–45 seconds. After landing, using the same-beam VLBI mode, the phase delay and phase reference mapping methods were used to determine the relative position of Yutu reaching an accuracy of 1 meter. The real-time and high-accuracy VLBI data greatly supported the CE-3 mission.

Keywords Real-time VLBI, lunar exploration, Delta-DOR, phase reference mapping, lunar surface positioning, orbit determination

1. Shanghai Astronomical Observatory, Chinese Academy of Sciences
2. Key Laboratory of Radio Astronomy, Chinese Academy of Sciences

1 Introduction

Chang'E-3 (CE-3) is China's first soft-landing and roving exploration on the Moon. It is also the first probe to soft-land on the Moon since Luna 24 in 1976. The mission objective is to demonstrate and develop key technologies for future lunar and deep-space exploration missions. The scientific objectives include the exploration of the lunar surface topography, a lunar surface material composition and resource survey, and the realization of lunar-based astronomical observations.

The CE-3 spacecraft was launched on 2 December 2013. It entered a 100-km-high polar orbit on 6 December, then adjusted to an elliptical orbit of 15×100 km, and finally realized a soft-landing on the Moon. CE-3 deployed the Yutu (Jade Rabbit) rover on 14 December 2013. The success of the CE-3 mission marks the transition of the Chinese Lunar Exploration Program from the first phase of orbital missions to the second phase of soft-landing. As the first soft-landing on the Moon since the Apollo missions, it is also one of the most complicated space exploration missions China has undertaken so far. To guarantee the high accuracy and high reliability, many new facilities and techniques were used for the first time.

The CE-3 mission used a combination of the Chinese space flight telemetry, tracking, and command (TT&C) network, the Chinese VLBI Network (CVN), and some ESA stations to compose the complex TT&C system [1]. Before the mission, the new Kashgar and Jiamusi deep-space stations joined the China TT&C network. Almost at the same time the Tianma 65-m antenna and the new VLBI Data Center of the CVN were put into operation.

There were five operation phases in the mission: the launch phase, the Earth-Moon transfer orbit phase,

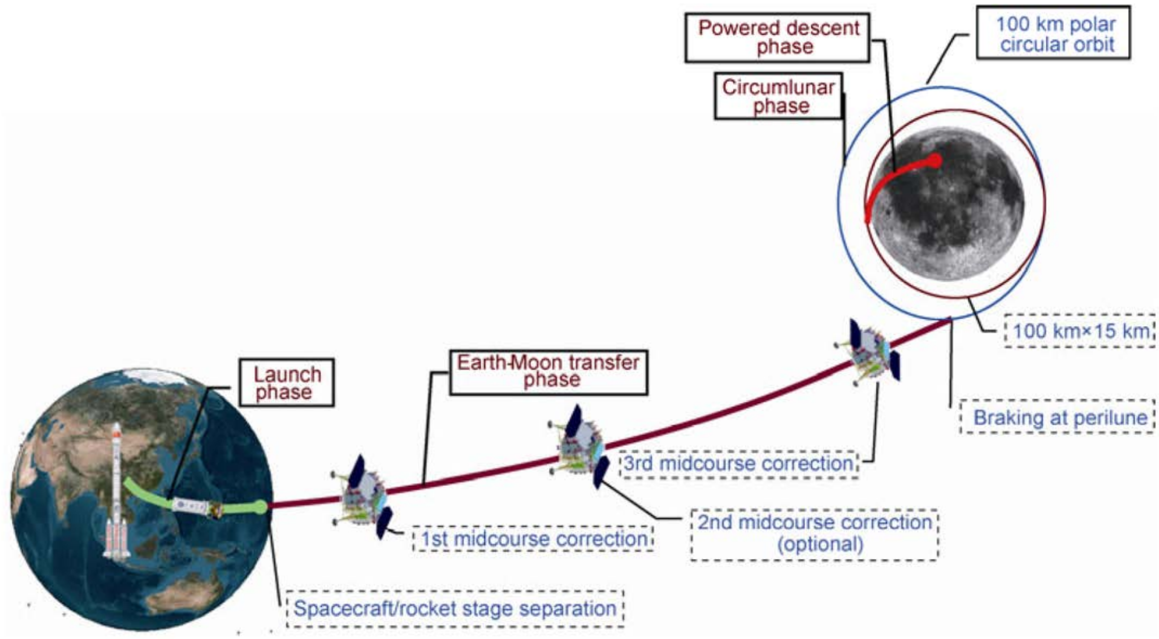

Fig. 1 CE-3 main trajectory (from Xinhua news agency).

the circum-lunar phase, the powered descent phase, and the lunar surface work phase. The TT&C working frequency changed from S-band to X-band with the Earth–Moon transfer phase. Shanghai station (including Tianma & Sheshan), Beijing station, Urumchi station, Kunming station, and the new CVN Data Center took part in tracking the probe from the Earth–Moon transfer phase to the power descent phase to the lunar surface working phase (Figure 1). The planned third mid-course correction (Trajectory Correction Maneuver, TCM-3) was canceled because of the high accuracy tracking.

Many new techniques and facilities improved the performance of the CVN. For using the real-time X-band Differential One-way Range (ΔDOR), the VLBI group delay was less than 0.5 ns (using a 5-second integration time), which is ten times better than that of the CE-1 mission. The total data turnaround time of the whole CVN system is shorter than one minute. The real-time performance of data transmission and processing featured tenfold increases, playing an irreplaceable role in time critical and important situations such as two mid-course corrections or Trajectory Course Maneuvers (TCMs), the braking of the Lunar Orbit Insertion (LOI), the powered descent, and the soft-landing. After landing, VLBI and three-way range data were used to determine the lander position to better than 100 meters. After the critical mission, using of the same-beam VLBI observation data, the relative position of Yutu to the lander was improved to about 1 meter by VLBI phase delay and phase reference mapping techniques.

2 CVN Status in the CE-3 Mission

According to the requirements of the TT&C system, the CVN should carry out the probe tracking and orbit/position determination. In the Earth–Moon transfer orbit phase and the circum-lunar phase, the CVN had to complete ΔDOR tracking, orbit/angular position determination, and orbit prediction. In the lunar surface phase, the CVN should complete lander and rover same-beam VLBI tracking, the lander 3D positioning, and the rover positioning relative to the lander. These are new tasks; for this reason, we have completed the station and Data Center upgrade before the mission.

The CVN consists of five stations and one Data Center (Figure 2). After the first construction stage of the Shanghai Tianma 65-meter antenna was completed, the antenna was equipped with an S/X-band observation system. The other four stations are Beijing Miyun (50-m), Urumchi Nanshan (25-m), Yunnan Kunming (40-m), and Shanghai Sheshan (25-m). The baseline Shanghai–Urumchi is the longest baseline with a length of 3,200 km.

Fig. 2 CVN configuration of five antennas and one Data Center in the CE-3 mission.

In order to improve the reliability, redundant designs were carried out in various aspects, such as the system design, the station observation system, the network system, and the data center.

Although three stations are the minimum configuration for CE-3 VLBI tracking, there are actually five stations. The strategy is to make sure three of four stations are always available during the critical mission period. There are two antennas at Shanghai station. The Tianma antenna is the main antenna and the Sheshan antenna is the backup antenna. The big Tianma antenna not only strengthens the CVN signal reception capacity, it also improves the reliability of Shanghai station. In the critical mission phase, the Tianma and Sheshan antennas tracked the CE-3 probe and sent the data to the VLBI Center simultaneously. But in the VLBI Center only data from Tianma were correlated, while data from the Sheshan antenna were just received and stored for offline data processing.

Before the mission, the new VLBI Data Center was successfully completed in the Sheshan park of Shanghai Astronomical Observatory (SHAO). The VLBI Center has eleven configuration items: e-VLBI data transfer, schedule, software correlator, hardware correlator, station monitoring, media error correction, group delay, phase delay, orbit determination, position determination, and system operation and management. To enhance reliability, there are two data pipelines. The one headed by the software correlator is the main pipeline, the one headed by the hardware correlator is the backup. The software correlator adopts parallel algorithm and runs on a set of blade-based clusters; the hardware correlator adopts FPGA technology. For the same reason, all operation positions have backups.

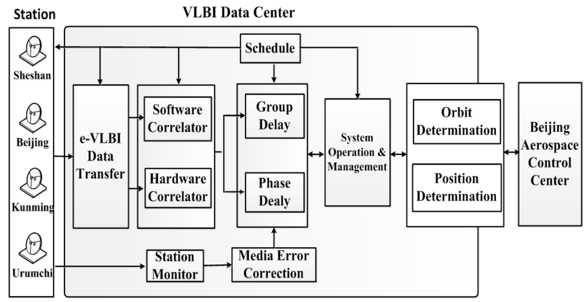

Fig. 3 CVN Data Center configuration.

3 New Techniques Improve the Orbit Determination and Position Accuracy

The techniques like real-time ΔDOR, same-beam lander and rover positioning were first used with the CE-3 mission (Table 1).

Table 1 Technique and device improvements of the CE-3 mission with respect to the CE-1/2 missions.

	CE-3	CE-2	CE-1
ΔDOR technique	First use	experiment	/
Same beam VLBI	First use	experiment	/
e-VLBI data rate	64 Mbps	32 Mbps or 16 Mbps	16 Mbps or 8 Mbps
Data Acquisition system	CDAS	CADS	ABBC
Station	5	4	4
VLBI Data center	Sheshan	Xu Jiahui	Xu Jiahui
Rover & lander positioning	First use	/	/
Noise level (5-second integration time)	<0.5 ns	$\sim$4–5 ns	<5.5 ns

3.1 *Real-time X-band ΔDOR*

The real-time X-band ΔDOR tracking technique was applied for the first time in CE-3. A special DOR beacon onboard the CE-3 probe substituted the S-band beacon used in CE-1/2. The DOR beacon emits two pairs of tones with higher onboard efficiency than the normal band limited continuous spectrum signals (Figure 4).

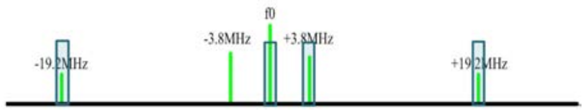

Fig. 4 Spectrum of X-band CE-3 DOR signal. Three tones and the carrier are recorded.

The carrier is denoted by f0. The second (lower-frequency) DOR tone is ± 3.8 MHz, which is used to resolve phase ambiguity. The first (high-frequency) DOR tone is ± 19.2 MHz, which determines the group delay accuracy [2]. Using the multiple signal synthesis technique, the measurement-limiting errors are inversely proportional to the spanned bandwidth of 38.4 MHz.

The CE-3 probe emitted two sets of carrier and DOR signals (one as backup). For each set of signals, the carrier, the upper second DOR tone, and the two first DOR tones were recorded in four channels. Hence, two pairs of DOR signals were recorded in eight BBC channels with 2 MHz bandwidth and 2-bit resolution. The total data rate per station thus amounts to $2 \times 4\,\mathrm{CH} \times 4\,\mathrm{MHz/CH} \times 2\,\mathrm{bit} = 64$ Mbps.

The frequency shift to X-band greatly reduces the ionosphere correction error (to a sixteenth part) compared to the S-band tracking system. To minimize the common-mode errors that arise from uncertainty in media delays, clock offsets, instrumental delays, and station locations, the differential measurement named ΔDOR was adopted [3]. The quasars with a small angular separation from the CE-3 spacecraft were the references. The scan sequence is Quasar–CE-3–Quasar–CE-3 with a switching interval of five minutes. The angular distance between CE-3 and the quasar is less than 10°. The big Tianma antenna was beneficial for quasar observations and improved the VLBI measurement accuracy.

The ΔDOR technique greatly improved the VLBI data accuracy. The formal error of the VLBI group delay was less than 0.2 ns. The delay residuals were at a level of 1 ns in trans-lunar orbit and decreased to a level of 0.5 ns in lunar orbit (Figure 5).

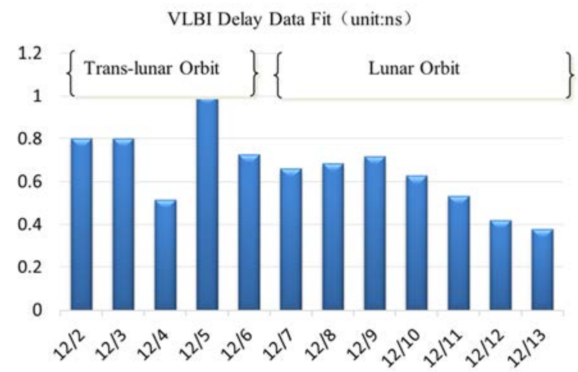

Fig. 5 Group delay residuals decreased to a level 0.5ns in the lunar orbit.

A ΔDOR test experiment had been run in the CE-2 mission. At that time, the data were correlated in the post-processing mode. But in the CE-3 mission, the CVN worked in real-time mode during the critical period from 2–20 December 2013. The planned total VLBI data turnaround time should be less than one minute, compared to ten minutes turnaround time in CE-1 and CE-2. This was a considerable challenge for the whole system.

Real-time e-VLBI is the fundamental technique. It consists of a station data transmitting unit, the Data Center receiving and distributing unit, and a Wide Area Network (WAN) link. The station data transmission unit is based on the Mark 5B+ system with specifically designed software to gather data from the CDAS digital terminal and to send data through a dedicated network. At the VLBI Center, the data servers received and distributed raw VLBI data to the software and hardware correlators in parallel. The raw data were stored on local disk arrays at the same time.

Each station had main and spare dedicated WAN fiber links to the VLBI Center protected by Border Gateway Protocol (BGP) for data transmission. There was a network management system to monitor the network status. If any one of the main lines was under unstable condition, it would switch to the backup line automatically. The switch time is shorter than 1 second to minimize the impact on the real-time data transmission.

In the VLBI Center, specific modules for e-VLBI data transfer, correlator, group delay, position determination, and system operation and management were designed to improve the real-time capability. They

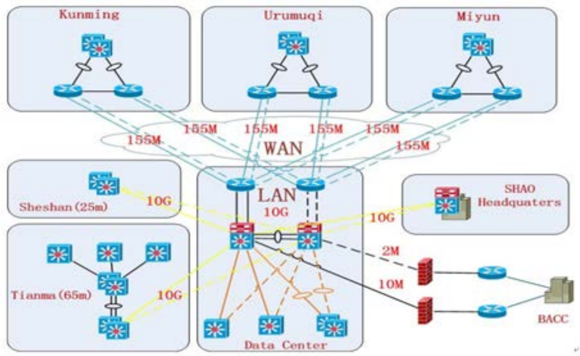

Fig. 6 CVN network with dual path connection.

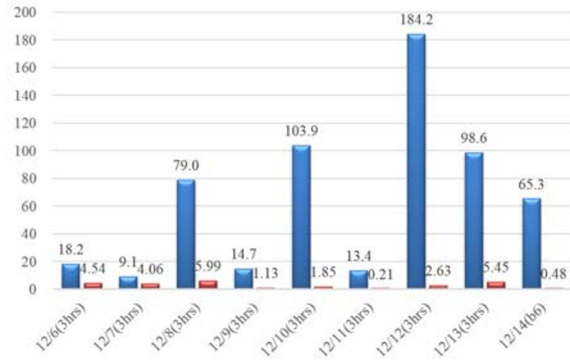

Fig. 7 POD of Lunar Orbit Compared with BACC(unit:m).

worked in pipeline mode. The intermediate data were exchanged through the Network File System (NFS) at a fixed rate. During the critical mission the shortest turnover time, from receiving the signal to producing the CE-3 angular position, was 25 seconds. In the special orbit maneuver procedure, when the software opened the onsite fringe search and delay model reconstruction function, the turnover time rose to 40 s.

3.2 High Accuracy VLBI Data Improve the Orbit Determination Results

In the CE-3 mission, the new facilities and techniques of the Chinese deep-space stations and the CVN improve the tracking capability of the range and delay data to a level of better than 1 m and 1 ns, respectively. The analysis reveals that the high eccentricity character of the trans-lunar orbit is not good for Precision Orbit Determination (POD) and that the orbit accuracy decreases as the probe flies away from the Earth. However, combining the VLBI data greatly improves the accuracy of the short arc orbit determination as compared to the result of using range data only in each phase of the mission. The orbit differences between the solutions from SHAO and Beijing Aerospace Control Center (BACC) in three dimensions are at the level of 1 km and 100 m in trans-lunar orbit and lunar orbit, respectively (Figure 7).

The strategy of estimating the empirical accelerations in the POD helps to reduce the impact of attitude control in the CE-3 mission. For 100×100 km and 100×15 km lunar orbits, the total position consistency is found to be at the level of 20 m (3 m in the radial direction) and 30 m (4 m in the radial direction), respectively. These are better than those for CE-2, which are at a level of 30 m (5 m in the radial direction) and 46 m (12 m in the radial direction) respectively; and they are much better than those for CE-1 with several hundreds of meters. The orbit accuracy of the CE-3 probe is at the same level as other contemporary lunar probes such as SELENE and LRO. The position error of the soft-landing trajectory is less than 100 m based on the kinematic POD method.

3.3 Lander and Rover Positioning

Because of the impact of range biases, the accuracy of the soft-landing trajectory and position of the lander with the range data only is up to a level of several km. However, VLBI data can improve the lander position accuracy to a level better than 100 m, and the relative position of the Yutu rover to the lander to a level of 1 m.

In the CE-3 mission, one of the important tasks of the CVN is to determine the locations of the lander and the rover. For the lander positioning task VLBI and range data were used; for the relative positioning of the rover to the lander same-beam VLBI was used.

The onboard range and DOR beacons were shut down about one hour after the soft landing. The lander directional antenna only transmitted wideband scientific data; the rover transmitted wideband scientific data through the directional antenna or transmitted narrowband telemetry signals through the omni-directional antenna according to the operational program. To avoid interrupting scientific data transmission, CVN stopped observing extragalactic radio sources after landing. So we only used the effective one-hour, three-way range and VLBI measurements to determine the lander position in the lunar body-fixed coordinate system. The conversion from the principal axes to mean axes is given by DE421. The lander position is in Table 2.

Table 2 Comparison of the lander locations determined by CVN and NASA.

	Latitude	Longitude	Height
CVN	44.1206°	−19.5124°	−2632.0 m
NASA	44.1214°	−19.5116°	−2640.0 m
Difference	24 m	17 m	4 m

In order to evaluate the position accuracy of the lander, the NASA Lunar Reconnaissance Orbiter (LRO) Digital Elevation Model (DEM), a spherical harmonic model of degree and order 2050 was used. The DEM spatial resolution is about 2.66 km. We input the lander longitude and latitude from the CVN into the DEM and got the elevation of −2636 m. On 25 December, LRO flew over the lander site and NASA published a lander position based on the images taken by the LRO camera [4]. The total difference of the CVN and LRO locations is less than 50 m.

On 15 December, the lander commenced deploying the Yutu rover. Yutu moved around the lander and they photographed each other at the parking positions A, B, C, D, and E. The CVN used same-beam VLBI to locate Yutu's relative position to the lander. The coordinates that describe the relative position between the lander and the rover are defined in the lander-centered NEG (North East Ground) coordinate system. The x-axis is pointing to the north, the y-axis is pointing to the east in the horizontal plane, and the z-axis is perpendicular to the x-axis and the y-axis, constructing a right-handed system [1].

VLBI observations were used to determine Yutu's relative position. During the mission, the relative position was calculated from the differential group delay and reached the 100-m level. After the critical mission, the differential phase delay as well as the phase-referencing mapping method were used; this greatly improved the position accuracy. The group delay noise was at the level of several ns, and that of phase delay was at the level of 1 ps with an ambiguity at a level of ns.

When utilizing phase delay data to determine the relative position, phase ambiguities for each baseline need to be solved. We solved for a VLBI phase delay bias for each baseline in relative positioning. Because the rover was close to the lander and the terrain at this location was relatively flat, we fixed the prior elevation parameter of the rover and set it the same as that of the lander.

In addition, the same-beam phase-referencing mapping method was adopted to obtain an accurate relative position for Yutu. Firstly, the software correlator output visibilities were converted to the uniformed FITS-IDI format, and then AIPS and Difmap, the astronomical mapping softwares, were utilized to complete the mapping and angular positioning of the Yutu antenna (Figure 8). A new positioning algorithm was developed to determine the rover lunar positions. We took advantage of same-beam observations with the signals of the lander and the rover being received in the same digital terminal to eliminate system errors.

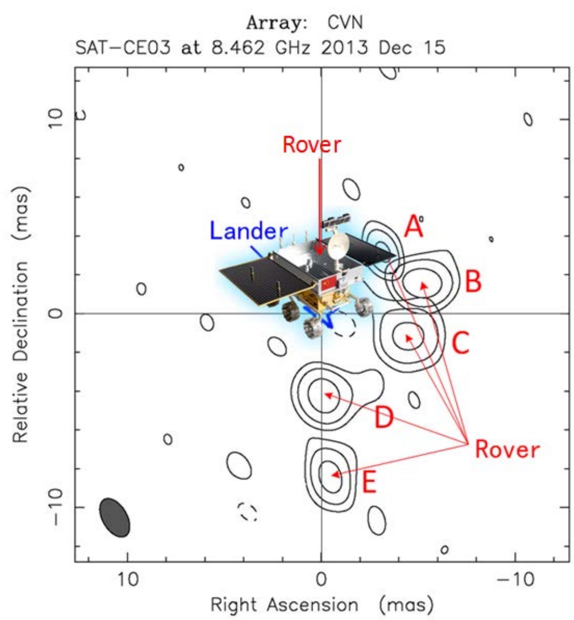

Fig. 8 Five rover positions with respect to the lander by a same-beam phase-referencing map.

The three VLBI relative positions from the group delay, phase delay, and VLBI map are compared with the results from the visual localization by the onboard Stereo Cameras (Table 3). The position differences are at a magnitude of hundreds of meters for the group delay data but decrease to about 1 m for phase delay and phase-referencing map data. Systematic errors in the differential group delay degrade the accuracy of the relative position, especially at point B. At that time, there were only about ten minutes of data from three antennas (Beijing, Kunming, and Tianma).

Table 3 Three VLBI relative position results compared with those from visual localization (unit: m).

Site		Visual	Group delay	Phase delay	Phase-referencing map
A	N	9.03	−4.2	11.25	9.47
	E	1.50	0.4	1.28	1.15
B	N	5.00	−269.8	5.89	5.12
	E	8.90	−640.8	7.56	9.30
C	N	−5.65	80.5	−4.92	−5.34
	E	8.36	10.0	8.02	8.86
D	N	−9.75	112.6	−8.73	9.51
	E	0.27	69.2	0.37	0.49
E	N	−19.76	59.0	−17.35	−19.26
	E	−0.20	32.0	−0.42	−0.29

Considering that the accuracy of the relative positions based on the visual localization method is about 4% of the distance between the lander and the rover, the position accuracy for the phase delay and phase-referencing map results can reach the 1-m level [5].

4 Conclusions

CE-3 is the first Chinese lunar probe that soft-landed on the surface of the Moon. Real-time and high accuracy VLBI has played a very import role in this mission. ΔDOR can improve the orbit determination and prediction accuracy remarkably, especially in the critical sections like TCM, LOI braking phase, or powered descent phase. Using VLBI and range data, the lander position can be better than 100 m. The relative position accuracy determined by same-beam VLBI is about one meter. Real-time ΔDOR and same-beam VLBI are anticipated to be used in the CE-5 rendezvous and docking mission as well as in other planetary exploration missions of China.

Acknowledgements

This paper is sponsored by the Natural Science Foundation of China General Program (11173052, 11373061), the state CNGI demonstration project, the State High-tech 863 R&D project (2012AA121603), the Key Laboratory of Radio Astronomy of Chinese Academy of Sciences, the Science & Technology Commission project of Shanghai Municipality (06DZ22101), the Program of Shanghai Subject Chief Scientist (14XD1404300) and the Chinese lunar exploration project. The authors appreciate the support from CVN Data Center.

References

1. Huang Yong, et al., Orbit determination of Chang'E-3 and positioning of the lander and the rover, Chinese Sciences Bulletin, in press.
2. DSN Telecommunications Link Design Handbook (810-005), Module 210, Delta-Differential One-way Ranging, Jet Propulsion Laboratory, Pasadena, California, 2004.
3. James S. Border, Innovations in Delta Differential One-Way Range: From Viking to Mars Science Laboratory, 21st International Symposium on Space Flight Dynamics, 2009.
4. http://www.nasa.gov/content/nasa-images-of-change-3-landing-site/#.UtUDbtLUNP.
5. Wang Baofeng, Zhou Jianliang, Tang Geshi, et al., Research on visual Localization method of Lunar Rover, Science China (F), 44(4), 452–460, 2014.

Research on Lunar Radio Measurements by Chang'E-3

Geshi Tang[1,2], Jianfeng Cao[1,2], Songtao Han[1,2], Songjie Hu[1,2], Tianpeng Ren[1,2], Lue Chen[1,2], Jing Sun[1,2], Mei Wang[1,2], Yifei Li[1,2], Li Li[1,2]

Abstract After the successful launch on December 2, 2013, the Chang'E-3 performed a soft landing on the lunar surface on December 14. The Chang'E-3 is designed to stand in place for more than one year, and it can transmit X-band signals when the transponder is switched on. With this signal ranging, doppler, carrier phase, and VLBI delay and delay rate can be acquired from ground TTC antennas and VLBI antennas. These techniques can be called Lunar Radio Measurement (LRM) collectively. By the LRM technique, more rich observations can be acquired nearly at the same time, so it should be more effective in contributing to space geodesy than LLR, which only provides ranging observations. To analyze the LRM technique, MEKAS (Moon Earth Kinematical Analysis Software) is developed, which can simulate all kinds of observations mentioned above, carry out covariance analysis, and determine the parameters including the CE'3 position on the lunar surface, ground site coordinates, UT1, EOP, and love numbers. A simulation is performed with MEKAS to analyze the ability of lunar lander positioning and estimation of earth rotation parameters. The results show that the LRM technique has wide prospects in terrestrial and lunar science.

Keywords Chang'E-3, Yutu Rover, X-band transponder, lunar radio measurements

1. National Key Laboratory of Science and Technology on Aerospace Flight Dynamics
2. Beijing Aerospace Control Center

1 Introduction

Lunar Laser Ranging (LLR) is a very important space geodetic technique in the sense that it can determine a huge number of parameters for lunar ephemerides, physical libration, the moon's interior structure, earth orientation parameters (EOP), and earth-moon dynamics. LLR can also be a powerful tool for testing Einstein's theory of general relativity. However, of all the ILRS observatories, only several sites are capable of carrying out Lunar Laser Ranging to retro-reflector arrays on the lunar surface, and 92% of the effective observations are concentrated in two sites (McDonald in the U. S. and Grasse in Europe). Furthermore, LLR observations are independent of the International Celestial Reference Frame (ICRF). It is difficult to tie lunar movement to the nearly inertial celestial reference frame. These deficiencies limit the increase of LLR's impact on terrestrial and lunar science. The successful launch of Chang'E-3 (CE-3) provides a new chance to break through these limitations. CE-3 was launched on December 2, 2013. It made a soft landing at the plains of Sinus Iridum (Rainbow Bay) successfully on the lunar surface on 14 December 2013. The lander will stand in place for at least one year. It is equipped with an X-band transponder, which can transmit an X-band signal to the ground when it is tracked by the Chinese Deep Space Network (CDSN). This signal not only can be utilized to provide range and Doppler observations by CDSN, but can also be received by widely distributed IVS antennas to provide VLBI observations. Combining these radio measurements from the earth to the moon, this technique can be called Lunar Radio Measurement (hereafter LRM) collectively. Based on these plentiful kinds of observations from CE-3, the LRM has at least four advantages as compared with

LLR. First, widely distributed IVS antennas provide a good PDOP (Position Dilution of Precision) factor. Secondly, VLBI is the unique technique to define inertial celestial frames; it can tie the lunar orbit to ICRF much more accurately. Third, range, doppler, carrier phase, time delay, and delay rate can be accessed at the same time, so it provides richer information than LLR. Fourth, an active radio signal can give a more intense observation. It is expected that the LRM will give more contributions to terrestrial and lunar science, especially in tying the earth-moon dynamical and kinematical frames. In view of this, it is of high interest to carry out research on the LRM utilizing the CE-3 signal.

2 Technique System

The LRM technique system includes two parts. One is a ground tracking and measurement system, and the other is a radio transponder on the spacecraft. The ground tracking and measurement system consists of CDSN, CVN, and BACC. The observations of CE-3 utilize the CDSN 66-m antenna at Jiamusi (JMS for short) and the 35-m antenna at Kashi (KSH for short). Two CDSN stations are responsible for receiving telemetry data and sending telecontrol instructions. They also provide range and range rate messages directly from baseband at the station, record raw data in the VSI or VSR formats, and transfer data to the correlation center at BACC for correlation of the time delays of the JMS—KSH baseline. Five CVN stations record raw data in Mark 5 and transfer the data to the SAO correlation center for correlation of the time delays of the SESHAN (TIANMA) — BEIJING — URUMQI — KUNM stations' baselines. All CDSN stations and CVN stations deployed an H-atomic clock, a GNSS receiver, and a WVR to ensure high performance of observations. To expand the ground observation distribution, an intercontinental IVS baseline is needed to provide a better PDOP factor. But because the CE-3 transmits signals only when CDSN is tracking, IVS antennas in Asia, Europe, Africa, and Australia are good candidates. Furthermore, the CE-3's signal is much stronger than an extragalactic radio source, so it is not essential to use a large antenna; perhaps a 12-m VGOS antenna is a better candidate. To test the performance of a small antenna, an old 12-m antenna at BACC/AFDL was reformed to receive the CE-3 signal. Because the LNA and the first level down-conversion are placed more than 60 meters away from the control room where the Rubidium atomic clock (HP5156) is placed, Active Phase Compensation Technology (APCT) was designed to ensure the down-conversion and to ensure that the A/D sampler gets stable LO when the local oscillation (LO) transfers from HP5156 to down-conversion and to the A/D sampler by optical fiber, By the APCT, the LO phase stability can be higher than 0.05 rad. With the ground antenna, the correlation center, and the CE-3 spacecraft, both the lander and the rover can be utilized as radio beacons on the lunar surface. These radio beacons are different from extragalactic radio sources in the follow aspects: (1) the lander and the rover can only work during the lunar day; (2) there are several single frequency signals (DOR and range tone) coherent with the uplink signal and with the high frequency stability($\sim$10-14) when the ground antenna's main carrier is uploaded to the lander; (3) the lander sends a wideband data transmission signal or DOR and range tone only when BACC gives instructions, and (4) the rover sends its telemetry signal all the time during the lunar day.

3 Experiments and Performance

By different tracking modes in the CE-3 mission, different observations can be achieved: (1) from baseband in the CDSN station, the range and the range rate can be acquired; (2) from the correlation center, the time delay and the delay rate of different baselines can be acquired; (3) from the correlation center, when the SBI mode is utilized, the difference in the time delay and the delay rate between the lander and the rover can be acquired, and (4) the VSI raw data in the digital backend and the carrier phase can be extracted, regardless of the baseband; if the ambiguities can be fixed, a higher phase range can be acquired. To get the time delay and the delay rate, the raw data recorded at different stations must be transferred to the correlation center. In the correlation center, a correlator must be deployed. With the development of the computer technique, the software correlator has become more and more popular. The BSCS (BACC Software Correlator System) is developed with the basic principle of DiFX at BACC. The software correlator has the ability to process VLBI data for both spacecraft navigation and quasars. The software is written modularly in the C programming language. The correlator is operated by shell script and is intended to run in clusters of the multiprocessor shared-memory machine. Figure 1 gives the performance of all kinds of observations in CE-3 tracking measurements.

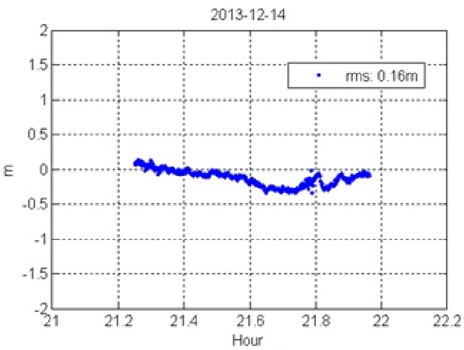

(a)delay

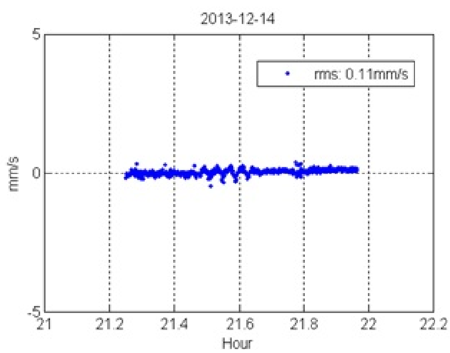

(b)delay rate

Fig. 1 Delta-DOR tracking observable accuracy. The random error is about 0.5 ns and 0.33 ps/s.

It shows that the Delta-DOR tracking observable accuracy is about 0.5 ns and 0.33 ps/s separately; SBI tracking shows the excellent agreement between the observation and the status of the rover and the lander. The movement of the rover can be identified to the order of 1 mm with SBI tracking data. Figure 3 also shows that the accuracy of the carrier phase can be better than 0.1 radians for the CDSN and 0.5 radians for the 12-m antenna, which means that an accuracy of 1-2 mm for phase ranging can be obtained if the ambiguity can be fixed.

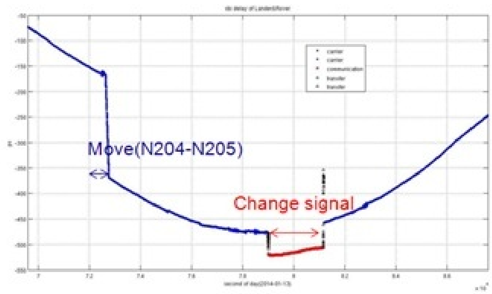

(a) identify the movement of rover

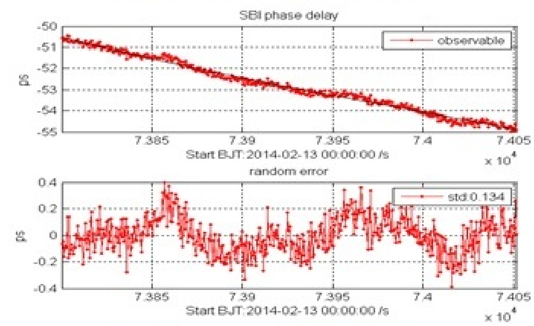

(b) random error of SBI is 0.134 ps

Fig. 2 SBI observing results.

4 Scientific Prospects

Now, with the radio measurement of the CE-3 lander, we can get a high precision and denser earth-moon observation ranging, and a greater contribution to terrestrial and lunar science is expected from the CE-3 program. To analyze the proper lunar science from the Lunar Radio Measurement technique, the MEKAS (Moon-Earth Kinetics Analysis Software) software is developed at the BACC. The software's main component is a collection of modules coded in FORTRAN. MEKAS has four main basic functions: observation simulation, generation of partial derivatives, estimation of uncertain parameters, and covariance analysis. The observations that can be processed in MEKAS include two-way/three-way Ranging and Doppler, VLBI delay and rate, DOR and DOD, Lunar laser Ranging, etc. The parameters that can be estimated or considered include locations of lunar landers or reflectors, station coordinates, earth rotation parameters, observation bias, and lunar love numbers, and the selection and settings of the parameters are flexible. The input to MEKAS is a card file named 'mmekas.dat'. In the input card file,

Table 1 The positioning accuracy of the lunar lander without IVS stations.

days	duration	case 1 std(x)	case 1 std(y)	case 1 std(z)	case 2 std(x)	case 2 std(y)	case 2 std(z)
1	1 hour	19.8951 m	0.9469 m	0.9547 m	28.2151 m	9.3839 m	9.5947 m
1	3 hour	19.4784 m	0.5687 m	0.9371 m	40.8174 m	6.9534 m	9.7245 m
2	1 hour	17.6182 m	0.7441 m	0.6484 m	42.3477 m	11.5982 m	8.1453 m
2	3 hour	12.0579 m	0.3046 m	1.2913 m	43.2007 m	8.4646 m	6.3751 m
5	1 hour	6.6759 m	0.5335 m	0.7352 m	46.9875 m	5.9377 m	13.7138 m
5	3 hour	3.8214 m	0.1899 m	0.3807 m	23.6102 m	7.2608 m	6.8793 m

Table 2 The positioning accuracy of the lunar lander with joint tracking from IVS stations.

days	duration	case 1 std(x)	case 1 std(y)	case 1 std(z)	case 2 std(x)	case 2 std(y)	case 2 std(z)
1	1 hour	30.9289 m	0.6526 m	3.3695 m	37.0099 m	0.80756 m	4.0622 m
1	3 hour	15.7896 m	0.3161 m	1.7339 m	21.5096 m	0.44933 m	2.4005 m
2	1 hour	7.0289 m	0.1572 m	0.7977 m	7.3167 m	0.20823 m	0.8411 m
2	3 hour	4.05749 m	0.0985 m	0.4622 m	4.5024 m	0.18013 m	0.5292 m
5	1 hour	0.6576 m	0.0881 m	0.0614 m	0.9487 m	0.1439 m	0.1042 m
5	3 hour	0.4142 m	0.0569 m	0.0365 m	0.8968 m	0.1409 m	0.0918 m

Table 3 The uncertainty of EOP estimation with the lunar lander.

Tracking arc	case 1 std(xp)	case 1 std(yp)	case 1 std($UT1-UTC$)	case 2 std(xp)	case 2 std(yp)	case 2 std($UT1-UTC$)
1 hour	0.22 mas	0.28 mas	0.05 ms	0.38 mas	0.41 mas	0.22 ms
2 hour	0.17 mas	0.19 mas	0.03 ms	0.37 mas	0.28 mas	0.20 ms
3 hour	0.17 mas	0.16 mas	0.03 ms	0.36 mas	0.20 mas	0.15 ms
4 hour	0.16 mas	0.13 mas	0.02 ms	0.35 mas	0.18 mas	0.09 ms

we can set the following items: (1) the location and the uncertainty of the lunar landers or lunar laser reflectors; (2) an observation to be processed in MEKAS and the weight settings; (3) the parameters to be estimated or considered in MEKAS, and (4) one or more observation files. With MEKAS, we performed some analysis. The following tables show the possible positioning accuracy of the lunar lander based upon the tracking data from CDSN and CVN. Because it is hard to determine the tracking data bias each pass in the positioning performance, a priori information for the elevation of the lunar lander with an uncertainty of ten meters is considered. Without regard to the uncertainty of the tracking station coordinates, the accuracy of the positioning gets better as the tracking arc increases. As the tracking data reaches five days, the results would be at a level of 1 m. Once an uncertainty of 15 cm for the tracking stations is taken into account, the accuracy may be decreased by ten meters. Table 1 lists the positioning accuracy of the lunar lander. Case 1 considers only the observation noise, while Case 2 also considers the uncertainty of the tracking station coordinates. With the assistance of IVS, VLBI stations in the southern hemisphere may join the tracking of the Chang'E-3 lunar lander. A simulation is performed with tracking stations from CDSN, CVN, and IVS. Table 2 shows the possible positioning accuracy of CE-3 with the joint tracking from IVS tracking stations. Case 1 and Case 2 are the same as in Table 1. The LLR retroreflector array principal axis coordinates were determined during the solution leading to development ephemerides. Comparing the LLR retroreflector coordinates from DE421 and DE430, there is also a shift of 1 m along the x axis. The results mean that the accuracy of the lunar lander is at the same level as that of the retroreflector, and the lunar lander can be treated as a lunar control point. Normally, the EOP is determined at the IERS Earth Orientation Center in the form of combined solutions derived from individual series, and the results are published in a bulletin with a delay of thirty days until the date of publication. The accuracy of polar motion is about 0.1 mas, and that of UT1 is 0.02 ms. Once the coordinates of the lander are determined precisely, it is possible to get the same accuracy as IERS distributed for EOP and UT1. Table 3 gives the possible accuracy for EOP estimation with a 1 m uncertainty of the lunar lander coordinates. Case 1 only considers the observation noise, while Case 2 considers observation noise and an uncertainty of 1 m for the lunar lander coordinates. In the construction of DE430,

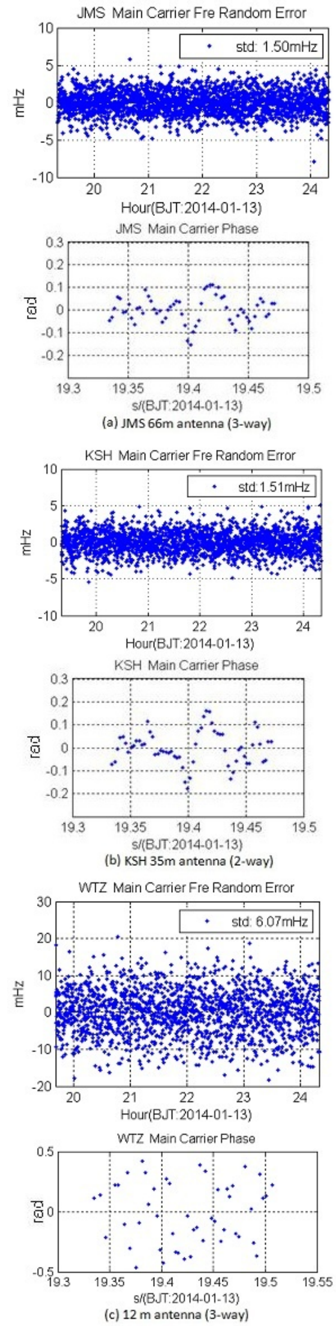

Fig. 3 Doppler and carrier phases at different antennas.

Lunar Love number h2 was estimated, while k2 was set equal to a GRAIL-determined value. The lunar displacement Love numbers from the solution leading to DE430 are h2=0.0476 and l2=0.0107. Comparing the h2 from DE421 and DE430, there is a shift of 0.01. With long term tracking of the lunar lander, it is also possible to estimate lunar love numbers. Table 4 gives the results from covariance analysis for the estimation of lunar love numbers. As the tracking arc reaches 30 days, the uncertainty is about 0.0053 for h2 and 0.0023 for l2 respectively. The LRM technique acting on the lunar lander can contribute to the estimation of lunar love number h2.

Table 4 The uncertainty of lunar love number estimation.

Arc	Lunar love numbers std($h2$)	Lunar love numbers std($l2$)
1 day	4.1576	5.7142
7 days	0.0355	0.0080
15 days	0.0123	0.0053
30 days	0.0053	0.0023

5 Summary

The CE-3 lander and the rover stand in place on the lunar surface, sending radio signals. After the positioning accuracy of the lunar lander improves to the sub-meter level, the lander can be utilized as a very good radio beacon to contribute to lunar and terrestrial science as LLR reflectors. The analysis results from MEKAS show that the current accuracy of radio measurements is expected to ensure one meter level positional precision of the CE-3 lander if the observing arc is enough, so it can be a good control point as a laser reflector; as a highly precise positional radio beacon on the moon's surface, its signal can be received by ordinary IVS antennas—even a 12-m antenna, when CDSN tracks the lander. Therefore, it is convenient and cheap to expand the ground observation distribution, a target that the LLR community will always be eager to pursue. This is expected to contribute more to terrestrial and lunar science; the geodetic VLBI technique's observation of quasars provides highly accurate positions for the ICRF, EOP, site coordinates etc. With the LRM technique's millimeter observational precision, if it is used with the LLR technique, it is possible to make great progress in many aspects of terrestrial and lunar science including lunar ephemerides, lunar physics, the moon's interior, various reference frames, earth orientation parameters, earth-moon dynamics, and testing Einstein's theory of general relativity.

Phase-based Radiometric System in Lunar Radio Measurements

Tian-Peng Ren[1,2], Ge-Shi Tang[1,2], An-Xu Zhang[3], Lue Chen[1,2], Song-Tao Han[1,2], Yi-Tang Dai[3]

Abstract In December 2013, the Chang'E-3 lunar lander carrying an X-band beacon made a successful soft landing in the Rainbow Bay area, which fulfills a prerequisite for lunar radio measurement (LRM). A new LRM system had been built before the Chang'E-3 launch. And a stable phase transfer for multiple frequencies has been studied, and high-precision phase has been estimated for phase-based radiometric measurements. Finally, signal processing on the satellite DOR carrier has been conducted, and 10 mHz frequency estimation precision and 0.02 circle (7.2°) phase conjunction precision have been achieved.

Keywords Lunar radio measurement (LRM), lunar laser ranging (LLR), phase-based radiometric system, Chang'E-3 lander

1 Introduction

Precise lunar measurements form the basis for research into lunar motion and lunar geodesy. The temporal and spatial lunar reference frame is almost built based on high-precision lunar measurements. After the first lunar laser ranging (LLR) in the Apollo 11 mission, America and the former Soviet Union placed four other lunar laser mirrors. In more than 40 years, lunar laser ranging has developed, but has been limited to measuring efficiency, which needs at least eight minutes to obtain one result. Up to now, only about 20,000 standard point results have been obtained.

Compared with LLR, lunar radio measurement (LRM) can be conducted without effects caused by weather conditions and the lunar phase, which will cause a systematic error in measuring. (To avoid a strong background noise, laser lunar tracking is almost always done when the moon is halfway between new and full—rarely when the moon is full and never when the moon is new.) Moreover, once the radio transmitter of a lunar lander works, the target can be continuously tracked with a high temporal resolution. In the 1960s, radio measurements were used to obtain the lunar landing point for the American Apollo project. After 1977, due to funding limitations, LMR was interrupted for about 30 years. In December 2013, the Chang'E-3 lunar lander carrying an X-band beacon made a successful soft landing in the Rainbow Bay area, which provides a chance for us to conduct LRM again.

In contrast to traditional ranging measurements that use a pseudo code or a sidetone, the phase of a carrier is estimated and applied for precise orbit determination with a high accuracy range in the proposed LRM. Because the carrier phase in LRM can easily be polluted by phase shifts caused by environmental temperature changes, mechanical vibrations, and so on, a new LRM system in which a stable phase transfer is studied and applied to eliminate the phase error was built before the Chang'E-3 launch.

2 Signal Model

After receiving a satellite downlink signal, the radio signal should be downconverted outdoors, and then

1. National Key Laboratory of Science and Technology on Aerospace Flight Dynamics (AFDL)
2. Beijing Aerospace Control Center (BACC)
3. Beijing University of Posts and Telecommunications (BUPT)

transmitted to a room via a cable. Suppose that the signal transmitted via the cable is presented as:

$$S(t) = A(t)\cos(2\pi f_c t + \phi)$$

With a link delay τ, the signal achieved indoors can be presented as:

$$S(t) = A(t)\cos[2\pi f_c(t-\tau) + \phi]$$

Due to changes in the environmental temperature and other influences, the link delay τ may fluctuate, which is defined as $\delta\tau$. In this case, the signal phase shift can be described as:

$$\delta\phi = 2\pi f_c \delta\tau$$

and $\delta\phi$ will cause a direct measurement error. To suppress the phase shift, we can compensate for the delay fluctuation $\delta\tau$ and apply a low frequency f_c. In the proposed system, we use an IF frequency f_c of about 70 MHz, which is far lower than the X-band and L-band frequencies.

To downconvert a radio signal to an IF signal, two levels of downconvertors are normally applied, where two local oscillator (LO) signals are required. In the proposed LRM system, we demonstrated a phase stabilization technique for multiple LO signals, where one of the LO signals is used as reference and round-trip transferred between the central station and remote end. Hence, the reference LO signal can carry the phase variation that arises from the fiber link. To stabilize the delay of the fiber link, the wavelength of the optical carrier is adjusted according to the phase variation of the reference LO signal. Obviously, the stability of the link delay will bring phase stabilities of other LO signals transferred through the same fiber link. Experimentally, LOs at frequencies of 1.21 GHz and two other values have been transferred through a fiber link; significant phase drift compression is observed. A recorded result is shown in Figures 1 and 2. The phase fluctuation of uncompensated delivery is 1.0 degree in a short time (the value will become much larger in hours). While the active compensation is on, the phase fluctuation is suppressed to about 0.05 degrees.

To obtain high-precision data products, the measurement accuracy of the system at X-band is required to be: frequency estimation accuracy better than 10 mHz and precision of relative range of about 1 mm.

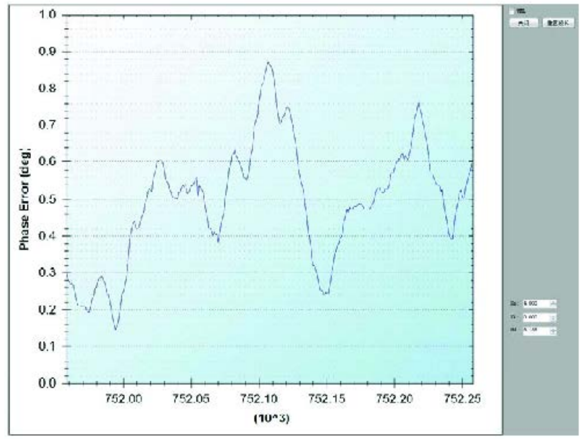

Fig. 1 Phase fluctuations of the reference signal without compensation.

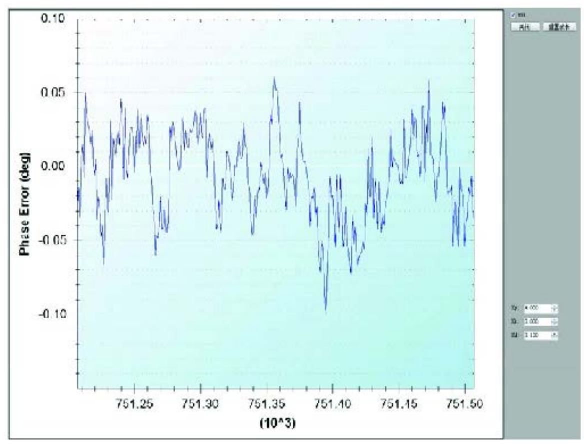

Fig. 2 Phase fluctuations of the reference signal with compensation.

The prerequisite for the overall accuracy is to eliminate each error source, including the phase drift of the RF signal.

3 Hardware System

3.1 Systematical Framework

The LRM system includes an S/X-band antenna, S-band and X-band radio links, a signal sampler, and a storage unit, as shown in Figure 3. Moreover, a phase-stable transmission sub-system for RF LO signals and a GNSS-based precise timing sub-system are built for phase-based range measuring.

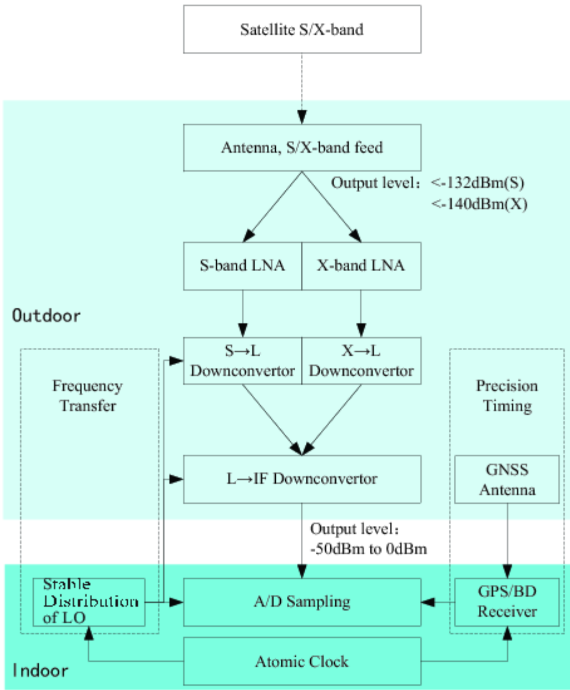

Fig. 3 Diagram of the LRM system.

Note that, to eliminate each measuring error, there are two innovations applied in the system: 1) RF LO signals, rather than an IF frequency reference signal, are transmitted to the down-converter directly, and a phase-stable transmission for RF LO signals is introduced, which has been discussed above, and 2) the down-converter is moved close to the low noise amplifier to shorten the RF cable.

3.2 Equipment

The LRM hardware system has been built completely and has received the downlink signal of the Chang'E-3 satellite. Part of the hardware equipment is presented in Figure 4.

4 Signal Processing

On 17 December 2013, the DOR signal transmitted from the Chang'E-3 lander was received. As a traditional signal processing, the received frequency has been estimated, as shown in Figure 5, where we can see that the precision of the estimation is about 10 mHz.

Fig. 4 Hardware equipment of the LRM system.

Moreover, the carrier phase of the DOR signal is also obtained for precise relative ranging, as shown in Figure 6. To avoid integer ambiguity, the phase skip between each processing conjunction is also given in Figure 6. Due to small phase skips during the observation, we believe there is no integer ambiguity.

Theoretically, the relative ranging between the lander (also the lunar) and the receiving antenna is smooth. Hence the phase of the carrier is also smooth. However, after a seventh order polynomial fitting, the residual is larger than the phase skip in Figure 6. And the fluctuation is clear, as shown in Figure 7. The reason is still unknown. If the fluctuation is caused by lunar motion with a high frequency, it will be very interesting.

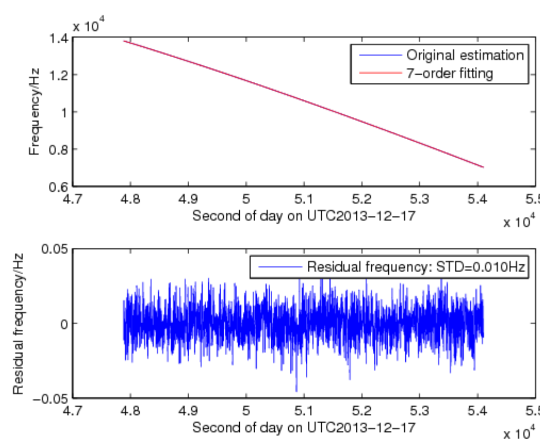

Fig. 5 Frequency estimation of the Chang'E-3 lander.

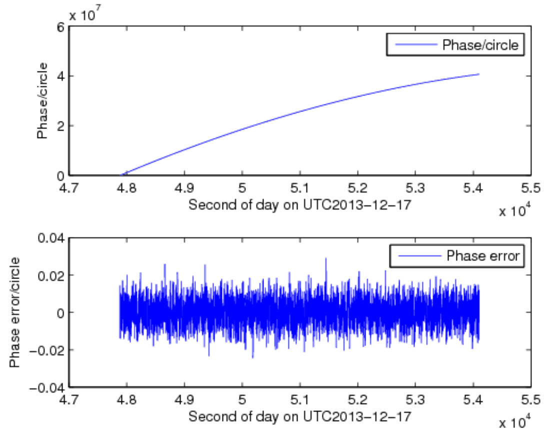

Fig. 6 Phase estimation and its conjunction error of the Chang'E-3 lander.

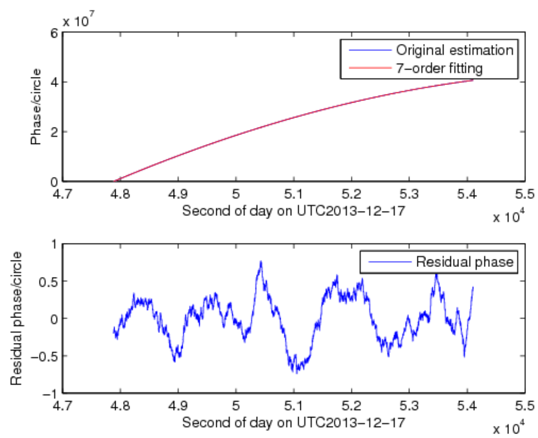

Fig. 7 Phase estimation and the residual with a seventh order polynomial fitting of the Chang'E-3 lander.

5 Conclusions

To obtain precise relative range data between the moon and the earth, a phase-based lunar radio measurement (LRM) system has been built to track the Chang'E-3 lunar lander. After proposing a stable phase transfer for multiple frequencies, the phase shift at the receiver is almost suppressed. Finally, the frequency and phase of a satellite DOR carrier are estimated with a frequency precision of 10 mHz and a phase conjunction precision of 0.02 circle (7.2°). Furthermore, after a seventh order polynomial fitting, there is an obvious fluctuation in the residual phase, which is very interesting and still needs to be explained.

References

1. P. L. Bender, D. G. Currie, S. K. Poultney, et al. The Lunar Laser Ranging Experiment: Accurate ranges have given a large improvement in the lunar orbit and new selenophysical information. Science, 182(4109), pp. 229–238, 19 Oct. 1973.
2. J. G. Williams, X. X. Newhall and J. O. Dickey. Relativity parameters determined from lunar laser ranging. Phys. Rev. D 53, 6730, 15 Jun. 1996.
3. J. G. Williams, S. G. Turyshev and D. H. Boggs. Progress in Lunar Laser Ranging Tests of Relativistic Gravity. Phys. Rev. Lett. 93, 261101, 29 Dec. 2004.
4. Davis, E. Darrell and Alan M. Victor. Synthesized multiple conversion receiver system with provision for avoiding receiver self-quieting spurious response. U.S. Patent No. 4551856. 5 Nov. 1985.
5. A. Zhang, Y. Dai, F. Yin, T. Ren, et al. Stable radio-frequency delivery by λ dispersion-induced optical tunable delay, Opt. Lett. 38, 2419–2421, 2013.

VLBI Software Correlator at the Interferometric Tracking Center of the China Deep Space Network

Songtao Han[1,2], Geshi Tang[1,2], Lue Chen[1,2], Jianfeng Cao[1,2], Tianpeng Ren[1,2], Mei Wang[1,2]

Abstract With the development of computer techniques, the VLBI software correlator is more and more popular. This article presents the development and performance of the software correlator used in the Interferometric Tracking Center. The software correlator has the ability of VLBI data processing both for spacecraft navigation and VLBI geodesy. Also, the data formats of VSR (VLBI Science Receiver) and VSI (VLBI Standard Interface) are accommodated. The correlator is written modularly in the C programming language and operated by shell script. The complex vector mathematics of the IPP (Intel Integrated Performance Primitive) library is induced because the efficiency of computing can be improved greatly. Parallel algorithm processing is adopted in the software. We present the results of the multi-agency VLBI experiment conducted with the ESA Spacecraft Venus Express in May 2013 and the Chinese Chang'e-3 lunar navigation in December 2013, which verifies the performance of the software correlator.

Keywords VLBI, software correlator, VSI, VSR

1 Introduction

In 2013, China Deep Space Stations JMS and KSH were deployed. At the same time the Interferometric Tracking Center of China Deep Space Network was founded in the Beijing Aerospace Control Center. The center takes the responsibility of organization tracking, making schedules, receiving raw VLBI data, monitoring the interferometric tracking system status, data processing, and so on. This paper focuses on the software correlator developed in BACC, which is named BSCS (BACC Software correlator system).

Fig. 1 Interferometric Tracking Center of the China DSN.

2 Software Development

The software correlator has a short history. With the pace of China DSN construction, the first generation software correlator was developed using Matlab, which is a convenient programming language for development, debugging, and graphical display. The second version was developed with the C programming language, with the basic complex structure and complex mathematics including an FFT developed by ourselves. The software runs in a multiprocessor shared-memory machine. To meet spacecraft navigation with a heavy data rate, the third version was developed under the ba-

1. National Key Laboratory of Science and Technology on Aerospace Flight Dynamics
2. Beijing Aerospace Control Center

sic principle from DiFX. The parallel algorithm processing is adopted in the software. The correlator is designed to run in Beowulf clusters of commodity machines. The parallel algorithm processing is adopted in the software. Then, two strategies are adopted: first, the correlator is designed to run in clusters combined with high performance computers, and the data streams of all the stations are distributed to each core computer according to the time stamp of the data. Second, each computer makes use of a number of threads to maximize performance. The core nodes make use of an allocatable number of threads to maximize performance on a heterogeneous cluster. The structure of the correlator system is shown in Figure 2. The manager node

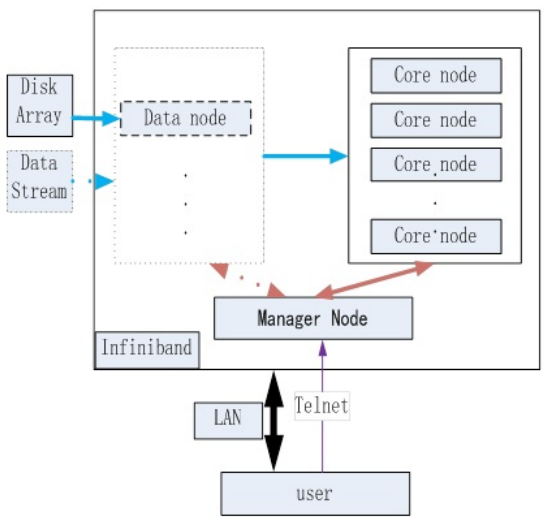

Fig. 2 Structure of the correlator system.

also performs cross multiplication and long-term accumulation, outputs the observable, and auto-crosses the spectrum, fringes, and logs. The core nodes take the key processing of the algorithm, including fringe rotation compensation, conversion to frequency-series, and fractional sample compensation. The cores act as short-term accumulators (STAs). These days, data stored in the disk is processed off-line, and the interface is preserved for real-time processing in the future. Data stream transfer within the cluster is handled via the Message Passing Interface standard. Local data storage consists of RAIDs with a total capacity of 100 TB. All the nodes are interconnected through a 20 Gbps InfiniBand. The control terminal and processing cluster are connected via a LAN. A trained operator signed in the manager node through telnet runs the software via shell script. Progress and running status information can be displayed in the shell window. Three files are necessary to run the correlator. The first is a MACHINES file, which contains all of the compute nodes in the cluster. Usually the file is unchanged unless any PC server is added or eliminated from the cluster. The second file is the run nodes file, which lists the necessary nodes on which the program will run. All the information used for data processing is listed in the configuration file. Data formats with protocol RDEF (Raw Data Exchange Format) and VSI (VLBI Standard Interface) are accommodated. These days, the output of the correlator is according to the OD system in BACC. The recording parameters include the sample rate, the quantization bit, and the number of channels. The correlator uses clock models in the form of a single clock offset and linear rate as a function of time per antenna. The delay model used for correlation is supplied by the OD group, in the form of high-order polynomials for each antenna.

3 Performance

After the deep space stations were deployed, the first multi-agency Delta-DOR experiment was conducted with the ESA spacecraft Venus Express in May 2013. One of the aims of this experiment is to verify the ability and the accuracy of the correlator. A total of eight stations participated in this co-operative observing, including SH/BJ/KM/UR of the CVN, KSH/JMS of the CDSN, and CEB/NNO of the ESA. We focused on the accuracy of the software correlator and the consistency of the observable values from the correlator, and ESOC indicates that an internal RMS accuracy of 0.2 ns was achieved. We can find that for quasar observations, the result has better consistency than for spacecraft observations. For scans 1, 3, 4, and 6, the consistency was on the order of 10 picoseconds, but for scans 2 and 5, on the order of 100 picoseconds. The differences may exist in the delay models used. The second important implication of the BACC Software Correlator System is for the China CE-3 project. All types of tracking raw data are transferred to BACC and processed with our correlator within 24 hours. Observables were used for high accuracy orbit determina-

Table 1 Comparison between BACC and ESOC.

Target	UTC	ESOC(ns)	BACC(ns)	Difference
0507+179	07:48:33	-4180977.909	-4180977.896	0.013ns
VEX	07:59:03	-91922.845	-91922.630	0.215ns
0507+179	08:10:33	-1636282.394	-1636282.428	0.036ns
0507+179	08:19:32	-569384.990	-569385.004	0.014ns
VEX	08:30:03	3451412.413	3451412.6590	0.246ns
0507+179	08:41:33	2089369.712	2089369.695	-0.017ns

tion including raw VLBI data, clock synchronization, and met data. These pictures show the interferometric fringes for quasar processing and CE-3 spacecraft. Observables include ranging, doppler tracking, delays and delay rates within the baselines of the CVN, and delays and delay rates within the baselines of the China DSN. All these observables are used for orbit determination. When we compared the observables within the China DSN with the high accuracy orbit, the residual delays were less than 1 ns, corresponding to a maximum angular error of tens of nanoradians with baseline length 4,350 km.

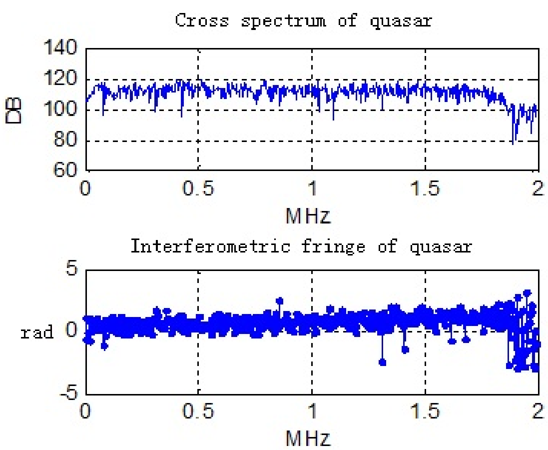

Fig. 3 Correlation results of quasar.

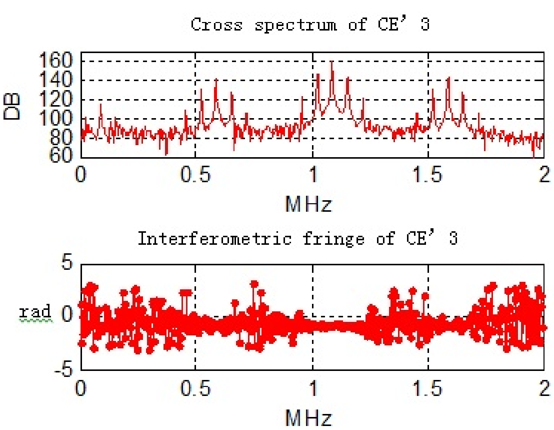

Fig. 4 Correlation results of CE-3.

Table 2 Accuracy statistics in the CE-3 project.

	Transfer orbit	Lunar orbit	After landing
Integration Time (s)	4.194304	4.194304	4.194304
Scan length (h)	5.3	13.2	0.7
Frequency	f1	f2	f2
Delay error (ns)	0.87	1.17	0.53
Delay rate error (ps/s)	0.90	0.77	0.37

4 Conclusions

As a new participant in the VLBI domain, we have successfully developed the software correlator and have successfully used it in VEX experiments and the China CE-3 project. In the future, packages of geometric delay modeling, station synchronization search, and propagation medium analysis will be integrated into the software correlator. Also we will improve the correlator system efficiency, extend the correlation cluster, and expand the output for different applications.

References

1. Deller, A. T., Tingay S. J., Bailes M., et al. DiFX: a software correlator for very long baseline interferometry using multiprocessor computing environments *Publications of the Astronomical Society of the Pacific*, 119(853), pages 318-336, 2007.
2. Kondo T., Kimura M., Koyama Y., et al. Current Status of Software Correlators Developed at Kashima Space Research Center*IVS 2004 General Meeting Proceedings* pages 186-190, NASA/CP-2004-212255, 2004.
3. Deller A. T., Brisken W. F., Phillips C. J., et al. DiFX-2: a more flexible, efficient, robust, and powerful software correlator*Publications of the Astronomical Society of the Pacific*, 123(901), pages 275-287, 2011.
4. Tingay S. J., Alef W., Graham D., et al. Geodetic VLBI correlation in software *Journal of Geodesy*, 83(11), pages 1061-1069, 2009.

Radio Navigation Beacons on the Moon, Lunar Geodetic VLBI System, Physical Libration of the Moon for Chang'E-3/4, Luna-Glob, Luna-Resource and SELENE-2 Projects

Alexander Gusev[1,2], Jinsong Ping[2], Hideo Hanada[3], Fuyuhiko Kikuchi[3], Alexander Kosov[4], Jinling Li[5], Oleg Titov[6]

Abstract The future lunar missions of Chang'E-3/4, Luna-Glob, Luna-Resource, and SELENE-2 will consist of a lander and an orbiter. Using the Lunar Same Beam, Differential and Inverse VLBI technologies, we anticipate to determine the coordinates of the radio beacons on the lunar surface with an accuracy of 1 mm for various space projects on the Moon. Small radio telescopes being installed on the surface of the Moon and incorporated into the existing network will help to improve the traditional IVS products by a factor of ten or even more. The model of the two-layer Moon gives several normal rotational modes—Chandler Wobble and Free Core Nutation. They can play an important role in the determination of the core parameters.

Keywords Lunar SBI, geodetic VLBI, lunar libration

1 Introduction

Many space agencies are planning lunar missions, including scientific observations in close proximity to and/or on the surface of the Moon. One of these experiments proposes to place two landers with radio beacons onto the lunar near side and to launch one or more orbiters into a lunar orbit. The difference of the distances between two radio beacons and Earth will be assumed to be measured by the methods of Inverse VLBI: the radio signal from various radio beacons will be sent to Earth antenna systems using the orbiter. The estimation of the physical libration angle accuracy is made for various locations and configurations for the radio beacons.

The geodetic VLBI network managed by the IVS provides high accurate positions of the reference radio sources, radio telescope coordinates, Earth Orientation Parameters (EOP), and so on. A small radio telescope being installed on the lunar surface (by the year 2020) and incorporated into the existing network will help to improve these traditional IVS products by a factor of ten or even more. This new instrument will be able to detect some known effects with an unprecedented accuracy as well as new effects, which are not available for other ground-based instruments or space missions.

2 Same Beam, Differential and Inverse VLBI for Lunar Space Projects

The future lunar missions of Chang'E-3/4, Luna-Glob, Luna-Resource, and SELENE-2 will consist of a lander and an orbiter. Using the Lunar Same Beam, Differential and Inverse VLBI technologies, we anticipate to be able to determine the coordinates of the radio beacons on the lunar surface with an accuracy of 1 mm for various space projects on the Moon. The radio sources installed on the orbiter and the lunar landing unit (lander or survival module) transmit three S-band signals (SELENE-2; Kikuchi, 2014; Sasaki, 2012) or an X-band and a Ka-band signal (Luna-Glob; Kosov, 2011) to the Earth. The double difference range between two lunar radio sources and the VLBI stations is measured with an error of less than 1 mm. This mea-

1. Kazan University
2. NAOC CAS
3. NAOJ
4. ISR(IKI)
5. SHAO CAS
6. Geoscience Australia

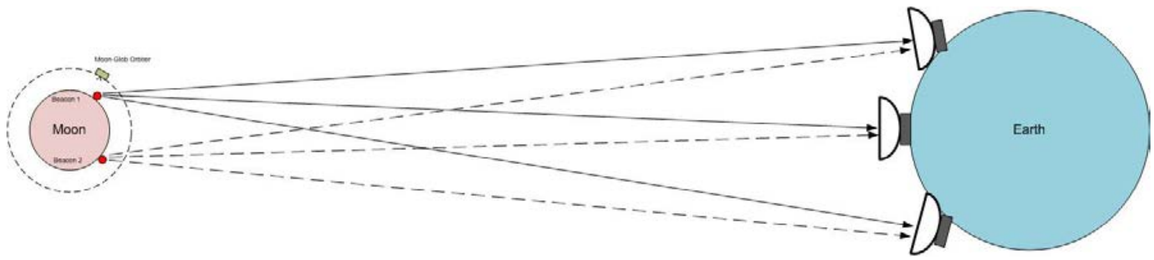

Fig. 1 Moon-Glob radio science experiment (2017).

surement will contribute to the determination of the position of the orbiter and the lunar landing unit.

The Radioscience Experiments (Kosov, 2011) will be performed with two lunar radio beacons on the lander and receiver of the "Luna-Glob" orbiter. **Science task 1:** Study of internal lunar motions using the phase-referencing method with support from ground radio telescopes for investigations of the internal structure of the Moon. **Science task 2:** Test the gravitational field (radio science of Lander and Orbiter). **Service task**: Provide radio-beacon service for future Landers and Orbiters. **Navigation task**: Determine the lander's position with an accuracy of 10 cm or better. The method of research will use D-VLBI technology. The planning cyclogram will contain each lunar day for 12–15 lunar days. The main features of the instruments are very high frequency stability and very narrow spectrum line width of the beacons' signals and the orbiter's receiver local oscillator signal. Such performance is possible due to the frequency standard used in the beacons and the orbiter's receiver.

The beacons will irradiate signals at two frequency bands: 8.4 GHz and 32 GHz. The 8.4-GHz signals will be directed to the Earth and, together with the VLBI ground-based network, will be used for celestial mechanics experiments and navigation. It will be possible to measure the beacon's positions with an accuracy of about 1 cm and to register lunar libration. The 32-GHz band will be used for orbiter navigation and gravitation field investigations. The Ka-band signal will be directed to zenith and will be received by the orbiter's receiver. An investigation of the non-uniformity of the lunar gravitation field (experiment INGL) will be performed in the vicinity of the landing regions with an accuracy of 3–5 mGal. The spatial resolution will be about 20 km. The experiment is based on precise Doppler shift measurements. The velocity and the acceleration will be recorded. It is planned to make beacons of an expected life time of five years and more. In first stage the beacons will be powered by solar batteries and then by nuclear power.

3 Lunar Geodetic VLBI

The geodetic VLBI network managed by the International VLBI Service provides high accurate positions of the reference radio sources, radio telescope coordinates, and Earth Orientation Parameters (EOP) (Schuh and Behrend, 2012). A small radio telescope being installed on the Moon surface and incorporated into the existing network will help to improve these traditional IVS products by a factor of ten or even more. In addition, this new instrument will be able to detect some known effects with an unprecedented accuracy and new effects, which are not available for other ground-based instruments or space missions.

3.1 Earth-Moon VLBI Project

The geodetic VLBI technique (Titov and Gusev, 2013) is capable of measuring the group delay between two radio telescopes with a formal error σ_τ of about 20 ps ($\approx$ 6 mm in linear scale). The accuracy of the different parameters (radio source positions, Earth orientation parameters, and VLBI station coordinates) can roughly be estimated as follows: $\sigma \sim \frac{\sigma_\tau}{\tau} = \frac{c\sigma_\tau}{B}$, where B is the length of the baseline between two radio telescopes and c is the speed of light. In accordance with the VGOS plans, the precision is likely to improve to 1 mm in linear scale (3.3 ps) (Petrachenko, 2010).

3.2 Orbital Geocentric Acceleration of the Moon

While the ground VLBI systems are not sensitive to the mutual acceleration between the radio telescopes, for the Earth-Moon baseline the VLBI group delay model must include the barycentric acceleration of the second station (Vlasov et al., 2012). For $B \sim 10^5$ km the time delay is about 1 s. For the precision of 1 mm the acceleration of 2 mm/s^2 must be implemented. The orbital geocentric acceleration of the Moon is about 3 mm/s^2. This means that all variations of the Moon acceleration are essential for accurate reductions. The time delay on the Earth–Moon baseline will be feeling the change of acceleration due to strong earthquakes (up to several m/s^2) and other seismic events. The ability to detect the acceleration of 20 μGal with high temporal resolution provides the opportunity to use this interferometer for gravimetric research.

3.3 General Relativity (PPN Parameters)

A long baseline could be effectively used for studying the propagation of electromagnetic waves in the gravitational field. The post-Newtonian parameters of the General Relativity will be substantially improved. Current LLR observations give an accuracy of the Earth–Moon range of about 1–2 cm. This results in an accuracy for the PPN parameters β and γ of about $\sim 10^{-3}$ and for the Einstein Strong Equivalence Principle (SEP) parameter of $\eta \sim 10^{-4}$ (Turyshev, Williams, 2006).

An improvement of the range measurement of the Earth–Moon VLBI baseline to 1 mm will improve the parameter estimation by a factor of 10, i.e., $\sim 10^{-4}$ for β and γ, and $\sim 10^{-5}$ for the SEP parameter η. In addition, a new set of parameters will be obtained after reduction of the Moon VLBI data (e.g., accurate Moon–Earth distance, Moon rotation parameters, Moon orbit parameters). A bunch of new opportunities for further Moon exploration will result from them (Dehant et al., 2012).

3.4 On the Way to ICRF3

Assuming that the precision of 1 mm is achieved for geodetic positions of the ground-based stations for each of the 24-hour sessions, the corresponding formal accuracy of the radio source position will be $\sim$33 μas. A longer baseline will reveal more small details which are not available with a shorter baseline. Variations of the intrinsic structure on the time scale from several days to several years will have the following effects: 1) the long-term effects in the radio source positions (apparent as a fake proper motion), 2) extra random-like noise, 3) correlated noise, or irregular variations of the astrometric positions. The realistic astrometric accuracy of the fundamental catalogs exceeds the formal errors calculated immediately from the global solutions due the reasons mentioned above (Titov, 2010). The Earth–Moon baseline will help to reveal the intrinsic structure variations and improve the final accuracy of the ICRF3 catalog.

3.5 Moon Tides and Other Benefits

It is worth noting that the following factors, which spoil the lifes of the VLBI data technicians and analysts, will be missed with the Moon-based radio telescope: 1) Earth ionosphere delay (if observed far enough from the Earth and Solar disks); 2) Wet troposphere delay with gradients; 3) Ocean loading; 4) Ocean tides; 5) Atmosphere and other non-tidal loading; 6) Tectonic velocities, especially, in the deformation zones; 7) Gravitational deformation of the antenna shape and mount; 8) Gravitational sag; and 9) RFI.

4 Interior Structure and Physical Librations of the Two-Layer Moon

Studies of the rotation of celestial objects give an understanding of their complex internal structure, especially when other (geophysical) methods are inapplicable. Physical libration of the Moon is a deviation of its rotation from uniform rotation described by Cassini's laws, determined by the misalignment of the rotation axis with the axes of inertia, and by perturbations from the Earth, Sun, and planets.

The Chandler Wobble (CW) is a motion of the rotation axis of the Moon around its dynamical figure axis due to the bulges of the lunar body. For the completely solid Moon the CW has a long period of 74.6 years in a frame tied to the Moon and is prograde. This mode was detected from LLR observation as a $3'' \times 8''$ (69 × 28 m) elliptical component in the oscillation (Rambaux & Williams, 2011).

The Free Core Nutation (FCN) represents a differential rotation of the liquid core relative to the rotation of the mantle. This mode does exist only if the core is liquid. It has a quasi-diurnal period in a frame connected to the Moon and is retrograde (Gusev & Petrova, 2008).

4.1 Modeling of Free Periods of the Moon

The dependence on the core's radius is very weak for both periods (CW and FCN), when the radius is set to vary within the range of 300 to 600 km, the periods are changed by less than one percent. Both periods P_{CW} and P_{FCN} depend very weakly on the core density. Only for radii greater than 400 km, the difference in density is observed. The difference in the periods between the eutectic composition with the density 5.5 g/cm^3 and the pure iron core (7 g/cm^3) is very small. The FCN-period is very sensitive to the core ellipticity. This property can be used to impose an additional constraint on the core's parameters, if the expected observation data allows detecting the FCN-mode in the polar motion. The expected amplitudes of the FCN lies at about 16 mas.

Table 1 Free librations of the two-layer Moon (Rambaux & Williams, 2011; Gusev, 2008).

Free modes	Values
Chandler Wobble (arcs)	$8.183'' \times 3.306''$
amplitude (m)	69 × 28 m
period	27,257.27 days = 74.626 years
Precession	$0.032''$
amplitude	0.27 m
period	8,822.88 days = 24.16 years
Longitude	$1.296''$
amplitude	11 m at the equator
period	1,056.12 days = 2.9 years
Free Core Nutation	$0.016''$
amplitude	0.14 m
P_{FCN} = 27.312 days, LRF	67,936 days = 186 years, ICRF

5 Summary

1) Lunar Same Beam, Differential and Inverse VLBI technologies will enable us to determine the coordinates of the radio beacons on the lunar surface with an accuracy of 1 mm for various space projects on the Moon. 2) Small radio telescopes installed on the Moon surface and incorporated into the existing network will help to improve these traditional IVS products by a factor of ten or even more. This new lunar instrument will be able to detect some known effects with an unprecedented accuracy and new effects which are not available for other ground-based instruments or space missions. 3) The model of the two-layer Moon gives several normal rotational modes—Chandler Wobble and Free Core Nutation. They can play an important role in the determination of the core's parameters: radius, density, and geochemical composition. Amplitudes and frequencies of the physical libration depend on the geophysical parameters of the model: the size, thickness, and density of the lunar mantle and core were calculated.

Acknowledgements

This work was supported by grant RFBR 14-02-92113. Thank you for partial support by the development program of Kazan Federal University for attending the IVS General Meeting.

References

1. V. Dehant, J. Oberst, R. Nadalini, U. Schreiber, N. Rambaux. Planetary and Space Science, 68, pp. 94–104, 2012
2. A. Gusev, N. Petrova. "Rotation, Physical libration and Interior of the Moon", Kazan Univ. Press, pp. 1–212, 2008
3. F. Kikuchi, K. Matsumoto, H. Hanada, S. Tsuruta, K. Asari, Y. Kono, R. Yamada, T. Iwata, S. Sasaki, K. Takahashi, Y. Uchibori, T. Komai, T. Nakamura. "Recent status of SELENE-2/VLBI instrument". Trans. JSASS Aerospace Tech. Japan. 2014 (in press)

4. A. S. Kosov. 2nd Moscow Solar System Symposium (2M-S3), IKI, Moscow, 2011
5. N. Rambaux , J. G.Williams. Celest. Mech. Dyn. Ast., 109, pp. 85–100, 2010
6. B. Petrachenko. Proc of the 6th IVS General Meeting, pp. 3–8, 2010
7. S. Sasaki, H. Hanada, H. Araki, H. Noda, F. Kikuchi, T. Iwata, K. Matsumoto, N. Kawano, S. Tsuruta, S. Tazawa, Q. Liu, K. Asari, T. Ishikawa, K. Funazaki, H. Kunimori, and SELENE-II group. “In Situ Measurements of Lunar Rotation for the Study of the Interior of the Moon”. Transaction of Japan Society for Aeronautical and Space Sciences, Aerospace Technology Japan, 8, pp.3_7–3_10, 2012
8. H. Schuh, D. Behrend Journal of Geodynamics, 61, pp. 68–80, 2012
9. O. Titov. MNRAS Letter, 407, L46, 2010
10. O. Titov, A. Gusev. 4nd Moscow Solar System Symposium (4M-S3), IKI, Moscow, 2013
11. I. Yu. Vlasov, V. E. Zharov, M. V. Sazhin. Astron. Rep., 12, pp. 984–987, 2012
12. J. Williams, S. Turyshev, D. H. Boggs, J. T. Ratcliff Advances in Space Research 37, pp. 67–71, 2006

On the Definition of Aberration

Minghui Xu[1,2], Guangli Wang[1]

Abstract There was a groundbreaking step in the history of astronomy in 1728 when the effect of aberration was discovered by James Bradley (1693–1762). Recently, the solar acceleration, due to the variations in the aberrational effect of extragalactic sources caused by it, has been determined from VLBI observations with an uncertainty of about 0.5 mm$\cdot$s$^{-1}\cdot$yr^{-1} level. As a basic concept in astrometry with a nearly 300-year history, the definition of aberration, however, is still equivocal and discordant in the literature. It has been under continuing debate whether it depends on the relative motion between the observer and the observed source or only on the motion of the observer with respect to the frame of reference. In this paper, we will review the debate and the inconsistency in the definition of the aberration since the last century, and then discuss its definition in detail, which involves the discussions on the planetary aberration, the stellar aberration, the proper motion of an object during the travel time of light from the object to the observer, and the way of selecting the reference frame to express and distinguish the motions of the source and the observer. The aberration is essentially caused by the transformation between coordinate systems, and consequently quantified by the velocity of the observer with respect to the selected reference frame, independent of the motion of the source. Obviously, this nature is totally different from that of the definition given by the IAU WG NFA (Capitaine, 2007) in 2006, which is stated as, "the apparent angular displacement of the observed position of a celestial object from its geometric position, caused by the finite velocity of light in combination with the motions of the observer and of the observed object."

1. Shanghai Astronomical Observatory, Chinese Academy of Science, Shanghai, China
2. Helmholtz Center Potsdam, GFZ German Research Center for Geosciences, Potsdam, Germany

Keywords Aberration, stellar aberration, planetary aberration, astrometry

1 Introduction

In 1725, English astronomer James Bradley conceived of the diameter of the earth orbit around the sun as a base line to detect the apparent displacement of Gamma Draconis during one year, namely the effect of parallax. But what he observed at that moment is the effect of aberration rather than that of parallax, because the parallax effect of Gamma Draconis is three magnitudes smaller than that of the aberration effect. The stellar aberration was discovered by him with the observations of more 200 stars (Gualandi and Bnoli, 2009).

The effect of aberration, based on the apparent variations in positions of the objects detected from observations, can be simply modeled as:

$$\delta\mathbf{k} = \frac{1}{c}\mathbf{k}\times(\mathbf{k}\times\mathbf{V}), \tag{1}$$

where c is the velocity of light in vacuum and $\mathbf{k}$ is the geometric direction to the object. The immediate question is, from both the theoretical and practical point of view, what the velocity $\mathbf{V}$ in Equation 1 is. Concerned with this question, there have been a lot of discussions and debates since the beginning of the last century. In the specialized note taken down by Turner (1909), that very question was put forward directly as the following: "Does the correction for aberration in the position of an observed heavenly body P depend on the velocity of the observer relative to P, or upon his absolute velocity in space?" Even though to speak of the absolute velocity of a body may be somewhat improper and can be misleading, it nevertheless explicitly proposes the question if the motion of the observed object is involved in the effect of aberration. After that the definition of aberration remains equivocal.

In light of the inconsistency associated with the aberration, this paper is dedicated to clarify the definition of aberration, to discuss various kinds of its notion involved, and eventually to get a consistent and basic definition for both theoretical consideration and practical applications. To abstract the inconsistency here, there are three reasons to discuss the definition of aberration. First, as one of the basic concepts with great importance in astronomy, the definition has undergone for a long time a debate, which lasts until present. Secondly, the inconsistency of two kinds of notions leads to the ambiguity and practical impacts on the calculation of this effect; and some recent studies of aberration even obtain results that cannot withstand a careful inspection. Thirdly, as will be discussed later in this paper, the nominal explanation of aberration given officially by the IAU WG can be misleading, which should be clarified and revised.

Regarding the basic concept of aberration, we think that the effect of aberration depends on the motion of the observer with respect to a selected reference frame, but not at all on the motion of the object; it describes the apparent displacement of position of the observed object caused by the variation in the motion of the observer. Moreover, the planetary aberration is pervasively called aberration as well, but it is more than that; the definition of planetary aberration, which depends on the relative motion of the observer and the object, contains two effects: the stellar aberration and the proper motion of the object during the travel time of light. However, the planetary aberration, both its definition and application, should be abandoned in order to avoid the potential misunderstanding. One crucial reason is that it is only an approximation of modeling these two effects based on some assumptions, which are not satisfied in most circumstances.

In Section 2 the exact expression for the aberration effect is derived in the context of Special Relativity, which is not an original work but is very helpful in explaining the pertinent notions of the next sections. In Section 3 we present the derivation of the model of the planetary aberration, and then we discuss the differences between planetary aberration and stellar aberration. Section 4 summarizes the arguments.

2 The Expression of the Aberration Effect

In the context of Special Relativity the derivation of the model of the aberration effect can be found in some excellent books, such as Green (1985). In order to have a clear understanding of its essence, a simple description of this procedure is given here.

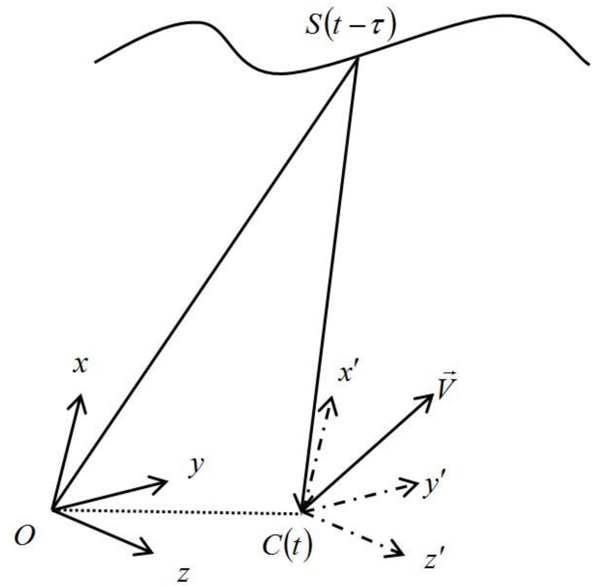

Fig. 1 Geometry of the observation.

As shown in Figure 1, imagine that an observer receives the photon at the time t_0 emitted from an object at an earlier time $(t_0 - \tau)$, τ being the travel time of the photon from the object to the observer. Suppose that two inertial reference frames, $O - xyz$ and $C - x'y'z'$, in relative motion with the velocity $\mathbf{V}$, exactly coincide at the observing time t_0. Let $C - x'y'z'$ be fixed to the observer and move with him. Therefore, the Lorentz transformation between these two frames, expressing C's coordinates in terms of O's, is given by:

$$
\begin{aligned}
x' &= \left[1+\frac{\gamma^2 V_x}{(\gamma+1)c^2}\right]x+\frac{\gamma^2 V_x V_y}{(\gamma+1)c^2}y+\frac{\gamma^2 V_x V_z}{(\gamma+1)c^2}z \\
&\quad -\gamma V_x(t-t_0), \\
y' &= \frac{\gamma^2 V_y V_x}{(\gamma+1)c^2}x+\left[1+\frac{\gamma^2 V_y}{(\gamma+1)c^2}\right]y+\frac{\gamma^2 V_y V_z}{(\gamma+1)c^2}z \\
&\quad -\gamma V_y(t-t_0), \\
z' &= \frac{\gamma^2 V_z V_x}{(\gamma+1)c^2}x+\frac{\gamma^2 V_z V_y}{(\gamma+1)c^2}y+\left[1+\frac{\gamma^2 V_z}{(\gamma+1)c^2}\right]z \\
&\quad -\gamma V_z(t-t_0), \qquad (2)\\
t' &= -\frac{\gamma V_x}{c^2}x-\frac{\gamma V_y}{c^2}y-\frac{\gamma V_z}{c^2}z-\gamma(t-t_0), \\
\gamma &= \sqrt{(1-V^2/c^2)}.
\end{aligned}
$$

Let the velocity of light in $C-x'y'z'$ be $\mathbf{V}(V_x,V_y,V_z)$. Its norm in general is a constant c independent of the observer. The travel path of the observed photon as measured in the frame $C-x'y'z'$ is expressed by the following form:

$$
\begin{aligned}
x &= v_x(t-t_0), \\
y &= v_y(t-t_0), \\
z &= v_z(t-t_0).
\end{aligned} \qquad (3)
$$

When the direction of the light path is the normalized velocity vector itself, then we have the apparent direction of the object in the rest frame of the observer, $C(t)S(t-\tau)$ denoted by a unit vector $\mathbf{k}'$:

$$\mathbf{k} = (-\frac{dx}{cdt},-\frac{dy}{cdt},-\frac{dz}{cdt}). \qquad (4)$$

Then, it is a straightforward matter to consider this process in the frame $O-xyz$. In this frame, denoting the velocity of light by $\mathbf{v}(v_x,v_y,v_z)$, its path is given by:

$$
\begin{aligned}
x' &= v'_x t', \\
y' &= v'_y t', \\
z' &= v'_z t'.
\end{aligned} \qquad (5)
$$

Consequently, the direction of the object as measured in the frame $O-xyz$, denoted by $\mathbf{k}$, is analogically expressed as:

$$\mathbf{k}' = (-\frac{dx'}{cdt'},-\frac{dy'}{cdt'},-\frac{dz'}{cdt'}). \qquad (6)$$

By using Lorentz transformation to relate Equations 4 and 6, we have the expression of $\mathbf{k}'$ in terms of $\mathbf{k}$,

$$\mathbf{k}' = [\frac{1}{\gamma}\mathbf{k}+\frac{\mathbf{V}}{c}+\frac{\gamma(\mathbf{k}\cdot\mathbf{V})\mathbf{V}}{(\gamma+1)}]/(1+\frac{\mathbf{k}\cdot\mathbf{V}}{c}). \qquad (7)$$

which is, in the context of Special Relativity, the complete formula for the aberration effect. It becomes more apparent when expanding it using the binomial theorem,

$$
\begin{aligned}
d\mathbf{k} = \mathbf{k}'-\mathbf{k} &= \frac{1}{c}\mathbf{k}\times(\mathbf{V}\times\mathbf{k}) + \\
&+\frac{1}{2c^2}\left[2(\mathbf{k}\cdot\mathbf{V})^2\mathbf{k}-(\mathbf{k}\cdot\mathbf{V})\mathbf{V}-\mathbf{V}^2\mathbf{k}\right] \qquad (8)\\
&+O\left(\mathbf{V}^3/c^3\right).
\end{aligned}
$$

The first term on the right-hand side of this equation is the classical model of the aberration effect, Equation 1, which merely contains the first order of the actual effect.

This process demonstrates how the aberration effect is introduced when one makes the Lorentz transformation. That is why, in the group delay model of VLBI observations, there is no need to consider the correction of the aberration effect for the source position in a direct way as the atmospheric effect does; it is implicitly hidden in that model as a result of the coordinate transformation (Petit & Luzum 2010). The effect of aberration indeed describes the apparent displacement in the positions of an object obtained by different observers in relative motion. So, when analyzing the measurements of direction, we need to portrait the motions of observers in a given frame and correspondingly make the correction for aberration according to Equations 7 or 8.

3 Planetary Aberration

The term planetary aberration is conventionally used to describe the displacement between the geometric direction and the apparent direction of the object at the time of observation t; while the term stellar aberration describes the displacement between the geometric direction of the object at the time of emission $t-\tau$ and its apparent direction at the time of reception t. Therefore, the planetary aberration actually includes the stellar aberration and the light-time correction, arising from the object's movement during the time interval τ.

Suppose that an observation is made at the instant of time t. Figure 2 shows the geometry of the object and the observer for this observation. Let the points C and S represent the observer and the object, respectively.

Let R be the displacement vector of the object due to its movement during τ, and U be its velocity relative to the barycenter of the solar system. Denote the vectors $C(t)S(t)$ and $C(t)S(t-\tau)$ by $\rho\mathbf{k}$ and $\rho'\mathbf{k}'$, where $\mathbf{k}$ and $\mathbf{k}'$ are unit vectors and then represent the geometric direction of the object at the instant $t-\tau$ and t, respectively. Clearly the geometry shows that

$$\rho\mathbf{k} - \rho'\mathbf{k}' = \mathbf{R}, \tag{9}$$

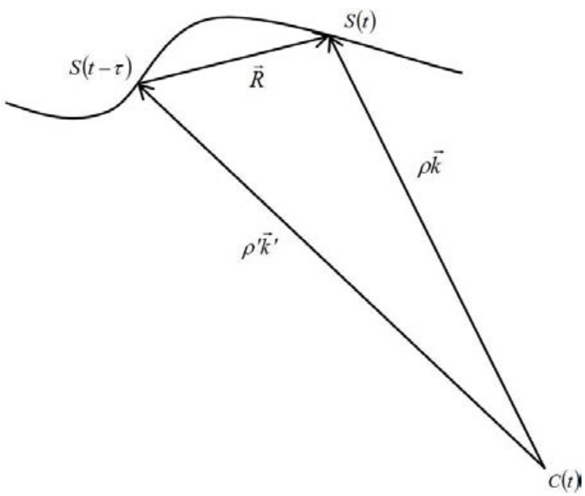

Fig. 2 Displacement of the source due to its motion during the light transmitting time.

Actually, this is the exact formula for the light-time correction. But, for its implicit and useful formula, two assumptions are required. If $R \ll \rho$, which satisfies that $\rho' \approx \rho$ and $\mathbf{k}' \cdot \mathbf{k} \approx 1$, after a little reduction, this equation can be written as,

$$\mathbf{k}' - \mathbf{k} = -\frac{1}{\rho}\mathbf{k} \times (\mathbf{R} \times \mathbf{k}). \tag{10}$$

The time interval τ by definition is $\tau = \frac{\rho}{c}$, and then the displacement vector of the object during this time can be found through integration,

$$\mathbf{R} = \int_{t-\tau}^{t} \mathbf{u}dt. \tag{11}$$

However, if we make the second assumption that within this interval τ the object is moving with a uniform velocity, it is more convenient to simply write Equation 11 as

$$\mathbf{R} = \mathbf{u}\tau = \frac{\mathbf{u}}{c}\rho. \tag{12}$$

The approximate expression for the light-time correction, by substituting Equation 12 into 10, can be found to be

$$\mathbf{k}' - \mathbf{k} = -\frac{1}{c}\mathbf{k} \times (\mathbf{u} \times \mathbf{k}). \tag{13}$$

This expression for the light-time correction closely parallels that for the aberration effect, as Equation 7. But as we can see from the derivation of it, provided that the motion of the object within the traveling time of the light can be regarded as constant, the light-time correction only depends on the motion of the object, which has the same form as that of stellar aberration to the first order. In addition, the light-time correction cannot have the terms of higher orders in Equation 8, and thus, the relative velocity of the observer and the object cannot be applied for the second order of Equation 8 or the exact expression (7). Their similarity ends to the first order and is mathematically accidental.

The correction for planetary aberration, according to its definition and Equations 1 and 13, then is given by

$$d\mathbf{k} = \frac{1}{c}\mathbf{k} \times [(\mathbf{V} - \mathbf{u}) \times \mathbf{k}]. \tag{14}$$

As one might expect, the displacement of planetary aberration depends on the relative motion of the observer and the object.

From both theoretical and practical considerations, the definition of planetary aberration, that aberration depends on the relative motion of the observer and the object, should be abandoned, because it can never be used for the stars and even for planets it is insufficient.

4 Discussion and Conclusions

In astrometry, the directly observed positions of a celestial object are affected by some systematical variations, such as parallax, aberration, atmospheric refraction, gravitational deflection, and so on. The basic principle for the data analysis, in order to make the measurements obtained by different observers comparable, is to take into account all kinds of effects caused by the personalities of the observers, referring to such a common fictitious observer as the barycenter of the solar system. After that, the proper motion caused by the motion of the object often remains, if detectable, as a signal embedded in the resulting time series of positions that can be analyzed and studied later. The aberration effect depends on the variation of the motion of the observer and is independent of the motion of the object.

Acknowledgements

Minghui Xu would like to thank the CAS-DAAD joint scholarship for supporting the exchange study at GFZ Potsdam.

References

1. Gualandi A, Bnoli F. The Search for Stellar Parallaxes and the Discovery of the Aberration of Light: The Observational Proofs of the Earth's Revolution, Eustachio Manfredi, and the "Bologna Case". Journal for the History of Astronomy, 2009, 40, 155–172
2. Hines C O. Planetary Aberration. Nature, 1949, 163, 249–249
3. Capitaine N, Andrei A H, Calabretta M, et al. Division I Working Group on 'Nomenclature for Fundamental Astronomy' (NFA). Transactions of the International Astronomical Union Series A, 2007, 26, 59–62
4. Capitaine N, Andrei A H, Calabretta M R, et al. Proposed terminology in fundamental astronomy based on IAU 2000 resolutions. Highlights of Astronomy, 2007, 14, 474–475
5. Robin M. Green, Spherical astronomy. Cambridge and New York: Cambridge University Press. 1985, 48–195
6. IAU 2006 NFA GLOSSARY, 2006, URL http://syrte.obspm.fr/iauWGnfa/

Earth Rotation Determination by Combining Ring Laser Gyroscopes and VLBI

E. Parselia[1], T. Nilsson[1], R. Heinkelmann[1], A. Gebauer[2], T. Klügel[3], U. Schreiber[2], H. Schuh[1]

Abstract Very Long Baseline Interferometry (VLBI) and ring laser gyroscopes are two techniques that sense the rotation of the Earth using different approaches; the former uses a geometric approach while the latter is based on a dynamic one. Combination of the two techniques could improve the determination of high frequency variations of Earth rotation. An attempt to combine recent data sets for the period from August 2011 until October 2013 of the "G" ring laser in Wettzell and VLBI observations was performed. In the cases where the VLBI data had a lower EOP sensitivity, the inclusion of the ring laser data could improve significantly the y-pole and the DUT1 estimates.

Keywords Earth rotation, VLBI, ring laser

1 Introduction

The rotation speed and the direction of the rotation axis of the Earth experience small variations in time. The variations at different scales are caused by various excitations of Earth rotation such as gravitational torques and processes in the atmosphere and the oceans. The rotation of the Earth is not uniform. It is described by the Earth Orientation Parameters (EOP). Presently, the EOP are mainly determined using space geodetic techniques such as GNSS and VLBI. GNSS is the most precise technique for observing polar motion, while VLBI is unique for measuring the coordinates of the Celestial Pole and DUT1. However, a novel technique called ring laser gyroscopes can be used to observe the instantaneous Earth rotation vector, which is different from (but related to) the Celestial Intermediate Pole (CIP) measured by geodetic techniques. Ring lasers are sensitive to high-frequency variations in Earth rotation and can provide an independent method for monitoring Earth rotation without the requirement of an external reference frame. One main drawback of this technique is that the ring laser measurements contain unknown drifts and offsets. Thus, combined with a space technique, ring lasers could be used for the estimation of precise high frequency EOP. A first successful attempt at combining VLBI observations and data from the "G" ring laser at Wettzell was done by Nilsson et al. (2012a). Because the accuracy of VLBI is about one order of magnitude better than the ring laser, the ring laser data had only a small impact in the combination. However, the quality of the ring laser data has been improving in terms of precision and stability within the last few years. In this work, an investigation of the potential gain from the combination of the two different techniques is made by using recent data sets for the period from 2011 until 2013.

2 Ring Laser Gyroscopes

Ring laser gyroscopes are instruments that can sense rotation about their sensitive axis. These sensing elements are commonly used in navigation systems for aircraft and marine applications. However, over the last two decades, a series of large ring lasers has been built in order to increase the scale factor and thus the precision of the measurements. These large ring

1. Helmholtz Centre Potsdam, GFZ German Research Centre for Geosciences
2. Forschungseinrichtung Satellitengeodäsie, TU München
3. Bundesamt für Kartographie und Geodäsie

lasers improved the sensitivity compared to commercial gyroscopes by more than six orders of magnitude (Schreiber et al., 2013). Thus, ring laser gyroscopes can be used for applications in geodesy by sensing high frequency variations in the rotation of the Earth.

In a ring laser gyroscope, two beams are transmitted in opposite directions. At the point at which the two laser beams interfere, the “Sagnac” frequency can be measured. This beat frequency is proportional to the rotation frequency of the ring, i.e., proportional to the projection of the rotation vector of the Earth onto the normal direction of the ring if the ring is fixed to the Earth’s surface. The Sagnac frequency observed by a ring laser is given by:

$$\Delta f_{SAG} = S \cdot \vec{n}\vec{\Omega} \tag{1}$$

where S is the scale factor, $\vec{n}$ the normal unit vector and $\vec{\Omega}$ the rotation vector of the Earth which can be written as $\vec{\Omega} = \Omega_0[m_x, m_y, 1+m_z]^T$. Ω_0 is the nominal value of the Earth rotation frequency and the terms m_x, m_y, m_z are related to polar motion (x_p and y_p) and DUT1 determined by space geodetic techniques such as VLBI (Brzezinski and Capitaine, 1993):

$$m = p - \frac{i}{\Omega}\frac{\partial p}{\partial t} \tag{2}$$

$$m_z = \frac{\partial DUT1}{\partial t} \tag{3}$$

where $m = m_x + im_y$ and $p = x_p + iy_p$.

The Sagnac frequency Δf is not stable but instead is drifting. Therefore the relative Sagnac frequency ΔS is used. For a horizontally mounted ring laser, the relative Sagnac frequency can be approximated by the following formula:

$$\Delta S = \cot(\phi)[m_x \cos(\lambda) + \sin(\lambda)] + m_z + \Delta S_{tilt} + \Delta S_{instr} \tag{4}$$

where ϕ and λ are the latitude and longitude and ΔS_{tilt} and ΔS_{instr} are the errors caused by the tilt and the instrument, respectively. Equations (2), (3), and (4) enable the ring laser observations to be expressed as a function of geodetic EOP.

3 VLBI and Ring Lasers

VLBI is sensitive to the complete rotation matrix between the network of terrestrial VLBI antennas being part of the ITRF (Altamimi et al., 2011) and the radio sources realizing the ICRF (Fey et al., 2009). The transformation between the two different Reference Frames is realized with the use of the Celestial Intermediate Pole (CIP). The CIP was introduced instead of the Instantaneous Rotation Pole (IRP) for simplicity. VLBI can determine the full set of the EOP:

- the coordinates of the CIP w.r.t. ICRF which rigorously describe the effects of precession, nutation, and frame bias,
- the coordinates of the CIP in the TRF (polar motion, x_p and y_p), and
- the rotation angle of the Earth (DUT1).

Ring laser gyroscopes can directly measure the position of the instantaneous rotation axis of the Earth including the Oppolzer terms. Figure 1 shows the measured relative Sagnac frequencies from the “G” ring laser mounted at the Geodetic Observatory Wettzell, corrected for the latitudinal tilt variations and the expected values due to EOP variations for the period from 5 September 2011 until 18 January 2012. The computed values were obtained from Equation 4, using the IAU 2000/2006A precession nutation model, an EOP series estimated from the Vienna VLBI software VieVS (Böhm et al., 2012) and the IERS high frequency EOP model (Petit and Luzum, 2010). At the beginning, the measured and the modelled relative Sagnac frequencies show small variations, while starting at about the middle of the period there is a significant drift. This drift is apparently caused by instrumental effects.

4 Data Analysis

The combination of the ring laser and the VLBI data was performed at the normal equation level (Nilsson et al., 2012b). Using the software VieVS, approximately 170 IVS-R1, IVS-R4, and CONT11 VLBI sessions were analyzed for the period from August 2011 until October 2013. For each session the normal equation matrices N_{VLBI} and the vectors of the right hand side b_{VLBI} were set up by the software. Polar motion and

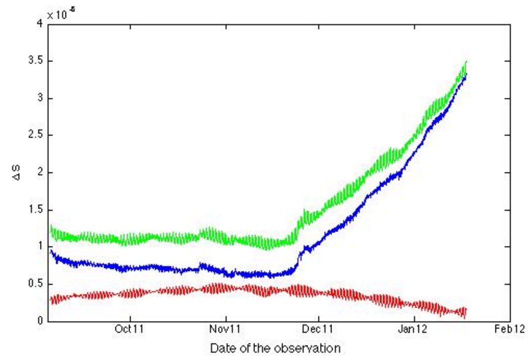

Fig. 1 Measured relative Sagnac frequencies ΔS by Wettzell ring laser (green (top) line). Expected values of ΔS due to EOP variation from VLBI (red (bottom) line). Difference between the modeled and the measured ΔS (blue (middle) line).

DUT1 were estimated with an hourly resolution, while the celestial coordinates of the CIP were fixed to the IAU 2006/2000A model plus the IERS 08 CO4 correction. The celestial coordinates of the CIP could not be estimated with an hourly resolution, because high correlation between the polar motion and celestial coordinates of the CIP would occur. Polar motion and DUT1 were computed by solving the normal equation system through the combination of the normal equation matrices of VLBI and ring laser:

$$N = N_{VLBI} + N_{RLG} \tag{5}$$

$$\overrightarrow{b} = \overrightarrow{b}_{VLBI} + \overrightarrow{b}_{RLG} \tag{6}$$

where N_{VLBI} and $\overrightarrow{b}_{VLBI}$ were obtained as described in Nilsson et al. (2012b).

5 Results

The estimates of polar motion and DUT1 were computed using two approaches: (i) from VLBI data only and (ii) combining VLBI and ring laser data. In order to compare the results from the two different approaches, the Root Mean Square (RMS) difference relative to the a priori IERS 08 C04 and the IERS high frequency EOP model were computed. Tables 1-3 show the mean RMS of the estimated polar motion and DUT1 computed for the session types IVS-R1, IVS-R4, and CONT11.

Table 1 RMS difference for X-pole estimated from VLBI only and from VLBI and ring laser.

Type of Session	X-pole VLBI only [mas]	X-pole VLBI+RL [mas]	Difference ["%"]
R1	0.403	0.407	+1
R4	0.447	0.434	-2.8
CONT11	0.2735	0.2731	-0.16

Table 2 RMS difference for Y-pole estimated from VLBI only and from VLBI and ring laser.

Type of Session	Y-pole VLBI only [mas]	Y-pole VLBI+RL [mas]	Difference ["%"]
R1	0.375	0.371	-1
R4	0.623	0.583	-7.5
CONT11	0.258	0.253	-1.8

Table 3 RMS difference for DUT1 estimated from VLBI only and from VLBI and ring laser.

Type of Session	DUT1 VLBI only [μ s]	DUT1 VLBI+RL [μ s]	Difference ["%"]
R1	21.5	20.9	-2.6
R4	25.8	24.1	-6.6
CONT11	17.3	16.8	-2.8

Since the accuracy of VLBI is approximately one order of magnitude better compared to the ring laser, the RMS differences for the two solutions show rather small but noticeable improvements up to 7.5%, as presented in Tables 1-3. Larger impacts can be detected on the y-pole and DUT1. Since the location of the ring laser is at a small longitude ($\sim$13°) and a middle latitude ($\sim$49°), its sensitivity is greater to the x and z components of the IRP. The x component of the IRP is related to the x-pole and time derivative of the y-pole of the CIP (Mendes et al., 2009b). Therefore, for the ring laser located at Wetzell, at high frequencies it is expected that the y-pole and DUT1 would be more significantly affected than the x-pole.

Figure 2 shows the estimated polar motion and DUT1 for session IVS-T2089 (23-24 April 2013). The original purpose of the IVS-T2 type of session was to determine high quality station coordinates without optimizing the EOP. The RMS values for polar motion/DUT1 estimated using only VLBI are 0.71 mas for x-pole, 0.62 mas for y-pole, and 64 μs for DUT1. The corresponding values when combining VLBI and ring laser are 0.68 mas for x-pole, 0.52 mas for y-pole, and 61 μs for DUT1. Polar motion and DUT1 estimates therefore improve when combined with the ring

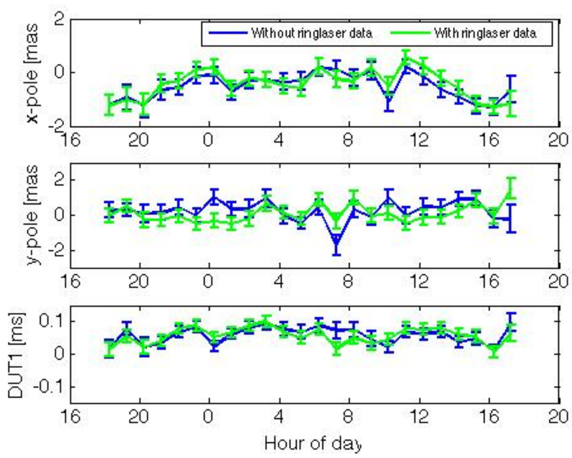

Fig. 2 Analysis of session IVS-T2089 (23-24 April 2013). The estimated polar motion and DUT1 are shown from only VLBI (blue line) and from the combination of VLBI and ring laser (green line).

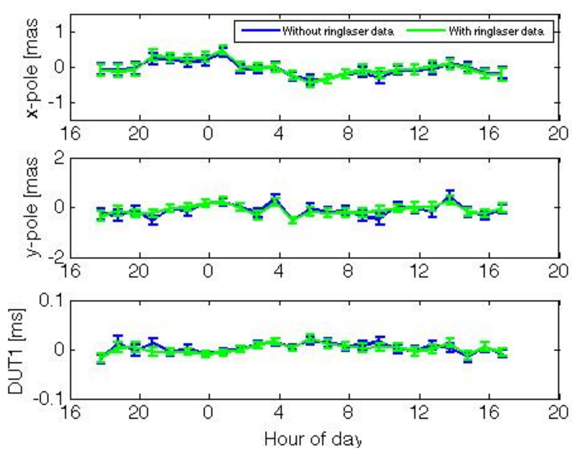

Fig. 3 Analysis of session IVS-R4574 (28-29 January 2013). The estimated polar motion and DUT1 are shown from only VLBI (blue line) and from the combination of VLBI and ring laser (green line).

laser data. The original purpose of the IVS-R4 type of session included also the accurate determination of the EOP. For session IVS-R4574 (28-29 January 2013), the VLBI data get a larger weight during the adjustment, and thus the impact of ring laser data in the combination is very small. In Figure 3, hardly any differences between the two solutions are noticeable.

6 Conclusions

The two different data types, ring laser and VLBI data, could be successfully combined for the period of August 2011 until October 2013. The inclusion of the ring laser in the combined solution with VLBI for the estimation of polar motion and DUT1 usually had a noticeable but small impact, since the accuracy of VLBI is higher. Only for the VLBI sessions where the estimates of polar motion and DUT1 had lower accuracy, the ring laser could significantly improve the results. If more ring lasers would be available, the improvement of polar motion and DUT1 estimates by ring lasers would be more significant as shown in simulations of Nilsson et al. (2012a). Furthermore, the quality of the ring laser data has improved in terms of precision and stability within the last years. If the accuracy of ring laser data continues to improve, it would be of great interest to operationally combine ring laser data and VLBI data.

References

1. Altamimi Z., Collilieux X., Métivier L., 2011. ITRF2008: an improved solution of the international terrestrial reference frame, Journal of Geodesy, Vol. 85, 457.
2. Böhm, J., Böhm, S., Nilsson, T., Pany, A., Plank, L., Spicakova, H., Teke, K., Schuh, H., 2012. The new Vienna VLBI software. In: Kenyon, S., Pacino, M.C., Marti, U. (Eds.), IAG Scientific Assembly 2009, IAG Symposium, vol. 136. Springer, Buenos Aires, Argentina, pp. 1007–1012.
3. Böhm, S., Brzezinski, A., Schuh, H. Complex demodulation in VLBI estimation of high frequency Earth rotation components. J. Geodyn., doi:10.1016/j.jog.2011.10.002.
4. Brzezinski, A., Bizouard, C., Petrov, S. D., 2002. Influence of the atmosphere on Earth rotation: what new can be learned from the recent atmospheric angular momentum estimates? Surv. Geophys. 23, 33–69.
5. Brzezinski, A., Capitaine, N., 1993. The use of the precise observations of the celestial ephemeris pole in the analysis of geophysical excitation of earth rotation. J. Geophys. Res. 98, 6667–6675, doi:10.1029/92JB02874.
6. Fey A., Gordon D., Jacobs C. S., 2009. The Second Realization of the International Celestial Reference Frame by Very Long Baseline Interferometry. IERS Technical Note. 35, Verlag des Bundesamts für Kartographie und Geodäsie, ISBN 3-89888-918-6, Frankfurt am Main.
7. Mendes Cerveira, P. J., Böhm, J., Schuh, H., Klügel, T., Velikoseltsev, A., Schreiber, K. U., Brzezinski, A., 2009a. Earth rotation observed by very long baseline interferometry and ring laser. Pure Appl. Geophys. 166, 1499–1517, doi:10.1007/s00024-004-0487-z.

8. Mendes Cerveira, P. J., Spicakova, H., Schuh, H., Klügel, T., Schreiber, K. U., Velikoseltsev, A., 2009b. Earth rotation parameters from very long baseline interferometry and ringlaser observables. In: Satake, K. (Ed.), Advances in Geosciences, vol. 13. Solid Earth. World Scientific Publishing Company, pp. 155–165.
9. Nilsson, T., Böhm, J., Schuh, H., 2010. Sub-diurnal Earth rotation variations observed by VLBI. Artif. Satellites 45, 49–55, doi:10.2478/v10018-010-0005-8.
10. Nilsson, T., Böhm, J., Schuh, H., 2012a. Determination of Earth rotation by combining VLBI and ring laser observations. In: Schuh, H., Böhm, S., Nilsson, T., Capitaine, N. (Eds.), Proc. Journées 2011, Vienna, Austria.
11. Nilsson, T., Böhm, J., Schuh, H., Schreiber, U., Gebauer, A., Klügel, T., 2012b. Combining VLBI and ring laser observations for determination of high frequency Earth rotation variation. J. Geodyn. doi: 10.1016/j.jog.2012.02.002.
12. Petit, G., Luzum, B. (Eds.), 2010. IERS Conventions. IERS Technical Note 36, Verlag des Bundesamts für Kartographie und Geodäsie, Frankfurt am Main, Germany.
13. Schreiber, K. U., Klügel, T., Velikoseltsev, A., Schlüter, W., Stedman, G.E., Wells, J. P. R., 2009. The large ring laser G for continuous earth rotation monitoring. Pure Appl. Geophys. 166, 1485–1498, doi:10.1007/s00024-004-0490-4.
14. Schreiber, K. U., Velikoseltsev, A., Rothacher, M., Klügel, T., Stedman, G. E., Wiltshire, D. L., 2004. Direct measurement of diurnal polar motion by ring laser gyroscopes. J. Geophys. Res., 109, doi:10.1029/2003JB002803.
15. Schreiber, K. U., Wells, J. P. R., 2013. Large Ring Lasers for Rotation Sensing. Review of Scientific Instruments 84: 041101.

About the Meeting

March 2-7, 2014

8th IVS GENERAL MEETING

Shanghai, China

Registered Participants

Name	Institution	Country	E-mail
Oleg Titov	Geoscience Australia	Australia	oleg.titov@ga.gov.au
Jim Lovell	University of Tasmania	Australia	jim.lovell@utas.edu.au
Stanislav Shabala	University of Tasmania	Australia	stanislav.shabala@utas.edu.au
Johannes Böhm	TU Vienna	Austria	johannes.boehm@tuwien.ac.at
Hana Krásná	TU Vienna	Austria	hana.krasna@tuwien.ac.at
Matthias Madzak	TU Vienna	Austria	matthias.madzak@tuwien.ac.at
Lucia Plank	TU Vienna	Austria	lucia.plank@tuwien.ac.at
Bill Petrachenko	NRCan Penticton	Canada	bill.petrachenko@nrc-cnrc.gc.ca
Hayo Hase	BKG Concepción	Chile	hayo.hase@bkg.bund.de
Hongzheng Cui	BACC Beijing	China	h.z.cui@hotmail.com
Songtao Han	BACC Beijing	China	justdoit_doing@126.com
Tian-Peng Ren	BACC Beijing	China	shemmer@126.com
Geshi Tang	BACC Beijing	China	afdl_bacc@163.com
Jinsong Ping	BAO Beijing	China	jsping@bao.ac.cn
Xin Lian	Equipment Academy	China	lianxin20032002@aliyun.com
Linwei Lv	Equipment Academy	China	137222635@qq.com
Hong Ma	Equipment Academy	China	978493189@qq.com
Shaojie Wei	Equipment Academy	China	sevenwsj@126.com
Jia-Cheng Liu	Nanjing University	China	jcliu@nju.edu.cn
Lin Fang	National Time Service Center	China	fanglin@ntsc.ac.cn
Jianjun Gong	National Time Service Center	China	gongjj@ntsc.ac.cn
Weichao Li	National Time Service Center	China	liwc@ntsc.ac.cn
Langming Ma	National Time Service Center	China	malm@ntsc.ac.cn
Xuhai Yang	National Time Service Center	China	yyang@ntsc.ac.cn
Ying Yang	National Time Service Center	China	yangying@ntsc.ac.cn
Zhong Chen	SHAO	China	zhchen@shao.ac.cn
Jiangying Gan	SHAO	China	jygan@shao.ac.cn
Shaoguang Guo	SHAO	China	sgguo@shao.ac.cn
Wu Jiang	SHAO	China	jiangwu@shao.ac.cn
Shuanggen Jin	SHAO	China	sgjin@shao.ac.cn
Jinling Li	SHAO	China	jll@shao.ac.cn
Qinghui Liu	SHAO	China	liuqh@shao.ac.cn
Maoli Ma	SHAO	China	mamaoli@shao.ac.cn
Fengchun Shu	SHAO	China	sfc@shao.ac.cn
Jing Sun	SHAO	China	sunjing@shao.ac.cn

Name	Institution	Country	E-mail
Guangli Wang	SHAO	China	wgl@shao.ac.cn
Maochun Wu	SHAO	China	mcwu@shao.ac.cn
Yajun Wu	SHAO	China	wuyajun@shao.ac.cn
Bo Xia	SHAO	China	bxia@shao.ac.cn
Minghui Xu	SHAO	China	mhxu@shao.ac.cn
Zhijun Xu	SHAO	China	xuthus@shao.ac.cn
Yun Yu	SHAO	China	yuyun@shao.ac.cn
Juan Zhang	SHAO	China	zhangjuan@shao.ac.cn
Xiuzhong Zhang	SHAO	China	xzhang@shao.ac.cn
Weimin Zheng	SHAO	China	zhwm@shao.ac.cn
Xin Zheng	SHAO	China	zhengxin@shao.ac.cn
Weiye Zhong	SHAO	China	wyzhong@shao.ac.cn
Renjie Zhu	SHAO	China	zhurj@shao.ac.cn
Xuechuan Li	Wuhan University	China	leexc0124@163.com
Xiang Liu	XAO Urumqi	China	liux@xao.ac.cn
Zhibin Zhang	XAO Urumqi	China	zhangzhibin@xao.ac.cn
Jia Wang	XSCC Xi'an	China	wj_ssl@126.com
Ke Xu	XSCC Xi'an	China	xk361@163.com
Dong Zhang	XSCC Xi'an	China	sandmanzd@163.com
Longfei Hao	YNAO Kunming	China	haolongfei@ynao.ac.cn
Romuald Bouffet	LAB Bordeaux	France	bouffet@obs.u-bordeaux1.fr
Patrick Charlot	LAB Bordeaux	France	charlot@obs.u-bordeaux1.fr
Sabine Bachmann	BKG Frankfurt	Germany	sabine.bachmann@bkg.bund.de
Volkmar Thorandt	BKG Leipzig	Germany	volkmar.thorandt@bkg.bund.de
Torben Schüler	BKG Wettzell	Germany	schueler@fs.wettzell.de
Jan Kodet	FESG Wettzell	Germany	kodet@fs.wettzell.de
Alexander Neidhardt	FESG Wettzell	Germany	neidhardt@fs.wettzell.de
Robert Heinkelmann	GFZ Potsdam	Germany	robert.heinkelmann@gfz-potsdam.de
Maria Karbon	GFZ Potsdam	Germany	maria.karbon@gfz-potsdam.de
Li Liu	GFZ Potsdam	Germany	liu.li@gfz-potsdam.de
Cuixian Lu	GFZ Potsdam	Germany	cuixian.lu@gfz-potsdam.de
Julian Andres Mora-Diaz	GFZ Potsdam	Germany	mora@gfz-potsdam.de
Tobias Nilsson	GFZ Potsdam	Germany	nilsson@gfz-potsdam.de
Virginia Raposo-Pulido	GFZ Potsdam	Germany	raposo@gfz-potsdam.de
Harald Schuh	GFZ Potsdam	Germany	schuh@gfz-potsdam.de
Benedikt Soja	GFZ Potsdam	Germany	bsoja@gfz-potsdam.de
Sebastian Halsig	IGG Bonn	Germany	halsig@igg.uni-bonn.de
Andreas Iddink	IGG Bonn	Germany	aiddink@uni-bonn.de
Axel Nothnagel	IGG Bonn	Germany	nothnagel@uni-bonn.de

Name	Institution	Country	E-mail
Alessandra Bertarini	MPIfR Bonn	Germany	abertari@mpifr-bonn.mpg.de
Richard Porcas	MPIfR Bonn	Germany	porcas@mpifr-bonn.mpg.de
Bo Zhang	MPIfR Bonn	Germany	bzhang@mpifr.de
Eberhard Sust	MT Mechatronics	Germany	eberhard.sust@mt-mechatronics.de
Thomas Zimmerer	MT Mechatronics	Germany	thomas.zimmerer@mt-mechatronics.de
Gino Tuccari	IRA/INAF Noto	Italy	g.tuccari@ira.inaf.it
Roberto Lanotte	e-GEOS Matera	Italy	roberto.lanotte@e-geos.it
Vincenza Tornatore	Politecnico di Milano	Italy	vincenza.tornatore@polimi.it
Yoshihiro Fukuzaki	GSI Tsukuba	Japan	fukuzaki@gsi.go.jp
Shinobu Kurihara	GSI Tsukuba	Japan	skuri@gsi.go.jp
Takahiro Wakasugi	GSI Tsukuba	Japan	t-wakasugi@gsi.go.jp
Mamoru Sekido	NICT Kashima	Japan	sekido@nict.go.jp
Yosuke Ishihara	TOYO Corporation	Japan	ishihara@toyo.co.jp
Harro Verkouter	JIVE	Netherlands	verkouter@jive.nl
Tim Natusch	AUT Auckland	New Zealand	tim.natusch@aut.ac.nz
Halfdan Pascal Kierulf	NMA Norway	Norway	halfdan.kierulf@kartverket.no
Ann-Silje Kirkvik	NMA Norway	Norway	ann-silje.kirkvik@kartverket.no
Line Langkaas	NMA Norway	Norway	line.langkaas@kartverket.no
Leif Morten Tangen	NMA Norway	Norway	leif.morten.tangen@kartverket.no
Luis R. dos Santos	Governo dos Açores	Portugal	luis.r.santos@azores.gov.pt
Ilya Bezrukov	IAA RAS	Russia	rbetra@gmail.com
Yuri Bondarenko	IAA RAS	Russia	bondarenko@ipa.nw.ru
Alexander Evstigneev	IAA RAS	Russia	aleksandr-evstigneev@yandex.ru
Anastasiia Girdiuk	IAA RAS	Russia	girdiuk@ipa.nw.ru
Gennadii Ilin	IAA RAS	Russia	igen@ipa.nw.ru
Alexander Ipatov	IAA RAS	Russia	ipatov@ipa.nw.ru
Irina Ipatova	IAA RAS	Russia	ir.ip@yandex.ru
Voytsekh Ken	IAA RAS	Russia	voitsekh@gmail.com
Sergei Kurdubov	IAA RAS	Russia	ksl@quasar.ipa.nw.ru
Dmitriy Marshalov	IAA RAS	Russia	marshalov.iaa@gmail.com
Alexey Melnikov	IAA RAS	Russia	myxtra@yandex.ru
Evgeny Nosov	IAA RAS	Russia	e84@mail.ru
Alexander Gusev	Kazan University	Russia	alexander.gusev@mail.ru
Sayan Basu	HartRAO	South Africa	sayan@hartrao.ac.za
Glenda Lorraine Coetzer	HartRAO	South Africa	glenda@hartrao.ac.za
Ludwig Combrinck	HartRAO	South Africa	ludwig@hartrao.ac.za
Denise Dale	HartRAO	South Africa	denise@hartrao.ac.za
Aletha de Witt	HartRAO	South Africa	alet@hartrao.ac.za
Marisa Nickola	HartRAO	South Africa	marisa@hartrao.ac.za

Name	Institution	Country	E-mail
Jungho Cho	KASI	South Korea	jojh@kasi.re.kr
Taehyun Jung	KASI	South Korea	thjung@kasi.re.kr
Younghee Kwak	KASI	South Korea	bgirl02@kasi.re.kr
Kiduk Ahn	NGII Sejong	South Korea	akd8319@korea.kr
Hongjong Oh	NGII Sejong	South Korea	stockoh11@korea.kr
Francisco Colomer	IGN Spain	Spain	f.colomer@oan.es
José A. López Fernández	IGN Spain	Spain	ja.lopez@oan.es
José Ferrandiz	University of Alicante	Spain	jm.ferrandiz@ua.es
Rüdiger Haas	Onsala Space Observatory	Sweden	rudiger.haas@chalmers.se
Niko Kareinen	Onsala Space Observatory	Sweden	niko.kareinen@chalmers.se
Tong Ning	Onsala Space Observatory	Sweden	tong.ning@chalmers.se
Benjamin Männel	ETH Zurich	Switzerland	maennelb@ethz.ch
Kamil Teke	Hacettepe University	Turkey	kteke@hacettepe.edu.tr
Doug Lamb	Exelis	U.S.A.	doug.lamb@exelisinc.com
Richard Gross	Jet Propulsion Laboratory	U.S.A.	richard.gross@jpl.nasa.gov
Christopher Jacobs	Jet Propulsion Laboratory	U.S.A.	christopher.s.jacobs@nasa.gov
Christopher Beaudoin	MIT Haystack Observatory	U.S.A.	cbeaudoin@haystack.mit.edu
Roger Cappallo	MIT Haystack Observatory	U.S.A.	rjc@haystack.mit.edu
Brian Corey	MIT Haystack Observatory	U.S.A.	bec@haystack.mit.edu
Arthur Niell	MIT Haystack Observatory	U.S.A.	aniell@haystack.mit.edu
Alan Whitney	MIT Haystack Observatory	U.S.A.	awhitney@haystack.mit.edu
Chopo Ma	NASA GSFC	U.S.A.	chopo.ma@nasa.gov
Dirk Behrend	NVI, Inc./NASA GSFC	U.S.A.	dirk.behrend@nasa.gov
Sergei Bolotin	NVI, Inc./NASA GSFC	U.S.A.	sergei.bolotin@nasa.gov
John Gipson	NVI, Inc./NASA GSFC	U.S.A.	john.m.gipson@nasa.gov
David Gordon	NVI, Inc./NASA GSFC	U.S.A.	david.gordon-1@nasa.gov
Daniel MacMillan	NVI, Inc./NASA GSFC	U.S.A.	daniel.s.macmillan@nasa.gov
Cynthia Thomas	NVI, Inc./NASA GSFC	U.S.A.	cynthia.c.thomas@nasa.gov
Ralph Gaume	U.S. Naval Observatory	U.S.A.	rgaume@usno.navy.mil

Author Index